NUREG/CR-6150
EGG-2720
Volume IV

SCDAP/RELAP5/MOD3.1 Code Manual Volume IV: MATPRO -- A Library of Materials Properties for Light-Water-Reactor Accident Analysis

Contributing Authors:

C. M. Allison
G. A. Berna
R. Chambers
E. W. Coryell
K. L. Davis
D. L. Hagrman
D. T. Hagrman
N. L. Hampton
J. K. Hohorst
R. E. Mason
M. L. McComas
K. A. McNeil
R. L. Miller
C. S. Olsen
G. A. Reymann
L. J. Siefken

Editor:
D. T. Hagrman

Manuscript Completed:
November 1993

Idaho National Engineering Laboratory
EG&G Idaho, Inc.
Idaho Falls, Idaho 83415

Prepared for the
Division of Systems Research
Office of Nuclear Regulatory Research
U. S. Nuclear Regulatory Commission
Washington, D. C. 20555
Under DOE Contract No. DE-AC07-761D01570
FIN No. W6095

ABSTRACT

The SCDAP/RELAP5 code has been developed for best estimate transient simulation of light-water-reactor coolant systems during a severe accident. The code models the coupled behavior of the reactor coolant system, the core, fission products released during a severe accident transient as well as large and small break loss of coolant accidents, operational transients such as anticipated transient without SCRAM, loss of offsite power, loss of feedwater, and loss of flow. A generic modeling approach is used that permits as much of a particular system to be modeled as necessary. Control system and secondary system components are included to permit modeling of plant controls, turbines, condensers, and secondary feedwater conditioning systems.

This volume, Volume IV, describes the material properties correlations and computer subroutines (MATPRO) used by SCDAP/RELAP5. Formulation of the materials properties are generally semi-empirical in nature. The materials property subroutines contained in this document are for uranium, uranium dioxide, mixed uranium-plutonium dioxide fuel, zircaloy cladding, zirconium dioxide, stainless steel, stainless steel oxide, silver-indium-cadmium alloy, cadmium, boron carbide, Inconel 718, zirconium-uranium-oxygen melts, fill gas mixtures, carbon steel, and tungsten. This document also contains descriptions of the reaction and solution rate models needed to analyze a reactor accident.

FIN NO. W6095-SCDAP/RELAP5 CODE IMPROVEMENT AND ASSESSMENT

EXECUTIVE SUMMARY

The specific features of SCDAP/RELAP5/MOD3.1 are described in this five volume set of manuals covering the theory, use, and assessment of the code for severe accident applications. This set replaces the SCDAP/RELAP5/MOD3 Code Manual, NUREG/CR-5273.

The SCDAP/RELAP5 computer code is designed to describe the overall reactor coolant system (RCS) thermal-hydraulic response, core damage progression, and in combination with VICTORIA[a], fission product release and transport during severe accidents. The code is being developed at the Idaho National Engineering Laboratory (INEL) under the primary sponsorship of the Office of Nuclear Regulatory Research of the U.S. Nuclear Regulatory Commission (NRC).

In an effort to prevent conflicting material data, SCDAP/RELAP5 contains a common set of material properties and correlations subroutines which all severe accident subroutines call. This grouping of subroutines is known as MATPRO. This volume, Volume IV, describes the material properties correlations and computer subroutines contained in MATPRO. Formulation of the material properties are generally semi-empirical in nature. The material property subroutines contained in this document are for uranium, uranium dioxide, mixed uranium-plutonium dioxide fuel, zircaloy cladding, zirconium dioxide, stainless steel, stainless steel oxide, silver-indium-cadmium alloy, cadmium, boron carbide, Inconel 718, zirconium-uranium-oxygen melts, fill gas mixtures, carbon steel, and tungsten. This document also contains descriptions of the reaction and solution rate models needed to analyze a reactor accident.

a. T. Heames et al., *VICTORIA: A Mechanistic Model of Radionuclide Behavior in the Reactor Coolant System Under Severe Accident Conditions*, NUREG/CR-5545, SAND90-0756, Rev. 1, December 1992.

ACKNOWLEDGMENTS

Development of a complex computer code such as SCDAP/RELAP5 is the result of a team effort. Acknowledgments are made to those who made significant contributions to the earlier versions of SCDAP/RELAP5 in particular for the contributions of G. H. Beers, E. R. Carlson, and T. M. Howe. Acknowledgment is also made of E. C. Johnsen for her work in code configuration control, to B. D. Reagan for her support in preparing figures and correcting equations, and to L. G. Price and N. Wade for technical editing support. The authors also acknowledge the RELAP5 development team, specifically R. J. Wagner, R. A. Riemke, and C. S. Miller for their contributions to SCDAP/RELAP5.

The SCDAP/RELAP5 Program is indebted to the technical monitors responsible for directing the overall program: Dr. Y. Chen of the U. S. Nuclear Regulatory Commission and Mr. W. H. Rettig of the Department of Energy Idaho Operations Office. Finally, acknowledgment is made of those many code users who have been very helpful in stimulating correction of code deficiencies with special appreciation to Dr. T. J. Haste and L. Nilsson for the many hours of technical review they provided.

CONTENTS

ABSTRACT iii

LIST OF FIGURES xvi

LIST OF TABLES xxvi

EXECUTIVE SUMMARY xxxi

ACKNOWLEDGMENTS xxxiii

1. INTRODUCTION 1-1

1.1 General Code Capabilities 1-1

1.2 Relationship to Other NRC-Sponsored Software 1-2

1.3 Quality Assurance 1-2

1.4 Organization of the SCDAP/RELAP5 Manuals 1-3

1.5 Organization of Volume IV 1-3

1.6 References 1-4

2. URANIUM DIOXIDE/MIXED OXIDES 2-1

2.1 Melting Temperature and Heat of Fusion (FHYPRP) 2-1

2.1.1 Melting Temperature 2-1
2.1.2 UO_2 and $(U,Pu)O_2$ Heat of Fusion 2-2
2.1.3 Reference 2-2

2.2 Specific Heat Capacity and Enthalpy (FCP, FENTHL) 2-2

2.2.1 Summary 2-2
2.2.2 Literature Review 2-4
2.2.3 Model Development 2-4
2.2.4 Model Comparisons with Data 2-10
2.2.5 Model Uncertainty 2-12
2.2.6 Bibliography 2-13
2.2.7 References 2-13

2.3 Thermal Conductivity (FTHCON) 2-14

2.3.1 Summary 2-14
2.3.2 Literature Review: Theory and Available Data 2-16
2.3.3 Model Development 2-34
2.3.4 Model Uncertainty 2-38
2.3.5 References 2-41

2.4 Emissivity (FEMISS) 2-43

2.4.1 Summary 2-43
2.4.2 Emissivity Data 2-43
2.4.3 Model Development 2-44
2.4.4 References 2-45

2.5 Thermal Expansion and Density (FTHEXP, FDEN) 2-46

2.5.1 Summary (FTHEXP) ... 2-46
2.5.2 Literature Review (FTHEXP) ... 2-47
2.5.3 Model Development (FTHEXP) ... 2-48
2.5.4 Model Data Comparison and Uncertainty (FTHEXP) ... 2-50
2.5.5 Implementation (FTHEXP) ... 2-51
2.5.6 Density (FDEN) ... 2-53
2.5.7 References ... 2-53

2.6 Elastic Moduli (FELMOD, FPOIR) ... 2-54

2.6.1 Summary (FELMOD) ... 2-55
2.6.2 Survey of Available Data (FELMOD) ... 2-56
2.6.3 Model Development (FELMOD) ... 2-62
2.6.4 Model Uncertainty (FELMOD) ... 2-63
2.6.5 Poisson's Ratio (FPOIR) ... 2-64
2.6.6 References ... 2-65

2.7 Creep (FCREEP) ... 2-66

2.7.1 Summary ... 2-67
2.7.2 Model Development ... 2-69
2.7.3 Evaluation of Constants and Data Comparison ... 2-72
2.7.4 References ... 2-78

2.8 Densification (FUDENS) ... 2-80

2.8.1 Summary ... 2-80
2.8.2 Uranium Dioxide and Mixed Oxide Densification Data and Models ... 2-81
2.8.3 Model Development ... 2-87
2.8.4 References ... 2-90

2.9 Swelling (FSWELL) ... 2-91

2.9.1 Summary ... 2-91
2.9.2 Solid Fission Product Swelling Model ... 2-92
2.9.3 Fission Gas Swelling Model ... 2-93
2.9.4 References ... 2-96

2.10 Pressure Sintering (FHOTPS) ... 2-97

2.10.1 Summary ... 2-98
2.10.2 Pressure Sintering Process and Data ... 2-99
2.10.3 Model Development and Uncertainties ... 2-104
2.10.4 References ... 2-107

2.11 Restructuring (FRESTR) ... 2-108

2.11.1 Summary ... 2-108
2.11.2 Restructuring Data ... 2-110
2.11.3 Model Development ... 2-112
2.11.4 Bibliography ... 2-115
2.11.5 References ... 2-116

2.12 Fracture Strength (FFRACS) ... 2-118

2.12.1 Summary ... 2-118
2.12.2 Out-of-Pile Uranium Dioxide Deformation ... 2-119
2.12.3 Uranium Dioxide Fracture Strength Model ... 2-123

2.12.4 References 2-124

2.13 Viscosity (FVISCO) 2-125

2.13.1 Summary 2-125
2.13.2 Fuel Viscosity Data 2-126
2.13.3 Model Development and Uncertainty 2-130
2.13.4 References 2-133

2.14 Vapor Pressure (FVAPRS) 2-133

2.14.1 Summary 2-133
2.14.2 Vapor Pressure Data 2-135
2.14.3 Model Development 2-143
2.14.4 Bibliography 2-153
2.14.5 References 2-153

2.15 Fuel Oxidation (FOXY, FOXYK) 2-156

2.15.1 Summary 2-156
2.15.2 Review of Literature 2-157
2.15.3 Model Development 2-157
2.15.4 Description of the FOXY and FOXYK Subcodes 2-160
2.15.5 References 2-161

3. URANIUM ALLOYS 3-1

3.1 Specific Heat Capacity and Enthalpy (UCP, UENTHL) 3-1

3.1.1 Specific Heat Capacity (UCP) 3-1
3.1.2 Enthalpy (UENTHL) 3-6
3.1.3 References 3-8

3.2 Thermal Conductivity (UTHCON) 3-9

3.2.1 Model Development 3-9
3.2.2 References 3-12

3.3 Thermal Expansion and Density (UTHEXP, UDEN) 3-12

3.3.1 Thermal Expansion (UTHEXP) 3-12
3.3.2 Density (UDEN) 3-13
3.3.3 References 3-13

3.4 Metallic Uranium Oxidation (UOXD, UOXWTK) 3-16

3.4.1 Model Development 3-16
3.4.2 Comparison With Data 3-18
3.4.3 Summary 3-18
3.4.4 References 3-18

4. ZIRCALOY 4-1

4.1 Melting and Phase Transformation Temperatures (CHYPRP) 4-1

4.1.1 Model Development 4-1
4.1.2 References 4-5

4.2 Temperature Required to Prevent Hydriding of a Given Concentration of Hydrogen in Zircaloy (CTSOL) 4-5

4.3 Cladding Specific Heat, the Effect of Hydride Solution on Cladding Specific Heat, and Enthalpy (CCP, CHSCP, CENTHL) 4-6

4.3.1 Specific Heat (CCP) 4-6
4.3.2 Effect of Hydride Solution (CHSCP) 4-10
4.3.3 Uncertainties in Specific Heat Predictions 4-11
4.3.4 Zircaloy Enthalpy (CENTHL) 4-12
4.3.5 References 4-16

4.4 Thermal Conductivity (CTHCON) 4-16

4.4.1 Summary 4-16
4.4.2 Literature Review 4-17
4.4.3 Model Development 4-18
4.4.4 References 4-23

4.5 Thermal Expansion, Density and Their Relation to Texture (CTHEXP, CDEN) 4-24

4.5.1 Summary (CTHEXP) 4-24
4.5.2 Literature Review (CTHEXP) 4-26
4.5.3 Model Development (CTHEXP) 4-29
4.5.4 Model Data Comparison and Uncertainty (CTHEXP) 4-38
4.5.5 Density (CDEN) 4-38
4.5.6 References 4-40

4.6 Elastic Moduli (CELMOD, CSHEAR, AND CELAST) 4-41

4.6.1 Summary 4-41
4.6.2 Review of Available Data 4-43
4.6.3 Model Development 4-48
4.6.4 Comparison of Models and Data Base 4-58
4.6.5 Expected Standard Error of the CELMOD and CSHEAR Codes 4-59
4.6.6 References 4-61

4.7 Axial Growth (CAGROW) 4-62

4.7.1 Summary 4-62
4.7.2 Background and Approach 4-63
4.7.3 Review of Experimental Data 4-63
4.7.4 The Effect of Texture on Axial and Circumferential Growth 4-67
4.7.5 Analysis of Irradiation-Induced Growth Factors Other Than Texture 4-70
4.7.6 Evaluation of the Model and Its Uncertainty 4-76
4.7.7 References 4-77

4.8 Creep (CCSTRN, CCSTRS, CABTP, CTP) 4-78

4.8.1 Summary 4-78
4.8.2 Survey of Available Data 4-81
4.8.3 Model Development 4-85
4.8.4 Model Uncertainty 4-95
4.8.5 References 4-96
4.8.6 Bibliography 4-97

4.9 Plastic Deformation (CSTRES, CSTRAN, CSTRNI, CANISO, CKMN) 4-100

4.9.1 Summary 4-100
4.9.2 Available Data 4-107
4.9.3 Model Development 4-110

4.9.4 Comparison to Burst Test Data 4-137
4.9.5 Uncertainties 4-138
4.9.6 References 4-139

4.10 Annealing (CANEAL) 4-142

4.10.1 Summary 4-142
4.10.2 Available Data 4-143
4.10.3 Model Development 4-149
4.10.4 Comparison of Annealing Models to Data 4-161
4.10.5 References 4-164

4.11 Mechanical Limits and Embrittlement (CMLIMT, CBRTTL) 4-165

4.11.1 Summary (CMLIMT) 4-165
4.11.2 Available Data 4-167
4.11.3 Model Development 4-171
4.11.4 Application of the Failure Criterion to Determine Cladding Shape After Burst 4-179
4.11.5 Summary (CBRTTL) 4-185
4.11.6 Literature Review 4-187
4.11.7 Model Development 4-187
4.11.8 Model for Fast Cooled Cladding 4-189
4.11.9 Model for Slow Cooled Cladding 4-191
4.11.10 Model Uncertainties 4-192
4.11.11 References 4-194

4.12 Cyclic Fatigue (CFATIG) 4-196

4.12.1 Summary 4-196
4.12.2 Basis for High Cycle Fatigue Material Constants 4-197
4.12.3 Basis for Low Cycle Fatigue Material Constants 4-199
4.12.4 References 4-200

4.13 Collapse Pressure (CCLAPS) 4-201

4.13.1 Model Development 4-201
4.13.2 References 4-201

4.14 Meyer Hardness (CMHARD) 4-202

4.14.1 Model Development 4-202
4.14.2 References 4-203

4.15 Zircaloy Oxidation in Water and Steam (CORROS, COBILD, COXIDE, COXWTK, COXTHK) 4-203

4.15.1 Summary 4-203
4.15.2 Zircaloy Oxidation Literature and Data 4-210
4.15.3 Model Development 4-211
4.15.4 Description of the CORROS, COBILD, COXIDE, COXWTK, and COXTHK Subcodes 4-225
4.15.5 References 4-227
4.15.6 Bibliography 4-229

4.16 Cladding Hydrogen Uptake (CHUPTK) 4-231

4.16.1 Summary 4-231

4.16.2 Background and Approach 4-233
4.16.3 Out of Pile Basis for the Model 4-233
4.16.4 Generalization to an In-Pile Model 4-235
4.16.5 References 4-236

4.17 Young's Modulus and Poisson's Ratio (CELMDR) 4-237

4.17.1 References 4-237

4.18 Zircaloy and Zirconium Heats of Fusion (PHYPRP) 4-238

4.18.1 References 4-238

4.19 Zirconium Transformation Temperature (PHYPRP) 4-238

4.19.1 References 4-238

5. ZIRCALOY OXIDES 5-1

5.1 Melting and Phase Transformation Temperatures (ZOPRP) 5-1

5.1.1 Model Development 5-1
5.1.2 References 5-3

5.2 Specific Heat Capacity and Enthalpy (ZOCP, ZONTHL) 5-3

5.2.1 Specific Heat (ZOCP) 5-3
5.2.2 Enthalpy (ZONTHL) 5-4
5.2.3 References 5-6

5.3 Thermal Conductivity (ZOTCON) 5-8

5.3.1 Model Development 5-8
5.3.2 References 5-15

5.4 Surface Emissivity (ZOEMIS) 5-15

5.4.1 Summary 5-16
5.4.2 Literature Review 5-17
5.4.3 Model Development 5-20
5.4.4 Uncertainty 5-23
5.4.5 References 5-23

5.5 Thermal Expansion and Density (ZOTEXP, ZODEN) 5-24

5.5.1 Thermal Expansion (ZOTEXP) 5-24
5.5.2 Density (ZODEN) 5-25
5.5.3 References 5-28

5.6 Elastic Moduli (ZOEMOD, ZOPOIR) 5-29

5.6.1 Young's Modulus (ZOEMOD) 5-29
5.6.2 Poisson's Ratio (ZOPOIR) 5-29
5.6.3 References 5-30

5.7 Mechanical Limits and Embrittlement (ZORUP) 5-31

5.7.1 Model Development 5-31
5.7.2 References 5-32

6. CONTROL ROD CLADDING 6-1

6.1 Melting Temperatures (SHYPRP) 6-1

6.1.1 Model Development 6-1
6.1.2 References 6-1

6.2 Specific Heat Capacity and Enthalpy (SCP, SENTHL) 6-1

6.2.1 Model Development 6-1
6.2.2 References 6-3

6.3 Thermal Conductivity (STHCON) 6-4

6.3.1 Model Development 6-4

6.4 Thermal Expansion and Density (STHEXP, SDEN) 6-6

6.4.1 Model Development 6-6
6.4.2 References 6-8

6.5 Stainless Steel Oxidation in Steam (SOXIDE, SOXWGN, SOXTHK) 6-8

6.5.1 Model Development 6-8
6.5.2 References 6-13

7. STAINLESS STEEL OXIDES 7-1

7.1 Specific Heat Capacity and Enthalpy (SOCP, SONTHL) 7-1

7.1.1 Specific Heat Capacity (SOCP) 7-1
7.1.2 Enthalpy (SONTHL) 7-3
7.1.3 References 7-8

7.2 Thermal Conductivity (SOTCON) 7-9

7.2.1 Model Development 7-9
7.2.2 References 7-10

7.3 Thermal Expansion and Density (SOTHEX, SODEN) 7-11

7.3.1 Thermal Expansion (SOTHEX) 7-11
7.3.2 Density (SODEN) 7-12
7.3.3 References 7-12

8. NEUTRON ABSORBERS (SILVER-INDIUM-CADMIUM CONTROL RODS AND BORON CARBIDE CONTROL BLADES) 8-1

8.1 Melting Temperature (AHYPRP) 8-1

8.1.1 Model Development 8-1
8.1.2 References 8-1

8.2 Specific Heat Capacity and Enthalpy (ACP, AENTHL) 8-2

8.2.1 Specific Heat Capacity of Ag-In-Cd (ACP) 8-2
8.2.2 Specific Heat Capacity for Boron Carbide(ACP) 8-2
8.2.3 Enthalpy of Ag-In-Cd (AENTHL) 8-3
8.2.4 Enthalpy of Boron Carbide (AENTHL) 8-5
8.2.5 References 8-5

8.3 Thermal Conductivity (ATHCON) 8-6

8.3.1 Thermal Conductivity of Ag-In-Cd (ATHCON) 8-6
8.3.2 Thermal Conductivity of Boron Carbide (ATHCON) 8-7
8.3.3 References 8-8

8.4 Thermal Expansion and Density (ATHEXP, ADEN) ... 8-10
8.4.1 Thermal Expansion Strain of Ag-In-Cd ... 8-10
8.4.2 Thermal Expansion Strain of Boron Carbide ... 8-10
8.4.3 Density Calculations for Ag-In-Cd and Boron Carbide ... 8-11
8.4.4 References ... 8-12
8.5 Surface Tension (ASTEN) ... 8-14
8.5.1 Model Development ... 8-14
8.5.2 References ... 8-14
8.6 Viscosity (AVISC) ... 8-14
8.6.1 Viscosity of Ag-In-Cd ... 8-14
8.6.2 Viscosity of Boron Carbide ... 8-15
9. CADMIUM ... 9-1
9.1 Specific Heat (CDCP) ... 9-1
9.2 Thermal Conductivity (CDTCON) ... 9-1
9.3 Density (CDDEN) ... 9-2
9.4 Enthalpy (CDENTH) ... 9-3
9.5 References ... 9-4
10. GRID SPACER MATERIAL (INCONEL) ... 10-1
10.1 Melting Temperatures (HPROP) ... 10-1
10.2 Enthalpy Correlations (USERP) ... 10-1
10.3 Thermal Conductivity (USERP) ... 10-2
10.4 Density (USERP) ... 10-3
10.5 References ... 10-3
11. ZIRCONIUM-URANIUM COMPOUNDS ... 11-1
11.1 Zirconium Uranium Oxygen Compound Melting, Solution, and Precipitation (PSOL, PLIQ, ZUSOLV, COEF) ... 11-4
11.1.1 Introduction ... 11-4
11.1.2 Data for the Zr-U-O System ... 11-5
11.1.3 Model Development ... 11-22
11.1.4 References ... 11-36
11.2 Specific Heat Capacity and Enthalpy (ZUCP, ZUNTHL, ZUCP1, ZUNTH1) ... 11-37
11.2.1 Zirconium-Uranium-Oxygen Compounds ... 11-37
11.2.2 Core Component Compounds ... 11-38
11.2.3 References ... 11-44
11.3 Thermal Conductivity (ZUTCON, ZUTCO1) ... 11-45
11.3.1 Zirconium-Uranium-Oxygen Compounds ... 11-45
11.3.2 Core Component Compounds ... 11-46
11.3.3 References ... 11-50

11.4 Thermal Expansion and Density (ZUTEXP, ZUDEN, ZUTEX1, ZUDEN1).....11-50

11.4.1 Zirconium-Uranium-Oxygen Compounds 11-50
11.4.2 Core Component Compounds 11-53
11.4.3 References 11-60

11.5 Zirconium-Uranium-Oxygen Compounds Coefficients of Friction (ZUFRIC) 11-60

11.6 Zirconium-Uranium-Oxygen Compounds Interfacial Surface Tension (ZUSTEN) 11-61

11.7 Zirconium-Uranium-Oxygen Compounds Viscosity (ZUVISC) 11-62

11.7.1 Model Development 11-62
11.7.2 References 11-63

11.8 Heat of Solution of Uranium Dioxide by Zirconium-Uranium-Oxygen Compounds (ZUSOLN) 11-63

11.8.1 Model Development 11-63
11.8.2 References 11-65

11.9 Heat of Fusion of Zirconium-Uranium-Oxygen Compounds (ZUFUSN) 11-65

11.10 Coefficient of Thermal Expansion of Liquefied Mix (ZUBET1).....11-65

11.11 Position of Advancing Zr-UO_2 Interface (PSUZ) 11-66

11.11.1 Summary 11-66
11.11.2 References 11-67

11.12 UO_2 Solubility in Oxygen Stabilized Zircaloy (PSLV).....11-67

11.12.1 Summary 11-67

11.13 Rate of Dissolution of UO2 in Zr-U-O (DISUO2, UO2DIS, UO2SOL) 11-67

11.13.1 Introduction 11-67
11.13.2 Data for the Zr-U-O System 11-68
11.13.3 Model Development 11-71
11.13.4 Uranium Dioxide Dissolution Kinetics 11-78
11.13.5 References 11-79

12. SILVER-ZIRCONIUM COMPOUNDS 12-1

12.1 Solubility of Zircaloy Cladding in Ag-In-Cd Absorber (ASOLV)..... 12-1

12.1.1 Summary 12-1
12.1.2 Solubility Data for Ag-In-Cd on Zircaloy..... 12-2
12.1.3 Model Development..... 12-3
12.1.4 References 12-5

13. NONCONDENSABLE GASES--HELIUM, ARGON, KRYPTON, XENON, HYDROGEN, NITROGEN, OXYGEN, CARBON MONOXIDE, CARBON DIOXIDE, WATER MIXTURES 13-1

13.1 Specific Heat Capacity (GCP)..... 13-1

13.1.1 Model Development..... 13-1
13.1.2 Reference..... 13-2

13.2 Thermal Conductivity, Gas Conductance, and Jump Distance (GASCON, GTHCON, GJUMP) ... 13-2
13.2.1 Summary ... 13-2
13.2.2 Gas Thermal Conductivity and Accommodation Coefficient Data ... 13-6
13.2.3 Model Development and Uncertainty Estimates ... 13-10
13.2.4 References ... 13-21
13.3 Effective Emissivity (GMISS) ... 13-24
13.3.1 Model Development ... 13-24
13.3.2 References ... 13-25
13.4 Viscosity (GVISCO) ... 13-26
13.4.1 Model Development ... 13-26
13.4.2 References ... 13-28
13.5 Mean Free Path (GMFP) ... 13-28
13.5.1 Model Development ... 13-28
13.5.2 Reference ... 13-29
14. VESSEL STEEL ... 14-1
14.1 Rupture Time and the Creep Damage Term Calculations (RUPTUR, TRUPT, CALTAV) ... 14-1
14.1.1 Model Description ... 14-1
14.1.2 Model Development ... 14-3
14.1.3 References ... 14-9
14.2 Carbon Steel ... 14-9
14.2.1 Enthalpy Correlations ... 14-9
14.2.2 Thermal Conductivity ... 14-10
14.2.3 Density Correlations ... 14-11
14.2.4 References ... 14-11
15. TUNGSTEN ... 15-1
15.1 Specific Heat (TUNGCP) ... 15-1
15.2 Thermal Conductivity (TUNGK) ... 15-1
15.3 Density Correlations (TUNGRO) ... 15-2
15.4 References ... 15-2
16. UTILITIES ... 16-1
16.1 Linear Interpolation (POLATE, POL8) ... 16-1
16.2 Cladding Texture Factors (CTXTUR) ... 16-1
16.2.1 Model Description ... 16-1
16.2.2 References ... 16-5
16.3 Collected Heats of Fusion (QFUSON) ... 16-5
16.3.1 Model Development ... 16-5
16.3.2 References ... 16-6

16.4 Mass Fraction Mole Fraction Conversions (PMOLE, PMASS) 16-6
16.5 Integral of the Reciprocal of Thermal Conductivity (ZUINT)..... 16-7
16.6 Atomic Fraction (ATOMFR) 16-8

FIGURES

Figure 2-1. Specific heat capacity as a function of temperature and oxygen-to-metal ratio for UO_2. 2-7

Figure 2-2. Specific heat capacity as a function of temperature and oxygen-to-metal ratio for (U0.8Pu0.2)O2+x. 2-8

Figure 2-3. Enthalpy of UO_2 as a function of temperature to 4,000 K. 2-9

Figure 2-4. Specific heat capacity of UO_2 from three experimenters compared with the FCP correlation (solid line) for UO_2. 2-11

Figure 2-5. Specific heat capacity of PuO_2 from Kruger and Savage compared with the FCP correlation (solid line) for PuO_2. 2-11

Figure 2-6. Specific heat capacity of (U0.8Pu0.2)O_2 from three experimenters compared with the FCP correlation (solid line) for mixed oxides. 2-12

Figure 2-7. Model prediction for thermal conductivity of 0.99% TD UO_2 compared to data from specimens with densities in the range 0.985 to 0.995% TD. 2-39

Figure 2-8. Model prediction for thermal conductivity of 0.98% TD UO_2 compared to data from specimens with densities in the range 0.975 to 0.985% TD. 2-39

Figure 2-9. Model prediction for thermal conductivity of 0.96% TD UO_2 compared to data from specimens with densities in the range 0.955 to 0.965% TD. 2-40

Figure 2-10. Model prediction for thermal conductivity of 0.95% TD UO_2 compared to data from specimens with densities in the range 0.945 to 0.955% TD. 2-40

Figure 2-11. Emissivity data and corresponding FEMISS predictions. 2-45

Figure 2-12. Correlation for the thermal expansion strain of UO_2 compared with its data base. 2-51

Figure 2-13. Correlation for the thermal expansion strain of PuO_2 compared with its data base. 2-52

Figure 2-14. Comparisons of the UO_2, PuO_2, and (U0.8, Pu0.2)O_2 correlations from 0 to 2,000 K. 2-52

Figure 2-15. Theoretical density of UO_2. 2-53

Figure 2-16. Young's modulus for stoichiometric UO_2 fuel at several temperatures and fractions of theoretical density. 2-57

Figure 2-17. Young's modulus for (U, Pu)O_2 with various oxygen-to-metal ratios. 2-58

Figure 2-18. Young's modulus data and least-squares linear fit for stoichiometric UO_2 fuel at room temperature and several different densities. 2-59

Figure 2-19. Ratio of Young's modulus for stoichiometric and nonstoichiometric fuels measured at room temperature compared to values predicted by de Novion's correlation. 2-61

Figure 2-20. Poisson's ratio as a function of temperature. 2-65

Figure 2-21. Comparison of unirradiated UO_2 experimental data with corresponding calculated values from FCREEP. 2-74

Figure 2-22. Comparison of irradiated UO_2 experimental data with corresponding calculated values from FCREEP. 2-75

Figure 2-23. Comparison of (U,Pu)O_2 experimental data with corresponding calculated values from FCREEP. 2-76

Figure 2-24. Comparison of UO_2 strain data of Rod 3C with corresponding calculated values from FCREEP. 2-77

Figure 2-25. Comparison of UO_2 strain data of Capsule 2 with corresponding calculated values from FCREEP. 2-77
Figure 2-26. The effect of burnup and fission rate on the fuel density change for EPRI fuel types 1, 2, and 4. 2-82
Figure 2-27. Change in fuel stack length of Halden fuel as a function of burnup. 2-84
Figure 2-28. Fuel stack length changes for 92% TD UO_2 processed by different techniques. 2-85
Figure 2-29. Graphical solution of Rolstad's model, where TD is percent of theoretical density, TS is sintering temperature (), and BU is burnup. 2-89
Figure 2-30. FUDENS calculations using EPRI fuel fabrication parameters and resintering values correlated with experimental EPRI in-pile data. 2-90
Figure 2-31. Unrestrained fission gas swelling. 2-95
Figure 2-32. Fuel volume changes calculated by FSWELL compared with experimental fuel swelling data. 2-95
Figure 2-33. Urania pressure sintering rates calculated using the FHOTPS model compared with data. 2-106
Figure 2-34. Mixed-oxide pressure sintering rates calculated using the FHOTPS model compared with data. 2-106
Figure 2-35. Threshold of columnar grain growth with temperature gradient of 4.0x105 K/m. 2-115
Figure 2-36. Comparison of Equation (2-128) in the elastic behavior regime with out-of-pile UO_2 fracture strength data normalized to 10-m grain size and 95% TD. 2-121
Figure 2-37. Comparison of Equation (2-129) in the elastic behavior regime with out-of-pile UO_2 fracture strength data normalized to 10-mm grain size and 95%TD. 2-122
Figure 2-38. Least squares regression fit of UO2 fracture strength in the elastic plastic regime to out-of-pile data of Cannon et al. 2-123
Figure 2-39. Calculated curves showing the predictions of FFRACS as a function of temperature for two fuel densities. 2-124
Figure 2-40. Uranium dioxide viscosities measured as a function of temperature. 2-130
Figure 2-41. Data from uranium dioxide samples compared with least-squares fit. 2-132
Figure 2-42. Viscosities calculated with Equation (2-130) (solid line) and upper and lower uncertainty estimates (dashed lines) compared with data. 2-132
Figure 2-43. Urania vapor pressure data. 2-138
Figure 2-44. Plutonia vapor pressure data. 2-139
Figure 2-45. Mixed oxide vapor pressure data. 2-140
Figure 2-46. FVAPRS calculations (solid line) compared to urania data. 2-147
Figure 2-47. FVAPRS calculations (solid line) compared to plutonia data. 2-148
Figure 2-48. FVAPRS calculations (solid line) compared to mixed oxide data. An oxygen-to-metal ratio of 2.0 was used in the FVAPRS calculations. 2-149
Figure 2-49. FVAPRS hypostoichiometric oxygen vapor pressure calculations (UOXVAP) compared to the data. 2-151
Figure 2-50. FVAPRS hyperstoichiometric oxygen vapor pressure calculations (DIOVAP) compared to the data. 2-152

Figure 2-51. FVAPRS vapor pressure calculations of plutonia (PUOVAP), urania (UO2VAP), mixed oxides (VAPMIX), and monatomic oxygen over urania (UOXVAP), using an oxygen-to-metal ratio of 2.0. 2-152
Figure 2-52. Computed weight gain as a function of temperature for constant time step size. 2-160
Figure 2-53. Computed weight gain as a function of time step size for constant temperature. 2-160
Figure 3-1. Specific heat capacity for uranium metal calculated by the function UCP. 3-6
Figure 3-2. Enthalpy change for uranium metal calculated by UENTHL. 3-8
Figure 3-3. Thermal conductivities calculated by UTHCON. 3-10
Figure 3-4. Thermal expansion strain as a function of temperature calculated by UTHEXP. 3-15
Figure 3-5. Density calculated by UDEN using the thermal strain calculated by UTHEXP. 3-16
Figure 3-6. Parabolic rate constant for the uranium-steam reaction as a function of temperature. 3-19
Figure 4-1. Zircaloy solidus and liquidus temperatures. 4-5
Figure 4-2. Specific heat of zircaloys as calculated by CCP for alloys without hydrides. 4-8
Figure 4-3. Available data, MATPRO expressions for specific heat, and estimated uncertainty of the MATPRO expression for temperatures from 300 to 1,000 K. 4-9
Figure 4-4. Available data, MATPRO expressions for specific heat, and estimated uncertainty of the MATPRO expression for temperatures from 1,000 to 2,000 K. 4-9
Figure 4-5. Data base for MATPRO prediction of the effect of hydride solution on specific heat, Scott's proposed curve for the specific heat of zirconium, and the MATPRO predictions for the effect of 28 and 300 ppm of hydrogen on the specific heat curve. 4-11
Figure 4-6. MATPRO predictions for apparent zircaloy specific heat for several hydrogen concentrations compared with the curve measured with as-received zircaloy-2. 4-12
Figure 4-7. Derivation of Equation (4-21). 4-14
Figure 4-8. Zircaloy enthalpy as a function of temperature. 4-15
Figure 4-9. Thermal conductivity data, least squares fit, and the two standard deviation limits. 4-17
Figure 4-10. Comparison of CTHEXP prediction with Douglass' data in the axial direction. 4-27
Figure 4-11. Comparison of CTHEXP prediction with Douglass' data in the circumferential direction. 4-27
Figure 4-12. Comparison of CTHEXP prediction with Kearns' model in the axial direction. 4-28
Figure 4-13. Comparison of CTHEXP prediction with Kearns' model in the circumferential direction. 4-28
Figure 4-14. Angles and orientation of the unit cell of zircaloy relative to a system of coordinates fixed in the lab frame of reference. 4-30
Figure 4-15. Elastic moduli for isotropic material compared to corresponding moduli for typical PWR cladding. 4-43
Figure 4-16. Reference directions selected for CELMOD/CSHEAR/CELAST analysis. 4-52
Figure 4-17. Measured values of axial Young's modulus compared to values predicted by the CELAST subcode for several oxygen concentrations and temperatures in the range of 300 to 1,500 K. 4-60
Figure 4-18. Measured values of circumferential Young's modulus compared to values predicted by the CELAST subcode for several oxygen concentrations and temperatures in the range of 300 to 1,500 K. 4-60

Figure 4-19. Comparison of the Young's modulus predicted with the CELAST code to the beta phase zirconium data of Padel and Groff, and Armstrong and Brown. 4-61
Figure 4-20. Model predictions and measured values of zircaloy tube axial growth as a function of fast neutron fluence, irradiation temperature, cold work, and texture coefficient, fz. 4-64
Figure 4-21. The growth of schematic unit cells in a grain..... 4-68
Figure 4-22. Model predictions and measured values of the growth of zircaloy tubes adjusted to a common texture coefficient of fz = 0.05..... 4-71
Figure 4-23. Zircaloy growth versus square root of fast neutron fluence for data adjusted to a common tube texture coefficient of fz = 0.05 with linear least-squares fits superimposed. 4-72
Figure 4-24. Zircaloy growth versus square root of fast neutron fluence for data adjusted to a common tube texture coefficient of fz = 0.05 and to a common temperature of 300°C with linear least squares fits superimposed. 4-75
Figure 4-25. Average tangential creep strain as a function of time at 140 MPa and 643 K reported by Stehle. 4-84
Figure 4-26. Radial displacement of cladding surface at 200 hours in Hobson's test 269-4. 4-87
Figure 4-27. Average tangential creep strain as a function of time at 15.86 MPa differential pressure. 4-89
Figure 4-28. Average tangential creep strain as a function of time at 14.48 MPa differential pressure. 4-90
Figure 4-29. Average tangential creep strain as a function of time from Hobson's in-reactor experiment at 13 to 13.5 MPa differential pressure and 5.4 x 1017 fast neutrons (m2/ s). 4-92
Figure 4-30. Steady-state creep rates reported by Fidleris for Tests R-6 and Rx-14 compared to model predictions for steady-state creepdown rates derived from these data. 4-95
Figure 4-31. Increase of the strain anisotropy constant A1E as a function of radial compressive strain in two tests. 4-114
Figure 4-32. Strain rate sensitivity exponent as a function of temperature and strain rate. 4-115
Figure 4-33. Increase of the strain rate sensitivity exponent at 1,173 K as a function of strain rate based on Chung, Garde, and Kassner's data. 4-116
Figure 4-34. Base data, MATPRO prediction, and uncertainty estimate for strain hardening exponent of annealed tubes. 4-117
Figure 4-35. Base data, MATPRO prediction, and uncertainty estimate for strain coefficient of annealed, isotropic cladding. 4-119
Figure 4-36. Data and least squares fit to strength coefficients as a function of cold work and irradiation at room temperature. 4-121
Figure 4-37. Data and analytical functions for strain hardening coefficient as a function of cold work and irradiation at room temperature. 4-122
Figure 4-38. Calculated ratios of the strength coefficients of zircaloy, containing oxygen (K) and the strength coefficients of as fabricated zircaloy (Ko) as a function of oxygen concentration for several temperatures. 4-128
Figure 4-39. Calculated curve and data showing the rate of change of the zircaloy strength coefficient with oxygen content as a function of temperature. 4-128

Figure 4-40. Calculated ratios of the strain hardening exponents of zircaloy containing oxygen (n) and the strain hardening exponents of as fabricated zircaloy (no) as a function of oxygen concentration for several temperatures. 4-130
Figure 4-41. Calculated curve and data showing the rate of change of the zircaloy strain hardening exponent as a function of temperature..... 4-131
Figure 4-42. Strain rate sensitivity exponent, m, data as a function of oxygen concentration from Chung..... 4-133
Figure 4-43. The ratio m/mo as a function of oxygen concentration showing Chung data and the line used to fit these data..... 4-134
Figure 4-44. Zircaloy oxygen phase diagram, taken from Chung. 4-134
Figure 4-45. Stress as a function of strain at a strain rate of 10-3/s for two oxygen concentrations at 600 K. 4-136
Figure 4-46. Stress as a function of strain at a strain rate of 10-3/s for two oxygen concentrations at 1,400 K. 4-136
Figure 4-47. Stress as a function of strain at a strain rate of 0.1 for two oxygen concentrations at 600 K. 4-137
Figure 4-48. Measured diametral strain versus MATPRO predictions for two initial values of cold work in tests conducted by Hardy at heating rates of 25 K/s..... 4-138
Figure 4-49. Measured diametral strain versus MATPRO predictions for Chung's test at 1,023 K and 5.2 MPa. 4-139
Figure 4-50. Local radial strains at burst versus temperature. 4-174
Figure 4-51. Average circumferential strains at failure versus temperature. 4-175
Figure 4-52. Local tangential stress at failure versus temperature..... 4-177
Figure 4-53. Base data and MATPRO correlation for effect of temperature variation on average circumferential elongation. 4-182
Figure 4-54. Schematic cross sections of cladding at burst. 4-182
Figure 4-55. Typical average circumferential strains predicted by the MATPRO correlations for typical engineering burst stress, true burst stress, and typical strain distributions at three different temperature differences..... 4-186
Figure 4-56. Hobson-Rittenhouse isothermal data for fast cooled cladding compared with the 0.65 and 0.70 wt% and the 90 and 95% filled criteria..... 4-190
Figure 4-57. Hobson-Rittenhouse and PBF data for fast-cooled rods compared with the critical fractional wall thickness as calculated from the 0.65 and 0.70 wt% and the 90 and 95% filled criteria. 4-191
Figure 4-58. Comparison of the Argonne data for slow-cooled cladding with the criterion that at least 0.3 mm of zircaloy with less than 1 wt% oxygen is required to survive thermal shock..... 4-193
Figure 4-59. Values of the CMHARD correlation and its data base..... 4-203
Figure 4-60. Idealized schematic of a uranium dioxide pellet in contact with the cladding, showing the layered structure..... 4-207
Figure 4-61. Schematic of posttransition oxide, showing an intact, rate-determining layer of varying thickness, with another oxide layer that does not affect the oxidation rate..... 4-213
Figure 4-62. Estimates of enhancements over out-of-pile oxidation rates when cladding is irradiated in typical BWR and PWR environments..... 4-217

Figure 4-63. Comparison of the predicted oxide layer thickness with the base data from average values of six Shippingport zircaloy-2 rods in a PWR environment at 277. 4-217
Figure 4-64. Comparison of the predicted oxide layer thickness with the base data from Saxton zircaloy-4 rods in a PWR at 340. 4-218
Figure 4-65. Comparison of the predicted oxide layer thickness with the base data from zircaloy-2 rods irradiated in the Vallecitos and Dresden BWRs at 286. 4-218
Figure 4-66. Comparison of calculated (solid lines) and measured ZrO2 thickness for six temperatures. 4-219
Figure 4-67. Data used by Urbanic and Heidrick to determine high temperature zircaloy oxidation rates. 4-221
Figure 4-68. Growth of Zr(O) and Zr(O)b layers as a function of temperature from Hofmann and Politis.4.15-16. 4-222
Figure 4-69. Linear power generation for a rod of initial diameter of 1.25 x 10-2 m as a function of temperature for various initial oxide thicknesses. 4-224
Figure 5-1. Zircaloy oxide solidus and liquidus temperatures. 5-3
Figure 5-2. Zircaloy oxide specific heat capacity as a function of temperature. 5-6
Figure 5-3. Zircaloy oxide enthalpy as a function of temperature. 5-8
Figure 5-4. Zircaloy oxide thermal conductivity data and correlations. 5-14
Figure 5-5. Zircaloy oxide thermal conductivity as a function of temperature. 5-15
Figure 5-6. Total hemispherical emittance of zircaloy-4 versus time at temperature in steam. 5-18
Figure 5-7. ZOEMIS calculations compared with the data base of the model. 5-22
Figure 5-8. Expected standard errors of emissivity for temperatures below 1,500 K and at 1,573 K. 5-24
Figure 5-9. Zircaloy oxide thermal strain. 5-26
Figure 5-10. Zircaloy oxide density as a function of temperature. 5-26
Figure 5-11. Zircaloy oxide thermal strain data compared to code prediction. 5-28
Figure 5-12. Data and calculated values of Young's modulus for zircaloy oxide. 5-30
Figure 5-13. Zircaloy oxide failure stress data and correlations versus temperature. 5-32
Figure 5-14. Zircaloy oxide failure stress calculated with the ZORUP function. 5-33
Figure 6-1. Stainless steel specific heat capacity at constant pressure. 6-3
Figure 6-2. Stainless steel enthalpy change at constant pressure. 6-4
Figure 6-3. Stainless steel thermal conductivity. 6-5
Figure 6-4. Stainless steel thermal expansion strain. 6-7
Figure 6-5. Stainless steel density. 6-7
Figure 6-6. Parabolic constant for oxygen weight gain. 6-10
Figure 6-7. Parabolic constant for oxide layer thickness. 6-11
Figure 6-8. Average power per meter during 1 second for a 1.25 x 10-2 m stainless steel rod with no initial oxide layer. 6-11
Figure 6-9. Oxygen uptake after 1 second with no initial oxidation. 6-12
Figure 6-10. Oxide layer thickness after 1 second with no initial oxidation. 6-12
Figure 7-1. Specific heat capacity for stainless steel oxide calculated by SOCP. 7-3
Figure 7-2. Enthalpy change for stainless steel oxide calculated by SONTHL. 7-9

Figure 7-3. Thermal conductivities for stainless steel oxide calculated by SOTCON. 7-11
Figure 7-4. Thermal expansion strain as a function of temperature calculated by SOTHEX. 7-13
Figure 7-5. Density calculated by SODEN using the thermal strain calculated by SOTHEX. 7-13
Figure 8-1. Silver-indium-cadmium absorber heat capacity. 8-4
Figure 8-2. Boron carbide absorber heat capacity. 8-4
Figure 8-3. Silver-indium-cadmium absorber enthalpy. 8-5
Figure 8-4. Boron carbide absorber enthalpy. 8-6
Figure 8-5. Thermal conductivity of silver-indium-cadmium alloy. 8-8
Figure 8-6. Thermal conductivity of silver-indium-cadmium absorber. 8-9
Figure 8-7. Thermal conductivity of boron carbide absorber. 8-9
Figure 8-8. Thermal expansion strain of silver-indium-cadmium absorber. 8-11
Figure 8-9. Thermal expansion strain of boron carbide absorber. 8-12
Figure 8-10. Density of silver-indium-cadmium absorber. 8-13
Figure 8-11. Density of boron carbide absorber. 8-13
Figure 8-12. Viscosity of silver-indium-cadmium absorber. 8-16
Figure 8-13. Viscosity of boron carbide absorber. 8-16
Figure 11-1. Compositions of Zr-U-O compounds on a Gibbs triangle plot. 11-2
Figure 11-2. Zirconium-zirconium dioxide phase diagram. 11-6
Figure 11-3. Uranium oxygen phase diagram. 11-8
Figure 11-4. Solidus and liquidus temperatures of uranium oxides according to Latta and Fryxell. 11-9
Figure 11-5. Oxygen saturated, alpha phase zirconium uranium dioxide isopleth. 11-12
Figure 11-6. Uranium dioxide zirconium dioxide quasi-binary phase diagram. 11-13
Figure 11-7. Uranium zirconium system liquidus and solidus. 11-14
Figure 11-8. Phases of the Zr-U-O system at 1,273 K. 11-15
Figure 11-9. Phases of the Zr-U-O system at 1,773 K. 11-16
Figure 11-10. Phases of the Zr-U-O system at 1,873 K. 11-17
Figure 11-11. Phases of the Zr-U-O system at 2,073 K. 11-18
Figure 11-12. Phases of the Zr-U-O system at 2,178 K. 11-19
Figure 11-13. Phases of the Zr-U-O system at 2,223 K. 11-20
Figure 11-14. Phases of the Zr-U-O system at 2,273 K. 11-21
Figure 11-15. Points that are connected to form the ternary Zr-O-U system liquidus lines. 11-23
Figure 11-16. Points that are connected to form the ternary Zr-O-U system solidus lines. 11-27
Figure 11-17. Solid and liquid phase boundaries with tie lines connecting compositions on the boundaries as they are represented for 2,500 K in the ZUSOLV code. 11-36
Figure 11-18. Specific heat capacity calculated for a 0.2 UO_2-0.8 ZrO_2 weight fraction compound. 11-39
Figure 11-19. Enthalpy calculated for a 0.2 UO_2-0.8 ZrO_2 weight fraction compound. 11-39
Figure 11-20. Thermal conductivity calculated for a 0.2 UO_2-0.8 ZrO_2 weight fraction compound. 11-46
Figure 11-21. Thermal strain calculated for a 0.2 UO_2-0.8 ZrO_2 weight fraction compound. 11-54

Figure 11-22. Density calculated for a 0.2 UO_2-0.8 ZrO_2 weight fraction compound.....11-54
Figure 11-23. Coefficient of friction calculated with the ZUFRIC function. 11-61
Figure 11-24. Viscosity of a compound composed of 0.33 mol% zirconium and 0.67 mol% uranium dioxide. 11-63
Figure 11-25. Effect of solvent composition of heat required to dissolve a kilogram of uranium dioxide. 11-65
Figure 11-26. Zirconium-zirconium dioxide phase diagram. 11-69
Figure 11-27. Uranium-oxygen phase diagram.....11-70
Figure 11-28. Oxygen saturated alpha phase zirconium - uranium dioxide isopleth.....11-72
Figure 11-29. Quasi binary phase diagram for the ZrO_2-UO_2 system from Reference 11.13-6. 11-73
Figure 11-30. Zr-U-O isothermal section at 2,273 K according to Hofmann and Politis.....11-74
Figure 11-31. Points connected to form the ternary Zr-U-O system. 11-76
Figure 11-32. Zr-U-O isothermal section at 2,273 K according to Hofmann and Politis (revised).....11-77
Figure 12-1. Silver-zirconium phase diagram..... 12-3
Figure 12-2. Computer generated graph of the calculated solubility of zircaloy in silver-indium-cadmium absorber material. 12-6
Figure 13-1. Thermal conductivity of helium as a function of temperature. 13-12
Figure 13-2. Thermal conductivity of argon as a function of temperature. 13-13
Figure 13-3. Thermal conductivity of krypton as a function of temperature..... 13-13
Figure 13-4. Thermal conductivity of xenon as a function of temperature..... 13-14
Figure 13-5. Thermal conductivity of hydrogen as a function of temperature. 13-14
Figure 13-6. Thermal conductivity of nitrogen as a function of temperature..... 13-15
Figure 13-7. Thermal conductivity of oxygen as a function of temperature..... 13-15
Figure 13-8. Thermal conductivity of carbon monoxide as a function of temperature. 13-16
Figure 13-9. Thermal conductivity of carbon dioxide as a function of temperature. 13-16
Figure 13-10. Thermal conductivity of helium xenon mixtures at 793 K..... 13-17
Figure 13-11. Gas viscosity as a function of temperature for pure helium, a binary mixture of helium and xenon, and for an equal molar mixture of helium, argon, krypton, and xenon. 13-27
Figure 14-1. Master creep rupture curve for A-508, Class 2 carbon steel..... 14-7
Figure 14-2. Master creep rupture curve for 316 stainless steel. 14-8
Figure 14-3. Master creep rupture curve for Inconel 600. 14-8
Figure 16-1. Schematic illustration showing the relation between basal pole intensity at one orientation (h,u) and the plotted value of the intensity at (r,u) on a pole figure..... 16-2
Figure 16-2. Input grid for CTXTUR subcode. 16-3
Figure 16-3. Relation between angles used in the definition of Kearn's texture factor (fu) and angles averaged by CTXTUR subcode. 16-5

TABLES

Table 2-1. Constants used in UO_2 and PuO_2 heat capacity and enthalpy correlations. 2-3
Table 2-2. UO_2 data from Christensen [2.3-21] 2-19
Table 2-3. UO_2 data from Godfrey et al.[2.3-18] 2-20
Table 2-4. UO_2 data from Bates[2.3-19] thermal diffusivity measurements 2-22
Table 2-5. UO2 data, Gibby's[2.3-27] thermal diffusivity measurements. 2-28
Table 2-6. UO_2 data from Weilbacher's[2.3-26] thermal diffusivity measurements. 2-30
Table 2-7. UO_2 data from Goldsmith and Douglas'[2.3-12] thermal diffusivity measurements. 2-31
Table 2-8. UO_2 data from Hobson's[2.3-13] thermal diffusivity measurements. 2-34
Table 2-9. Values of b0 and b1 from various density groups 2-36
Table 2-10. Parameters used in UO_2 and PuO_2 solid phase thermal expansion correlations..... 2-47
Table 2-11. Summary of Young's moduli measured in nonstoichiometric fuel at room temperature. 2-60
Table 2-12. Least squares constants for data of Figure 2-16. 2-63
Table 2-13. Pressure sintering data. 2-103
Table 2-14. UO_2 viscosity data from Tsai and Olander[2.13-4] 2-127
Table 2-15. UO_2 viscosity data from Woodley[2.13-5] 2-128
Table 2-16. Measured and calculated weight gain. 2-158
Table 2-17. Glossary of FORTRAN names. 2-161
Table 3-1. Alpha phase uranium specific heat capacity data. 3-2
Table 3-2. Beta phase uranium specific heat capacity data. 3-4
Table 3-3. Gamma phase uranium specific heat capacity data. 3-4
Table 3-4. Uranium metal thermal conductivity from Touloukian et al. 3-10
Table 3-5. Uranium thermal expansion data from Touloukian et al.[3.3-1] for temperature < 942 K. 3-13
Table 3-6. Uranium thermal expansion data from Touloukian et al.[3.3-1] 942 K < T < 1,045 K. 3-14
Table 3-7. Uranium thermal expansion data from Touloukian et al.[3.3-1] T > 1,045 K. 3-15
Table 3-8. Parabolic Rate Law Constants for the Uranium Steam Reaction. 3-18
Table 4-1. Oxygen content parameters for zircaloy. 4-2
Table 4-2. Zircaloy specific heat capacities for CCP. 4-7
Table 4-3. Specific heat as a function of temperature--beta phase. 4-8
Table 4-4. Uncertainties in specific heat of zircaloy. 4-13
Table 4-5. Values of mass for zircaloy. 4-14
Table 4-6. Uncertainty of zircaloy enthalpy. 4-15
Table 4-7. Zircaloy thermal conductivity data base. 4-19
Table 4-8. Comparison of Mehan and Wiesinger plate expansion with MATPRO model. 4-29
Table 4-9. Bunnell's circumferential thermal expansion data. 4-33
Table 4-10. Bunnell's axial thermal expansion data. 4-35
Table 4-11. Comparison of model predictions and Bunnell's alpha phase data in the diametral direction. 4-39
Table 4-12. Comparison of model predictions and Bunnell's alpha phase data in the axial direction. 4-39

Table 4-13. Beta-phase zirconium Young's Modulus measured by Armstrong and Brown. 4-45
Table 4-14. Beta phase zirconium Young's Modulus measured by Padel and Groff. 4-46
Table 4-15. Young's Modulus measurements by Busby. 4-47
Table 4-16. Young's Modulus measurements by Spasic et al. 4-48
Table 4-17. Young's Modulus measurement by Mehan. 4-49
Table 4-18. Elastic moduli measurements by Northwood et al. 4-50
Table 4-19. Relations between fourth-rank tensor elements and traditional matrix elements..... 4-53
Table 4-20. Measurements of growth in zircaloy tubing. 4-65
Table 4-21. Zircaloy growth data as a function of cold work and fluence. 4-76
Table 4-22. Determination of cold work coefficient. 4-76
Table 4-23. Surface coordinates of probes which measure radial displacement. 4-85
Table 4-24. Radial displacements at 200 hours in Hobson's Test 269-4 (10-3 mm).a 4-86
Table 4-25. Strength coefficient calculated with data of L. S. Rubenstein. 4-125
Table 4-26. Rate of change of K/Ko with oxygen content. 4-127
Table 4-27. Rate of change of n/n_o with oxygen content. 4-129
Table 4-28. Room temperature ultimate strengths of cladding annealed for 1 hour from Howe and Thomas. 4-145
Table 4-29. 644 K test results for unirradiated transient annealed cladding[4.10-2] 4-146
Table 4-30. 644 K test results for irradiated transient annealed cladding[4.10-3] 4-147
Table 4-31. 644 K test results for irradiated isothermally annealed cladding[4.10-3] 4-148
Table 4-32. Strength and residual strength coefficients after isothermal anneals. 4-153
Table 4-33. Strength and residual strength coefficients with modified cold work annealing model. 4-155
Table 4-34. Strength and residual strength coefficients after transient anneals (tests with equal maximum temperature). 4-156
Table 4-35. Strength and residual strength coefficients after transient anneals (test with equal heating rates). 4-157
Table 4-36. Comparison of model predictions of K and n with data base fo unirradiated cladding. 4-162
Table 4-37. Comparison of model predictions of K and n with data base for transient anneals of irradiated cladding. 4-162
Table 4-38. Comparison of model predictions of K and n with data base for isothermal anneals of irradiated cladding. 4-164
Table 4-39. Summary of multirod burst test data employed in CMLIMT. 4-168
Table 4-40. Summary of data from the Hobson-Rittenhouse tests. 4-169
Table 4-41. Summary of data from the Chung-Kassner tests. 4-170
Table 4-42. Summary of data from the Bauer tests 4-171
Table 4-43. Uncertainties in digitized Argonne data. 4-193
Table 4-44. Crack growth rate versus stress intensity range from Rao. 4-198
Table 4-45. Low cycle fatigue material parameters. 4-200
Table 4-46. Rate constants for oxidation by steam. 4-208
Table 4-47. Rate constants for oxidation by UO2. 4-209
Table 4-48. 90% joint confidence intervals for the parabolic rate constants for oxide layer growth, alpha layer growth, and total oxygen uptake 4-220

Table 4-49. Time temperature layer thickness data from Hoffman's[4.15-16] out-of-pile experiments.... 4-222
Table 4-50. Rate equations for hydrogen uptake.... 4-235
Table 5-1. Zircaloy cladding oxide specific heat capacity data from Gilchrist[5.2-3] 5-6
Table 5-2. Stabilized zircaloy dioxide thermal conductivity data from Adams[5.3-1] 5-9
Table 5-3. Zircaloy oxide thermal conductivity data reported by Maki[5.3-2] 5-10
Table 5-4. Zircaloy dioxide thermal conductivity data of Lapshov and Bashkatov[5.3-3] 5-11
Table 5-5. Zircaloy oxide thermal conductivity data of Gilchrist[5.3-4].... 5-12
Table 5-6. Emissivity of thin oxide films as reported by Murphy and Havelock.... 5-19
Table 5-7. Emissivity data from Burgoyne and Garlick.... 5-19
Table 5-8. Emissivity versus oxide thickness from Juenke and Sjodahl's data.... 5-21
Table 5-9. Standard errors of ZOEMIS predictions.... 5-23
Table 5-10. Zircaloy dioxide thermal expansion data by Fulkerson[5.5-3].... 5-27
Table 5-11. Zircaloy dioxide thermal expansion data from Brassfield et al.[5.5-4] 5-28
Table 5-12. Zircaloy dioxide modulus of elasticity data from Brassfield et al.[5.6-1] 5-30
Table 5-13. Zircaloy dioxide tensile strength data from Brassfield et al.[5.7-1] 5-32
Table 6-1. Rate constants for use with Equation (6-13) to predict oxidation.... 6-9
Table 7-1. FeO specific heat capacity data.... 7-4
Table 7-2. Fe2O3 specific heat capacity data.... 7-5
Table 7-3. Fe3O4 specific heat capacity data.... 7-8
Table 7-4. Stainless steel oxide thermal conductivity from Touloukian.... 7-10
Table 8-1. Molar heat capacity constants for Equation (8-1) from Reference 8.2-1.... 8-3
Table 8-2. Thermal conductivity values for Ag-In-Cd recommended by Cohen et al.[8.3-1] 8-7
Table 9-1. Cadmium specific heat as a function of temperature.... 9-1
Table 9-2. Cadmium thermal conductivity as a function of temperature.... 9-2
Table 9-3. Cadmium density as a function of temperature.... 9-3
Table 9-4. Cadmium enthalpy as a function of temperature.... 9-4
Table 10-1. Enthalpy of Inconel as a function of temperature.... 10-1
Table 10-2. Thermal conductivity of Inconel as a function of temperature.... 10-2
Table 11-1. Solidus and liquidus temperatures of UO_{2+x} from Latta and Fryxell.....11-9
Table 11-2. Correlations for liquidus compositions.....11-24
Table 11-3. Correlations for solidus compositions.....11-28
Table 11-4. Data used to produce liquidus correlations.....11-31
Table 11-5. Data used to produce solidus correlations.....11-33
Table 11-6. ZUNTHL calculations and Deem's data11.2-1 for a 0.2 UO_2-0.8 ZrO_2 weight fraction compound.....11-40
Table 11-7. ZUNTHL calculations and Deem's data[11.2-1] for 0.32 UO_2-0.68 ZrO_2 weight fraction compound.....11-40
Table 11-8. ZUNTHL calculations and Deem's data11.2-1 for a 0.5 UO_2-0.5 ZrO_2 weight fraction compound.....11-42
Table 11-9. ZUNTHL calculations and Deem's data[11.2-1] for 0.94 UO_2-0.06 ZrO_2 weight fraction compound.....11-43
Table 11-10. ZUTCON calculations and Deem's results[11.3-3] for 0.2 UO_2-0.8 ZrO_2 weight fraction compound.....11-47

Table 11-11. ZUTCON calculations and Deem's Results[11.3-3] for 0.32 UO_2-0.68 ZrO_2 weight fraction compound. 11-47
Table 11-12. ZUTCON calculations and Deem's results[11.3-3] for 0.5 UO_2-0.5 ZrO_2 weight fraction compound. 11-48
Table 11-13. ZUTCON calculations and Deem's results11.3-3 for a low-density 0.32 UO_2-0.68 ZrO_2 weight fraction compound. 11-49
Table 11-14. ZUTCON calculations and Deem's results11.3-3 for 0.94 UO_2-0.06 ZrO_2 weight fraction compound. 11-49
Table 11-15. ZUTEXP calculations and Deem's data[11.4-1] for a 0.2 UO_2-0.8 ZrO_2 weight fraction compound. 11-55
Table 11-16. ZUTEXP calculations and Deem's data[11.4-1] for 0.32 UO_2-0.68 ZrO_2 weight fraction compound. 11-55
Table 11-17. ZUTEXP calculations and Deem's data[11.4-1] for a 0.5 UO_2-0.5 ZrO_2 weight fraction compound. 11-56
Table 11-18. ZUTEXP calculations and Deem's data[11.4-1] for 0.94 UO_2-0.06 ZrO_2 weight fraction compound. 11-57
Table 11-19. ZUDEN calculations and Deem's compound density data[11.4-1] 11-57
Table 11-20. Constants for thermal expansion strain. 11-58
Table 11-21. Call variable to the subroutine ZUBET1. 11-66
Table 12-1. Data used to find the liquidus in the Ag-rich region. 12-4
Table 12-2. Data used to find the liquidus in the Zr-rich region. 12-5
Table 13-1. Constants used to calculate C_p. 13-2
Table 13-2. Constants used in gas thermal conductivity correlations. 13-4
Table 13-3. Uncertainty of the gas thermal conductivity correlations. 13-5
Table 13-4. Surface accommodation coefficients. 13-6
Table 13-5. Pure gas conductivity references. 13-7
Table 13-6. Coefficients used to calculate CW. 13-26
Table 14-1. Constants used to solve creep rupture equation. 14-4
Table 14-2. Creep rupture data of A-508 pressure vessel carbon steel. 14-4
Table 14-3. Tensile test data of A-508 pressure vessel carbon steel. 14-5
Table 14-4. Stainless steel creep rupture data. 14-5
Table 14-5. Inconel 600 creep rupture data. 14-6
Table 14-6. Enthalpy of carbon steel as a function of temperature. 14-9
Table 14-7. Thermal conductivity of carbon steel as a function of temperature. 14-10
Table 14-8. Density of carbon steel as a function of temperature. 14-11
Table 15-1. Specific heat of tungsten as a function of temperature. 15-1
Table 15-2. Thermal conductivity of tungsten as a function of temperature. 15-2
Table 16-1. Heats of fusion calculated in QFUSON. 16-6

SCDAP/RELAP5/MOD3.1 Code Manual Volume IV: MATPRO—A Library of Materials Properties for Light-Water-Reactor Accident Analysis

1. INTRODUCTION

The SCDAP/RELAP5 computer code is designed to describe the overall reactor coolant system (RCS) thermal-hydraulic response, core damage progression, and, in combination with VICTORIA,[1-1] fission product release and transport during severe accidents. The code is being developed at the Idaho National Engineering Laboratory (INEL) under the primary sponsorship of the Office of Nuclear Regulatory Research of the U.S. Nuclear Regulatory Commission (NRC).

1.1 General Code Capabilities

The code is the result of merging the RELAP5/MOD3[1-2] and SCDAP[1-3] models. The RELAP5 models calculate the overall RCS thermal hydraulics, control system interactions, reactor kinetics, and transport of noncondensable gases. Although previous versions of the code have included the analysis of fission product transport and deposition behavior using models derived from TRAP-MELT, this capability is being replaced through a data link to the detailed fission product code, VICTORIA, as a result of an effort to reduce duplicative model development and assessment. The SCDAP models calculate the damage progression in the core structures and the formation, heatup, and melting of debris.

SCDAP/RELAP5 is capable of modeling a wide range of system configurations from single pipes to different experimental facilities to full-scale reactor systems. The configurations can be modeled using an arbitrary number of fluid control volumes and connecting junctions, heat structures, core components, and system components. Flow areas, volumes, and flow resistances can vary with time through either user control or models that describe the changes in geometry associated with damage in the core. System structures can be modeled with RELAP5 heat structures, SCDAP core components, or SCDAP debris models. The RELAP5 heat structures are one-dimensional models with slab, cylindrical, or spherical geometries. The SCDAP core components include representative light water reactor (LWR) fuel rods, silver-indium-cadmium (Ag-In-Cd) and B_4C control rods and/or blades, electrically heated fuel rod simulators, and general structures. A two-dimensional, finite element model based upon the COUPLE[1-4] code may be used to calculate the heatup of debris and/or surrounding structures. This model takes into account the decay heat and internal energy of newly fallen or formed debris and then calculates the transport by conduction of this heat in the radial and axial directions to the wall structures and water surrounding the debris. Perhaps the most important use of this model is to calculate the heatup of the vessel wall so that the time at which the vessel may rupture can be determined. Other system components available to the user include pumps, valves, electric heaters, jet pumps, turbines, separators, and accumulators. Models to describe selected processes, such as reactor kinetics, control system response, and tracking noncondensable gases, can be invoked through user control.

The development of the current version of the code was started in the spring of 1992. This version contains a number of significant improvements since the last versions of the code, SCDAP/RELAP5/MOD2.5 and SCDAP/RELAP5/MOD3[7af], were released. These improvements include the addition of several new models to describe the earlier phases of a severe accident, changes in the late phase models to

provide more “physically intuitive” behavior for full plant calculations, and changes to improve the overall reliability and usability of the code. The improvements in the early phase models include the addition of models to treat (a) the effects of grid spacers including the effects of Inconel spacer grid-zircaloy cladding material interactions, (b) BWR B_4C control blade-zircaloy channel box material interactions, and (c) accelerated heating, melting, and hydrogen generation during the reflood of damaged fuel rods. An extension to the molten pool models to treat the sporadic growth of the boundaries of the molten pool into adjacent regions of relatively intact assemblies or rubble debris beds is the most significant change to the late phase models. Improvements in overall reliability and usability of the code for plant calculations include changes in the overall code numerics to reduce the likelihood of numerical instabilities or code failures and changes in the codes input/output processors. The most noticeable of these for the code users is the conversion of the SCDAP input to a form more compatible with the RELAP5 style. In addition to these modeling and coding changes, SCDAP/RELAP5/MOD3.1 has also been subjected to (a) an intensive effort of verification testing to identify and resolve outstanding code errors and (b) a systematic assessment of the code to quantify uncertainties in the predicted results.

1.2 Relationship to Other NRC-Sponsored Software

SCDAP/RELAP5 and RELAP5 are developed in parallel and share a common configuration. Both codes share a common source deck. Separate codes are formed only prior to compilation, so changes made to the source deck are automatically reflected in both codes.

The development and application of the code is also related to several other NRC-sponsored software packages. Theoretical work associated with the development of PARAGRASS-VFP[1-5] has resulted in model improvements for fission product release. A data link to the VICTORIA code will allow for the detailed treatment of phenomena such as fission product and aerosol transport, deposition, and resuspension. A link with PATRAN[1-6] and ABAQUS[1-7] provides the user with the means to calculate the details of lower head failure. Animated plant response displays are possible through links to the Nuclear Plant Analyzer (NPA)[1-8] display software, which gives the user an efficient way of analyzing the large amount of data generated. Detailed plant simulations from accident initiation through release of fission products to the atmosphere are made available through links to the CONTAIN[1-9] containment response and CRAC2[1-10] or MACCS[1-11] atmospheric dispersion consequence codes.

1.3 Quality Assurance

SCDAP/RELAP5 is maintained under a strict code configuration system that provides a historical record of the changes made to the code. Changes are made using an update processor that allows separate identification of improvements made to each successive version of the code. Modifications and improvements to the coding are reviewed and checked as part of a formal quality program for software. In addition, the theory and implementation of code improvements are validated through assessment calculations that compare the code-predicted results to idealized test cases or experimental results.

1.4 Organization of the SCDAP/RELAP5 Manuals

The specific features of SCDAP/RELAP5/MOD3.1 are described in a five-volume set of manuals covering the theory, use, and assessment of the code for severe applications. Although Volume I describes (a) the overall code architecture, (b) interfaces between the RELAP5 system models, and (c) any system models unique to SCDAP/RELAP5, the code user is referred to the companion set of six volumes which describe the RELAP5[1-2] system thermal hydraulics and associated models.

Volume I presents a description of SCDAP/RELAP5/MOD3.1-specific thermal-hydraulic models (relative to RELAP5/MOD3), and interfaces between the thermal-hydraulic models and damage progression models.

Volume II contains detailed descriptions of the severe accident models and correlations. It provides the user with the underlying assumptions and simplifications used to generate and implement the basic equations into the code, so an intelligent assessment of the applicability and accuracy of the resulting calculation can be made.

Volume III provides the user's guide and code input for the severe accident modeling. SCDAP input was recently changed to be consistent with the free-form input used by RELAP5. User guidelines are produced specifically for the severe accident code. The user should also refer to the RELAP5/MOD3 Code Manual Volume V: User Guidelines for a complete set of guidelines.

Volume IV describes the material property library, MATPRO. It contains descriptions of the material property subroutines available for severe accident analysis.

Volume V documents the assessments of SCDAP/RELAP5/MOD3.1 performed on versions released since the 1993 deficiency resolution effort. It includes nodalization sensitivity studies and time-step sensitivity studies, assessments using standard PWR and BWR plant models, and assessments using code-to-data comparisons.

1.5 Organization of Volume IV

Publication of a set of materials properties descriptions intended to provide a common base for reactor analysis began in 1974. The descriptions have been revised from time to time, as required by new data or consideration of new materials and temperature ranges.[1-12 - 1-19] This MATPRO document is the only formal description of the package published since the last release of the SCDAP/RELAP5 code manuals.[1-20] This volume contains descriptions of all MATPRO subroutines used by SCDAP/RELAP5 (subroutines dealing with fission product transport and deposition have been replaced by a data link to VICTORIA). Also, material properties have been updated. The materials whose properties were updated include: uranium dioxide, uranium alloys, zircaloy, Inconel, and zirconium-uranium compounds. Furthermore, three new materials descriptions were added. They are cadmium, carbon steel, and tungsten.

The descriptive detail provided for the subroutines presented in this document varies because the subroutine documentation came from many different resources, including the MATPRO-11 Revision 2 document,[1-12] a series of informal reports dealing with materials properties subroutines that have been incorporated into SCDAP/RELAP5, and previously undocumented materials properties subroutines that

are contained in the SCDAP/RELAP5 computer code or in the MATPRO library of materials properties subroutines. The correlations used in MATPRO-11 Revision 2 were developed using an extensive literature search, whereas later correlations were developed as their need became evident or new and relevant experimental data became available, such as the dissolution model for UO_2 in zircaloy. A less extensive literature search was used to develop the correlations used to calculate the materials properties in the models developed after the publication of the MATPRO-11 Revision 2 document.

1.6 References

1-1. T. Heames et al., *VICTORIA: A Mechanistic Model of Radionuclide Behavior in the Reactor Coolant System Under Sever Accident Conditions,* NUREG/CR-5545, SAND90-0756, Rev. 1, December 1992.

1-2. C. M. Allison, C. S. Miller, N. L. Wade (Eds.) *RELAP5/MOD3 Code Manual,* Volumes I through IV, NUREG/CR-5535, EGG-2596, June 1990.

1-3. C. M. Allison and G. H. Beers, "Comparisons of the SCDAP Computer Code with Bundle Data Under Severe Accident Conditions," *Seventh International SMIRT Conference,* Chicago, Illinois, August 22-26, 1983.

1-4. E. C. Lemmon, *COUPLE/FLUID: A Two-Dimensional Finite Element Thermal Conduction and Advection Code*, EGG-ISD-SCD-80-1, February 1980.

1-5. J. Rest and S. A. Zawadzki, "FASTGRASS-VFP/PARAGRASS-VFP Version 50531, Users Guide," *Argonne National Laboratory Quarterly Report, January-March 1983,* Volume I, NUREG/CR-3689, ANL-83-85 Volume I, June 1983.

1-6. *PATRAN Plus User's Manual*, Release 2.4, PDA Engineering, Costa Mesa, California, 1987.

1-7. *ABAQUS User's Manual*, Version 4.6, Hibbitt, Karlsson & Sorensen, Inc., Providence, Rhode Island, 1987.

1-8. D. M. Snider, K. L. Wagner, W. Grush, *Nuclear Plant Analyzer (NPA) Reference Manual Mod1*, EGG-EAST-9096, April 1990.

1-9. K. D. Bergeron et al., *User's Manual for CONTAIN 1.0, A Computer Code for Severe Nuclear Reactor Accident Containment Analysis*, NUREG/CR-4085, SAND84-1204, May 1985.

1-10. L. T. Ritchie et al., *CRAC2 Model Description*, NUREG/CR-2552, SAND82-0342, March 1984.

1-11. D. I. Chanin et al., *MELCOR Accident Consequence Code System (MACCS Version 1.5)*, NUREG/CR-4691, SAND86-1562, July 1988, DRAFT.

1-12. D. L. Hagrman, G. A. Reyman, R. E. Mason, *MATPRO-Version 11 (Revision 2), A Handbook of Materials Properties for Use in the Analysis of Light Water Reactor Fuel Rod Behavior*, NUREG/CR-0479, TREE-1280, Revision 2, August 1981.

1-13. R. L. Miller, R. R. Hobbins, V. F. Baston, and W. A. Yuill, *FRAP-T: A Computer Code for the Transient Analysis of Oxide Fuel Rods. Vol. 2, MATPRO Materials Properties Subcode,* I-243-2, 1974.

1-14. P. E. MacDonald and L. B. Thompson (eds.), *MATPRO A Handbook of Materials Properties for Use in the Analysis of Light Water Reactor Fuel Rod Behavior,* ANCR-1263, February 1976.

1-15. P. E. MacDonald and L. B. Thompson (eds.), *MATPRO-Version 09 A Handbook of Materials Properties for Use in the Analysis of Light Water Reactor Fuel Rod Behavior,* TREE-NUREG-1005, December 1976.

1-16. G. A. Reymann (ed.), *MATPRO-Version 10 A Handbook of Materials Properties for Use in the Analysis of Light Water Reactor Fuel Rod Behavior*, TREE-NUREG-1180, February 1978.

1-17. D. L. Hagrman and G. A. Reymann (eds.), *MATPRO-Version 11 A Handbook of Materials Properties for Use in the Analysis of Light Water Reactor Fuel Rod Behavior,* NUREG/CR-0497, TREE-1280, February 1979.

1-18. D. L. Hagrman, G. A. Reymann, and R. E. Mason (eds.), *MATPRO-Version 11 (Revision 1) A Handbook of Materials Properties for Use in the Analysis of Light Water Reactor Fuel Rod Behavior,* NUREG/CR-0497, TREE-1280, Rev. 1, February 1980.

1-19. D. L. Hagrman, G. A. Reymann, and R. E. Mason (eds.), *MATPRO Version 11 (Revision 2) A Handbook of Materials Properties for Use in the Analysis of Light Water Reactor Fuel Rod Behavior,* NUREG/CR-0497, TREE-1280, Rev.# 2, August 1981.

1-20. C. M. Allison et. al, *SCDAP/RELAP5/MOD3 Code Manual*, Volumes I through IV, NUREG/CR-5273, EGG-2555, September 1990.

2. URANIUM DIOXIDE/MIXED OXIDES

Sixteen materials properties of LWR fuel have been modeled for inclusion in MATPRO. The approaches range from (a) a least-squares fit to available data using a polynomial or other function having little or no theoretical basis to (b) a semiempirical correlation employing an analytical expression suggested by theory with constants determined by comparison with data. The intent of current and future work is to take the second approach wherever possible.

All 16 MATPRO fuel subcodes have temperature as an argument. In addition, many are functions of burnup, plutonia content, density, time, and other variables.

2.1 Melting Temperature and Heat of Fusion (FHYPRP)

2.1.1 Melting Temperature

The subroutine FHYPRP calculates the lowest temperature with a liquid phase (solidus) and the highest temperature with a solid phase (liquidus) of UO_2 and $(U,Pu)O_2$. These temperatures are calculated as a function of burnup and plutonia content.

2.1.1.1 ***Model Development.*** The equations used to calculate the UO_2 and $(U,Pu)O_2$ melting points utilize 3,113.15 K as the melting temperature of uranium (experimentally by Brassfield,[2.1-1)] and a least-squares fit to parabolic equations for the solidus and liquidus boundaries from the Lyon and Baily[2.1-2] phase diagram for the stoichiometric $(U,Pu)O_2$ mixed oxide. The equations used are as follows:

For plutonia compositions > 0,

$$T_{sol} = 3{,}113.15 - 5.41395\ C + 7.468390 \times 10^{-3}\ C^2 - 3.2 \times 10^{-3}\ FBu. \quad (2\text{-}1)$$

$$T_{liq} = 3{,}113.15 - 3.21660\ C - 1.448518 \times 10^{-2}\ C^2 - 3.2 \times 10^{-3}\ FBu. \quad (2\text{-}2)$$

For plutonia compositions = 0,

$$T_{sol} = 3{,}113.15 - 3.2 \times 10^{-3}\ FBu. \quad (2\text{-}3)$$

$$T_{liq} = T_{sol} \quad (2\text{-}4)$$

where

T_{sol}	=	the solidus temperature (K)
T_{liq}	=	the liquidus temperature (K)
C	=	PuO_2 content (wt%)
FBu	=	burnup (MWd/tU).

2.1.2 UO_2 and $(U,Pu)O_2$ Heat of Fusion

The two calorimetrically determined values for the heat of fusion of unirradiated UO_2 are in good agreement. Specifically, Hein and Flagella[2.1-3] found 76.1 ± 2 kJ/mol, and Leibowitz[2.1-4] reported a value of 74 kJ/mol. These results suggest that the heat of fusion of unirradiated UO_2 is adequately known from present analyses. The routine PHYPRP uses Leibowitz's calorimetry value of 2.74×10^5 J/kg for the heat of fusion of UO_2.

Leibowitz[2.1-5] determined a heat of fusion for mixed oxides of 67 kJ/mol from three tests. This 10% agreement between UO_2 and mixed oxide values for the heat of fusion is reasonable because of the similarity in crystal structure and atomic bonding. Therefore, unless conflicting data become available, the UO_2 value will be used for the heat of fusion of mixed oxides.

2.1.3 Reference

2.1-1 H. C. Brassfield et al., *Recommended Property and Reactor Kinetics Data for Use in Evaluating a Light-Water-Coolant Reactor Loss-of-Coolant Incident Involving Zircaloy-4 or 304-SS-Clad UO_2*, GEMP-482, April 1968.

2.1-2 W. F. Lyon and W. E. Baily, *The Solid-Liquid Phase Diagram for the UO_2-PuO_2 System*, Journal of Nuclear Materials, 22, 332, 1967.

2.1-3 A. Hein and P. N. Flagella, *Enthalpy Measurements of UO_2 and Tungsten to 3,260 K*, GE-NMPO-578, February 1968.

2.1-4 L. Leibowitz et al., *Enthalpy of Liquid Uranium Dioxide to 3,500 K, Journal of Nuclear Material, 39* (1971), p. 115.

2.1-5 L. Leibowitz, D. F. Fischer, and M. G. Chasanov, *Enthalpy of Molten Uranium-Plutonium Oxide*, ANL-8082, February 1975.

2.2 Specific Heat Capacity and Enthalpy (FCP, FENTHL)

The specific heat capacity of nuclear fuel is needed for time dependent temperature calculations. The stored energy, or enthalpy, is calculated from the specific heat capacity. Stored energy is important in reactor transient analysis because the severity of the transient is greatly affected by the initial stored energy of the fuel.

2.2.1 Summary

The specific heat capacity and enthalpy of nuclear fuel are modeled empirically as functions of four parameters: temperature, composition, molten fraction, and oxygen to metal ratio. Since UO_2 and PuO_2 are the principal LWR fuels, they are the constituents considered. The correlations for fuel specific heat and enthalpy are valid for temperatures from 300 K to more than 4,000 K.

Equations for the specific heat and enthalpy of solid UO_2 and PuO_2 are assumed to have the same form, but with different constants. The basic equations are

$$FCP = \frac{K_1 \theta^2 e^{\left(\frac{\theta}{T}\right)}}{T^2 \left[e^{\left(\frac{\theta}{T}\right)} - 1 \right]^2} + K_2 T + \frac{Y K_3 E_D}{2RT^2} e^{\left(\frac{-E_D}{RT}\right)} \tag{2-5}$$

and

$$FENTHL = \frac{K_1 \theta}{e^{(\theta/T)} - 1} + \frac{K_2 T^2}{2} + \frac{Y}{2} \{ K_3 e^{[-E_D/(RT)]} \} \tag{2-6}$$

where

FCP	=	specific heat capacity (J/k**g** · K)
FENTHL	=	fuel enthalpy (J/kg)
T	=	temperature (K)
Y	=	oxygen to metal ratio
R	=	universal gas constant = 8.3143 (J/mol · K)
θ	=	the Einstein temperature (K)

and the constants are given in Table 2-1.

Table 2-1. Constants used in UO_2 and PuO_2 heat capacity and enthalpy correlations.

Constant	UO_2	PuO_2	Units
K_1	296.7	347.4	J/kg · K
K_2	2.43×10^{-2}	3.95×10^{-4}	J/kg · K^2
K_3	8.745×10^{7}	3.860×10^{7}	J/kg
θ	535.285	571.000	K
E_D	1.577×10^{5}	1.967×10^{5}	J/mol

The specific heat capacities of UO_2 and PuO_2 in the liquid state are given by

$$FCP = 503 \text{ J/kg} \cdot \text{K}. \tag{2-7}$$

For a mixture of UO_2 and PuO_2, the specific heat capacity of the solid is determined by combining the contribution from each constituent in proportion to its weight fraction. When the material is partially molten, the heat capacity is determined similarly with a weighted sum. The standard error of the UO_2 specific heat capacity correlation is ± 3 J/kg · K; and, for the mixed oxide specific heat capacity correlation, it is 6 to 10 J/kg · K, depending on the fraction of PuO_2. For nonstoichiometric fuels, these uncertainties are approximately doubled.

Inspection of Equations (2-5) and (2-6) shows that the fuel enthalpy correlation is simply the integral of fuel specific heat correlation from 0 K to T (K). Because the specific heat correlation is only valid above a fuel temperature of about 300 K, the fuel enthalpy correlation is not valid below a temperature of about 300 K. Therefore, it is necessary to calculate fuel enthalpy with respect to a reference temperature $\geq$ 300 K. Thus, the fuel enthalpy at any desired temperature T, is calculated by evaluating Equation (2-6) at T and a reference temperature, T_{ref}, of 300 K and taking the difference [FENTHL (T) - FENTHL (T_{ref})]. For temperatures greater than 2 K below melting, the molten fraction and heat of fusion are used to interpolate between the enthalpy of unmelted fuel and just melted fuel at the melting temperature

Section 2.2.2 is a review of the surveyed literature. The model development is presented in Section 2.2.3. Model predictions are compared with data in Section 2.2.4. An uncertainty analysis is given in Section 2.2.5.

2.2.2 Literature Review

An important source for fuel specific heat capacity data is the extensive review by Kerrisk and Clifton.[2.2-1] Additional data from Kruger and Savage[2.2-2] are used to find the parameters for PuO_2 in Equation (2-5). The heat capacity of liquid fuel is taken from Leibowitz.[2.2-3] Literature relevant to the heat of fusion, which is used for the enthalpy model is discussed in Section 2.2.

2.2.2.1 ***Limitations of the Data Source.*** The data used by Kerrisk and Clifton cover a wide range of temperatures (483 to 3,107 K), but these data are restricted to nearly stoichiometric material (oxygen to metal ratio between about 2.00 and 2.015). The data of Kruger and Savage are limited in that the highest reported temperature was only 1,400 K, which is well below the melting point of PuO_2, about 2,600 K. Their data are also restricted to approximately stoichiometric PuO_2. The oxygen-to-metal ratio has been shown to be significant by Gronvold[2.2-4] and by Affortit and Marcon.[2.2-5]

The specific heat capacity of liquid fuel taken from Leibowitz is applicable to UO_2 only. The assumption is made that the liquid UO_2 value is also valid for liquid PuO_2. Although departures from stoichiometry were found to be significant for solid fuel, no experimental effort has been made to assess the importance of this parameter in the liquid state.

2.2.2.2 ***Other Data Sources.*** Several other data sources are used to estimate the uncertainty of the model but not in its development. These sources are cited in Section 2.2.5, where the uncertainty is analyzed.

2.2.3 Model Development

The most common technique of determining specific heat capacity is to measure the enthalpy of a sample by drop calorimetry and deduce the heat capacity by finding the rate of enthalpy change with temperature. Generally, the enthalpy data are fitted using an empirical function, often a simple polynomial equation. Whereas the accuracy of this approach is good, a function based on first principles is preferable because it allows the identification of the physical processes involved and can be extrapolated beyond its temperature base with some degree of confidence. This approach was used by Kerrisk and Clifton and is adopted here.

2.2.3.1 ***Specific Heat Capacity of a Typical Solid.*** The lattice specific heat capacity of solids at constant volume can be characterized theoretically quite well using the Debye model for specific heat. Except at low temperatures, a similar but simpler theory developed earlier by Einstein is also adequate.

These theories are described in the most basic solid state textbooks, such as Kittel.[2.2-6] The Einstein formulation is used here because of its simplicity. This formulation is

$$C_V = \frac{K_1 \theta^2 e^{\left(\frac{\theta}{T}\right)}}{T^2 \left[e^{\left(\frac{\theta}{T}\right)} - 1 \right]^2} \tag{2-8}$$

where

C_v	=	specific heat capacity (J/kg · K)
K_1	=	constant to be determined (J/kg · K).

Equation (2-8) gives the specific heat capacity at constant volume. In most reactor situations, the specific heat capacity at constant pressure, C_p, is more appropriate. The relationship between the two is[2.2-7]

$$C_p = C_V + \left(\alpha^2 \frac{V}{\beta}\right) T \tag{2-9}$$

where

α	=	coefficient of thermal expansion (K^{-1})
β	=	coefficient of compressibility (Pa^{-1})
V	=	molar volume (m^3).

The temperature dependence of α^2 (V/β) in Equation (2-9) is complicated. The compressibility of a liquid or a solid is nearly constant with temperature, but the molar volume and the coefficient of thermal expansion change with temperature. However, expressing the quantity (C_p-C_v) as a function of a constant times temperature yields results well within the scatter of the data. Therefore, C_p is expressed as

$$C_p = C_v + K_2 T \tag{2-10}$$

where C_v is given by Equation (2-8) and K_2 is a constant to be determined by comparison with data.

2.2.3.2 *Defect Energy Contribution to the Specific Heat Capacity.* At temperatures > 1,500 K, the specific heat capacity data show a rapid increase not described by Equation (2-10). This increase is generally attributed to the energy necessary to form Frenkel defects.[2.2-7,2.2-8,2.2-9] Some investigators [2.2-4,2.2-8] have suggested that Schottky defects may also contribute to this rapid increase. However, the assumption used in this model is that the rapid increase in specific heat capacity > 1,500 K is due to formation of Frenkel defects. The functional form of the extra term that should be added to Equation (2-10) may be found from the defect energy contribution to the enthalpy given by[2.2-6]and R and T were previously defined in Equation (2-5). To determine the defect contribution to the specific heat capacity, the derivative of H_D with respect to temperature, C_D is given by

$$H_D = K_3 e^{(-E_D/RT)} \tag{2-11}$$

where

H_D	=	defect energy contribution to enthalpy (J)
E_D	=	activation energy for Frenkel defects (J/mol)
K_3	=	constant to be determined (J)

and R and T were previously defined in Equation (2-5). To determine the defect contribution to the specific heat capacity, the derivative of H_D with respect to temperature, C_D is given by

$$C_D = \frac{K_3 E_D}{RT^2} e^{\left(-\frac{E_D}{RT}\right)}. \tag{2-12}$$

Combining Equations (2-8), (2-10), and (2-12) gives the general expression for specific heat capacity

$$C_p = \frac{K_1 \theta^2 e^{\left(\frac{\theta}{T}\right)}}{T^2\left[e^{\left(\frac{\theta}{T}\right)} - 1\right]^2} + K_2 T + \frac{K_3 E_D}{RT^2} e^{\left(-\frac{E_D}{RT}\right)}. \tag{2-13}$$

2.2.3.3 ***Determination of the Constants in the Model.*** For UO_2, the values of the five constants, K1, K2, K3, q, and E_D, are taken from Kerrisk and Clifton. For PuO_2, the constants are determined by fitting the data of Kruger and Savage. In both cases, the fuel was nearly stoichiometric. Data sources for pure PuO_2 are scarce. One potential source is the work of Affortit and Marcon. However, they give only correlations determined from fitting the data and not the actual data. Also, they do not present an uncertainty analysis. Without knowing the number or accuracy of the data on which their correlations are based, it is not possible to estimate what weight to give to their results. Therefore, their correlations were not used to determine the constants of Equation (2-13). However, their work was useful for the assessment of the effects of departure from stoichiometry.

It should be noted that the constants determined for Equation (2-13) are only valid at fuel temperatures > 300 K. Data < 300 K were not used to determine the constants of Table 2-1, and the Einstein formulation assumes temperatures above the Einstein temperature, θ.

2.2.3.4 ***Effect of Nonstoichiometry.*** Several investigators have found the oxygen-to-metal ratio of fuel to influence the specific heat capacity.[2.2-1,2.2-5,2.2-8,2.2-10] At temperatures > 1,300 K, departures from stoichiometry typical of those found in LWR fuel have caused changes in the specific heat capacity greater than the data scatter. The most complete analysis of this effect has been done by Affortit and Marcon. Even though their results are quantitatively different (see Figures 2-1 and 2-2), made from their correlations) from sources used to develop this model, they illustrate well the qualitative aspects of this effect. Figure 2-1 is for UO_2, and Figure 2-2 is for mixed oxide fuels. These figures show that the specific heat capacity increases as the oxygen-to-metal ratio becomes larger than 2.

Very hyperstoichiometric materials, such as U_4O_9 and U_3O_8, have specific heat capacities considerably larger than that of UO_2.[2.2-4,2.2-11] In addition, these materials exhibit peaks in specific heat capacity at temperatures associated with phase transitions. However, the incidence of these states in LWR fuel is infrequent and their influence is neglected in this model.

In reactor fuel, nonstoichiometry is believed to be due to oxygen interstitials for hyperstoichiometric fuel and oxygen vacancies for hypostoichiometric fuel.[2.2-8] Excess oxygen tends to increase and an oxygen deficiency tends to decrease the probability of formation of Frenkel and Schottky defects, thereby changing the specific heat capacity. Thus, the logical adjustment to Equation (2-13) to account for the oxygen-to-metal ratio effect is in its last term, which includes the effect of defect formation. By multiplying the term by the oxygen-to-metal ratio divided by 2.0, the following desirable features are produced.

1. The correlation is unaffected for stoichiometric fuel.
2. The proper temperature dependence is obtained.
3. The specific heat capacity is increased for hyperstoichiometry and decreased for hypostoichiometry, in accordance with the data.

Therefore, this correction has been made to Equation (2-13), giving Equation (2-5). This is the model used for the specific heat capacity of solid UO_2 and PuO_2.

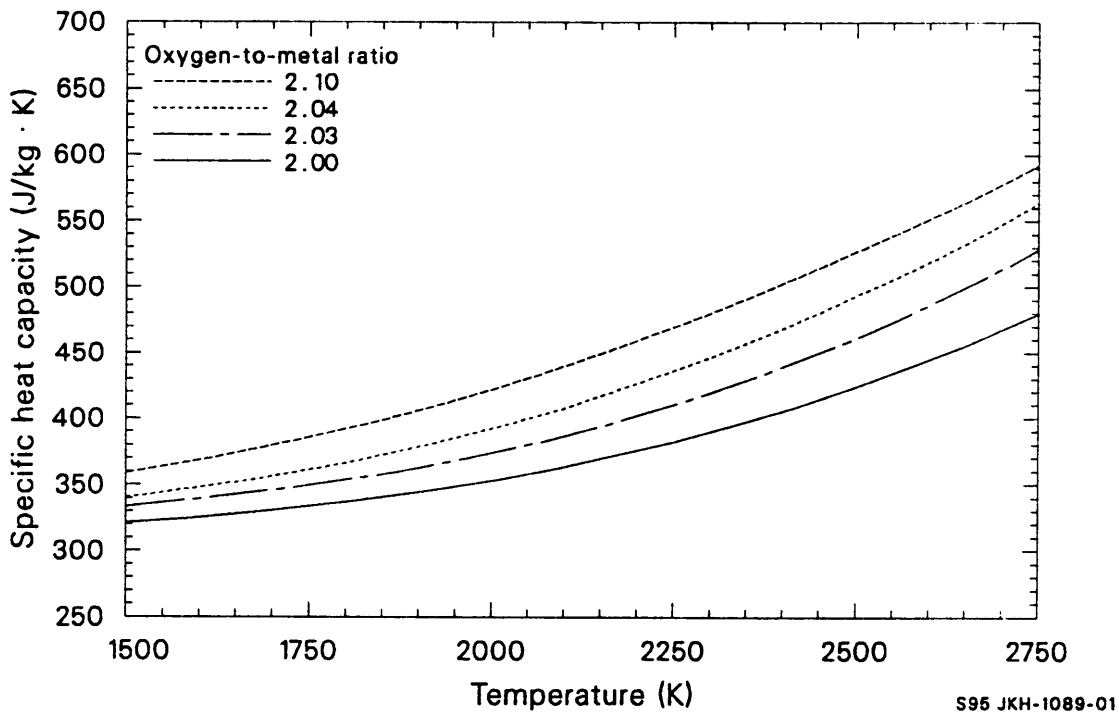

Figure 2-1. Specific heat capacity as a function of temperature and oxygen-to-metal ratio for UO_2.

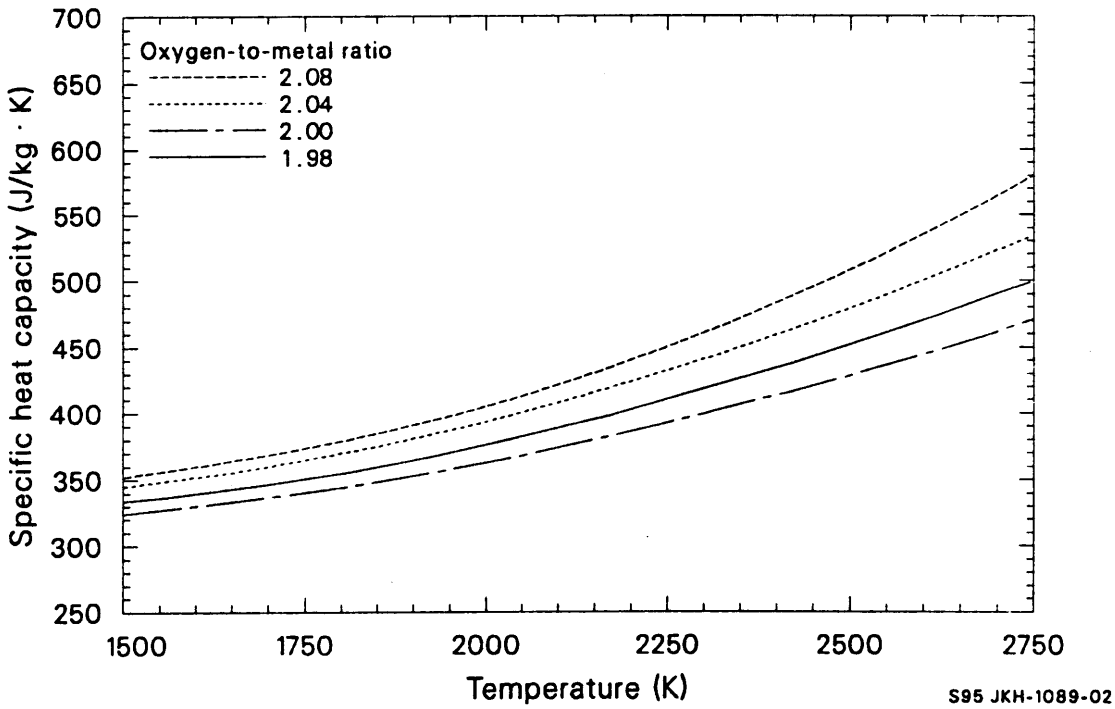

Figure 2-2. Specific heat capacity as a function of temperature and oxygen-to-metal ratio for $(U_{0.8}Pu_{0.2})O_{2+x}$.

If the fuel consists of a mixed oxide (MO_2) with a weight fraction of PuO_2 equal to FCOMP, then the specific heat capacity of the mixed oxide fuel is calculated by the expression

$$FCP_{MO_2} = FCP_{UO_2}(1 - FCOMP) + FCP_{PuO_2} \cdot FCOMP. \tag{2-14}$$

If the fuel temperature is greater than the fuel melting temperature, FTMELT, plus the liquid solid coexistence temperature, then the fuel specific heat capacity is not calculated using Equation (2-5) but is set equal to the specific heat of liquid fuel, 503 J/kg · K, for both UO_2 and PuO_2 fuel. If the fuel temperature is equal to the fuel melting temperature, TMELT, then the specific heat capacity is calculated by the expression

$$FCP = (1.0 - R)\ FCP\ (T - TMELT) + R \cdot FCPMOL \tag{2-15}$$

where

R = fraction of fuel that is molten (unitless)

FCPMOL = specific heat capacity of liquid fuel (503 J/kg · K).

Fuel enthalpy, FENTHL, for solid fuel is found by integrating Equation (2-5) with respect to temperature over the interval 0 K to T K. The result of the integration is the expression

$$\mathrm{FENTHL} = \frac{K_1\theta}{e^{(\theta/T)} - 1} + \frac{K_2T^2}{2} + \frac{Y}{2}\left[K_3 e^{\left(-\frac{E_D}{RT}\right)}\right]. \tag{2-16}$$

Figure 2-3 shows the enthalpy of UO_2 versus temperature calculated using Equation (2-6).

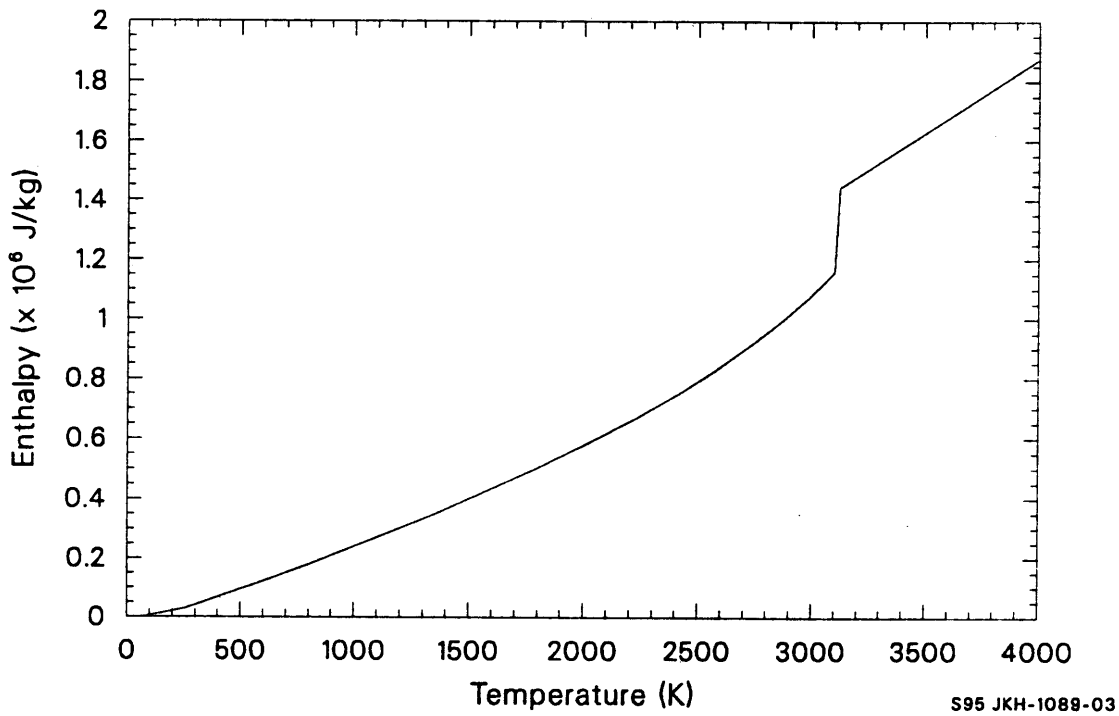

Figure 2-3. Enthalpy of UO_2 as a function of temperature to 4,000 K.

If the fuel consists of a mixed oxide with a weight fraction of PuO_2 equal to FCOMP, then the enthalpy of the mixed oxide fuel is calculated by the expression

$$\mathrm{FENTHL}_{MO_2} = \mathrm{FENTHL}_{UO_2}(1 - \mathrm{FCOMP}) + \mathrm{FENTHL}_{PuO_2} \cdot \mathrm{FCOMP}. \tag{2-17}$$

If the fuel temperature is equal to the fuel melting temperature, FTMELT, then the fuel enthalpy is calculated by the expression

$$\mathrm{FENTHL} = \mathrm{FENTHL(FTMELT)} + \mathrm{FHEFUS} \bullet \mathrm{FACMOT} \tag{2-18}$$

where

FTMELT = melting temperature minus a vanishingly small increment (K)

FHEFUS = heat of fusion of the fuel (J/kg)

FACMOT = fraction of the fuel that is molten (unitless).

If the fuel temperature, FTEMPT, is greater than the fuel melting temperature, then the fuel enthalpy is calculated by the expression

$$\text{FENTHL} = \text{FENTHL(FTMELT)} + \text{FHEFUS} + (\text{FTEMP} - \text{FTMELT}) \cdot \text{FCPMOL} \tag{2-19}$$

where FCPMOL is the specific heat capacity of molten fuel (J/kg · K).

2.2.4 Model Comparisons with Data

Figure 2-4 shows the specific heat capacity correlation, FCP, for UO_2 compared with data from three sources.[2.2-4,2.2-12,2.2-13] These data were taken from experiments using stoichiometric UO_2. At the high end of the temperature interval (a few hundred K below the melting temperature), the data fall below the model calculations. (This is probably the result of partial melting due to a nonuniform temperature distribution within the sample.) For example, the measured specific heat capacity would be smaller because the specific heat capacity in a liquid is considerably lower than in a solid. A similar comparison is shown in Figure 2-5 for PuO_2. In this instance, the correlation is compared with its own data base. This was necessary due to the lack of a broad data base for PuO_2 fuel. A better test of the accuracy of the model is found by comparing its predictions with mixed oxide data,[2.2-5,2.2-10,2.2-14] as shown in Figure 2-6. None of the data shown in this figure were used in the development of the model. The agreement is relatively good except for the low values reported by Affortit and Marcon. Other experimenters[2.2-3,2.2-10] have pointed out that the results of Affortit and Marcon are generally low when compared with their data and have excluded the Affortit and Marcon measurements from their data base. No one has proposed an adequate explanation for the discrepancy. On the other hand, at least one investigator[2.2-9] has given considerable weight to the work done by Affortit and Marcon. In this document, the Affortit and Marcon results are used only in the analysis of the effect of departure from stoichiometry on the specific heat capacity.

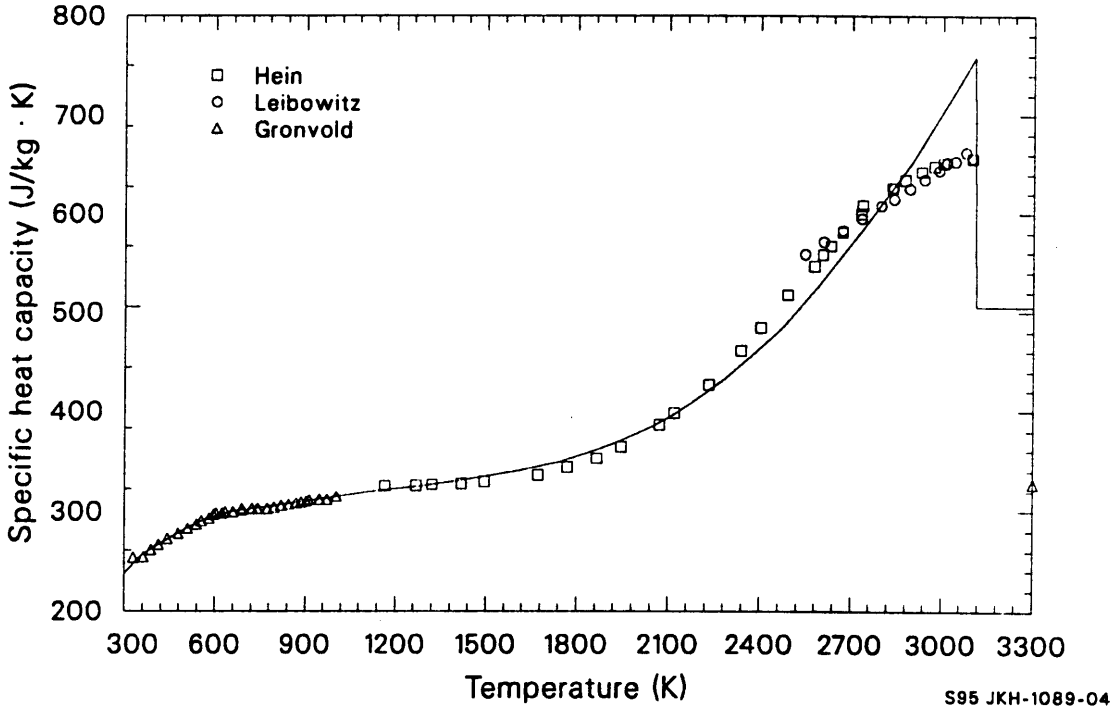

Figure 2-4. Specific heat capacity of UO_2 from three experimenters compared with the FCP correlation (solid line) for UO_2.

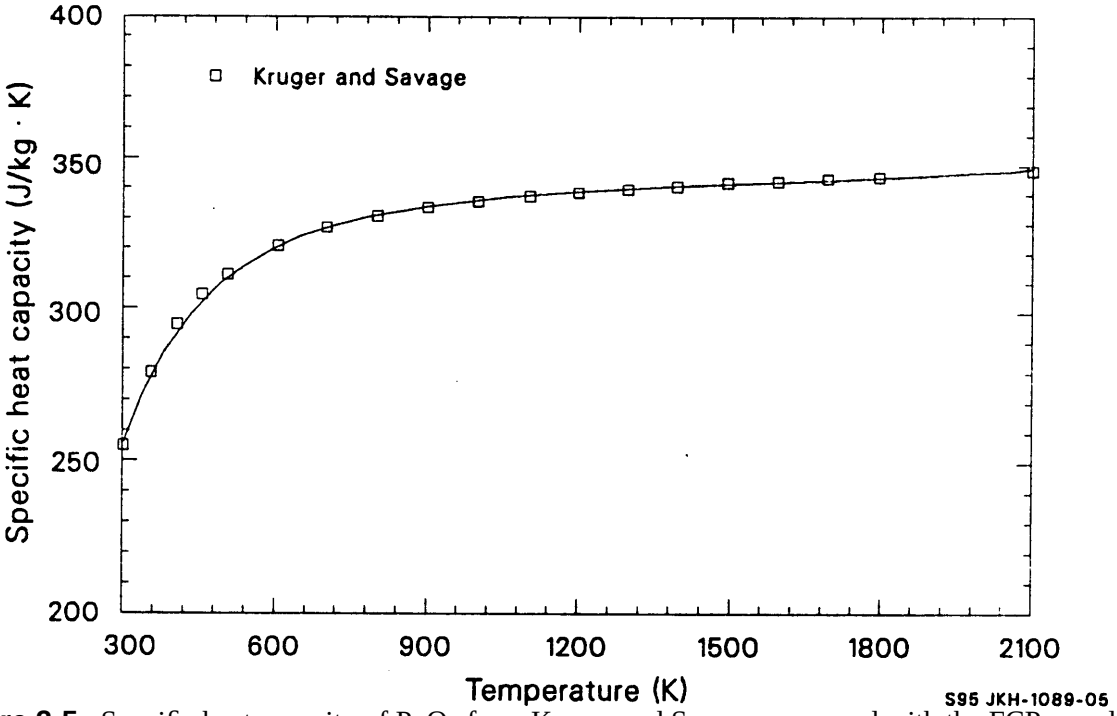

Figure 2-5. Specific heat capacity of PuO_2 from Kruger and Savage compared with the FCP correlation (solid line) for PuO_2.

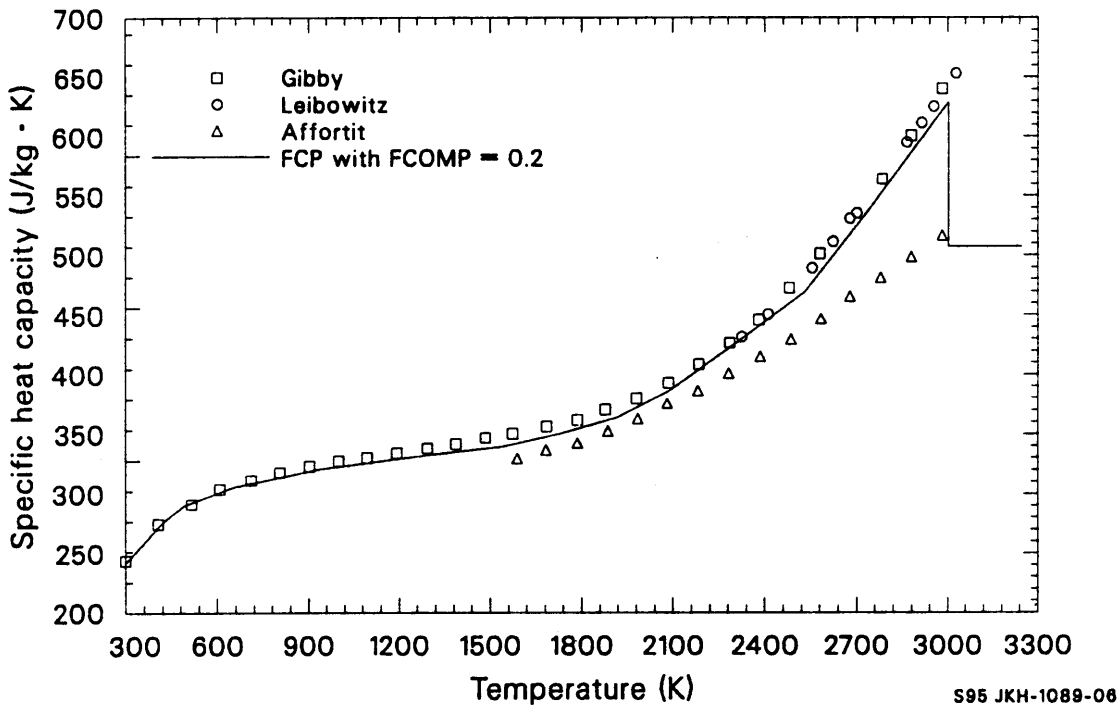

Figure 2-6. Specific heat capacity of $(U_{0.8}Pu_{0.2})O_2$ from three experimenters compared with the FCP correlation (solid line) for mixed oxides.

2.2.5 Model Uncertainty

As would be expected, the accuracy of the FCP model when compared with its own data base is quite good. A better test was found by comparing the correlations with data not used during their development. The UO_2 and mixed oxide fuel correlations are analyzed separately in this section.

2.2.5.1 ***Uncertainty in UO_2 Model.*** Kerrisk and Clifton report an accuracy of ±3% for their correlation over the temperature range 300 to 3,000 K, with an approximately uniform distribution relative to temperature. When the calculations of the correlation are compared with the data of Gronvold for stoichiometric oxide, the agreement is even better, having a standard error of only 2.0 J/kg · K. This is a good test of the model, since these data were not used to develop the correlation. The paper by Affortit and Marcon gives correlations fit to their data. Arbitrarily taking 200 K intervals over their temperature range from 600 to 3,000 K and using their correlations, the standard error is 46 J/kg · K. Affortit and Marcon's predictions are smaller at all temperatures, and the residuals increase with temperature.

2.2.5.2 ***Uncertainty in the Mixed Oxide Model.*** Because of the limited number of data for PuO_2, the accuracy of the correlation for mixed oxide fuel was used as a test for this correlation. Data were taken from Leibowitz,[2.2-14] Gibby,[2.2-10] and Affortit and Marcon.[2.2-5] The model presented in this paper, using a weighted sum of the UO_2 and PuO_2 results, calculates specific heat capacities that are slightly larger than all but two of the 55 data points reported by Gibby and Leibowitz. At the highest and lowest applicable temperatures (3,000 and 300 K), the differences are negligible, < 1.0 J/kg · K. At intermediate temperatures, around 1,600 K, the residuals are approximately 10.0 J/kgK, falling off smoothly from this temperature. The standard error of the model relative to these three data sets is 5.6 J/kg · K. This is equivalent to a maximum percentage error of < 2.5%. Since these residuals are smaller than the scatter in the data,

the model represents these data sets adequately. When the model is compared with that of Affortit and Marcon, again taking 200 K steps from 1,600 K to melting, the standard error is 46 J/kg · K. Affortit and Marcon always have the smaller value, and the residuals increase with increasing temperature, as with the UO_2 results. Because of the lack of actual data, the results of Affortit and Marcon are not included in the standard error estimate.

2.2.6 Bibliography

The following data sources were used in previous EG&G Idaho Inc. reports dealing with fuel specific heat models but are not quoted in this version. They are included here for completeness.

2. C. E. Wicks and F. E. Block, *Thermodynamics of 65 Elements--Their Oxides, Halides, Carbides, and Nitrides*, Bureau of Mines Bulletin No. 605, 1963.

3. M. L. Bleiberg, R. M. Berman, and B. Lustman, *Effects of High Burnup on Oxide Ceramic Fuels*, WAPD-T-1455, 1962.

4. A. E. Ogard and J. A. Leary, *Thermodynamics of Nuclear Materials*, IAEA, Vienna, 1968, p. 651.

5. R. L. Gibby, *Enthalpy and Heat Capacity of* $^{U}0.75^{Pu}0.25^{O}2\text{-}x$ *(25-1490C)*, HEDL-TIME-73-19, 1973.

6. L. Leibowitz, D. F. Fischer, and M. G. Chasanov, *Enthalpy of Molten Uranium Plutonium Oxides*, ANL-8042, 1974.

2.2.7 References

2.2-1 J. F. Kerrisk and D. G. Clifton, "Smoothed Values of the Enthalpy and Heat Capacity of UO_2," Nuclear Technology, 16, December 1972, pp. 531-535.

2.2-2 O. L. Kruger and H. Savage, "Heat Capacity and Thermodynamic Properties of Plutonium Dioxide," *Journal of Chemical Physics, 45*, November 1968, pp. 4540-4544.

2.2-3 L. Leibowitz et al., "Enthalpy of Liquid Uranium Dioxide to 3,500 K," *Journal of Nuclear Materials, 39*, 1971, pp. 115-116.

2.2-4 F. Gronvold et al., "Thermodynamics of the UO_{2+x} Phase I. Heat Capacities of $UO_{2.017}$ and $UO_{2.254}$ from 300 to 1,000 K and Electronic Contributions," *Journal of Chemical Thermodynamics, 2*, 1970, pp. 665-679.

2.2-5 C. Affortit and J. Marcon, "Chaleur Specifique a Haute Temperature des Oxydes D'Uranium et de Plutonium," *Revue Internationale des Hautes Temperatures et des Refractaires, 7*, 1970, pp. 236-241.

2.2-6 C. Kittel, *Introduction to Solid State Physics*, 3rd Edition, New York: John Wiley and Sons Inc., 1966.

2.2-7 D. R. Olander, *Fundamental Aspects of Nuclear Reactor Fuel Elements*, TID-26711-P1, 1976.

2.2-8 R. Szwarc, "The Defect Contribution to the Excess Enthalpy of Uranium Dioxide Calculation of the Frenkel Energy," *Journal of Chemistry and Physics of Solids, 30*, 1969, pp. 705-711.

2.2-9 E. A. Fscher, P. R. Kinsman, and R. W. Ohse, "Critical Assessment of Equations of State for UO_2," *Journal of Nuclear Materials, 59*, 1976, pp. 125-136.

2.2-10 R. L. Gibby et al., "Analytical Expressions for Enthalpy and Heat Capacity for Uranium--Plutonium Oxide," *Journal of Nuclear Materials, 50*, 1974, pp. 155-161.

2.2-11 H. Inaba, H. Shimizu, and K. Naito, "Lambda Type Heat Capacity Anomalies in U_3O_8," *Journal of Nuclear Materials*, 64, 1977, pp.66-70.

2.2-12 R. A. Hein, L. H. Sjodahl, and R. Swarc, "Heat Content of Uranium Dioxide from 1,200 to 3,100 K," *Journal of Nuclear Materials, 25*, 1968, pp. 99-102.

2.2-13 L. Leibowitz, L. W. Mschler, and M. G. Chasanov, "Enthalpy of Solid Uranium Dioxide from 2,500 K to its Melting Point," *Journal of Nuclear Materials, 29*, 1969, pp. 356-358.

2.2-14 L. Leibowitz, D. F. Fischer, and M. G. Chasanov, "Enthalpy of Uranium Plutonium Oxides $(U_{0.8},Pu_{0.2})\ O_{1.07}$ from 2,350 to 3,000 K," *Journal of Nuclear Materials, 42*, 1972, pp. 113-116.

2.3 Thermal Conductivity (FTHCON)

In this section, a correlation is presented for the thermal conductivity of uncracked UO_2 and (U, Pu)O_2 fuels. This property and the closely associated models for the effect of fuel cracking on temperature distributions within the fuel are critical to accurate predictions of fuel rod behavior in both steady state operation and off-normal transients because fuel rod behavior is strongly dependent on temperature.

2.3.1 Summary

The FTHCON subcode determines the fuel thermal conductivity and its derivative with respect to temperature as a function of temperature, density, oxygen to metal (O/M) ratio, and plutonium content of the fuel. Burnup is also required input but is used only to calculate the melt temperature.

The data base shows no significant effect of porosity at temperatures above about 1,600 K, probably because of the effects of radiation and gas conductivity, which increase pore conductivity at high temperatures. The thermal conductivity of liquid fuel was estimated from physical considerations because no data for the conductivity of molten fuel were found.

With the exception of minor modifications made to eliminate discontinuities in slope in the temperature range from 1,364 to 2,300 K, the expression used to model thermal conductivity of solid fuel is

$$k = \left[\frac{D}{1 + (6.5 - 0.00469T')\ (1 - D)}\right]\left[\frac{C_V}{(A + BT'')\ (1 + 3e_{th})}\right] + 5.2997\times10^{-3}Te^{\left[\frac{-13358}{T}\right]}\left\{1 + 0.169\left[\left(\frac{13358}{T}\right) + 2\right]^2\right\} \tag{2-20}$$

where

k	=	thermal conductivity (W/m · K)
D	=	fraction of theoretical density (unitless)
C_v	=	phonon contribution to the specific heat at constant volume (J/kg · K). The first term of the MATPRO correlation for fuel specific heat capacity is used for this factor[a]

e_{th}	=	linear strain caused by thermal expansion when temperature is > 300 K (unitless). The MATPRO correlation for fuel thermal expansion is used for this factor
T	=	fuel temperature (K)
T'	=	fuel temperature if < 1,364 K. For temperatures > 1,834 K, the porosity factor, D{1+ [6.5-0.00469T']}, is equal to -1; and for temperatures in the range 1,364 to 1,834 K, the factor is found by interpolation, as explained in Subsection 2.3.3
T"	=	fuel temperature if < 1,800 K. For temperatures > 2,300 K, T" is equal to 2,050 K; for temperatures in the range 1,800 to 2,300 K, T" is found by interpolation, as explained in Subsection 2.3.3
A	=	a factor proportional to the point defect contribution to the phonon mean free path (m · s/kg · K). The correlation used for this factor is 0.339 + 12.6 x absolute value (2.0 - O/M ratio)
B	=	a factor proportional to the phonon-phonon scattering contribution to the phonon mean free path (m · s/kg · K). The correlation used for this factor is 0.06867 x (1 + 0.6238 x plutonium content of fuel).

The first term of Equation (2-20) represents the phonon contribution to specific heat, and the second term represents the electronic (electron hole) contribution. The expression is valid only in the range 90 to 100% of theoretical density. When the fuel is molten, the first term is neglected.

The expected error of the thermal conductivity model has been estimated by computing the standard error of the model with respect to its data base. For stoichiometric UO_2 samples, the standard error was 0.2 (W/m · K); and for stoichiometric (U, Pu)O_2 with 2% Pu, the standard error was 0.3 (W/m · K). On the basis of these results, the following expression is used to calculate the expected standard error of the thermal conductivity of the solid fuel:

$$UK = [0.2(1 - COMP) + 0.7\ \ COMP] \times (1.0 + |2 - OTM|\ 10) \qquad (2\text{-}21)$$

where

UK	=	expected standard error of solid fuel thermal conductivity (W/m · K)
COMP	=	PuO_2 content of the fuel (ratio of weight of PuO_2 to total weight)
OTM	=	O/M ratio of fuel (unitless).

---

a. The analytical expression for C_v as a function of temperature, T, and plutonium content, COMP, is

$$C_V = \frac{297.7\,(535.285)^2}{T^2\left[e^{\left[\frac{535.285}{T}\right]} - 1\right]^2}\left[e^{\left[\frac{535.285}{T}\right]}\right](1 - COMP) + \frac{COMP \cdot (347.4)\ (571)^2}{T^2\left[e^{\left[\frac{571}{T}\right]} - 1\right]^2} e^{\left[\frac{571}{T}\right]} \quad .$$

The following subsection is a review of the general theories and data used to derive the model for thermal conductivity. Section 2.3.3 describes the development of the model, and Section 2.3.4 is a discussion of the uncertainty of the model.

2.3.2 Literature Review: Theory and Available Data

The mechanistic basis for a description of the thermal conductivity of solid unirradiated UO_2 and (U, Pu)O_{2+x} is well documented.[2.3-1 to 2.3-4] The thermal conductivity is the sum of contributions due to lattice vibrations, electron hole pairs, and radiant heat transfer. At temperatures below 1,500 K, the lattice component, k_p, (Equation 2-22) is the most important contribution. At temperatures above 2,000 K, sufficient thermal energy exists to create significant numbers of electron hole pairs. These pairs contribute to the thermal conductivity[2.3-4] if the solid is not doped with donors or acceptors. The radiant heat transfer contribution to the thermal conductivity is small in polycrystalline fuel,[2.3-1] presumably because the material is transparent only at long wavelengths.

$$k_p = \rho\, C_v u \lambda / 3 \tag{2-22}$$

where

k_p	=	lattice vibration (phonon) contribution to thermal conductivity (W/m · K)
ρ	=	density of the solid (kg/m^3)
C_v	=	phonon contribution to the specific heat at constant volume (J/kg · K)
u	=	mean phonon speed (m/s)
λ	=	phonon mean free path (m).

$$k_e = 2\left(\frac{k_b}{e}\right)^2 T\left[\sigma + \frac{2\sigma_e\sigma_h}{\sigma}\left(\frac{E_q}{2k_B T} + 2\right)^2\right] \tag{2-23}$$

where

k_e	=	electronic contribution to thermal conductivity (W/m · K)
k_B	=	Boltzmann's constant, 1.38x10^{-23} (J/K)
e	=	electron charge, 1.6x10^{-19} (coul)
σ_e	=	electron contribution to electrical conductivity (1/ohm · m)
σ_h	=	hole contribution to electrical conductivity (1/ohm · m)
σ	=	$\sigma_e + \sigma_h$ [1/(ohm · m)]
E_g	=	energy gap between conduction and valence bands (J)
T	=	temperature (K).

The application of Equation (2-23) is simplified by the existence of accurate measurements of the electrical conductivity of UO_2. Bates, Hinman, and Kawada[2.3-5] report electrical conductivities above 1,400 K to be given by

$$\sigma = 3.569\times10^{7} e^{\left(-\frac{E_g}{2k_B T}\right)} \tag{2-24}$$

where

σ	=	electrical conductivity (1/ohm · m)
E_g	=	energy gap between conduction and valence bands, 3.688 x 10^{-19} (J).

Equation (2-23) can be combined with Equation (2-24) to obtain

$$k_e = 2\left(\frac{k_B}{e}\right)^2 (3.569\times10^{7}T)\left[e^{\left(-\frac{E_g}{2k_B T}\right)}\right]\left[1+\frac{2f}{(1+f)^2}\left(\frac{E_g}{2k_B T}+2\right)^2\right] \tag{2-25}$$

where $f = \sigma_h / \sigma_e$ and the other symbols have been defined in conjunction with the two previous equations. Equation (2-25) contains only one undetermined parameter, the ratio of f.

Unfortunately, the application of Equation (2-22) for the lattice contribution to thermal conductivity is complex. C_v and ρ are available from the MATPRO routines for fuel specific heat and fuel thermal expansion and u is approximately the speed of sound in the lattice, but the phonon mean free path, λ, is not a directly measured quantity. For the purpose of applying Equation (2-22) to (U, Pu)O_2, it is sufficient to point out that the quantity $u\lambda/3$ in Equation (2-22) at temperatures in the range from 500 to 3,000 K is determined by two main contributions--the deflection or scattering of lattice vibrations from permanent defects in the regular lattice pattern and the scattering of lattice vibrations from each other.[a] The first contribution is primarily a function of the O/M ratio and the impurity content of the fuel, and the second contribution is a function of temperature and the plutonium content of the fuel.[2.3-1] When the two main contributions to the phonon mean free path are incorporated in Equation (2-22), the appropriate expression for the lattice vibration contribution to the thermal conductivity of solid fuel is

$$k_p = \frac{\rho C_V}{A+BT} \tag{2-26}$$

where A is a function of the number of permanent defects in the lattice and B is a measure of the probability that lattice vibrations interfere with each other. The second term in the denominator is proportional to temperature because the density of lattice vibrations is proportional to temperature in the range of 500 to 3,000 K.

For porous materials, some modification of Equation (2-26) is required because the pores do not have the same conductivity as the lattice. This physical problem has been discussed extensively in the literature,[2.3-1,2.3-6 to 2.3-10] where the effect of porosity has been shown to be a function of the porosity fraction (volume of pores/total volume), the pore shape, the thermal conductivity of any gas trapped within the pores, and the emissivity of the lattice.

Unfortunately, the detailed mechanistic analysis presented in the literature cannot be applied to most of the published thermal conductivity data because the pore shape and the composition of the gas trapped within the pores are usually not reported. Most authors interested in obtaining usable expressions[2.3-11 to 2.3-14] have adopted some form of either the modified Loeb equation

a. The interested reader will find detailed physical discussions in References (2.3-3) and (2.3-4).

$$\frac{k}{k_{100}} = 1 - \alpha P \tag{2-27}$$

or the Maxwell-Eucken equation

$$\frac{k}{k_{100}} = \frac{1 - P}{1 + \beta P} \tag{2-28}$$

where

k	=	thermal conductivity of a porous sample (W/m · K)
k_{100}	=	thermal conductivity of a sample with no pores (W/m · K)
P	=	volume of pores/total sample volume (unitless)
α,β	=	factors depending on the shape and distribution of the pores (unitless).

These authors usually assume α or β to be linear functions of temperature and fit the linear functions to data from a limited set of samples.

None of the known previous studies of the effect of porosity on thermal conductivity has used the large collection of available experimental data. These data will be used in Section 2.3.3. The correlation will be based on the Maxwell-Eucken relation because from mechanistic studies both Marino[2.3-6] and Ondracek[2.3-10] recommend using this relation.

The remainder of this literature review discusses the available experimental measurements of thermal conductivity. Two general types of experiments will be encountered: the radial heat flow method and the transient heat pulse method. In the radial heat flow method, heat is supplied internally to a specimen and the thermal conductivity is deduced from measurements of the heat input and the steady state temperature difference across the sample. In the transient heat pulse method, the measured quantity is the thermal diffusivity,[2.3-3]

$$\alpha = \frac{k}{C_P \rho} \tag{2-29}$$

where

α	=	thermal diffusivity (m^2/s)
k	=	thermal conductivity (W/m · K)
C_p	=	fuel specific heat at constant pressure (J/kg · K)
ρ	=	fuel density (kg/m^3).

The available UO_2 data are contained in References 2.3-11 through 2.3-27. Several of these sources were not used in the present analysis: Hedge[2.3-15] and Kingery[2.3-16] used samples with densities between 70 and 75% theoretical density (TD) – far below those used in commercial fuel. Asamoto,[2.3-14] Reiswig,[2.3-23] Stora,[2.3-24] and Hetzler[2.3-17] employed radial heat flow methods in which the electrically heated center conductor may have been in contact with the oxide sample, so that Joule heating of the oxide could result and indicate anomalously high conductivity. The data of Hetzler and Asamoto also show

unusually large scatter, probably because of cracking during the measurements. The data of Ferro[2.3-25] show such large scatter that they were rejected for this reason alone. The temperature data of Lyons[2.3-22] were derived from observation of postirradiation grain growth and restructuring, a method considered less reliable than that used by other investigators. The data of Van Craeynest and Stora,[2.3-11] and Lucks and Deem[2.3-20] showed anomalously low conductivity compared to data from fuels with similar density. The low conductivity was probably caused by cracking before the reported data were taken.

Christensen's data[2.3-21] are the most suspect of those used. The apparatus used in his radial heat flow experiment is not well described. Possibly the sharp increase in thermal conductivity at high temperature reported by Christensen is due to electrical contact with the heating element. Because of this possibility and because the specimen composition changed from $UO_{2.01}$ to $UO_{1.99}$ during the test, Christensen's data for temperatures above 1,800 K were not used. The data from Christensen that were used are listed in Table 2-2.

The data of Godfrey[2.3-18] are the most reliable radial heat flow data reviewed in this section. Granular alumina insulation and careful positioning of the center heater were used to minimize electrical contact between the center heater and the sample. Runs which resulted in a change in the O/M ratio were reported as suspect and not used. Thermocouple errors were analyzed carefully, and runs at temperatures above 1,373 K were identified as not valid because of thermocouple problems.

Unfortunately, Godfrey used only samples of 93.4% TD. Also, the data were corrected to TD by dividing by the fraction of theoretical density. The unsatisfactory nature of this correction would no doubt have become evident if samples of varying density had been used. This correction was removed before the data were used to develop the model described here.

The data with the density correction removed are listed in Table 2-3. Several runs are represented, and there is no systematic variation from run to run. Data at temperatures below 500 K are not included in Table 2-3 because the low temperature data cannot be used with Equation (2-26). (The equation is valid only when temperatures are well above the Debye temperature.)

The remaining five sets of UO_2 data used were all obtained with the heat pulse method. Bates[2.3-19] measured the thermal diffusivity of three samples, all with a density of 98.4% TD. Some data which correspond to runs taken when the samples had a metallic second phase at the grain boundaries were not used. Table 2-4 is a list of the values of thermal conductivity deduced from Bates' thermal diffusivity data, Equation (2-29), and the MATPRO expressions for fuel specific heat at constant pressure and for thermal expansion (see Sections 2.2 and 2.5). Systematic variation does not occur in the data either from run to run or sample to sample.

Table 2-2. UO_2 data from Christensen [(2.3-21)]

Temperature (K)	Density (fraction of)	Thermal Conductivity
.13120E+04	.9400E+00	.287000E+01
.13890E+04	.9400E+00	.287000E+01
.14320E+04	.9400E+00	.270000E+01
.14960E+04	.9400E+00	.272000E+01

Table 2-2. UO_2 data from Christensen [2.3-21] (Continued)

Temperature (K)	Density (fraction of)	Thermal Conductivity
.15520E+04	.9400E+00	.271000E+01
.15870E+04	.9400E+00	.256000E+01
.16120E+04	.9400E+00	.257000E+01
.16560E+04	.9400E+00	.280000E+01
.17470E+04	.9400E+00	.248000E+01
.18380E+04	.9400E+00	.259000E+01

Table 2-3. UO_2 data from Godfrey et al.[2.3-18]

Temperature (K)	Density (Fraction of theoretical)	Thermal Conductivity [W/(m•K)]	Run Number
.57400E+03	.9340E+00	.540400E+01	2
.67300E+03	.9340E+00	.475400E+01	2
.76700E+03	.9340E+00	.432200E+01	2
.87700E+03	.9340E+00	.390200E+01	2
.97600E+03	.9340E+00	.355900E+01	2
.10740E+04	.9340E+00	.326500E+01	2
.67500E+03	.9340E+00	.461000E+01	3
.87000E+03	.9340E+00	.379400E+01	3
.86900E+03	.9340E+00	.383200E+01	3
.97100E+03	.9340E+00	.348700E+01	3
.10720E+04	.9340E+00	.318200E+01	3
.11650E+04	.9340E+00	.298500E+01	3
.11730E+04	.9340E+00	.297500E+01	3
.12790E+04	.9340E+00	.277400E+01	3
.12820E+04	.9340E+00	.275500E+01	3
.57200E+03	.9340E+00	.518700E+01	4

Table 2-3. UO_2 data from Godfrey et al.[2.3-18] (Continued)

Temperature (K)	Density (Fraction of theoretical)	Thermal Conductivity [W/(m•K)]	Run Number
.87000E+03	.9340E+00	.373700E+01	4
.87000E+03	.9340E+00	.369000E+01	4
.87200E+03	.9340E+00	.368100E+01	4
.11710E+04	.9340E+00	.288800E+01	4
.11750E+04	.9340E+00	.287000E+01	4
.57000E+03	.9340E+00	.514000E+01	5
.57200E+03	.9340E+00	.511100E+01	5
.67300E+03	.9340E+00	.458900E+01	5
.67300E+03	.9340E+00	.455700E+01	5
.77400E+03	.9340E+00	.407700E+01	5
.77400E+03	.9340E+00	.409600E+01	5
.87500E+03	.9340E+00	.371100E+01	5
.87500E+03	.9340E+00	.373400E+01	5
.97300E+03	.9340E+00	.341600E+01	5
.97300E+03	.9340E+00	.341700E+01	5
.10710E+04	.9340E+00	.316900E+01	5
.10710E+04	.9340E+00	.316400E+01	5
.11730E+04	.9340E+00	.295000E+01	5
.12710E+04	.9340E+00	.275100E+01	5
.13230E+04	.9340E+00	.268200E+01	5
.57600E+03	.9340E+00	.523200E+01	6
.57600E+03	.9340E+00	.522900E+01	6
.67100E+03	.9340E+00	.469100E+01	6
.67100E+03	.9340E+00	.469100E+01	6
.67100E+03	.9340E+00	.470500E+01	6
.87400E+03	.9340E+00	.382100E+01	6

Table 2-4. UO_2 data from Bates (2.3-19) thermal diffusivity measurements

Temperature (K)	Density (Fraction of Theoretical)	Thermal Conductivity [W/(m•K)]	Sample	Cycle Number
.53900E+03	.9840E+00	.650000E+01	RR1	3
.53900E+03	.9840E+00	.657000E+01	RR1	3
.75600E+03	.9840E+00	.482000E+01	RR1	3
.76100E+03	.9840E+00	.502000E+01	RR1	3
.89500E+03	.9840E+00	.411000E+01	RR1	3
.89100E+03	.9840E+00	.435000E+01	RR1	3
.99400E+03	.9840E+00	.383000E+01	RR1	3
.99500E+03	.9840E+00	.391000E+01	RR1	3
.11800E+04	.9840E+00	.328000E+01	RR1	3
.11850E+04	.9840E+00	.313000E+01	RR1	3
.13250E+04	.9840E+00	.285000E+01	RR1	3
.13250E+04	.9840E+00	.289000E+01	RR1	3
.14890E+04	.9840E+00	.251000E+01	RR1	3
.14910E+04	.9840E+00	.255000E+01	RR1	3
.16660E+04	.9840E+00	.240000E+01	RR1	3
.16550E+04	.9840E+00	.237000e+01	RR1	3
.17780E+04	.9840E+00	.224000E+01	RR1	3
.17800E+04	.9840E+00	.213000E+01	RR1	3
.18630E+04	.9840E+00	.219000E+01	RR1	3
.18660E+04	.9840E+00	.219000E+01	RR1	3
.19770E+04	.9840E+00	.210000E+01	RR1	3
.19720E+04	.9840E+00	.224000E+01	RR1	3
.20930E+04	.9840E+00	.232000E+01	RR1	3
.21020E+04	.9840E+00	.225000E+01	RR1	3
.21740E+04	.9840E+00	.226000E+01	RR1	3
.21870E+04	.9840E+00	.225000E+01	RR1	3

Table 2-4. UO_2 data from Bates (2.3-19) thermal diffusivity measurements (Continued)

Temperature (K)	Density (Fraction of Theoretical)	Thermal Conductivity [W/(m•K)]	Sample	Cycle Number
.23730E+04	.9840E+00	.249000E+01	RR1	3
.23730E+04	.9840E+00	.264000E+01	RR1	3
.22800E+04	.9840E+00	.229000E+01	RR1	3
.22850E+04	.9840E+00	.242000E+01	RR1	3
.15990E+04	.9840E+00	.237000E+01	RR1	3
.16010E+04	.9840E+00	.249000E+01	RR1	3
.16090E+04	.9840E+00	.232000E+01	RR1	3
.13600E+04	.9840E+00	.283000E+01	RR1	4
.14530E+04	.9840E+00	.242000E+01	RR1	4
.15620E+04	.9840E+00	.248000E+01	RR1	4
.16490E+04	.9840E+00	.237000E+01	RR1	4
.17500E+04	.9840E+00	.239000E+01	RR1	4
.19070E+04	.9840E+00	.213000E+01	RR1	4
.20050E+04	.9840E+00	.210000E+01	RR1	4
.20070E+04	.9840E+00	.231000E+01	RR1	4
.21090E+04	.9840E+00	.219000E+01	RR1	4
.21040E+04	.9840E+00	.227000E+01	RR1	4
.21950E+04	.9840E+00	.235000E+01	RR1	4
.22950E+04	.9840E+00	.247000E+01	RR1	4
.23840E+04	.9840E+00	.242000E+01	RR1	4
.57100E+03	.9840E+00	.572000E+01	RR2	2
.57700E+03	.9840E+00	.603000E+01		
.57700E+03	.9840E+00	.616000E+01		
.66100E+03	.9840E+00	.533000E+01		
.68200E+03	.9840E+00	.541000E+01		
.78600E+03	.9840E+00	.448000E+01		
.78400E+03	.9840E+00	.445000E+01		

Table 2-4. UO_2 data from Bates (2.3-19) thermal diffusivity measurements (Continued)

Temperature (K)	Density (Fraction of Theoretical)	Thermal Conductivity [W/(m•K)]	Sample	Cycle Number
.78500E+03	.9840E+00	.454000E+01		
.86600E+03	.9840E+00	.415000E+01		
.86700E+03	.9840E+00	.415000E+01		
.96100E+03	.9840E+00	.373000E+01		
.96100E+03	.9840E+00	.363000E+01		
.96100E+03	.9840E+00	.396000E+01		
.10690E+04	.9840E+00	.335000E+01		
.10710E+04	.9840E+00	.331000E+01		
.10690E+04	.9840E+00	.351000E+01		
.11710E+04	.9840E+00	.304000E+01		
.11740E+04	.9840E+00	.307000E+01		
.11730E+04	.9840E+00	.324000E+01		
.12700E+04	.9840E+00	.280000E+01		
.12690E+04	.9840E+00	.287000E+01		
.12700E+04	.9840E+00	.281000E+01		
.13610E+04	.9840E+00	.255000E+01		
.13610E+04	.9840E+00	.263000E+01		
.13610E+04	.9840E+00	.259000E+01		
.13610E+04	.9840E+00	.263000E+01		
.14710E+04	.9840E+00	.254000E+01		
.14720E+04	.9840E+00	.267000E+01		
.14690E+04	.9840E+00	.226000E+01		
.15690E+04	.9840E+00	.240000E+01		
.15710E+04	.9840E+00	.241000E+01		
.15690E+04	.9840E+00	.246000E+01		
.16830E+04	.9840E+00	.233000E+01		
.16830E+04	.9840E+00	.237000E+01		

Table 2-4. UO_2 data from Bates (2.3-19) thermal diffusivity measurements (Continued)

Temperature (K)	Density (Fraction of Theoretical)	Thermal Conductivity [W/(m•K)]	Sample	Cycle Number
.17580E+04	.9840E+00	.230000E+01		
.17560E+04	.9840E+00	.219000E+01		
.17600E+04	.9840E+00	.228000E+01		
.67300E+03	.9840E+00	.553000E+01	RR3	3
.12830E+04	.9840E+00	.275000E+01		
.67300E+03	.9840E+00	.542000E+01		
.11000E+04	.9840E+00	.360000E+01	RR3	1
.10890E+04	.9840E+00	.340000E+01		
.10900E+04	.9840E+00	.354000E+01		
.10990E+04	.9840E+00	.341000E+01		
.81300E+03	.9840E+00	.486000E+01		
.79700E+03	.9840E+00	.480000E+01		
.50700E+03	.9840E+00	.646000E+01	RR3	2
.58300E+03	.9840E+00	.640000E+01		
.67600E+03	.9840E+00	.542000E+01		
.67900E+03	.9840E+00	.551000E+01		
.76300E+03	.9840E+00	.501000E+01		
.76400E+03	.9840E+00	.513000E+01		
.87300E+03	.9840E+00	.450000E+01		
.87600E+03	.9840E+00	.429000E+01		
.97900E+03	.9840E+00	.395000E+01		
.98100E+03	.9840E+00	.396000E+01		
.10650E+04	.9840E+00	.374000E+01		
.10720E+04	.9840E+00	.369000E+01		
.11880E+04	.9840E+00	.317000E+01		
.11870E+04	.9840E+00	.336000E+01		
.12770E+04	.9840E+00	.309000E+01		

Table 2-4. UO_2 data from Bates (2.3-19) thermal diffusivity measurements (Continued)

Temperature (K)	Density (Fraction of Theoretical)	Thermal Conductivity [W/(m•K)]	Sample	Cycle Number
.12850E+04	.9840E+00	.319000E+01		
.12840E+04	.9840E+00	.328000E+01		
.10710E+04	.9840E+00	.370000E+01		
.88000E+03	.9840E+00	.457000E+01		
.87900E+03	.9840E+00	.452000E+01		
.87900E+03	.9840E+00	.452000E+01		
.67800E+03	.9840E+00	.534000E+01		
.57300E+03	.9840E+00	.618000E+01	RR3	3
.58300E+03	.9840E+00	.589000E+01		
.68000E+03	.9840E+00	.536000E+01		
.68100E+03	.9840E+00	.524000E+01		
.67800E+03	.9840E+00	.533000E+01		
.77600E+03	.9840E+00	.488000E+01		
.77500E+03	.9840E+00	.496000E+01		
.89100E+03	.9840E+00	.417000E+01		
.89500E+03	.9840E+00	.430000E+01		
.96800E+03	.9840E+00	.388000E+01		
.97300E+03	.9840E+00	.396000E+01		
.10870E+04	.9840E+00	.345000E+01		
.10810E+04	.9840E+00	.348000E+01		
.11720E+04	.9840E+00	.328000E+01		
.11730E+04	.9840E+00	.316000E+01		
.12920E+04	.9840E+00	.285000E+01		
.12910E+04	.9840E+00	.281000E+01		
.13770E+04	.9840E+00	.265000E+01		
.13800E+04	.9840E+00	.263000E+01		
.14730E+04	.9840E+00	.254000E+01		

Table 2-4. UO_2 data from Bates (2.3-19) thermal diffusivity measurements (Continued)

Temperature (K)	Density (Fraction of Theoretical)	Thermal Conductivity [W/(m•K)]	Sample	Cycle Number
.14770E+04	.9840E+00	.259000E+01	RR3	3
.15780E+04	.9840E+00	.230000E+01		
.15840E+04	.9840E+00	.245000E+01		
.16730E+04	.9840E+00	.223000E+01		
.16790E+04	.9840E+00	.220000E+01		
.17690E+04	.9840E+00	.209000E+01		
.17920E+04	.9840E+00	.224000E+01		
.17860E+04	.9840E+00	.219000E+01		
.15950E+04	.9840E+00	.206000E+01		
.15960E+04	.9840E+00	.241000E+01		
.14000E+04	.9840E+00	.261000E+01		
.13990E+04	.9840E+00	.256000E+01		
.11660e+04	.9840E+00	.329000E+01		
.10790E+04	.9840E+00	.344000E+01		
.10850E+04	.9840E+00	.350000E+01		
.84700E+03	.9840E+00	.443000E+01		
.84700E+03	.9840E+00	.445000E+01		
.57700E+03	.9840E+00	.598000E+01		
.55300E+03	.9840E+00	.622000E+01		

Gibby[2.3-27] reported the thermal diffusivity of a UO_2 sample as part of a study on the effect of plutonium additions. The sample had a density of 95.8% TD. The thermal conductivity data calculated from Gibby's diffusivities are shown in Table 2-5.

Weilbacher[2.3-26] reported the thermal diffusivity of a UO_2 sample as part of a study of the effect thorium additions. The sample had a density of 98.0% TD. These data are important because they include temperatures up to melting and because the low temperature part of the data falls within the narrow scatter of the data reported by Bates for his samples of similar density. The close agreement of the Bates and Weilbacher data provide support for the idea that the thermal diffusivity data on uncracked samples are consistent. The thermal conductivity data calculated from Weilbacher's thermal diffusivity data using the same MATPRO expressions used with Bates' data are listed in Table 2-6.

The data of Goldsmith and Douglas[2.3-12] provide more support for the idea that thermal diffusivity data on uncracked samples are consistent. When the MATPRO expressions for specific heat and thermal expansion are employed to convert the thermal diffusivity data of Goldsmith and Douglas to thermal conductivity, the resultant thermal conductivities fall within the scatter of the data of several authors who performed extensive measurements on a limited number of samples. The thermal conductivities obtained from Goldsmith and Douglas' data are presented in Table 2-7. The thermal conductivity data from 98.2 and 97.7% TD samples agree with the data of Bates and Weilbacher, the 95.1 and 95.8% dense sample data agree with the data of Gibby, the 95.2 and 94.7% dense sample data agree with the data of Hobson[2.3-13] (which will be discussed in the next paragraph), and the 93.2 and 93.0% dense sample data agree with the data of Godfrey.[a]

Table 2-5. UO_2 data, Gibby's[2.3-27] thermal diffusivity measurements.

Temperature (K)	Density (fraction of theoretical)	Thermal Conductivity [W/(m•K)]
.57500E+03	.9580E+00	.624000E+01
.57800E+03	.9580E+00	.636000E+01
.58600E+03	.9580E+00	.628000E+01
.58700E+03	.9580E+00	.587000E+01
.58800E+03	.9580E+00	.563000E+01
.66500E+03	.9580E+00	.512000E+01
.67500E+03	.9580E+00	.520000E+01
.67900E+03	.9580E+00	.531000E+01
.69000E+03	.9580E+00	.512000E+01
.84600E+03	.9580E+00	.430000E+01
.84600E+03	.9580E+00	.440000E+01
.85200E+03	.9580E+00	.453000E+01
.85300E+03	.9580E+00	.465000E+01
.86500E+03	.9580E+00	.430000E+01
.86500E+03	.9580E+00	.440000E+01
.89300E+03	.9580E+00	.429000E+01

a. The thermal conductivities determined from each author's data will be compared with each other and the MATPRO model in a series of figures presented in Section 2.3.4.

Table 2-5. UO_2 data, Gibby's[2.3-27] thermal diffusivity measurements. (Continued)

Temperature (K)	Density (fraction of theoretical)	Thermal Conductivity [W/(m•K)]
.90800E+03	.9580E+00	.429000E+01
.90700E+03	.9580E+00	.420000E+01
.96400E+03	.9580E+00	.384000E+01
.96400E+03	.9580E+00	.392000E+01
.96900E+03	.9580E+00	.402000E+01
.96900E+03	.9580E+00	.412000E+01
.10000E+04	.9580E+00	.370000E+01
.10310E+04	.9580E+00	.394000E+01
.10310E+04	.9580E+00	.384000E+01
.10710E+04	.9580E+00	.366000E+01
.10800E+04	.9580E+00	.347000E+01
.10800E+04	.9580E+00	.355000E+01
.12040E+04	.9580E+00	.324000E+01
.12040E+04	.9580E+00	.334000E+01
.12800E+04	.9580E+00	.313000E+01
.12880E+04	.9580E+00	.299000E+01
.12880E+04	.9580E+00	.292000E+01
.12890E+04	.9580E+00	.299000E+01
.13230E+04	.9580E+00	.301000E+01
.13350E+04	.9580E+00	.290000E+01
.13840E+04	.9580E+00	.292000E+01
.13900E+04	.9580E+00	.280000E+01
.13950E+04	.9580E+00	.270000E+01
.13990E+04	.9580E+00	.280000E+01
.14120E+04	.9580E+00	.295000E+01
.14910E+04	.9580E+00	.278000E+01

Table 2-5. UO_2 data, Gibby's[2.3-27] thermal diffusivity measurements. (Continued)

Temperature (K)	Density (fraction of theoretical)	Thermal Conductivity [W/(m•K)]
.15020E+04	.9580E+00	.244000E+01
.15080E+04	.9580E+00	.262000E+01
.15100E+04	.9580E+00	.266000E+01

Table 2-6. UO_2 data from Weilbacher's[2.3-26] thermal diffusivity measurements.

Temperature (K)	Density (fraction of theoretical)	Thermal Conductivity [W/(m•K)]
.97400E+03	.9800E+00	.358000E+01
.97400E+03	.9800E+00	.381000E+01
.11710E+04	.9800E+00	.309000E+01
.11710E+04	.9800E+00	.325000E+01
.13770E+04	.9800E+00	.262000E+01
.13760E+04	.9800E+00	.285000E+01
.15750E+04	.9800E+00	.231000E+01
.15750E+04	.9800E+00	.251000E+01
.17780E+04	.9800E+00	.218000E+01
.17760E+04	.9800E+00	.239000E+01
.29790E+04	.9800E+00	.219000E+01
.19800E+04	.9800E+00	.233000E+01
.21800E+04	.9800E+00	.226000E+01
.21820E+04	.9800E+00	.239000E+01
.22810E+04	.9800E+00	.231000E+01
.22840E+04	.9800E+00	.245000E+01
.23790E+04	.9800E+00	.245000E+01

Table 2-6. UO_2 data from Weilbacher's[2.3-26] thermal diffusivity measurements. (Continued)

Temperature (K)	Density (fraction of theoretical)	Thermal Conductivity [W/(m•K)]
.23790E+04	.9800E+00	.254000E+01
.24840E+04	.9800E+00	.261000E+01
.24830E+04	.9800E+00	.273000E+01
.25770E+04	.9800E+00	.274000E+01
.25770E+04	.9800E+00	.286000E+01
.26740E+04	.9800E+00	.291000E+01
.26740E+04	.9800E+00	.302000E+01
.27730E+04	.9800E+00	.310000E+01
.27730E+04	.9800E+00	.321000E+01
.28750E+04	.9800E+00	.332000E+01
.28750E+04	.9800E+00	.344000E+01
.30250E+04	.9800E+00	.366000E+01
.30270E+04	.9800E+00	.383000E+01

Table 2-7. UO_2 data from Goldsmith and Douglas'[2.3-12] thermal diffusivity measurements.

Temperature (K)	Density (fraction of theoretical)	Thermal Conductivity [W/m•K]
.67000E+03	.960E+00	.557000E+01
.67000E+03	.9860E+00	.553000E+01
.67000E+03	.9860E+00	.559000E+01
.67000E+03	.9820E+00	.531000E+01
.67000E+03	.9770E+00	.543000E+01
.67000E+03	.9610E+00	.519000E+01
.67000E+03	.9580E+00	.498000E+01
.67000E+03	.9520E+00	.485000E+01

Table 2-7. UO_2 data from Goldsmith and Douglas'[2,3-12] thermal diffusivity measurements. (Continued)

Temperature (K)	Density (fraction of theoretical)	Thermal Conductivity [W/m•K]
.67000E+03	.9470E+00	.508000E+01
.67000E+03	.9320E+00	.455000E+01
.67000E+03	.9300E+00	.461000E+01
.67000E+03	.9060E+00	.440000E+01
.67000E+03	.9040E+00	.420000E+01
.87000E+03	.9860E+00	.468000E+01
.87000E+03	.9860E+00	.467000E+01
.87000E+03	.9860E+00	.470000E+01
.87000E+03	.9820E+00	.444000E+01
.87000E+03	.9770E+00	.460000E+01
.87000E+03	.9610E+00	.438000E+01
.87000E+03	.9580E+00	.410000E+01
.87000E+03	.9520E+00	.416000E+01
.87000E+03	.9470E+00	.426000E+01
.87000E+03	.9320E+00	.380000E+01
.87000E+03	.9300E+00	.388000E+01
.87000E+03	.9060E+00	.369000E+01
.87000E+03	.9040E+00	.349000E+01
.10700E+04	.9860E+00	.396000E+01
.10700E+04	.9860E+00	.394000E+01
.10700E+04	.9860E+00	.394000E+01
.10700E+04	.9820E+00	.375000E+01
.10700E+04	.9770E+00	.387000E+01
.10700E+04	.9610E+00	.370000E+01
.10700E+04	.9580E+00	.356000E+01
.10700E+04	.9520E+00	.346000E+01

Table 2-7. UO_2 data from Goldsmith and Douglas'[2.3-12] thermal diffusivity measurements. (Continued)

Temperature (K)	Density (fraction of theoretical)	Thermal Conductivity [W/m•K]
.10700E+04	.9470E+00	.361000E+01
.10700E+04	.9320E+00	.324000E+01
.10700E+04	.9300E+00	.330000E+01
.10700E+04	.9060E+00	.310000E+01
.10700E+04	.9040E+00	.291000E+01
.12700E+04	.9860E+00	.327000E+01
.12700E+04	.9860E+00	.326000E+01
.12700E+04	.9860E+00	.332000E+01
.12700E+04	.9820E+00	.316000E+01
.12700E+04	.9770E+00	.323000E+01
.12700E+04	.9610E+00	.312000E+01
.12700E+04	.9580E+00	.301000E+01
.12700E+04	.9520E+00	.295000E+01
.12700E+04	.9470E+00	.301000E+01
.12700E+04	.9320E+00	.266000E+01
.12700E+04	.9300E+00	.275000E+01
.12700E+04	.9060E+00	.259000E+01
.12700E+04	.9040E+00	.246000E+01

The final set of UO_2 data to be discussed are those of Hobson et al.[2.3-13] These authors have apparently measured the thermal diffusivity of a series of UO_2 samples. However, they reported only data from a single sample with a density of 10.40 x 10^3 kg/m^3 (94.9% TD). Their thermal diffusivity data were converted to thermal conductivity and are listed in Table 2-8.

The data appropriate for modeling the thermal conductivity of mixed (U, Pu)$O_{2\pm x}$ include the (U, Pu)O_2 measurements that are available,[2.3-11,2.3-17,2.3-27 to 2.3-34] and $UO_{2\pm x}$ data with $x \neq 0$.[2.3-12,2.3-13,2.3-17] The $UO_{2\pm x}$ data are important because the effect of nonstoichiometry in mixed oxide fuels is at least as important as the effect of variations in the weight fraction PuO_2. Unfortunately, the resources available to produce the present model were too limited to allow for a careful review of the (U, Pu)$O_{2\pm x}$ or the $UO_{2\pm x}$ data. For that reason, the stoichiometric data from References 2.3-27 to 2.3-30 and the model proposed by Olander[2.3-1] for the effect of O/M ratio variations will be adopted without modification.

Kim et al[2.3-35] provided the data which allow a calculation of the thermal conductivity of liquid fuel (UO_2 or UO_2-PuO_2 mixtures). They measured the thermal diffusivity of 0.813 and 1.219 mm layers of molten UO_2 in the temperature range of 3,187 through 3,315 K. The diffusivity values obtained of 1.90×10^{-6} to 3.23×10^{-6} m^2/s can be used with specific heat and density measurements to calculate the thermal conductivity of liquid fuel.

2.3.3 Model Development

The development of the model for thermal conductivity of $(U, Pu)O_{2\pm x}$ was based directly on the theory and data which have just been reviewed. The first step in producing the model was the determination of an expression for the effect of density. The UO_2 data were grouped by density, with second degree polynomials in temperature fit to the data in each group. Inspection of the data[a] revealed a regular pattern of decreasing thermal conductivity with decreasing density at low temperature but almost no density effect at high temperature. For this reason, the polynomials representing the thermal conductivity of the various groups were evaluated at 600 and 1,000 K and the average thermal conductivities obtained were used with Equation (2-28) to obtain linear functions of the form

$$\beta = \beta_0 + \beta_1 T \tag{2-30}$$

corresponding to pairs of porosity groups. The resultant values of β_0 and β_1 are listed in Table 2-9.

.

Table 2-8. UO_2 data from Hobson's[2.3-13] thermal diffusivity measurements.

Temperature (K)	Density (fruition of theoretical)	Thermal Conductivity [W/m•K]
.54700E+03	.9490E+00	.576000E+01
.60700E+03	.9490E+00	.541000E+01
.64200E+03	.9490E+00	.533000E+01
.73200E+03	.9490E+00	.496000E+01
.78800E+03	.9490E+00	.463000E+01
.83400E+03	.9490E+00	.445000E+01
.88500E+03	.9490E+00	.426000E+01
.94400E+03	.9490E+00	.413000E+01
.99500E+03	.9490E+00	.401000E+01
.10460E+04	.9490E+00	.386000E+01

a. The data and model predictions are illustrated in Section 2.3.4

Table 2-8. UO_2data from Hobson's[2.3-13] thermal diffusivity measurements.

Temperature (K)	Density (fruition of theoretical)	Thermal Conductivity [W/m•K]
.10830E+04	.9490E+00	.375000E+01
.11330E+04	.9490E+00	.362000E+01
.11500E+04	.9490E+00	.351000E+01
.11750E+04	.9490E+00	.353000E+01
.12790E+04	.9490E+00	.323000E+01
.13300E+04	.9490E+00	.315000E+01
.13920E+04	.9490E+00	.304000E+01
.14490E+04	.9490E+00	.297000E+01
.15000E+04	.9490E+00	.281000E+01
.15320E+04	.9490E+00	.284000E+01
.16210E+04	.9490E+00	.263000E+01
.16380E+04	.9490E+00	.269000E+01
.17490E+04	.9490E+00	.252000E+01
.17600E+04	.9490E+00	.258000E+01
.18070E+04	.9490E+00	.246000E+01
.18710E+04	.9490E+00	.260000E+01
.19130E+04	.9490E+00	.248000E+01
.19930E+04	.9490E+00	.245000E+01
.20160E+04	.9490E+00	.252000E+01
.20590E+04	.9490E+00	.247000E+01
.21540E+04	.9490E+00	.243000e+01
.21540E+04	.9490E+00	.249000E+01
.22430E+04	.9490E+00	.247000E+01
.23360E+04	.9490E+00	.251000E+01
.24120E+04	.9490E+00	.263000E+01
.25030E+04	.9490E+00	.266000E+01

The scatter in the values of β_0 and β_1 is caused by unknown variations of pore shape and content, as

discussed in Section 2.3.2. In subsequent model development steps, all three sets of β_0 and β_1, as well as their average values, were tested to determine which produced the model with the smallest standard error. Since very little difference was found, the average values of β_0 and β_1 were adopted.

The second step in the development of the model was the determination of the constants A and B of Equation (2-26). This determination was done with a least-squares-fit technique and the UO_2 thermal conductivity data for temperatures between 500 and 1,000 K.[a] The data were normalized to 100% TD with Equation (2-28) before the fit was carried out.

The third step in developing the UO_2 model was the determination of a value for the constant f in Equation (2-25) through the use of the high temperature data. Since Equation (2-25) models the electronic contribution to thermal conductivity, a value for f was determined with a least-squares fit to the difference between the experimental thermal conductivities and the lattice vibration contribution predicted with Equation (2-26). The factor (A + BT) in Equation (2-26) was limited to its value at T = 2,050 K because the mean free path of the phonons is about equal to the interatomic distance at this temperature.[2.3-1] No normalization for density was applied to the high temperature data.

.

Table 2-9. Values of β_0 and β_1 from various density groups

Groups Compared[a]	β_0	β_1
2 and 5	9.6	-0.00946
2 and 7	4.1	-0.00281
4 and 7	5.8	-0.00181
AVERAGES	6.5	-0.00469

a. Group 2 contains densities between 0.975 and 0.985 of theoretical

Group 4 contains densities between 0.955 and 0.965 of theoretical.

Group 5 contains densities between 0.945 and 0.955 of theoretical.

Group 7 contains densities between 0.925 and 0.935 of theoretical.

The final steps in the development of the UO_2 model were a trivial smoothing of two discontinuities in the slope of the predicted thermal conductivities as a function of temperature and the provision of an estimate for liquid fuel. The discontinuities are caused by limiting β in Equation (2-28) to values larger than -1 and limiting the phonon mean free path to at least the interatomic distance. Each discontinuity was removed by replacing temperature with an interpolated temperature in a range above the cutoff value and requiring the interpolated temperature to produce continuous functions and slopes at the ends of the range. For liquid fuel, the lattice vibration contribution to thermal conductivity was set equal to zero.

Several preliminary assumptions have been made to provide at least an approximate model for effects of variations in the plutonium content and the O/M ratio of ceramic fuels:

a. Data below 500 K were not used because Equation (2-26) is not valid near the Debye temperature.

1. The effects of variations in density of mixed oxide fuels have been assumed to be described by the porosity correction derived with UO_2 data.

2. The high temperature electronic contribution to thermal conductivity has been assumed to be the same for PuO_2, UO_2, and nonstoichiometric fuels.

3. Variations in plutonium content have been assumed to affect only the phonon-phonon scattering term in Equation (2-26).

4. Variations in O/M ratio have been assumed to affect only the defect term of Equation (2-26).

The change in the phonon-phonon scattering term of Equation (2-26) was modeled by fitting reported thermal conductivities[2.3-27 to 2.3-30,2.3-33] of (U, Pu)O_2 to Equation (2-26) with B replaced by

$$B' = B_{UO_2}(1 + b \cdot COMP) \tag{2-31}$$

where

B'	=	coefficient of temperature in Equation (2-26) for mixed oxides
B_{UO_2}	=	coefficient of temperature in Equation (2-26) for UO_2
COMP	=	UO_2 content of the fuel (ratio of weight of PuO_2 to total weight)
b	=	constant to be determined.

The resultant value of b was 0.6238.

Olander's expression[2.3-1] for the effect of O/M ratio on the defect term of Equation (2-26) was adopted to provide a preliminary model for the effect of variations from stoichiometry. The fractional change in the defect term was estimated by Olander to be

$$\frac{\Delta A}{A} = \frac{400x}{A'} \tag{2-32}$$

where

x	=	absolute value of (O/M ratio - 2.0).
A'	=	defect term in Olander's version of Equation (2-26)
$\frac{\Delta A}{A}$	=	fractional change in the defect term of Equation (2-20).

The expression for A which resulted from this adaptation is given in Equation (2-20).

The thermal diffusivity values of 1.90 x 10^{-6} through 3.23 x 10^{-6} m^2/s measured for the 0.813 and 1.219 mm layers of molten UO_2 in the temperature range of 3,187 through 3,315 K by Kim et al[2.3-35] can be used with specific heat and density measurements to calculate the thermal conductivity of molten UO_2 or UO_2-PuO_2 mixtures from the relation

$$K = C_p \rho \alpha \tag{2-33}$$

where

K	=	thermal conductivity of molten UO_2 or UO_2 - PuO_2($W/m \cdot K$)
C_p	=	specific heat capacity ($J/kg \cdot K$)
ρ	=	density (kg/m^3
α	=	thermal diffusivity (m^2/s).

Substitution of the MATPRO values for C_p and ρ at melting into Equation (2-33) yields thermal conductivities in the range 8.5 to 14.5 $W/m \cdot K$.

Kim et al.[2.3-35] interpret this unusually high conductivity as being due to internal infrared radiation heat transfer in the liquid UO_2 that is not allowed in the solid because of the effect of scattering centers, such as grain boundaries or voids. Although they caution that radiative thermal diffusivity depends on the thickness of the material as well as on the emissivity of the boundary surfaces, the variations they estimate are only 0.10 to 0.30 times the measured value. The constant 11.5 ($W/m^2 \cdot s$) used for the thermal conductivity of liquid fuel (UO_2 or UO_2-PuO_2 mixtures) in the FTHCON subroutine is the average of a range of values calculated from the data of Kim, et al. An uncertainty of $\pm$ 0.3 times the given liquid conductivity is estimated from the range of values measured.

2.3.4 Model Uncertainty

The standard error[a] of the FTHCON model for thermal conductivity with respect to its UO_2 data base is $\pm$ 0.20 $W/m \cdot K$. The standard error with respect to the $(U,Pu)O_2$ data base is $\pm$ 0.29 $W/m \cdot K$. The first two terms of Equation (2-21), the expression of model uncertainty which has been added to the FTHCON subcode, were constructed to reproduce these uncertainties at 0 and 20% PuO_2 content. The third term of Equation (2-21) provides an engineering estimate of the increase in the error of the model for nonstoichiometric fuel.

Figures 2-7 through 2-10 illustrate the model predictions and the UO_2 data base for several densities. Each figure shows data within $\pm$0.005 of the fraction of theoretical density assumed for the model prediction. The UO_2 data of each investigator show scatter nearly as large as the standard error of the model. This fact suggests that this part of the model is complete.

Mixed oxide data have not been compared to the current model because the part of the model that applies to mixed oxide (fuel) is preliminary.

a. The standard error was estimated with the expression (sum of squared residuals/number of residuals minus the number of constants used to fit the data)$^{1/2}$. Five constants were used for the UO_2 data, and six were used for the PuO_2 data.

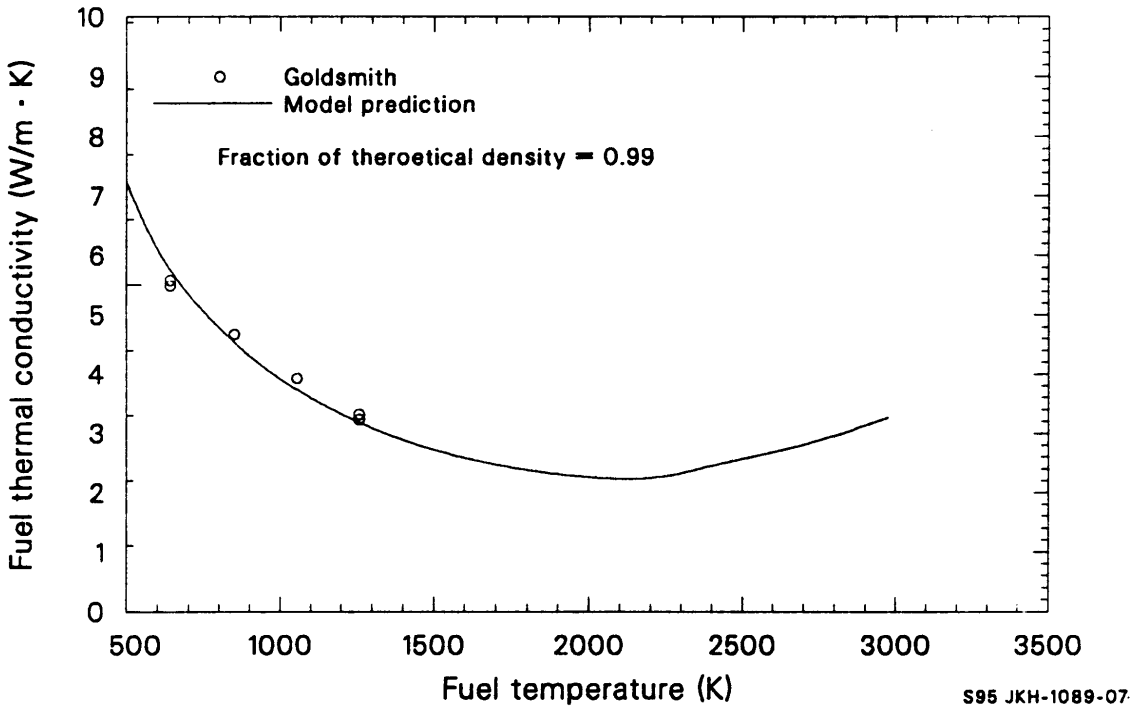

Figure 2-7. Model prediction for thermal conductivity of 0.99% TD UO_2 compared to data from specimens with densities in the range 0.985 to 0.995% TD.

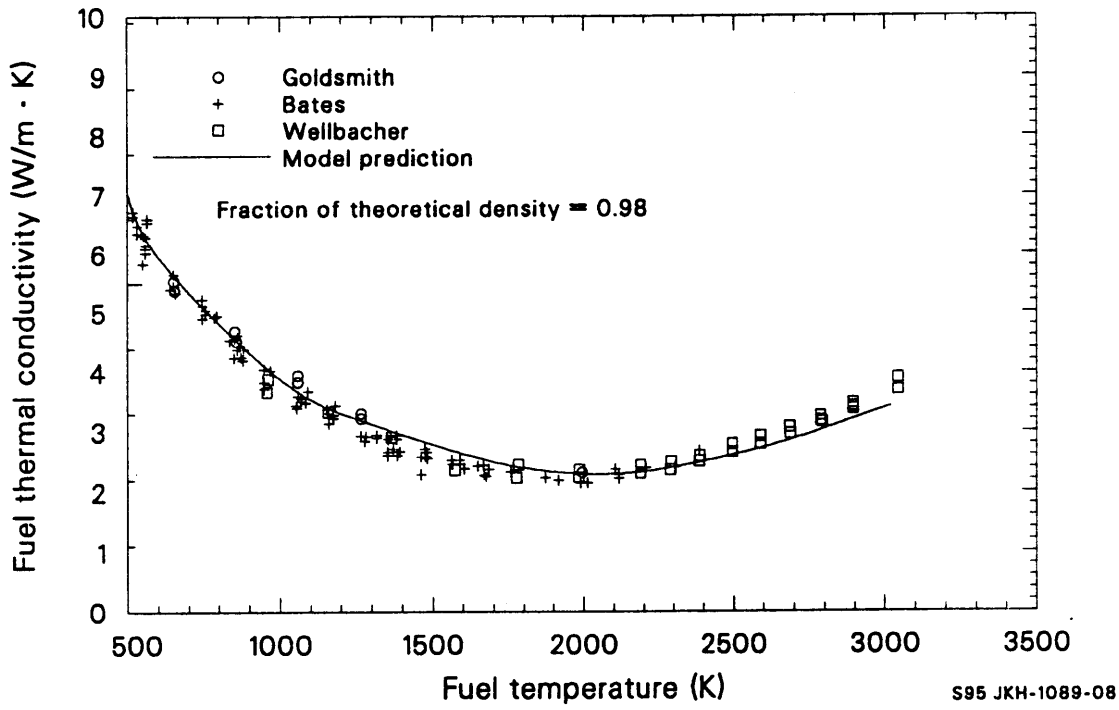

Figure 2-8. Model prediction for thermal conductivity of 0.98% TD UO_2 compared to data from specimens with densities in the range 0.975 to 0.985% TD.

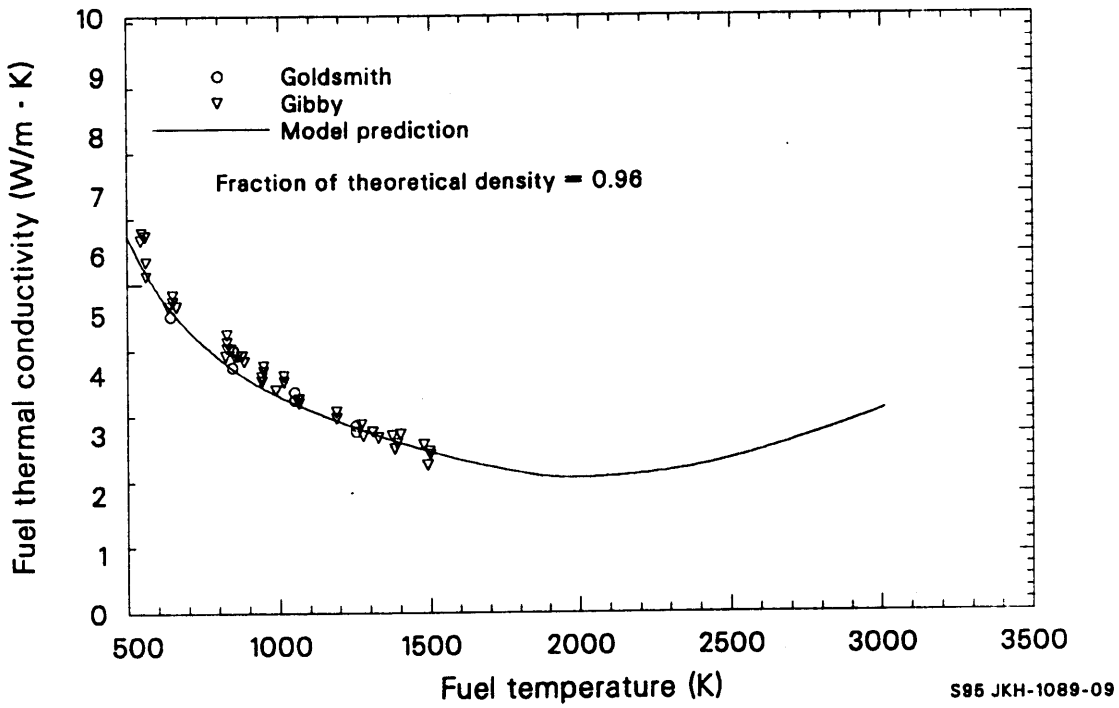

Figure 2-9. Model prediction for thermal conductivity of 0.96% TD UO_2 compared to data from specimens with densities in the range 0.955 to 0.965% TD.

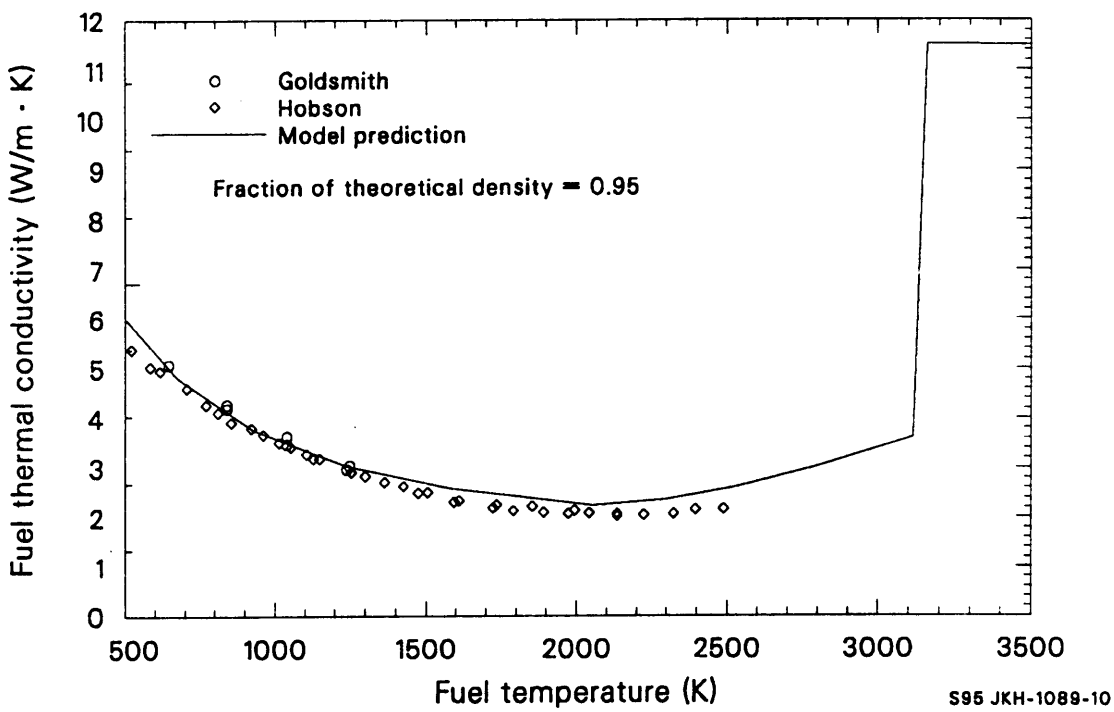

Figure 2-10. Model prediction for thermal conductivity of 0.95% TD UO_2 compared to data from specimens with densities in the range 0.945 to 0.955% TD.

2.3.5 References

2.3-1 D. R. Olander, *Fundamental Aspects of Nuclear Reactor Fuel Elements*, TID-26711-P1, 1976.

2.3-2 C. Kittel, *Introduction to Solid State Physics*, New York: John Wiley and Sons, Inc., 1956.

2.3-3 R. Berman, *Thermal Conduction in Solids*, Oxford: Clarendon Press, 1976.

2.3-4 H. J. Goldsmith, *The Thermal Properties of Solids*, New York: Dover Publications, Inc., 1965.

2.3-5 J. L. Bates, C. A. Hinman, T. Kawada, "Electrical Conductivity of Uranium Dioxide," *Journal of the American Ceramic Society, 50*, 1967, pp. 652-656.

2.3-6 G. P. Marino, "The Porosity Correction Factor for the Thermal Conductivity of Ceramic Fuels," *Journal of the American Ceramic Society, 38*, 1970, pp. 178-190.

2.3-7 A. L. Loeb, "Thermal Conductivity: A Theory of Thermal Conductivity of Porous Materials," *Journal of the American Ceramic Society, 37*, 1954, pp. 96-99.

2.3-8 J. R. MacEwan, R. L. Stoute, and M. F. Notley, "Effect of Porosity on the Thermal Conductivity of UO_2," *Journal of Nuclear Materials, 24*, 1967, pp. 109-112.

2.3-9 A. Biancheria, "The Effect of Porosity on Thermal Conductivity of Ceramic Bodies," *Transactions of the American Nuclear Society, 9*, 1966, p. 15.

2.3-10 G. Ondracek and B. Schulz, "The Porosity Dependence of the Thermal Conductivity for Nuclear Fuels," *Journal of Nuclear Materials, 46*, 1973, pp. 253-258.

2.3-11 J. C. VanCraeynest and J. P. Stora, "Effect de la Porosite sur la Variation de Conductubilite Thermique du Bioxyde d'Uranium en Fonction de la Temperature," *Journal of Nuclear Materials, 37*, 1970, pp. 153-158.

2.3-12 L. A. Goldsmith and J. A. M. Douglas, "Measurements of the Thermal Conductivity of Uranium Dioxide at 670-1270 K," *Journal of Nuclear Materials, 47*, 1973, pp. 31-42.

2.3-13 I. C. Hobson, R. Taylor, and J. B. Ainscough, "Effect of Porosity and Stoichiometry on the Thermal Conductivity of Uranium Dioxide," *Journal of Physics Section D: Applied Physics, 7*, 1974 pp. 1003-1015.

2.3-14 R. R. Asamoto, F. L. Anselin, and A. E. Conti, "The Effect of Density on the Thermal conductivity of Uranium Dioxide," *Journal of Nuclear Materials, 29*, 1969, pp. 67-81.

2.3-15 J. C. Hedge, *Measurement of Thermal Conductivity of Uranium Dioxide*, AECU-3881, September 20, 1956.

2.3-16 W. K. Kingery et al., "Thermal Conductivity X: Data for Several Pure Oxide Materials Corrected to Zero Porosity," *Journal of the American Ceramic Society, 37*, 1954, pp.107-110.

2.3-17 F. J. Hetzler et al., *The Thermal Conductivity of Uranium and Uranium Plutonium Oxides*, GEAP-4879, August 1967.

2.3-18 T. G. Godfrey et al., *Thermal Conductivity of Uranium Dioxide and Armco Iron by an Improved Radial Heat Flow Technique*, ORNL-3556, June 1964.

2.3-19 J. Lambert Bates, *High Temperature Thermal Conductivity of "Round Robin" Uranium Dioxide*, BNWL-1431, July 1970.

2.3-20 C. F. Lucks and H. W. Deem, "Thermal Conductivity and Electrical Conductivity of UO_2," *Progress Relating to Civilian Applications During June 1960*, BMI-1448, July1, 1960.

2.3-21 J. A. Christensen, et al., "Uranium Dioxide Thermal Conductivity," *Transactions of the American Nuclear Society, 7*, 1964, pp. 391-392.

2.3-22 M. F. Lyons et al., *UO_2 Pellet Thermal Conductivity from Irradiations with Central Melting*, GEAP-4624, July 1964.

2.3-23 R. D. Reiswig, "Thermal Conductivity of UO_2 to 2,100^{o}C," *Journal of the American Ceramic Society, 44*, 1961, pp. 8-49.

2.3-24 J. Stora et al., *Thermal Conductivity of Sintered Uranium Oxide Under In-Pile Conditions*, EURAEC 1095, CEA-R 2585, August 1964.

2.3-25 C. Ferro, C. Patimo, and C. Piconi, "Thermal Diffusivity of Mixed H_{1-x}, U_x Oxides and Some Materials to be Used as Reference in the Range 650-2,700 K," *Journal of Nuclear Materials, 43*, 1972 pp. 272-276.

2.3-26 J. C. Weilbacher, "Diffusivite Thermique de l'Oxyde d'Uranium et de l'Oxyde de Thorium a Haute Temperature," *High Temperatures--High Pressure, 4*, 1972, pp. 431-438.

2.3-27 R. L. Gibby, "The Effect of Plutonium Content on the Thermal Conductivity of $(U,Pu)O_2$ Solid Solutions," *Journal of Nuclear Materials, 38*, 1971, pp. 163-177.

2.3-28 R. L. Gibby, *The Thermal Diffusivity and Thermal Conductivity of Stoichiometric, $(U_{0.8}\ Pu_{0.2})O_2$*, BNWL-704, May 1968.

2.3-29 R. L. Gibby, *The Effect of Oxygen Stoichiometry on the Thermal Diffusivity and Conductivity of $U_{0.75}Pu_{0.25}O_{2-x}$*, BNWL-927, January 1969.

2.3-30 L. A. Goldsmith and J. A. M. Douglas, "The Thermal Conductivity of Plutonium Uranium Dioxide at Temperatures up to 1,273 K," *Journal of Nuclear Materials, 43*, 1972, pp. 225-233.

2.3-31 M. Serizawa et al., "Thermal Diffusivity and Thermal Conductivity of Uranium Plutonium Dioxide," *Journal of Nuclear Materials, 34*, 1970, pp. 224-226.

2.3-32 J. C. VanCraeynest and J. C. Weilbacher, "Etude de la Conductibility Thermique des Oxides Mixed d'Uranium et de Plutonium," *Journal of Nuclear Materials, 26*, 1968, pp. 132-136.

2.3-33 H. E. Schmidt, "Die Waermeleitfaehigkeit von Uran and Uran Plutonium Dioxyd bei Hohen Temperaturen," *Forschung, Ingenieur-Wesen, 38*, 1972, pp. 149-151.

2.3-34 H. E. Schmidt, "Die Waermeleitfaehigkeit von Uran and Uran Plutonium Dioxyd bei Hohen Temperaturen," *High Temperatures--High Pressure, 3*, 1971, p. 345.

2.3-35 C. S. Kim et Al., "Measurement of Thermal Diffusivity of Molten UO_2," *Proceedings of the Seventh Symposium on Thermophysical Properties at the National Bureau of Standards, Gaithersberg, MD, May 10-12, 1977*, CONF 770537-3, pp. 338-343.

2.4 Emissivity (FEMISS)

The fuel emissivity subcode FEMISS calculates total hemispherical UO_2 emissivity (emissivity integrated over all wavelengths) as a function of temperature. Fuel emissivity is defined as the ratio of radiant energy emitted from a material to that emitted by a black body at the same temperature. The subcode is used to calculate radiant energy transfer from fuel to cladding in conjunction with thermal conduction. Radiant energy transfer can be a significant heat transfer mechanism, depending on the gap size, temperature gradient across the gap, and plenum gas.

2.4.1 Summary

According to the Stefan-Boltzmann law, the total radiant power per unit area emitted by a body at temperature T is

$$P = e\sigma T^4 \tag{2-34}$$

where

P	=	radiant power per unit area (W/m^2)
e	=	total hemispherical emissivity (unitless)
σ	=	the Stefan-Boltzmann constant (5.672×10^{-8} $W/m^2 \cdot K$)
T	=	temperature (K).

The expression used in the FEMISS subcode to describe total emissivity is

$$e = 0.7856 + 1.5263 \times 10^{-5}\ T. \tag{2-35}$$

The standard error of estimate of Equation (2-35) with respect to its data base is ± 6.8%. The emissivity data were measured at temperatures up to approximately 2,400 K, and use of FEMISS above this temperature is speculative because of possible high temperature effects that are not modeled. At the time of model development, there were no data to develop a $(U, Pu)O_2$ emissivity equation, so Equation (2-35) is also recommended for $(U, Pu)O_2$.

The data base for Equation (2-35) is discussed in Section 2.4.2. Model development is discussed in Section 2.4.3.

2.4.2 Emissivity Data

Emissivity data have been reported by Held and Wilder,[2.4-1] Cabannes,[2.4-2] Jones and Murchison,[2.4-3] Claudson,[2.4-4] Belle,[2.4-5] and Ehlert and Margrave.[2.4-6]

Held and Wilder reported hemispherical spectral (emissivity at one wavelength) emissivity data of UO_2. These data are also documented by Touloukian and Dewitt.[2.4-7] They determined the emissivity of UO_2 having O/M ratios between 1.95 and 2.29 and bulk densities between 8×10^3 and 10.6×10^3 kg/m^3. The measurements were taken at wavelengths of 0.656 and 0.7 μm and at temperatures between 450 and

2,400 K. The data show no observable emissivity trend as a function of the fuel O/M ratio or density, but scatter of the data is large (±10%) and may obscure trends. Their data indicate that emissivity increases with temperature between 450 and 2,200 K and then drops a few percent at temperatures near 2,400 K. Whether or not the emissivity continues to drop at higher temperatures is uncertain because of lack of data. Since this decrease in emissivity at high temperatures is less than the scatter of the data, the trend cannot be considered to continue until more high temperature data are obtained.

Cabannes measured reflectance (1.0--emissivity) of UO_2 up to 2,200 K as a function of wavelength and temperature. He found that the emissivity approaches1.0 at wavelengths above 20 μm but remains between 0.9 and 0.8 for wavelengths below 10 μm. He also found that emissivity did not change with thermal cycling. Since a polished surface normally deteriorates during thermal cycling, the study implies little sensitivity of emissivity data to the surface polish of the UO_2 samples.

Jones and Murchison reported reflectivity of UO_2 at wavelengths between 0.4 and 0.7 μm. The emissivity of the samples varied between 0.81 and 0.84. They found emissivity to be smallest (0.81) at a wavelength of about 0.5 μm. It increased 1 to 3% for wavelengths other than 0.5 μm. Emissivity also varied less than 3% for O/M ratios between 2.003 and 2.203.

Data reported by Claudson and Belle indicate that emissivity decreases from 0.85 to 0.37 as temperature increases from 1,000 to 2,200 K. This decrease with decreasing temperature is in direct contradiction to the Held and Wilder, Cabannes, and Jones and Murchison data. Cabannes has reviewed Claudson's data and concludes that the discrepancy is possibly due to an error in Claudson's measurement technique.

Ehlert and Margrave reported two data points from UO_2 pellets. They measured the emissivity of UO_2 at 2,073 K and approximately 3,000 K and found the emissivities to be 0.416 and 0.40, respectively.

2.4.3 Model Development

The subcode FEMISS calculates total emissivity of fuel at a particular temperature. The hemispherical spectral data of Held and Wilder and the emissivity data of Cabannes and Jones and Murchison were used in developing the FEMISS model. Data of Claudson and Ehlert and Margrave were not used because of possible errors in measurement technique.[2.4-2]

Spectral emissivity data were also used to develop the total emissivity subcode FEMISS for the following reasons. Jones and Murchison indicate that spectral emissivities do not vary more than 2 or 3% at wavelengths between 0.4 and 0.7 μm, well within the uncertainty of the data. The Cabannes data show that UO_2 emissivity is about 0.85 at all wavelengths below 10 μm. Since spectral data measured at wavelengths smaller than 10 μm do not vary more than a few percent as wavelength varies, spectral data can be used to develop a total emissivity correlation. This assumption is valid in general for FEMISS calculations, since the radiation emitted from a black body or any material has maximum intensities at wavelengths smaller than 10 μm at temperatures for which radiant energy transfer is important.

Besides the emitted wavelength, emissivity can be a function of material properties, such as density, porosity, surface finish, O/M ratio, and temperature. Analysis of the data showed no dependence of emissivity on any of the above properties except temperature. The Held and Wilder data and the Cabannes data were used in a linear regression program to obtain Equation (2-35). A standard error of estimate of ± 6.8% was also determined using Equation (2-35) and the data base.

The emissivity data of Held and Wilder and Cabannes are shown in Figure 2-11 as a function of temperature. The emissivity predictions of FEMISS at temperatures between 300 and 3,000 K are shown as a solid line in the figure. The dashed lines in the figure represent predicted $\pm 1\sigma$ values. The decreasing emissivities of the Held and Wilder data at temperatures near 2,400 K can be seen in Figure 2-11. There are no data past this temperature to determine whether the drop is a real effect or experimental error. If the trend is real, no data exist to indicate what happens to the emissivity beyond 2,400 K; so until more data at higher temperatures are obtained, the drop of the Held and Wilder data near 2,400 K is assumed to be experimental error.

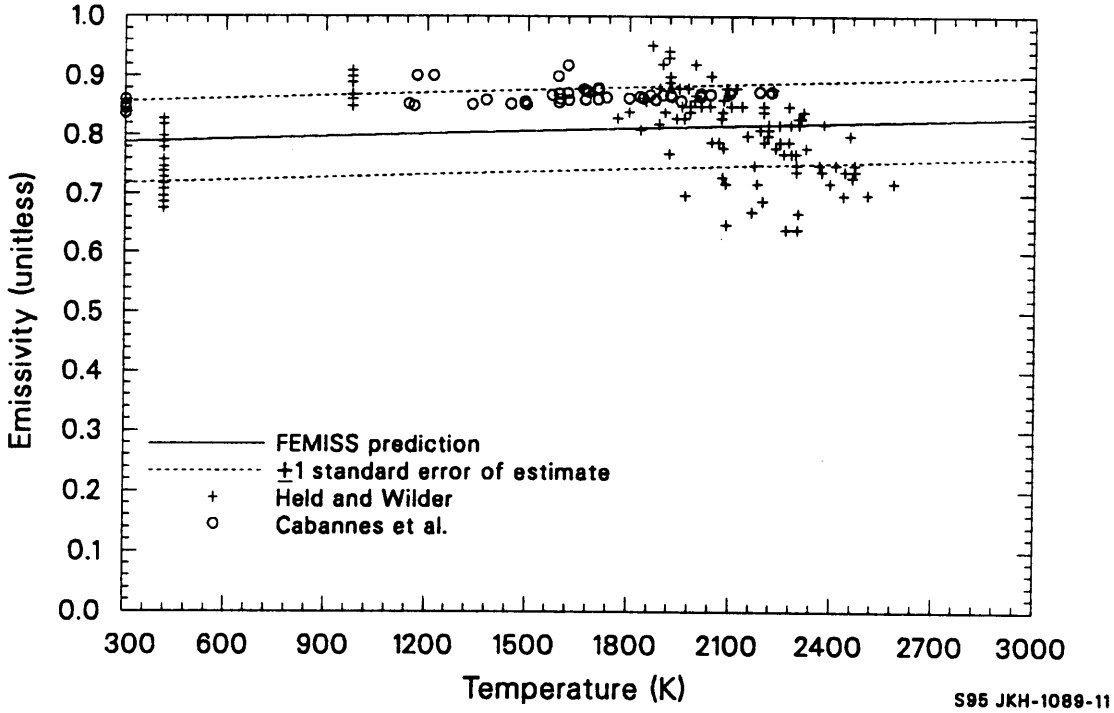

Figure 2-11. Emissivity data and corresponding FEMISS predictions.

2.4.4 References

2.4-1 P. C. Held and D. R. Wilder, "High Temperature Hemispherical Spectral Emittance of Uranium Oxides at 0.65 and 0.70 µm," *Journal of the American Ceramic Society*, 52, 1969.

2.4-2 M. M. F. Cabannes, J. P. Stora, and J. Tsakiris, "ORTIQUE-MOLECULAIRE-Fracteurs de re'flexion et d'e'mission de UO_2 a' haute Temperature," *C. R. Acad. Sc. Paris, t. 264*, January 1967.

2.4-3 J. M. Jones and D. G. Murchison, "Optical Properties of Uranium Oxides," *Nature, 205*, 4972, 1965, pp. 663-665.

2.4-4 T. T. Claudson, *Emissivity Data for Uranium Dioxides*, HW-55414, November 5, 1958.

2.4-5 J. Belle (ed.), *Uranium Dioxide: Properties and Nuclear Applications*, TID-7546, 1961.

2.4-6 T. C. Ehlert and J. L. Margrave, "Melting Point and Spectral Emissivity of Uranium Dioxide," *Journal of the American Ceramic Society, 41*, 1958, p. 330.

2.4-7 Y. S. Touloukian and D. P. Dewitt, “Thermal Radiative Properties of Nonmetallic Solids,” *Thermophysical Properties of Materials, 8*, New York-Washington: IFI/Plemung, 1972.

2.5 Thermal Expansion and Density (FTHEXP, FDEN)

The FTHEXP function models dimensional changes in unirradiated fuel pellets caused by changes in temperature. It is capable of dealing with any combination of UO_2 and PuO_2 in solid, liquid, or states with both phases and includes expansion due to the solid liquid phase change. The FDEN function determines the theoretical density of UO_2 using room temperature data and thermal expansion strains calculated by the FTHEXP subcode.

Fuel dimensional changes affect the pellet to cladding gap size, which is a major factor in determining gap heat transfer and thus the stored energy, an important quantity for safety analysis.

2.5.1 Summary (FTHEXP)

The function FTHEXP models fuel thermal expansion as a function of temperature, fraction of PuO_2, and the fraction of fuel which is molten. The O/M ratio is not included. When the departure from stoichiometry, |O/M-2.0|, is greater than 0.2, there is clearly an effect.[2.5-1 to 2.5-3] This effect is ignored in modeling thermal expansion, since typical reactor fuels only deviate about a tenth this much from the stoichiometric composition.

The equations for the thermal expansion of UO_2 and PuO_2 have the same form. In the solid phase, the equation is

$$\frac{\Delta L}{L_0} = K_1 T - K_2 + K_3 e^{\left(-\frac{E_D}{kT}\right)} \tag{2-36}$$

where

$\frac{\Delta L}{L_0}$	=	linear strain caused by thermal expansion (equal to zero at 300 K) (unitless)
T	=	temperature (K)
E_D	=	energy of formation of a defect (J)
k	=	Boltzmann's constant (1.38×10^{-23} J/K)

and K_1, K_2, and K_3 are constants to be determined. K_1, K_2, K_3, and E_D are given in Table 2-10.

For mixed UO_2 and PuO_2, the thermal expansion of the solid is found by combining the contribution from each constituent in proportion to its weight fraction.

During melting, an expansion equal to a linear strain of 0.043 occurs. If the fuel is partially molten, the strain due to thermal expansion is given by

$$\frac{\Delta L}{L_0} = \frac{\Delta L}{L_0}(T_m) + 0.043 \cdot FACMOT \tag{2-37}$$

where

$\frac{\Delta L}{L_0}(T_m)$ = thermal expansion strain of solid fuel from Equation with $T = T_m$

T_m = melting temperature of the fuel (K)

FACMOT = reaction of the fuel which is molten (unitless).

If FACMOT = 0.0, the fuel is all solid; if FACMOT = 1.0, the fuel is all molten.

The correlation used to describe the expansion of entirely molten fuel is

$$\frac{\Delta L}{L_0} = \frac{\Delta L}{L_0}(T_m) + 0.043 + 3.6\times10^{-5}\,[T - (T_m + \Delta T_m)] \tag{2-38}$$

The solid to liquid phase transition is isothermal only for pure UO_2 or pure PuO_2. For $(U,Pu)0_2$, the transition occurs over a finite temperature range, denoted in Equation (2-38) by ΔT_m. That is, ΔT_m is the liquidus minus the solidus temperature for the $(U,Pu)O_2$ considered.

Table 2-10. Parameters used in UO_2 and PuO_2 solid phase thermal expansion correlations.

Constant	UO_2	PuO_2	Units
K_1	1.0×10^{-5}	9.0×10^{-6}	K^{-1}
K_2	3.0×10^{-3}	2.7×10^{-3}	Unitless
K_3	4.0×10^{-2}	7.0×10^{-2}	Unitless
E_D	6.9×10^{-20}	7.0×10^{-20}	J

The uncertainty of the pooled data was found to be temperature dependent, increasing approximately linearly with temperature. Therefore, a percentage error is given rather than a fixed number. The $\pm\sigma$ limits were found to be within ±10% of the calculated value.

Section 2.5.2 contains a discussion and evaluation of the sources used. Section 2.5.3 presents the development of the model. In Section 2.5.4, the model predictions are compared with data and an uncertainty estimate is given. Implementation of FTHEXP is described in Section 2.5.5. In Section 2.5.6. the subcode FDEN is described.

2.5.2 Literature Review (FTHEXP)

Data were taken from nine sources for UO_2,[2.5-1 to 2.5-9] and two sources for PuO_2.[2.5-3,2.5-10] For UO_2, the data cover a temperature range from 300 to 3,400 K; and for PuO_2, the data cover a range from 300 to 1,700 K.

In four of the UO_2 experiments,[2.5-1,2.5-2,2.5-8,2.5-9] x-ray measuring techniques were used. This type of measurement gives the change in the lattice parameter rather than the bulk thermal expansion. Several investigators[2.5-2,2.5-11,2.5-12] have noted that the change in the lattice parameter is appreciably smaller than the bulk thermal expansion measured using dilatometric or interferometric methods, especially at high

(>1,000 K) temperature. In general, the difference is attributed to the creation of Schottky defects.[2.5-2,2.5-11,2.5-12] Hock and Momin[2.5-9] obtained results where there was no discrepancy between their x-ray results and bulk results. However, the bulk of the data support the Schottky defect theory, since the x-ray data consistently fall below other data at high temperatures where defects begin to appear in large numbers. Therefore, x-ray data were used in the data base only at low temperatures(< 800 K).

2.5.3 Model Development (FTHEXP)

While most authors simply fit their data with a polynomial, in this report correlations based on more physical grounds are used.

2.5.3.1 ***Low Temperature Thermal Expansion.*** The simplest theory of the linear expansion of a solid near room temperature is found in most elementary physics texts, such as Sears and Zemansky.[2.5-13]

$$\Delta L = L_0 K_1 (T - T_0) \tag{2-39}$$

or

$$\frac{\Delta L}{L_0} = K_1 T - K_1 T_0 \tag{2-40}$$

where

ΔL	=	linear expansion (m)
K_1	=	the average coefficient of linear expansion (K^{-1})
T_0	=	a reference temperature (K)
L_0	=	length at reference temperature (m).

At the reference temperature, $\Delta L = 0$ or, equivalently, $L = L_0$.

The low temperature(< 800 K) data were fit by the method of least-squares to a generalized form of Equation (2-40)

$$\frac{\Delta L}{L_0} = K_1 T - K_2 \tag{2-41}$$

This fit was done separately for UO_2 and PuO_2, and the coefficients K_1 and K_2 for each material are listed in Table 2-10. The numbers in the table have been rounded off to two significant figures. Comparison of Equations (2-40) and (2-41) shows that $T_o = K_2/K_1$, which for both fuels is 300 K, a temperature typical of the reference temperatures where $\Delta L = 0$ in data bases. These correlations describe low temperature thermal expansion within the data scatter.

2.5.3.2 ***High Temperature Thermal Expansion.*** For both UO_2 and PuO_2, Equation (2-41) was inadequate at higher temperatures (T > 1,000 K), most likely due to the formation of Schottky defects. Fenkel defects will also be present but should have no measurable effect on the thermal expansion.[2.5-2,2.5-

[9] The contribution from Schottky defects should be directly proportional to their concentration, which is given by[2.5-2,2.5-14]

$$N/N_o = K_3\ e^{(-E_D/(kT))} \tag{2-42}$$

where

N	=	number of Schottky defects in the crystal
N_o	=	number of atoms in the crystal
E_D	=	energy of formation of a defect (J)
k	=	Boltzmann's constant (1.38×10^{-23} J/K)
K_3	=	constant to be determined (unitless).

The difference between the thermal strain calculated with Equation (2-41) and each data point was found. These differences were assumed to be the defect contribution to the thermal expansion strain and were fit by the method of least-squares to an equation of the form

$$\left(\frac{\Delta L}{L_0}\right)_D = K_3 e^{(-E_D/kT)} \tag{2-43}$$

where $\left(\frac{\Delta L}{L_0}\right)_D$ is the defect contribution to the thermal expansion (unitless).

The values for K_3 and E_D resulting from these fits are given in Table 2-10.

Baldock[2.5-2] did a similar analysis using UO_2 data and those data of Conway.[2.5-4] Both the preexponential factor, K_3, and the energy of formation, E_D, were larger than those listed in Table 2-10. The differences mean that Baldock's Schottky term is smaller than the one found here at low temperatures and larger at high temperatures. The magnitude of the Schottky term determined this way is strongly dependent on the low temperature correlation used. Since Equation (2-41) has been found using a much broader data base than Baldock's, the values for K_3 and E_D in Table 2-10 should be the more accurate and are the ones used in his model.

2.5.3.3 ***Mixed Oxide Thermal Expansion.*** When the fuel is composed of a mixture of UO_2 and PuO_2, the thermal expansion is found by taking a weighted average of the contributions from each component

$$\left(\frac{\Delta L}{L_0}\right)(U, Pu)\,O_2 = \left(\frac{\Delta L}{L_0}\right)UO_2 \cdot (1 - FCOMP) + \left(\frac{\Delta L}{L_0}\right)PuO_2 \cdot FCOMP \tag{2-44}$$

where FCOMP is the PuO_2 weight fraction.

2.5.3.4 ***Thermal Expansion of Partially Molten Fuel.*** Christensen[2.5-6] has determined that UO_2 experiences a linear thermal strain of 0.043 on melting. His measurements show considerable scatter but are the only data available. No comparable measurements exist for PuO_2. The structure of the two fuels

is similar enough, however, so that no serious error should be introduced by equating the PuO_2 expansion on melting with that of UO_2. For partially molten fuel, the thermal expansion strain is given by

$$\frac{\Delta L}{L_0} = \frac{\Delta L}{L_0} T_m + 0.043 \cdot FACMOT. \tag{2-45}$$

The various terms of Equation (2-37) are defined in Section 2.5.1.

2.5.3.5 ***Thermal Expansion of Entirely Molten Fuel.*** The experiment of Christensen on UO_2 again produced the only data available and must be used for all combinations of $(U, Pu)O_2$.

A least-squares fit to his limited data yields

$$\frac{\Delta L}{L_0} = \frac{\Delta L}{L_0} T_m + 0.043 + 3.6\times10^{-5} [T - (T_m + \Delta T_m)] \tag{2-46}$$

where all the variables have been defined previously in Section 2.5.1.

2.5.4 Model Data Comparison and Uncertainty (FTHEXP)

Figure 2-12 compares the correlation for UO_2 with its data base. The three very low points around 1,500 K are all from Christensen.[2.5-6] Other data from Christensen fit well to the curve, and there is no obvious reason for the large deviation of these points. At the highest temperatures, there are several data considerably above the curve. These are also from Christensen. (At these temperatures, the possibility exists that the fuel was melted in the sample.) The large expansion which occurs on melting could easily explain the deviation of these data from the solid UO_2 data.

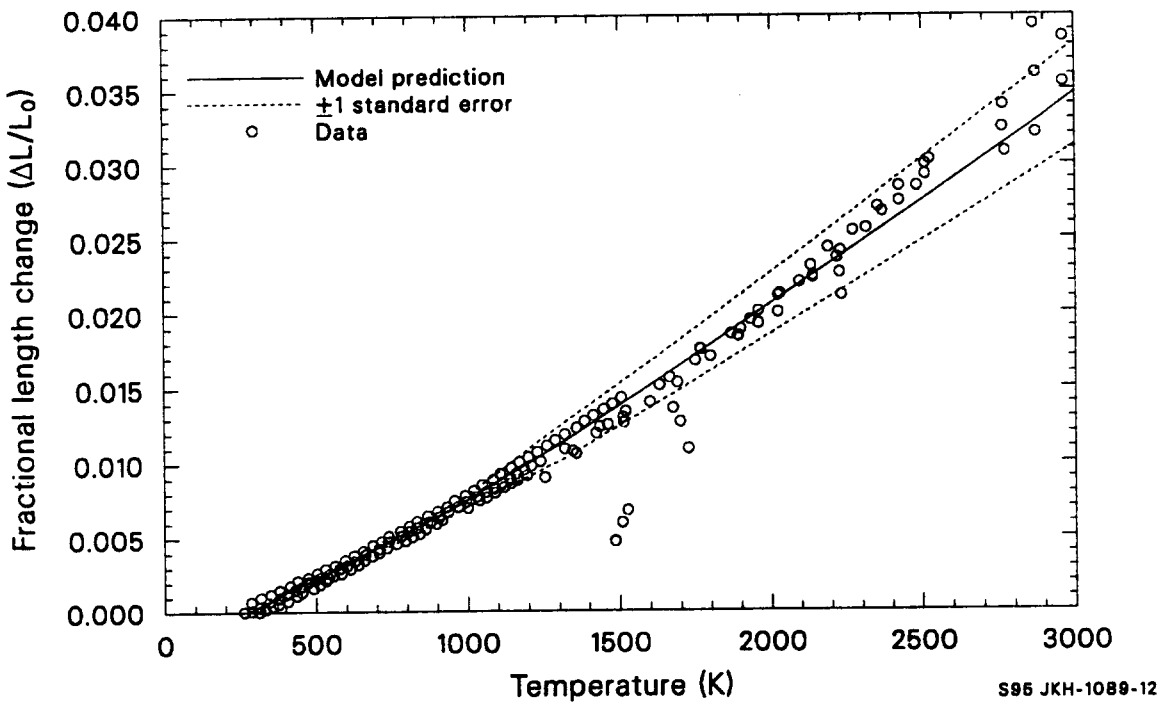

Figure 2-12. Correlation for the thermal expansion strain of UO_2 compared with its data base.

A similar comparison of the correlation and the data is shown in Figure 2-13 for PuO2. Figure 2-14 shows a comparison of the expansion curves for UO2 and PuO2 and (U0.8, Pu0.2)O2. No data are shown on this curve because thermal expansion data for mixed oxides are not available. The figures show that the thermal expansion behavior of the two materials differ, but only slightly.

Error bands, calculated from the sum of the squared residuals, are shown in Figure 2-12 and Figure 2-13. as dotted lines. These reflect a standard error of ± 10% of the calculated value found from the UO_2 data set. A percentage uncertainty is given because the error increases with temperature. A single valued uncertainty can lead to a nonphysical possibility in this model. For example, the standard error for UO_2 is ± 0.0012, which equals the thermal expansion strain at 420 K. Thus, for any temperature less than 420 K, the lower limit implied by the uncertainty would be negative, implying that as the fuel heats from 300 to 400 K, it contracts. A percentage error automatically precludes this.

The error for PuO_2 was somewhat smaller, probably due to the limited number of sources. The ± 10% error limit is also used for PuO_2 to avoid assigning unrealistic accuracy to these data.

2.5.5 Implementation (FTHEXP)

The function FTHEXP is coded as described in the preceding sections to calculate the thermal expansion strains of UO_2 and PuO_2. As used in SCDAP/RELAP5, this function has the ability to calculate the thermal expansion strains with PuO_2 disabled. (A PuO_2 fractional composition of 0.0, making the fuel pure UO_2, is hard-wired into the coding.) By inputting the PuO_2 composition fraction by argument list or common block, the PuO_2 thermal expansion strain can be restored.

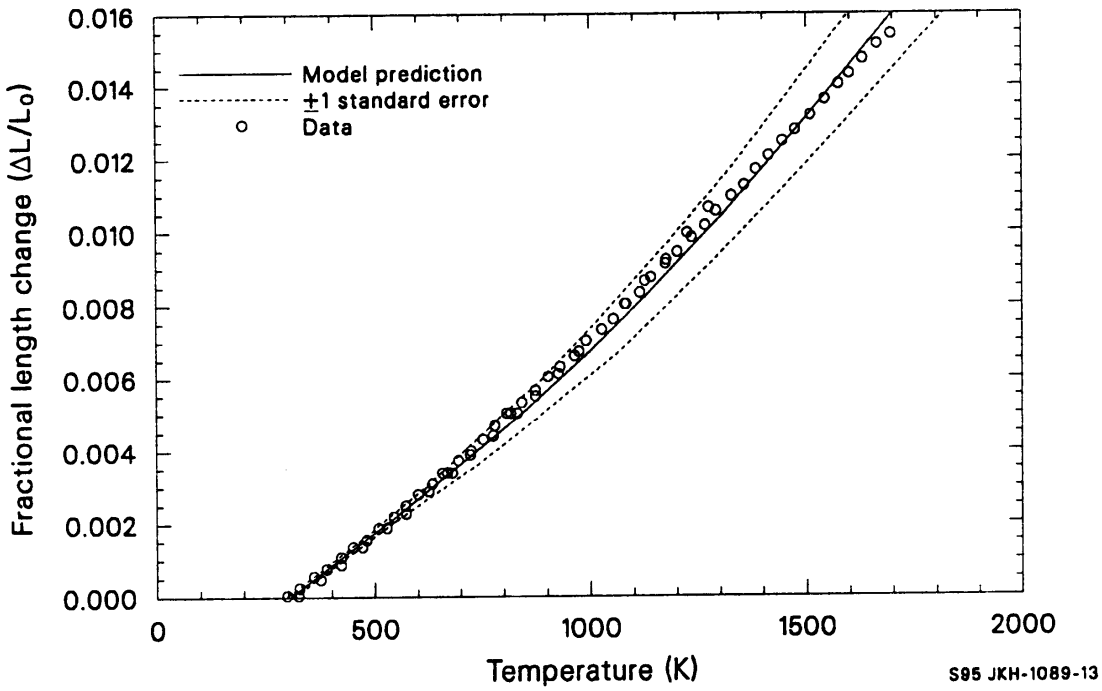

Figure 2-13. Correlation for the thermal expansion strain of PuO_2 compared with its data base.

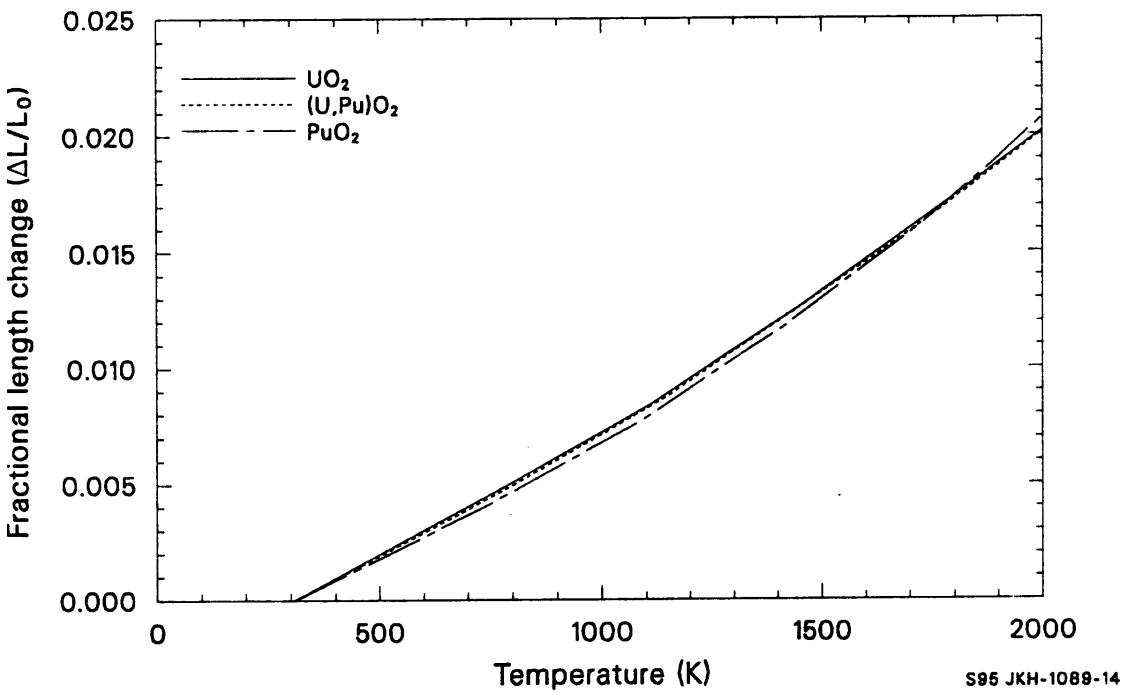

Figure 2-14. Comparisons of the UO_2, PuO_2, and $(U_{0.8}, Pu_{0.2})O_2$ correlations from 0 to 2,000 K.

2.5.6 Density (FDEN)

The FDEN function determines the theoretical density of UO_2 using room temperature data and thermal expansion strains calculated by the FTHEXP subcode. The relation used is

$$\rho = \rho_0 (1 - 3\varepsilon_{UO_2}) \tag{2-47}$$

where

ρ	=	theoretical density of UO_2 (kg/m^3)
ρ_0	=	room temperature density of UO_2 = 10,980 (kg/m^3)
ε_{UO_2}	=	linear thermal expansion strain calculated for UO_2, using a reference (zero strain) temperature of 300 K (m/m).

The room temperature density, 10,980 kg/m3, was taken from Olander[2.5-15] and is accurate to ± 20 kg/m^3. Figure 2-15 shows the theoretical density of uranium dioxide as calculated by FDEN.

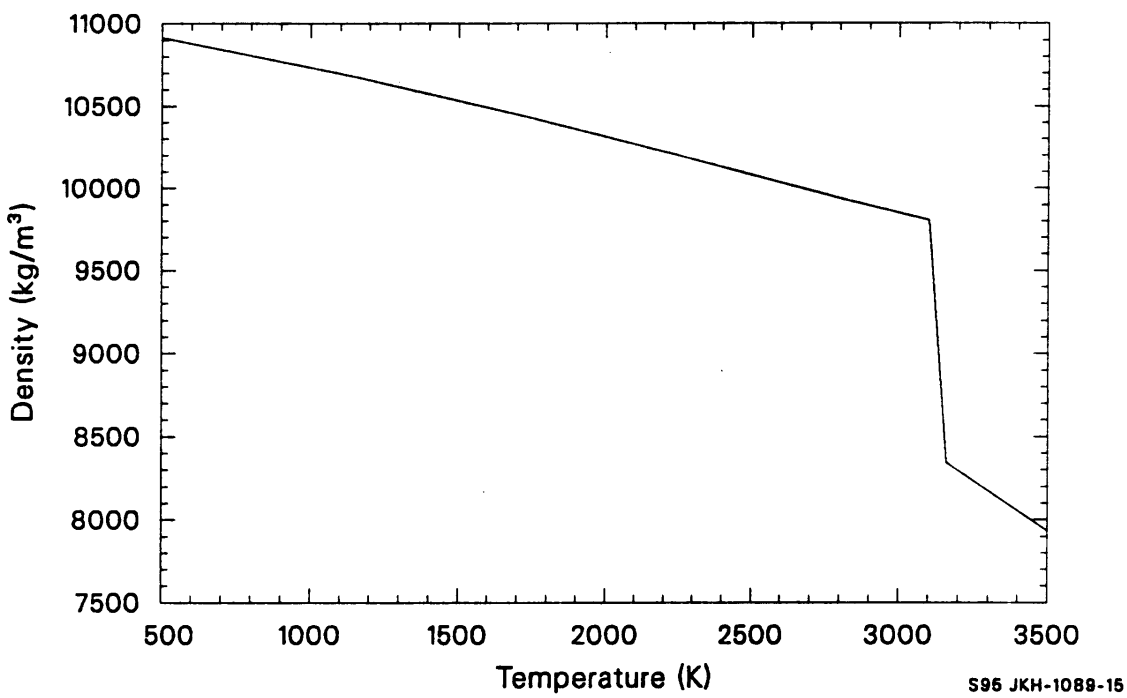

Figure 2-15. Theoretical density of UO_2.

2.5.7 References

2.5-1 F. Gronvold, "High Temperature X-ray Study of Uranium Oxides in the UO_2-U_30_8 Region," *Journal of Inorganic and Nuclear Chemistry, 1,* 1955, pp. 357-370.

2.5-2 P. J. Baldock et al., "The X-ray Thermal Expansion of Near Stoichiometric UO_2," *Journal of Nuclear Materials, 18*, 1966, pp. 305-313.

2.5-3 N. H. Brett and L. E. Russel, "The Thermal Expansion of PuO_2 and Some Other Actinide Oxides Between Room Temperature and 1,000^{o}C," *Proceedings of the Second International Conference on Plutonium Metallurgy, Grenoble, France, April 19-22, 1960*, pp. 397-410.

2.5-4 J. B. Conway et al., *The Thermal Expansion and Heat Capacity of UO_2 to 2,200^oC*, TM-63-6-6, 1963.

2.5-5 M. D. Burdick and H. S. Parker, "Effect of Particle Size on Bulk Density and Strength Properties of Uranium Dioxide Specimens," *Journal of the American Ceramic Society, 39*, 1956, pp. 181-187.

2.5-6 J. A. Christensen, "Thermal Expansion and Change in Volume of Uranium Dioxide on Melting," *Journal of the American Ceramic Society, 46*, 1963, pp. 607-608.

2.5-7 W. A. Lambertson and J. H. Handwerk, *The Fabrication and Physical Properties of Urania Bodies*, ANL-5053, 1956.

2.5-8 C. P. Kempter and R. E. Elliott, "Thermal Expansion of UN, UO_2, UO_2-ThO_2, and ThO_2, *Journal of Chemical Physics, 30*, 1958, pp. 1524-1526.

2.5-9 M. Hoch and A. C. Momin, "High Temperature Thermal Expansion of UO_2 and ThO_2," *High Temperature High Pressures, 1*, 1969, pp. 401-407.

2.5-10 M. Tokar and A. W. Nutt, "Thermal Expansion of PuO_2 from 25 to 1,420^{o}C," *Transactions of the American Nuclear Society, 10*, June 1972, pp. 210-211.

2.5-11 M. Tokar et al., "Linear Thermal Expansion of Plutonium Dioxide," *Nuclear Technology, 17*, 1973.

2.5-12 R. W. Siegel, "Vacancy Concentration in Metals," *Journal of Nuclear Materials, 69 and 70*, 1978, pp. 117-146

2.5-13 F. W. Sears and M. W. Zemansky, *University Physics*, 3rd Edition, Reading, MA: Addison-Wesley Publishing Company, 1967, p. 347.

2.5-14 C. Kittel, *Introduction to Solid State Physics*, 3rd Edition, New York: John Wiley and Sons, Inc., 1966.

2.5-15 D. R. Olander, *Fundamental Aspects of Nuclear Reactor Fuel Elements*, TID-26711-P1, 1976, p.114.

2.6 Elastic Moduli (FELMOD, FPOIR)

The FELMOD subcode calculates values for Young's modulus for UO_2 and (U, Pu)O_2. An estimate of the standard error expected with FELMOD is also calculated. FELMOD and FPOIR are intended for use with mechanical codes like FRACAS,[2.6-1] which predict pellet deformation.

The FELMOD code is discussed in Sections 2.6.1 through 2.6.4, and the FPOIR code is discussed in Section 2.6.5.

2.6.1 Summary (FELMOD)

The Young's modulus of ceramic fuels is affected by the temperature, density, and, to a lesser extent, the oxygen-to-metal ratio (O/M) and burnup of the fuel. Although published $(U,Pu)O_2$ mixed oxide data are very limited, several authors indicate that the addition of PuO_2 to UO_2 causes an increase in Young's modulus which is at least as large as the standard error of the UO_2 correlation. The increase has therefore been included in the model.

The subcode was constructed by considering values of Young's modulus measured at high temperatures typical of normal and abnormal LWR operation. Extensive room temperature data were available but were used only to help evaluate the uncertainty of the model.

The correlation developed to model Young's modulus for stoichiometric UO_2 fuel below the melting temperature is

$$ES = 2.334 \times 10^{11} [1 - 2.752 (1 - D)] [1 - 1.0915 \times 10^{-4} T] \quad (2\text{-}48)$$

where

ES	=	Young's modulus for stoichiometric UO_2 fuel (N/m^2)
D	=	fuel density (fraction of the theoretical density)
T	=	temperature (K).

For nonstoichiometric fuel or fuel which contains PuO_2, the Young's modulus below melting temperature is

$$E = ES\, e^{(-Bx)} [1 + 0.15f] \quad (2\text{-}49)$$

where

E	=	Young's modulus (N/m^2)
ES	=	Young's modulus for stoichiometric UO_2 fuel (N/m^2)
B	=	1.34 for hyperstoichiometric fuel or 1.75 for hypostoichiometric fuel
x	=	the magnitude of the deviation from stoichiometry in $MO_{2\pm X}$ fuel
f	=	PuO_2 content of the fuel (weight fraction).

The estimated standard error[a] of FELMOD for stoichiometric fuel is

(1) for temperatures between 450 and 1,600 K,

a. The standard error is estimated with a set of data by the expression (sum of squared residuals/number of residuals minus the number of constants used to fit the data)$^{1/2}$.

$$S_{ES} = 0.06 \times 10^{11} \tag{2-50}$$

(2) for temperatures between 1,600 and 3,113 K,

$$S_{ES} = 0.06 \times 10^{11} + ES\ (T-1600)/6052.6 \tag{2-51}$$

where S_{ES} is the estimated standard error for stoichiometric UO_2 fuel (N/m^2) and ES and T were previously defined.

For nonstoichiometric fuel or fuel that contains PuO_2, the estimated standard error is

$$S_E = [(S_{ES})^2 + (E - ES)^2]^{1/2} \tag{2-52}$$

where S_E is the estimated standard error (N/m^2) for nonstoichiometric fuel and E, ES, and S_{ES} were previously defined.

The following subsection is a review of the available Young's modulus data for UO_2 and $(U,Pu)O_2$ fuel. Section 2.6.3 describes the approach used to formulate the model, and Section 2.6.4 is a discussion of the uncertainty of the model.

2.6.2 Survey of Available Data (FELMOD)

Young's modulus for UO_2 and $(U,Pu)O_2$ fuel has been measured by bending techniques[2.6-2,2.6-3] and by resonant frequency methods. The bending techniques measure an isothermal Young's modulus that is more characteristic of reactor operating conditions than the adiabatic Young's modulus measured with resonant frequency methods. However, bending technique measurements are not as accurate as resonance frequency methods and will therefore not be used in the data base for this model. Also, the difference between adiabatic and isothermal Young's moduli is small, only about 0.1% of the measured value.[2.6-4]

2.6.2.1 ***Stoichiometric Fuels at Reactor Operating Temperatures.*** Data from Padel and de Novion,[2.6-5] Belle and Lustman,[2.6-6] and Hall[2.6-7] are most important because they include temperatures characteristic of reactors. Figure 2-16 illustrates values of Young's modulus for stoichiometric UO_2 at several temperatures and densities. The modulus decreases with increasing temperature and decreasing density. Moreover, the temperature dependence of the modulus at each density is nearly linear.

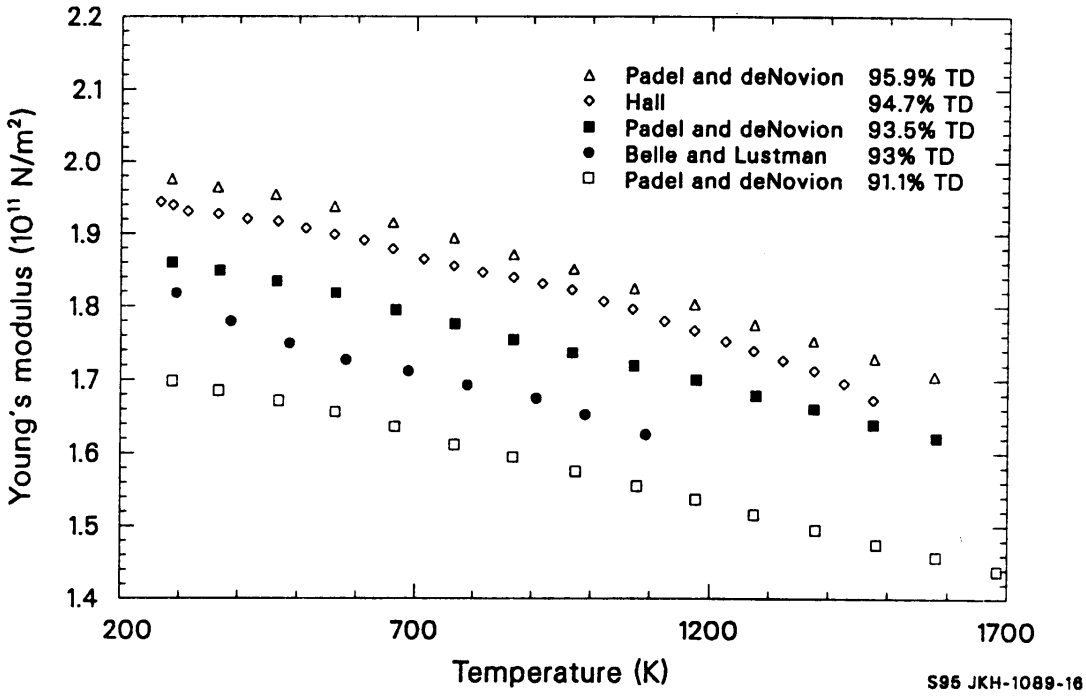

Figure 2-16. Young's modulus for stoichiometric UO_2 fuel at several temperatures and fractions of theoretical density.

Padel and de Novion have reported measurements of mixed oxide (with 20% PuO_2) moduli as a function of temperature and O/M ratio, but their report includes only room temperature data and curves representing the fractional decrease in Young's modulus with increasing temperature on 95% dense fuel. Room temperature, mixed oxide data from Padel and de Novion and from Boocock et al.,[2.6-8] as well as curves from Padel and de Novion, are shown in Figure 2-17. The effect of temperature on the (U, Pu)O_2 Young's modulus is similar to its effect on UO_2, but the stoichiometric mixed oxide samples have a larger Young's modulus than stoichiometric UO_2 samples.

Boocock's results suggest that Padel and de Novion have exaggerated the increase of Young's modulus in mixed oxides. Boocock's measurements are supported by the following observations: (a) plutonium and uranium are transition elements with presumably similar atomic bonding; (b) more recent results that showed a 3% increase in Young's modulus due to the addition of PuO_2 have been quoted elsewhere;[2.6-9] and (c) Nutt et al.[2.6-10] have published a correlation for the effect of porosity on (U,Pu)O_2 oxides that agrees with Boocock's measurements. The 3% increase due to an addition of 20% PuO_2 to UO_2 is probably the most reliable estimate, since it is based on the more recent data of de Novion.[2.6-11]

In-reactor measurements of Young's modulus as a function of neutron fluence[2.6-12] have indicated that irradiation increases Young's modulus by about 2% at saturation. Since the effect is small and could be explained by in-reactor densification of the fuel, no separate model for such burnup related changes as fission product accumulation and fuel lattice damage appears necessary at this time.

2.6.2.2 ***Room Temperature Measurements of Young's Modulus.*** The effect of changes in fuel density shown in Figure 2-16. is confirmed by room temperature measurements of Young's modulus as a function of density. Numerous data obtained with stoichiometric UO_2 fuels between 90 and 100% of

theoretical density[2.6-5 to 2.6-8 and 2.6-13 to 2.6-15] are reproduced in Figure 2-18. The data are plotted both as a function of density and porosity (1minus the density). The room temperature data for porosities between 0 and 0.1 can be described with the least-squares regression line also shown in Figure 2-18. The equation represented by the line is

$$ES = 2.334 \times 10^{11} - 5.63 \times 10^{11} P \qquad (2\text{-}53)$$

where

ES = the Young's modulus for stoichiometric UO_2 fuel (N/m^2)

P = porosity (1-D).

The standard deviation of this fit is $\pm 0.6 \times 10^{11}$ N/m^2.

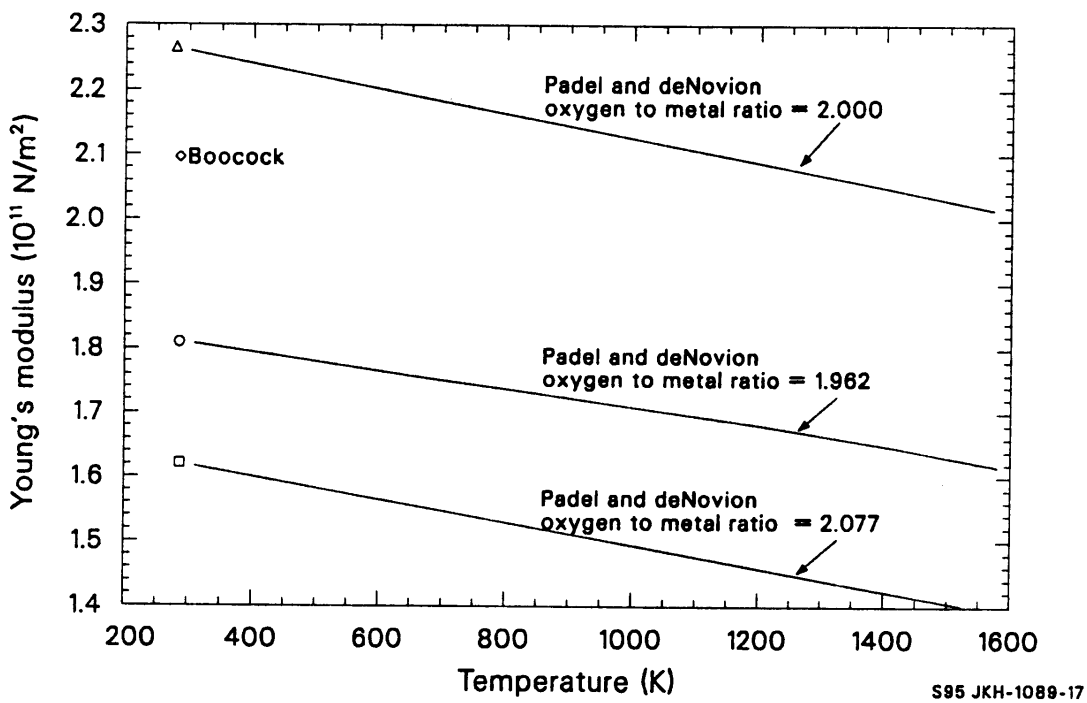

Figure 2-17. Young's modulus for (U, Pu)O_2 with various oxygen-to-metal ratios.

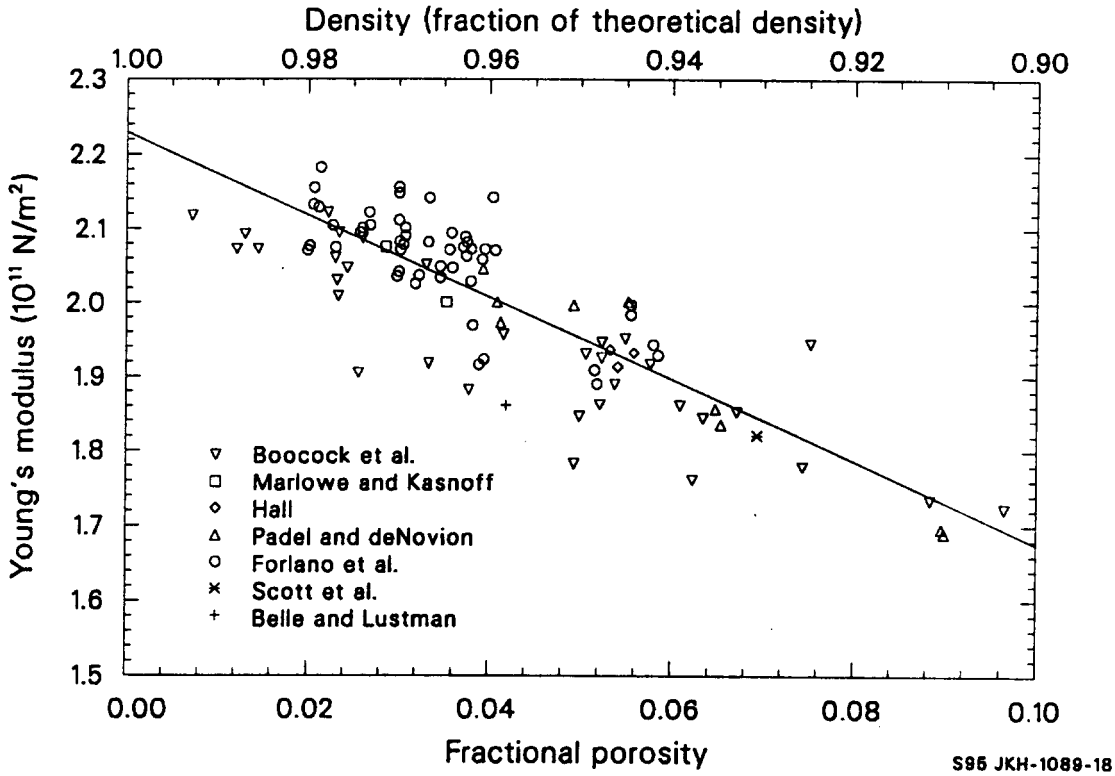

Figure 2-18. Young's modulus data and least-squares linear fit for stoichiometric UO_2 fuel at room temperature and several different densities.

2.6.2.3 ***Nonstoichiometric Fuels.*** The data available to describe the effect of variations in the O/M ratio on Young's modulus are difficult to interpret. For example, the significant variation of Young's modulus with changes in stoichiometry reported by Padel and de Novion (see Figure 2-17) is not seen in low density fuel studies by Nutt et al.[2.6-10] Data attributed to de Novion et al. by Matthews show an intermediate effect.

Table 2-11 summarizes relevant nonstoichiometric fuel data taken at room temperature.

The ratio (Young's modulus in nonstoichiometric fuel/Young's modulus in stoichiometric fuel) is plotted as a function of the fuel's O/M ratio in Figure 2-19. Most of the points show a decrease in Young's modulus when the fuel is either hypo- or hyperstoichiometric, but there is little agreement about the magnitude of the decrease.

It is possible that the fabrication history of the fuel is more significant than the O/M ratio in determining the Young's modulus. However, the inconsistent data of Nutt et al. are from fuel of uncharacteristically low density (9.5 g/cm^3) and may not apply to more dense fuels. Therefore, the correlation selected for modeling the effects of nonstoichiometric fuel is that attributed to de Novion et al. by Matthews.

$$E = ES\, e^{(-Bx)} \qquad (2\text{-}54)$$

where the terms of the equation were previously defined.

Table 2-11. Summary of Young's moduli measured in nonstoichiometric fuel at room temperature.

Composition	O/M Ratio	Porosity	Young's Modulus (10^{11} N/m^2)	Fraction of Stoichiometric Value
Padel and de Novion:				
20% $PuO_{2\pm X}$	1.962	0.051	1.808	0.798
20% $PuO_{2\pm X}$	2.000	0.050	2.265	1.000
20% $PuO_{2\pm X}$	2.077	0.050	1.620	0.715
Scott et al.:				
$UO_{2\pm X}$	2.000	0.042	1.860	1.000
$UO_{2\pm X}$	2.160	0.042	1.240	0.666
de Novion et al. as quoted by Matthews:				
20% $PuO_{2\pm X}$	2.000	--	--	1.000
20% $PuO_{2\pm X}$	1.967	--	0.926	
20% $PuO_{2\pm X}$	1.963	--	--	0.919
20% $PuO_{2\pm X}$	1.926	--	--	0.873
20% $PuO_{2\pm X}$	1.911	--	--	0.848
20% $PuO_{2\pm X}$	1.904	--	--	0.871
20% $PuO_{2\pm X}$	1.900	--	--	0.876
20% $PuO_{2\pm X}$	2.022	--	0.960	
20% $PuO_{2\pm X}$	2.050	--	--	0.929
20% $PuO_{2\pm X}$	2.052	--	--	0.915
20% $PuO_{2\pm X}$	2.089	--	--	0.903
20% $PuO_{2\pm X}$	2.111	--	--	0.895
20% $PuO_{2\pm X}$	2.142	--	--	0.816
20% $PuO_{2\pm X}$	2.168	--	--	0.812
Nutt et al.:				
20% $PuO_{2\pm X}$	2.000	--	--	1.000

Table 2-11. Summary of Young's moduli measured in nonstoichiometric fuel at room temperature. (Continued)

Composition	O/M Ratio	Porosity	Young's Modulus (10^{11} N/m^2)	Fraction of Stoichiometric Value
20% $PuO_{2\pm X}$	1.968	--	--	0.996
20% $PuO_{2\pm X}$	1.971	--	--	0.996
20% $PuO_{2\pm X}$	1.982	--	--	0.998
20% $PuO_{2\pm X}$	2.006	--	--	1.006
20% $PuO_{2\pm X}$	2.008	--	--	1.002
20% $PuO_{2\pm X}$	2.008	--	--	1.005

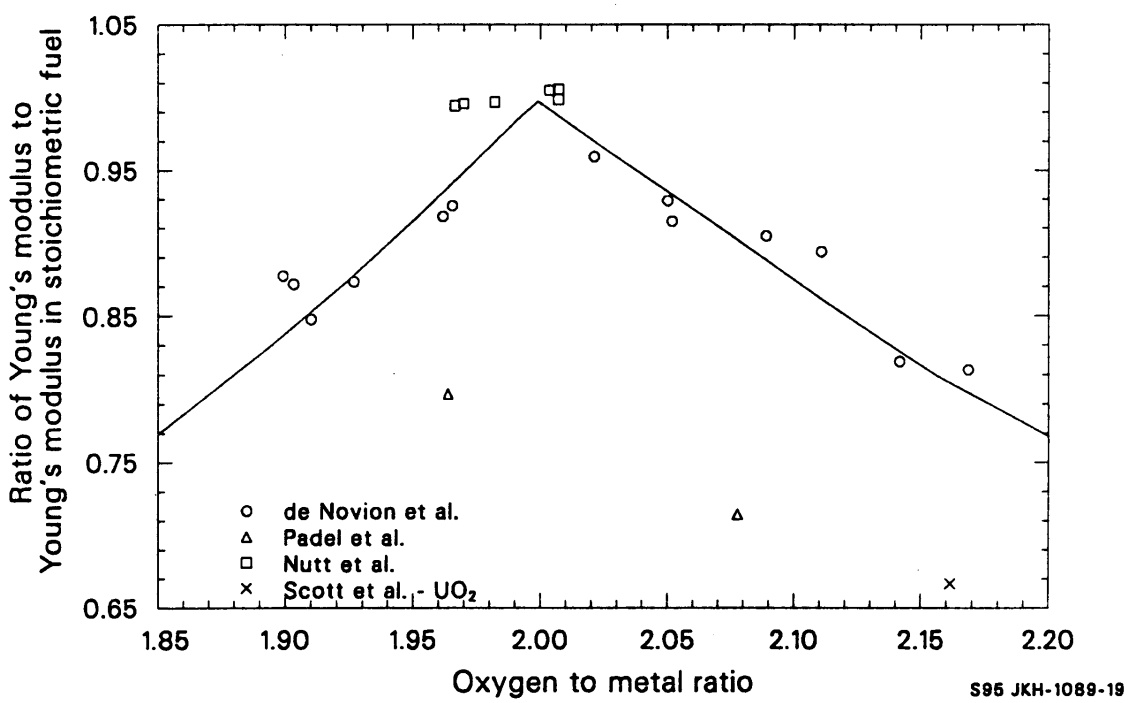

Figure 2-19. Ratio of Young's modulus for stoichiometric and nonstoichiometric fuels measured at room temperature compared to values predicted by de Novion's correlation.

Since typical in-reactor values of the O/M ratio are 1.96 to 2.04,[2.6-16] the effect of nonstoichiometry is a reduction of Young's modulus by 0 to 5%.

2.6.3 Model Development (FELMOD)

The model for Young's modulus is based primarily on the available UO_2 fuel data. A correlation for the Young's modulus of stoichiometric UO_2 fuel in the temperature range 450 to 1,600 K was developed first, then extrapolated to the approximate melting temperature and modified to predict a slight increase proportional to the weight fraction of PuO_2. The rate of increase with PuO_2 was set to reproduce the factor of 1.03, which was estimated in Section 2.6.2 for 20% PuO_2. A second modification for the estimated effect of nonstoichiometric fuel was also included in the model. The section describes the development of the model for stoichiometric UO_2 fuel.

The most realistic correlation for the effect of temperature on Young's modulus is the exponential form proposed by Wachtman et al.[2.6-17] However, the data in the temperature range 300 to 1,600 K shown in Figure 2-16 of Section 2.6.2 can be described with an expression of the form

$$E = a\,(1 + bT) \tag{2-55}$$

where a and b are constants.

A similar approximation is possible to describe the effect of porosity on Young's modulus in the limited range of porosities of interest. The approximation is used because the information necessary to use detailed discussions of the effects of very large porosities[2.6-18,2.6-19] and pore shape variation[2.6-8,2.6-20] is most often not available. The room temperature data of Figure 2-18 for porosities between 0 and 0.1 can be described with an expression of the form

$$E = c\,(1 + dP) \tag{2-56}$$

where c and d are constants.

Equation (2-56) was used to describe the effect of porosity on Young's modulus at temperatures above 450 K. However, the constants c and d were not evaluated with the room temperature data because (a) sufficient high temperature data exist to evaluate the effect of porosity in the temperature range of interest and (b) the room temperature data exhibit considerable scatter. The expression used to correlate the combined effects of porosity and temperature on Young's modulus is

$$E = e\,(1 + fT)\,(1 + gP) \tag{2-57}$$

where E, T, and P have been defined previously and e, f, and g are constants.

The constants e, f, and g were evaluated using a two step fitting procedure. In the first step, least-squares constants a and b of Equation (2-55) were determined for each UO_2 fuel sample shown in Figure 2-16. The result of the fits is summarized in Table 2-12.

The constant a is equivalent to the product of the factors e (l+gP) in Equation (2-57) for each UO_2 fuel sample, and the constant b is equivalent to the constant f in Equation (2-57). The second step of the fitting procedure was therefore the determination of a linear least-squares regression equation of constant a

on P in order to find the best fit values of e and g. The least-squares fit produced values of e = 23.34 x 10^{10} N/m^2 and g = 2.752. These values were combined with the average of the values for f = b from Table 2-12 to produce the correlation

$$E = 23.34 \times 10^{10} (1 - 1.0915 \times 10^{-4} T) (1 - 2.752 P) \quad (2\text{-}58)$$

where the terms have been previously defined. The correlation is equivalent to Equation (2-48).

No data are available for solid UO_2 fuel above 1,500 K. Equation (2-58) was simply extrapolated to estimate Young's modulus between 1,600 K and the approximate melting temperature (3,113 K)

.

Table 2-12. Least squares constants for data of Figure 2-16.

Reference	Fraction of Theoretical Density	a (10^{10} N/m^2)	b (10^{-4}/K)
Padel and de Novion	0.911	17.605	-1.1053
Padel and de Novion	0.935	19.221	-1.0056
Padel and de Novion	0.959	20.549	-1.0665
Belle and Lustman	0.93	18.742	-1.1957
Hall	0.947	20.175	-1.0843

2.6.4 Model Uncertainty (FELMOD)

The standard error of Equation (2-58) with respect to its own data base is 0.021 x 10^{11} N/m^2 (about 1% of the predicted value), and the standard error of the equation with respect to the room temperature data of Figure 2-18 is 0.073 x 10^{11} N/m^2.[a] These numbers represent lower and upper bounds for the standard error to be expected in applying the model to stoichiometric UO_2 fuel in the range 450 to 1,600 K. The first number does not include possible variations to be expected with samples not in the data base, and the second number was obtained using data taken at a low temperature where the linear expression for the effect of temperature systematically overpredicts Young's modulus. The best estimate for the standard error to be expected with this model is the standard deviation of Equation (2-53). The value, 0.06 x 10^{-11} N/m^2, includes the effect of sample to sample variation but does not include the artificial error due to the extrapolation of the temperature coefficient.

a. Since three constants were used to fit the stoichiometric UO_2 fuel data base, the number of degrees of freedom is equal to the number of measurements minus three.

For temperatures above 1,600 K, there are no data and no rigorous ways to test the model. In Equation (2-51), the standard error estimate for 400 to 1,600 K has been increased by an additive term, which is zero at 1,600 K and increases to one fourth of the predicted value at the approximate melting temperature (3,113 K).

The modifications to the basic UO_2 fuel correlation to predict the effects of nonstoichiometry and PuO_2 additions are based on limited data and are therefore uncertain. The standard error estimate expressed in Equation (2-52) assumes an independent error equal to the change produced by the models for nonstoichiometry and PuO_2 addition. That is, the net estimated standard error is taken to be the square root of the sum of the square of the standard error of the prediction for the stoichiometric UO_2 fuel elastic modulus and the square of the net change produced by the models for nonstoichiometric and PuO_2 fuels.

2.6.5 Poisson's Ratio (FPOIR)

Poisson's ratio for both UO_2 and $(U,Pu)O_2$ fuels is calculated by the routine FPOIR as a function of fuel temperature and composition.

Poisson's ratio can be related to Young's modulus and the shear modulus as follows:[2.6-21]

$$\mu = \frac{E}{2G} - 1 \tag{2-59}$$

where

μ	=	Poisson's ratio (unitless)
E	=	Young's modulus (N/m^2)
G	=	shear modulus (N/m^2).

Wachtman et al.[2.6-22] report mean values for the Young's modulus and shear modulus of UO_2 from two experiments as $E = 2.30 \times 10^{11}$ N/m^2 and $G = 0.874 \times 10^{11}$ N/m^2. Consequently, the value of Poisson's ratio is 0.316 and the routine FPOIR returns this value for UO_2. The Wachtman et al. paper only considers single crystal UO_2 data at 25°C. However, Padel and de Novion have reported values of 0.314 and 0.306 for the Poisson's ratio of polycrystalline UO_2. These values are in reasonable agreement with Wachtman's value of 0.316.

Nutt et al. determined Poisson's ratio for $U_{0.8}Pu_{0.2}0_{2-x}$ at room temperature by determining the Young's modulus and the shear modulus and calculating Poisson's ratio using Equation (2-59). Nutt and Allen's room temperature Poisson's ratio for $(U,Pu)O_2$ fuel of 0.276 ± 0.094 was found to be independent of density and is returned by FPOIR for mixed oxides.

Poisson's ratio for the fuel is shown in Figure 2-20 as a function of temperature and fuel composition. As can be seen from the figure, any plutonia content is assumed to reduce Poisson's ratio, which is independent of temperature.

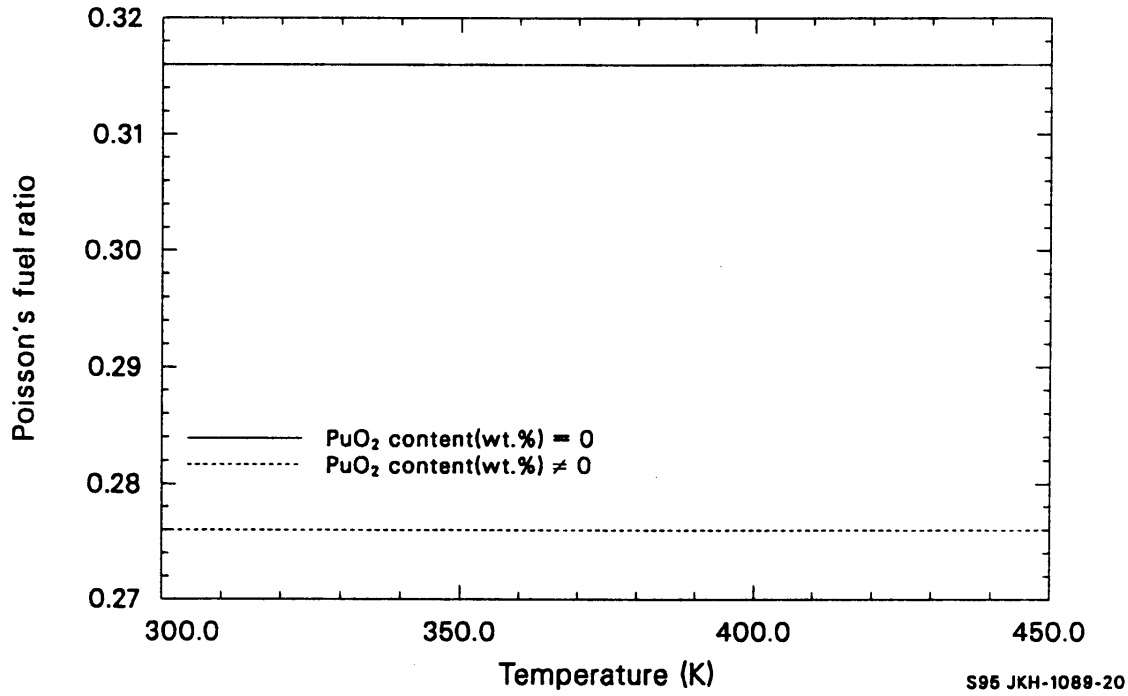

Figure 2-20. Poisson's ratio as a function of temperature.

2.6.6 References

2.6-1 M. P. Bohn, *FRACAS - A Subcode for the Analysis of Fuel Pellet Cladding Mechanical Interaction*, TREE-NUREG-1028, April 1977.

2.6-2 W. A. Lambertson and J. H. Handwerk, *The Fabrication and Physical Properties of Urania Bodies*, ANL-5053, February 1956.

2.6-3 J. T. A. Roberts and Y. Ueda, "Influence of Porosity and Deformation and Fracture of UO_2," *Journal of the American Ceramic Society, 55*, 1972, pp. 117-124.

2.6-4 I. J. Fritz, "Elastic Properties of UO_2 at High Pressure," *Journal of Applied Physics, 47*, 1976, pp. 4353-4358.

2.6-5 A. Padel and C. de Novion, "Constants Elastiques des Carbures, Nitures et Oxydes d'Uranium et de Plutonium," *Journal of Nuclear Materials, 33*, 1969, pp. 40-51.

2.6-6 J. Belle and B. Lustman, "Properties of UO_2," *Fuel Elements Conference, Paris, France, November 18-23, 1957*, TID-7546, March 1958, pp.480-481.

2.6-7 A. R. Hall, "Elastic Moduli and Internal Friction of Some Uranium Ceramics," *Journal of Nuclear Materials, 37*, 1970, pp. 314-323. Also AERE-R 5650, 1967.

2.6-8 J. Boocock, A. S. Furzer, and J. R. Matthews, The Effect of Porosity on the Elastic Moduli of UO_2 as Measured by an Ultrasonic Technique, AERE-M 2565, September 1972.

2.6-9 J. R. Matthews, *Mechanical Properties and Diffusion Data for Carbide and Oxide Fuels, Ceramics Data Manual Contribution*, AERE-M2643, 1974.

2.6-10 A. W. Nutt, Jr., A. W. Allen, and J. H. Handwerk, "Elastic and Anelastic Response of Polycrystalline UO_2-PuO_2," *Journal of the American Ceramic Society, 53*, 1970, p. 205.

2.6-11 A. de Novion et al., "Mechanical Properties of Uranium Plutonium Based Ceramics," *Nuclear Metallurgy, 17*, 1970, pp. 509-517.

2.6-12 V. M. Baranov et al., "In-Reactor Measurements of the Modulus of Elasticity of Uranium Dioxide," *Soviet Atomic Energy, 40*, 1976, pp. 37-39.

2.6-13 M. O. Marlowe and A. I. Kaznoff, "Elastic Behavior of Uranium Dioxide," *Journal of the American Ceramic Society, 53*, 1970, pp. 90-99.

2.6-14 R. J. Forlano et al., "Elasticity and Anelasticity of Uranium Oxides at Room Temperature: I Stoichiometric Oxide," *Journal of the American Ceramic Society, 50*, 1967, pp. 92-96.

2.6-15 R. Scott et al., "The Plastic Deformation of Uranium Oxides Above 800°C," *Journal of Nuclear Materials, 1*, 1959, pp. 39-48.

2.6-16 D. R. Olander, *Fundamental Aspects of Nuclear Reactor Fuel Elements*, TID-26711-P1, 1976, pp. 160-166.

2.6-17 J. B. Wachtman et al., "Exponential Temperature Dependence of Young's Modulus for Several Oxides," *Physics Review, 122*, 6, 1961, pp. 1754-1759.

2.6-18 M. O. Marlowe and D. R. Wilder, "Elasticity and Internal Friction of Polycrystalline Yttrium Oxide," *Journal of the American Ceramic Society, 48*, 1965, pp. 227-233.

2.6-19 N. Igata and K. Domoto, "Fracture Stress and Elastic Modulus of Uranium Dioxide Including Excess Oxygen," *Journal of Nuclear Materials, 45*, 1972/73, pp. 317-322.

2.6-20 D. P. H. Hasselman and R. M. Fulrath, "Effect of Cylindrical Porosity on Young's Modulus of Polycrystalline Brittle Materials," *Journal of the American Ceramic Society, 48*, 1965, p. 545.

2.6-21 I. S. Sokolnikoff and R. D. Specht, *Mathematical Theory of Elasticity*, 2nd Edition, NewYork: McGraw-Hill Book Company, Inc., 1956.

2.6-22 J. B. Wachtman, Jr., M. L. Wheat, H. J. Anderson, and J. L. Bates, "Elastic Constants of Single Crystal UO_2 at 25°C," *Journal of Nuclear Materials, 16*, 1, 1965, p. 39.

2.7 Creep (FCREEP)

The fuel creep model, FCREEP, calculates creep rate of UO_2 and (U, Pu)O_2 fuels. Fuel creep affects the width of the gap between fuel pellets and cladding and hence the temperature gradient in the fuel rod. FCREEP was developed through use of both out-of-pile and in-pile data. The samples were high density (generally above 95% theoretically dense) and were irradiated to burnups too low for swelling to be a major factor. Therefore, the fuel dimensional changes calculated with the FCREEP subcode should simply be added to the dimensional changes calculated using other MATPRO correlations.

2.7.1 Summary

The FCREEP model calculates creep deformation of UO_2 or mixed oxide fuels. The model includes a time dependent creep rate for UO_2, valid for both steady state and transient reactor conditions. Fuel creep is modeled as a function of time, temperature, grain size, density, fission rate, oxygen to metal (O/M) ratio, and external stress.

At a transition stress (σ_t), the creep rate changes from a linear stress dependence to a creep rate proportional to stress to a power n. The transition stress is defined by

$$\sigma_t = \frac{1.6547\times10^7}{G^{0.5714}} \tag{2-60}$$

where

σ_t	=	transition stress (Pa)
G	=	fuel grain size (μm).

The creep function is dependent on an Arrhenius type activation energy. This energy is found to be a function of the fuel O/M ratio. Increasing the O/M ratio increases the creep rate, all other things being constant. The activation energy of UO_2 below the transition stress is given by

$$Q_1 = 17884.8\,\{e^{\left[\frac{-20}{\ln(x-2)}-8\right]}+1\}^{-1} + 72124.23 \tag{2-61}$$

where

Q_1	=	activation energy below the transition stress (cal/mol)
x	=	O/M ratio.

The activation energy of UO_2 above the transition stress is

$$Q_2 = 19872\left[e^{\left(\frac{-20}{\ln(x-2)}-8\right)}+1\right]^{-1} + 111543.5 \tag{2-62}$$

where Q_2 is the activation energy above the transition stress (cal/mol).

The steady state creep rate of UO_2 is determined using

$$\dot{\varepsilon} = \frac{(A_1 + A_2\dot{F})\,\sigma e^{\left(-\frac{Q_1}{RT}\right)}}{(A_3 + D)\,G^2} + \frac{(A_4 + A_8\dot{F})\,\sigma^{4.5} e^{\left(-\frac{Q_2}{RT}\right)}}{A_6 + D} + A_7\sigma\dot{F}e^{\left(\frac{Q_3}{RT}\right)} \tag{2-63}$$

where

$\dot{\varepsilon}$	=	steady state creep rate (s^{-1})

A_1	=	0.3919
A_2	=	1.3100×10^{-19}
A_3	=	-87.7
A_4	=	2.0391×10^{-25}
A_6	=	-90.5
A_7	=	3.72264×10^{-35}
A_8	=	0.0
$\dot{F}$	=	fission rate (fissions/m3)/s
σ	=	stress (Pa)
R	=	universal gas constant (J/mol · K)
T	=	temperature (K)
D	=	density (percent of theoretical density)
G	=	grain size (μm)
Q3	=	2.6167 x 103(J/mol).

For mixed oxides, the steady state creep rate is found using the equation

$$\dot{\varepsilon}_s = \frac{(B_1 + B_2 F)\,\sigma}{G^2} e^{\left[-\frac{Q_3}{RT} + B_3(1-D) + B_4 C\right]} + (B_5 + B_6 F)\,\sigma^{4.5} e^{\left[-\frac{Q_4}{RT} + B_7(1-D) + B_4 C\right]} \tag{2-64}$$

where

B_1	=	0.1007
B_2	=	7.57×10^{-20}
B_3	=	33.3
B_4	=	3.56
B_5	=	6.469×10^{-25}
B_6	=	0.0
B_7	=	10.3
Q_3	=	55354.0
Q_4	=	70451.0
C	=	PuO_2 concentration (weight percent)

and the other terms have been previously defined.

When the applied stress (σ) is less than the transition stress (σ_t), the applied stress is used in the first term of Equation (2-63) or (2-64). For stresses greater than σ_t, the transition stress is used in the first term and the external stress is used in the second term of both equations.

When the fuel first experiences stress, usually during initial irradiation, or when a higher stress than in any other time step is applied, the strain rate is time dependent and is calculated using the equation

$$\dot{\varepsilon}_T = \dot{\varepsilon}_S \left[2.5e^{(-1.40\times10^{-6}t)} + 1\right] \tag{2-65}$$

where

$\dot{\varepsilon}_T$	=	the total strain rate (s^{-1})
$\dot{\varepsilon}_S$	=	steady state strain rate defined by Equation (2-63) (s^{-1})
t	=	time since the largest stress was applied (s).

Equation (2-65) is the total creep rate function prescribed by the subcode FCREEP.

2.7.2 Model Development

Fuel deforms through a number of creep mechanisms depending on the stress, density, temperature, O/M ratio, irradiation level, and grain size. The FCREEP model is based on vacancy diffusion at low stress, dislocation climb at high stress, and a time dependent creep rate at all stresses at times less than 300 hours after a stress increase. The time dependent creep increases the creep rate over the steady state value for times less than 300 hours but contributes little at longer times. Only constant volume creep is modeled in FCREEP, whereas hot pressing processes are being considered separately.

This subcode incorporates the UO_2 steady state creep model proposed by Bohaboy,[2.7-1] with modifications suggested by Solomon[2.7-2] for fission enhanced and fission induced creep. The subcode also incorporates the $(U,Pu)O_2$ creep equation proposed by Evans et al.[2.7-3] modified in a similar manner to include fission enhanced creep. The constants proposed by Bohaboy and Solomon for UO_2 creep and by Evans for $(U,Pu)O_2$ creep were fit to the data base.

2.7.2.1 ***Steady State Creep.*** Steady state creep for ceramic fuel can be modeled as a two process phenomenon: (a) low stress creep based on vacancy diffusion and (b) power law creep based on dislocation climb.

The theoretical model[2.7-4 to 2.7-6] for viscous creep is based upon diffusion of vacancies from grain boundaries in tension to grain boundaries in compression. This model results in a creep rate that is (a) proportional to the vacancy diffusion coefficient, (b) inversely proportional to the square of the grain size, and (c) proportional to stress. Low stress creep can be written as

$$\dot{\varepsilon}_S = \left(\frac{A_1}{G^2}\right) \sigma e^{\left(-\frac{Q_2}{RT}\right)} \tag{2-66}$$

where the terms of the equation have been previously defined.

Equation (2-66) is based upon the assumption that volume diffusion controls the creep rate. Therefore, the creep rate is inversely proportional to the square of the grain size with an activation energy determined for volume diffusion. However, Coble[2.7-7] has shown that if the diffusion path is along grain boundaries, the creep rate should be inversely proportional to the cube of the grain size with an associated activation energy that corresponds to grain boundary diffusion. Equation (2-66) is derived solely for diffusion of vacancies, but grain boundary sliding has been observed during low stress creep deformation of UO_2.[2.7-8,2.7-9] Both grain boundary sliding and diffusional creep have the characteristics of linear stress dependence and an activation energy nearly that of self diffusion. Therefore, it is not possible to distinguish between mechanisms of grain boundary sliding and diffusion. Regardless of which mechanism predominates, the form of Equation (2-66) is still applicable.

At high stresses, the movement of dislocations due to external shear stresses within the crystal structure results in a macroscopic movement of material. At high temperatures, dislocation climb can occur, which results in an increase in deformation rate by allowing dislocations to surmount barriers which normally would restrict movement. Weertman[2.7-10] has proposed a model based upon dislocation climb which results in a creep rate proportional to stress raised to the 4.5 power. In this case, creep rate is not a function of grain size. This power law model for steady state creep rate is

$$\dot{\varepsilon}_S = A_2 \sigma^{4.5} e^{\left(-\frac{Q_2}{RT}\right)} \tag{2-67}$$

where the terms of the equation have been previously defined.

2.7.2.2 ***Irradiated Fuel Creep.*** Equations (2-62) and (2-63) were modified to model enhanced creep rate due to irradiation following the method suggested by Solomon. Solomon concluded that in-reactor creep of UO_2 is composed of (a) an elevated temperature regime, in which normal thermal creep mechanisms are enhanced, and (b) a low temperature regime, in which the fission process induces fuel creep. At temperatures less than 1,173 K, the creep rate is linearly proportional to fission rate and to stress. All the data appeared to lie within a broad scatter band that is insensitive to temperature. Evidence was insufficient to determine whether scatter is due primarily to variations of material properties (density, grain size, stoichiometry, and impurity concentration), or test conditions (temperature, stress, and fission rate).

Solomon consolidated the results of Perrin[2.7-11] and used Bohaboy's equation to arrive at the following expression:

$$\dot{\varepsilon}_S = \frac{(A_4 + A_8\dot{F})}{(A_6 + D)} \sigma^{4.5} e^{\left(-\frac{Q_2}{RT}\right)} + \frac{(A_1 + A_2\dot{F})}{(A_3 + D)\, G^2} \sigma e^{\left(\frac{Q_1}{RT}\right)} + A g \sigma \dot{F} \tag{2-68}$$

where A_1, A_2, A_3, A_4, A_6, A_8, and A_9 are constants and the other terms of the equation have been previously defined. This equation assumes a fivefold increase in creep rate instead of the fourfold increase reported by Perrin at a fission rate of 1.2 x 10^{19} fission/m^3/s. The five-fold increase is also assumed at higher stresses where dislocation creep occurs but where no experimental data are available.

Brucklacher et al.[2.7-12] reported an equation for the fission induced creep up to 2.5% burnup of

$$\dot{\varepsilon} = 5.6 e^{\left[-\frac{2616.8}{T}\right]} \dot{F} \tag{2-69}$$

where $\dot{\varepsilon}$ is the creep rate (s^{-1}).

Equation (2-69) is used in place of the last term of Equation (2-68), resulting in the final form of the UO_2 steady state creep Equation (2-63).

For the creep of mixed oxides, the equation suggested by Evans et al. is adopted with similar modification for fission enhanced creep. The steady state, mixed oxide creep rate equation is

$$\dot{\varepsilon}_s = \frac{(B_1 + B_2\dot{F})}{G^2}\sigma e^{\left[-\frac{Q_1}{RT} + B_3(1-D) + B_4C\right]} + (B_5 + B_6\dot{F})\,\sigma^{4.5} e^{\left[-\frac{Q_2}{RT} + B_7(1-D) + B_4C\right]} \tag{2-70}$$

where B_1, B_2, B_3, B_4, B_5, B_6, and B_7 are constants and the other terms of the equation have been previously defined.

2.7.2.3 ***Transition Stress.*** Wolfe and Kaufman[2.7-13] pointed out that the stress at which the transition from viscous creep to power law creep occurs is only mildly dependent upon temperature, but more strongly affected by grain size. Seltzeret al.[2.7-14,2.7-15] performed an analysis of the transition stress that presents circumstantial evidence for a power law creep rate with a 4.5 stress coefficient and a viscous creep rate with an inverse dependence on the square of the grain size. At the transition, Equations (2-66) and (2-67) can be equated:

$$\frac{A_1\sigma}{G^2} e^{\left(-\frac{Q_1}{RT}\right)} = A_2\sigma^{4.5} e^{\left(-\frac{Q_2}{RT}\right)} \tag{2-71}$$

where the terms of the equation have been previously defined.

Solving Equation (2-71) for the stress at the transition (σ_t):

$$\sigma_t = \left(\frac{A_1}{A_2}\right)^{1/3.5} G^{-0.57} e^{\left[\frac{(Q_2 - Q_1)}{3.5RT}\right]}. \tag{2-72}$$

If the activation energies, Q_2 and Q_1, are about the same magnitude, then the temperature dependence of σ_t should be minimal and the resulting transition stress is calculated using

$$\sigma_t = AG^{-0.57}. \tag{2-73}$$

2.7.2.4 ***Time Dependent Creep.*** The time dependent creep rate is based on an anelastic creep equation and is used in FCREEP to calculate the creep rate of water reactor fuel during the first 300 hours after the stress on the fuel has been increased. The strain resulting from the time dependent stress can be a major portion of the total creep deformation.[2.7-16] A number of time dependent creep functions were compared with transient creep data. In particular, time to a power used by other authors to describe UO_2 transient creep[2.7-17] was tried; but the function found to best predict the transient creep data was the exponential function

$$\dot{\varepsilon}_t = 2.5\,[1 + e^{(-at)}] \tag{2-74}$$

where

$\dot{\varepsilon}_t$	=	time dependent creep rate (s^{-1})
a	=	constant
t	=	time (s).

Since this subcode is to be used to calculate both steady state and transient reactor conditions, the anelastic form of time dependent creep was used because it better predicted the creep data for all times. The anelastic equation is multiplied by the steady state creep rate to obtain the total creep rate.

$$\dot{\varepsilon}_T = [1 + 2.5e^{(-at)}]\,\varepsilon_s \tag{2-75}$$

where $\dot{\varepsilon}_T$ is the total creep rate (s^{-1}) and the other terms of the equation have been previously defined.

2.7.3 Evaluation of Constants and Data Comparison

Data selection for code development use was based on the following requirements:

1. The data results from compressive creep tests were considered.

2. The initial O/M ratio was measured and documented.

3. The temperature was measured and documented.

4. The grain size was measured and documented.

Requirement (2) prevented the use of some data in determining the constants of FCREEP. These data were used after the creep model was developed (with an assumed O/M ratio) as an extra data comparison, and no significant deviation was noted.

2.7.3.1 ***Evaluation of Steady State Creep Constants.*** The basic form of the steady state equation of Solomon and Evans et al. was retained, but some of the constants were refit to include the effect of the fuel O/M ratio. The activation energies of Equation (2-61) and (2-62) were determined by calculating the creep rate using the data reported by Burton and Reynolds,[2.7-18,2.7-19] Seltzer et al.,[2.7-15] and Bohaboy et al.[2.7-1] These were data of UO_2 under different stresses, temperatures, and O/M ratios. Fitting the equations to the available data gave effective activation energies, which changed less as the O/M ratio increased than is reported in the literature.[2.7-15]

Other creep data considered while developing the subcode are Bohaboy and Asamoto,[2.7-20] Speight,[2.7-21] Brucklacher and Dienst,[2.7-22] Solomon,[2.7-23] Scott et al.,[2.7-24] and Armstrong and Irvine.[2.7-25]

The activation energies found to give the best fit to the base data were

(1) for low stresses,

$$Q_1 = 17884.8 \{ e^{\left[\frac{-20.0}{\log(x-2.0)} - 8.0\right]} + 1.0 \}^{-1} + 72124.23 \tag{2-76}$$

(2) for high stresses,

$$Q_2 = 19872.0 \{ e^{\left[\frac{-20.0}{\log(x-2.0)} - 8.0\right]} + 1.0 \}^{-1} + 112142.4 \tag{2-77}$$

After the approximate activation energies were determined, the equations were further evaluated against the data of Bohaboy et al.[2.7-1] to refine the constants. Figure 2-21 shows the calculated creep rates plotted against experimental data. Those data which did not have a documented O/M ratio are shown, along with the data used to develop the code. Figure 2-22 shows the calculated creep rates for irradiated fuel compared to the experimental data base. The uncertainty of the FCREEP calculations was determined as the standard deviation of the log of the calculated creep rate compared with the log of the corresponding creep rate. The uncertainty range is shown as dashed lines in Figures 2-21 and 2-22. The uncertainty creep rates can be calculated using the equation:

$$\dot{\varepsilon}_u = \dot{\varepsilon} \times 10^U \tag{2-78}$$

where

$\dot{\varepsilon}_u$	=	upper and lower bounds of creep rate (s^{-1})
$\dot{\varepsilon}$	=	FCREEP calculated creep rate (s^{-1})
U	=	$\pm$ 1.25.

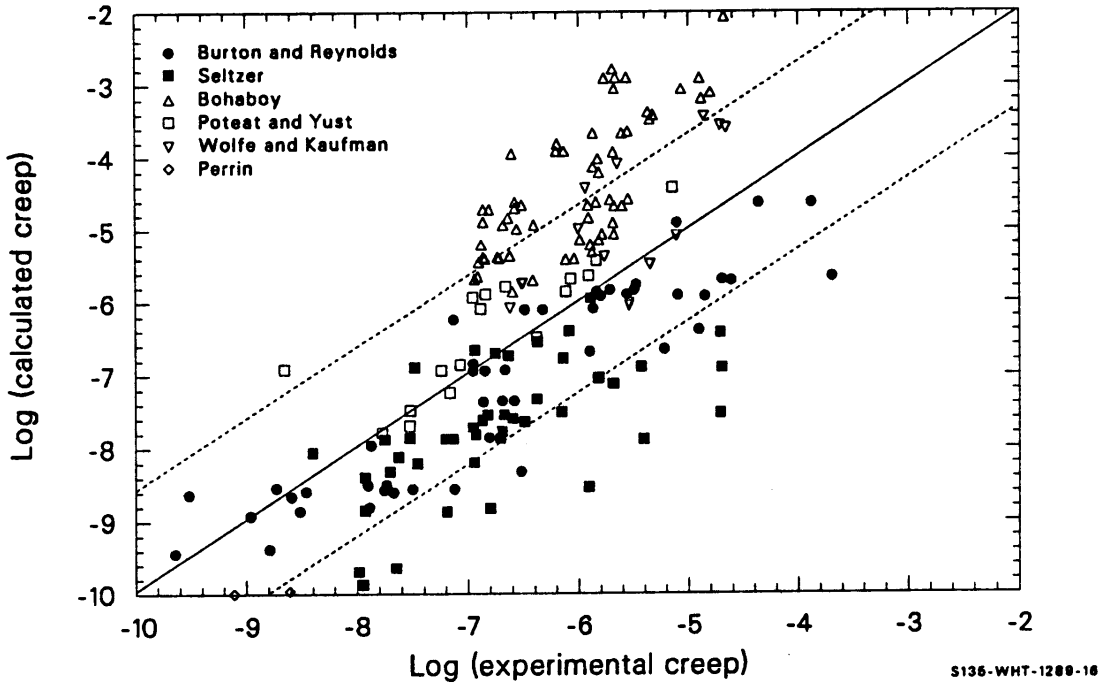

Figure 2-21. Comparison of unirradiated UO_2 experimental data with corresponding calculated values from FCREEP.

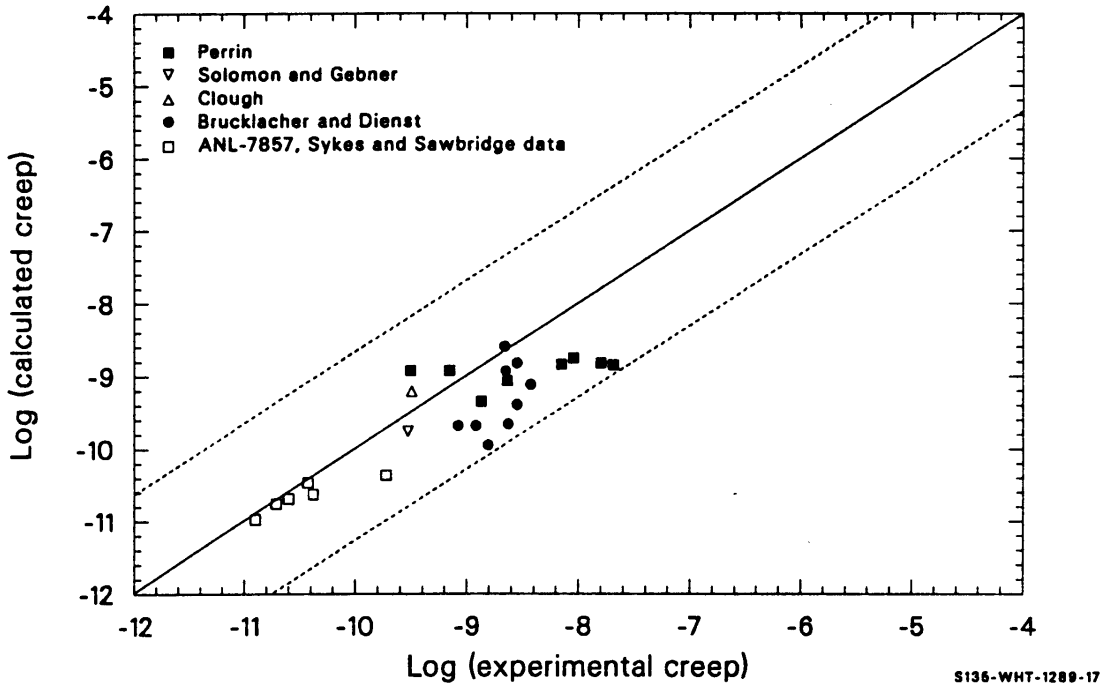

Figure 2-22. Comparison of irradiated UO_2 experimental data with corresponding calculated values from FCREEP.

2.7.3.2 ***Evaluation of Constants for Irradiation Enhanced Creep.*** The data sources used to evaluate the constants for the last term of Equation (2-63) are the fission induced creep tests of Sykes and Sawbridge,[2.7-26] Clough,[2.7-27] Brucklacher and Dienst,[2.7-28] and Solomon and Gebner[2.7-29] and in-pile creep measurements of Perrin,[2.7-11] Vollath,[2.7-30] and Slagle.[2.7-31] These data were considered by Solomon,[2.7-2] who developed Equation (2-63) except for the last term, which was proposed by Brucklacher et al.[2.7-12]

In Figure 2-23, the predictions of FCREEP are compared with mixed oxide creep data selected from compressive experiments with O/M ratios between 1.95 and 1.98. This comparison includes data from Evans et al.,[2.7-3] Routbort et al.,[2.7-32] and Perrin.[2.7-33] Good agreement is obtained for O/M ratios between 1.95 and 1.96 and grain sizes between 18 and 23 μm. However, measured values for the 4-μm material used by Evans et al.[2.7-3] are one to two orders of magnitude higher than the corresponding values calculated by FCREEP. Also, the high stress data of Routbort[2.7-32] (in the dislocation controlled creep regime) compare favorably with FCREEP calculations even though the O/M ratio is slightly higher than 1.95. The low stress data lie about an order of magnitude higher than calculated by the FCREEP model, indicating the significance of the stoichiometry on the diffusion mechanism in the viscous creep regime. Perrin's[2.7-33] data were used to determine the constants for fission enhanced creep in the linear stress creep of Equation (2-70). Reasonably good agreement is achieved for the irradiated material, but the calculated values for unirradiated material are about an order of magnitude less than experimental values. The solid line represents perfect agreement between experimental and calculated values.

2.7.3.3 ***Evaluation of Constants for Time Dependent Creep.*** Much of the reported creep rate data do not include the time dependent creep contribution, and the reported steady state data probably include those contributions, making an accurate analysis difficult. Some excellent creep studies reporting both time dependent and steady state creep have been reported. A comprehensive study was conducted by Battelle Columbus Laboratories.[2.7-11,2.7-34,2.7-35] They evaluated creep of UO_2 under both irradiated and unirradiated conditions. These data were used as the data base, along with the data reported by Solomon,[2.7-29,2.7-36] Clough,[2.7-37] Dienst,[2.7-38] and Brucklacher and Dienst.[2.7-22]

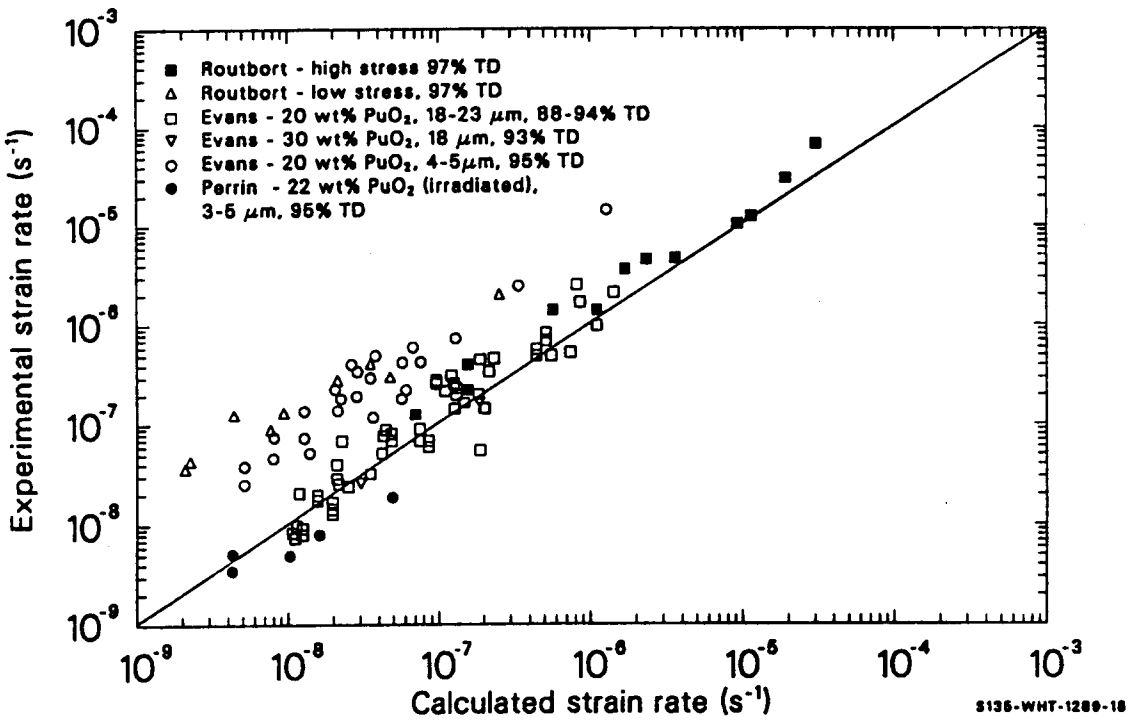

Figure 2-23. Comparison of $(U,Pu)O_2$ experimental data with corresponding calculated values from FCREEP.

Evaluation of the time dependent creep equation was carried out, using the reported steady state creep rate and then determining the appropriate function to follow the curve and have the appropriate magnitude after a number of iterations. The best estimate equation is

$$\dot{\varepsilon}_t = 2.5e^{(-1.4\times10^{-6}t)}\,\dot{\varepsilon}_s \tag{2-79}$$

where the terms of the equation have been previously defined.

Examples of the strain determined using the final strain rate equation are shown in Figures 2-24 and 2-25. They show the FCREEP calculated strain compared with the base data and show a reasonably good fit.

$$\dot{\varepsilon}_t = [2.5e^{(-1.4\times10^{-6}t)} + 1]\,\dot{\varepsilon}_s \tag{2-80}$$

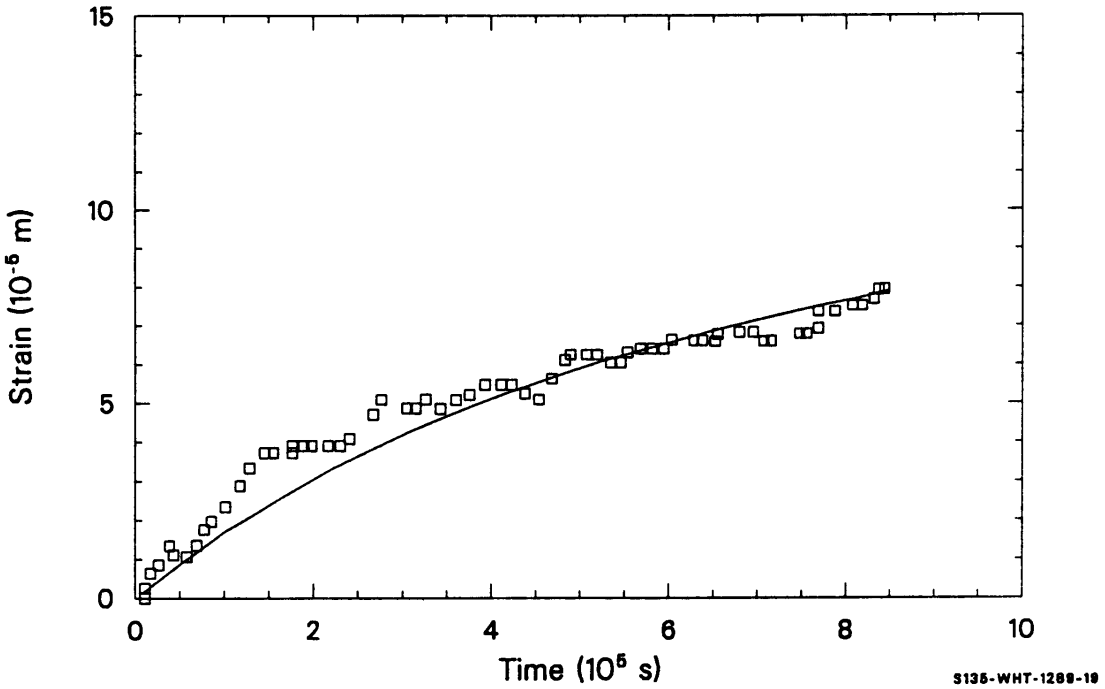

Figure 2-24. Comparison of UO_2 strain data of Rod 3C with corresponding calculated values from FCREEP.

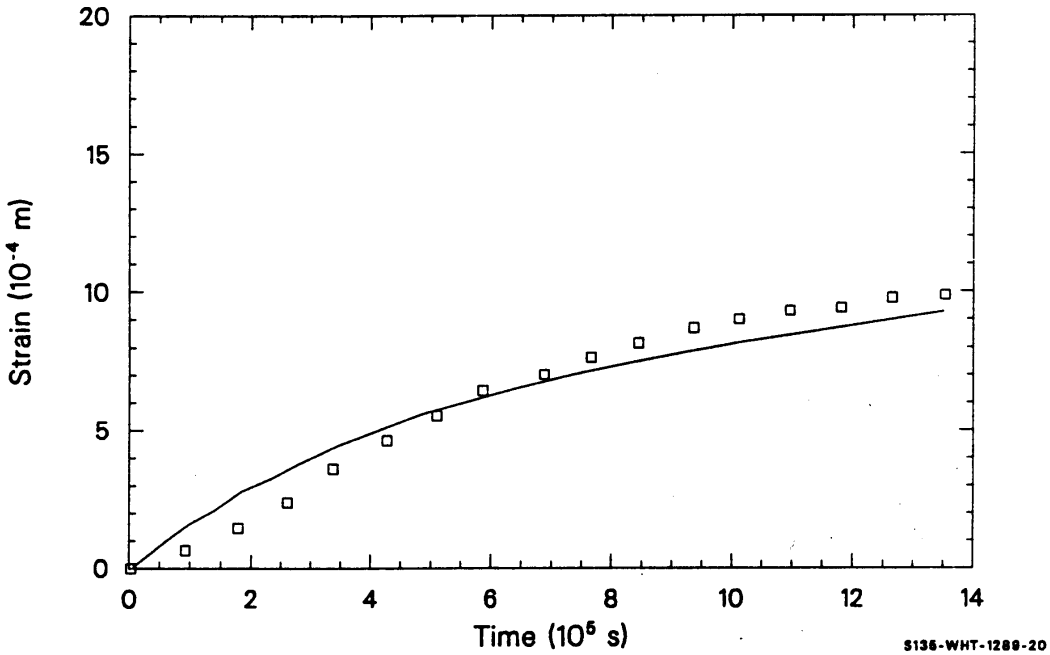

Figure 2-25. Comparison of UO_2 strain data of Capsule 2 with corresponding calculated values from FCREEP.

2.7.4 References

2.7-1 P. E. Bohaboy, R. R. Asamoto, and A. E. Conti, *Compressive Creep Characteristics of Stoichiometric Uranium Dioxide*, GEAP-10054, May 1969.

2.7-2 A. A. Solomon, J. L. Routbort, and J. C. Voglewede, *Fission Induced Creep of UO_2 and Its Significance to Fuel Element Performance*, ANL-7857, September 1971.

2.7-3 S. K. Evans, P. E. Bohaboy, and R. A. Laskiewicz, *Compressive Creep of Urania Plutonia Fuels*, GEAP-13732, August 1971.

2.7-4 J. S. Perrin and W. R. D. Wilson, *Effect of Irradiation on the Creep of Uranium Dioxide*, BMI-1899, March 1971.

2.7-5 F. R. N. Nabarro, Report of a Conference on the Strength of Solids, *Physical Society, London 1949*, p. 75.

2.7-6 C. Herring, "Diffusional Viscosity of Poly-Crystalline Solid," *Journal of Applied Physics, 21*, 1950, p. 437.

2.7-7 R. L. Coble, "A Model for Boundary Diffusion Controlled Creep in Poly-Crystalline Materials," *Journal of Applied Physics, 34*, 1963, p. 1679.

2.7-8 W. M. Armstrong, W. R. Irvine, and R. H. Martinson, "Creep Deformation of Stoichiometric Uranium Dioxide," *Journal of Nuclear Materials, 7, 2*, 1962, pp.133-141.

2.7-9 L. E. Poteat and C. S. Yust, *Grain Boundary Reactions During Deformation*, ORNL-P-2371, 1965.

2.7-10 J. Weertman, "Steady State Creep Based Through Dislocation Climb," *Journal of Applied Physics, 28*, 1957, p. 362.

2.7-11 J. S. Perrin, "Irradiation Induced Creep of Uranium Dioxide," *Journal of Nuclear Materials, 39*, 1971, pp. 175-182.

2.7-12 D. Brucklacher, W. Dienst, and F. Thummler, *Creep Behavior of Oxide Fuels Under Neutron Irradiation*, translated from German by J. L. Routbort, Argonne National Laboratory, ANL-Trans-942, May 1973.

2.7-13 R. A. Wolfe and S. F. Kaufman, *Mechanical Properties of Oxide Fuels*, WAPD-TM-587, October 1967.

2.7-14 M. S. Seltzer, A. H. Clauer, and B. A. Wilcox, "The Stress Dependence for High Temperature Creep of Polycrystalline Uranium Dioxide," *Journal of Nuclear Materials, 34*, 1970, pp. 351-353.

2.7-15 M. S. Seltzer, J. S. Perrin, A. H. Clauer, and B. A. Wilcox, "A Review of Creep Behavior of Ceramic Nuclear Fuels," *Reactor Technology, 14*, 2, January 1971, pp. 99-135.

2.7-16 J. R. Matthews, *Mechanical Properties and Diffusion Data for Carbide and Oxide Fuels*, AERE-M-2643, September 1974.

2.7-17 R. G. Sachs, *Reactor Development Program Progress Report*, ANL-RDP-16, April-May 1973.

2.7-18 B. Burton and G. L. Reynolds, "The Diffusional Creep of Uranium Dioxide: Its Limitation by Interfacial Processes," *Acta Metallurgical, 21*, August 1973, pp. 1073-1078.

2.7-19 B. Burton and G. L. Reynolds, "The Influence of Deviations from Stoichiometric Composition on the Diffusional Creep of Uranium Dioxide," *Acta Metallurgical, 21*, December 1973, pp. 1641-1647.

2.7-20 P. E. Bohaboy and R. R. Asamoto, "Compressive Creep Characteristics of Ceramic Oxide Nuclear Fuels: Part I: Uranium Dioxide," *Presented at American Ceramic Society Nuclear Division, Pittsburgh, PA, October 6-8, 1968*.

2.7-21 M. V. Speight, *Enhancement of Diffusion Creep Under Irradiation*, Central Electricity Generating Board, RD/B/N-2402, August 1972.

2.7-22 D. Brucklacher and W. Dienst, "Creep Behavior of Ceramic Nuclear Fuels Under Irradiation," *Journal of Nuclear Materials, 42*, 1972, pp. 285-296.

2.7-23 A. A. Solomon, "Effect of c-Radiation on the Deformation of UO_2," *Journal of Nuclear Materials, 47*, 1973, pp. 345-346.

2.7-24 R. Scott, A. R. Hall, and J. Williams, "The Plastic Deformation on Nonstoichiometric Uranium Dioxide," *Journal of Nuclear Materials, 1*, 1959, pp. 39-48.

2.7-25 W. M. Armstrong and W. R. Irvine, "Creep Deformation on Nonstoichiometric Uranium Dioxide," *Journal of Nuclear Materials, 9*, 2, 1963, pp. 121-127.

2.7-26 E. C. Sykes and P. T. Sawbridge, *The Irradiation Creep of Uranium Dioxide*, Central Electricity Generating Board, RD/BN/1489, November 1969.

2.7-27 D. J. Clough, "Irradiation Induced Creep of Ceramic Fuels," *Proceedings on Fast Reactor Fuel and Fuel Elements, GFK Karlsruhe, 1970*, p. 321.

2.7-28 D. Brucklacher and W. Dienst, "Kontinuierliche Messung Des Kriechens von UO_2 Unter Bestrahlung," *Journal of Nuclear Materials, 36*, 1970, pp. 244-247.

2.7-29 A. A. Solomon and R. H. Gebner, Instrumented Capsule for Measuring Fission Induced Creep of Oxide Fuels," *Nuclear Technology, 13*, February 1972, p. 177.

2.7-30 D. Vollath, "Thermisches Kriechen von Plutonium-Haltigen Oxidischen Kernbrennstoffen," *Reactor Meeting, Bonn, Germany, March 30, 1971*, pp. 558-561.

2.7-31 O. D. Slagle, *High Temperature Creep of UO_2-20 wt% PuO_2*, HEDL-TME-71-28, August 1971.

2.7-32 J. L. Routbort, N. A. Javed, and J. C. Voglewede, "Compressive Creep of Mixed Oxide Fuel Pellets," *Journal of Nuclear Materials, 44*, 1972, pp. 247-259.

2.7-33 J. S. Perrin, "Effect of Irradiation on Creep of UO_2-PuO_2," *Journal of Nuclear Materials, 42*, 1972, pp. 101-104.

2.7-34 J. S. Wilson and R. D. William, *Effect of Irradiation on the Creep of Uranium Dioxide*, BMI-1899, March 1971.

2.7-35 W. R. D. Wilson and J. S. Perrin, "Anisothermal Effects During In-Pile Creep Testing of Uranium Dioxide, *Nuclear Science and Engineering, 45,* 1971.

2.7-36 A. S. Solomon, "Radiation Induced Creep of UO_2," *Journal of the American Ceramic Society, 56,* March 1973.

2.7-37 D. J. Clough, "Creep Properties of Oxide and Carbide Fuels Under Irradiation," *Journal of Nuclear Materials, 65,* 1977.

2.7-38 W. Dienst, "Irradiation Induced Creep of Ceramic Nuclear Fuels," *Journal of Nuclear Materials, 65,* 1977.

2.8 Densification (FUDENS)

The subcode FUDENS calculates fuel dimensional changes due to irradiation induced densification of UO_2 and $(U,Pu)O_2$ fuels during the first few thousand hours of water reactor operation. Densification is calculated as a function of fuel burnup, temperature, and initial density. This subcode is based on data of fuel that had small amounts of hydrostatic stress applied. Densification can result from hydrostatic stress on the fuel due to contact with the cladding, which is considered in Section 2.10. Both models describe the same physical process; the model which calculates the greater densification should be used.

The data used to develop FUDENS were taken from irradiated fuel which was also swelling. If fuel densification is much greater than swelling during the first 1,000 hours of irradiation, then, to a first approximation, swelling can be neglected during this period. That was done for the development of the FUDENS model. A suggested calculation procedure, combining calculations of models given in this section with pressure sintering and fuel swelling models, is discussed in Section 2.9.

2.8.1 Summary

The subcode FUDENS uses one of two methods to calculate the maximum density change during irradiation. The density change observed during a resintering test (1,973 K for more than 24 hours) in a laboratory furnace is the preferred input for the calculation. If a resintering density change is not input, the code uses the initial unirradiated density of the fuel and the fuel fabrication sintering temperature for the calculations. These inputs are used in the following equations to calculate the maximum densification length change during irradiation.

If a nonzero value for the resintering density change is input,

when FTEMP < 1,000 K,

$$\left(\frac{\Delta L}{L}\right)_m = -(0.0015)\,RSNTR. \tag{2-81}$$

When FTEMP ≥ 1,000 K,

$$\left(\frac{\Delta L}{L}\right)_m = -(0.00285)\,RSNTR. \tag{2-82}$$

If zero is input for the resintering density change,

when FTEMP < 1,000 K,

$$\left(\frac{\Delta L}{L}\right)_m = \frac{-22.2\,(100 - DENS)}{(TSINT - 1453)}. \tag{2-83}$$

When FTEMP > = 1,000K,

$$\left(\frac{\Delta L}{L}\right)_m = \frac{-(66.6)\,(100 - DENS)}{(TSINT - 1453)} \tag{2-84}$$

where

$\left(\frac{\Delta L}{L}\right)_m$	=	maximum possible dimension change of fuel due to irradiation (percent)
RSNTR	=	resintered fuel density change (kg/m^3)
FTEMP	=	fuel temperature (K)
DENS	=	theoretical density (percent)
TSINT	=	sintering temperature (K).

Densification as a function of burnup is calculated using

$$\frac{\Delta L}{L} = \left(\frac{\Delta L}{L}\right)_m + e^{[-3\,(FBU + B)]} + \left(2.0e^{[-35\,(FBU + B)]}\right) \tag{2-85}$$

where

$\left(\frac{\Delta L}{L}\right)$	=	dimension change (percent)
FBU	=	fuel burnup (MWd/kgU)
B	=	a constant determined by the subcode to fit the boundary condition: $\Delta L/L$ when FBU = 0.

The FUDENS subcode uses Equation (2-85) to calculate total densification and then subtracts the densification from the previous time step to obtain the incremental densification. The incremental densification for the time step being considered is the output of the subcode FUDENS.

2.8.2 Uranium Dioxide and Mixed Oxide Densification Data and Models

The sintering of cold pressed UO_2 powder may be divided usefully into three regimes: (a) the formation of necks between particles, (b) the decrease of interconnected porosity, and (c) the subsequent volume reduction of isolated pores.[2.8-1] The last stage begins when 92 to 95% theoretical density (TD) is reached. Two types of porosities, open along grain edges and closed along grain boundaries, are present in low density fuels, less than 92% TD, sintered at low temperatures. However, at higher sintering temperatures, accelerated grain growth occurs; and closed porosity may be found inside the grains even in low density fuel pellets.[2.8-2] In-reactor densification involves the third sintering regime in which fine, isolated, closed porosity (located either at grain boundaries or within the grains) is annihilated.

2.8.2.1 ***Uranium Dioxide and Mixed Oxide Densification Data.*** Edison Electric Institute/ Electric Power Research Institute (EEI/EPRI)[2.8-3,2.8-4] performed a comprehensive study of UO_2 fuel densification. The fuel was tested in the RAFT (Radially Adjustable Facility Tubes) of the General Electric Test Reactor (GETR), located in Pleasanton, CA. Pre- and postirradiation physical properties were reported on fuel subjected to burnups of up to 3.5 MWd/kgU. It was concluded that irradiation induced densification can be correlated with fuel microstructure, that is, the largest in-reactor density changes occurred for fuel types having a combination of the smallest pore size, the largest volume percent of porosity less than 1 μm in diameter, the smallest initial grain size, and the lowest initial density. The volume fraction of porosity less than 1 μm in diameter contributed significantly to densification of the fuel types studied; and density increases were accompanied by a significant decrease in volume fraction of pores in this size range. The volume fraction of pores ranging in diameter from 1 to 10 μm initially increased with densification but decreased with continued densification. Significant density increases occurred during irradiation, with only minimal increases in grain size.

Analysis of the EPRI data also shows that pellets in low burnup, low fission rate, and low temperature regions densify less than pellets irradiated to the same burnup but in higher fission rate and temperature positions, as shown in Figure 2-26. At higher fission rates and temperatures, densification occurs rapidly, with pellets approaching maximum densities at a burnup of 1 MWd/kgU. At lower fission rates, densification appears to be increasing with a fuel burnup of 2 MWd/kgU.

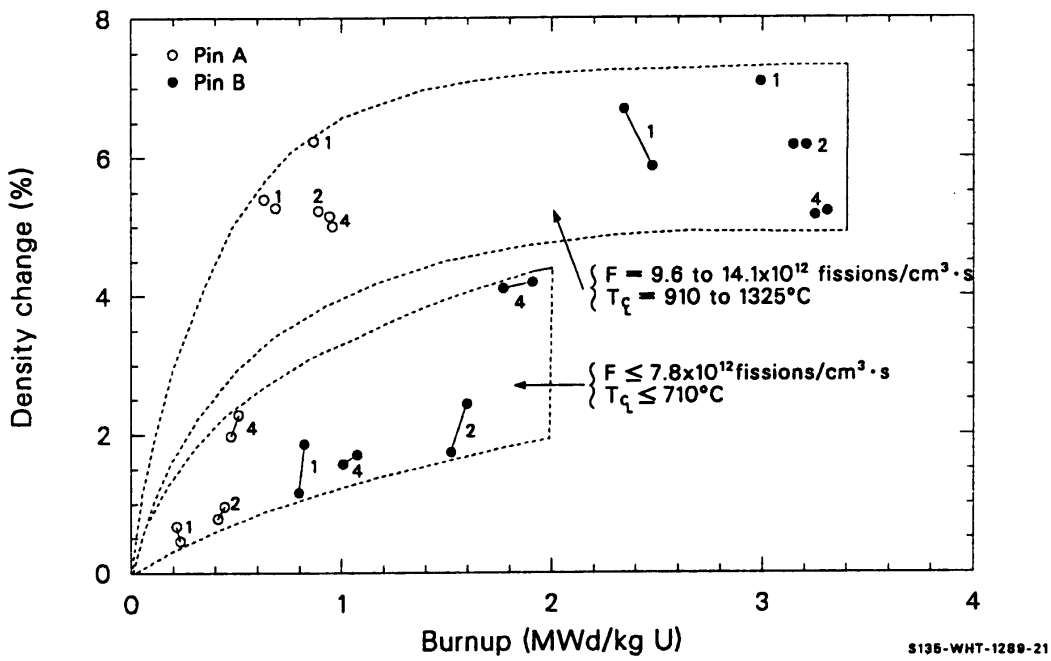

Figure 2-26. The effect of burnup and fission rate on the fuel density change for EPRI fuel types 1, 2, and 4.

Rolstad et al.[2.8-5] measured the fuel stack length change of UO_2 in the Halden HBWR reactor. Fuel densities (87, 92, and 95% TD), fabrication sintering temperatures, irradiation power levels, and fuel cladding gap sizes were used to study irradiation induced densification. Rolstad found that fuel sintered at the highest temperature densified the least (stable fuel) and fuel sintered at the lowest temperature densified the most (unstable fuel). The axial length change, measured during irradiation and as a function of burnup

(Figure 2-27) for different power levels, did not depend on reactor power levels or fuel temperatures. Hanevik et al.[2.8-6] proposed that this may be attributed to the fact that temperatures of the outer edges (shoulders) of the pellet would be within 200 to 300 K of each other at both power levels. Since the shoulders of the pellet are much colder than its center, the axial in-reactor length change measurements are probably a measurement of the shrinkage in these regions (low temperature irradiation densification). The amount of fuel stack length change of the Halden fuel was found to depend on out-of-pile thermal fuel stability, initial density, and burnup.

Collins and Hargreaves[2.8-7] compared measurements of out-of-pile sintering rates at temperatures greater than 1,600 K with the sintering rates of fuel irradiated in the Windscale Advanced Gas Cooled Reactor (WAGR). The observed out-of-pile densification was attributed to the sintering of grain boundary porosity and was characterized by an activation energy of 2.9×10^5 J/mol for grain boundary diffusion. Extrapolation of these results to 1,000 K, the approximate temperature of the in-pile material, indicated that negligible thermal sintering would be expected after a few hundred hours at this temperature. In addition, no evidence of sintering was observed in out-of-pile annealing tests conducted at 1,173 K and a pressure of 2.06 MPa. However, fuel irradiated to less than 0.3% burnup at temperatures between 1,000 and 1,100 K experienced significant reduction in diameter. This shrinkage was attributed to irradiation induced sintering, which decreased the initial fuel porosity volume. Pores with diameters less than 3 μm were reported by Collins and Hargreaves to be the major source of increased density. Pores with diameters greater than 10 μm were reported stable during irradiation at temperatures below 1,500 K.

Ferrari et al.[2.8-8] measured UO_2 fuel pellet densification in commercial reactors using both movable in-core flux detectors and postirradiation examination of selected test rods. The densification rate of the fuel was reported to occur rapidly during the early stages of irradiation and then slow or even stop after about 6 to 10 MWd/kgU, as shown in Figure 2-28. These results are consistent with the measurements of Rolstad et al. For 92% TD, the extent of densification was reported to vary significantly with microstructure, but no microstructure details were reported. Ferrari et al. reported that power levels between 4.9 and 55.8 kW/m did not significantly affect densification. This result is in agreement with Rolstad et al. The axial shrinkage was suggested to be controlled by densification in the shoulder of the fuel pellets, a region of the fuel pellets where the temperature is generally below 1073 K, a temperature too low for in-pile densification to be attributed to thermal mechanisms. Ferrari et al. proposed that the kinetics of densification are compatible with irradiation enhanced diffusion processes.

Metallographic measurements on the fuel by Ferrari et al. indicated that the irradiation enhanced densification was associated with the disappearance of fine pores and that pore shrinkage significantly decreased with increasing pore size. These results correspond to the EPRI findings. Ferrari et al. suggested that densification could be reduced through both microstructural control of the fuel pellet and a reduction of the fine porosity content. Both of these factors are influenced by the fabrication process, especially the sintering temperature and the use of so called pore formers. Ferrari et al. reported that experimental fuel of 89% theoretical density has been made and demonstrated to be relatively stable in the Saxton reactor.

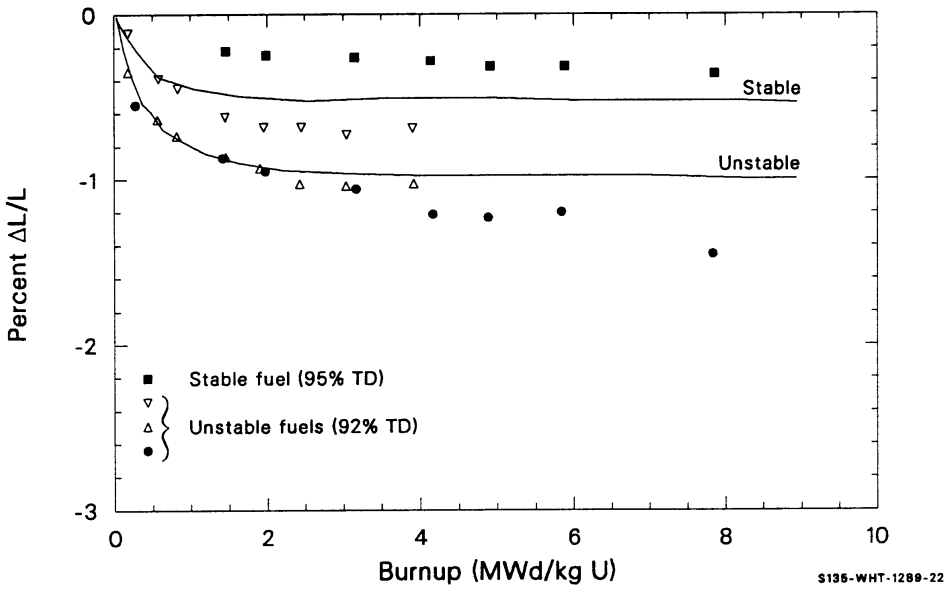

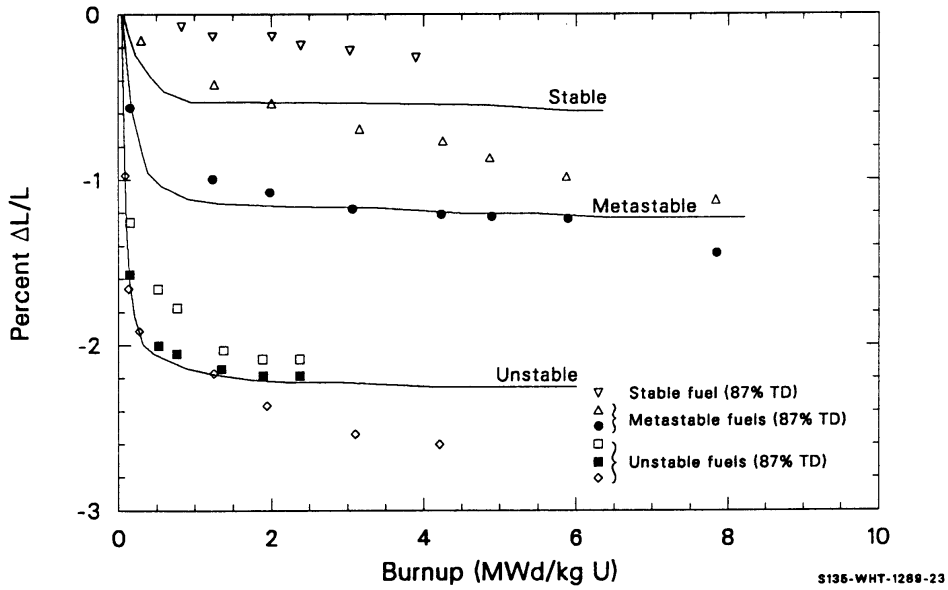

Figure 2-27. Change in fuel stack length of Halden fuel as a function of burnup.

Heal, et al.[2.8-9] reported that they have developed UO_2 fuel which does not densify significantly by controlling the pore size. They assumed that shrinkage of the pores would continue until the internal pressure of trapped gas in the pores matched the surface tension forces. Their calculations show shrinkage in pores of diameters greater than 20 μm and that pores of 10 μm shrink only to 6 to 7 μm before gas stabilization occurs, whereas voids of 1.0 μm or less shrink to 0.2 μm or less before gas stabilization occurs, causing considerable densification. Fuel pellets fabricated with porosity sizes greater than 25 μm were irra-

diated by Heal et al. to 1.4 x 10^{26} fissions/m^3 with center temperatures up to 1,873 K. Postirradiation examination of these pellets showed significantly less than 1% volume densification.

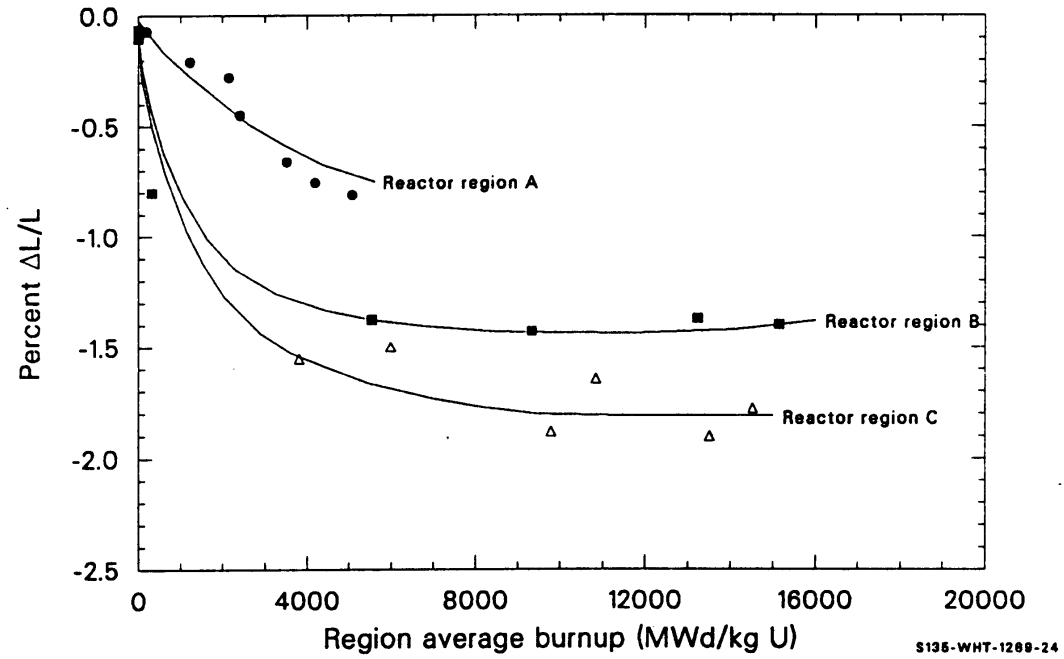

Figure 2-28. Fuel stack length changes for 92% TD UO_2 processed by different techniques.

Ross[2.8-10] has shown that fuel after an irradiation of 2 x 10^{25} fission/m^3 has lost most pores with radii less than 0.5 μm. He found that fuels with burnups even as low as 2 x 10^{24} fissions/m^3 had lost most pores with radii less than 0.3 μm.

Burton and Reynolds[2.8-11] measured the shrinkage of three fuel pellets of 96.5% TD UO_2 with isolated porosity at grain boundaries during the final stage of out-of-pile sintering. The densification rate was initially large but decreased with longer sintering times. (The shapes of these curves are very similar to those obtained for the in-pile densification of UO_2; however, in-pile densification occurs at much lower temperatures.) This reduction in the densification rate with time can arise for several reasons: (a) grain boundaries may migrate away from cavities; (b) when significant entrapped gas is present, cavities may shrink until they become stabilized as the internal gas pressure becomes equal to the surface tension of the cavity, as proposed by Heal et al.; and/or (c) the number of cavities can progressively decrease as densification proceeds. The first and second reasons were rejected by Burton and Reynolds because the majority of the cavities in their samples remained on grain boundaries during sintering and smaller cavities centered to closure. Therefore, Burton and Reynolds suggested that the reduction in the densification rate with time is only due to the progressive reduction in the number of cavities.

The reported irradiation induced densification data indicate that it is affected by porosity and pore size distribution, fuel density, and irradiation temperature. The lack of a temperature dependence of the fuel densification data reported by Ferrari et al. and Rolstad et al. is probably a result of the technique used to measure the length change in the low temperature pellet edges.

2.8.2.2 *Survey of Densification Models.* Densification models proposed by Rolstad, Meyer,[2.8-12] Collins and Hargreaves, Voglewede and Dochwat,[2.8-13] Stehle and Assmann,[2.8-14] Marlowe,[2.10-15] Hull and Rimmer,[2.10-16] and MacEwen and Hastings[2.10-17] are reviewed in this section.

Rolstad et al.[2.10-5] used two equations to correlate their data. In the first, the shortening $(\Delta L/L)_m$ is a function of the current theoretical density (DENS) and sintering temperature in degrees centigrade (TSINT) at a burnup of 5,000 MWd/tUO_2:

$$\left(\frac{\Delta L}{L}\right)_m = \frac{-22.2\,(100 - \mathrm{DENS})}{(\mathrm{TSINT} - 1453)} \tag{2-86}$$

The effect of burnup was introduced through the use of a master curve created by shifting all curves vertically to agreement at 5,000 MWd/tU and then horizontally to achieve the best agreement at the low burnup portion of the curve. The master curve is

$$\left(\frac{\Delta L}{L}\right) = -3.0 + 0.93e^{(-BU)} + 2.07e^{(-35BU)} \tag{2-87}$$

where

$\left(\frac{\Delta L}{L}\right)$ = the percent shrinkage of the fuel

BU = the burnup (MWd/kgU).

This equation results in a rapid length change at low burnups (< 1.0 MWd/kgU) and a small length change at higher burnup levels. Very little additional densification is calculated after a burnup greater than 5,000 to 6,000 MWd/kgU.

Meyer developed a conservative model based on resintering of fuel at 1,973 K for 24 hours. The change in density of fuel after resintering was used as an upper limit. Two equations were used to calculate densification, one for fuels that resintered less than 4% and one for fuels which resintered more than 4%. Meyer's model was based on a log function of burnup and the resintering density change. Meyer reports that his model adequately bounds all in-reactor densification data at his disposal.

Collins and Hargreaves developed an empirical densification expression based on the initial porosity and an exponential burnup function. They suggested that a complete description of the densification rate of irradiated uranium dioxide demands a knowledge of the initial porosity size distribution of the as manufactured UO_2 fuel in addition to the total porosity volume because of the differing sintering rates associated with different pore sizes. However, the pore morphology of their fuel was not determined.

Voglewede and Dochwat developed an equation for final stage densification of mixed oxide fuels based on EBR-II reactor data. It is a semiempirical approach based on porosity, stress, and temperature.

Stehle and Assmann proposed a vacancy controlled densification model as a function of initial fuel porosity, fission rate, initial pore radius, fuel temperature, and vacancy diffusion. Their equation considers pores of only one diameter; therefore, application of this equation to practical engineering problems requires that the equation be integrated over all pore sizes existing in the fuel. Their approach predicts that irradiation induced densification is temperature dependent because of the dependence of the volume diffusion coefficient, D_v, on temperature. The authors used approximate values for D_v and found that the densi-

fication rate should change at approximately 1,023 K. This corresponds very well with the experiment results found in the EPRI densification study.

Marlowe proposed a model for diffusion controlled densification and modified the model to include fuel swelling contributions to the density change, as well as an irradiation induced diffusivity, which provides atomic mobility for grain growth densification. This model is based on densification and grain growth rate, which must be determined experimentally for any particular fuel. These rates strongly affect the predicted in-reactor densification behavior through grain size modification. Because the model allows complete pore elimination and, in fact, densities greater than theoretical for the matrix material, an upper limit to the density must be calculated to limit the densification change.

Hull and Rimmer developed an empirical densification equation based on grain boundary diffusion and temperature. They report reasonably good agreement with the Burton and Reynolds data despite the approximations required to evaluate the equation and the errors in determining the porosity distribution of the samples. Both the shape of the predicted curve and the absolute magnitude of the values were reported to be in good agreement with experimental data, demonstrating that the decrease in sintering rate with time is associated only with the progressive reduction in the number of cavities. The calculation assumed a constant cavity spacing for each time step in changing from one volume size to the next. The similarity between out-of-pile and in-pile densification strongly suggests the importance of pore size distribution and volume for in-reactor densification.

MacEwen and Hastings developed a model describing the rate change of pore diameter based on the time dependence of vacancy and interstitial concentrations, fission gas concentrations, and internal pore pressures. Two equations were used, one describing the diametral change of pores on the grain boundaries and the other describing intergranular pore shrinkage. Use of this model also requires vacancy jump frequencies. The model is thus difficult to use in engineering applications with the present in-reactor fuel data base.

Fuel densification models proposed in References 2.10-11 and 2.10-13 through 2.10-17 attempted to correlate fuel densification with fundamental material properties. These theoretical or semiempirical approaches will eventually be the preferred modeling techniques, but current versions of these models are based on estimates of material properties such as diffusion coefficients, void concentrations, and jump frequencies. These properties are not sufficiently defined to be used to predict in-reactor densification. As Meyer pointed out in his review, the use of complicated theoretical approaches is not justified unless they can be supported with material property data, which allow significantly better predictions than fully empirical correlations. An empirical approach similar to the Meyer model is best for modeling densification.

2.8.3 Model Development

The relation between densification and burnup suggested by Rolstad et al. Equation (2-87) has been adopted for use in the FUDENS subcode. Densification is assumed to consist of a rapidly varying component, represented by the term $2.0\ e^{[-35(FBU + B)]}$ in Equation (2-85), and a slowly varying component, represented by the term $e^{[-3(FBU + B)]}$ in Equation (2-85). The expression was adopted because it successfully describes the burnup dependence of both the original Rolstad e tal. data and recent EPRI data.

The Rolstad et al. model,[2.8-5] as originally proposed, is solved graphically, as indicated in Figure 2-29. The curves in Figure 2-29a are defined by Equation (2-86) for various sintering temperatures, and the curve in Figure 2.29b is defined by Equation (2-87).

The use of these equations to find the length change as a function of burnup is also shown in Figure 2-29. For an initial density of 91% TD and sintering temperature of 1,500°C, the left scale of Figure 2-29 shows that the eventual length change will be about 0.6%. To determine the change as a function of burnup, new axes are drawn in Figure 2-29b, as shown by the dashed lines. With the (x,y) origin of these new axes interpreted to be zero burnup and zero length change, the solid curve in Figure 2-29b then gives $\Delta L/L$ as a function of burnup. The 0.6% fractional length change is then seen to require about 5,000 MWd/tU burnup.

The numerical equivalent to this graphical solution is incorporated into the subroutine FUDENS. Newton's method[2.8-18] was selected for the iterative determination of the new origin because of its rapid convergence. Between four and ten iterations are typically required to determine the position of the new axes, with a 0.0002% convergence criterion defined by

$$E = 100\,(X - X_1)/X \tag{2-88}$$

where

E	=	calculated convergence
X	=	current value of burnup in Equation (2-88)
X_1	=	preceding value of burnup in Equation (2-88).

The maximum densification term, $(\Delta L/L)m$ in Equation(2-85), determines the in-reactor densification limit. Four different expressions, Equations (2-81) through (2-84), are used by the FUDENS code to determine a number for this term. When a measurement of fuel densification during a resintering test at 1,973 K is available, this measurement is the basis of the model's prediction for the maximum in-pile shrinkage. The resintering density change found during a resintering test at 1,973 K for at least 24 hours is appropriate for use in calculating the maximum in-pile densification because in-pile densification and thermal resintering are both dependent on porosity removal. Meyer's assumption that the change in length during a resintering test is equal to the maximum in-pile densification is too conservative for a best estimate code. Therefore, the maximum irradiation induced densification calculated by FUDENS is a fraction of the density change found during a resintering test. If resintering test data are not available, the FUDENS model defaults to the expression suggested by Rolstad et al., Equation (2-83). This provides a reasonable estimate of in-pile densification but cannot account for variations in pore size distribution.

Constants in the expressions used by FUDENS for maximum in-pile shrinkage were determined separately for high (> 1,000 K) and low temperatures. The separate expressions were used because a temperature dependence was found in the EPRI data and because of irregularities between the Halden and the EPRI high temperature data sets. The Rolstad et al. model, which predicts the Halden data well, fits the EPRI low temperature data but not the high temperature EPRI data. Hanevik et al. suggested that the Halden data were probably measurements of the densification of fuel pellet edges, that is, the cooler regions of the pellet. The Rolstad et al. model is assumed by the FUDENS code to apply to low temperature densification, and the high temperature densification is assumed to be three times as large.

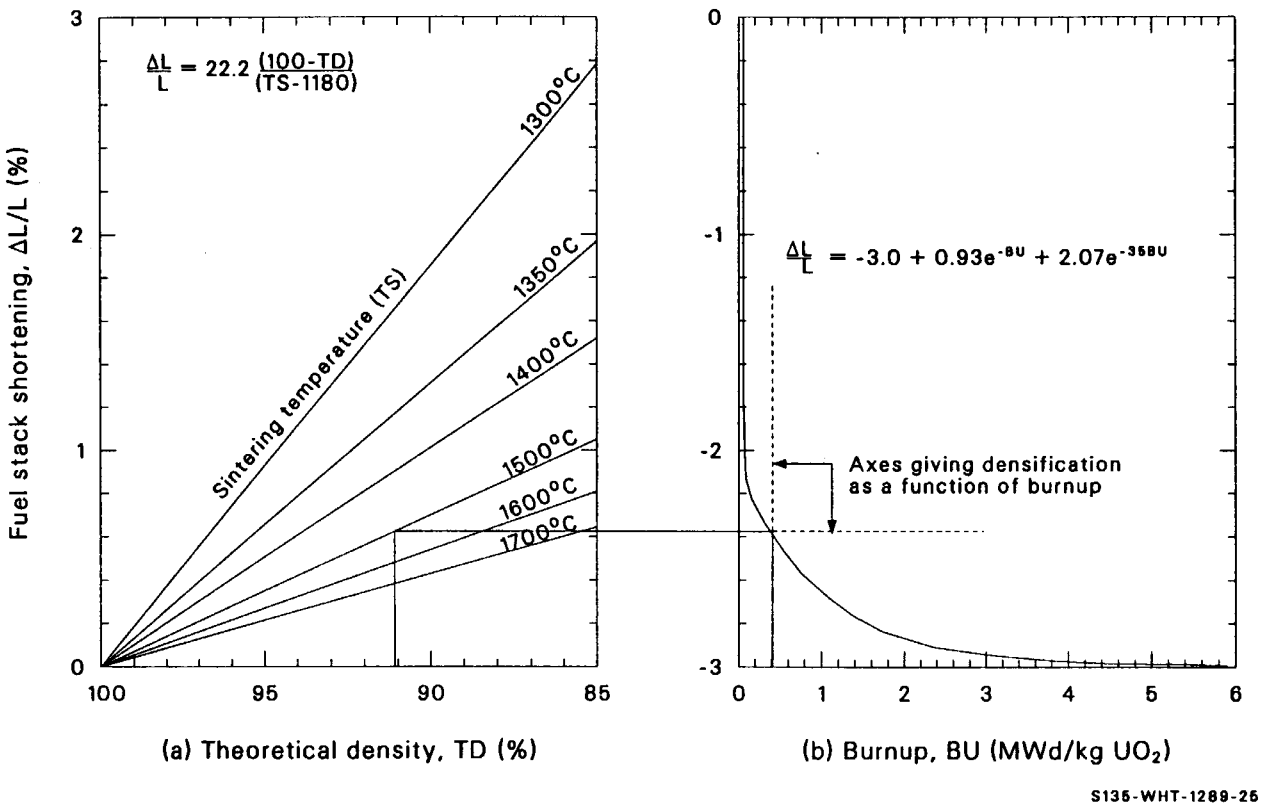

Figure 2-29. Graphical solution of Rolstad's model, where TD is percent of theoretical density, TS is sintering temperature (°C), and BU is burnup.

The constants in Equations (2-81) through (2-84) were determined by inspection to provide the best fit to the maximum density change of the EPRI data. Model predictions and the data base used are shown in Figures 2-27 and Figure 2-30. Mixed oxide fuel is assumed to densify in the same manner as UO_2 due to lack of data to show otherwise.

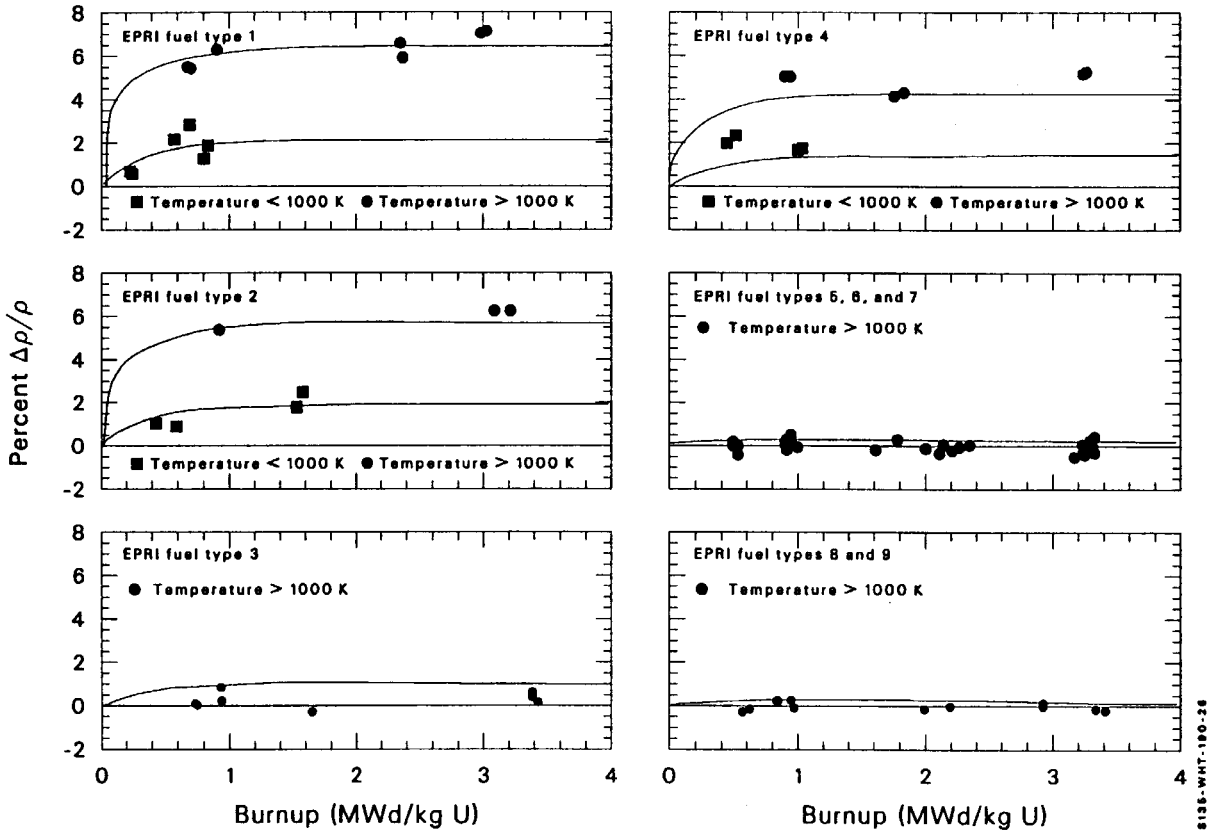

Figure 2-30. FUDENS calculations using EPRI fuel fabrication parameters and resintering values correlated with experimental EPRI in-pile data.

2.8.4 References

2.8-1 W. Beere, "The Sintering and Morphology of Interconnected Porosity in UO_2 Powder Compacts," J*ournal of Materials Science, 5*, 1973, pp. 1717-1724.

2.8-2 W. M. Armstrong, W. R. Irvine, and R. H. Martinson, "Creep Deformation of Stoichiometric Uranium Dioxide," J*ournal of Nuclear Materials, 7*, 1962, pp. 133-141.

2.8-3 D. W. Brite et al., *EEI/EPRI Fuel Densification Project, Research Project131 Final Report*, revised June 1975.

2.8-4 M. D. Freshley et al., "The Effect of Pellet Characteristics and Irradiation Conditions on UO_2 Fuel Densification," *ANS/CNA Topical Meeting on Commercial Nuclear Fuel Current Technology, Toronto, Canada, April 1975.*

2.8-5 E. Rolstad et al., "Measurements of the Length Changes of UO_2 Fuel Pellets During Irradiation," *Enlarged HPG Meeting on Computer Control and Fuel Research, June 4-7, 1974.*

2.8-6 A. Hanevik et al., "In-Reactor Measurements of Fuel Stack Shortening," *BNES Nuclear Fuel Performance Conference, London, October 15-19, 1973*, Paper No. 89.

2.8-7 D. A. Collins and R. Hargreaves, "Performance Limiting Phenomena in Irradiated UO_2," *BNES Nuclear Fuel Performance Conference, London, October 15-19, 1973*, Paper No. 50.

2.8-8 H. M. Ferrari et al., "Fuel Densification Experience in Westinghouse Pressurized Water Reactors," *BNES Nuclear Fuel Performance Conference, London, October 15-19, 1973*, Paper No. 54.

2.8-9 T. J. Heal et al., "Development of Stable Density UO_2 Fuel," *BNES Nuclear Fuel Performance conference, London, October 15-19, 1973*, Paper No. 52.

2.8-10 A. M. Ross, "Irradiation Behavior of Fission Gas Bubbles and Sintering Pores in UO_2," *Journal of Nuclear Materials, 30*, April 1969, pp. 134-142.

2.8-11 B. Burton and G. L. Reynolds, "The Sintering of Grain Boundary Cavities in Uranium Dioxide," *Journal of Nuclear Materials, 45*, 1972/73, pp. 10-14.

2.8-12. R. O. Meyer, *The Analysis of Fuel Densification*, NUREG-0085, July 1976.

2.8-13 J. C. Voglewede and S. C. Dochwat, *Reactor Development Program Progress Report*, ANL-RDP-33, December 1974, pp. 5-1-5-2.

2.8-14 H. Stehle and H. Assmann, "The Dependence of In-Reactor UO_2 Densification on Temperature and Microstructure," *Journal of Nuclear Materials, 52*, 1974, pp. 303-308.

2.8-15 M. O. Marlowe, "Predicting In-Reactor Densification Behavior of UO_2," *Transactions of the American Nuclear Society, 17*, November 1973, pp. 166-169.

2.8-16 D. Hull and D. E. Rimmer, "The Growth of Grain Boundary Voids Under Stress," *Philosophical Magazine, 4*, 1959, p. 673.

2.8-17 S. R. MacEwen and I. J. Hasting, "A Model for In-Reactor Densification of UO_2," *The Philosophical Magazine, 31*, 1, January 1975, pp. 135-143.

2.8-18 R. W. Hamming, *Introduction to Applied Numerical Analysis*, New York: McGraw-Hill Book Company, Inc., 1971.

2.9 Swelling (FSWELL)

The computer subcode FSWELL calculates fuel swelling, which is caused by the buildup of solid and gaseous fission products during irradiation. In order to calculate the overall fuel dimensional changes, fuel swelling (FSWELL) must be combined with the effects of creep induced elongation (FCREEP) and densification due to pressure sintering (FHOTPS) and irradiation (FUDENS).

2.9.1 Summary

The expression used in FSWELL to calculate swelling due to solid fission products is

$$S_s = 2.5 \times 10^{-29} B_s \tag{2-89}$$

where

S_s = fractional volume change due to solid fission products (m^3volume change/m^3

fuel)

B_s = burnup during a time step (fissions/m^3).

The correlation employed for swelling due to gaseous fission products when the temperature is below 2,800 K is

$$S_g = 8.8 \times 10^{-56} (2800 - T)^{11.73} e^{[-0.0162 (2800-T)]} e^{[-8.0 \times 10^{-27} B]} B_s \quad (2\text{-}90)$$

where

S_g = fractional volume change due to gas fission products (fissions/m^3)

T = temperature (K)

B = total burnup of fuel (fissions/m^3).

For temperatures greater than 2,800 K, S_g is zero because the gas that causes swelling is assumed to have been released.

2.9.2 Solid Fission Product Swelling Model

Volume changes caused by the buildup of nongaseous atoms are difficult to measure. However, a number of studies have been undertaken to determine the relative amounts of fission product elements and compounds, as well as their chemical states and locations within the fuel.[2.9-1 to 2.9-15]

Anselin[2.9-8] calculated swelling as a function of burnup using room temperature data with an assumed fission product yield and chemical state for each element. He found a maximum solid fission product swelling rate of 0.13% Δ V/V per 10^{26} fissions/m^3, if the fuel completely utilized the vacancies created during irradiation, and 0.54% Δ V/V per 10^{26} fissions/m^3 if none of the vacancies are used. He proposed an average of 0.35% Δ V/V per 10^{26} fissions/m^3 for all conditions but cautioned that there is no unique value for the swelling rate, since the irradiation conditions, fuel pin design, and fuel properties all contribute to swelling.

Harrison and Davies[2.9-10] calculated solid fission product swelling as a function of thermal neutron flux and concluded that the swelling rate decreases monotonically with increasing flux. They reported swelling rates of 0.45% Δ V/V per 10^{26} fissions/m^3 and 0.39% Δ V/V per 10^{26} fissions/m^3 for thermal neutron fluxes of 10^{18} and 10^{21} n/$m^2 \cdot$ s, respectively.

Olander[2.9-16]obtained a solid fission product swelling rate of 0.32% Δ V/V per atom percent burnup, which corresponds closely to Anselin's average value of 0.35% Δ V/V per 10^{26} fissions/m^3. However, this calculation does not account for fission product migration and is influenced by uncertainties in the physical and chemical states of the fission products, leading to an error of ±50% in the predicted value. Olander found a minimum swelling rate of 0.16% Δ V/V per atom percent burnup for initially hypostoichiometric UO_2 and a maximum of 0.48% Δ V/Vper atom percent burnup for initially hyperstoichiometric fuel or fuel irradiated to high burnups.

Rowland[2.9-17] conducted an extensive study of oxide fuel swelling and found the maximum total swelling due to both solid and gaseous fission products to be 0.4% Δ V/V per 10^{26} fissions/m^3.

Frost[2.9-18] obtained 0.21% Δ V/V per 10^{26} fissions/m^3, and Whapman and Sheldon[2.9-19] obtained 0.20% Δ V/V per 10^{26} fissions/m^3.

The FSWELL model was developed by choosing a swelling rate between Anselin's rate of swelling when vacancies are utilized and General Electric's maximum swelling rate due to both solid and gaseous fission products. The best solid fission product swelling rate at both low burnups and high burnups, where much of the fission gas is released and solid fission product swelling dominates, is 0.25% Δ V/V per 10^{26} fissions/m^3. Thus, the correlation for swelling due to solid fission products is given by Equation (2-89) where the terms are previously defined. This equation has been modified in FSWELL, where burnup is given in terms of MW-s/kg-U. To make the proper conversion between units, the correlation must be

$$soldsw = 7.435 \times 10^{-13}\ fdens\ (bu - bu_1) \tag{2-91}$$

where

soldsw	=	fractional volume change due to solid fission products
fdens	=	initial input density of the fuel (kg/m^3)
bu	=	input burnup to end of current time step (MW-s/kg-U)
bu_1	=	input burnup to end of last time step (MW-s/kg-U).

2.9.3 Fission Gas Swelling Model

Fuel swelling is primarily a result of the increase in fission gas bubbles within the fuel pellets. The physical mechanisms that cause the fuel to swell are complex and are not considered in detail in the FSWELL subcode. Swelling due to fission gas is modeled using a correlation for unrestrained swelling as a function of temperature and burnup. This correlation is based on the data reported by Battelle Columbus Laboratories,[2.9-20 to 2.9-24] Turnbull,[2.9-25 to 2.9-27] Kuz'min and Lebedev,[2.9-28] and Grando et al.[2.9-29] for unrestrained swelling caused by the growth of intergranular gas bubbles and tunnels on the grain boundaries, edges, and corners at temperatures between 1,373 and 1,973 K. The model considers two gross mechanisms, depending on the temperature of the fuel. Above 1,573 K, macropores begin to grow, causing a significant increase in fuel rod swelling. At very high temperatures (1,973 K to the melting point), columnar grains form, fission gas is released, and swelling is reduced.

The fuel volume changes listed by Chubb et al.[2.9-20] and Turnbull[2.9-27] were used to correlate the unrestrained isothermal swelling rate. The fission gas swelling rate equation was determined by comparing the calculated swelling curve with the data and adjusting the equation until the predicted values matched the measured data. The shape of the unrestrained isothermal curve was determined by assuming that (a) at temperatures below 1,000 K, the gases remain in very small bubbles and/or as single atoms in the matrix so that little swelling occurs; (b) between 1,000 and 2,000 K, bubbles grow at the grain boundaries, edges, and corners, creating volume changes; and (c) above 2,000 K, dense (98% of theoretical density) columnar grains form and gas is removed, making fission gas swelling insignificant compared to solid fission product swelling. The equation describing this process is

$$F_g = 8.8\times10^{-56}\,(2800 - T)^{11.73}\,e^{[-0.0162\,(2800 - T)]} \tag{2-92}$$

where

F_g	=	fractional volume change/burnup (m^3/fission)
T	=	temperature (K).

The unrestrained fuel swelling predicted by Equation (2-92) is shown in Figure 2-31. The values calculated by FSWELL are compared with the data of Turnbull and Chubb et al. in Figure 2-32.

Fission gas swelling must also be modeled as a function of burnup. Data reported by Battelle Columbus Laboratories, Turnbull, and Kuz'min and Lebedev indicate that fission gas swelling saturates at relatively low burnups (< 10^{26} fissions/m^3). An exponential burnup function has been included in the FSWELL model to account for swelling saturation. The swelling dependence on burnup is

$$S_g = F_g B_S e^{(-8.0\times10^{-27}B)} B_S \tag{2-93}$$

where

S_g	=	fractional volume change due to gaseous fission products
B	=	total burnup (fissions/m^3).

When Equation (2-92) is substituted into Equation (2-93), the correlation for swelling due to gaseous fission products is given by Equation (2-90)

for T < 2,800 K, and

$$S_g = 0.0 \tag{2-94}$$

for T ≥ 2,800 K.

Converting fissions/m^3 to MW-s/kg-U gives

$$\text{gaswl} = 2.617\times10^{-39}\,\text{fdens}\,(\text{bu} - \text{bu}_1)\,(2800 - T)^{11.73} \tag{2-95}$$

$$e^{[-0.0162\,(2800 - T)]}\, e^{(-2.4\times10^{-10}\text{bu}\cdot\text{fdens})}$$

where gaswl is the fractional volume change due to gaseous fission products.

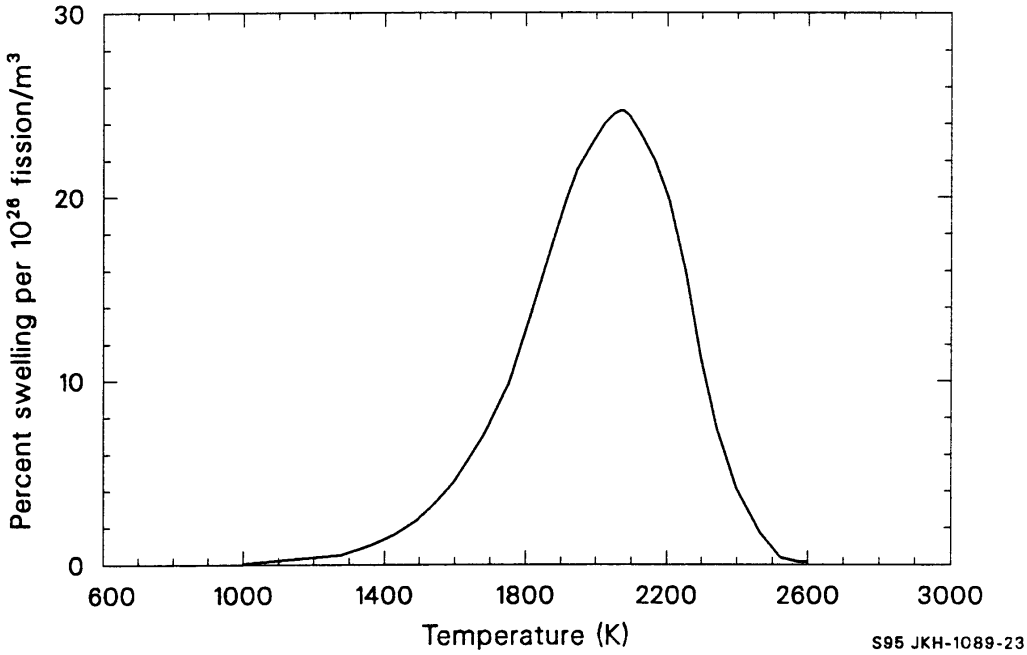

Figure 2-31. Unrestrained fission gas swelling.

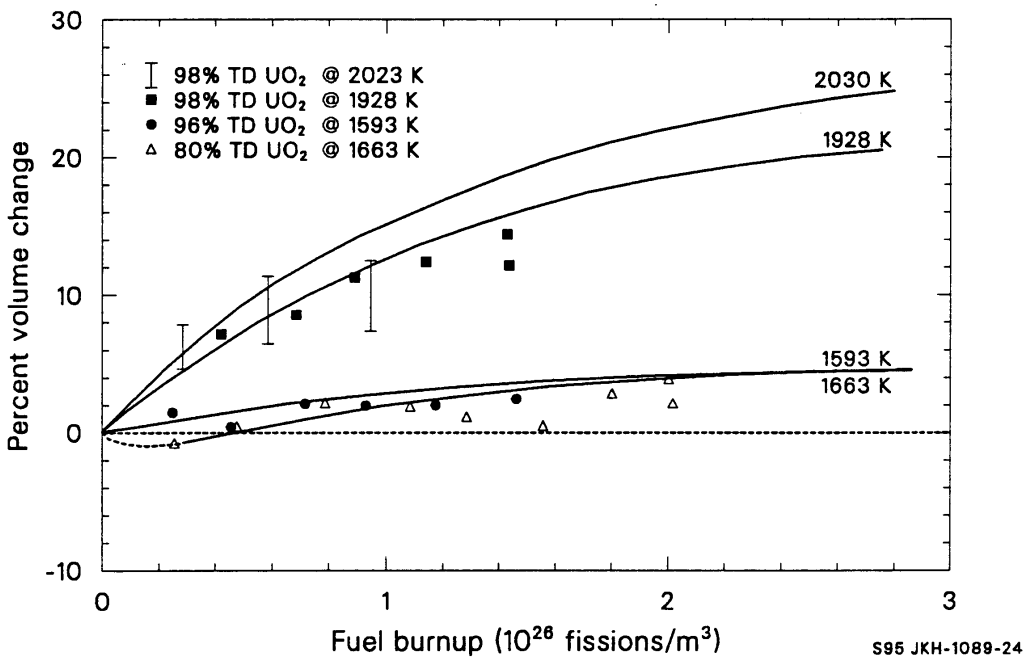

Figure 2-32. Fuel volume changes calculated by FSWELL compared with experimental fuel swelling data.

2.9.4 References

2.9-1 B. T. Bradbury and B. R. T. Frost, *Studies in Radiation Effects on Solids*, NewYork: Gordon and Breach, 1967.

2.9-2 B. T. Bradbury, J. T. Demant, P. M. Martin, and D. M. Poole, *Journal of Nuclear Materials, 17*, 1965.

2.9-3 B. T. Bradbury, J. T.Demant, and P. M. Martin, AERE-R-5149, 1966.

2.9-4 G. M. Jeffery, *Journal of Nuclear Materials, 22*, 1964.

2.9-5 J. L. Bates, *Metallic Uranium in Irradiated UO_2*, HW-82263, 1964.

2.9-6 D. R. O'Boyle, F. L. Prown, and J. E. Saneck, "Solid Fission Product Behavior in Uranium - Plutonium Oxide Fuel Irradiated in a Fast Neutron Flux," *Journal of Nuclear Materials, 29*, 1969, pp.27-42.

2.9-7 I. J. Hastings, D. H. Rose, and J. Barid, "Identification of Precipitates Associated with Intergranular Fission Gas Bubbles in Irradiated UO_2 Fuel," *Journal of Nuclear Materials, 61*, 1976, pp. 229-231.

2.9-8 F. Anselin, *The Role of Fission Products in the Swelling of Irradiated UO_2 and $(U,Pu)O_2$ Fuel*, GEAP-5583, January 1969.

2.9-9 F. Anselin and W. E. Baily, "The Role of Fission Products in the Swelling of Irradiated UO_2 and $(U,Pu)O_2$ Fuels," *Transactions of the American Nuclear Society, 10*, 1967.

2.9-10 J. W. Harrison and L. M. Davies, "The Variation of Solid Fission Product and Gas Swelling in Uranium Compounds with Thermal Neutron Dose Rate," *Journal of Nuclear Materials, 27*, 1968.

2.9-11 B. Lustman, *Technical Progress Report, PWR Project*, WAPD MRP11, October 1964 - January 1965.

2.9-12 J. H. Davies, R. F. Boyle, D. Weidenbaum, and J. Hanson, "On the Composition of Metallic Ingots Formed in High Performance Ceramic Fuel Elements," *Transactions of the American Nuclear Society, 9*, 63, 1966.

2.9-13 J. H. Davies, *Some Considerations Regarding the Behavior of Fission Products in the Fast Ceramic Reactor*, GEAP-4872.

2.9-14 M. L. Bleiberg, R. M. Berman, and B. Lustman, *Effect of High Burnup on Oxide Ceramic Fuels*, WAPD-T-1455, 1962.

2.9-15 I. G. Lebedev, V. I., Kuz'min, and A. S. Piskum, "Swelling of Hot Oxide Fuel," *Soviet Journal of Atomic Energy, 28*, 1970.

2.9-16 D. R. Olander, *Fundamental Aspects of Nuclear Reactor Fuel Elements*, TID-26711-P, 1967.

2.9-17 T. C. Rowland, M. O. Marlowe, and R. B. Elkins, *Fission Product Swelling BWR Fuels*, NEDP-20702, November 1974.

2.9-18 B. R. T. Frost, "Studies of Irradiation Effects in Ceramic Fuel at Harwell," *Journal of the American Ceramic Society*, 1969.

2.9-19 A. D. Whapham and B. E. Sheldon, *Electron Microscope Observation of the Fission Gas Bubble Distribution in UO_2*, AERE-R-4970, April 1966.

2.9-20 W. Chubb, V. W. Storhok, and D. L. Keller, "Observations Relating to the Mechanisms of Swelling and Gas Release in Uranium Dioxide of High Temperatures," *Journal of Nuclear Materials, 44*, 1972, pp. 136-152.

2.9-21 W. Chubb, V. W. Storhok, and D. L. Keller, "Factors Affecting the Swelling of Nuclear Fuel at High Temperatures," *Nuclear Technology, 18*, June 1973, pp. 231-255.

2.9-22 W. Chubb and D. L. Keller, *Implication of High Temperature Irradiation Data for Low Temperature Reactor Design*, BMI-1918, July 1971, pp. B98-B112.

2.9-23 R. F. Hilbert, W. J. Zielenbach, D. E. Lozier, R. B. Clark, and V. W. Storhok, *Irradiation Behavior of Oxide Fuels at High Temperatures*, BMI-1918, July 1971, pp. B2-B43.

2.9-24 R. F. Hilbert, V. W. Storhok, W. Chubb, and D. L. Keller, "Mechanisms of Swelling and Gas Release in Uranium Dioxide," *Journal of Nuclear Materials, 38*, 1971, pp. 26-34.

2.9-25 J. A. Turnbull, "The Effect of Grain Size on the Swelling and Gas Release Properties of UO_2 During Irradiation," *Journal of Nuclear Materials, 50*, 1974, pp. 62-68.

2.9-26 J. A. Turnbull, "The Mobility of Intragranular Bubbles in Uranium Dioxide During Irradiation," *Journal of Nuclear Materials, 62*, 1976, pp. 325-328.

2.9-27 J. A. Turnbull and M. O. Tucker, "Swelling in UO_2 under Conditions of Gas Release," *The Philosophical Magazine, 30*, July 1974, pp. 47-64.

2.9-28 V. I. Kuz'min and I. G. Lebedev, "Effect of Temperature Distribution on the Swelling of UO_2 and UO_2-PuO_2 Cores," *Power Atomic Energy, 28*, January 1975.

2.9-29 C. Grando, M. Montgomery, and A. Strasser, "Unrestrained Swelling and Fission Gas Release of Fast Reactor Fuels," *Proceedings of the Conference on Fast Reactor Fuel Element Technology, New Orleans, LA, April 13-15, 1971*, Ruth Farmakes, ed., pp. 771-784.

2.10 Pressure Sintering (FHOTPS)

Urania or mixed oxide fuel pellets densify when exposed to sufficiently high hydrostatic pressures (pressure sintering), high temperatures (thermal sintering), and irradiation. This report discusses a densification model based on published out-of-pile fuel pressure sintering data. The pressure sintering model complements the irradiation dependent densification model described in Section 2.8 of this report.

A summary of the pressure sintering model, FHOTPS, is contained in Section 2.10.1. Section 2.10.2 describes pressure sintering theories and examines their applicability to modeling urania and mixed oxide pressure sintering data. Section 2.10.3 describes the development of the FHOTPS model, provides standard error estimates, and compares FHOTPS calculated results with experimental data, and the references are given in Section 2.10.4.

2.10.1 Summary

Fuel densification in a reactor environment is a function of temperature, stress, and irradiation. Temperature and stress densification mechanisms are driven by a stress, P, expressed by

$$P = P_e - P_i + 2\gamma/a \tag{2-96}$$

where

P_e	=	external hydrostatic stress (Pa)
P_i	=	internal pore pressure (Pa)
γ	=	surface energy per unit area (J/m^2)
a	=	grain size (m).

Pressure sintering is the dominant densification process if the stress (P_e-P_i) is much larger than the surface energy stress, 2c/a. If an external hydrostatic stress, P_e, is present, it will dominate the densification of in-pile fuel because the internal pore pressure, P_i, and the surface energy stress, 2c/a, are generally much smaller than the externally applied stress. Over an extended irradiation period and at zero P_e, the internal pore pressure, P_i, could cause fuel swelling and the surface energy stress could cause some fuel densification. However, these changes in fuel volume are small compared with densification caused by applied stress and are not considered in the development of the FHOTPS model.

Equation (2-96) does not include an irradiation related driving stress. It is assumed that the irradiation densification driving stress would be added to the right side of Equation (2-96). Since the irradiation densification driving stress is a linear term, it is treated independently as a separate model (the FUDENS model, see Section 2.8). The values calculated with the FUDENS model should, therefore, be added to the FHOTPS model described in this section. The reader should, however, be cautioned that data used to develop the FUDENS model were in-pile data that may include some pressure sintering effects so that combining the two model outputs may be conservative. There are no in-pile data available that will allow separation of these effects.

A lattice diffusion creep equation was fit to the data of Solomon[2.10-1] to give the equation used for urania in the FHOTPS model

$$\frac{1}{\rho}\frac{d\rho}{dt} = 48939\left(\frac{1-\rho}{\rho}\right)^{2.7}\frac{P}{TG^2}e^{\left(\frac{Q_u}{RT}\right)} \tag{2-97}$$

where

ρ	=	fraction of theoretical density (unitless)
t	=	time (s)
P	=	hydrostatic pressure (Pa)
T	=	temperature (K)
G	=	grain size (μm)

Q_u = activation energy (J/mole)

R = 8.314 (J/mole · K).

The activation energy of urania pressure sintering for Equation (2-97) is calculated with the oxygen to metal dependent equation

$$Q_u = R\left(9000e^{\left[\frac{20-8|\log(x-1.999)|}{|\log(x-1.999)|}+1.0\right]^{-1}} + 36294.4\right) \tag{2-98}$$

where x is the oxygen to metal ratio.

The lattice diffusion creep equation was fit to the mixed oxide data of Routbort[2.10-2] to give the mixed oxide fuel pressure sintering equation

$$\frac{1}{\rho}\frac{d\rho}{dt} = 1.8\times10^7\left(\frac{1-\rho}{\rho}\right)^{2.25}\frac{P}{TG^2}e^{\left(-\frac{450000}{RT}\right)} \tag{2-99}$$

The estimated standard error of estimate for both equations is ± 0.5% of the calculated density.

Care must be exercised when using these models out of the 1,600-1,700 K and 2-6 MPa data base range. Pressure sintering not represented in the data base may be controlled by a different creep densification mechanism, as discussed below. Pressure sintering rates would then be much different than those calculated by Equations (2-97) or (2-99).

2.10.2 Pressure Sintering Process and Data

Pressure sintering or volume creep consists of several modes of creep. One of these modes of creep mechanisms can dominate the others, depending on the fuel temperature, pressure, porosity, and grain size conditions, as will be discussed below. Equations representing each creep mechanism combined with the theoretical constants for UO_2 were used by Routbort[2.10-2] to determine the most probable dominating (contributes the highest densification rate) mechanism under reactor operating conditions. These equations, their use, and the published experimental data used to develop the FHOTPS model are described in this section.

2.10.2.1 ***Creep Densification.*** Several distinct mechanisms, such as lattice diffusion (Narbarro-Herring creep) or rate independent plasticity (yielding or dislocation glide), contribute to fuel densification.[2.10-3] Each mechanism imposes specific stress porosity temperature dependent functions. One or any combination of these creep mechanisms can dominate densification, depending on the grain size and stress porosity temperature conditions. There is no single mechanism that will always dominate the densification process. Therefore, an equation representing each creep mechanism is presented so that all possible densification parameter dependencies are described.

Pressure sintering by grain boundary diffusion creep (grain boundary acting as a diffusion path) is usually dominant at temperatures less than one half the melting temperature.[2.10-3,2.10-4] The densification rate by grain boundary creep is expressed by

$$\frac{d\rho}{dt} = \frac{4.5\delta D_b \Omega}{kTb^3} \frac{P}{1-(1-\rho)^{1/3}} \tag{2-100}$$

where

δ	=	grain boundary thickness
D_b	=	grain boundary diffusion coefficient
Ω	=	atomic volume
P	=	applied stress
k	=	Boltzman's constant
b	=	grain size.[a]

Pressure sintering by grain boundary diffusion creep can dominate only if the grain sizes remain small, so that the diffusion paths along the grain boundaries are small.

Pressure sintering by lattice diffusion creep often dominates at temperatures greater than half the melting temperature and before significant grain growth has occurred. Densification by lattice diffusion creep is expressed by

$$\frac{d\rho}{dt} = \frac{3D_V \Omega P}{kTb^2} \tag{2-101}$$

where D_V is the lattice diffusion coefficient. This equation is used to calculate densification by vacancy flow from the surface of a pore to sinks on nearby grain boundaries.[2.10-3]

Pressure sintering by power law creep can dominate at high fuel temperatures or pressures. Densification by power law creep (dislocation creep) has been derived by Wilkinson and Ashby[2.10-4] and by Wolfe and Kaufman.[2.10-5] The densification rate equation is

$$\frac{d\rho}{dt} = \frac{SA}{T} e^{\frac{Q}{kT}\left(\frac{\rho(1-\rho)}{[1.0-(1-\rho)^{1/n}]^n}\right)} \left(\frac{3|\rho|^n}{2n}\right) \tag{2-102}$$

where

S	=	sign of pressure
A	=	constant
Q	=	power law activation energy (J/mole)
n	=	stress and porosity exponent.

Equation (2-102) assumes steady-state creep and densification independent of the grain size and is valid even after extensive grain growth.

---

a. It was assumed here and in the following equations that the effective particle radius is the grain size. This is consistent with the model that is based on the assumption of about one pore to every grain in the compact.

The fourth pressure sintering mechanism, plastic flow, operates at low temperatures or very high strain rates and is defined by the expression

if $\rho \geq 1 - e^{(\frac{-3P}{2\sigma_y})}$

$$\frac{dq}{dt} = 0 \tag{2-103}$$

$$\text{else } \frac{dq}{dt} = \infty \tag{2-104}$$

where σ_y is the yield stress. Densification by the plastic flow mechanism is assumed to occur instantaneously. 2.10-3

The stress dependency of the above equations has been shown by Rossi and Fulrath,[2.10-6] McCelland,[2.10-7] Fryer,[2.10-8] and Wolf[2.10-5] to be dependent on the applied stress and the fuel porosity. Porosity in fuel increases stress in the vicinity of the pores and results in a vacancy concentration difference between the pore surfaces and the grain boundaries. Various porosity dependent functions have been proposed by the above authors, but the porosity dependent function of Fryer[2.10-8] is the most generally accepted effective stress porosity dependent function. The form of Fryer's expression is

$$P = \left(\frac{1-\rho}{\rho}\right)^n \tag{2-105}$$

where

P	=	effective stress (Pa)
ρ	=	fractional density (unitless)
n	=	1.0.

Routbort[2.10-2] found that the porosity exponent, n, of Equation (2-105) was not constant for mixed oxides but varied with the pressure sintering temperature. Routbort mapped pressure sintering of mixed oxides (determined the most dominant mechanism using theoretical material properties) using predominantly urania material constants. It was found that the lattice diffusion mechanism dominates under LWR conditions (fuel temperatures between 1,100 and 3,136 K, pressures < 100 MPa, and fuel densities > 0.90% of theoretical density). This conclusion, however, must be exercised with caution because the densification rate equations depend on the grain size and the oxygen-to-metal ratio and neither were included in the pressure sintering map analysis. The oxygen-to-metal ratio has been shown by Seltzer[2.10-9 to 2.10-11] to strongly influence the activation energy and thereby drastically alter the densification rates predicated by Equations (2-100) through (2-102).

The final pressure sintering mechanism is lattice diffusion modified to include an effective applied stress. The expression describing this mechanism is

$$\frac{1}{\rho}\frac{d\rho}{dt} = A\left(\frac{1-\rho}{\rho}\right)^n \frac{P}{TG^2} e^{(\frac{Q}{RT})} \tag{2-106}$$

where

A	=	constant
Q	=	activation energy (J/mole).

2.10.2.2 ***Pressure Sintering Data.*** The models presented in Section 2.10.1 are based on data published in the open literature that deal with final stage sintering of urania and mixed oxide fuels. These models are based on the urania pressure sintering data of Solomon[2.10-1] and the mixed oxide pressure sintering data of Routbort.[2.10-2] Other data were used as comparison data, but fuel resintering data or final stage sintering data are used because these data most closely resemble what is occurring in a reactor. Measurement techniques and urania and mixed oxide data published in the open literature are presented in this section.

2.10.2.2.1 Measurement Techniques--Immersion density and specimen length change measurements are used to obtain densification data. From the more accurate immersion density measurements, is the more accurate technique, but only the initial and final densities are obtained. Densities from specimen length changes provide time density data and are calculated by density changes determined from length change measurements have several inherent sources of error. The most critical error is the change in length during the initial densification of the test sample, caused by seating and alignment changes. This strain error affects only the initial1 to 2% of sample densification. Creep (nonvolumetric strain) of the sample and loading column is another source of error. Routbort measured the final densities using both the immersion and length change techniques and found about a 5% difference.

$$\frac{\rho}{\rho_f} = \left(\frac{l_f}{l}\right)^3 \qquad (2\text{-}107)$$

where

ρ	=	initial fraction of theoretical density (unitless)
ρ_f	=	final fraction of theoretical density (unitless)
l_f	=	final length (mm)
l	=	initial length (mm).

2.10.2.2.2 Urania Densification Data--Pressure sintering data of UO_2 fuel have been published by Solomon,[2.10-1] Kaufman,[2.10-12] Amato,[2.10-13] Hart,[2.10-14] Fryer,[2.10-8] and Warren and Chaklader.[2.10-15] Fuel resintering or final stage sintering data from other sources were used only as comparison data.

Solomon[2.10-1] measured pressure sintering rates of UO_2 fuel pellets with pretest theoretical densities between 92 and 94% at 1,673 K for up to 136 hours. A summary of the experimental conditions used by Solomon is provided in Table 2-13. These pressure sintering tests indicate that (a) significant densification occurred prior to the application of pressure, (b) internal pore pressures were possible influences on the densification rate, (c) pressure sintering rates are approximately linear with applied stress ($\sigma^{1.03}$ to $\sigma^{1.2}$), and (d) activation energy for specimens at different temperatures and constant density was 0.290 MJ/g · mole. The activation energy of 0.480 MJ/g · mole obtained from two isothermal tests was reported to be more accurate. Pressure cycling tests showed that the specimens swelled after the applied pressure was removed and that the applied pressure densification and released pressure swelling rates were reversible.

Kaufman[2.10-12] reported experimental urania pressure and sintering data of fuel with initial theoretical densities of 80.7 to 83.7%. Immersion densities were taken before and after pressure sintering with a ±0.2% accuracy. These data are intermediate sintering data and can only be used to check the FHOTPS model densification rates. Kaufman observed in his experiments that no densification from heating occurred prior to the application of the load. From experimental results, Kaufman determined the stress exponent values for Equation (2-105) to be between 1 and 4.5.

Table 2-13. Pressure sintering data.

	Solomon	Kaufman	Amato	Routbort
O/M ratio	2.004 + 0.001	--	2.00	1.98+0.01[a]
Presintering				
Temperature (K)	1,783 ± 1	2,023	--	--
Time (h)	3	12 to 24	--	--
Pressure sintering				
Theoretical density (%)	92 to 98	80 to 92	68 to 96	90 to 99
Temperature (K)	1,673 ± 1	2,123	1,373 to 1,473	1,598≤T≤1,823
Time (s)	$0<t<5 \times 10^5$	--	900<t<3600	--
Pressure (MPa)	--	3.86 to 3.96×10^7	2.76 to 5.52×10^7	7.6 to 76
Stress exponent	1.03<n<1.2	--	--	1.33
Porosity exponent	2.7	--	--	2.25
Initial Grain size (mm)	3.354	10 to 40	--	8.0

a. Mixed oxide pellets consisted of 25 wt% PuO_2 and 75 wt% UO_2 (20%^{235}U enriched).

Amato[2.10-13] used a graphite die plunger lined with alumina to obtain hot pressing data in pressure sintering tests conducted in a vacuum of 10^{-5}torr. A summary of test conditions is given in Table 2-13. This intermediate and final stage sintering data is used to check the densification rates and is not part of the FHOTPS data base.

The fabrication pressure sintering data reported by Hart[2.10-14] and Fryer,[2.10-8] which include initial, intermediate, and final stage densification, and the chemical reaction sintering data reported by Warren and

Chaklader were not useful in the MATPRO modeling effort, since the densification and chemical reaction rate equations change at each stage.

2.10.2.2.3 Mixed Oxide Densification Data--The experimental results of Routbort[2.10-2] and Voglewede[2.10-16,2.10-17] were the only mixed oxide pressure sintering data published in the open literature. The test conditions used by Routbort for his experiments are summarized in Table 2-13. Routbort determined a porosity exponent of from 1.5 at 1,673 K to 2.25 at 1,823 K. His results also showed pressure sintering to be a nonlinear function of stress, with a stress exponent of 1.33.

2.10.3 Model Development and Uncertainties

The pressure sintering model, FHOTPS, calculates the volume reduction rate of fuel under hydrostatic pressures and elevated temperatures. The model is based on the urania and plutonia data described above and the semiempirical equation suggested by Solomon, Routbort, and Voglewede. The model simulates the removal of closed porosity developed during fuel pellet fabrication and porosity created by released fission gases.

The appropriate pressure sintering mechanism to model reactor fuel behavior is best determined by comparing the densification rates calculated using the theoretical equations described in Section 2.10.2. The equation indicating the largest densification rate at expected reactor pressures and temperatures is the best model for in-reactor pressure sintering. Both Routbort, from his analysis of mixed oxides using mostly UO_2 physical constants, and Solomon, from his analysis of urania densification rates, determined lattice diffusion to be the controlling mechanism. The lattice diffusion equation is therefore used as the framework for the final FHOTPS model.

The constants used in Equation (2-97) were obtained from the general equation for lattice diffusion, Equation (2-106), and the data of Solomon. Determining constant A of Equation (2-106) constituted equation fitting to the data. Trial and error adjustments of the constant A were made until the standard error of estimate from Equation (2-106) and the data converged to the smallest error possible. The porosity exponent, n, for urania was obtained by using the average slope value of $1/\rho(d/\rho dt)$ plotted versus $\ln[(1-\rho)/\rho]$. The average slope value was determined to be 2.7.

The lattice diffusion equation, Equation (2-106), was fit to the Solomon data using a porosity exponent of 2.7, an initial grain size of 3.5 μm, an assumed activation energy of 0.48 MJ/mole, the reported hydrostatic pressure, and isothermal temperature. This fitted equation calculated a larger densification rate than indicated by the intermediate stage sintering data of Amato. This was opposite to the expected results because intermediate sintering is usually faster than final stage sintering. The lattice diffusion equation was then refit to the Solomon data, using an apparent activation energy closer to 0.290 MJ/mole (apparent activation energy obtained by Solomon from specimen data taken at different temperatures). The activation energy used in the urania pressure sintering model was calculated using Equation (2-98). This activation energy equation and the resulting activation energy were used to be consistent with the FCREEP model of the MATPRO package. With the oxygen-to-metal ratio of 2.004, an apparent activation energy of 0.332 MJ/mole was calculated using Equation (2-98), which is relatively close to the lower Solomon activation energy. Using this activation energy, Equation (2-106) was fit by trial and error adjustments of constants to fit the Solomon data, with a final error estimation of $\pm 0.48\%$. Calculations using Equation (2-97) compared with the Solomon data are shown in Figure 2-33.

The mixed oxide pressure sintering rate equation suggested by Routbort was used as the FHOTPS mixed oxide model except with the grain size dependence of the theoretical lattice diffusion equation con-

sistent with the urania model. The 0.4 MJ/mole activation energy for mixed oxides suggested by Routbort, with an oxygen-to-metal ratio of 1.98, was used in the model. This activation energy is assumed not to vary with the oxygen-to-metal ratio because of a lack of data. The porosity exponent is also assumed constant at 2.25, the value determined by Routbort for samples tested at 1,823 K. Although Routbort observed a temperature dependence of the porosity exponent, a model for the dependence was not developed because data on which this conclusion was based were not included in the published report.

Equation (2-106) was fit to the Routbort data using an activation energy of 0.4 MJ/g mole, a porosity exponent of 2.25, and an initial grain size of 9 μm. Constants were adjusted until the smallest standard error estimate was obtained. The final standard error of estimate is 0.5%. Figure 2-34 shows a comparison of the mixed oxide densification rates corresponding to the Routbort data and those calculated with the FHOTPS model.

The FHOTPS model calculates a density change rate. These calculations are easily modified to obtain strain rate by multiplying calculational results by -1/3. This is a result of the following analysis. Using a fuel mass, g, a change in density can be expressed.

$$\frac{1}{\rho}\frac{d\rho}{dt} = \frac{\frac{g}{V} - \frac{g}{V_0}}{\frac{g}{V_T}}\frac{1}{\Delta t} \tag{2-108}$$

where

g	=	fuel mass
V	=	final volume
g	=	fuel mass
V_o	=	initial volume
V_T	=	volume of the mass, g, at theoretical density
Δt	=	time step.

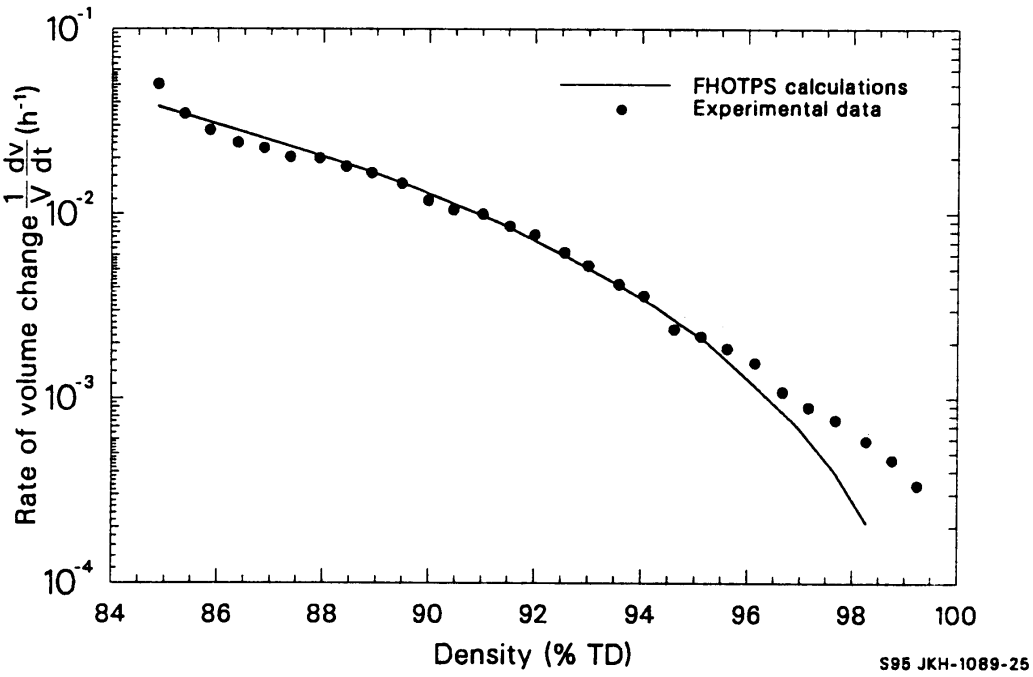

Figure 2-33. Urania pressure sintering rates calculated using the FHOTPS model compared with data.

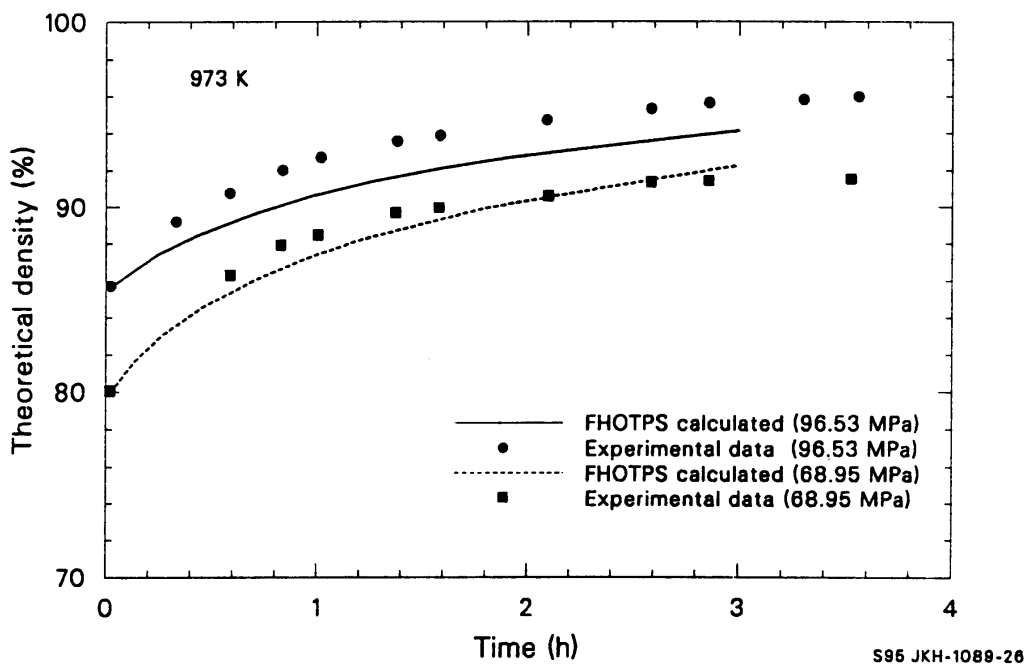

Figure 2-34. Mixed-oxide pressure sintering rates calculated using the FHOTPS model compared with data.

Eliminating and multiplying denominator and numerator by V_T gives

$$\frac{1}{\rho}\frac{d\rho}{dt} = V_T\left(\frac{V - V_0}{VV_0}\right)\frac{1}{\Delta t}. \tag{2-109}$$

Assuming that $V_T \cong |V$, Equation (2-109) relates a densification strain rate to a volume strain rate by

$$\frac{1}{\rho}\frac{d\rho}{dt} = \left(\frac{V - V_0}{V_0}\right)\frac{1}{\Delta t}. \tag{2-110}$$

This can be reduced to a linear strain rate by using the assumption that

$$\frac{1}{3}\frac{\Delta V}{V_0 \Delta t} = \frac{\Delta L}{L_0}\frac{1}{\Delta t}. \tag{2-111}$$

Equations (2-97) and (2-99) must be used with caution because the models are based on very limited data. Both equations are based on one data set, and these data cover only a small portion of the temperatures, pressures, oxygen to metal ratios, and grain sizes possible in a reactor environment. An additional concern is that a significant change in any one of these parameters could result in a different creep mechanism.

2.10.4 References

2.10-1 A. A. Solomon, K. M. Cochran, and J. H. Habermeyer, *Modeling Hot-Pressing of UO_2*, NUREG/CR-PUR-2023, March 1981.

2.10-2 J. L. Routbort, J. C. Voglewede, and D. S. Wilkinson, "Final Stage Densification of Mixed Oxide Fuels," *Journal of Nuclear Materials, 80*, 1979, pp. 348-355.

2.10-3 D. S. Wilkinson and M. F. Ashby, "The Development of Pressure Sintering Maps," *Proceedings of the Fourth International Conference on Sintering and Related Phenomena, May 26-28, 1975.*

2.10-4 D. S. Wilkinson and M. F. Ashby, "Pressure Sintering by Power Law Creep," *Acta Metallurgica, 23*, November 1975.

2.10-5 R. A. Wolfe and S. F. Kaufman, *Mechanical Properties of Oxide Fuels (LSBR/LWB) Development Program*, WAPD-TM-58, October 1967.

2.10-6 R. C. Rossi and R. M. Fulrath, "Final Stage Densification in Vacuum Hot Pressing of Alumina," *Journal of the American Ceramic Society, 48*, 1965, pp. 558-564.

2.10-7 J. D. McCelland, *Kinetics of Hot Pressing*, NAA-SR-5591, 1961.

2.10-8 G. M. Fryer, "Hot Pressing of Alumina: A New Treatment of Final Densification," *Transactions of the British Ceramics Society, 66*, 1967, pp. 127-134.

2.10-9 M. S. Seltzer, A. H. Claver, and B. A. Wilcox, "The Influence of Stoichiometry on Compression Creep of Uranium Dioxide Single Crystals," *Journal of Nuclear Materials, 44*, 1972, pp. 43-56.

2.10-10 M. S. Seltzer et al., "A Review of Creep Behavior of Ceramic Nuclear Fuels," *Reactor Technology, 14*, 2, January 1971, pp. 99-135.

2.10-11 M. S. Seltzer, A. H. Calver, and B. A. Wilcox, "The Stress Dependence for High Temperature Creep of Polycrystalline Uranium Dioxide," *Journal of Nuclear Materials, 34*, 1970, pp. 351-353.

2.10-12 S. F. Kaufman, *The Hot Pressing Behavior of Sintered Low Density Pellets of UO_2, ZRO_2-UO_2, THO_2 and THO_2-UO_2*, WAPD-TM-751, May 1969.

2.10-13 I. Amato, R. L. Colombo, and A. M. Petrucciolo Balzari, "Hot Pressing of Uranium Dioxide," *Journal of Nuclear Materials, 20*, 1966, pp. 210-214.

2.10-14 P. E. Hart, "Fabrication of High Density UO_2 and $(U_{0.75}\ Pu_{0.25})O_2$ by Hot Pressing," *Journal of Nuclear Materials, 51*, 1974, pp. 199-202.

2.10-15 I. H. Warren and A. C. D Chaklader, "Reactive Hot Pressing of Nonstoichiometric Uranium Dioxide," *Metallurgical Transactions, 1*, 1970, pp. 199-205.

2.10-16 J. C. Voglewede, *Reactor Development Program Progress Report*, ANL-RDP-26, March 1974.

2.10-17 J. C. Voglewede, *Reactor Development Program Progress Report*, ANL-RDP-29, June 1974.

2.11 Restructuring (FRESTR)

The morphology and structural integrity of oxide fuel changes while power is being produced in LWRs. These changes are a function of time, temperature, burnup, and energy density. These structural changes affect the effective fuel thermal conductivity, fuel swelling, fission gas release, and fuel creep. The structure of irradiated fuel can be grouped into four categories: as-fabricated unrestructured fuel, equiaxial grains which are enlarged fuel grains with all sides approximately the same length, columnar grains that have their long axes parallel to the radial temperature gradient, and shattered or desintered grains consisting of fuel grains which are fractured free of bonds to other grains during high power transients. The physical processes which create restructured fuel and models to predict the modified fuel structures are discussed in the following sections.

2.11.1 Summary

The FRESTR subroutine is used to calculate equiaxial grain size, columnar grain size, and regions of fuel shattering during normal or transient reactor operation. Grain growth is driven by a potential difference across a curved grain boundary or by a temperature gradient, with the growth rate is controlled by the motion of impurities at the grain boundaries. Since impurities and migration mechanisms are probably the same in UO_2 and $(U,Pu)0_2$, the model described in the following paragraphs is assumed to apply for both fuel types.

The growth rate of equiaxial fuel grains is calculated using the expression

$$g = \left(\frac{1.0269\times10^{-13} t e^{\left(-\frac{35873.2}{T}\right)}}{(1.0 + 5.746\times10^{-6} B)^2 T} + g_0^4 \right)^{1/4} \tag{2-112}$$

where

g	=	grain size at the end of a time interval (m)
g_o	=	grain size at beginning of the time interval (m)
t	=	time interval (s)
T	=	temperature (K)
B	=	burnup (MWs/kg).

The standard error of Equation (2-112) with respect to its data base is $\pm$ 8.4 x 10^{-6}m.

Columnar grains form behind lenticular (large lens shaped) pores, moving up the temperature gradient in the fuel at a rate given by the equation

$$V = \frac{49.22 \nabla T e^{\left(-\frac{44980}{T}\right)}}{T^2} \tag{2-113}$$

where

V	=	rate of pore movement (M/s)
∇T	=	temperature gradient (K/m)
T	=	temperature (K).

Columnar grain formation is characterized by a threshold temperature and temperature gradient. This threshold temperature is defined by the time, temperature, and temperature gradient combination required to move a grain boundary or bubble across one-tenth of the pellet diameter (approximately 0.0005 m) during a time step. The long axis of a columnar grain is the smaller of the length of the pore migration during a time step or the distance to the center of the pellet.

Formation of shattered fuel is characterized in FRESTR by an integer switch, NSHATR, which is unity if the fuel is shattered and zero if the fuel is not shattered.

If $E \geq E_o$ and $T < T_m$ and columnar grains have not formed

$$NSHATR = 1 \ . \tag{2-114}$$

If $E < E_o$ or $T > T_m$ or columnar grains have formed

$$NSHATR = 0 \ . \tag{2-115}$$

where

E	=	energy density deposited during a transient (J/m^3)
E_o	=	energy density required to fracture the fuel at the grain boundaries (J/m^3)

T_m = fuel melting temperature (K)

T = fuel temperature (K).

The energy density required to fracture the fuel at the grain boundaries is determined by the expression

$$E_0 = \frac{8.64\times10^{-14}}{g}(T - 1673) \tag{2-116}$$

The following paragraphs discuss restructuring data and the code development approach. Section 2.11.2 is a discussion of restructuring data. Section 2.11.3 describes the approach used to develop the FRESTR code. Section 2.11.4 is a list of references, and Section 2.11.5 is a bibliography of literature reviewed during code development but not referenced directly in text.

2.11.2 Restructuring Data

The FRESTR restructuring subcode is based on a fit of equation constants to data available in the literature. A complete data base requires both unirradiated isothermal and irradiated restructuring data, with accompanying well documented temperature profiles. Unirradiated isothermal restructuring data are relatively easy to obtain, and a number of good data sets are available for the data base. Irradiated restructuring data with well documented temperature and time histories, on the other hand, are difficult to obtain, especially at burnups above 20,000 MWd/t. The following paragraphs discuss data available in the open literature and the merits of those data for the FRESTR code data base.

The data of Ainscough,[2.11-1] Singh,[2.11-2] MacEwan,[2.11-3] Stehle,[2.11-4] Brite,[2.11-5] and Freshley[2.11-6] are useful for equiaxial grain growth model development. Data analysis published by Singh, Michels and Poeppel[2.11-7] and Oldfield and Brown[2.11-8] show surface diffusion as the mechanism controlling boundary migration; and data published by Gulden,[2.11-9] Williamson and Cornell,[2.11-10] Brite,[2.11-5] and Michels and Poeppel[2.11-7] (for fission gas bubbles) show either volume diffusion or vapor transport as the controlling mechanism. Since no data unequivocally demonstrate which mechanism is controlling grain growth and since more available data indicate volume diffusion or vapor transport as the controlling mechanism, volume diffusion equations were used to develop the FRESTR code. A detailed discussion of the data sets used is contained in this section.

Lenticular pore migration velocity data of Kawamata,[2.11-11] Oldfield and Brown,[2.11-8] and Ronchi and Sari[2.11-12] were used to develop the FRESTR columnar grain growth model. Other available data sets were used only qualitatively to determine specific mechanisms. These data sets are also discussed in this section. Lenticular pore migration data indicate that the probable diffusion mechanism controlling columnar grain growth rates is volume diffusion or vapor phase transport. Each mechanism results in a velocity migration rate equation of the form discussed in the model development section.

Ainscough[2.11-1] conducted a thorough investigation of equiaxial grain growth in urania using samples with initial theoretical densities between 0.94 and 0.99%, temperatures between 1,273 and 1,773 K, and times up to 24 weeks (1.45152×10^7 seconds). The densities and the O/M ratios of the samples remained constant during testing and showed little grain growth at temperatures below 1,500 K. Above 1,500 K, the grain growth rate increased rapidly with increasing temperatures. Ainscough also reported some data from irradiated fuel that were received through personal communications. These data had bur-

nup values approaching 14,000 MWd/t at temperatures representative of LWRs. Therefore, the Ainscough data were considered to be the best available for determining the effect of burnup or grain growth rates.

Singh[2.11-2] measured isothermal grain growth rates of urania at temperatures between 2,073 and 2,373 K for times up to 21 hours (75,600 seconds). Equiaxial grains formed during their experiments, with no accompanying change in O/M ratio. Singh concluded from his data analysis that urania grain growth follows the cubic vapor transport law and determined pore sizes to be at equilibrium with the surface tension. He also observed test sample densities to decrease during the experiments. These observations suggest vapor phase transport growth with a pore size gas pressure equilibrium.

MacEwan[2.11-3] measured grain growth of urania at constant temperatures between 1,828 and 2,713 K for times up to 700 hours (2.52×10^6 seconds). The MacEwan data are excellent for model development because of the long times and appropriate temperatures.

Stehle[2.11-4] reported grain growth measured at temperatures between 1,823 and 2,373 K and at times up to 120 hours (4.32×10^5 seconds). These data are also an excellent source for the FRESTR data base.

Hausner[2.11-13] studied grain growth while sintering green urania pellets (cold pressed and unsintered) and grain growth in some presintered pellets. Grain growth rates in presintered pellets were measured at temperatures between 2,223 and 2,853 K. Sintering grain growth of green pellets is different than the grain growth being modeled in FRESTR, so the Hausner data were not used in the FRESTR data base.

Brite[2.11-5] reported extensive UO_2 densification, and Freshley[2.11-6] reported mixed oxide densification grain growth and porosity measurements in both isothermal and in-reactor environments. Although these data were useful for determining the effect of burnup on grain growth rate, they were less useful than desired because most of the data were obtained at temperatures where little grain growth occurs.

Eichenberg[2.11-14] reported three grain growth data taken from samples at 2,273, 2,473 and 2,573 K and annealed at these temperatures for 900 seconds. These data were used as part of the FRESTR data base.

Runfors[2.11-15] and Padden[2.11-16] measured grain growth in UO_2 during sintering from green compacts. These data do not represent growth rates of final sintering or resintering pellets and are, therefore, of no value for FRESTR code development.

Williamson and Cornell[2.11-10] observed bubble migration rates in single crystal UO_2. Although the FRESTR code does not consider pore velocities or rates for equiaxial grain growth, these observation are interesting in that they demonstrate possible migration mechanisms of pores or impurities that control the growth rate of equiaxial grains.

Data provided by Kawamata[2.11-11] dealt with columnar grain formation. His results demonstrated that columnar grains are formed by pores migrating up a temperature gradient with migration velocities between 2.389×10^{-9} and 4.0×10^{-8} m/s.

Buescher and Meyer[2.11-17] measured migration velocities of 3×10^{-10} m/s for helium gas bubbles in single crystal urania. Their results were not useful for the FRESTR data base because intragranular bubbles do not control grain boundary movement.

Oldfield and Brown[2.11-8] published from experimental results lenticular pore migration velocities up to 1.5 x 10^{-8} m/s and columnar grain growth measurements. These data were used in the data base for the FRESTR grain growth model.

Michels and Poeppel[2.11-7] measured migration velocities of fission gas bubbles and fission product inclusions in mixed oxides. The migration velocities of fission product inclusions were found to be dependent on the size of the inclusion. These data were used only to help define maximum and minimum migration rates.

Gulden[2.11-9] measured bubble migration velocities at the equilibrium pressures of long lived or stable fission gas species, using irradiated fuel with burnups of approximately 10^{26} fissions/m^3 (~3.0 x 10^{25} krypton and xenon atoms/m^3 UO_2). These data are interesting in that they show the probable bubble migration mechanism but were not useful for developing the detailed thermal gradient correlation for bubble migration contained in the FRESTR subcode.

Ronchi and Sari[2.11-12] measured lenticular pore migration rates and grain boundary migration rates at temperatures between 2,200 and 3,000 K. These data were useful in developing the FRESTR subcode.

In-pile restructuring data from EG&G Idaho, Inc.[2.11-18 to 2.11-20] and out-of-pile data from Argonne tests[2.11-21] were all that are available on fuel shattering. These data were used to determine an approximate fuel shattering model in spite of the large uncertainty of the temperature.

2.11.3 Model Development

An equiaxial grain growth and pore migration model based on theory and a fit of the data, was developed for use in the FRESTR subcode. Many of the material properties used in developing the theoretical equations are not well defined and are, therefore, included in the fitted constants. The theoretical derivation proves very beneficial in that the dependence of restructuring on temperature, time, power density, and impurity particle size can be determined.

The equiaxial and columnar grain growth equations are based on the equations developed in a paper by Shewman,[2.11-22] who considers three possible diffusion mechanisms: surface diffusion, volume diffusion, and vapor transport. These mechanisms describe the motion of impurities, bubbles, or inclusions on the grain boundaries that retard and control the motion of the grain boundaries. As discussed in the previous section, much of the data show volume diffusion as the controlling mechanism for grain boundary migration. The equation Shewman obtained for volume diffusion migration is

$$V = \frac{\alpha D_V F_a}{T} \tag{2-117}$$

where

V	=	velocity of atom movement (m/s)
α	=	constant
D_v	=	volume diffusion coefficient (m^2/s)
F_a	=	force driving atom (N)
T	=	temperature (K).

Equation (2-117) was used for columnar grain growth for the following reasons. The data discussed in Section 2.11.3 indicate volume diffusion or possibly vapor transport at constant pressure as the controlling mechanism for lenticular pores forming large columnar grains. Shewman[2.11-22] showed that an approach similar to that described previously for vapor transport produced an equation of the same form as Equation (2-117), thus making this equation proper assuming either mechanism.

The approach used by Nichols[2.11-23] and Shewman[2.11-22] to relate the force on each atom to the force driving the entire bubble and grain boundary was used to further develop Equation (2-117) into a usable form, resulting in the following equation for equiaxial grain growth.

$$\frac{dx}{dt} = \frac{\beta D_V}{r^3 T} \tag{2-118}$$

where

x	=	the migration distance (m)
t	=	time (s)
β	=	constant
r	=	bubble radius (m).

If the migration distance is assumed to be equal to the grain boundary migration distance and the particle radius is assumed to be proportional to the grain size and burnup, then

$$r = \beta' (1 - \beta B) g \tag{2-119}$$

where

β', β	=	constants
B	=	burnup (MWs/kg)
g	=	grain size (m).

Substitution of Equation (2-119) into Equation (2-118) and use of a common temperature dependent form for the volume diffusion constant results in the expression

$$\frac{dg}{dt} = \frac{a D_0 e^{(\theta/T)}}{T (1 - \beta B)^2 g^3} \tag{2-120}$$

where

D_o	=	diffusion coefficient (m^2/s)
θ	=	activation energy divided by the gas constant (K).

Combining the equation constants and integrating gives the final form of the equiaxial grain growth equation

$$g^4 - g_0^4 = \frac{D\Delta t e^{(\theta/T)}}{T(1-\beta B)^2} \tag{2-121}$$

where

g	=	final grain size (m)
g_o	=	grain size at beginning of increment (m)
D	=	constant.

The constants D and θ of Equation (2-121) were determined by fitting the data of Singh,[2.11-2] MacEwan,[2.11-3] Stehle,[2.11-4] and Ainscough[2.11-1] with $\beta = 0$ (no irradiation). The constant β was then determined by fitting the equation to the irradiation data of Ainscough.[2.11-1]

The movement of columnar grains can be derived using Equation (2-117). For columnar grain growth, the grain boundary driving force is derived from a temperature gradient in the fuel. This analysis was done by Shewman, who obtained the following expression for the bubble velocity

$$V = \frac{C\nabla T e^{(\theta/T)}}{T^2} \tag{2-122}$$

where

V	=	pore migration velocity (m/s)
C	=	constant
∇T	=	temperature gradient (K/m).

The constants in Equation (2-122) were then fit to the data of Ronchi and Sari,[2.11-12] Michels and Poeppel[2.11-7] (for upper and lower bounds), Buescher,[2.11-17] Oldfield and Brown,[2.11-8] and Kawamata.[2.11-11]

Equation (2-122) was used to calculate the onset of columnar grain growth. An assumption, suggested by Nichols,[2.11-24] that columnar grains form only if lenticular pores are able to migrate one-sixth of the pellet radius, was required to define columnar grain growth in the subcode. On the basis of this criterion, columnar grains form only if the migration distance per time step is greater than 0.0005 m. If this criterion is not met, the grain size is determined by equiaxial grain size calculations and the columnar grain growth switch, NCOLGN, is set to zero. If columnar grains were formed in a previous time step, the preceding calculations are bypassed and NCOLGN remains unity. If columnar grains are formed, their length is the smaller of the migration distance during the time step or the distance from the ring edge to the center of the fuel pellet. Figure 2-35 shows typical columnar growth threshold as a function of time and temperature with an average temperature gradient of 4.0×10^5 K/m.

The model for fuel shattering is taken from a study of this effect by Cronenberg and Yackle,[2.11-25] using data from the reactivity initiated accident (RIA) tests by EG&G Idaho and direct electrical heating tests by Argonne. They found the fuel shattered at the grain boundaries when the stress resulting from the deposited energy is greater than the fracture strength. Their expression for the energy density at fracture is

$$E = \frac{8.64\times10^{-14}(T-1673)}{g} \tag{2-123}$$

The FRESTR subcode uses Equation (2-123) to determine whether the fuel in the region of fuel being considered has fractured at the grain boundaries. If the input energy density is greater than E, the fuel temperature is less than melting, and columnar grains have not formed, the fuel is assumed to be shattered and the shattering parameter, NSHATR, is set to unity.

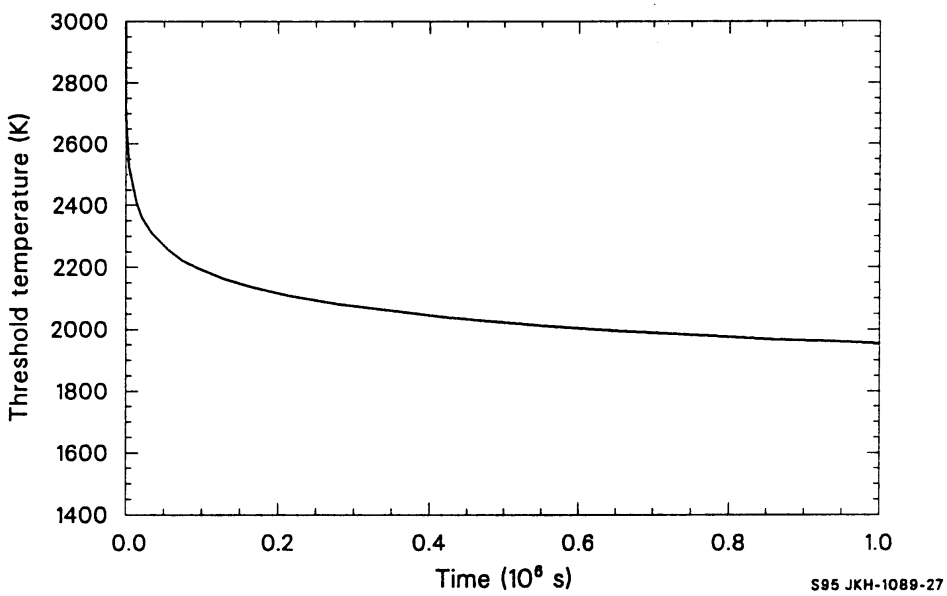

Figure 2-35. Threshold of columnar grain growth with temperature gradient of 4.0×10^5 K/m.

2.11.4 Bibliography

1. W. L. Baldewicz, A. R. Wazzan, and D. Okrent, "Grain Growth in Nuclear Fuels Containing Fission Gas," *Transactions of the American Nuclear Society, 23*, 1978.

2. P. F. Sens, "The Kinetics of Pore Movement in UO_2 Fuel Rods," *Journal of Nuclear Materials, 43*, 1972, pp. 293-307.

3. D. R. DeHalas and G. R. Horn, "Evolution of Uranium Dioxide Structure During Irradiation of Fuel Rods," *Journal of Nuclear Materials, 8*, 1963, pp. 207-220.

4. W. Oldfield and A. J. Markworth, "Effects of Impurities on the Migration of Lenticular Pores in UO_2," *Scripta Metallurgica, 6*, 1972, pp. 277-762.

5. F. A. Nichols, "Pore Migration in Ceramic Fuel Elements," *Journal of Nuclear Materials, 27*, 1968, pp. 137-146.

6. F. A. Nichols, "Kinetics of Diffusional Motion of Pores in Solids," *Journal of Nuclear Materials, 30*, 1969, pp. 143-165.

7. W. D. Whapman, "Electron Microscope Observation of the Fission Gas Bubble Distribution in UO_2," *Nuclear Applications, 2*, 1966.

8. W. Beere and G. L. Reynolds, "The Morphology and Growth of Interlinked Porosity in Irradiated UO_2," *Journal of Nuclear Materials, 47*, 1973, pp. 51-57.

9. M. V. Speight, "The Migration of Gas Bubbles in Materials Subject to a Temperature Gradient," *Journal of Nuclear Materials, 13*, 1964, pp. 207-209.

10. F. A. Nichols, "Movement of Pores in Solids," *Journal of Nuclear Materials, 19*, 1969.

11. J. R. MacEwan and V. B. Lawson, "Grain Growth in Sintered Uranium Dioxide: II, Columnar Grain Growth," *Journal of the American Ceramic Society, 45*, 1962.

12. W. D. Kingery and B. Francois, "Grain Growth in Porous Compacts," *Journal of the American Ceramic Society, 48*, 1965.

13. W. Oldfield and A. J. Markworth, "The Theory of Bubble Migration Applied to Irradiated Materials," *Material Science and Engineering, 4*, 1969, pp. 353-366.

14. A. J. Markworth, "Growth Kinetics of Inert Gas Bubbles in Polycrystalline Solids," *Journal of Applied Physics, 43*, 1972.

15. D. R. DeHalas, "The Shape of Migrating Voids," *Journal of Nuclear Materials, 23*, 1967, pp. 118-120.

16. J. A. Christensen, "In-Pile Void Migration in Uranium Dioxide," *Transactions of the American Nuclear Society, 8*, 1965, pp. 44-45.

17. J. A. Christensen, "Columnar Grain Growth in Oxide Fuels," *Transactions of the American Nuclear Society, 15*, 1972.

18. M. F. Lyons, D. H. Coplin, and B. Weidenbaum, *Analysis of UO_2 Grain Growth Data from "Out of Pile" Experiments*, GEAP-4411, 1963.

19. R. O. Meyer and J. C. Voglewede, "Thermal Gradient Migration of Pores in UO_2," *Reactor Development Program Progress Report*, ANL-7753, 1970.

20. M. V. Speight and G. W. Greenwood, "Grain Boundary Mobility and Its Effect in Materials Containing Inert Gases," *Philosophical Magazine, 9*, 1964, pp. 683-688.

21. J. A. Turnbull, "The Mobility of Intragranular Bubbles in Uranium Dioxide During Irradiation," *Journal of Nuclear Materials, 62*, 1976, pp. 325-328.

22. K. Smidoda, W. Gottschalk, and H. Gleifer, "Diffusion in Migrating Interfaces," *Acta Metallurgica, 26*, 1978, pp. 1833-1836.

2.11.5 References

2.11-1 J. B. Ainscough, B. W. Oldfield and J. O. Ware, “Isothermal Grain Growth Kinetics in Sintered UO_2 Pellets,” *Journal of Nuclear Materials, 49*, 1973/74, pp. 117-128.

2.11-2 R. N. Singh, “Isothermal Grain Growth Kinetics in Sintered UO_2 Pellets,” *Journal of Nuclear Materials, 64*, 1977, pp. 174-178.

2.11-3 J. R. MacEwan, *Grain Growth in Sintered Uranium Dioxide*, AECL-1184, 1961.

2.11-4 V. H. Stehle, "Kornwachstrum von UO_2," *Bericht der Deutschen Keramische Gesellshaft*, 1963, pp. 129-135.

2.11-5 D. W. Brite et al., *EEI/EPRI Fuel Densification Project 131-Final Report*, 1975.

2.11-6 M. D. Freshley et al., *Plutonia Fuel Study*, EPRI NP-637, 1978.

2.11-7 L. C. Michels and R. B. Poeppel, "In-Pile Migration of Fission Product Inclusions in Mixed Oxide Fuel," *Journal of Applied Physics, 44*, 1973.

2.11-8 W. Oldfield and J. B. Brown, Jr., "Bubble Migration in UO_2-A Study Using a Laser Image Furnace," *Material Science and Engineering, 6*, 1970, pp.361-370.

2.11-9 M. E. Gulden, "Migration of Gas Bubbles in Irradiated Uranium Dioxide," *Journal of Nuclear Materials, 23*, 1967, pp. 30-36.

2.11-10 G. K. Williamson and R. M. Cornell, "The Behavior of Fission Product Gases in Uranium Dioxide," *Journal of Nuclear Materials, 13*, 1974, pp. 278-280.

2.11-11 H. Kawamata, H. Kaneko, H. Furuya, and M Koizumi, "Migration Rate of Lenticular Voids in UO_2 Under the Influence of Temperature Gradient," *Journal of Nuclear Materials, 68*, 1977, pp. 48-53.

2.11-12 C. Ronchi and C. Sari, "Properties of Lenticular Pores in UO_2, $(U,Pu)O_2$" *Journal of Nuclear Materials, 50*, 1974, pp. 91-97.

2.11-13 H. Hausner, "UO_2 Grain Growth and Melting Studies," *High Performance Quarterly Progress Reports*, GEAP-3771-5, 3771-6, 3771-7, 1962, 1963.

2.11-14 J. D. Eichenberg, *Effects of Irradiation on Bulk UO_2*, WAPD-183, 1957.

2.11-15 U. Runfors et al., "Sintering of Uranium Dioxide," *Proceedings of 2nd International Conference on Peaceful Uses of Atomic Energy, 6*, Paper P/142, September 1958, p. 605.

2.11-16 T. R. Padden, "Behavior of Uranium Oxide as a Reactor Fuel," *Proceedings of 2nd International Conference on Peaceful uses of Atomic Energy, 6*, Paper P/2404, September 1958, pp. 569-586.

2.11-17 B. J. Buescher and R. O. Meyer, "Thermal Gradient Migration of Helium Bubbles in Uranium Dioxide," *Journal of Nuclear Materials, 48*, 1973, pp. 143-156.

2.11-18 P. E. MacDonald et al., *Response of Unirradiated and Irradiated PWR Fuel Rods Tested Under Power Cooling Mismatch Conditions*, TREE-NUREG-1196, January 1978.

2.11-19 R. W. Garner et al., *Gap Conductance Test Series-2, Test Results Report of Tests GC2-1, GC2-2, and GC2-3*, NUREG/CR-0300, TREE-1268, 1978.

2.11-20 R. J. Buckland, C. E. White, and D. G. Abbott, *Experimental Data Report for Test RIA1-1 (Reactivity Initiated Accident Test Series)*, NUREG/CR-0516, TREE-1236, 1979.

2.11-21 R. G. Sachs and J. A. Kyger, *Light Water Reactor Safety Research Program: Quarterly Progress Report*, ANL-77-59, April-June 1977, pp.76-111.

2.11-22 P. G. Shewman, "The Movement of Small Inclusions in Solids by a Temperature Gradient," *Transactions of the Metallurgical Society of AIME, 230*, 1964.

2.11-23 F. A. Nichols, "Theory of Grain Growth in Porous Compacts," *Journal of Applied Physics, 37*, 1966, pp. 4599-4062.

2.11-24 F. A. Nichols, "Theory of Columnar Grain Growth and Central Void Formation in Oxide Fuel Rods," *Journal of Nuclear Materials, 22*, 1977, pp. 214-222.

2.11-25 A. W. Cronenberg and T. R. Yackle, *An Assessment of Intergranular Fracture Within Unrestructured UO_2 Fuel Due to Film Boiling Operation*, NUREG/CR-0595, TREE-1330, March 1979.

2.12 Fracture Strength (FFRACS)

FFRACS calculates the UO_2 fracture strength as a function of fuel temperature and fractional fuel density.

2.12.1 Summary

FFRACS calculates the fracture strength of UO_2 as a function of fractional fuel density and temperature up to 1,000 K, the lowest temperature at which plasticity has been observed in-pile. For temperatures above 1,000 K, a constant value is used for the in-pile fracture strength of plastic UO_2. The UO_2 fracture model is given by the following equations:

For $273 < T \leq 1{,}000$ K,

$$\sigma_F = 1.7\times10^8 \left[1 - 2.62\,(1 - D)\right]^{1/2} e^{\left(-\frac{1590}{8.314}T\right)} \tag{2-124}$$

For $T > 1{,}000$ K,

$$\sigma_F = \sigma_F\,(1000\text{K}) \tag{2-125}$$

where

σ_F	=	fracture strength (Pa)
D	=	fraction of theoretical density
T	=	temperature (K)
σ_F(1,000 K)	=	fracture strength found with T = 1,000 K.

Equation (2-124) is based upon out-of-pile UO_2 data and describes the behavior of brittle UO_2. Because no in-pile measurements of fracture strength have been made, Equation (2-125) is based upon theoretical considerations and fragmentary out-of-pile data and applies to plastic UO_2. The transition from brittle to ductile material is accompanied by a discontinuity in fracture strength and occurs at temperatures below the usual out-of-pile brittle ductile transition temperature due to fission induced plasticity. Equation (2-124) has a standard deviation with respect to experimental data of 0.19×10^8 Pa. The uncertainty in Equation (2-125) is not estimated because of lack of in-pile data.

2.12.2 Out-of-Pile Uranium Dioxide Deformation

The out-of-pile deformation of UO_2 exhibits either elastic or elastic plastic behavior. Elastic behavior is characterized by stress being linearly proportional to strain up to the fracture point.[2.12-1 to 2.12-5] Elastic plastic behavior is characterized by the stress strain curve, which is initially elastic (to the elastic proportional limit) and which then exhibits plastic behavior.[2.12-1 to 2.12-5]

2.12.2.1 ***Review of Out-of-Pile Uranium Dioxide Elastic Behavior Data and Theory.*** At temperatures below a ductile brittle transition temperature, T_c, UO_2 deforms elastically up to the fracture point.[2.12-1 to 2.12-5] In such cases, the fracture strength, σ_F, is much less than the yield strength, σ_y, so that no yielding occurs prior to fracture. The fracture topography of near theoretically dense UO_2 exhibits the cleavage fracture mode of a brittle material. However, this fracture mode is affected by the amount of porosity and grain size, where, in general, the relative proportion of brittle to ductile fracture decreases with an increase in porosity and a decrease in grain size.[2.12-6]

The crack initiator[2.12-1,2.12-2,2.12-4,2.12-6] has been suggested as the largest pore. The Griffith fracture theory[2.12-7] can be applied to theoretically examine the parameters that affect the fracture strength. Griffith showed that the fracture stress or critical stress required to propagate an elliptical crack of length 2c with an infinitely small radius of curvature is given by Equation (2-126):

$$\sigma_F = \left(\frac{2\gamma E}{\pi c\,(1-\nu^2)} \right)^{1/2} \tag{2-126}$$

where

E	=	elastic modulus (Pa)
γ	=	surface energy (J/m^2)
c	=	crack length (m)
ν	=	Poisson's ratio (unitless).

This equation applies to planar strain conditions and to an infinitely thick section of purely elastic material.

In Equation (2-126), the fracture strength is proportional to the square root of the elastic modulus, which, in turn, linearly decreases with porosity and temperature, as discussed in Section 2.6.1 of this report. Therefore, the fracture strength should decrease with increasing temperature. However, the fracture strength of UO_2 has been observed to increase slightly with temperature.[2.12-2, 2.12-4] These measurements can be explained by the fact that γ in Equation (2-126) probably increases with temperature[2.12-4] at a faster rate than the rate of decrease of E with temperature.

Hasselman[2.12-8] has shown that when a material contains numerous elliptical cracks of length 2c spaced a distance 2h from each other. Equation (2-126) becomes for planar strain conditions

$$\sigma_F = \left(\frac{E\gamma}{2\,(1-\nu^2)\,h} \right)^{1/2} \cot\left(\frac{\pi c}{2h}\right) \tag{2-127}$$

where the terms are previously defined.

Equation (2-127) and Equation (2-126) both predict a UO_2 fracture strength that is dependent on porosity because of the effect of porosity on the elastic modulus. Equation (2-127) also predicts a crack spacing effect upon fracture strength, which, in turn, depends upon both the pore size and volume of porosity. A fracture strength dependence upon the pore morphology (size, shape, and distribution) has also been observed by Roberts and Ueda.[2.12-1]

2.12.2.2 ***Out-of-Pile Elastic Models.*** Experimental data[2.12-1,2.12-2,2.12-6,2.12-9, 2.12-10] for fracture strength in the brittle region were fit to Equation (2-128) using a linear least-squares regression analysis [after reducing Equation (2-128) to a linear form] to determine the coefficients A, m, and Q

$$\sigma_F = A\,[1 - 2.62\,(1 - D)]^{1/2}\,G^{-m} e^{(-Q/RT)} \qquad (2\text{-}128)$$

where

G	=	grain size (μm)
R	=	gas constant (8.314 J/mol · K)

and the other terms of the equation have been previously defined. The following values of A, m, and Q were determined:

A	=	1.70×10^8 Pa
m	=	0.047
Q	=	1590 J/mol.

The expression $[1\text{-}2.62\,(1\text{-}D)]^{1/2}$ arises from the proportionality between σ_F and $\sqrt{E}$ in Equations (2.-(2-126) and (2-127) and the relation between E and D (see Section 2.6.1 of this report). The expression between fracture strength and grain size was based upon the suggestion of Orowan[2.12-11] and Petch[2.12-12] and the data of Igata and Domoto,[2.12-13] which relate the strength of a material to $G^{-1/2}$. In general terms, this factor is written G^{-m}. The Boltzmann factor was selected to represent the temperature dependence. The effects of pore morphology have been ignored because of a lack of appropriate data. In Figure 2-36, Equation (2-128) is compared with experimental data normalized to a 10-μm grain size and to 95% TD using Equation (2-128).

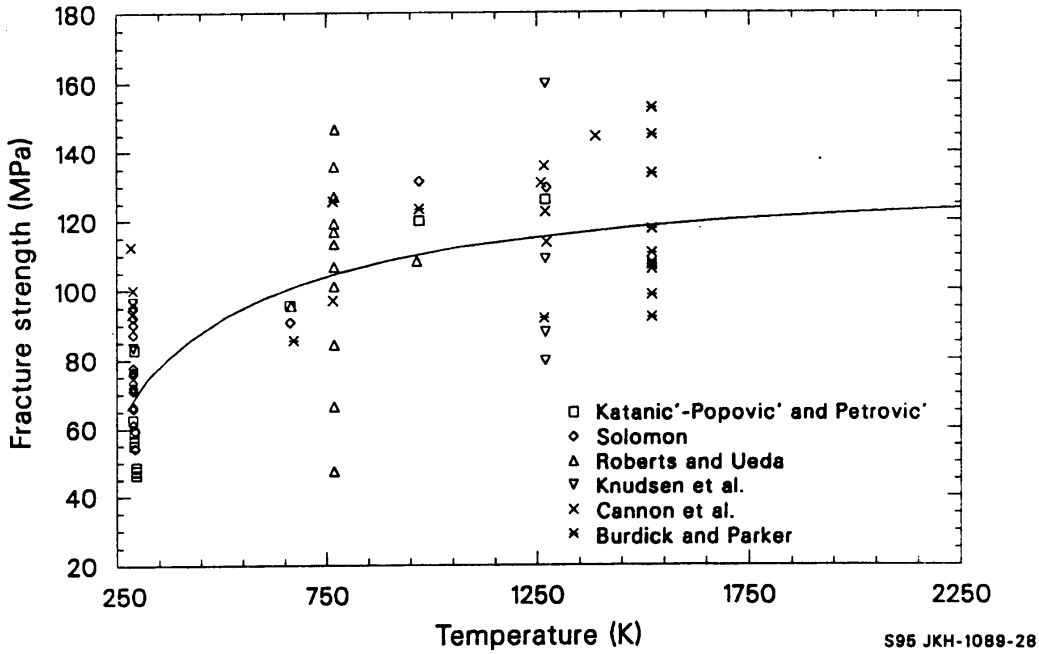

Figure 2-36. Comparison of Equation (2-128) in the elastic behavior regime with out-of-pile UO_2 fracture strength data normalized to 10-μm grain size and 95% TD.

Knudsen[2.12-14] proposed the following empirical equation relating fracture strength to grain size and porosity:

$$\sigma_F = AG^{-m} e^{[-b(1 - D)]} \tag{2-129}$$

where

1 - D	=	porosity
b	=	constant

the other terms have been previously defined, and constants are given below.

Knudsen suggested that this relation describes the strength of chromium carbide and thoria reasonably well. This expression was fit to UO_2 fracture strength data, except that the Arrhenius term from Equation (2-128) was added to provide a temperature dependence. The resultant expression was reduced to a linear form; and a linear, multiple variable regression analysis was used to determine the coefficients A, m, b, and Q. The results are:

A	=	1.7108×10^8 Pa
m	=	0.05136
b	=	2.412
Q	=	1649 J/mol.

Equation (2-129) is compared with experimental data in Figure 2-37.

Both Equations (2-128) and (2-129) indicate a very small effect of grain size upon the fracture strength. Values of m on the order of 0.5 are expected theoretically[2.12-11,2.12-12]; but values of 0.05 were obtained, indicating a very insignificant effect of grain size on UO_2 fracture strength. Much scatter exists in the data with respect to Equations (2-128) and (2-129) and is attributed to differences in pore morphology not accounted for in these equations and also not reported with the data.

In some cases, porosity has not been the initiator of cracks in UO_2. Instead, silica or alumina[2.12-15] precipitated at grain boundaries has considerably reduced the fracture strength, whereas small additions of titania increased the fracture strength of UO_2.[2.12-9] These additions are not normally part of the fabrication process and were not considered in the UO_2 fracture strength model.

2.12.2.3 ***Out-of-pile Transition Temperature.*** The transition temperature, T_c, is defined to be the temperature at which the stress strain curve departs from (linear) elastic to plastic behavior. Density, grain size, and strain rate are expected to affect this transition temperature, but data are insufficient to obtain a precise relationship.

Cannon et al.[2.12-2] reported out-of-pile transitions at 1,100, 1,375, and 1,450°C for strain rates of 0.092, 0.92, and 9.2/h, respectively, in material with an 8 m average grain size. Transitions at 1,050 and 1,100°C occurred for a strain rate of 0.092/h in material with 15 and 31 µm average grain sizes, respectively. Evans and Davidge[2.12-4] reported transition temperatures of 1,200 and 1,300°C for 8 and 25 µm materials. A transition temperature of 1,250°C is assumed for FFRACS, since that is the midpoint of the 1,050 to 1,450°C range.

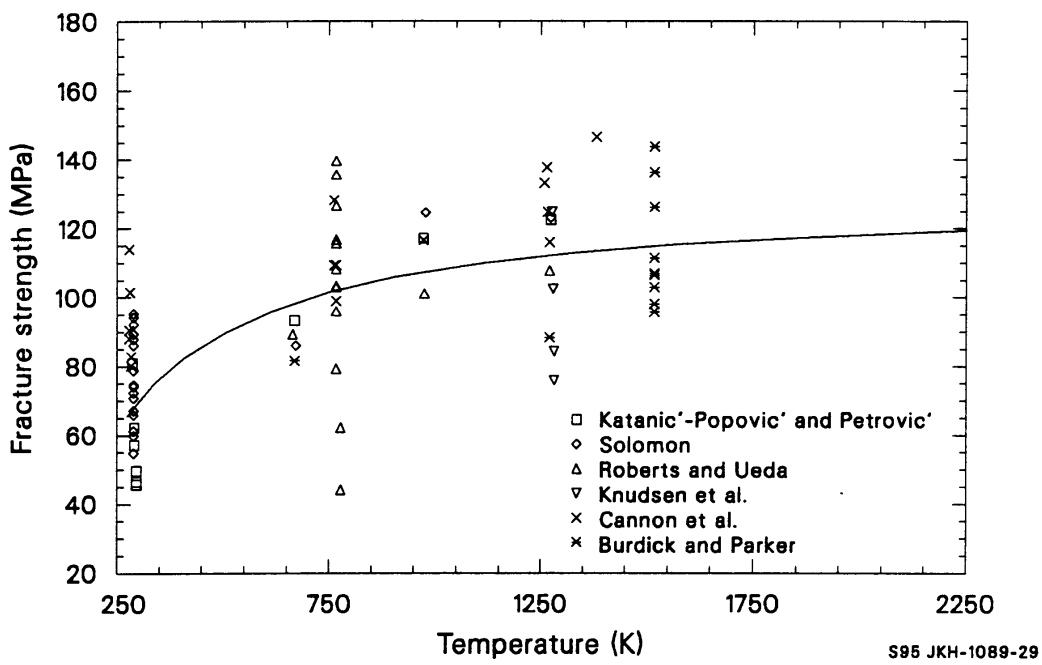

Figure 2-37. Comparison of Equation (2-129) in the elastic behavior regime with out-of-pile UO_2 fracture strength data normalized to 10-µm grain size and 95%TD.

2.12.2.4 ***Out-of-pile Uranium Dioxide Elastic Plastic Behavior.*** At temperatures above the transition temperature, the deformation of UO_2 exhibits plastic behavior after some elastic deformation has occurred. The fracture mode is mostly intergranular, and a significant contribution to the deformation

arises from grain boundary sliding. Figure 2-38 shows the fracture strength of UO_2 as a function of temperature. At temperatures above T_c, the ultimate tensile strength decreases with increasing temperature. The effect of strain rate is significant, but the effect of grain size is negligible for grain sizes up to about 30 µm. Strain rate effects and grain boundary sliding strongly suggest that creep plays a dominant role at these temperatures. When the creep rate for a given temperature is nearly the same order of magnitude as the strain rate, stress relaxation reduces the fracture stress. This effect is shown in Figure 2-38 by the increase in fracture strength with the increase in strain rate.

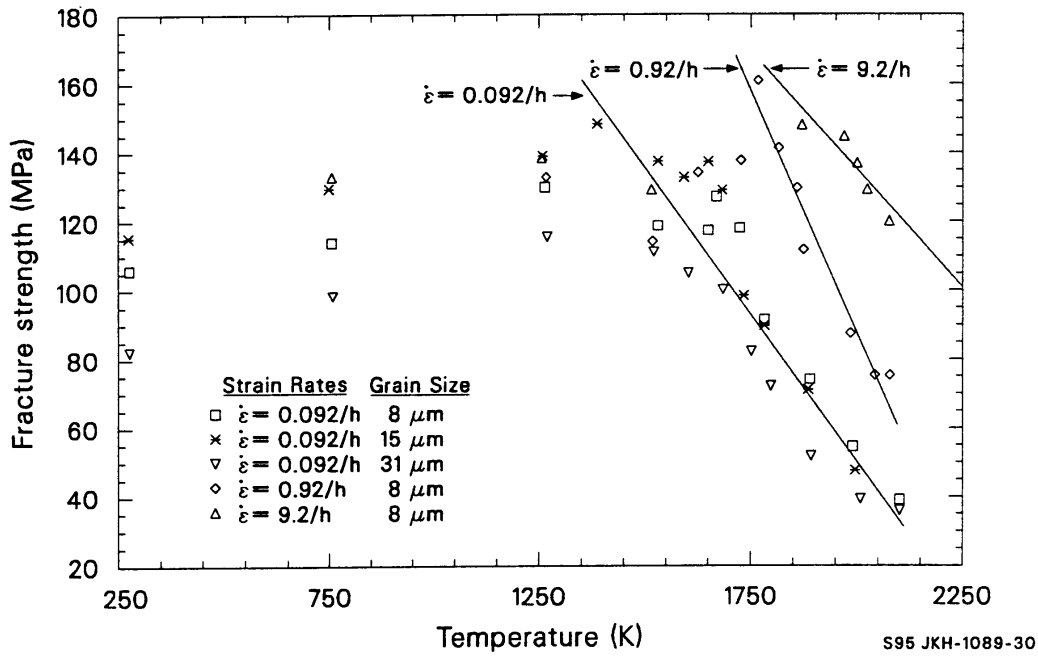

Figure 2-38. Least squares regression fit of UO_2 fracture strength in the elastic plastic regime to out-of-pile data of Cannon et al.

2.12.3 Uranium Dioxide Fracture Strength Model

Irradiation substantially reduces the ductile brittle transition temperature. As discussed in Section 2.7, in-pile creep measurements show that plasticity exists in UO_2 at temperatures as low as 1,000 K. UO_2 is assumed to be brittle below this temperature, and Equation (2-128) (without the grain size term) is selected for the low temperature fracture strength model for UO_2. Equations (2-128) and (2-129), each with a standard deviation of about 1.9×10^7 Pa, predict the experimental out-of-pile fracture strength about equally well; but Equation (2-128) has more theoretical foundation.

Above 1,000 K, irradiation and thermal effects enhance the plasticity of UO_2 so that a decrease in fracture strength with increasing temperature may not occur. A strain rate effect may also exist, but the experimental data available are not sufficient to quantify a strain rate effect. Therefore, the in-pile fracture strength for plastic UO_2 at temperatures higher than 1,000 K is taken to be that found with the low temperature correlation at 1,000 K. This ensures calculational continuity between the two correlations.

The in-pile UO_2 fracture strength model is summarized by Equations (2-124) and (2-125).

Equation (2-124) can be used for temperatures up to about 1,323 K for out-of-pile use. The predictions of FFRACS for two different fuel densities as a function of temperature are shown in Figure 2-39.

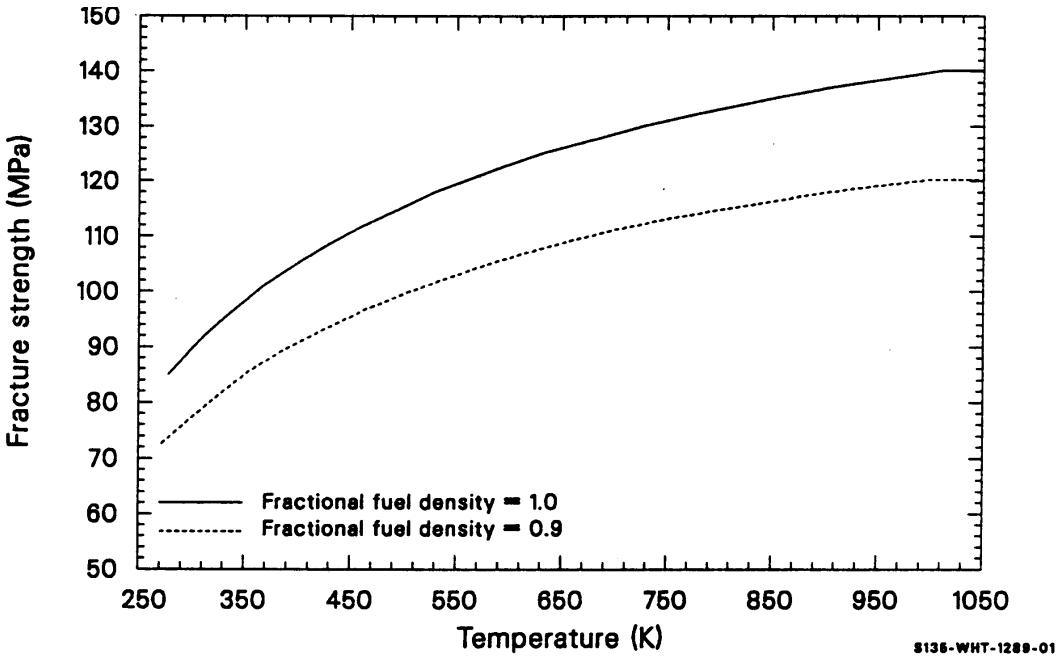

Figure 2-39. Calculated curves showing the predictions of FFRACS as a function of temperature for two fuel densities.

2.12.4 References

2.12-1 J. T. A. Roberts and Y. Ueda, "Influence of Porosity on Deformation and Fracture of UO_2," *Journal of the American Ceramic Society, 55,* 3, 1972, pp. 117-124.

2.12-2 R. F. Cannon, J. T. A. Roberts, and R. J. Beals, "Deformation of UO_2 at High Temperatures," *Journal of the American Ceramic Society, 54,* 1971, pp. 105-112.

2.12-3 Y. Guerin, "Etude par Compression a Hautes Temperatures de la Deformation Plastique du Bioxyde d'Uranium Polycristallin," *Journal of Nuclear Materials, 56,* 1975, pp. 61-75.

2.12-4 A. G. Evans and R. W. Davidge, "The Strength and Fracture of Stoichiometric Polycrystalline UO_2," *Journal of Nuclear Materials, 33,* 1969, pp. 249-260.

2.12-5 C. R. Tottle, *Mechanical Properties of Uranium Compounds,* ANL-7070, November 1965.

2.12-6 J. Katanic'-Popovic' and V. Petrovic', "Strength Dependence on Microstructure Characteristics of Sintered UO_2," *Physics Sintering, 5,* 2, 1973, pp. 95-105.

2.12-7 A. Tetelman and A. McEvily, Jr., *Fracture of Structural Materials,* New York: John Wiley and Sons, 1967, p. 53.

2.12-8 D. Hasselman, "Analysis of the Strain at Fracture of Brittle Solids with High Densities of Microcracks," *Journal of the American Ceramic Society, 52,* 1969, pp. 458-459.

2.12-9 F. P. Knudsen, H. S. Parker, and M. D. Burdick, "Flexural Strength of Specimens Prepared from Several Uranium Dioxide Powders: Its Dependence on Porosity and Grain Size and the Influence of Additions of Titania," *Journal of the American Ceramic Society, 43*, 1960, pp. 641-647.

2.12-10 M. C. Burdick and H. S. Parker, "Effect of Particle Size on Bulk Density and Strength Properties of Uranium Dioxide Specimens," *Journal of the American Ceramic Society, 39*, 1956, pp. 181-187.

2.12-11 E. Orowan, "Die Erhohte Festigkeit Dunner Faden, die Joffe-Effekt, und Verwandte Erscheinungen vom Standpunkt der Griffithschen Bruchtheorie," *Zeitschrift Fuer Physik, 3/4*, pp. 195-213.

2.12-12 N. J. Petch, "Cleavage Strength of Polycrystals," *Journal of the Iron Steel Institute, 174*, Part I, 1953, pp. 25-28.

2.12-13 N. Igata and K. Domoto, "Fracture Stress and Elastic Modulus of Uranium Dioxide Including Excess Oxygen," *Journal of Nuclear Materials, 45*, 1972/73, pp. 317-322.

2.12-14 F. P. Knudsen, "Dependence of Mechanical Strength of Brittle Polycrystalline Specimen on Porosity and Grain Size," *Journal of the American Ceramic Society, 42*, 1959, pp. 376-387.

2.12-15 A. A. Solomon, "Influence of Impurity Particles on the Fracture of UO_2," *Journal of the American Ceramic Society, 55*, 1972, pp. 622-627.

2.13 Viscosity (FVISCO)

The function FVISCO calculates the dynamic viscosity of UO_2. The viscosity is one of the parameters needed to model the motion of fuel during severe core damage.

The effects of departure from stoichiometry and the range of temperatures where liquid and solid UO_2 can coexist are not modeled. Also, the model does not consider any possible contamination of the molten UO_2. Uncertainty estimates are provided based on the data used in the model.

2.13.1 Summary

Viscosity of UO_2 is modeled as a function of temperature, melting temperature (solidus), and the fraction of the fuel that has liquefied. Input arguments describing the oxygen-to-metal ratio and PuO_2 content are not used in the current correlations for viscosity.

Viscosity is calculated by one of three equations, depending on whether the temperature is below the melting point for UO_2, in the range of temperatures where liquid and solid UO_2 can coexist, or above this range.

The equation used to model the viscosity of completely liquefied fuels is

$$\eta_e = 1.23 \times 10^{-2} - 2.09 \times 10^{-6}\ T \qquad (2\text{-}130)$$

where

η_e = dynamic viscosity of the liquid (Pa · s)

T = temperature (K).

For solid UO_2, the viscosity is modeled with the expression

$$\eta_s = 1.38 e^{(4.942 \times 10^4 / T)} \tag{2-131}$$

where η_s is the dynamic viscosity of the UO_2 for temperatures below melting (Pa · s).

In the temperature range where liquid and solid UO_2 phases can both exist, the viscosity is modeled with the expression

$$\eta = \eta_S (1 - f) + \eta_e f \tag{2-132}$$

where

η = dynamic viscosity of the liquid solid mixture (Pa · s)

f = fuel fraction that is liquid (unitless).

The estimated uncertainty of the values computed with Equations (2-130) through (2-132) is computed with the FVISCO subcode but not returned as an output argument. The expressions used for this uncertainty are

$$U = \eta A (1 + |\gamma - 2|) \tag{2-133}$$

where

U = estimated uncertainty (Pa · s)

A = 0.33 for temperatures above melting 0.67 for temperatures below melting

Y = oxygen to metal ratio of the fuel (unitless).

Details of the development of the fuel viscosity model used in the FVISCO function are presented in the following sections. Section 2.13.2 is a review of the data, and Section 2.13.3 is a discussion of the model development.

2.13.2 Fuel Viscosity Data

Viscosities for solid UO_2, $UO_{2.06}$, and $UO_{2.15}$ have been reported by Scott, Hall, and Williams.[2.13-1] Viscosities for the nonstoichiometric oxides are lower than the viscosity of UO_2 at corresponding temperatures and could be measured over a sufficient range to establish the following relation for nonstoichiometric UO_2:

$$g_s = A\, e^{(-B/T)} \tag{2-134}$$

where A and B are material constants. The viscosity of UO_2 was determined to be 2 x 10^{11} Pa · s at 1,923 K and to be in excess of 10^{17} Pa · s at 1,273 K.

Viscosity data at much higher temperatures were obtained by Nelson.[2.13-2,2.13-3] An early measurement (0.145 Pa · s at a temperature of 3,028 K) was reported to correspond to incomplete melting of the sample. Subsequent data (0.045 Pa · s at 3,028 K and 0.036 at 3,068 K) represent a viscous fluid at temperatures below the melt temperature used in this report.[a] These data are not suitable for use in the viscosity model because all three measurements have indicated viscosities well above the more extensive viscosity measurements at temperatures where the UO_2 is known to be completely liquefied.

Two useful sources of data with completely molten UO_2 were available. Tsai and Olander[2.13-4] published data from two samples, and Woodley[2.13-5] published more extensive data from a single sample. The data are tabulated in Tables 2-14 and 2-15 and plotted in Figure 2-40. The precision of the data by Woodley is noticeably higher than the precision of the other data, but there is a larger difference between the two experiments than can be explained by random measurement error. This difference is discussed by Woodley, but no definite reason for it was found. The model developed in the next section therefore contains the assumption that the difference between the data of Tsai and Olander and the data of Woodley is caused by some material parameter that has not been considered (oxygen to metal ratio, for instance).

Table 2-14. UO_2 viscosity data from Tsai and Olander.[2.13-4]

	Temperature (K)	Viscosity (Pa · s)
Sample 1	3,153	0.00583
	3,153	0.00739
	3,153	0.00594
	2,333	0.00514
	3,113	0.00628
	3,113	0.00686
	3,173	0.00762
Sample 2	3,083	0.00921
	3,188	0.00869
	3,188	0.00771
	3,138	0.00781
	3,328	0.00602
	3,328	0.00602

a. The melt temperature for UO_2 is given as 3,113 K in the PHYPRP subcode of the MATPRO package.

Table 2-14. UO_2 viscosity data from Tsai and Olander.[2.13-4] (Continued)

Temperature (K)	Viscosity (Pa · s)
3,328	0.00765
3,248	0.00808
3,248	0.00682

Table 2-15. UO_2 viscosity data from Woodley.[2.13-5]

Temperature (K)	Viscosity (Pa · s)
3,143	0.00425
3,148	0.00365
3,148	0.00326
3,193	0.00441
3,193	0.00434
3,193	0.00444
3,258	0.00420
3,258	0.00417
3,258	0.00415
3,213	0.00426
3,213	0.00428
3,218	0.00427
3,178	0.00432
3,183	0.00436
3,183	0.00434
3,163	0.00424
3,163	0.00420
3,163	0.00423
3,158	0.00418
3,158	0.00428

Table 2-15. UO_2 viscosity data from Woodley.[2.13-5] (Continued)

Temperature (K)	Viscosity (Pa · s)
3,163	0.00425
3,198	0.00417
3,208	0.00418
3,198	0.00419
3,263	0.00399
3,263	0.00405
3,263	0.00402
3,298	0.00398
3,298	0.00395
3,303	0.00394
3,273	0.00399
3,273	0.00398
3,273	0.00397
3,218	0.00409
3,213	0.00406
3,218	0.00404
3,178	0.00412
3,178	0.00406
3,178	0.00413

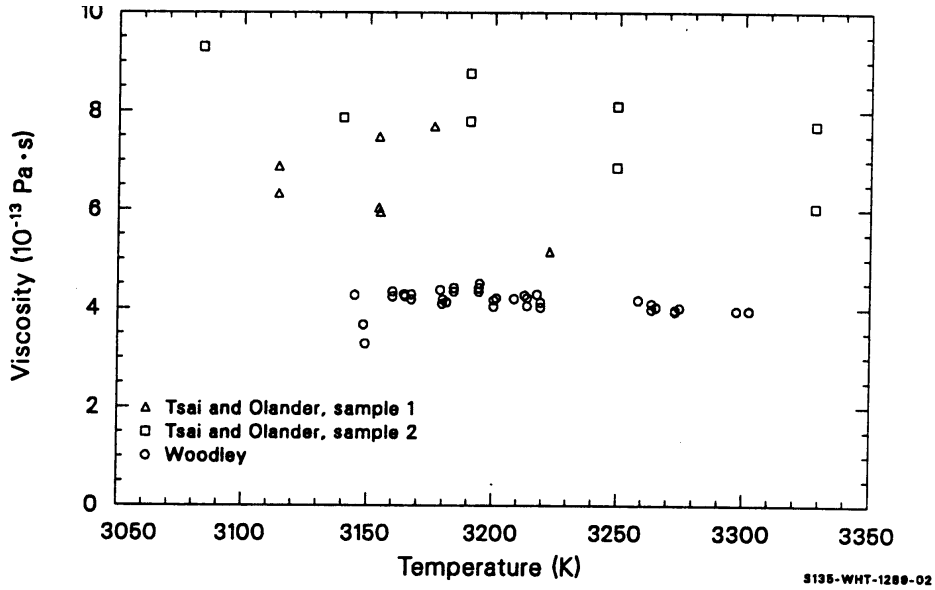

Figure 2-40. Uranium dioxide viscosities measured as a function of temperature.

2.13.3 Model Development and Uncertainty

The correlation for the viscosity of UO_2 below the melt temperature was obtained by solving Equation (2-134) for the values of the two material constants that reproduce the viscosity measured by Scott, Hall, and Williams at 1,273 K and the minimum viscosity reported by these authors for UO_2 at 1,273 K. The fact that this procedure produces only a crude engineering estimate of viscosity is expressed by assigning a large fractional uncertainty, two thirds, to the predicted viscosity of solid UO_2.

Equation (2-130), the correlation for viscosity of liquid UO_2, was obtained from the data of Tsai and Olander and the data of Woodley. The less precise data of Tsai and Olander were used because Woodley used only one sample and the viscosities measured by Tsai and Olander with their samples differ from Woodley's data by more than the scatter of their measurements.

The traditional Arrhenius relation [Equation (2-134)] was not used to correlate the liquid viscosities because a simpler linear expression fits the data as well as the exponential form. A linear least-squares fit to the data of Woodley (with the two anomalously low viscosities at 3,148 K omitted) produced the equation

$$\eta_e = 1.09 \times 10^{-2} - 2.09 \times 10^{-6}\ T\ . \qquad (2\text{-}135)$$

The data of Tsai and Olander yielded the following correlation

$$\eta_e = 1.60 \times 10^{-2} - 2.77 \times 10^{-6}\ T \qquad (2\text{-}136)$$

The viscosities predicted by Equations (2-135) and (2-136) are compared with the data in Figure 2-41. By inspection of this figure, it was concluded that the best mathematical description of the difference in the viscosities measured for the different lots of UO_2 is to assume that the viscosities of the two different lots differ by an additive constant.[a]

To recognize the more precise measurements of Woodley, yet account for the probable lot to lot variation indicated by the data of both authors, the least-squares fit to the data of Tsai and Olander was repeated with the added constraint that the slope of the correlation match the slope obtained from the data of Woodley. The resultant correlation for the data of Tsai and Olander is

$$\eta_e = 1.38 \times 10^{-2} - 2.09 \times 10^{-6}\ T\ . \qquad (2\text{-}137)$$

The final step in the derivation of Equation (2-130) was to average Equations (2-137) and (2-135). With a lot to lot variation present, this step assumes that each lot of UO_2 is equally probable.

The estimated uncertainty of the values of viscosity computed with Equation (2-137) was determined using the assumption that the important difference in the measurements of the two references is the unknown difference in the two lots of UO_2. The resultant standard deviation is

$$\sigma = 2 \times 10^{-3}\ \mathrm{Pa \cdot s} \qquad (2\text{-}138)$$

which is approximately one-third the predicted value of the viscosity. The increased uncertainty for nonstoichiometric UO_2 shown in Equation (2-133) is simply an estimate that has been included to indicate that the model contains no dependence on the oxygen-to-metal ratio of the fuel.

Figure 2-42 illustrates the viscosities calculated with Equation (2-130) for liquid UO_2. The dashed lines are the upper and lower uncertainty limits obtained by adding ± 1/3 of the predicted viscosity and an assumed melt temperature of 3,113 K.

a. The interpretation corresponds to the assumption mentioned at the end of Section 2.15.2; the difference in viscosities is caused by some unknown material parameter of the UO_2.

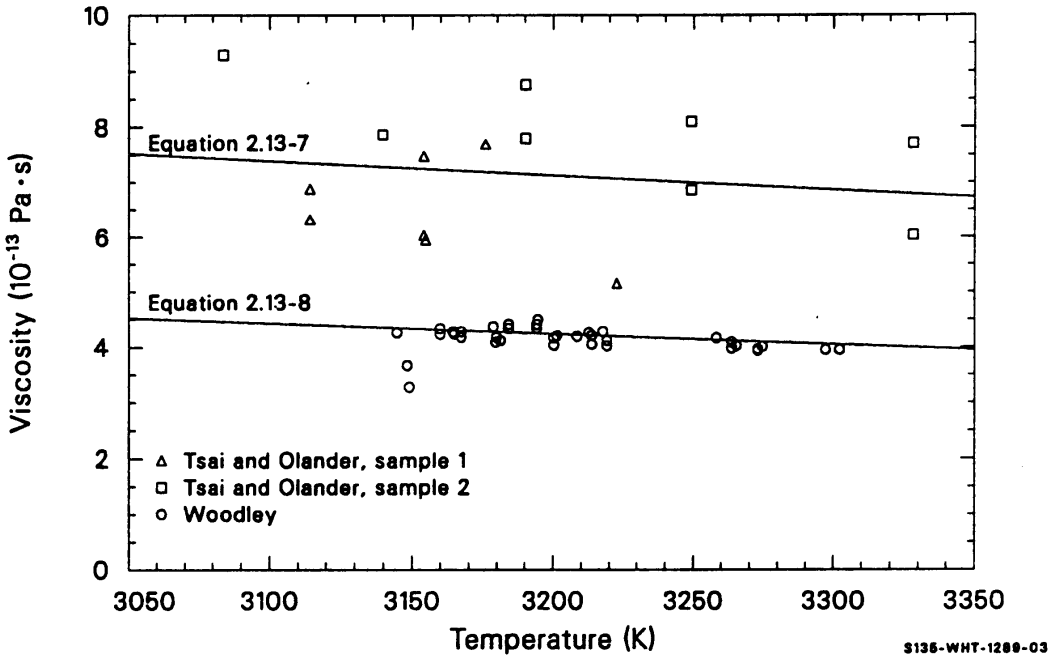

Figure 2-41. Data from uranium dioxide samples compared with least-squares fit.

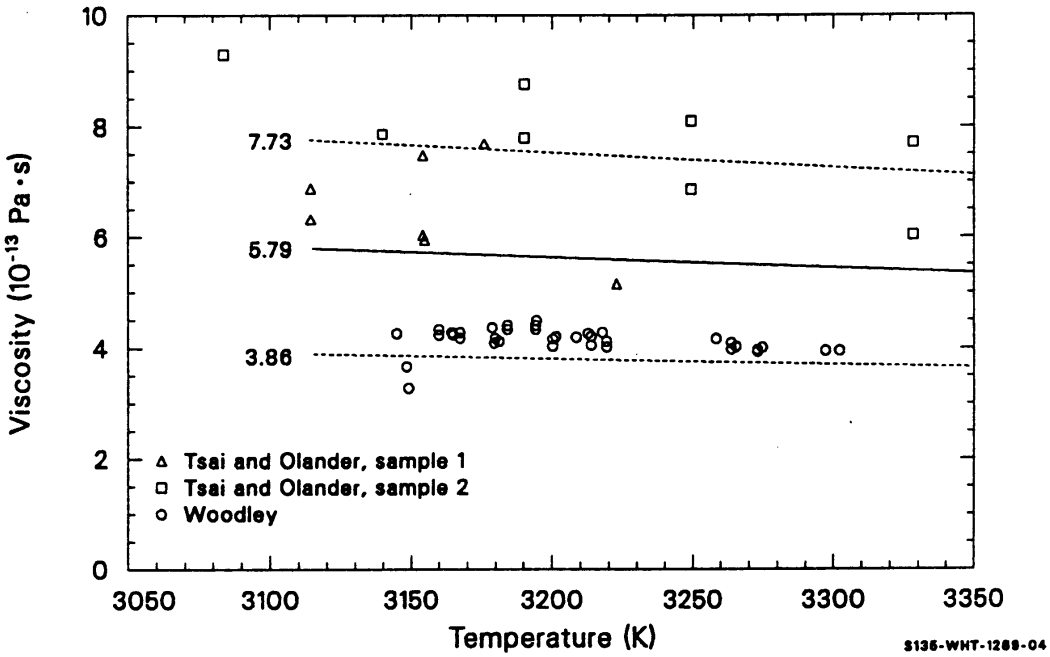

Figure 2-42. Viscosities calculated with Equation (2-130) (solid line) and upper and lower uncertainty estimates (dashed lines) compared with data.

Equation (2-132), which is employed only in the temperature range where liquid and solid can both exist (for temperatures between the fuel melting temperature and the melt temperature plus the liquid solid coexistence temperature range), is obtained from the assumption that the viscosity is the volume weighted average of the solid and liquid viscosities in this temperature range.

2.13.4 References

2.13-1 R. Scott, A. R. Hall, and J. Williams, "The Plastic Deformation of Uranium Oxides Above 800 K," *Journal of Nuclear Material, 1*, 1959, pp. 39-48.

2.13-2 W. F. Sheely ed., *Quarterly Progress Report, July-September, 1969, Reactor Fuels and Materials Development Programs for Fuels and Materials Branch of USAEC Division of Reactor Development and Technology*, BNWL-1223, November 1969.

2.13-3 W. F. Sheely ed., *Quarterly Progress Report, October-December, 1969, Reactor Fuels and Materials Development Programs for Fuels and Materials Branch of USAEC Division of Reactor Development and Technology*, BNWL-1279, February 1970.

2.13-4 H. C. Tsai and D. R. Olander, "The Viscosity of Molten Uranium Dioxide," *Journal of Nuclear Materials, 44*, 1972, pp. 83-86.

2.13-5 R. E. Woodley, "The Viscosity of Molten Uranium Dioxide," *Journal of Nuclear Materials, 50*, 1974, pp. 103-106.

2.14 Vapor Pressure (FVAPRS)

During very high temperature excursions, evaporating reactor fuel (urania or plutonia urania mixtures) can create pressures that equal or exceed plenum gas or fission gas pressures in the fuel rod. This pressure will influence the failure mechanism of the cladding and may cause the melted portion of the fuel to froth and swell. Significant volume changes of the fuel may also result from phase changes due to non-congruent evaporation (composition of the vapor phase being different than that of the fuel). A number of compounds are present in fuel vapors. These are actinide and actinide oxide vapors (UO_2, UO_3, UO_4, U, PuO_2, PuO,Pu) and oxygen vapors (0 to 0_2). The total pressure (sum of all partial pressures) of the actinides and actinide oxides is calculated.

The vapor pressure equations described in this section are to be used in transient fuel codes, mechanistic gas release codes, or restructuring codes that require vapor pressures of calculate bubble migration by evaporation condensation.

2.14.1 Summary

The FVAPRS model determines the saturated actinide vapor and oxygen vapor pressures over urania, plutonia, and mixed oxides as a function of fuel O/M ratio and temperature. Semiempirical equations based on the Clausius-Clapeyron equation are used. The standard error of estimate (SEOE) with respect to the log of the data base is given for each equation.

For urania,

$$\log_{10}(P) = -11191/T + 9.9932 \ln(T) - 0.00132\, T - 69.174 \qquad (2\text{-}139)$$

and SEOE ($\log_{10}P$) = ± 0.206

For plutonia,

$$\log_{10}(P) = (-5404.1 + 6854.6x)/T + 18.166 \ln(T) - 0.003389\ T - 130.65 \quad (2\text{-}140)$$

and SEOE ($\log_{10}P$) = ± 0.559

where

P	=	vapor pressure (Pa)
x	=	deviation from stoichiometry (absolute value of O/M-2)
T	=	temperature (K).

Equation (2-139) is used to calculate the vapor pressure of urania at all O/M ratios. Plutonia vapor pressures are calculated in the FVAPRS code for hypostoichiometric fuel using Equation (2-140). Because it is improbable that plutonia or mixed oxides will be hyperstoichiometric, the FVAPRS code uses a default value of 2.0 for all O/M ratios greater than 2.0. Mixed oxide vapor pressures are obtained by multiplying the plutonia and urania equations by the weight fraction of each material and adding the two resulting calculated pressures.

Similar equations are used for the oxygen vapor pressure ($P(O_2)$ or $P(O)$) over urania.

For O/M ratios > 2.004,

$$\log_{10}(P(O_2)) = -14638.2/T + 21.7752x + 6.2062 \quad (2\text{-}141)$$

and SEOE ($\log_{10} P(O_2)$) = + 0.545.

For O/M ratios < 1.999,

$$\log_{10}(P(O)) = -(49535 + 1418.1 \ln x)/T + 15.181 \quad (2\text{-}142)$$

and SEOE ($\log_{10} P(O)$) = + 0.801.

For O/M ratios < 2.004 but > 1.999,

$$\log_{10}(P'(O_2)) = -\frac{14638}{T} + 1.8036 \ln(x + 0.004) + 6.2933 \quad (2\text{-}143)$$

and SEOE $(\log_{10} P'(O_2)) = \pm 9.0$

where $P'(O_2)$ is the diatomic oxygen pressure for 1.999 < O/M < 2.004.

The rapid decrease of the pressure predicted by Equation (2-143) as stoichiometric composition is approached is limited by imposing the following restrictions:

If $-52708/T + 23.32 \geq \log_{10}(P'(0_2))$,

$$\log_{10}(P(O_2)) = -52708/T + 23.32 \tag{2-144}$$

If $-52708/T + 23.32 < \log_{10}(P'(0_2))$,

$$\log_{10}(P(O_2)) = \log_{10}(P'(O_2)). \tag{2-145}$$

The following sections contain a discussion of the information and techniques used to develop Equations (2-139) through (2-145). Section 2.14.2 is a discussion of data described in the literature and methods used by each investigator to obtain those data. Section 2.14.3 is a discussion of vapor pressure theory, FVAPRS subcode development, and comparisons of the FVAPRS subcode with literature data. Section 2.14.5 contains a bibliography of references studied but not used to develop the FVAPRS subcode.

2.14.2 Vapor Pressure Data

Vapor pressure data for urania, plutonia, and mixed oxides are obtained, using a number of different experimental techniques, such as transpiration, effusion, Knudsen effusion, laser heating, electron beam heating, free evaporation, static testing, and boiling point pressures. Of these techniques, transpiration, Knudsen effusion, static testing, and laser heating are most widely used. Reported vapor pressures are generally determined indirectly, calculated from measurements of sample weight loss, sample momentum, weight of deposit on a target, or by analysis of the ions in a gas stream. Techniques such as coulorimetric or x-ray analysis are used to determine vapor pressure when the O/M ratio of the sample is known. These measurement techniques are discussed in the following text in enough detail to indicate their advantages or disadvantages.

The transpiration technique is one of the techniques that can be used to measure vapor pressure in the presence of large concentrations of other gases. It is most accurate at temperatures where the confining material does not contribute significantly to the measured vapor pressure. Since it is not limited by the pressure of the gas being measured, a distinct advantage of this technique is that a carrier gas can be used to control the composition of the sample. Using this technique, the vapor pressure of a sample is determined from measurements of sample weight loss, weight of vapor condensed in a cold trap, or by monitoring molecular species in the carrier gas. A disadvantage of the technique is that vapor pressure is independent of the carrier gas flow rate in only a narrow band of flow rates which depend on other experimental conditions.

The Knudsen effusion technique[2.14-1] and a similar technique, the Langmuir free evaporation technique, are good measurement methods for vapor pressures below 15 Pa. An advantage of the Knudsen technique to measure vapor pressure is that there are very small temperature gradients in the sample and its surroundings.

The application of lasers or electron beams to heat the surface of materials that melt at very high temperatures has provided an experimental method to study materials at temperatures above those that would

melt the retaining crucibles. Vapor pressure data gathered when intense pulses of laser or electron beams impinge on the surface of the samples are derived from sample weight loss, evaporation depth, recoil momentum, torsion, or by mass spectrometry ion intensity measurements. These experiments must be analyzed with caution because equilibrium vapor pressure may not be the pressure measured.

2.14.2.1 ***Urania Vapor Pressure.*** The measurement techniques described previously have been used to measure urania vapor pressures discussed in the following paragraphs.

Szwarc and Latta[2.14-2] reported total equilibrium vapor pressure data of hypostoichiometric urania, using the transpiration technique with the oxygen potential of the carrier gas controlled with H_2/H_2O mixtures. They found that the initial O/M ratios remained stable to within ± 0.005 but that the vapor pressure changed an order of magnitude as the O/M ratio varied between 1.88 to 1.94.

Bober[2.14-3] measured urania vapor pressure, using the laser heating technique to attain temperatures between 4,100 and 4,400 K and found vapor pressures between 0.608 and 1.01 MPa.

Reedy and Chasanov[2.14-4] used the transpiration technique to obtain total vapor pressure data. They determined the O/M ratio of remaining residues and found final O/M ratios to be dependent on the testing temperatures.

Ackermann[2.14-5] determined the vapor pressure of hypostoichiometric urania between 1,580 to 2,400 K, using effusion rate measurements, with an assumed vapor of UO. Mass spectrometric measurements on the system found the UO vapor pressure to be about 10 times greater than the UO_2 and U vapor pressures.

Tetenbaum and Hunt[2.14-6] measured total vapor pressure of hypostoichiometric and nearly stoichiometric urania, using the transpiration technique. The O/M ratio of their samples increased with increasing temperatures, and the fuel vapor pressure increased as the O/M ratio approached the hypostoichiometric phase boundary. Their reported vapor pressure data are in very good agreement with those of Szwarc and Latta for $UO_{1.88}$ but are approximately 1.5 to 2 times greater for $UO_{1.92}$ and $UO_{1.94}$. They also reported an order of magnitude pressure change as the O/M ratio of the samples changed.

Benezech[2.14-7] used the transpiration technique to obtain urania vapor pressure data at temperatures between 2,200 and 2,600 K with O/M ratios varying between 2.0 and 2.15. He reported large temperature gradients in the crucible and found the dominant vapor species (UO_2 or UO) to be dependent on the composition of the carrier gas.

Ohse[2.14-8, 2.14-9] reported vapor pressures of urania at temperatures up to 4,710 K, using the laser heating technique. These data are important because they were taken at temperatures above melting and show the vapor pressure at very high temperatures to increase with increasing temperature at a much slower rate than it does below the melting temperatures.

Alexander[2.14-10] measured total vapor pressure and oxygen dissociation pressures of urania, thoria, zirconia, and combinations of the three, using the transpiration technique at temperatures between 2,000 and 3,000 K. They reported vapor pressures of thoria urania mixtures to be an order of magnitude less than urania vapor pressures.

Ackermann[2.14-11,2.14-12] reported vapor pressures for urania at temperatures between 1,600 and 2,800 K, using the Knudsen effusion technique. These data were later revised and reported after the results of later experiments were analyzed.[2.14-13] Their reported results, urania vapor pressure invariant to 2,700

K and melting at 2,678 K, conflict with results previously discussed by other investigators. Their sample composition probably varied from pure urania, containing impurities that affected the measured vapor pressures and the melting point. However, the magnitude and the slope of the pressure as a function of temperature are within the data scatter bands of other investigators' data.

Chapman and Meadows[2.14-14,2.14-15] investigated nonstoichiometric urania of compositions between $UO_{2.02}$ and $UO_{2.63}$ in the UO_{2+x} and U_3O_{8-x} and U_3O_{8-y} phase regions at temperatures between 1,273 and 1,873 K, using a thermogravimetric technique to obtain the vapor pressure data. They reported evidence of UO_4 vapor instead of UO or UO_2 and an equilibrium O/M ratio, in a vacuum at temperatures above 1,973 K, to be less than the ratio 2.0 obtained by other investigators.

Ohse[2.14-16] measured urania vapor pressures between 1×10^{-6} and 3.4×10^{-4} MPa in an effusion cell at temperatures between 2,278 and 2,768 K.

Benson[2.14-17] investigated vapor pressures of urania, using an electron beam to heat the samples to temperatures between 4,500 and 7,200 K.

Babelot[2.14-18] reported urania vapor pressure data obtained at temperatures between 3,300 and 4,700 K, using a laser to heat the samples. The slope and magnitude of these data agree very well with those reported by Benson.

The literature data discussed in this section generally indicate that urania evaporates bivariantly as a function of O/M ratio and temperature. A composition change from stoichiometry can, at temperatures less than 2,500 K, cause the vapor pressure to increase 10 times or more as the urania becomes increasingly hypostoichiometric. The data are insufficient to determine how much effect deviation from stoichiometry has on vapor pressures in the hyperstoichiometric region. Tetenbaum and Hunt observed little effect of urania nonstoichiometry on the vapor pressure at temperatures near melting with hypostoichiometric fuel. Data at temperatures above melting and not having O/M ratios reported can therefore be used. There is no observed discontinuity of vapor pressure at the urania melting temperature, although the temperature dependence does begin to decrease. The early data of Ackermann[2.14-12] are considered in error by the authors[2.14-15] and are therefore not useful for model development. Also, the Chapman and Meadows data are not applicable for model development because the scatter is large due to unreported O/M ratios much greater than 2.0. All the rest of the data discussed are amenable to model development, although some scatter between data sets occurs. Data discussed in this section are displayed in Figure 2-43. The urania vapor pressure as a function of temperature can be seen in each figure. The decreasing rate of change at temperature above 3,000 K can also be seen.

2.14.2.2 ***Plutonia Vapor Pressure.*** Plutonia (PuO_2) is very similar to urania in many of its material properties. The plutonia vapor pressure data presently available in the literature are briefly discussed in the following paragraphs.

Ohse and Ciani[2.14-19] reported vapor pressures of urania, at 1,800, 2,000, and 2,200 K, and plutonia, with O/M ratios between 1.51 and 1.61, based on effusion cell measurements. They found it very difficult to obtain good data with O/M ratios greater than 1.94 due to rapid change of fuel O/M ratios, or vapor O/M ratios, or both.

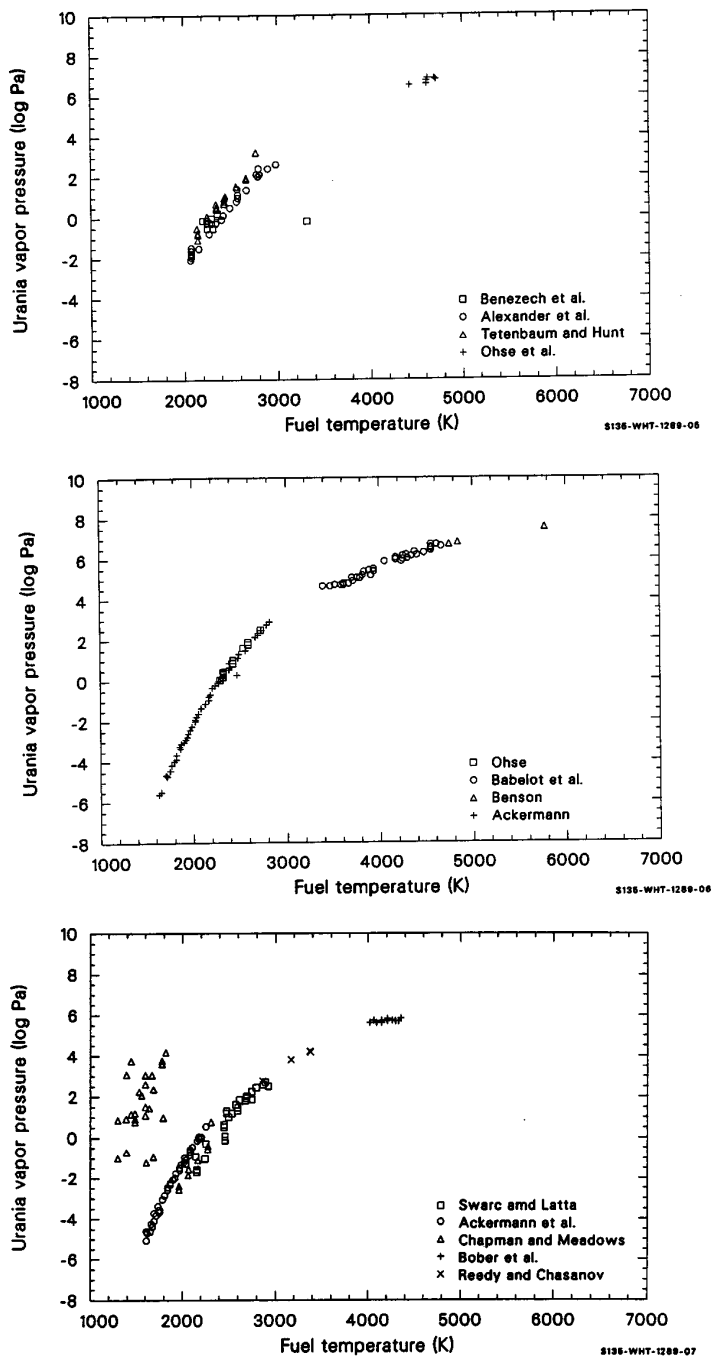

Figure 2-43. Urania vapor pressure data.

Ackermann[2.14-20] measured plutonia vapor pressures of hypostoichiometric plutonia in effusion cells. Investigating the effects of both temperature and composition on the total vapor pressures, he found

the evaporation rate to decrease more than 30% from the initial rate after 8 hours and found the composition to change with time. Chemical and x-ray analyses determined the O/M ratios to be 1.923 to 1.916 and 1.90 to 1.93, respectively.

Phipps[2.14-21] used the Knudsen effusion method to measure vapor pressures between 1,589 and 2,060 K. The vapor pressure data reported were derived from radiochemical analysis of the deposit on the effusion target. Phipps reported that oxygen reacted with the vapor flow and, therefore, had to be included in the vapor pressure calculations.

Pardue and Keller[2.14-22] measured the vapor pressure of plutonia in three atmospheres of air, argon, and oxygen at temperatures between 1,723 and 2,048 K, using the transpiration technique to obtain their data.

Mulford and Lamar[2.14-23] reported plutonia vapor pressure data measured at temperatures between 2,000 and 2,400 K, using the Knudsen effusion technique, that were significantly different than those observed by Phipps.

The plutonia data reviewed include vapor pressures of plutonia between 1,600 and 2,500 K and O/M ratios between 1.5 and 2.0. These data are shown in Figure 2-44. Vapor pressures of plutonia decrease as the hypostoichiometric phase boundary is approached. Vapor pressures were observed between 10^{-6} and 10 Pa. Large scatter in the data can be seen in Figure 2-44, partially a result of O/M ratio effects not recorded by many of the investigators. Therefore, only the data of Ackermann[2.14-20] and Ohse and Ciani[2.14-19] are used for model development.

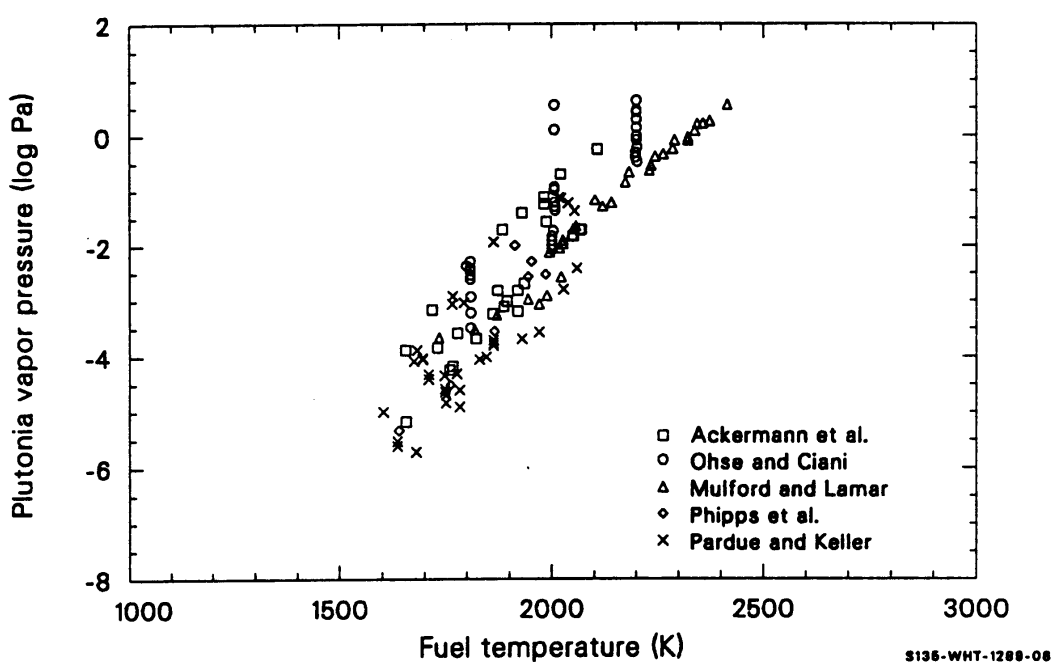

Figure 2-44. Plutonia vapor pressure data.

2.14.2.3 ***Mixed Oxide Vapor Pressure.*** Some mixed oxide data have appeared in the literature. These are discussed briefly.

Tetenbaum[2.14-24] reported the results of an investigation of total vapor pressure of actinide bearing species over the U-Pu-O system, using the transpiration technique. The data indicate that mixed oxides of composition $(U_{0.8}, Pu_{0.2})0_{2-x}$ have vapor pressures between 0.1 and 1Pa at temperatures between 2,150 and 2,450 K. Analysis of these data shows the urania vapor pressure to be approximately 0.85 of the total vapor pressure and plutonia is approximately 0.15 of the total.

Ohse and Olson[2.14-25] reported the vapor pressures of coprecipitated mixed oxide with a composition of $(U_{0.85}Pu_{0.15})O_{2-x}$ obtained in a tungsten effusion cell heated by an electron beam. The measurements were taken at temperatures between 1,800 and 2,350 K, with the O/M ratios varying between 2.0 and 1.94. Ohse and Olson observed urania vapor pressures to be about 10 times greater than for any of the other oxides present.

Battles[2.14-26] reported vapor pressures of mechanically mixed urania and plutonia $(U_{0.8}Pu_{0.2})O_{2-x}$ with the O/M ratio between 1.92 and 2.01 and the temperature approximately 2,240 K. They used the Knudsen effusion technique with a mass spectrometer to determine the vapor pressure. They reported the urania vapor pressure to be much greater than the plutonia vapor pressure.

Ohse[2.14-8,2.14-9] reported mixed oxide data measured at very high temperatures (4,000 to 7,000 K), using the laser heating technique. These test samples were melted prior to laser heating and vapor pressure measurements.

The four data sets just reviewed all show the vapor pressure of urania to be on the order of 10 times greater than the pressure of other chemical species present. The O/M ratios between 1.91 and 2.00 were investigated at temperatures between 2,100 and 2,500 K. Vapor pressures ranged from approximately 0.01 Pa at 2,150 K to approximately 12 MPa at 7,000 K. Figure 2-45 shows the mixed oxide data just discussed. The high temperature data show a significant decrease in the rate of vapor pressure increase. The data also show scatter bands of about an order of magnitude at temperatures below 3,000 K.

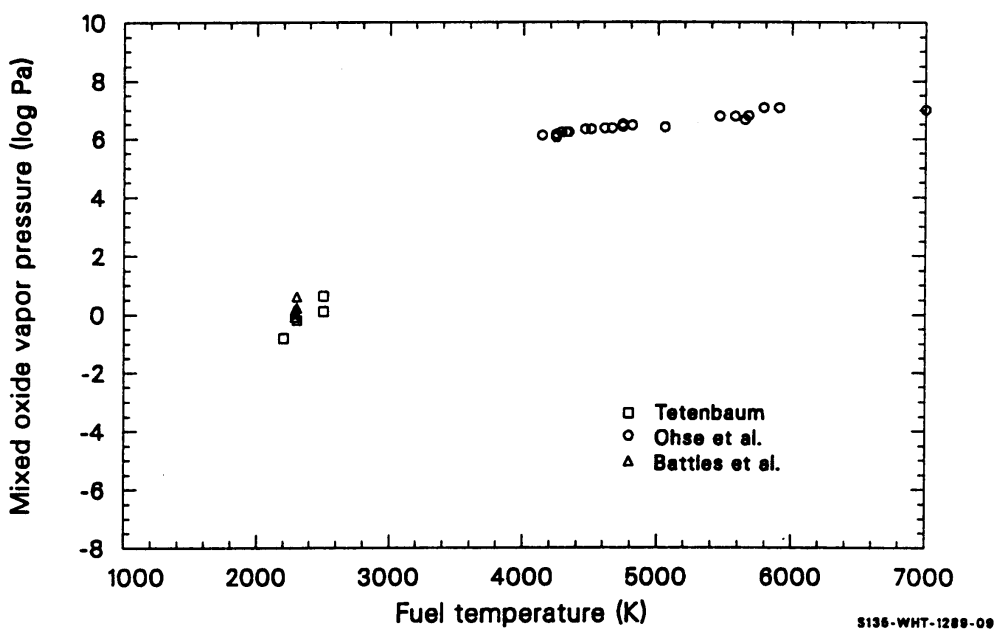

Figure 2-45. Mixed oxide vapor pressure data.

2.14.2.4 ***Oxygen Vapor Pressure.*** Although actinide oxide vapors constitute the most prominent vapors evolving from reactor fuels, oxygen vapors (O and O_2) do evaporate and thereby change the chemical composition of the fuel. A number of investigators have found metallic uranium in otherwise pure urania after heating above 2,073 in a vacuum. For example, Aitken[2.14-27] found both hypo- and hyperstoichiometric urania to change with time and temperature until an O/M ratio of 1.88 was reached. Vaporization of oxygen from the fuel not only changes the composition of the fuel but is directly related to the oxidation of the internal surfaces of the cladding. Oxygen vapor pressures have been determined for urania up to approximately 2,900 K. Most of this oxygen data is derived from measurement of moisture content of carrier gases, sample weight, or composition changes. Only one set of oxygen vapor pressure data for plutonia[2.14-28] was found. This data set was at temperatures too low (less than 1,323 K) and is inefficacious until more data are available. Modeling of plutonia oxygen pressures was therefore not attempted. Data reported for oxygen pressures over urania are described in the following paragraphs.

Tetenbaum and Hunt[2.14-29] used the transpiration technique to measure the oxygen partial pressure of hypostoichiometric urania. Monatomic oxygen pressures were determined up to 2,700 K. Vapor pressure measurements were determined for compositions ranging from $UO_{2.0}$ to approximately $UO_{1.86}$. Their data show oxygen vapor pressure to increase sharply near the stoichiometric composition at the lower temperatures measured. This pressure increase near the stoichiometric composition is not as steep at the higher temperatures.

Markin[2.14-30] used a unique method (sample composition measurements after equilibrium was reached) to obtain monatomic oxygen vapor pressure data for hypostoichiometric and hyperstoichiometric urania. The O/M ratios reported are accurate to within ± 0.005. Measurements were obtained for hypostoichiometric urania between 2,000 and 2,400 K and for hyperstoichiometric urania between 1,600 and 1,700 K. Their data agree will with that of Tetenbaum and Hunt.

Wheeler[2.14-31] measured the monatomic oxygen vapor pressure of urania between 1,800 and 2,000 K. He used a technique of equilibrating UO_{2-x} in an oxygen atmosphere controlled by the equilibrium reaction

$$C + O_2 = CO_2 \,. \tag{2-146}$$

Data were obtained from urania with O/M ratios between 2.0 and 1.98. These data agree well with both data sets just described.

Javed[2.14-32] reported diatomic oxygen vapor pressure data of urania, using the transpiration technique at temperatures between 1,873 and 2,173 K. The O/M ratios were obtained from chemical, x-ray, and metallographic techniques. These oxygen vapor pressure data tend to be higher than those of Tetenbaum and Hunt, Marken, and Wheeler.

Aitken[2.14-27] used free evaporation and flowing gas transpiration techniques to obtain the oxygen pressure of urania between 2,023 and 2,223 K. These data were reported as diatomic oxygen pressures. Aitken observed the O/M ratio of the urania to approach 1.88 for both hypo- and hyperstoichiometric urania when the samples were heated above 2,000 K. The oxygen vapor pressure implied by these data is approximately two to ten times that of the Tetenbaum and Hunt data. Tetenbaum and Hunt suggest that the discrepancy is a result of the Aitken data not having reached equilibrium pressures.

Roberts and Walter[2.14-33] investigated diatomic oxygen equilibrium vapor pressure of urania with compositions between $UO_{2.00}$ and $UO_{2.3}$ and at temperatures between 1,273 and 1,723 K. Temperature measurements were obtained, using a tensimetric technique (direct measurement of pressure). The technique is crude, and there was no control of the sample O/M ratio. The investigators found deposits of mixtures of the U_4O_9 and $UO_{2.61}$ phases in cooler parts of the furnace, indicating that the O/M ratio of the samples was changing. The authors also suggest that an equilibrium vapor pressure may not have been obtained. These data were therefore not used as part of the data base for model development.

Hagemark and Broli[2.14-34] conducted an extensive investigation of diatomic oxygen pressures of urania with O/M ratios between 2.0 and 2.25 and at temperatures between 1,173 and 1,773 K. Oxygen vapor pressure measurements were obtained from thermobalance measurements during testing.

Alexander[2.14-10] used the transpiration technique to determine the oxygen dissociation pressure of urania. They investigated oxygen vapor pressures of urania compositions of $UO_{2.03}$, $UO_{2.0}$, and $UO_{1.97}$ with compositions accurate to ± 0.01 units at temperatures between 1,950 and 2,720 K.

Blackburn[2.14-35] used the Knudsen effusion technique to measure the diatomic oxygen vapor pressure of urania. He obtained oxygen vapor pressure data for O/M ratios between 2.1 and 2.6 at temperatures between 1,263 and 1,400 K. For purposes of the FVAPRS code and this report, only the data of O/M ratios less than 2.2 can be used. This is roughly the boundary of urania-oxygen solid solution at temperatures above 1,273 K. These data are in fair agreement with those reported by other investigators.

Aronson and Belle[2.14-36] used an electrochemical measurement technique (emf measurements on urania half cells) to measure the diatomic oxygen vapor pressure of urania. Vapor pressures for urania compositions between $UO_{2.0}$ and approximately $UO_{2.5}$ at temperatures between 1,150 and 1,350 K were investigated. Only the urania data with O/M ratios below 2.2 were considered for model development.

Kiukkola[2.14-37] used emf measurements from galvanic cells to obtain diatomic vapor pressures over urania. Vapor pressure measurements of urania at compositions of $UO_{2.01}$ to $UO_{2.67}$ were obtained at temperatures between 1,073 and 1,473 K. Here again, only those data points with urania O/M ratios less than $UO_{2.0}$ were considered.

Markin and Bones[2.14-38] used emf measurements of urania with O/M ratios between 2.00 and 2.003 in a high temperature galvanic cell. Diatomic oxygen pressures of urania between the temperatures of 973 and 1,673 K were investigated. The O/M ratios were controlled and determined by coulorimetric titration of oxygen ions, using NiO as a source of oxygen. The main purpose of their investigations was to obtain thermodynamic functions and not oxygen vapor pressures, so there is very little discussion of the vapor pressure data. Their data indicate a steep slope (decrease in vapor pressure) as the composition of the urania approaches stoichiometry. This is consistent with other data in this composition range. These data are therefore useful in the modeling effort.

Aukrust[2.14-39] determined equilibrium oxygen pressures over hyperstoichiometric urania. The O/M ratios were determined by a thermogravimetric method, and oxygen pressures were determined from known CO_2/CO or O_2/Ar gas mixtures and O/M ratio measurements. Data were obtained at temperatures between 1,373 and 1,673 K. They report O/Mratios accurate to within +0.0002 and the $\log_{10}P_{O2}$ accurate to ±0.02.

The data discussed in this section must be divided into two groups; hypostoichiometric and hyperstoichiometric. For hypostoichiometric fuel, the data of Tetenbaum and Hunt, Markin, Wheeler, and Alex-

ander are the best available. The data of Javed and Atkins were probably measured under nonequilibrium conditions and should not be used. For hyperstoichiometric fuel and oxygen pressure, data of Hagemark and Broli are the most extensive and are the best. The rest are within an order of magnitude of these data and have been used.

2.14.3 Model Development

The equations used in FVAPRS are based on thermodynamic equations fitted to the data. The following section is a discussion of thermodynamic and chemical theory and the technique used to develop the FVAPRS correlations.

2.14.3.1 ***Review of Basic Theory.*** Evaporation is a change in chemical state obeying the law of conservation of mass. Equations can therefore be used to show which elements or compounds could be expected to be present in the vapor phase above a fuel substrate. Possible reactions of urania are [2.14-12]

$$UO_{2\,(\beta)} \rightarrow UO_{(g)} + \frac{(1-\alpha)}{2} O_{2\,(g)} + \alpha O_{(g)} \tag{2-147}$$

$$UO_{2\,(\beta)} \rightarrow \frac{1}{2} UO_{2\,(g)} + \frac{(2-3\alpha)}{4} O_{2\,(g)} + \alpha \frac{3}{2} O_{(g)} + \frac{1}{2} U_{(\beta)} \tag{2-148}$$

$$UO_{2\,(\beta)} \rightarrow \frac{1}{2} UO_{(g)} + \frac{1}{2} UO_{3\,(g)} \tag{2-149}$$

$$UO_{2\,(\beta)} \rightarrow \frac{1}{3} U_{(g)} + \frac{2}{3} UO_{3\,(g)} \tag{2-150}$$

$$UO_{2\,(\beta)} \rightarrow UO^{+}{}_{2\,(g)} + e^{-}_{(g)} \tag{2-151}$$

$$UO_{(\beta)} \rightarrow UO_{(g)} \tag{2-152}$$

$$2UO_{2\,(\beta)} \rightarrow (UO_2)_{2\,(g)} \tag{2-153}$$

where β denotes that the material is in the solid or liquid phase and g denotes the gas phase. These equations apply only in the oxygen solid solution regions of solid and liquid urania. Of these possible compounds, one is usually much more prominent than the others. Analysis of the data indicates that for substrate temperatures < 2,000 K, the magnitude of the actinide oxide vapors follow the order, $P_{UO} > P_{UO_2} > P_U > P_{UO_3}$, where P is the vapor pressure. At about 3,000 K, the order of partial pressures is $P_{UO_2} \approx P_{UO} > P_{UO_3}, \approx P_U$; and at temperatures > 3,500 K, the partial pressure order is $P_{UO_2} > P_{UO_3} > P_{UO} > P_U$. The oxygen partial pressure at all temperatures is generally much smaller than the combined vapor pressure of the actinide oxides.

For plutonia, the chemical reactions are similar to those of urania

$$PuO_{2\,(\beta)} \rightarrow PuO_{(g)} + \frac{(1-\alpha)}{2} O_{2\,(g)} + \alpha O_{(g)} \tag{2-154}$$

$$PuO_{2(\beta)} \rightarrow \frac{1}{2}PuO_{2(g)} + \frac{(2-3\alpha)}{4}O_{2(g)} + \alpha\frac{3}{2}O_{(g)} + \frac{1}{2}Pu_{(\beta)} \quad (2\text{-}155)$$

$$PuO_{2(\beta)} \rightarrow \frac{1}{2}PuO_{(g)} + \frac{1}{2}PuO_{3(g)} \quad (2\text{-}156)$$

$$PuO_{2(\beta)} \rightarrow \frac{1}{3}Pu_{(g)} + \frac{2}{3}PuO_{3(g)} \quad (2\text{-}157)$$

$$PuO_{2(\beta)} \rightarrow PuO^{+}_{2(g)} + e^{-}_{(g)} \quad (2\text{-}158)$$

$$PuO_{(\beta)} \rightarrow PuO_{(g)} \quad (2\text{-}159)$$

$$2PuO_{2(\beta)} \rightarrow (PuO_2)_{2(g)}. \quad (2\text{-}160)$$

It is experimentally determined that PuO is the prominent species of plutonia up to an O/M ratio of approximately 1.99, where PuO_2 becomes more prominent.

Evaporation can be described by simple thermodynamic considerations of a first order phase transition of a pure substance, solid to vapor or liquid to vapor, at constant temperature and pressure. At the phase transition

$$dG_\beta = dG_g \quad (2\text{-}161)$$

where

dG_β	=	change in Gibbs free energy for the solid or liquid
dG_g	=	change in Gibbs free energy for the gas.

Since the process is reversible for a first order phase transition at constant temperature and pressure,

$$dG_\beta = V_\beta dp - S_\beta dT . \quad (2\text{-}162)$$

$$dG_g = V_g dp - S_g dT \quad (2\text{-}163)$$

where

V_β	=	molar volume of solid or liquid
V_g	=	molar volume of gas
p	=	pressure (Pa)
S_β	=	entropy of solid or liquid
S_g	=	entropy of gas

T = temperature (K).

Combining Equations (2-161) through (2-163) and rearranging gives

$$(S_g - S_\beta)\, dT = (V_g - V_\beta)\, dp \quad . \tag{2-164}$$

Since V_g is generally much greater than $V\beta$, Equation (2-164) can be reduced to

$$\Delta S/V_g = dp/dT. \tag{2-165}$$

From the second law of thermodynamics, we know that

$$\Delta S = \int_\beta^g \frac{dQ}{T} \tag{2-166}$$

where dQ is the differential of heat for a reversible phase transition proceeding at constant temperature and pressure.

The first law and the definition of system enthalpy can be used to relate dQ to enthalpy. From the first law,

$$dU = dQ - pdV \tag{2-167}$$

where U is the internal energy and V is the volume. The differential of the system enthalpy for a reversible process is

$$dH = dU + pdV + Vdp. \tag{2-168}$$

At constant pressure, Equations (2-167) and (2-168) imply

$$dQ = dH. \tag{2-169}$$

The change of enthalpy can then be written as

$$\Delta S = \int_\beta^g \frac{dH}{T}. \tag{2-170}$$

Integrating Equation (2-170) at constant temperature gives

$$\Delta S = \frac{\Delta H}{T} \tag{2-171}$$

where ΔH is the enthalpy change of the phase transition.

Since the enthalpy change of the phase transition is a function of heat capacity, which is different for solids and gases at different temperatures, the temperature dependence of ΔH must be taken into account for the vapor pressure to be evaluated accurately. The temperature dependence of ΔH can be approximated by the second order empirical equation

$$\Delta H = a + f(x) + bT + cT^2 \tag{2-172}$$

where

f(x)	=	a function of composition
a,b,c	=	constants.

Substituting Equation (2-172) into Equation (2-171) and the resultant expression into Equation (2-165) gives

$$\frac{dp}{dT} = \left[\frac{a + f(x)}{T} + b + cT\right] V_g^{-1} \tag{2-173}$$

If the vapor behaves as an ideal gas,

$$V_g = RT/p \tag{2-174}$$

where R is the universal gas constant (m^3Pa/mole · K). Equation (2-173) reduces to

$$\frac{dp}{p} = \left[\frac{a + f(x)}{T^2} + \frac{b}{T} + c\right] R^{-1} dT \tag{2-175}$$

and integrating gives

$$\ln(p) = \left[-\frac{a + f(x)}{T} + b\ln(T) + cT + D\right] R^{-1} \tag{2-176}$$

where D is a constant of integration.

2.14.3.2 ***Evaluation of Constants.*** Constants used in Equation (2-139) were obtained from fitting of Equation (2-176) to literature data. Hyperstoichiometric and hypostoichiometric data were fit separately.

The urania model is based on the data discussed in Section 2.14.2.1 except for that of Chapman and Meadows[2.14-14] and Ackermann,[2.14-12] for the reasons discussed in that section. The data of Tetenbaum and Hunt indicate the urania total pressure to be dependent on the urania O/M ratio, but this dependence diminishes near the melting temperature. Since many of the data have been obtained at temperatures where the O/M ratio seems to have little effect and most of the data do not include the O/M ratio, the FVAPRS

urania correlation was developed disregarding the vapor pressure dependence on the fuel composition. The low temperature data of Ackermann,[2.14-5] Alexander,[2.14-10] and Benezech[2.14-7] were used, assuming that their test samples did not deviate greatly from stoichiometry. The best fit correlations prediction (solid line) is shown in Figure 2-46 compared to the urania data in Section 2.14.2.1. The standard error of estimate of the FVAPRS equation and log of the data is ± 0.206.

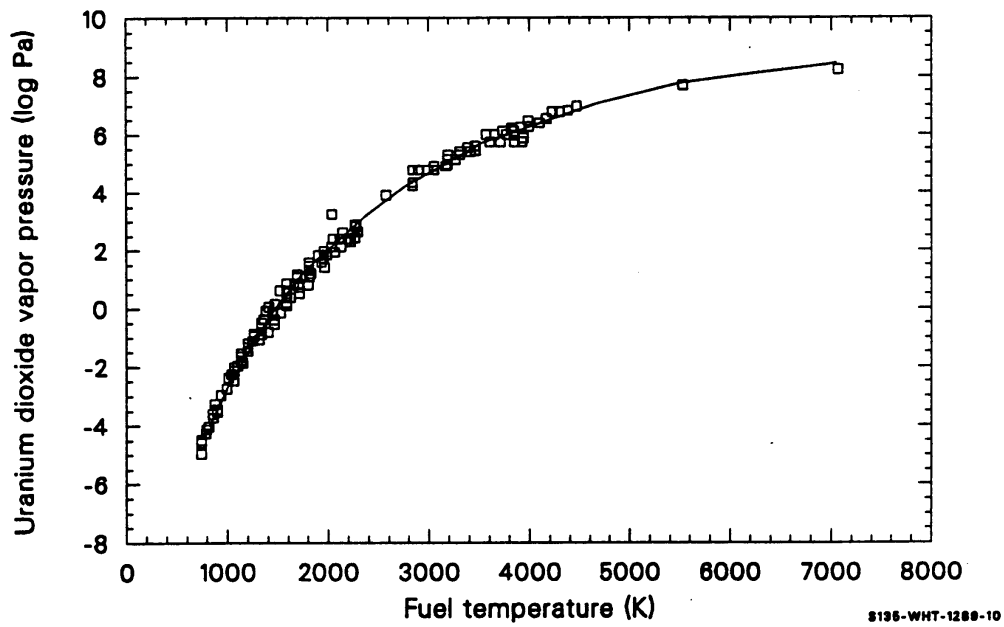

Figure 2-46. FVAPRS calculations (solid line) compared to urania data.

Material constants of Equation (2-139) for hypostoichiometric plutonia were obtained by fitting the vapor pressure data of Ackermann[2.14-20] and Ohse and Ciani.[2.14-19] The data of Mulford and Lamar,[2.14-23] Phipps,[2.14-21] and Pardue and Keller[2.14-22] were not used because these data did not include O/M ratios. As a result of the vapor pressure studies of mixed oxides at temperatures between 4,000 and 7,000 K (which indicate maximum pressures of 100 MPa), the data of Ohse[2.14-8] were modified and used to find the plutonia constants for temperatures above 4,000 K. The data of Ohse were modified by multiplying by the weight fraction of plutonia in the samples. This modification of observed vapor pressure approximates the ratios of urania and plutonia vapor pressures over the mixed oxides observed in the Tetenbaum[2.14-24] data. The fitting method followed this sequence.

Data in a narrow O/M ratio band near stoichiometry were used to determine a normalization curve. The resulting equation was then used with all applicable data to normalize the data with respect to temperature, while a best fit slope as a function of deviation from stoichiometry was determined. This O/M dependent function was then used to determine the final equation as a function of temperature and O/M ratio. Figure 2-47 shows FVAPRS plutonia subcode predictions, using O/M ratios of 2.0 (bottom curve) and 1.5 (top curve). The data with O/M ratio between 1.5 and 2.0 are seen to lie between the two lines

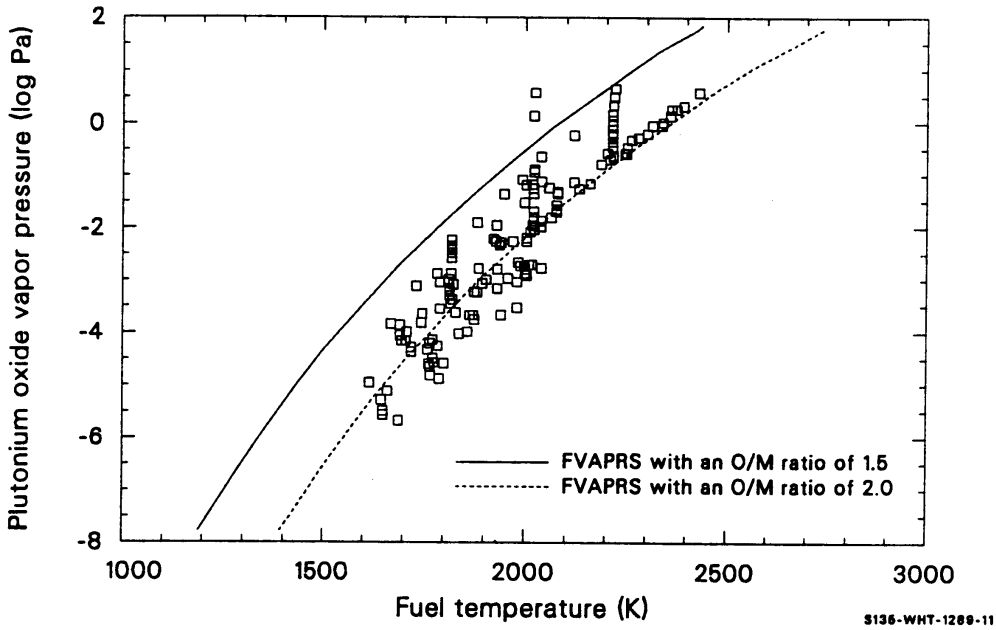

Figure 2-47. FVAPRS calculations (solid line) compared to plutonia data.

The FVAPRS correlation for mixed oxide vapor pressure was obtained by combining the equation calculations of urania and plutonia. This is accomplished by multiplying the weight fraction of urania and plutonia times the calculated vapor pressure of urania and plutonia, respectively. This approach was used rather than modeling the mixed oxide directly because mixed oxide data at typical mixture ratios (<10%) have not been investigated and Tetenbaum's[2.14-24] plutonia pressures are roughly the same fraction of the total pressure as the weight fraction. A comparison of the FVAPRS mixed oxide predictions (VAPMIX) to data is shown in Figure 2-48. The fit is good at temperatures below 5,000 K but becomes too large by about an order of magnitude at 6,000 K, well above the temperatures for which this subcode will usually be used.

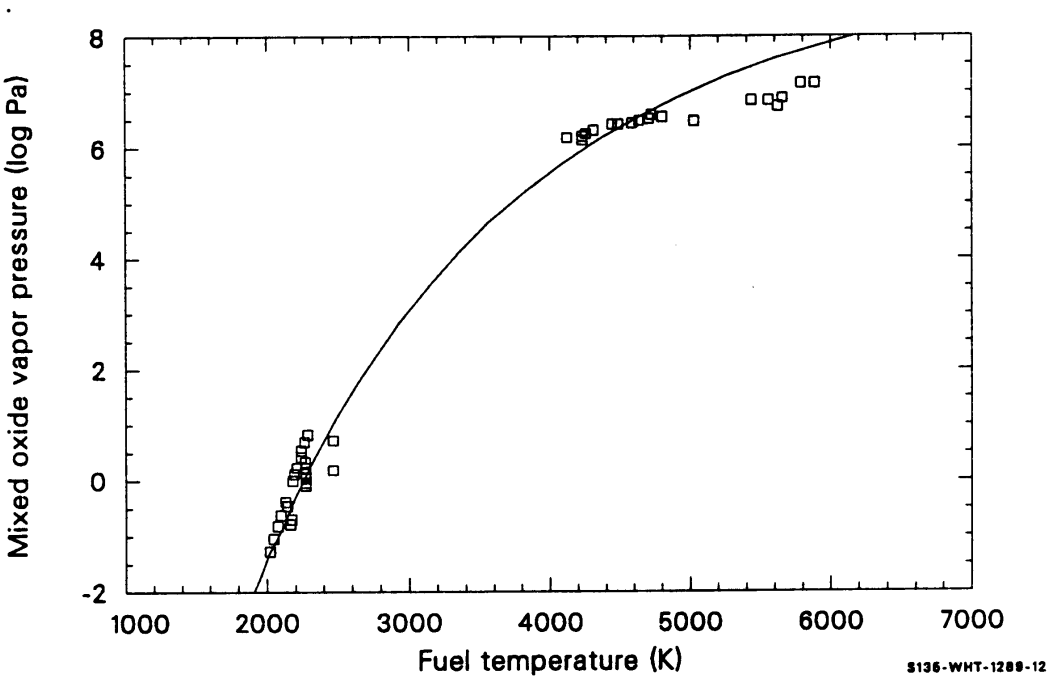

Figure 2-48. FVAPRS calculations (solid line) compared to mixed oxide data. An oxygen-to-metal ratio of 2.0 was used in the FVAPRS calculations.

FVAPRS oxygen vapor pressure calculations for hypostoichiometric urania are for monatomic oxygen up to O/M ratios of 1.999. Because of the scatter in the data, a simplified form of Equation (2-175) was used. The resultant expressions are Equations (2-141) through (2-145). The constants of the equations were obtained by a simple least-squares fit technique. A log function of the deviation from stoichiometry is reported to describe the oxygen vapor pressure for hypostoichiometric fuel. This was used in Equation (2-142) with good results. The fit procedure was to first determine a composition normalization factor from a narrow range of temperature (1,300 to 1,400 K). This was then used to normalize the data and develop the temperature dependent function. The data of Tetenbaum and Hunt,[2.14-29] Markin,[2.14-30] Wheeler,[2.14-31] and Alexander[2.14-10] were used to develop the equation constants.

FVAPRS oxygen vapor pressure for hyperstoichiometric urania is defined in two composition regimes, 1.999 to 2.004 and 2.004 to 2.2. Data, especially those of Hagemark and Broli,[2.14-34] show an approximately linear increase in pressure as the O/M ratios increase from 2.004 to 2.2; they show an exponential increase as O/M ratios increased from 1.999 to 2.004. Equations (2-141) and (2-143) were developed by determining a composition normalization factor, using the data of Hagemark and Broli.[2.14-34] These normalization factors were then used in a least-squares fit subroutine, using the data of Hagemark and Broli, Blackburn,[2.14-35] Aronson and Belle,[2.14-36] and Markin and Bones[2.14-38] to obtain the final Equations (2-141) and (2-142).

To ensure that no discontinuity exists between the hyperstoichiometric and hypostoichiometric calculations, thermodynamic equations must be applied. At equilibrium, the reaction $O_2 \leftrightarrow 2O$ implies that

$$2\mu_O = \mu_{O_2} \tag{2-177}$$

where

μ_O = monatomic oxygen chemical potential

μ_{O_2} = diatomic oxygen chemical potential.

For ideal gases at equilibrium, the chemical potentials are

$$\mu_O = \Delta G^\circ_0 + RT\ln(P(O)) \tag{2-178}$$

$$\mu_{O_2} = \Delta G^\circ_{0_2} + RT\ln(P(O_2)) \tag{2-179}$$

where

ΔG°_O = heat of formation of monatomic oxygen (J)

$\Delta G^\circ_{O_2}$ = heat of formation of diatomic oxygen (J)

R = universal gas constant (J/K)

T = temperature (K)

P(O) = monatomic vapor pressure (Pa)

$P(O_2)$ = diatomic vapor pressure (Pa).

Since $\Delta G^\circ_{O_2}$ is defined as zero, combining Equations (2-177) through (2-179) and solving for $\log P(O_2)$ gives

$$1/2 \log P(O_2) - \Delta G^\circ_O (2.303RT)^{-1} = \log P(O) . \tag{2-180}$$

The heat of formation, or ΔG°_O, of Equation (2-180) has been reported by Markin[2.14-30] and Breitung[2.14-40] among others. For the FVAPRS code, the Markin value was used

$$\Delta G^\circ_O = 61250 - 16.1\,T \tag{2-181}$$

which gives the following expression when substituted into Equation (2-179):

$$\log[P(O_2)] = 2.0\left[\log(P(O)) + \frac{13384.57}{T} + 3.52\right] . \tag{2-182}$$

Equation (2-182) is used with Equation (2-142) to find the diatomic pressure and limits the calculation of Equation (2-142) to the maximum calculated by Equation (2-141) at an O/M ratio of 1.999. Equation (2-182) does not always produce reasonable results (especially at low temperatures) when used to compare different data sets. It should, therefore, be used with caution except in this case of defining continuity of equations.

Figure 2-49 shows the FVAPRS hypostoichiometric oxygen vapor pressure correlation (UOXVAP) predictions compared to the literature data. The FVAPRS predictions, using O/M ratios of 1.8 and 2.0

(solid lines) show fair agreement, and the correlation predictions bound vapor pressure data having O/M ratios between 1.6 and 2.0. Figure 2-50 compares the FVAPRS hyperstoichiometric oxygen vapor pressure calculation (DIOVAP) at O/M ratios of 2.004 and 2.2 to the literature data having O/M ratios greater than 2.004. These calculations are also seen to yield pressures in the same range as the data. Because of the large scatter in the data, the standard error of estimate of the log of the data is large, ± 0.545 in the case of hyperstoichiometric oxygen pressures and ± 0.806 for hypostoichiometric oxygen pressures.

Correlations for urania (UO2VAP), plutonia (PUOVAP), mixed oxide (VAPMIX), and monatomic oxygen (UOVAP) are compared in Figure 2-51. The calculated urania vapor pressures are the largest, with plutonia vapor pressures about an order of magnitude less and the oxygen vapor pressures (for O/M ratios less than 2.0) even smaller. Oxygen vapor pressure calculations are probably not accurate above 4,000 K (much above the data base temperatures), and the plutonia vapor pressure calculations are useful only to about 5,500 K.

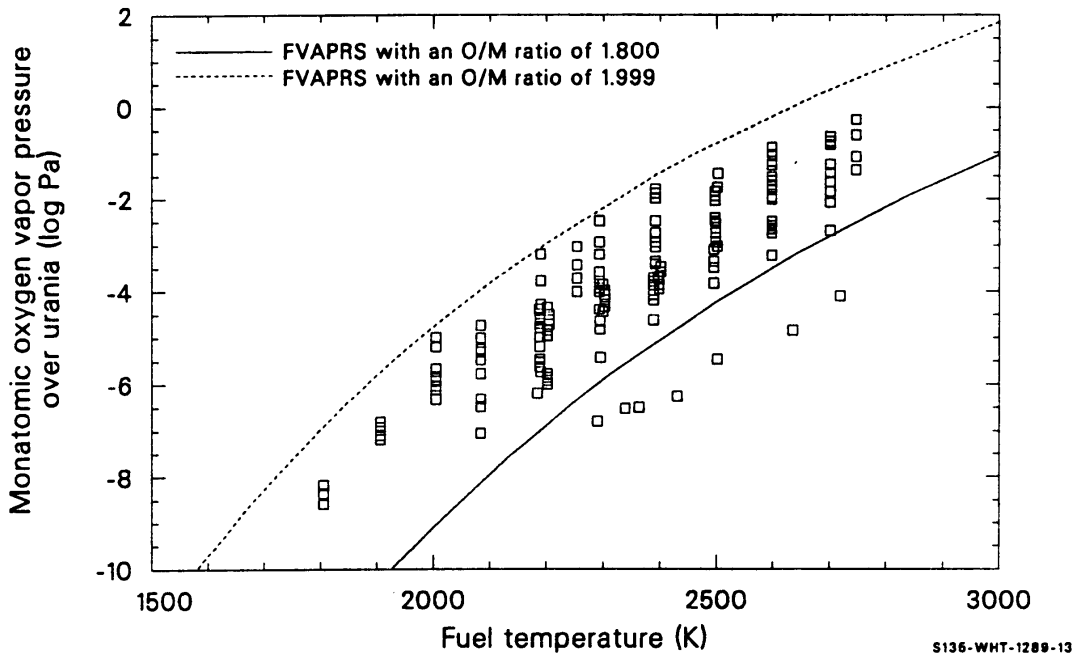

Figure 2-49. FVAPRS hypostoichiometric oxygen vapor pressure calculations (UOXVAP) compared to the data.

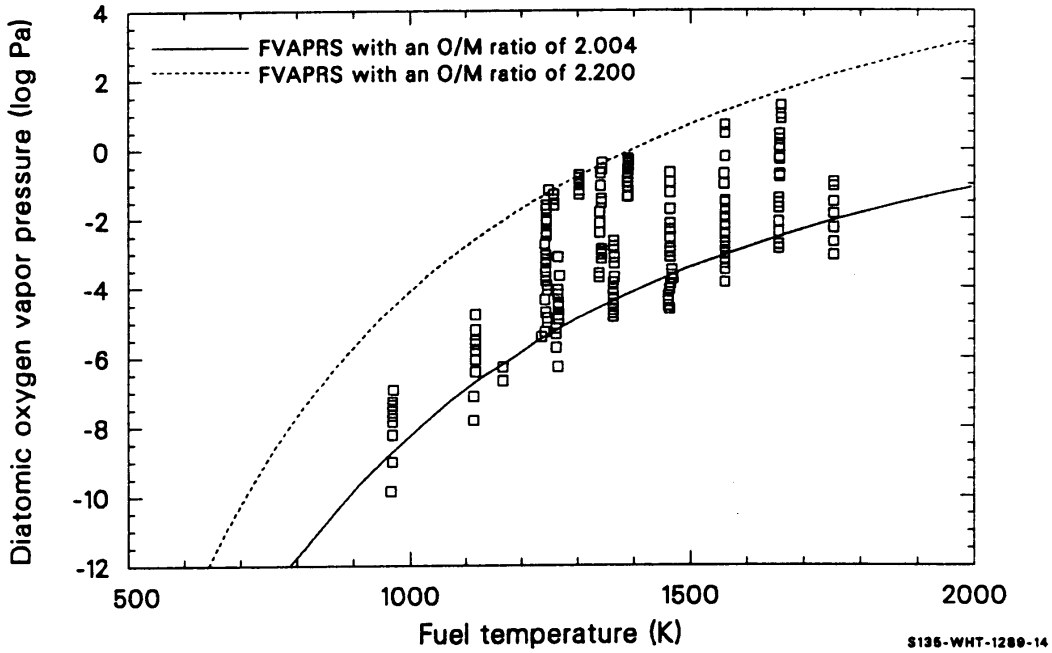

Figure 2-50. FVAPRS hyperstoichiometric oxygen vapor pressure calculations (DIOVAP) compared to the data.

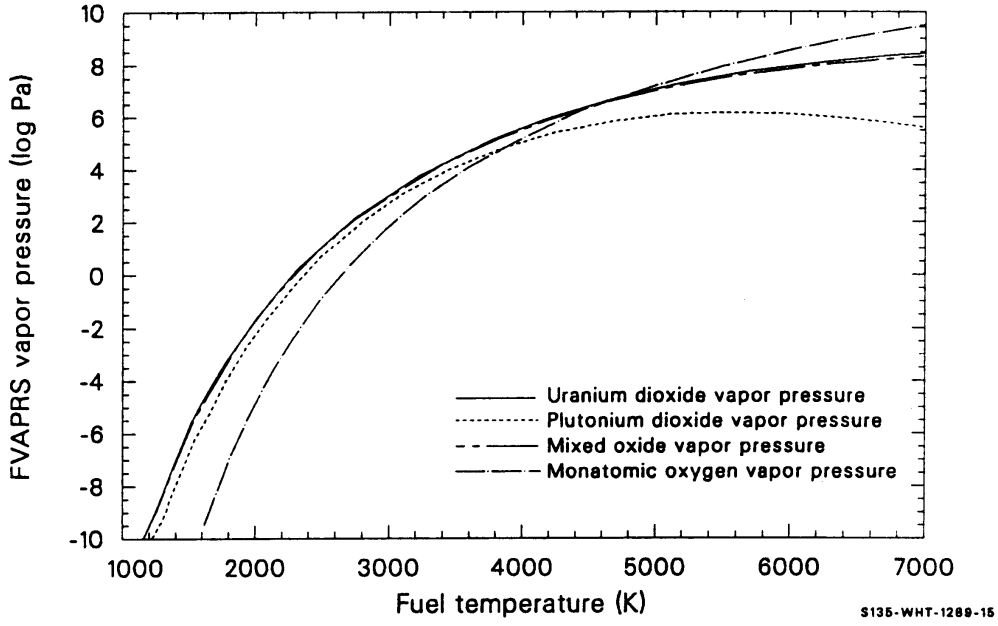

Figure 2-51. FVAPRS vapor pressure calculations of plutonia (PUOVAP), urania (UO2VAP), mixed oxides (VAPMIX), and monatomic oxygen over urania (UOXVAP), using an oxygen-to-metal ratio of 2.0.

2.14.4 Bibliography

The following list of reference material is pertinent to a literature review and was consulted by the FVAPRS code developer.

1. J. Dorwart, A. Pattoret, and S. Smoes, *Procedure of the British Ceramic Sociey, 8*, 1967, p. 67.

2. G. H. Winslow, "An Examination of the Total Pressure Over Hypostoichiometric Uranium Dioxide," *High Temperature Science, 7*, 1975, pp. 81-102.

3. P. A. Finn, A. Sheth, and L. Leibowitz, "Equation of State of Uranium Dioxide," *Journal of Nuclear Material, 79*, 1979, pp. 14-19.

4. R. A. Meyer and B. E. Wolfe, "High Temperature Equation of State of Uranium Dioxide," *Transactions of the American Nuclear Society, 7*, 1964, pp. 14-17.

5. R. K. Edwards, M. S. Chandrasekharaish, and P. M. Danielson, "The Congruently Evaporating Compositions of Urania," *High Temperature Science, 1*, 1969, pp. 98-113.

6. R. A. Meyer and B. E. Wolfe, "High Temperature Equation of State of Uranium Dioxide," *Transactions of the American Nuclear Society, 7*, 1964.

7. G. H. Winslow, "An Examination of the Oxygen Pressure Over Hypostoichiometric Uranium Dioxide," *High Temperature Science, 5*, 1973, pp. 176-191.

8. J. L. Margrave, *The Characterization of High Temperature Vapors*, New York: John Wiley and Sons, Inc., 1967.

9. J. R. Thorn and G. H. Winslow, *Journal of Chemical Physics, 44*, 1966.

2.14.5 References

2.14-1 T. E. Phipps, G. W. Sears, and O. C. Simpson, “The Volatility of Plutonium Dioxide,” *Journal of Chemical Physics, 8*, 1950.

2.14-2 R. Szwarc and R. E. Latta, “Vapor Pressure of Hypostoichiometric Urania as a Function of Composition,” *Journal of the American Ceramic Society, 51*, 1968.

2.14-3 M. Bober, H. U. Karow, and K. Schretzmann, “Vapor Pressure Measurements of Oxide Fuel Between 3000 and 5000 K Using Laser Heating,” *Nuclear Technology, 26*, 1975.

2.14-4 G. T. Reedy and M. G. Chasanov, “Total Pressure of Uranium Bearing Species Over Molten Urania,” *Journal of Nuclear Materials, 42*, 1972, pp. 341-344.

2.14-5 R. J. Ackermann, E. G. Rauh, and M. S. Chandrasekharaish, “A Thermodynamic Study of the Urania-Uranium System,” *Journal of Physical Chemistry, 73*, 1969, pp. 762-769.

2.14-6 M. Tetenbaum and P. D. Hunt, “Total Pressure of Urania Bearing Species Over Oxygen Deficient Urania,” *Journal of Nuclear Materials, 34*, 1970, pp. 86-91.

2.14-7 G. Benezech, J. P. Coutures, and M. Fox, *Transpiration Study of Uranium Dioxide Vaporization Processes Between 2,200 and 2,600 K*, ANL-TRANS-972, 1974.

2.14-8 R. W. Ohse, P. G. Berrie, H. G. Bogensberger, and E. A. Fischer, "Extension of Vapor Pressure Measurements of Nuclear Fuels $(U,Pu)O_2$ and UO_2 to 7,000 K for Fast Reactor Safety Analysis," *Journal of Nuclear Materials, 59*, 1976, pp. 112-124.

2.14-9 R. W. Ohse, P. G. Berrie, H. G. Bogensberger, and E. A. Fischer, "Measurement of Vapor Pressure of $(U,Pu)O_2$ and UO_2 to 5,000 K for Fast Reactor Safety Analysis and the Contribution of the Radial Cs Distribution to Fuel Pin Failure," *Thermodynamics of Nuclear Materials, 1*, IAEA-SM-190/8, Vienna 1975.

2.14-10 C. A. Alexander, J. S. Ogden, and G. W. Cunningham, *Thermal Stability of Zirconia and Thoria Based Fuels*, BMI-1789, 1967.

2.14-11 R. J. Ackermann, *The High Temperature, High Vacuum Vaporization and Thermodynamic Properties of Uranium Dioxide*, ANL-5482, 1955.

2.14-12 R. J. Ackermann, P. W. Gilles, and R. J. Thorn, "High Temperature Thermodynamic Properties of Uranium Dioxide," *Journal of Chemical Physics, 25*, 1956.

2.14-13 R. J. Ackermann et al., *Journal of Chemical Physics, 49*, 1968) p.4739.

2.14-14 A. T. Chapman and R. E. Meadows, "Volatility of UO_2+x and Phase Relations in the System Uranium Oxygen," *Journal of the American Ceramic Society, 47*, 1964.

2.14-15 A. T. Chapman and R. E. Meadows, *The Volatility of UO_2+x and Phase Relations in the Uranium Oxygen System*, ORNL-3587, 1964.

2.14-16 R. W. Ohse, "High Temperature Vapor Pressure Studies of UO_2 by the Effusion Method and Its Thermodynamic Interpretation," *Journal of Chemical Physics, 44*, 1966.

2.14-17 D. A. Benson, *Application of Pulsed Electron Beam Vaporization to Studies of UO_2*, SAND-77-0429, 1977.

2.14-18 J. R. Babelot, G. D. Brumme, P. R. Kinsmann, and R. W. Ohse, "Vapor Pressure Measurement Over Liquid UO_2 and $(U,Pu)O_2$ by Laser Surface Heating up to 5,000 K," *Atomwirtschaft*, 1977.

2.14-19 R. W. Ohse and C. Ciani, "Evaporation Behavior and High Temperature Thermal Analysis of Substoichiometric Plutonium Oxide for 1.51<O/Pu<2.00," *Thermodynamics of Nuclear Materials*, Vienna: IAEA, 1968.

2.14-20 R. J. Ackermann, R. L. Faircloth, and M. H. Rand, "A Thermodynamic Study of the Vaporization Behavior of the Substoichiometric Plutonium Dioxide Phase," *Journal of Physical Chemistry, 70*, 1966.

2.14-21 T. E. Phipps, G. W. Sears, and O. C. Simpson, "The Volatility of Plutonium Dioxide," *Journal of Chemical Physics, 8*, 1950.

2.14-22 W. M. Pardue and D. L. Keller, "Volatility of Plutonium Dioxide," *Journal of Chemical Physics, 8*, 1950.

2.14-23 R. N. R. Mulford and L. E. Lamar, "The Volatility of Plutonium Oxide (31)," Plutonium 1960--*The Proceedings of the Second International Conference on Plutonium Metallurgy, Grenoble, France, 1960*, pp. 411-429.

2.14-24 M. Tetenbaum, "Total Pressures of Uranium and Plutonium Bearing Species Above the U-Pu-O System," *Transactions of the American Nuclear Society, 23*, 1976.

2.14-25 R. W. Ohse and W. M. Olson, "Evaporation Behavior of Substoichiometric $(U,Pu)O_2$," *Proceedings of the 4th International Conference on Plutonium and Other Actinides, Santa Fe, NM, 1970.*

2.14-26 J. E. Battles, W. A. Shinn, P. E. Blackburn, and R. K. Edwards, "A Mass Spectrometric Investigation of the Volatization Behavior of $(U_{0.8}\ Pu_{0.2})O_{2-x}$," *Proceedings of the 4th International Conference on Plutonium and Other Actinides, Santa Fe, NM, 1970.*

2.14-27 E. A. Aitken, H. C. Brassfield, and R. E. Fryxell, "Thermodynamic Behavior of Hypostoichiometric UO_2," *Thermodynamics*, Vienna: IAEA, 1966.

2.14-28 T. L. Markin and M. H. Rand, "Thermodynamic Data for Plutonium Oxides," *Thermodynamics*, Vienna: IAEA, 1965, pp. 145-156.

2.14-29 M. Tetenbaum and P. D. Hunt, "High Temperature Thermodynamic Properties of Oxygen Deficient Urania," *Journal of Chemical Physics, 49*, 1968.

2.14-30 T. L. Markin, V. J. Wheeler, and R. J. Bones, "High Temperature Thermodynamic Data for UO_{2+x}," *Journal of Inorganic Nuclear Chemistry, 30*, 1968.

2.14-31 V. J. Wheeler, "High Temperature Thermodynamic data for UO_{2-x}," *Journal of Nuclear Materials, 39*, 1971, pp. 315-318.

2.14-32 N. A. Javed, "Thermodynamic Study of Hypostoichiometric Urania," *Journal of Nuclear Materials, 43*, 1972, pp. 219-224.

2.14-33 L. E. J. Roberts and A, H, Walter, "Equilibrium Pressures and Phase Relations in the Uranium Oxide System," *Journal of Inorganic Nuclear Chemistry, 22*, 1961, pp. 213-229.

2.14-34 K. Hagemark and M. Broli, "Equilibrium Oxygen Pressures Over Nonstoichiometric Uranium Oxides Between UO_{2+x} and U_3O_{8-z} at Higher Temperatures," *Journal of Inorganic Nuclear Chemistry, 28*, 1966.

2.14-35 P. E. Blackburn, "Oxygen Dissociation Pressures Over Uranium Oxides," *Journal of Physical Chemistry, 8*, 1958, pp. 897-902.

2.14-36 S. Aronson and U. Belle, "Nonstoichiometry in Uranium Dioxide," *Journal of Chemical Physics, 29*, 1958.

2.14-37 K. Kiukkola, "High Temperature Electrochemical Study of Uranium Oxides in the UO_{2-x} Region," *Acta Chemical Scandinavica, 16*, 1962, pp, 327-345.

2.14-38 T. L. Markin and R. J. Bones, *The Determination of Some Thermodynamic Properties of Uranium Oxides with O/U Ratios Between 2.00 and 2.03 Using a High Temperature Galvanic Cell*, AERE-R 4178, 1962.

2.14-39 E. Aukrust, T. Forland and K. Hagemark, "Equilibrium Measurements and Interpretation of Nonstoichiometry in UO_{2+x}," *Procedures of the IAEA Symposium on Thermodynamics of Nuclear Materials, Vienna, 1962.*

2.14-40 W. Breitung, *Calculation of Vapor Pressures of Oxide Fuels up to 5000 K for Equilibrium and Nonequilibrium Evaporation*, KfK-2091, 1975.

2.15 Fuel Oxidation (FOXY, FOXYK)

The fuel oxidation models, FOXY and FOXYK, calculate UO_2 oxygen uptake in steam for UO_2 temperatures above 1,150 K. The UO_2 oxidation weight gain is modeled using parabolic kinetics. Oxidation of UO_2 affects its chemical composition, which, in turn, significantly affects most of the other material properties of the fuel (i.e.,thermal conductivity and melting temperature).[2.15-1] Changes in the material properties of the UO_2 may have an impact on core behavior during severe reactor accidents involving potential liquefaction of the fuel matrix.[2.15-2]

2.15.1 Summary

The equation used to model UO_2 oxygen uptake in steam is

$$W^2 = 24.4e^{\left(-\frac{26241}{T}\right)} \Delta t + W_0^2 \tag{2-183}$$

where

W	=	oxidation weight gain at end of time step (kg/m^2)
T	=	temperature of the UO_2 surface (K)
Δt	=	oxidation time (s)
W_o	=	initial oxidation weight gain (kg/m^2).

The standard error[a] of the model with respect to its data base is $0.027 kg/m^2$, or 21% of the average measured weight gain.

An estimate of the power resulting from the oxidation of UO_2 is given by the equation

$$P = \frac{(W - W_0)\ (1.84 \times 10^5)}{\Delta t} \tag{2-184}$$

where P is the rate of heat generation (W/m^2).

a. $\text{standard error} = \left[\sum_{i=1}^{n} \frac{(C_i - M_i)^2}{n-1}\right]^{1/2}$

where
C_i = calculated weight gain
M_i = measured weight gain
n = number of data points.

An estimate of the power resulting from the oxidation of UO_2 is given by the equation

$$P = \frac{(W - W_0)\ (1.84\times10^5)}{\Delta t} \tag{2-185}$$

where P is the rate of heat generation (W/m^2).

2.15.2 Review of Literature

The only published data for UO_2 oxygen uptake are provided by Bittel et al.[2.15-3] The constants used in Equation (2-183) came from this source. The data represent temperatures from 1,158 to 2,108 K. These constants appear to be independent of fuel density and surface to volume ratio. However, additional data are needed for oxidation at UO_2 temperatures in excess of 2108 K and, in particular, for molten UO_2.

2.15.3 Model Development

The model for UO_2 oxygen uptake is based on parabolic kinetics. That is, the rate of oxygen weight gain is inversely proportional to the amount of excess oxygen present, or

$$\frac{dW}{dt} = \frac{k}{W} \tag{2-186}$$

where

t	=	time (s)
k	=	rate constant ($kg^2/m^4 \cdot s$).

Solution of this differential equation yields

$$W^2 - W_0 = 2k\Delta t = K_p\Delta t \tag{2-187}$$

where

K_p	=	$2k\ (kg^2/m^4 \cdot s)$
	=	$24.4e^{(-26241/T)}$.

Equation (2-187) is equivalent to Equation (2-183). The parabolic rate constant, K_p, was determined in Reference 2.17-3 using a least-squares data fit. Table 2-16 contains a list of the data used to determine K_p, along with the corresponding calculated value of W.

Although experimental data were recorded only for temperatures ranging from 1,158 to 2,108 K, the correlation of Equations (2-183) and (2-187) is used for any temperature up to the melting temperature of UO_2 (3,100 K). When the fuel temperature exceeds 3,100 K, oxidation is assumed to continue at a temperature of 3,100 K.

As an estimate of the heat of reaction for oxidation of UO_2, one percent of the heat of reaction per kg of oxygen in the oxidation of zircaloy was used. The correlation for the rate of heat generation is

$$P = \frac{(W - W_0)\ (0.01)\ (6.45\times10^6)\ (2.85)}{\Delta t} \tag{2-188}$$

where

6.45×10^6 = heat of reaction per kg Zr(J/kg)

2.85 = ratio of weight of Zr to O_2 in ZrO_2.

Equation (2-188) is equivalent to Equation (2-184).

A standard error of 0.027 kg/m^2 was calculated using the measured and calculated values of oxygen weight gain given in Table 2-16. This number was converted to a fraction of the measured value of oxygen uptake because the fractional error was more nearly constant over the temperature range of the data than the absolute error. The standard error of 0.027 kg/m^2 is about 21% of the mean measured oxygen uptake (0.1306 kg/m^2).

Table 2-16. Measured and calculated weight gain.

Temperature (K)	Test Time (s)	Test Weight Gain (kg/m^2)	Correlation Weight Gain (kg/m^2)
2,108	600	0.2313	0.2397
2,068	600	0.2036	0.2125
1,993	600	0.1679	0.1674
1,988	600	0.1401	0.1646
1,898	1,200	0.1636	0.1703
1,883	1,200	0.1904	0.1611
1,873	1,800	0.2574	0.1901
1,793	1,200	0.1117	0.1136
1,773	1,140	0.1170	0.1019
1,768	2,400	0.1351	0.1448
1,768	4,740	0.1672	0.2035
1,678	3,600	0.1897	0.1191
1,673	6,900	0.1365	0.1611
1,668	5,700	0.1619	0.1430

Table 2-16. Measured and calculated weight gain. (Continued)

Temperature (K)	Test Time (s)	Test Weight Gain (kg/m^2)	Correlation Weight Gain (kg/m^2)
1,663	2,400	0.1004	0.09065
1,478	7,020	0.07352	0.05775
1,478	11,800	0.08825	0.07487
1,373	11,860	0.02577	0.03807
1,368	10,500	0.04287	0.03459
1,273	24,480	0.02373	0.02582
1,158	17,400	0.01445	0.00782

Development of the model is based on the following assumptions:

1. Enough oxygen is always available for the oxidation process.

2. The correlation [Equations (2-183) and (2-186)] applies for UO_2 temperatures below 1,158 K and above 2,108 K up to 3,100 K, where no data exist.

3. For UO_2 temperatures above 3,100 K, oxidation will continue at the rate corresponding to a UO_2 temperature of 3,100 K.

Figures 2-52 and 2-53 show the computed weight gain as functions of temperature and time, respectively. In Figure 2-52, the UO_2 temperatures range from 1,158 K to 3,400 K at a constant oxidation time of 60 seconds. The exponential nature of the curve can be seen up to temperatures of 3,100 K. Above this temperature, weight gain calculations are constant using temperature of 3,100 K. Figure 2-53 shows the weight gain for times ranging from1 to 200 seconds at a constant UO_2 temperature of 1,600 K. This curve is parabolic in shape.

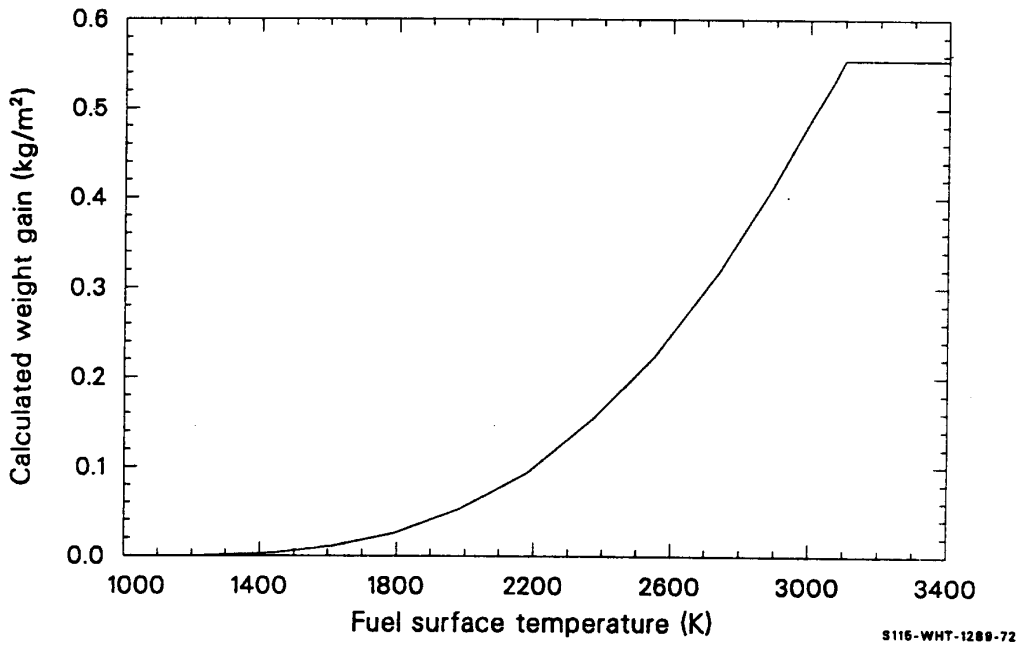

Figure 2-52. Computed weight gain as a function of temperature for constant time step size.

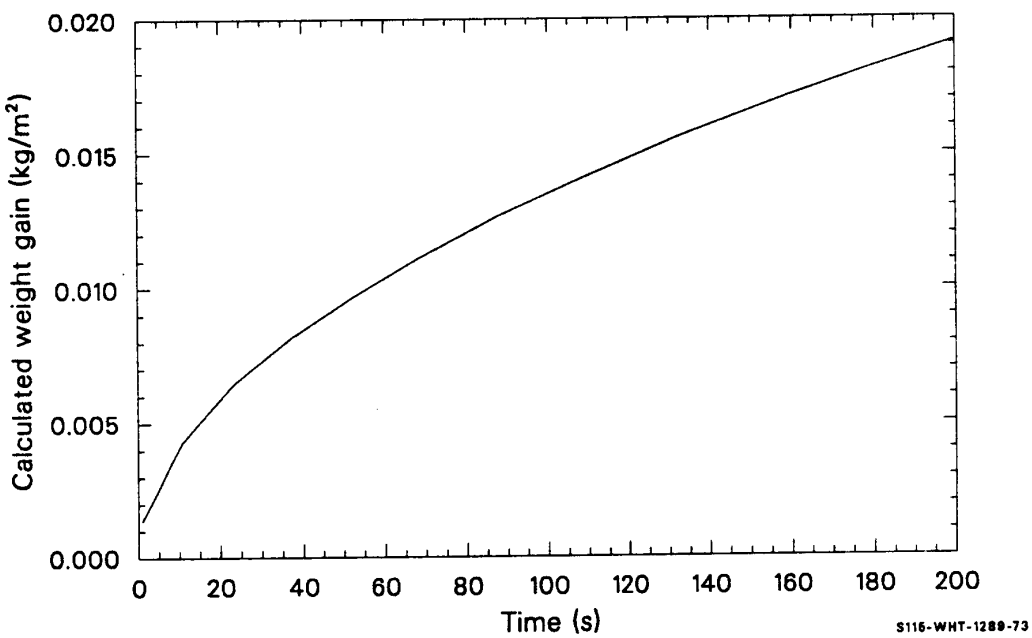

Figure 2-53. Computed weight gain as a function of time step size for constant temperature.

2.15.4 Description of the FOXY and FOXYK Subcodes

The following input variables or information are needed for FOXY: the time duration of oxidation(s), fuel temperature (K), and initial oxidation weight gain (kg/m^2). The FOXY subcode will output the total oxide weight gain at the end of the time step and a preliminary estimate of the power generated from this

oxidation (W/m^2). Also, the value of the parabolic rate constant, [K_p in Equation (2-186)] is made available by FOXYK. Table 2-17 is a list of the FORTRAN names for these variables.

Table 2-17. Glossary of FORTRAN names.

Variable	Input or Output	Definition	Units
FTEMP	Input	Fuel surface temperature	K
DT	Input	Time step	s
UO2OXI	Input	Initial oxide weight gain	kg/m^2
UO2OXF	Output	Final oxide weight gain	kg/m^2
P	Output	Power generated by oxidation	W/m^2
FOXYK	--	Parabolic rate constant	$kg^2/m^4 \cdot s$

The input will be accepted in the following ranges:

FTEMP $\geq$ 0

DT $>$ 0

UO2OXI $>$ 0.

Whenever the fuel temperature is nonpositive or the time step size or initial oxide weight gain is negative, the final oxide weight gain and the power are set to one. A diagnostic message is printed if any one of these input errors is noted but was not noted during the previous execution of FOXY. This message states, "Input Error in FOXY." The entire input is then printed.

2.15.5 References

2.15-1 D. L. Hagrman, *Melting Temperatures of Uranium-Zirconium-Oxygen Compounds (PSOL and PLIQ) and Uranium Dioxide Solubility in Zircaloy (PSLV)*, EGG-CDAP-5303, January 1981.

2.15-2 C. M. Allison et al., *Severe Core Damage Analysis Package (SCDAP), Code Conceptual Design Report*, EGG-CDAP-5397, April 1981.

2.15-3 J. T. Bittel, L. H. Sjodahl, and J. F. White, "Steam Oxidation Kinetics and Oxygen Diffusion in UO_2 at High Temperatures," *Journal of the American Ceramic Society, 52*, 1969, pp. 446-451.

3. URANIUM ALLOYS

As the need for uranium metal materials properties became apparent, correlations for the specific heat capacity (UCP), enthalpy (UENTHL), thermal conductivity (UTHCON), thermal expansion (UTHEXP), and density (UDEN) were developed for the MATPRO package of materials properties subcodes. Descriptions of these subcodes and required input are given in this section.

3.1 Specific Heat Capacity and Enthalpy (UCP, UENTHL)

The function UCP calculates the specific heat capacity of uranium metal as a function of temperature. The function UENTHL calculates the enthalpy of uranium metal as a function of temperature and a reference temperature (for which the enthalpy change will be zero).

3.1.1 Specific Heat Capacity (UCP)

The function UCP calculates the specific heat capacity of uranium metal from equations derived from data reported by Touloukian[3.1-1] and listed in Tables 3-1 through 3-3. Specific heat capacity data for the alpha phase ($300 \leq T < 938$ K) were approximated using a least squares fit to a second degree polynomial. An average of the data for the beta ($938 \leq T < 1{,}049$ K) and gamma ($1{,}049 \leq T < 1{,}405.6$ K) phases was used to determine a constant specific heat capacity for these phases because sample to sample variation was greater than variation with temperature. Since no data were found for the liquid specific heat capacity, the gamma phase specific heat capacity was used as an estimate.

The following expressions were used to calculate the specific heat capacity of uranium metal:

For $T < 938$ K,

$$C_p = 104.82 + 5.3686 \times 10^{-3}\, T + 10.1823 \times 10^{-5}\, T^2 \quad . \tag{3-1}$$

For $938 \leq T < 1049$ K,

$$C_p = 176.41311 \tag{3-2}$$

For $T \geq 1049$ K,

$$C_p = 156.80756 \tag{3-3}$$

where

C_p	=	uranium metal specific heat capacity (J/kg K)
T	=	uranium metal temperature (K).

The first three equations represent the alpha, beta, and gamma solid phases of uranium, while the fourth equation represents the liquid phase.

Figure 3-1 is a plot of the specific heat capacity for uranium metal calculated by the function UCP.

Table 3-1. Alpha phase uranium specific heat capacity data.

Temperature (K)	Specific Heat Capacity (cal/g · K)
300.104	0.02779
307.465	0.02793
327.514	0.02834
337.489	0.02853
347.549	0.02868
304.95	0.02789
314.904	0.02806
323.15	0.0268
373.15	0.0284
573.15	0.0345
623.15	0.0362
673.15	0.0378
723.15	0.0394
773.15	0.041
823.15	0.0425
873.15	0.044
298.	0.02758
300.	0.0276
400.	0.0295
500.	0.0323
600.	0.03543
700.	0.03873
800.	0.04212

Table 3-1. Alpha phase uranium specific heat capacity data. (Continued)

Temperature (K)	Specific Heat Capacity (cal/g · K)
900.	0.0455
935.	0.04676
373.15	0.0278
473.15	0.0296
573.15	0.0324
673.15	0.0353
773.15	0.0392
873.15	0.0437
933.15	0.0466
323.15	0.0283
373.15	0.02919
423.15	0.03022
473.15	0.03135
523.15	0.03257
573.15	0.03388
623.15	0.03529
673.15	0.03681
723.15	0.03846
773.15	0.04031
823.15	0.04253
873.15	0.04521
923.15	0.04818
941.15	0.0493

Table 3-2. Beta phase uranium specific heat capacity data.

Temperature (K)	Specific Heat Capacity (cal/g · K)
935	0.0436
950	0.0436
1,000	0.0436
1,045	0.0436
953.15	0.0394
973.15	0.0396
1,043.15	0.0397
1,063.15	0.034
1,073.15	0.034
941.15	0.04262
973.15	0.04262
1,023.15	0.04262
1,047.15	0.04262

Table 3-3. Gamma phase uranium specific heat capacity data.

Temperature (K)	Specific Heat Capacity (cal/g · K)
1,045	0.03822
1,100	0.03822
1,200	0.03822
1,300	0.03822
1,047.15	0.03843
1,073.15	0.03843
1,123.15	0.03843

Table 3-3. Gamma phase uranium specific heat capacity data.

Temperature (K)	Specific Heat Capacity (cal/g · K)
1,173.15	0.03843

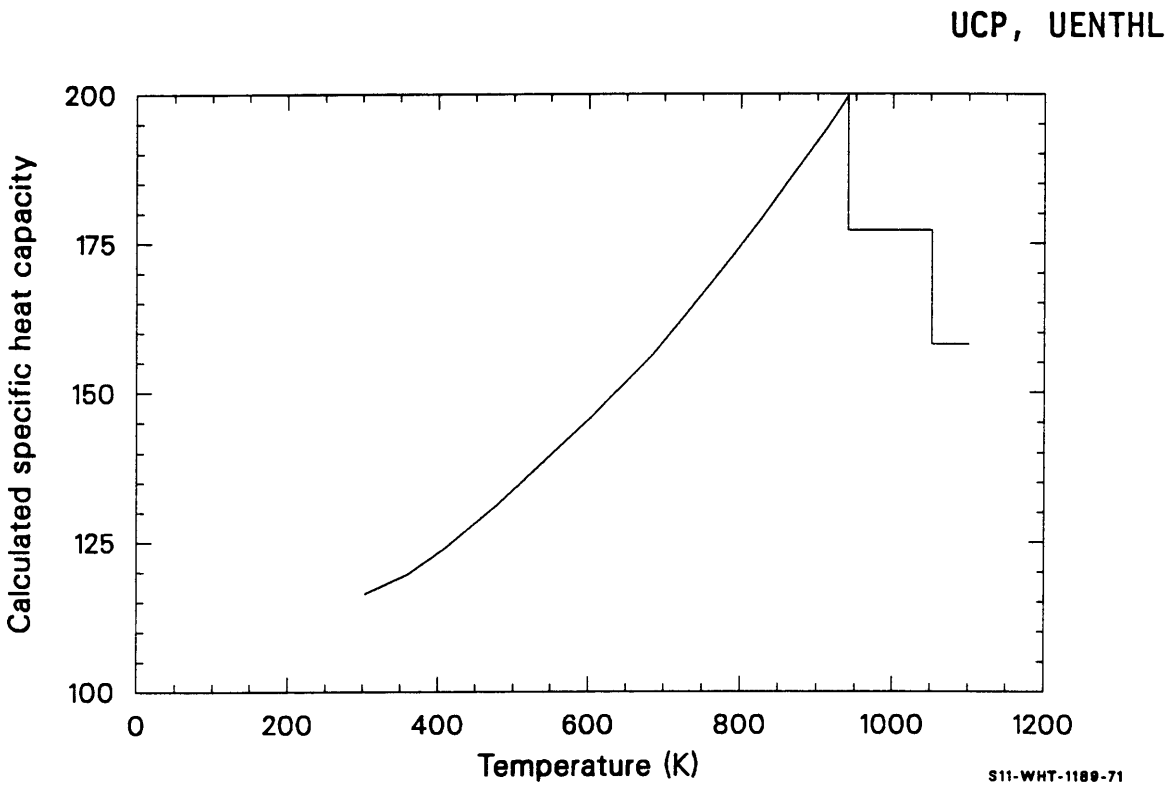

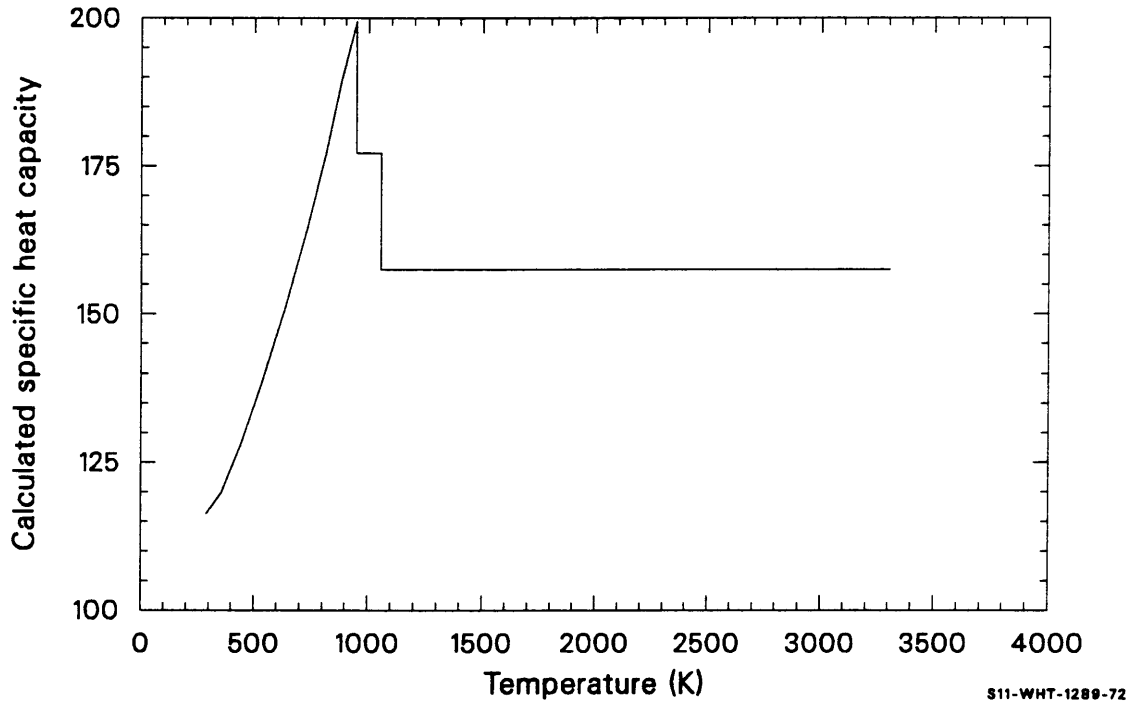

Figure 3-1. Specific heat capacity for uranium metal calculated by the function UCP.

3.1.2 Enthalpy (UENTHL)

The function UENTHL calculates the change in enthalpy of the uranium metal during a constant pressure change from the reference temperature of 300 K to the temperature of the uranium metal. The uranium specific heat capacity equations calculated in UCP were integrated piecewise over the alpha, beta, and gamma temperature ranges to determine the uranium enthalpy. A constant of integration was determined to force an enthalpy of zero at 300 K. (This number will not affect code calculations because the subroutine UENTHL uses a reference temperature of 300 K and subtracts the calculated enthalpy at this reference temperature from the calculated enthalpy at the temperature of interest.) Heats of transformation taken from Tipton[3.1-2] were:

alpha-to-beta	12,500 J/kg
beta-to-gamma	20,060 J/kg
gamma-to-liquid	82,350 J/kg.

The expressions used to calculate the enthalpy of the uranium metal in this function are as follows:

For 300 < T < 938 K,

$$H_u = -3.255468 \times 10^4 + T[1.0466 \times 10^2 + T(2.685 \times 10^{-03} + 3.389 \times 10^{-05}\ T)] \quad . \qquad (3\text{-}4)$$

For $938 \leq T < 1049$ K,

$$H_u = -5.1876776 \times 10^4 + 1.7092 \times 10^2 T \quad . \tag{3-5}$$

For $1{,}049 \leq T < 1405.6$ K,

$$H_u = -2.0567496 \times 10^{-4} + 1.602 \times 10^2 T \quad . \tag{3-6}$$

For $T \geq 1{,}405.6$ K,

$$H_u = 6.177850 \times 10^5 + 1.602 \times 10^2 T \tag{3-7}$$

where

H_u	=	uranium metal enthalpy (J/kg)
T	=	uranium metal temperature (K).

The first three equations represent the alpha, beta, and gamma solid phases of uranium, while the fourth equation represents the liquid phase.

Figure 3-2 is a plot of the specific heat capacity for uranium metal calculated by the function UCP.

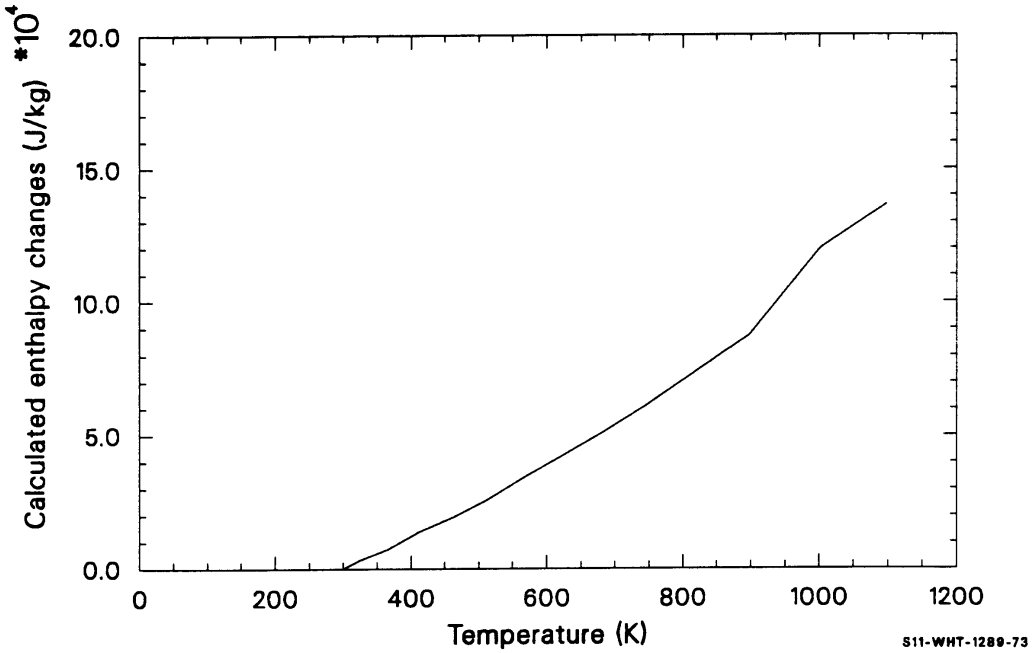

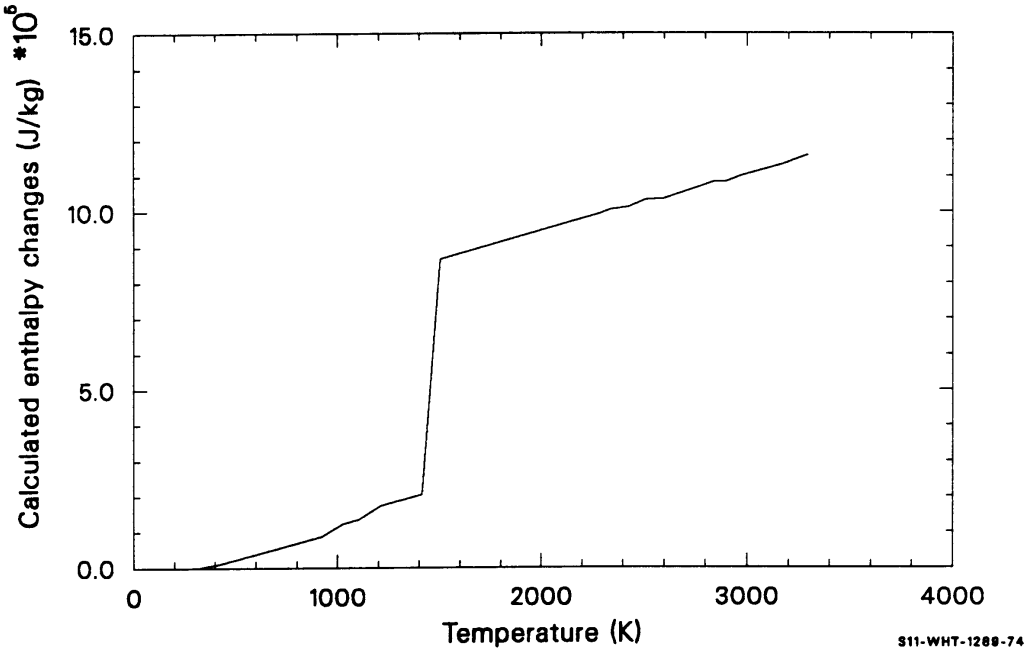

Figure 3-2. Enthalpy change for uranium metal calculated by UENTHL.

3.1.3 References

3.1-1 Y. S. Touloukian and E. H. Buyco, *Thermal Physical Properties of Matter, V4, Specific Heat - Metallic Elements and Alloys*, New York: IFI/Plenum, 1970, p. 270.

3.1-2 C. R. Tipton, Jr., *Reactor Handbook*, New York: Interscience Publishers, Inc., p. 113

3.2 Thermal Conductivity (UTHCON)

The thermal conductivity of uranium metal as a function of temperature is calculated by the function UTHCON. The only input required is the temperature of the uranium metal (UTEMP).

3.2.1 Model Development

Since the thermal conductivity of uranium metal is not significantly affected by the phase changes that take place during the heating of uranium metal, the single equation used to calculate the thermal conductivity of uranium metal for temperatures less than the melting point (1,405.6 K) is obtained from a polynomial fit of the temperatures and thermal conductivity values obtained in Reference 3.2-1. These values are shown in Table 3-4. The correlation used to calculate the thermal conductivity is as follows:

$$K_s = 20.457 + 1.2047 \times 10^{-2}\, T - 5.7368 \times 10^{-6}\, T^2 \qquad (3\text{-}8)$$

where

K_s	=	uranium metal thermal conductivity (W/m · K)
T	=	uranium metal temperature (K).

The expected standard error of the predicted conductivities is $\pm$ 0.2 times the calculated conductivity. A plot of the thermal conductivities calculated by UTHCON is shown in Figure 3-3.

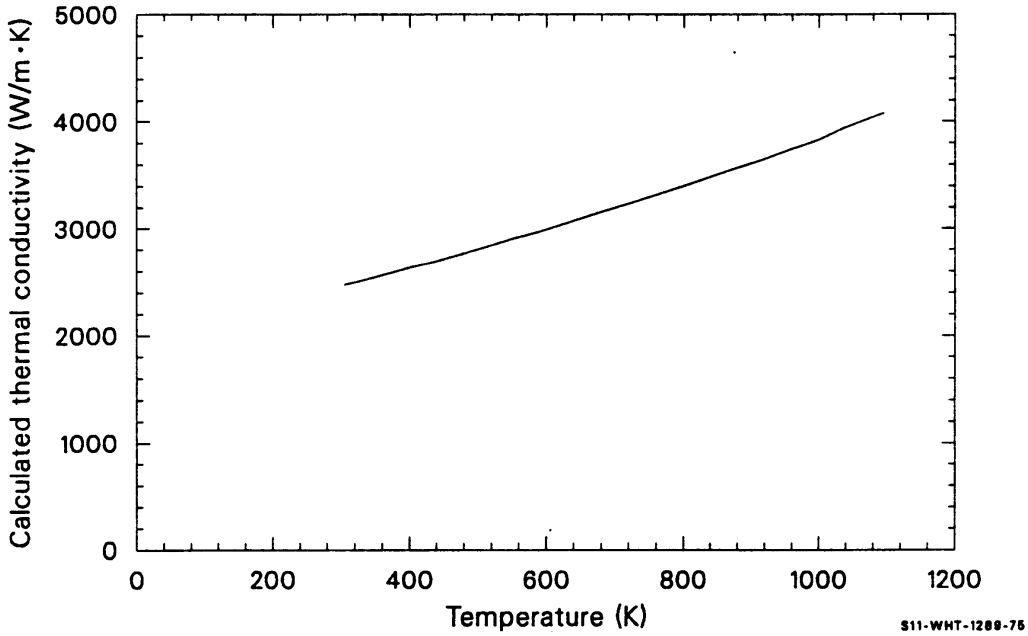

Figure 3-3. Thermal conductivities calculated by UTHCON.

Table 3-4. Uranium metal thermal conductivity from Touloukian et al.

Temperature (K)	Thermal Conductivity [W/(m · K)]
255.4	21.4
255.4	22.6
310.9	22.4
310.9	23.5
311.2	25.5
318.2	25.5
323.2	24.3
353.2	26.4
353.2	24.5
358.2	25.9
383.2	26.8
398.2	28.5

Table 3-4. Uranium metal thermal conductivity from Touloukian et al.

Temperature (K)	Thermal Conductivity [W/(m · K)]
408.2	27.2
422.1	24.4, 25.4
423.2	30.1
458.2	29.3
469.2	27.5
473.2	28.6
533.2	26.5, 27.4
548.2	34.7
567.9	29.5
573.2	30.9
644.3	28.6, 29.3
673.3	33.1
755.4	31.1, 31.1
773.2	35.4
866.5	33.6, 33.2
873.2	37.3
933.2	34.8
949.9	35.9
973.3	40.0
977.6	36.9
1,002.6	37.4
1,005.4	37.9
1,033.2	38.9
1,073.2	42.3
1,173.2	44.6

3.2.2 References

3.2-1 Y. S. Touloukian, R. W. Powell, C. Y. Ho, and P. G. Klemens, *Thermal Physical Properties of Matter, V1, Thermal Conductivity Metallic Elements and Alloys*, New York: IFI/Plenum, 1970, pp. 429-440.

3.3 Thermal Expansion and Density (UTHEXP, UDEN)

The function UTHEXP calculates the polycrystalline uranium metal thermal expansion strain, and the function UDEN computes the density from 300 K to the melting point of the uranium metal, 1,132.3 K. Input values required for UTHEXP are the uranium metal temperature and a reference temperature (for which the thermal strain will be zero), while UDEN requires only the uranium metal temperature.

3.3.1 Thermal Expansion (UTHEXP)

The expressions used to calculate the uranium metal thermal expansion strains are:

For $300 < T < 942$ K,

$$\varepsilon_u = [-0.30033 + T(7.1847 \times 10^{-4} + 1.0498 \times 10^{-6}\, T)]/100 \quad . \tag{3-9}$$

For $942 \leq T < 1045$ K,

$$\varepsilon_u = (-0.28340 + 1.9809 \times 10^{-3}\, T)/100 \tag{3-10}$$

For $1{,}045 \leq T \leq 1132.3$ K,

$$\varepsilon_u = (-0.27120 + 2.2298 \times 10^{-3}\, T)/100 \tag{3-11}$$

where

ε_u	=	uranium metal thermal strain (m/m)
T	=	uranium metal temperature (K).

At the present time, the phase change to liquid is not modeled.

A polynomial fit of the thermal expansion data from Touloukian[3.3-1] shown in Table 3-5 yields an expression that can be integrated to produce Equation (3-9). Equations (3-10) and (3-11) are derived by using a linear fit of the thermal expansion rates given in Tables 3-6 and 3-7, respectively. The constant of integration is ignored because the quantity returned by UTHEXP is the strain calculated by Equations (3-9), (3-10), or (3-11) at the given temperature minus the strain calculated at the reference temperature (300 K).

Uranium metal goes through two phase changes, one at approximately 942 K and another at approximately 1,045 K. The discontinuous change in thermal strain at these phase changes is the reason three different equations are used to calculate ε_u. Each equation calculates the thermal expansion strain of one phase. (The expected standard error for these curves is about 0.1 times the calculated value).

3.3.2 Density (UDEN)

The function UDEN uses the general relation between density and thermal strain, together with a reference density of 1.905 x 10^4 kg/m^3, the density of uranium at 300 K.[3.3-1] The thermal expansion strain as a function of temperature calculated by UTHEXP using a reference temperature of 300 K is illustrated in Figure 3-4, and the density calculated by UDEN using the thermal strain calculated by UTHEXP is shown in Figure 3-5.

3.3.3 References

3.3-1 Y. S. Touloukian, R. K. Kirby, R. E. Taylor, and P. D. Desai, *Thermal Physical Properties of Matter, V12, Thermal Expansion - Metallic Elements and Alloys*, New York: IFI/Plenum, 1970, pp. 336-372.

Table 3-5. Uranium thermal expansion data from Touloukian et al.[3.3-1] for temperature < 942 K.

Temperature (K)	Thermal Strain (10^{-3} m/m)		
0	-.263	-.18	
20	-.267	-.184	-.265
40	-.312	-.257	
60	-.306	-.258	-.296
80	-.302	-.237	-.280
100	-.259	-.215	-.258
120	-.233	-.192	-.234
140	-.206	-.170	-.207
160	-.179	-.148	-.180
180	-.159	-.126	-.153
200	-.123	-.104	-.126
220	-.095	-.081	-.099
240	-.068	-.059	-.072

Table 3-5. Uranium thermal expansion data from Touloukian et al.[3.3-1] for temperature < 942 K. (Continued)

Temperature (K)	Thermal Strain (10^{-3} m/m)		
260	-.179	-.148	-.180
273	-.022	-.022	
280	-.013	-.015	-.018
291	-.0032		
293	0.00		
300	.014	.009	.008
373	.127	.118	
473	.306	.268	
573	.424	.506	
673	.728	.594	
773	.972	.780	
873	1.238	1.000	

Table 3-6. Uranium thermal expansion data from Touloukian et al.[3.3-1] 942 K $\leq$ T < 1,045 K.

Temperature (K)	Thermal Strain (10^{-3}m/m)
935	1.618
942	1.515
948	1.643
973	1.577
973	1.685
998	1.731
1,000	1.629
1,023	1.743
1,045	1.813

Table 3-7. Uranium thermal expansion data from Touloukian et al.[3.3-1] T ≥ 1,045 K.

Temperature (K)	Thermal Strain (10^{-3}m/m)
1,045	2.061
1,073	2.116
1,123	2.232
1,173	2.347
1,223	2.457
1,273	2.572
1,323	2.679
1,373	2.786

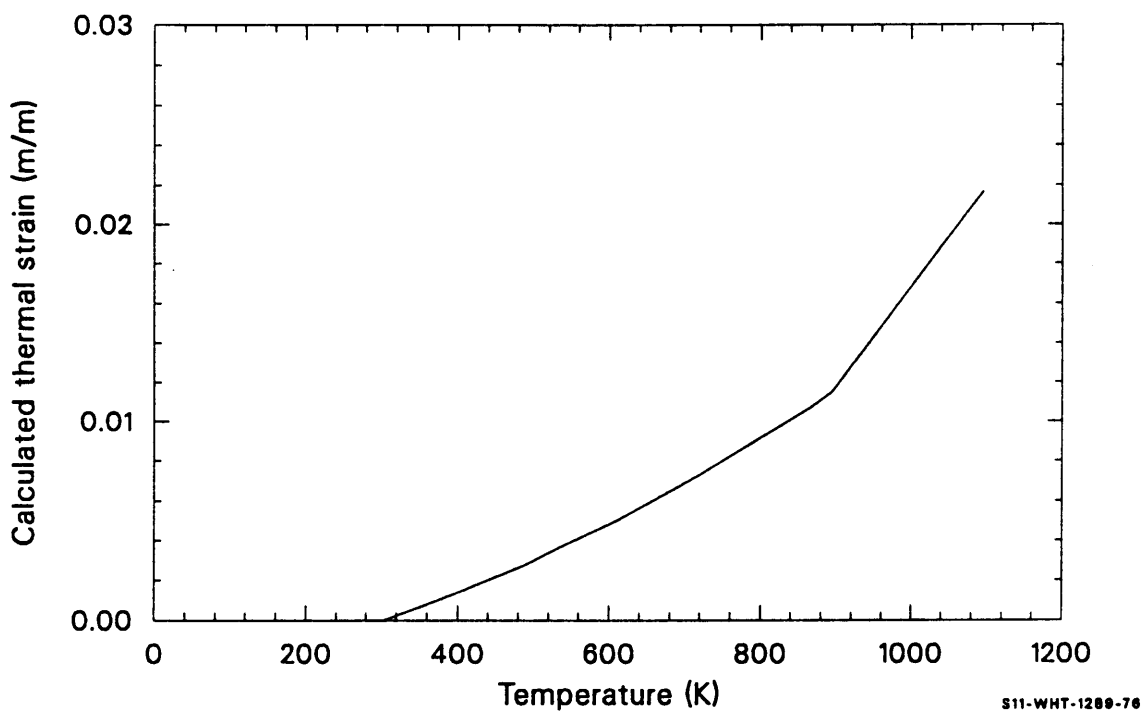

Figure 3-4. Thermal expansion strain as a function of temperature calculated by UTHEXP.

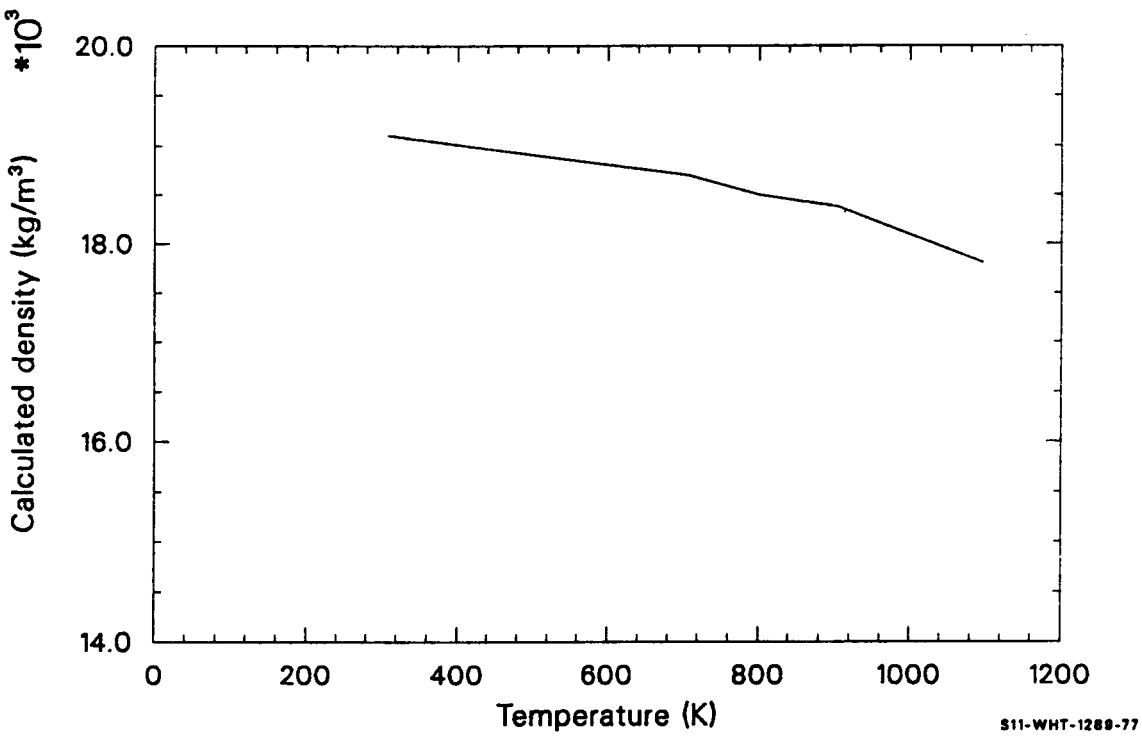

Figure 3-5. Density calculated by UDEN using the thermal strain calculated by UTHEXP.

3.4 Metallic Uranium Oxidation (UOXD, UOXWTK)

3.4.1 Model Development

To calculate the oxidation rates for metallic uranium, the subroutines UOXD and UOXWTK were developed from analytical data reported by Wilson et al.[3.4-1] Subroutine UOXWTK returns the parabolic oxidation constant while UOXD will calculate oxygen weight gain, steam removal rate, hydrogen generation rate, and oxidation heat generation. These subroutines describe the following reaction:

$$U + 2H_2O \rightarrow UO_2 + 2H_2 + \Delta H_U \quad . \tag{3-12}$$

In UOXWTK, the parabolic rate constant for uranium at a given temperature is calculated using the following expression:

For T > 1,473 K,

$$K_{UO} = 1.3503 \exp(-25000/(R\ UTEMP)) \quad . \tag{3-13}$$

For T ≤ 1,473 K,

$$K_{UO} = 0.1656 \exp(-18600/(R\ UTEMP)) \tag{3-14}$$

where

R	=	the gas constant 1.987kcal/(mole deg K)
K_{UO}	=	the parabolic rate constant for the oxidation of uranium (kg^2/m^4 s)
UTEMP	=	temperature of the uranium (K).

The oxygen weight gain, uwg, is evaluated by:

$$uwg = \sqrt{uwg0^2 - K_{UO} \times deltc} \tag{3-15}$$

where

uwg0	=	weight gain from previous time step (kg/m^2)
deltc	=	time step (s).

The oxygen weight gain is limited by the availability of metallic uranium and steam.

The hydrogen generation rate (h2uox), steam removal rate (sroux), and oxidation heat generation (quox) are calculated as follows:

$$h2uox = \frac{(uwg - uwg0) \times slbwd \times dzcond}{8 \times deltc} \tag{3-16}$$

$$quox = \frac{(\frac{238}{32}) \times uheat \times (uwg - uwg0) \times slbwd}{deltc} \tag{3-17}$$

$$sruox = h2uox \times 9 \tag{3-18}$$

where

slbwd	=	fuel element width (m)
dxcond	=	axial node height (m)
uheat	=	heat of reaction for uranium reacted (J/kg).

3.4.2 Comparison With Data

The original work by Wilson was measured in volume of hydrogen produced at STP. The conversions to more usable units for MATPRO have been done above, but the data here will be presented in original form. Parabolic rates for the uranium steam reaction are shown in Table 3-8, and a plot of the data versus the calculations is shown in Figure 3-6.

3.4.3 Summary

According to Wilson,[3.4-1] the oxide produced at high temperatures exhibited no tendency to leave the surface of the uranium at reaction temperatures, and remained quite adherent until cooling to temperatures of approximately 570 K when it would audibly "ping" and flake off. The flakes were of large size and may contribute to blockage. Under these flakes the original metal was shiny and exhibited no visible oxidation. The oxides formed in these reactions were nearly pure UO_2.

Oxides produced at lower temperature (T < 773 K) did not exhibit the same adherence as the higher temperature UO_2 and it is likely that these were categorized by the formation and rapid oxidation of uranium hydrides. These oxides continually flaked off the metal, and offered no protection to the metal below.

3.4.4 References

3.4-1 R. E. Wilson et al., "Isothermal Reaction of Uranium with Steam between 400 and 1,600°C," *Nuclear Science and Engineering, 25,* 1966, pp. 109-115.

Table 3-8. Parabolic Rate Law Constants for the Uranium Steam Reaction

Temperature °C	**Parabolic Rate K ([ml H_2 (at STP)/cm^2]^2/min**	**Error (±)**
500	4.5	1.1
600	3.36	0.33
700	15.6	1.9
900	67	14
1,000	120	11
1,200	341	1
1,300	504	49
1,400	848	18
1,500	1335	55
1,600	1976	122

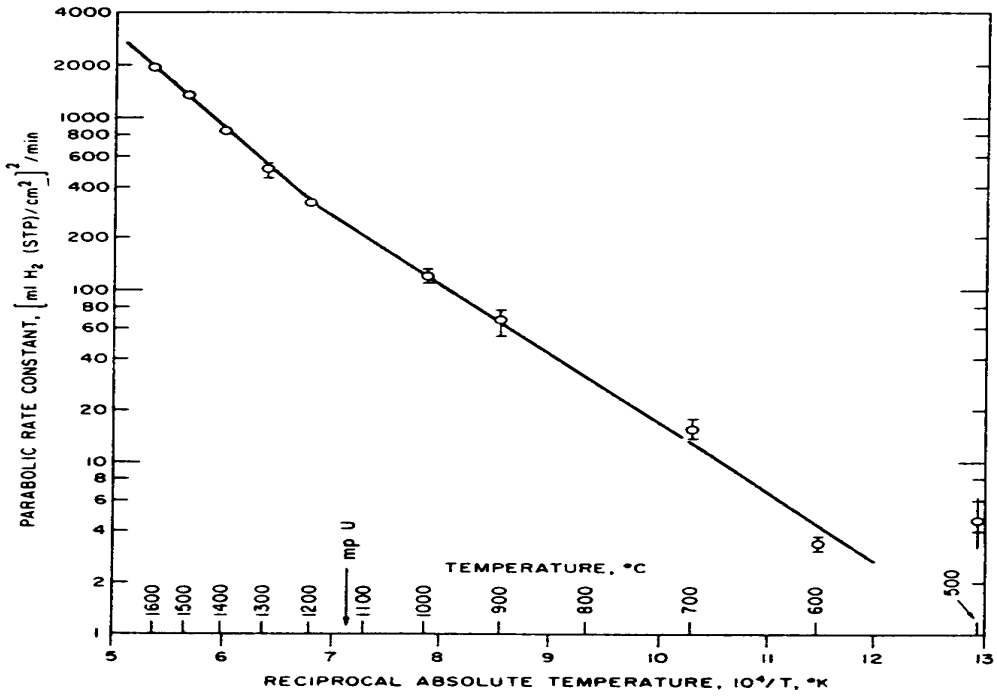

Figure 3-6. Parabolic rate constant for the uranium-steam reaction as a function of temperature.

4. ZIRCALOY

Twenty seven materials properties of LWR fuel rod cladding (zircaloy-2 or -4) have been modeled for inclusion in the SCDAP/RELAP5 materials properties subcode package. Modeling approaches range from a choice of experimental data with linear interpolation or extrapolation or both to a semiempirical expression suggested by theory.

All 27 properties are modeled as a function of the cladding temperature. In addition, such variables as fast neutron flux, fluence, cold work, stress, time, and impurity content are used as arguments. Some of the subcodes are interconnected, employing in part identical or very similar correlations (for example, strain versus stress, stress versus strain, and cladding ultimate strength). Some subcodes call upon others, such as the physical properties subcode, PHYPRO; but all of the information needed to run a given subcode is contained in this report.

4.1 Melting and Phase Transformation Temperatures (CHYPRP)

To perform an accurate analysis of reactor behavior during an accident involving the core, it is necessary to know the melting and phase transformation temperatures of zircaloy. The subroutine CHYPRP calculates the zircaloy phase transition temperatures of interest for use in LWR analysis. The only input required in this subroutine is the excess weight fraction oxygen content of the zircaloy. From this input, the subroutine calculates the solidus temperature (appearance of lowest temperature liquid phase), the liquidus temperature (melting of the last solid phase), the alpha to alpha plus beta phase boundary, and the alpha plus beta to beta phase boundary for zircaloy.

4.1.1 Model Development

Four parameters are often used to describe the oxygen concentration in zircaloy. Table 4-1 shows the relationship between the one used in CHYPRP and the others. The first column gives the excess weight fraction oxygen content. The second column gives the corresponding values for the total weight fraction oxygen, assuming an as received oxygen concentration of 0.0012 by weight. The third column presents corresponding values for the atomic fraction of oxygen in the compound. The atomic fraction oxygen is related to the mass fraction oxygen in zirconium oxide by the equation

$$x = \frac{WFOX}{WFOX + \frac{GMWT(0)}{GMWT(Zr)}(1 - WFOX)} \tag{4-1}$$

where

x	=	the atomic fraction of oxygen in zircaloy containing oxygen (atoms of oxygen/ atoms of compound)
WFOX	=	mass fraction of oxygen in zircaloy containing oxygen (kg oxygen/kg compound)

Table 4-1. Oxygen content parameters for zircaloy.

Excess mass oxygen fraction	Total mass oxygen fraction (WFOX)	Atomic oxygen fraction	Oxygen to Metal Ratio
O/kg Zr(O)	[kg O/kg Zr(O)]	(O/atoms compound)	Atoms O/ atoms metal
0.0000	0.0012	0.007	0.007
0.0100	0.0112	0.061	0.065
0.0200	0.0212	0.110	0.124
0.0300	0.0312	0.155	0.183
0.0400	0.0412	0.197	0.245
0.0500	0.0512	0.235	0.307
0.0600	0.0612	0.271	0.372
0.0657	0.0669	0.290	0.408

GMWT(O) = molecular weight of an oxygen atom [16 kg (O)/kg · mole]

GMWT(Zr) = molecular weight of a zircaloy atom [91.22 kg (Zr)/kg · mole]

As-received zircaloy is presumed to have 0.0012 weight fraction oxygen.

The fourth column gives the corresponding values of the oxygen to metal ratio. This ratio is related to the atomic fraction oxygen by the following equation for zirconium oxide (which approximates zircaloy oxide):

$$YE = \frac{x}{1 - x} \tag{4-2}$$

where YE is the oxygen to metal ratio (atoms of oxygen/atoms of zirconium).

To convert the input excess weight fraction oxygen to an atomic fraction for oxygen in the zircaloy, the as received oxygen weight fraction for the zircaloy is added to the input weight fraction oxygen prior to calculating the atomic fraction of the oxygen in the zircaloy. From the calculated atomic fraction oxygen, the melting and phase transformation temperatures are calculated using equations from the PYHPRP, PSOL, and PLIQ subcodes. To calculate the solidus temperature from the atomic fraction of oxygen in zircaloy, the following relationships are used:

For $x \leq 0.1$,

$$T_{sol} = 2098 + 1150\ x\ . \tag{4-3}$$

For $0.1 < x \leq 0.18$,

$$T_{sol} = 2213\ . \tag{4-4}$$

For $0.18 < x \leq 0.29$,

$$T_{sol} = 1389.5317 + 7640.0748\ x - 17029.172\ x^2\ . \tag{4-5}$$

For $0.29 < x \leq 0.63$,

$$T_{sol} = 2173\ . \tag{4-6}$$

For $0.63 < x \leq 0.667$,

$$T_{sol} = -11572.454 + 21818.181\ x\ . \tag{4-7}$$

For $x > 0.667$,

$$T_{sol} = -11572.454 + x(1.334 - x)\ 21818.181 \tag{4-8}$$

where T_{sol} is the solidus temperature (K).

The liquidus temperatures are calculated using the following relationships:

For $x \leq 0.19$,

$$T_{liq} = 2125. + 1632.1637\ x - 5321.6374\ x^2\ . \tag{4-9}$$

For $0.19 < x \leq 0.41$,

$$T_{liq} = 2111.6553 + 1159.0909\ x - 2462.1212\ x^2\ . \tag{4-10}$$

For $0.41 < x \leq 0.667$,

$$T_{liq} = 895.07792 + 3116.8831\ x\ . \tag{4-11}$$

For x > 0.667,

$$T_{liq} = 895.07792 + (1.34 - x)\ 3116.8831 \qquad (4\text{-}12)$$

where T_{liq} is the liquidus temperature (K).

The subcode CHYPRP also calculates the low and high temperature boundaries of the alpha plus beta phase region as a function of the total weight fraction oxygen in the compound. If the compound weight fraction oxygen is less than 0.025, then the low temperature boundary of the two-phase region is calculated as follows:

$$\text{ctranb} = 1094. + \text{WFOX} \cdot (-1.289 \times 10^{3} + \text{WFOX} \cdot 7.914 \times 10^{5}\ ) . \qquad (4\text{-}13)$$

If the total weight fraction is greater than 0.025, then the low temperature boundary is calculated using the following equation:

$$\text{ctranb} - 1556.4 + 3.8281 \times 10^{4} \cdot (\text{WFOX} - 0.025)\ . \qquad (4\text{-}14)$$

where ctranb is the low temperature boundary of the alpha plus beta phase region (K). If the lower alpha plus beta transition temperature is equal to or larger than the calculated solidus temperature, then the alpha plus beta lower boundary phase temperature is set equal to the solidus temperature.

The high temperature alpha plus beta phase region boundary temperatures are calculated using the following relationships, which use the input oxygen content rather than weight fraction. With an input oxygen content less than 4.7308937×10^{-3}, the upper phase boundary temperature is calculated using the following correlation:

$$\text{ctrane} = 392.46 \cdot [(100 \cdot \text{WFOX})^{2} + 3.1417]\ . \qquad (4\text{-}15)$$

If the oxygen content is greater than $4.7308937 \times 10^{-03}$, then the equation used to calculate the upper alpha plus beta phase boundary temperature is

$$\text{ctrane} = (100 \cdot \text{WFOX}) \cdot 491.157 + 1079.639 \qquad (4\text{-}16)$$

where ctrane is the high temperature boundary of the alpha plus beta phase region (K). If the upper boundary temperature of the alpha plus beta phase region is greater than the calculated solidus temperature, then the upper boundary alpha plus beta phase temperature is set equal to the solidus temperature. The alpha plus beta boundaries expressions are based on data from Chung and Kassner.[4.1-1]

Figure 4-1 shows the calculated zircaloy solidus and liquidus temperatures and the calculated alpha plus beta phase region boundaries.

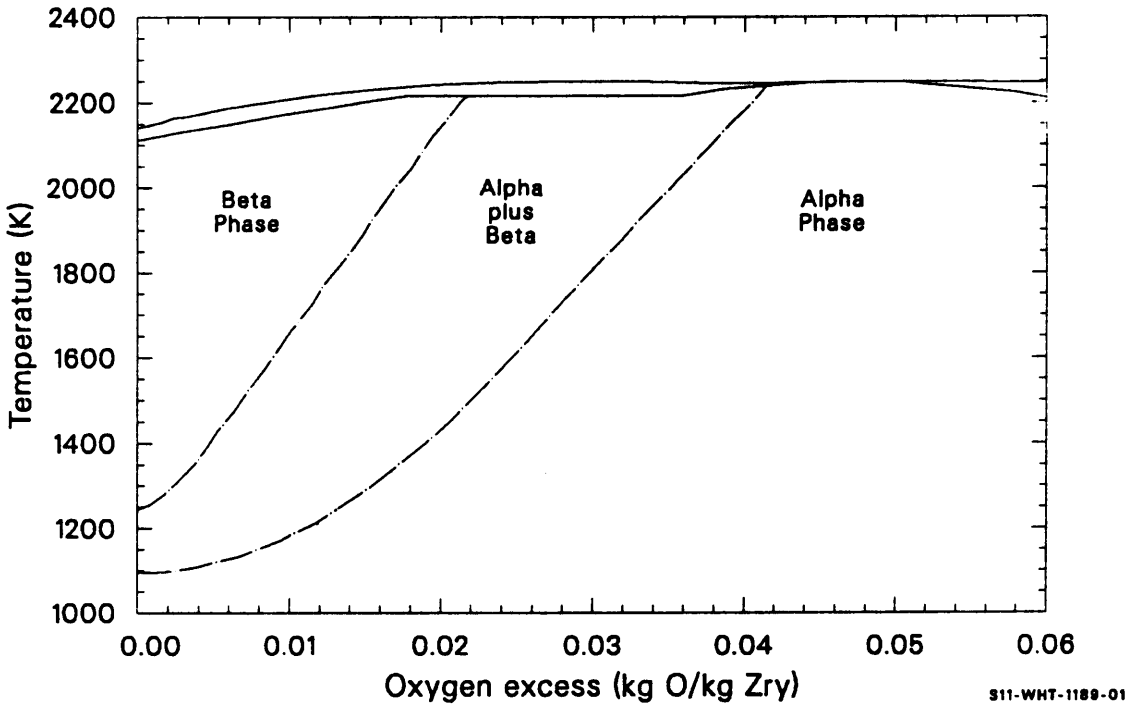

Figure 4-1. Zircaloy solidus and liquidus temperatures.

4.1.2 References

4.1-1 H. M. Chung and T. F. Kassner, "Pseudobinary Zircaloy Oxygen Phase Diagram," *Journal of Nuclear Materials, 84,* 1979, pp. 327-339.

4.2 Temperature Required to Prevent Hydriding of a Given Concentration of Hydrogen in Zircaloy (CTSOL)

An estimate of the temperature at which hydride precipitates begin to form in zircaloy cladding is useful for estimating when hydriding will begin to embrittle the cladding. The function CTSOL calculates the minimum temperature for complete solution of a given concentration of hydrogen. The expression used for the calculation is

$$\mathrm{CTSOL} = \frac{4401\mathrm{K}}{\ln\left(\frac{1.332\times10^{5}}{\mathrm{H}}\right)} \tag{4-17}$$

where

CTSOL = minimum temperature for complete solution of a concentration of hydrogen in zircaloy (K)

H = hydrogen concentration (parts per million by weight).

The development of this equation is discussed in Section 4.3 in conjunction with the derivation of the model for the effect of hydride solution on zircaloy cladding specific heat.

4.3 Cladding Specific Heat, the Effect of Hydride Solution on Cladding Specific Heat, and Enthalpy (CCP, CHSCP, CENTHL)

Two function subcodes are used to describe the apparent specific heat of the zircaloys. The first, CCP, describes the true specific heat at constant pressures for the alloys. The second, CHSCP, describes the apparent addition to the specific heat because of energy used to dissolve the hydrides present in zircaloys. Uncertainty estimates have been determined and are returned by each function.

CCP requires only temperature as input, while CHSCP requires both temperature and the concentration of hydrogen. The hydrogen concentration may be supplied directly by the user or it may be calculated by the MATPRO function CHUPTK.

4.3.1 Specific Heat (CCP)

For the alpha phase of the zircaloys (temperature less than 1,090 K), CCP returns linear interpolations for the points listed in Table 4-2. (Linear interpolation is computed by the subcode POLATE described in Section 16.1.)

Table 4-2 is based on precise data taken by Brooks and Stansbury[4.3-1] with a zircaloy-2 sample that had been vacuum annealed at 1,075 K to remove hydrogen. The standard error[a] of the CCP interpolation (that is, the precision of the fit to the data) was based on the 90 points in the data base and was found to be temperature dependent. For the 57 data points between 300 and 800 K, the standard error is 1.1 J/kg K. Between 800 and 1,090 K, it is 2.8 J/kg K.

a. The standard error is estimated for a data set by the expression: [sum of squared residuals/number of residuals minus number of constants used to fit the data)]$^{1/2}$.

Table 4-2. Zircaloy specific heat capacities for CCP.

Temperature (K)	Specific Heat Capacity (J/kgK)
300	281
400	302
640	331
1,090	375
1,093	502
1,113	590
1,133	615
1,153	719
1,173	816
1,193	770
1,213	619
1,233	469
1,248	356

For temperatures from 1,,090 to 1,300 K (where Brooks and Stansbury do not report results), values of specific heat proposed by Deem and Eldridge[4.3-2] are adopted by MATPRO. The Deem and Eldridge values, shown in Table 4-3, are based on measurements of enthalpy and temperature which provide considerably less precise specific heat data than the results of Brooks and Stansbury.[4.3-1]

The standard error as estimated by the Deem and Eldridge data in the region 1,090 through 1,310 K is 10.7 J/kg·K. Again, this standard error is a measure only of the precision of the fit, since only a single data source is employed.

The specific heat as calculated by CCP is shown in Figure 4-2. Figures 4-3 and 4-4 also show the CCP prediction, using an expanded scale at lower temperatures and illustrating the base data from Brooks and Stansbury as well as alpha phase (300 to 1,090 K) data from Deem and Eldridge that were not used in constructing CCP.

At temperatures up to 900 K, the Brooks and Stansbury data agree with the Deem and Eldridge data within 3%. Above the alpha plus beta to beta transformation temperature (about 1,250 K) and up to about 1,320 K, a constant value of 355.7 J/kg·K was reported by Deem and Eldridge. This value agrees well with a value of 365.3 reported by Coughlin and King[4.3-3] for pure beta zirconium.

Table 4-3. Specific heat as a function of temperature--beta phase.

Temperature (K)	Specific Heat (J/kg·K)
1,093	502
1,113	590
1,133	615
1,153	719
1,173	816
1,193	770
1,213	619
1,233	469
1,248	356

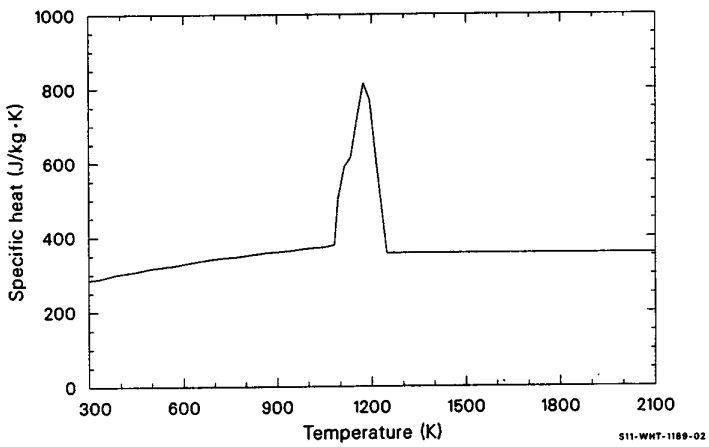

Figure 4-2. Specific heat of zircaloys as calculated by CCP for alloys without hydrides.

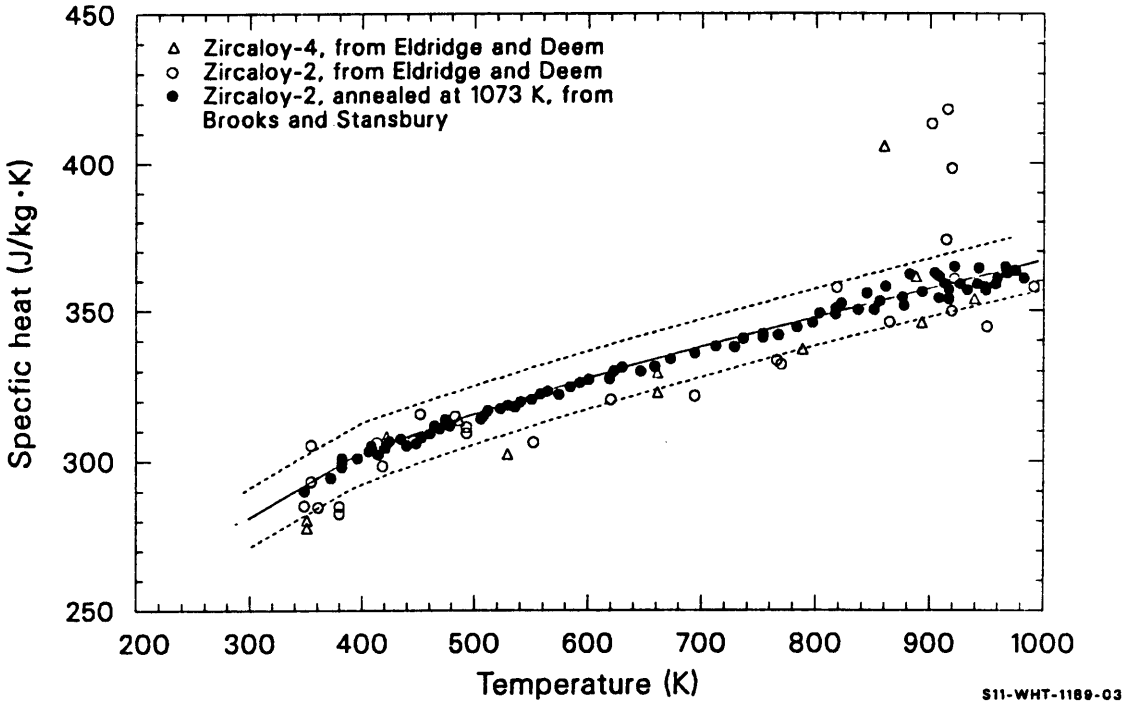

Figure 4-3. Available data, MATPRO expressions for specific heat, and estimated uncertainty of the MATPRO expression for temperatures from 300 to 1,000 K.

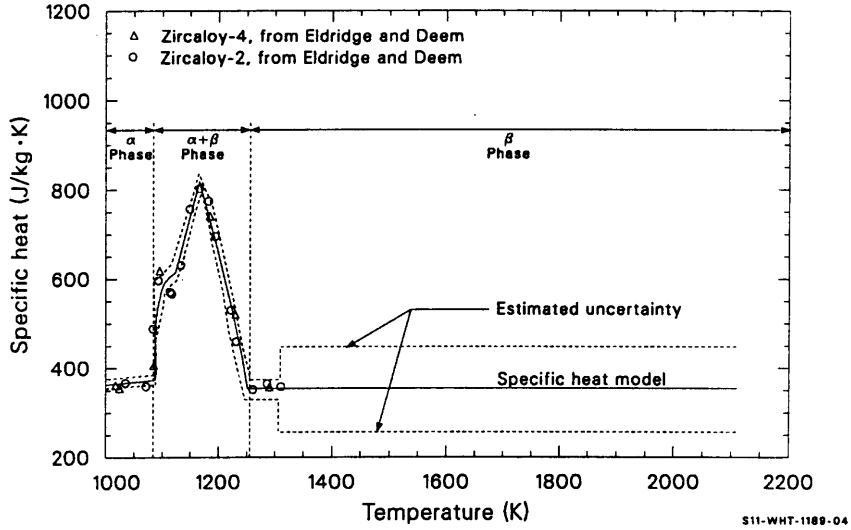

Figure 4-4. Available data, MATPRO expressions for specific heat, and estimated uncertainty of the MATPRO expression for temperatures from 1,000 to 2,000 K.

The estimated standard error of CCP for data consisting of a random sample from all zircaloy-2 and zircaloy-4 claddings is also shown in Figures 4-3 and 4-4. This standard error is discussed in Section 4.3.3 after the discussion of the effect of hydride solution.

4.3.2 Effect of Hydride Solution (CHSCP)

Values returned by the function CHSCP for the addition to the specific heat due to energy used in solution of hydrides are:

$$CHSCP = \frac{ABC}{T^2}\left[\exp\left(-\frac{B}{T}\right)\right]\left[\exp\left(\frac{T - TSOL}{0.02TSOL}\right) + 1\right]^{-1} \tag{4-18}$$

where

CHSCP	=	addition to true specific heat due to hydride solution (J/kg·K)
T	=	cladding temperature (K)
TSOL	=	minimum temperature for complete solution of the hydrogen concentration, as determined with Equation (4-19) (K)
A	=	1.332×10^5 (ppm hydrogen)
B	=	4.401×10^3 (K)
C	=	45.70(J/kg ppm hydrogen).

TSOL, the minimum temperature required for complete solution of the hydrogen in the cladding, is determined from the expression

$$TSOL = \frac{B}{\ln\left(\frac{A}{H}\right)} \tag{4-19}$$

where

A and B	=	constants given in conjunction with Equation (4-18)
H	=	hydrogen concentration (ppm by weight).

A value of H can be determined with the function CHUPTK (Section 4.16).

Equations (4-18 and 4-19) are based on data reported by Scott[4.3-4] for zirconium with and without intentional additions of hydrogen. For temperatures below 830 K, Scott (Figure 16 of Reference 4.3-4) finds the logarithm of the terminal solubility of hydrogen in zirconium to be proportional to temperature. Below the temperature TSOL, when hydrides are not completely dissolved,

Energy to dissolve hydride = constant x exp(negative constant/temperature). (4-20)

It is assumed in this expression that the terminal solubility will be attained as long as undissolved

hydrogen is present. The heat of solution per gram atom of hydrogen may be taken as the average of two values given by Scott (Table VII of Reference 4.3-4). Equation (4-18) results from differentiation of this expression with respect to temperature and multiplication by the empirical factor

$$\left[\exp\left(\frac{T - TSOL}{0.02TSOL}\right) + 1\right]^{-1}$$

to express the fact that the data do not show an instant termination of hydride solution with increasing temperature.

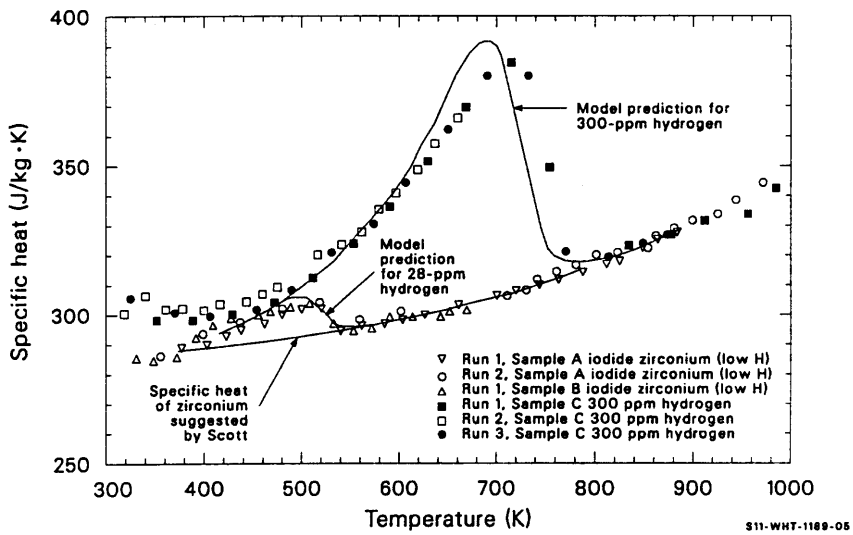

Figure 4-5. Data base for MATPRO prediction of the effect of hydride solution on specific heat, Scott's proposed curve for the specific heat of zirconium, and the MATPRO predictions for the effect of 28 and 300 ppm of hydrogen on the specific heat curve.

Figure 4-5 illustrates Scott's data for two samples of zirconium iodide and a single sample of zirconium intentionally doped with approximately 300 ppm of hydrogen. The two zirconium iodide samples apparently contained some hydrogen and were fit by the MATPRO correlation [Equation (4-19)], assuming they contained 28 ppm hydrogen. Figure 4-5 also shows the MATPRO correlation assuming 300 ppm hydrogen and the curve recommended by Scott for pure zirconium.

4.3.3 Uncertainties in Specific Heat Predictions

The systematic error (the estimated variation between values obtained with different samples) is larger than the imprecision in the base data of CCP and CHSCP.

The standard error of CCP, reflecting the systematic error for a random sample of cladding zircaloys, is estimated to be ± 10 J/kg· K (±3%) in the alpha phase. This value is based on the difference between values of specific heat estimated by Deem and Eldridge from their data[4.3-2] and the more precise data from one sample of zircaloy-2 used by MATPRO. In the alpha beta phase region and the beta region to 1,300 K,

a roughly estimated standard error of 25 J/kg·K is assigned to CCP, based on the decreased precision of the measurements and on the lack of confirming data in this temperature range. Above 1,300 K, the only basis for the assumed constant value of specific heat is the prediction of the Debye model of heat capacity for temperatures above the Debye temperature. Since no data are available, a standard error of ± 100 J/kg·K is listed.

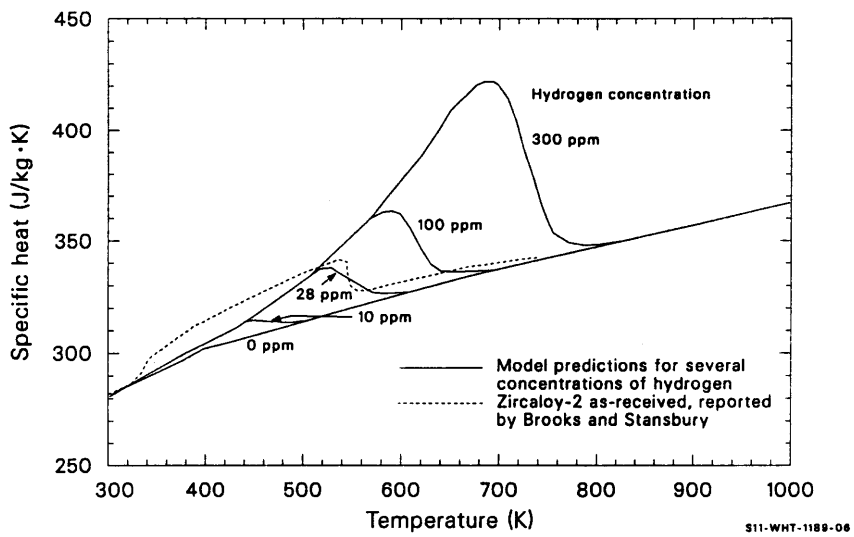

Figure 4-6. MATPRO predictions for apparent zircaloy specific heat for several hydrogen concentrations compared with the curve measured with as received zircaloy-2.

The basis for the estimate of the standard error of CHSCP over a random sample of cladding zircaloy is shown in Figure 4-6, which compares MATPRO predictions for several concentrations of hydrogen with a curve published by Brooks and Stansbury[4.3-1] for the specific heat of zircaloy-2 tested without prior heat treatment. The unpublished data are reported to be within 1% of this curve, and the MATPRO prediction is as far as 3% (10 J/kg·K) below the reported curve. Since the prediction of CCP in this temperature range is based on precise data (± 1.1 J/kg·K) taken with vacuum annealed samples of the same alloy, shown by a dashed line in Figure 4-6, most of the discrepancy (between the dashed line and the 28 ppm H solid line) is presumed to be due to errors inherent in the application by CHSCP to the zirconium data of Scott for zircaloy. A standard error of 50% in the hydrogen induced increment to apparent specific heat is, therefore, assigned to the model.

The uncertainties in CCP are summarized in Table 4-4.

4.3.4 Zircaloy Enthalpy (CENTHL)

The function CENTHL provides zircaloy enthalpy for temperatures above 300 K. The CENTHL enthalpy subcode requires a temperature and a reference temperature for which the enthalpy will be set equal to zero.

Table 4-4. Uncertainties in specific heat of zircaloy.

Temperature Range	Standard Error in CPP
300 < T < 1,090 K	±10 J/kg·K
1,090 < T < 1,300 K	±25 J/kg·K
T < 1,300 K	±100 J/kg·K

Zircaloy enthalpy is modeled by integrating the expressions used in the cladding specific heat subcode, CCP. Since CCP utilizes linear interpolation on the set of points reproduced in Table 4-2, the CENTHL routine uses the expression

$$H(T) - H(300) = \sum_{j=1}^{i} \Delta H_j + C_{p_i}(T - T_i) + \frac{(T - T_i)^2}{2(T_{i+1} - T_i)}(C_{p_{i+1}} - C_{p_i}) \tag{4-21}$$

where

H(T)	=	enthalpy of zircaloy at temperature T (J/kg)
T_i	=	i-th temperature in Table 4-2 (K)
C_p	=	specific heat capacity at T_i (J/kg • K)
ΔH	=	change in enthalpy of zircaloy between T_{i-1} and T_i
T	=	temperature (K).

To find the enthalpy at a temperature greater than or equal to T_i, but less than T_{i+1}. Equation (4-21) can be derived by inspection of Figure 4-7. The first term is the enthalpy between T_1 and T_i, that is the area under the line segments which connect C_{p1} to C_{pi}. The second term is the area of rectangle B, and the third term is the area of triangle A. The sum of these two areas is the enthalpy between T_i and T. Table 4-5 lists values of $\varepsilon\Delta H_j$ corresponding to the values of C_p in Table 4-2. The entries for 2,098 and 2,099 K incorporate the heat of fusion for melting zircaloy. The melt temperature and heat of fusion were taken from the MATPRO-11, Revision 2, PHYPRP subcode, and do not include the effect of oxidation on these quantities.

For temperatures greater than 2,099 K, an enthalpy consistent with a constant specific heat capacity above 2,099 K is calculated by omitting the third term on the right-hand side of Equation (4-21). Table 4-6 lists engineering estimates for the expected standard error of the enthalpy predicted by CENTHL with a reference temperature of 300 K.

A code generated plot of zircaloy enthalpy change as a function of temperature is presented in Figure 4-8.

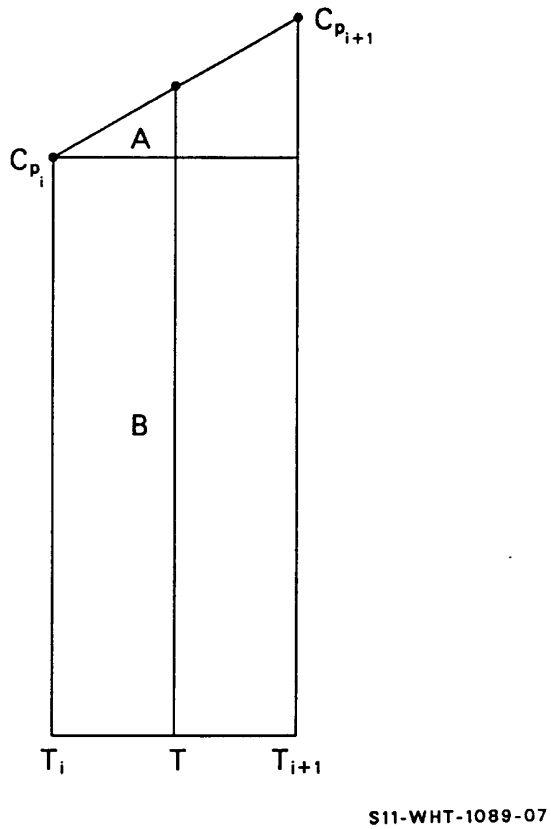

Figure 4-7. Derivation of Equation (4-21).

Table 4-5. Values of mass for zircaloy.

Temperature (K)	$\sum_{j=1}^{i-1} \Delta H_j$ (10^4 J/kg)
300	0.000
400	2.915
640	10.511
1,090	26.396
1,093	26.52755
1,113	27.61955
1,133	28.82455
1,153	30.15855

Table 4-5. Values of mass for zircaloy. (Continued)

Temperature (K)	$\sum_{j=1}^{i-1} \Delta H_j$ (10^4J/kg)
1,173	31.69355
1,193	33.27955
1,213	34.66855
1,233	35.67655
1,248	36.29530
2,098	66.5553
2,099	89.0909

Table 4-6. Uncertainty of zircaloy enthalpy.

Temperature Range (K)	Expected Standard Error of CNTHL (fraction of predicted value)
$300 \leq T \leq 1{,}090$	0.03
$1{,}090 \leq T \leq 2{,}656.67$	3×10^{-4} (T-1,090) + 0.03
$2{,}656.67 \leq T$	0.5

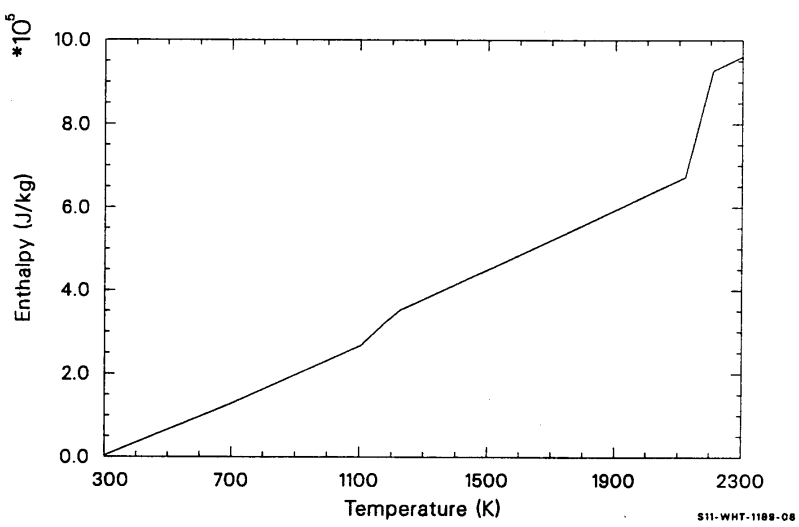

Figure 4-8. Zircaloy enthalpy as a function of temperature.

4.3.5 References

4.3-1 C. R. Brooks and E. E. Stansbury, "The Specific Heat of Zircaloy-2 from 50 to 700°C," *Journal of Nuclear Materials, 18*, 1966, p. 223.

4.3-2. H. W. Deem and E. A. Eldridge, *Specific Heats and Heats of Transformation of Zircaloy-2 and Low Nickel Zircaloy-2*, USAEC BM1-1803, May 31, 1967.

4.3-3. J. P. Coughlin and E. G. King, "High Temperature Heat Contents of Some Zirconium Containing Substances," *Journal of the American Chemical Society, 72*, 1950, p. 2262.

4.3-4. J. Scott, *A Calorimetric Investigation of Zirconium, Titanium, and Zirconium Alloys from 60 to 960°C*, Ph.D. Thesis, University of Tennessee, 1957.

4.4 Thermal Conductivity (CTHCON)

The transfer of heat from the fuel pellet to reactor coolant depends partly on the thermal conductivity of the cladding. Accurate predictions of fuel temperatures require knowledge of zircaloy thermal conductivities. An expression has been developed for the thermal conductivity of zircaloy-2 and -4 based on the pooled data from eight reports. This expression and the uncertainty in the correlation are presented in this section.

4.4.1 Summary

The thermal conductivity of alloys is primarily a function of temperature. Other characteristics, such as residual stress levels, crystal orientation, and minor composition differences (zircaloy-2 versus zircaloy-4, for example), may have a secondary influence on thermal conductivity. Considering only temperature as the defining parameter, the thermal conductivity of zircaloy for temperatures less than 2,098 K and its uncertainty are found to be:

$$k = 7.51 + 2.09 \times 10^{-2}\, T - 1.45 \times 10^{-5}\, T^2 + 7.67 \times 10^{-9}\, T^3 \qquad (4\text{-}22)$$

$$\sigma_k = 1.01 \quad . \qquad (4\text{-}23)$$

For temperatures greater than or equal to 2,098 K, the thermal conductivity and uncertainty are:

$$K = 36 \qquad (4\text{-}24)$$

$$\sigma_k = \pm 5 \qquad (4\text{-}25)$$

where

k	=	thermal conductivity of zircaloy (W/m•K)
T	=	temperature (K)

σ_k = standard deviation (W/m•K).

This equation predicts k very well from room temperature to the data limit of about 1,800 K and may be extrapolated with some confidence to the melting point. The standard deviation (σ_k) of the data with respect to this correlation appears to be temperature independent over the data range (Figure 4-9). Least squares regression analysis indicates that the standard deviation for each of the constants in Equation (4-22) is 20-30% of the value of the constant.

The correlations for zircaloy thermal conductivity at high temperatures required only consideration of the effect of melting on thermal conductivity. No data for liquid zircaloy thermal conductivity have been found; but Nazare, Ondracek, and Schulz[4.4-1] have reported that the ratios of solid state conductivities to liquid state conductivities at the melting temperatures for metals like zircaloy with eight nearest neighbor atoms is 1.6 $\pm$ 0.2.[a] Since the solid state conductivity predicted by the CTHCON function is 58 W/m•K, the liquid state conductivity should be about 36 $\pm$5 W/m• K.

4.4.2 Literature Review

Anderson[4.4-2] reported thermal conductivity data for zircaloy-2 in the temperature range of 380 to 872 K. Chirigos et al.[4.4-3] reported thermal conductivity data for zircaloy-4 between 370 and 1,125 K. Feith[4.4-4] studied the thermal conductivity of zircaloy-4 between 640 and 1,770 K. Lucks and Deem[4.4-5] measured the thermal conductivity of zircaloy-2 in the temperature range of 290 to 1,075 K. Powers[4.4-6] reported three sets of thermal conductivity data for zircaloy taken from Battelle Memorial Institute (BMI) letter reports. These data cover both zircaloy-2 and -4 over temperature ranges of approximately 300 to 1,000 K. Scott[4.4-7] reported the thermal conductivity of zircaloy-4 between 400 and 1,060 K. Numerical values of his data were reported by Touloukian et al.[4.4-8] These data are presented in Table 4-7.

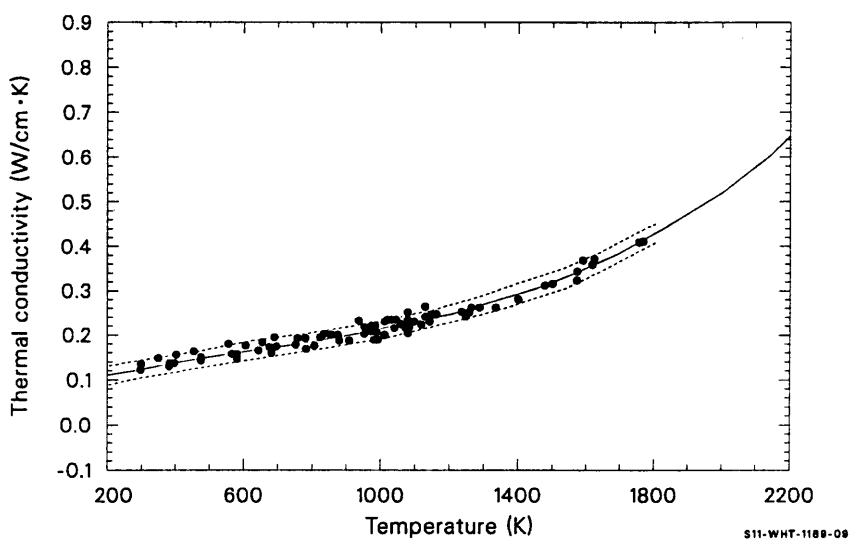

Figure 4-9. Thermal conductivity data, least squares fit, and the two standard deviation limits.

a. The body-centered cubic lattice of beta-phase zircaloy has eight nearest neighbors.

4.4.3 Model Development

The data reported in Section 4.4.2 refer to zircaloy-2 and zircaloy-4 having various textures and pre-test histories. The alloy chemistry and heat transfer properties of zircaloy-2 and-4 are similar enough to consider them to be a single material. The differences in thermal conductivity between the materials appears to be of the same magnitude as the statistical scatter in the data.

Texture may have an effect in the alpha phase temperature region. Zircaloy is crystallized in a hexagonal, close packed configuration in the low temperature alpha phase; and there may be some difference in the thermal conductivity along the prismatic and basal directions. At higher temperatures, the material is body centered cubic and will not exhibit texture effects. In any case, contributions to the thermal conductivity due to texture are probably well within the scatter of the experimental data used to develop models for this property.

All of the available data for thermal conductivity of zircaloy-2 and -4 were combined and analyzed using a least squares polynomial fit of the third degree. The equation is:

$$k = 7.51 + 2.09 \times 10^{-2}\, T - 1.45 \times 10^{-5}\, T^2 + 7.67 \times 10^{-9}\, T^3 \quad . \qquad (4\text{-}26)$$

where

k	=	zircaloy thermal conductivity (W/m•K)
T	=	temperature of cladding (K).

A comparison of calculated thermal conductivities and the data is shown in Figure 4-9.

The standard deviation of the data with respect to Equation (4-26) is 1.01 W/m• K. Thirty two of the points fall outside $\pm$ 1σ from the curve. Four points fall outside $\pm$ 2σ (Figure 4-9). The standard deviations of the coefficients of Equation (4-26) are about 20-30% of the absolute value of the coefficients.

The standard deviation is small enough so that the user may have considerable confidence in the model. Jensen[4.4-9] performed a parametric analysis of several variables involved in estimation of fuel and cladding temperatures. Both steady state and transient analyses showed that variations of $\pm$ 20% resulted in calculated cladding temperature variations of about 2.8 K. Fuel centerline temperatures are more sensitive to cladding thermal conductivity and showed variations of 28 K. Similar findings were reported by Korber and Unger.[4.4-10]

Table 4-7. Zircaloy thermal conductivity data base.

Temperature (K)	Experimental Thermal Conductivity [W/(m•K)]	Calculated Thermal Conductivity [W/(m•K)]	Difference Between Calculated and Experimental Thermal Conductivity	Reference	Material
380.4	13.50	13.78	-0.28	W. K. Anderson et al.	Zircaloy-2
469.3	14.43	14.92	-0.49		
577.6	15.68	16.22	-0.54		
685.9	17.10	17.50	-0.40		
774.8	18.42	18.57	-0.15		
872.0	19.91	19.80	0.11		
373.2	13.60	13.69	-0.09	J. N. Chirigos et al.	.Zircaloy-4
473.2	14.30	14.97	-0.67		
573.2	15.20	16.17	-0.97		
673.2	16.40	17.35	-0.95		
773.2	18.00	18.55	-0.55		
873.2	20.10	19.81	0.29		
973.2	22.50	21.19	1.31		
1,073.2	25.20	22.72	2.48		
1,123.2	26.60	23.56	3.04		
642.2	16.30	16.98	-0.68	A. D. Feith	Zircaloy-4
678.2	16.10	17.41	-1.31		
746.2	17.60	18.22	-0.62		
780.2	18.40	18.63	-0.23		
800.2	17.70	18.88	-1.18		
819.2	19.80	19.12	0.68		
833.2	20.10	19.29	0.81		
847.2	19.60	19.47	0.13		
850.2	20.00	19.51	0.49		
902.2	19.00	20.20	-1.20		
925.2	23.10	20.51	2.59		
943.2	21.80	20.76	1.04		

Table 4-7. Zircaloy thermal conductivity data base. (Continued)

Temperature (K)	Experimental Thermal Conductivity [W/(m•K)]	Calculated Thermal Conductivity [W/(m•K)]	Difference Between Calculated and Experimental Thermal Conductivity	Reference	Material
946.2	20.40	20.80	-0.40		
960.2	22.10	21.00	1.10		
963.2	21.50	21.04	0.46		
969.2	21.40	21.13	0.27		
981.2	21.20	21.30	-0.10		
1,005.2	22.90	21.66	1.24		
1,012.2	23.60	21.76	1.84		
1,019.2	21.10	21.87	-0.77		
1,021.2	21.20	21.90	-0.70		
1,023.2	22.60	21.93	0.67		
1,025.2	23.20	21.96	1.24		
1,035.2	21.80	22.12	-0.32		
1,037.2	22.50	22.15	0.35		
1,040.2	22.90	22.19	0.71		
1,054.2	22.70	22.41	0.29		
1,063.2	24.00	22.56	1.44		
1,066.2	21.70	22.61	-0.91		
1,079.2	21.40	22.82	-1.42		
1,093.2	23.30	23.05	0.25		
1,122.2	22.50	23.54	-1.04		
1,128.2	24.50	23.65	0.85		
1,139.2	23.10	23.84	-0.74		
1,152.2	24.40	24.07	0.33		
1,161.2	24.20	24.24	-0.04		
1,232.2	25.30	25.60	-0.30		
1,243.2	24.70	25.82	-1.12		
1,253.2	25.20	26.02	-0.82		
1,269.2	26.20	26.36	-0.16		
1,289.2	26.50	26.79	-0.29		
1,331.2	26.40	27.73	-1.33		
1,401.2	27.80	29.43	-1.63		

Table 4-7. Zircaloy thermal conductivity data base. (Continued)

Temperature (K)	Experimental Thermal Conductivity [W/(m•K)]	Calculated Thermal Conductivity [W/(m•K)]	Difference Between Calculated and Experimental Thermal Conductivity	Reference	Material
1,404.2	27.90	29.50	-1.60		
1,484.2	31.10	31.67	-0.57		
1,508.2	31.70	32.36	-0.66		
1,576.2	32.60	34.46	-1.86		
1,581.2	34.60	34.63	-0.03		
1,594.2	36.80	35.05	1.75		
1,624.2	36.30	36.07	0.23		
1,625.2	37.30	36.10	1.20		
1,755.2	41.40	41.00	0.40		
1,771.2	41.80	41.66	0.14		
293.2	12.60	12.58	0.02	C. F. Lucks and H. W. Deem	Zircaloy-2
373.2	13.40	13.69	-0.29		
473.2	14.50	14.97	-0.47		
573.2	15.60	16.17	-0.57		
673.2	17.00	17.35	-0.35		
773.2	18.40	18.55	-0.15		
873.2	19.90	19.81	0.09		
973.2	21.50	21.19	0.31		
1,073.2	23.10	22.72	0.38		
373.2	14.11	13.69	0.42	A. E. Powers	Zircaloy-2
473.2	14.80	14.97	-0.17		
573.2	15.32	16.17	-0.85		
673.2	16.01	17.35	-1.34		
773.2	17.05	18.55	-1.50		
873.2	1.18	19.81	-1.63		
973.2	19.42	21.19	-1.77		
1,073.2	20.77	22.72	-1.95		
293.2	12.55	12.58	-0.03		

Table 4-7. Zircaloy thermal conductivity data base. (Continued)

Temperature (K)	Experimental Thermal Conductivity [W/(m•K)]	Calculated Thermal Conductivity [W/(m•K)]	Difference Between Calculated and Experimental Thermal Conductivity	Reference	Material
373.2	13.29	13.69	-0.40		
473.2	14.37	14.97	-0.60		
573.2	15.58	16.17	-0.59		
673.2	16.88	17.35	-0.47		
773.2	18.42	18.55	-0.13		
873.2	19.91	19.81	0.10		
973.2	21.52	21.19	-0.33		
1,073.2	23.02	22.72	0.30		
293.2	13.42	12.58	0.84		
373.2	13.67	13.69	-0.02		
473.2	14.16	14.97	-0.81		
573.2	15.13	16.17	-1.04		
673.2	16.39	17.35	-0.96		
773.2	18.00	18.55	-0.55		
873.2	20.17	19.81	0.36		
973.2	22.55	21.19	1.36		
403.2	15.60	14.08	1.52	D. B. Scott, Y. S. Touloukian et al.	Zircaloy-4
452.1	16.30	14.70	1.60		
476.5	14.50	15.01	-0.51		
546.5	18.30	15.85	2.45		
557.6	15.80	15.99	-0.19		
602.6	17.60	16.52	1.08		
649.9	18.50	17.03	1.47		
682.1	19.20	17.45	1.75		
694.3	17.10	17.60	-0.50		
753.2	18.90	18.30	0.60		
770.3	18.90	18.51	0.39		
812.1	19.60	19.03	0.57		
826.5	20.10	19.21	0.89		

Table 4-7. Zircaloy thermal conductivity data base. (Continued)

Temperature (K)	Experimental Thermal Conductivity [W/(m•K)]	Calculated Thermal Conductivity [W/(m•K)]	Difference Between Calculated and Experimental Thermal Conductivity	Reference	Material
982.1	19.70	21.32	-1.62		
1,000.9	20.30	21.59	-1.29		
1,058.1	21.70	22.48	-0.78		

4.4.4 References

4.4-1 S. Nazare, G. Ondracek, and B. Schulz, "Properties of Light Water Reactor Core Melts," *Nuclear Technology, 32*, 1977, pp. 239-246.

4.4-2 W. K. Anderson, C. J. Beck, A. R. Kephart, and J. S. Theilacker "Zirconium Alloys," *Reactor Structural Materials: Engineering Properties as Affected by Nuclear Reactor Service*, ASTM-STP-314, 1962, pp. 62-93

4.4-3 J. N. Chirigos et al., "Development of Zircaloy-4," *Fuel Element Fabrication*, New York: Academic Press, 1961, pp. 19-55.

4.4-4 A. D. Feith, *Thermal Conductivity and Electrical Resistivity of Zircaloy-4*, GEMP-669, October 1966.

4.4-5 C. F. Lucks and H. W. Deem, *Progress Relating to Civilian Applications During June, 1958*, R. W. Dayton and C. R. Tipton, Jr., (eds.), BMI-1273, 1958, pp. 7-9.

4.4-6 A. E. Powers, *Application of the Ewing Equation for Calculating Thermal Conductivity from Electrical Conductivity*, KAPL-2146, April 7, 1961.

4.4-7 D. B. Scott, *Physical and Mechanical Properties of Zircaloy-2 and -4*, WCAP-3269-41, May 1965, pp. 5, 9.

4.4-8 Y. S. Touloukian, R. W. Powell, C. Y. Ho, and P. G. Klemens, *Thermophysical Properties of Matter, Volume 1, Thermal Conductivity*, NewYork: Plenum Press, 1970, pp. 888-889.

4.4-9 S. E. Jensen, *Parametric Studies of Fuel Pin Temperature Response*, IDO-17295, February 1969.

4.4-10 H. Korber and H. E. Unger, "Sensitivity Study on Core Heatup and Meltdown by Variation of Heat Conductivity and Thermal Emissivity," *Transactions of the American Nuclear Society, 18*, 1974, pp. 234-235.

4.5 Thermal Expansion, Density and Their Relation to Texture (CTHEXP, CDEN)

The model described herein calculates components of the thermal expansion strain for single crystal zircaloy. By use of pole figures to ascertain the average orientation of single crystals in a multicrystalline sample, such as zircaloy fuel rod cladding, these single crystal values may be applied to find the thermal expansion strain of any sample.

Thermal expansion strain, especially in the diametral direction, is important in safety analyses because it is a major factor in determining the pellet cladding gap, and thus the pellet temperature and its stored energy. Since zircaloy is an anisotropic solid, strains parallel and perpendicular to the basal pole direction of single crystal grains are needed to find the diametral strain in a multicrystalline sample. The subcode CTHEXP treats this strain as a tensor and uses pole figures to calculate the thermal expansion strain.

The subroutine CDEN returns the density of zircaloy from room temperature data and thermal expansion strains calculated with the CTHEXP subcode.

4.5.1 Summary (CTHEXP)

A total of six correlations that are functions of temperature only are used to find single crystal thermal strains. In addition, basal plane symmetry ($\varepsilon_{11} = \varepsilon_{22}$) is assumed. The model was developed for as fabricated zircaloy-4, but comparisons with zircaloy-2 and zirconium data also show good agreement for these materials.

The correlations for single crystal thermal strains are:

For 300 < T < 1,083 K,

$$\varepsilon_{11} = 4.95 \times 10^{-6}\, T - 1.485 \times 10^{-3} \tag{4-27}$$

$$\varepsilon_{33} = 1.26 \times 10^{-5}\, T - 3.78 \times 10^{-3} \tag{4-28}$$

where

ε_{11}	=	circumferential thermal expansion (m/m)
ε_{33}	=	axial thermal expansion (m/m)
T	=	temperature (K).

For 1,083 ≤ T ≤ 1244 K,

$$\varepsilon_{11} = \left[2.77763 + 1.09822 \cos\left(\frac{T - 1083}{161}\pi\right)\right] \times 10^{-3} \tag{4-29}$$

$$\varepsilon_{33} = \left[8.76758 + 1.09822\cos\left(\frac{T-1083}{161}\pi\right)\right]\times 10^{-3} \tag{4-30}$$

where the arguments of the cosines are in radians.

For 1,244 K ≤ T ≤ 2098 K,

$$\varepsilon_{11} = 9.7 \times 10^{-6}\,T - 1.04 \times 10^{-2} \tag{4-31}$$

$$\varepsilon_{33} = 9.7 \times 10^{-6}\,T - 4.4 \times 10^{-3}\ . \tag{4-32}$$

For temperatures > 2,098 K, consideration of the volume change associated with melting is required. Since no data have been found, a typical 2% volume increase at melt is assumed. The expressions used for the thermal strain in liquid zirconium (temperatures ≥ 2,098 K) are thus

$$\varepsilon_p = \frac{2}{3}\varepsilon_{11} + \frac{1}{3}\varepsilon_{33} + 0.0067 \tag{4-33}$$

where

ε_p	=	thermal expansion strain in liquid zircaloy (m/m)
ε_{11}	=	circumferential thermal expansion strain of a single crystal of zircaloy at 2,098 K (m/m)
ε_{33}	=	axial thermal expansion strain of a single crystal of zircaloy at 2,098 K (m/m).

Equations (4-29) and (4-30) are used to calculate ε_{11} and ε_{33}.

To obtain cladding strains from these single crystal strains, it is necessary to do a volume weighted averaging over the entire cladding section. Such an averaging requires a pole figure and is described in Section 16.2. The results are

$$\langle\varepsilon'_{11}\rangle = \langle\sin^2\phi\rangle\varepsilon_{11} + \langle\cos^2\theta\cos^2\phi\rangle\varepsilon_{22} + \langle\sin^2\theta\cos^2\phi\rangle\varepsilon_{33} \tag{4-34}$$

$$\langle\varepsilon'_{22}\rangle = \langle\cos^2\phi\rangle\varepsilon_{11} + \langle\cos^2\theta\sin^2\phi\rangle\varepsilon_{22} + \langle\sin^2\theta\sin^2\phi\rangle\varepsilon_{33} \tag{4-35}$$

$$\langle\varepsilon'_{33}\rangle = \langle\sin^2\theta\rangle\varepsilon_{22} + \langle\cos^2\theta\rangle\varepsilon_{33} \tag{4-36}$$

where primed strains refer to the laboratory system (cladding and unprimed strains to the single crystals),

θ	=	angle between the radial direction of the cladding and the c-axis of the single crystals
ϕ	=	angle between the circumferential direction of the cladding and the projection of the c-axis at a grain onto the circumferential--axial plane at the cladding.

As an example, the strains for a typical LWR cladding tube (zircaloy-4) are, for T < 1,083 K

$$\langle \varepsilon'_{11} \rangle = 6.48\times10^{-6}T - 1.95\times10^{-3} \tag{4-37}$$

$$\langle \varepsilon'_{22} \rangle = 5.63\times10^{-6}T - 1.69\times10^{-3} \tag{4-38}$$

$$\langle \varepsilon'_{33} \rangle = 1.04\times10^{-5}T - 3.11\times10^{-3}. \tag{4-39}$$

Equations (4-37) through (4-39) are valid for $<\cos^2\theta> = 0.71013$ and $<\sin^2\phi> = 0.30822$.

Section 4.5.2 contains a review of the literature consulted. The model development is given in Section 4.5.3, and Section 4.5.4 contains a model data comparison with an uncertainty analysis.

4.5.2 Literature Review (CTHEXP)

The most important source is the model on cladding plastic deformation, Section 4.9, where the volume weighted averages of the direction cosines for typical LWR cladding are given. These averages were used with thermal expansion data from an EPRI report by Bunnell[4.5-1] to make the basic model. Since Bunnell does not report data in the beta phase (T > 1,244 K) for circumferential expansion, the data can be used only for an alpha phase model. The EPRI data do not show ε_{11} or ε_{22} equal to zero at 300 K, and therefore each point was shifted by an amount such that this requirement was met. To determine the validity of the resulting data, they were checked against the older data sources of Douglas,[4.5-2] Mehan and Wiesinger,[4.5-3] Scott,[4.5-4] and Kearns.[4.5-5] The correlations given here compare well with those of Douglass and Kearns, as shown in Figures 4-10 through 4-13. The Mehan and Wiesinger data are for plates. To be compared with Equations (4-27) and (4-28), these equations must be converted from single crystal form to plate form. Since Mehan and Wiesinger give no detailed texture information, typical values for texture coefficients from Hann[4.5-6] were used. The results are shown in Table 4-8.

The differences shown in Table 4-8 can be easily explained by the unknown texture differences between the samples from which the data sets were derived.

All data sets had to be adjusted to give $\Delta L = 0$ at 300 K. This was done by adding or subtracting the strain at 300 K. This technique is not exact for engineering strains but results in negligible error when the strains are small, as in the case here.

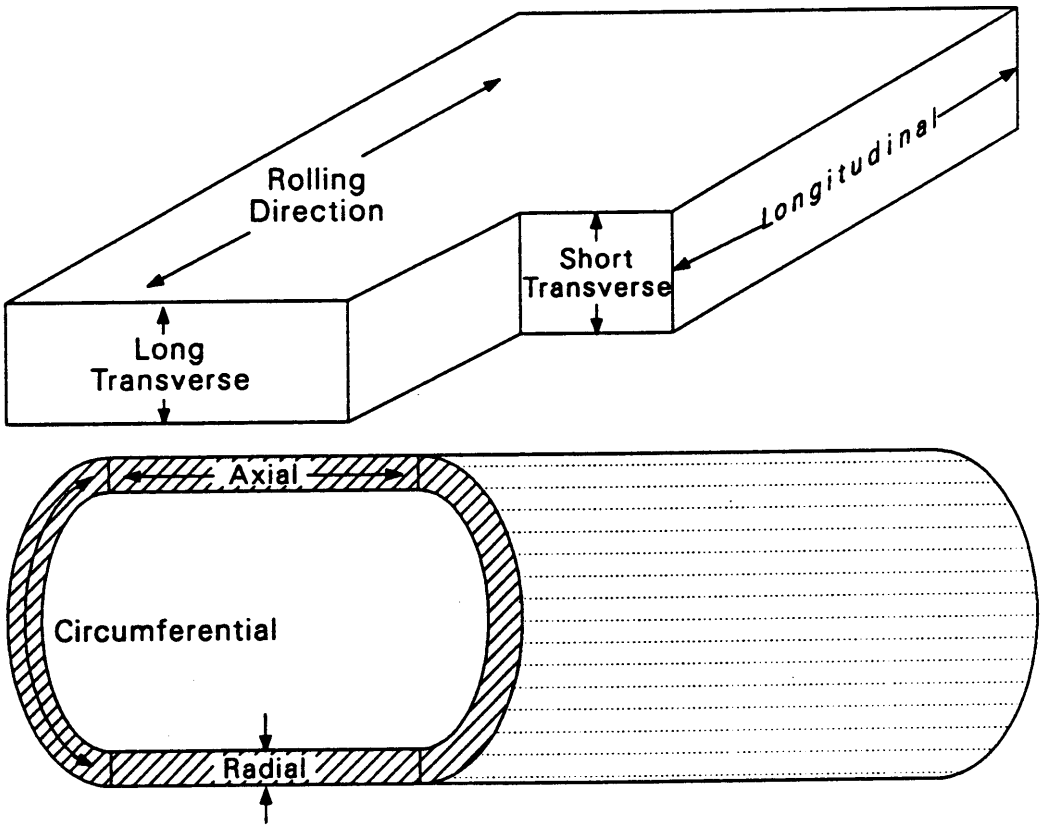

Figure 4-10. Comparison of CTHEXP prediction with Douglass' data in the axial direction.

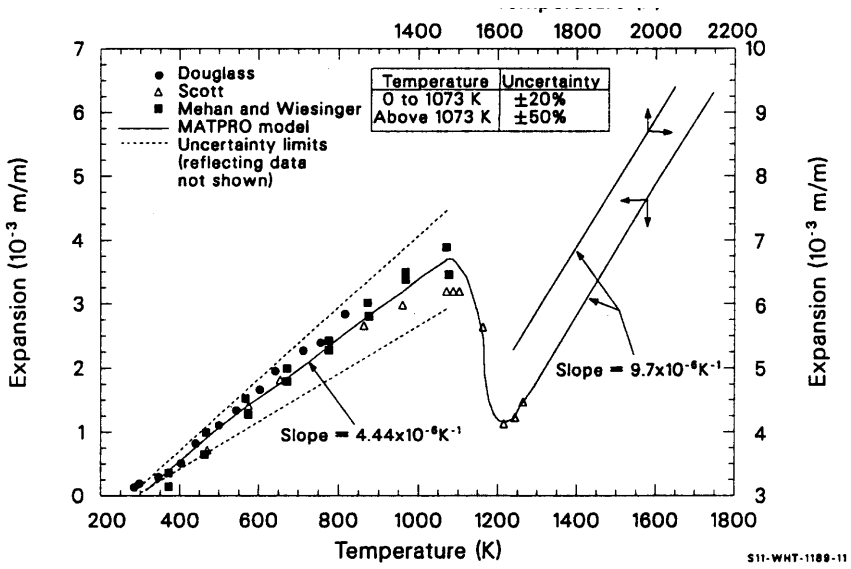

Figure 4-11. Comparison of CTHEXP prediction with Douglass' data in the circumferential direction.

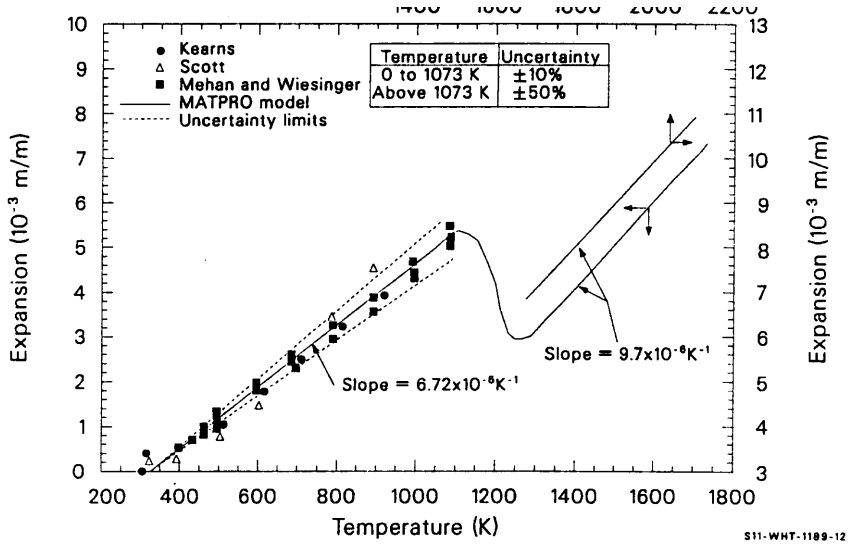

Figure 4-12. Comparison of CTHEXP prediction with Kearns' model in the axial direction.

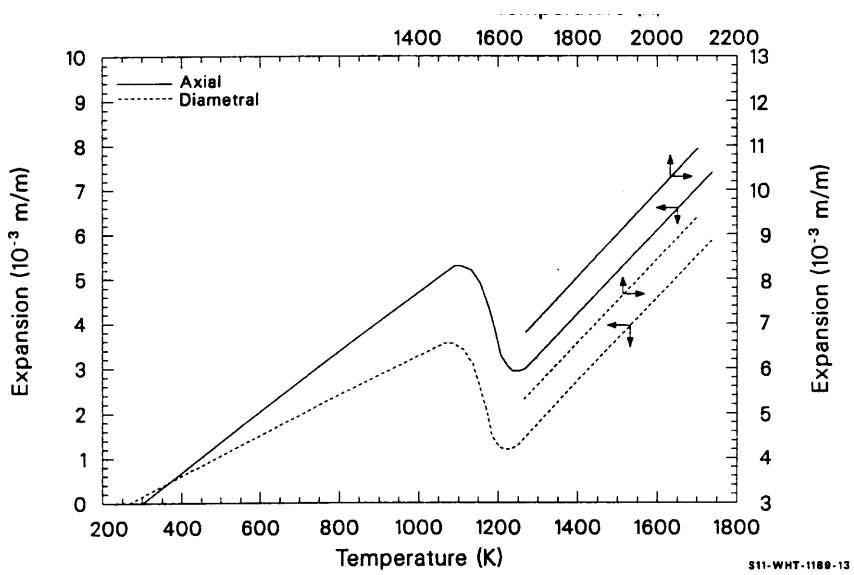

Figure 4-13. Comparison of CTHEXP prediction with Kearns' model in the circumferential direction.

Table 4-8. Comparison of Mehan and Wiesinger plate expansion with MATPRO model.

Direction	Mehan and Wiesinger	MATPRO Model	Difference (%)
Longitudinal	4.62×10^{-6}	$5.41 \times 10^{-}6$	-14.60
Transverse	6.58 x 10-6	7.10×10^{-6}	-7.32

These comparisons show that the Bunnell data are adequate in the alpha phase. Therefore, this data set is used as the data base in the low temperature (T < 1,083 K) range.

In the transition region between the alpha and beta phases (1,083 ≤ T ≤ 1,244 K), the volume strain was found using lattice constants for alpha zirconium from Douglass and for beta zirconium from Kittel.[4.5-7] This strain was divided by 3.0 to find an approximate linear strain, which was assumed to be equal in all three directions. A cosine function was fit to the strains to match the values at the end of the alpha phase and the beginning of the beta phase. For the beta phase, the coefficient of expansion for zirconium from Skinner and Johnston[4.5-8] was used.

The correlations for T > 1,083 K are approximate. However, at these temperatures, the cladding is so soft that typical in-reactor stresses cause a significantly greater strain than the strain due to thermal expansion.

4.5.3 Model Development (CTHEXP)

The model development is divided into three sections, depending on the temperature: an alpha phase region, a transition phase region, and a beta phase region.

4.5.3.1 ***Thermal Expansion in the Alpha Phase.*** The basic equations used to model thermal expansion in the alpha phase are tensor transformation equations relating cladding strain components to single crystal strain components and parameters that describe the distribution of grain orientations in the cladding. The model is based on measured thermal strains in two directions for cladding with known texture. The inverse of the transformation is used to deduce single crystal thermal expansions from data.

Since strain is a second rank tensor, it is necessary to do a formal rotation of axes to describe single crystal strains viewed from a laboratory system. The rotation is shown schematically in Figure 4-14, which was taken from Section 4.6. To derive the various tensors, first consider the transformation necessary to obtain the laboratory unit vectors expressed in terms of the single crystal unit vectors. Since the single crystal is isotropic in planes perpendicular to the c-axis, assume for this transformation that the y-axis (single crystal) is in the same plane as the c-axis and the radial direction of the tube. Primed coordinates refer to those fixed in the laboratory system, and the unprimed coordinates refer to those fixed in the single crystals. The resulting transformation is

$$\hat{x}' = \sin\phi\hat{x} + \cos\theta\cos\phi\hat{y} + \sin\theta\cos\phi\hat{z} \tag{4-40}$$

$$\hat{y}' = -\cos\theta\hat{x} + \cos\theta\sin\phi\hat{y} + \sin\theta\sin\phi\hat{z} \tag{4-41}$$

$$\hat{z}' = -\sin\theta\hat{y} + \sin\theta\cos\theta\hat{z} \tag{4-42}$$

where θ and ϕ are defined in Figure 4-14.

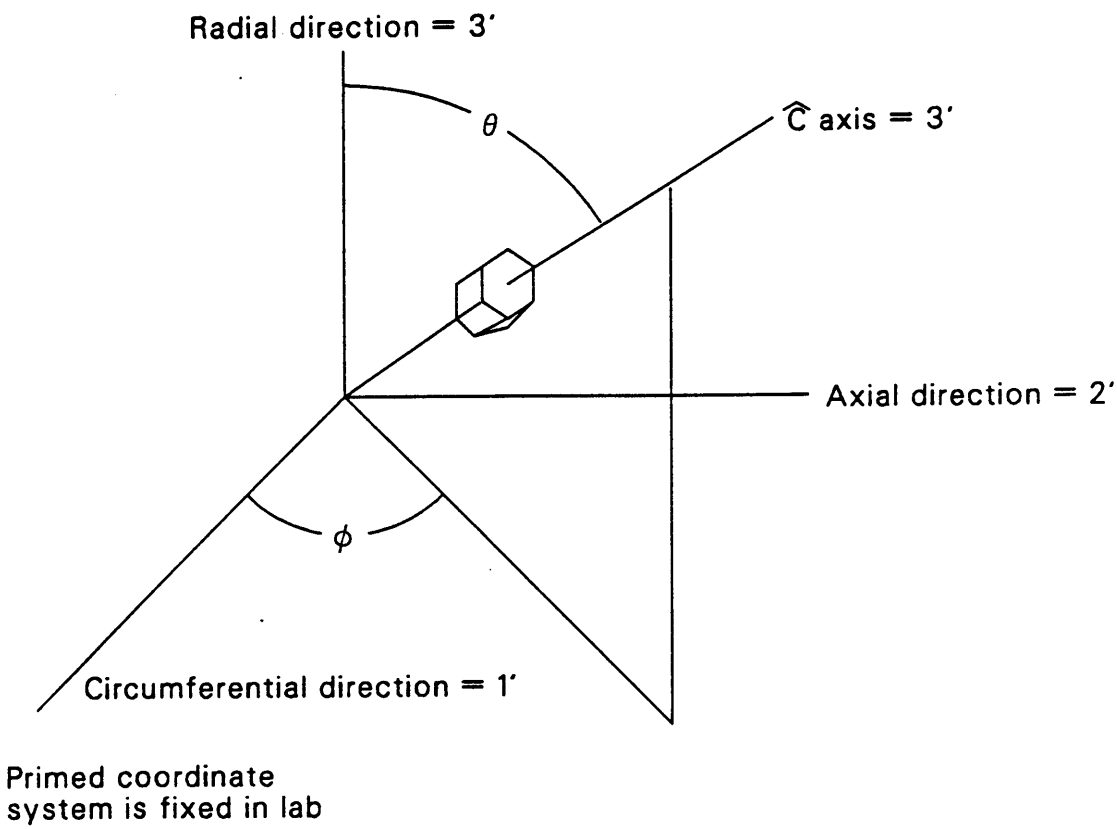

Figure 4-14. Angles and orientation of the unit cell of zircaloy relative to a system of coordinates fixed in the lab frame of reference.

Equations (4-40) through (4-42) show a first rank tensor transformation.

$$\hat{x}_i^i = c_{ij}\hat{x}_j \tag{4-43}$$

where c_{ij} is the transformation coefficient.

The corresponding transformations for strains (2nd-rank tensors) are

$$\varepsilon'_{ij} = \sum_{s=1}^{3}\sum_{t=1}^{3} C_{is}C_{jt}\varepsilon_{st} \tag{4-44}$$

where C_{is} is the coefficient from the first order tensor transformation [Equations (4-40) through (4-42)]. For example, $C_{11} = \sin\phi$, $C_{12} = \cos\theta\cos\phi$, and $C_{13} = \sin\theta\ \cos\phi$.

Applying Equation (4-44) to find ε'_{11} gives

$$\begin{aligned}\varepsilon'_{11} = {} & (C_{11}C_{11}\varepsilon_{11} + C_{12}C_{11}\varepsilon_{21} + C_{13}C_{11}\varepsilon_{31}) + \\ & (C_{11}C_{12}\varepsilon_{12} + C_{12}C_{12}\varepsilon_{22} + C_{13}C_{12}\varepsilon_{32}) + \\ & (C_{11}C_{13}\varepsilon_{13} + C_{12}C_{13}\varepsilon_{23} + C_{13}C_{13}\varepsilon_{33})\end{aligned} \tag{4-45}$$

Substituting the appropriate C_{ij}'s into Equation (4-45) gives

$$\begin{aligned}\varepsilon'_{11} = {} & \sin^2\phi\varepsilon_{11} + \cos\theta\cos\phi\sin\phi\varepsilon_{21} + \sin^2\theta\cos\phi 3\varepsilon_{31} + \\ & \sin\phi\cos\theta\cos\phi\varepsilon_{12} + \cos^2\theta\cos^2\phi\varepsilon_{22} + \sin^2\theta\cos\phi\varepsilon_{32} + \\ & \sin\phi\cos\phi\sin\theta\varepsilon_{13} + \cos\theta\cos\phi\sin\theta\varepsilon_{23} + \sin^2\theta\cos^2\phi\varepsilon_{33}\end{aligned} \tag{4-46}$$

The volume weighted averages of the strain tensors are needed. These are given by

$$\langle\varepsilon'_{ij}\rangle = \int_0^{2\pi}\int^{\pi} \varepsilon'_{ij}(\theta,\phi)\,\rho(\theta,\phi)\,\sin\theta d\theta d\phi \tag{4-47}$$

where

$\langle\varepsilon'_{ij}\rangle$	=	volume fraction weighted average of e_{ij} (m/m)
$\varepsilon'_{ij}(\theta,\phi)$	=	thermal expansion strain (m/m)
$\rho(\theta,\phi)$	=	volume fraction of grains with their c-axis oriented in the region $\sin\theta\ d\theta\ d\phi$ about θ and ϕ.

Putting Equation (4-46) into Equation (4-47) gives

$$\begin{aligned}\langle\varepsilon'_{ij}\rangle = {} & \varepsilon_{11}\int_0^{2\pi}\int_0^{\pi}\sin^2\phi\rho(\theta,\phi)\,\sin\theta d\theta d\phi + \\ & \varepsilon_{21}\int_0^{2\pi}\int_0^{\pi}\cos\theta\cos\phi\sin\phi\rho(\theta,\phi)\,\sin\theta d\theta d\phi\ldots\end{aligned} \tag{4-48}$$

The integral $\int_0^{2\pi}\int_0^{\pi}\varepsilon_{11}\sin^2\phi\rho(\theta,\phi)\,\sin\theta d\theta d\phi = \langle\sin^2\phi\rangle$, the volume weighted average of $\sin^2\phi$. Similarly,

the third integral.

$$\varepsilon_{31}\int_0^{2\pi}\int_0^{\pi}\sin^2\theta\cos\phi\rho(\theta,\phi)\,\sin\theta d\theta d\phi = \langle\sin^2\theta\cos\phi\rangle = \langle\sin^2\theta\rangle\langle\cos\phi\rangle = 0.0 \tag{4-49}$$

because averaged over the 0 to 2π interval, $\cos\phi$ equals zero. In the same way, $\sin\phi$, $\sin\theta$, and $\cos\theta$ are zero. Only a squared function has a nonzero average. These averages may be found with the CTXTUR subcode of Section 16.2, using a pole figure for input texture information.

All nine of the tensor elements $\langle\varepsilon_{ij}\rangle$ may be found using Equations (4-44) and (4-47). The only non-zero ones are listed in Equations (4-34) through (4-36).

$$\langle\varepsilon'_{11}\rangle = \langle\sin^2\phi\rangle\varepsilon_{11} + \langle\cos^2\theta\cos^2\phi\rangle\varepsilon_{22} + \langle\sin^2\theta\cos^2\phi\rangle\varepsilon_{33} \tag{4-50}$$

$$\langle\varepsilon'_{22}\rangle = \langle\cos^2\phi\rangle\varepsilon_{11} + \langle\cos^2\theta\sin^2\phi\rangle\varepsilon_{22} + \langle\sin^2\theta\sin^2\phi\rangle\varepsilon_{33} \tag{4-51}$$

$$\langle\varepsilon'_{33}\rangle = \langle\sin^2\theta\rangle\varepsilon_{22} + \langle\cos^2\theta\rangle\varepsilon_{33}. \tag{4-52}$$

From Section 4.9, the coefficients of the strains in Equations (4-34) through (4-36) may be found for the cladding used by Bunnell. Substituting these values into Equations (4-34) through (4-36), following equations are obtained.

$$\langle\varepsilon'_{11}\rangle = 0.18\varepsilon_{11} + 0.54\varepsilon_{22} + 0.28\varepsilon_{33} \tag{4-53}$$

$$\langle\varepsilon'_{22}\rangle = 0.82\varepsilon_{11} + 0.12\varepsilon_{22} + 0.06\varepsilon_{33} \tag{4-54}$$

$$\langle\varepsilon'_{33}\rangle = 0.34\varepsilon_{22} + 0.66\varepsilon_{33}\ . \tag{4-55}$$

In a single crystal, the circumferential strain, ε_{11}, is equal to the diametral strain, ε_{22}, so Equations (4-53) through (4-55) reduce to

$$\langle\varepsilon'_{11}\rangle = 0.72\varepsilon_{11} + 0.28\varepsilon_{33} \tag{4-56}$$

$$\langle\varepsilon'_{22}\rangle = 0.94\varepsilon_{11} + 0.06\varepsilon_{33} \tag{4-57}$$

$$\langle\varepsilon'_{33}\rangle = 0.34\varepsilon_{22} + 0.66\varepsilon_{33}\ . \tag{4-58}$$

Bunnell's data were taken in the laboratory frame. Therefore, Equations (4-56) through (4-58) must be inverted to find the single crystal strains in terms of the cladding strains

$$\varepsilon_{11} = -0.27\langle\varepsilon'_{11}\rangle + 1.27\langle\varepsilon'_{22}\rangle \tag{4-59}$$

$$\varepsilon_{33} = 4.27\langle\varepsilon'_{11}\rangle - 3.27\langle\varepsilon'_{22}\rangle \tag{4-60}$$

$$\varepsilon_{22} = \varepsilon_{11} \quad . \tag{4-61}$$

Bunnell's data, adjusted so the strain is zero at 300 K, are given in Tables 4-9 and 4-10 for circumferential and axial thermal expansion, respectively.

Using the data listed in these tables, the next step is to find the single crystal strains as a function of temperature. Since temperatures in the two tables do not always correspond, it was necessary to use Bunnell's correlations, which he used to fit those data, again adjusting them so the strains are zero at 300 K. A least squares fit was done, with the constraint that the strains are zero at 300 K. The results are given in Equation 4-27 and Equation 4-28.

Equations 4-27 and 4-28 are the models for the alpha phase of zircaloy single crystals. If one has a pole figure for cladding, Equations (4-47) through (4-49) may be used to find the cladding thermal expansion, remembering that $\varepsilon_{22} = \varepsilon_{11}$.

4.5.3.2 ***Thermal Expansion in the Transition Region.*** To obtain single crystal thermal expansion, both the axial and circumferential cladding thermal expansions are necessary. While axial data in the transition region are available, circumferential data are not. Due to this lack of data and the insignificance of thermal strain at these temperatures, an approximation was made.

For zirconium in the alpha phase at 1,123 K, the Douglass[4.5-2] correlation gives the lattice constants as c = 5.193 x 10^{-10}m and a = 3.245 x 10^{-10}m, giving a volume of 47.356 x 10^{-30}m^3. Kittel[4.5-7] gives the lattice constant for beta zirconium at the same temperature as 3.61 x 10^{-10}m, implying a unit cell volume of 47.046 x 10^{-30} m^3. This decrease in volume as the material changes from the alpha close packed structure to the generally more open beta body centered cubic is surprising, although it has been reported by many[4.5-2,4.5-4,4.5-8] The volume strain is ~0.66%, in good agreement with Skinner and Johnston.[4.5-8] To model the transition region, it is assumed that each dimension contributes equally to this volume strain

Table 4-9. Bunnell's circumferential thermal expansion data.

Temperature (K)	$\varepsilon_{11}\times10^{-3}$ (unitless)	Temperature (K)	$\varepsilon_{11}\times10^{-3}$ (unitless)
394.15	1.806	616.15	2.326
398.15	1.136	620.15	2.516
401.15	1.266	625.15	1.916
405.15	0.716	627.15	2.926
439.15	1.336	663.15	2.636
444.15	1.516	667.15	2.826
444.15	2.206	671.15	2.226
447.15	0.926	673.15	3.396
481.15	1.616	708.15	2.986

Table 4-9. Bunnell's circumferential thermal expansion data. (Continued)

Temperature (K)	$\varepsilon_{11}\times10^{-3}$ (unitless)	Temperature (K)	$\varepsilon_{11}\times10^{-3}$ (unitless)
485.15	1.786	712.15	3.126
488.15	1.196	716.15	2.516
488.15	2.196	718.15	3.736
523.15	1.876	751.15	3.266
528.15	2.016	755.15	3.456
531.15	1.416	759.15	2.856
532.15	2.516	761.15	3.916
568.15	2.096	794.15	3.646
572.15	2.216	797.15	3.756
577.15	1.626	802.15	3.166
579.15	2.776	804.15	4.346
836.15	4.026	964.15	4.806
840.15	4.096	969.15	5.026
844.15	3.476	972.15	4.376
846.15	4.396	975.15	4.676
878.15	4.086	1008.15	5.006
881.15	4.436	1013.15	5.326
885.15	3.786	1017.15	4.656
888.15	4.506	1019.15	4.616
920.15	4.606	1044.15	4.736
925.15	4.716	1044.15	4.876
929.15	4.136	1044.15	5.646
931.15	4.706	1044.15	5.406

Table 4-10. Bunnell's axial thermal expansion data.

Temperature (K)	$\varepsilon_{11}\times10^{-3}$ (unitless)	Temperature (K)	$\varepsilon_{11}\times10^{-3}$ (unitless)
376.15	0.461	569.15	1.321
380.15	0.421	569.15	1.621
389.15	0.531	578.15	1.311
396.15	0.461	579.15	1.631
396.15	0.611	581.15	1.401
398.15	0.481	588.15	1.731
403.15	0.561	599.15	1.451
406.15	0.481	604.15	1.661
411.15	0.581	604.15	1.811
421.15	0.591	613.15	1.901
424.15	0.661	616.15	1.571
428.15	0.741	620.15	1.841
436.15	2.061	627.15	1.551
441.15	0.681	629.15	1.461
444.15	0.811	630.15	1.921
445.15	0.671	646.15	1.701
449.15	0.691	646.15	2.031
456.15	0.901	651.15	1.851
462.15	0.941	653.15	2.111
466.15	0.801	663.15	1.841
468.15	0.901	663.15	2.031
477.15	1.031	671.15	2.151
482.15	0.901	673.15	1.831
489.15	1.121	675.15	1.871
490.15	0.911	686.15	2.221
496.15	1.201	691.15	1.991
504.15	1.201	694.15	2.271

Table 4-10. Bunnell's axial thermal expansion data. (Continued)

Temperature (K)	$\varepsilon_{11}\times10^{-3}$ (unitless)	Temperature (K)	$\varepsilon_{11}\times10^{-3}$ (unitless)
506.15	1.021	697.15	2.221
511.15	1.181	704.15	2.061
512.15	1.251	707.15	2.111
523.15	1.111	711.15	2.351
524.15	1.351	718.15	2.101
531.15	1.451	721.15	2.111
532.15	1.101	726.15	2.401
535.15	1.131	833.15	2.511
540.15	1.141	734.15	2.251
548.15	1.481	738.15	1.051
550.15	1.211	740.15	2.481
557.15	1.441	749.15	2.531
563.15	1.581	750.15	2.381
760.15	2.351	930.15	3.281
763.15	2.321	932.15	3.221
764.15	2.631	932.15	3.471
771.15	2.691	946.15	3.431
776.15	2.481	948.15	3.601
782.15	2.721	955.15	3.661
790.15	2.751	961.15	3.741
794.15	2.591	963.15	3.521
804.15	2.611	964.15	3.691
804.15	2.811	973.15	3.541
806.15	2.601	973.15	3.741
812.15	2.851	975.15	3.451
819.15	2.721	991.15	3.671
826.15	2.961	991.15	3.801
828.15	2.941	998.15	3.931

Table 4-10. Bunnell's axial thermal expansion data. (Continued)

Temperature (K)	$\varepsilon_{11}\times10^{-3}$ (unitless)	Temperature (K)	$\varepsilon_{11}\times10^{-3}$ (unitless)
835.15	2.781	1003.15	3.581
843.15	3.031	1007.15	3.781
844.15	2.821	1007.15	3.851
848.15	2.761	1015.15	3.941
851.15	3.081	1017.15	3.081
862.15	2.961	1021.15	3.711
868.15	3.171	1032.15	3.901
869.15	3.191	1035.15	3.961
877.15	3.051	1042.15	4.181
878.15	3.181	1044.15	3.671
882.15	3.261	1047.15	3.821
886.15	3.061	1048.15	4.041
889.15	2.941	1052.15	4.071
890.15	3.321	1052.15	4.421
904.15	3.181	1052.15	4.161
908.15	3.401	1054.15	4.341
910.15	3.401	1084.15	4.461
919.15	3.291		
919.15	3.381		
923.15	3.461		

$$\frac{\Delta l}{l_0} = \frac{1}{3}\frac{\Delta V}{V_0} = \frac{1}{3}\frac{3.1\times10^{-31}}{(3.61\times10^{10})^3} = 2.196\times10^{-3} \tag{4-62}$$

where

Δl = change in length (m)

l_o = reference length (m)

ΔV = change in volume (m^3)

V_o = reference volume (m^3).

At the start of the transition (T = 1,083 K), from Equations (4-27) and (4-28), $\varepsilon_{11} = 3.88\text{x}10^{-3}$ and

ε_{33} = 9.87x10^{-3}; and at the end of the transition, ε_{11} = 1.68x10^{-3} and ε_{33} = 7.67x10^{-3}. A simple pair of correlations fit these numbers.

For 1083 ≤ T ≤ 1244 K,

$$\varepsilon_{11} = \left[2.77763 + 1.09822\cos\left(\frac{T-1083}{161}\pi\right)\right]\times 10^{-3} \tag{4-63}$$

$$\varepsilon_{33} = \left[8.76758 + 1.09822\cos\left(\frac{T-1083}{161}\pi\right)\right]\times 10^{-3} \tag{4-64}$$

where the arguments for the cosines are in radians. There are more significant figures in Equations (4-63) and (4-64) than in other parts of the model to avoid discontinuities, not to reflect more accurate data.

4.5.3.3 ***Thermal Expansion in the Beta Region.*** For the transition region, there are insufficient data to construct a detailed model for the thermal expansion in the beta region. However, the strain due to thermal expansion is relatively unimportant to the total strain at these high temperatures. The model for T > 1,244 K, based on the expansivity for zirconium reported by Skinner and Johnston,[4.5-8] is

$$\varepsilon_{11} = 9.7 \times 10^{-6}\, T - 1.04 \times 10^{-2} \tag{4-65}$$

$$\varepsilon_{33} = 9.7 \times 10^{-6}\, T - 4.4 \times 10^{-3}\,. \tag{4-66}$$

4.5.4 Model Data Comparison and Uncertainty (CTHEXP)

The only data to which the model is compared are from Bunnell's correlations in the alpha phase. The predictions of the model using Equations (4-27) and (4-28) are compared with the data predictions in Tables 4-11 and 4-12 using Bunnell's correlations and Equations (4-67) and (4-68). The first table is for circumferential strain, and the second is for axial strain; both tables are for a single crystal.

From these tables, the standard error of estimate is ± 12% for the circumferential direction and ± 8% for the axial direction. These uncertainties are somewhat artificial, since the model is compared to its own data base.

In the transition region and the beta phase, the uncertainty is expected to be much larger. An uncertainty of ± 50% was arbitrarily assigned to these regions until appropriate data are available for a better model.

4.5.5 Density (CDEN)

The CDEN function determines zirconium density from room temperature data and the thermal expansion strains calculated with the CTHEXP subroutine. By definition

$$\rho = \frac{m}{V} \tag{4-67}$$

where

ρ	=	density (kg/m^3)
m	=	mass of a sample of material (kg)
V	=	volume of the given mass of material (m^3).

Table 4-11. Comparison of model predictions and Bunnell's alpha phase data in the diametral direction.

Temperature (K)	Model (Unitless)	(Bunnell) (Unitless)	(Bunnell-Model)/Model
300	0	0	--
400	0.0007	0.0009	0.28
500	0.0014	0.0016	0.14
600	0.0021	0.0022	0.05
700	0.0028	0.0028	0.00
800	0.0035	0.0035	0.00
900	0.0043	0.0043	0.00
1,000	0.0050	0.0050	0.00
1,100	0.0057	0.0055	-0.04

Table 4-12. Comparison of model predictions and Bunnell's alpha phase data in the axial direction.

Temperature (K)	(Model)	(Bunnell)	
300	0	0	--
400	0.0005	0.0006	0.20
500	0.0011	0.0011	0.00
600	0.0016	0.0016	0.00
700	0.0022	0.0021	-0.05
800	0.0027	0.0027	0.00
900	0.0032	0.0032	0.00
1,000	0.0038	0.0038	0.00
1,100	0.0042	0.0045	-0.07

Thermal expansion changes only the volume. The volume is related to a reference volume by

$$V = V_0 \exp(\varepsilon_x) \exp(\varepsilon_y) \exp(\varepsilon_z) \tag{4-68}$$

where

V_o = volume of the mass m when strains are zero (m^3)

$\varepsilon_x, \varepsilon_y, \varepsilon_z$ = true strains for any orthogonal coordinate system (m/m).

Substitution of Equation (4-68) into Equation (4-67) shows

$$\rho = \rho_0 \exp(-\varepsilon_x) \exp(-\varepsilon_y) \exp(-\varepsilon_z) \tag{4-69}$$

where ρ_0 is the density at any reference temperature (kg/m^3).

Since thermal strains are always much less than one,

$$\rho \approx \rho_0 (1-\varepsilon_x-\varepsilon_y-\varepsilon_z) \ . \tag{4-70}$$

The three orthogonal strains are provided by CTHEXP, and the reference density used is the value of 6.5510^3 kg/m^3 at 300 K reported by Scott.[4.5-4] This value is consistent with the high temperature value of 6,490 kg/m^3 often used in material properties subcodes. The predicted zircaloy thermal strains are estimated in material properties subroutines to have an expected standard error near 10% of their predicted valves for temperatures below 1,090 K and 50% for higher temperatures.

4.5.6 References

4.5-1 L. R. Bunnell et al., *High Temperature Properties of Zircaloy Oxygen Alloys*, EPRI NP-524, March 1977.

4.5-2 D. L. Douglass, "The Physical Metallurgy of Zirconium," *Atomic Energy Review*, *1*, 4, December 1963, pp. 73-74.

4.5-3 R. L. Mehan and F. W. Wiesinger, *Mechanical Properties of Zircaloy-2*, KAPL-2110, February 1961.

4.5-4 P. B. Scott, *Physical and Mechanical Properties of Zircaloy-2 and -4*, WCAP-3269-41, May 1965.

4.5-5 J. J. Kearns, *Thermal Expansion and Preferred Orientation in Zircaloy*, WAPD-TM-472, November 1965, pp. 17-18.

4.5-6. C. R. Hann et al., *Transient Deformation Properties of Zircaloy for LOCA Simulation*, NP-526, Volume 3, March 1978.

4.5-7 C. Kittel, *Introduction to Solid State Physics*, 3rd Edition, NewYork: John Wiley and Sons, Inc.,

1966, p. 29.

4.5-8 G. B. Skinner and H. L. Johnston, "Thermal Expansion of Zirconium Between 298 and 1,600 K," *Journal of Chemical Physics, 21*, August 1953, pp. 1383-1384.

4.6 Elastic Moduli (CELMOD, CSHEAR, AND CELAST)

Elastic moduli are required to relate stresses to strains. The elastic moduli are defined by the generalized form of Hooke's law as elements of the fourth rank tensor that relates the second rank stress and strain tensors below the yield point. In practice, cladding is frequently assumed to be an isotropic material. In such a case, only two independent elastic moduli are needed to describe the relation between elastic stress and strain. These two constants, the Young's modulus and the shear modulus, are calculated by the functions CELMOD and CSHEAR. Elements of the tensor necessary to describe anisotropic cladding are calculated by the subroutine CELAST.

4.6.1 Summary

Cladding elastic moduli are affected primarily by temperature and oxygen content. Fast neutron fluence, cold work, and texture effects are also included in the models described herein; but they are not as important as temperature and oxygen content for typical LWR fuel rod cladding. The models are based primarily on data published by Bunnell et al.,[4.6-1] Fisher and Renken,[4.6-2] Armstrong and Brown,[4.6-3] and Padel and Groff,[4.6-4] since these data include the best description of texture for the temperature range in which they were used. Data from several other sources[4.6-5 to 4.6-11] are used to evaluate the expected standard error of the CELMOD and CSHEAR codes and to estimate the effect of fast neutron fluence.[4.6-12] To calculate zircaloy elastic moduli at temperatures greater than the melting temperature of zircaloy (2,098 K), the moduli are set to zero. (Actually, 1.0×10^{-10} is used to avoid dividing by zero.)

The expressions used in the CELMOD subcode to calculate the isotropic Young's modulus are:

a. In the alpha phase,

$$Y = (1.088 \times 10^{11} - 5.475 \times 10^{7}\, T + K_1 + K_2)/K_3 \qquad (4\text{-}71)$$

b. In the beta phase,

$$Y = 9.21 \times 10^{10} - 4.05 \times 10^{7}\, T \qquad (4\text{-}72)$$

where

Y	=	Young's modulus for zircaloy-2 and -4 with random texture (Pa)
T	=	cladding temperature (K)
K_1	=	modification to account for the effect of oxidation (Pa)
K_2	=	modification to account for the effect of cold work (Pa)

K_3 = modification to account for the effect of fast neutron fluence (unitless).

In the alpha plus beta phase, Y is the value obtained by linear interpolation of values calculated at the alpha to alpha plus beta and the alpha plus beta to beta boundaries.

The expressions used to model the effects of oxidation, cold work, and fast neutron fluence are

$$K_1 = (6.61 \times 10^{11} + 5.912 \times 10^{8}\ T)\ \Delta \tag{4-73}$$

$$K_2 = -2.6 \times 10^{10}\ C \tag{4-74}$$

$$K_3 = 0.88 + 0.12 \exp\left(-\frac{\Phi}{10^{25}}\right) \tag{4-75}$$

where

Δ = average oxygen concentration minus oxygen concentration of as-received cladding (kg oxygen/kg zircaloy). As-received oxygen concentrations are so small (0.0012 kg oxygen/kg zircaloy) that the exact magnitude of the as-received concentration will not affect the correlation predictions.

C = cold work (unitless ratio of areas)

Φ = fast neutron fluence (n/m^2).

The standard error of the CELMOD code is 6.4×10^{9} Pa.

The expressions used in the CSHEAR subcode to calculate the isotropic shear modulus are:

a. In the alpha phase,

$$G = \frac{(4.04\times10^{10} - 2.168\times10^{7}T + K_1 + K_2)}{K_3} \tag{4-76}$$

b. In the beta phase,

$$G = 3.49 \times 10^{10} - 1.66 \times 10^{7}\ T\ . \tag{4-77}$$

In the alpha plus beta phase, G is the value obtained by linear interpolation of values calculated at the alpha to alpha plus beta and the alpha plus beta to beta boundaries, where the other terms have been defined in conjunction with Equations (4-71) and (4-72).

The expression used to model the effect of oxidation for shear modulus is

$$K_1 = (7.07 \times 10^{11} - 2.315 \times 10^{8}\ T)\ \Delta \tag{4-78}$$

where the terms have been previously defined. The standard error of the CSHEAR code is 9 x 10^9 Pa.

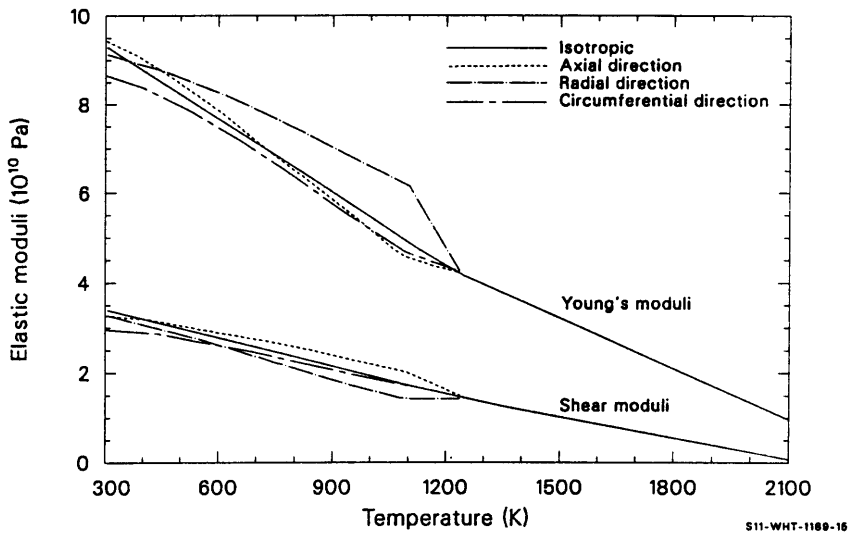

Figure 4-15. Elastic moduli for isotropic material compared to corresponding moduli for typical PWR cladding.

The subcode CELAST calculates elastic compliance constants for isotropic cladding. This subcode is discussed in the model development Section 4.15 because it is the basis for the much simpler CELMOD and CSHEAR codes. The elastic moduli predicted by CELAST for typical textures are reasonably close to the moduli for isotropic cladding. Figure 4-15 illustrates this. The solid lines represent the Young's and shear moduli for isotropic (random texture) material. The six broken lines represent reciprocal compliance constants corresponding to diagonal elements of the traditional S-matrix. Three of these quantities may be interpreted as the apparent Young's moduli for stresses in the direction indicated, and the other three may be interpreted as the apparent shear moduli for shears acting normal to the direction indicated. The only modulus which departs significantly from the isotropic moduli is the Young's modulus in the radial direction. It should be noted that this modulus was based on zirconium single crystal data because appropriate zircaloy data are not available. The axial and circumferential Young's moduli are based on zircaloy-4 data, and they are very similar to the isotropic Young's modulus. The increased Young's modulus in the radial direction is not expected to affect code predictions, even if zircaloy data do confirm the difference shown by the zirconium data.

Details of the elastic modulus models are presented in the following sections. Section 4.6.2 is a review of available data, and Section 4.6.3 describes the model development. Section 4.6.4 is a comparison of the model and its data base. Uncertainties are discussed in Section 4.6.5.

4.6.2 Review of Available Data

Elastic moduli measurements may be classified as either static or dynamic. The static moduli are based on measurements of stress and strain under conditions which can, in principle, be representative of

in-reactor cladding. However, the accuracy of the static moduli are typically limited by the accuracy of the measurement of the strain. Dynamic measurements avoid this difficulty by vibrating a sample of known dimensions in a resonant mode and inferring the moduli from accurate measurements of resonant frequency. The advantage in accuracy of the dynamic measurements is somewhat compromised by the fact that these measurements are made with the small cyclic strains associated with resonant modes. To date, static measurements have not achieved sufficient accuracy to show significant discrepancies with the dynamic measurements, so the dynamic measurements are used as a basis for the models discussed herein.

The most complete set of applicable elastic moduli measurements available are the dynamic measurements of zirconium single-crystal moduli by Fisher and Renken.[4.6-2] Measured values of the stiffness moduli,[a] C_{11}, C_{33}, C_{44}, C_{13}, and C_{12}, are reported at 50 K intervals from 4 K to the alpha plus beta phase transition at 1,135 K. The C_{11}, C_{33}, C_{44}, and C_{13} moduli vary almost linearly with temperature between 300 and 1,135 K, while the C_{12} modulus is reported to increase in a nonlinear fashion with temperature. Least-squares polynomial fits to Fisher and Renken's data yield the following correlations when the data at 300 K or greater are used:

$$C_{11} = 1.562 \times 10^{11} - 4.484 \times 10^{7}\ T \tag{4-79}$$

$$C_{33} = 1.746 \times 10^{11} - 3.282 \times 10^{7}\ T\ . \tag{4-80}$$

$$C_{44} = 3.565 \times 10^{10} - 1.281 \times 10^{7}\ T \tag{4-81}$$

$$C_{12} = 6.448 \times 10^{10} + (3.1882 \times 10^{7} - 1.2318 \times 10^{4}\ T)\ T \tag{4-82}$$

$$C_{13} = 6.518 \times 10^{10} - 6.817 \times 10^{5}\ T \tag{4-83}$$

where C_{ij} are the five independent stiffness moduli for a hexagonal crystal (Pa). (The subscripts 1, 2, 3 refer to orthogonal coordinate axes arranged with the direction labeled 3 parallel to the c-axis. By basal plane symmetry, the 1 and 2 axes are any orthogonal axes in the basal plane.)

Single-crystal constants have not been determined for the high-temperature beta phase, so measurements on polycrystalline materials of unknown texture are used. The models are based on dynamic measurement of the Young's modulus[b] of zirconium by Armstrong and Brown[4.6-3]and by Padel and Groff.[4.6-4] The data from these two sources are reproduced in Tables 4-13 and 4-14. The measurements differ by less than 5% at corresponding temperatures. As discussed in Section 4.6.3, compliance constants (elements of the inverse of the stiffness matrix) are obtained by assuming that the beta phase is isotropic.

The alpha-phase data of Fisher and Renken do not help one to address three of the effects under consideration in this report-the effects of zircaloy-alloying elements, of oxidation, and of variations in texture.

---

a. The definition of elastic stiffness moduli is reviewed in Subsection 4.6.3 in conjunction with the development of the model for the effect of texture variations.

b. Young’s modulus is defined as stress in a given direction divided by strain in the same direction.

These considerations are addressed with the help of Young's moduli measurements in the axial and circumferential direction by Bunnell et al.[4.6-1] Bunnell's data provide important additional information because (a) they were taken with zircaloy cladding, (b) the samples contained various amounts of oxygen, and (c) an estimate of the initial texture of the material is available. Unfortunately, the texture information is only available for the as-received samples and consists of a basal pole figure published by Chapman.[4.6-13]

Bunnell's data were analyzed using the model for the effect of texture developed in Section 4.6.3. The axial and circumferential Young's modulus data are used to establish correlations for the effect of temperature and oxygen on two of the five independent compliance constants. The correlations for as received and homogenized (annealed) cladding agree closely with the compliance constants obtained by inverting Equations (4-79) through (4-83) and lend confidence to the assumption that single crystal zirconium data are a good approximation to zircaloy data when oxygen concentrations are on the order of 0.001 weight fraction. The latter assumption is necessary because the data from zircaloy cladding are not sufficient to determine all five independent compliance constants.

Table 4-13. Beta-phase zirconium Young's Modulus measured by Armstrong and Brown.

Temperature (K)	Young's Modulus (10^{10} Pa)
1,173	4.426
1,223	4.233
1,273	4.047
1,323	3.861
1,373	3.675
1,423	3.488
1,473	3.302

Table 4-14. Beta phase zirconium Young's Modulus measured by Padel and Groff.

Temperature (K)	Young's Modulus (10^{10} Pa)
1,143	4.578
1,156	4.544
1,181	4.311
1,234	4.233
1,266	4.111
1,281	4.122
1,311	3.922
1,340	3.833
1,380	3.611
1,395	3.544
1,409	3.422
1,449	3.278
1,474	3.167

Data relevant to modeling the effect of irradiation and cold work are limited both in quantity and in completeness. The Saxton CoreII Fuel Performance Evaluation[4.6-12] reports elastic moduli at 630 K for irradiated cladding. The moduli were measured with a static method in the axial direction, but no pole figure was provided so the effects of irradiation could not be separated from the effects of texture.

Data relevant to modeling the effect of cold work are contained (but not discussed as such) in the report by Bunnell et al.[4.6-1] The as-received material was cold-worked to about 0.75 and stress-relieved for 4 hours at 770 K.[4.6-13] The homogenized material was completely annealed. Unfortunately, the effect of cold work suggested by Bunnell's dynamic measurements of Young's modulus is opposite to the trend reported by Shober et al.[4.6-10] from static measurements. The dynamic measurements show a slight decrease in Young's modulus with cold work, and the static measurements show a slight increase in Young's modulus with cold work. Since neither source provides usable texture information, it is impossible to tell whether the change with cold work is due to associated changes in texture, to a separate effect associated with the cold work, or to a fundamental difference in the quantity that is being measured with the different techniques. The small decrease implied by Bunnell's data was tentatively included in the models for elastic moduli because of the greater precision of the dynamic data.

Several measurements of Young's and shear moduli were not used in constructing the models for elastic moduli because texture information was not available. The data are useful, however, as an independent test of the two approximate models for isotropic cladding. Busby[4.6-5] reported the axial Young's

modulus for zircaloy-4 between 300 and 645 K for five combinations of cold work and heat treatment. Busby's data are reproduced in Table 4-15. Spasic et al.[4.6-6] reported values of the static elastic modulus from room temperature to 675 K. Their data are reproduced in Table 4-16. The material used by Spasic et al., was not characterized as to cold work or texture. It is assumed that unirradiated material in the annealed condition was used in these tests. Mehan[4.6-7] and Mehan and Wiesinger[4.6-8] reported Young's modulus data from room temperature to 1,090 K. The data were taken with both static and dynamic techniques on unirradiated, vacuum annealed zircaloy-2 plates. Table 4-17 is a summary of Mehan's measurement. Northwood et al.[4.6-9] reported Young's modulus and shear modulus data from 293 to 773 K. The data were obtained with a resonance method and are accompanied by an excellent discussion of the effects of texture. The zircaloy-2 samples were machined from bar stock that had been annealed for 1 hour at 1,061 K. Table 4-18 is a summary of the zircaloy-2 data reported by Northwood et al.

Table 4-15. Young's Modulus measurements by Busby.

Material	Temperature (K)	Young's Modulus (10^{10} Pa)	Effective Cold Work Predicted by the Subcode CANEAL
78% cold work 922 K recrystallization for 5 hours	297	9.686	0%
78% cold work 922 K recrystallization for 5 hours	516	8.018	0%
78% cold work 922 K recrystallization for 5 hours	644	7.515	0%
15-20% cold work 783 K stress relief for 5 hours	297	10.031	5%
15-20% cold work 783 K stress relief for 5 hours	561	8.583	5%
15-20% cold work 783 K stress relief for 5 hours	559	8.349	5%
74% cold work 783 K stress relief for 5 hours	297	9.907	25%
73% cold work 783 K stress relief for 5 hours	644	7.708	25%

Table 4-16. Young's Modulus measurements by Spasic et al.

Temperature (K)	Young's Modulus (10^{10} Pa)
300	10.10
373	9.25
423	8.78
473	8.52
673	7.70
673	*7.40*

4.6.3 Model Development

The equations used in the CELMOD and CSHEAR subcodes are simplified forms of the more complex expressions used in the CELAST subcode. These coefficients, and the closely related elastic stiffness coefficients, are defined by the relations[4.6-14]

$$\varepsilon_i = S_{ij}\sigma_j \tag{4-84}$$

$$\sigma_i = C_{ij}\varepsilon_j \tag{4-85}$$

where

ε_i	=	strain components
σ_i	=	stress components
S_{ij}	=	compliance matrix elements
C_{ij}	=	stiffness matrix elements.

Also, the usual tensor summation convention is assumed.

By inspection of Equations (4-84) and (4-85), it is clear that the compliance matrix is the reciprocal of the stiffness matrix. The author has elected to use compliance coefficients.

4.6.3.1 ***Effect of Texture Variations.*** Texture effects are modeled using techniques which have become fairly standard.[4.6-9,4.6-15,4.6-16] Macroscopic compliance matrix elements for polycrystalline materials are computed as the average of corresponding single-crystal values, weighted by the volume

fraction of grains at each orientation.

Table 4-17. Young's Modulus measurement by Mehan.

Temperature (K)	Young's Modulus (10^{10} Pa)	Method/Direction
300	9.493	Static/not reported
300	9.473	Static/not reported
300	9.459	Static/not reported
300	9.500	Static/not reported
589	7.928	Static/not reported
589	7.790	Static/not reported
297	9.804	Dynamic/transverse
427	9.142	Dynamic/transverse
593	8.273	Dynamic/transverse
704	7.715	Dynamic/transverse
298	9.921	Dynamic/transverse
422	9.238	Dynamic/transverse
594	8.466	Dynamic/transverse
711	7.784	Dynamic/transverse
811	7.246	Dynamic/transverse
300	9.893	Dynamic/transverse
424	9.128	Dynamic/transverse
598	8.294	Dynamic/transverse
703	7.715	Dynamic/transverse
809	7.852	Dynamic/transverse
298	9.452	Dynamic/longitudinal
428	8.659	Dynamic/longitudinal
591	7.535	Dynamic/longitudinal
703	6.991	Dynamic/longitudinal
814	6.356	Dynamic/longitudinal
298	9.445	Dynamic/longitudinal

Table 4-17. Young's Modulus measurement by Mehan. (Continued)

Temperature (K)	Young's Modulus (10^{10} Pa)	Method/Direction
430	8.597	Dynamic/longitudinal
593	7.604	Dynamic/longitudinal
698	6.908	Dynamic/longitudinal
814	6.219	Dynamic/longitudinal
303	9.445	Dynamic/longitudinal
422	8.597	Dynamic/longitudinal
594	7.535	Dynamic/longitudinal
707	6.942	Dynamic/longitudinal
822	6.253	Dynamic/longitudinal

Table 4-18. Elastic moduli measurements by Northwood et al.

Temperature (K)	Young's Modulus Longitudinal (10^{10} Pa)	Young's Modulus Transverse (10^{10} Pa)	Shear Modulus Torsional Resonant Mode (10^{10} Pa)
293	9.67	9.61	3.48
373	9.01	8.98	3.36
473	8.64	8.60	3.18
573	7.99	8.01	2.94
673	7.38	7.34	2.79
773	6.78	6.81	2.53

$$\overline{S'_{ij}} = \iiint S'_{ij}(\theta, \phi)\, \rho(\theta, \phi)\, dv \qquad (4\text{-}86)$$

where

S'_{ij} = macroscopic compliance constants (Pa^{-1})

$S'_{ij}(\theta, \phi)$ = single-crystal compliance constants defined relative to a fixed set of coordinates. Figure 4-16 defines the coordinates and the angles θ and ϕ.

$\rho(\theta,\phi)$ = volume fraction of grains with their c-axis orientated at angles θ and ϕ relative to the fixed set of coordinates.

The volume fraction of grains at angles θ and ϕ can be determined from c-axis pole figures.

$$\rho(\theta,\phi) = \frac{I(\theta,\phi)}{\int_0^{2\pi}\int_0^{\pi} I(\theta,\phi)\sin\theta\, d\theta\, d\phi} \tag{4-87}$$

where $I(\theta,\phi)$ is the diffracted ray intensity of the basal planes as plotted in basal pole figures.

Expressions for the various single-crystal compliance constants, referred to a fixed coordinate system in $S'_{ij}(\theta,\phi)$ Equation (4-86), are obtained by applying standard tensor rotation techniques[4.6-17] to single crystal compliances defined relative to a set of coordinates attached to each grain, S_{ij}.[a] The traditional matrix notation is converted to a formal fourth-rank tensor using the relations listed in Table 4-19.[4.6-14] The coordinate system is rotated with the equation

a. In this section, primed compliance constants are referred to a system of coordinates that are fixed. Unprimed compliance constants are referred to a system of coordinates which are determined by the orientation of each grain, as shown in Figure 4-16.

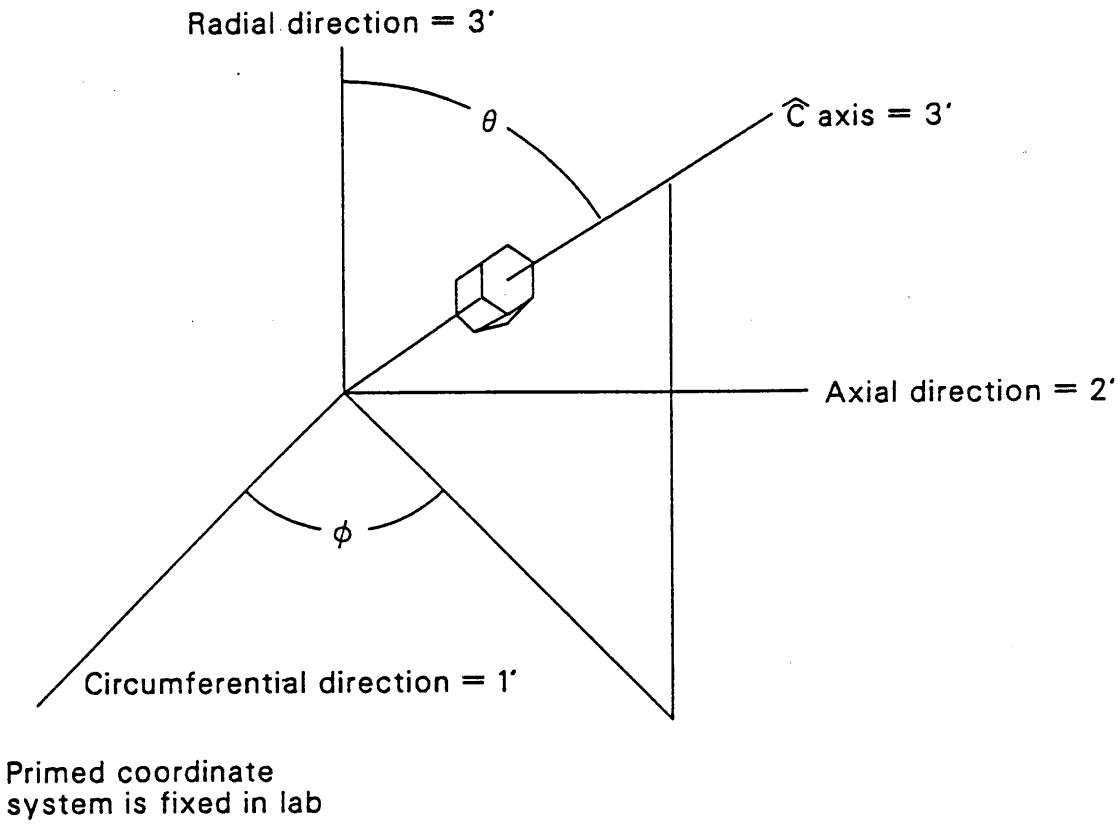

Figure 4-16. Reference directions selected for CELMOD/CSHEAR/CELAST analysis.

$$S'_{ijke}(\theta, \phi) = C_{ir}C_{js}C_{kt}C_{eu}S_{rstu} \tag{4-88}$$

where

$S'_{ijke}(\theta, \phi)$ = single-crystal compliance tensor elements measured with respect to the fixed (primed) coordinate system shown in Figure 4-16 (Pa^{-1})

S_{rstu} = single-crystal compliance tensor elements measured with respect to a coordinate system attached to each grain (Pa^{-1})

C_{ij} = elements of the rotation matrix

$$\begin{bmatrix} \cos\alpha & \sin\alpha\cos\theta & \sin\alpha\sin\theta \\ -\sin\alpha & \cos\alpha\cos\theta & \cos\alpha\sin\theta \\ 0 & -\sin\theta & \cos\theta \end{bmatrix}$$

α = complement of ϕ.

The expressions that result from combining the relations in Table 4-19 and Equations (4-87) and

(4-88) are available in the CELAST subcode listing. As an example, the equation relating the macroscopic elastic compliance constant S_{33} to the single-crystal compliance constants is

$$\overline{S'_{33}} = (1 - 2\langle\cos^2\theta\rangle + \langle\cos^4\theta\rangle)\, S_{11} + (\langle\cos^2\theta\rangle - \langle\cos^4\theta\rangle)\,(2S_{13} + S_{44}) + \langle\cos^4\theta\rangle S_{33} \tag{4-89}$$

where

S'_{33}	=	macroscopic elastic compliance constant relating radial stress to radial strain (Figure 4-16) (Pa^{-1})
$S_{11}, S_{13}, S_{33}, S_{44}$	=	single-crystal compliance constants (Pa^{-1})
$\langle\cos^2\theta\rangle$	=	volume fraction weighted average of the squared cosine of the angle θ (Figure 4-16)
$\langle\cos^4\theta\rangle$	=	volume fraction weighted average of the fourth power of the angle θ.

Table 4-19. Relations between fourth-rank tensor elements and traditional matrix elements.

Complete Compliance Tensor Elements	Traditional Matrix Elements
$(S_{11ij}) =$	$\begin{bmatrix} S_{11} & (1/2)\,S_{16} & (1/2)\,S_{15} \\ (1/2)\,S_{16} & S_{12} & (1/2)\,S_{14} \\ (1/2)\,S_{15} & (1/2)\,S_{14} & S_{13} \end{bmatrix}$
$(S_{12ij}) =$	$\frac{1}{2}\begin{bmatrix} S_{61} & (1/2)\,S_{66} & (1/2)\,S_{65} \\ (1/2)\,S_{66} & S_{62} & (1/2)\,S_{64} \\ (1/2)\,S_{65} & (1/2)\,S_{64} & S_{63} \end{bmatrix}$

Table 4-19. Relations between fourth-rank tensor elements and traditional matrix elements.

Complete Compliance Tensor Elements	Traditional Matrix Elements
$(S_{13ij}) =$	$\frac{1}{2}\begin{bmatrix} S_{51} & (1/2)\,S_{56} & (1/2)\,S_{55} \\ (1/2)\,S_{56} & S_{52} & (1/2)\,S_{54} \\ (1/2)\,S_{55} & (1/2)\,S_{54} & S_{53} \end{bmatrix}$
$(S_{22ij}) =$	$\begin{bmatrix} S_{21} & (1/2)\,S_{26} & (1/2)\,S_{25} \\ (1/2)\,S_{26} & S_{22} & (1/2)\,S_{24} \\ (1/2)\,S_{25} & (1/2)\,S_{24} & S_{23} \end{bmatrix}$
$(S_{23ij}) =$	$\frac{1}{2}\begin{bmatrix} S_{41} & (1/2)\,S_{46} & (1/2)\,S_{45} \\ (1/2)\,S_{46} & S_{42} & (1/2)\,S_{44} \\ (1/2)\,S_{45} & (1/2)\,S_{44} & S_{43} \end{bmatrix}$
$(S_{33ij}) =$	$\begin{bmatrix} S_{31} & (1/2)\,S_{36} & (1/2)\,S_{35} \\ (1/2)\,S_{36} & S_{32} & (1/2)\,S_{34} \\ (1/2)\,S_{35} & (1/2)\,S_{34} & S_{33} \end{bmatrix}$
$(S_{rsij}) =$	S_{srij}

4.6.3.2 ***Effect of Temperature.*** The effect of temperature on single-crystal elastic compliance constants is modeled separately for the alpha and beta phases of zircaloy.

Correlations for two of the five independent elastic constants, S_{11} and S_{44}, are developed from Bunnell's measurements of the axial and circumferential Young's modulus of unoxidized zircaloy-4.[4.6-14] The other three single-crystal alpha phase constants, S_{33}, S_{12}, and S_{13}, are modeled by finding the matrix inverse of the stiffness moduli for zirconium [Equations (4-79) to (4-83)]. The expressions obtained from Bunnell's data are an improvement over the alternate expressions that could be obtained from the zirconium data because Bunnell's data were taken with zircaloy-4 cladding.

To use the zircaloy-4 data, the pole figure provided by Chapman is input to the MATPRO subcode CTXTUR to find the orientation angle averages relating single crystal elastic compliance constants to $\overline{S'_{11}}$' and $\overline{S'_{22}}$ for this cladding. The resultant expressions are:

$$\overline{S'_{11}} = 0.65106\ S_{11} + 0.09210\ S_{33} + (0.12842)(2\ S_{13} + S_{44}) \tag{4-90}$$

$$\overline{S'_{22}} = 0.88030\ S_{11} + 0.01900\ S_{33} + (0.05035)(2\ S_{13} + S_{44}) \tag{4-91}$$

where $\overline{S'_{11}}$, $\overline{S'_{22}}$ are the macroscopic elastic compliance constants (Pa^{-1}).

Inspection of the defining relation for the elastic compliance constant [Equation (4-75)] and the reference direction conventions used in the report (Figure 4-16) shows that $\overline{S'_{11}}$ is the reciprocal of Young's modulus measured in the circumferential direction of the cladding and $\overline{S'_{22}}$ is the reciprocal of Young's modulus measured in the axial direction of the cladding. Thus, Equations (4-86) and (4-87) can be used with Bunnell's measurements of the circumferential and axial Young's modulus of this cladding and the inverse matrix values of S_{33} and S_{13} to find least squares correlations for S_{11} and S_{44} as a function of temperature.

The correlations found from a least squares fit to Bunnells's data are:

$$S_{11} = 0.1028 \times 10^{-10} + T\ (-0.5417 \times 10^{-14} + T\ 0.1476 \times 10^{-16}) \tag{4-92}$$

$$S_{44} = 0.3904 \times 10^{-10} + T\ (-0.8118 \times 10^{-14} + T\ 0.2115 \times 10^{-16}) \tag{4-93}$$

where the terms of the equations have been previously defined.

Equation (4-92) predicts values of S_{11} which vary from zero to 10% below the value of S_{11} predicted by the zirconium data of Fisher and Renken.[4.6-2] Equation (4-93) predicts values of S_{44} which are about 20% above the value of S_{44} predicted by the zirconium data of Fisher and Renken.[4.6-2]

In the beta phase,[a] only two independent single crystal compliance constants are employed. The independent constants are S_{11} and S_{44}. By classical symmetry arguments, $S_{33} = S_{11}$ and $S_{23} = S_{13} = S_{12}$. A correlation for one of the constants is obtained from a least squares fit to the beta phase zirconium Young's modulus data of Armstrong and Brown[4.6-3] and Padel and Groff.[4.6-4] The expression is

$$S_{11}^{-1} = Y = 9.21 \times 10^{10} - 4.05 \times 10^{7}\ T \tag{4-94}$$

where

S_{11} = elastic compliance constant for beta phase zircaloy (Pa^{-1})

a. The beta phase is body-centered cubic and has therefore been assumed isotropic.

Y = Young's modulus for beta phase zircaloy (Pa).

Since no measurements of the shear modulus in beta phase zirconium are available, the second constant, S_{44}, is estimated by extrapolation of an approximate expression for the shear modulus of isotropic alpha phase zirconium to the higher temperatures of the beta phase.

The phase boundaries of the alpha, alpha plus beta, and beta phases are determined with correlations based on data from Figure III.33 of Reference 4.6-18. Compliance constants in the alpha plus beta phase region are obtained by interpolating between these constants at the boundaries of this region.

4.6.3.3 ***Effect of Oxygen.*** The only data available to model the effect of oxygen on the single-crystal compliance constants are Bunnell's measurements of axial and circumferential Young's moduli as a function of oxygen concentration.[4.6-1] The effect of oxygen on the alpha phase compliance constants is modeled in much the same way that Bunnell's data were used to correlate changes in the single crystal compliance constants S_{11} and S_{44} with temperature. The three-step procedure is outlined as follows:

a. Equation (4-91) is used with measured values of the axial Young's modulus ($1/S'_{22}$), approximate (zirconium) values of S_{33}, S_{13}, and S_{44} in the small terms containing these factors and the measured values of oxygen concentration to find a leas-squares fit correlation between S_{11} and the oxygen concentration.

b. Equation (4-90) is used with measured values of the circumferential Young's modulus ($1/S'_{11}$), the expression for S_{11} obtained in step (1), approximate (zirconium) values of S_{33} and S_{13}, and the measured values of oxygen concentration to find a least-squares fit correlation for S_{44} as a function of oxygen concentration. The correlations obtained are

$$1/S_{11} = 1/(S_{11})_o + (6.61 \times 10^{11} + 5.912 \times 10^{8}\ T)\Delta \qquad (4\text{-}95)$$

$$1/S_{44} = 1/(S_{44})_o + (7.07 \times 10^{11} + 2.315 \times 10^{8}\ T)\Delta \qquad (4\text{-}96)$$

where

S_{11}, S_{44} = elastic compliance constants for oxidized zircaloy (Pa^{-1})

$(S_{11})_o$, $(S_{44})_o$ = elastic compliance constants for as-received zircaloy (Pa^{-1})

Δ = average oxygen concentration minus oxygen concentration of as-received cladding (kg oxygen/kg zircaloy).

c. Equation (4-96) is assumed to apply to S_{13}, S_{33}, and S_{12}.

The effect of oxygen in the beta phase has been neglected because no relevant data are available and because an exact knowledge of elastic moduli at the high temperatures of the beta phase is not likely to be important to code applications.

4.6.3.4 ***Effect of Cold Work.*** Bunnell's measurements of the Young's modulus of cold worked, stress-relieved cladding were compared to his Young's modulus measurements of homogenized (annealed)

cladding to estimate cold work effects. Measured values of the axial Young's modulus for the stress relieved material are related to S_{11} with Equation (4-91). The differences between $(S_{11})^{-1}$ in the cold worked material and (S_{11}) computed for annealed material [Equation (4-92)] are assumed to be proportional to the cold work (assumed = 0.5). The correlation resulting from an average of the six low temperature data on as-received cladding is

$$1/S_{11} = 1/(S_{11})_o - 2.6 \times 10^{10}\ C \qquad (4\text{-}97)$$

where

S_{11}	=	elastic compliance constant for cold worked zircaloy (Pa^{-1})
$(S_{11})_o$	=	elastic compliance constant for annealed zircaloy (Pa^{-1})
C	=	cold work (unitless ratio of areas).

No modification of S_{44} was implied by Bunnell's measurements of the Young's modulus in the circumferential direction.

4.6.3.5 ***Effect of Irradiation.*** Data from the Saxton Core II Fuel Performance Evaluation[4.6-12] are used to estimate fast neutron fluence effects on elastic compliance constants. Since no pole figures for this material were found, measured values of the axial Young's modulus for the irradiated material are related to S_{11}, S_{33}, S_{13}, and S_{44} with Equation (4-95). The four compliance constants are assumed to decrease by a single factor due to the fluence, and the factor is determined by comparing the measured values of Young's modulus to the values predicted for unirradiated material. The factor which results from the comparison is:

$$S_{ij}/(S_{ij})_o = 0.88 \qquad (4\text{-}98)$$

where

S_{ij}	=	each of the compliance constants for the irradiated cladding (Pa^{-1})
$(S_{ij})o$	=	each of the compliance constants predicted for unirradiated cladding (Pa^{-1}).

Measured values of fast neutron fluences received by the Saxton rods varied from 2.2 to 3.4 10^{25}n/m^2, and no correlation with the fluence was found. The fluence dependence is therefore modeled by replacing Equation (4-100) with an assumed fluence dependent expression

$$H = 0.88 + 0.12 \exp(-\Phi/10^{25}) \qquad (4\text{-}99)$$

where

H	=	ratio of compliance constants for irradiated material to compliance constants for unirradiated material
Φ	=	fast neutron fluence (n/m^2).

4.6.3.6 ***Derivation of the CELMOD and CSHEAR Codes from the CELAST Code.*** It has been mentioned in Section 4.6.3.2 that the compliance tensor contains only two independent constants for isotropic (random distribution of c-axes) cladding. Moreover, the definition of the compliance tensor implies that the constants may be interpreted as the reciprocals of Young's modulus and the shear modulus

$$(\overline{S'_{ij}})_{isotropic} = \begin{bmatrix} Y^{-1} & a & a & 0 & 0 & 0 \\ a & Y^{-1} & a & 0 & 0 & 0 \\ 0 & 0 & Y^{-1} & 0 & 0 & 0 \\ 0 & 0 & 0 & G^{-1} & 0 & 0 \\ 0 & 0 & 0 & 0 & G^{-1} & 0 \\ 0 & 0 & 0 & 0 & 0 & G^{-1} \end{bmatrix} \tag{4-100}$$

where

$(S'_{ij})_{isotropic}$ = compliance matrix for isotropic cladding (Pa^{-1})

Y = Young's modulus for isotropic cladding (Pa)

G = shear modulus for isotropic cladding (Pa)

a = $1/Y - 1/2G$ (Pa^{-1}).

Expressions for the isotropic Young's modulus and shear modulus in the alpha phase are obtained by computing S_{11} and S_{44} for the isotropic case with the CELAST code. Isotropic values of the several averages required by the code are computed by taking $I(\theta,\phi) = 1$ in Equation (4-87). The resultant values of the isotropic Young's and shear moduli decreased nearly linearly with temperature for temperatures above 450 K. The isotropic alpha phase Young's and shear moduli are therefore modeled with simple linear correlations obtained by fitting straight lines to their values at 623 and 1023 K. The resultant correlations are:

$$Y = 1.088 \times 10^{10} - 5.475 \times 10^{7}\ T \tag{4-101}$$

$$G = 4.040 \times 10^{10} - 2.168 \times 10^{7}\ T \tag{4-102}$$

where the terms have been defined in Equation (4-100).

Equation (4-102) is extrapolated to the high temperatures of beta phase zircaloy because no high temperature shear modulus data are available. The expression used in CELMOD for the Young's modulus of isotropic cladding is identical to the expression used in the CELAST code [Equation (4-72)].

Expressions for the change in Young's and shear moduli with increased oxygen, cold work, and fast neutron fluence are taken directly from the CELAST code. Expressions for the changes in the reciprocal of S_{11} are applied to Young's modulus, and changes in the reciprocal of S_{44} are applied to the shear modulus.

4.6.4 Comparison of Models and Data Base

Figures 4-17 and 4-18 compare predictions obtained with the CELAST code to the measurements of

axial and circumferential Young's moduli by Bunnell. Predicted moduli increase with increasing oxygen and decrease with increasing temperature. Both predicted and measured axial Young's moduli for homogenized (annealed) cladding at room temperature are larger than the corresponding circumferential Young's moduli, but the difference disappears at temperatures above 800 K. Even at room temperature, the difference is only slightly larger than the standard error of the model predictions. However, the low value of the circumferential Young's modulus is consistent with a minimum in predicted Young's modulus versus c-axis direction reported by Northwood.[4.6-9]

Figure 4-19 is a comparison of the Young's modulus predicted using the CELAST code with the beta phase zirconium data of Armstrong and Brown[4.6-3] and Padel and Groff.[4.6-4] The data show very little scatter, but are based on measurements of the Young's modulus of zirconium. The CELAST code has introduced a slight discontinuity in slope at 1,240 K, the alpha plus beta to beta phase boundary. For higher concentrations of oxygen, this discontinuity would appear at higher temperatures. The discontinuity is significant only in interpreting the physical meaning of the code predictions.

4.6.5 Expected Standard Error of the CELMOD and CSHEAR Codes

An estimate of the uncertainty of the CELMOD code is obtained by computing the standard error[a] of the code with the data of Tables 4-15 through 4-18. For this calculation, the small effects of cold work are ignored. The standard error is 6.4×10^9 Pa. Since (a) the data used to estimate standard error are not used in the data base of the model; (b) the effects of texture, cold work, oxygen, and irradiation are not large compared to temperature effects; and (c) the residuals do not vary in any irregular fashion with temperature, this number is assumed to be a reasonable estimate of the expected standard error of the CELMOD code for in-reactor problems. At normal LWR temperatures, this standard error is 10% of the predicted value.

a. The standard error is estimated with a data set by the expression: [sum of squared residuals/(number of residuals - number of constants used to fit the data)]$^{1/2}$.

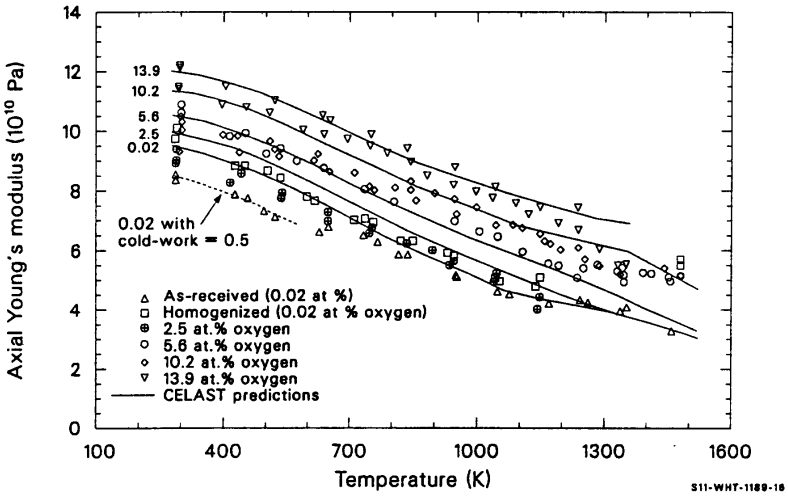

Figure 4-17. Measured values of axial Young's modulus compared to values predicted by the CELAST subcode for several oxygen concentrations and temperatures in the range of 300 to 1,500 K.

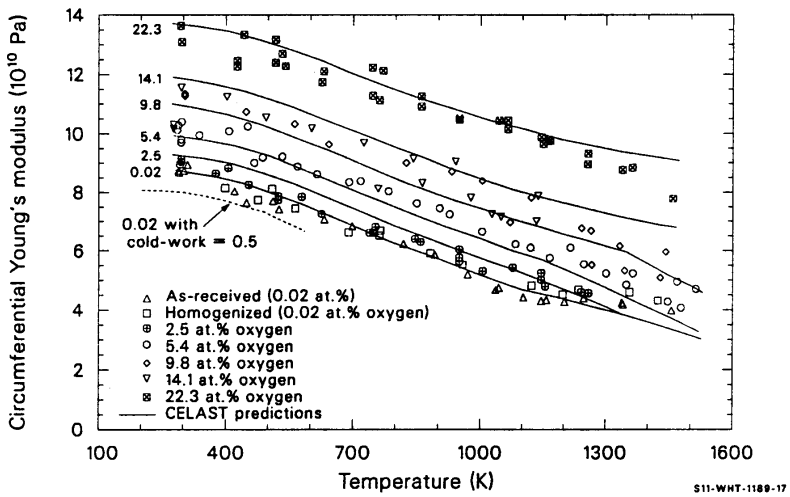

Figure 4-18. Measured values of circumferential Young's modulus compared to values predicted by the CELAST subcode for several oxygen concentrations and temperatures in the range of 300 to 1,500 K.

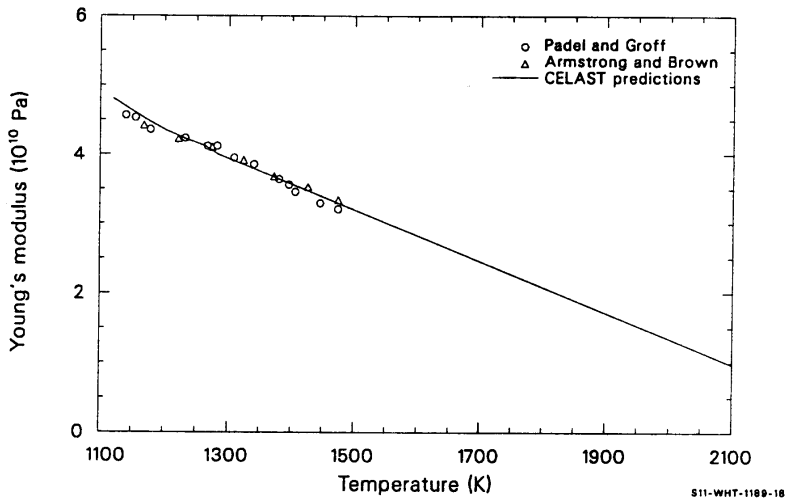

Figure 4-19. Comparison of the Young's modulus predicted with the CELAST code to the beta phase zirconium data of Padel and Groff, and Armstrong and Brown.

The uncertainty of the CSHEAR code is estimated by computing the standard error of the code with a large block of data (214 measurements) reported by Bunnell.[4.6-1] The data were not used in the development of the codes described here because the author was not able to interpret the effect of texture on the torsional wave used by Bunnell to measure shear modulus. The standard error, assuming the cladding was isotropic, is 9 x 10^9 Pa. At normal LWR temperatures, the standard error of the isotropic shear is 30% of the predicted value.

4.6.6 References

4.6-1 L. R. Bunnell et al., *High Temperature Properties of Zircaloy Oxygen Alloys*, EPRI NP-524, March 1977.

4.6-2 E. S. Fisher and C. J. Renken, "Single-Crystal Elastic Moduli and the HCP-BCC Transformation in Ti, Zr, and Hf," *Physical Review, 135 2A*, July 20, 1964, pp. A482-494.

4.6-3 P. E. Armstrong and H. L. Brown, "Dynamic Young's Modulus Measurements above 1000°C on Some Pure Polycrystalline Metals and Commercial Graphites," *Transactions of the Metallurgical Society of AIME 230*, August 1964, pp. 962-966.

4.6-4 A. Padel and A. Groff, "Variation du Module de Young du Zirconium b en Function de la Temperature," *Journal of Nuclear Materials 59*, 1976, pp. 325-326.

4.6-5 C. C. Busby, *Properties of Zircaloy-4 Tubing*, WAPD-TM-585, December 1966, p. 65.

4.6-6 Z. Spasic et al., *Conference on the Use of Zirconium Alloys in Nuclear Reactors*, Marlanske Lanze, Czechoslovakia, USAEC CONF-681086, 1968, pp. 277-284.

4.6-7 R. L. Mehan, *Modulus of Elasticity of Zircaloy-2 Between Room Temperature and 1000°F*, KAPL-M-RLM-16, July 1958.

4.6-8 R. L. Mehan and F. W. Wiesinger, *Mechanical Properties of Zircaloy-2*, KAPL-2110, February 1961, pp. 11-12.

4.6-9 D. O. Northwood et al., "Elastic Constants of Zirconium Alloys," *Journal of Nuclear Materials, 55*, 1975, pp. 299-310.

4.6-10 F. B. Shober et al., *The Mechanical Properties of Zirconium and Zircaloy-2*, BMI-1168, 1957.

4.6-11 C. L. Whitmarsh, *Review of Zircaloy-2 and Zircaloy-4 Properties Relevant to N. S. Savannah Reactor Design*, ORNL-3281, 1962.

4.6-12 W. R. Smalley, *Saxton Core II Fuel Performance Evaluation Part I: Materials*, WCAP-3385-56, September 1971.

4.6-13 R. H. Capman, *Characterization of Zircaloy-4 Tubing Procured for Fuel Cladding Research Programs*, ORNL/NUREG/TM-29, July 1976.

4.6-14 G. E. Dieter, *Mechanical Metallurgy*, New York: McGraw-Hill Book Company, Inc., 1976.

4.6-15 J. J. Kearns, *Thermal Expansion and Preferred Orientation in Zircaloy*, WAPD-TM-472, November 1965.

4.6-16 H. S. Rosenbaum and J. E. Lewis, "Use of Pole Figure Data to Compute Elasticity Coefficient of Zirconium Sheet," *Journal of Nuclear Materials, 67*, 1977, pp. 273-282.

4.6-17 R. B. Leighton, *Principles of Modern Physics*, New York: McGraw-Hill Book Company, Inc., New York, 1959.

4.6-18 H. M. Chung et al., "Mechanical Properties of Zircaloy Containing Oxygen," *In Light-Water-Reactor Safety Research Program: Quarterly Progress Report for January-March 1976*, ANL-76-49.

4.7 Axial Growth (CAGROW)

A model for calculating the fractional change in length of zircaloy tubes due to irradiation induced growth is presented in this section. Effects of fast neutron fluence, tubing texture, cladding temperature, and cold work are included and apply equally well to zircaloy-2 and zircaloy-4. The change in length of commercial fuel rods due to irradiation growth is small; however, it can be a significant fraction of the clearance between the rod and the top and bottom assembly nozzles. Contact with the nozzles can cause rods to bow and possibly fail at points where rods contact each other.

4.7.1 Summary

The following equation has been developed to model the irradiation growth of zircaloy tubes at temperatures between 40 and 360 °C (the normal range of cladding temperatures in LWRs).

$$\Delta L/L = A\,[\exp(240.8/T)]\,(\Phi t)^{1/2}\,(1 - 3f_z)\,(1 + 2.0\,CW) \qquad (4\text{-}103)$$

where

$\Delta L/L$	=	fractional change in length due to growth
A	=	1.407×10^{-16} $(n/m^2)^{1/2}$
T	=	cladding temperature (K)
Φ	=	fast neutron flux (n/m^2s) (E > 1.0 MeV)
t	=	time (s)
f_z	=	texture factor[a] for the tubing axis
CW	=	cold work (fraction of cross sectional area reduction).

Axial growth for temperatures below 40C is approximated by using T = 40°C in Equation (4-103), and growth above 360°C is approximated by using T = 360°C.

A comparison of values calculated by the CAGROW subroutine for fully annealed material with experimental results is presented in Figure 4-20. Comparison with the data shown from cold worked tubes was not possible because the exact amount of cold work was not reported.

4.7.2 Background and Approach

The irradiation growth of zircaloy cladding appears to be quite sensitive to texture; therefore, the effects of texture were considered first. The data were normalized to a standard texture (f_z = 0.05) before considering other effects on axial growth. The model was developed further by modeling the effects of fluence and irradiation temperature on the growth of annealed specimens. Finally, the effect of cold work was modeled after removing the effects of texture, fluence, and temperature from the cold worked specimen data, using the model based on annealed specimens. (The data were normalized to a texture of 0.05, a fluence of 2×10^{25} n/m2, and a temperature of 300°C.) It should be noted, however, that the effect of cold work may not be treated completely, since the limited data base did not allow treatment of interactions between cold work and fluence, temperature, and texture.

In CAGROW, it is assumed that fast neutron flux and temperature both affect the growth rate by varying the concentration of interstitials which are free to migrate and cause growth. Since theoretical considerations imply a complex relation between temperature, fast neutron flux, time, and rate of growth, an empirical approach was used to approximate these effects. An empirical approach was also used to model the effect of cold work on zircaloy tube growth. The limited data were fit using an independent factor of the form (1 + constant x cold work), the least complex form consistent with the data available. The main conclusion is that cold work increases the rate of growth at low fluence. At higher fluences, the growth rate of annealed tubing may decrease rapidly. Cold-worked tubing continues to grow at higher fluences at nearly the rate established during early radiation.

4.7.3 Review of Experimental Data

Samples of zirconium, zircaloy-2, and zircaloy-4 irradiated in a fast neutron flux (E > 1 MeV) to flu-

a. f_z is the effective fraction of cells aligned with their <0001> axis parallel to the tubing axis, as determined by ray diffraction analysis. A value of f_z = 0.05 is typical.[4.7-1]

ences of 10^{25} n/m^2 show typical axial growth on the order of 0.1% of length or less. Since the effects of fuel-cladding mechanical interactions and pressure differentials across the cladding compete with the smaller effects of irradiation growth, the relatively plentiful data[4.7-2 to 4.7-4] are not directly useful in

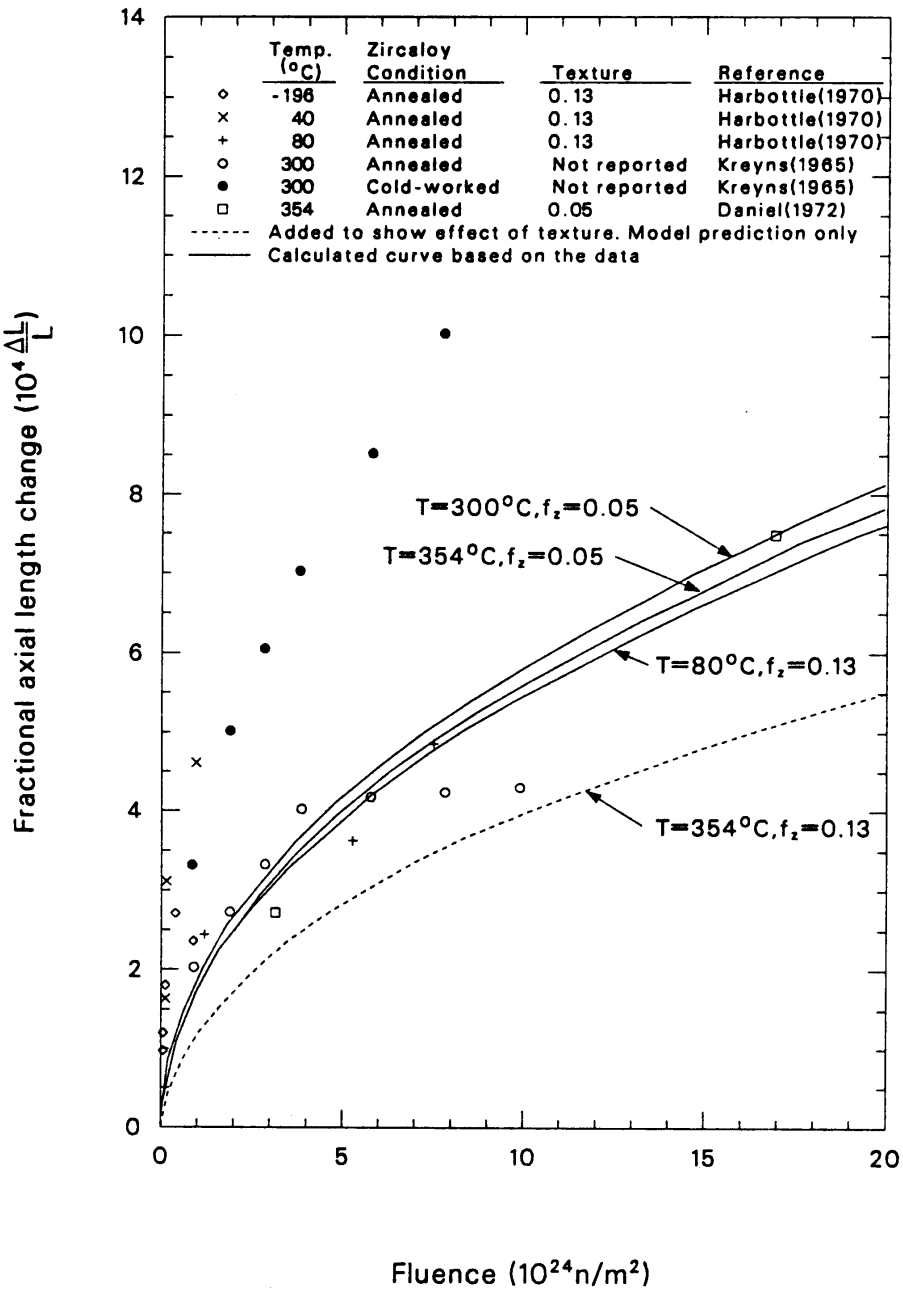

Figure 4-20. Model predictions and measured values of zircaloy tube axial growth as a function of fast neutron fluence, irradiation temperature, cold work, and texture coefficient, f_z.

smaller effects of irradiation growth, the relatively plentiful data[4.7-2 to 4.7-4] are not directly useful in determining the change in cladding length due to irradiation growth. Data on thimble tubes or other structural elements relatively free of confounding effects would be useful. Table 4-20 summarizes the data used for

development of the model.

Early data on irradiation-induced axial growth of zircaloy-4 tubing at 300°C were obtained by Kreyns.[4.7-5] His experiments indicated that growth of cold-worked tubing is proportional to the square root of the fast neutron fluence up to its maximum fluence (10^{25}n/m^2). Growth of annealed tubing appeared to saturate at a fluence of 4 x 10^{24} n/m^2 and a fractional length change of 4 x 10^{-4}. However, subsequent data taken by other investigators have indicated that saturation is not determined by fluence or net growth.

Harbottle[4.7-6] reported the difference in growth strains of transverse and longitudinal strips cut from zircaloy-2 pressure tubes. The strips were annealed and then irradiated at 196, 40, and 80°C. The basal pole texture was found to be 13% in the direction of the tube axis and 36% in the circumferential direction, both before and after the cutting and annealing process. Harbottle's differential growth strains were converted to absolute values of axial growth strains by using the equation

Table 4-20. Measurements of growth in zircaloy tubing.

Source	ΔL/L (10^{-4})	Differential[a] ΔL/L (10^{-4})	Fast Fluence (10^{22}n/m^{2}s)	Material	Fast Flux (10^{17}n/m^2·s)	Irradiation Temperature (°C)
Kreyns[4.7-5]	2		100	Annealed zircaloy-4	(?)	300
	2.7		200			
	3.3		300			
	4.0		400			
	4.15		600			
	4.2		800			
	4.3		1,000			
	3.3		100	Cold worked zircaloy-4	(?)	300
	5		200			
	6		300			
	7		400			
	8.5		600			
	10		800			

Table 4-20. Measurements of growth in zircaloy tubing. (Continued)

Source	ΔL/L (10^{-4})	Differential[a] ΔL/L (10^{-4})	Fast Fluence (10^{22}n/m^{2}s)	Material	Fast Flux (10^{17}n/m^2·s)	Irradiation Temperature (°C)
Daniel (4.7-1, 4.7-7)	2.7		310	Annealed zircaloy-4	12.5	354
	7.5		1700			
Harbottle (4.7-6)		1.2 ± 0.2	4.9	Annealed zircaloy-2	3	-196
		1.5 ± 0.3	9.7			
		2.3 ± 0.3	19			
		3.5 ± 0.5	50			
		3.0 ± 0.1	98			
		2.1 ± 0.2	8.2	Annealed	3	40
		4.0 ± 0.2	29	zircaloy-2		
		5.6 ± 0.4	100			
		3.1 ± 0.4	130	Annealed	12	80
		4.7 ± 0.4	54	zircaloy-2		
		6.3 ± 1.0	770			

a. Only the difference between longitudinal and transverse changes in length was reported.

$$\frac{1-3f_z}{1-3f_\theta} = \frac{\text{growth strain in axial direction}}{\text{growth strain in circumferential direction}}$$

where f_z and f_θ are the texture factors in the axial and circumferential directions, respectively.

A somewhat different approach was taken by Daniel[4.7-1,4.7-7] in a series of experiments that measured both diameter and length changes of fuel rods. The effects of fuel cladding interactions and pressure differentials across the cladding on measured changes in rod length could be separated from the effect of cladding growth, since no fuel cladding mechanical interaction was present in one experiment series. The separation was achieved by noting that the expected ratio of length-to-diameter changes is very different for fuel cladding interactions, creep due to pressure differentials across the rod, and irradiation-induced growth. In particular, the fractional change in diameter due to growth was predicted to be very small for typical cladding diameters and textures. Therefore, a plot of the measured change in length as a function of the measured change in diameter at a single fluence could be used to determine the change in length due to growth by simply extrapolating to zero changes in diameter with data that did not contain fuel cladding mechanical interactions. Daniel determined the fractional change in length at two values of fluence. His

results[a] are particularly significant because they provide a measure of growth of annealed cladding at high fluence and do not show the saturation which Kreyns[4.7-5] observed.

4.7.4 The Effect of Texture on Axial and Circumferential Growth

Single-crystal texture effects are related to polycrystalline growth. Growth is pictured simply as a reduction of the c axis dimension of individual grains and an increase of the basal plane dimensions of the grains. The analysis is carried out with the help of an abstract picture of grains made up of schematic immobile unit cells, which decrease their c-axis length by a fraction and increase their a_1, a_2, and a_3 axis length by a fraction m. Although the picture of changing unit cell size does not represent atomic behavior within the grain, the growth of the grain is reproduced by the abstract picture.

Figure 4-21 illustrates the change in the axis lengths of the schematic unit cells. Growth of the three axes in the basal plane is assumed to be equal because of the symmetry of the lattice. The relation between the decrease of the c-axis dimension and the increase of the a axes is dependent on the details of the atomic model used to describe growth. For models that imply that the volume of the grain (and schematic unit cell) remains constant, $(1 + m) = (1 - n)^{-1/2}$. This value for 1 + m will be assumed at the last stage of the derivation of the effect of texture. It should be noted that the assumption is not made on the basis of a detailed atomic model. The constant volume assumption is made on the basis of experimental evidence,[4.7-8,4.7-9] and this evidence has been somewhat contradictory.

4.7.4.1 ***Use of the X-ray Diffraction Orientations Parameter to Relate Single Crystal Models to Polycrystalline Results.*** The effective fraction of grains aligned with their c-axis parallel to a reference direction (axial, circumferential, or radial direction of the tube) is usually taken to be an orientation parameter[4.7-10] determined from ray diffraction studies. This parameter is formally defined as the average of the squared cosine of the azimuthal angle between the c-axis of individual grains and the reference direction, weighted by the volume fraction, V_i, occupied by cells at a given azimuthal angle, θ_i. That is,

$$F = \frac{\sum_i V_i \cos^2\theta_i}{\sum_i V_j} . \qquad (4\text{-}104)$$

It is shown in Reference 4.7-10 that polycrystalline bulk properties in a reference direction can be expressed as

$$P_{ref} = fP|| + (1 - f)\, P_{\perp} \qquad (4\text{-}105)$$

if the property has the following characteristics:

a. $$P_{\eta} = P|| \cos^2\eta + P_{\perp} \sin^2\eta \qquad (4\text{-}106)$$

a. A growth component of strain equal to 7.5×10^{-4} at a fluence of 17×10^{24} n/m^2 and a growth strain of 2.7×10^{-4} at a fluence of 3.1×10^{24} n/m^2 were indicated by Daniel.[4.7-1,4.7-7]

where

P_η	=	the single-crystal property in a direction at an angle η to the axis
$P\|\|$	=	the single-crystal property along the c-axis
$P_\perp$	=	the single-crystal property perpendicular to the c-axis

and

b. The property in a reference direction of the polycrystalline sample is the volume weighted summation of this property in its individual crystals.

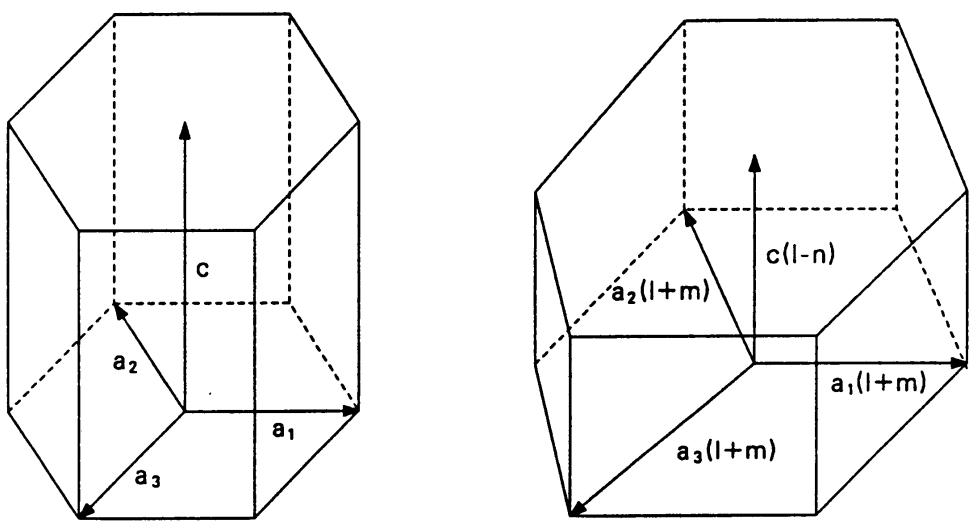

Figure 4-21. The growth of schematic unit cells in a grain.

A property of the schematic unit cells that satisfies condition (a) is the square of the distance between two points imbedded in the schematic unit cell. That is, if (-x/2,-y/2,-z/2) and (x/2,y/2,z/2) are coordinates of two points in the cell relative to an origin at the middle of the cell, the squared distance between the points is

$$l^2 = Z^2 + X^2 + Y^2 \tag{4-107}$$

or

$$l^2 = l_o^2 (1 - n)^2 \cos^2 \; + l_o^2 (1 + m)^2 \sin^2\theta \tag{4-108}$$

where

l_o	=	the distance between the points
n and m	=	parameters that describe cell change
θ	=	the angle between the c-axis and the line between the points.

It is assumed here that condition (b) of the previous paragraph is also satisfied.

Equations (4-105) and (4-108) can be used to express the fractional change in the distance between two points of a polycrystalline sample. $P\|$ and $P\perp$ of Equation (4-105) are identified as $l_o^2 (1 - n)^2$ and $l_o^2 (1 + m)^2$ in Equation (4-108) so that l^2 (the square of the distance between points of a polycrystalline sample) is

$$l^2 = f (1 - n)^2 l_o^2 + (1 - f) (1 + m)^2 l_o^2 \quad . \tag{4-109}$$

The fractional change in length along the reference direction of a polycrystalline sample will then be

$$\Delta l/l_o = (l - l_o)/l = [f(1 - n)^2 + (1 - f)(1 + m)^2]^{1/2} - 1 \quad . \tag{4-110}$$

The parameters n and m represent the average fractional growth of single crystals along the c and a axes. Since growth in zirconium alloys is typically less than 1%, n and m are small numbers and a Taylor series expansion of the radical about n = m = 0 is possible. The expansion yields

$$\frac{\Delta l}{l_0} \approx 1 + m - (n + m) f + \text{terms of order } n^2, m^2, \text{ and } mn. \tag{4-111}$$

If (1 + m) is taken equal to $(1 - n)^{-1/2}$ to impose the restriction of a constant volume on the grain, the Taylor series expansion yields

$$\frac{\Delta l}{l_0} \approx \frac{n}{2} (1 - 3f) + \text{terms of order } n^2. \tag{4-112}$$

The assumption of constant volume is made here in lieu of a successful atomic level model for kinetics of growth.

4.7.4.2 *Application of the Result of Section 4.7.3.1 to Measurements of Growth in Different Directions.* Equations (4-111) and (4-112) have been derived without reference to any particular direction. Thus, for the axial component of growth, $\Delta l/l_0$ is measured along the tubing axis and f is the axial orientation parameter, f_z. If a change in tubing circumference (or diameter of the tube since the diameter is π-1 times the circumference) is being considered, $\Delta l/l_0$ is the fractional change in the tubing diameter or circumference and f is f_θ, the tangential orientation parameter.

4.7.5 Analysis of Irradiation-Induced Growth Factors Other Than Texture

The fast neutron flux (in addition to fluence) and the residual stress in the tubing may affect growth (References 4.7-6 and 4.7-11), but no attempt has been made to include these effects due to lack of data. Also, no significant difference in the growth rates of zirconium, zircaloy-2, and zircaloy-4 has been reported, so no distinction between their growth rates has been incorporated into the model. As mentioned in Section 4.7.2, the first step in developing the model was to account for differences in growth due to differences in texture. The factor (1 + 3f) of Equation (4-112) was used to adjust growth measured with arbitrary textures to values expected for f = 0.05. The results are illustrated in Figure 4-22.

4.7.5.1 ***The Effect of Fast Neutron Fluence on Irradiation-Induced Growth.*** Many investigators have treated the effect of fast fluence by fitting in the empirical expression

$$\text{Growth strain} = (\text{fluence})^q \tag{4-113}$$

to the data,[4.7-6,4.7-8] with resultant values of q in the range from 0.3 to 0.8. Although good agreement can be obtained by allowing q to vary for each set of data, the results of such empirical fits are somewhat misleading. Hesketh[4.7-12] has derived a dependence on the square root of fluence [q = 0.5 in Equation (4-113)], and data from individual irradiations have not demonstrated a clear departure (other than saturation effects) from this rule. This point is illustrated in Figure 4-23 by showing a plot of axial growth as a function of the square root of the fluence.

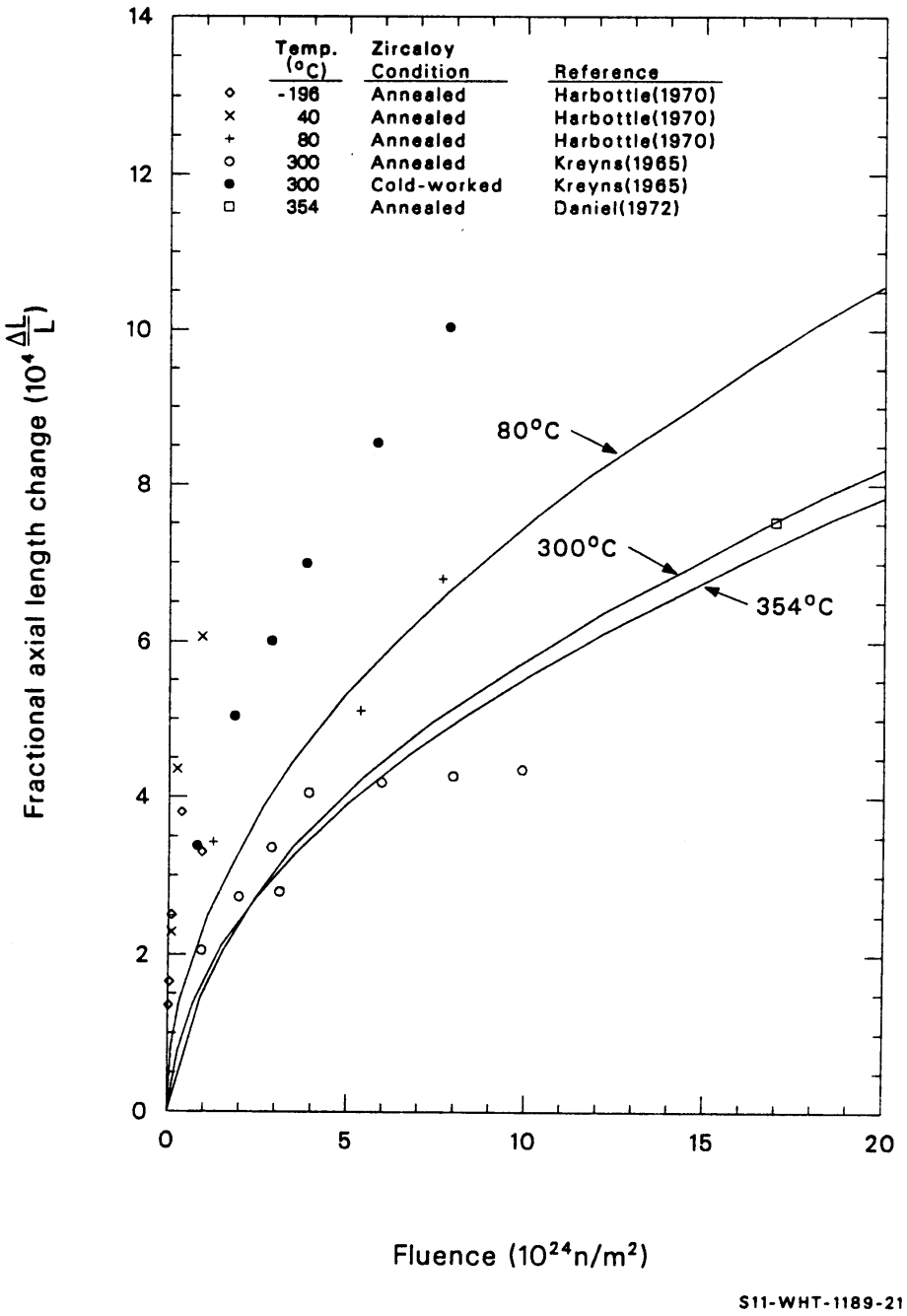

Figure 4-22. Model predictions and measured values of the growth of zircaloy tubes adjusted to a common texture coefficient of $f_z = 0.05$.

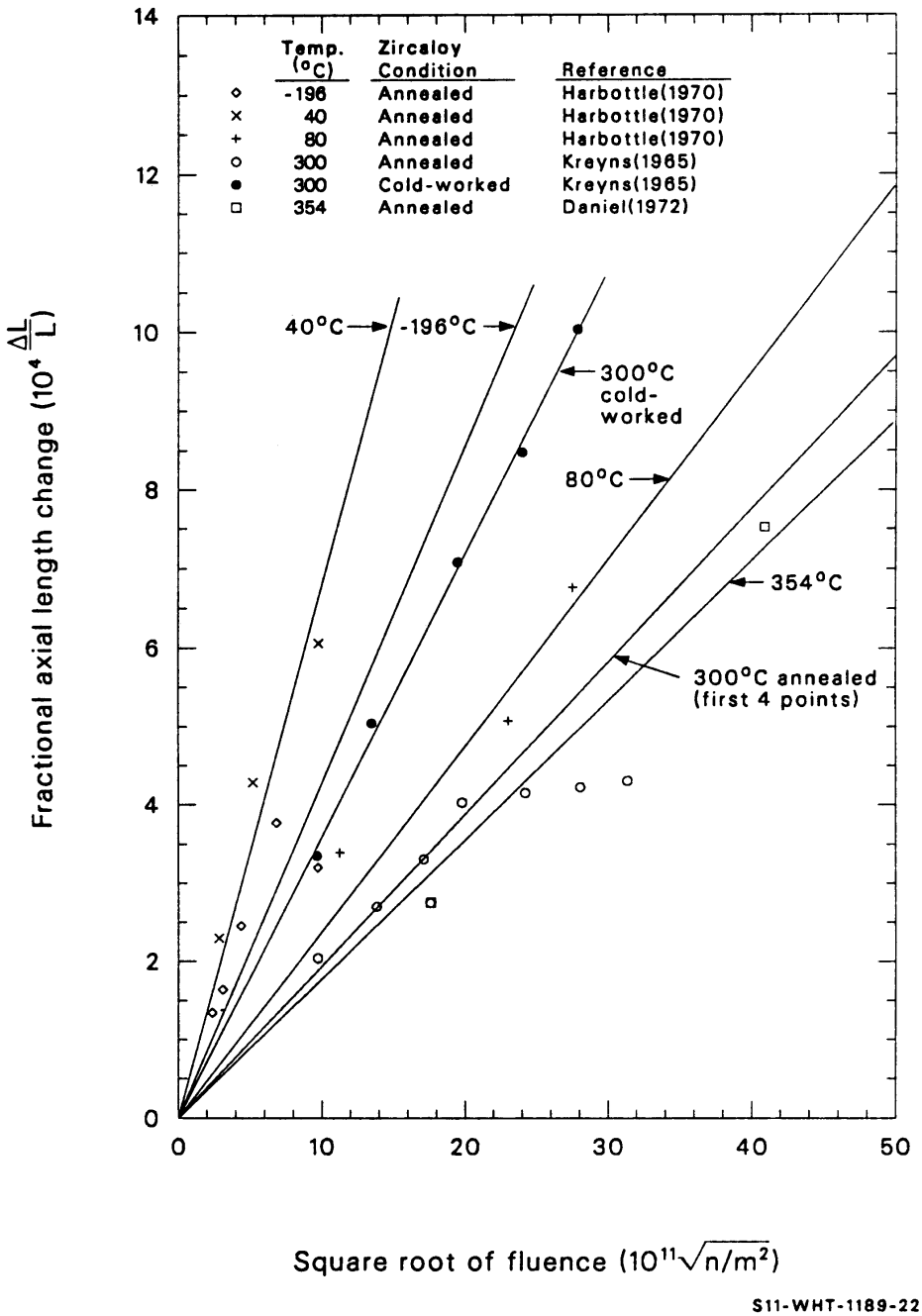

Figure 4-23. Zircaloy growth versus square root of fast neutron fluence for data adjusted to a common tube texture coefficient of $f_z = 0.05$ with linear least-squares fits superimposed.

Departures from q = 0.5 would be indicated by curvature of the data in Figure 4-23. Except for apparent saturation effects on annealed tubes at 300°C, these departures are much less pronounced than differences due to different temperatures, fluences, and cold work. Moreover, there is a physical basis for expecting temperature and flux to modify the effect of given fluence. Therefore, the exponent in Equation

(4-109) is fixed in the model at 0.5.

4.7.5.2 ***The Effect of Temperature on Irradiation-Induced Growth.*** It has been suggested by Harbottle[4.7-6] that growth is proportional to the instantaneous concentration of interstitials. This implies that growth should be directly proportional to the rate of interstitial production (which is proportional to neutron flux Φ) and inversely proportional to the rate of interstitial removal. Since interstitial removal is proportional to exp (interstitial migration energy/RT), the following expression for growth should apply.

$$\frac{\Delta L}{L} \propto \Phi \exp\left(\frac{E_M}{RT}\right) \tag{4-114}$$

where

E_M	=	interstitial migration energy
R	=	gas constant.

When Equation (4-114) is compared to data, E_M varies with temperature as expected; but any simple variation of E_M with temperature is not consistent with all experiments. A constant value for E_M has been used in the model, due to these inconsistencies and because it has been suggested that the dependence of E_M on temperature is too complex[4.7-13] to evaluate with existing data. E_M will actually change, in poorly defined steps, as the modes of interstitial migration change with increasing temperature. However, Figures 4-20, 4-22, and 4-23 indicate that there is a relatively small temperature dependence in the normal operating temperature range for LWRs. Use of a small and constant value for E_M is therefore justified. A comparison of Equation (4-114) with the data shown in Figure 4-23 results in the following correlation:

$$\frac{\Delta L}{L} \propto \exp\left(\frac{240.8}{T}\right). \tag{4-115}$$

The fast flux factor of Equation (4-114) has been incorporated in the constant A of the full expression for growth, Equation (4-103).

The detailed data comparisons made while deriving Equation (4-115) provide justification for the functional dependence shown. When Harbottle's[4.7-6] data for growth under fast fluxes differing by a factor of two (at 40 and 80°C, see Table 4-20) are compared, they are consistent with a value of E_M = 0.3 eV. This value of E_M is reasonable for atomic migration in that temperature range. When other data are examined, values of E_M = 0.075 eV result at -196°C and of E_M = 0.157 eV at 354°C. This range of values is also reasonable,[4.7-14] lending confidence to the functional dependence given by Equations (4-114) and (4-115).

4.7.5.3 ***The Effect of Cold Work on Irradiation Induced Growth.*** The observed effects of cold work have not been successfully explained in detail in the literature. For this model, general conclusions have been drawn from the available measurements and an empirical expression has been formed. The data taken by Kreyns[4.7-5] on cold worked zircaloy-4 tubes at 300°C agree very well with a square root of fluence dependence, as shown in Figure 4-24. To compare these results with those for annealed tubes, the annealed data shown in Figure 4-23 were normalized to 300°C using Equation (4-115). Figure 4-24 then indicates that the net effect of cold work is to increase the growth rate in the unsaturated range of flu-

ence. Neither the dependence on the square root of the fluence nor the intercept at zero fluence are changed by cold work.

The only available data on the effect of varying the amount of cold work are reported in Figure 19 of Reference 4.7-8, which indicates the following approximate irradiation growth fractions in the longitudinal direction of zircaloy-4 plate specimens at 300°C (Table 4-21). The data are reasonably consistent with a linear relationship between growth and cold work and have been incorporated into the model by assuming a factor of the form (1 + D x coldwork). Values of D determined from the data at three different fluences are listed in Table 4-22 where

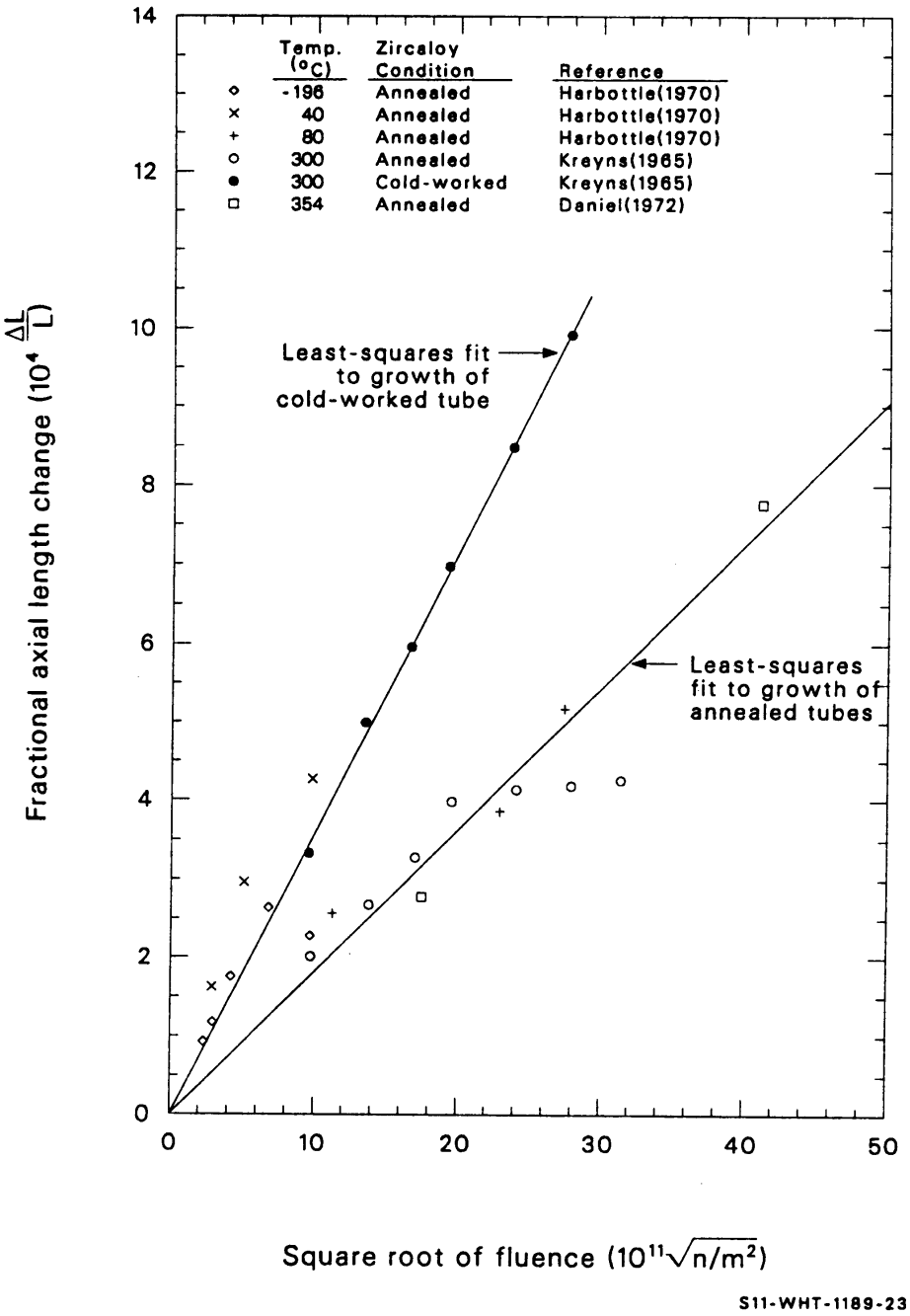

Figure 4-24. Zircaloy growth versus square root of fast neutron fluence for data adjusted to a common tube texture coefficient of $f_z = 0.05$ and to a common temperature of 300°C with linear least squares fits superimposed.

Table 4-21. Zircaloy growth data as a function of cold work and fluence.

	Cold Work		
Fast Fluence (10^{24}n/m^2)	**0%**	**20%**	**78%**
14	7.4×10^{-4}	7.8×10^{-4}	17.4×10^{-4}
20	8.2×10^{-4}	11.7×10^{-4}	24.4×10^{-4}
30	9.2×10^{-4}	17.3×10^{-4}	$35.7.3 \times 10^{-4}$

Table 4-22. Determination of cold work coefficient.

Fast Fluence (10^{24}n/m^2)	D
14	1.7
20	2.0
30	3.8

$$D = \frac{1}{\text{cold work}}\left[\frac{\text{growth with cold work}}{\text{growth without cold work}} - 1\right]. \tag{4-116}$$

The value D = 2.0, given by the data at the lower fluences, is used in the model, since the measured growth with 0% cold work (Table 4-21) shows gross saturation effects similar to the effects apparent in the high fluence data of Kreyns. The model thus sacrifices a description of these gross saturation effects in order to fit the cold work data and the majority of annealed tubing data.

4.7.6 Evaluation of the Model and Its Uncertainty

The normalization of all the annealed data to identical conditions (texture coefficient f = 0.05, temperature at 300°C), as shown in Figure 4-24, provides a test of the model. The model predicts irradiation-induced growth reasonably well except for data taken at fluences less than 10^{24} n/m^2 and except for greater-than-normal saturation effect seen in some annealed samples. Figure 4-20 leads to the same conclusion and also indicates the relative effects of the temperature, texture, and fluence variables as predicted by the model. [The factor A used in Equation (4-103) for these curves was derived from a linear least-squares fit to the data of Figure 4-24.]

Further refinement of the model to explain the relatively high growth measured at low fluence and to explain the gross saturation effects observed on some samples has not been attempted. In the low-fluence case, there are competing processes that may explain the high values sometimes found; and there is no way

to distinguish between them without additional data. These effects are:

1. Stress relief causing additional length changes (Reference 4.7-11)
2. Variation in fast flux causing different growth rates (Reference 4.7-6)
3. Variation in interstitial migration energy with temperature, causing error in the temperature model (as discussed in Section 4.7.4.2).

Similar problems exist with attempts to model the gross saturation effects observed in some experiments by Kreyns, using tubing, and Fidleris,[4.7-8] using plate samples. There are sufficient data to indicate clearly that these saturation effects in growth are not simply a function of the fluence or the growth of the strain. However, few data are available to appraise correlations between saturation and other parameters.

An estimate of the uncertainty can be obtained by comparing predictions to the model with data not used in formulating the model. For example, the plate specimen data listed in Table 4-21 for 0% cold work (and 300°C) were not used to formulate the predicted growth of annealed tubes. When these data are compared with the model predictions for annealed growth at 300°C, a discrepancy of approximately 10% is found. This 10% discrepancy is consistent with the scatter of the data at fluences above 10^{24} n/m^2 in Figure 4-24 and thus is a reasonable estimate of the model's uncertainty in the temperature range from 40 to 360°C.

The uncertainty for temperatures outside of this range and for fluences less than 10^{24}n/m^2 may be substantially greater than 10%. In the low-fluence range, inspection of Figure 4-24 suggests uncertainties on the order of 100%. Such large discrepancies may be due to stress relief effects.[4.7-11] For temperatures much outside the range 40 to 360°C, increased error will be caused by the presence of different modes of interstitial or vacancy migration, causing different rates of zircaloy growth.

4.7.7 References

4.7-1 R. C. Daniel, “In-Pile Dimensional Changes of Zircaloy-4 Tubing Having Stresses (Light Water Breeder Reactor Development Program),” *Nuclear Technology, 14*, May 1972, pp. 171-186.

4.7-2 W. R. Smalley, *Evaluation of Saxton Core III Fuel Materials Performance*, WCAP 3385-87, 1974.

4.7-3 J. B. Melehan, *Yankee Core Evaluation Program Quarterly Progress Report for the Period Ending September 1969*, WCAP-3017-6091, December 1969.

4.7-4 E. T. Laats and P. E. MacDonald, *Halden Project Fuel Behavior Test Program--Experimental Data Report for Test Assemblies IFA-226 and IFA-239*, NRC-OECD, March 1975.

4.7-5 P. H. Kreyns, quoted by E. Duncombe et al., *Comparisons with Experiment of Calculated Changes and Failure Analysis of Irradiated Bulk Oxide Fuel Test Rods Using the CYGRO-1 Computer Program*, WAPD-TM-583, September 1966.

4.7-6 J. E. Harbottle, “The Temperature and Neutron Dose Dependence of Irradiation Growth in Zircaloy-2,” *Irradiation Effect on Structural Alloys for Nuclear Reactor Applications*, ASTM-STP-485, 1970, pp. 287-299.

4.7-7 R. Daniel, *In-Pile Dimensional Changes of Zircaloy-4 Tubing Having Low Hoop Stresses*

(LWBR Development Program), WAPD-TM-973, July 1971.

4.7-8 V. Fidleris, "Summary of Experimental Results on In-Reactor Creep and Irradiation Growth of Zirconium Alloys," *Atomic Energy Review, 13*, 1975, p. 51.

4.7-9 S. N. Buckley, "Discussion at Institute of Metals Spring Meeting," *Journal of the Institute of Metals, 97*, 1969, p. 61.

4.7-10 J. J. Kearns, *Thermal Expansion and Preferred Orientation in Zircaloy*, WAPD-TM-472, November 1965.

4.7-11 V. Fidleris, "The Effect of Cold Work and Stress Relieving on the Irradiation Growth Behavior of Zirconium Alloys," *Journal of Nuclear Materials, 46*, 1973, pp. 356-360.

4.7-12 R. V. Hesketh, "Nonlinear Growth in Zircaloy-4," *Journal of Nuclear Materials, 30*, 1969, pp. 217-222.

4.7-13 S. H. Bush, *Irradiation Effects in Cladding and Structural Materials*, NewYork: Rowman and Littlefield, 1965, p. 143.

4.7-14 A. Seeger and H. Mehren, "Analysis of Self Diffusion and Equilibrium Measurements," *Vacancies and Interstitials Metals*, A.Seeger (ed.), NewYork: American Elsevien Publishing Co., Inc., 1970, p. 892.

4.8 Creep (CCSTRN, CCSTRS, CABTP, CTP)

Cladding creep due to coolant pressure during steady-state operation is important in modeling the size of the fuel cladding gap and initial stored energy at the start of transients. For fuel rods with low internal pressure, the creep may be sufficiently rapid to also affect fuel relocation and effective conductivity of fuel pellets. Subroutines for finding creep strain as a function of stress and stress required to produce a given creep strain are presented in this section. The model used in these subroutines is based primarily on surface displacement data from the HOBBIE-1 test conducted by the U. S. Nuclear Regulatory Commission and the Energieonderzock Centrum Nederland (ECN).

4.8.1 Summary

The basic equation used in both the CCSTRN and CCSTRS subroutines is

$$\dot{\varepsilon}(t) = BA - \int_0^t B\exp\left[-(t-t')\left(\frac{\Phi}{\Psi}+\frac{1}{\gamma}\right)\right]\dot{\varepsilon}(t')\,dt' \qquad (4\text{-}117)$$

where

$\dot{\varepsilon}(t)$	=	tangential component of creep strain rate (s^{-1})
t	=	time since creep strain was zero (s)
t'	=	integration variable
B	=	rate constant (s^{-1}), Equation (4-119)

A	=	ultimate strain for infinite correlation (unitless), Equation (4-118)
Φ	=	fast neutron flux [n/(m^2·s)], E > 1 MeV
Ψ	=	correlation fluence, Equation (4-120) (n/m^2), E > 1 MeV
γ	=	zero flux correlation time, Equation (4-121) (s).

Correlations for the parameters A and B used in the CCSTRN and CCSTRS subroutines are contained in the CABTP and CTP subcodes. These correlations were obtained from out of pile creep strain versus time data. CABTP is called from CCSTRN, and CTP is called from CCSTRS. Both CABTP and CTP use the following expressions to calculate the needed parameters:

$$A = 3.83\times10^{-19}|\sigma|^{r}\frac{\sigma}{|\sigma|} \tag{4-118}$$

$$B = 4.69\times10^{-6}|\sigma|^{r}\exp\left(-\frac{25100}{T}\right) \text{ for } T \geq 615 \text{ K}$$

$$= 1.9519804\times10^{-16}|\sigma|^{r}\exp\left(-\frac{10400}{T\sigma}\right) \text{ for } T<615 \text{ K} \tag{4-119}$$

where

σ	=	tangential component of stress (Pa)
T	=	temperature (K) (input temperatures are limited to the range 450 to 750 K)
r	=	2.0 for stress between 0.2 and 0.75 times the strength coefficient of cladding
	=	0.5 for stress between 0 and 0.2 times the strength coefficient of cladding
	=	25.0 for stress less than 0.75 times the strength coefficient of cladding. The strength coefficient is approximated by the linear expression 1.5 x 10^9 -1.5 x 10^6 T, and the constants in Equation (4-119) are modified when stress is outside the range 0.2 to 0.75 times the strength coefficient to guarantee continuity at the boundaries of this range.

Expressions for the correlation fluence, Ψ, and zero flux correlation time, γ, were obtained from the slope of secondary creep rates versus temperature under tensile stress. These expressions are

$$\Psi = 2.9\times10^{6}\exp\left(\frac{25100}{T}\right) \text{ or } T \geq 615 \text{ K}$$

$$= 6.967795\times10^{16}\exp\left(\frac{10400}{T}\right) \text{ for } T < 615 \text{ K} \tag{4-120}$$

$$\gamma = 8.6\times10^{-11}\exp\left(\frac{25100}{T}\right) \text{ for } T \geq 615 \text{ K}$$

$$= 2.0663116\exp\left(\frac{10400}{T}\right) \text{ for } T < 615 \text{ K} \ . \tag{4-121}$$

The CCSTRN subroutine calculates the tangential component of cladding creep strain at the end of a time step with constant cladding temperature, flux, and stress. For time step intervals less than a time to steady state, the infinite correlation approximation[a] is used to integrate Equation (4-117). The resultant expression for creep strain is

$$\varepsilon_{final} = [A - \varepsilon_{boundary}]\,[1 - \exp(B\Delta t)] + \varepsilon_{initial} \tag{4-122}$$

where

ε_{final}	=	tangential component of creep strain at the end of the time step (unitless)
$\varepsilon_{initial}$	=	tangential component of creep strain at the start of the time step (unitless)
$\varepsilon_{boundary}$	=	a boundary condition parameter used to force the creep rate to be continuous at the time step boundary when temperature and stress do not change (unitless); this parameter is zero for the first time step and is determined by Equations (4-145) and (4-146) for subsequent time steps
Δt	=	time step duration (s).

For time step durations longer than the time to steady state, the steady-state approximation $[\ddot{\varepsilon}(t) \approx 0]$ is used to integrate Equation (4-117). The resultant expression for creep strain is

$$\varepsilon_{final} = (A - \varepsilon_{boundary})\,[1 - \exp(-B\Delta t_{ss})] + \frac{BA\left[\frac{\Phi}{\Psi} + \frac{1}{\gamma}\right](\Delta t - \Delta t_{ss})}{1 + \frac{\Phi}{\Psi} + \frac{1}{\gamma}} + \varepsilon_{initial} \tag{4-123}$$

where Δt_{ss} is the time to steady state (s). The time to steady state is defined to be the time when creep strain rates given by Equations (4-122) and (4-123) are equal

$$\Delta t_{ss} = -\frac{1}{B}\ln\left[\frac{A}{1 + \frac{B}{\frac{\Phi}{\Psi} + \frac{1}{\gamma}}}\,\frac{1}{(A - \varepsilon_{boundary})}\right] \tag{4-124}$$

or 0 if the argument of the log term is outside the range 0 < argument < 1.

Subroutine CCSTRS uses an interaction technique and trial assumptions to solve Equation (4-116) or (4-123) for stress when ε_{final}, $\varepsilon_{initial}$, and Δt are known. The procedure begins by solving Equation 116) with the implied assumption that Δt is $< \Delta t_{ss}$. In this case, the possible range of stresses is bounded and the

a. The exponent in Equation (4-117) is approximated by a one.

function is monotonic. The range is cut in half in each of several iterations by testing stress at the midpoint of the possible range. If substitution of the trial solution into Equation (4-124) yields a Δt_{ss} that is > Δt, the trial solution is adopted.

A second trial solution is obtained by solving Equation (4-123) for $|\sigma|^r$ with the assumption that Δt_{ss} is zero. If this trial solution yields $\Delta t_{ss} = 0$ in Equation (4-124), it is adopted.

If neither of the two trial solutions are adopted, the technique used in CCSTRS employs the observation that the initial trial solution provides a maximum $|\sigma|^r$ and the second trial solution provides a minimum initial slope. The implied range of possible stress is then cut in half in each of several iterations by testing in Equations (4-124) and (4-123) with stress at the midpoint of the range.

Uncertainty estimates for creep strain and stress are provided by CCSTRN and CCSTRS. Both estimates are based on the observation that the only creep data with compressive stresses are at a temperature of 644 K and stresses in the range 120 to 140 MPa. The expression used to estimate the uncertainty of the strain calculated in CCSTRN is

$$f_{\varepsilon^+} = 1 + 0.3\left(1 + 2\left|\frac{\sigma + 130\times10^6}{130\times10^6}\right| + 5\left|\frac{T - 644}{644}\right|\right) \tag{4-125}$$

$$f_{\varepsilon^-} = \frac{0.4}{\left(1 + 2\left|\frac{\sigma + 130\times10^6}{130\times10^6}\right| + 5\left|\frac{T - 644}{644}\right|\right)} \tag{4-126}$$

where $f_{\varepsilon^\pm}$ are the upper and lower uncertainty estimates of the calculated creep strain increment magnitude.

The expression used to estimate the uncertainty of stress calculated in CCSTRS is

$$f_{\sigma^+} = 1 + 0.075\left(1 + 2\left|\frac{\sigma + 130\times10^6}{130\times10^6}\right| + 5\left|\frac{T - 644}{644}\right|\right) \tag{4-127}$$

$$f_{\sigma^-} = \frac{0.85}{\left(1 + 2\left|\frac{\sigma + 130\times10^6}{130\times10^6}\right| + 5\left|\frac{T - 644}{644}\right|\right)} \tag{4-128}$$

where $f\sigma\pm$ are the upper and lower uncertainty estimates of the calculated stress magnitude expressed as a function of the calculated stress magnitude.

The following subsections discuss available data and development of the model.

4.8.2 Survey of Available Data

Data that measure creep under tensile stress are being supplemented by data for creep with compressive stress in very limited ranges of temperature and stress. The available theories and data for creep under compressive stress are surveyed in this section. A bibliography of extensive literature on tensile creep experiments is provided in Section 4.8.6.

Currently, there are no theories directed specifically at compressive stress; but Dollins and Nichols,[4.8-1] Piercy,[4.8-2] MacEwen,[4.8-3] and Nichols[4.8-4,4.8-5] have discussed similar physical models that explain the general features of in-pile creep of cladding under tensile stress. For the temperature range 523 to 623 K, these authors believe the controlling mechanism for in-pile creep at stresses < 70 to 100 MPa is the preferred alignment of irradiation-induced dislocation loops during nucleation. At higher stresses, the effective stress at dislocations is thought to be sufficiently large to allow dislocation glide between the neutron produced depleted zones. The creep rate would then be controlled by combined rates of dislocation glide between depleted zones and climb out of these zones. Although some of Nichol's ideas have been challenged,[4.8-5,4.8-6,4.8-7] the predicted linear stress dependence of strain rate at low stress is supported by several authors;[4.8-8,4.8-9] and his prediction that the strain rate at high stress is proportional to approximately the one-hundredth power of stress in the 523 to 623 K temperature range is consistent with the MATPRO models for cladding plastic deformation at high stress (see Section 4.9). Unfortunately, Nichols predicts a complex relation between strain rate and stress for intermediate stress. The dependence of strain rate on stress is expected to vary from the tenth power of stress to the first power and then to the fourth power as stress increases. The physical model proposed by Nichols has been consulted but not used directly because the cost associated with the use of such a detailed model is not justified until compressive creep data confirm the model.

A similar, but less physically founded, stress dependence is proposed by Fidleris in his review of experimental data.[4.8-9] He reported that creep rate varies linearly with stress at temperatures around 570 K and stresses less than one-third the yield stress. With increasing stress, the strain rate is reported to be proportional to higher powers of stress, reaching a power of 100 at stresses of 600 MPa. The model for creepdown uses only the general features of the stress dependence reported by Fidleris because insufficient creepdown data exist to support detailed modeling.

The data referenced by Fidleris show that the in-reactor creep rate depends on material, flux temperature, and direction of testing, as well as stress. At temperatures below half the melting temperature (1,050 K) and stresses lower than the yield stress, the in-reactor creep reaches a constant rate, while the out of reactor creep rate becomes negligibly small with time. The steady-state creep rate is stated to be independent of test history or strain, at least for fast neutron fluences below 3×10^{24} n/m^2 (E > 1 MeV).

Below 450 K, temperature is reported to have little effect and, for stresses below the yield stress, the strain is < 0.001. The out-of-reactor creep data of Fidleris can be described by

$$\varepsilon = A \log t + B \qquad (4\text{-}129)$$

where

ε	=	strain
t	=	time (s)
A,B	=	constants.

In the range 450 to 800 K, Fidleris reports that the out-of-reactor creep strain is often represented by equations of the type

$$\varepsilon = At^m + B \qquad (4\text{-}130)$$

where ε, t, A, and B were defined in conjunction with Equation (4-129) and m is a constant between zero and one. Recovery of some of the strain is possible in this temperature range, and dynamic strain aging[4.8-10] frequently causes anomalously low creep strains and rates.

Equations (4-129) and (4-130) and other conclusions in Fidleris' review are based on his own extensive data for uniaxial, tensile creep of zirconium alloys, both in and out of reactor.[4.8-11] From these data, Fidleris concluded that the in-reactor creep is approximately proportional to the fast neutron flux for all temperatures. Other investigators treat the effect of fast neutron flux on creep in different ways.[4.8-12] Although most authors have treated in-reactor creep as the sum of the out-of-reactor creep and an additional irradiation-induced creep proportional to fast neutron flux to some power, a, there is disagreement about the magnitude of the exponent a. Ross-Ross and Hunt[4.8-8] report that creep rate is directly proportional to the fast flux, Wood[4.8-13,4.8-14] uses a = 0.85, Kohn[4.8-15] uses a = 0.65, and Gilbert[4.8-16] finds a = 0.5 for yielding creep at moderate stress levels. MacEwen [4.8-3] and Nichols[4.8-4] have resolved this apparent conflict by suggesting that the flux exponent can have values from 0 (Nichols) or 0.5 (MacEwen) to 1.0, depending on the flux and temperature.

The expressions for calculating creepdown models the effect of fast neutron flux on creep with an expression that is proportional to fast neutron flux for large fluxes but less dependent on flux for smaller fluxes. Equation (4-130), Fidleris' equation for creep strain versus time with tensile stress, has not been used because it is inconsistent with data obtained from tests with compressive stress.

The effects of grain size annealing and texture are addressed by several authors. Fidleris[4.8-9] finds that the zircaloy-2 creep rate increases continuously with grain size at 573 K. However, within the limited range of grain sizes formed in his recrystallized zircaloy-2 (6 to 20 μm), very little variation is reported. Stehle[4.8-17] reports creep strains in cold worked material that are more than twice as large as the creep strains in recrystallized cladding. He also reports that the short time creep strain of stress relieved tubes is larger than that of recrystallized tubes but that plots of creep strain versus time for stress relieved and recrystallized cladding intersect at about 6,000 hours. Kohn[4.8-15] reported that the biaxial creep rate of Zr-2.5 Nb fuel cladding is about 10 times higher than that of pressure tube material under similar conditions. He states that texture differences between the materials and the overaged precipitate structure in the as manufactured cladding can explain the difference in creep rates. The importance of texture is disputed by Stehle,[4.8-17] who reported that mechanical anisotropy (especially in longtime creep) is surprisingly low compared to the anisotropy in short time creep at room temperature. The effects of grain size, annealing, and texture have not been considered in the creepdown model because an explicit model for these effects on creepdown was premature at the time of model development.

Theories surveyed above may be misleading when applied to compressive creep because they are based primarily on tensile stress data. Picklesimer,[4.8-18] Lucas and Bement,[4.8-19] and Stehle[4.8-17] have pointed out that deformation with compressive stress differs from tensile deformation. Stehle has obtained data showing that the magnitude of creep strain of tubes under external pressure can be as small as half the creep strain of tubes under internal pressure.

The biaxial compressive stress data available include out-of-reactor measurements at three stresses and one temperature. Results from a single in-reactor experiment are also available. All experiments

except one were conducted by Hobson using tubes from a shipment of typical pressurized water reactor cladding purchased specifically for use in fuel cladding research programs sponsored by the NRC.[4.8-20]

The only biaxial compressive strain data from a different lot of cladding were reported by Stehle.[4.8-17] His measurements of the tangential creep as a function of time for standard stress relieved tubing fabricated according to KwU (Kraftwerke Union) specifications are reproduced in Figure 4-25. The tangential stress in this test was 140 MPa, and the temperature was 643 K. The magnitudes of the measured creep strains are somewhat smaller than the out-of-pile strains computed from Hobson's out-of-pile data at the same temperature but are within the range of the scatter reported by Stehle for cladding with varying cold work and stress relief annealing histories. Since the details of the stress relief anneal on the lot of cladding used by Stehle are not reported, the data will be used only to assess the uncertainty of the creepdown model.

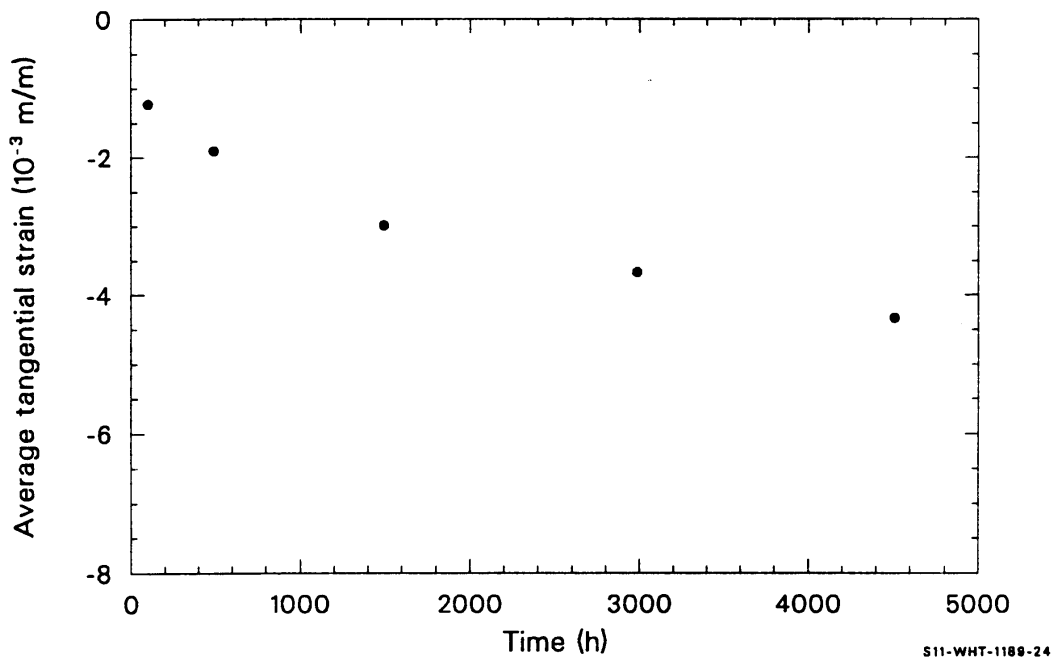

Figure 4-25. Average tangential creep strain as a function of time at 140 MPa and 643 K reported by Stehle.

The data reported by Hobson[4.8-21 to4.8-24] are radial displacements of the cladding surface at various azimuthal angles and axial positions (6.34 mm apart). The 20 probes used to measure the displacement were arranged in a double helix pattern over a 50.8 mm length of cladding, as shown by probe number in Table 4-23. This table is arranged so that the location of the probes may be visualized by thinking of the cladding surface as split along the cylinder axis and rolled out in the plane of the page. Hobson has pointed out[4.8-23] that the exact shape of the cladding surface cannot be determined with point-by-point data from a few radial probes and that the exact stress state at any point in the sample is related to the geometry of the

sample. In spite of these complications, the data can be analyzed to obtain the average tangential strain, as discussed in the next section of this report. Hobson data play a dominant role in the development of the creepdown model because the cladding is typical of LWR cladding, the stress is compressive, the cladding displacement is reported as a function of time at 2-hour intervals, and the temperature is typical of the cladding temperatures predicted by the FRAPCON-2 code. The only atypical feature of the data is the magnitude of the stresses employed by Hobson, 125 and 135 MPa. These stresses are characteristic of low pressure rods, so extrapolation to smaller stress magnitudes is necessary to model current fuel rod prepressurization levels.

4.8.3 Model Development

It has been concluded that the most relevant data for modeling cladding creepdown under the compressive stress of steady-state LWR reactor conditions are the data of Hobson. Extensive theory and tensile creep data are useful only to provide a tentative extension of the model to stresses and temperatures where no creepdown data are available.

The first step in the analysis of Hobson's data was to estimate the average tangential strain from radial displacements measured by probes at the locations shown in Table 4-23. This was done by inspecting plots of the radial displacement measured for each test. Table 4-24 and Figure 4-26 are examples of the results. The table was constructed from Hobson's data for Test 269-4 (14.4 MPa pressure) at 200 hours, and the figure is a polar plot of the radial displacement as a function of the azimuthal angle of the probe. The plot exaggerates the radial displacement by a factor of 10 compared to the scale of the circle, which represents zero displacement. From an inspection of the figure, it can be seen that the radial displacements at 200 hours in Test 269-4 are consistent with the assumption that the cladding surface was an ellipse, with major axis between 0 and 45 degrees and the center displaced slightly toward the 180 to 270-degree quadrant. There is some variation with axial position, as shown by the scatter in the displacements with common azimuthal angles and different axial positions.

Table 4-23. Surface coordinates of probes which measure radial displacement.

Axial Position	**Azimuthal Angle (degrees)**							
(mm)	0	45	90	135	180	225	270	315
0.00	1	--	--	--	13	--	--	--
6.35	--	4	--	--	--	16	--	--
12.70	--	--	7	--	--	--	19	--
19.05	--	--	--	10	--	--	--	22
25.40	2	--	8	--	14	--	20	--
31.75	--	5	--	--	--	17--	--	

Table 4-23. Surface coordinates of probes which measure radial displacement. (Continued)

Axial Position	Azimuthal Angle (degrees)							
(mm)	0	45	90	135	180	225	270	315
38.10	--	--	9	--	--	--	21	--
44.45	--	--	--	11	--	--	--23	
50.80	3	--	--	--	15	--	--	--

Table 4-24. Radial displacements at 200 hours in Hobson's Test 269-4 (10^{-3} mm).[a]

(mm)	0	45	90	135	180	225	270	315
0.00	4	--	--	--	12	--	--	--
6.35	--	6	--	--	--	12	--	--
12.70	--	--	48	--	--	--	12	--
19.05	--	--	--	-19	--	--	--	-29
25.40	31	--	-63	--	40	--	-58	--
31.75	--	3	--	--	--	31	--	--
38.10	--	--	-77	--	--	--	-60	--
44.45	--	--	--	-36	--	--	--	-38
50.8031	--	--	--	32	--	--	--	

a. 14.48 MPa pressure differential and 0.2127 mm pellet cladding gap.[4.8-23]

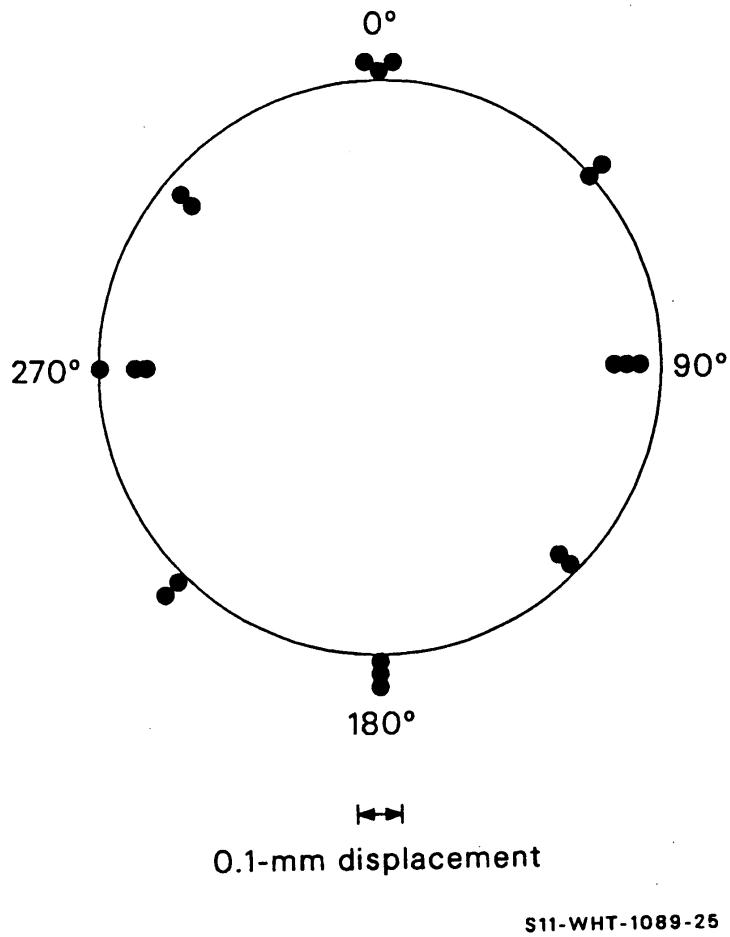

Figure 4-26. Radial displacement of cladding surface at 200 hours in Hobson's test 269-4.

The elliptical shape and gradual axial variations are also consistent with general descriptions of cladding surfaces after creepdown given by Stehle[4.8-25] and Bauer.[4.8-26] On the basis of several plots like Figure 4-26 and the general descriptions just mentioned, the author has concluded that (a) an ellipse is a reasonable approximation for the cladding surface at any given height prior to extensive fuel cladding interaction and (b) the major and minor axes (length or orientation or both) vary slowly with axial position.

The assumption that the cladding surface at any axial position is an ellipse allows calculation of the average tangential strain, as outlined in the six steps below.

1. The circumference of the elliptical surface was related to the major and minor semi-axis lengths with the approximate expression

$$c = 2\pi\left[\frac{(a^2 + b^2)}{2}\right]^{1/2} \tag{4-131}$$

where

c	=	circumference (m)
a,b	=	semi-axis lengths (m).

2. The average tangential strain was defined as

$$\varepsilon_\theta = \int_{\text{circumference}} \frac{1}{s} ds \cong \frac{c_{final} - c_{initial}}{c_{initial}} \tag{4-132}$$

where

ε_θ	=	average tangential strain (unitless)
s	=	arc length
$c_{initial}$	=	initial circumference (m)
c_{final}	=	final circumference (m).

3. Equations (4-131) and (4-132) were combined to obtain

$$\varepsilon_\theta = \left(\frac{a_{final}^2 + b_{final}^2}{a_{initial}^2 + b_{initial}^2} \right)^{1/2} - 1 \tag{4-133}$$

4. $a_{initial}$ and $b_{initial}$ were assumed equal to r_0, and a_{final} and b_{final} were set equal to the initial values plus Δa and Δb.

5. A Taylor series expansion to order $\Delta a/r_o$ and $\Delta b/r_o$ was used with Equation (4-133) and Step 4 above to find

$$\varepsilon_\theta \cong \frac{1}{2} (\Delta a + \frac{\Delta b}{r_0}) \tag{4-134}$$

where

r_o	=	initial radius of the outside (circular) surface of the cladding (m)
Δa, Δb	=	change of the major and minor semi-axes lengths (m).

6. Measurements of the radial displacements at one axial position (25.4 mm) and azimuthal angles of 0, 90, 180, and 270 degrees are available from Hobson's data. If these four measurements happen to occur along the major and minor axes of the ellipse, Equation (4-134) is sufficient to convert the data to an expression for the average circumferential component of the strain. When the radial displacements at 25.4 mm are not measured along the major and minor axes of the ellipse, the derivation is more complex; but the result (to order $\Delta a/r_r$ in the Taylor series expansion) is an equation of the same form as Equation(4-134), with Δa and Δb replaced by the average radial displacements along any two axes at right angles to each other and at any angle to the major and minor axes of the ellipse. The expression then becomes

$$\varepsilon_\theta \cong \frac{1}{2} (\Delta a' + \frac{\Delta b'}{r_0}) \tag{4-135}$$

where $\Delta a'$ and $\Delta b'$ are the change of the cladding radius measured along any mutually perpendicular axes at one axial position (m).

The second part of the analysis of Hobson's data was to describe the average tangential strains obtained from the data and Equation (4-135). Figure 4-27 displays the calculated average tangential strain from two out-of-pile tests at 15.86 MPa differential pressure. During the first 600 hours, the strains are remarkably consistent. During the last 400 hours of the tests, the strain in Test 269-27 was noticeably larger than that of Test 269-8. Test 269-27 had a large simulated axial gap centered about the axial position of the four probes used to determine the strain. Test 269-8 had only a small axial gap. The difference in strain at long times is probably due to the effect of the different contact times with the simulated fuel.

Figure 4-28 illustrates the strain versus time results obtained from the 14.48 MPa out-of-pile test. The magnitude of the strain at any time is significantly smaller than the strains obtained with the the 15.86 MPa tests.

In an effort to describe the strain-versus-time data shown in Figures 4-27 and 4-28, the constants in Equations (4-129) and (4-130) for tensile creep were fit to selected strain-time pairs. Each equation was then tested by extrapolating to longer or shorter times and comparing the predicted strains to strain-time pairs not used in determining the constants A and B. Neither equation passed this test. Equation (4-129) consistently had too much curvature,[a] and Equation (4-130) had too little curvature.

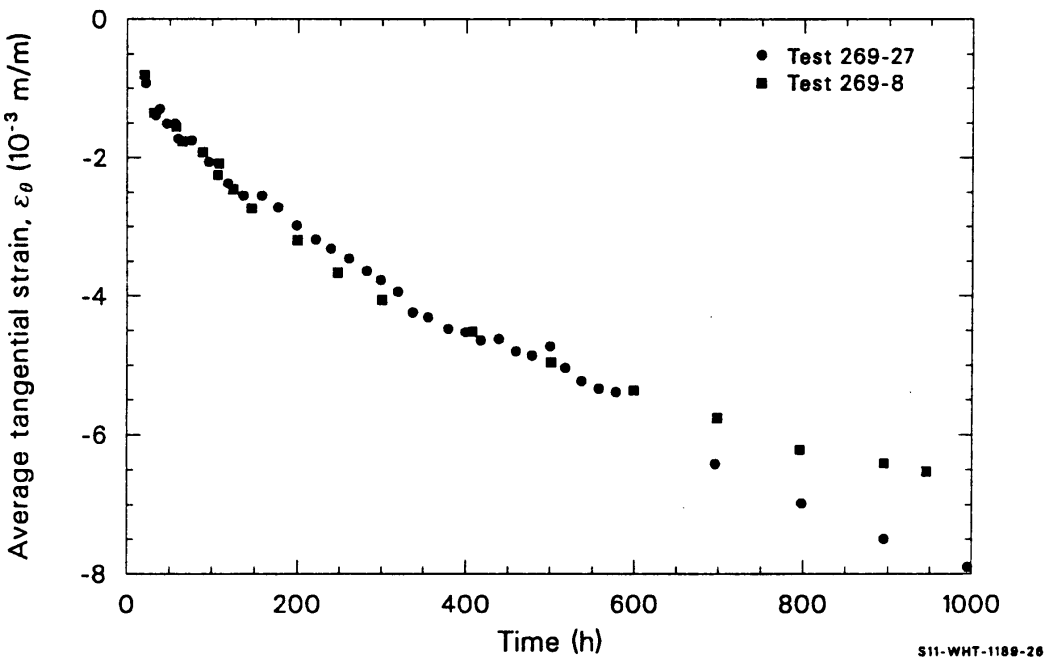

Figure 4-27. Average tangential creep strain as a function of time at 15.86 MPa differential pressure.

a. $d^2\varepsilon_\theta)/dt^2$ too large.

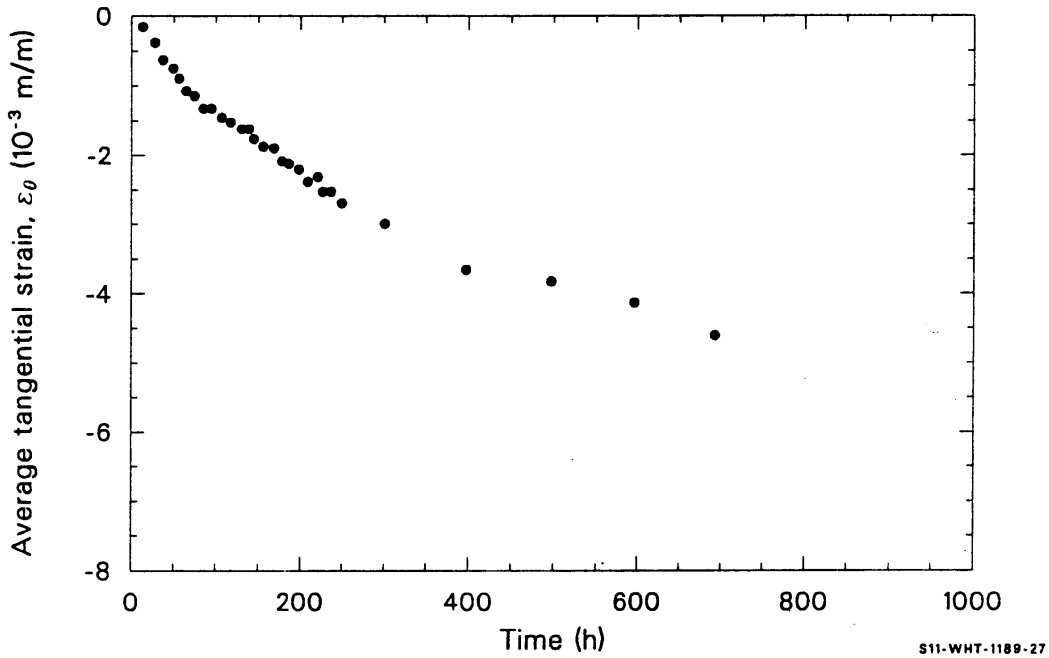

Figure 4-28. Average tangential creep strain as a function of time at 14.48 MPa differential pressure.

The equation finally adopted for short time out-of-pile tests was

$$\varepsilon_\theta = A[1 - \exp(-Bt)] \tag{4-136}$$

where

ε_θ	=	average tangential strain (m/m)
t	=	time (s)
A,B	=	functions of stress and temperature.

For the 14.48 MPa test, A = -5.32 x 10^{-3} and B = 7.64 x 10^{-7} seconds. For the 15.86 MPa tests, A = -6.32 x 10^{-3} and B = 9.17 x 10^{-7}seconds. The values of A and B for each stress were determined with a two step process:

1. A value of B was guessed and one strain time pair (ε_o,t_o) was selected as a reference. Other strain time pairs (ε_j, t_j) were then used to find an improved guess for B according to the relation

$$B_j = \ln\left(1 - \frac{\varepsilon_j\,[1 - \exp(-B_{guessed}t_0)]}{\varepsilon_0}\right). \tag{4-137}$$

2. Once a single value of B that worked for several strain-time pairs was determined, a least-squares fit was carried out to determine A.

The two sets of values for A and B were used to estimate the effect of change in stress. A and B were assumed to be dependent on stress to some power, n; and n was calculated from A and B at the two stresses where they are known

$$n = \frac{\ln(A\,at\,15.86\,MPa / A\,at\,14.48\,MPa)}{\ln\left(\frac{15.86}{14.48}\right)} = 1.89 \qquad (4\text{-}138)$$

$$n = \frac{\ln(B\,at\,15.86\,MPa / B\,at\,14.48\,MPa)}{\ln\left(\frac{15.86}{14.48}\right)} = 1.89\,. \qquad (4\text{-}139)$$

In view of the limited number of tests, both values of n were assumed to be 2. This result implies a strain rate proportional to the fourth power of stress,[a] a conclusion that agrees with one of the intermediate stress regions suggested by Dollins and Nichols[4.8-1] in Section 4.8.2.

The resultant expressions for the stress-dependence of A and B near 125 MPa and at a temperature of 644 K are

$$A = -5.32 \times 10^{-3}\ \{\sigma^2/[(1.245 \times 10^8)^2]\} \qquad (4\text{-}140)$$

$$B = 7.64 \times 10^{-7}\ \{\sigma^2/[(1.245 \times 10^8)^2]\} \qquad (4\text{-}141)$$

where σ is the tangential component of stress.

The data from Hobson's in-reactor experiment were converted to average tangential strains with the same technique used for the out-of-reactor experiment. Figure 4-29 displays the resultant average tangential strains as a function of time, along with the predicted out-of-reactor average strain from Equations (4-136), (4-140), and (4-141). The temperature during the in-reactor experiment was approximately the same as the temperature of Hobson's out-of-reactor experiments, but pressure varied from 13 to 13.5 MPa, so the tangential stress (116 MPa) was smaller in magnitude than stresses of the out-of-pile experiments.

Interpretation of the in-reactor data is complicated by absence of data for the first 80 hours, by reactor shutdown from 540 to 610 hours, and by the apparent positive average tangential strains from 80 to 200 hours. Hobson[4.8-24] has discussed the apparent positive average strains during the early part of the experiment and suggests that the positive readings come from the effects of a reactor scram at 50 hours on the experiment electronics.

a. The time derivative of Equation (4-136) is proportional to A x B.

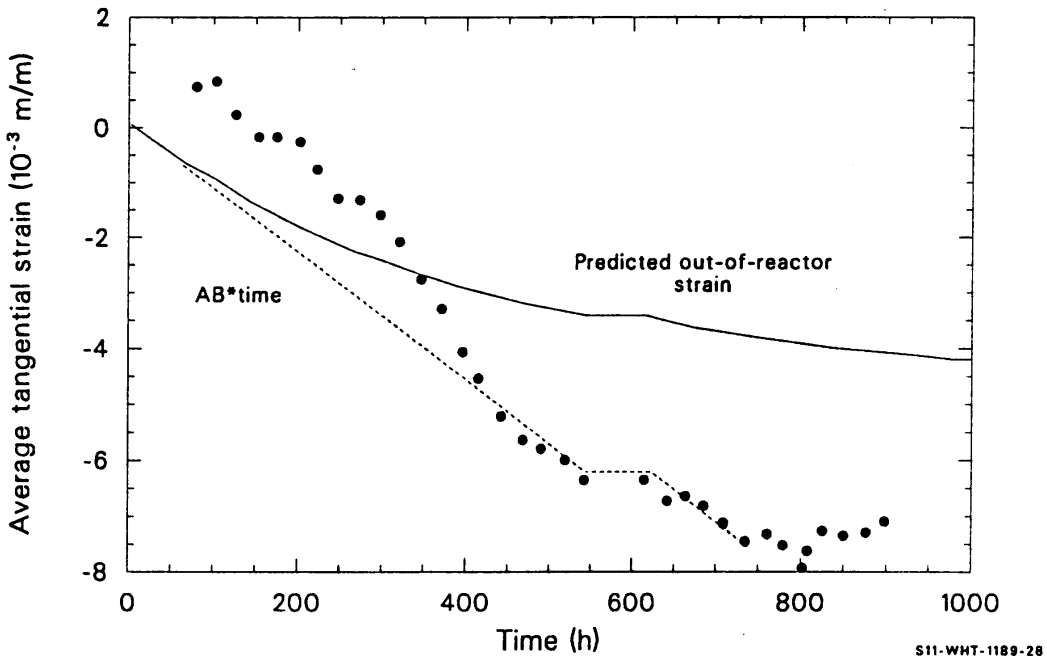

Figure 4-29. Average tangential creep strain as a function of time from Hobson's in-reactor experiment at 13 to 13.5 MPa differential pressure and 5.4 x 10^{17} fast neutrons (m^2/•s).

The in-reactor strains shown in Figure 4-29 are consistent with a simple relation between the out-of-reactor strains and the in-reactor strains [for fast neutron flux of 5.4 x 10^{17} n/m^2s). The dashed line of the figure is the strain predicted by assuming that the initial out-of-reactor strain rate, AB, is maintained throughout the in-reactor experiment. The strains are described to within the experimental uncertainty by this line.

If this simple relation between initial out-of-reactor creep rates and in-reactor creep is confirmed by subsequent experiments with compressive stress, the implications for model development are significant. The result implies that irradiation-induced creep for compressive stress is not an independent additional creep (as virtually all the models based on tensile deformation data have assumed) but simply the result of destruction of some effect associated with prior creep strain that impedes further creep strain. In the absence of any data other than those from Hobson's experiments, the assumption must be made that either (a) the in-reactor creep rate is related to the initial out of reactor creep rate for compressive stress at temperatures near 644 K or (b) the fast neutron flux, stress magnitude, and temperature are coincidentally at values that make the independent irradiation-induced creep rate equal to the initial out-of-reactor creep rate. The author has selected assumption (a) and has developed a model for cladding creepdown that is consistent with this assumption.

To be consistent with the assumption that some effect associated with prior creep strain impedes further creep strain, the independent variable in Equation (4-136) was changed from time to prior strain. The

equation was then differentiated with respect to time, and the differentiated expression was used with Equation (4-136) to eliminate time, resulting in the expression

$$\dot{\varepsilon}_\theta = B(A - \varepsilon_\theta) \tag{4-142}$$

where $\dot{\varepsilon}_\theta$ is the time derivative of the tangential strain (s^{-1}).

If fast neutron flux destroys some effect associated with prior creep strain, the appropriate modification of Equation (4-142) to describe in-reactor creep will reduce or eliminate the term, $-B\varepsilon_\theta$, when a fast neutron flux is present. This was accomplished by adapting the idea of an auto-correlation function from statistical mechanics.[4.8-27] The total strain in Equation (4-142) is replaced by the integral of the strain increment at a prior time, t', times a correlation function that approximates the rate of destruction of the effect of prior strain on the current strain rate. In the absence of detailed information, the correlation function is represented by an exponential. The resultant generalization of Equation (4-142) is

$$\dot{\varepsilon}_\theta = B\left(A - \int_0^t \exp\left[-(t-t')\left(\frac{\Phi}{\Psi} + \frac{1}{\gamma}\right)\right] d\varepsilon(t')\right) \tag{4-143}$$

where

Φ	=	fast neutron flux ($n/m^2 \cdot s$)
Ψ	=	correlation fluence (n/m^2)
γ	=	zero flux correlation time (s)

and other symbols have been previously defined.

New parameters introduced in Equation (4-143) can be given a physical interpretation without defining a detailed mechanistic model. The correlation fluence, Ψ, is the amount of radiation damage required to destroy most of the effect of prior strain on current strain rate; and the zero flux correlation time, s, is the time at the temperature required to anneal most of the effect of prior strain in zero flux. Since Equation (4-117) is an alternate form of Equation (4-143), the same interpretation can be applied to Equation (4-117).

CCSTRN Equations (4-122) and (4-123) are approximations derived from Equation (4-117). Equation (4-122) is obtained from Equation (4-117) by assuming

$$t\left(\frac{\Phi}{\Psi} + \frac{1}{\gamma}\right) \ll 1. \tag{4-144}$$

And integrating Equation (4-117) from an initial to a final time, t. Equation (4-123) uses the steady state approximation to Equation (4-117), derived by setting the time derivative of Equation (4-117) equal to zero and solving for the steady-state creep rate. If the creep rate at the given final time of a time step interval is greater than or equal to the steady-state creep rate, Equation (4-122) is employed for the entire time interval. If the creep rate at the given final time of a time step interval is less than the steady state

creep rate, the time to steady-state is calculated with Equation (4-124) and Equation (4-123) is used to calculate the final strain from the assumption that the creep rate after the time interval given by Equation (4-124) has passed. The time interval to steady state is found by solving the time derivative of Equation (4-122) for the time when the creep rate is equal to the steady state creep rate.

Equations (4-122) and (4-123) contain a term, $\varepsilon_{boundary}$, which is the initial creep strain for any time step in which the temperature and stress are the same as the previous time step. For time steps in which the temperature, stress, or fast neutron flux has changed, Equation (4-117) implies that the creep rate should respond immediately to changes in the product AB (a function of stress and temperature); but the response of the creep rate to changes in the factor, $\Phi/\Psi + 1/\gamma$ (a function of flux and temperature) should be more gradual. A boundary condition is therefore required to make the initial creep rate of Equation (4-122) equal to the creep rate at the end of the prior step. The appropriate condition is:

For prior steps not in steady state,

$$.\varepsilon_{boundary} = APexp\ (-BP\Delta tp) + eP_{boundary}[1 - exp) -BP\Delta tP)] \tag{4-145}$$

For prior steps in steady state,

$$\varepsilon_{boundary} = \frac{AP\,BP}{\frac{\Phi P}{\Psi P} + \frac{1}{\gamma P} + BP} \tag{4-146}$$

(4-147)

where AP, BP, ΔtP, $\varepsilon P_{boundary}$, ΦP, ΨP, and γP are equal to A, B, Δt, $\varepsilon_{boundary}$, Φ, Ψ, and γ during the previous time step.

Values for the parameters A and B at 644 K and stresses near 125 MPa have been determined from Hobson's out-of-reactor data. These data can also be used in conjunction with the modeling ideas just developed to find a minimum value for the zero flux correlation time, γ, at 644 K. The strains shown in Figure 4-27 show that a steady-state creep rate (a straight line plot for strain versus time) did not occur prior to 600 hours in either of the out-of-reactor experiments represented in the figure. Equation (4-124), with $\Phi = 0$ and Δt_{ss} at least as large as 600 hours, implies aγ of at least 6.8×10^6 seconds. This value was adopted as an interim estimate for γ at 644 K, since the strains calculated from Test 269-27 (test that simulated an axial gap in the fuel pellets) are consistent with steady-state creep after 600 hours.

The temperature-dependent factors in Equations (4-119) through (4-121) are interim estimates because they are based on the temperature dependence of tensile creep data. The data from Fidleris' tests, R-6 and Rx-14,[4.8-11] were selected to estimate the temperature dependence of B, γ, and Ψ because these tests were carried out at stress magnitude that closely approximates the magnitude of the stress in Hobson's experiments.

Figure 4-30 illustrates the steady-state creep rates reported by Fidleris for a stress of 138 MPa at several temperatures. The in-reactor data are at fast neutron fluxes of 6.8×10^{16} or 6.0×10^{16} n/m^2•s. The

range of steady-state creep rates predicted by the model for creepdown at 644 K is also represented. A solid square is used to represent the steady-state creep rate seen in Hobson's experiment at a fast neutron flux of 5.4 x 10^{17} n/m^2 s. The slope of the tensile stress data at temperatures > 614 K (1/T < 1.626 x 10^3) corresponds to a temperature-dependent factor of the form exp (-25,100/T). The in-reactor data < 615 K correspond to a temperature-dependent factor of the form exp (-10,400/T). The temperature-dependent factors in Equations (4-119) through (4-121) are the most convenient way of forcing the steady-state creep rate implied by Equation (4-123) to correspond to the temperature-dependence shown by the Fidleris equation.

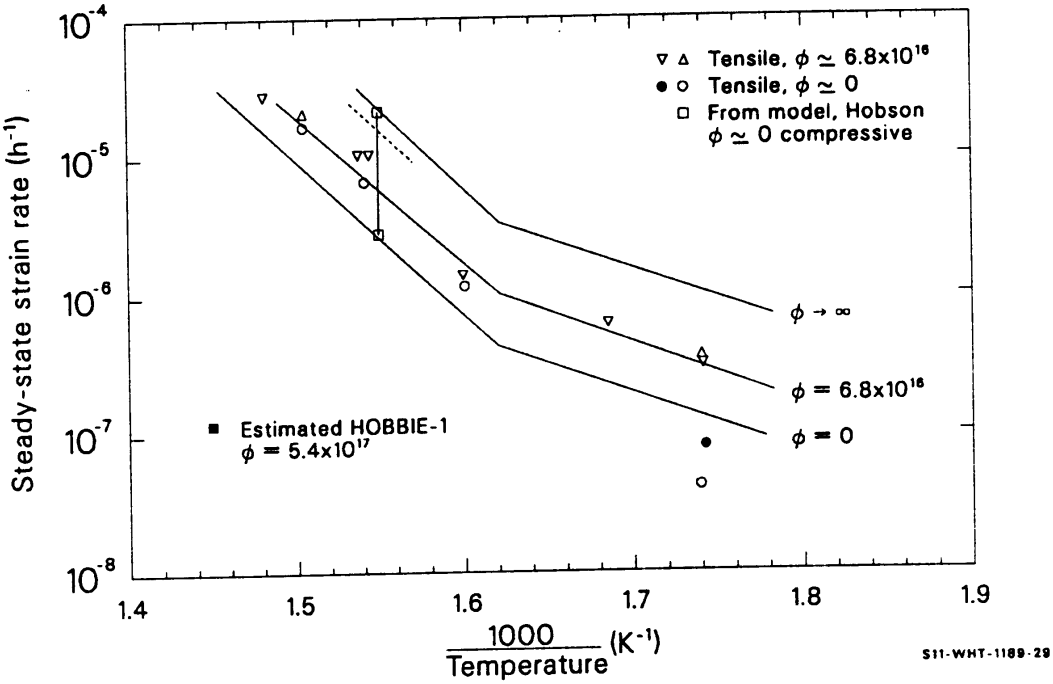

Figure 4-30. Steady-state creep rates reported by Fidleris for Tests R-6 and Rx-14 compared to model predictions for steady-state creepdown rates derived from these data.

The constants 2.9 x 10^6 and 6.967795 x 10^{16} in Equation (4-120) are the result of a least-squares fit to the steady-state creep rate data of Fidleris. As expected from the previous discussion, the resultant prediction of the steady-state creep rate for Hobson's in-reactor creep rate at 5.4 x 10^{17} n/m^2• s with a compressive stress is slightly too high. The predicted rate, s^{-1}, is shown in Figure 4-30 by the dashed line.

4.8.4 Model Uncertainty

Lack of an extensive data base for creep under compressive stress makes the assignment of uncertainty limits very tentative. The data of Stehle (illustrated in Figure 4-25) are the only other compressive stress data available. These data show creep strains of about half the magnitude of the model-predicted strains. Since these are the only appropriate data not used in developing the model, they were used to esti-

mate fractional error of 0.6 and +0.3 in strain at 644 K and 130 MPa stress. The remaining terms of the uncertainty estimate for the strain predicted by CCSTRN [Equations (4-125) and (4-126)] are simply engineering judgments that estimate 100% error when the stress differs from 130 MPa by more than 65 MPa or the temperature differs from 644 K by more than 60 K.

Equations (4-127) and (4-128), the expressions for the uncertainty of the stress calculated by CCSTRS, were derived from Equations (4-125) and (4-126) and the observation that the predicted strain is usually proportional to the fourth power of stress. The resultant uncertainty in stress expressed as a fraction of stress is one-fourth the fractional uncertainty in strain.

4.8.5 References

4.8-1 C. C. Dollins and F. A. Nichols, "Mechanisms of Irradiation Creep in Zirconium-Base Alloys," *Zirconium in Nuclear Applications*, ASTM-STP-551, 1974, pp. 229-248.

4.8-2 G. R. Piercy, "Mechanisms for the In-Reactor Creep of Zirconium Alloys," *Journal of Nuclear Materials, 2*, 1968, pp. 18-50.

4.8-3 J. R. MacEwen, "The Effect of Neutron Flux on Dislocation Climb," *Journal of Nuclear Materials, 54*, 1974, pp.85-96.

4.8-4 F. A. Nichols, "Point Defects and the Creep of Metals," *Journal of Nuclear Materials, 69 and 70*, 1978, pp. 451-464.

4.8-5 F. A. Nichols, "On the SIPA Contribution to Irradiation Creep," *Journal of Nuclear Materials, 84*, 1979, pp. 207-221.

4.8-6 D. O. Northwood, "Comments on In-Pile Dimensional Changes in Neutron Irradiated Zirconium Base Alloys," *Journal of Nuclear Materials, 64*, 1977, pp. 316-319.

4.8-7 E. F. Ibrahim, "In-Reactor Creep of Zirconium Alloys by Thermal Spikes," *Journal of Nuclear Materials, 58*, 1975, pp. 302-310.

4.8-8 P. A. Ross-Ross and C. E. L. Hunt, "The In-Reactor Creep of Cold-Worked Zircaloy-2 and Zirconium-2.5 wt Niobium Pressure Tubes," *Journal of Nuclear Materials, 26*, 1968, pp. 2-17.

4.8-9 V. Fidleris, "Summary of Experimental Results on In-Reactor Creep and Irradiation Growth of Zirconium Alloys," *Atomic Energy Review, 13*, 1976, pp. 51-80.

4.8-10 E. D. Warda, V. Fidleris, and E. Teghtsoonian, "Dynamic Strain Aging During Creep of α-Zr," *Metallurgical Transactions, 4*, 1972/1973, pp. 302-316.

4.8-11 V. Fidleris, "Uniaxial In-Reactor Creep of Zirconium Alloys," *Journal of Nuclear Materials, 26*, 1968, pp. 51-76.

4.8-12 W. J. Duffin and F. A. Nichols, "The Effect of Irradiation on Diffusion-Controlled Creep Processes," *Journal of Nuclear Materials, 45*, 1972/1973, pp. 302-316.

4.8-13 D. S. Wood, "Dose Dependence of Irradiation Creep of Zircaloy-2," *Properties of Reactor Structural Alloys After Neutron or Particle Irradiation*, ASTM-STP-570, 1975, pp. 207-217.

4.8-14 D. S. Wood and B. Watkins, "A Creep Limit Approach to the Design of Zircaloy-2 Reactor

Pressure Tubes at 275°C," *Journal of Nuclear Materials, 41*, 1971, pp. 327-340.

4.8-15 E. Kohn, "In-Reactor Creep of Zr-2.5Nb Fuel Cladding," *Zirconium in the Nuclear Industry*, ASTM-STP-633, 1977, pp. 402-417.

4.8-16 E. R. Gilbert, "In-Reactor Creep of Reactor Materials," *Reactor Technology, 14*, Fall 1971, pp. 258-285.

4.8-17 H. Stehle et al., "Mechanical Properties of Anisotropy and Microstructure of Zircaloy Canning Tubes," *Zirconium in the Nuclear Industry*, ASTM-STP-633, American Society for Testing and Materials, December 1977, pp. 486-507.

4.8-18 M. L. Picklesimer, "Deformation, Creep, and Fracture in Alpha-Zirconium Alloys," *Electrochemical Technology, 4*, 1966, pp. 289-300.

4.8-19 G. E. Lucas and A. L. Bement, "Temperature Dependence of the Zircaloy-4 Strength Differential," *Journal of Nuclear Materials, 48*, 1975, pp. 163-170.

4.8-20 R. H. Chapman, *Characterization of Zircaloy-4 Tubing Procured for Fuel Cladding Research Programs*, ORNL/NUREG/TM-29, 1976.

4.8-21 D. O. Hobson and C. V. Dodd, *Interim Report on the Creepdown of Zry Fuel Cladding*, ORNL/NUREG/TM-103, May 1977.

4.8-22 D. O. Hobson, *Quarterly Progress Report on the Creepdown and Collapse of Zircaloy Fuel Cladding for January-March 1977*, ORNL/NUREG/TM-125, July 1977.

4.8-23 D. O. Hobson, *Creepdown of Zircaloy Fuel Cladding-Initial Tests*, ORNL/NUREG/TM-181, April 1978.

4.8-24 D. O. Hobson, *Preliminary Analysis of Surface Displacement Results in the Creepdown Irradiation Experiment HOBBIE-1*, NUREG/CR-0810 and ORNL/NUREG/TM-310, June 1979.

4.8-25 H. Stehle et al., "Uranium Dioxide Properties for LWR Fuel Rods," *Nuclear Engineering and Design, 33*, 1975, pp. 230-260.

4.8-26 A. A. Bauer et al., *Progress on Evaluating Strength and Ductility of Irradiated Zircaloy During July-September 1975*, BMI-1938, September 1975.

4.8-27 C. Kittle, *Elementary Statistical Physic*s, New York: John Wiley and Sons, Inc., 1958.

4.8.6 Bibliography

This section is a list of additional references from the extensive literature on creep experiments. The list is reported here because one of the objectives of this report is to provide lists of available literature for future studies of material behavior. In most cases, the additional references were not used in the development of the model for creepdown because literature for the different case of creep under compressive stress has become available.

1. G. Dressler et al., "Determination of Complete Plane Stress Yield of Zircaloy Tubing," *Zirconium in Nuclear Applications*, ASTM-STP-551, 1974, pp. 72-103.

2. D. G. Franklin and W. A. Franz, "Numerical Model for the Anisotropic Creep of Zircaloy," *Zirconium in the Nuclear Industry*, ASTM-STP-633, 1977, pp. 365-384.

3. P. J. Pankaskie, *Irradiation Effects on the Mechanical Properties of Zirconium and Dilute Zirconium Alloys--A Review*, BN-SA-618, July 1976, updated November 1976.

4. C. E. Coleman, "Tertiary Creep in Cold Worked Zircaloy-2," *Journal of Nuclear Materials, 43*, 1971, pp. 180-190.

5. C. C. Busby and L. S. White, *Some High Temperature Mechanical Properties of Internally Pressurized Zircaloy-4*, WAPD-TM-1243, February 1976.

6. M. Gartner and H. Stehle, *In-Pile Creep Behavior of Zircaloy-4 Cladding Tubes at 400°C*, Siemens Aktiengesellschaft Reaktortechnik, September 1972.

7. M. Bernstein, "Diffusion Creep in Zirconium and Certain Zirconium Alloys," *Transactions of the Metallurgical Society of AIME, 329*, 1969, pp. 1518-1522.

8. F. A. Nichols, "On the Mechanisms of Irradiation Creep in Zirconium Base Alloys," *Journal of Nuclear Materials, 26*, 1967, pp. 51-76.

9. H. P. Kreyns and M. W. Burkart, "Radiation Enhanced Relaxation in Zircaloy-4 and Zr/2.5wt Nb/ 0.5wt Cu Alloys," *Journal of Nuclear Materials, 26*, 1968, pp. 87-104.

10. F. L. Yagee and A. Purohit, "Biaxial Creep Characteristics of GCFR Cladding at 650° and 32.4 ksi Hoop Stress," *Transactions of the American Nuclear Society, 22*, November 1975, p. 182.

11. E. F. Ibrahim and C. E. Coleman, "Effect of Stress Sensitivity on Stress Rupture Ductility of Zircaloy-2 and Zr-2.5 wt%Nb," *Canadian Metallurgical Quarterly, 12*, 3, 1973, pp. 285-287.

12. V. Fidleris, "The Effect of Texture and Strain Aging on Creep of Zircaloy-2," *Applications of Related Phenomena for Zirconium and Its Alloys*, ASTM-STP-458, 1969, pp. 1-17.

13. F. J. Azzarto et al., "Unirradiated In-Pile and Postirradiation Low Strain Rate Tensile Properties of Zircaloy-4," *Journal of Nuclear Materials, 30*, 1969, pp. 208-218.

14. W. R. Smalley, Saxton Plutonium Program: *Semi Annual Progress Report for the Period Ending June 30, 1969*, WCAP-3385-20, October 1969.

15. T. E. Caye and W. R. Smalley, *Saxton Plutonium Project: Quarterly Progress Report for the Period Ending December 31, 1970*, WCAP-3385-26, March 1971.

16. E. F. Ibrahim, "In-Reactor Tubular Creep of Zircaloy-2 at 260°C and 300°C," *Journal of Nuclear Materials, 46*, 1973, pp. 196-182.

17. H. Conrad, "Experimental Evaluation of Creep and Stress Rupture," *Mechanical Behavior of*

Materials at Elevated Temperatures, NewYork: McGraw-Hill Book Company, Inc., 1961, p.149.

18. F. A. Nichols, "Theory of the Creep of Zircaloy During Neutron Irradiation," *Journal of Nuclear Materials, 30*, 1969, pp. 249-270.

19. V. Fidleris and C. D. Williams, "Influence of Neutron Irradiation of Zircaloy-2 at 300°C," *Journal of Electrochemical Technology, 4*, May-June 1966, pp. 258-267.

20. E. F. Ibrahim, "In-Reactor Creep of Zirconium-2.5 Nb Tubes at 570 K." *Zirconium in Nuclear Industry*, ASTM-STP-551, 1974, pp. 249-262.

21. C. E. Ells and V. Fidleris, "Effect of Neutron Irradiation on Tensile Properties of the Zirconium-2.5 Weight Percent Niobium Alloy," *Journal of Electrochemical Technology, 4*, May-June 1966, pp. 268-274.

22. E. R. Gilbert, "In-Reactor Creep of Zr-2.5wt Nb," *Journal of Nuclear Materials, 26*, 1968, pp.105-111.

23. W. J. Langford and L. E. J. Mooder, "Metallurgical Properties of Irradiated Cold Worked of Zr2.5 wt% Nb Pressure Tubes," *Journal of Nuclear Materials, 30*, 1969, pp. 292-302.

24. E. F. Ibrahim, "In Reactor Creep of Zirconium Alloy Tubes and Its Correlation with Uniaxial Data," *Applications Related Phenomena for Zircaloy and Its Alloys*, ASTM-STP-458, 1969, pp.18-36.

25. T. M. Frenkel and M. Weisz, "Effect of the Annealing Temperature on the Creep Strength of Cold-Worked Zircaloy-4 Cladding," *Zirconium in Nuclear Applications*, ASTM-STP-551, 1974, pp. 140-144.

26. K. Kallstrom et al., "Creep Strength of Zircaloy Tubing at400#C as Dependent on Metallurgical Structure and Texture," *Zirconium in Nuclear Applications*, ASTM-STP-551, 1974, pp. 160-168.

27. C. R. Woods (ed)., *Properties of Zircaloy-4*, WAPD-TM-585, December 1966.

28. O. D. Sherby and A. K. Miller, *Development of the Materials Code, MATMOD (Constitutive Equations for Zircaloy)*, NP-567, December 1977.

29. D. G. Franklin and H. D. Fisher, "Requirements for In-Reactor Zircaloy Creep Measurements for Application in the Design of PWR Fuel," *Journal of Nuclear Materials, 65*, 1977, pp. 192-199.

30. W. R. Smalley, *Saxton Core II Fuel Performance Evaluation Part I: Materials*, WCAP-3385-56, September 1971.

31. W. R. Smalley, *Evaluation of Saxton Core III Fuel Materials Performance*, WCAP-3385-57, July 1974.

32. A. A. Bauer et al., *Evaluating Strength and Ductility of Irradiated Zircaloy, Quarterly Progress Report, January-March 1977*, BMI-NUREG-1971, April 1977.

4.9 Plastic Deformation (CSTRES, CSTRAN, CSTRNI, CANISO, CKMN)

This section is a description of materials properties subcodes for cladding stress and plastic deformation. The subroutine CSTRES calculates instantaneous cladding stress as a function of plastic strain, strain rate, temperature, cold work, fast neutron fluence, and average oxygen concentration. The subroutine CSTRAN calculates instantaneous cladding strain as a function of strain rate, stress, temperature, cold work, fast neutron fluence, and average oxygen concentration. CSTRNI calculates the cladding strain at the end of a time step of specified length as a function of the initial strain, average stress during the time step, temperature, cold work, fast neutron fluence, and average oxygen concentration.

The stresses and strains used with CSTRES, CSTRAN, and CSTRNI are effective stresses and strains. The subcode CANISO provides coefficients of anisotropy for converting given stress and plastic strain components to effective stresses and strains. CANISO includes a preliminary model for the change in texture with deformation. The subcode CKMN provides the parameters for the cladding equation of state as a function of temperature, average oxygen concentration, fast neutron fluence, and cold work.

4.9.1 Summary

All input strain or stress components are assumed by MATPRO mechanical property routines to be true strain or true stress.[a] The basic equation used to relate stress and plastic strain is

$$\sigma = K\varepsilon^{n}\left(\frac{\dot{\varepsilon}}{10^{-3}}\right)^{m} \tag{4-148}$$

where

σ	=	true effective stress (Pa)
ε	=	true effective plastic strain (unitless)
$\dot{\varepsilon}$	=	rate of change of true effective plastic strain (s^{-1})
K,n,m	=	parameters which describe the metallurgical state of the cladding.

Equation (4-148) is the expression used in CSTRES to calculate effective stress.

The strain returned by CSTRAN is obtained from the solution of Equation (4-148) for strain. The strain returned by CSTRNI is obtained from the time integral of the strain-dependent factors of Equation (4-148), assuming stress is constant during the time interval

a. True strain equals the change in length divided by the length at the instant of change integrated from the original to the final length. True stress equals the force per unit cross-sectional area determined at the instant of measurement of the force.

$$\varepsilon_f = \left[\left(\frac{n}{m} + 1\right) 10^{-3} \left(\frac{\sigma}{K}\right)^{1/m} \Delta t + \varepsilon_i^{\left(\frac{n}{m}+1\right)} \right]^{\frac{m}{n+m}} \tag{4-149}$$

where

ε_f	=	true effective strain at the end of a time interval (unitless)
ε_i	=	true effective strain at the start of a time interval (unitless)
Δt	=	duration of the time interval (s).

Effective stress for use with the CSTRAN and CSTRNI subroutines is obtained from stress components and the equation

$$\sigma = [A1S\,(\sigma_1 - \sigma_2)^2 + A2S\,(\sigma_2 - \sigma_3)^2 + A3S\,(\sigma_3 - \sigma_1)^2]^{1/2} \tag{4-150}$$

where

σ	=	effective stress (Pa)
$\sigma_1, \sigma_2, \sigma_3$	=	principal axis stress components (Pa)
A1S,A2S,A3S	=	coefficients of anisotropy provided by the CANISO subcode.

Effective strain for use with the CSTRES code is obtained from strain components with the equation

$$d\varepsilon = \left[\frac{1}{A1EA2E + A2EA3E + A3EA1E}\right] (A1E\,(A2E\,d\varepsilon_1 - A3Ed\,\varepsilon_2)^2 + A2E\,(A3Ed\,\varepsilon_2 - A1Ed\,\varepsilon_3)^{(2)} \tag{4-151}$$

$$A3E\,(A1Ed\,\varepsilon_3 - A2Ed\,\varepsilon_1)^2\,)^{1/2}$$

where

$d\varepsilon$	=	effective plastic strain increment
$d\varepsilon_1, d\varepsilon_2, d\varepsilon_3$	=	axial, circumferential, and radial strain component increments
A1E,A2E,A3E	=	coefficients of anisotropy provided by the CANISO subroutine.

Once effective stress and strain are known, along with the input values of either strain or stress components, the unknown components of either stress or strain can be obtained from the Prandtl-Reuss flow rule[4.9-1]

$$d\varepsilon_1 = \frac{d\varepsilon}{\sigma}\,[\sigma_1\,(A1E + A3E) - \sigma_2 A1E - \sigma_3 A3E] \tag{4-152}$$

$$d\varepsilon_2 = \frac{d\varepsilon}{\sigma}\,[-\sigma_1\,(A1E + \sigma_2\,(A1E + A2E) - \sigma_3 A2E)] \tag{4-153}$$

$$d\varepsilon_3 = \frac{d\varepsilon}{\sigma}\,[-\sigma_1 A3E - \sigma_2 A2E + \sigma_3\,(A3E + A2E)] \tag{4-154}$$

where all the terms have been previously defined.

As mentioned in conjunction with Equations (4-150) and (4-151), coefficients of anisotropy are provided by the CANISO subroutine. The information required by this subroutine is the temperature, the three principal components of plastic strain during a time interval, three constants related to the cladding basal pole distribution at the start of the time interval, and three constants related to the deformation history of the cladding prior to the time interval. For each time step, the subroutine updates the six constants required and provides the six coefficients of anisotropy required by Equations (4-150) through (4-154). Initial (no plastic deformation) values of the pole figure and deformation history constants will be discussed in conjunction with the following summary of the equations used in the CANISO subcode.

For undeformed cladding, with σ_1, σ_2, σ_3 of Equation (4-150) defined to be the axial, circumferential, and radial components of stress, the expressions used to find the stress anisotropy constants are

$$A1S = (1.5f_r - 0.5)\, g(T) + 0.5 \tag{4-155}$$

$$A2S = (1.5f_z - 0.5)\, g(T) + 0.5 \tag{4-156}$$

$$A3S = (1.5f_\theta - 0.5)\, g(T) + 0.5 \tag{4-157}$$

where

g(T)	=	a function which is 1.0 for temperatures < 1,090 K, 0 for temperatures >1,255 K, and found by linear interpolation for temperatures between 1090 and 1,255 K.
f_r, f_z, f_θ	=	average of the squared cosine between the c-axis of grains in the cladding and the radial, axial, and tangential reference directions, respectively, weighted by the volume fraction of grains at each orientation. These averages can be obtained from a pole figure and the CTXTUR subroutine (f_r = COSTH2, f_z = COSF12 - CT2CF2, and f_θ = 1-COSTH2 - COSFI2 + CT2CF2 in the notation of the CTXTUR subroutine). Values of f_r, f_z, and f_θ for typical cladding textures are $f_r = 0.66$, $f_z = 0.06$, and $f_\theta = 0.28$.[4.9-2]

The change of the factors, f_r, f_θ, and f_z, of Equations (4-155) through (4-157) due to deformation is modeled with the following correlations

$$\Delta f'_r = -d\varepsilon_3\, [-1.505T\, (0.00895)] \tag{4-158}$$

$$\Delta f'_\theta = -d\varepsilon_1\, [-1.505T\, (0.00895)] \tag{4-159}$$

$$\Delta f'_z = -d\varepsilon_2\, [-1.505T\, (0.00895)] \tag{4-160}$$

where

$\Delta f'_r \Delta f'_z \Delta f'_\theta =$ change in f_r, f_z, and f_θ due to deformation

T = 644 K, for temperature < 644 K, the temperature for > 644 temperature ≤ 1,090 K, 1,090 K for temperature > 1,090 K.

The strain anisotropy coefficients A1E, A2E, and A3E are given by Equations (4-155) through (4-160), with A1S, A2S, and A3S replaced by A1E, A2E, and A3E when the cladding temperature is below 650 K. However, limited data at temperatures above 800 K suggest initial strain anisotropy coefficients of 0.5 (the isotropic values). The description of high temperature strain anisotropy thus requires a separate set of f values, set initially at the isotropic values and changed during each time step by an amount given by Equations (4-158) through (4-160). The expressions for A1E, A2E, and A3E which are used to model this rather complex switching from texture-dependent to deformation-dependent strain anisotropy are

$$A1E = \frac{A1S + [(1.5f'_r - 0.5)\,g(T) + 0.5]\exp\left[\frac{(T-725)}{18}\right]}{\exp\left[\frac{(T-725)}{18}\right] + 1} \tag{4-161}$$

$$A2E = \frac{A2S + [(1.5f'_z - 0.5)\,g(T) + 0.5]\exp\left[\frac{(T-725)}{18}\right]}{\exp\left[\frac{(T-725)}{18}\right] + 1} \tag{4-162}$$

$$A3E = \frac{A3S + [(1.5f'_\theta - 0.5)\,g(T) + 0.5]\exp\left[\frac{(T-725)}{18}\right]}{\exp\left[\frac{(T-725)}{18}\right] + 1} \tag{4-163}$$

where f'_r, f'_z, and f_θ are deformation-dependent parameters set equal to 1/3 at zero deformation and changed like the parameters f_r, f_z, and f_θ in Equations (4-158) through (4-160).

Effects of cladding temperature, cold work, irradiation, in-reactor annealing, and oxidation on mechanical properties are expressed as changes in the strength coefficient, K; the strain hardening exponent, n; and the strain rate sensitivity exponent, m; of Equations (4-148) and (4-149). For fully annealed isotropic zircaloy-2 or zircaloy-4 cladding, the temperature and strain rate dependent values of m, n, and K are as shown below.

(1) Values of the strain rate sensitivity exponent, m[a]:

For T ≤ 730 K,

$$m = 0.02 \quad . \tag{4-164}$$

For 730 ≤ T < 900 K,

$$m = 2.063172161 \times 10^{1} + T\{-7.704552983 \times 10^{-2} + T[9.504843067 \times 10^{-5} + T(-3.860960716 \times 10^{-8})]\} \quad . \tag{4-165}$$

a. Eight to ten significant figures are used in these expressions to minimize discontinuities.

For $900 \leq T < 1{,}090$ K,

$$m = -6.47 \times 10^{-2} + 2.203 \times 10^{-4}\, T \quad . \tag{4-166}$$

For $1{,}090 \leq T \leq 1{,}172.5$ K,

$$m = -6.47 \times 10^{-2} + 2.203 \times 10^{-4}\, T, \text{ for } \dot{\varepsilon} \geq 6.34 \times 10^{-3} s^{-1}$$

$$= -6.47\times10^{-2} + 2.203\times10^{-4}T + 6.78\times10^{-2}\left(\frac{T-1090}{82.6}\right)\ln\left(\frac{6.34\times10^{-3}}{\dot{\varepsilon}}\right) \text{ for } \dot{\varepsilon} < 6.34\times10^{-3}s^{-1} \quad . \tag{4-167}$$

For $1{,}172.5 < T < 1{,}255$ K,

$$m = -6.47 \times 10^{-2} + 2.203 \times 10^{-4}\, T, \text{ for } \dot{\varepsilon} \geq 6.34 \times 10^{-3} s^{-1}$$

$$= -6.47\times10^{-2} + 2.203\times10^{-4}T + 6.78\times10^{-2}\left(\frac{1255-T}{82.6}\right)\ln\left(\frac{6.34\times10^{-3}}{\dot{\varepsilon}}\right) \text{ for } \dot{\varepsilon} < 6.34\times10^{-3}s^{-1} \quad . \tag{4-168}$$

For $1{,}255 \leq T \leq 2{,}100$ K,

$$m = -6.47 \times 10^{-2} + 2.203 \times 10^{-4}\, T \quad . \tag{4-169}$$

(2) Values of the strain hardening exponent, n:

For $T < 1{,}099.0772$ K,

$$n = -9.490 \times 10^{-2} + T[1.165 \times 10^{-3} + T(-1.992 \times 10^{-6} + T9.588 \times 10^{-10})] \quad . \tag{4-170}$$

For $1{,}099.0722 \leq T < 1{,}600$ K,

$$n = -0.22655119 + 2.5 \times 10^{-4}T \quad . \tag{4-171}$$

For $T \geq 1{,}600$ K,

$$n = 0.17344880 \tag{4-172}$$

When the strain is < n/(1 + m), the strain hardening exponent is modified to a larger value than the one given by Equations (4-170) through (4-172). The expression used to modify n for strains < n/(1 + m) is

$$n' = \text{the smaller of ANL or } n^2/[(1 + m)\cdot \varepsilon] \quad (4\text{-}173)$$

where

ANL	=	0.17 for $T \leq 730$ K; 0.056T - 11.218 for $730 < T < 780$ K; or 0.95 for $T \geq 780$ K
n	=	the number given by Equations (4-170) through (4-172)
n	=	the revised number to be used with Equation (4-148) or (4-149) in place of n.

(3) Values of the strength coefficient, K:

For $T < 750$ K,

$$K = 1.17628 \times 10^9 + T\{4.54859\times10^5 + T[-3.28185 \times 10^3 + T(1.72752)]\} \quad (4\text{-}174)$$

For $750 \leq T < 1{,}090$ K,

$$K = 2.522488 \times 10^6 \exp(2.8500027 \times 10^6/T^2) \quad (4\text{-}175)$$

For $1{,}090 \leq T < 1{,}255$ K,

$$K = 1.841376039 \times 10^8 - T1.4345448 \times 10^5 \quad (4\text{-}176)$$

For $1{,}255 \leq T \leq 2{,}100$ K.

$$K = 4.3302 \times 10^7 + T[-6.685 \times 10^4 + T(3.7579 \times 10^1 - T7.33 \times 10^{-3})] \quad (4\text{-}177)$$

The changes in form of Equations (4-164) through (4-177) in various temperature ranges are caused by changes in the physical mechanism of the plastic deformation. At 700 to 900 K, the deformation becomes significantly strain-rate-dependent, the strength of the material begins to decrease rapidly with temperature, and strain hardening becomes relatively unimportant. This change is generally attributed to thermal creep at high temperature, but the specific deformation system change has not been identified. The 1,090 to 1,255 K region is the $\alpha + \beta$ phase region for zircaloy, and the region above 1,255 K is the β phase region for this material.

The change in the strain hardening exponent due to irradiation and cold-working of cladding is described by multiplying the value of n given in Equations (4-170) through (4-172) by

$$RIC = [0.847\exp(-39.2COLDW) + 0.153 + COLDW(-9.16\times10^{-2} + 0.229COLDW)] \exp\left(\frac{-\Phi^{1/3}}{3.73\times10^7 + 2\times10^8 COLDW}\right) \quad (4\text{-}178)$$

where

RIC	=	strain hardening exponent for irradiated and cold-worked material divided by

the expression in Equations (4-170) through (4-172)

COLDW = effective cold work for strain hardening exponent (unitless ratio of areas). (Changes in the effective cold work as a function of time and temperature are modeled by the CANEAL subroutine discussed in Section 4.10.)

Φ = effective fast neutron fluence (neutrons > 1.0 MeV/m^2). (Changes in the effective fast neutron fluence are modeled by the CANEAL subroutine discussed in Section 4.10.)

The change in the strength coefficient due to irradiation and cold-working of the cladding is modeled with the expression

$$DK = (0.546\ COLDW + 9.76 \times 10^{-27}\Phi)\ K \tag{4-179}$$

where ΔK is the strength coefficient for irradiated and cold-worked material minus the expression in Equations (4-174) through (4-177) (Pa). The strain rate sensitivity exponent does not change as a function of irradiation or cold work.

Correlations for the changes in the strain hardening exponent, strength coefficient, and strain rate sensitivity exponent due to the oxidation of the cladding are

$$RNO = 1 + \left[1250 - \frac{1250}{\exp\left[\frac{(T - 1380)}{20}\right] + 1} \right] Y \tag{4-180}$$

$$RKO = 1 + \left[1120 - \frac{990}{\exp\left[\frac{(T - 1300)}{61}\right] + 1} \right] Y \tag{4-181}$$

and

$$RMO = \exp(-69Y) \tag{4-182}$$

where

RNO = strain hardening exponent for oxidized cladding divided by strain hardening exponent for as fabricated cladding

RKO = strength coefficient for oxidized cladding divided by strength coefficient for as fabricated cladding

RMO = strain rate sensitivity exponent for oxidized cladding divided by strain rate sensitivity exponent for as fabricated cladding

T = temperature (K)

Y = average oxygen concentration increase (kg oxygen/kg zircaloy). (Changes in oxygen concentration are modeled by the COBILD subroutine).

Estimates have been made for the expected error of the strength coefficient, strain hardening exponent, and strain rate sensitivity exponent. The expressions for these uncertainties are

$$UK = \begin{cases} 77\times10^{6} \text{ for } T < 700K \\ 110.43693\times10^{6} - T4.7767045\times10^{4} \text{ for } 700 \le T \le 800K \\ \dfrac{(\text{strength coefficient})}{3} \text{ for } T > 800K \end{cases} \tag{4-183}$$

$$Un = \begin{cases} 0.017 \text{ for } T < 700K \\ -2.8405405\times10^{-2} + 1.64864864\times10^{-5}T \text{ for } 700 \le T \le 1255K \\ 0.053 \text{ for } T > 800K \end{cases} \tag{4-184}$$

$$Um = \begin{cases} 0.01 \text{ for } T < 700K \\ -2.97992\times10^{-2} + 5.6856\times10^{-5} \text{ for } 700 \le T \le 1255K \\ 0.16\ (\text{strain rate sensitivity exponent}) \text{ for } T \ge 1255 \end{cases} \tag{4-185}$$

where

UK = expected error of the strength coefficient (fraction of value)

Un = expected error of the strain hardening exponent (fraction of value)

Um = expected error of the strain rate sensitivity exponent (fraction of value).

The following section is a review of the data used to derive the expressions summarized in this section. Section 4.9.3 describes the development of the plastic deformation models, and Section 4.9.4 is a comparison of model predictions to data not used to develop the models. Uncertainties are discussed in Section 4.9.5.

4.9.2 Available Data

A number of references which discuss zircaloy plastic deformation are available.[4.9-2 to 4.9-37] However, many of the data are from uniaxial load elongation tests on poorly characterized material. Also, the basic data used to construct models are often not published. The critical data for analysis of cladding deformation stress and strain versus time in tests with biaxial stress using well characterized cladding are sparse. This section is a review of the theoretical results and data available for use in cladding plastic deformation models. The general features of zircaloy plastic deformation are reviewed first, followed by reviews of uniaxial and biaxial test data.

4.9.2.1 ***Modes of Deformation.*** Zircaloy has a hexagonal, close packed crystal structure at temperatures in the range from 300 to 1,090 K. At temperatures of 1,255 to 2,100 K, the alloy has a body-centered cubic structure. Since the structure changes, significant changes in the plastic deformation must also be expected in the temperature range 1,090 to 1,255 K. Moreover, the alpha (hexagonal), alpha + beta, and beta (body-centered cubic) phase boundaries change with increasing oxygen content. Thus, the

temperatures at which one expects discontinuities in cladding plastic deformation change with oxygen content.

The alpha phase (at least in unirradiated zircaloy) is anisotropic. This means the texture (orientation of individual grains) of the material is important at temperatures below 1,090 K. Theories exist to deal with anisotropic plastic deformation[4.9-30,4.9-38] under varying stress-states, but they rely on the assumption that the physical process responsible for plastic deformation does not change significantly as a function of the stress state. That is, a single plastic potential[4.9-38] or a single stress-strain law[4.9-29] is assumed at each temperature. There is evidence that indicates that this is an oversimplification.[4.9-3, 4.9-31] Both slip and twinning systems are expected to operate in zircaloy, and the operable system is related to the orientation of grains with respect to the applied stress. As multiaxial stress versus strain data become available, it is likely that different stress strain laws (equations of state) will be developed for each mode of deformation, along with conditions for specifying when each mode is active. There is not enough detailed biaxial data to develop equations of state for separate modes of deformation; therefore, an equation of state has been developed based on existing uniaxial data and compared to limited biaxial data to see if discrepancies exist. Analysis discussed in Section 4.9.3 of this report indicates that the discrepancies may be significant.

Modeling zircaloy plastic deformation is further complicated by the fact that deformation is caused by true stress, which is not measured in any of the tests reported because none of the investigators measured the minimum cross sectional area of the sample during deformation. The problem was addressed by other experiments,[4.9-37] but zircaloy data from these tests were not included in the model.

4.9.2.2 ***Uniaxial Test Data.*** The low temperature part of the equation of state used in MATPRO for fully annealed cladding, Equation (4-148), in conjunction with Equations (4-170) through (4-177), is based primarily on data in Section VI of a review by Woods.[4.9-5] He reports strength coefficients and strain hardening exponents derived from load elongation tests at temperatures from 300 to 783 K. Strain rates of 1.25×10^{-2} and 5×10^{-4}/s were used in the tests, and cladding samples with several different annealing histories were studied. Reciprocal pole figures were provided to specify the texture of each cladding group, but these figures are not sufficiently detailed to allow an accurate characterization of the texture. Considerable scatter has no doubt been introduced into the data base because the details of the material texture are not accurately known and because models for cold work effects had to be used to try to account for the different annealing histories of the samples.

Ultimate strength data from Bauer[4.9-27] have been used to supplement the data from Woods for the low temperature equation of state. These data were from well characterized cladding,[4.9-39] but the full stress-strain curve was not published. To use these data, a stress-strain law of the form of Equation (4-148) had to be assumed.

Since neither Woods nor Bauer reported strain rate sensitivities, data from tests on zircaloy sheet specimens were used for the low temperature correlation for the strain rate sensitivity exponent, Equation (4-164). The values of m obtained with zircaloy-2 plate by Mehan and Wiesinger[4.9-6] and those reported for zircaloy-4 plate in the transverse direction by Lee and Backofen[4.9-9] were employed.

With two important exceptions, which will be discussed in the next subsection, all of the correlations for plastic deformation above 783 K are based on ultimate strength, uniform elongation, and strain rate sensitivity measurements by Chung, Garde, and Kassner[4.9-20] and on ultimate strength data reported by

Brassfield.[4.9-7] Such data are not satisfactory for deriving an equation of state because (a) the form of the equation of state must be assumed to use the data and (b) even if the assumed form of the equation of state is correct, the parameters obtained from those data in the alpha phase may apply to a mode of deformation not active when biaxial stress is applied. The high temperature data just discussed were used in MATPRO because there have been so few publications on biaxial isothermal measurements of stress and strain versus time at high temperature.

Equations (4-178) and (4-179) for the effects of cold work and irradiation on plastic deformation are based primarily on a study by Bement.[4.9-8] The study was conducted with well characterized zircaloy-2 plates irradiated to fast neutron fluences of 10^{25} fast n/m^2. The entire load elongation curve was used to deduce values of the strength coefficient and strain hardening exponent. Unfortunately, specimen irradiation was conducted at 333 K and testing was at room temperature. It is, therefore, possible that irradiation at reactor operating temperature produces different results.[4.9-40] For that reason, the data from this study were compared with limited and less well characterized data from Cowan and Langford[4.9-12] and Howe and Thomas.[4.9-10] The latter data were obtained from material irradiated at reactor operating temperatures. The load elongation tests of References 4.9-10 and 4.9-12 were conducted at room temperature and 573 K.

The most applicable data for modeling the effect of irradiation and cold work are the measurements of ultimate strengths, yield strengths, and uniform elongation reported by Bauer.[4.9-26,4.9-28] His measurements were taken with cladding irradiated in the Carolina Power and Light H. B. Robinson reactor to fast neutron fluences of 4 x 10^{25}n/m^2. Testing was performed at 644 K. Unfortunately, Bauer was unable to test unirradiated samples from the lot of tubing they used. Use of this data must therefore rely on nominal preirradiated values of ultimate strength.[4.9-28]

The models for the effect of cladding oxidation on plastic deformation are based on ultimate strength data from Rubenstein[4.9-11] and additional work by Chung, Garde, and Kassner.[4.9-23] The tensile strength data by Rubenstein were measured at temperatures in the range 300 to 644 K and oxygen concentrations up to 6330 ppm. Unfortunately, neither load elongation curves nor values of uniform elongation were published.

Chung, Garde, and Kassner[4.9-23] published constants based on a fit of stress strain data. The temperature range (1,123 to 1,673 K) and oxygen concentrations (0.46 to 1.10 wt% oxygen) make the data unique. An approximate model was developed by reformulating correlations so that they could be used in the MATPRO package.

4.9.2.3 ***Biaxial Test Data.*** Tube burst tests provide strain versus time data that are usable for stress versus strain modeling of multiaxial stress states. These experiments are important because it is possible that a change in the deformation mode under multiaxial stress will lead to a completely different equation of state for relating stress and strain under biaxial stress.

The earliest attempt at providing data for a biaxial stress strain law is the work of Hardy.[4.9-34] Zircaloy-4 cladding tubes were heated in an inert environment, and both temperature and internal pressure were recorded. The important feature of these tests is that tests with similar initial pressures and heating rates were stopped by venting internal pressure before burst temperature occurred. The posttest diameter measurements from tests with the same input conditions provide a reasonable measure of strain during a typical test. Only the diametral expansion was reported, so only one component of strain can be obtained

from these tests. Their primary value is for checking predicted diametral strain versus time. At least two components of strain are needed to construct an (effective stress)-(effective strain) expression.

Similar biaxial data have been provided by Chung[4.9-23,4.9-24] using a laser and high-speed camera. In most cases, only diameter versus time was reported; but the data are a valuable supplement to Hardy's measurements of diametral strain versus time. In a few cases,[4.9-24] both diameter and length versus time were reported. Unfortunately, those cases include only preoxidized cladding; and it has been shown[4.9-23] that the presence of an oxide changes the properties of the composite specimen considerably.

The most useful data available to date are measurements of cladding diameter and length versus time by Hann.[4.9-2] The cladding is well characterized, and experimental details are discussed. The principal difficulty with using these data are possible local effects variations in temperatures and cladding wall thickness, which will cause the measured strain to be an average of local strains. The published data from two of the tests described in Reference 4.9-2 have been analyzed and are discussed in Section 4.9.3.

4.9.3 Model Development

The equation of state used in MATPRO to provide a description of zircaloy cladding plastic deformation under tensile stress is based on the Holloman relation

$$\sigma = K\varepsilon^n \tag{4-186}$$

where

σ	=	true effective stress (Pa)
K	=	strength coefficient (Pa)
n	=	strain hardening exponent (unitless)
ε	=	true effective strain (unitless).

Holloman's equation was modified to include the effect of strain rate because this parameter was found to be more important than strain in high temperature, uniaxial stress tests. The resultant form of the equation of state is

$$\sigma = K\varepsilon^n \left(\frac{\dot{\varepsilon}}{10^{-3}} \right)^m \tag{4-187}$$

where

ε	=	rate of change of true effective strain (s^{-1})
m	=	strain rate sensitivity exponent (unitless).

Several more complex relations between stress and strain have been proposed,[4.9-18,4.9-20,4.9-30] and a few highly simplified equations have been successfully employed in limited temperature ranges.[4.9-32,4.9-33] Equation (4-148) was selected because it is efficient for code use and consistent with available data

The following subsections discuss the development of equations for the coefficients of anisotropy used to determine effective stress and strain from their components. Equations (4-164) through (4-177) form, n, and K as a function of temperature are developed in Subsection 4.9.3.2. Subsection 4.9.3.3 discusses Equation (4-178) and (4-179) for the change in n and K with cold work and irradiation. Finally, Equations (4-180) through (4-182) for the effect of oxidation on the equation of state are developed in Subsection 4.9.3.4.

4.9.3.1 ***Coefficients of Anisotropy.*** The model for the effects of texture is based on Hill's quadratic expression for plastic potential[4.9-38] [for principal axes, Equation (4-150)]. As Hill and several others have pointed out, the expression implies that the effect of tensile stress is the same as compressive stress. Since compressive and tensile stress of equal magnitude produce different strains in zircaloy,[4.9-3] Hill's theory is not sufficient to model plastic strain for all states of stress. The theory has been used because (a) it is compatible with the mechanics package of the FRAPCON and FRAP-T codes[4.9-1] and (b) there are not enough data to modify Hill's theory in the temperature range from 500 to 1,255 K.

The constants A1S, A2S, and A3S in Equation (4-150) have been assumed to be proportional to the texture factors defined in conjunction with Equations (4-155) through (4-157) and to correspond to isotropic material in the beta phase. The assumption is ad hoc and intended to reflect the general observation that effective stress is smaller when stress is applied in directions with heavy concentrations of basal poles. Its justification is that it reduces the scatter in measured values of cladding strength for material with different textures, as discussed in Subsection 4.9.3.2.

The appropriate texture factor to use to estimate each anisotropy constant was determined simply by considering uniaxial tests. For example, in a test with $\sigma_2 = \sigma_3 = 0$ and σ_1 = axial stress, Equation (4-150) becomes

$$\sigma = \begin{cases} (A1S + A3S)^{1/2}\sigma_z \\ \left[\frac{3}{2}(f_r + f_\theta)\right]^{1/2}\sigma_z \\ \left[\frac{3}{2}(1 - f_z)\right]^{1/2}\sigma_z \end{cases} \tag{4-188}$$

where the symbols have been defined previously. For a texture with basal poles strongly concentrated in the axial direction, f_z could be nearly 1.0 and the effective stress small. For the small values of f_z more characteristic of cladding, the effective stress would be relatively large.

For a perfect crystal, the empirical constants A1S, A2S, and A3S would imply that there is no deformation at all in the basal pole direction. Since twinning is known to occur and allow deformation along the basal pole direction, the estimated values of A1S, A2S, and A3S can be expected to overestimate the effect of texture when the largest stress differences in the expression for effective stress

$$\sigma = [1.5 f_r (\sigma_z - \sigma_\theta)^2 + 1.5 f_z (\sigma_\theta - \sigma_r)^2 + 1.5 f_\theta (\sigma_r - \sigma_z)^2]^{1/2} \tag{4-189}$$

multiply small texture factors.

The uniaxial stress tests by Busby[4.9-18] agree well with both the effective stress predicted by Equation (4-189) and with the strain ratios predicted when A1E, A2E, and A3E in Equations (4-152) through (4-154) are presumed to be equal to the anisotropy coefficients just discussed for effective stress. However, an analysis of recent experimental data at 811 and 1,089 K has indicated that the anisotropy coefficients given in Equation (4-189) are not appropriate for a closed tube burst test in the temperature range 800 to 1,090 K. For these tests, strain anisotropy coefficients derived from the data are characteristic of isotropic material for small strain but change rapidly with increasing strain. A similar result has been reported by Stehle.[4.9-35]

It is likely that the change in the strain anisotropy is due to a change in the physical mechanism of plastic deformation that is, in turn, caused either by increased temperature or the biaxial stress state of the data. The data that could be used to tell whether the important difference between Busby's tests and later tests is the temperature or the stress state were not published at the time of model development. If the stress state changes the mechanism of plastic deformation, a second equation of state and a second set of anisotropy coefficients would be required to describe this second mode of deformation.

An attempt has been made to include the second mode of deformation by defining experimentally determined strain anisotropy coefficients that are different than the texture related stress anisotropy coefficients previously discussed. The experimental data used to define the high temperature strain anisotropy coefficients are measurements of length, diameter, and internal pressure versus time for isothermal cladding burst tests at 810 and 1,089 K by Hann.[4.9-2] With the incompressibility assumption, the data can be used to calculate the three components of strain as a function of the stress components. With the additional assumption that the deformation of these samples was symmetric, at least during the early part of the test, plastic strain components were calculated and compared to the predictions of Equations (4-152) through (4-154) using the texture determined values for A1E, A2E, and A3E. These predicted results were totally inconsistent with the measured strain components. However, consistent results were obtained by assuming that the constants A1E, A2E, and A3E were all initially 0.5. Moreover, if the anisotropy coefficients are interpreted as texture coefficients, the change in the anisotropy coefficients with deformation was consistent with the general rule suggested by Busby (Reference 4.9-18), i.e., that "the basal planes of zircaloy tend to become aligned parallel to the direction of positive (tensile) strain and perpendicular to negative (compressive) strain."

Unfortunately, a direct solution for A1E, A2E, and A3E from the measured strain components and Equations (4-152) through (4-154) is not possible. The equations are not independent, since the sum of the strain increments is zero. However, the assumption that the coefficients of anisotropy are proportional to the volume average of some texture coefficients gives another independent equation

$$A1E + A2E + A3E = 1.5 \tag{4-190}$$

With this relation, it is possible, in principle, to solve two of Equations (4-152) through (4-154) and Equation (4-190) in terms of stress and strain components. However, the expressions for $d\varepsilon$ and σ are complicated functions, so an alternate approach, taking $d\varepsilon/\sigma$ as a fourth unknown, was used. With this approach, the expressions for two of the three unknowns A1E, A2E, and A3E in terms of a third and measured stress and strain components are Equation (4-190) and

$$\frac{de_\theta}{de_z} = \frac{A1E\ (\sigma_\theta - \sigma_z) + A2E\ (\sigma_\theta - \sigma_r)}{A3E\ (\sigma_z - \sigma_r) + A1E\ (\sigma_z - \sigma_\theta)}. \tag{4-191}$$

The idea that the basal poles of zircaloy should tend to become aligned in the direction of compressive strain leads to the conclusion that A2E, the coefficient proportional to the axial concentration of basal poles, should change very little because the axial strain observed in closed tube burst tests is small. With this assumption and using Equation (4-190), the increase in A1E and the decrease in A3E are of equal magnitude. Substitution of

$$A1E = 1/2 + \delta \tag{4-192}$$

$$A2E = 1/2 \tag{4-193}$$

$$A3E = 1/2 - \delta \tag{4-194}$$

into Equation (4-191) allows δ (and thus A1E, A2E, and A3E) to be determined from measured quantities.

Figure 4-31 shows the results obtained for the two tests from Reference 4.9-2 at 810 and 1,089 K. The increase in the anisotropy coefficient that has been assumed proportional to the effective concentration of basal poles in the radial direction (A1E) is approximately proportional to the radial compressive strain in each test. The rate of change appears to increase with temperature. The expressions for the change of anisotropy coefficients with compressive strain, Equations (4-158) through (4-160), were obtained by least-squares fits to the two sets of data shown in Figure 4-31, assuming a linear temperature dependence. Extrapolation of this correlation to 644 K predicts no significant departure of the coefficients A1E, A2E, and A3E from their initial values until strains of about 0.15 are produced. This is the approximate strain for which Busby reported significant departure in his tests.

4.9.3.2 *Plastic Deformation Parameters m, n, and K as Functions of Temperature.*

The strain rate sensitivity constant, m, of zircaloy-2 and zircaloy-4 was evaluated with data obtained from References 4.9-5, 4.9-20, 4.9-6, 4.9-9, and 4.9-16. The data are plotted in Figure 4-32. Most of the values of m at temperatures higher than 900 K were given in Reference 4.9-20 as a function of engineering strain for strain rate changes centered around 10^{-3}/s. No significant dependence on strain was indicated, so m is modeled without strain dependence. Outside the $\alpha - \beta$ phase transition region (taken as from 1,090 to 1,255 K), significant dependence of m on strain rate again was not observed. Within the $\alpha - \beta$ transition region and at strain rates below 6.34×10^{-3}, m was a strong function of the strain rate

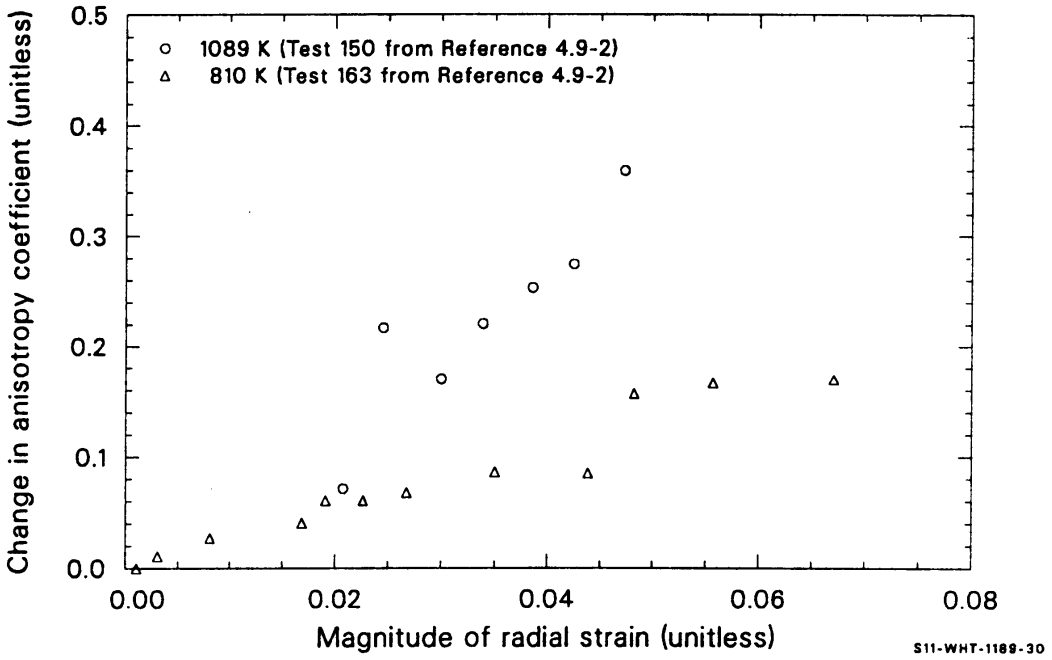

Figure 4-31. Increase of the strain anisotropy constant A1E as a function of radial compressive strain in two tests.

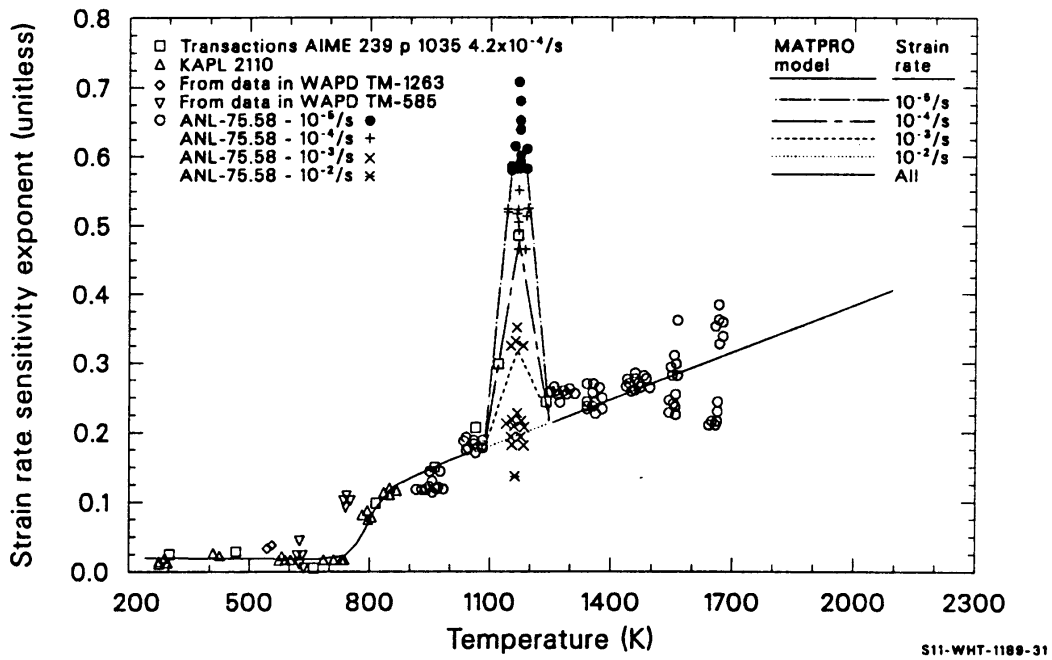

Figure 4-32. Strain rate sensitivity exponent as a function of temperature and strain rate.

In the MATPRO plastic deformation models, values of m from data taken at temperatures below 730 K are approximated with a constant (m = 0.02), while data for temperatures above 900 K and outside the $\alpha - \beta$ phase transition region are modeled as a linear function of temperature. The value of m in the region from 730 to 900 K is modeled by a third-degree polynomial in temperature with the constants determined so that the values and slopes of the polynomial match the values and slopes of the expressions form outside the boundaries of the 730 to 900 K region. The values of m predicted by Equations (4-164) through (4-169) are illustrated in Figure 4-32, along with the data. The two points at 561 K are particularly interesting because they are estimates based on high-strain-rate (4/s) tests with irradiated material. They do not appear to be significantly different from the values of m obtained at lower strain rates with unirradiated material.

Most of the values of m in the $\alpha - \beta$ transition region were also obtained from data presented in Reference 4.9-20. The strain-rate-dependent values measured at 1,173 K were assumed to reflect an additive increase in m due to the mixed phases. When the increase is plotted against the logarithm of the strain rate, the effect of varying strain rates on m can be closely approximated by a straight line of the form

$$\Delta m = 0.1253 + 0.1562 \log (10^{-3} s^{-1} / \text{STRAIN RATE}) \qquad (4\text{-}195)$$

which was obtained by a least-squares fit to the data. The fit is illustrated in Figure 4-33. For strain rates outside the range 10^{-5}/s to 6.34 x 10^{-3}/s, the change in m is taken to be equal to its value at the nearest point

of this range.

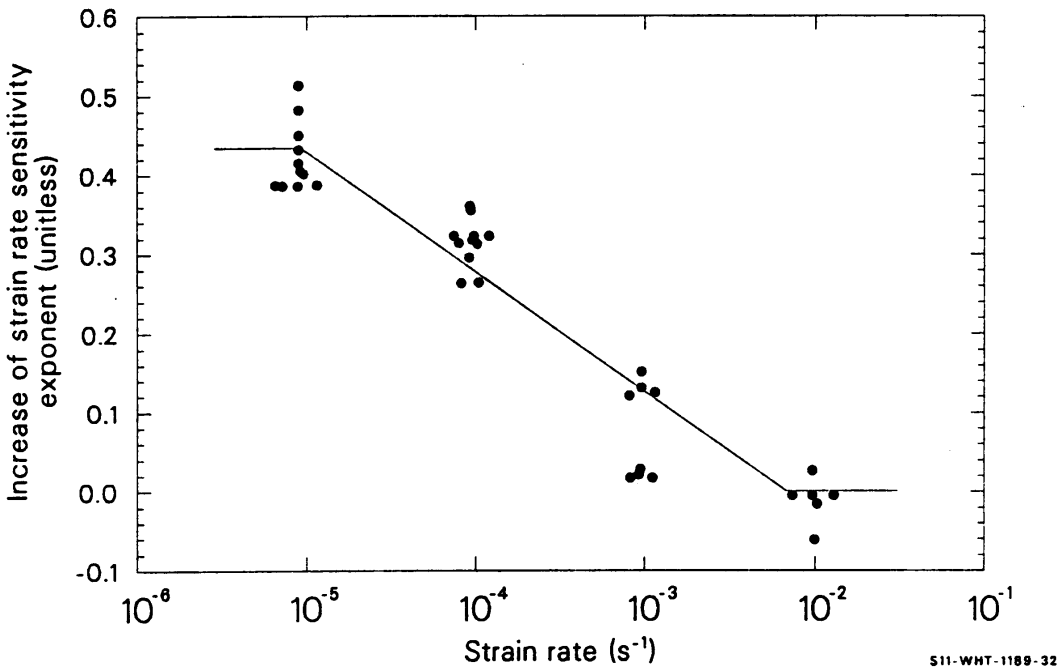

Figure 4-33. Increase of the strain rate sensitivity exponent at 1,173 K as a function of strain rate based on Chung, Garde, and Kassner's data.

In this model, it is assumed that m increases linearly from its value at the edges of the $\alpha - \beta$ transition region to a maximum at 1,172.5 K in the center of the region, as shown in Figure 4-32. Additional data on values of m as a function of temperature and strain rate in the $\alpha - \beta$ transition region will be required if this approximation is to be refined. However, the need for such refinement is questionable, at least until biaxial data confirm a similar effect.

Values of the strain hardening exponent, n, as a function of temperature from room temperature to 755 K are based on data from tensile tests on zircaloy-4 tubes.[4.9-5] The data and the values of n predicted by the MATPRO correlation Equations (4-170) through (4-172) are shown in Figure 4-34. At temperatures above 850 K, the only datum from a full stress strain curve is the point from EPRI NP526.[4.9-2] This value was obtained by a double regression fit to data derived from EPRI Test 150. The majority of the estimates for the high temperature strain hardening exponent are simply the values of uniform strain reported by Garde.[4.9-20] Use of the uniform strain as an estimate is based on the theoretical result that the maximum force in a uniaxial test on a material which obeys Equation (4-148) will occur at a strain of n/(1 + m).

The very large value of n at 811 K was obtained from a double regression analysis of EPRI Test 163, which will be discussed in more detail later in this subsection. The large value of n is either due to an unfortunate feature of the double regression fitting technique or an indication that the stress-strain law for

cladding plastic deformation is significantly different when biaxial (closed tube burst tests) rather than uniaxial stress drives the deformation.

Equations (4-174) through (4-177) for the strength coefficients, K, of fully annealed, isotropic cladding are based on uniaxial tests of cladding,[4.9-5,4.9-27] on a uniaxial plate test,[4.9-20] and on two closed tube burst tests.[4.9-2] For the low temperature data, the effects of varying amounts of cold work and stress relief in the tubing tested were removed prior to including the measured values of K in the data base. This was done by using the cladding annealing model discussed in Section 4.10 and the models for the effects of irradiation and cold work, which will be described in the next subsection. The effects of different strain rates were similarly removed with the model discussed in previous paragraphs of this section.[a]

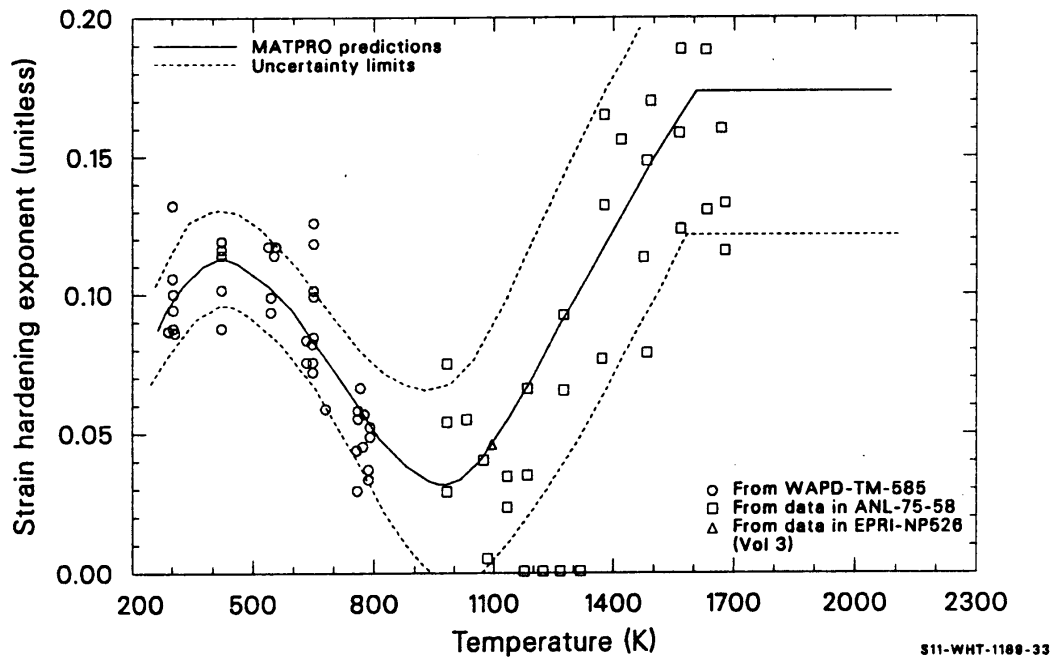

Figure 4-34. Base data, MATPRO prediction, and uncertainty estimate for strain hardening exponent of annealed tubes.

---

a. Strain rate effects and annealing effects were removed from K by redefining K' (from the expression $\sigma = K'\varepsilon^m$)[4.9-5] as

$$K' = K\left[\frac{\dot{\varepsilon}}{10^{-3}s^{-1}}\right]^m$$

Then, the fractional change in K expected from varying amounts of cold work and annealing was removed to give values for the K of annealed tubing consistent with the model for the effects of cold work and annealing.

The strength coefficients based on uniaxial tests of cladding were modified to apply to isotropic cladding using the empirical anisotropy coefficients discussed in the previous subsection. This was done by substituting values of effective stress from Equation (4-150) and values of effective strain from Equation (4-152) into the equation of state, Equation (4-148) to obtain

$$\sigma_z = \left[\frac{K}{(1.5f_r + 1.5f_\theta)^{\frac{(1+m+n)}{2}}} \right] \varepsilon_n^z \left[\frac{\dot{\varepsilon}_z}{10^{-3}} \right]^m . \tag{4-196}$$

Thus, the isotropic strength coefficient is related to the strength coefficient determined in a uniaxial test by the expression

$$K = K_{\text{axial test}} (1.5f_r + 1.5f_\theta)^{1+m+n/2} . \tag{4-197}$$

This approach is different than the usual practice of taking the uniaxial test as the equation of state.[4.9-41] The new approach reduces the scatter in values of K because the texture of the material being tested is considered.

Unfortunately, values of f_r and f_θ were not given in Reference 4.9-5, so estimated values based on the texture factors were employed. The approximation that worked best to reduce the scatter in values of the strength coefficient was

$$f_r + f_\theta = 1 - [\text{axial (002) texture coefficient}]/4 . \tag{4-198}$$

The factor of 1/4 was determined by requiring the sum of the axial, tangential, and radial (002) texture coefficients of Reference 4.9-5 to be approximately 1.5 (f factors sum to1).

The base data and the values of the strength coefficient predicted by the MATPRO correlation of the strength coefficient Equations (4-174) through (4-177) are shown in Figure 4-35. Discontinuities in the slope of the predicted strength coefficient as a function of temperature occur at 750, 1,090, and 1,255 K.

Values of the strength coefficient from BMI-NUREG-1961,[4.9-27] GEMP-482,[4.9-7] and ANL-75-58[4.9-20] were calculated from ultimate tensile strengths (presumed equal to maximum engineering strength at constant engineering strain rate). To estimate $K_{\text{axial test}}$, the axial stress and strain rate are converted to their engineering equivalents,[a] the true strain at maximum engineering stress is found,[b] and this true strain is substituted into Equation (4-148) to find

$$K_{\text{axial test}} = \frac{S_{max} \exp\left(\frac{n}{1+m}\right)}{\left(\frac{n}{1+m}\right)^m \left[\dot{e} \exp\left(-\frac{n}{1+m}\right) \times 10^3 \right]^m} \tag{4-199}$$

a. Engineering stress = true stress x exp (true strain) inside the exp of the first equation, true strain rate = engineering strain rate x exp (true strain).

b. The true strain at maximum engineering stress with constant engineering strain rate is 1 = m/n.

where

S_{max} = maximum engineering stress (Pa)

$\dot{e}$ = engineering strain rate (s^{-1}).

This approach is not very satisfactory because it neglects possible necking of the test sample. It is used because true stress/true strain curves were not available.

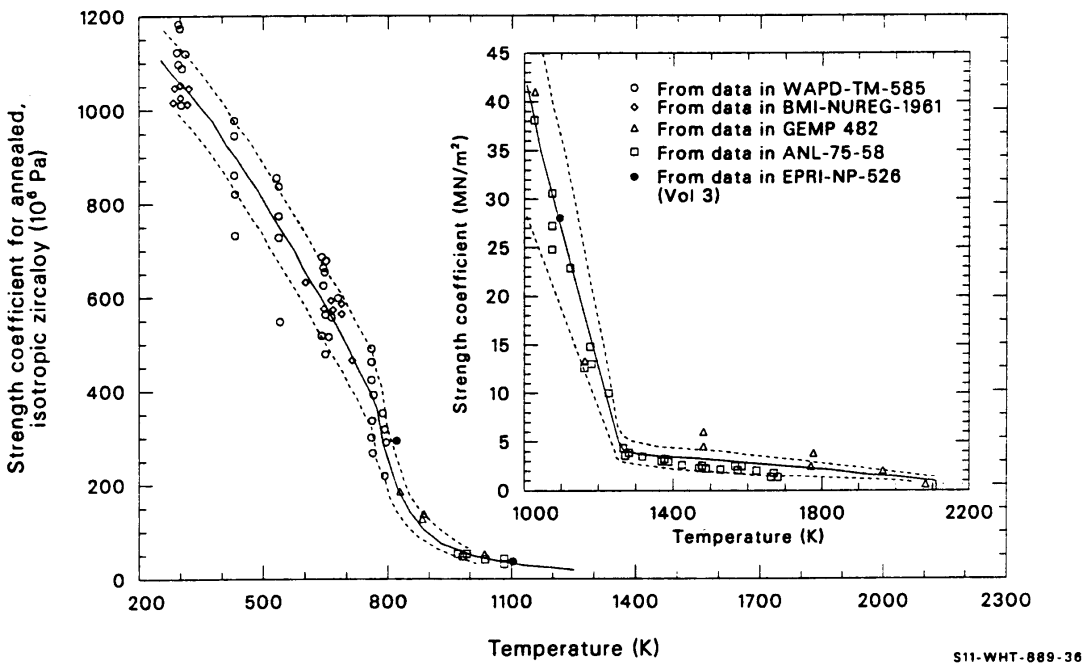

Figure 4-35. Base data, MATPRO prediction, and uncertainty estimate for strain coefficient of annealed, isotropic cladding.

The most important strength coefficient data shown in Figure 4-35 are the two values determined from data in EPRI NP-526, Volume 3.[4.9-2] These strength coefficients were determined with a least squares regression technique that found the values of K, n, and m of Equation (4-148) that best fit the measured values of the stress and plastic strain.[a]

As previously discussed, the anisotropy coefficients calculated from strain components did not agree with the anisotropy coefficients determined from the materials texture. An effort was made to construct a plastic deformation equation of state by assuming that the experimentally determined strain anisotropy coefficients were also the stress anisotropy coefficients. This approach leads to strength coefficients of 469 MPa at 810 K and 32.9 MPa at 1,089 K--results that differ from the uniaxial strength coefficients sig-

a. Elastic strains were calculated with the CELAST model and subtracted from the total strain components.

nificantly. With this approach, a second equation of state is required; but there were only two tests available and no useful model could be produced. The approach was, therefore, abandoned; and it was assumed that stress anisotropy coefficients are different than strain anisotropy coefficients at high temperatures. The anisotropy coefficients determined from material texture were used for stress, and the experimentally determined strain anisotropy coefficients were retained for strain only. The corresponding values of strength coefficients were 360 MPa at 810 K and 27.9 MPa at 1,089 K--results consistent with the uniaxial strength coefficients.

The most plausible explanation of these results is that the kind of deformation assumed in Equation (4-189) does not occur because some other mode is activated first. The physical arguments for this explanation have been advanced by Picklesimer.[4.9-3] If the empirical anisotropy coefficients in Equation (4-181) are considered acceptable, then Picklesimer's ideas are confirmed by the fact that (a) the largest shear stress for $\sigma_\theta \approx 2\sigma_z$ and $\sigma \approx 0$ in Equation (4-189) is multiplied by a very small texture coefficient, f_z, and (b) the strength coefficients found when experimentally determined anisotropy coefficients are used to calculate effective stress are larger than those calculated for basal plane slip. The first fact means that basal plane slip is not likely in the EPRI tests because of the relationship between the applied stress and the material texture. The second fact means that the second mode of deformation will be seen only when the effective stress for basal plane slip is low, because the second mode produces much less strain than the basal plane slip when the effective stresses for the two modes are equal.

Unfortunately, this interpretation cannot yet be exploited because the two sets of values for K, n, m, and the anisotropy coefficients are also the only values available to use to construct an equation of state for the second mode of deformation in the temperature range from 600 to 1,255 K. The values of K obtained with effective stresses calculated from Equation (4-189) have thus been incorporated into the data base for MATPRO (after the 810 K value was corrected for cold work effects) to help force reasonable predictions even though the model is probably incomplete.

4.9.3.3 ***Irradiation and Cold Work Effects.*** Irradiation and cold work effects on cladding plastic deformation have been incorporated into the equation of state for plastic deformation by repeating the analysis discussed in Section 4.9.3.2 for uniaxial tests and noting the changes in the strain rate sensitivity exponent (m), the strain hardening exponent (n), and the strength coefficient (K) with varying amounts of cold work and irradiation. No change in the strain rate sensitivity exponent with irradiation or cold work was found, but the other two parameters did vary with both cold work and irradiation. The effect of cold work on K and n will be discussed first, followed by the effect of irradiation.

Strength coefficients from Reference 4.9-8 are plotted in Figure 4-36. Although texture effects are evident in annealed material and irradiation does tend to increase the strength coefficient slightly, the dominant correlation is a linear increase in the strength coefficient with cold work. A linear least squares fit yields the room temperature correlation

$$K' = 624.4 + 341\ CWK = 624.4\ (1 + 0.546\ CWK) \qquad (4\text{-}200)$$

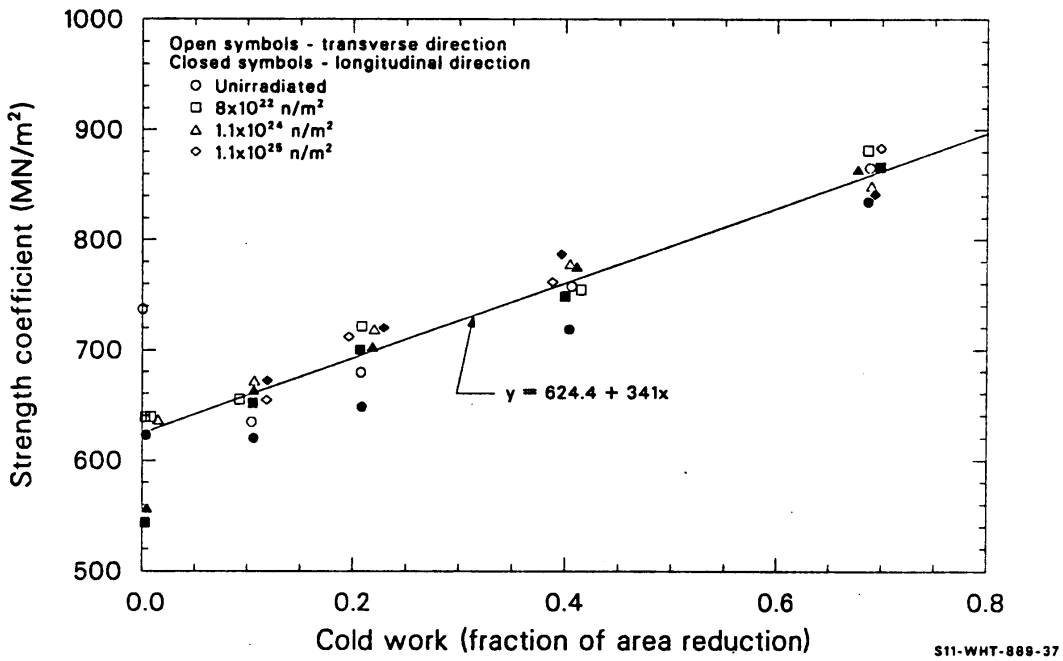

Figure 4-36. Data and least squares fit to strength coefficients as a function of cold work and irradiation at room temperature.

where

CWK	=	the cold work for strength coefficient
K'	=	strength coefficient at room temperature (MN/m^2).

To estimate the effect of temperature on this correlation, values of the strength coefficient determined from the limited data from References 4.9-12 and 4.9-10 at temperatures of 553 and 573 K were also fit to a straight line, with the resultant correlation

$$K' = 373 + 238\ CWK = 373\ (1 + 0.64)\ CWK\ . \qquad (4\text{-}201)$$

Comparison of the two results show that they are consistent with a temperature dependent expression of the form

$$K' = K\ (T)\ [1 + \text{constant}\ CWK] \qquad (4\text{-}202)$$

where K(T) is the temperature dependent function describing the behavior of the strength coefficient of annealed zircaloy [Equations (4-174) through (4-177)]. The form of Equation (4-202) has, therefore, been

assumed. The constant coefficient of the cold work is taken to be 0.546, as determined at room temperature, because the room temperature data exhibit much less scatter then the high temperature data taken from several different sources.

Figure 4-37 illustrates the effect of cold work and irradiation on the strain hardening exponent, n, as determined at room temperature in Reference 4.9-8. The strain hardening exponent of unirradiated material shown in Figure 4-37 can be described by the empirical relation

$$n = 0.11 \exp(-39.2\ CWN) + 0.03(CWN)^2 - 0.12(CWN) + 0.021 \qquad (4\text{-}203)$$

where CWN is the effective cold work for the strain hardening exponent. This expression is essentially a decreasing exponential function for small values of cold work and a slowly increasing parabola for large values of cold work.

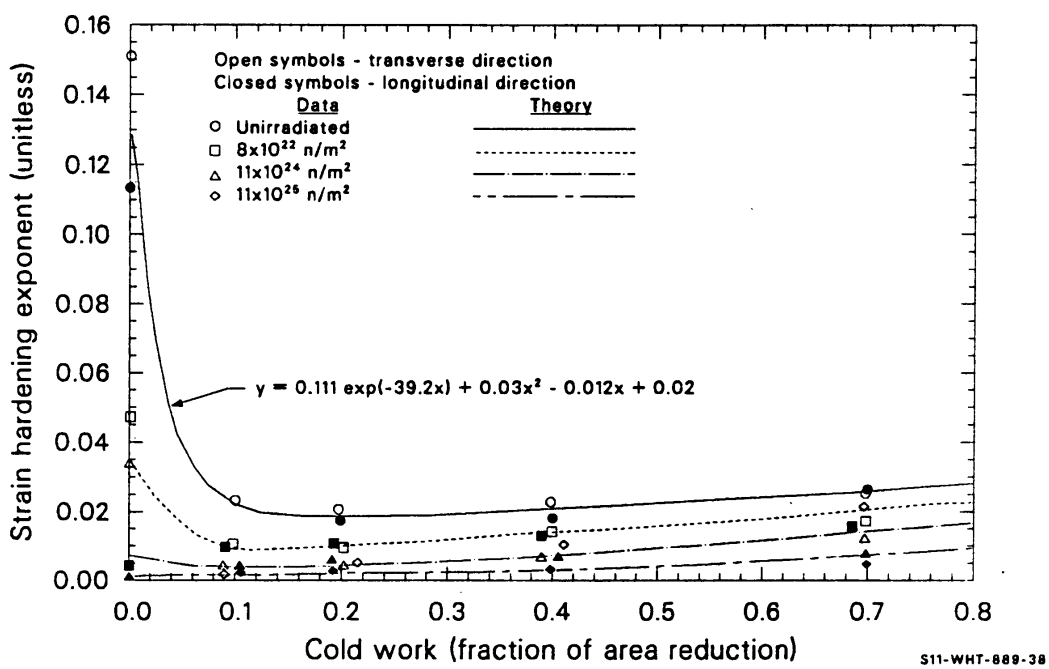

Figure 4-37. Data and analytical functions for strain hardening coefficient as a function of cold work and irradiation at room temperature.

At higher temperatures, trends exhibited by the limited and scattered values of n (which have been obtained at 553[4.9-12] and 573K[4.9-10]) are consistent with the assumption that the fractional changes in n with cold work are similar to the fractional changes in n at room temperature. The following functional relationship is assumed in the present model

$$n(T, \text{cold work}) = n(T) \frac{n(\text{cold work})}{n(\text{at } 0 \text{ cold work})} \quad . \tag{4-204}$$

When the expression for n as a function of cold work given by Equation (4-203) is substituted into Equation (4-204), the following expression is obtained:

$$n = n(T) \frac{0.11 \exp[-39.2(CWN)] + 0.03CWN^2 - 0.012CWN + 0.021}{0.132} \tag{4-205}$$

where n(T) is given by Equations (4-170) through (4-172).

The data from Reference 4.9-8 plotted in Figure 4-36 show little effect of irradiation on the strength coefficient. However, the irradiation of these samples were conducted at 333 K, and it is probable that irradiation at reactor operating temperature produces different results.[4.9-40]

The most applicable data for modeling the effect of irradiation on cladding are the measurements of ultimate strength and uniform elongation reported by Bauer.[4.9-26,4.9-28] Their measurements were taken with cladding irradiated in the Carolina Power and Light H. B. Robinson Reactor to fast neutron fluences of 4×10^{25} fast n/m^2. Testing was performed at 644 K. Unfortunately, they were unable to test unirradiated samples from the lot of tubing they used, so use of their data must rely on nominal preirradiated ultimate strengths.[4.9-28]

Bauer's data are most representative of in-reactor irradiation damage and are, therefore, used instead of the data from Reference 4.9-8 to find an expression for the effect of irradiation on temperature. Strength coefficients for irradiated cladding at 644 K were determined with Equation (4-199) and tensile test results given in Table I of Reference 4.9-26 (samples P8-20, P8-34, and P8-46). Equations (4-174) and (4-202) were then used to estimate the strength coefficient for annealed cladding and the cold work contribution to the strength coefficient (for typical cold work of 0.5) at 644 K. The difference between the strength coefficient of the irradiated material and the predicted strength coefficient of cold worked material is presumed to be due to irradiation effects. Furthermore, the effect of irradiation is assumed to be proportional to the fast neutron fluence. The second term of Equation (4-179) resulted from these assumptions.

At present, the best evidence in support of a linear dependence of K on fast neutron fluence is the fact that the small effect of irradiation on the samples of Reference 4.9-8 is not inconsistent with the predictions of Equation (4-179) for the relatively low fluences reported in that reference.

The effect of irradiation on the strain hardening exponent, n, is complex. Figure 4-37 shows that the fractional change in n due to irradiation at 333 K is large in annealed material and somewhat less in material that has been heavily cold worked. Furthermore, the effect of irradiation is highly nonlinear. Increasing amounts of irradiation produce continually decreasing changes in n.

These features are described empirically in the irradiation model by expressing the ratio of the value of n after irradiation to the value of n before irradiation as an exponential multiplier with a moderating cold work dependent term in the argument of the exponent. The strain hardening exponent of irradiated material is then

$$n = n\ (\text{unirradiated})\ \exp\left[-(\text{fluence})^{1/3}/(A + BCWN)\right] \tag{4-206}$$

where

$A = 3.73 \times 10^{7}\ (n/m^{2})^{1/3}$

$B = 2.0 \times 10^{8}\ (/m^{2})^{1/3}$

and n (unirradiated) is defined in Equation (4-205).

4.9.3.4 ***Effects of Oxygen.*** The effects of oxygen on cladding plastic deformation have been incorporated into the equation of state for plastic deformation by developing correlations for the changes in the strength coefficient, the strain hardening exponent, and the strain rate sensitivity exponent with increasing oxygen content. The derivation of the expressions for the change in the strength coefficient is presented first, followed by a discussion of the effects of oxygen on the strain hardening exponent and the strain rate sensitivity exponent.

4.9.3.4.1 ***Effect of Oxygen Concentration on the Strength Coefficient--***There are no data that may be used directly to find the influence of oxygen on the strength coefficient. However, data do exist that may be manipulated to yield this information. Because different types of data are available for high and low temperatures, different analytical techniques were used for these temperature ranges and the analyses are presented separately.

(1) Low Temperature Strength Coefficient Data. In the range 300 to 650 K, which includes typical LWR operating temperatures, the effect of oxygen concentration may be obtained from measurements of the change in the ultimate tensile strength (UTS) of zircaloy as a function of oxygen content. The true strain at maximum engineering stress, that is, the engineering stress at the onset of plastic instability in a tensile test on sheet specimens at constant strain rate, is given by Equation (4-199), which is rewritten here for convenience

$$K = \frac{S_{max} \exp\left(\frac{n}{1+m}\right)}{\left(\frac{n}{1+m}\right)^{m} \left(\dot{\varepsilon} \times 10^{3}\right)^{m}} \tag{4-207}$$

where S_{max} is the ultimate tensile strength in a tensile test (Pa). When ε was specified in the data, it was 10^{-3}/s. Since 10^{-3}/s is a typical value for ε in tensile tests, this value was assumed when not specified. In this case, Equation (4-207) reduces to

$$K = S_{max} \left[\frac{\exp\left(\frac{n}{m+1}\right)}{\left(\frac{n}{m+1}\right)^{n}} \right]. \tag{4-208}$$

A paper by Rubenstein[4.9-11] gives values for the UTS as a function of oxygen concentration for temperatures ranging from about 300 to 650 K. For this range, MATPRO estimates an m of 0.02 for as received zircaloy. Therefore, m has very little effect on the value of K calculated with Equation (4-207) and can be neglected. The value for n predicted by MATPRO varies from 0.119 to 0.144 in this temperature range, causing the term $\exp(n)/n^{n}$ of Equation (4-208) (with m = 0) to vary from 1.45 to 1.53. If this

term is replaced by 1.49 for all temperatures, the maximum error introduced is smaller than 3%, which is substantially less than the scatter in the data. Therefore, the strength coefficient in this temperature range has been calculated by simply multiplying the UTS by 1.49. Strength coefficients calculated in this way using data taken from Rubenstein are presented in Table 4-25. The lowest concentration for each temperature (9×10^{-3} weight fraction) was assumed to be the concentration of the as-fabricated zircaloy. With this information, the ratio K/K_o, where K_o is the strength coefficient of as received zircaloy, may be calculated; and these data are also shown in the table.

(2) High Temperature Strength Coefficient Data. All of the information used to model the effects of oxygen concentration on the high temperature plastic deformation of zircaloy was taken from a report by Chung, Garde, and Kassner,[4.9-23] of Argonne National Laboratory. Rather than reporting the stress associated with a given strain, however, the Argonne group made a computer fit of their data to a flow curve equation known as the Ludwik equation,[4.9-41]

$$\sigma = K\varepsilon^n + \sigma_0 \tag{4-209}$$

and reported only the parameters K, n, and σ_0 for many different strain intervals and oxygen concentrations. The additional variable, σ_0, will cause the stress, σ, resulting from Equation (4-209) for a given ε to differ from that of Equation (4-150) for the same K and n.

Table 4-25. Strength coefficient calculated with data of L. S. Rubenstein.

Temperature (K)	Oxygen Content (weight fraction)	Ultimate Tensile Strength (MPa)	Calculated K (MPa)	K/K_o
297	0.0009	524	781	1.00
297	0.0018	616	918	1.18
297	0.0034	785	1,170	1.50
297	0.0063	949	1,414	1.81
422	0.0009	354	527	1.00
422	0.0034	544	811	1.54
422	0.0063	680	1,013	1.92
533	0.0009	266	396	1.00
533	0.0018	298	444	1.12
533	0.0034	361	538	1.36
533	0.0063	462	688	1.74

Table 4-25. Strength coefficient calculated with data of L. S. Rubenstein. (Continued)

Temperature (K)	Oxygen Content (weight fraction)	Ultimate Tensile Strength (MPa)	Calculated K (MPa)	K/K_o
644	0.0009	227	338	1.00
644	0.0018	241	359	1.06
644	0.0034	283	422	1.25
644	0.0063	373	556	1.64

The Argonne curves generally start at strains of 0.0004, and their data are fit accurately to the Ludwik equation by dividing the flow curve into two or three strain intervals with different values of K, n, and σ_0 for each interval. There are scattered examples in the Argonne results, indicating that this approach may be inappropriate for small strains. In several of these cases, $\sigma < 0$. Since σ_0 can be interpreted as the yield stress,[4.9-41] a negative value indicates a physical inconsistency. To avoid these problems, the Argonne correlations were used only for strains greater than an arbitrarily chosen minimum of 0.002.

To get a base for a model, data were generated using Equation (4-209) and fit to Equation (4-150) (the Holloman equation). The strain interval (from 0.002 to the maximum reported strain) was divided into 20 equally spaced intervals for each temperature oxygen content combination. The Ludwik equations were then used to find a stress associated with each strain, and the resulting stress strain pairs were fit by the method of least squares to the Holloman equation. Only those tests where $\varepsilon = 10^{-3}$/s were used. This included 82 equations describing 60 different samples. The fluctuations in the resulting strength coefficient and the strain hardening exponent were much smaller for the Holloman equation than they were for the Ludwik equation.

For these derived data, the ratio (K/K_o) was calculated, as was done with the low temperature data. As with the Rubenstein data, (K/K_o) increases with oxygen concentration for all temperatures.

(3) Correlation for the Effect of Oxygen Concentration on the Strength Coefficient. Because little is known about the physical mechanism causing the strength coefficient of zircaloy to change with oxygen concentration, a model based on theory is not possible. An empirical fit to the data is, therefore, the approach chosen. In addition to fitting the data, the correlation should satisfy the obvious condition that $(K/K_o) = 1$ when $C = C_o$. A quite simple correlation that does this is

$$K/K_o = 1 + a(C - C_o) \tag{4-210}$$

where

C	=	oxygen concentration (weight fraction)
C_o	=	oxygen concentration of as received zircaloy (weight fraction)
a	=	a function of temperature to be determined (weight fraction)$^{-1}$.

An equation of the form of Equation (4-210) for each temperature was generated by a least squares fit technique using the data. The results are presented in Table 4-26.

The ratio (K/K_o) derived from Equation (4-210) is plotted as a function of oxygen concentration for all temperatures used in Figure 4-38. The data from Table 4-26 are shown in the same figure. The six lowest temperatures are represented by a single line with a = 130 because they are too close together to be distinguishable.

The general characteristics of the temperature dependence of a are that it is relatively constant until about 1,200 K, rises rapidly between 1,200 and 1,400 K, and then begins to level off. The leveling off is based on only the data point at the highest temperature. However, there are too few data to justify a sophisticated correlation. A single function can be found which fits the data with acceptable accuracy over the entire temperature range, thus having the advantages of automatically avoiding discontinuities and fitting compactly into a computer routine. For 300 < T < 1,673 K, the function is

$$a = 1120 - \frac{990}{\exp\left[\frac{(T - 1301.5)}{61}\right] + 1}. \tag{4-211}$$

Equation (4-211) is plotted as the function of temperature in Figure 4-39, where it is compared with the data from Table 4-26.

Table 4-26. Rate of change of K/Ko with oxygen content.

Temperature (K)	a
297	160
422	178
533	137
644	115
1,123	89
1,173	95
1,223	343
1,273	541
1,323	676
1,373	891
1,673	1116

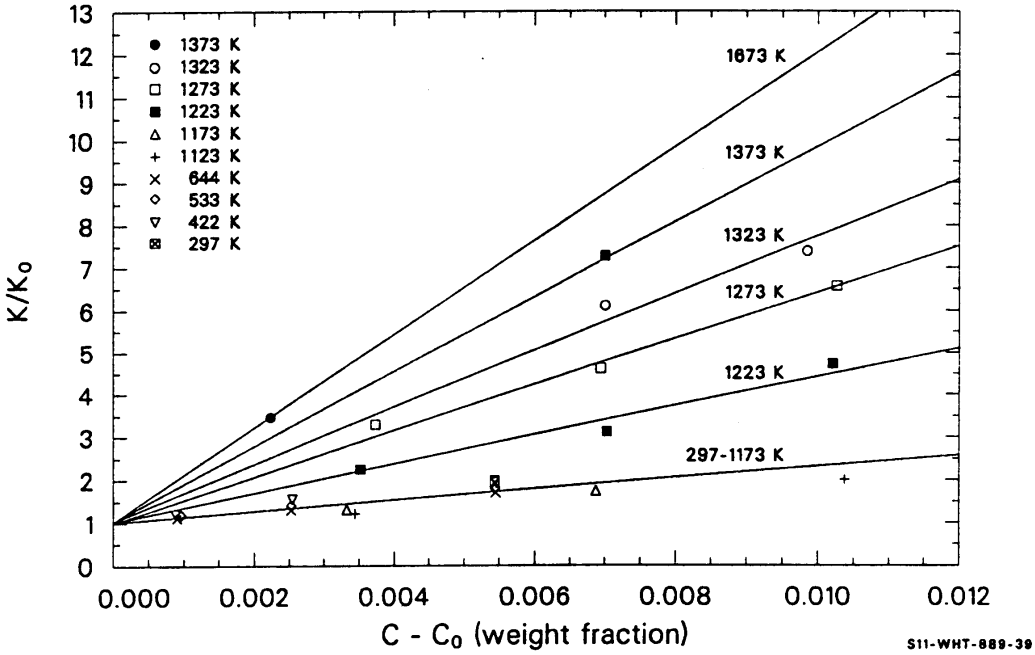

Figure 4-38. Calculated ratios of the strength coefficients of zircaloy, containing oxygen (K) and the strength coefficients of as fabricated zircaloy (K_o) as a function of oxygen concentration for several temperatures.

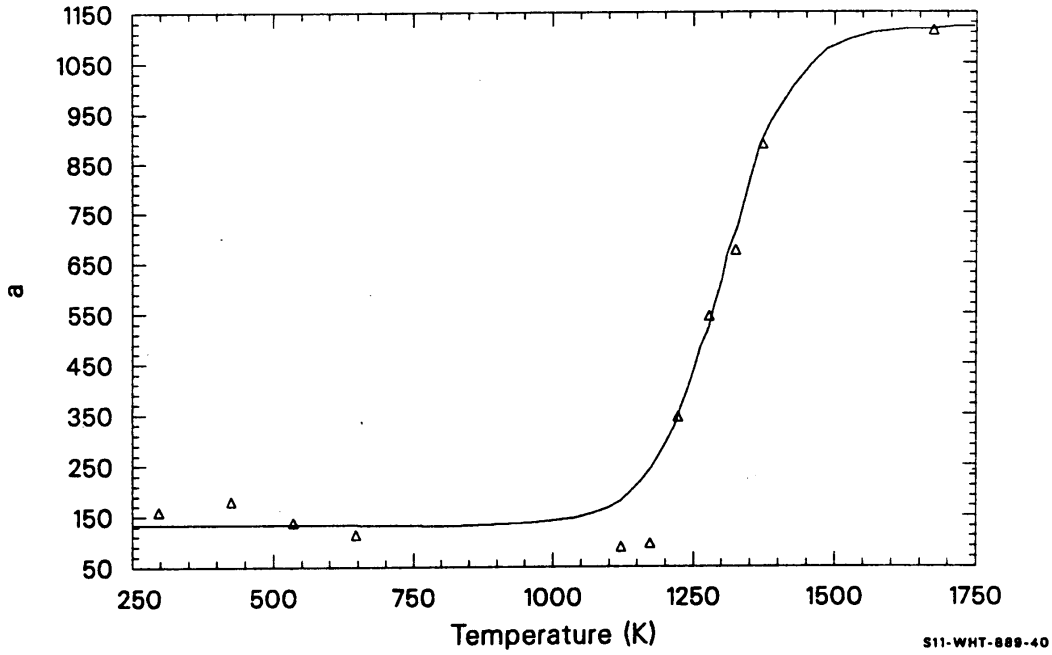

Figure 4-39. Calculated curve and data showing the rate of change of the zircaloy strength coefficient with oxygen content as a function of temperature.

A comparison of the values of (K/K_o) predicted by Equations (4-210) and (4-211) with the data shows that the average percentage error is 12%. All the points except those at 1,123 and 1,173 K have percentage errors of this size or less. At these two temperatures, the average percentage error is 45%. These uncertainties can serve only as a rough guide in assessing the accuracy of the model, since they were calculated by comparing the correlation to its own data base.

4.9.3.4.2 ***Effect of Oxygen Concentration on the Strain Hardening--***The methods of development and the form of the equations used to correlate oxygen content with changes in the strain hardening exponent, n, are identical to those used for the analogous changes in the strength coefficient.

(1) High Temperature Strain Hardening Exponent Data. The only data available are those from Chung, which were all taken at high temperature.

(2) Correlation for the Effect of Oxygen Concentration on the Strain Hardening Exponent. The ratio(n/n_o) is modeled using the equation

$$n/n_o = 1 + b(C - C_o) \tag{4-212}$$

where b is a function of temperature to be determined. A fit of Equation (4-212) to the data gives the value forb listed in Table 4-27.

The lines given by Equation (4-212) using the values of b listed in Table 4-27 are plotted in Figure 4-40 with their data bases.

The data presented in Table 4-27 and Figure 4-40 show considerable scatter. It is possible that this is a reflection of actual physical processes. Systematic oscillations in such things as the total strain at failure and the strain at maximum engineering stress have been repeatedly documented in the Argonne Quarterly Reports,[4.9-22,4.9-23 to 4.9-26] and these oscillations may be due in part to variations in the strain hardening exponent. More data are needed to accurately quantify these variations. Therefore, only the general features of the coefficient b in Equation (4-212) are treated in the model. It is small below about 1,300 K, rises rapidly between 1,300 and 1,400 K, and then levels off about 1,500 K. The function used is

Table 4-27. Rate of change of n/n_o with oxygen content.

Temperature (K)	b
1,123	-19.0
1,173	4.9
1,223	-12.7
1,273	-11.1
1,323	340.0

Table 4-27. Rate of change of n/n_o with oxygen content.

Temperature (K)	b
1,373	244.3
1,673	1,245.0

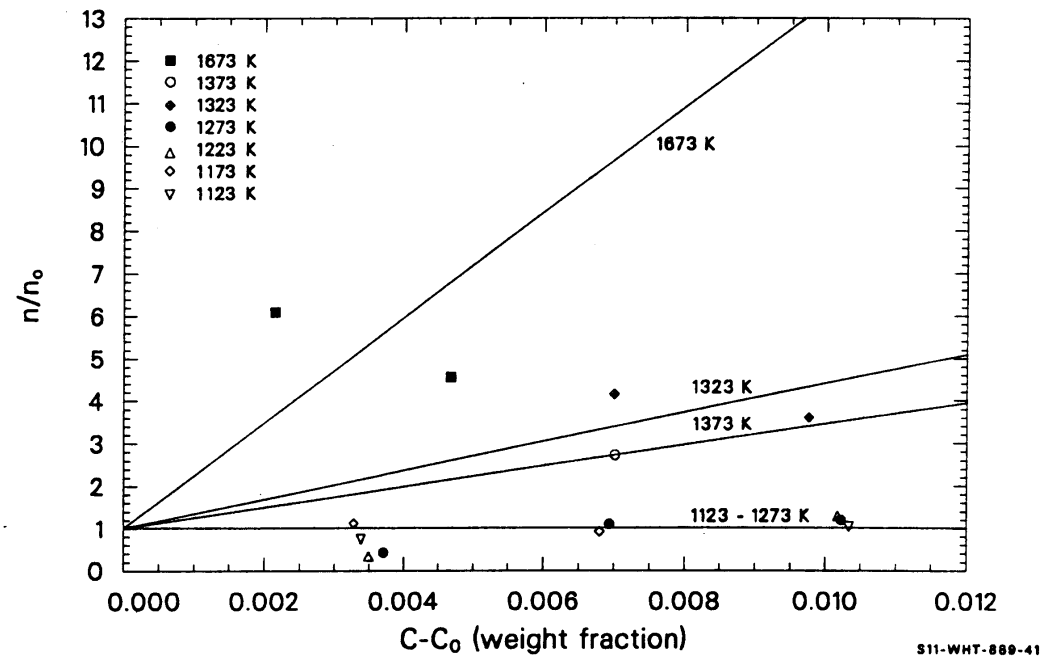

Figure 4-40. Calculated ratios of the strain hardening exponents of zircaloy containing oxygen (n) and the strain hardening exponents of as fabricated zircaloy (n_o) as a function of oxygen concentration for several temperatures.

$$b = 1250 - \frac{1250}{\exp\left[\frac{(T-1380)}{20}\right] + 1} \tag{4-213}$$

for 1,123 < T < 1,673K.

Equation (4-213) is plotted in Figure 4-41, where it is compared with the data from Table 4-27.

At temperatures below 1,100 K, b calculated with Equation (4-213) is negligibly small, so that $(n/n_o) = 1$. This means that the strain hardening exponent is unchanged by the presence of oxygen. Therefore, the lower limit of the model may be extended down to operating temperatures without affecting the stress-strain laws now in MATPRO.

The uncertainty in the predictions of Equations (4-212) and (4-213) when compared with the data base is quite large. The one standard deviation limits are ± 42%. There are two data which are in error by more than 100%; but since the data indicate that the strain hardening exponent changes by a factor of five or more in some cases, the model is certainly better than entirely neglecting oxygen effects.

4.9.3.4.3 ***Effect of Oxygen Concentration on the Strain Rate Sensitivity Exponent--***As with the strength coefficient and the strain hardening exponent, the data used for determining the effect of oxygen concentration on the strain rate sensitivity exponent of Equation (4-150) are taken from Chung. In this case, however, the data may be used directly, since they are consistent with the Holloman equation, Equation (4-150), as will be shown in the next subsection.

(1) Experimental Technique. Chung[4.9-19] measured m by quickly changing the strain rate during a stress strain test, causing a change in the stress, σ. If the change occurs rapidly, the strain itself does not change significantly during the transient, and m may be found from the equation

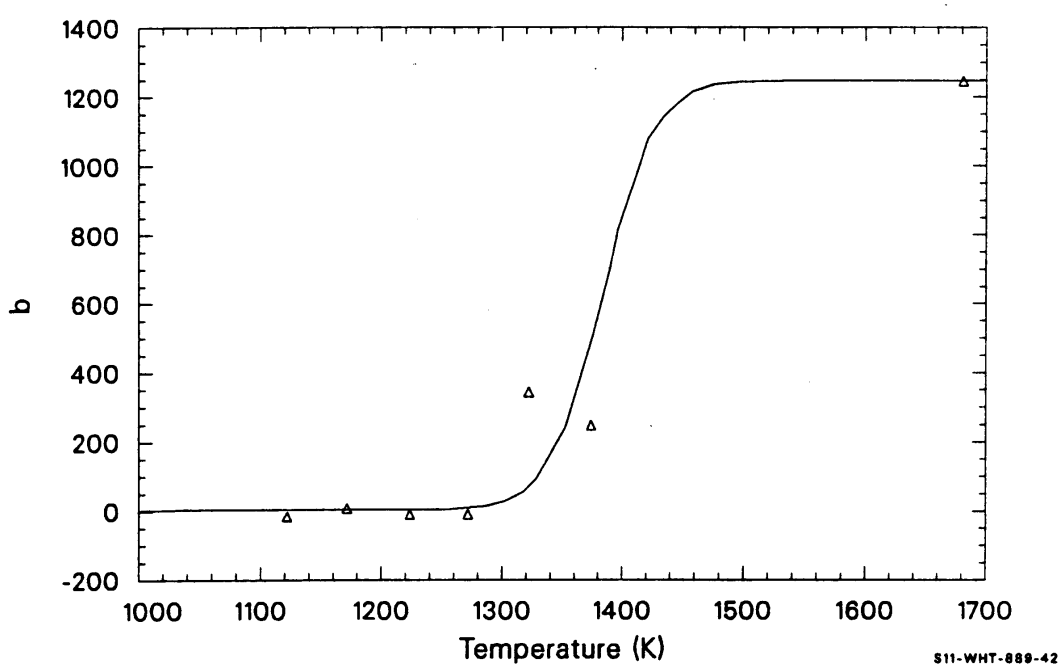

Figure 4-41. Calculated curve and data showing the rate of change of the zircaloy strain hardening exponent as a function of temperature.

$$\left(\frac{\sigma_1}{\sigma_2}\right) = \left(\frac{\dot{\varepsilon}_1}{\dot{\varepsilon}_2}\right)^m \tag{4-214}$$

or

Zircaloy

$$m = \frac{\ln\left(\frac{\sigma_1}{\sigma_2}\right)}{\ln\left(\frac{\dot{\varepsilon}_1}{\dot{\varepsilon}_2}\right)} \tag{4-215}$$

where

σ_1	=	stress immediately before the transient (Pa)
σ_2	=	stress immediately after the transient (Pa)
$\dot{\varepsilon}_1$	=	strain rate before the transient (s^{-1})
$\dot{\varepsilon}_2$	=	strain rate after the transient (s^{-1}).

Taking the logarithm of both sides of Equation (4-148) for two cases with different stresses and strain rates, but the same strain,

$$\ln(\sigma_1) = \ln(K) + n\,[\ln(\varepsilon)] + m\,(\ln(\varepsilon_1)) - m\,(\ln(10^{-3})) \tag{4-216}$$

$$.\ln(\sigma_2) = \ln(K) + n\,[\ln(\varepsilon)] + m\,(\ln(\varepsilon_2)) - m\,(\ln(10^{-3})) \tag{4-217}$$

Subtracting Equation (4-217) from Equation (4-216) yields Equation (4-215), so the strain rate sensitivity exponents measured by Chung may be used directly in Equation (4-148).

(2) High Temperature Strain Rate Sensitivity Exponent Data. The data were taken from two Argonne Quarterly Reports[4.9-22,4.9-23] and, as with the strain hardening exponent, cover the temperature range from 1,123 to 1,673 K. These data are shown in Figure 4-42, where m is plotted as a function of oxygen concentration for seven temperatures. The change in m is plotted as a function of oxygen concentration for seven temperatures. The changes in m with temperature reflect the changes predicted by MATPRO. The 1,173 K curve is anomalous because the as received zircaloy is in the alpha + beta transition phase region at this temperature.[a] It is evident that m decreases with increasing C in all cases; and each curve resembles an exponential decay, although the scatter in the data precludes quantification of the temperature dependence.

Only the ratio (m/m_o) as a function of concentration was modeled, as shown in Figure 4-43. The equation used was

$$m/m_o = \exp\,[-69\,(C - C_o)] \tag{4-218}$$

where m_o is the strain rate sensitivity constant for as received material. The number 69 in the argument of the exponent in Equation (4-218) was obtained by a least squares fit of the data to the equation.

The quality of the fit of Equation (4-218) using Chung's values for m_o can be seen in Figure 4-43.

---

a. This explanation will not suffice to explain the low values of m at 1,473 K, where the material remains in the beta region over the entire range of oxygen concentrations reported, as may be seen in the phase diagram taken from Chung.[4.9-23]

Although a quantitative statement cannot be made at this time, the scatter may be partly the result of phase transitions which can occur even isothermally with changes in oxygen content (Figure 4-44). For example, at 1,123 K, m_o is measured using material which is midway through the alpha plus beta transition phase; while the material at the highest oxygen concentration point at 1,123 K is oxygen stabilized, alpha-phase zircaloy. The fact that this point is quite far from the calculated curve may be a reflection of the failure to consider the effects of the phase transition.

To include the 68% of the data that should fall within one standard deviation from the calculated line, the coefficient 69 of Equation (4-218) must be given quite large uncertainty limits, $\pm$ 40. The data lying below the calculated line in Figure 4-43, especially those for which $(C - C_o) = 10^{-3}$, contribute much to the uncertainty because they require particularly large values to make the curve drop abruptly enough from its starting point to pass through them.

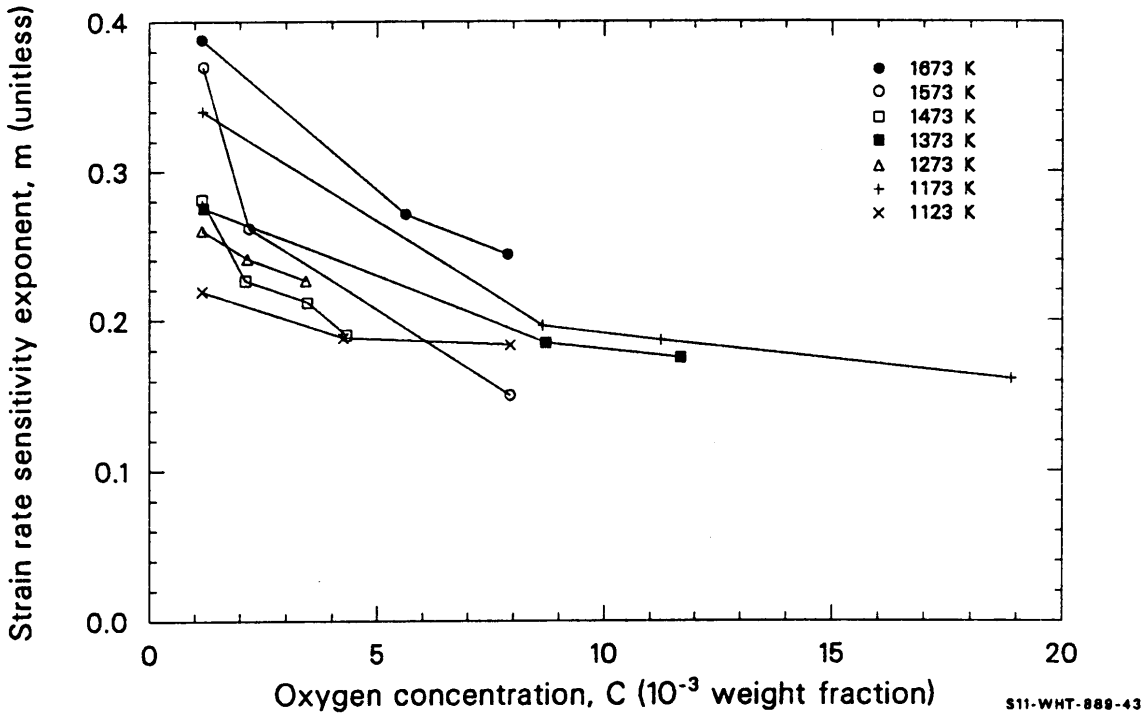

Figure 4-42. Strain rate sensitivity exponent, m, data as a function of oxygen concentration from Chung.

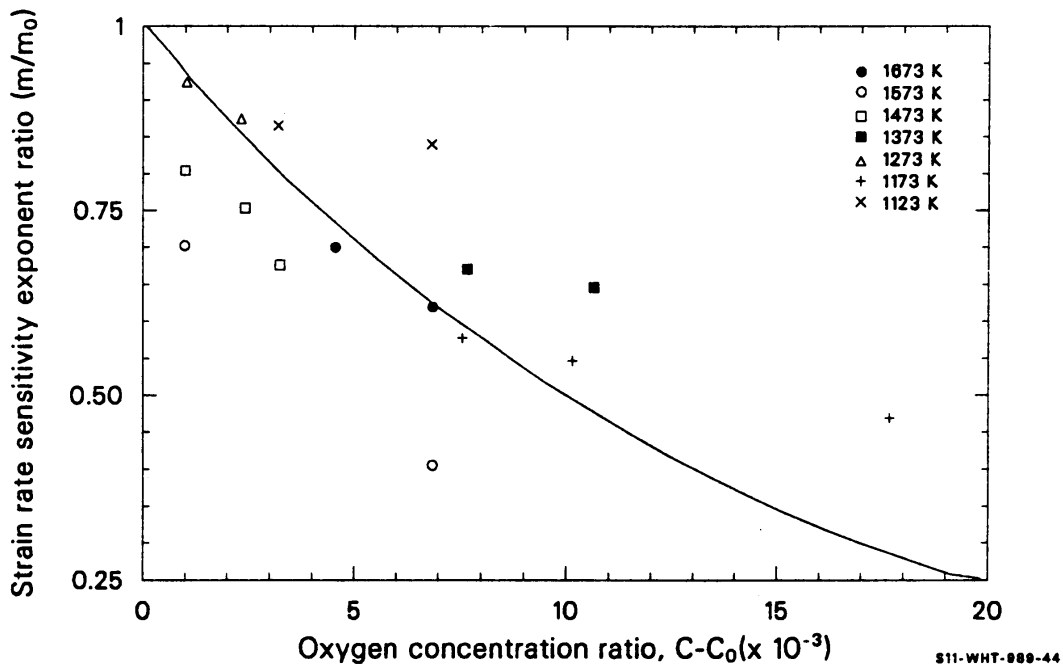

Figure 4-43. The ratio m/m_o as a function of oxygen concentration showing Chung data and the line used to fit these data.

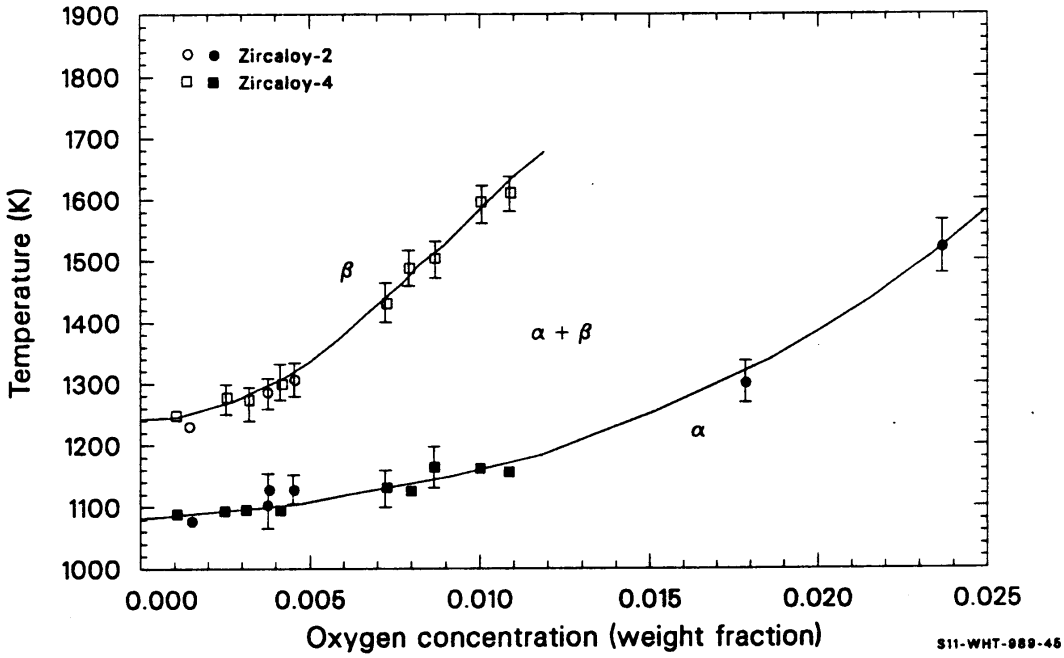

Figure 4-44. Zircaloy oxygen phase diagram, taken from Chung.

4.9.3.4.4 ***Flow Curves Showing the Effect of Oxygen Concentration--***Three figures are presented in this section to show how oxygen concentration affects the plastic deformation por-

tion of the stress strain curves predicted by MATPRO. Equations (4-210) through (4-213) and Equation (4-218) were used in conjunction with the MATPRO subroutines to generate these plots. All plots show two curves, one for as fabricated zircaloy ($C - C_o = 0$) and one for zircaloy containing a total of about five times the as fabricated oxygen level ($C - C_o = 0.005$ weight fraction). Unless otherwise specified, the as fabricated oxygen content, C_o, was assumed to be 0.0012 weight fraction.

Figure 4-45 shows the flow curves at 600 K, a temperature typical of PWR normal operation. The strain rate was taken as 10^{-3}/s, so that the strain rate dependence on oxygen content was not a factor. At this temperature, Equations (4-212) and (4-213) predict a completely negligible change in n, the strain hardening exponent. The entire difference between the curves thus results from the change in K which, for these conditions, increases by a factor of 1.65.

Figure 4-46 shows flow curves for conditions the same as those of Figure 4-45 except that the temperature is 1,400 K, which is characteristic of the temperature postulated for reactor transients, such as a loss of coolant or a power cooling mismatch. At this temperature, K increases by a factor of 5.8 and n by a factor of 5.6. Since the curve with $C = C_o = 0$ is nearly flat except at very small strains, the increasing slope of the curve for $C - C_0 \neq 0$ is largely due to the change in n caused by the extra oxygen.

Figure 4-47 shows the stress required to cause a strain of 0.1 at various strain rates. This figure is included to illustrate the effect of oxygen concentration on the strain rate exponent. Nearly all of the difference between the oxidized and unoxidized cladding is caused by the change in the strength coefficient. Careful examination of the curves will show a slightly increasing separation between them as the strain rate increases. The separation of the curves increases by only 2.5% as the strain rate changes from 10^{-4} to 10^{-2}. However, under these conditions, if m were unchanged by oxygen concentration but K were affected, the increase would be 9.3%. In general, the effect of oxygen concentration on m is to increase $d\sigma / d\varepsilon$ for $\varepsilon < 10^{-3}$/s and to decrease $d\sigma / d\varepsilon$ for $\varepsilon > 10^{-3}$/s. For the strain rate range of Figure 4-47, approximately nine-tenths of the strain rates are greater than 10^{-3}/s; therefore, the net effect is a slope smaller than would be found if m were not a function of oxygen concentration. These observations must still be regarded as tentative, since Equation (4-186) was derived from data taken at strain rates close to 10^{-3}/s, and these data included large scatter.

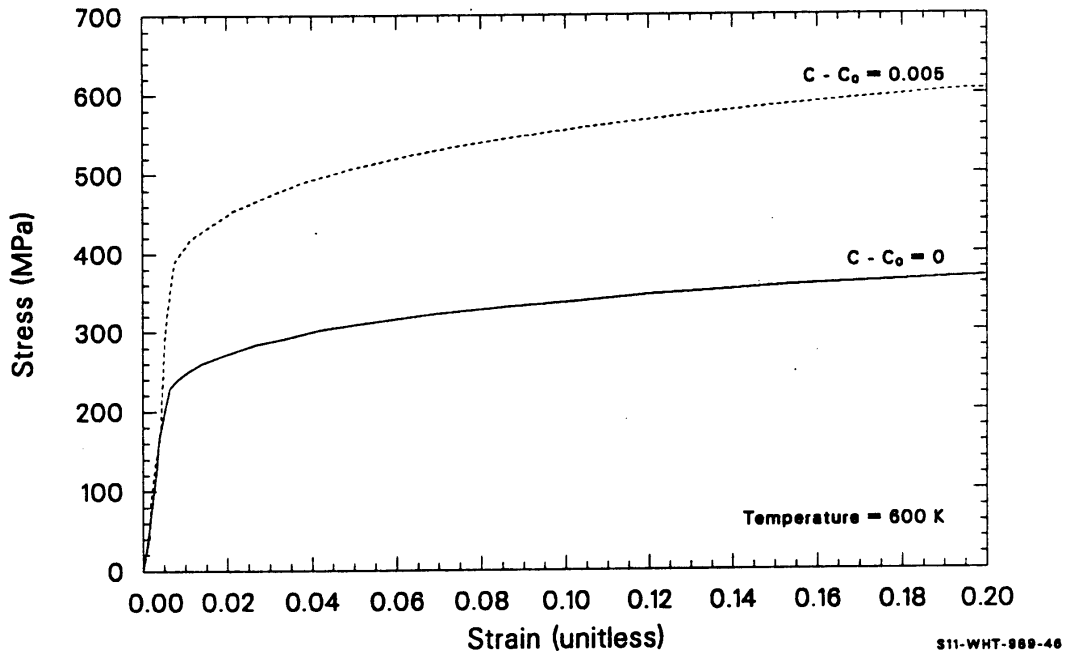

Figure 4-45. Stress as a function of strain at a strain rate of 10^{-3}/s for two oxygen concentrations at 600 K.

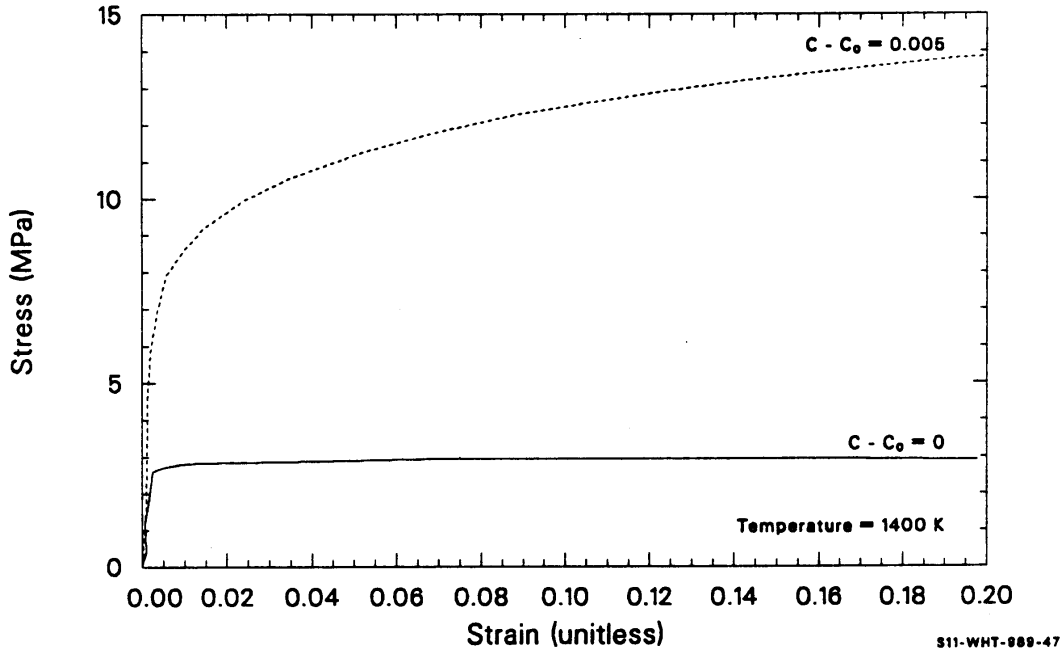

Figure 4-46. Stress as a function of strain at a strain rate of 10^{-3}/s for two oxygen concentrations at 1,400 K.

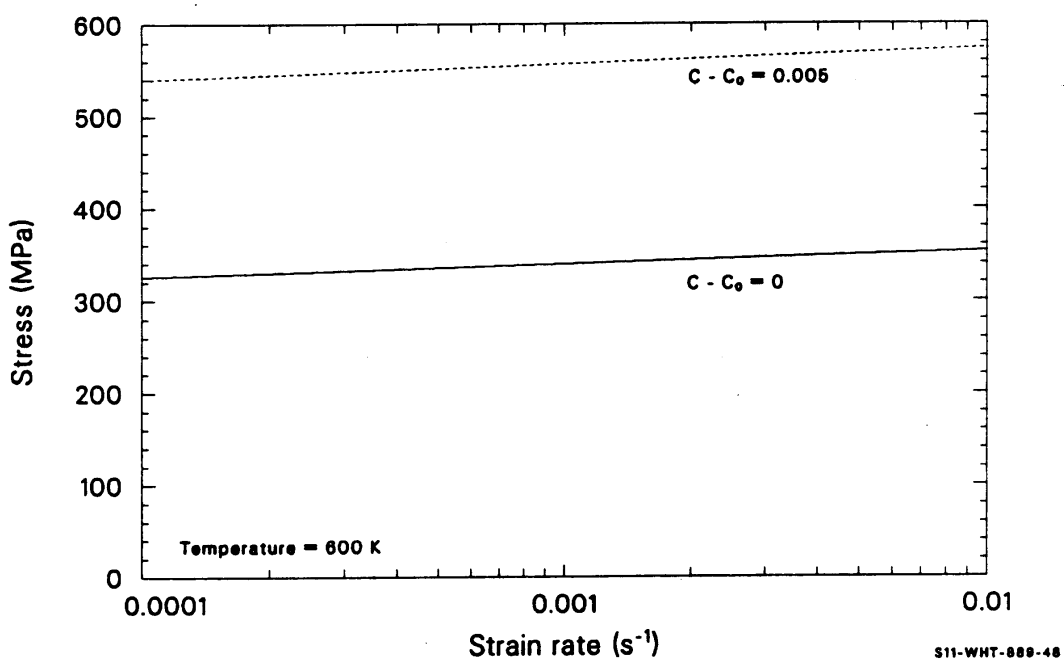

Figure 4-47. Stress as a function of strain at a strain rate of 0.1 for two oxygen concentrations at 600 K.

4.9.4 Comparison to Burst Test Data

The transient temperature tests by Hardy[4.9-34] discussed in Section 4.9.2 offer an opportunity to test the model at temperatures in the range 900 to 1,400 K. Figure 4-48 is a comparison of predicted versus measured strains for four of Hardy's tests at a heating rate of 25 K/s and initial pressures of 5.5, 2.8, 1.4, and 0.3 MPa. Since Hardy did not report the cladding texture, typical values were assumed (f_r = 0.66, f_z = 0.06, and f_θ = 0.28).

Details of the stress relief were also not reported, so two predicted strains are shown for each series--one for fully annealed material and one for a very light stress relief. With the exception of the highest temperature data (where slight oxidation due to residual water vapor in the vacuum chamber may have affected the experiment), the predictions are within $\pm$25 K of the experimental value.

It is somewhat surprising that a model based on uniaxial deformation and empirical texture coefficients stays within about 25 K of these biaxial data. Apparently, the temperature dependence of the strength coefficient for the second mode of deformation is similar to the temperature dependence of the mode observed with uniaxial tests. Inspection of the predicted strain curves and Hardy's data seems to confirm the different (large) strain hardening exponent found with the biaxial test by Hann. Strains are systematically underpredicted when they are small and tend to be overpredicted when they are large. It is also possible that the relatively large initial strain is caused by an as yet unmodeled annealistic deformation.

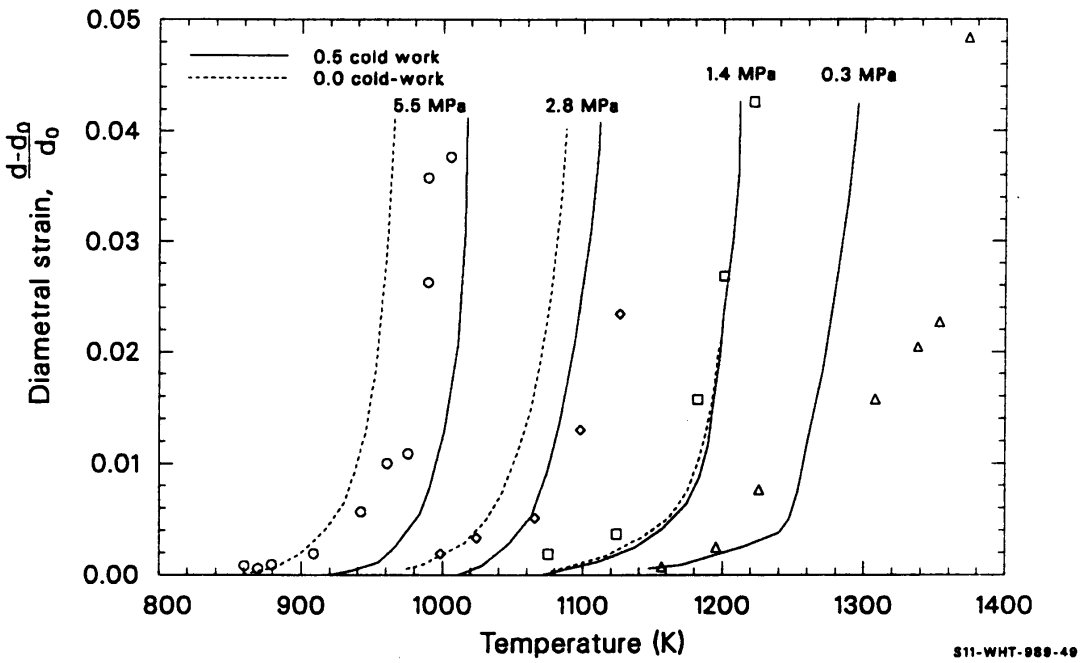

Figure 4-48. Measured diametral strain versus MATPRO predictions for two initial values of cold work in tests conducted by Hardy at heating rates of 25 K/s.

A more sensitive test is provided by a stress rupture experiment reported by Chung.[4.9-24] In this test, temperature and pressure were set at 1,023 K and 5.2 MPa. Chung's data and the MATPRO model predictions for 1,023 and 1,048 K are shown in Figure 4-49. The model overpredicts cladding strength at 1,023 K, but the prediction at 1,048 K approximates Chung's data fairly well out to strains of 0.2, where ballooning becomes important.

4.9.5 Uncertainties

Equations (4-183) through (4-185) for the expected error of the constants K, n, and m were obtained by comparing values predicted by Equations (4-164) through (4-177) with their own data base. Two points should be emphasized for users of these expressions: (a) they are not standard errors, and (b) they do not apply to irradiated or oxidized material. Standard error was not used as a measure of uncertainty because the scatter in the data is a function of temperature. Use of a single standard error would lead to nonphysical predictions, such as negative strengths at high temperatures, and there are not enough data to define a more reasonable distribution than the Gaussian distribution of the usual standard error definition. The error estimates of Equations (4-157) through (4-170) seem to be consistent with the comparison to burst tests that were discussed in the previous section. That is, the error from Equations (4-164) through (4-177) (strength coefficient/3.0) is approximately equivalent to an error of 25 K. The limited burst test data also were found to be in error by 25 K.

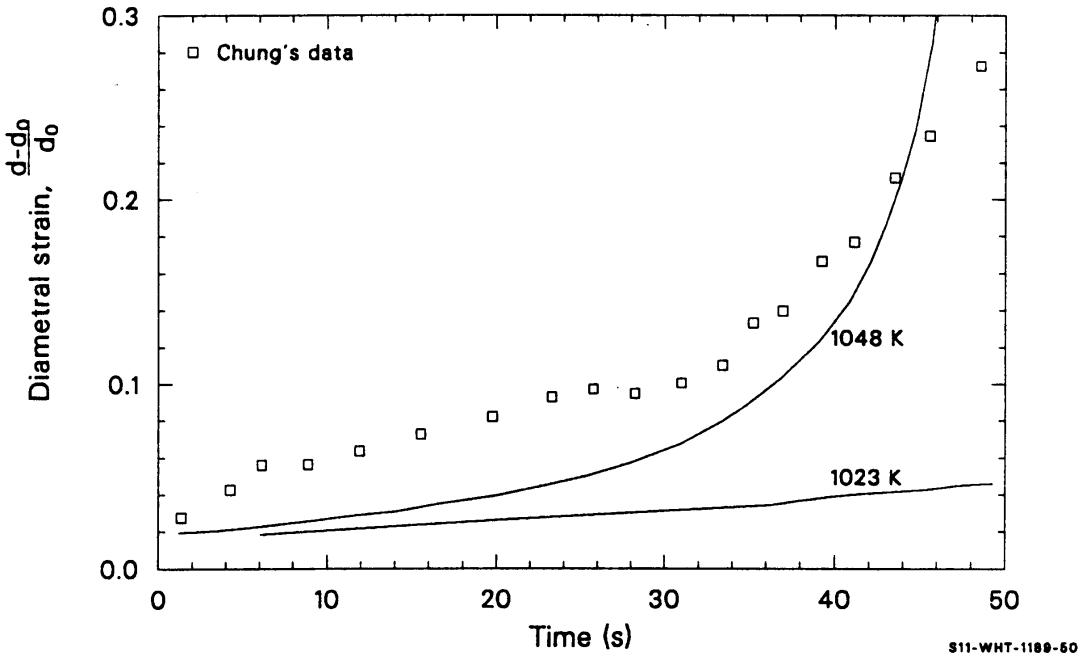

Figure 4-49. Measured diametral strain versus MATPRO predictions for Chung's test at 1,023 K and 5.2 MPa.

4.9.6 References

4.9-1 L. J. Siefken, M. P. Bohn, S. O. Peck, and J. A. Dearien, *FRAP-T5: A Computer Code for the Transient Analysis of Oxide Fuel Rods*, NUREG/CR-0840, TREE-1281, June 1979.

4.9-2 C. R. Hann et al., *Transient Deformation Properties of Zircaloy for LOCA Simulation*, NP-526, Volume 3, March 1978.

4.9-3 M. L. Picklesimer, "Deformation, Creep and Fracture in Alpha-Zirconium Alloys," *Journal of Electrochemical Technology, 4*, July-August 1966, pp. 289-300.

4.9-4 P. L. Rittenhouse and M. L. Picklesimer, "Research on the Mechanical Anisotropy of Zircaloy-2," *Journal of Electrochemical Technology, 4*, July-August 1966, pp. 322-329.

4.9-5 C. R. Woods (ed.), *Properties of Zircaloy-4 Tubing*, WAPD-TM-585, December 1966.

4.9-6 R. L. Mehan and F. W. Wiesinger, *Mechanical Properties of Zircaloy-2*, KAPL 2110, February 1, 1961.

4.9-7 H. C. Brassfield, J. F. White, L. Sjodahl, and J. T. Bittel, *Recommended Property and Reaction Kinetics Data for Use in Evaluating a Light Water Cooled Reactor Loss of Coolant Incident Involving Zircaloy-4 or 304-SS-Clad UO_2*, GEMP-482, April 1968.

4.9-8 A. L. Bement, Jr., *Effects of Cold Work and Neutron Irradiation on the Tensile Properties of*

Zircaloy-2, HW-74955, April 1963.

4.9-9 D. Lee and W. A. Backofen, "Superplasticity in Some Titanium and Zirconium Alloys," *Transactions of the Metallurgical Society of AIME, 239*, July 1967, pp. 1034-1040.

4.9-10 L. M. Howe and W. R. Thomas, "The Effects of Neutron Irradiation on the Tensile Properties of Zircaloy-2," *Journal of Nuclear Materials, 2*, 1960, pp. 248-260.

4.9-11 L. S. Rubenstein et al., "Effect of Oxygen on the Properties of Zircaloy-2," *Transactions of the American Society for Metals, 54*, 1961, pp. 20-30.

4.9-12 A. Cowan and W. J. Langford, "Effects of Hydrogen and Neutron Irradiation on the Failure of Flawed Zircaloy-2 Pressure Tubes," *Journal of Nuclear Materials, 30*, 1969, pp. 271-281.

4.9-13 C. C. Busby and K. B. Marsh, *High Temperature Deformation and Burst Characteristics of Recrystallized Zircaloy-4 Tubing*, WAPD-TM-900, January 1970.

4.9-14 D. O. Pickman, "Properties of Zircaloy Cladding," *Nuclear Engineering and Design, 21*, 1972, pp. 212-236.

4.9-15 G. F. Fieger and D. Lee, "Strength and Ductility of Neutron Irradiated and Textured Zircaloy-2," *Zirconium in Nuclear Applications*, ASTM-STP-551, 1973, pp. 355-369.

4.9-16 P. J. Crescimanno, *High Strain Rate Tensile Tests of Zircaloy at 550°F* (LWBR Development Program), WAPD-TM-1263, February 1976.

4.9-17 Y. Miyamoto, Y. Komatsu, N. Nagai, "Mechanical Behavior of Zircaloy-2 Tubing Under Biaxial Stresses," *Journal of Nuclear Materials, 61*, 1976, pp. 53-65.

4.9-18 C. C. Busby and K. B. Marsh, *High Temperature, Time Dependent Deformation in Internally Pressurized Zircaloy-4 Tubing*, WAPD-TM-1043, October 1974.

4.9-19 H. M. Chung, A. M. Garde, and T. F. Kassner, *Light-Water-Reactor Safety Research Program: Quarterly Progress Report*, January-March, 1975, ANL-75-28, June 12, 1975.

4.9-20 H. M. Chung, A. M. Garde, and T. F. Kassner, *Light-Water-Reactor Safety Research Program: Quarterly Progress Report, April-June, 1975*, ANL-75-58, June 13, 1975.

4.9-21 H. M. Chung, A. M. Garde, and T. F. Kassner, *Light-Water-Reactor Safety Research Program: Quarterly Progress Report, July-September, 1975*, ANL-75-72, no date.

4.9-22 H. M. Chung, A. M. Garde, and T. F. Kassner, *Light-Water-Reactor Safety Research Program: Quarterly Progress Report, October-December, 1975*, ANL-76-15, no date.

4.9-23 H. M. Chung, A. M. Garde, and T. F. Kassner, *Light-Water-Reactor Safety Research Program: Quarterly Progress Report, January-March, 1976*, ANL-76-49, no date.

4.9-24 H. M. Chung, A. M. Garde, and T. F. Kassner, *Light-Water-Reactor Safety Research Program: Quarterly Progress Report, July-September, 1976*, ANL-76-121, no date.

4.9-25 H. M. Chung, A. M. Garde, and T. F. Kassner, *Light-Water-Reactor Safety Research Program: Quarterly Progress Report, January-March, 1977*, ANL-77-34, no date.

4.9-26 A. A. Bauer, L. M. Lowry, and J. S. Perrin, *Evaluating Strength and Ductility of Irradiated Zir-*

caloy: Quarterly Progress Report April-June, 1976, BMI-NUREG-1956, July 1976.

4.9-27 A. A. Bauer, L. M. Lowry, and J. S. Perrin, *Evaluating Strength and Ductility of Irradiated Zircaloy: Quarterly Progress Report July-September, 1976*, BMI-NUREG-1961, October 1976.

4.9-28 A. A. Bauer, L. M. Lowry, and J. S. Perrin, *Evaluating Strength and Ductility of Irradiated Zircaloy: Quarterly Progress Report October-December, 1976*, BMI-NUREG-1967, January 1977.

4.9-29 D. Lee et al., *Plasticity Theories and Structural Analysis of Anisotropic Metals--Zircaloys*, NP-500, May 1977.

4.9-30 O. D. Sherby and A. K. Miller, *Development of the Materials Code, MATMOD (Constitutive Equations of Zircaloy)*, NP-567, December 1977.

4.9-31 E. Tenckhoff, "Operable Deformation Systems and Mechanical Behavior of Textured Zircaloy Tubing," *Zirconium in Nuclear Applications*, ASTM-STP-551, 1974, pp. 179-200.

4.9-32 B. D. Clay and G. B. Redding, "Creep Rupture Properties of Alpha Phase Zircaloy Cladding Relevant to the Loss of Coolant Accident," *J. Br.Nucl. Energy Soc., 15*, 1976, pp. 253-256.

4.9-33 J. R. Stanbridge and B. A. Keen, "Strain in the Zircaloy Clad of Fuel Pins in Loss of Coolant Accidents," *J. Br. Nucl. Energy Soc., 16*, 1977, pp. 341-346.

4.9-34 D. G. Hardy, "High Temperature Expansion and Rupture Behavior of Zircaloy Tubing," *Topical Meeting on Water Reactor Safety, Salt Lake City, UT, March 26-28, 1973*, CONF-730304.

4.9-35 H. Stehle, H. Steinberg, and E. Tenckhoff, "Mechanical Properties Anisotropy and Microstructure of Zircaloy Canning Tubes," *Zirconium in the Nuclear Industry*, ASTM-STP-663, pp. 486-507.

4.9-36 K. H. Matucha and G. Dressler, "Yield and Fracture of Biaxially Stressed Zircaloy-4 Cladding Tubes at Room Temperature and at 400°C," *Zirconium in the Nuclear Industry*, ASTM-STP-663, pp. 508-522.

4.9-37 C. S. Hartley, "Properties of Reactor Materials at Constant True Strain Rates," Progress Report July 1, 1977-June 30, 1978, NUREG/CR-0235, August 1978.

4.9-38 R. Hill, "A Theory of the Yielding and Plastic Flow of Anisotropic Metals," *Proceedings of the Royal Society of London, Series A, Mathematical and Physical Sciences, 193*, 1948, pp. 281-297.

4.9-39 R. H. Chapman, *Characterization of Zircaloy-4 Tubing Procured for Fuel Cladding Research Programs*, ORNL/NUREG/TM-29, July 1976.

4.9-40 D. R. Olander, *Fundamental Aspects of Nuclear Reactor Fuel Elements*, TID-26711-P1, 1976.

4.9-41 G. E. Dieter, *Mechanical Metallurgy*, New York: McGraw-Hill Book Company, Inc., 1976, pp. 28-32.

4.10 Annealing (CANEAL)

The equation of state for cladding plastic deformation described in Section 4.9 contains terms which are dependent on cold work and fast neutron fluence. This section is a description of a subcode that determines the thermal annealing of cold work and fast neutron fluence. The annealing is modeled with empirical rate equations, which are used to keep track of the remaining effective cold work and fast neutron fluence for use in the equation of state for cladding plastic deformation.

4.10.1 Summary

The CANEAL subcode requires input values of temperature at the start of a time step, an estimate of the rate of change of temperature during the time step, time step size, fast neutron flux, and start-of-step values of cold work and fast neutron fluence.

The expression used to find the ratio of effective cold work for the strength coefficient at the end of a time step divided by effective cold work at the beginning of an isothermal time step with temperature < 1,255 K is

$$FK = \exp\left[-1.504\,(1 + 2.2 \times 10^{-25}\,\Phi_{KO})\,(t)\,\exp\left(-2.33 \times 10^{18}/T^{6}\right)\right] \tag{4-219}$$

where

FK	=	effective cold work for the strength coefficient at the end of a time step divided by effective cold work at the start of the time step
Φ_{KO}	=	effective fast neutron fluence for strength coefficient at the start of the time step (n/m^2)
t	=	time step size (s)
T	=	cladding temperature (K).

The effective fast neutron fluence for calculating the strength coefficient after an isothermal time step with temperature < 1,255 K is computed with the expression

$$\frac{10^{20}}{\Phi_K} = 2.49\times10^{-6}\,(t)\,\exp\left(\frac{-5.35\times10^{23}}{T^{8}}\right) + \frac{10^{20}}{\Phi_{KO}} \tag{4-220}$$

where Φ_K is the effective fast neutron fluence for the strength coefficient at the end of a time step (n/m^2).

For temperatures < 1,255 K, the expression used to find the ratio of effective cold work for the strain hardening exponent at the end of an isothermal time step to the effective cold work for strain hardening at the start of the time step is

$$FN = \exp\left[-12.032\,(1 + 2.2\times10^{-25}\Phi_{NO})\,(t)\,\exp\left(\frac{-2.23\times10^{18}}{T^{6}}\right)\right] \tag{4-221}$$

where

FN	=	effective cold work for strain hardening exponent at the end of a time step divided by effective cold work for strain hardening exponent at the start of the time step
Φ_{NO}	=	effective fast neutron fluence for the strain hardening exponent at the start of the time step (n/m^2).

For temperatures < 1,255 K, the effective fast neutron fluence for calculating the strain hardening exponent after an isothermal time step is computed with the expression

$$\frac{10^{20}}{\Phi_N} = 2.49\times10^{-6}\,(t)\,\exp\left(\frac{-5.35\times10^{23}}{T^8}\right) + \frac{10^{20}}{\Phi_{NO}} \tag{4-222}$$

where Φ_N is the effective fast neutron fluence for the strain hardening exponent at the end of a time step (n/m^2).

If the time step is not isothermal, Equations (4-219) through (4-222) must be modified to include the effect of varying temperature. The modification used is

$$\exp\left(\frac{-Q}{T^m}\right) = \exp\left(\frac{-Q}{TO^m}\right)\left[\frac{\exp\left[Q\left(\frac{dT}{dt}\right)t\left(\frac{m}{TO^m+1}\right)\right]-1}{Q\left(\frac{dT}{dt}\right)t\left(\frac{m}{TO^m+1}\right)}\right] \tag{4-223}$$

where

Q,m	=	the constants that appear in the isothermal expression
TO	=	temperature at the start of the time step (K)
dT/dt	=	average rate of change of temperature expected during the time step (K/s).

Expression (4-222) is exact for a constant rate of temperature change and is only an approximation for nonlinear temperature changes.

If the temperature during the time step is as high as 1,255 K, the effective cold works and fast neutron fluences are set equal to zero.

The following section is a discussion of the data that were available to use to develop annealing rate equations. The model development itself is presented in Section 4.10.3.

4.10.2 Available Data

Howe and Thomas[4.10-1] reported postirradiation annealing studies on annealed, 13.1% cold worked, and tempered 25.5% cold worked zircaloy-2 irradiated at 493 and 553 K with integrated fast neutron fluences of 3.6 x 10^{23} n/m^2 and 2.7 x 10^{24} n/m^2. Specimens were given 1 hour anneals in vacuum at various temperatures. The nominal room temperature ultimate stresses measured with these samples are listed in

Table 4-28.

The data from irradiated annealed zircaloy-2 show that irradiation induced hardening in this material is completely annealed out after 1 hour at temperatures above 775 K and that most of the recovery occurs in the temperature range from 575 to 675 K. From their recovery data with 25.5% cold worked zircaloy-2, Howe and Thomas concluded that:

1. The recovery occurring in the temperature range 550 to 725 K is the annealing out of irradiation damage rather than cold work.
2. The irradiation damage in cold worked material is completely annealed out after 1 hour at approximately 725 K.
3. The recovery from 725 to 973 K for irradiated material is fairly similar to that for unirradiated material. However, there is an indication that the irradiated material recovers slightly faster.

Since the 1 hour anneals of Howe and Thomas represent times which are long compared to loss of coolant accident blowdown and refill times, the data were used only for general guidance and verification of the models developed from shorter annealing times reported by Bauer. In particular, the data support the ideas that (a) irradiation damage anneals before cold work and (b) irradiation damage affects the rate of annealing of cold work.

Bauer reported yield strengths, ultimate strength, uniform elongations (engineering strain at maximum load), and total elongations from annealing studies of both cold worked and irradiated cold worked zircaloy cladding material.[4.10-2,4.10-3] The unirradiated cold worked cladding was from a standard lot of tubing which has been characterized by Chapman.[4.10-4] The irradiated cladding was obtained from spent fuel rods irradiated in the Carolina Power and Light H. B. Robinson Plant to a fast neutron fluence of

approximately 4.4 x 10^{25} n/m^2.

Table 4-28. Room temperature ultimate strengths of cladding annealed for 1 hour from Howe and Thomas.

Cold Work (%)	Neutron Fluence (n/m^2)	Annealing Temperature (K)	Ultimate Strength (MPa)
0	3.6 x 10^{23}	555	634
0	3.6 x 10^{23}	625	588
0	3.6 x 10^{23}	675	513
0	3.6 x 10^{23}	725	513
0	3.6 x 10^{23}	775	500
0	3.6 x 10^{23}	875	500
0	3.6x10^{23}	975	499
25.5	0	555	619
25.5	0	675	614
25.5	0	775	603
25.5	0	875	530
25.5	0	975	512
25.5	2.7x10^{24}	555	728
25.5	2.7x10^{24}	625	712
25.5	2.7x10^{24}	675	675
25.5	2.7x10^{24}	725	626
25.5	2.7x10^{24}	775	579
25.5	2.7x10^{24}	875	504
25.5	2.7x10^{24}	975	486

Ultimate strengths and uniform elongations obtained at 644 K and a strain rate of 0.025/minutes with the unirradiated cladding are listed in Table 4-29. With a heating rate of 5.6 K/s, most of the recovery of both strength and uniform elongation occurs between temperatures of 894 and 978 K. However, the recovery has barely started at 978 K when the heating rate is 27.8 K/s. Since the annealing times at temperature are short, the maximum temperature required to anneal these samples is considerably higher than the temperatures reported by Howe and Thomas.

Tables 4-30 and 4-31 are a summary of Bauer's measurements of ultimate strengths and uniform elongations of annealed irradiated tubing. The measurements were performed at 644 K and a strain rate of

0.025/minutes. The results in Table 4-30 were obtained with transient anneals similar to those used with the unirradiated tubing. Table 4-31 summarizes results from isothermal anneals similar to the anneals carried out by Howe and Thomas.

The annealing behavior of the irradiated cladding is different than the behavior of the unirradiated material. Ultimate strengths obtained with irradiated material which had little or no annealing are substantially higher than the ultimate strengths of the unirradiated material. However, transient anneals that begin to affect the strength of cold worked material (5.6 K/s to 866 and 894 K or 27.8 K/s to 978 K) leave the irradiated material with strengths below the strengths of the unirradiated material after corresponding anneals. It is possible that these differences are due to the fact that the tubing does not come from the same lot, but a similar trend has been shown by the studies of Howe and Thomas on material from one lot. It has thus been concluded that irradiation for long times at reactor operating temperatures causes a significant increase in the strength of zircaloy cladding and enhances the annealing of the strength increase due to cold work.

Comparison of uniform elongation measurements with the unirradiated cladding (Tables 4-29 and 4-30) shows that the effect of irradiation on this parameter is different than its effect on ultimate strength. The uniform elongation of the unannealed irradiated material is less than the uniform elongation of the unannealed unirradiated material, but there is no obvious increase in the rate of recovery from cold work effects because of the irradiation. Therefore, models that describe annealing by keeping track of effective cold work and effective fluence should be set up to use different values of these parameters for predicting strength and elongation.

Table 4-29. 644 K test results for unirradiated transient annealed cladding.[4.10-2]

Specimen Number[a]	Heating Rate (K/s)	Maximum Temperature (K)	Ultimate Strength (MPa)	Uniform Elongation (%)
As received	--	*644*	*434.5*	*4.1*
0781-8	5.6	811	434	4.1
0781-7	5.6	866	432	4.1
0781-6	5.6	894	409	4.8
0781-5	5.6	978	252	24.3
0781-4	27.8	811	434	3.6
0781-3	27.8	866	438	3.3
0781-2	27.8	894	432	3.6
0781-1	27.8	978	422	4.6

a. The number 0781 is the rod number.

Table 4-30. 644 K test results for irradiated transient annealed cladding. [4.10-3]

Specimen Number[a]	Heating Rate (K/s)	Maximum Temperature (K)	Ultimate Strength (MPa)	Uniform Elongation (%)
PB-20	--	644	622.8	4.10
PB-34	--	644	650.3	4.00
PB-46	--	644	660.9	2.80
H10-20	--	644	694.0	3.80
P4-50-55	0.6	700	674.0	2.10
P4-55-60	0.6	755	633.0	2.70
P4-89-1/2-94-1/2	0.6	811	574.5	2.30
P4-94-1/2-99-1/2	0.6	894	286.1	9.57
Pr-89-1/2-104-1/2	0.6	978	268.9	9.21
P4-111-116	5.6	700	653.0	2.00
P4-45-50	5.6	755	676.0	2.40
P4-35-3/4-46-3/4	5.6	811	595.2	2.35
Pr-70-3/4-75-3/4	5.6	866	349.3	2.94
Pr-75-3/4-80-3/4	5.6	894	313.7	4.77
Pr-80-1/2-89-1/2	5.6	978	287.3	10.56
014-106-1/2-111-1/2	13.9	755	717.0	2.40
A8-120-3/4-125-3/4	13.9	811	652.7	2.27
P4-16-1/2-21-1/2	13.9	866	577.9	2.50
P4-21-1/2-26-1/2	13.9	894	456.2	2.16
P4-26-1/2-31-1/2	13.9	978	304.5	5.74
P4-65-70	27.8	755	671.0	2.10
A1-29-1/2-34-1/2	27.8	811	721.6	2.70
A8-105-3/4-110-3/4	27.8	866	671.0	2.70
A8-110-3/4-115-3/4	27.8	894	597.5	2.06
A8-115-3/4-120-3/4	27.8	978	348.2	3.49

Table 4-30. 644 K test results for irradiated transient annealed cladding. (Continued)[4.10-3]

Specimen Number[a]	Heating Rate (K/s)	Maximum Temperature (K)	Ultimate Strength (MPa)	Uniform Elongation (%)
P4-116-21	27.8	1033	329.0	4.70
014-111-1/2-116-1/2	27.8	1144	338.0	8.60
014-37-42	27.8	1255	340.0	10.50

a. The letter and number, letter, or number before the first hyphen identifies the rod number; that is Rod P8, Rod P4-9, Rod 014, etc.

Table 4-31. 644 K test results for irradiated isothermally annealed cladding.[4.10-3]

Specimen Number[a]	Temperature (K/s)	Time at Temperature (minutes)	Ultimate Strength (MPa)	Uniform Elongation (%)
P8-20	644	--	622.8	4.10
P8-34	644	--	650.3	4.00
P8-46	644	--	660.9	2.80
H10-20	644	--	694.0	3.80
H10-5	700	60	615.9	3.35
H10-41	755	10	590.6	2.85
H10-17	755	60	556.2	3.06
P4-60-65	811	1	560	2.90
A1-24-1/2-29-1/2	811	10	363.1	3.20
H10-18	811	30	371.1	5.10
A1-105-3/4-110-3/4	866	1	332.1	4.52
A1-99-104	866	5	311.4	8.03
H10-3	866	30	321.7	10.10
A1-110-3/4-115-3/4	894	1	308.9	7.90
H10-4	894	30	319.4	13.93
A1-116-1/2-121-1/2	978	1	305.6	7.67
H10-16	978	30	311.4	11.80

a. The letter and number before the first hyphen identifies the rod number; that is, Rod P8, Rod H10, and Rod A1.

The isothermal annealing effects reproduced in Table 4-31 are similar to those of Table 4-30 in that recovery of ultimate strength precedes recovery of uniform elongation. However, several additional features of the annealing of cold-worked and irradiated zircaloy cladding become apparent from the isothermal data.

1. The four tests at 644 K show that approximately 10% sample to sample scatter should be expected in the measured values of strength. In particular, rod H10 shows consistently high strength. Variation on the order of a percent seems to be present in the uniform elongation data. Models for annealing will therefore have to emphasize general trends and avoid exact fits to individual measurements.

2. Irradiation effects on the strength of zircaloy cladding do not seem to saturate at the low fluences used by Howe and Thomas. The two 60 minute anneals show strengths at 644 K similar to the room temperature strengths measured after similar anneals by Howe and Thomas. If the tensile test data had been taken at similar temperatures, the cladding measured by Bauer would show considerably greater strength.

3. Time at temperature during annealing is less important for the irradiated material than for the unirradiated material. The exponential dependence on time of the model developed in Section 4.10.3 for annealing of the effect of cold work on strength predicts that the log of the departure of strength parameters from their annealed values for two isothermal anneals that differ only in the time at temperature should be proportional to the reciprocal ratio of the annealing times. The major component of the increase of the strengths in Table 4-31 is much less dependent on time at temperature than this relation would imply.[a]

The net impression left by the data of Tables 4-28 through 4-31 is that at least two different processes are important in the annealing of cold worked and irradiated cladding and that the annealing of the irradiation caused component follows a rate equation that is different than the rate equation for the cold work component. Data that could be used to model these separate processes (for example, annealing studies with one lot of material irradiated to several different fluences) were not available for use in the development of the annealing model for MATPRO. Therefore, the model developed in the next section is a strictly empirical attempt to reproduce the available data with a reasonably concise set of correlations. Also, there were no data for annealing rates at temperatures corresponding to the beta phase (temperature > 1,255 K).

4.10.3 Model Development

The approach used to develop the annealing models presented here was to develop a model for the annealing of cold worked cladding and modify it to fit data from cold worked and irradiated material in the alpha and alpha plus beta phase temperature range. The model for recovery kinetics in cold worked cladding is based on a result reported by Byrne.[4.10-5] He found that recovery[b] data frequently conform to the

a. For example, the 10- and 60-minute anneals at 775 K have ultimate strengths that are 279.2 and 244.8 MPa above the fully annealed ultimate strength sample H10-16. An equation with the exponential time dependence of Equation (4-219) would imply that the ratio of the logs of the two strengths should be 1/6, or 0.17. The ratio is 0.98.

assumption that the rate of recovery of a property from its cold worked value is proportional to the instantaneous value of the property. If the property is the strength coefficient,[a] the rate equation for recovery is

$$dK/dt = -f_T (K - K_A) \tag{4-224}$$

where

K	=	strength coefficient of cold worked cladding (MPa)
t	=	time (s)
f_T	=	a temperature-dependent factor
K_A	=	strength coefficient of annealed cladding (MPa).

Since isothermal annealing data with unirradiated cold worked tubing are not available, the effect of temperature on the factor f_T in Equation (4-224) had to be determined from the limited transient annealing data of Table 4-29. The method used to do this is outlined as follows:

(1) The change of the factor f_T in Equation (4-224) is assumed to be represented by the expression

$$f_T = B \exp (Q/T^m) \tag{4-225}$$

where

B,Q,m	=	positive constants
T	=	temperature (K)

(2) Equation (4-224) is integrated over a very short (approximately isothermal) time interval to produce a differential expression for the change in strength coefficient

$$\frac{K_{final} - K_A}{K_{initial} - K_A} = \exp\left[-B\,(t_{final} - t_{initial})\,\exp\left(-\frac{Q}{T^m}\right)\right] \tag{4-226}$$

(3) The long interval beginning at a temperature T_i, and ending at a temperature T_f is divided into η small intervals, and the temperature during any small interval is assumed constant. The net change in K is the product of η terms like Equation (4-226) for each interval

$$\frac{K_{final} - K_A}{K_{initial} - K_A} = \prod_{j=1}^{\eta} \exp\left[-B\left(\frac{t_{final} - t_{initial}}{\eta}\right)\exp\left(-\frac{Q}{T_j^m}\right)\right] \tag{4-227}$$

---

b. A separate model for recrystallization kinetics was developed but not used because only limited recrystallization data were available.

a. Since the change in the strength coefficient is modeled as a linear function of cold work, one can use cold work instead of the strength coefficient in this equation.

$$= \exp\left[-b\left(\frac{t_{final} - t_{initial}}{\eta}\right)\sum_{j=1}^{\eta}\exp\left(-\frac{Q}{T_j^m}\right)\right]$$

where T_j is the temperature during the j-th interval.

(4) When the temperature change is a linear function of time, T_j in Equation (4-227) can be obtained by interpolation between the initial and final temperatures. The linear interpolation,[a] a Taylor series expansion, and a power series summation yield

$$\sum_{j=1}^{\eta}\exp\left(-\frac{\dot{Q}}{T_j^m}\right) = \sum_{j=1}^{\eta}\exp\left(\frac{-Q}{\left[T_f - \left(\frac{T_f - T_i}{2\eta}\right) - (\eta - j)\left(\frac{T_f - T_i}{\eta}\right)\right]^m}\right)$$

$$= \sum_{j=1}^{\eta}\exp\left(\frac{-Q}{\left[T_f - \left(\frac{T_f - T_i}{2\eta}\right)\right]^m}\left[1 + \frac{m(\eta - j)\frac{(T_f - T_i)}{\eta}}{T_f - \left(\frac{T_f - T_i}{2\eta}\right)} + \ldots\right]\right)$$

$$= \exp\left(\frac{-Q}{\left[T_f - \left(\frac{T_f - T_i}{2\eta}\right)\right]^m}\right)\left[\frac{1 - \exp\left(\frac{-m(T_f - T_i)Q}{\left[T_f - \left(\frac{T_f - T_i}{2\eta}\right)\right]^{m+1}}\right)}{1 - \exp\left(\frac{-m(T_f - T_i)Q}{\eta\left[T_f - \left(\frac{T_f - T_i}{2\eta}\right)\right]^{m+1}}\right)}\right] \quad (4\text{-}228)$$

---

a. The interpolation may start with the final temperature as is done here

$$T_j = T_f - \left(\frac{T_f - T_i}{2\eta}\right) - (\eta - j)\left(\frac{T_f - T_i}{\eta}\right)$$

or it may start with the initial temperature so that

$$T_j = T_i + \left(\frac{T_f - T_i}{2\eta}\right) + j\left(\frac{T_f - T_i}{\eta}\right) \quad .$$

The second form was used for coding the annealing model because it yields a result in terms of the initial temperature.

(5) Equation (4-228) is substituted into Equation (4-227), and the limit as the number of short intervals approaches infinity($n \rightarrow \infty$) is determined. The resultant expression is

$$\frac{K_f - K_A}{K_i K_A} = \exp\left(-B\left[\exp\left(-\frac{Q}{T_f^m}\right)\right]\left[\frac{1-\exp\left(\frac{-Q\,(T_f - T_i)^m}{T_f^{m+1}}\right)}{\frac{Q\,(T_f - T_i)^m}{T_f^{m+1}}}\right](t_{final} - t_{initial})\right). \quad (4\text{-}229)$$

(6) Ultimate strengths and uniform elongations from Table 4-29 are used to determine the strength coefficient[a] after the various anneals described in this table.

(7) The strength coefficients of Step (6) are used to determine Q, B, and m. For the current MATPRO version, the values of K_f after the anneals to 866 and 978 K at 5.6 K/s were used with the value of K_i from the as-received material and Equation (4-229) to determine B and Q with assumed trial values of K_A between 364 and 442 MPa and assumed trial integral values of m between1 and 9. Finally, the values of Q, B, K_i, K_A, and m for each trial were used in Equation (4-229) to predict K_f for the six anneals that were not already considered. The predictions were compared with the data. The trial values of K_A and m that most successfully predicted both the postanneal data and the as received strength coefficient (using the stress relief annealing schedule provided in Reference 4.10-4) were K_A = 406 MPa and m = 6. The value m = 6 and the values of Q and B which produced the successful predictions (Q = 2.33 x 10^{18} and B = 1.504) were therefore adopted for the model.

A procedure similar to the one described in the previous seven steps could be used to develop a model for the effect of cold work annealing on the strain hardening exponent. However, the complex form of the expression relating cold work and the strain hardening exponent would complicate the solution considerably. For the time being, the rate of annealing of effective cold work for the strain hardening exponent is assumed to be proportional to the rate of the effective cold work for the strength coefficient. The best fit was obtained with a value of B which is eight times as large as the B used for the strength coefficient.

The rest of this section describes the development of models for the annealing of cold worked and irradiated cladding. It was concluded in Section 4.10.2 that the principal features of the annealing data with irradiated cladding are:

1. Fast neutron fluence increases the rate of recovery from cold work effects.
2. The annealing kinetics of the irradiation caused increase in strength do not have the exponential time dependence that characterizes the recovery from cold work effects.

Based on these conclusions, the first step in producing the model for the effect of annealing on the strength coefficient of irradiated cladding was to modify the model for cold work annealing to include the irradiation caused enhancement of the recovery of the strength coefficient from cold work effects. The

a. The procedure used to determine a strength coefficient from ultimate strength and uniform elongation data is discussed in Section 4.9.

modification of the cold work annealing model was based on the information in Table 4-32.[a] The first two columns identify the annealing tests, and the third column lists the strength coefficients calculated from the ultimate strengths and uniform elongations of Bauer's isothermal annealing tests (Table 4-31). The column

Table 4-32. Strength and residual strength coefficients after isothermal anneals.

Temperature (K)	Time at Temperature (min)	Strength Coefficient (Mpa)	Residual Strength Coefficient (MPa)	CW/CW_o
644	As received	750.7	191.7	1
644	As received	781.5	222.5	1
644	As received	763.4	204.4	1
644	As received	828.9	205.9	1
700	60	724.8	101.8	1
755	10	683.5	61.0	0.997
755	60	648.2	28.3	0.982
811	1	649.7	94.5	0.975
811	10	425.2	-100.1	0.780
811	30	460.8	-72.6	0.475
866	1	387.9	-125.1	0.700
866	5	417.2	-14.3	0.167
866	30	451.6	-0.9	0.000
894	1	411.3	-54.7	0.392
894	30	483.2	-30.7	0.000
978	1	406.0	0	0.002
978	30	452.5	0	0.000

entitled “Residual Strength Coefficient” is the strength coefficient minus the sum of the strength coefficient for annealed cladding and the contribution of cold work calculated with the unmodified model for cold work annealing. The column entitled CW/CW_o is the initial cold work divided into the postanneal cold work predicted by the unmodified cold work annealing model. Comparison of the residual strengths

a. A similar table was constucted from Bauer’s transient annealing data. The transient data have no new information.

and the column titled CW/CW_o shows that the residual strength coefficient is negative whenever the cold-work is predicted to be partly annealed (CW/CW_o in the range 0.4 to 0.8). The most reasonable interpretation of this feature is to assume that the irradiation enhances the rate of annealing of the cold work. The change required to model this effect is to replace the constant B in Equation (4-229) by a function which increases with increasing fluence. The expression adopted for the strength coefficient annealing model was

$$B = 1.504\,[1 + 2.22 \times 10^{-25}]\,\Phi \qquad (4\text{-}230)$$

where

B	=	the rate constant in Equation (4-229)
Φ	=	fast neutron fluence (n/m^2).

Table 4-33 lists the information of Table 4-32 using the revised rate constant of Equation (4-230). The residual strength coefficients are close to zero for temperatures above 866 K and for the two long isothermal anneals at 811 K.

The second step in producing a model for the effect of annealing on the strength coefficient of irradiated cladding was the derivation of expressions to describe the annealing of the residual strength coefficient. The expressions for the annealing of the residual strength coefficient are based on the values of this parameter presented in Table 4-33 and on residual strengths obtained with the transient test data of Table 4-30.

Tables 4-34 and 4-35 are summaries of the strength coefficient and residual strength coefficients obtained with the transient test data. Table 4-34 groups the tests with equal maximum temperature

Table 4-33. Strength and residual strength coefficients with modified cold work annealing model.

Temperature (K)	Time at Temperature (minutes)	Strength Coefficient (MPa)	Residual Strength Coefficient (MPa)	CW/CW_o
644	As received	750.7	191.7	1
644	As received	781.5	222.5	1
644	As received	763.4	204.4	1
644	As received	828.9	205.9	1
700	60	724.8	101.8	1
755	10	683.5	65.8	0.969
755	60	648.2	54.7	0.827
811	1	649.7	239.9	0.025
811	10	425.2	19.2	0.000
811	30	460.8	8.3	0.000
866	1	387.9	-18.1	0.000
866	5	417.2	11.2	0.000
866	30	451.6	-0.9	0.000
894	1	411.3	5.3	0.000
894	30	483.2	30.7	0.000
978	1	406.0	0	0.000
978	30	452.5	0	0.000

Table 4-34. Strength and residual strength coefficients after transient anneals (tests with equal maximum temperature).

Heating Rate (K/s)	Maximum Temperature (K)	Strength Coefficient (MPa)	Residual Strength Coefficient (MPa)	CW/CWo
As received	644	750.7	191.7	1
As received	644	781.5	222.5	1
As received	644	763.4	204.4	1
As received	644	828.9	205.9	1
0.6	700	758.5	199.5	1
5.6	700	732.4	173.4	1
0.6	755	728.8	169.7	0.999
5.6	755	769.4	210.4	1.0
13.9	755	816.5	257.5	1.0
27.8	755	755.4	196.4	1.0
0.6	811	651.8	111.0	0.881
5.6	811	676.5	119.5	0.987
13.9	811	739.7	181.5	0.995
27.8	811	830.7	272.1	0.997
5.6	866	405.5	-115.0	0.749
13.9	866	660.5	118.2	0.891
27.8	866	772.4	220.0	0.944
0.6	894	397.0	-9.0	0.000

Table 4-34. Strength and residual strength coefficients after transient anneals (tests with equal maximum temperature). (Continued)

Heating Rate (K/s)	Maximum Temperature (K)	Strength Coefficient (MPa)	Residual Strength Coefficient (MPa)	CW/CWo
5.6	894	385.8	-79.7	0.389
13.9	894	514.9	4.0	0.685
27.8	894	681.8	149.2	0.828
0.6	978	370.1	-35.9	0.000
5.6	978	407.1	1.1	0.000
13.9	978	384.9	-22.4	0.009
27.8	978	411.6	-8.7	0.932
27.8	1,033	403.6	-2.4	0.001
27.8	1,144	458.7	52.7	0.000
27.8	1,255	481.1	75.1	0.000

Table 4-35. Strength and residual strength coefficients after transient anneals (test with equal heating rates).

Heating Rate (K/s)	Maximum Temperature (K)	Residual Strength Coefficient (MPa)
As received	644	191.7
As received	644	222.5
As received	644	204.4
As received	644	205.4
0.6	700	199.5
0.6	755	169.7
0.6	811	111.0
0.6	894	-9.0
0.6	978	-35.9
5.6	700	173.4
5.6	755	210.4

Table 4-35. Strength and residual strength coefficients after transient anneals (test with equal heating rates). (Continued)

Heating Rate (K/s)	Maximum Temperature (K)	Residual Strength Coefficient (MPa)
5.6	811	119.5
5.6	866	-115.0
5.6	894	-79.7
5.6	978	
13.9	755	257.5
13.9	811	181.5
13.9	866	118.2
13.9	894	4.0
13.9	978	-22.4
27.8	755	196.4
27.8	811	272.1
27.8	866	222.0
27.8	894	149.2
27.8	978	-8.7
27.8	1033	-2.4
27.8	1144	52.7
27.8	1255	75.1

together, and Table 4-35 groups tests with equal heating rates together. Several trends used to develop the model for the annealing of the residual strength coefficient are apparent from an inspection of Tables 4-34 and 4-35.

Inspection of the data in Table 4-35 shows that the residual strength coefficient does not anneal significantly in any of the tests with a maximum temperature of 755 K or less. All of the tests with maximum temperature of 978 K show essentially complete annealing. The tests with maximum temperatures of 811 K show varying amounts of annealing, but the effect of different heating rates (or, said another way, different times at temperature) on the residual strength coefficient is much less than one would expect from an expression with an exponential time dependence like Equation (4-229). If an equation of the form of equation (4-229) were used to model the annealing of the residual strength coefficient, the ratio of the logs of the measured residual strength coefficients after two anneals to the same maximum temperature would be predicted to be proportional to the heating rates. The four residual strengths measured after anneals with a maximum temperature of 811 K (where annealing changes are greater than the scatter of the data) show

significantly less dependence on heating rate. This observation is supported by the isothermal annealing data of Table 4-33, which also show relatively little dependence on the time at a given temperature.

When the transient data are grouped with equal heating rates together (Table 4-35), a very strong dependence of residual strength on maximum temperature is apparent. For all of the heating rates, the annealing of the residual strength occurs over a range of maximum temperatures only about 75 K wide. Moreover, the center of this 75 K band is increased by only about 100 K when the heating rate is increased by a factor of 50.

The approach used to model the annealing of the residual strength coefficient was to assume that this component is not subject to the rate equation used for the annealing of cold work effects. The assumption is logical, not only because of the information in Tables 4-33 and 4-34 but also because the probable cause of the residual strength coefficient is radiation damage--vacancies, interstitials, and dislocation loops--rather than cold work effects. To describe the annealing of the residual strength coefficient, an empirical rate equation which is a generalized form of Equations (4-224) and (4-225) was written[a]

$$dv/dt = -B \exp(-Q/T^m)\, y^P \tag{4-231}$$

where

y	=	irradiation contribution to the strength coefficient (MPa)
T	=	temperature (K)
t	=	time (s)

and B, Q, m, and P are positive constants to be evaluated by comparison to the residual strength coefficient data of Tables 4-33 through 4-35. The procedure used with the rate equation for the annealing of cold work effects [Steps (2) to (5) after Equation (4-225)] was repeated with Equation (4-231) to produce a differential expression for the change in y during a time interval with a linear change in temperature. The differential expression is

$$\frac{1}{y_f^p - 1} = [p-1]\, B\left[\exp\left(-\frac{Q}{T_f^m}\right)\right]\left[\frac{1-\exp\left(\dfrac{-Q\,(T_f - T_i)^m}{T_f^{m+1}}\right)}{\dfrac{Q\,(T_f - T_i)^m}{T_f^{m+1}}}\right](t_f - t_i) + \frac{1}{y_i^p - 1} \tag{4-232}$$

where terms with subscripts i refer to initial values and terms with subscripts f refer to final values of the terms in Equation (4-231).

a. Since the change in the strength coefficient due to irradiation is modeled as a linear function of fast neutron fluence, one could use the fast neutron fluence in place of the variable y. The net effect would be a change of the constant B.

No completely analytical method to obtain a best fit of Equation (4-231) to the data has been found. However, several observations aided in finding values of B, Q, m, and P that provide a fit that is within the scatter of the data.

(1) The factor

$$\frac{1 - \exp\left(\frac{-Q\,(T_f - T_i)^m}{T_f^{m+1}}\right)}{\frac{Q\,(T_f - T_i)^m}{T_f^{m+1}}}$$

can be viewed as a correction for the fact that the temperature did not remain at T_f throughout the anneal. It is not relevant to the fundamental annealing properties of the cladding.

(2) Increasing m increases the effect of temperature on the change in y because the factor exp $[-Q/(T_f)^m]$ is more sensitive to temperature when m is larger.

(3) Increasing P decreases the sensitivity of the change in y to the time span t_f - t_i. This is most easily seen by noting that for large y_i, y_f is proportional to (t_f - t_i) - 1/(P - 1). For large values of P, the 1/(P - 1)-th root of t_f - t_i is relatively insensitive to t_f - t_i.

The residual strength data of Tables 4-33 and 4-35 were fit by trying integral values of m and P and using pairs of residual strengths from Table 4-35 in conjunction with the average value of the as received residual strength (206 MPa) and Equation (4-232) to solve for trial values of Q and B. Predictions of Equation (4-232) with each trial set of m, P, Q, and B were then compared to all the residual strengths in Tables 4-33 and 4-34. The best fit to the residual strength data was obtained with m = 8, P = 2, Q = 5.35×10^{23}, and B = 4.50×10^{-3}.[a]

Two trivial steps were required to convert Equation (4-232) to the form actually used in MATPRO subcodes.

1. The equation was transformed to an equivalent expression in terms of the initial temperature and heating rate. This transformation allows all the required input information to be parameters at the beginning of a time step. The transformation was carried out by using an alternate linear interpolation for temperature, as noted in conjunction with Equation (4-228).

2. The equation was modified to express the change in residual strength in terms of an effective fluence.

The expression for the rate of annealing of the effective fast neutron fluence for strain hardening [Equation (4-222)] was obtained by assuming that the rate of annealing of the effective fast neutron fluence for the strain hardening exponent is proportional to the rate of annealing of the effective fluence for the

a. The 13.9-K/s anneals to 811 and 866 K were used to find these values of Q and B.

strength coefficient. The model development was complicated by the fact that the cladding used to construct the model experienced three periods at high temperature in addition to the actual annealing test.

1. The stress relief anneal
2. The 2-year in-reactor life of the rod
3. The normal thermal transients during postirradiation handling of the rods.[4.10-6]

The effective fast neutron fluence for the strain hardening exponent at the start of the actual annealing test can be estimated from Bauer's as received data (Table 4-30 or 4-31). A maximum effective fluence of 8.4 x 10^{22} n/m^2 (for zero effective cold work) was found. Since the measured fast neutron fluence was 4.3 x 10^{25} n/m^2, considerable annealing of the radiation damage component that determines the strain hardening exponent must be assumed either in-reactor or during postirradiation handling of the rods.

The constants used in Equation (4-222) were obtained by (a) assuming as received effective fast neutron fluences in the range 1 x 10^{21} to 8 x 10^{22} n/m^2; (b) determining a constant of proportionality between the annealing rates of effective fast neutron fluences for strength and strain hardening that yields a prediction consistent with the annealing data; and (c) checking the first two steps by applying the annealing model to the in-reactor history to see if the assumed as-received effective fast neutron fluence and annealing rate are consistent. Self consistent results were obtained with an as received effective fast neutron fluence for strain hardening of 2 x 10^{22} n/m^2 and a constant of proportionality of 1,000.

Since no data are available for beta phase annealing, an approximation is necessary. The effective cold works and fast neutron fluences are set equal to zero whenever the temperature is as high as 1,255 K, the approximate equilibrium phase boundary for beta zircaloy.

4.10.4 Comparison of Annealing Models to Data

Tables 4-36 through 4-37 are comparisons of the predicted strength coefficients and strain hardening exponents to the data base used to construct the annealing models. The limited data for unirradiated cladding appear in Table 4-35. The cladding used in these tests had been 70% cold worked, then stress relieved according to schedules published by Chapman.[4.10-4] Equations (4-219) and (4-221) predict an effective cold work of 50% for the strength coefficient and 4% for the strain hardening exponent after the stress relief anneal. Both strength coefficient and strain hardening exponent are well predicted by the model.

Tables 4-37 and 4-38 compare model predictions for strength coefficients and strain hardening exponents with corresponding values derived from Bauer's measurements with cold worked and irradiated cladding. No annealing schedule has been published for this material, but published nominal preirradiation values[4.10-7] are consistent with the assumption that the annealing schedule was similar to the unirradiated cladding. Therefore, the effective cold works of 50% and 4% were also used to describe the irradiated

cladding.

Table 4-36. Comparison of model predictions of K and n with data base for unirradiated cladding.

Heating Rate (K/s)	Maximum Temperature (K)	Strength Coefficient (MPa) From Data	Strength Coefficient (MPa) Predicted	Strain Hardening Exponent From Data	Strain Hardening Exponent Predicted
As received	644	524	524	0.040	0.040
5.6	811	524	524	0.040	0.040
5.6	866	520	521	0.040	0.047
5.6	894	503	515	0.047	0.062
5.6	978	444	457	0.218	0.119
27.8	811	515	524	0.035	0.040
27.8	866	514	524	0.033	0.041
27.8	894	513	522	0.035	0.044
27.8	978	516	505	0.045	0.087

Table 4-37. Comparison of model predictions of K and n with data base for transient anneals of irradiated cladding.

Heating Rate (K/s)	Maximum Temperature (K)	Strength Coefficient (MPa) From Data	Strength Coefficient (MPa) Predicted	Strain Hardening Exponent From Data	Strain Hardening Exponent Predicted
As received	644	750.7	765.1	0.040	0.024
As received	644	781.5	765.1	0.039	0.024
As received	644	763.4	765.1	0.028	0.024
As received	644	828.9	765.1	0.037	0.024
0.6	700	758.5	764.6	0.021	0.024
0.6	755	728.5	721.3	0.027	0.024
0.6	811	651.8	574.1	0.023	0.029
0.6	894	397.0	442.7	0.091	0.092
0.6	978	370.1	409.9	0.088	0.100
5.6	700	732.4	765.1	0.020	0.024
5.6	755	769.4	759.9	0.024	0.024

Table 4-37. Comparison of model predictions of K and n with data base for transient anneals of irradiated cladding. (Continued)

Heating Rate (K/s)	Maximum Temperature (K)	Strength Coefficient (MPa) From Data	Strength Coefficient (MPa) Predicted	Strain Hardening Exponent From Data	Strain Hardening Exponent Predicted
5.6	811	76.5	706.2	0.023	0.025
5.6	866	405.5	598.7	0.029	0.030
5.6	894	385.8	547.0	0.047	0.041
5.6	978	407.1	441.0	0.100	0.083
13.9	755	816.5	762.9	0.024	0.024
13.9	811	739.7	736.9	0.022	0.024
13.9	866	680.5	660.5	0.025	0.026
13.9	894	514.9	511.6	0.021	0.031
13.9	978	384.9	482.9	0.056	0.071
27.8	755	755.4	764.0	0.021	0.024
27.8	811	830.7	750.2	0.027	0.024
27.8	866	772.4	700.6	0.027	0.025
27.8	894	681.8	662.1	0.026	0.027
27.8	978	411.6	532.3	0.034	0.054
27.8	1,033	403.6	476.4	0.046	0.074
27.8	1,144	458.7	439.7	0.083	0.081
27.8	1,255	481.1	428.7	0.100	0.084

Table 4-38. Comparison of model predictions of K and n with data base for isothermal anneals of irradiated cladding

Heating Rate (K/s)	Maximum Temperature (K)	Strength Coefficient (MPa) From Data	Strength Coefficient (MPa) Predicted	Strain Hardening Exponent From Data	Strain Hardening Exponent Predicted
644	As received	750.7	765.1	0.040	0.024
644	As received	781.5	765.1	0.039	0.024
644	As received	763.4	765.1	0.028	0.024
644	As received	828.9	765.1	0.037	0.024
700	60	724.8	700.8	0.033	0.024
755	10	683.5	567.7	0.028	0.028
755	60	648.2	512.7	0.030	0.036
811	1	649.7	547.9	0.029	0.032
811	10	425.2	421.9	0.031	0.080
811	30	460.8	409.5	0.050	0.100
866	1	387.9	428.5	0.044	0.080
866	5	417.2	411.3	0.077	0.097
866	30	451.6	408.0	0.096	0.106
894	1	411.3	420.4	0.076	0.088
894	30	483.2	407.8	0.130	0.108
978	1	406.0	414.2	0.074	0.093
978	30	452.5	407.6	0.112	0.110

4.10.5 References

4.10-1 L. M. Howe and W. R. Thomas, “The Effect of Neutron Irradiation on the Tensile Properties of Zircaloy-2,” *Journal of Nuclear Materials, 2*, 1960, pp. 248-260.

4.10-2 A. A. Bauer, L. M. Lowry, and J. S. Perrin, *Evaluating Strength and Ductility of Irradiated Zircaloy: Quarterly Progress Report, July-September 1976*, BMI-NUREG-1961, October 1976.

4.10-3 A. A. Bauer, L. M. Lowry, and J. S. Perrin, *Evaluating Strength and Ductility of Irradiated Zircaloy: Quarterly Progress Report, April-June 1976*, BMI-NUREG-1956, July 1976.

4.10-4 R. H. Chapman, *Characterization of Zircaloy-4 Tubing Procured for Research Programs*, ORNL/NUREG/TM-29, July 1976.

4.10-5 J. G. Byrne, *Recovery, Recrystallization and Grain Growth*, New York: The Macmillan Company, 1965.

4.10-6 A. A. Bauer, L. M. Lowry, and J. S. Perrin, *Progress on Evaluating Strength and Ductility of Irradiated Zircaloy During July-September 1975*, BMI-NUREG-1938, September 1975.

4.10-7 A. A. Bauer, L. M. Lowry, and J. S. Perrin, *Evaluating Strength and Ductility of Irradiated Zircaloy: Quarterly Progress Report, October-December 1976*, BMI-NUREG-1967, January 1977.

4.11 Mechanical Limits and Embrittlement (CMLIMT, CBRTTL)

Cladding deformation and failure under stress is characterized by several boundaries that define important changes in the physical response of the cladding to stress. This section is a description of these boundaries and the two subcodes used to model them. The first subcode, CMLIMT, defines the elastic-plastic transition and cladding failure under tensile stress. The second subcode, CBRTTL, defines the amount of oxygen the cladding can absorb without becoming brittle.

4.11.1 Summary (CMLIMT)

Cladding mechanical limits are important to code predictions of both the number and shape of failed rods. This section describes expressions used to determine the most important limits, the elastic-plastic transition (yield) and cladding failure under tensile stress, as well as the ultimate engineering strength and the uniform elongation under uniaxial stress.

Failure expressions are related to the amount of detail the user chooses to consider in mechanical models. The fundamental failure criterion is derived for codes that model cladding plastic deformation without assuming azimuthally symmetric deformation. Alternate expressions are presented for less sophisticated codes that assume symmetric deformation, and one simplified correlation is presented for users who do not model plastic deformation at all.

The input parameters for the CMLIMT subcode are temperature, cold work, fast neutron fluences (> 1 MeV), average oxygen concentration, and strain rate. The equations used are

$$\text{true strain at yield} = \left[\frac{K}{E}\left(\frac{\dot{\varepsilon}}{10^{-3}}\right)^{m}\right]^{\frac{1}{(1-n)}} \tag{4-233}$$

$$\text{true yield strength} = \left[\frac{K}{E^{n}}\left(\frac{\dot{\varepsilon}}{10^{-3}}\right)^{m}\right]^{\frac{1}{(1-n)}} \tag{4-234}$$

$$\text{true strain at maximum load} = \frac{n}{1+m} \tag{4-235}$$

$$\text{true ultimate strength} = K\left(\frac{\dot{\varepsilon}}{10^{-3}}\right)^{m}\left(\frac{n}{1+m}\right)^{n} \tag{4-236}$$

where

K	=	strength coefficient (Pa)
E	=	Young's modulus (Pa)
$\dot{\varepsilon}$	=	true strain rate (s^{-1})

n	=	strain hardening exponent (unitless)
m	=	strain rate sensitivity constant (unitless).

K, n, and m are calculated with the subcode CKMN discussed in the description of CSTRES (Section 4.9), E is obtained by calling the function CELMOD (Section 4.6), and e is required input information.

Arguments are presented in Section 4.11.3 that demonstrate that cladding failure should be predicted by comparing the tangential component of true stress to the burst stress. Heating rate and strain rate do not affect this criterion, but irradiation and cold work increase it somewhat. The burst stress as a function of temperature is given by the following equations:

For $T \leq 750$ K,

$$\sigma_{\theta B} = 1.36 K_A \quad . \tag{4-237}$$

For $750 < T \leq 1{,}050$ K,

$$\sigma_{\theta B} = 46.861429 K_A \exp\left(\frac{-1.9901087\times10^6}{T^2}\right) \quad . \tag{4-238}$$

For $T > 1{,}050$ K,

$$\sigma_{\theta B} = 7.7 K_A \quad . \tag{4-239}$$

where

$\sigma_{\theta B}$	=	tangential component of true stress at burst (Pa)
K_A	=	strength coefficient for annealed cladding as determined with the MATPRO CKMN subcode (Pa)
T	=	temperature (K).

For cold worked or irradiated cladding, the burst stress is increased by four tenths of the increase of the strength coefficient due to irradiation and cold work.

The standard error[a] of Equations (4-237) through (4-239) is

$$U\sigma_{\theta B} = 0.17\sigma_{\theta B} \tag{4-240}$$

where $U\sigma_{\theta B}$ is the standard error of $\sigma_{\theta B}$.

a. The standard error of a model is estimated with a set of data by the expression: (sum of squared residuals/number of residuals minus the number of constants used to fit the data)$^{1/2}$.

Section 4.11.2 is a review of the available data. Equations (4-233) through (4-238) are derived in Section 4.11.3, and alternate methods of applying Equation (4-237) are derived in Section 4.11.4.

4.11.2 Available Data

The data reported as yield points, strain at maximum load (uniform strain), and ultimate strength have been reviewed in conjunction with the description of the CSTRES code (Section 4.9). This subsection will review only the data used in development of the CMLIMT subcode failure criterion. The number of these data has been severely restricted by the requirement that they be sufficiently complete to allow an estimate of local stresses and strains at failure.

The most useful data have been produced by the Multirod Burst Test Program sponsored by the NRC. All of these data were obtained with internal heaters and an external steam environment. Heating rates varied from 0 to 28 K/s. Estimated burst temperatures, burst pressures, and burst strains (average circumferential elongation) have been published for a number of single rod tests.[4.11-1,4.11-2] In addition, calibrated photographs of cross sections through the burst regions of some of the tests have been published.[4.11-2 to 4.11-5] These cross sections were needed to estimate wall thickness at burst[a] for the calculation of local stress at failure. The other required information for the local stress analysis developed in Section 4.11.3 is an estimate of the axial radius of curvature at burst. This information was not published but could be estimated from side view photographs of the burst tubes.[4.11-6-4.11-8] Table 4-39 is a summary of the Multirod Burst Test Program Data used.

Data from tests by Hobson and Rittenhouse[4.11-9] were also employed. The Hobson-Rittenhouse tests were conducted using a radiant heating furnace on BWR cladding in an argon environment with heating rates from 5.6 to 56 K/s. There was no significant difference in the local failure stress predicted from the Hobson-Rittenhouse tests conducted in argon and that predicted from the tests in a steam environment. It is possible that longtime tests in steam will show a difference in local stress at failure. However, it is also possible that specimens that accumulate thick, oxygen rich layers before significant deformation occurs will show that the oxygen rich layers of the cladding rupture before the oxygen poor layers. In the latter case, oxidation would have a significant effect on the early (small strain) deformation but little effect on the stress at failure.

Table 4-40 is a summary of the data that were used from the tests of Hobson and Rittenhouse. Burst temperatures, wall thickness measurements, and the average circumferential elongation were obtained from figures in Reference 4.11-9. Burst pressures were obtained by private communication from Chapman, and axial radii of curvature were estimated from samples sent by Hobson.

---

a. Most burst edges displayed one or more cleavage-like lines approximately 45 degrees from the radial direction. The wall thickness was measured adjacent to this line or, if the line could not be distinguished, 0.25 mm from the burst tear.

Table 4-39. Summary of multirod burst test data employed in CMLIMT.

Test No.	Burst Temperature (K)	Differential Pressure at Burst (MPa)	Average Circumferential Strain (m/m)	Wall Thickness at Burst (mm)	Axial Radius of Curvature (cm)
PS-10	1,174[a]	6.000[a]	0.20[a]	0.079[c]	2.1[c]
PS-17	1,051[a]	12.130[a]	0.25[a]	0.176[c]	1.2[c]
PS-18	1,444[a]	0.772[a]	0.24[a]	0.111[d]	0.9[g]
PS-19	1,232[a]	2.590[a]	0.28[a]	0.079[c]	0.6[c]
SR-23	1,350[a]	0.960[a]	0.35[a]	0.164[e]	1.1[h]
SR-25	1,365[a]	0.960[a]	0.78[a]	0.077[e]	0.6[i]
SR-34	1,039[b]	5.820[b]	0.316[b]	0.109[b]	1.6[c]
SR-35	1,048[b]	4.470[b]	0.290[b]	0.073[f]	3.1[c]
SR-37	1,033[b]	13.560[b]	0.231[b]	0.263[f]	3.7[c]
SR-41	1,030[b]	9.765[b]	0.274[b]	0.199[b]	2.7[c]
SR-43	1,046[b]	7.620[b]	0.290[b]	0.179[b]	3.5[c]

a. Reference 4.11-1.

b. Reference 4.11-2.

c. From photographs sent by R. H. Chapman.

d. Reference 4.11-3.

e. Reference 4.11-4.

f. Reference 4.11-5.

g. Reference 4.11-6.

h. Reference 4.11-7.

i. Reference 4.11-8.

Table 4-40. Summary of data from the Hobson-Rittenhouse tests.

Test No.	Burst Temperature (K)	Differential Pressure at Burst (MPa)	Average Circumferential Strain (m/m)	Wall Thickness at Burst (mm)	Axial Radius of Curvature (cm)
35	1,061	6.170	0.63	0.25	2.9
34	1,081	7.584	0.58	0.23	1.8
40	1,111	4.654	0.79	0.18	1.8
18	1,145	4.826	1.25	0.18	3.0
17	1,158	4.205	0.57	0.20	2.5
19	1,160	4.895	0.51	0.23	1.8
21	1,171	3.102	0.30	0.18	1.7
8	1,179	3.826	0.22	0.20	1.3
16	1,195	3.999	0.42	0.25	1.7
5	1,196	3.757	0.44	0.20	1.0
26a	1,205	3.068	0.27	0.28	1.8
27	1,213	2.241	0.55	0.15	1.1
15	1,214	2.275	0.41	0.18	1.1
37	1,215	2.344	0.40	0.18	1.4
26	1,220	3.033	0.53	0.13	1.5
9	1,235	1.448	0.43	0.20	2.7
28	1,253	1.413	0.85	0.18	2.8
11	1,299	1.434	0.68	0.25	1.5
32	1,302	0.745	0.93	0.25	2.1
29	1,432	0.676	0.92	0.23	2.5
36	1,440	0.827	0.50	0.23	1.5
4	1,472	0.689	1.11	0.20	2.5
36a	1,487	0.662	0.74	0.25	1.5

Table 4-41 is a summary of data obtained by Chung and Kassner[4.11-10] that were used in the devel-

opment of the CMLIMT code. The burst temperature, differential pressure at burst, average circumferential strain, and axial radius of curvature were obtained from Reference 4.11-10. The wall thickness at burst was obtained from photographs of cross sections from Chung by private communication. An important factor is that all of the samples in Table 4-41 were constrained by an internal mandrel, which applied an unknown axial stress to the cladding.

None of the data mentioned so far were obtained from irradiated cladding or at temperatures below 1,000 K. The only available low temperature data with irradiated cladding were obtained from studies by Bauer, Lowry, Gallagher, Markworth and Perrin[4.11-11 to 4.11-13] on cladding obtained from the H. B. Robinson reactor. The data from Bauer's tests which have been used in the development of CMLIMT are presented in Table 4-42. Tests M12-16, M-12-4, and M12-15 were conducted on as received cladding; while Tests D9-7, D9-8, D9-13, and D9-14 were conducted on cladding that had been annealed. Wall thicknesses adjacent to the burst were obtained from unpublished photographs similar to Figure 7 of Reference 4.11-11. The axial radii of curvature in these tests have not been reported.

Two sources of in-reactor data were employed. One is the irradiation effects Test IE-5, conducted in the Power Burst Facility at EG&G Idaho, Inc.[4.11-14,4.11-15] The measured (Rod IE-19) internal pressure in this test was reported to be 5.2 MPa in excess of the coolant pressure, and the cladding temperature was estimated from microstructure studies to be near 1,100 K. The average circumferential elongation was reported to be 25%.[4.11-15] The wall thickness at burst was estimated to be 0.09 mm, using figures from the postirradiation examination results report;[4.11-15] and the axial radius of curvature was estimated to be approximately four times the rod diameter from the posttest side view in Reference 4.11-15.

The second source of in-reactor data is a series of tests in the FR2 reactor in Germany.[4.11-16] Complete data from three tests (A2.3, B1.2, and B1.3) were presented, but two of the cladding cross sections showed evidence of contact with the shroud (burst edges rolled in). For that reason, only data from Test B1.2 were used. The average circumferential elongation, axial radius of curvature, burst pressure, and temperature for this test were taken from Reference 4.11-16 (0.249, 1.5 cm, 4.52 MPa, and 1,188 K).

Table 4-41. Summary of data from the Chung-Kassner tests.

Test No.	Burst Temperature (K)	Differential Pressure at Burst (MPa)	Average Circumferential Strain (m/m)	Wall Thickness at Burst (mm)	Axial Radius of Curvature (cm)
AS-40	1,089	5.302	1.01	0.39	2.9
AS-36	1,310	0.558	1.11	0.26	2.9
AS-9	1,329	1.282	1.24	0.12	3.2
AS-5	1,348	1.334	1.02	0.42	1.6

Table 4-42. Summary of data from the Bauer tests

Test No.	Burst Temperature (K)	Burst Strength (MPa)	Average Circumferential Strain (m/m)	Wall Thickness at Burst (mm)
M12-16	477	749.4	0.026	0.57
M12-4	644	659.1	0.052	0.60
M12-15	644	684.6	0.028	0.61
D9-7	644	356.4	0.212	0.45
D9-8	644	350.9	0.204	0.46
D9-13	644	372.3	0.225	0.51
D9-14	644	367.5	0.292	0.48

a. From Reference 4.11-12.

b. From photographs sent by Bauer and Lowry.

The coolant pressure was assumed to be the typical value of 0.3 MPa quoted in Reference 4.11-16.

One out-of-pile test result from Germany[4.11-17] was used in developing the CMLIMT failure model. The test was performed in air (one atmosphere) with an internal heater. The burst temperature, internal pressure at burst, average circumferential strain, and wall thickness at burst (1,114 K, 7.1 MPa, 0.37, and 0.215 mm) were taken from Reference 4.11-17. The axial radius of curvature was estimated to be approximately three times the cladding radius at burst by inspection of x-ray photos of similar tests just prior to burst.

4.11.3 Model Development

The expressions used to describe the elastic-plastic transition (yield) do not correspond to the usual definition of yield (stress at 0.2% strain). In order to provide expressions that are consistent with code requirements for continuous stress-strain expressions, the yield point is taken to be the nonzero intersection of the stress-strain curves given by Hooke's law for the elastic region

$$\sigma = E\varepsilon \tag{4-241}$$

and by the modified power law used in CSTRES and CSTRAN for the plastic region

$$\sigma = K\varepsilon^{n} (\dot{\varepsilon}\times 10^{3})\, m \tag{4-242}$$

where

σ = true stress (Pa)

E	=	Young's modulus (Pa)
ε	=	true strain (unitless)
K	=	strength coefficient (Pa)
n	=	strain hardening exponent (unitless)
$\dot{\varepsilon}$	=	true strain rate (s^{-1})
m	=	strain rate sensitivity exponent (unitless).

Solution of these simultaneous equations gives the yield strain and yield strength described by Equations (4-233) and (4-234), respectively.

The point of maximum load in a one-dimensional stress test at constant engineering strain rate is found by converting the true stress and true strain rate in Equation (4-242) to their engineering equivalents

$$\sigma = (S) \exp(\varepsilon) \tag{4-243}$$

$$\dot{\varepsilon} = \frac{\dot{e}}{\exp(\varepsilon)} \tag{4-244}$$

where

S	=	engineering stress (Pa)
$\dot{e}$	=	engineering strain rate (s^{-1}).

The derivative of S with respect to ε is zero at the true strain given by Equation (4-235), and the true stress at this strain is given by Equation (4-236).

The development of Equation (4-239) was preceded by a review of several different cladding failure criteria in use. Two previously used criteria, average circumferential elongation and engineering hoop stress, were rejected because they ignore the effect of local wall thinning and because this effect is now realized to vary considerably from test to test.[4.11-4,4.11-10,4.11-16] Two other possible criteria, strain rate at failure and strain-fraction rules (strain increment/strain at failure), were considered and rejected because these criteria would require a considerable collection of strain-versus-time data. Such a collection did not exist in the publicly available literature at the time the model was developed. The remaining criteria, local strain at failure and local stress at failure, were investigated with the data presented in Section 4.11.2.

Local strain at failure was determined using the measured wall thickness adjacent to the burst[a]

$$\varepsilon_r = \ln\left(\frac{t_B}{t_0}\right) \tag{4-245}$$

a. Since the material is not compressible, the sum of the axial and circumferential strains is ε_r.

where

ε_r	=	true radial strain at burst
t_o	=	initial cladding wall thickness
t_B	=	cladding wall thickness adjacent to burst.

Figure 4-50 is a plot of the local radial strains at burst versus temperature. The relevant observations are:

1. The scatter of the local strains at failure is much smaller than the scatter of the average circumferential strains at failure for these tests. The average strains are shown in Figure 4-51.

2. An important series of tests by Chapman (SR-37, SR-41, SR-34, and SR-35), with decreasing pressures and heating rates but similar heaters, burst temperatures, and average circumferential elongations, show a regularly decreasing wall thickness (more negative radial strain) with decreasing pressure. The Chapman data are identified by test number and burst pressure in Figure 4-50.

These observations suggest that the local stress is the common parameter of cladding about to burst. The data in the plot of local strains at failure versus temperature are scattered by neglected variations in circumferential radii of curvature, axial radii of curvature, and burst pressure; and the data in the plot of average circumferential strains at failure are scattered further by circumferential variations in strain. More evidence for using stress as the failure criterion is provided by the observations that (a) failure cross sections usually show a fracture surface or surfaces at 45° to the tangential direction and in the direction of maximum shear stress and (b) the fracture line is usually longitudinal. In cases where the fracture line is circumferential, there is good reason to suspect large axial stress components (Reference 4.11-10).

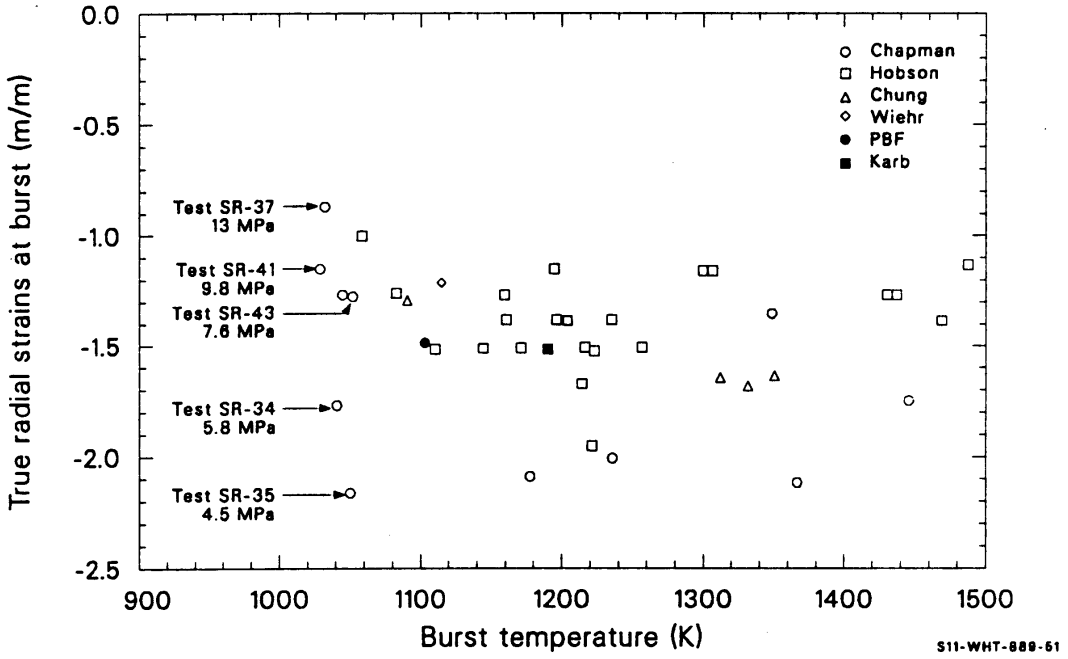

Figure 4-50. Local radial strains at burst versus temperature.

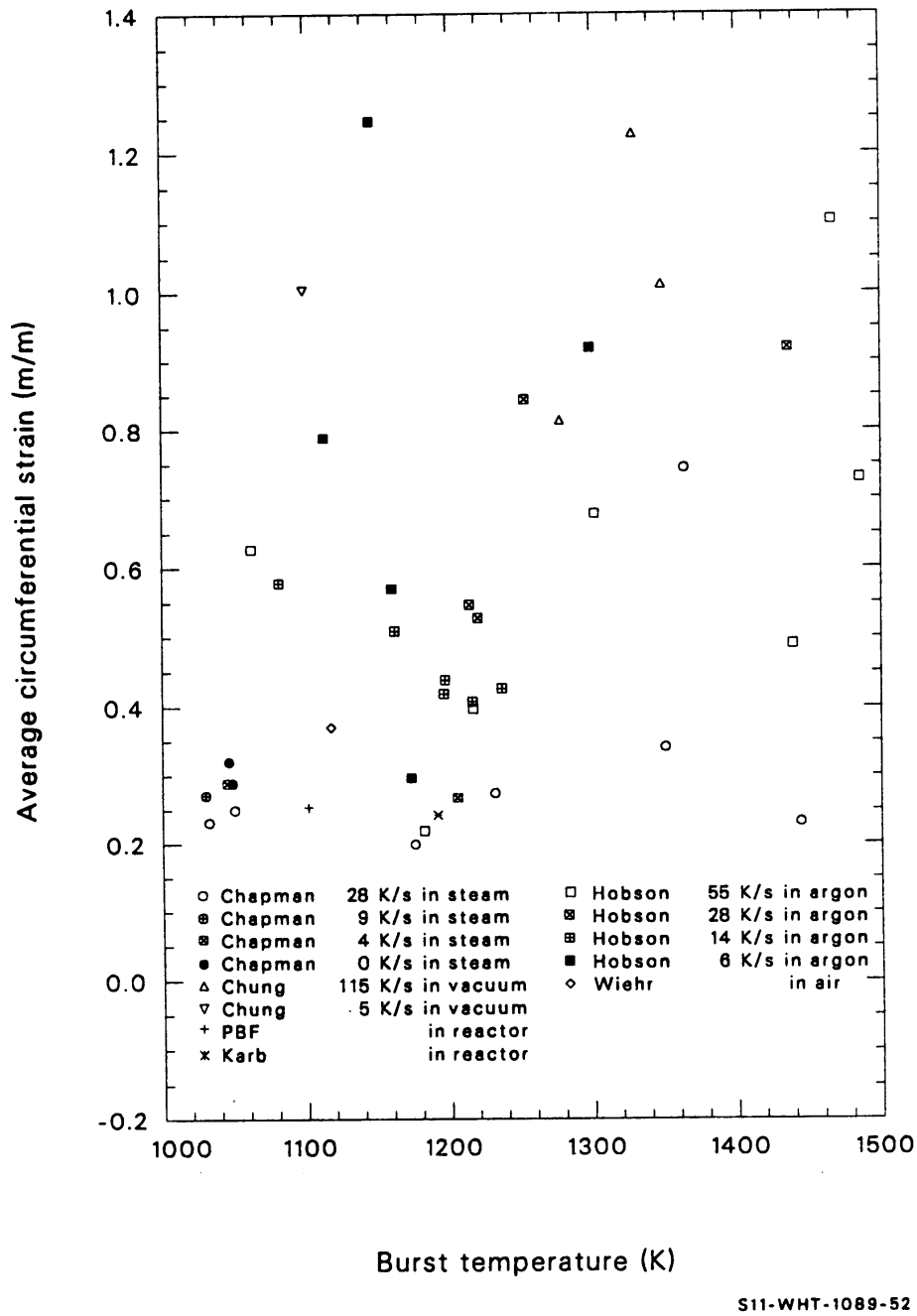

Figure 4-51. Average circumferential strains at failure versus temperature.

Local stresses at failure were estimated from the data presented in Section 4.11.2 and the equilibrium equation for a membrane element at the moment of failure[4.11-18]

$$\frac{\sigma_{ZB}}{r_Z} + \frac{\sigma_{\theta B}}{r_\theta} = \frac{P_B}{t_B} \tag{4-246}$$

where

σ_{ZB}	=	axial stress at burst (Pa)
$\sigma_{\theta B}$	=	tangential stress at burst (Pa)
P_B	=	difference between gas pressure and coolant pressure at burst (Pa)
r_z	=	axial radius of curvature at burst (m)
r_θ	=	circumferential radius of curvature at burst (m)
t_B	=	cladding thickness at burst (m).

Two approximations are needed to deduce $\sigma_{\theta B}$ from Equation (4-246) and the data presented in Section 4.11.2. The first approximation is that the azimuthal cross section shortly before burst is approximately circular

$$r_\theta = \text{undeformed radius } (1 + \text{average circumferential strain}). \tag{4-247}$$

The second approximation is needed to estimate σ_{ZB}. The range of possible values for σ_{ZB} is severely limited by physical considerations. It must have been greater than the yield stress for significant ballooning to occur,[4.11-18] and it must have been less than $\sigma_{\theta B}$ for the failure to occur along an axial line. Since r_z is typically several times r_θ, the first term of Equation (4-246) is small; and any value of σ_{ZB} in the range between the yield stress and $\sigma_{\theta B}$ will estimate the first term of the equation with an uncertainty that is less than the uncertainty in the terms containing r_θ and t_B. The CMLIMT expression for failure stress was developed with the assumption that the axial and tangential stresses are nearly equal to burst because that assumption tends to underpredict $\sigma_{\theta B}$, while the assumption of Equation (4-247) tends to overpredict $\sigma_{\theta B}$.[a] The resultant expression for the tangential stress at burst is

$$\sigma_{\theta B} = \frac{P_B}{t_B}\left(\frac{1}{\frac{1}{r_Z} + \frac{1}{r_\theta}}\right) . \tag{4-248}$$

Figure 4-52 is a plot of the local tangential failure stress obtained from Equation (4-248) and the data reviewed in Section 4.11.2. Approximate heating rates during burst are indicated to show that there is no systematic variation with heating rate. Comparison of the burst stresses obtained from Hobson's tests with both Chapman's tests and the two in-reactor data show that there is no significant effect of oxide films or alpha layers on the burst stress, at least at heating rates used in these tests. The most probable interpretation of this observation is the suggestion that the relatively thin oxide and alpha layers are cracked before the burst stress of the underlying beta layers is achieved.

Most of the burst stresses shown in Figure 4-52 are located near a curve that looks very similar to the plot of the strength coefficient for plastic deformation, which was obtained in Figure 4-35 of Section 4.9.3.2. The exceptions are not scattered randomly about the curve. They all lie above the curve. Upon closer inspection, it was noticed that the tests that yielded unusually high tangential burst stresses had some feature which caused one of the assumptions used in calculating tangential burst stress to be questionable.

a. Local ballooning will cause the actual value of r_θ to be less than the value predicted with Equation (4-246).

These features are discussed, test by test, in the next several paragraphs. The exceptional data are individually labeled in Figure 4-52.

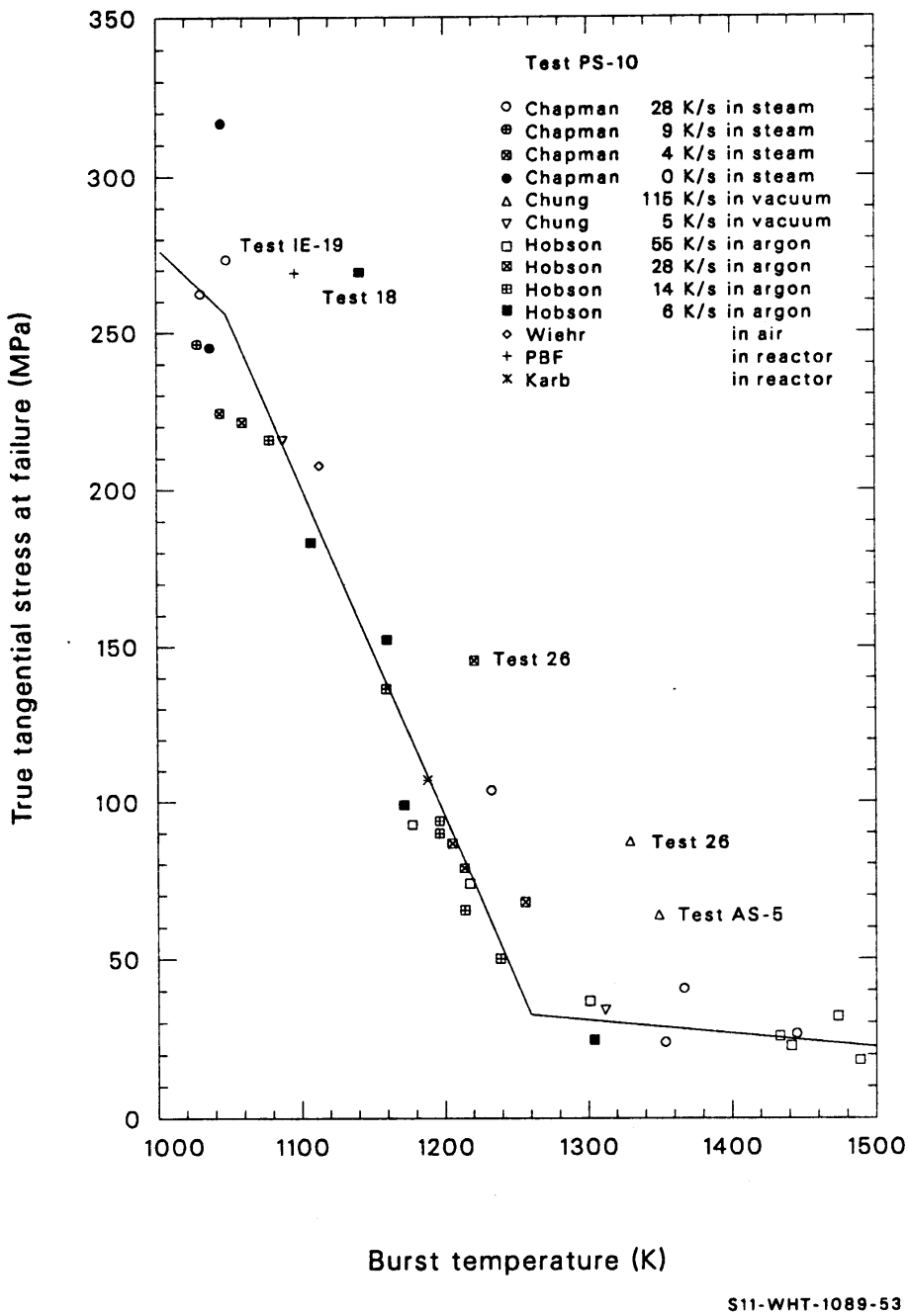

Figure 4-52. Local tangential stress at failure versus temperature.

In the PBF Test IE-5 (Rod IE-19), the maximum temperature of the cladding burst region was determined by metallography to be approximately 1,100 K. Postirradiation examination results[4.11-15] show that

the maximum temperature of the fracture area was less than the maximum cladding temperature at other azimuthal locations in the axial plane of the fracture. The interpretation given to this information in the postirradiation examination results report is that 1,100 K was also the burst temperature because no increase in temperature could have occurred on the protruding fracture tips. This conclusion may be slightly overstated. The Test Results Report[4.11-19] shows that the adjacent 45° thermocouple, which also protruded, experienced a 50 K temperature rise after the initial increase. It is therefore probably more realistic to estimate the burst temperature of the cladding in Rod IE-19 at 1,000 to 1,050 K.

Test PS-10 from Chapman's studies was performed with a heater which had an unusually large circumferential variation in temperature.[4.11-20] In this case, very local ballooning is likely; and Equation (4-247) is probably a poor approximation for the circumferential radius of curvature near burst. Because of the questionable validity of Equation (4-247) for this test and because of the large difference between the calculated burst stress of this test and several other data obtained at similar burst temperatures, this test was omitted from the CMLIMT failure analysis.

Test 18 from the Hobson-Rittenhouse series burst at a thermocouple temperature of 1,145 K, yet had an average circumferential strain characteristic of temperatures in the alpha phase. Moreover, the axial profile of this test is almost triangular (Reference 4.11-9). In all probability, the axial radius of curvature in Table 4-40 (estimated from the bottom half of the sample) is much too large. The test was therefore eliminated from the CMLIMT data base.

Test 26 from the Hobson-Rittenhouse series is the only sample in the entire test series that did not exhibit approximate mirror symmetry of wall thickness about a plane through the burst area and the cladding centerline. In this test, one half of the cross section is essentially undeformed, and one half is uniformly thin. Thus, both the axial and circumferential radii of curvature estimated for this test are questionable; and the test was removed from the CMLIMT data base.

Tests AS-9 and AS-5 by Chung are the most difficult of all the data shown in Figure 4-52 to understand. One might assume that the constraining mandrel used in these tests caused a large axial stress that somehow perturbed the test; however, the argument given in conjunction with Equation (4-248) shows that the local axial stress near the failure area was between the yield and the burst stresses. Moreover, Test AS-36, which differed only in heating rate from AS-5 and AS-9, does not differ from the Hobson or Chapman tests that burst at similar temperatures. Tests AS-5 and AS-9 were tentatively removed from the CMLIMT data base solely because they differ markedly from the two tests by Chapman that were conducted in steam with an internal heater, two features that are believed to make Chapman's tests more representative of in-reactor cladding failure.

The remaining data shown in Figure 4-52 and reviewed in Section 4.11.2 were used to find an expression for the tangential burst stress at failure above 1,000 K. The failure stress was divided by the strength coefficient used with Equation (4-242), and the quotients were averaged. For the alpha phase data with burst temperatures above 1,000 K, the average quotient is 7.48 ± 0.91; for the alpha $\pm$ beta region, it is 7.54 ± 1.03; and for the beta phase, it is 8.14 ± 1.84. Since there is no significant variation of the quotient, the average obtained for the entire temperature range above 1,000 K, 7.70 ± 1.29, was used to produce Equations (4-239) and (4-240).

Equations (4-247) and (4-248)[a] were also used with the low-temperature data of Table 4-42 in an attempt to find low temperature failure stresses. In this case, the ratios of failure stress to strength coefficient obtained were much smaller than those of the high temperature data 0.84 ± 0.03 for the annealed cladding and 0.80 ± 0.06 for the irradiated cladding. These ratios were not used for the CMLIMT failure stress correlation because the axial radii of curvature used to calculate them were assumed. Instead, the measured failure strains were used with Equation (4-242), an assumed strain rate sensitivity exponent of zero, and typical anisotropy coefficients[b] to calculate failure stresses consistent with Equation (4-240) and the measured strain. The approximation is more reasonable than guessing axial radii of curvature at low temperature because (a) the unknown strain rate at failure is unimportant at low temperature and (b) the stress strain curve at low temperature is very flat; (i.e., small uncertainties in stress are equivalent to large uncertainties in strain). The factor of 1.36 for annealed cladding and an increase of burst strength equal to four-tenths of the increase in the strength coefficient due to cold work or irradiation in Equation (4-237) reproduce the failure strains listed in Table 4-42. Equation (4-238) is simply an assumption contrived to extrapolate between the two regions where data are available without producing unreasonable predictions for failure strain in the temperature range where it is used.

4.11.4 Application of the Failure Criterion to Determine Cladding Shape After Burst

Equations (4-237) through (4-239) are sufficient to provide a complete description of both the time of cladding failure and the shape of failed cladding if they are used with an equation of state for plastic deformation and a mechanical code that models circumferential and axial variations in strain as a function of applied stress and time. The expressions derived in this section are intended as consistent alternatives to the direct use of Equations (4-237) through (4-239). They also illustrate the effect of deformation history on cladding shape after burst.

The first alternate expression is intended for use with codes like the FRAP-T5 ballooning subcode,[4.11-18] which treat asymmetric deformation but do not calculate local stress. The recommended test for failure is a comparison of wall thickness to the minimum wall thickness given by the following approximate expressions for the strain at failure in a azimuthally symmetric test:

$$\varepsilon_r = \varepsilon_{\theta SYM} \tag{4-249}$$

and

$$\varepsilon_{\theta SYM} = \ln\left(\frac{\sigma_{ZB} t_0}{2 P_B r_Z} + \left(\frac{t_0 \sigma_{\theta B}}{P_B r_0}\right)^{1/2} + \frac{1}{2}\left(\frac{\sigma_{ZB} t_0}{P_B r_Z}\right)^2\right) \tag{4-250}$$

where

ε_r = local true radial strain at failure (m/m)

a. The axial radius of curvature was assumed to be three times the circumferential radii of annealed cladding and infinite for the irradiated cladding.

b. The irradiated cladding was assumed to be isotropic when effective stress and strains were calculated, but the annealed cladding was assumed to have the typical anisotropy coefficients given in Section 4.10.

$\varepsilon_{\theta SYM}$	=	true tangential strain at failure for azimuthally symmetric deformation (m/m)
σ_{ZB}	=	axial component of true stress at burst (Pa)
t_o	=	initial cladding wall thickness (m)
P_B	=	pressure differential across cladding at burst (Pa)
r_z	=	axial radius of curvature at burst (m).
$\sigma_{\theta B}$	=	tangential component of true stress at burst (Pa) given by Equation (4-237) through (4-239)
r_o	=	initial cladding radius (m).

If ballooning is neglected ($r_z = \infty$), Equation (4-250) reduces to

$$\varepsilon_{\theta SYM} = \ln\left(\frac{r_{\theta B}}{S_{\theta B}}\right)^{1/2} \tag{4-251}$$

where $S_{\theta B}$ is the tangential component of engineering stress at burst (Pa). An outline of the derivation of Equation (4-250) follows:

1. Following Reference 4.11-21, the cladding deformation is considered to be composed of the strain for cylindrical deformation plus a perturbation due to ballooning. Axial strains for isotropic, closed-tube, cylindrical deformation are zero; and it is shown in Reference 4.11-21 that the change in axial strain due to a balloon with negligible tangential displacement is also zero. It is, therefore, reasonable to assume that the axial strain for typical bursts is small compared to the radial and tangential strains.

2. From the incompressibility relation (true strains sum to zero) and Step 1, the true radial strain equals the negative of the true tangential strain in an azimuthally symmetric burst test.

3. For an azimuthally symmetric burst test, the circumferential radius of curvature and the cladding thickness at burst are related to their initial values through the tangential strain

$$r_\theta = r_0 \exp(\varepsilon_{\theta SYM}) \tag{4-252}$$

$$t_B = t_0 \exp(-\varepsilon_{\theta SYM}) \ . \tag{4-253}$$

4. Substitution of Equations (4-252) and (4-253) into Equation (4-246) and a Taylor series expansion with

$$\frac{\sigma_{ZB}}{r_Z} \ll \frac{\sigma_{\theta B}}{r_\theta}$$

yields Equation (4-242) for $\varepsilon_{\theta SYM}$.

5. If the burst test does not have azimuthal symmetry, Equation (4-252) will overpredict the

circumferential radius of curvature[4.11-18] and Equation (4-253) will overpredict the cladding wall thickness at failure. However, this is not a serious fault because the local deformation near failure is very rapid. The average strains, and thus the average elongation, will be only slightly underpredicted by using Equations (4-252) and (4-250) to predict strain at failure.

The second alternate set of expressions for determining cladding shape after failure and burst stress at failure are intended for codes that assume azimuthally symmetric cladding plastic deformation in spite of known temperature differences during the burst. An approximate expression for the effect of temperature variation on circumferential elongation was obtained by correlating to data taken at temperatures near 1,050 K.[4.11-10,4.11-22] The data and least-squares correlation used to describe them are shown in Figure 4-53. The least-squares expression obtained by fitting an exponential function to the data is

$$\varepsilon_\theta = -0.94\exp(-0.01\Delta T) \tag{4-254}$$

where

$$\bar{\varepsilon}_\theta = \frac{\text{Circumferential at burst} - \text{initial circumference}}{\text{initial circumference}}$$

ΔT = approximate temperature difference during burst (K).

If the 0.94 of Equation (4-253) is replaced by the more general expression of Equation (4-250), the resultant expression for the average circumferential elongation in a typical burst test near 1,050 K is

$$\bar{\varepsilon}_\theta = \left[\left(\frac{t_0\sigma_{\theta B}}{P_B r_0}\right)^{1/2} - 1\right]\exp(-0.01\Delta T) \tag{4-255}$$

where ΔT is the estimated temperature variation around the circumference during burst (K) and the other symbols have been defined previously.

A mechanical model that assumes azimuthal symmetry cannot independently calculate the average circumference and the maximum stress of asymmetric deformation. However, it is possible to define an effective stress that is consistent with Equations (4-253) and (4-237). This effective burst stress is derived by considering the three cross sections shown in Figure 4-54.

Figure 4-54A represents the actual asymmetric cladding with local thinning at a hot spot and relatively little deformation elsewhere. Figure 4-54B represents an idealized symmetric deformation modeled by analytical codes that do not consider asymmetric deformation. The circumferences of Figures 4-54A and 4-54B are equal. Figure 4-54C represents a symmetrically deformed cladding with true stress equal to the maximum hoop stress of the actual asymmetric cladding.

The maximum tangential component of true stress of the asymmetric deformation is approximately

$$\sigma_{\theta B} = \frac{P_B r_a}{t_B} \tag{4-256}$$

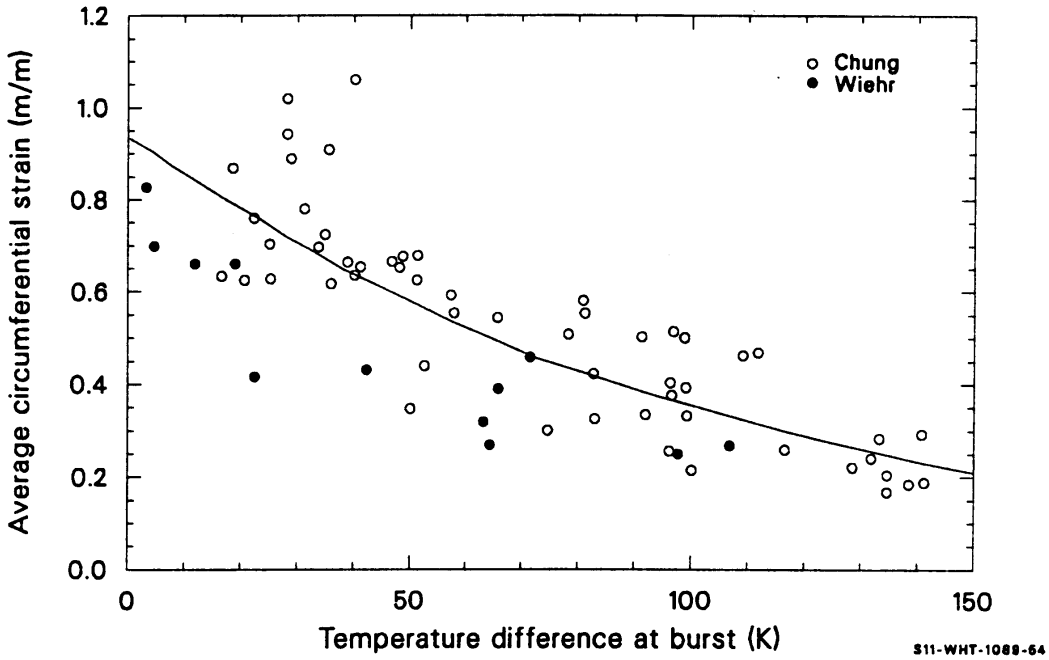

Figure 4-53. Base data and MATPRO correlation for effect of temperature variation on average circumferential elongation.

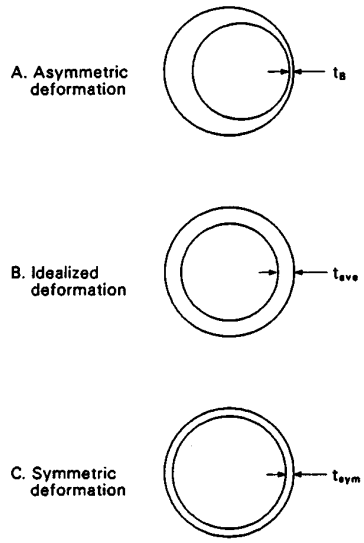

Figure 4-54. Schematic cross sections of cladding at burst.

where r_a is the radius of the cladding (m) and other symbols have been defined previously. The circumferential stress which will be used to predict the idealized deformation is

$$\sigma_{\theta B} = \frac{P_B r_a}{t_{ave}} \tag{4-257}$$

where t_{ave} is the wall thickness of the cladding predicted with idealized symmetric deformation (m). From Equations (4-256) and (4-257), the tangential stress at failure calculated with idealized deformation is related to the true burst stress by the equation

$$\sigma_{\theta B} = \sigma_{\theta B} \frac{t_B}{t_{ave}} \quad . \tag{4-258}$$

The ratio t_B/t_{ave} in Equation (4-258) is related to the reduction in circumferential elongation at failure. Since the maximum true local stress of asymmetric deformation and the circumferential stress of symmetric deformation are both equal to the burst stresses,

$$\frac{P_B r_a}{t_B} = \frac{P_B r_{SYM}}{t_{SYM}} \tag{4-259}$$

where

r_{SYM}	=	radius of symmetrically deformed cladding (m)
t_{SYM}	=	wall thickness of symmetrically deformed cladding (m)

and the other terms were defined previously.

The incompressibility relations with the simplifying assumption that axial strain is less than radial or circumferential strain imply that the areas of the idealized and symmetrically deformed cladding are equal. This in turn implies

$$r_a t_{ave} = r_{SYM} t_{SYM} \tag{4-260}$$

Equations (4-259) and (4-260) can be combined to show

$$\frac{t_B}{t_{ave}} = \left(\frac{r_a}{r_{SYM}}\right)^2 \quad . \tag{4-261}$$

The radii r_a and r_{SYM} are related to the circumferential elongation of A and C, (Figure 4-54)

$$r_a = r_0(1.0 + \varepsilon_\theta) \tag{4-262}$$

$$r_{SYM} = r_0(1.0 + \varepsilon_{\theta SYM}) \tag{4-263}$$

$$= r_0 \exp(\varepsilon_{\theta SYM})$$

where r_o is the initial radius of the cladding.

Substitution of Equation (4-251) into Equation (4-263), Equations (4-262) and (4-263) into Equation (4-261), and the resultant expression into Equation (4-258) yields the following result for effective burst stress

$$\sigma_{\theta B} = S_{\theta B} (1 + \varepsilon_\theta)^2 \tag{4-264}$$

where $\sigma_{\theta B}$ is the effective burst stress to be used when azimuthally symmetric deformation is assumed in spite of known circumferential temperature differences.

The instability strain returned by CMLIMT is also determined with the correlation for typical strain distribution. The expression used in the CMLIMT subcode for instability strain is

$$\bar{\varepsilon}_{\theta l} = \max \left\{ \begin{matrix} 0.05 \text{ or} \\ \left(\dfrac{1.15 K t_0}{10^{2m_p} r_0} \right)^{1/2} - 1 \end{matrix} \right\} \exp\left(\frac{-\Delta T}{100}\right) \tag{4-265}$$

where

$$\bar{\varepsilon}_{\theta l} = \frac{\text{circumference at instability} - \text{initial circumference}}{\text{initial circumference}}$$

P = pressure differential across cladding (Pa).

Equation (4-265) was derived by setting the true strain rate in Equation (4-242) equal to 10^{-1}/s and employing the following simplifying assumptions:

l. Isotropic texture coefficients and closed tube stress radios were assumed ($\sigma = 0.866\sigma_\theta$ and $\varepsilon = \varepsilon_\theta/0.866$),

2. $\sigma_\theta = S_{\theta exq} (2\varepsilon_\theta)$,

3. Equation (4-254) relates average strain to symmetric strain at instability as well as at burst.

The third alternate expression for describing cladding failure is intended for users who choose to ignore all the details of the deformation history of the cladding. The quantity returned is a typical engineering burst stress obtained by correlating tests without regard for either the distribution of strain during the tests or the variation of pressure and temperature with time during the test. If the user is willing to accept the uncertainty associated with using typical burst stresses (pressure) for a given temperature, he can use this relation with all of the previous relations to determine typical average circumferential elongations as a function of burst temperature and the circumferential temperature variation during burst. The correlation used for typical engineering burst stresses is

$$\log_{10}(S) = 8.42 + T[2.78 \times 10^{-3} + T(-4.87 \times 10^{-6} + T\ 1.49 \times 10^{-9})] \quad (4\text{-}266)$$

where

S = typical engineering hoop stress at burst (Pa)

T = temperature at rupture (K).

Equation (4-266) was obtained by correlating engineering burst stress to burst temperature using data obtained from several sources.[4.11-9,4.11-23 to 4.11-29] Since all information about the local stress and strain has been ignored in producing this correlation, it provides only a typical engineering burst stress as a function of temperature.

Figure 4-55 shows typical average tangential strains as a function of temperature obtained by substituting typical engineering burst stresses from Equation (4-266), true stress at burst from Equation (4-237), and several assumed temperature differences during burst into Equation (4-255).

4.11.5 Summary (CBRTTL)

Cladding may fail because of embrittlement by oxygen. In embrittled cladding, failure occurs at low temperatures with no plastic strain. Several hypothetical reactor transients can cause cladding to reach the high temperature necessary for extensive oxygen diffusion. These transients include power cooling mismatch, reactivity insertion, and loss of coolant. In the cooling following these transients, the cladding will be subjected to thermal stresses that may cause its fragmentation. Therefore, oxygen embrittlement is an important safety consideration.

A model is presented in this report defining limits for the amount of oxygen that may diffuse into zircaloy without causing it to become embrittled. This model is restricted to outside oxidation.

The model deals with cladding that has reached a temperature of at least 1,244 K at least once in its lifetime. At this point, zircaloy has completed a phase transition from its low temperature, hexagonal, close packed structure, called the alpha phase, to a body centered cubic structure called the beta phase. This threshold is chosen because oxygen uptake increases exponentially with temperature and, for typical postulated transients, not enough oxygen to cause embrittlement will diffuse into the cladding until beta temperatures are reached. However, for transients lasting more than about one half hour at around 1,300 K, the model is not adequate. The model is divided into two parts to account for both fast and slow cooling rates.

For fast cooling rates (>100 K/s) such as are found following film boiling, the cladding is characterized as embrittled if:

1. The oxygen concentration in the beta phase is greater than 90% of the saturation concentration at the beginning of the fast quench,
2. The average oxygen concentration in the beta phase exceeds 0.65 percent by weight, or
3. The maximum temperature exceeds 1,700 K.

The first two of these restrictions are of the type proposed by Pawel, of Oak Ridge National Laboratory (ORNL).[4.11-30] The last is based on data obtained at EG&G Idaho, Inc.[4.11-31]

During a LOCA transient, there are two cladding cooling rates. One is a rather slow rate during refill, and the other is a rapid rate due to quench. If the slow decrease brings the cladding below the temperature of the beta phase, it is this rate that is important for embrittlement. In these cases, the cladding is characterized as embrittled if 0.3 mm or more of the beta phase contains more than 1 wt% oxygen. This criterion is similar to one proposed by Chung, Garde, and Kassner.[4.11-32]

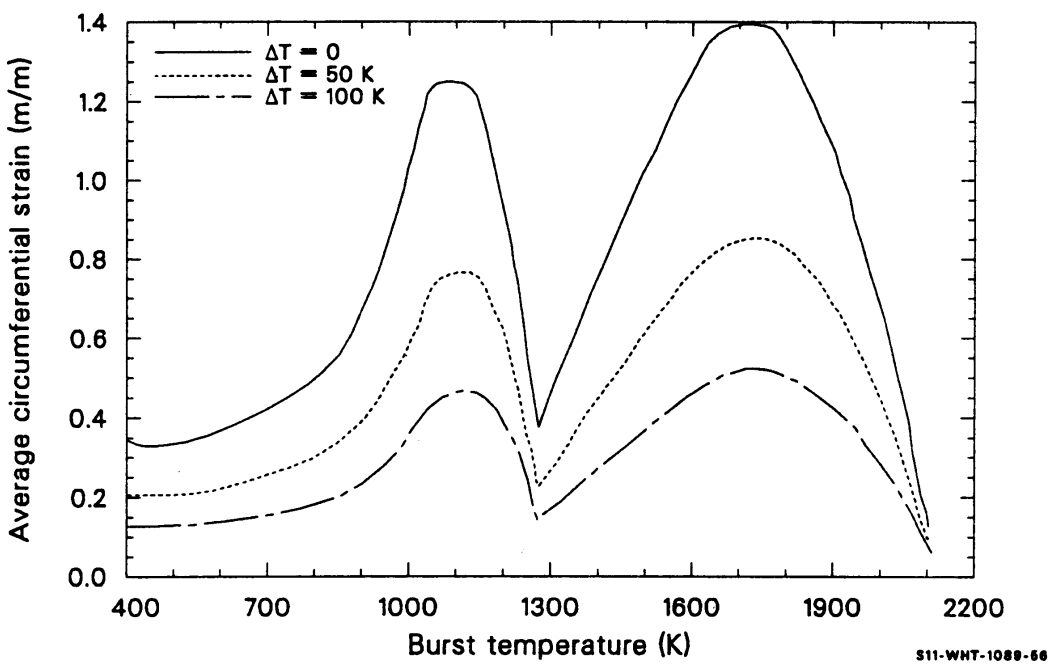

Figure 4-55. Typical average circumferential strains predicted by the MATPRO correlations for typical engineering burst stress, true burst stress, and typical strain distributions at three different temperature differences.

The inputs required by the model are the temperature and oxygen profiles in the beta phase zircaloy. At EG&G Idaho, Inc., these are found with the FRAP codes,[4.11-18,4.11-33] in conjunction with the COBILD high temperature oxidation subcode (see Section 4.15). When the oxygen concentration exceeds the limits defined above, the model indicates that the cladding is critically embrittled.

Section 4.11.6 contains a discussion of the literature reviewed. The model development is presented in Section 4.11.7, along with model data comparisons and a discussion of the uncertainty.

4.11.6 Literature Review

The paper by Pawel[4.11-30] is the basis for the part of CBRTTL describing fast-cooled cladding. The criteria presented by Pawel are modified based on in-pile data taken at EG&G Idaho, Inc.[4.11-31] The embrittlement criterion for slow cooled cladding is based on data taken from a recent series of reports from ANL.[4.11-32,4.11-34,4.11-35] These data sets are described in the following subsections.

4.11.6.1 ***Data for Fast Cooling.*** Data taken in-pile at the Power Burst Facility (PBF) reactor of EG&G Idaho, Inc., are extensively documented.[4.11-31] In this reactor, fuel rods about 3 feet in length but otherwise of typical PWR dimensions are brought into film boiling. The rods are externally pressurized with a pressure differential of at least 10 MPa. The oxidizing agent is steam, since data were taken from areas experiencing film boiling. The rods were oxidized under nonisothermal conditions. In some cases, the cladding temperature varied by as much as 800 K during a single experiment. An important feature of the PBF tests is that the source of heat was actual fuel pellets, which can relocate causing pellet-cladding thermal and mechanical interactions.

A major disadvantage of the PBF data base is that it is quite small. Competing embrittlement effects, such as chemical reactions at the inside surface from pellet-cladding interaction and aggressive fission products, present another difficulty. The fact that the PBF data conform well to Pawel's criteria developed from data taken out of pile,[4.11-36] where such competing effects are absent, suggests that this latter disadvantage may not be important and that oxygen uptake is the dominant embrittlement process.

4.11.6.2 ***Data for Slow Cooling.*** Many out of pile data were taken from recent reports by Chung, Garde, and Kassner.[4.11-32,4.11-34,4.11-35] The samples were 30 cm zircaloy tubes with inner and outer diameters typical of LWR cladding. About one-half of the tube length was filled with alumina ($A1_20_3$) pellets to simulate the fuel. The experimental procedure was to heat the sample by induction heating to the test temperature from room temperature at 10 K/s. This temperature was held for the desired time period, after which the sample was cooled at 5 K/s to approximately 810 K and then rapidly quenched by bottom flooding with water. The tubes ruptured during the heating phase due to an initial internal pressure, typically about 7 MPa. During the entire experiment, a steam generator circulated steam at about 0.15 MPa pressure past the specimen. After each experiment, the tubes were examined and classified in one of three ways:

1. Tubes that failed during the quench.
2. Tubes that survived quench but failed in normal handling required to remove them from the experimental apparatus.
3. Tubes that remained intact.

The ANL experiments provide a good test of the ability of zircaloy cladding, embrittled by nearly isothermal oxidation, to withstand the thermal shock of reflood after a hypothetical LOCA. The principal disadvantage of these tests is that the experiment environment may not apply the same stresses as cracked and relocated fuel.

4.11.7 Model Development

Ideally, a model for embrittlement by oxygen uptake would specify a maximum acceptable stress as a function of oxygen content in the cladding. The available data, however, are not amenable to such an

approach because neither the stress nor the strain at failure are measured. For some cases, the stress or strain could be calculated; but this is clearly not possible for those rods which failed during normal handling at the ANL. Therefore, a more empirical process is used, wherein several commonly used embrittlement criteria are tested against the data and the most appropriate ones are subjected to sensitivity studies to determine the best boundary conditions.

Several embrittlement criteria are now in use or have been proposed. In this subsection, the more prominent ones are compared to the data. The COBILD code was used to calculate oxide layer thicknesses, oxygen uptake, and oxygen profiles in the beta phase.

4.11.7.1 ***Presently Used Acceptance Criteria.*** For reactor licensing purposes, the present oxidation limits for an acceptable emergency core cooling system are defined in the Code of Federal Regulations, Title 10, Section 50. The code specifies:

(a) That the peak cladding temperature must not exceed 2,200^{o}F (1,477.5 K)

(b) That the oxide thickness that would result if all oxygen uptake produced ZrO_2 (called the equivalent cladding reacted) must not exceed 17% of the original cladding wall thickness.

Both of these criteria have been shown to be conservative for out-of-pile tests[4.11-32,4.11-34] and inconsistent for in-pile tests.[4.11-31]

4.11.7.2 ***Fraction of Wall Thickness That is Beta Phase Criterion.*** Scatena[4.11-37] suggested an embrittlement criterion based on the quantity F_w, where

$$F_W = \frac{\text{remaining beta phase thickness}}{\text{original unoxidized wall thickness}} \quad . \tag{4-267}$$

If $F_w \leq 0.5$, the material is considered embrittled. This criterion was not found to work well for either the out-of-pile or in-pile data, being conservative in both cases.

4.11.7.3 ***Argonne Impact Energy Criterion.*** In these tests, the tubes were treated as described in Section 4.11.6. In an effort to quantify the embrittlement, those rods that emerged intact from quenching and handling were subject to impact testing with a pendulum device. Impact energies of 0.03 and 0.30 J were used, causing additional rods to fail. However, unless an allowable impact energy is specified, classification of tubes shattered by impact as failed is not useful. If such energy is specified, an embrittlement model based on these data will become attractive.

4.11.7.4 ***ORNL Correlation of Embrittlement with Oxygen Content in the Beta Phase.*** Using data from a report by Hobson and Rittenhouse,[4.11-36] Pawel[4.11-30] arrived at two embrittlement criteria for zircaloy. He considered the cladding embrittled if the oxygen content of the beta phase exceeded 95% of the saturation content, or 0.7 wt%. This model, slightly modified, is used for fast-cooled cladding in this section. The saturation oxygen concentration is determined from a zircaloy-oxygen phase diagram published by Chung.[4.11-38]

4.11.7.5 ***Argonne Correlation of Embrittlement with Oxygen Content in the Beta Phase.*** Using a computer code developed at ANL, Chung[4.11-32] found an embrittlement criterion that fits their data very well. Their criterion states that the cladding will not be embrittled if there is at least 0.1 mm of beta with less than 1.0 wt% oxygen. The limits set by the ANL group are consistent with the conclu-

sions of a more qualitative study by Sawatzky,[4.11-39] who states that the maximum temperature and total oxygen content have little or no effect on the tensile properties of zircaloy-4. Sawatzky used a maximum cooling rate of 160 K/s for about 10% of his samples; but the other 90% were cooled at rates of 21 K/s or less, so his conclusions apply primarily to slow cooled cladding. The ANL model is also modified and used for slow cooled cladding in this section.

4.11.8 Model for Fast Cooled Cladding

The Pawel criteria, slightly modified and with the additional limit that the peak cladding temperature must not exceed 1,700 K, are adopted for the fast-cooled cladding model. Physically, a percent saturation limit makes sense, at least qualitatively, because as the oxygen content of the beta phase approaches saturation, any local oxygen excess is relieved by the formation of brittle oxygen-stabilized alpha precipitates, often in the form of incursions originating in the normal alpha-phase layer and extending into the beta phase. The presence of these oxygen-rich alpha incursions is always associated with a loss of ductility. They may also form during cooling because as the temperature decreases, so does the oxygen solubility, often making the beta phase super-saturated with oxygen.

The criterion specifying a maximum oxygen weight fraction is needed because the diffusivity of oxygen also decreases with temperature. If the cooling rate is high enough, there will not be sufficient time for incursions to form during cooling and only those formed at high temperature will be present. Since the ductility of zircaloy decreases even without incursions as its oxygen content increases, there must be a critical oxygen concentration that causes embrittlement. The 1,700 K limit, although in contradiction to the conclusions of Sawatzsky,[4.11-39] was necessary to fit the data.

Pawel's limits of 95% saturation and 0.70 wt% oxygen were subjected to a brief sensitivity analysis to examine the effect of varying these limits. Combinations that were tried included 0.70 and 0.65 wt% and saturations of 90 and 95%. The results are shown in Figure 4-56, along with data from the Hobson-Rittenhouse experiment. The plot shows little to be gained by changing the limits. These criteria do not specify a single thickness for the beta layer necessary to retain ductility. However, for a given original wall thickness, it is possible to find a critical beta thickness as a function of temperature corresponding to the limits of this model. This thickness is usually expressed as a ratio

$$(F_W)_{crit} = \frac{\text{critical thickness of beta layer}}{\text{original unoxidized wall thickness}} \quad . \tag{4-268}$$

An $(F_w)_{crit}$ criterion corresponding to limits such as those specified by Pawel is particularly useful because it contains no explicit reference to time and may therefore be generalized to more realistic situations where the rod temperature changes. Time is still a necessary parameter to make the calculations; but, in the evaluation of the ductility, only the oxygen content and the temperature at a time are required. For this part of the model, the time and temperature used are those at the end of the last time temperature segment when the cladding was entirely in the beta phase. In Figure 4-57, $(F_w)_{crit}$ is plotted as a function of temperature. The solid lines are for 0.7 wt% and 95% filled, and the dashed lines are for 0.65 wt% and 90% filled. Also shown in the figure are data from the Hobson-Rittenhouse out-of-pile isothermal tests and the in-pile PBF nonisothermal tests. All the points, as well as the limiting lines, were calculated with the COBILD subcode. As with Figure 4-56, the data apply for a specific wall thickness, chosen here to be

0.60 mm to correspond to the PBF data. However, COBILD runs show that the limiting lines in Figure 4-57 move less than 1% when the wall thickness changes by as much as 40% from 0.60 mm.

An obvious feature of these figures is that three in-pile rods failed when they apparently should not have. These rods were at temperatures of 1,405, 1,418, and 1,523 K. Postirradiation examination of the inner surface oxidation showed that these rods had a wall defect in the vicinity of the failure, allowing steam to enter. Hot zircaloy exposed to stagnant steam will absorb an abnormally large amount of hydrogen,[4.11-40] and the failures of these three rods show evidence of hydride influence.[4.11-31] These rods are therefore not deemed suitable examples of the simple failure by oxygen embrittlement.

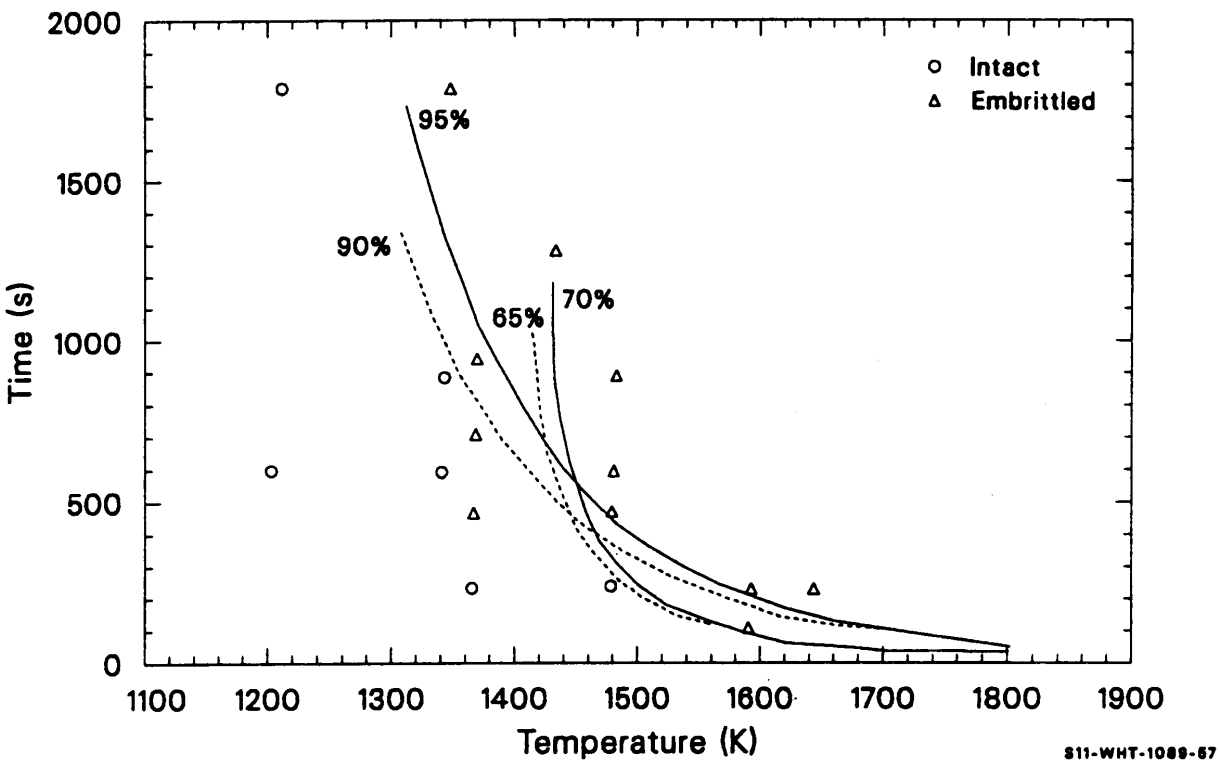

Figure 4-56. Hobson-Rittenhouse isothermal data for fast cooled cladding compared with the 0.65 and 0.70 wt% and the 90 and 95% filled criteria.

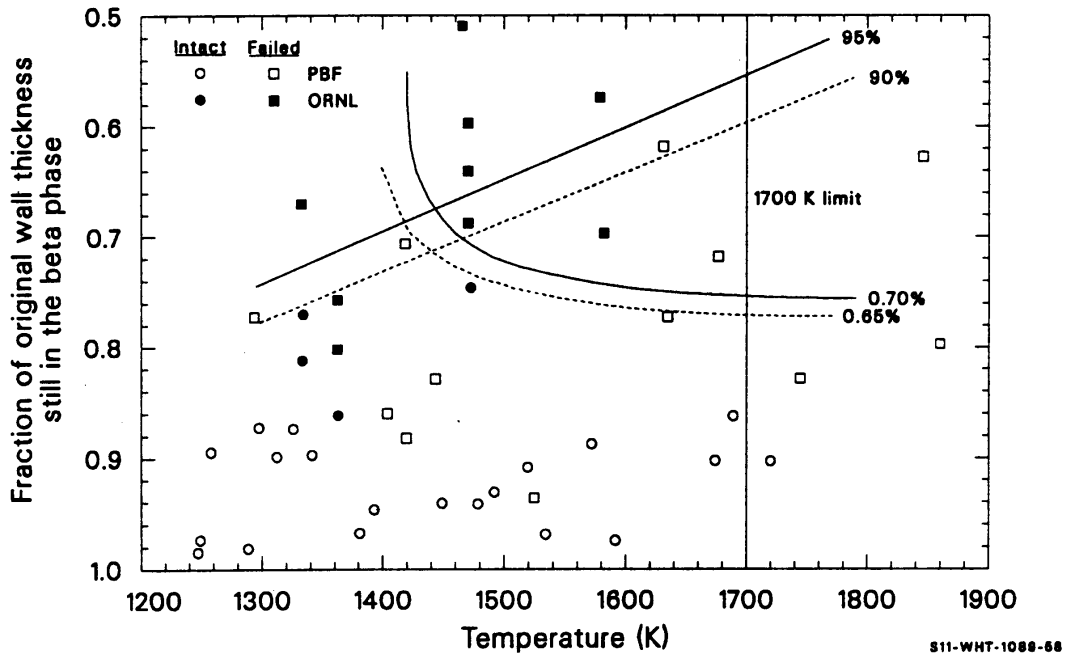

Figure 4-57. Hobson-Rittenhouse and PBF data for fast-cooled rods compared with the critical fractional wall thickness as calculated from the 0.65 and 0.70 wt% and the 90 and 95% filled criteria.

It is clear from Figure 4-57 that the lower limits of 90% saturation and 0.65 wt% oxygen include more of the failed rods than do Pawel's original limits. Consequently, the model for fast-cooled cladding is considered embrittled if the oxygen content of the beta phase exceeds (a) 90% of the saturation content or (b) 0.65% of weight. A third criterion limiting the maximum cladding temperature to < 1,700 K is added to fit the highest temperature data.

The data are still too limited to consider this model final; however, the accuracy is encouraging, especially considering the differences in the experiments. The Hobson-Rittenhouse samples were oxidized on both sides, out of pile, and quenched rapidly, while the PBF samples were oxidized primarily on the outside, in pile, and quenched slowly.

4.11.9 Model for Slow Cooled Cladding

Designation of this part of the model as being applicable to slow cooled cladding is slightly misleading; it is meant to apply during the prequench of a LOCA. As described in Section 4.11.2.2 of this report, Chung, Garde, and Kassner[4.11-32,4.11-34,4.11-35] have completed many out-of-pile tests of this sort and have developed an embrittlement criterion requiring at least 0.1 mm of cladding thickness with < 1 wt% oxygen. When the criterion was checked using COBILD, it was found that at least 0.3 mm with < 1 wt% oxygen are required to avoid failure by thermal shock. No reason for the difference between this and the ANL minimum thickness of 0.1 mm has been found. It possibly lies in the mechanics of the two codes.

Until a comparison of the ANL code and COBILD can be performed, the criterion established with COBILD is recommended for use with the MATPRO package.

In Figure 4-58, this criterion is compared with the data. Only temperatures > 1,244 K are considered, since this is the lower range of validity for COBILD. Not all of the data are shown in the figure because many are coincident, or nearly so. Of the 146 intact rods, 16 (or 11%) are predicted to fail; and of the 57 failed rods, 4 (or 7%) are predicted to remain intact. In the entire data set, < 10% of the predictions are incorrect. Given the scatter in the data, this is considered acceptable accuracy.

Since all the tubes tested at ANL had a wall thickness of 0.635 mm, it is impossible to conclude whether 0.30 mm is the actual minimum thickness required to retain ductility or if there is some minimum F_W. The former is more reasonable on physical grounds because it seems logical that there should be a minimum thickness of ductile material necessary for ductility.

If the embrittlement criteria for fast-cooled rods are compared with the slow-cooled data, failure would be predicted in most cases, contrary to experimental observation. Similarly, the criterion used for the slow cooled rods almost never predicts a failure when compared to the fast-cooled data. These facts underscore the importance and complexity of cooling rate on the ductility of zircaloy at high temperature and further emphasize the importance of clearly specifying the cooling rate.

4.11.10 Model Uncertainties

A primary source of uncertainty for both models is in temperature measurement. For the Hobson-Rittenhouse data set, the temperature uncertainty is estimated by comparing the temperature reported for a given layer thickness with that calculated using isothermal oxidation kinetics published by Cathcart[4.11-41] for the same thickness. From this analysis, the root mean square of the temperature difference is about 50 K. A similar technique was used for the PBF and ANL data. Seiffert and Hobbins[4.11-31] also arrived at an uncertainty of about 50 K, while Chung[4.11-34] found an 85 K uncertainty. This technique should give a reasonable estimate because Cathcart's correlations are based on a careful analysis of his own data. This analysis shows the data to have a high degree of consistency, and the major error in measurement should be the temperature, the layer thickness being much easier to obtain with accuracy.

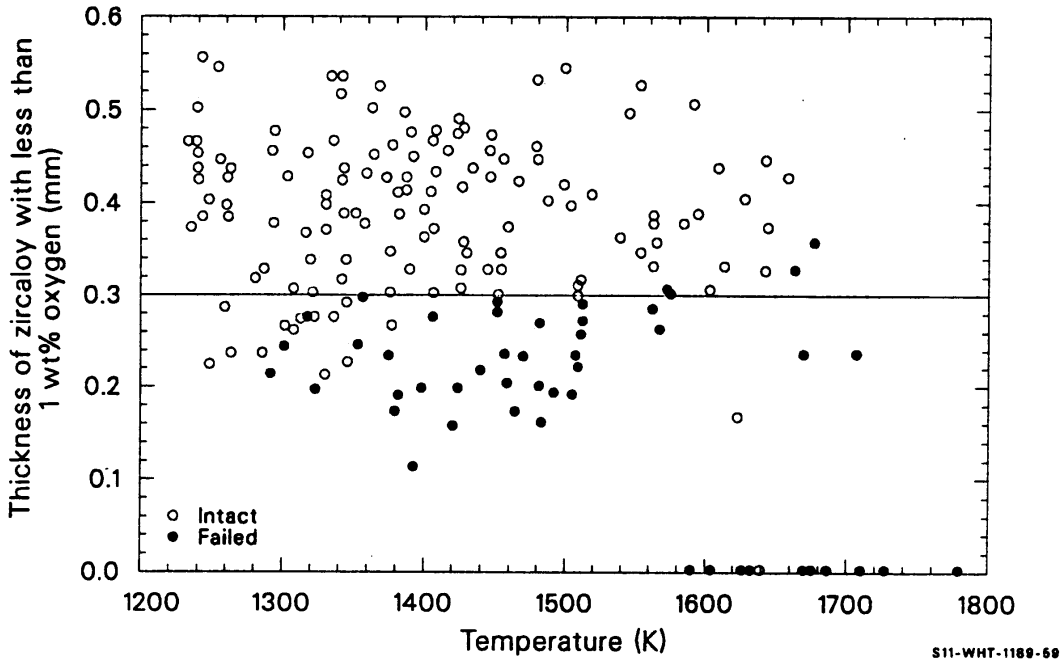

Figure 4-58. Comparison of the Argonne data for slow-cooled cladding with the criterion that at least 0.3 mm of zircaloy with less than 1 wt% oxygen is required to survive thermal shock.

There is another potentially important source of systematic error in the ANL data. They were presented in graphical rather than tabular form. A digitizer was used to obtain numerical values. The data were generally plotted as the logarithm of the time versus reciprocal temperature, so larger errors result for long times or high temperatures. By repeating the digitizing from the same plots, the uncertainties listed in Table 4-43 were found.

An idea of the effect of errors for fast cooled cladding may be obtained by examining Figure 4-55. For slow-cooled cladding, a sensitivity analysis is required to find what change in beta phase thickness with less than 1% oxygen content would result from the given uncertainties. Such an analysis has not been carried out.

Table 4-43. Uncertainties in digitized Argonne data.

Temperature (K)	ΔTemperature (K)	Time (s)	ΔTime (s)
1,250	16	10^2	2.50
1,650	28	10^4	2.50

4.11.11 References

4.11-1 R. H. Chapman, *Multirod Burst Test Program Quarterly Progress Report for April-June 1977*, ORNL/NUREG/TM-135, December 1977.

4.11-2 R. H. Chapman, J. L. Crowley, A. W. Longest and E. G. Sewell, *Effect of Creep Time and Heating Rate on Deformation of Zircaloy-4 Tubes Tested in Steam With Internal Heaters*, ORNL/NUREG/TM-245 and NUREG/TM-74, October 1978.

4.11-3 R. H. Chapman, *Multirod Burst Test Program Quarterly Progress Report for April-June 1976*, ORNL/NUREG/TM-74, January 1977.

4.11-4 R. H. Chapman, *Multirod Burst Test Program Quarterly Progress Report for July-December 1977*, ORNL/NUREG/CR-0103, June 1978.

4.11-5 R. H. Chapman, *Multirod Burst Test Program Quarterly Progress Report for January-March 1978*, NUREG/CR-0225, ORNL/NUREG/TM-217, August 1978.

4.11-6 R. H. Chapman, *Multirod Burst Test Program Quarterly Progress Report for January-March 1976*, ORNL/NUREG/TM-36, September 1976.

4.11-7 R. H. Chapman, *Multirod Burst Test Program Quarterly Progress Report for October-December 1976*, ORNL/NUREG/TM-95, April 1977.

4.11-8 R. H. Chapman, *Multirod Burst Test Program Quarterly Progress Report for January-March 1977*, ORNL/NUREG/TM-108, May 1977.

4.11-9 D. O. Hobson and P. L. Rittenhouse, *Deformation and Rupture Behavior of Light Water Reactor Fuel Cladding*, ORNL-4727, October 1971.

4.11-10 H. M. Chung and T. F. Kassner, *Deformation Characteristics of Zircaloy Cladding in Vacuum and Steam Under Transient-Heating Conditions: Summary Report*, NUREG/CR-0344, ANL-77-31, July 1978.

4.11-11 A. A. Bauer, L. M. Lowry, and J. S. Perrin, *Evaluating Strength and Ductility of Irradiated Zircaloy: Quarterly Progress Report for January-March 1976*, BMI-NUREG-1948, March 1976.

4.11-12 A. A. Bauer, W. J. Gallagher, L. M. Lowry, and A. J. Markworth, *Evaluating Strength and Ductility of Irradiated Zircaloy: Quarterly Progress Report for July-September 1977*, BMI-NUREG-1985, October 1977.

4.11-13 A. A. Bauer, W. J. Gallagher, L. M. Lowry, and A. J. Markworth, *Evaluating Strength and Ductility of Irradiated Zircaloy: Quarterly Progress Report for October-December 1977*, NUREG/CR-0026, BMI-1992, January 1978.

4.11-14 D. W. Croucher, *Behavior of Defective PWR Fuel Rods During Power Ramp and Film Boiling Operation*, NUREG/CR-0283, TREE-1267, February 1979.

4.11-15 T. F. Cook, S. A. Ploger, and R. R. Hobbins, *Postirradiation Examination Results for the Irradiation Effects Test IE-5*, TREE-NUREG-1201, March 1978.

4.11-16 E. H. Karb, "Results of the FR-2 Nuclear Tests on the Behavior of Zircaloy Clad Fuel Rods," *6th NRC Water Reactor Safety Research Information Meeting, Gaithersburg, MD, November 7,*

1978.

4.11-17 K. Wiehr and H. Schmidt, *Out-of-Pile Versuche zum Aufblahvorgang von Zirkaloy Hullen Ergenbnisse aus Vorversuchen mit verkurzten Brennstabsimulatoren*, KfK 2345, October 1977.

4.11-18 L. J. Siefken, M. P. Bohn, S. O. Peck, and J. A. Dearien, *FRAP-T5: A Computer Code for the Transient Analysis of Oxide Fuel Rods*, TREE-1281, NUREG-CR-0840, June 1979.

4.11-19 D. W. Croucher, T. R. Yackle, C. M. Allison, and S. A. Ploger, *Irradiation Effects Test Series IE-5 Test Results Report*, TREE-NUREG-1130, January 1978.

4.11-20 R. H. Chapman, *Multirod Burst Test Program Quarterly Progress Report for October-December 1975*, ORNL/NUREG/TM-10, May 1976.

4.11-21 J. M. Kramer and L. W. Deitrich, *Cladding Failure by Local Plastic Instability*, ANL-77-95, December 1977.

4.11-22 K. Wiehr et al., *Jahreskolloquim 1977 des Projekts Nukleare Sicherheit.*

4.11-23 C. C. Busby and K. B. Marsh, *High Temperature Deformation and Burst Characteristics of Recrystallized Zircaloy-4 Tubing*, WAPD-T-900, January 1970.

4.11-24 D. G. Hardy, "Burst Testing of Zircaloy Cladding from Irradiated Pickering-Type Fuel Bundles," *Symposium on the Effects of Radiation on Substructure and Mechanical Properties of Metal and Alloys, Los Angeles, CA, June 25-30, 1972*, ASTM-STP-529, 1973, pp. 415-435.

4.11-25 M. F. Osborne and G. W. Parker, *The Effect of Irradiation on the Failure of Zircaloy-Clad Fuel Rods*, ORNL-3626, January 1972.

4.11-26 D. O. Hobson, M. F. Osborne, and G. W. Parker, "Comparison of Rupture Data from Irradiated Fuel Rods and Unirradiated Cladding," *Nuclear Technology, II*, August 1971.

4.11-27 D. G. Hardy, "The Effect of Neutron Irradiation on the Mechanical Properties of Zirconium Alloy Fuel Cladding in Uniaxial and Biaxial Tests," *Symposium on Irradiation Effects on Structural Alloys for Nuclear Reactor Applications, Niagara Falls, Canada, June 29-July 1, 1970*, ASTM-STP-484, 1971, pp. 215-216.

4.11-28 W. J. Landford, "Metallurgical Properties of Cold Worked Zircaloy-2 Pressure Tubes Irradiated Under CANDU-PHW Power Reactor Conditions," *Symposium on Irradiation Effects on Structural Alloys for Nuclear Reactor Applications, Niagara Falls, Canada, June 29-July 1, 1970*, ASTM-STP 484, 1971, pp. 259-286.

4.11-29 W. R. Smalley, *Saxton Core II Fuel Performance Evaluation Material*, WCAP-3385-56, September 1971, pp.4-84,4-65; W. R. Smalley, *Evaluation of Saxton Core III Fuel Materials Performance*, WCAP-3385-57, July 1974, pp. 3-69, 3-132, 3-134.

4.11-30 R. E. Pawel, "Oxygen diffusion in Beta Zircaloy During Steam Oxidation," *Journal of Nuclear Materials, 50*, 1974, pp. 247-258.

4.11-31 S. L. Seiffert and R. R. Hobbins, *Oxidation and Embrittlement of Zircaloy-4 Cladding from High Temperature Film Boiling Operation*, TFBP-TR-292, October 1978.

4.11-32 H. M. Chung, A. M. Garde, and T. F. Kassner, *Light Water Reactor Safety Research Program:*

Quarterly Progress Report for January-March 1978, ANL-78-49, p. 56.

4.11-33 G. A. Berna et al., *FRAPCON-1: A Code for the Steady State Analysis of Oxide Fuel Rods*, CDAP-TR-78-032-R1, November 1978.

4.11-34 H. M. Chung, A. M. Garde, and T. F. Kassner, *Light-Water Reactor Safety Research Program: Quarterly Progress Report, for July-September 1977*, ANL-78-3, January 1978, pp. 47-75.

4.11-35 H. M. Chung, A. M. Garde, and T. F. Kassner, *Light-Water Reactor Safety Research Program: Quarterly Progress Report, for October-December 1977*, ANL-78-25, May 1978, pp.31-44.

4.11-36 D. O. Hobson and P. L. Rittenhouse, *Embrittlement of Zircaloy-Clad Fuel Rods by Steam During LOCA Transients*, ORNL-4758, January 1972.

4.11-37 C. J. Scatena, *Fuel Cladding Embrittlement During a Loss-of-Coolant Accident*, NEDO-10674, General Electric, October 1972.

4.11-38 H. M. Chung, A. M. Garde, and T. F. Kassner, *Light-Water Reactor Safety Research Program: Quarterly Progress Report for January-March 1976*, ANL-76-49.

4.11-39 A. Sawatzsky, "Oxygen Embrittlement of Zircaloy-4 Fuel Cladding," *6th Water Reactor Safety Research Information Meeting, Gaithersburg MD, November 6, 1978.*

4.11-40 C. Roy, "An Experiment to Clarify the Effect of Dissolved Oxygen on the Terminal Solubility of Hydrogen in Zirconium," *Journal of Nuclear Materials, 13*, 1964.

4.11-41 J. V. Cathcart et al., *Zirconium Metal Water Oxidation Kinetics VI Reaction Rate Studies*, ORNL/NUREG-17, August 1977.

4.12 Cyclic Fatigue (CFATIG)

The subcode CFATIG provides preliminary estimates of material constants in a format compatible with the use of fracture mechanics to model the effect of cyclic fatigue as described in the following equations.

4.12.1 Summary

High cycle (nominally elastic strain) fatigue uses material constants in an equation of the following form:

For $\Delta K \geq 9.5 \times 10^6$ MN/m$^{1.5}$,

$$dl/dN = B\,(\Delta K)^m \quad . \tag{4-269}$$

And for $\Delta K < 9.5 \times 10^6$ MN/m$^{1.5}$,

$$dl/dN = 0 \tag{4-270}$$

where

dl/dN	=	the change in crack length per cycle (m/cycle)
ΔK	=	the stress intensity range ($MN/m^{1.5}$)
B,m	=	material parameters returned by the CFATIG code.

The exponent m is

$$m = 15 - 12 \exp(-\Phi/10^{24}) \tag{4-271}$$

where Φ is the fast neutron fluence (n/m^2).

The parameter B in Equation (4-269) is computed from the following expressions for fast neutron fluences less than 10^{25} n/m^2:

$$B = 2 \times 10^{-11} \{15.531432^{12} [\exp(-\Phi/10^{24}) - 1]\} . \tag{4-272}$$

For fast neutron fluences of 10^{25} n/m^2 or more,

$$B = 1.0165786 \times 10^{-25.} \tag{4-273}$$

Low cycle (plastic strain) fatigue uses material constants intended for use in the equation proposed by Tomkins.[4.12-1]

$$\frac{dl}{dN} = K(\Delta\varepsilon)^{1/\alpha} l \tag{4-274}$$

where

$\Delta\varepsilon$	=	plastic strain amplitude (unitless)
l	=	crack length (m)
α, K	=	material parameters.

The value returned by CFATIG for the dimensionless material parameter K is 10.7, and the value for α is 0.6.

4.12.2 Basis for High Cycle Fatigue Material Constants

Constants for the description of high-cycle crack propagation are based on data taken by Rao[4.12-2] and preliminary measurements by Walker and Kass.[4.12-3] S-N (stress versus number of cycles to failure) data reported by O'Donnell and Langer[4.12-4] are not incorporated into the model because the effect of varying initial crack sizes is not known.

Rao's measurements of crack growth rates as a function of stress intensity (from Figure 4 of Reference 4.12-2) are reproduced in Table 4-44. The parameter m in Equation (4-269) is equal to the slope of a plot of log dl/dN against log ΔK. The value of m obtained from a least-squares fit to a plot of the data of Table 4-44 is 3.3.

The preliminary data of Walker and Kass (Figure 9 of Reference 4.12-2) were analyzed with the same approach used for the data of Rao. The straight line used by Walker and Kass to summarize data from unirradiated samples is equivalent to a value of m = 2.8 in Equation (4-269).

Walker and Kass also reported crack growth rates from eleven samples which received fast neutron fluences from 5 to 19 x 10^{24} n/m^2. A linear least-squares fit to a [log (stress intensity) versus log (crack growth rate)] plot of these measurements suggests that a value of m = 15.7 in Equation (4-269) would yield the best description of irradiated zircaloy.

The exponential form of Equation (4-271) is an estimate relating the values of m = 3 for unirradiated zircaloy and m = 15 for zircaloy irradiated to a fast neutron fluence of 10^{25} n/m^2. A decreasing exponential is typical of the change of material constants with fluence.

Value of the parameter B for unirradiated zircaloy were determined by substituting measurements of crack growth rate and stress intensity range into Equation (4-269) with m = 3. Values of B determined from the two sets of data shown in Table 4-44 were averaged to obtain 12.7 and 6 x 10^{-30} or stress intensities in N/$m^{1.5}$. Two additional estimates for B were obtained by repeating the solution of Equations (4-272) and (4-273) with Rao's measurements of crack growth rates at constant stress intensity (Figure 9 of Reference 4.12-2). Analysis of data from these two samples yielded B = 19.3 x 10^{-30} and B = 16 x 10^{-30}. A fifth estimate for B in unirradiated zircaloy was obtained using the Walker and Kass summary of their data with unirradiated material. Their straight line fit corresponds to a value of B = 48 x 10^{-30}.

Table 4-44. Crack growth rate versus stress intensity range from Rao.

Stress Intensity Range (MN/$m^{1.5}$)	Crack Growth Rate (10^{-8}m/cycle)
20.5	4.0
25.5	11.3
31.6	22.1
37.4	37.8
45.3	69.2
54.9	134.5
20.5	9.4
25.5	22.4

Table 4-44. Crack growth rate versus stress intensity range from Rao. (Continued)

Stress Intensity Range ($MN/m^{1.5}$)	Crack Growth Rate (10^{-8}m/cycle)
31.6	42.5
37.4	71.4
45.3	116.7
54.9	203.8

The only data used to find B for irradiated zircaloy are the eleven measurements of crack growth rate and stress intensity factor range by Walker and Kass discussed earlier in this section. The average value of B from these data and Equation (4-269) with m = 15 was $B = 10^{-25}$.

The expression used to model B [Equation (4-272)] is a fit to the average of the five estimates for B at zero fast neutron fluence and the one value of B at fluences on the order of 10^{25} n/m^2. The functional dependence of B on fast neutron fluence is an estimate based on the data at zero and 10^{25} n/m^2. The value of B for fluences between 10^{24} and 10^{25} n/m^2 has been determined to cause the predicted value of crack growth rate to remain constant at stress intensity factors of 15.531432 $MN/m^{1.5}$.

The value $\Delta K_{min} = 9.5$ $MN/m^{1.5}$ in Equation (4-269) is based on a test by Rao at this stress intensity range. No change in crack length was observed in this test.

4.12.3 Basis for Low Cycle Fatigue Material Constants

The values returned for the material parameters in Equation (4-274) are based on the data and analysis of Pettersson.[4.12-5] Pettersson has shown that Equation (4-274) can be integrated and expressed in the form of the Coffin-Manson relationship

$$\Delta E = CN_f^{-\alpha} \tag{4-275}$$

where

ΔE	=	plastic strain range
N_f	=	number of cycles to failure
C,α	=	material parameters.

The constant α in Equation (4-275) is the same material parameter as the constant a in Equation (4-274). Pettersson shows that the constant C in Equation (4-275) is related to the material constant K of Equation (4-274) by the following expressions:

for uniaxial straining,

$$C^{1/\alpha} = \frac{\ln\left(\frac{l_f}{l_0}\right)}{K} = \frac{4.83}{K} \tag{4-276}$$

for bend tests,

$$C^{1/\alpha} = \frac{1}{K}\int_{\frac{l_0}{t}}^{\frac{l_f}{t}} \frac{dX}{X\,(1-X)^{1/\alpha}} = \frac{6.26}{K} \tag{4-277}$$

where

l_o	=	the initial crack length (m)
l_f	=	the final crack length (m)
t	=	the specimen thickness (m).

The constants α and log C, which Pettersson reports from fits to his data, are listed in Table 4-45, along with the constant K obtained from Equation (4-277).

Table 4-45. Low cycle fatigue material parameters.

Fast Fluence $(n/m)^2$	Material Parameter, α (Unitless)	log C (Unitless)	Material Parameter, K (Unitless)
0	0.60	1.87	10.3
1.3×10^{24}	0.64	1.96	11.7
2.6×10^{24}	0.56	1.75	10.1
Average	0.6	--	10.7

4.12.4 References

4.12-1 B. Tomkins, "Fatigue Crack Propagation - An Analysis," *Philosophical, 18*, 1968, p. 1041.

4.12-2 V. S. Rao, *High Cycle Fatigue Crack Growth of Two Zirconium Alloys*, AE-486, March 1974.

4.12-3 T. J. Walker and J. N. Kass, "Variation of Zircaloy Fracture Toughness in Irradiation," *Zirconium in Nuclear Applications*, ASTM-STP-551, 1974, pp. 328-254.

4.12-4 W. J. O'Donnell and B. F. Langer, "Fatigue Design Basis for Zircaloy Components," *Nuclear Science and Engineering, 20*, 1, 1964

4.12-5 K. Pettersson, "Low Cycle Fatigue Properties of Zircaloy Cladding," *Journal of Nuclear Materials, 56*, 1975, pp. 91-102.

4.13 Collapse Pressure (CCLAPS)

The subcode CCLAPS was produced to aid in the prediction of cladding collapse into axial gaps between fuel pellets. It is based on a correlation developed by Hobson,[4.13-1] which predicts collapse pressure for temperatures between 590 and 700 K. This version of the subcode does not apply to the description of high temperature (900 K) collapse or waisting of cladding into pellet to pellet gaps, which has been observed during power cooling mismatch (PCM) accident tests.[4.13-2]

4.13.1 Model Development

The required input parameters for the function CCLAPS are cladding temperature (K), the largest pellet to pellet gap in the node considered (m), and the room temperature midwall diamond pyramid hardness number (DPH) of the cladding. An additional input argument, pellet-to-cladding gap size (m) is not used by this version of the model but is included in the argument list to allow for future improvement of the model. The function returns the pressure at which collapse is predicted by Hobson's correlation.

When measured values of hardness for the particular lot of tubing under consideration are not available, it is suggested that the user input Hobson's measured values. These were reported[4.13-3] as follows: for 80% cold worked and 775 K stress relieved material, hardness equals 238 DPH; for fully recrystallized material, hardness equals 180 DPH.

The expression for collapse pressure derived by Hobson[4.13-1] is

$$P = 6895\left[15660 + \frac{G}{2.17\times10^{-4}G - 4.57\times10^{-7}} - 183H + 0.729H^2 - 7.40\times10^{-4}H^3 - 3762T\right] \qquad (4\text{-}278)$$

where

P	=	collapse pressure (Pa)
G	=	pellet to pellet gap (m)
H	=	room temperature midwall hardness (DPH)
T	=	test temperature (K).

Hobson's correlation is based on out-of-pile tests with unirradiated cladding and pellet-to-cladding gaps of 0.20 mm (0.008 in.). Some tests were conducted with other pellet-to-cladding gaps sizes[4.13-3] but were not included in the data base of the correlation.

4.13.2 References

4.13-1 D. O. Hobson, *Quarterly Progress Report on the Creepdown and Collapse of Zircaloy Fuel Cladding Program Sponsored by the NRC Division of Reactor Safety Research for April-June 1976*, ORNL/NUREG/TM-52, October 1976.

4.13-2 J. B. Ferguson (ed.), *Quarterly Technical Progress Report on Water Reactor Safety Programs Sponsored by the Nuclear Regulatory Commission's Division of Reactor Safety Research for October-December 1976*, TREE-NUREG-1070, April 1977, p.37.

4.13-3 D. O. Hobson, *Quarterly Progress Report on the Creepdown and Collapse of Zircaloy Fuel Cladding Program Sponsored by the NRC Division of Reactor Safety Research for January-March 1976*, ORNL/NUREG/TM-51, October 1976.

4.14 Meyer Hardness (CMHARD)

The routine CMHARD calculates Meyer hardness as a function of cladding temperature.

4.14.1 Model Development

One of the parameters required for calculating fuel-to-cladding contact conductance is hardness. As the contact pressure between the two surfaces increases, the points of contact enlarge due to localized plastic deformation and the solid-to-solid thermal conductance is improved. The Meyer hardness is used by Ross and Stoute[4.14-1] in their heat transfer correlation as an indication of the hardness of resistance to deformation of the softer (zircaloy) material.

The Meyer hardness number is a measure of indentation hardness and is defined in conjunction with Meyer's law,

$$L = ad^n \tag{4-279}$$

where

L	=	load
d	=	the diameter of impression at the surface of a specimen in a static ball test
n	=	the Meyer work hardening coefficient
a	=	a material constant.

The Meyer hardness number (MH) is defined as $4L/\pi d^2$. Other hardness numbers are available (Brinell, Rockwell, etc.), and conversion from one to another is possible. However, the routine CMHARD was created to provide information required by the Ross and Stoute gap conductance model.

Meyer hardness numbers for temperatures from 298 to 877 K were taken from Peggs and Godin.[4.14-2] A regression analysis of the reciprocal of the Meyer hardness values versus the log of temperature was used to obtain the analytical expression used in CMHARD. The correlation used is given by

$$MH = \exp\{ 2.6034 \times 10^{1} + T \{-2.6394 \times 10^{-2} + T [4.3504 \times 10^{-5} + T (2.5621 \times 10^{-8})]\}\} \tag{4-280}$$

where

MH	=	Meyer hardness (N/m^2)
T	=	temperature (K).

Figure 4-59 illustrates the correlation and its data base. The Meyer hardness decreases rapidly with increasing temperature, beginning at 2 x 10^9 MPa at room temperature and decreasing to 2 x 10^8 MPa at 875 K. The hardness is presumed to continue its rapid rate of decrease at temperatures above 875 K. The minimum Meyer hardness number of zircaloy cladding is 1.0 x 10^5 N/m^2.

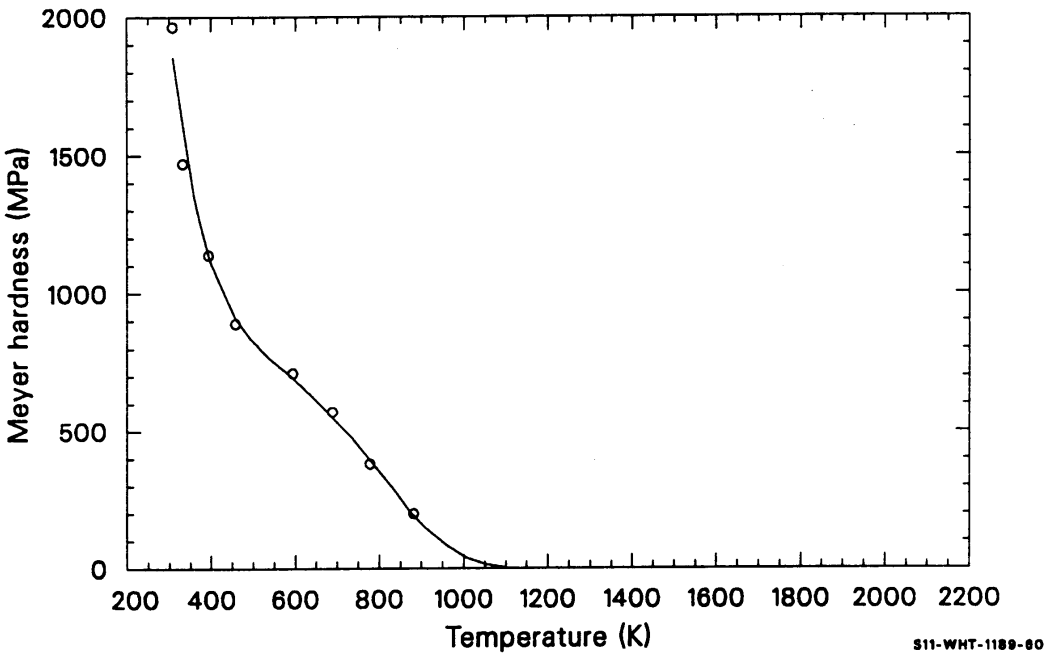

Figure 4-59. Values of the CMHARD correlation and its data base.

4.14.2 References

4-14.1 A. M. Ross and R. L. Stoute, *Heat Transfer Coefficient Between UO_2 and Zircaloy-2*, AECL-1552, June 1962.

4-14.2 I. D. Peggs and D. P. Godin, "The Yield Strength-Hot Hardness Relationship of Zircaloy-4," *Journal of Nuclear Materials, 57*, 1975, pp. 246-248.

4.15 Zircaloy Oxidation in Water and Steam (CORROS, COBILD, COXIDE, COXWTK, COXTHK)

The oxidation of zircaloy cladding is an important subject because the thermal and mechanical properties of oxidized zircaloy are significantly different than the unoxidized properties. Moreover, the oxidation is highly exothermic. It can proceed rapidly enough at high temperatures to cause the reaction heat to significantly influence temperatures.

4.15.1 Summary

Low temperature (523 to 673 K) oxidation is modeled with the CORROS subcode, and high-temper-

ature (1,273 to 2,100 K) oxidation is modeled with the COBILD, COXIDE, COXWTK and COXTHK subcodes. These codes provide information for other MATPRO subcodes, which describe the mechanical properties of zircaloy containing oxygen. This information includes oxygen concentrations, layer thicknesses, and the linear heating rate due to the zirconium-water reaction.

Oxide layer thickness is the only quantity calculated by the CORROS subcode. No other layers are found in zircaloy oxidized at 523 to 673 K.

COBILD, a FORTRAN adaptation of the BASIC BUILD5 code by Pawel, of Oak Ridge National Laboratory, calculates high-temperature oxygen concentrations, layer thicknesses, and the heating rate due to the zirconium steam reaction. The temperature at the beginning and end of a time step and the time step duration are required input information. The time step is divided into five substeps. During each substep, the average temperature obtained from a linear interpolation of the input temperatures is used with the isothermal correlations that are discussed below.

Calculations in COXIDE are isothermal. The input time step is not divided, and the temperature provided is assumed to be the average temperature for the entire step. Also, the oxygen concentration calculations of COBILD are not carried out in COXIDE.

COXWTK and COXTHK provide only oxidation rate constants for the high temperatures. The rate constants are provided in separate subcodes so that they are available for use with routines that calculate the coupled effects of oxidation heat, temperature, and geometry.

4.15.1.1 ***Low Temperature Oxidation (CORROS).*** The subroutine CORROS returns an expression for the thickness of the oxide layer on zircaloy cladding during typical reactor operation at temperatures of 523 to 673 K. Required input values are temperature at the outer surface of the oxide, initial oxide film thickness, length of time at the given temperature, type of reactor (BWR or PWR), heat flux across the oxide layer, and zircaloy oxide thermal conductivity.

Cladding oxidation during normal LWR operation occurs in two stages, depending on the oxide thickness and to some extent on the temperature of the oxide. For thin oxides, the rate of oxidation is controlled by the entire oxide layer. When the oxide layer becomes thicker, a change of the outer portion occurs; and further oxidation is controlled by the intact inner layer. The transition between stages is described in terms of thickness of the oxide layer at transition:

$$X_{TRAN} = 7.749\times10^{-6}\exp\left(-\frac{790}{T}\right) \tag{4-281}$$

where

X_{TRAN} = thickness of the oxide layer at transition point (m) (typically 1.9 x 10^{-6} m thick)

T = temperature of the oxide-metal interface (K).

Values of the thickness of the oxide layer on the outside of the cladding are given by Equations (4-282) through (4-284) for pretransition and posttransition oxide films.

For pretransition oxide films:

$$X_{PRE} = \left[4.976\times10^{-9}\,(At)\exp\left(-\frac{15660}{T}\right) + X_0^3\right]^{1/3} \tag{4-282}$$

For posttransition oxide films when X_o, the initial oxide thickness, is less than X_{TRAN}:

$$X_{POST} = 82.88A\,(t - t_{TRAN})\exp\left(-\frac{14080}{T}\right) + X_{TRAN}. \tag{4-283}$$

When X_o is greater than the transition thickness:

$$X_{POST} = 82.88\,(At)\exp\left(-\frac{14080}{T}\right) + X_0 \tag{4-284}$$

where

X_{PRE}	=	thickness of the oxide layer when a pretransition oxide film exists (m)
A	=	a parameter describing enhancement of the cladding oxidation rate in a reactor environment. Typical reactor coolant chemistry, temperatures, and flux levels result in a value of A = 1.5 and 9 for a PWR and BWR, respectively. However, the factor is a function of temperature, as discussed in Section 4.15.3. A value for A is determined by correlations in the subcode using user specification of BWR or PWR chemistry with an input parameter ICOR.
t	=	time at temperature (days)
T	=	temperature of the oxide metal interface calculated by the subcode from the input value of the temperature at the outer oxide surface, the heat flux across the oxide, and the thermal conductivity of the oxide layer (K).
X_o	=	initial thickness of the cladding oxide layer (m). (This term can be approximated as $X_o = 0$ for etched cladding, but it becomes important if extensive prefilming has occurred or if oxidation is carried out in several steps which take place at different temperatures or in different coolant chemistries.)
X_{POST}	=	thickness of the oxide layer when the oxide film is in the posttransition state (m)
t_{TRAN}	=	time of transition between states (pre- and post-transition). [This time is calculated in the subcode from the inverse of Equation (4-282)].
X_{TRAN}	=	thickness of the oxide layer at the transition point (m) [Equation (4-281)].

4.15.1.2 ***High Temperature Oxidation (COBILD, COXIDE, COXWTK, COXTHK).*** For the high temperature range (1,273 to 2,100 K), neither the heat flux nor the coolant chemistry has an important influence on the extent of oxidation. At these reactor operating temperatures, the coolant has become steam; and oxidation proceeds much more rapidly than at normal LWR operating temperatures. Zircaloy normally has a body-centered cubic structure in this temperature range, called the beta phase, but the presence of oxygen causes two other possibilities. If the oxygen concentration is greater than about 0.25 weight fraction, one of several zirconium dioxide structures is formed. For oxygen weight fractions

around 0.04, a hexagonal, close-packed phase called oxygen stabilized alpha zircaloy is formed. Thus, high-temperature oxidation of zircaloy in steam produces three layers: the ductile inner beta layer with minimal dissolved oxygen, an intermediate oxygen-stabilized alpha-zircaloy layer, and a zirconium-dioxide layer near the zircaloy steam interface.

When zircaloy cladding is exposed not only to steam on its outer surface but also to firm contact with uranium dioxide on the inside surface, three distinct inside layers are formed as oxygen and uranium diffuse into the cladding. A schematic cross section of a fuel rod with fuel and pellet in contact is shown in Figure 4-60. The layers shown in this figure are

ZrO_2	=	a zirconium dioxide layer formed by the metal water reaction
α-Zr(O)	=	an oxygen stabilized alpha zircaloy layer formed with oxygen from the coolant
β	=	a beta zircaloy layer with some dissolved oxygen
α-$Zr(O)_a$	=	oxygen stabilized alpha zircaloy layer formed with oxygen from the fuel
α-$Zr(O)_b$	=	oxygen stabilized alpha zircaloy layer formed with oxygen from the fuel
(U,Zr)	=	a thin layer of zircaloy uranium alloy.

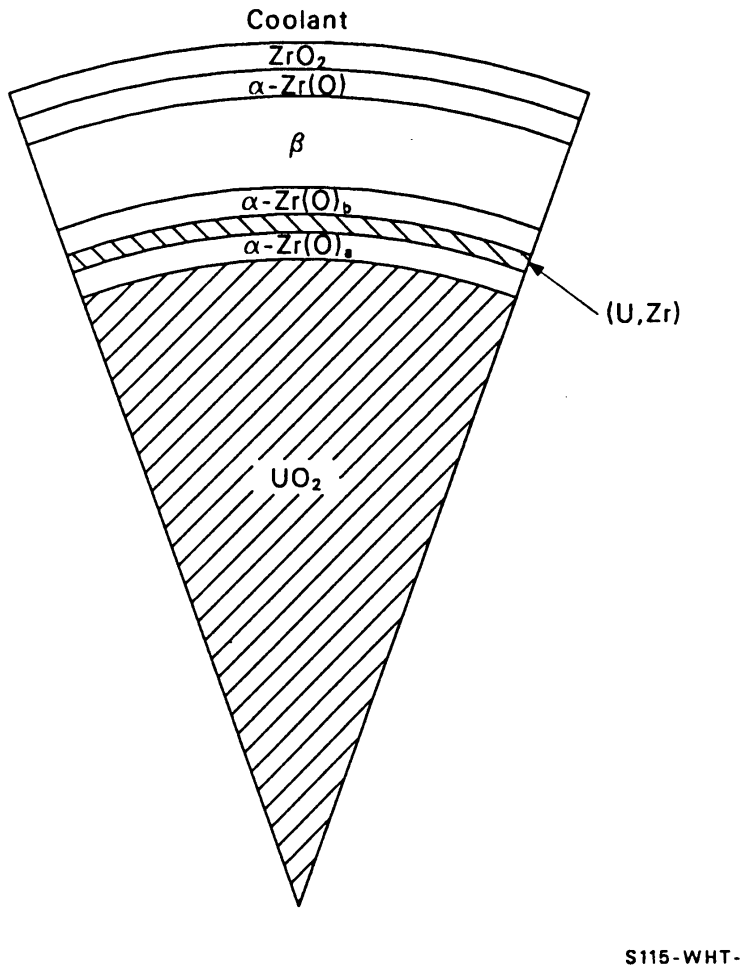

Figure 4-60. Idealized schematic of a uranium dioxide pellet in contact with the cladding, showing the layered structure.

COBILD works in time steps. At the start of each time step, it should be supplied with quantities including the duration of the time step, the temperature at the beginning and end of the step, the original unoxidized cladding dimensions, the thickness of the various layers and their oxygen concentrations, and the total oxygen uptake at the beginning of the timestep. After updating or recalculating several of these to conform to conditions at the end of the time step, it returns values for each of them.

The equations used to model the growth of the outside layers exposed to steam are all of the form

$$Z_f = \left(Z_i^2 + 2A\exp\left(-\frac{B}{T}\right)\Delta t\right)^{1/2} \tag{4-285}$$

where

Z_f = value of oxidation parameter (oxide layer thickness, alpha layer thickness, or zircaloy weight gain per unit surface area due to oxidation) at the end of a time span of length Δt

Z_i	=	value of oxidation parameter at the start of the time span
T	=	temperature of the oxide layer (K)
A,B	=	rate constants.

Table 4-46 lists the rate constants used with Equation (4-285) to model the various oxidation parameters for steam oxidation. In all cases, the model assumes that there is sufficient steam to provide the indicated weight gain. The parabolic rate constants for the α-Zr(O) thicknesses in this table are not valid when the beta zircaloy layer becomes small.

Table 4-46. Rate constants for oxidation by steam.

Parameter	A	B
	$Zr0_2$ thickness (m)	
For temperature ≤ 1,853 K	1.126×10^{-6} m^2/s	1.806×10^4 K
For temperature > 1,853 K	1.035×10^{-6} m^2/s	1.6014×10^4 K
a-Zr(O) thickness (m)	7.615×10^{-5} m^2/s	2.423×10^4 K
	Weight gain per unit surface area (kg/m^2)	
For temperature ≤ 1,853 K	1.680×10^1 $(kg/m^2)^2/s$	2.006×10^4 K
For temperature ≥ 1,853 K	5.426×10^1 $(kg/m^2)^2/s$	1.561×10^4 K

Equation (4-285) is also used to model the growth of the inside of the α-$Zr(O)_a$ and α-$Zr(O)_b$ layers. For these layers, the growth rate is modeled as zero unless there is pellet cladding contact. For those time steps when there is pellet-cladding mechanical interaction, the constants given in Table 4-47 are used with Equation (4-285) to calculate the layer thickness.

The expression used to calculate the rate of heat generation due to the exothermic oxidation of zircaloy by steam is

$$P = 1.15\times10^8 \frac{R_0 (W_f - W_i)}{\Delta t} \tag{4-286}$$

where

P	=	rate of heat generation per unit length (W/m)
R_o	=	cladding outside radius without oxidation (m)
W_f	=	mass gain per unit surface area due to oxidation at end of time step (kg/m^2)
W_i	=	mass gain per unit surface area due to oxidation at start of time step (kg/m^2).

COBILD calculations for the oxygen profiles are completed after the oxide and alpha surface layer

thicknesses are determined. The remaining beta thickness is divided into eight sections (nine nodes), and the oxygen concentrations are calculated with the expression

$$C(X, t+\Delta t) = C(X, t) + \frac{D\Delta t}{\Delta X^2}[C(X+\Delta X, t) - 2C(X, t) + C(X-\Delta X, t)] \quad (4\text{-}287)$$

where

C(X,t)	=	oxygen concentration at position X and time t (kg/m^3)
D	=	diffusion constant of oxygen in zircaloy (m^2/s) [see Equation (4-288)]
ΔX	=	one-eighth of the beta layer thickness (m).

Table 4-47. Rate constants for oxidation by UO_2.

Parameter	A	B
a-$Zr(O)_a$ thickness (m)	1.6×10^{-5} m^2/s	2.47×10^4 K
a-$Zr(O)_b$ thickness (m)	3.5×10^{-5} m^2/s	2.21×10^4 K

The diffusion constant is found with a correlation of experimental data versus temperature

$$D = 2.63\times10^{-6}\exp\left(-\frac{14200}{T}\right). \quad (4\text{-}288)$$

In solving Equation (4-287) for oxygen concentrations, it is assumed that the concentration at the alpha beta interface (the first node) is always the saturation concentration for beta zircaloy,[a] that diffusion of oxygen into the beta region does not begin until the temperature is greater than 1,239 K, and that the initial oxygen concentration throughout the as fabricated metal is 0.0012 weight fraction.

The oxygen profiles calculated with Equation (4-287) are used to calculate the average mass of oxygen added to the beta layer. The expression used is

$$F = \frac{M}{6490B} - 0.0012 \quad (4\text{-}289)$$

where

F	=	oxygen weight fraction in the beta layer in excess of the as-fabricated content (dimensionless)
M	=	total oxygen in beta layer per unit surface area (kg/m^2)
B	=	thickness of beta layer (m).

Since the oxygen weight fraction in the alpha phase is nearly constant at 0.047, no calculation is nec-

a. Equations (4-310) through (4-312) are used to determine this concentration.

essary for this parameter. It is simply listed in the COBILD code.

Section 4.15.2 is a review of the literature on zircaloy oxidation. The models that have just been presented are developed in Section 4.15.3. Section 4.15.4 is a description of the zircaloy oxidation subcodes. References are listed in Section 4.15.5, and a bibliography is presented in Section 4.15.6.

4.15.2 Zircaloy Oxidation Literature and Data

The review of oxidation data is divided into separate discussions of low and high-temperature data.

4.15.2.1 ***Low Temperature Oxidation (CORROS).*** Investigators generally agree[4.15-1,4.15-2] that oxidation of zirconium alloys by water in the temperature range from 573 to 673 K proceeds by the migration of oxygen vacancies from the oxide metal interface through the oxide layer to the oxide coolant surface (and the accompanying migration of oxygen in the opposite direction). The vacancies at the metal oxide surface are generated by the large chemical affinity of zirconium for oxygen. Although the rate of oxidation is controlled in part by vacancy migration, the process of oxygen transfer from coolant to metal is not complete until the vacancy is annihilated by an oxygen ion at the oxide coolant surface. It is thus reasonable to expect the complex array of both bulk oxide properties effects and surface (coolant chemistry) effects that are reported in the literature.

Well-characterized data for out-of-pile oxidation are available from numerous experiments. The principal features of these data are:

a. There is a transition between initial oxidation kinetics and later oxidation kinetics. The transition is a function of temperature and oxide layer thickness.

b. The pretransition oxidation rate is time dependent and inversely proportional to the square of the oxide thickness.

c. The posttransition oxidation rate of a macroscopic surface is constant.

Detailed mechanisms to explain the time dependencies of zircaloy oxidation have not been established in the literature.[4.15-3,4.15-4] Proposed mechanisms are discussed in conjunction with the models developed in Section 4.15.3.

Empirical relations based on out of pile data are published in Reference 4.15-2. These relations are as follows:

$$\text{pretransition oxidation} = (27.1 \pm 0.8) \times 10^3 t^{1/3} e^{\left(-\frac{5220}{T}\right)} \tag{4-290}$$

$$\text{posttransition oxidation} = (23.0 \pm 0.7) \times 10^8 t e^{\left(-\frac{14400}{T}\right)} \tag{4-291}$$

$$\text{weight gain at transition} = (123 \pm 4)\, e^{\left(-\frac{790}{T}\right)} \tag{4-292}$$

where

oxidation = weight gain (mg/dm^2)

T	=	temperature (K)
t	=	time (days).

The correlations were reported to be accurate to $\pm$ 4%.

In-reactor oxidation is not successfully predicted by Equations (4-290) through (4-292). This oxidation is enhanced by physical mechanisms that are not completely clear. It is known that the enhancement is different in BWR environments than in PWR environments and that the enhancement is more pronounced at the lower end of the 573 to 673 K temperature range. An adequate data base for a careful prediction of oxidation enhancements in reactor environments is not available in spite of several past studies, which have concentrated on the effects of dissolved oxygen,[4.15-5,4.15-6] fast neutron flux,[4.15-6] fast neutron fluence,[4.15-7] and gamma irradiation.[4.15-8]

4.15.2.2 ***High Temperature Oxidation.*** Many of the complications observed with low temperature oxidation are absent at high temperatures. The use of parabolic kinetics to describe the total oxygen uptake by zircaloy from steam and the ZrO_2 and oxygen-stabilized alpha layers has been extensively documented by experimenters in several countries. In the United States, there has been a series of reports from ORNL[4.15-9,4.15-10] and from Worcester Polytechnic Institute.[4.15-11] There have been similar reports by Urbanic in Canada,[4.15-12] Leistikow in Germany,[4.15-13] and Kawasaki in Japan.[4.15-14] The only published data above 1853 K are the measurements by Urbanic and Heidrick[4.15-15] at temperatures between 1,320 and 2,120 K. These data show a discontinuity in the oxidation rate at about 1853 K. Since this temperature is near the monoclinic-to- cubic transformation of the oxide, it is suspected that the change in oxidation rate is due to the oxide structure change. No discontinuity was observed in the oxygen-stabilized α-Zr(O) layer, and none would be expected because the growth rate of this layer is controlled by the rate of oxygen diffusion into the beta-phase zircaloy. Urbanic and Heidrick calculate rate constants from the slope of the linear portion of a plot of their $(\text{weight gain})^2$ data versus time.

Several papers have been published describing the UO_2-Zr reaction responsible for the inside α-Zr(O) layers observed when cladding contacts UO_2 fuel. Hoffmann and Politis[4.15-16] have published a particularly useful article. Other important papers are by Mallet[4.15-17] and Rooney and Grossman.[4.15-18] These investigators agree that a layered structure exists next to the fuel and that the inner surface reaction layer farthest from the UO_2 is oxygen stabilized alpha zirconium. Next, a (U,Zr) alloy is found, which is primarily uranium. The different authors disagree in their description of this (U,Zr) alloy, and there is a further difference among them about the oxygen-stabilized alpha layer adjacent to the fuel.

An attempt to model the UO_2-Zr reaction analytically has been made by Cronenberg and El-Genk.[4.15-19] However, their analysis deals only with the diffusion of oxygen from the fuel and describes the resulting oxygen gradients in both the fuel and the zirconium. Their model has the advantage of being based largely on first principles, but it does not give the detail observed experimentally by the other investigators.

4.15.3 Model Development

Oxidation of materials that form a protective oxide layer is frequently found to conform to the assumption that the rate determining process is the diffusion of oxygen atoms across the oxide.[4.15-20] In this case, the rate of oxygen diffusion across the oxide layer is given by Fick's law

$$J_x = -D\frac{\partial N}{\partial X} \tag{4-293}$$

where

J_x	=	flux of oxygen atoms (atoms/m^2•s)
D	=	a function of temperature (m^2/s)
N	=	concentration of oxygen atoms (atoms/m^3)
X	=	direction perpendicular to the oxide surface (m).

If the concentration of oxygen atoms at both surfaces of the oxide surface is fixed, Equation (4-293) implies that the rate of formation of the oxide thickness will be inversely proportional to the oxide thickness

$$\frac{dy}{dt'} = \frac{D\,(N_s - N_i)}{Cy} \tag{4-294}$$

where

y	=	oxide layer thickness (m)
t'	=	time (s)
N_s	=	concentration of oxygen atoms at oxide surface (atoms/m^3)
N_i	=	concentration of oxygen atoms at oxide metal interface (atoms/m^3)
C	=	concentration of oxygen atoms in the oxide layer (atoms/m^3).

Integration of this equation from $y = Z_i$ at $t' = 0$ to $y = Z_f$ at $t' = \Delta t$ yields the parabolic time dependence of Equation (4-285), which is observed experimentally for high temperature oxidation.

4.15.3.1 ***Low Temperature Oxidation (CORROS).*** The fact that low temperature oxidation does not obey a parabolic time dependence implies that oxygen diffusion across the oxide is not the rate-controlling step. However, a slight extension of the derivation of the parabolic oxidation produces a result consistent with the measured time dependence of zircaloy corrosion. As mentioned at the beginning of Section 4.15.2.1, the migration of oxygen from the oxide surface to the metal-oxide interface may actually be caused by the migration of oxygen vacancies from the oxide metal interface through the oxide layer to the oxide-coolant surface. If the vacancies have a long lifetime, their migration should obey Fick's law. If the vacancies have a lifetime that is short compared to the time required to diffuse across the oxide layer, the flux of vacancies arriving at the oxide-coolant surface will be proportional to the inverse of the time, $t_{diffusion}$, required for a vacancy to diffuse to the oxide-coolant surface. Since this time is proportional to the square of the average diffusion distance $t_{diffusion} \alpha y^2$, the vacancy flux arriving at the oxide-coolant surface, and thus the rate of oxidation, should be proportional to the inverse of the square of the oxide thickness that the vacancies must cross.

From the physical arguments of the last paragraph, the vacancy lifetime limited rate of oxide growth should be $dy/dt' = M/y^2$, where M is not a function of time or oxide thickness. Integration of the rate equation from $y = X$ at $t' = 0$ to $y = X$ at $t' = t$, gives $X = (3Mt + X_0^3)^{1/3}$, which is the observed result. If the

vacancy concentration at the metal oxide surface is assumed to be given by an expression of the form $M = R \exp(-T_0/T)$, where R and T_0 are constants and T is the temperature of the interface, the resultant expression for pretransition oxidation is

$$X = \left[(3Rt) \exp\left(-\frac{T_0}{T}\right) + X_0^3 \right]^{1/3} . \tag{4-295}$$

Posttransition oxidation is viewed in this section as a series of pretransition modes. An inner oxide layer shown schematically in Figure 4-61, with thickness that varies as a function of surface position, is presumed to control the rate of oxidation until this inner layer grows to the transition thickness. At this time, the inner layer changes to an outer layer that does not affect the oxidation rate and growth of a new inner layer begins. The representation is adopted because it successfully relates pretransition and posttransition oxidation rates for out-of-pile data.

If the representation with an inner oxide film of varying thickness is correct, the rate controlling inner part of the oxide layer should join the outer layer at a thickness approximately equal to the transition thickness but at a time determined by local conditions. After several cycles, the growth rates of the inner oxide layer at different locations on the surface of a macroscopic oxide film will be out of phase; and the rate of growth of the entire surface film at any time (which is what is observed in most experiments) will be the time-average rate of growth at any one place on the surface:

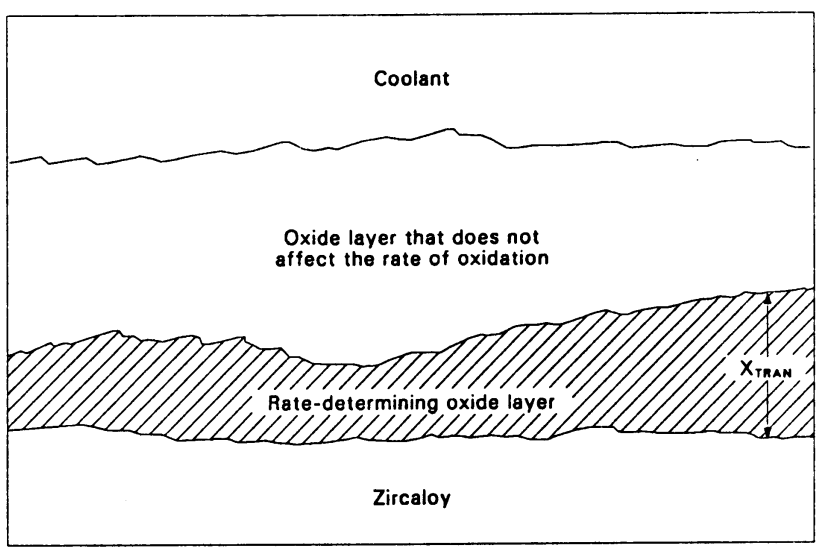

Figure 4-61. Schematic of posttransition oxide, showing an intact, rate-determining layer of varying thickness, with another oxide layer that does not affect the oxidation rate.

$$\frac{dy}{dt_{surface\ average}} = \frac{X_{TRAN}}{t_{TRAN_0}} = \frac{3R\exp(-\frac{T_0}{T})}{X_{TRAN}^2} \tag{4-296}$$

where

y	=	oxide layer thickness (m)
X_{TRAN}	=	thickness of the oxide layer at transition (m)
t_{TRAN_0}	=	time necessary for an oxide film to grow from almost zero thickness to the transition thickness, according to Equation (4-283) (s)
T	=	temperature (K)
T_o	=	constant (K)
R	=	constant (m^3/day).

Since the posttransition oxidation is viewed as being a series of pretransition modes that are separated by local loss of the inside oxide film, one would expect to obtain the pre-and post-transition oxidation rates with a single set of constants. In fact, the empirical constants determined by Van der Linde[4.15-2] for the pre-and post-transition oxidation rates [Equations (4-290) and (4-291)] can be reproduced with a single set of parameters, T_o = 14,080 K, R = 1.659 x 10^{-9} m^3/day, and X_{TRAN} = 7.749 x 10^{-6}m exp (-790/T). Oxidation rates obtained using these constants and Equations (4-295) and (4-296) are within the $\pm$ 4% error reported by Van der Linde for oxidation rates obtained using Equations (4-290) and (4-291).

Changes in oxidation due to in-pile chemical effects are incorporated into the present model with an enhancement factor, A, which describes a multiplicative in-pile enhancement of the out-of-pile oxidation rate due to an increased supply of oxygen ions. The explanation of an increased supply of oxygen ions[4.15-8] was adopted over an alternate explanation, which suggests that in-pile corrosion enhancement is due to irradiation damage of the oxide layer,[4.15-21,4.15-22] because the former can be modeled by a simple change in the rate constant while the latter would require adding a new mechanism to the model. There are no definitive experiments to indicate which approach is correct.

Rate equations for in pile oxidation are thus:

For the pretransition regime,

$$\frac{dX}{dt_{pre}} = \frac{AR\exp(-\frac{T_0}{T})}{X^2} \quad . \tag{4-297}$$

For the posttransition regime,

$$\frac{dX}{dt_{post}} = \frac{3AR\exp(\frac{-T_0}{T})}{X_{TRAN}^2} \tag{4-298}$$

where the terms of the equations have been previously defined.

The integrated forms of these equations are:

$$X_{PRE} = \left[3ARt\exp\left(-\frac{T_0}{T}\right) + X_0^3\right]^{1/3} \tag{4-299}$$

and

$$X_{POST} = \frac{3AR\,(t - t_{TRAN})\exp\left(-\frac{T_0}{T}\right)}{X_{TRAN}^2} + X_{TRAN} \tag{4-300}$$

if X_o is less than X_{TRAN}. If X_o is greater than X_{TRAN},

$$X_{POST} = \frac{3AR\,(t_{exp})\exp\left(-\frac{T_0}{T}\right)}{X_{TRAN}^2} + X_0 \ . \tag{4-301}$$

An interesting result (and a good test of the theory if time-dependent in-reactor data become available) is the fact that the rate enhancement factor A does not result in a linear change in the oxide thickness for pretransition films. That is, although the oxidation rate is enhanced by factor A, the pretransition oxide film thickness at a given time is merely $A^{1/3}$ as thick as it would have been without the in-pile enhancement. Since the posttransition oxidation is linear in time, both the rate and change in oxide thickness at a particular time are enhanced by factor A.

The metal-oxide temperature is computed from the temperature at the outer oxide surface, the heat flux across the oxide surface, and the thermal conductivity of the oxide layer by the expression

$$T = T_c + Q\left(\frac{X}{KO2}\right) \tag{4-302}$$

where

T	=	temperature of the oxide-metal interface (K)
T_c	=	temperature of the outer surface of the oxide (K)
Q	=	heat flux across the oxide layer (W/m^2)
X	=	oxide layer thickness (m)
KO2	=	thermal conductivity of the oxide layer (W/m + K).

Since the term Q(X/KO2) normally is a small correction to the temperature of the outer oxide surface, the correction to the temperature is approximated with an iteration. For the first step, X is approximated as the initial oxide thickness. The oxide thickness is then computed with Equation (4-299), (4-300), or (4-301), and the resultant value is inserted for X in Equation (4-302).

Expressions for the enhancement factor, A, were obtained by correlating BWR and PWR data to temperature. Values of the enhancement factor for BWRs shown in Figure 4-62 were proposed in References 4.15-22 and 4.15-23. The point attributed to Megerth is the average value, A = 9, found necessary to obtain a reasonable fit of the model developed here to the oxidation data presented in References 4.15-24 and 4.15-25. The analytical expression used in CORROS to represent these BWR enhancement factors in the temperature range 500 < T < 673 K is

$$A = 4.840\times10^{5}\exp(-1.945\times10^{-2}T_c) \quad (4\text{-}303)$$

where

A	=	the enhancement factor
T_c	=	the temperature at the outer oxide surface (K).

Enhancement factors have been reported to be about 2.4[4.15-26] for zircaloy-2 rods in the Shippingport PWR. A fit of Equation (4-283) to values of oxide thickness reported in Reference 4.15-25 agreed with this value. A similar fit of the equation to values reported from Saxton PWR rods[4.15-27,4.15-28] resulted in a value of A = 1.5. These values are also plotted in Figure 4-62. The relatively small value of A in PWR environments (which do not contain dissolved oxygen in the bulk coolant) is consistent with the picture of enhanced oxygen atom and ion supply rates due to ionization of dissolved oxygen. As in the case of BWR environments, the straight line sketched between these points is used by CORROS to estimate the enhancement in a typical PWR environment. The equation for $500 < T < 673$ K is

$$A = 1.203 \times 10^{2} \exp(-7.118 \times 10^{-3} T_c) \quad (4\text{-}304)$$

where

A	=	the enhancement factor
T_c	=	the temperature at the oxide coolant surface (K).

The predictions of the model developed in this section are compared with the values reported for individual samples in Figures 4-63 through 4-65. There is considerable scatter in the data from individual rods, with maximum measured values of oxide thickness as large as twice the average values. In some cases, such as the Shippingport data of Figure 4-63, variations are generally consistent with the idea that temperature variations are responsible. In other cases, such as the Saxton data of Figure 4-64, variations are not explained solely by temperature variation; and the cause is probably related to local variations in coolant quality or chemistry caused by nucleate boiling or to contaminants. Similarly, variations in the coolant along the BWR rods could contribute to the large scatter in the BWR data of Figure 4-65. Note that the duration of the pretransition period varies considerably in Figures 4-63 through 4-65. Figures 4-63 and 4-64 refer to PWRs with relatively low oxidation rate enhancements. However, the temperature is higher in the case of Figure 4-64, producing a shorter pretransition period due to more rapid oxidation. Figure 4-65 refers to a BWR with low temperatures but a large oxidation enhancement factor (9 in this case). This results in a long pretransition period so that the relatively rapid posttransition oxidation is predicted to start late for the BWR.

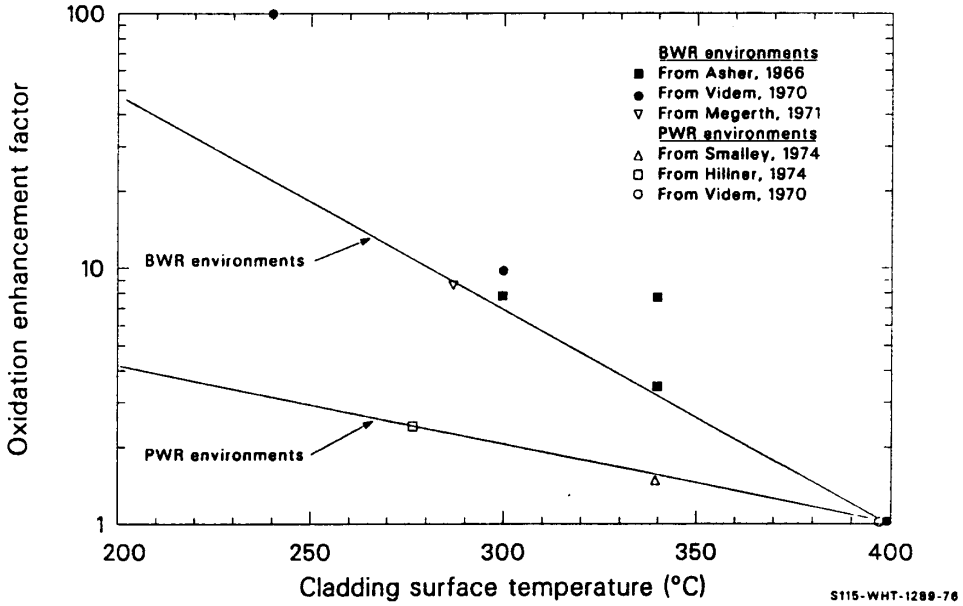

Figure 4-62. Estimates of enhancements over out-of-pile oxidation rates when cladding is irradiated in typical BWR and PWR environments.

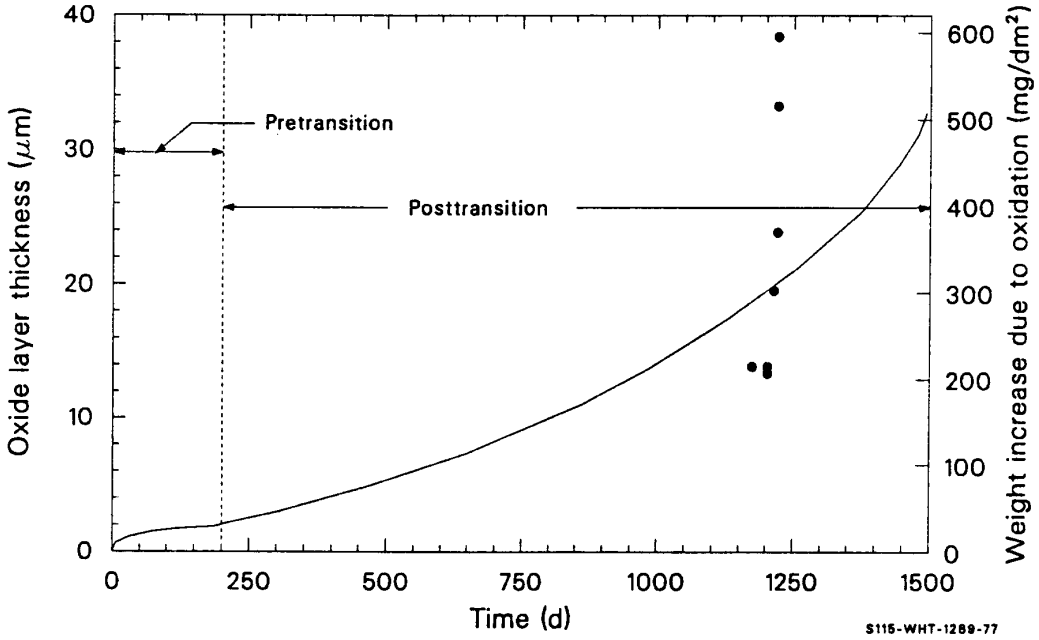

Figure 4-63. Comparison of the predicted oxide layer thickness with the base data from average values of six Shippingport zircaloy-2 rods in a PWR environment at 277°C.

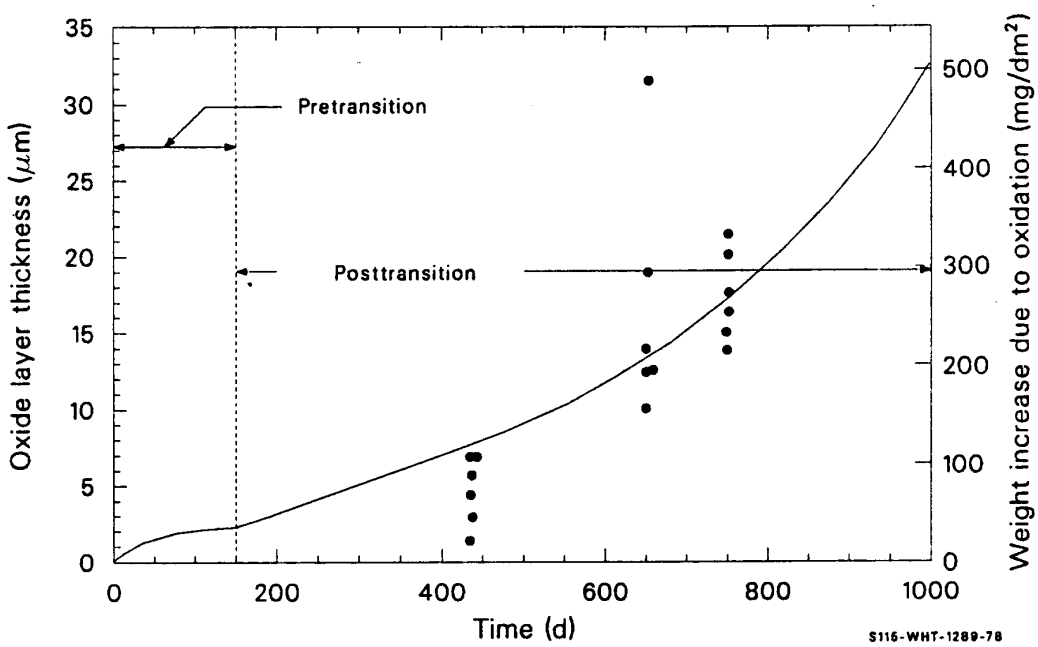

Figure 4-64. Comparison of the predicted oxide layer thickness with the base data from Saxton zircaloy-4 rods in a PWR at 340°C.

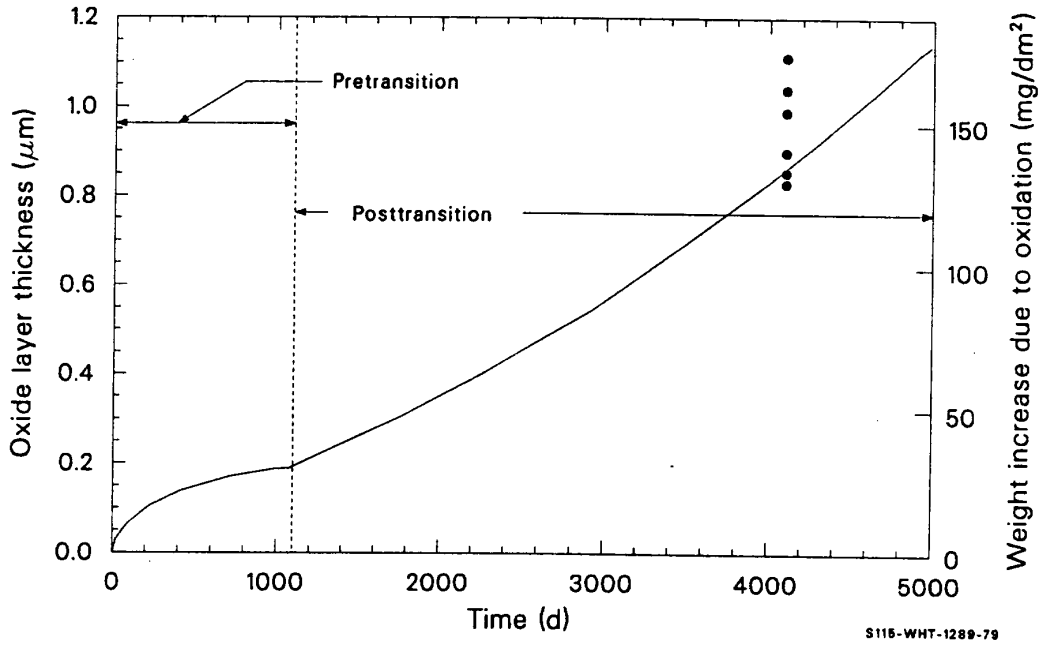

Figure 4-65. Comparison of the predicted oxide layer thickness with the base data from zircaloy-2 rods irradiated in the Vallecitos and Dresden BWRs at 286°C.

4.15.3.2 ***High Temperature Oxidation (COBILD, COXIDE).*** The COBILD and COXIDE subcodes were adapted from another code, BUILD5, written by Pawel, of Oak Ridge National Laboratory. Although BUILD5 was written in the computer language BASIC and the MATPRO codes are in

FORTRAN, the computational techniques are similar. COBILD and COXIDE have been expanded to include oxidation of the cladding on the inside surface by oxygen released from the fuel. The oxygen weight fraction in the beta phase and the linear power generation from the metal-water reaction are also calculated in COBILD and COXIDE but not BUILD5.

The correlations for ZrO_2 thickness, α-Zr(O) thickness, and weight gain due to steam reaction between 1,239 and 1,853 K were taken from Cathcart,[4.15-9,4.15-10] because Cathcart's expressions give the best fit to the pooled data from all the sources mentioned in Section 4.15.2.[a] A comparison with data of the ZrO_2 thicknesses calculated with Cathcart's equation is shown in Figure 4-66. A similarly good fit is obtained when the alpha thickness and weight gain correlations are compared with the data. Rate constants for temperatures between 1,853 and 2,100 K were taken from Urbanic and Heidrick.[4.15-15] In order to convert the correlations for zircaloy consumed given by Urbanic and Heidrick to oxygen consumed, the parabolic rate constant for zircaloy consumed was multiplied by the square of the ratio of oxygen consumed to zircaloy consumed given in Equation (4-305).

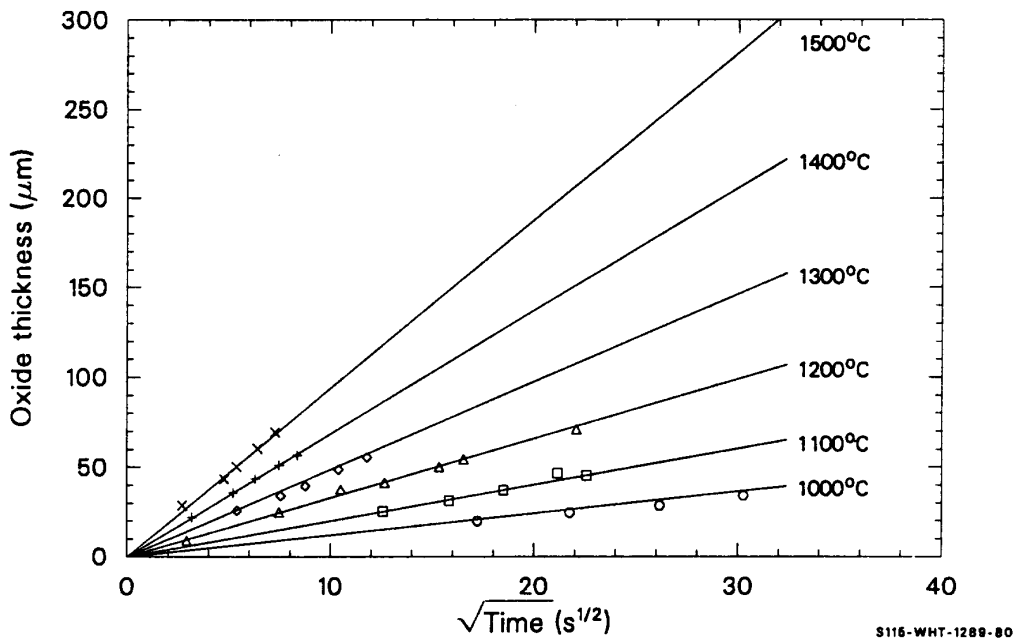

Figure 4-66. Comparison of calculated (solid lines) and measured ZrO_2 thickness for six temperatures.

Cathcart has thoroughly analyzed the uncertainty in his measurement.[4.15-29] In an earlier report [4.15-30] he reported joint 90% confidence levels for the rate constants [A exp (-B/T)] of Table 4-46. The word "joint" is used to indicate the uncertainty of the rate constant as a whole rather than uncertainties in the parameters A and B separately. His conclusions are presented in Table 4-48. These uncertainties are recommended for use with the oxidation codes in the temperature range where Cathcart's correlations are used.

a. Cathcart recommends these correlations only to 1,773 K. The authors extrapolated to 1,853 K, where the data of Urbanic and Heidrick suggest a discontinuity.

The numbers given in Table 4-48 are for isothermal oxidation only. There are no comparable statistics available for time dependent problems, largely because of the difficulty in obtaining reliable temperature measurements under transient conditions.

The standard error[a] of the weight gain correlation of Urbanic and Heidrick with respect to its own data base is 0.49 kg/m^2.

Only the linear portions of the entire data curves shown in Figure 4-67 were used by Urbanic and Heidrick to determine the high temperature correlation. Since these data did not pass through the origin, the resulting offset is the main contributor to the standard error.

Table 4-48. 90% joint confidence intervals for the parabolic rate constants for oxide layer growth, alpha layer growth, and total oxygen uptake

	Percent Deviation from Expected Value		
	1,323 K	1,523 K	1,773 K
Oxide	+4.9	+2.5	+4.3
Layer	-4.7	-2.4	-4.1
Alpha	+12.1	+6.1	-10.1
Layer	-10.8	-5.8	-9.2
Oxygen	+3.4	+1.7	+3.0
Uptake	-3.3	-1.7	-2.9

a. The expression used to calculate the standard error, σ, is

$$\sigma = \sum_{i=1}^{n} \frac{(C_i - M_i)^2}{n-1}$$

where

C_i = calculated weight gain

M_i = measured weight gain

n = number of data used.

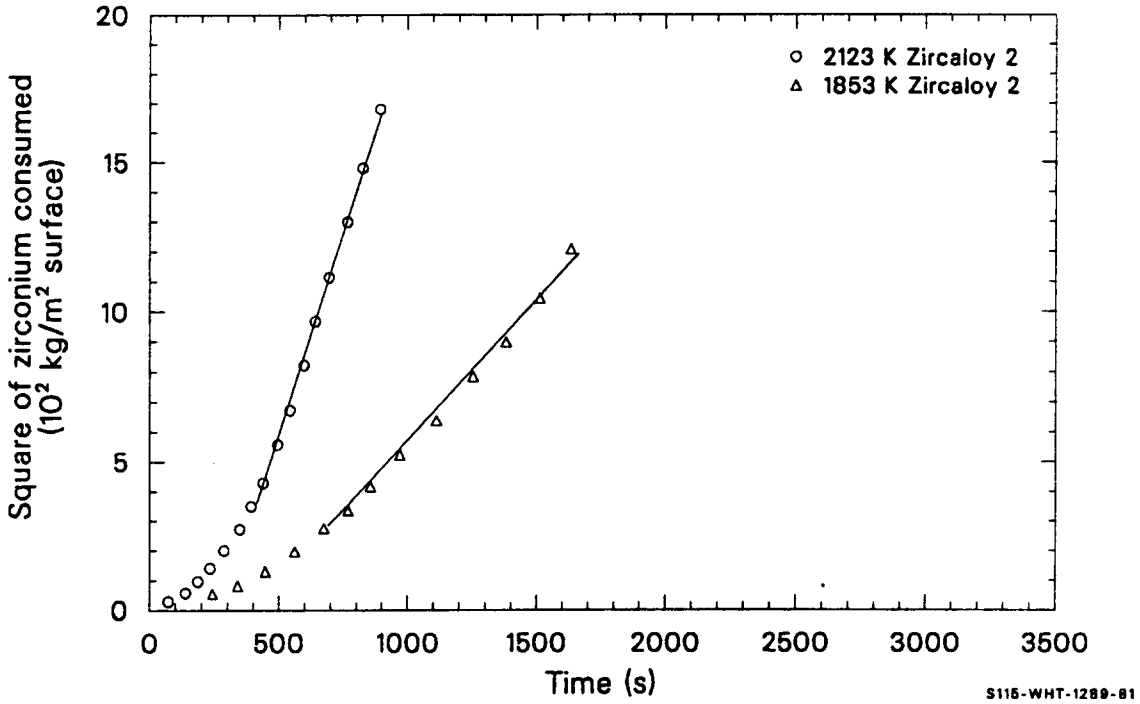

Figure 4-67. Data used by Urbanic and Heidrick to determine high temperature zircaloy oxidation rates.

The layers of alpha zircaloy on the inside cladding surface of unruptured cladding are caused by zircaloy-UO_2 interaction. The model for cladding oxidation by UO_2 is taken from Hofmann's results[4.15-16] for two reasons. His time and temperature data base is wider than that of Grossman and Rooney or of Mallet, and Hofmann gives correlations which can be integrated to become part of the high-temperature oxidation subcodes.

In Figure 4-68, Hofmann's correlations for the α-Zr(O) layers are compared with his data; and the data are presented in Table 4-49. The standard deviations of the correlations with respect to their own data bases are $\pm$ 18% for $Zr(O)_a$ for T < 1,600 K and $\pm$ 16% for $Zr(O)_b$ for T < 1,760 K.

Calculations of the rate of heat generation are based on the heat of reaction of zirconium, 6.45 x 10^6 J/kg of zirconium converted to ZrO_2 by steam.[4.15-31] Since the weight fraction of oxygen in ZrO_2 is 0.26, the ratio of zirconium consumed to oxygen added is

$$\frac{\Delta Zr}{\Delta W} = \frac{1 - 0.26}{0.26} \tag{4-305}$$

where

ΔZr	=	zirconium per unit surface area consumed by oxidation during the given time increment (kg/m^2)
ΔW	=	mass gain per unit surface area due to oxidation during a given time increment (kg/m^2).

The mass of zirconium consumed per unit length for a cylindrical rod is the mass per unit surface area times the circumference. The rate of heat generation per unit length is thus

$$P = \frac{0.74}{0.26}\frac{\Delta W}{\Delta t} 2\pi R_0 6.45\times10^6 \frac{J}{m} \quad . \tag{4-306}$$

This expression is equivalent to Equation (4-286).[a]

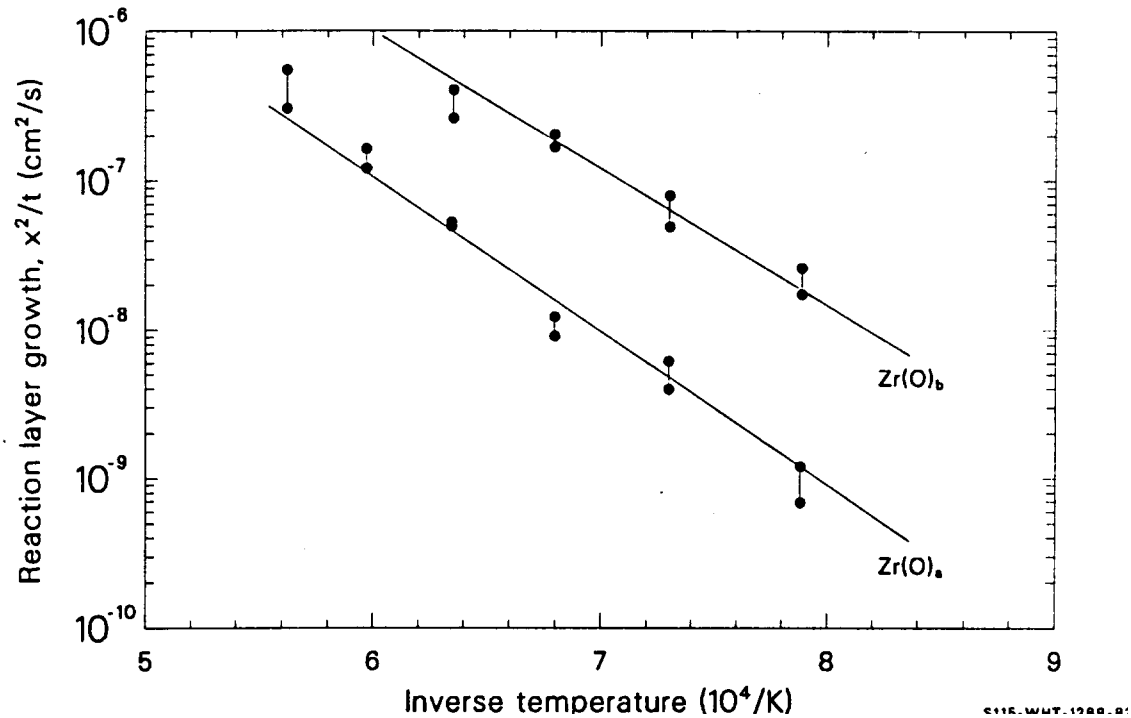

Figure 4-68. Growth of Zr(O) and $Zr(O)_b$ layers as a function of temperature from Hofmann and Politis.[4.15-16]

Table 4-49. Time temperature layer thickness data from Hoffman's[4.15-16] out of pile experiments

	Depth of Reaction Layers (mm)		
Temperature (^{0}C)	**Time (min)**	**$Zr(O)_a$**	**$Zr(O)_b$**
1,000	10	7	41
1,000	20	10	50
1,000	30	12	61

a. The derivation of Equation (4-306) uses the oxygen weight gain rather than the ZrO_2 thickness correlation because some of the oxygen consumed appears in the α-Zr(O) and beta layers.

Table 4-49. Time temperature layer thickness data from Hoffman's[4.15-16] out of pile experiments (Continued)

		Depth of Reaction Layers (mm)	
Temperature (^oC)	**Time (min)**	**$Zr(O)_a$**	**$Zr(O)_b$**
1,000	60	22	80
1,100	10	16	67
1,100	20	28	100
1,100	30	32	95
1,100	60	38	136
1,200	6	19	79
1,200	10	25	114
1,200	20	34	157
1,200	30	44	198
1,200	60	70	270
1,300	3	32	90
1,300	6	48	108
1,300	10	50	130
1,300	20	84	241
1,300	30	82	240
1,400	3	53	116
1,400	6	70	110
1,400	10	96	156
1,400	20	152	--
1,500	3	90	76
1,500	61	18	--
1,500	10	162	--
1,500	20	290	--

Figure 4-69 is a plot of P versus temperature for a fuel rod with an initial radius $R_o = 6.25 \times 10^{-3}$ m. Several initial oxide thicknesses are shown, and a time step of 1 second is assumed in each case. The exponential increase in power with temperature is evident, as is the proportional relation between instantaneous power and reciprocal oxide thickness.

Equation (4-306) may underpredict the oxidation heating rate because it uses the heat released in the reaction

$$2H_2O + Zr \rightarrow 2H_2 + ZrO_2 + Q \quad . \tag{4-307}$$

With Q = 6.5 x 10^6 J/kg of zircaloy reacted, Q is smaller by nearly a factor of two than Q_1, the heat released in the following reaction:

$$Zr + O_2 \rightarrow ZrO_2 + Q_1 \tag{4-308}$$

where Q_1 is 1.204 x 10^7 J/kg of zircaloy reacted.[15.2-32]

The difference arises because Equation (4-307) includes the heat required for the endothermic dissociation of water reaction

$$2H_2O + Q_2 \rightarrow 2H_2 + O_2 \quad .2H_2O + Q_2 \rightarrow 2H_2 + O_2 \quad . \tag{4-309}$$

The dissociation described by Equation (4-309) must take place either at the oxide-to-coolant interface or within the coolant itself. The oxygen thus liberated then diffuses through the oxide layer and combines with the zircaloy at the metal-to-oxide interface according to Equation (4-308). It is clearly Q_1 and not Q that causes the cladding to heat. However, Q_2 must ultimately come from the rod as well, cooling it. In a closed system, Equation (4-307) would be adequate. A problem can arise because the system is not strictly closed. As an example, dissociation may occur near one rod, cooling it, and oxidation may occur within an adjacent rod, heating it. The assumption made here is that these processes average out and Equation (4-307) is satisfactory.

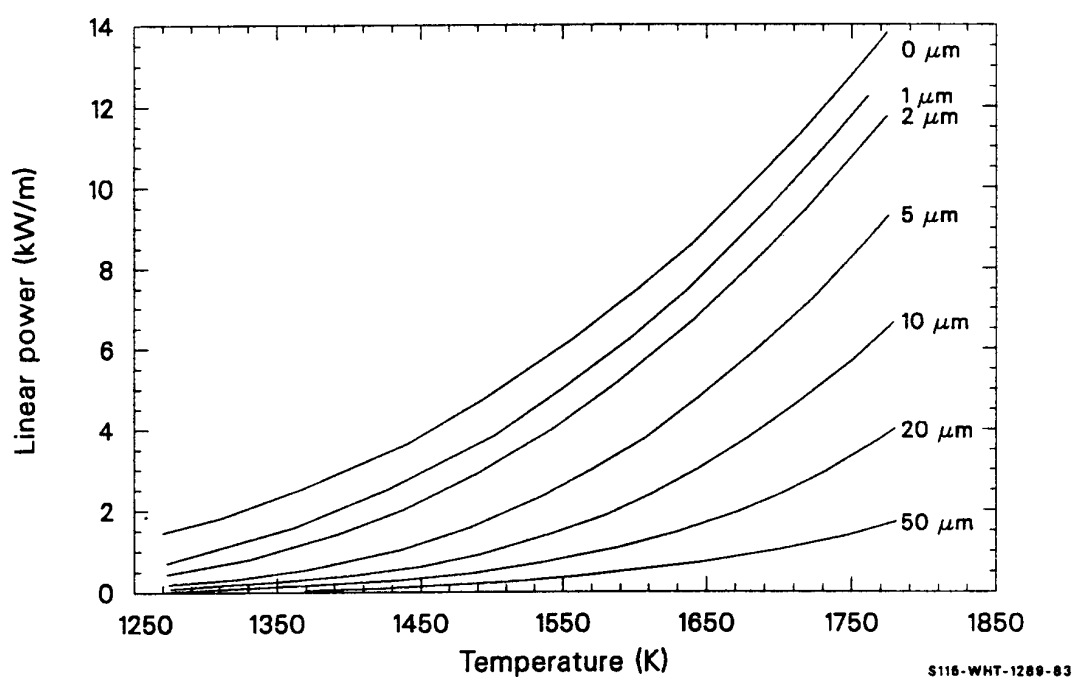

Figure 4-69. Linear power generation for a rod of initial diameter of 1.25 x 10^{-2} m as a function of temperature for various initial oxide thicknesses.

COBILD calculations for the oxygen profile in the beta region, Equation (4-287) are taken directly from a computer code described by Pawel.[4.15-33] Equation (4-288), the diffusion constant used in the oxygen profile calculation, is from Perkins[4.15-34,4.15-35] (converted from oxygen 18 to oxygen 16); and the following correlation is used to determine the saturation concentration of oxygen in beta zircaloy.

For T < 1,239 K,

$$CS = 0.0012 \quad . \tag{4-310}$$

For 1,239 ≤ T < 1,373 K,

$$CS = [-0.0042807 + (T/392.46 - 3.1417)^{1/2}]/100 \quad . \tag{4-311}$$

For T ≥ 1,373 K,

$$CS = (T-1081.7)/(4.91157 \times 10^4) \quad . \tag{4-312}$$

where CS is the saturation concentration of oxygen in beta zircaloy (weight fraction).

Equation (4-289), the expression used to calculate the oxygen weight fraction in the beta layer, is derived easily. To find the ratio of oxygen to zircaloy, the total oxygen per unit surface area in the beta region is divided by the product of the density of zircaloy (6,490 kg/m^3) and the beta layer thickness. The weight fraction of as-fabricated zircaloy, 0.0012, is subtracted to find the excess oxygen.

4.15.4 Description of the CORROS, COBILD, COXIDE, COXWTK, and COXTHK Subcodes

The first calculation is a check of the input parameters to determine the appropriate value of the error index. If impossible input parameter values are detected, no further calculations are attempted. If one of the input temperatures is below 1,239 K, only that portion of the time step above 1,239 K is used.

The input pellet-cladding interface pressure is checked to see if there is pellet cladding mechanical interaction during the given time step. If there is interaction, the cladding will be treated as two one-sided oxidation problems with steam supplying the outside source of oxygen and fuel providing the inside source of oxygen. The input initial cladding thickness is thus multiplied by 0.5.

Next, the step-average heat up rate, average temperature, beta saturation concentration, and diffusion constant for oxygen in beta zircaloy are calculated. The input time step size is divided by five to determine a substep size for later calculations, and the initial oxygen weight gain is saved because it will be needed to calculate the power of the oxidation reaction.

The next two sections of the program interpolate to find beta phase concentrations of oxygen if there has been a change from pellet-cladding mechanical interaction to no interaction, or vice versa. The input parameter IP2 is used to determine the prior step status and is updated to indicate current step status in the

process.

Initialization of the dimensioned quantities AA(1) to AI(1) at the initial beta-phase oxygen concentrations in the nine outside nodes is performed next. If there is no pellet-cladding mechanical interaction, these nine nodes span the entire beta layer. If there is interaction, the nine nodes span the outer half of the beta layer. The switch IP2 determines which of these cases is present. IP is set equal to zero to indicate that the nine outer nodes are being modeled, since the same coding may later be used to model the nine inside nodes.

The initial thickness of the beta layer being modeled is determined by subtracting the outside alpha layer thickness and two-thirds of the oxide layer thickness from the initial thickness of the region under consideration. The factor of two thirds is found by equating the mass per unit surface area of the oxide to the sum of the zircaloy and oxygen masses that produced the oxide:

$$\rho_{ZrO_2} X = \rho_{Zr} Y + 0.26 \rho_{ZrO_2} X \tag{4-313}$$

where

X	=	oxide layer thickness (m)
Y	=	thickness of zircaloy consumed to make the oxide (m)
ρ_{Zr}	=	density of zircaloy (kg/m^3) = 6,490
ρ_{ZrO_2}	=	density of zircaloy oxide (kg/m^3) = 5,820.

The constant 0.26 represents the mass fraction of oxygen in the oxide. Solution of Equation (4-313) for the ratio Y/X yields the required ratio. If the nine nodes under consideration span the entire cladding beta region (IP2 = 0 for no contact), the inside alpha layer thicknesses are also subtracted.

An iteration over five substeps is used to calculate the oxide layer thickness, outside alpha layer thickness, and weight gain due to oxidation by steam. Each substep is assumed to be isothermal, and the temperature is determined by linear interpolation of the input temperatures.

The two layer thicknesses are used to calculate the end of step thickness of the beta zircaloy layer spanned by the outside nine nodes. This thickness is stored as the variable AL80 for possible later addition to the beta thickness spanned by nine inside nodes.

Next, the change in the beta layer is compared with one-eighth of the initial layer. If the change is greater than one-eighth of the initial beta layer, the following message is printed: “DECREASE IN BETA LAYER IS GREATER THAN 1/8 INITIAL LAYER..., TIME STEP TOO LARGE OR BETA LAYER TOO DEPLETED.” Also, the error index is changed to one. Physically, the condition implies either that the time step is too long or that the beta layer is nearly completely converted to alpha-zircaloy.

A second check is made to determine if the finite-difference equation of Pawel, Equation (4-287), will be stable. If this condition is violated, the following message is printed: “DIFFUSION IS OCCURRING TOO RAPIDLY FOR COBILD TO ACCURATELY CALCULATE OXYGEN CONCENTRATIONS.” Also, the input parameter index is set equal to one.

Since the beta layer boundary moves during the time step, the input oxygen concentrations will not apply to the positions of the nodes at the end of the time step. Thus, two calculations are used to find the oxygen concentration in the beta layer. First, it is assumed that the alpha beta interface jumps immediately to its end-of-step position. A parabolic interpolation is used to find the start of step concentrations at the end of step positions. In the second part of the calculation, Equation (4-287) is applied over five small sub-steps but always at the end of step positions.

Simpson's rule is used to integrate the oxygen concentrations over the beta layer width in order to find the net oxygen. The net oxygen is stored as AQ20 for possible addition to the net oxygen in the region spanned by the nine inside nodes.

The final concentrations, AA(6) to AI(6), are stored as the output variables AA0 to AI0.

If there is no pellet-cladding interaction, the outer nine nodes span all of the beta layer so the calculation of oxygen concentrations in the beta layer is complete. In this case, the percent saturation, average oxidation power, and average oxygen concentration in the beta layer are calculated and the COBILD calculation is complete.

If there is pellet-cladding interaction, the sequence of calculations for the oxygen concentration is repeated for the inside nine nodes of the beta layer before the percent saturation, average oxidation power, and average oxygen concentration in the beta layer are calculated.

The COXIDE logic is similar to the COBILD logic, but the calculations of oxygen concentration in the beta phase have been omitted.

4.15.5 References

4.15-1 E. Hillner, *Hydrogen Absorption in Zircaloy During Aqueous Corrosion, Effect of Environment*, WAPD-TM-411. November 1964.

4.15-2 A. VanderLinde, *Calculation of the Safe Life Time Expectancy of Zirconium Alloy Canning in the Fuel Elements of the Nero Reactor*, RCN-41, July 1965.

4.15-3 B. Cox, "Comments on the Paper 'The Influence of Oxide Stress on the Breakaway Oxidation of Zircaloy-2' By D. H. Bradhurst and P. M. Heuer," *Journal of Nuclear Materials, 41*, 1970, p. 96.

4.15-4 D. H. Bradhurst and P. M. Heuer, "Reply to Comments by B. Cox on 'The Influence of Oxide Stress on the Breakaway Oxidation of Zircaloy-2," *Journal of Nuclear Materials, 41*, 1971, p.101.

4.15-5 A. B. Johnson, Jr., "Effects of Nuclear Radiation on the Corrosion, Hydriding, and Oxide Properties of Six Zirconium Alloys," *Applications Related Phenomena for Zirconium and Its Alloys*, ASTM-STP-458, 1969, pp. 301-324.

4.15-6 W. A. Burns, *Effects of Fast Neutron Irradiation, Fabrication History, and Water Oxygen on the Environmental Behavior of Zirconium Alloys*, BNWL-88, 1965.

4.15-7 A. B. Johnson, Jr., and J. E. Irvin, *Radiation-Enhanced Oxidation of Zircaloy-2 in pH-10 LiOH and pH-10 NH_4OH*, BNWL-463, 1967.

4.15-8 L. Lunde and K. Videm, "Effects of Surface Treatment on the Irradiation Enhancement of Corrosion of Zircaloy-2 in HBWR," *Zirconium in Nuclear Applications*, ASTM-STP-551, 1974, pp.514-526.

4.15-9 J. V. Cathcart, *Quarterly Progress Report on the Zirconium Metal-Water Oxidation Kinetics Program Sponsored by the NRC Division of Reactor Safety Research for April-June 1978*, ORNL/NUREG/TM-41, August 1976.

4.15-10 J. V. Cathcart, *Quarterly Progress Report on the Zirconium Metal-Water Oxidation Kinetics Program Sponsored by the NRC Division of Reactor Safety Research for October-December 1976*, ORNL/NUREG/TM-87, February 1977.

4.15-11 R. G. Ballinger, W. G. Dobson, and R. R. Bierderman, "Oxidation Reaction Kinetics of Zircaloy-4 in an Unlimited Steam Environment," *Journal of Nuclear Materials, 62*, November 1976, pp. 213-220.

4.15-12 V. F. Urbanic, "Method for Estimating the Exposure Time and Temperature for Zircaloy Oxidation in Steam," *Journal of Nuclear Materials, 59*, 1976, pp. 90-94.

4.15-13 S. Leistikow et al., "Untersuchen zur Hochtemperature-Wasserdampf-Oxidation von Zircaloy-4 Hullrohen," *PBS Halbjahresbericht 1976/2*, KfK 2435, February 1977.

4.15-14 S. Kawasaki et al., *Reaction of Zircaloy Cladding with Steam Under Simulated Loss-of-Coolant Accident Conditions*, JAERI-M-6181, July 1975.

4.15-15 V. F. Urbanic and T. R. Heidrick, "High Temperature Oxidation of Zircaloy-2 and Zircaloy-4 in Steam," *Journal of Nuclear Materials, 75*, 1978, pp. 251-261.

4.15-16 P. Hofmann, and C. Politis, "Chemical Interaction Between UO_2 and Zry-4 in the Temperature Range Between 900 and 1,500^{o}C," *Fourth International Conference on Zirconium in the Nuclear Industry, Stratford-upon-Avon, England, June 26-29, 1979.*

4.15-17 M. W. Mallet et al., *The Zirconium-Uranium Dioxide Reaction*, BMI-1210, July 1975.

4.15-18 D. M. Rooney, and L. N. Grossman, *Interfacial Reaction Between UO_2 and Zircaloy-2*, GEAP-4679, April 1965.

4.15-19 A. W. Cronenberg, and M. S. El-Genk, *An Assessment of Oxygen Diffusion During UO_2--Zircaloy Interaction*, TREE-NUREG-1192, January 1978.

4.15-20 W. Jost, *Diffusion in Solids, Liquids, Gases*, NewYork: Academic Press Inc., 1972, p. 341.

4.15-21 D. H. Bradhurst, P. J. Shirvington, and P. M. Heuer, "The Effects of Radiation and Oxygen on the Aqueous Oxidation of Zirconium and its Alloys at 290°C," *Journal of Nuclear Materials, 46*, 1973, p. 53.

4.15-22 R. C. Asher et al., "Effects of Radiation on the Oxidation and Hydrogen Absorption of Zirconium Alloys in Steam," *Electrochemical Technology, 4*, 1966, p. 231.

4-15-23 K. Videm, "Properties of Zirconium Base Cladding Materials Corrosion and Hydrogen Pickup," *Advanced Course on Limiting Aspects of Fuel Element Performance in Water Cooled Power Reactors at the Institute for Atomenergi in Kjeller, Norway, August 24-28, 1970.*

4.15-24 F. H. Megerth, C. P. Ruiz, and U. E. Wolff, *Zircaloy-Clad UO_2 Fuel Rod Evaluation Program*, GEAP-10371, June 1971.

4.15-25 H. E. Williamson et al., *AEC Fuel Cycle Program Examination of UO_2, Fuel Rods Operated in the VBWR to 10,000 MWD/TU*, GEAP-4597, 1965.

4.15-26 E. Gillner, "Corrosion and Hydriding Performance in Zircaloy Tubing after Extended Exposure in the Shippingport PWR," *Zirconium in Nuclear Applications*, ASTM-STP-551, 1974, pp. 449-462.

4.15-27 W. R. Smalley, *Saxton Core II Fuel Performance Evaluation, Part I: Materials*, WCAP-3385-56, 1971.

4.15-28 W. R. Smalley, *Saxton Core III Fuel Materials Performance*, WCAP-3385-57, 1974.

4.15-29 J. V. Cathcart, *Quarterly Progress Report on the Zirconium Metal-Water Oxidation Kinetics Program Sponsored by the NRC Division of Reactor Safety Research for January-March 1976*, ORNL/NUREG/TM-17, May 1976.

4.15-30 J. V. Cathcart, *Quarterly Progress Report on the Zirconium Metal-Water Oxidation Kinetics Program Sponsored by the NRC Division of Reactor Safety Research for July-September 1976*, ORNL/NUREG/TM-62, December 1976.

4.15-31 L. Baker and L. C. Just, *Studies of Metal-Water Reactions at High Temperatures-III. Experimental and Theoretical Studies of the Zirconium Water Reaction*, ANL-6548, May 1962.

4.15-32 S. Malang, *SIMTRAN I-A Computer Code for the Simultaneous Calculation of Oxygen Distributions and Temperature Profiles in Zircaloy During Exposure to High Temperature Oxidizing Environments*, ORNL-5083, November 1975.

4.15-33 R. E. Pawel, "Diffusion in a Finite System with a Moving Boundary," *Journal of Nuclear Materials, 49*, January 1974, pp. 281-290.

4.15-34 R. A. Perkins, *Zirconium Metal Water Oxidation KineticsII, Oxygen-18 Diffusion in Beta Zircaloy*, ORNL/NUREG/TM-19, 1976, p. 33.

4.15-35 R. E. Pawel, R. A. Perkins, R. A. McKee, J. V. Cathcart, G. J. Yurek, and R. E. Druschel, "Diffusion of Oxygen in Beta-Zircaloy and the High Temperature Zircaloy Steam Reaction," *Zirconium in the Nuclear Industry*, ASTM-STP-663, 1977, pp. 119-133.

4.15.6 Bibliography

The following references contain information pertinent to zircaloy oxidation.

1. A. W. Lemmon, *Studies Relating to the Reaction Between Zirconium and Water at High Temperatures*, BMI-1154, 1957.

2. D. H. Bradhurst and P. M. Heuer, "The Influence of Oxide Stress on the Breakway Oxidation of Zircaloy-2," *Journal of Nuclear Materials, 37*, 1970, pp. 35-47.

3. D. O. Hobson and P. L. Rittenhouse, *Embrittlement of Zircaloy-Clad Fuel Rods by Steam During LOCA Transients*, ORNL-4758, January 1972.

4. R. E. Pawel, "Oxygen Diffusion in Beta Zircaloy During Steam Oxidation," *Journal of Nuclear Materials, 50*, 1974, pp. 247-258.

5. R. R. Biederman and W. G. Dobson, "A Study of Zircaloy-Steam Oxidation Reaction Kinetics," *Fifth Interim Progress Report*, Worchester Polytechnic Institute, January 16-April 15, 1976.

6. T. G. Odekirk, *Detailed Test Plan Report for PBF Test Series PCM-20: The Behavior of Unirradiated PWR Fuel Rods Under Power-Cooling-Mismatch Conditions*, ANCR-1095, April 1974.

7. A. W. Urquhart and D. A. Vermilyea, "Characterization of Zircaloy Oxidation Films," *Zirconium in Nuclear Applications*, ASTM-STP-551, 1974, pp. 463-478.

8. R. E. Pawel, *Zirconium Metal-Water Oxidation Kinetics III. Oxygen Diffusion in Oxide and Alpha Zircaloy Phases*, ORNL/NUREG-5, October 1976.

9. J. V. Cathcart, *Quarterly Progress Report on the Zirconium Metal-Water Oxidation Kinetics Program Sponsored by the NRC Division of Reactor Safety Research for July-September 1975*, ORNL-5148, December 1975.

10. J. V. Cathcart, *Quarterly Progress Report on the Zirconium Metal-Water Oxidation Kinetics Program Sponsored by the NRC Division of Reactor Safety Research for October-December 1975*, ORNL/TM-5248, March 1976.

11. J. V. Cathcart, *Quarterly Progress Report on the Zirconium Metal-Water Oxidation Kinetics Program Sponsored by the NRC Division of Reactor Safety Research for October-December 1976*, ORNL/NUREG/TM-87, February 1977.

12. R. R. Biederman and W. G. Dobson, "A Study of Zircaloy Steam Oxidation Reaction Kinetics," *Fourth Interim Progress Report*, Worchester Polytechnic Institute, October 1, 1975 - January 15, 1976.

13. G. Schanz and S. Leistikow, "Anwnedung und Experimentelle Überprüfung des Codes SIMTRAN-1 zur Beschreibung der Zircaloy Wasserdampf-HT-Oxidation," *Atomwirtschaft*, August 1976, pp. 409-410.

14. S. L. Seiffert and T. F. Cook, *Power-Cooling-Mismatch Test Series Test PCM-4 Postirradiation Examination*, NUREG/CR-02381, TREE-1230, July 1978.

15. D. L. Douglass, "Oxide Plasticity in the Oxidation Mechanism of Zirconium and its Alloys," *Corrosion Science, 5*, 1965, pp. 255-268.

16. H. M. Chung and T. F. Kassner, "Pseudobinary Zircaloy-Oxygen Phase Diagram," *Journal of Nuclear Materials, 84*, 1979, pp. 327-339.

17. E. A. Garcia, "Diffusion in a Semi-Infinite System with a Moving Interface at Constant Temperature for Application to a Zirconium Oxidation at High Temperature," *Journal of Nuclear Materials, 92*, 1980, pp. 249-256.

18. E. A. Garcia, "Diffusion in a Semi-Infinite Medium with a Moving Boundary During a Temperature Gradient," *Journal of Nuclear Materials, 96*, 1981, pp. 118-126.

19. A. Denis and E. A. Garcia, "Diffusion in a Semi-Infinite System with a Moving Interphase Considering Solvent Density Change: Application to the Oxidation of Zirconium," *Journal of Nuclear Materials, 96*, 1981, pp. 127-140.

20. G. Schanz and S. Leistikow, "ZrO_2-Scale Degradation During Zircaloy-4 High Temperature Steam Exposure; Microstructural Mechanisms and Consequences for PWR Safety Analysis," *Topical Meeting on Reactor Safety Aspects of Fuel Behavior, Sun Valley, ID, August 2-6, 1981.*

21. G. J. Yurek, J. V. Cathcart, and R. E. Pawel, "Microstructures of the Scales Formed on Zircaloy-4 in Steam at Elevated Temperatures," *Oxidation of Metals, 10*, 1976, pp. 255-276.

22. R. E. Pawel, J. V. Cathcart, and J. J. Campbell, "The Oxidation of Zircaloy-4 at 900 and 1,100^{o}C in High Pressure Steam," *Journal of Nuclear Materials, 82*, 1979, pp. 129-139.

23. R. E. Pawel, J. V. Cathcart and R. A. McKee, "'Anomalous' Oxide Growth During Transient-Temperature Oxidation of Zircaloy-4," *Oxidation of Metals, 14*, 1980, pp. 1-13.

24. R. E. Pawel, "Oxygen Diffusion in the Oxide and Alpha Phases During Reaction of Zircaloy-4 with Steam from 1,000 to 1,500^{o}C," *Journal of the Electrochemical Society, 126*, 1979, pp. 1111-1118.

25. R. E. Pawel and J. J. Campbell, "The Oxidation of Pure Zirconium in Steam from 1,000 to 1,416^{o}C," *Journal of the Electrochemical Society, 128*, 1981, pp. 1999-2005.

26. R. E. Pawel, J. V. Cathcart and R. A. McKee, "The Kinetics of Oxidation of Zircaloy-4 in Steam at High Temperature," *Journal of the Electrochemical Society, 126*, 1979, pp. 1105-1111.

27. R. E. Pawel and J. J. Campbell, "The Observation of Effects of Finite Specimen Geometry on the Oxidation Kinetics of Zircaloy-4," *Journal of the Electrochemical Society, 127*, 1980, pp. 2188-2194.

4.16 Cladding Hydrogen Uptake (CHUPTK)

This subroutine calculates the average weight fraction of hydrogen in zircaloy cladding during typical reactor operation at temperatures of 523 to 650 K. Required inputs are: as-received hydrogen concentration in the cladding, initial fuel water content, fuel pellet diameter, type of cladding (zircaloy-2 or zircaloy-4), cladding inside and outside diameters, type of reactor (BWR or PWR), oxide thickness at the start and end of the current time step, temperature at the oxide-coolant interface, heat flux, zirconium oxide thermal conductivity, and the average weight fraction of hydrogen in the cladding at the start of the current time step.

4.16.1 Summary

The average weight fraction of hydrogen in zircaloy cladding during steady state conditions is

$$H = H_o + H_1 + H_c \tag{4-314}$$

where

H = net weight fraction of hydrogen in the cladding (ppm)

H_o = initial concentration of hydrogen in the cladding due to impurities introduced during manufacturing and autoclaving (ppm). Typical values are 8 to 30 ppm[4.16-1,4.16-2]

H_1 = concentration of hydrogen in the cladding due to internal outgassing of water absorbed by the fuel (ppm)

H_c = concentration of hydrogen in the cladding due to absorption of hydrogen from the coolant (ppm).

H_o is an input parameter. H_1 is calculated by the routine using the input values for parts per million water vapor in the fuel, the input cladding dimensions, and the input fuel pellet diameter. CHUPTK assumes that all the hydrogen from the water vapor in the fuel is picked up by the cladding.

The primary consideration in determining H is the determination of H_c. Analytical expressions for H_c are divided into three parts: Equation (4-315) for oxide films thinner than the transition thickness,[a] Equation (4-316) for oxide films equal to the transition thickness at some point in the current time step, and Equation (4-317) for oxide films greater than the transition thickness during the current time step. In these equations, the variable H_c has been converted from a fraction of the oxide's oxygen increase to units of average parts per million by weight in the cladding.

$$H_{cf} = \left[\frac{(9\times10^5)\,d_o}{d_o^2 - d_i^2}\right]\frac{B}{8A}\,(X_f - X_i) + H_{ci} \tag{4-315}$$

$$H_{cf} = \left[\frac{(9\times10^5)\,d_o}{d_o^2 - d_i^2}\right]\left[\frac{B}{8A}\,(X_f - X_i) + \frac{C}{8A}\,(X_f - X_{TRAN})\right] + H_{ci} \tag{4-316}$$

$$H_{cf} = \left[\frac{(9\times10^5)\,d_o}{d_o^2 - d_i^2}\right]\frac{C}{8A}\,(X_f - X_{TRAN}) + H_{ci} \tag{4-317}$$

where

H_{cf} = weight fraction of hydrogen added to the cladding from the coolant at the end of the current time step (ppm by weight)

H_{ci} = weight fraction of hydrogen added to the cladding from the coolant at the start of the current time step (ppm by weight)

d_o = cladding outside diameter (m)

d_i = cladding inside diameter (m)

B = fraction of hydrogen liberated by the reaction with the coolant that is absorbed by the cladding during pretransition oxidation. The value of B is a function of the input parameters ICOR (BWR or PWR chemistry) and ICM (zircaloy-2 or zircaloy-4). Values of B for zircaloy-2 are 0.48 in a PWR environment and 0.29

a. Oxide film growth is discussed in conjunction with the description of the cladding oxidation subcode, CORROS. The terms pre- and post-transition refer to two different stages in the growth of the oxide film. A transition between the two stages occurs when the oxide film has added approximately 30 mg of oxide per dm^2 of oxide surface.

in a BWR environment. For zircaloy-4, B = 0.12

C	=	fraction of hydrogen liberated by the reaction with the coolant that is absorbed by the cladding during posttransition oxidation. The value of C is a function of the input parameter ICM (zircaloy-2 or zircaloy-4). The value of C for zircaloy-2 is 1.0. For zircaloy-4, C = 0.12
A	=	a parameter describing the enhancement of the oxidation rate of the cladding in the reactor environment. The parameter is discussed in conjunction with the description of the cladding oxidation subcode, CORROS. The value for A is determined in the subcode by user specification of BWR and PWR chemistry with the input parameter ICOR
X_i	=	oxide layer thickness at the start of the current time step (m)
X_f	=	oxide layer thickness at the end of the current time step (m)
X_{TRAN}	=	oxide layer thickness at the transition point (typically, 2×10^{-6} m). The value of X_{TRAN} is calculated by the CHUPTK subcode using the expression developed for CORROS (Section 4.15) and the input information.

The approach and general physical picture used to model hydrogen uptake are summarized in Section 4.16.2. Section 4.16.3 develops the basic out-of-pile model, and Section 4.16.4 generalizes the basic model so that it describes in-pile hydrogen uptake.

4.16.2 Background and Approach

It is generally agreed[4.16-3,4.16-4] that oxidation of zirconium alloys by water in the temperature range from 523 to 673 K proceeds by the migration of oxygen vacancies in the oxide layer. Change and physical size considerations imply that the mechanism of introduction of hydrogen into the zirconium metal through an oxide film is by entry of neutral hydrogen atoms into oxygen vacancies in the lattice. (H_2 is too large and H^+ is too positive.) The constant ratio of absorbed hydrogen to oxygen taken up by the cladding (the 'pickup fraction') is explained as having been determined by the competition between possible subsequent reactions of the atomic hydrogen created by corrosion. (The atomic hydrogen can combine to form a gas or enter a surface vacancy in the oxide lattice.)

In this approach, the close relationship between the hydrogen weight gain and the oxygen weight gain from the coolant is viewed as a consequence of the fact that the oxygen and hydrogen usually come from a common source (the water molecule) and are transported to the metal by a common carrier (oxygen vacancies). The hydrogen pickup fraction is determined by the composition of the coolant-oxide surface. In particular, it is suspected that nickel oxide from the nickel in zircaloy-2 absorbs atomic hydrogen at the surface of the oxide and thereby enhances the fractional hydrogen uptake for zircaloy-2.

4.16.3 Out of Pile Basis for the Model

The in-pile model is based primarily on out-of-pile data because well characterized data on hydrogen uptake as a function of time and temperature have been published only for out-of-pile corrosion. At least two plausible suggestions for a hydrogen uptake model can be presented from the approach discussed in Section 4.16.2. According to both of these suggestions, the dependent variable is the ratio of the corrosion

liberated hydrogen to oxygen absorbed by the metal, although the independent variables differ. A brief, summary of the two models, and a third less probable model, follows.

4.16.3.1 ***Simple Probabilistic Hydrogen Pickup Model.*** In this model, the fraction of released hydrogen absorbed by the oxide surface is assumed to be proportional to the rate of appearance of oxide vacancies at the oxide coolant interface. In the discussion of the cladding oxidation model, CORROS, it is shown that the vacancies appear at a rate proportional to the inverse of the square of the oxygen weight gain during the pretransition phase of oxidation. During the posttransition phase of oxidation, the surface averaged rate of appearance of oxide vacancies is constant and proportional to three times the inverse of the square of the weight of the oxide layer at transition. This model ignores any details of the surface chemistry involved in the absorption of atomic hydrogen by the oxide vacancies.

4.16.3.2 ***Surface-Controlled Hydrogen Pickup Model.*** In this model, the fraction of released hydrogen absorbed by the oxide surface is a constant determined by the metallurgy of the oxide surface. The model assumes that the effect of absorption of atomic hydrogen is dominant in the capture of hydrogen by the oxide film's outer surface.

4.16.3.3 ***Diffusion-Controlled Hydrogen Pickup Model.*** It is also conceivable that the time rate of hydrogen input into the metal is controlled by some as-yet-unconsidered independent diffusion process. In the case of diffusion-controlled hydrogen uptake, the net time rate of hydrogen pickup is proportional to the inverse thickness of the oxide layer.

The rate equations implied by the three alternate pictures are summarized in Table 4-50. Pretransition expressions were formulated simply by writing down the mathematical equivalent of the descriptions above. Posttransition expressions for the hydrogen pickup fraction were derived by replacing powers of X (proportional to the oxide thickness) in the pretransition expressions with powers of X averaged over a rate- determining oxide thickness that randomly varies from zero to the transition thickness of the oxide film. A discussion of the posttransition oxide film and this approach to describing posttransition rates is included in the description of the cladding oxidation subcode CORROS in Section 4.15.

When the three very different expressions for hydrogen uptake obtained with these models were integrated and compared with the pretransition data of Tables 7 and 9 of Reference 4.16-3, the pretransition data for zircaloy-2 and zircaloy-4 were found to conform best to the assumption that the rate is surface-controlled. The surface-controlled model is therefore used.

Comparison of experimental pretransition and posttransition hydrogen pickup fractions[4.15-3] for zircaloy-2 show that the posttransition rate is about twice the pretransition rate. For zircaloy-4, the pre- and post-transition rates are similar. The reason for this difference between zircaloy-2 and-4 is not well understood but may be related to the presence of nickel, which absorbs atomic hydrogen in zircaloy-2.

The simple surface-controlled hydrogen pickup model of Table 4-50 has, therefore, been modified slightly.

For pretransition,

$$\frac{dH}{dX} = \frac{B}{8} \quad . \tag{4-318}$$

For posttransition,

$$\frac{dH}{dX} = \frac{C}{8} \tag{4-319}$$

where B and C are determined by the oxide surface metallurgy of the particular alloy and 8 accounts for the different weights of hydrogen and oxygen in water so that dH/dX = 1/8 for complete pickup.

Table 4-50. Rate equations for hydrogen uptake.

Pretransition Rates	Posttransition
(1) Simple probabilistic pickup fraction determination	
$dH/dX = G/X^2$	$dH/dX = G/X^2_{ave} = 3G/X^2_{TRAN}$
(2) Surface-controlled pickup fraction determination	
$dH/dX = P$	$dH/dX = P$
(3) Diffusion-controlled time rate	
$dH/dX = Q/X$	$dH/dX = Q/X_{ave} = 2Q/X_{TRAN}$

Where

H = hydrogen weight gain(mg/dm^2)

X = oxygen weight gain (mg/dm^2, corresponds to oxide thickness)

t = time at temperature

X_{TRAN} = the transition weight of the oxide layer (mg/dm^2)

X^2_{ave} = the average of X^2 with values of X distributed at random between 0 and the transition thickness, X_{TRAN} (mg/dm^2)

X_{ave} = the space average of X with values of X distributed at random between 0 and the transition thickness (mg/dm^2)

G,P,Q = constants

4.16.4 Generalization to an In-Pile Model

Prediction of in-pile corrosion is complicated because important variables (local temperature and reactor chemistry) are not always reported and because data on the time-dependence of corrosion are limited. Enhancement of the hydrogen uptake factors by the reactor environment is treated by determining the value of the pickup fractions B and C for each reactor environment. Changes in the rate of hydrogen picked up caused by changes in the oxidation rate are described with the parameter A, which is discussed in conjunction with the oxidation model, CORROS. Thus, separate parameters are specified to describe the separate processes involved in determining the total rate of hydrogen uptake.

The basic equations for the fraction of hydrogen pickup with respect to the amount of oxygen pickup (dH/dX) are discussed at the end of Section 4.16.3 [Equations (4-318) and (4-319)]. Those equations reference out-of-pile oxidation. For in-pile pickup, the enhancement factor A must again be used. It is presumed that the effect that enhances the oxidation rate in the reactor does not enhance the rate of hydrogen uptake. Thus, the enhancement of the oxidation rate by a factor A will decrease the fractional hydrogen uptake by a factor 1/A.

The rate equations for in-pile oxidation and for fractional pickup of hydrogen are summarized in Equations (4-320) and (4-321) for both pre- and posttransition regimes.

For the pretransition in-pile regime,

$$\frac{dH}{dX} = \frac{B}{8} \ . \tag{4-320}$$

For the posttransition in-pile regime,

$$\frac{dH}{dX} = \frac{C}{8} \ . \tag{4-321}$$

Integration of Equations (4-320) and (4-321) and conversion of the integrated forms from weight gains to oxide thickness and parts per million hydrogen by weight leads to Equations (4-315) through (4-317).

An out-of-pile value of the parameter B has been determined in Reference 4.16-4 (from unpublished data) to be B = 0.33 for zircaloy-2. For zircaloy-4, a value of B = 0.12 was obtained from Figure 12 of Reference 4.16-3. The result is consistent with a value of 10% recommended by Reference 4.16-4.

When values of B were fit to the average hydrogen pickup values for the zircaloy-4 rods of the Saxton reactor,[4.16-5,4.16-6] an average value of B = 0.104 $\pm$ 0.04 was obtained. Thus, the out of pile determined value of B = 0.12 is apparently adequate for zircaloy-4 rods in PWRs. Since no data on zircaloy-4 cladding in a BWR are available, the PWR value, B = 0.12, is returned for the unlikely case of zircaloy-4 in a BWR. Values of B obtained by fitting the zircaloy-2 PWR hydrogen pickup reported in Reference 4.16-2 were B = 0.48 $\pm$ 0.07, while a fit to the BWR hydrogen pickup data on the zircaloy-2 rods of Reference 4.16-7 produced B = 0.29 $\pm$ 0.06. Since the PWR environment has an overpressure of hydrogen and it is known that hydrogen overpressures enhance the out-of-pile pickup fraction,[4.16-7] it is suggested that the difference in PWR and BWR values for B with zircaloy-2 is an effect of the different environments.

4.16.5 References

4.16-1 F. H. Megerth, C. P. Ruiz, and U. E. Wolff, *Zircaloy-Clad UO_2 Fuel Rod Evaluation Program*, GEAP-10371, June 1971.

4.16-2 E. Hillner, "Corrosion and Hydriding Performance of Zircaloy Tubing after Extended Exposure in the Shippingport PWR," *Zirconium in Nuclear Applications*, ASTM-STP-551, 1974, pp. 449-462.

4.16-3 E. Hillner, *Hydrogen Absorption in Zircaloy During Aqueous Corrosion, Effect of Environment,* WAPD-TM-411, November 1964.

4.16-4 A. VanderLinde, *Calculation of the Safe Life Time Expectancy of Zirconium Alloy Canning in the Fuel Elements of the Nero Reactor*, RCN-41, July 1965.

4.16-5 W. R. Smalley, *Saxton Core II Fuel Performance Evaluation, Part I: Materials*, WCAP-3385-56, July 1971.

4.16-6 W. R. Smalley, *Saxton Core III Fuel Materials Performance*, WCAP-3385-57, July 1974.

4.16-7 H. E. Williamson et al., *AEC Fuel Cycle Program Examination of UO_2 Fuel Rods Operated in the VBWR to 10,000 MWD/TU*, GEAP-4597, 1965.

4.17 Young's Modulus and Poisson's Ratio (CELMDR)

Subroutine CELMDR will return temperature dependent values for Young's modulus and a constant value of 0.30 for poisson's ratio. Subroutine CELMDR[4.17-1] does not account for fast neutron fluence, cold work, or oxygen concentration as does subroutine CELMOD. Young's modulus, Y (Pa), is calculated in the following manner:

If $T \leq 1090$ K,

$$Y = 1.088 \times 10^{11} - (5.47 \times 10^{7})\, T \quad . \tag{4-322}$$

If $1090\ K < T \leq 1240$ K,

$$Y = 4.912 \times 10^{10} - 4.827 \times 10^{7}\, (T - 1090) \quad . \tag{4-323}$$

If $1240\ K < T$,

$$Y = \text{maximum of} \begin{cases} 1.0 \times 10^{10} \\ 9.21 \times 10^{10} - (4.05 \times 10^{7})\, T \end{cases} \tag{4-324}$$

where,

T = Temperature (K).

4.17.1 References

4.17-1 D. L. Hagrman et al., *MATPRO-Version 11 (Revision 1), A Handbook of Materials Properties for Use in the Analysis of Light Water Reactor Fuel Rod Behavior*, NUREG/CR-0497, February

1980.

4.18 Zircaloy and Zirconium Heats of Fusion (PHYPRP)

The heat of fusion of zircaloy depends to some extent on its composition and the extent of oxidation. Brassfield[4.18-1] has suggested that the heat of fusion of zircaloy-4 differs little from that of zirconium and list the heat of fusion of zirconium as 20.5 kJ/mol. However, Quill[4.18-2] lists the heat of fusion of zirconium as 23 kJ/mol with uncertainty. The routine PHYPRP returns Brassfield's listed heat of fusion for zirconium of 2.25 x 10^5 J/kg.

4.18.1 References

4.18-1 H. C. Brassfield et al., *Recommended Property and Reactor Kinetic Data for Use in Evaluating a Light-Water-Coolant Reactor Loss-of-Coolant Incident Involving Zircaloy-4 or 304-SS-Clad UO_2*, GEMP-482, April 1968.

4.18-2 L. L. Quill, *Chemistry and Metallurgy of Miscellaneous Material, Thermodynamic, National Nuclear Energy Series, IV*, 19B, New York: McGraw-Hill Book Company, Inc., 1950.

4.19 Zirconium Transformation Temperature (PHYPRP)

Pure zirconium isothermally transforms from the α phase to the β phase at 1,135 K.[4.19-1] The routine PHYPRP returns 1,135.15 K for the zirconium transformation temperature when the variable, CTRANSZ, is called.

4.19.1 References

4.19-1 B. Lustman and F. Kerze, *The Metallurgy of Zirconium*, New York: McGraw-Hill Book Company, Inc., 1955.

5. ZIRCALOY OXIDES

The materials properties correlations needed for the oxides of the zircaloy fuel cladding formed at high temperatures were developed and are described in this section. The subcodes described in this section are for melting temperature (ZOPRP), specific heat capacity (ZOCP), enthalpy (ZONTHL), thermal conductivity (ZOTCON), thermal expansion (ZOTEXP), density (ZODEN), emissivity (ZOEMIS), elastic moduli (ZOEMOD, ZOPOIR), and mechanical limits and embrittlement (ZORUP).

5.1 Melting and Phase Transformation Temperatures (ZOPRP)

The subcode ZOPRP calculates the transition temperatures between the monoclinic, tetragonal, cubic, and liquid phases of zircaloy oxide. The oxygen-to-metal ratio of the oxide is the only required input to the subroutine. The monoclinic-to-tetragonal and tetragonal-to-cubic transition temperatures are constants that have been reported for ZrO_2 (1,478 and 2,558 K).[5.1-1] These temperatures are assumed to apply to zircaloy oxide, in spite of the fact that the oxide is slightly substoichiometric and may be under stress.

5.1.1 Model Development

Since atomic fraction oxygen in the zircaloy oxide compound is used as a basis to determine the solidus (appearance of the first liquid phase) and the liquidus (melting of the last solid phase) temperatures of the zircaloy oxide, the input oxygen-to-metal ratio is converted to atomic fraction using the following relationship:

$$x = \frac{YE}{(1 + YE)} \tag{5-1}$$

where

x	=	atomic fraction oxygen (atoms of oxygen/atoms of compound)
YE	=	oxygen-to-metal ratio in compound (atoms of oxygen/atoms of zirconium).

With a known atomic fraction oxygen for the zirconium oxide, the correlations developed for the PSOL and PLIQ subroutines described in Subsection 11.1 were used to calculate the solidus temperatures. These correlations are as follows:

For $x \leq 0.1$,

$$T_{sol} = 2{,}098 + 1{,}150 \quad . \tag{5-2}$$

For $0.1 < x \leq 0.18$,

$$T_{sol} = 2{,}213 \quad . \tag{5-3}$$

For $0.18 < x \leq 0.29$,

$$T_{sol} = 1{,}389.5317 + 7{,}640.0748\ x - 17{,}029.172\ x^2 \quad . \tag{5-4}$$

For $0.29 < x \leq 0.63$,

$$T_{sol} = 2{,}173 \quad . \tag{5-5}$$

For $0.63 < x \leq 0.667$,

$$T_{sol} = -11{,}572.454 + 21{,}818.181\ x \quad . \tag{5-6}$$

For $x > 0.667$,

$$T_{sol} = -11{,}572.454 + x(1.334 - x)\ 21{,}818.181 \quad . \tag{5-7}$$

where T_{sol} is the solidus temperature (K).

The liquidus temperatures are calculated using the following relationships:

For $x \leq 0.19$,

$$T_{liq} = 2{,}125 + 1{,}632.1637\ x - 5{,}321.6374\ x^2 \quad . \tag{5-8}$$

For $0.19 < x \leq 0.41$,

$$T_{liq} = 2{,}111.6553 + 1{,}159.0909\ x - 2{,}462.1212\ x^2 \quad . \tag{5-9}$$

For $0.41 < x \leq 0.667$,

$$T_{liq} = 895.07792 + 3{,}116.8831\ x \quad . \tag{5-10}$$

For $x > 0.667$,

$$T_{liq} = 895.07792 + (1.334 - x)\ 3{,}116.8831\ x \tag{5-11}$$

where T_{liq} is the liquidus temperature (K).

Figure 5-1 shows the zircaloy oxide solidus and liquidus temperatures as calculated by the subroutine for oxygen-to-metal ratios greater than 1.5.

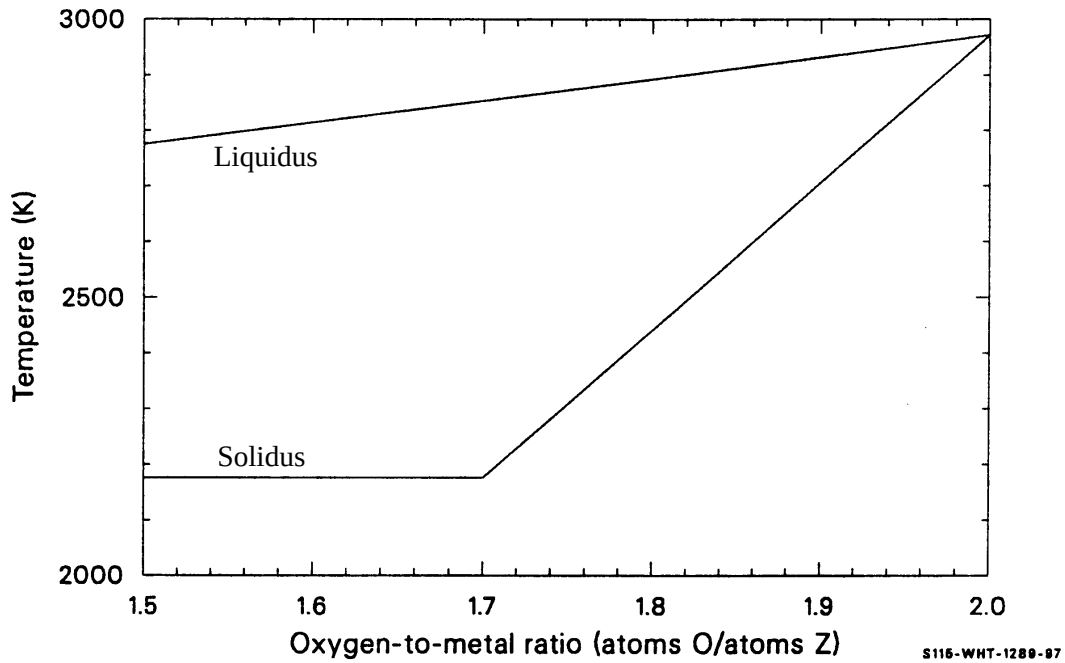

Figure 5-1. Zircaloy oxide solidus and liquidus temperatures.

5.1.2 References

5.1-1 R. R. Hammer, *Zircaloy-4, Uranium Dioxide and Materials Formed By Their Interaction. A Literature Review with Extrapolation of Physical Properties to High Temperatures*, IN-1093, September, 1967.

5.2 Specific Heat Capacity and Enthalpy (ZOCP, ZONTHL)

The functions ZOCP and ZONTHL return zircaloy oxide specific heat capacity and enthalpy. ZOCP requires only temperature as input, while the two enthalpy subcodes require temperature and a reference temperature for which the enthalpy will be set equal to zero.

5.2.1 Specific Heat (ZOCP)

Zircaloy oxide specific heat is modeled by the ZOCP function with the following expressions, which were taken from Reference 5.2-1:

For 300 < T < 1,478 K (monoclinic $Zr0_2$),

$$C_p^o = 565 + 6.11 \times 10^{-2}\, T - 1.14 \times 10^{7}\, T^{-2} \quad . \tag{5-12}$$

For $1{,}478 \leq T \leq 2{,}000$ K (tetragonal $Zr0_2$),

$$C_p^o = 604.5 \quad . \tag{5-13}$$

For $2{,}000 < T < 2{,}973$ K (tetragonal and cubic $Zr0_2$),

$$C_p^o = 171.7 + 0.2164\ T \quad . \tag{5-14}$$

For $T \geq 2{,}973$ K (liquid $Zr0_2$),

$$C_p^o = 815\ \text{J/kg}\bullet\text{K} \tag{5-15}$$

where

C_p^o	=	specific heat of zircaloy oxide (J/kg•K)
T	=	temperature (K).

The several equations correspond to the several phases of $Zr0_2$.

5.2.2 Enthalpy (ZONTHL)

Zircaloy oxide enthalpy is modeled in the ZONTHL function with the integrated version of Equations (5-13) through (5-15), estimates of the changes of enthalpies at the phase changes and an estimate of the heat of fusion of $Zr0_2$.[a]

For $300 < T < 1{,}478$ K (monoclinic $Zr0_2$),

$$H^0\ (T) - H^0\ (300) = 565\ T + 3.055 \times 10^{-2}\ T^2 + 1.14 \times 10^7\ T^{-1} - 2.102495 \times 10^5 \quad . \tag{5-16}$$

For $1{,}478 \leq T \leq 2{,}000$ K[a] (tetragonal $Zr0_2$),

$$H^0\ (T) - H^0\ (300) = 604.5\ T - 1.46 \times 10^5 \quad . \tag{5-17}$$

For $2{,}000 < T < 2{,}558$ K (tetragonal and cubic $Zr0_2$),

$$H^0\ (T) - H^0\ (300) = 171.7\ T + 0.1082\ T^2 + 2.868 \times 10^5 \quad . \tag{5-18}$$

---

a. Monoclinic to tetragonal transition ΔH = 48,200 J/kg; tetragonal to cubic transition ΔH = 102,000 J/kg; heat of fusion = 706,000 J/kg.

For $2{,}558 \leq T < 2{,}973$ K,

$$H^0(T) - H^0(300) = 171.7\,T + 0.1082\,T^2 + 3.888 \times 10^5 \quad . \tag{5-19}$$

For $T \geq 2{,}973$ K (liquid $Zr0_2$),

$$H^0(T) - H^0(300) = 815\,T + 1.39 \times 10^5 \tag{5-20}$$

where

$H^o(T)$	=	enthalpy of zircaloy oxide at temperature T (J/kg)
T	=	oxide temperature (K).

The principal contribution to the expected standard error of the enthalpy and specific heat capacity predictions for cladding oxide is not the uncertainty of the correlations for $Zr0_2$ because C_p measurements are typically accurate to several percent. It is the probability that the oxide film that appears on cladding differs significantly from the $Zr0_2$ used to produce the correlations. The oxide is substoichiometric and has enough stress from the volume expansion during oxidation to cause significant changes of the phase transition temperatures.[5.2-2] Therefore, a relatively large expected standard error of $\pm$ 0.2 times the given values is suggested for both the predicted specific heat capacity and enthalpy of zircaloy oxide.

The specific heat capacity predicted with the ZOCP function is shown in Figure 5-2. Comparison of the predicted specific heat capacity with data reported by Gilchrist,[5.2-3] which are reproduced in Table 5-1, suggests an expected standard error of $\pm$ 150 J/kg• K. Figure 5-3 is a plot of the zircaloy oxide enthalpy predicted with the ZONTHL function. The numerous steps are heats of transitions for the several phase changes of zircaloy dioxide.

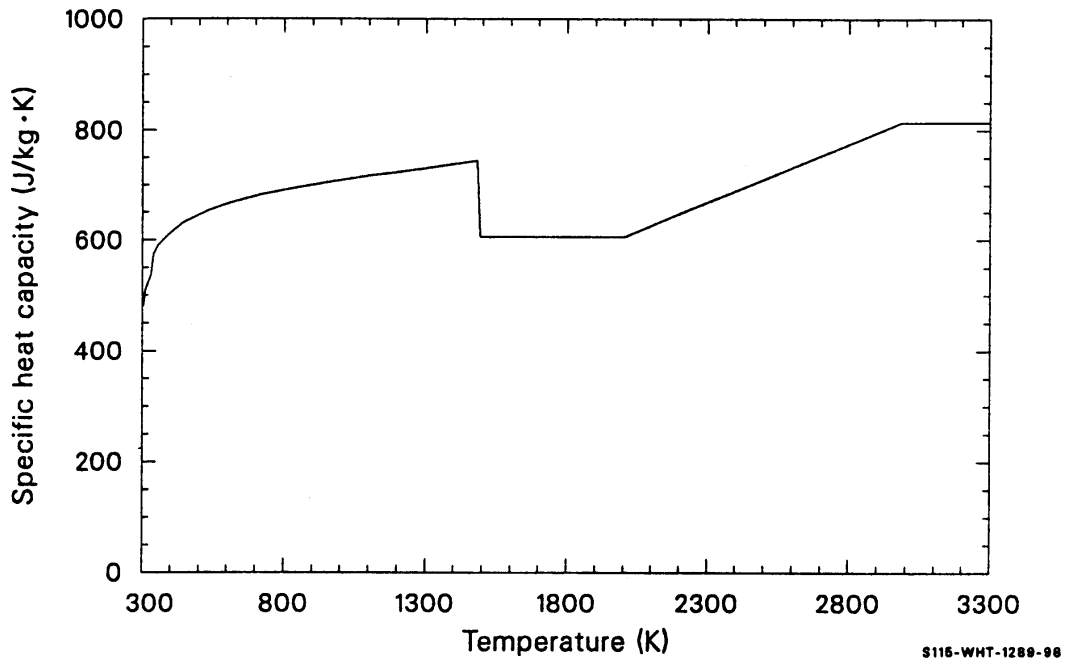

Figure 5-2. Zircaloy oxide specific heat capacity as a function of temperature.

5.2.3 References

5.2-1 R. R. Hammer, *Zircaloy-4, Uranium Dioxide, and Materials Formed by Their Interaction. A Literative Review with Extrapolation of Physical Properties to High Temperatures*, IN-1093, September 1967.

5.2-2 R. E. Pawel, J. V. Cathcart, J. J. Campbell, and S. H. Jury, *Zirconium Metal Water Oxidation Kinetics V. Oxidation of Zircaloy in High Pressure Steam*, ORNL/NUREG-31, December 1977.

5.2-3 K. E. Gilchrist, "Thermal Property Measurements on Zircaloy-2 and Associated Oxide Layers," *Journal of Nuclear Materials, 62*, 1976, pp. 257-264.

Table 5-1. Zircaloy cladding oxide specific heat capacity data from Gilchrist.[5.2-3]

Temperature	Specific Heat Capacity	Comment
324	462	Measured by Gilchrist
348	481	Measured by Gilchrist
377	486	Measured by Gilchrist

Table 5-1. Zircaloy cladding oxide specific heat capacity data from Gilchrist.[5.2-3] (Continued)

Temperature	Specific Heat Capacity	Comment
422	402	Measured by Gilchrist
462	510	Measured by Gilchrist
500	523	Measured by Gilchrist
598	543	Measured by Gilchrist
698	566	Measured by Gilchrist
801	569	Measured by Gilchrist
899	592	Measured by Gilchrist
945	598	Measured by Gilchrist
975	601	Measured by Gilchrist
1,004	603	Measured by Gilchrist
772	563	Measured by Smithells
373	437	Measured by Washburn
774	525	Measured by Washburn
1,272	631	Measured by Washburn
325	442	Reported by Gilchrist as data from "Thermophysical Properties of Solid Material"
399	486	Reported by Gilchrist as data from "Thermophysical Properties of Solid Material"
494	510	Reported by Gilchrist as data from "Thermophysical Properties of Solid Material"
598	535	Reported by Gilchrist as data from "Thermophysical Properties of Solid Material"
692	555	Reported by Gilchrist as data from "Thermophysical Properties of Solid Material"
790	576	Reported by Gilchrist as data from "Thermophysical Properties of Solid Material"
1,198	606	Reported by Gilchrist as data from "Thermophysical Properties of Solid Material"
1,398	612	Reported by Gilchrist as data from "Thermophysical Properties of Solid Material”

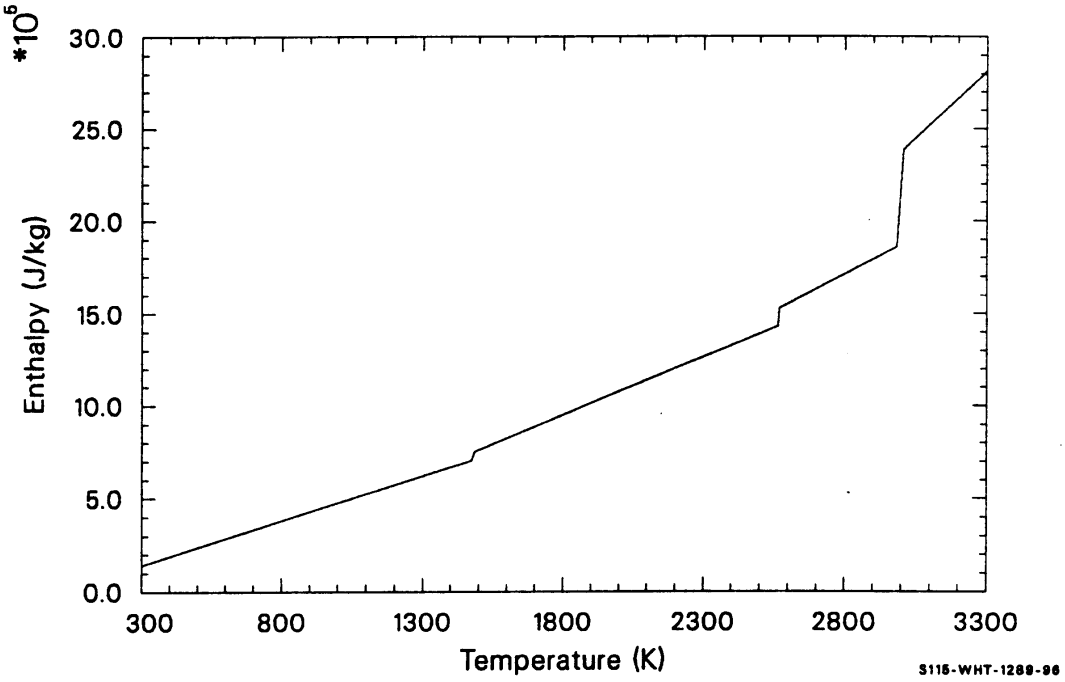

Figure 5-3. Zircaloy oxide enthalpy as a function of temperature.

5.3 Thermal Conductivity (ZOTCON)

The function ZOTCON returns zircaloy oxide thermal conductivity. The only input information required is the temperature of the material.

5.3.1 Model Development

To obtain an accurate value of zircaloy oxide thermal conductivity, accurate calculations of the peak cladding temperature during the rapid heating of cladding due to oxidation that occurs at high temperature are important. Data from the one sample that Adams reports[5.3-1] are presented in Table 5-2. Additional sources of data are Maki,[5.3-2] Lapshov and Bashkatov,[5.3-3] and Gilchrist.[5.3-4]

Data of Maki[5.3-2] from two samples oxidized in steam are reproduced in Table 5-3. The data cover a small temperature range and show a sharp increase in conductivity between 400 and 500 K. The principal recommendation for the data is that they were taken with black oxide from zircaloy tubes. Two sets of data attributed to Waldman by Maki are also shown in the table.

The data of Lapshov and Bashkatov[5.3-3] are presented in Table 5-4. These data are from films formed by plasma sputtering of zirconium dioxide on tungsten substrates. Since sputtered coatings are quite porous, not of the same oxygen-to-metal ratio as cladding oxide, and may not be very adherent to the substrate, these data may not be representative of zircaloy cladding oxide conductivity.

Table 5-54 presents the data of Gilchrist.[5.3-4] Two types of oxide films were employed, one nodular oxide and the other a black oxide characteristic of the kinds of layers usually reported in high temperature tests with cladding. The black oxide thermal conductivities are much lower than the nodular oxide thermal conductivities, and both kinds of oxide have conductivities that are significantly lower than the stabilized zircaloy dioxide conductivities reported by Adams. Considerable uncertainty is reported by Gilchrist because of difficulty in measuring oxide film thickness.

Table 5-2. Stabilized zircaloy dioxide thermal conductivity data from Adams.[5.3-1]

Temperature	Thermal Conductivity	Thermal Conductivity Corrected to 5820 kg/m
370	1.69	1.88
460	1.69	1.88
547	1.70	1.89
641	1.78	1.98
698	1.73	1.91
743	1.74	1.93
817	1.74	1.93
882	1.74	1.93
945	1.76	1.95
993	1.79	1.98
1,059	1.78	1.97
1,123	1.79	1.98
1,187	1.86	2.06
1,245	1.89	2.09
1,285	1.95	2.16
1,305	1.92	2.13
1,329	1.93	2.14
1,338	1.94	2.15
1,354	1.96	2.17
1,390	1.96	2.18
1,405	1.99	2.20
1,427	1.98	2.19

Table 5-2. Stabilized zircaloy dioxide thermal conductivity data from Adams.[5.3-1] (Continued)

Temperature	Thermal Conductivity	Thermal Conductivity Corrected to 5820 kg/m
1,440	2.02	2.24
1,448	2.08	2.31
1,480	2.01	2.23
1,485	2.03	2.25
1,505	2.01	2.23
1,554	2.01	2.23
1,566	2.02	2.24
1,583	2.01	2.23

Table 5-3. Zircaloy oxide thermal conductivity data reported by Maki.[5.3-2]

Outside Temperature	Thermal Conductivity	Comment
401	0.70	Sample 4
434	4.78	Sample 4
488	6.35	Sample 4
536	5.41	Sample 4
588	5.45	Sample 4
400	1.07	Sample 5
437	4.50	Sample 5
490	5.76	Sample 5
536	6.11	Sample 5
589	6.27	Sample 5
373	0.90	Data from Waldman
373	1.35	Data from Waldman

Table 5-4. Zircaloy dioxide thermal conductivity data of Lapshov and Bashkatov.[5.3-3]

Temperature (K)	Thermal Conductivity
571	0.509
618	0.636
642	0.508
654	0.627
664	0.715
684	0.474
721	0.652
739	0.448
755	0.441
771	0.558
802	0.430
817	0.512
827	0.605
855	0.456
882	0.522
929	0.477
969	0.506
984	0.509
999	0.509
1,006	0.472
1,050	0.509
1,071	0.522
1,088	0.493
1,097	0.587
1,104	0.527
1,162	0.563

Table 5-4. Zircaloy dioxide thermal conductivity data of Lapshov and Bashkatov.[5.3-3] (Continued)

Temperature (K)	Thermal Conductivity
1,189	0.636
1,201	0.577
1,220	0.555
1,250	0.623
1,302	0.623
1,354	0.577
1,366	0.661
1,380	0.663
1,491	0.708
1,527	0.656
1,558	0.717
1,626	0.801
1,638	0.776
1,685	0.788
1,735	0.854

Table 5-5. Zircaloy oxide thermal conductivity data of Gilchrist.[5.3-4]

Temperature	Thermal Conductivity	Comment
297	1.354	Black oxide
668	0.955	Black oxide
712	0.958	Black oxide
806	1.048	Black oxide
854	1.060	Black oxide
916	1.090	Black oxide
983	1.163	Black oxide
1,043	1.242	Black oxide

Table 5-5. Zircaloy oxide thermal conductivity data of Gilchrist.[5.3-4] (Continued)

Temperature	Thermal Conductivity	Comment
1,193	1.443	Black oxide
1,260	1.407	Black oxide
1,327	1.393	Black oxide
1,386	1.487	Black oxide
1,450	1.586	Black oxide
299	0.324	Nodular oxide
659	0.137	Nodular oxide
733	0.160	Nodular oxide
806	0.192	Nodular oxide
867	0.219	Nodular oxide
944	0.271	Nodular oxide
1,018	0.410	Nodular oxide
1,141	0.606	Nodular oxide
1,222	0.825	Nodular oxide
1,246	0.864	Nodular oxide
1,326	0.743	Nodular oxide
1,425	0.700	Nodular oxide

Figure 5-4 is a plot of the data in Tables 5-2 through 5-5. The plot shows that, with the exception of the anomalously high data of Maki, the principal uncertainty in thermal conductivity is caused by sample-to-sample variations. Measurement inaccuracies with any one sample are much smaller than sample-to-sample variations. It is also clear from an inspection of Figure 5-4 that the slopes of the measurements on individual samples are quite consistent. The difference between the various samples is essentially a displacement of a line with a constant slope.

The slope of the thermal conductivity of a given sample was determined with a least-squares linear fit to the data of Adams. These data were used because they extend over a large temperature range and were made with the most accurate experimental technique. The equation which results from this fit is

$$K_{ZrO_2} = 1.67 + 3.62 \times 10^{-4}\ T \qquad (5\text{-}21)$$

where K_{ZrO_2} is zircaloy dioxide thermal conductivity (W/m•K).

Since the black oxide data of Gilchrist are the most representative of the oxide found on cladding, Equation (5-21) is modified for zircaloy oxide by dividing the right hand side by two. The resultant expression is

$$K_o = 0.835 + 1.81 \times 10^{-4}\ T \qquad (5\text{-}22)$$

where K_o is zircaloy cladding oxide thermal conductivity (W/m•K).

Values of K_{ZrO_2} and K_o calculated with Equations (5-21) and (5-22) are shown with the data in Figure 5-4. Inspection of the figure suggests an expected standard error of + 0.75 of the measured value for K_o. For material that is known to be ZrO_2, the expected standard error is much less, approximately 10% of the value of K_{ZrO_2}.

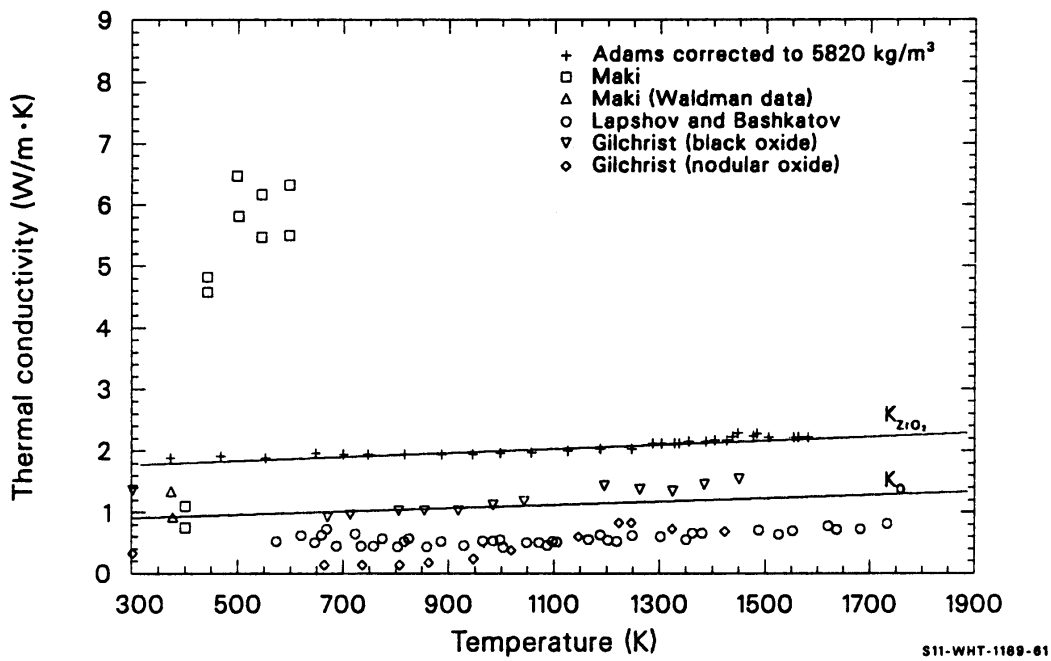

Figure 5-4. Zircaloy oxide thermal conductivity data and correlations.

For liquid zircaloy oxide (temperature > 2,973 K), the conductivity is assumed to be approximately the value of K_o at the melting temperature of ZrO_2:

$$K_{o(liquid)} = 1.4\ \text{W/m•K}\ . \qquad (5\text{-}23)$$

This number is a compromise between the decrease in conductivity at melt due to the loss of the phonon contribution and the increase in conductivity at melt due to the loss of porosity.

Figure 5-5 is a plot of the thermal conductivity predicted by the function ZOTCON as a function of temperature.

5.3.2 References

5.3-1 M. Adams, Thermal Conductivity: III, Prolate Spheroidal Envelope Method," *Journal of the American Ceramic Society, 37*, 1954, pp. 74-79.

5.3-2 H. Maki, "Heat Transfer Characteristics of Zircaloy-2 Oxide Film," *Journal of Nuclear Science and Technology, 10*, 1973, pp. 107-175.

5.3-3 V. N. Lapshov and A. V. Bashkatov, "Thermal Conductivity of Coatings of Zirconium Dioxide Applied by the Plasma Sputtering Method," *Heat Transfer, Soviet Research, 5*, 1973, pp. 19-22.

5.3-4 K. E. Gilchrist, "Thermal Property Measurements on Zircaloy-2 and Associated Oxide Layers, *Journal of Nuclear Materials, 62*, 1976, pp. 257-264.

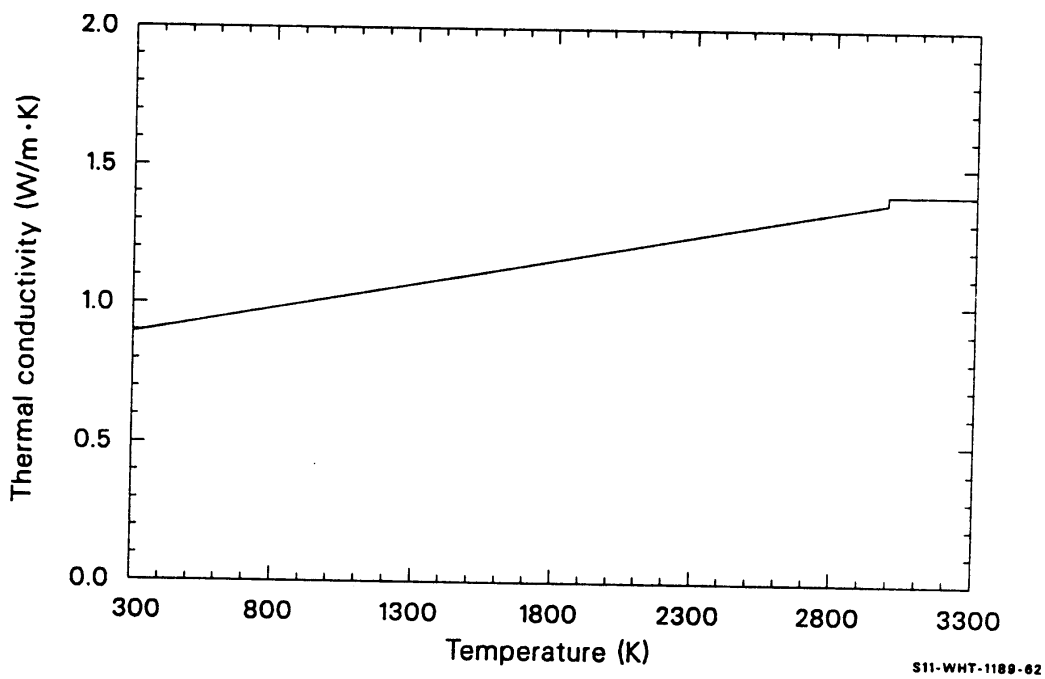

Figure 5-5. Zircaloy oxide thermal conductivity as a function of temperature.

5.4 Surface Emissivity (ZOEMIS)

One of the important modes of heat transfer to and from cladding surfaces during an abnormal transient is radiant heat transfer. Since the energy radiated is directly proportional to the emissivity of the inner and outer cladding surfaces, surface emissivity is important in descriptions of abnormal transients.

5.4.1 Summary

Surface emissivities are significantly affected by surface layers on the cladding. For cladding with thin oxide coatings, the oxide surface thickness is only a few wavelengths of near infrared radiation and is partly transparent. Oxide thickness is an important parameter for these thin coatings. Thicker oxide layers are opaque, so the oxide thickness is not as important as the nature of the outer oxide surface, which is affected by temperature and by chemical environment. The effect of temperature has been modeled, but variations in crud on the external cladding surface and chemical reaction products on the inside surface are not modeled explicitly.

The model for emissivity was constructed by considering measured emissivities reported by several investigators.[5.4-1,5.4-2,5.4-3] Expressions used to predict the emissivity of zircaloy cladding surfaces are summarized below.

When the cladding surface temperature has not exceeded 1,500 K, emissivities are modeled by Equations (5-24) and (5-25). For oxide layer thicknesses less than 3.88×10^{-6} m,

$$\varepsilon_1 = 0.325 + 0.1246 \times 10^6 \, d \quad . \tag{5-24}$$

For oxide layer thicknesses of 3.88×10^{-6} m or greater,

$$\varepsilon_1 = 0.808642 - 50.0 \, d.^{a} \tag{5-25}$$

where

ε_1	=	hemispherical emissivity (unitless)
d	=	oxide layer thickness (m).

When the maximum cladding temperature has exceeded 1,500 K, emissivity is taken to be the larger of 0.325 and

$$\varepsilon_2 = \varepsilon_1 \exp\left[\frac{1500 - T}{300}\right] \tag{5-26}$$

where

ε_1	=	value for emissivity obtained from Equation (5-24)
T	=	maximum cladding temperature (K).

The standard error expected from the use of Equation (5-24) to predict emissivity in a reactor when cladding surface temperature has never exceeded 1,500 K is

---

a. The use of six significant figures in Equation (5-25) ensures an exact match of the values of ε_1 at $d = 3.88 \times 10^{-6}$ m.

$$\sigma_1 = \pm 0.1 \quad . \tag{5-27}$$

When cladding temperature has exceeded 1,500 K, the expected standard error is estimated by σ_2 in the expression

$$\sigma_2 = \pm 0.1 \exp\left[\frac{T - 1500}{300}\right] \tag{5-28}$$

If Equations (5-26) and (5-28) predict values of $\varepsilon_2 \pm \sigma_2$ that fall inside the range of physically possible values of emissivity (0.0-1.0), the value σ_2 is returned as the expected standard error. If the prediction $\varepsilon_2 + \sigma_2$ is greater than 1 or if $\varepsilon_2 - \sigma_2$ is less than 0, the standard error of Equation (5-28) is modified to limit $\varepsilon_2 + \sigma_2$ at 1 and/or $\varepsilon_2 - \sigma_2$ at 0.

The following subsection is a review of the available data on cladding emissivity. The approach used to formulate the model for emissivity is described in Section 5.4.3, and Section 5.4.4 is a discussion of the uncertainty of the model for cladding emissivity.

5.4.2 Literature Review

Measurements of zircaloy-2 emissivities as a function of temperature and dissolved oxygen content were reported by Lemmon.[5.4-1] The measurements utilized the hole-in-tube method and were carried out in vacuum. Data from samples with an oxide film were reported, but the nonoxidizing environment of the sample during emissivity measurements caused the emissivity to change with time. Moreover, the thicknesses of the oxide films were not reported. The Lemmon data were not used in formulating the ZOEMIS subcode because the unknown oxide thickness probably influenced the emissivity and because of complications caused by the vacuum environment.

The emissivity of zircaloy-4 was reported by Juenke and Sjodahl[5.4-2] from measurements on oxidized zircaloy in vacuum and from measurements in steam during the isothermal growth of oxide films. These authors reported a decrease in the emissivity measured in vacuum, which they attributed to the formation of a metallic phase in the oxide. This metallic phase did not form in the presence of steam. The data taken in steam were used in constructing ZOEMIS because the steam environment is similar to an abnormal reactor environment.

Figure 5-6 is a reproduction of the Juenke and Sjodahl steam data. The data suggest that emissivity decreases when oxide films become very thick (long times or high temperatures). In fact, Juenke and Sjodahl expect the total emissivity of very thick films to approach 0.3 or 0.4, which is characteristic of pure ZrO_2. However, the decrease in emissivity at temperatures greater than about 1,200°C is greater than one would predict from oxide layer thickness alone. The correlation of this emissivity data with oxide layer thickness is discussed in Section 5.4.3.

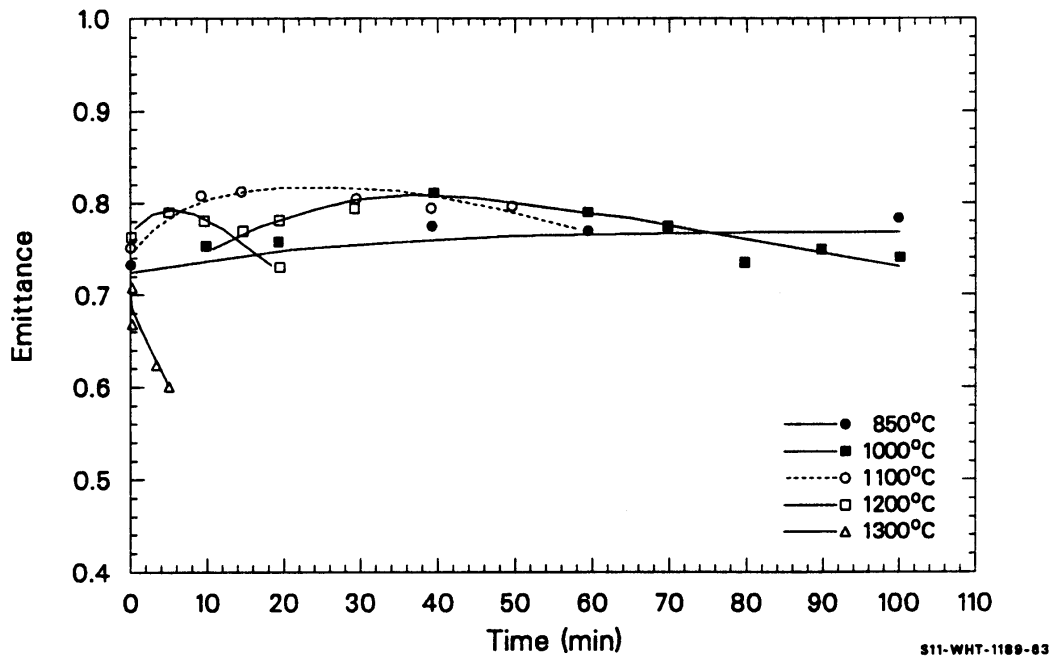

Figure 5-6. Total hemispherical emittance of zircaloy-4 versus time at temperature in steam.

Juenke and Sjodahl do not include very thin oxide films but do report that the total emittance rises almost instantaneously from about 0.2 to 0.7 with the introduction of steam. Data relevant to thin films are discussed below.

The emissivity of oxide films measured in air at temperatures in the range 100 to 400°C were reported by Murphy and Havelock[5.4-3] and are reproduced in Table 5-6. The emissivities are not strongly dependent on temperature but do increase rapidly with oxide thickness for the thin oxide layers measured. The one value of emissivity measured with an oxide thickness of 94 x 10^{-6} m is important because the oxide was approximately 30 times the thickness associated with the transition from black oxide layers to white oxide layers. The emissivity of this oxide, described as white by the authors, has a measured emissivity characteristic of surfaces which are black in the infrared region of the spectrum. Since (a) the Murphy and Havelock data were taken in an oxidizing environment and (b) the emissivity of the 94 x 10^{-6} m oxide film agrees with the emissivity of films measured in steam, all of the Murphy and Havelock data were used in the formulation of ZOEMIS.

Additional data were reported by Burgoyne and Garlick at the OECD-CSNI meeting on the Behavior of Water Reactor Fuel Elements under Accident Conditions in Spinad, Norway, on September 13-16, 1976. Using a hot filament calorimeter, these authors measured the emissivity of zircaloy-2 cladding surfaces coated with uniform oxide, nodular oxide, and crud. The emissivities were measured in vacuum. However, the following arguments are presented in favor of including some of these data in the data base of ZOEMIS: (a) a significant decrease in emissivity was not noticed with initial oxide thicknesses greater than 10^{-5} m until the samples were heated above approximately 800°C (the alpha beta phase transition of zircaloy); and (b) the low temperature values of emissivity data taken with nodular and crud coated sur-

faces are representative of in-reactor surfaces not represented in other data. Data from Burgoyne and Garlick that did not show the sudden decrease in emissivity characteristic of the change caused by a vacuum environment were used in ZOEMIS. Table 5-7 is a summary of the measurements used..

Table 5-6. Emissivity of thin oxide films as reported by Murphy and Havelock.

		Emissivity				
Surface Condition	**Oxide Thickness (μm)**	**100°C**	**150°C**	**200°C**	**300°C**	**400°C**
Pickled + 2 days in air at 400°C	0.9	0.424	0.414	0.416	0.434	0.433
Pickled + 10 days in air at 400°C	1.48	0.521	0.542	0.557	0.588	--
Pickled + 55 days in 400°C steam under a pressure on 10.4 MPa	2.3	--	0.582	0.599	0.620	--
Pickled + 30 days in air at 400°C + 73 days in air at 500°C	94	--	0.748	--	--	--

Table 5-7. Emissivity data from Burgoyne and Garlick.

Cladding Surface	Surface Layer Thickness (μm)	Measurement Temperature (K)	Emissivity (unitless)
Uniform oxide	10	735	0.748
	10	805	0.770
	10	876	0.773
	10	885	0.773
	10	978	0.774
	10	986	0.767
	10	1,072	0.791
Uniform oxide	28	784	0.834
	28	884	0.818
	28	987	0.832
	28	1,080	0.829
Nodular oxide	130	654	0.860

Table 5-7. Emissivity data from Burgoyne and Garlick. (Continued)

Cladding Surface	Surface Layer Thickness (μm)	Measurement Temperature (K)	Emissivity (unitless)
	130	769	0.845
	130	775	0.857
	130	868	0.849
	130	885	0.850
	130	965	0.849
	130	975	0.837
	130	1,066	0.866
	130	1,149	0.841
Crud	35	677	0.918
	35	683	0.930
	35	769	0.890
	35	777	0.888
	35	870	0.899
	35	876	0.888
	35	966	0.913
	35	977	0.903

5.4.3 Model Development

Near infrared radiation has a wavelength of 1×10^{-6} m. Oxide films up to a few wavelengths thick should be partly transparent to infrared radiation and should therefore have emissivities strongly dependent on oxide thickness. The emissivity versus oxide thickness data of Murphy and Havelock[5.4-3] were fit with standard least-squares residual analysis to deduce Equation (5-24).

The equation for the emissivity of oxide films thicker than 4×10^{-6} m is based on the data of Burgoyne and Garlick, Juenke and Sjodahl,[5.4-2] and one measurement from Murphy and Havelock,[5.4-3] as discussed in Section 5.4.2. Oxide thicknesses were calculated from the time and temperatures reported by Juenke and Sjodahl using the correlation published by Cathcart.[5.4-4]

$$X = [2.25 \times 10^{-6} \exp(-18{,}063/T)t]^{1/2} \qquad (5\text{-}29)$$

where

X = the oxide layer thickness (m)

T = temperature (K)

t = time at temperature (s).

Table 5-8 lists the emissivity, time, and temperature reported by Juenke and Sjodahl, together with the oxide thickness predicted using Equation (5-29). Values of emissivity and oxide layer thickness from Tables 5-6 through 5-8 were used to establish Equation (5-25).

Figure 5-7 is a comparison of the curves generated by Equations (5-24) and (5-25) with the data base used to derive these equations. Predicted values of emissivity increase rapidly until the surface oxide layer thickness is 3.88×10^{-6} m, then decrease very slowly with increasing surface layer thickness.

Table 5-8. Emissivity versus oxide thickness from Juenke and Sjodahl's data.

Temperature (K)	Time (s)	Calculated Oxide Thickness μm	Measured Emissivity (unitless)
1,125	1,200	17	0.755
1,125	2,400	24	0.755
1,125	6,000	38	0.785
1,275	600	31	0.750
1,275	1,200	43	0.773
1,275	1,800	53	0.795
1,275	3,600	75	0.790
1,275	4,200	81	0.775
1,275	4,800	86	0.738
1,275	5,400	92	0.755
1,275	6,000	96	0.740
1,375	600	51	0.808
1,375	900	63	0.815
1,375	1,200	72	0.780
1,375	3,000	114	0.798
1,375	3,600	125	0.775
1,475	300	57	0.795
1,475	600	80	0.780
1,475	900	98	0.775
1,475	1,200	113	0.722

Table 5-8. Emissivity versus oxide thickness from Juenke and Sjodahl's data. (Continued)

Temperature (K)	Time (s)	Calculated Oxide Thickness μm	Measured Emissivity (unitless)
1,575	210	70	0.620
1,575	300	83	0.600

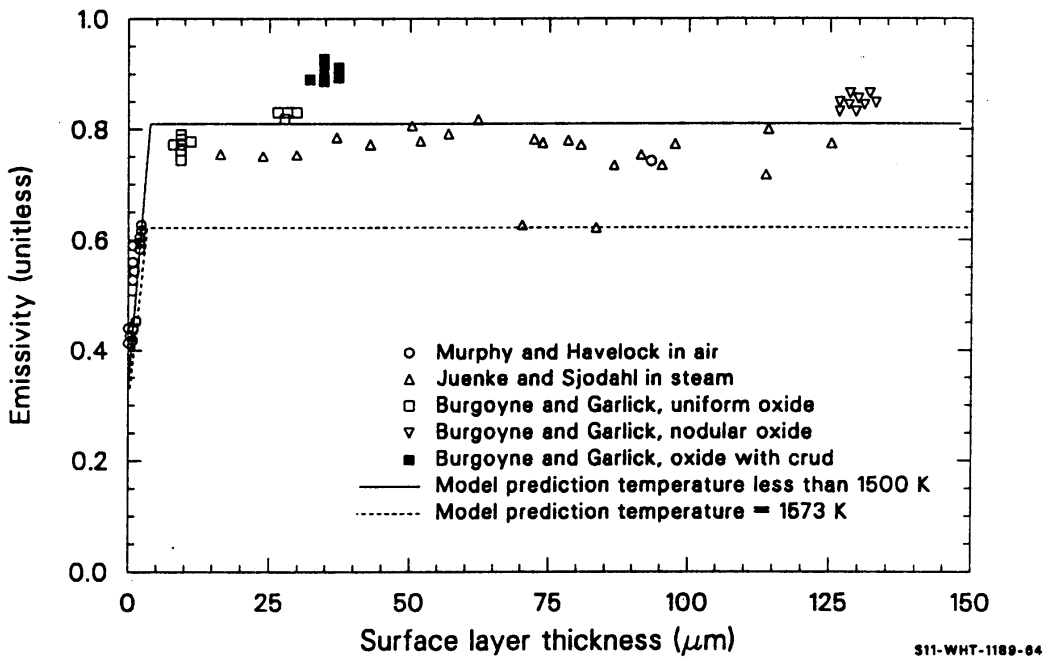

Figure 5-7. ZOEMIS calculations compared with the data base of the model.

The values of emissivity measured by Juenke and Sjodahl at 1,575 K (0.62 and 0.60) are significantly below the measured emissivities at lower temperatures. Since thicker oxide films were formed at lower temperatures, the low emissivity is not due to the thickness of the oxide film. Moreover, the low values of emissivities measured by Juenke and Sjodahl at high temperature are supported by posttest observations of cladding surfaces that have been at high temperatures.[5.4-5] Cladding surfaces that experienced film boiling, and therefore high temperatures, showed spalled oxide and somewhat whiter oxide surfaces in the region of the film boiling. The observations reported (Reference 5.4-5) and the trend toward lower values of emissivity at higher temperatures reported by Juenke and Sjodahl at 1,475 and 1,575 K imply that lower cladding surface emissivities are likely at temperatures above approximately 1,500 K. This trend in the limited data has been included in ZOEMIS by (a) adding a multiplicative factor to the expression for emissivity,

$$\exp[(1500 - T)/300] \tag{5-30}$$

where T is the greater of 1,500 K and the maximum cladding temperature, and (b) limiting the minimum emissivity to 0.325, the value predicted by the model for zero oxide thickness.

5.4.4 Uncertainty

The standard errors obtained with Equations (5-24) and (5-25) and the data base used to develop these equations are listed in Table 5-9.

Standard errors shown in Table 5-9 for oxide layers without the complicating features of nodular oxides or surface crud are consistent with measurement errors of $\pm$3% estimated by Lemmon.[5.4-1] However, the model is intended to predict the emissivity of cladding surfaces with crud or UO_2 fission products as well as the oxide layer. The data from Burgoyne and Garlick (illustrated in Figure 5-7) suggest that crud layers introduce a systematic error of approximately $\pm$0.1. The value of $\pm$0.1 is therefore included in ZOEMIS as the best estimate for the standard error of the model prediction for emissivity during abnormal reactor operation at temperatures below 1,500 K.

Table 5-9. Standard errors of ZOEMIS predictions.

Surface Description	Standard Error
Oxide films < 3.88×10^{-6} m	$\pm$ 0.04
Pure oxide films > 3.88×10^{-6} m	$\pm$ 0.05
Oxide films including samples with nodular oxides and crud	$\pm$ 0.07

The uncertainty of the prediction for emissivities above 1,500 K is difficult to estimate. Equation (5-28) was selected as a reasonable expression for the expected standard error of Equation (5.4-3), simply because the expression $\pm$0.1 exp{-(1,500 - maximum cladding temperature)/300] predicts a standard error approximately equal to the change in emissivity caused by the empirical multiplicative factor of Equation (5-30).

In Figure 5-8, the data base and model predictions shown in Figure 5-7 are repeated. The standard error expected with ZOEMIS for temperatures below 1,500 K is shown by the cross-hatched area centered on the solid line. The cross-hatched area centered on the dashed line shows the standard error estimated for temperatures of 1,573 K.

5.4.5 References

5.4-1 A. W. Lemmon, Jr., *Studies Relating to the Reaction Between Zirconium and Water at High Temperatures*, BMI-1154, January 1957.

5.4-2 E. F. Juenke and L. H. Sjodahl, "Physical and Mechanical Properties: Emittance Measurements," *AEC Fuels and Materials Development Program*, GEMP-1008, 1968, pp. 239-242.

5.4-3 E. V. Murphy and F. Havelock, "Emissivity of Zirconium Alloys in Air in the Temperature Range 100-400°C," *Journal of Nuclear Materials, 60*, 1976, pp. 167-176.

5.4-4 J. V. Cathcart, *Quarterly Progress Report on the Zirconium Metal Water Oxidation Kinetics Program Sponsored by the NRC Division of Reactor Safety Research for April-June 1976*, ORNL/NUREG-TM-41, August 1976.

5.4-5 *Quarterly Technical Progress Report on Water Reactor Safety Programs Sponsored by the Nuclear Regulatory Commission's Division of Reactor Safety Research. October-December 1975*, ANCR-NUREG-1301, May 1976, p. 67.

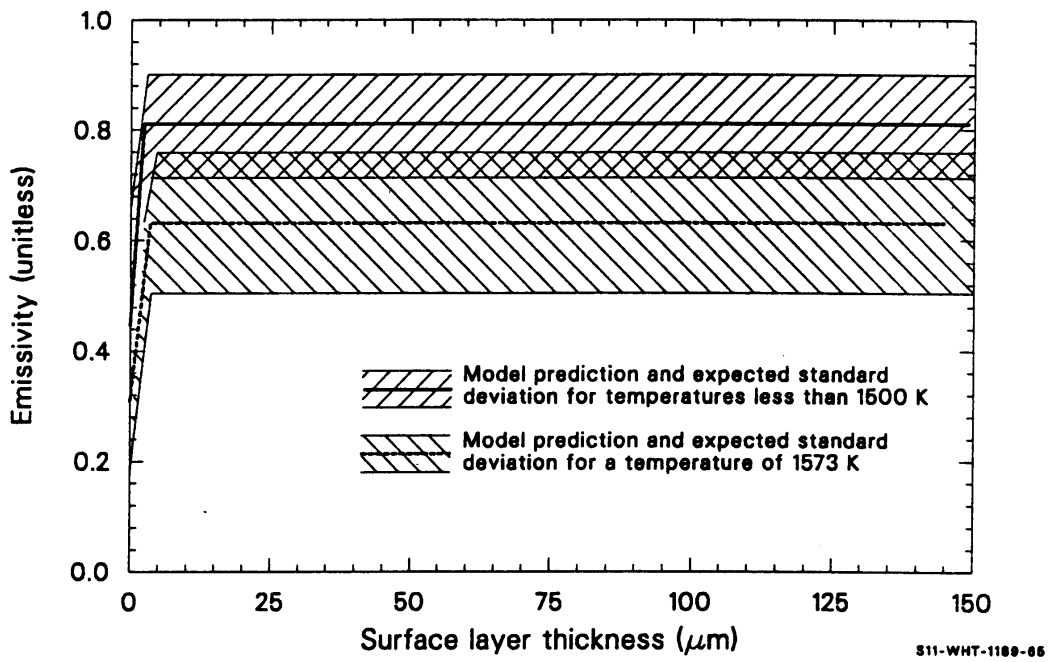

Figure 5-8. Expected standard errors of emissivity for temperatures below 1,500 K and at 1,573 K.

5.5 Thermal Expansion and Density (ZOTEXP, ZODEN)

The subroutine ZOTEXP calculates the zircaloy oxide thermal strain, using a reference temperature for which the thermal strain will be zero and the zircaloy oxide temperature. The subroutine ZODEN calculates the zircaloy oxide density from the zircaloy oxide temperature.

5.5.1 Thermal Expansion (ZOTEXP)

Expressions used in ZOTEXP to calculate the thermal strains of solid zirconium oxide are taken from Hammer:[5.5-1]

For 300 < T < 1,478 K (monoclinic $Zr0_2$),

$$\varepsilon_0 = 7.8 \times 10^{-6}\, T - 2.34 \times 10^{-3} \quad . \tag{5-31}$$

For 1,478 ≤ T < 2,973 K (tetragonal and cubic $Zr0_2$),

$$\varepsilon_0 = 1.302 \times 10^{-5}\ T - 3.338 \times 10^{-2} \tag{5-32}$$

where ε_0 is the linear thermal strain of zircaloy oxide(m/m). These expressions show a 7.7% decrease in volume at the monoclinic tetragonal phase change (1,478 K).

For liquid zirconium oxide, a 5% reduction in volume is assumed when the oxide melts. This assumption corresponds to the assumption that the 5% porosity of the oxide is removed when it melts. The resultant expression is

$$\varepsilon_0 = -1.1 \times 10^{-2}, \tag{5-33}$$

for $T \geq 2{,}973$ K.

5.5.2 Density (ZODEN)

Thermal expansion Equations (5-31) through (5-33) are used in ZODEN to calculate the density of zircaloy oxide. The relation employed is

$$\rho_x = \rho_{xo}\ (1 - 3\varepsilon_0) \tag{5-34}$$

where

ρ_x = zirconium oxide density at the given temperature (kg/m^3)

ρ_{xo} = zirconium oxide density at 300 K (kg/m^3).

The value of ρ_{xo} used is the density of black oxide reported by Gilchrist,[5.5-2] 5,800 kg/m^3.

The expected standard error of Equations (5-31) and (5-32) is large, the greater of half the predicted value or $\pm$ 5 x 10^{-3}, because the equations are based on zircaloy dioxide data. The cladding oxide is not only substoichiometric but is formed under large stress because of the different densities of the oxide and the zircaloy on which it is formed.

The zircaloy dioxide thermal strains predicted by ZOTEXP are shown in Figure 5-9, and the density of the oxide predicted by ZODEN is illustrated in Figure 5-10. $Zr0_2$ thermal expansion data by Fulkerson[5.5-3] and from pages 17 and 70 of Brassfield et al.[5.5-4] are listed in Tables 5-10 and 5-11 and included in Figure 5-11 so that they may be compared with code predictions.

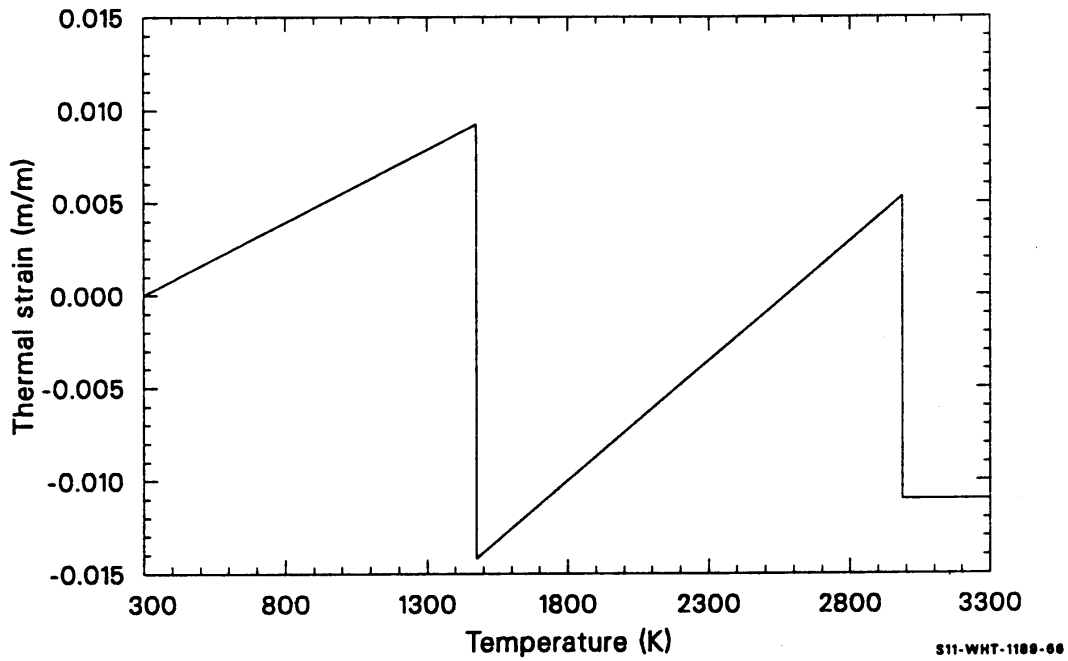

Figure 5-9. Zircaloy oxide thermal strain.

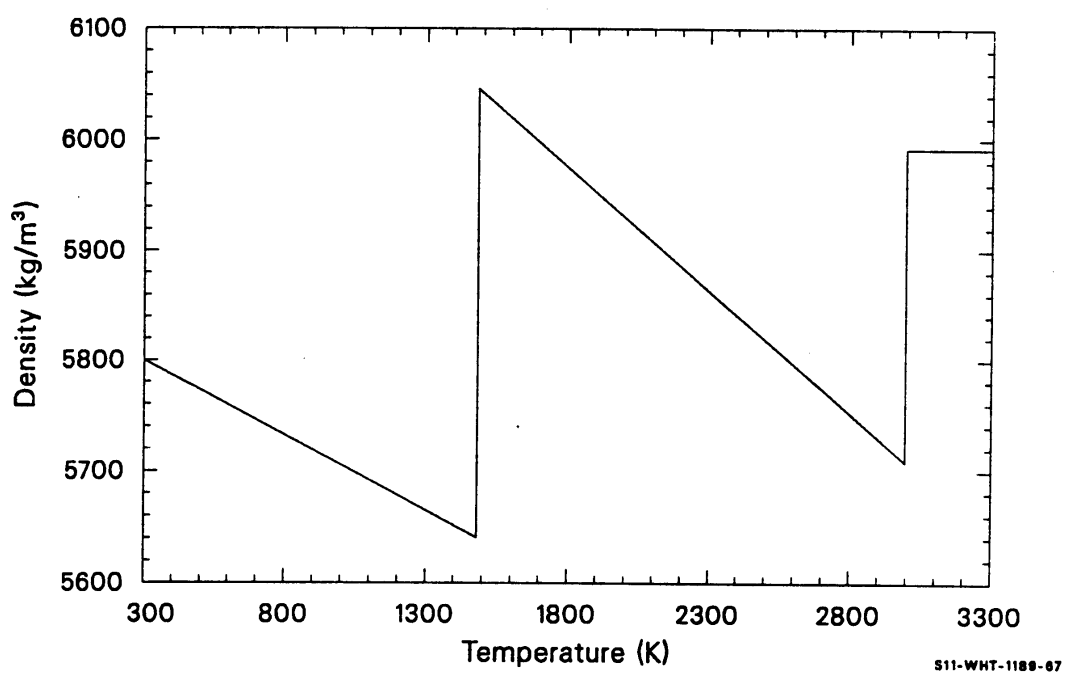

Figure 5-10. Zircaloy oxide density as a function of temperature.

Table 5-10. Zircaloy dioxide thermal expansion data by Fulkerson.[5.5-3]

Temperature (K)	Thermal Strain (10^{-3}m/m)
289	0
473	1.34
571	2.05
673	2.82
773	3.64
818	4.02
922	4.78
1,019	5.61
1,119	6.63
1,222	7.51
1,308	8.06
1,330	8.25
1,349	8.33
1,369	8.38
1,390	8.34
1,430	7.63
1,450	6.10
1,466	3.27
1,487	1.16
1,508	0.17
1,529	-0.38
1,550	-0.82
1,571	-1.05

Table 5-11. Zircaloy dioxide thermal expansion data from Brassfield et al.[5.5-4]

Temperature (K)	Thermal Strain (10^{-3}m/m)
300	0
537	2.1
778	3.7
1,031	5.05
1,238	7.35
1,383	9.10
1,488	-1.8

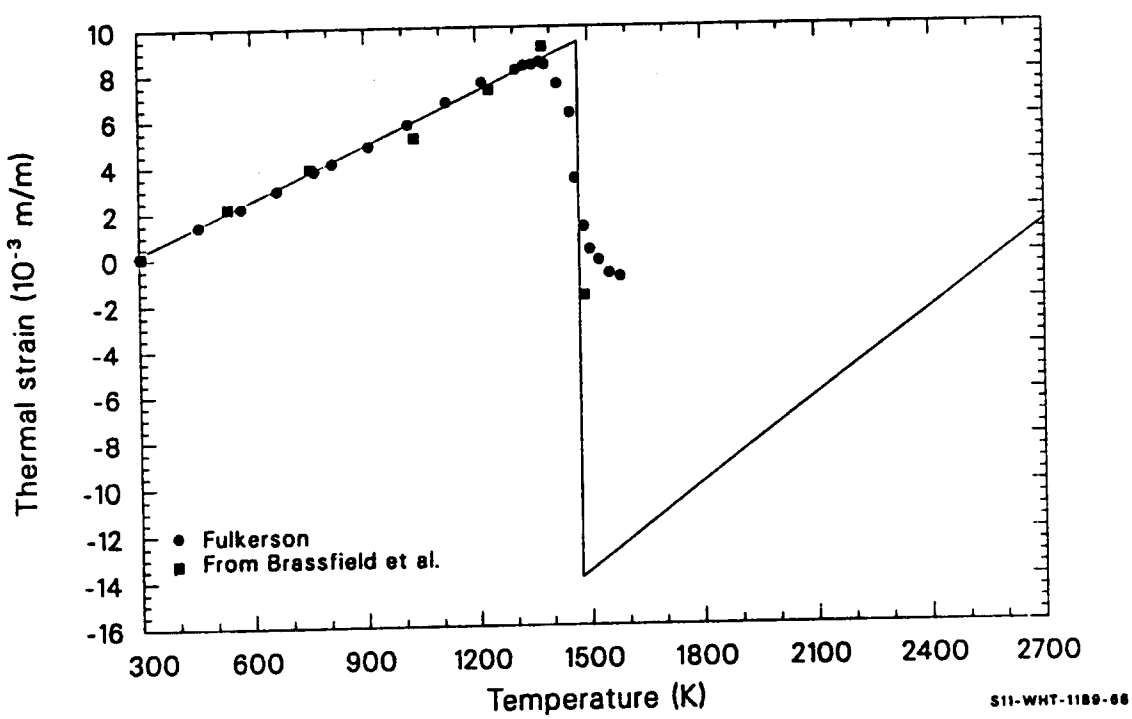

Figure 5-11. Zircaloy oxide thermal strain data compared to code prediction.

5.5.3 References

5.5-1 R. R. Hammer, *Zircaloy-4, Uranium Dioxide and Materials formed by their Interaction. A Literature Review with Extrapolation of Physical Properties to High Temperatures,* IN-1093, September 1967.

5.5-2 K. E. Gilchrist, "Thermal Property Measurements on Zircaloy-2 and Associated Oxide Layers," *Journal of Nuclear Materials, 62,* 1976, pp. 257-264.

5.5-3 S. D. Fulkerson, *Apparatus for Determining Linear Thermal Expansions of Materials in Vacuum or Controlled Atmosphere*, ORNL-2856, 1960, p. 20.

5.5-4 H. C. Brassfield, J. F. White, L. Sjodahl, and J. T. Bittel, *Recommended Property and Reaction Kinetics Data for Use in Evaluating a Light Water Cooled Reactor Loss-of-Coolant Incident Involving Zircaloy-4 or 304-SS Clad $U0_2$*, GEMP 482, 1968.

5.6 Elastic Moduli (ZOEMOD, ZOPOIR)

The function ZOEMOD calculates Young's modulus for zircaloy oxide from the zircaloy oxide temperature and oxygen-to-metal ratio. The function ZOPOIR calculates the Poisson's ratio for liquid and solid zircaloy oxide.

5.6.1 Young's Modulus (ZOEMOD)

Young's modulus for zircaloy oxide is returned by the ZOEMOD function. Oxide temperature and oxide oxygen-to-metal ratio are the only required inputs. The function uses the following correlation to calculate the modulus for 300 < T < 1,478 K (monoclinic phase):

$$Y_0 = -3.77 \times 10^7 T + 1.637 \times 10^{11} \quad . \tag{5-35}$$

For $1{,}478 \leq T < T_{SOL}$ (tetragonal and cubic phase),

$$Y_0 = -8.024 \times 10^7 T + 2.255 \times 10^{11} \quad . \tag{5-36}$$

For $T \geq T_{SOL}$,

$$Y_0 = 1 \tag{5-37}$$

where

Y_o	=	zircaloy oxide Young's modulus (Pa)
T	=	oxide temperature (K)
T_{SOL}	=	zircaloy oxide solidus temperature (K) (obtained from the ZOPRP subroutine).

The equations are least squares fits to data from Brassfield et al.[5.6-1] Table 5-12 reproduces the data, and Figure 5-12 shows the data and values of Y_o calculated with the ZOEMOD function. The function sets Y_o = 1 Pa for temperatures above 2,810 K where Equation (5-36) would predict a negative modulus. Since so few data are available, a large expected standard error of $\pm$0.2 times the predicted value is recommended.

5.6.2 Poisson's Ratio (ZOPOIR)

ZOPOIR returns constant values of 0.3 and 0.5 for the Poisson's ratios of solid and liquid zircaloy oxide, respectively. No data for these ratios have been found. The number 0.3 is merely typical of many

solid materials, and 0.5 is the constant volume, isotropic material value of Poisson's ratio. The expected standard error is therefore large, ±0.2

5.6.3 References

5.6-1 H. C. Brassfield, J. F. White, L. Sjodahl, and J. T. Bittel, *Recommended Property and Reaction Kinetics Data for Use in Evaluating a Light Water Cooled Reactor Loss-of-Coolant Incident Involving Zircaloy-4 or 304-SSClad UO_2*, GEMP 482, 1968, p. 89.

Table 5-12. Zircaloy dioxide modulus of elasticity data from Brassfield et al.[5.6-1]

Temperature (K)	Elastic Modulus (10^{10} Pa)	Comment
1,323	11.38	Monoclinic phase
1,453	10.89	Monoclinic phase
1,498	10.48	Tetragonal phase
1,563	10.10	Tetragonal phase
1,633	9.41	Tetragonal phase

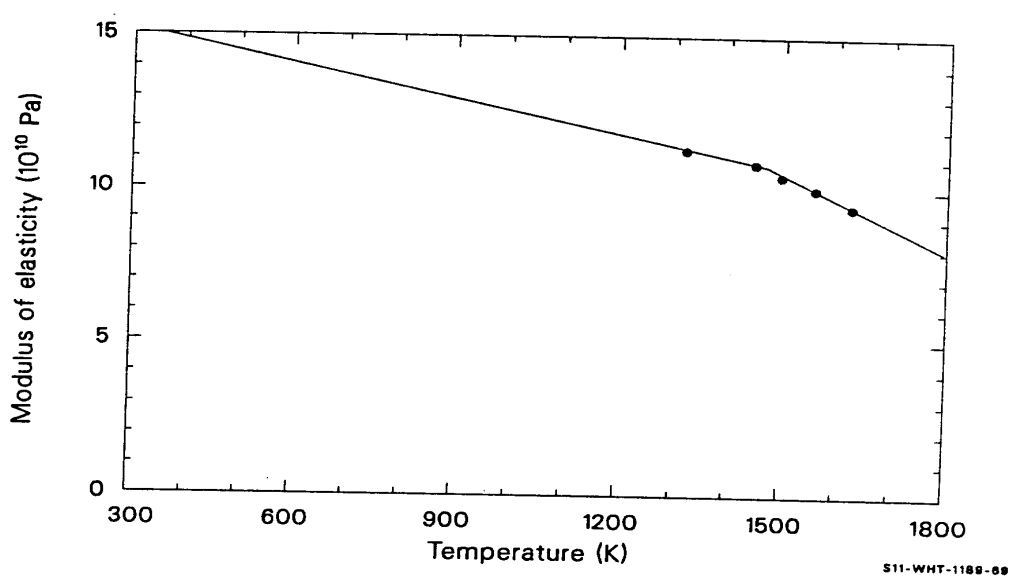

Figure 5-12. Data and calculated values of Young's modulus for zircaloy oxide.

5.7 Mechanical Limits and Embrittlement (ZORUP)

The function ZORUP returns zircaloy oxide failure stress as a function of temperature. The correlations used in the function ZORUP to calculate the oxide failure stress are listed below.

5.7.1 Model Development

For $300 \leq T \leq 1{,}200$ K (monoclinic phase of $Zr0_2$),

$$S_B = 96.28 \times 10^6 \quad . \tag{5-38}$$

For $1{,}200 < T < 1{,}478$ K (monoclinic phase of $Zr0_2$),

$$S_B = -5.06 \times 10^4\, T + 1.57 \times 10^8 \quad . \tag{5-39}$$

For $1{,}478 \leq T < 1{,}869.4$ K (tetragonal and cubic phases of $Zr0_2$),

$$S_B = -2.075 \times 10^5\, T + 3.889 \times 10^8 \quad . \tag{5-40}$$

For $1{,}869.4 \leq T \leq T_{SOL}$,

$$S_B = 10^6 \quad . \tag{5-41}$$

For $T > T_{SOL}$,

$$S_B = 0 \tag{5-42}$$

where

S_B	=	circumferential or axial stress on the oxide at failure (Pa)
T	=	oxide temperature (K)
T_{SOL}	=	zircaloy oxide solidus temperature (K) (Obtained from the ZOPRP subroutine).

These correlations are fits to the three $Zr0_2$ tensile strength data sets reported by Brassfield et al.[5.7-1] The data are shown in Table 5-13 and are compared with the correlation values in Figure 5-13.

The values and shape of the curve are similar to the values and shape of the more extensive data for $U0_2$ failure. In the temperature range of the data, the oxide failure stress is about three times the failure stress of zircaloy. In spite of these similarities, the very limited data used to construct the expressions for oxide failure stress suggest a large expected standard error for the correlation, $\pm$ 0.7 times the predicted value.

Figure 5-14 is a plot of the failure stresses returned by the function.

5.7.2 References

5.7.1 H. C. Brassfield, J. F. White, L. Sjodahl, and J. L. Bittel, *Recommended Property and Reaction Kinetics Data for Use in Evaluating a Light Water Cooled Reactor Loss-of-Coolant Incident Involving Zircaloy-4 or 304-SS Clad UO_2,* GEMP 482, 1968, p. 89.

Table 5-13. Zircaloy dioxide tensile strength data from Brassfield et al.[5.7-1]

Temperature (K)	Tensile Strength (MPa)
1,303	91.2
1,473	82.6
1,813	12.7

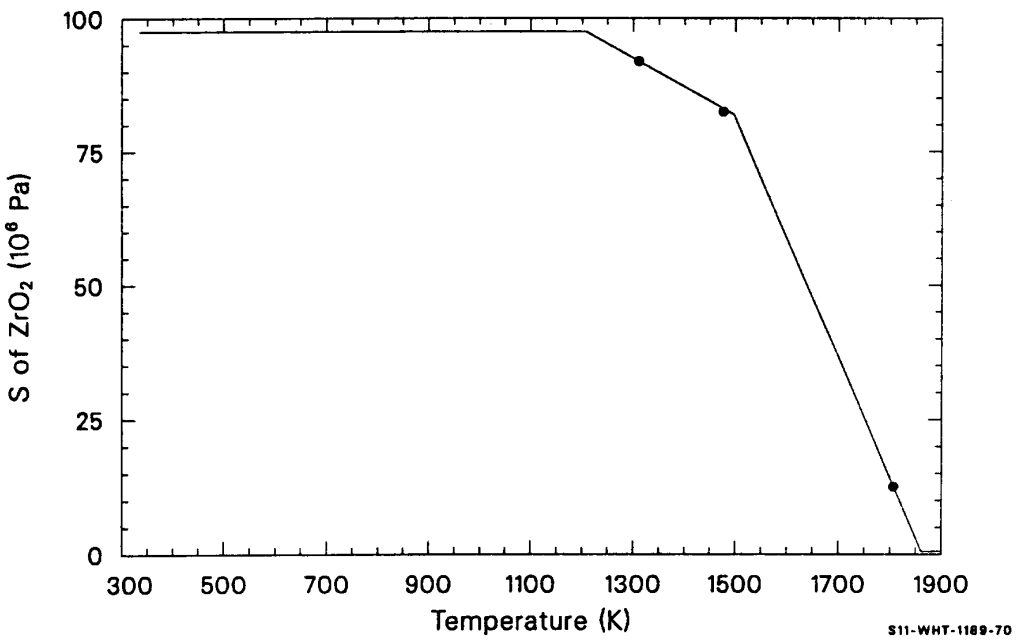

Figure 5-13. Zircaloy oxide failure stress data and correlations versus temperature.

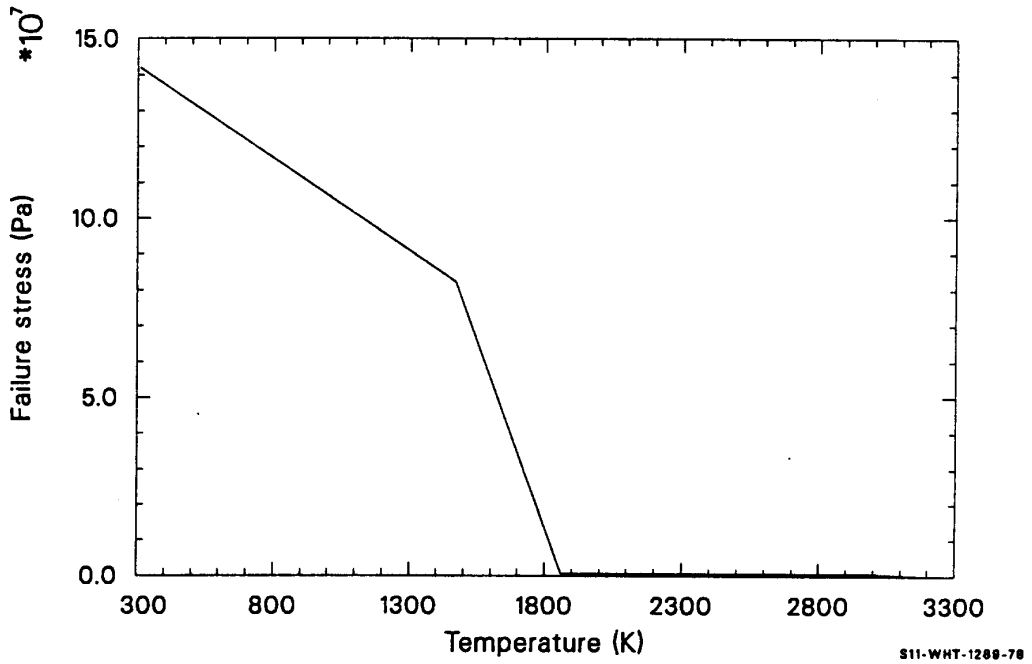

Figure 5-14. Zircaloy oxide failure stress calculated with the ZORUP function.

6. CONTROL ROD CLADDING

A collection of properties of 304 stainless steel has been prepared to allow modeling of temperature dependent phenomena and possible failure by melting or oxidation of stainless steel control rod cladding. Properties included are melting temperatures (SHYPRP), specific heat capacity (SCP), enthalpy (SENTHL), thermal conductivity (STHCON), thermal expansion (STHEXP), and density (SDEN).

6.1 Melting Temperatures (SHYPRP)

The subroutine SHYPRP provides 304 stainless steel melting temperatures. There is no required input.

6.1.1 Model Development

For this alloy, page 19-3 of Reference 6.1-1 reports a melting range of 1,671 to 1,727 K. These numbers are used for the solidus (first liquid phase appears) and liquidus (last solid phase melts) temperatures of control rod cladding.

6.1.2 References

6.1-1 D. Peckner and I. M. Bernstein (eds.), *Handbook of Stainless Steel*, New York: McGraw-Hill Book Company, 1977.

6.2 Specific Heat Capacity and Enthalpy (SCP, SENTHL)

The function SCP returns the specific heat capacity of 304 stainless steel as a function of temperature. SENTHL uses the specific heat capacity to calculate the enthalpy change of the cladding as a function of temperature and a reference temperature for which the enthalpy change will be zero. The reference temperature used is 300 K.

6.2.1 Model Development

For specific heat capacity, two expressions are used. The first [Equation (6-1)] is a fit to the specific heat capacity values of 398 J/kg•K at 263 K, 488 J/kg• K at 700 K, and 540 J/kg•K at 1,119 K. These values were obtained from a curve by Peckner and Bernstein.[6.2-1] The curve reaches a maximum between 1,558 and 1,559 K, and Equation (6-2) uses the maximum value of 558.228 J/kg• K for temperatures above 1,558 K.

For $300 \leq T < 1{,}558$ K,

$$C_{ps} = 326 + 0.298\,T - 9.56 \times 10^{-5}\,T^2 \quad . \tag{6-1}$$

For $T \geq 1{,}558$ K,

$$C_{ps} = 558.228 \tag{6-2}$$

where

C_{ps}	=	control rod cladding specific heat capacity (J/kg• K)
T	=	cladding temperature (K).

SENTHL returns the enthalpy change of 304 stainless steel as a function of temperature. For temperatures below 1,671 K, at which 304 stainless steel begins to melt, the integrals of Equations (6-1) and (6-2) with respect to temperature are used [Equations (6-3) and (6-4)]. From 1,671 to 1,727 K, the melting range for 304 stainless steel given in Reference 6.2-1, a heat of fusion is included in the specific heat capacity. The heat of fusion of 2.8×10^5 was added linearly over the melting range, and this is responsible for the additional 5,000 J/kg• K in Equation (6-5). This heat of fusion was calculated from the heats of fusion for chromium, iron, and nickel given by Brassfield et al.[6.2-2] and the composition of 304 stainless steel given by Murfin et al.[6.2-3] The heat of fusion for the alloy was assumed to be the atomic fraction of each element times its elemental heat of fusion. Equation (6-6) is a continuation of Equation (6-4) used to estimate the enthalpy change of the liquidus.

For $300 < T \leq 1{,}558$ K,

$$h_s = 326\,T + 0.149\,T^2 - 3.187 \times 10^{-5}\,T^3 \quad . \tag{6-3}$$

For $1{,}558 < T < 1671$ K,

$$h_s = -1.206610 \times 10^5 + 558.228\,T \quad . \tag{6-4}$$

For $1{,}671 \leq T \leq 1727$ K,

$$h_s = -8.475661 \times 10^6 + 5558.228\,T \quad . \tag{6-5}$$

For $T > 1{,}727$ K,

$$h_s = 1.593390 \times 10^5 + 558.228\,T \tag{6-6}$$

where

h_s	=	control rod cladding enthalpy (J/kg)
T	=	control rod cladding temperature (K).

The expected standard error of Equations (6-1) through (6-6) is $\pm$ 0.10 of the predicted values. Figures 6-1 and 6-2 illustrate the calculated values of specific heat capacity and enthalpy change (relative to a reference temperature of 300 K) over temperature.

6.2.2 References

6.2-1 D. Peckner and I. M. Bernstein (eds.), *Handbook of Stainless Steel*, New York: McGraw-Hill Book Company, 1977, pp. 19-3, 19-26.

6.2-2 H. C. Brassfield, J. F. White, L. Sjodahl, and J. T. Bittel, *Recommended Property and Reaction Kinetics Data for Use in Evaluating a Light Water Cooled Reactor Loss-of-Coolant Incident Involving Zircaloy-4 of 304-SS Clad UO_2*, GEMP482, 1968, p. 89.

6.2-3 W. B. Murfin et al., *Core Meltdown Experimental Review*, SAND74-0382, NUREG-0205, 1977, p. 4-8.

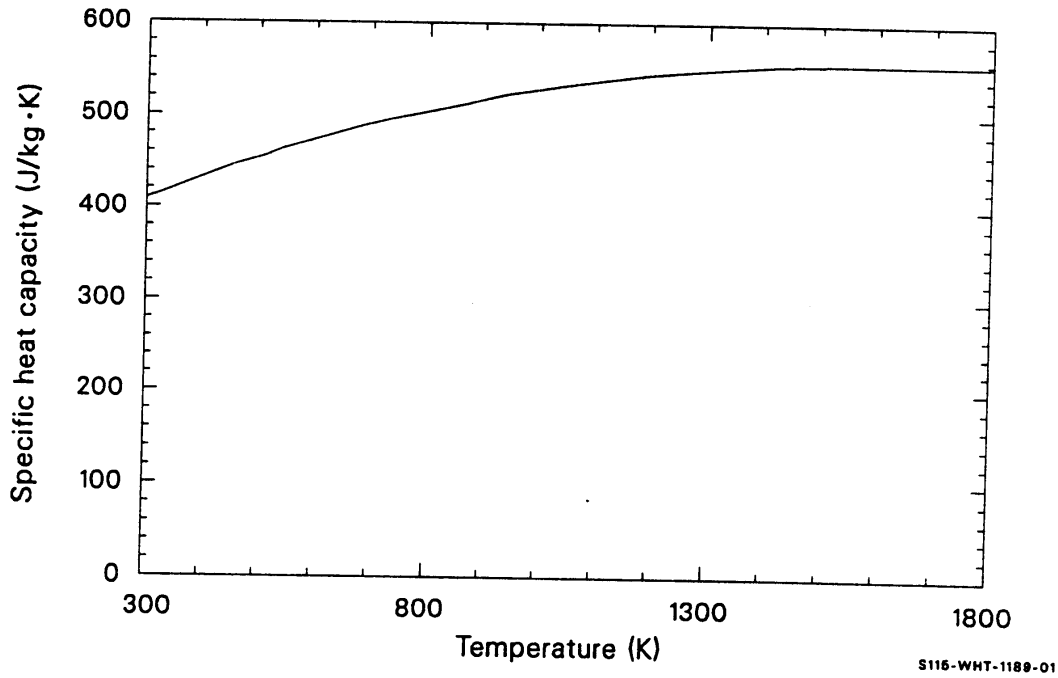

Figure 6-1. Stainless steel specific heat capacity at constant pressure.

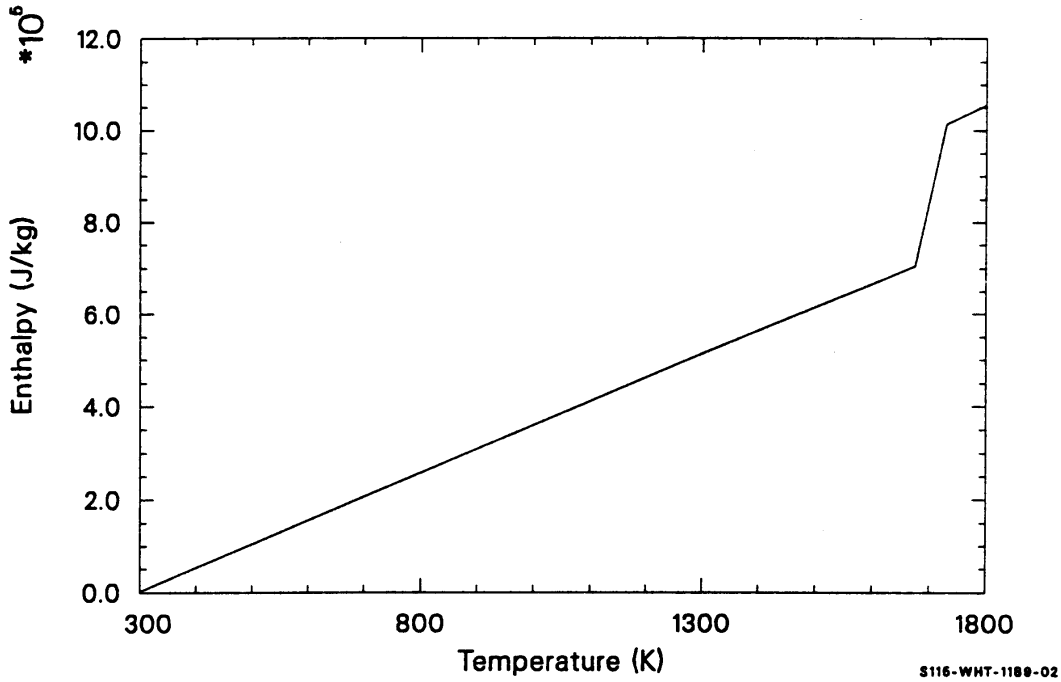

Figure 6-2. Stainless steel enthalpy change at constant pressure.

6.3 Thermal Conductivity (STHCON)

6.3.1 Model Development

The thermal conductivity of 304 stainless steel as a function of temperature is calculated by the STHCON function. Equation (6-7) is a fit to the values of 14.65 W/m•K at 374 K and 25.83 W/m•K at 965 K obtained from page 19-18 of Reference 6.3-1. Equation (6-9) is an approximation of the thermal conductivity at the lowest temperature for which the steel is completely melted. To obtain this approximation, Equation (6-7) was evaluated at 1,727 K and then reduced by 50%, noting that the thermal conductivity of a metal with a face-centered cubic structure like 304 stainless steel is reduced by half when melted.[6.3-2] Equation (6-8) interpolates between the result of Equation (6-9) predicted at 1,671 K and the value predicted by Equation (6-9) at and above 1,727 K.

For $300 \leq T < 1{,}671$ K,

$$K_s = 7.58 + 0.0189\ T \quad . \tag{6-7}$$

For $1{,}671 \leq T < 1{,}727$ K,

$$K_s = 610.9393 - 0.3421767\ T \quad . \tag{6-8}$$

For T ≥ 1,727 K,

$$K_s = 20 \tag{6-9}$$

where

K_s	=	control rod cladding thermal conductivity (W/m•K)
T	=	control rod cladding temperature (K).

The expected standard error of the predicted conductivities is ± 0.02 of the predicted conductivity. The predicted thermal conductivity as a function of temperature is shown in Figure 6-3.

6.3.2 References

6.3-1 D. Peckner and I. M. Bernstein (eds.), *Handbook of Stainless Steel*, New York: McGraw-Hill Book Company, 1977.

6.3-2 S. Nazare, G. Ondracek, and B. Schulz, "Properties of Light Water Reactor Core Melts," *Nuclear Technology, 32*, 1977, pp. 239-246.

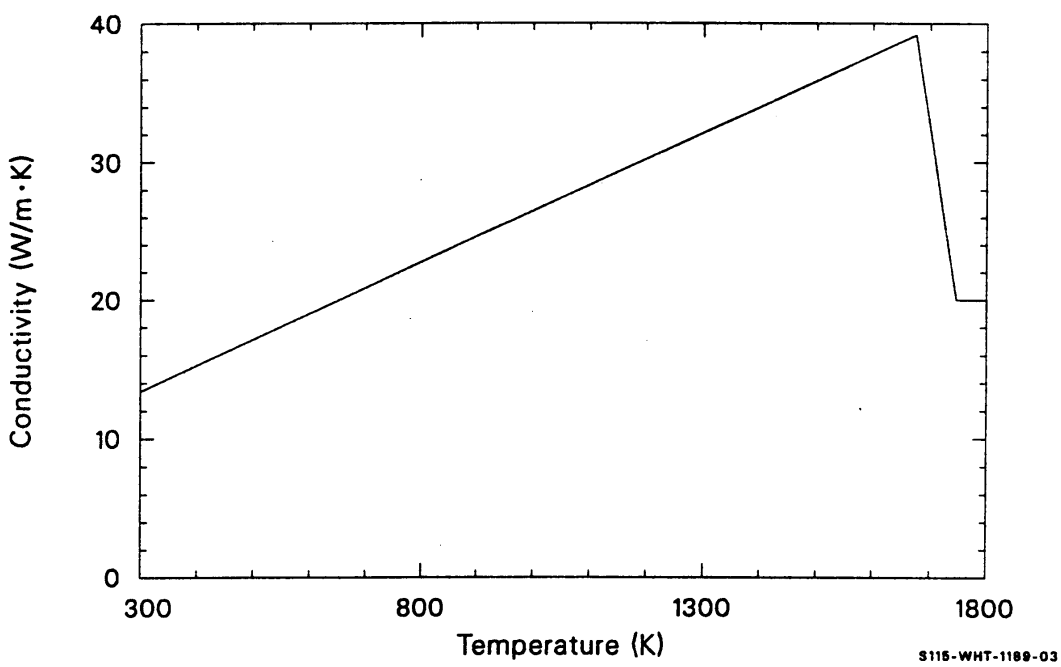

Figure 6-3. Stainless steel thermal conductivity.

6.4 Thermal Expansion and Density (STHEXP, SDEN)

The function STHEXP calculates 304 stainless steel thermal expansion strain, and SDEN computes the density of this material. STHEXP requires the control rod cladding temperature and a reference temperature (for which thermal strain will be zero), while SDEN requires only the temperature.

6.4.1 Model Development

The expressions used to calculate thermal expansion strains are

For $300 \leq T < 1{,}671$ K,

$$\varepsilon_s = 1.57 \times 10^{-5} \times T + 1.69 \times 10^{-9} \times T^2 \quad . \tag{6-10}$$

For $1{,}671 \leq T < 1{,}727$ K,

$$\varepsilon_s = -2.986634 \times 10^{-1} + 1.972573 \times 10^{-4} \times T \quad . \tag{6-11}$$

For $T \geq 1{,}727$ K,

$$\varepsilon_s = 4.2 \times 10^{-2} \tag{6-12}$$

where

ε_s	=	control rod cladding thermal strain (m/m)
T	=	control rod cladding temperature (K).

Equation (6-10) is derived from thermal expansion rates of 17.2×10^{-6} and 18.9×10^{-6} m/m•K at 455 and 959 K. These values were taken from a curve on page 197 of Reference 6.4-1. A linear fit to the thermal expansion rates yields an expression which can be integrated to produce Equation (6-10). The constant of integration is ignored because the quantity returned by STHEXP is the strain predicted by Equations (6-10) through (6-12) at the given temperature minus the strain predicted at the reference temperature. Equation (6-12) is the strain predicted by Equation (6-10) at the lowest temperature for which the steel is completely melted, 1,727 K, plus an assumed additional expansion of 1% (3%volume increase) because of the melting. Equation (6-11) is a linear interpolation of the values predicted by Equation (6-10) at 1,671 K and Equation (6-12) at 1,727 K. The expected standard error of these expressions is about 0.10 of the predicted value.

The function SDEN uses the general relation between density and thermal strain, together with a reference density of 7.9×10^3 kg/m^3 at 300 K obtained from page 87 of Reference 6.4-2. The expected standard error of this density is the uncertainty of reference density, $\pm$ 50 kg/m^3.

The thermal expansion strain returned by STHEXP for a reference temperature of 300 K is illustrated in Figure 6-4, and the density calculated with the SDEN function is shown in Figure 6-5.

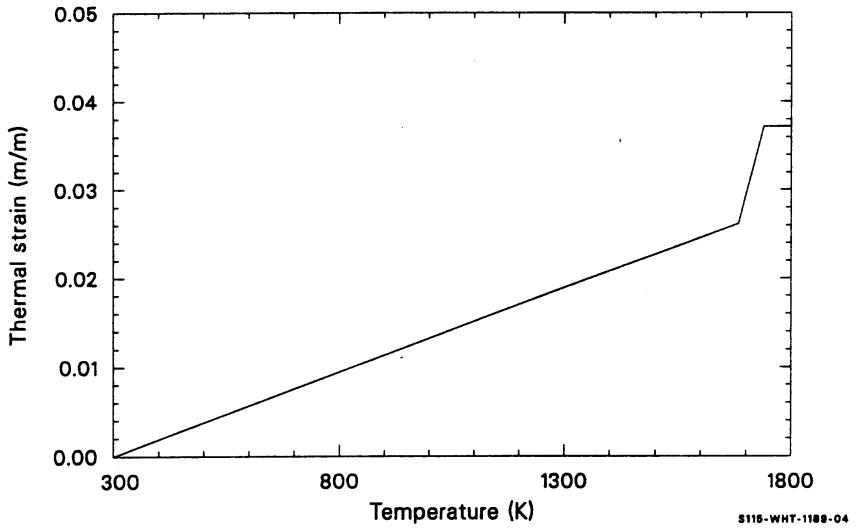

Figure 6-4. Stainless steel thermal expansion strain.

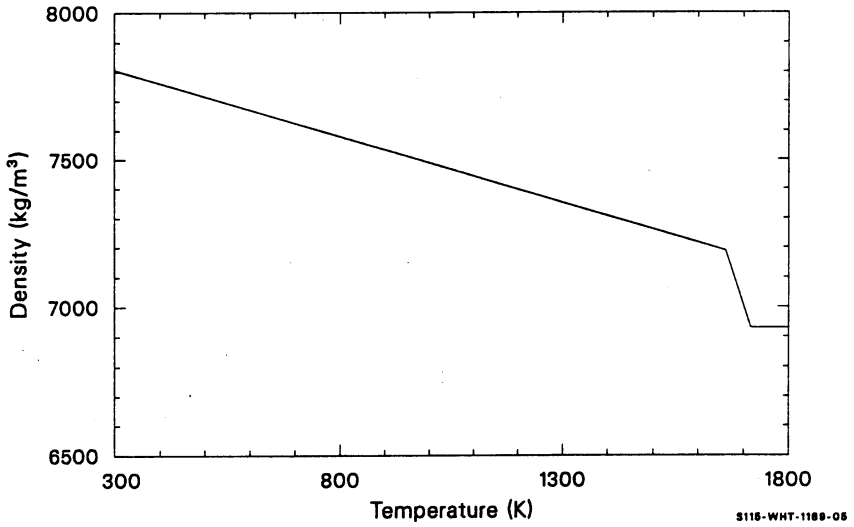

Figure 6-5. Stainless steel density.

6.4.2 References

6.4-1 D. Peckner and I. M. Bernstein (eds.), *Handbook of Stainless Steel*, New York: McGraw-Hill Book Company, 1977.

6.4-2 H. C. Brassfield, J. F. White, L. Sjodahl, and J. T. Bittel, *Recommended Property and Reaction Kinetics Data for Use in Evaluating a Light Water Cooled Reactor Loss-of-Coolant Incident Involving Zircaloy-4 of 304-SS Clad UO_2*, GEMP 482, 1968.

6.5 Stainless Steel Oxidation in Steam (SOXIDE, SOXWGN, SOXTHK)

Three subcodes are employed to describe the oxygen uptake of 304 stainless steel. The SOXIDE subroutine returns the linear power generated by the oxidation of stainless steel, the oxidation weight gain at the end of a time step, and an estimate of the oxide layer thickness at the end of a time step. Required input information is the cladding temperature, the time step duration, the outside diameter of the as fabricated cladding, the initial weight gain, and the initial oxide layer thickness. SOXWGN is a function that returns the parabolic rate constant for the oxidation weight gain of stainless steel as a function of temperature. The parabolic rate constant for the oxide layer thickness is calculated by SOXTHK as a function of temperature.

6.5.1 Model Development

The equation used to model the oxidation parameters is of the form

$$Z_f = \left[Z_i^2 + 2A\exp\left(-\frac{B}{T}\right)\Delta t \right]^{1/2} \tag{6-13}$$

where

Z_f	=	value of the oxidation parameter (oxide layer thickness or cladding weight gain per unit surface area due to oxidation) at the end of a time span of Δt
Z_i	=	value of the oxidation parameter at the start of the time span
T	=	temperature of the oxide layer (K)
Δt	=	time span (s)
A,B	=	rate constants.

There is some question as to the exact value of the A coefficient for the oxide thickness version of Equation (6-13). The values currently considered are 300 m^2/s and 30,000 m^2/s. The former is currently used in the code.

Table 6-1 lists the rate constants used with Equation (6-13) to model weight gain or oxide layer thickness. The parabolic rate constants calculated by SOXWGN and SOXTHK are the quantities

$$R = 2A \exp(-B/T) \tag{6-14}$$

where R is the parabolic rate constant for oxidation parameter described by rate constants A and B.

The expression used to model the linear power generated by the oxidation of stainless steel is

$$P = 4.85\times10^{6} D_0 \frac{(M_f - M_i)}{\Delta t} \tag{6-15}$$

where

P	=	rate of heat generation per unit length of 304 stainless steel cladding (W/m)
D_o	=	cladding outside diameter without oxidation (m)
M_f	=	mass gain per unit surface area due to oxidation at end of time step (kg/m^2)
M_i	=	mass gain per unit surface area due to oxidation at start of time step (kg/m^2).

The power represented by this equation is about one tenth the power represented by the corresponding equation for zircaloy oxidation when the mass gains are similar.

Table 6-1. Rate constants for use with Equation (6-13) to predict oxidation.

Oxidation Parameter	A	B
Cladding weight gain (kg/m^2 surface)	1.2×10^8 $kg^2/m^4 \cdot s$	42,428 K
Oxide thickness	300 m^2/s	42,428 K

Equation (6-13), with oxidation rate constants for weight gain, was taken from page 50 of Reference 6.5-1. If the composition and density of the oxide are known, the rate constant for the oxide layer thickness can be determined from the rate constant for oxidation weight gain:

$$A = \frac{B}{WFOX^2 p^2} \tag{6-16}$$

where

A	=	rate constant for oxide layer thickness (m^2/s)
B	=	rate constant for oxidation weight gain ($kg^2/m^4 \cdot s$)
$WFOX$	=	mass fraction oxygen in the oxide (kg oxygen/kg oxide)
p	=	density of the oxide film (kg/m^3).

However, determination of a rate constant for the oxide layer thickness is complicated by uncertainty about the oxide density because of considerable foaming of the stainless steel during oxidation.[6.5-1,6.5-2]

Moreover, page 53 of Reference 6.5-1 reports very complex oxide structures. The oxide is expected to contain some FeO, Fe_3O_4, Fe_2O_3, CrO_3, Cr_2O_3, NiO, and mixed spinels. The rate constant in Table 6-1 was calculated by assuming the composition of FeO and a density of 3,000 kg/m^3 (about half the density of nonporous FeO).

Equation (6-15) for the linear power generated by oxidation is derived by subtracting the heat required to dissociate H_2O, 2.4182x10^5 J/mole,[6.5-3] from the heat of reaction of iron and oxygen to form-FeO, 2.67 x 10^5 J/mole.[6.5-4] The resultant heat of formation for one mole of FeO from one mole of H_2O is multiplied by the rate of oxygen uptake in moles and the circumference of the cladding to obtain Equation (6-15).

The expected standard deviation of the oxide layer thickness is $\pm$ 50% of the predicted thickness. The expected standard deviation of the oxidation weight gain and oxidation power is somewhat less, $\pm$25% of the predicted value, because the oxide composition and density do not affect the prediction of these quantities.

Figures 6-6 and 6-7 illustrate the parabolic constants calculated with the SOXWGN and SOXTHK functions. The time step averaged power per meter of rod calculated with SOXIDE for a 1.25 x 10^{-2}m diameter rod with no initial oxide layer and a 1 second time step is shown in Figure 6-8. Figures 6-9 and 6-10 illustrate oxygen uptake and the oxide layer thickness expected after a 1 second time step with no initial oxidation.

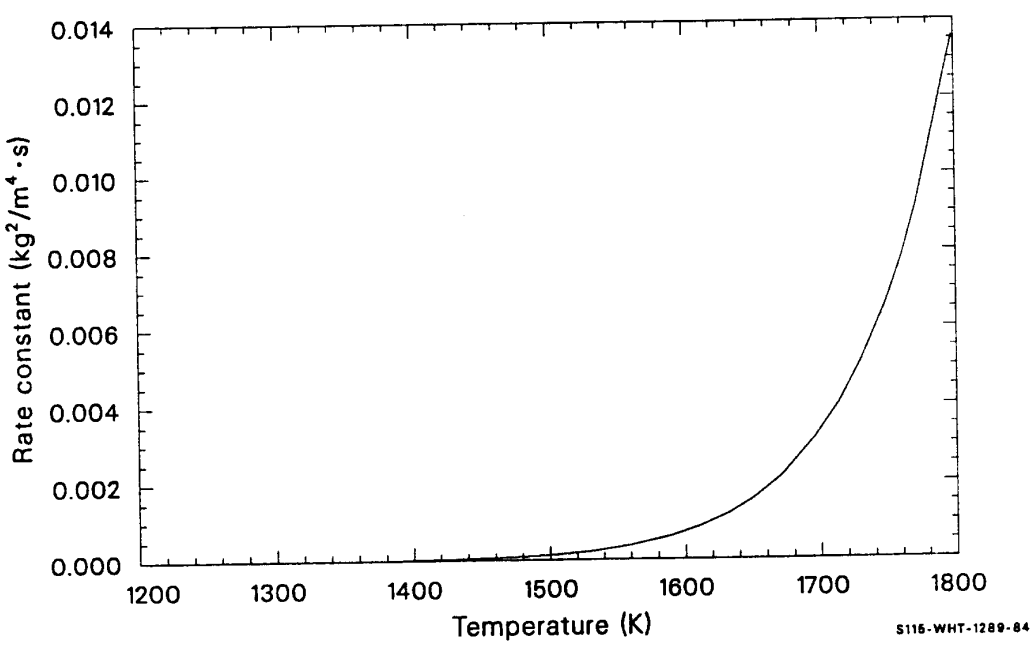

Figure 6-6. Parabolic constant for oxygen weight gain.

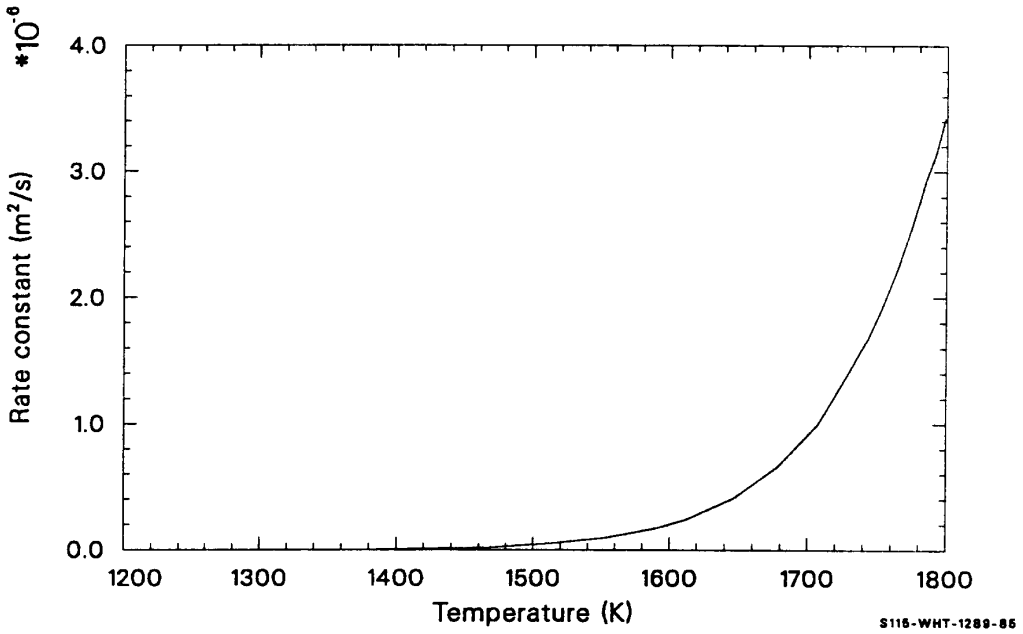

Figure 6-7. Parabolic constant for oxide layer thickness.

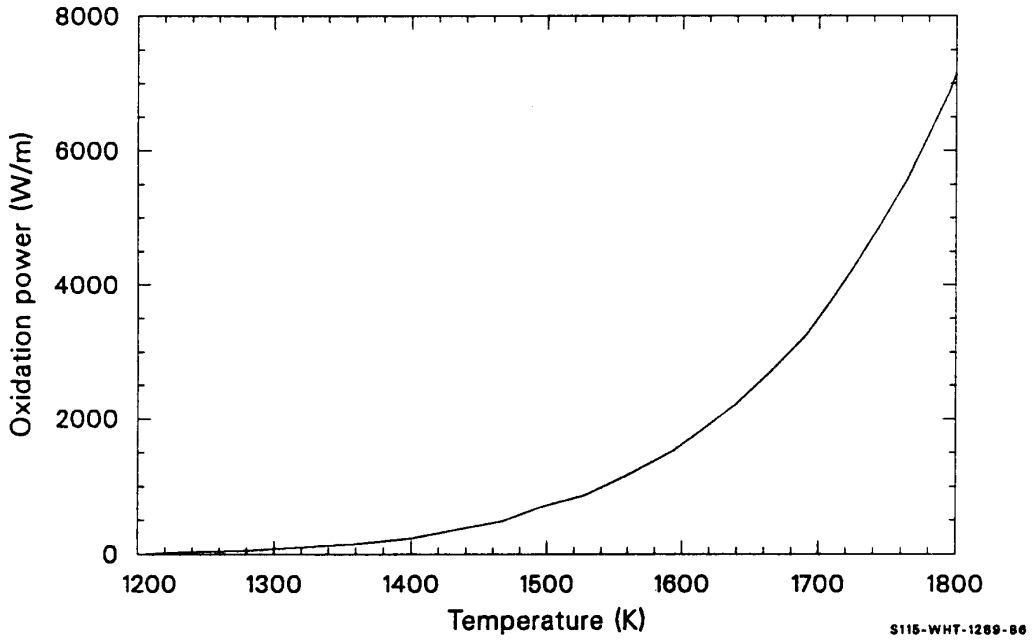

Figure 6-8. Average power per meter during 1 second for a 1.25 x 10^{-2} m stainless steel rod with no initial oxide layer.

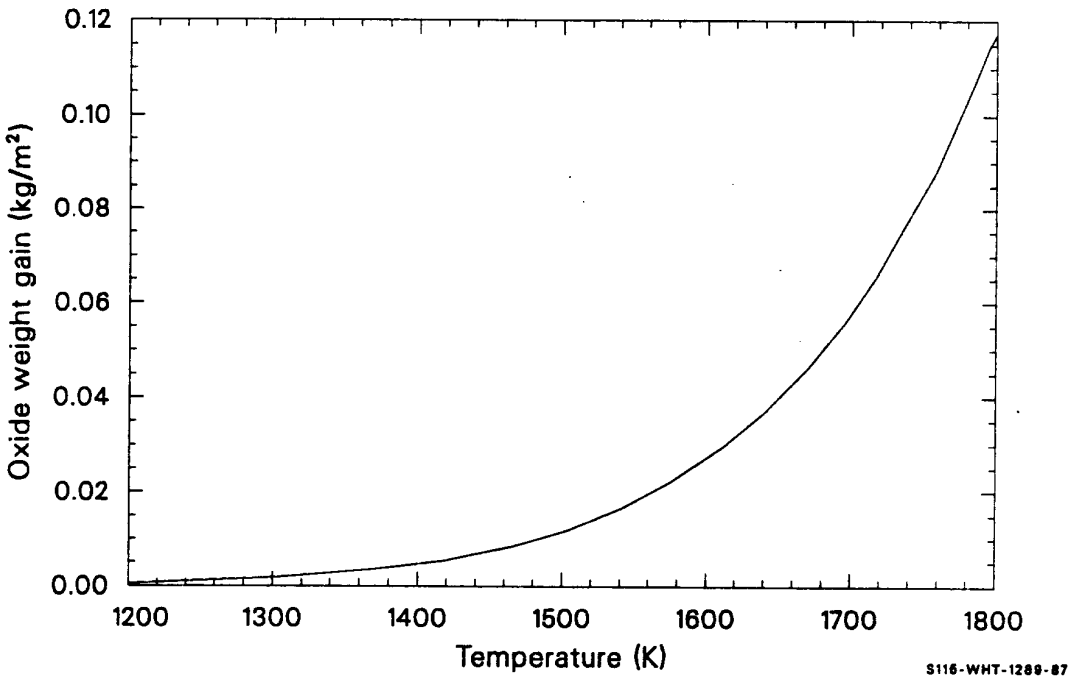

Figure 6-9. Oxygen uptake after 1 second with no initial oxidation.

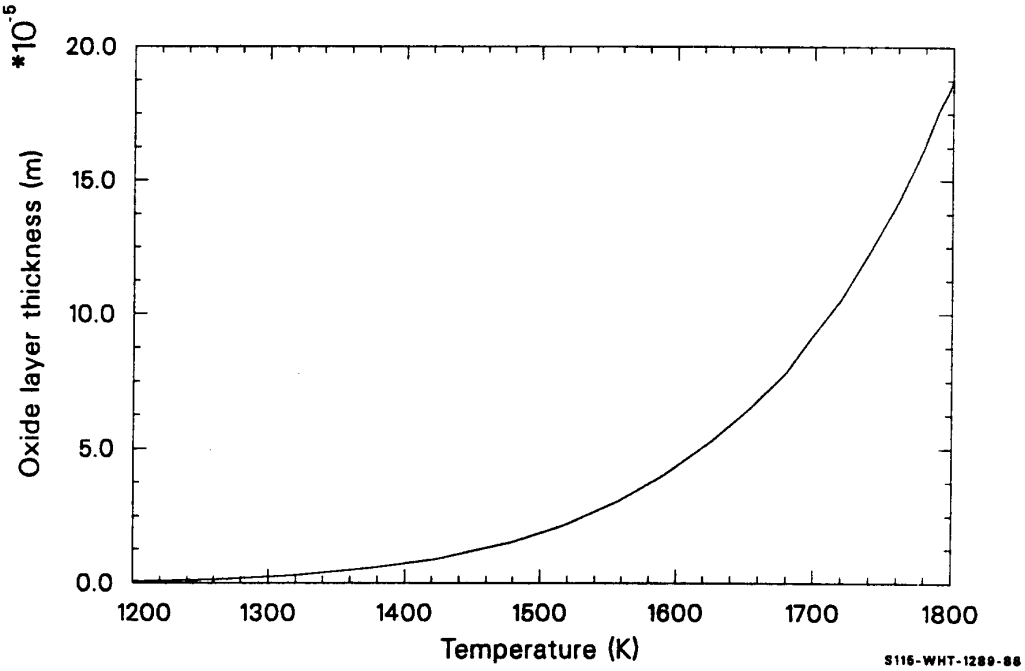

Figure 6-10. Oxide layer thickness after 1 second with no initial oxidation.

6.5.2 References

6.5-1 H. C. Brassfield, J. F. White, L. Sjodahl, and J. T. Bittel, *Recommended Property and Reaction Kinetics Data for Use in Evaluating a Light Water Cooled Reactor Loss-of-Coolant Incident Involving Zircaloy-4 of 304SS Clad UO_2*, GEMP 482, 1968.

6.5-2 J. C. Hesson et al., *Laboratory Simulations of Cladding--Steam Reactions Following Loss of Coolant Accidents in Water Cooled Power Reactors*, ANL-7609, 1970, pp. 12-18.

6.5-3 J. A. Dean (ed.), *Lange's Handbook of Chemistry*, 12th Edition, New York: McGraw-Hill Book Company, 1979.

6.5-4 F. D. Rossini et al., *Selected Values of Chemical Thermodynamic Properties, Circular of the National Bureau of Standards 500*, Washington, D. C.: United States Government Printing Office, 1952.

7. STAINLESS STEEL OXIDES

With the expansion of severe accident analysis computer codes to include boiling water reactors (BWR) using stainless steel control blades, it became apparent that materials properties information was needed for the stainless steel oxides formed at high temperatures. Correlations were developed to calculate specific heat capacity (SOCP), enthalpy (SONTHL), thermal conductivity (SOTCON), thermal expansion (SOTEXP), and density (SODEN).

7.1 Specific Heat Capacity and Enthalpy (SOCP, SONTHL)

The function SOCP calculates the specific heat capacity for stainless steel oxide at constant pressure as a function of temperature. The function SONTHL calculates the enthalpy change for stainless steel oxide at constant pressure as a function of temperature and a reference temperature, for which the enthalpy change will be zero.

7.1.1 Specific Heat Capacity (SOCP)

The function SOCP returns the specific heat capacity at constant pressure for a mixture of the iron oxides, FeO, Fe_2O_3, and Fe_3O_4, as a function of temperature. These iron oxides are presumed to be the major components of stainless steel oxide. The expressions used to calculate specific heat capacity are:

FeO:

For $300 < T \leq 1{,}642$ K (solid phase),

$$C_p = 676.2 + 0.1432\ T \quad . \tag{7-1}$$

For $T > 1{,}642$ K (liquid phase),

$$C_p = 989 \quad . \tag{7-2}$$

Fe_2O_3:

For $300 < T \leq 950$ K (alpha phase),

$$C_p = 337.6 + T(1.099 - 2.372 \times 10^{-05}\ T) \quad . \tag{7-3}$$

For $950 < T \leq 1{,}050$ K (beta phase),

$$C_p = 1248 \ . \tag{7-4}$$

For 1,050 < T ≤ 1,838 K (gamma phase),

$$C_p = 829.9 + 4.26 \times 10^{-02}\ T \quad . \tag{7-5}$$

For T > 1,838 K (liquid phase),

$$C_p = 829.9 + 4.26 \times 10^{-02}\ T \quad . \tag{7-6}$$

Fe_3O_4:

For 300 < T ≤ 1,000 K (alpha phase),

$$C_p = 394.9 + T(0.8705 - 4.976 \times 10^{-07}\ T) \quad . \tag{7-7}$$

For 1,000 < T ≤ 1,864 K (beta phase),

$$C_p = 866.5 \quad . \tag{7-8}$$

For T > 1,864 K (liquid phase),

$$C_p = 866.5 \quad . \tag{7-9}$$

Since no data were found for the liquid phase specific heat capacity, the specific heat capacity at the melting point of each oxide was used as an estimate. The final specific heat capacity for stainless steel oxide calculated by the SOCP subroutine is a simple average of the calculated specific heat capacities of each oxide of iron.

$$SOCP_F = \frac{[SOCP_{(FeO)} + SOCP_{(Fe\ O_3)} + SOCP_{(Fe\ O_4)}]}{3} . \tag{7-10}$$

Figure 7-1 shows the calculated specific heat capacity for stainless steel oxide as a function of temperature. Tables 7-1 to 7-3 contain the specific data from Touloukian[7.1-1] that were used to derive the equations used in the calculation.

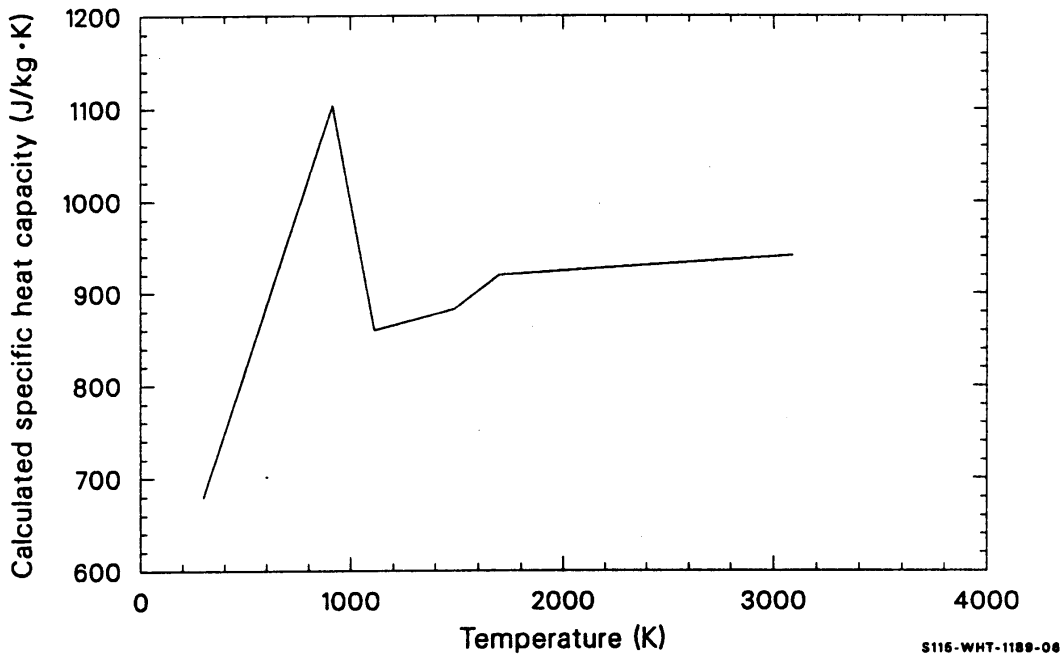

Figure 7-1. Specific heat capacity for stainless steel oxide calculated by SOCP.

7.1.2 Enthalpy (SONTHL)

The function SONTHL calculates the enthalpy change for stainless steel oxide as a function of temperature and a reference temperature of 300 K. At 300 K, the enthalpy change is zero. The expressions used to calculated the enthalpy of stainless steel oxide are:

For $300 < T < 950$ K,

$$h_s = -1.7264166 \times 10^5 + T[469.6 + T(0.3521 - 2.691 \times 10^{-6}\, T)] \quad . \tag{7-11}$$

For $950 \leq T < 1{,}000$ K,

$$h_s = -2.9379084 \times 10^5 + T[773.0 + T(0.1690 - 5.53 \times 10^{-7}\, T)] \quad . \tag{7-12}$$

For $1000 \leq T < 1{,}050$ K,

$$h_s = -3.530784 \times 10^5 + T(930.2 + 2.387 \times 10^{-2}\, T) \quad . \tag{7-13}$$

For $1{,}050 \leq T \leq 1{,}642$ K,

$$h_s = -1.6657291 \times 10^5 + T(790.0 + 3.07 \times 10^{-02}\ T)\ . \tag{7-14}$$

For $T > 1{,}642$ K,

$$h_s = -2.7403984 \times 10^5 + T(895.1 + 7.1 \times 10^{-03}\ T) \tag{7-15}$$

where

h_s	=	the enthalpy change for stainless steel oxide (J/kg)
T	=	the stainless steel oxide temperature (K).

The above enthalpy expressions were obtained by averaging at each temperature range the enthalpies of FeO, Fe_2O_3, and Fe_3O_4, the main components presumed to be present in the oxide of stainless steel. For each iron oxide, the enthalpies that were averaged were obtained by integrating the polynomials obtained from fitting the specific heat capacity data from Touloukian et al.[7.1-1] The specific heat capacity data used to obtain the polynomials are presented in Tables 7-1 through 7-3.

Table 7-1. FeO specific heat capacity data.

	Temperature (K)	**Specific Heat Capacity (cal/gK)**
Solid phase:		
	300	0.1672
	400	0.1747
	500	0.1789
	600	0.184
	700	0.1876
	800	0.191
	900	0.1942
	1,000	0.1973
	1,100	0.2004
	1,200	0.2034

Table 7-1. FeO specific heat capacity data. (Continued)

	Temperature (K)	Specific Heat Capacity (cal/gK)
	1,300	0.2064
	1,400	0.2094
	1,500	0.2123
	1,600	0.2153
	1,650	0.2168
Liquid phase:		
	1,650	0.2366
	1,700	0.2366
	1,800	0.2366

Table 7-2. Fe_2O_3 specific heat capacity data.

	Temperature	Specific Heat Capacity
Alpha phase:		
	391.0	0.182
	393.5	0.184
	414.0	0.186
	450.5	0.197
	490.5	0.204
	493.0	0.207
	508.0	0.207
	533.0	0.217
	419.2	0.187
	435.0	0.189
	463.0	0.211
	479.5	0.217

Table 7-2. Fe_2O_3 specific heat capacity data. (Continued)

Temperature	Specific Heat Capacity
483.7	0.206
505.5	0.214
535.0	0.222
567.0	0.22
592.5	0.223
626.5	0.238
654.5	0.264
682.0	0.272
685.5	0.273
701.5	0.27
715.5	0.287
737.5	0.271
763.0	0.288
799.0	0.291
823.0	0.298
840.0	0.314
880.0	0.335
904.0	0.342
864.0	0.326
870.5	0.32
889.0	0.322
936.0	0.328
941.0	0.358
301.23	0.1563
310.2	0.1592
319.04	0.1616
327.77	0.164
336.53	0.1664

Table 7-2. Fe_2O_3 specific heat capacity data. (Continued)

	Temperature	Specific Heat Capacity
	345.42	0.1687
	300.0	0.1796
	400.0	0.1922
	500.0	0.2044
	600.0	0.2163
	700.0	0.2281
	800.0	0.2399
	900.0	0.2516
	950.0	0.2575
Beta phase:		
	973.0	0.367
	991.5	0.376
	950.0	0.2254
	1,000.0	0.2254
	1,050.0	0.2254
Gamma phase:		
	1,050.0	0.2101
	1,100.0	0.2106
	1,200.0	0.2118
	1,300.0	0.2128
	1,400.0	0.214
	1,500.0	0.2154
	1,600.0	0.2162
	1,700.0	0.2172
	1,750.0	0.2178

Table 7-3. Fe_3O_4 specific heat capacity data.

	Temperature	Specific Heat Capacity
Alpha phase:		
	300.0	0.1569
	400.0	0.1778
	500.0	0.1986
	600.0	0.2193
	700.0	0.2402
	800.0	0.261
	900.0	0.2818
Beta phase:		
	1,100.0	0.2073
	1,200.0	0.2073
	1,300.0	0.2073
	1,400.0	0.2073
	1,500.0	0.2073
	1,600.0	0.2073
	1,700.0	0.2073
	1,800.0	0.2073

Figure 7-2 is a plot of the enthalpy change for stainless steel oxide calculated by the subroutine SONTHL.

7.1.3 References

7.1-1 Y. S. Touloukian, E. H. Buyco, *Thermal Physical Properties of Matter, V5, Specific Heat - Non-metallic Solids*, New York: IFI/Plenum, 1970, p. 107-117.

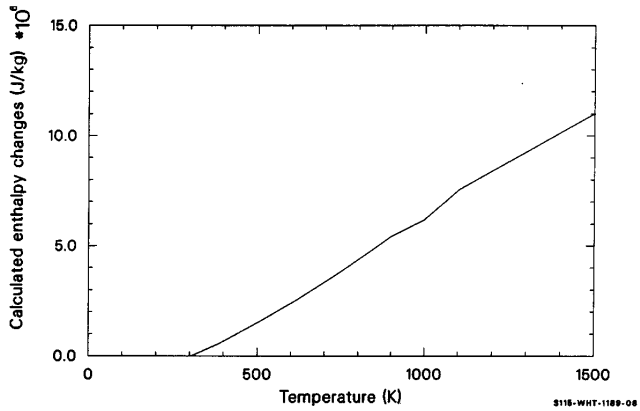

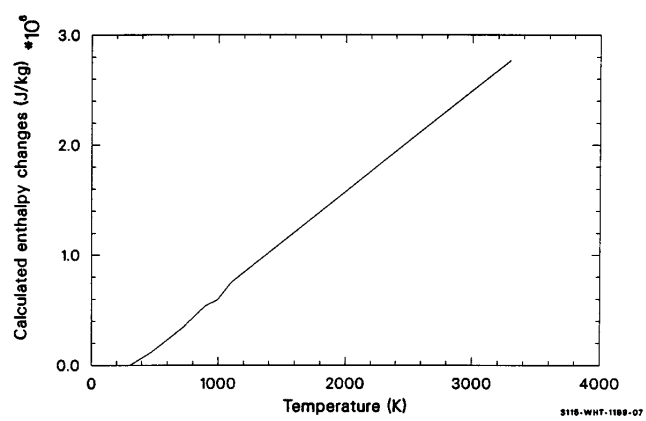

Figure 7-2. Enthalpy change for stainless steel oxide calculated by SONTHL.

7.2 Thermal Conductivity (SOTCON)

The thermal conductivity of stainless steel oxide as a function of temperature is calculated by the function SOTCON. The only input required is the temperature of the stainless steel oxide (SOTEMP).

7.2.1 Model Development

The correlation used to calculate the thermal conductivity is derived from a polynomial fit of data (Table 7-4) from Reference 7.2-1. Due to lack of available data, the calculation was truncated at a temperature of 800 K. The equation used to calculate the thermal conductivity is:

$$K_s = 4.6851 + 100\ T(-3.3292 \times 10^{-7} - 2.5618 \times 10^{-8}\ T) \qquad (7\text{-}16)$$

where

K_s	=	the stainless steel oxide thermal conductivity (W/m K)
T	=	the stainless steel oxide temperature (K).

The expected standard error of the predicted conductivities is $\pm$ 0.2 times the calculated conductivity for temperatures in the range from 300 to 800 K. For temperatures greater than 800 K, the uncertainty of the calculation increases. A plot of the thermal conductivities calculated by the function SOTCON is shown in Figure 7-3.

7.2.2 References

7.2-1 S. Touloukian, R. W. Powell, C. Y. Ho, and P. G. Klemens, *Thermal Physical Properties of Matter, V2, Thermal Conductivity - Non-Metallic Solids,* New York: IFI/Plenum, 1970, pp. 154-156.

Table 7-4. Stainless steel oxide thermal conductivity from Touloukian.

Temperature	Thermal Conductivity
317.1	0.0444
335.7	0.0435
353.9	0.0435
385.6	0.0431
453.2	0.0414

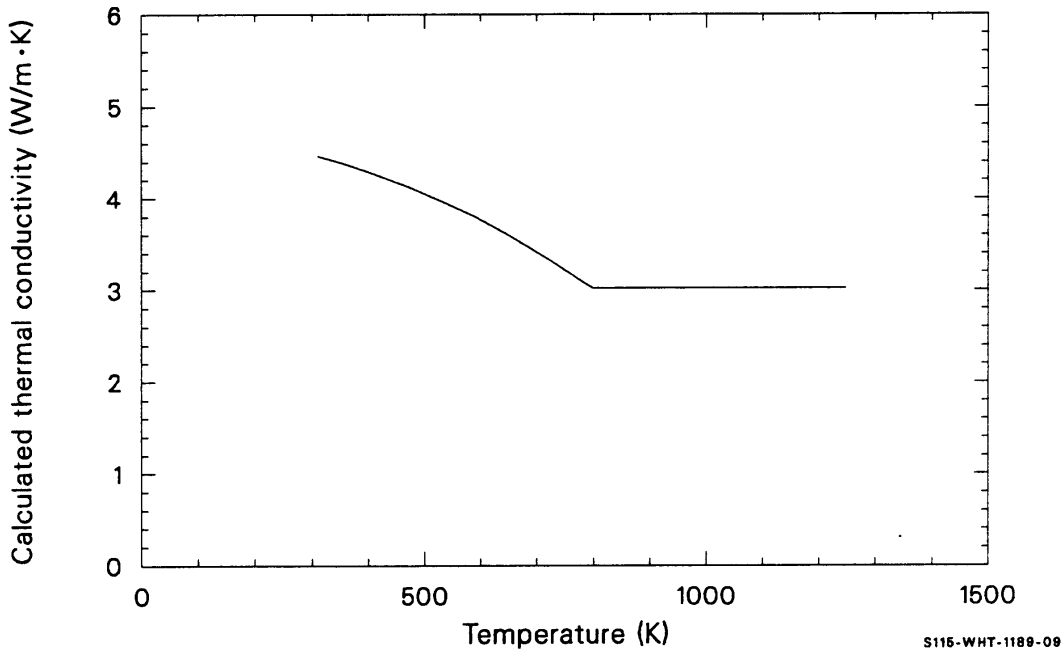

Figure 7-3. Thermal conductivities for stainless steel oxide calculated by SOTCON.

7.3 Thermal Expansion and Density (SOTHEX, SODEN)

The subcode SOTHEX calculates the stainless steel oxide thermal expansion strain, and the subcode SODEN computes the density from room temperature to the oxide melting point. SOTHEX requires the temperature of the stainless steel oxide and a reference temperature (for which the thermal strain will be zero), while SODEN requires only the temperature of the stainless steel oxide.

7.3.1 Thermal Expansion (SOTHEX)

The thermal expansion value calculated for stainless steel oxide was obtained by taking an average of the calculated thermal expansion of FeO, Fe_2O_3, and Fe_3O_4. The equations used were obtained from Reference 7.3-1 and are as follows:

$$\varepsilon_{s(FeO)} = -0.409 + 1.602 \times 10^{-3}\,T - 7.913 \times 10^{-7}\,T^2 + 5.348 \times 10^{-10}\,T^3 . \quad (7\text{-}17)$$

$$\varepsilon_{s\,(Fe_2O_3)} = -2.537 + 7.30 \times 10^{-4}\,T + 4.964 \times 10^{-7}\,T^2 - 1.140 \times 10^{-10}\,T^3 . \quad (7\text{-}18)$$

$$\varepsilon_{s\,(Fe_3O_4)} = -0.214 + 6.929 \times 10^{-4}\,T - 1.107 \times 10^{-7}\,T^2 + 8.078 \times 10^{-10}\,T^3 . \quad (7\text{-}19)$$

$$\varepsilon_{s\,(average)} = \frac{\varepsilon_{s\,(FeO)} + \varepsilon_{s\,(Fe_2O_3)} + \varepsilon_{s\,(Fe_3O_4}}{3} \quad (7\text{-}20)$$

where

$\varepsilon_{s(FeO)}$	=	the thermal expansion strain for FeO (m/m)
$\varepsilon_{s(Fe_2O_3)}$	=	the thermal expansion strain for Fe_2O_3 (m/m)
$\varepsilon_{s(Fe_3O_4)}$	=	the thermal expansion strain for Fe_3O_4 (m/m)
$\varepsilon_{s(average)}$	=	the thermal expansion strain taken as the average of the calculated strains for the three oxides (m/m)
T	=	the temperature of the stainless steel oxide (K).

The calculated thermal expansion strain for stainless steel oxide was obtained by averaging the thermal expansion strains calculated for each oxide of iron. This average strain value was used as an approximation for the thermal expansion strain of stainless steel oxide because no data for the thermal expansion strain of the oxide mixture found on oxidized stainless steel surfaces are available.

The thermal expansion strains computed by the function SOTHEX for stainless steel oxide using a reference temperature of 300 K is illustrated in Figure 7-4.

7.3.2 Density (SODEN)

The function SODEN uses the general relation between density and thermal expansion strain to calculate the density of stainless steel oxide. A density of 5.2×10^3 kg/m^3 at 300 K[7.3-2] is used as a reference density. The expected standard error of $\pm$ 0.5 kg/m^3 for the density of stainless steel oxide is due to the uncertainty of the reference density. Figure 7-5 shows the density of stainless steel oxide calculated by the function SODEN using the thermal expansion strains calculated in SOTHEX.

7.3.3 References

7.3-1 Y. S. Touloukian, R. K. Kirby, R. E. Taylor, and P. D. Desai, *Thermal Physical Properties of Matter, V12, Thermal Expansion - Metallic Elements and Alloys*, New York: IFI/Plenum, 1970, pp. 366-372.

7.3-2 *Handbook of Chemistry and Physics*, The Chemical Rubber Company, 50th Edition, 1969-1970.

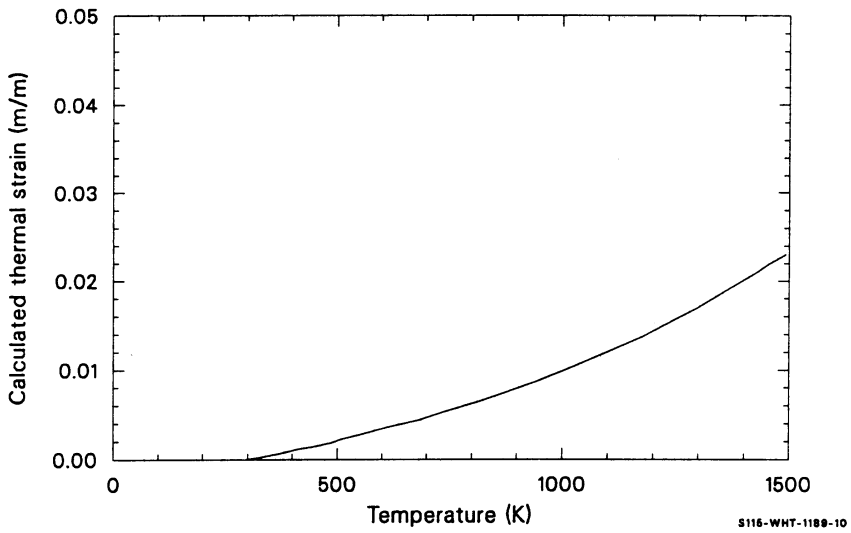

Figure 7-4. Thermal expansion strain as a function of temperature calculated by SOTHEX.

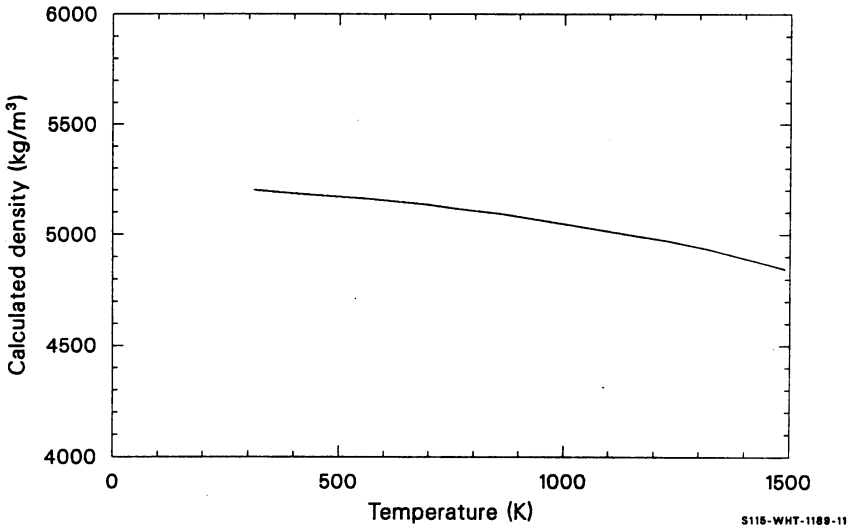

Figure 7-5. Density calculated by SODEN using the thermal strain calculated by SOTHEX.

8. NEUTRON ABSORBERS (SILVER-INDIUM-CADMIUM CONTROL RODS AND BORON CARBIDE CONTROL BLADES)

A set of control rod neutron absorber properties for silver-indium-cadmium (Ag-In-Cd) alloys (80% Ag, 15% In, 5% Cd by weight) and boron carbide (B_4C) has been prepared to allow modeling of the possible flow and freezing of these materials during a severe core disruption. Properties for both substances have been included in each subcode. An input argument, ICTYPE, is used to determine which substance properties are returned. (ICTYPE = 1 for the Ag-In-Cd control rod properties, and ICTYPE = 2 for the BWR B_4C control rod properties.)

No models have been provided for mixtures of neutron absorbers and their stainless steel cladding because it has been reported[8-1] that Ag-In-Cd alloy is insoluble in stainless steel and because the very different melting temperatures of stainless steel (1700 K) and B_4C (2700 K)[8-2] make it likely that the stainless steel will oxidize or melt and run away from hot regions before B_4C and stainless steel mix.

References

8-1 W. B. Murfin et al., *Core Meltdown Experimental Review*, SAND74-0382, NUREG-0205, 1977, p. 4-38.

8-2 Chase et al., *JANAF Thermochemical Tables*, 1986, pp. 541-543.

8.1 Melting Temperature (AHYPRP)

The subroutine AHYPRP provides absorber solidus (appearance of the first liquid phase) and liquidus (melting of the last solid phase) temperatures. There is no required input other than a parameter to identify which absorber material is used.

8.1.1 Model Development

For the typical Ag-In-Cd alloy, Reference 8.1-1 reports an approximate melting range of 1,073 to 1,123 K. These numbers are thus used for the solidus and liquidus temperatures of the alloy.

The melting temperature of 2,743 K reported on page 541 of Reference 8.1-2 is used for the solidus and liquidus temperature of B_4C.

8.1.2 References

8.1-1 D. A. Petti, *Silver-Indium-Cadmium Control Rod Behavior and Aerosol Formation in Severe Reactor Accidents*, NUREG/CR-4876, EGG-2501, April 1987.

8.1-2 Chase et al., *JANAF Thermochemical Tables*, 1986, pp. 541-543.

8.2 Specific Heat Capacity and Enthalpy (ACP, AENTHL)

The function ACP provides absorber specific heat capacities as a function of temperature. AENTHL returns the absorber enthalpies as a function of temperature and a reference temperature for which the enthalpy will be zero.

8.2.1 Specific Heat Capacity of Ag-In-Cd (ACP)

The expressions used for the specific heat capacity of Ag-In-Cd are atomic fraction weighted averages of the specific heat capacities of silver, indium, and cadmium

$$C_p = \frac{0.808 C_{pm_{Ag}} + 0.143 C_{pm} + 0.049 C_{pm_{Cd}}}{0.109 \frac{kg}{mole} \text{Alloy}} \tag{8-1}$$

where

C_p	=	alloy specific heat capacity (J/kg• K)
$C_{pm_{Ag}}$	=	molar heat capacity of silver (J/mole•K)
$C_{pm_{In}}$	=	molar heat capacity of indium (J/mole• K)
$C_{pm_{Cd}}$	=	molar heat capacity of cadmium (J/mole• K).

Expressions for the silver, indium, and cadmium molar heat capacities up to the beginning of melting, 1,073 K, were taken from Table 2-24 of Reference 8.2-1. All are correlations of the form

$$C_{pm} = a + b \times 10^{-3} T + d \times 10^{5} T^{-2} \tag{8-2}$$

where

C_{pm}	=	molar heat capacity (J/mole•K)
T	=	temperature (K)

and the constants a, b, and d are listed in Table 8-1. For temperatures above 1,073 K, C_p is assumed to be equal to its value at 1,073 K. Figure 8-1 shows the heat capacity of Ag-In-Cd calculated by ACP. A standard error of 10% of the calculated value is predicted.

8.2.2 Specific Heat Capacity for Boron Carbide(ACP)

The expressions used for the specific heat capacity of B_4C are listed below:

For T < 2,700 K,

$$C_p = 563 + T\,(1.54 - T\,2.94 \times 10^{-4}) \quad . \tag{8-3}$$

For $T \geq 2{,}700$ K,

$$C_p = 2{,}577.740 \quad . \tag{8-4}$$

Equations (8-3) and (8-4) were developed from a curve given on page 588 of Reference 8.2-2. Figure 8-2 shows the heat capacity of boron carbide as calculated by the function ACP. The prediction has a standard error near 0.10 of its value.

8.2.3 Enthalpy of Ag-In-Cd (AENTHL)

Integrals of Equation (8-2), (8-3), or (8-4) are used to compute enthalpy changes in the AENTHL function for the Ag-In-Cd absorber (ICTYPE = 1). The heat of fusion which is included in the AENTHL function is an estimate. The Ag-In-Cd heat of fusion, 9.5610^4 J/kg, was estimated by multiplying the molar heats of fusion of silver, indium, and cadmium by the atomic fraction of each element in the alloy; summing the calculated fractional heats of fusion; and dividing the sum by 0.109, the weight of a g-mole of the alloy in kilograms. The elemental heats of fusion were obtained from Tables 2 through 24 of Reference 8.2-1. Figure 8-3 shows the enthalpy changes calculated for Ag-In-Cd by AENTHL. The prediction has a standard error near 0.10 of its value.

Table 8-1. Molar heat capacity constants for Equation (8-1) from Reference 8.2-1.

Metal	a (J/mole• K)	b (J/mole• K)	d (J• K/mole)
Silver	21.3	4.27	1.51
Indium	24.3	10.5	0
Cadmium	22.2	12.3	0

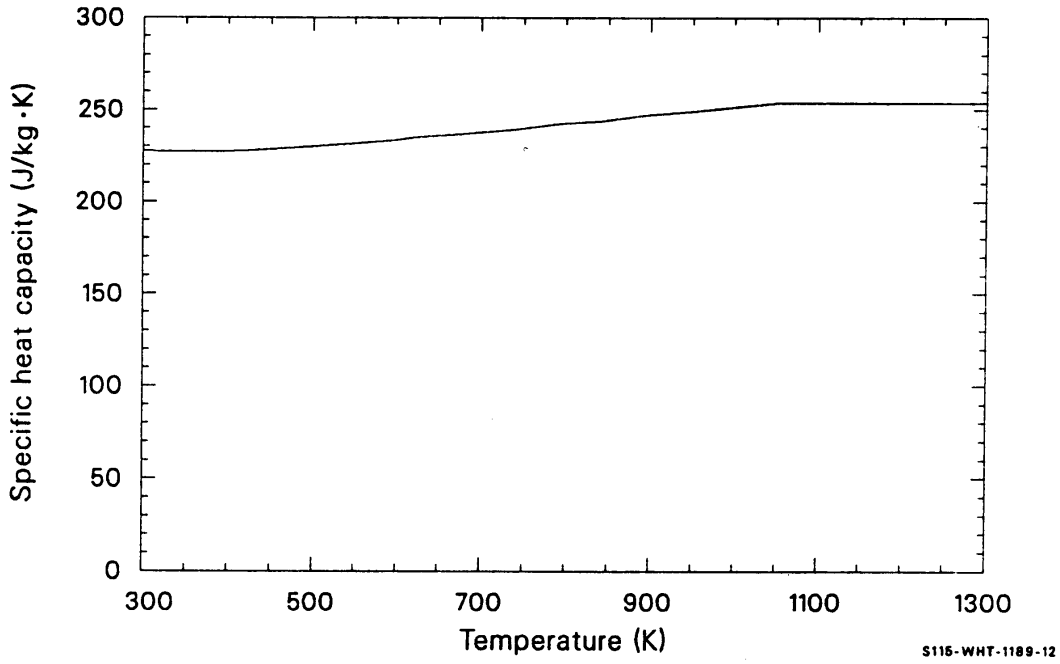

Figure 8-1. Silver-indium-cadmium absorber heat capacity.

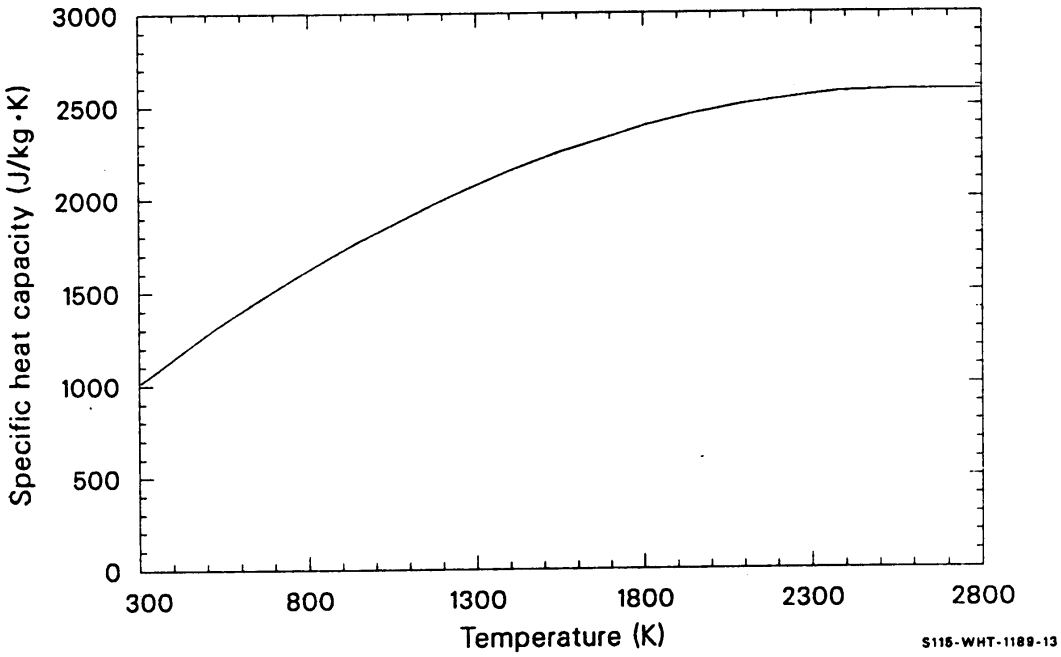

Figure 8-2. Boron carbide absorber heat capacity.

8.2.4 Enthalpy of Boron Carbide (AENTHL)

An integral of Equation (8-3) is used to compute enthalpy changes in the AENTHL function for the B_4C absorber (ICTYPE = 2). The estimated heat of fusion for B_4C was taken to be that of UO_2, 2.74 x 10^5 J/kg. Figure 8-4 shows the enthalpy changes calculated for B_4C by AENTHL. The prediction has a standard error near 0.10 of its value.

8.2.5 References

8.2-1 C. T. Lynch (ed.), *Handbook of Materials Science, II: Metals, Composites and Refractory Materials*, Cleveland: CRC Press, Inc.

8.2-2 Aerojet Nuclear Company, *Materials Properties Data Book*, AGC2275, 1970.

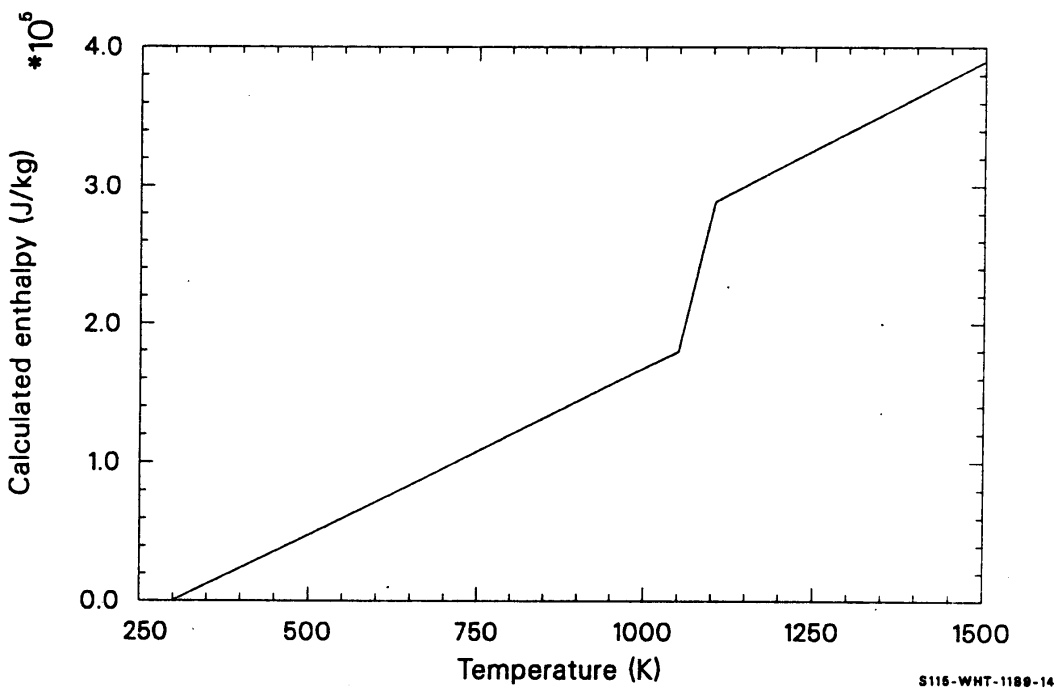

Figure 8-3. Silver-indium-cadmium absorber enthalpy.

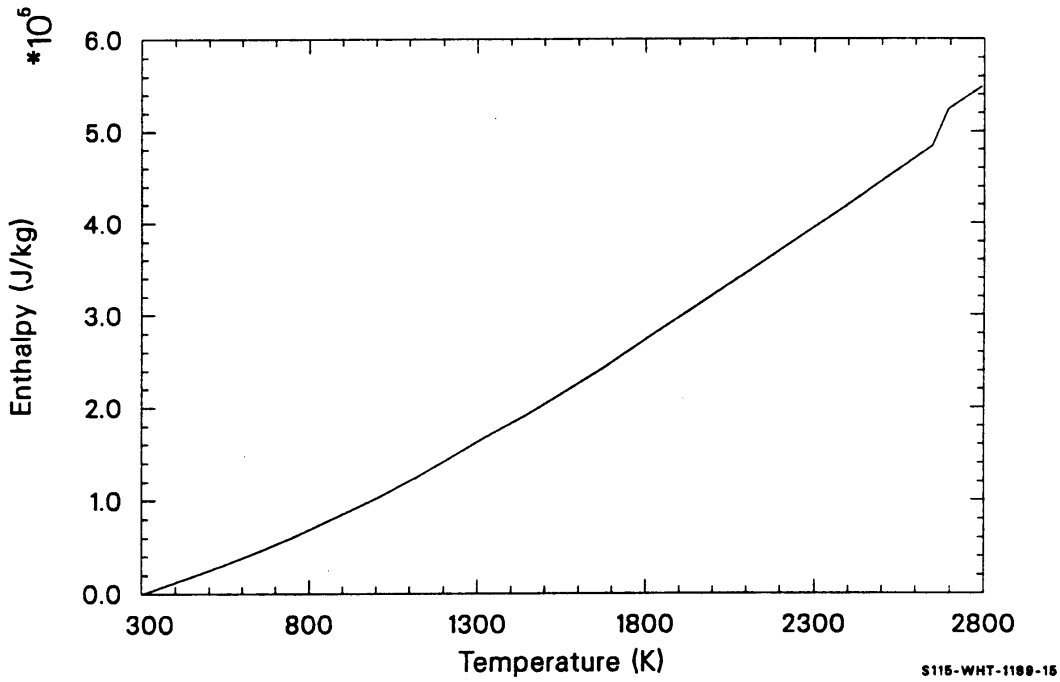

Figure 8-4. Boron carbide absorber enthalpy.

8.3 Thermal Conductivity (ATHCON)

The only input required by ATHCON to calculate the thermal conductivity of Ag-In-Cd or B_4C is the absorber temperature.

8.3.1 Thermal Conductivity of Ag-In-Cd (ATHCON)

The expressions used for Ag-In-Cd are listed below:

For $300 \leq T < 1{,}073$ K,

$$K_a = 2.805 \times 10^1 + T\,(1.101 \times 10^{-1} - 4.436 \times 10^{-5}\,T) \quad . \tag{8-5}$$

For $1{,}073 \leq T < 1{,}123$ K,

$$K_a = 1.119736 \times 10^3 - 0.954592\,T \quad . \tag{8-6}$$

For $T \geq 1{,}123$ K,

$$K_a = 47.730 \tag{8-7}$$

where

K_a = absorber thermal conductivity (W/m•K)

T = absorber temperature (K).

The correlation (8-5) was derived by fitting a second degree polynomial to the first, fourth, and seventh entries of a table of properties provided by Reference 8.3-1. The table is reproduced as Table 8-2. Equation (8-7) was derived by dividing the conductivity predicted by Equation (8-5) for 1,098 K (the middle of the melting range) by two to estimate the conductivity when this face centered cubic solid[8.3-1] melts. The method for estimating liquid conductivities follows recommendations by Nazare et al.[8.3-2] Equation (8-6) is simply a linear interpolation between the conductivity predicted by Equation (8-5) at the beginning of melting (1,073 K) and Equation (8-7) when melting is complete. Figure 8-5 is a comparison of the predictions of Equations (8-5) through (8-7) with the recommended values of Table 8-2. Figure 8-6 shows the thermal conductivity of the Ag-In-Cd absorber calculated by ATHCON. An expected standard error of 0.20 is recommended.

Table 8-2. Thermal conductivity values for Ag-In-Cd recommended by Cohen et al.[8.3-1]

Temperature (K)	Thermal Conductivity (W/m•K)
323	59.0
373	62.8
473	70.3
573	76.6
673	82.0
773	86.6
873	90.4

8.3.2 Thermal Conductivity of Boron Carbide (ATHCON)

For B_4C, thermal conductivity, the following expressions are used:

For T < 1,700 K,

$$K_a = \frac{1}{1.79\times10^{-2} + 4.98\times10^{-5}T} \quad . \tag{8-8}$$

For T ≥ 1700 K,

$$K_a = 9.750390 \quad . \tag{8-9}$$

The expression is a fit to values of 23.37 and 13.76 W/m• K at 500 and 1,100 K, respectively, obtained from the 150 lb•m/ft^3 curve presented on page 947 of Reference 8.3-3. An expected standard deviation of 50% is recommended because of the significant effect of density of the material. Figure 8-7 shows the predicted values for the thermal conductivity of B_4C.

8.3.3 References

8.3-1 I. Cohen, E. F. Losco, and J. D. Eichenberg, "Metallurgical Design and Properties of Silver-Indium-Cadmium Alloys for PWR Control Rods," *Bettis Technical Review*, 1958.

8.3-2 S. Nazare, G. Ondracek, and B. Schulz, "Properties of Light Water Reactor Core Melts," *Nuclear Technology, 32*, 1977, pp. 239-246.

8.3-3 A. Goldsmith, T. E. Waterman, and H. J. Hirschhorn, *Handbook of Thermophysical Properties of Solid Materials, Revised Edition, Volume III: Ceramics*, New York: The MacMillan Company, 1961.

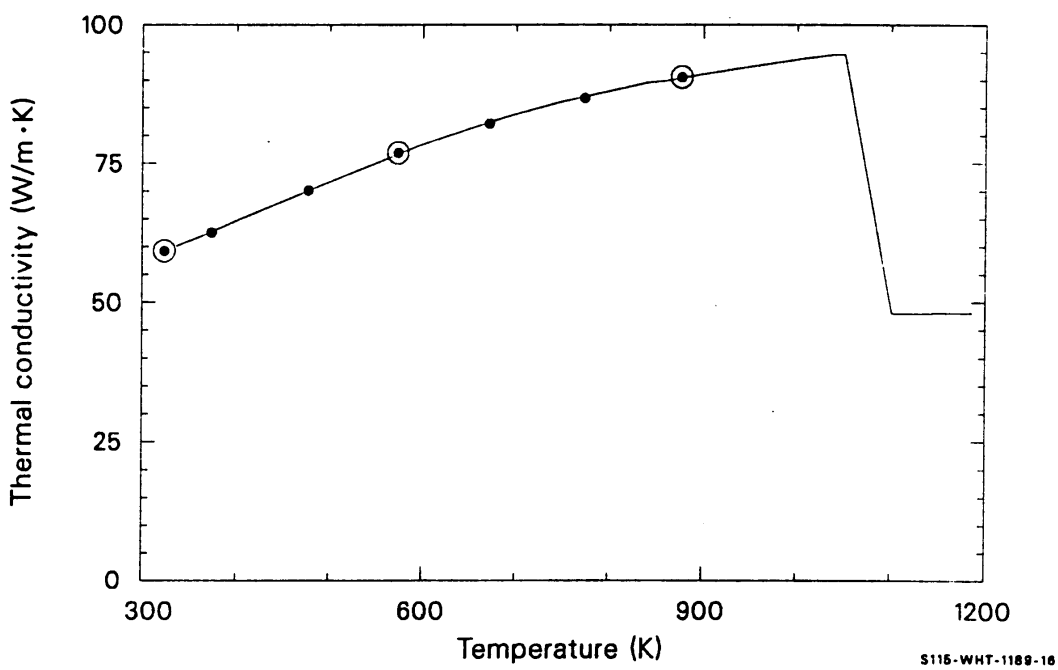

Figure 8-5. Thermal conductivity of silver-indium-cadmium alloy.

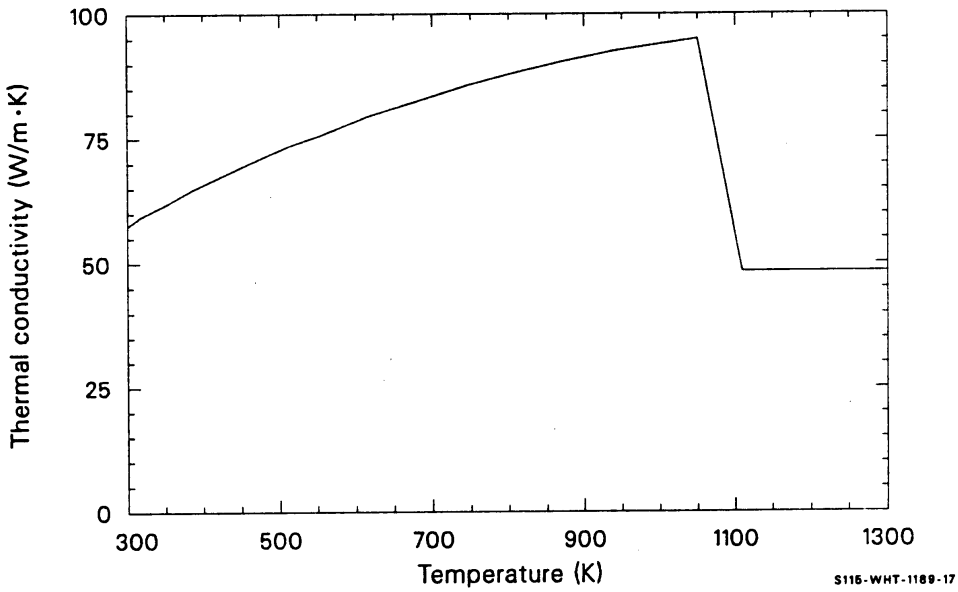

Figure 8-6. Thermal conductivity of silver-indium-cadmium absorber.

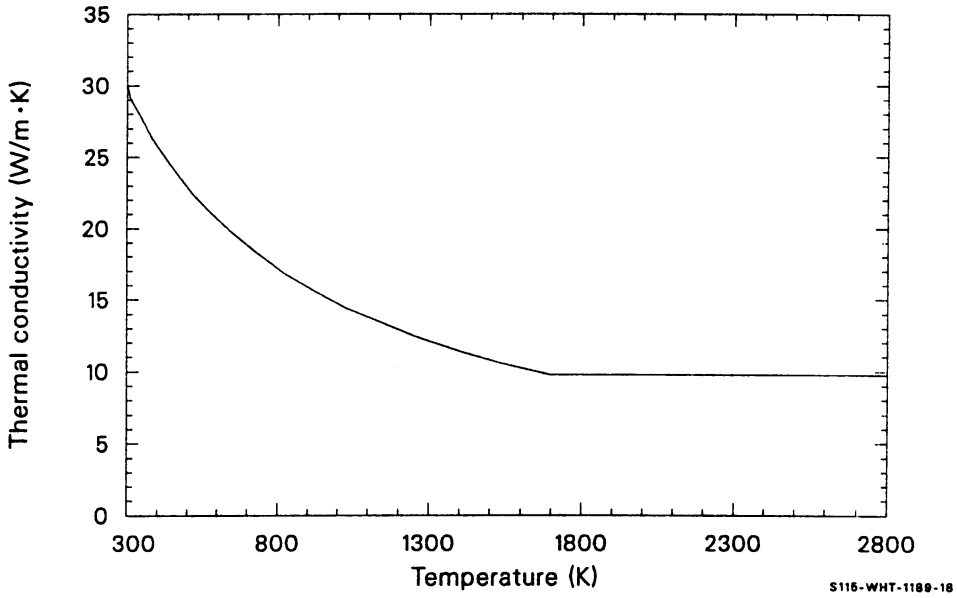

Figure 8-7. Thermal conductivity of boron carbide absorber.

8.4 Thermal Expansion and Density (ATHEXP, ADEN)

The function ATHEXP calculates absorber thermal expansion strain, while ADEN is designed to use this information to calculate absorber densities. ATHEXP requires input values of the materials temperature and a reference temperature (for which strain will be taken as zero). ADEN requires only temperature.

8.4.1 Thermal Expansion Strain of Ag-In-Cd

The expressions used for the thermal expansion strain of Ag-In-Cd absorbers are listed below:

For $300 \leq T < 1{,}073$ K,

$$\varepsilon_a = 2.25 \times 10^{-5} (T - 300) \quad . \tag{8-10}$$

For $1{,}073 \leq T < 1{,}123$ K,

$$\varepsilon_a = -0.25875 + 2.625 \times 10^{-4} \times T \quad . \tag{8-11}$$

For $T \geq 1{,}123$ K,

$$\varepsilon_a = 3.0 \times 10^{-2} \tag{8-12}$$

where

ε_a	=	absorber thermal expansion strain (m/m)
T	=	absorber temperature (K).

Equation (8-10) is taken from Table V of Reference 8.4-1. Equation (8-12) was obtained by modifying the prediction of Equation (8-10) to allow for an increase of 0.038 in volume (0.013 in length) at the center of the melting range of 1,073 to 1,123 K because page 186 of Reference 8.4-2 reports this value for the change in volume of silver, the major component of the alloy, during melting. Equation (8-11) is a linear interpolation between the predictions of Equations (8-10) and (8-12) for the beginning and end of the melting range. The expected standard error of Equations (8-10) through (8-12), $\pm$ 0.10 of the predicted strain, is small because the data cover most of the range of the correlations. Figure 8-8 shows the predicted thermal expansion strain for Ag-In-Cd.

8.4.2 Thermal Expansion Strain of Boron Carbide

The expression used to calculate thermal expansion strains of B_4C is

$$\varepsilon_a = -1.10 \times 10^{-3} + T (3.09 \times 10^{-6} + 1.88 \times 10^{-9} T) \quad . \tag{8-13}$$

This correlation is a fit to values of 0, 2.58 x 10^{-3}, and 5.32 x 10^{-3} at 300, 800 and 1,200 K, respectively, obtained from a curve presented on page 949 of Reference 8.4-3. The expected standard error is $\pm$ 0.2 of the predicted strain. Figure 8-9 shows the predicted thermal expansion strain for B_4C.

8.4.3 Density Calculations for Ag-In-Cd and Boron Carbide

The function ADEN uses the general relation between density and thermal strain, together with reference densities of 10.17 x 10^3 kg/m^3 at 300 K for Ag-In-Cd (Reference 8.4-1, Table V) and 2.5 x 10^3 kg/m^3 at 300 K for B_4C (page 943 of Reference 8.4-3). For Ag-In-Cd, the expected standard error is only 0.02 of the predicted density; but for B_4C, it is $\pm$ 0.30 of the predicted density.

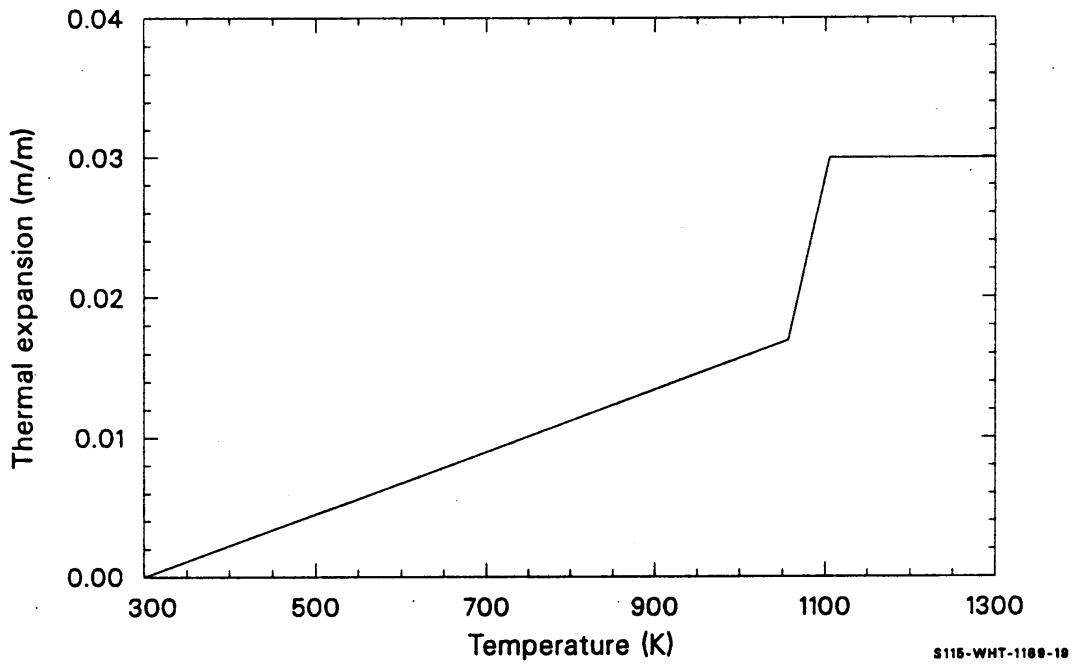

Figure 8-8. Thermal expansion strain of silver-indium-cadmium absorber.

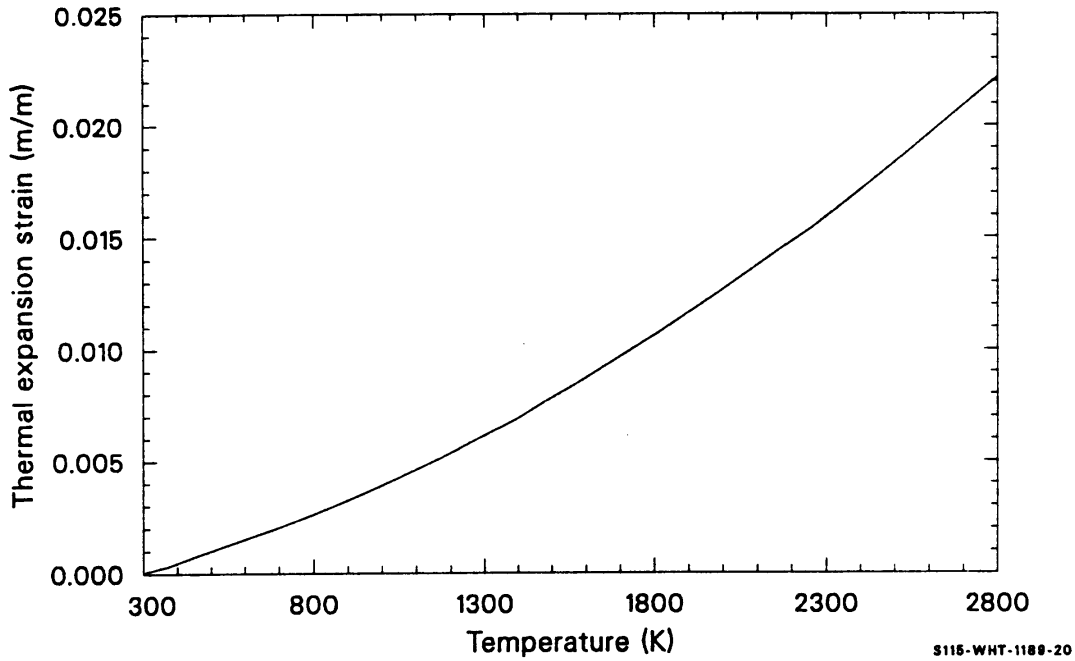

Figure 8-9. Thermal expansion strain of boron carbide absorber.

The prediction for Ag-In-Cd and B_4C versus temperature given by the function are shown in Figures 8-10 and 8-11.

8.4.4 References

8.4-1 I. Cohen, E. F. Losco and J. D. Eichenberg, "Metallurgical Design and Properties of Silver-Indium-Cadmium Alloys for PWR Control Rods," *Bettis Technical Review*, 1958.

8.4-2 C. J. Smithells and E. A. Brandes (eds.), *Metals Reference Book*, London and Boston: Butterworths, 1956.

8.4-3 A. Goldsmith, T. E. Waterman, and H. J. Hirschhorn, *Handbook of Thermophysical Properties of Solid Materials. Revised Edition Volume III: Ceramics*, New York: The MacMillan Company, 1961.

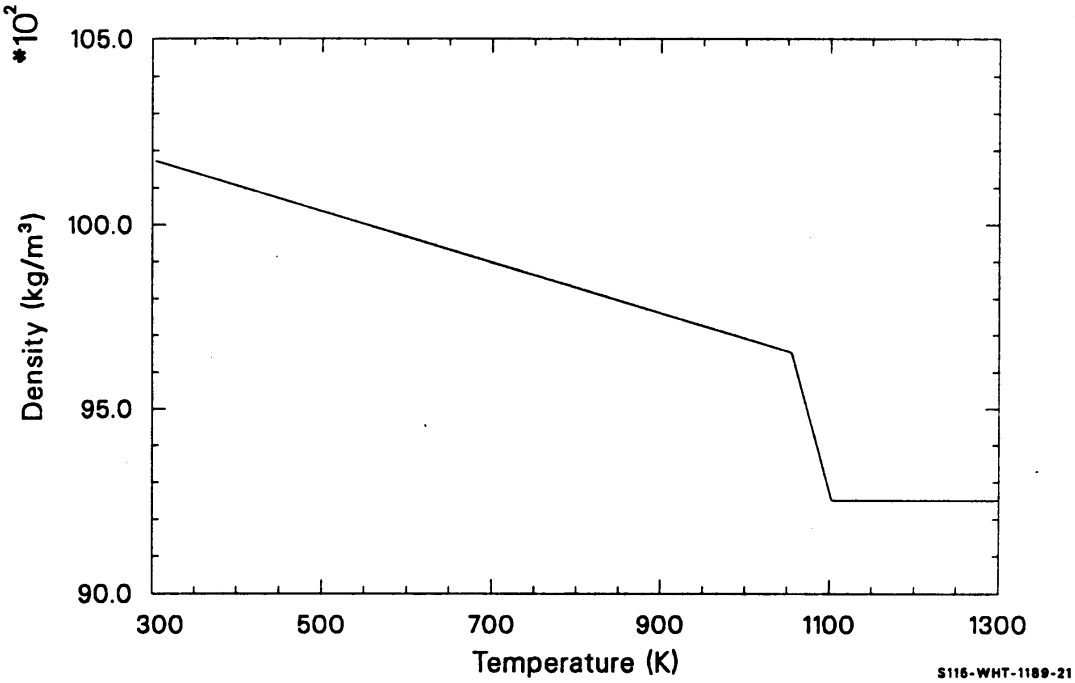

Figure 8-10. Density of silver-indium-cadmium absorber.

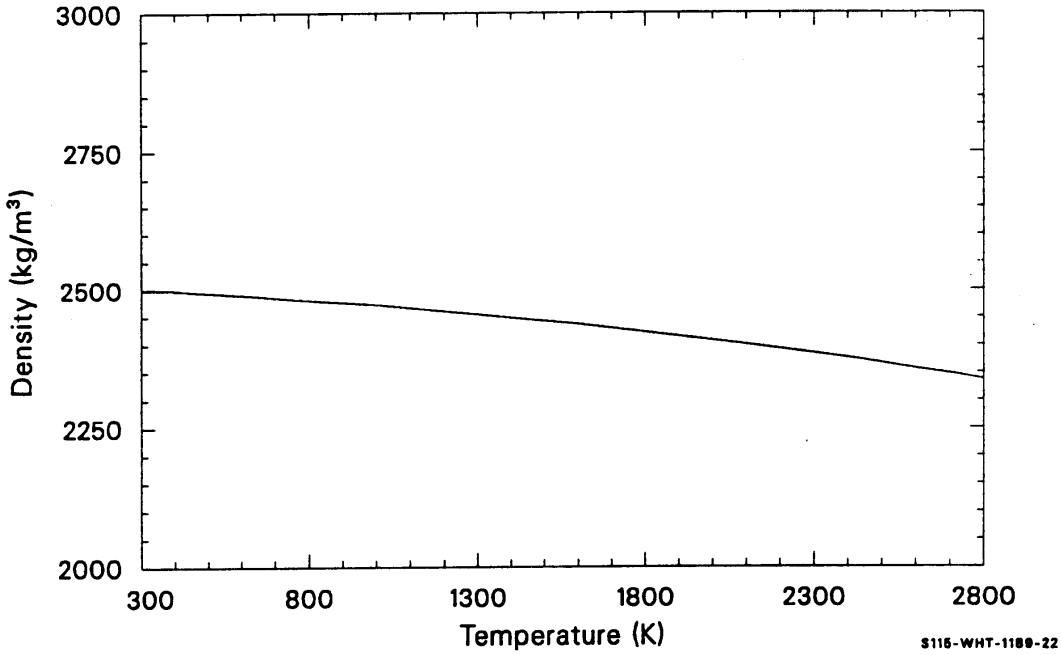

Figure 8-11. Density of boron carbide absorber.

8.5 Surface Tension (ASTEN)

8.5.1 Model Development

The function ASTEN returns the interfacial surface tension of absorber material on stainless steel cladding. The value used for both the Ag-In-Cd and B_4C absorbers is

$$ST = 0.3 \tag{8-14}$$

where ST is the interfacial surface tension (N/m).

The number used is an engineering estimate based on the relative magnitudes of zirconium and silver liquid surface tensions given by Allen[8.5-1] and the interfacial surface tension for zircaloy and zirconium-uranium-oxygen compounds given in the ZUSTEN function of Section 11.6. The expected error of this number is +2.0,-0.2.

8.5.2 References

8.5-1 B. C. Allen, "The Surface Tension of Liquid Transition Metals at Their Melting Points," *Transactions of the Metallurgical Society of AIM, 227*, 1963, pp. 1175-1183.

8.6 Viscosity (AVISC)

The function AVISC returns an estimate of the viscosity of Ag-In-Cd or B_4C neutron absorbers as a function of temperature.

8.6.1 Viscosity of Ag-In-Cd

For Ag-In-Cd, a viscosity of 10^{10} Pa• s is returned for temperatures below 1,050 K. When the temperature is above 1,100 K, a mole fraction weighted average of the alloy component viscosities is used.

$$\eta_1 (f_{Ag}\, \eta_{Ag} + f_{In}\, \eta_{In} + f_{Cd}\, \eta_{Cd}) \tag{8-15}$$

where

η_1	=	viscosity of liquid absorber (Pa•s)
f_{Ag}	=	mole fraction of silver in the alloy, 0.808
η_{Ag}	=	viscosity of silver (Pa•s)
f_{In}	=	mole fraction of indium in the alloy, 0.143
η_{In}	=	viscosity of indium (Pa•s)
f_{cd}	=	mole fraction of cadmium in the alloy, 0.049
η_{Cd}	=	viscosity of cadmium (Pa• s).

The component viscosities are calculated with expressions obtained from procedures recommended by Nazare, Ondracek, and Schulz.[8.6-1]

$$\eta_{Ag} = 2.95\times10^{-4}\exp\left(\frac{3187}{T}\right) \quad . \tag{8-16}$$

$$\eta_{In} = 3.18\times10^{-4}\exp\left(\frac{768}{T}\right) \quad . \tag{8-17}$$

$$\eta_{Cd} = 3.19\times10^{-4}\exp\left(\frac{1190}{T}\right) \tag{8-18}$$

where T is the absorber temperature (K).

When the temperature is between 1,050 and 1,100 K, an interpolation scheme is used

$$\eta = \frac{\eta_l\,(T - 1050) + 10^{10}\,(1100 - T)}{50} \tag{8-19}$$

where η is the viscosity of the absorber in the two-phase temperature range, 1,050 to 1,100 K (Pa• s). Figure 8-12 is a plot showing the calculated liquid phase viscosity of Ag-In-Cd. The expected standard error is $\pm$ 0.8 of the predicted value because there are no data to support the model.

8.6.2 Viscosity of Boron Carbide

For B_4C absorbers, a viscosity of 10^{10} Pa•s is returned for temperatures less than 2,700 K. When the temperature is at or above 2,700 K, the expression used is

$$\eta_{B_4C} = 1.21\times10^{-4}\exp\left(\frac{9158}{T}\right) \tag{8-20}$$

where ηB_4C is the viscosity of liquid B_4C absorber (Pa• s).

Figure 8-13 is a plot showing the calculated liquid phase viscosity of B_4C. The expected error of the B_4C viscosity models is $\pm$ 0.8 of the predicted value because there are no data in support of the model.

8.6.3 References

8.6-1 S. Nazare, G. Ondracek, and B. Schulz, "Properties of Light Water Reactor Core Melts," *Nuclear Technology*, *32*, 1977, pp. 239-246.

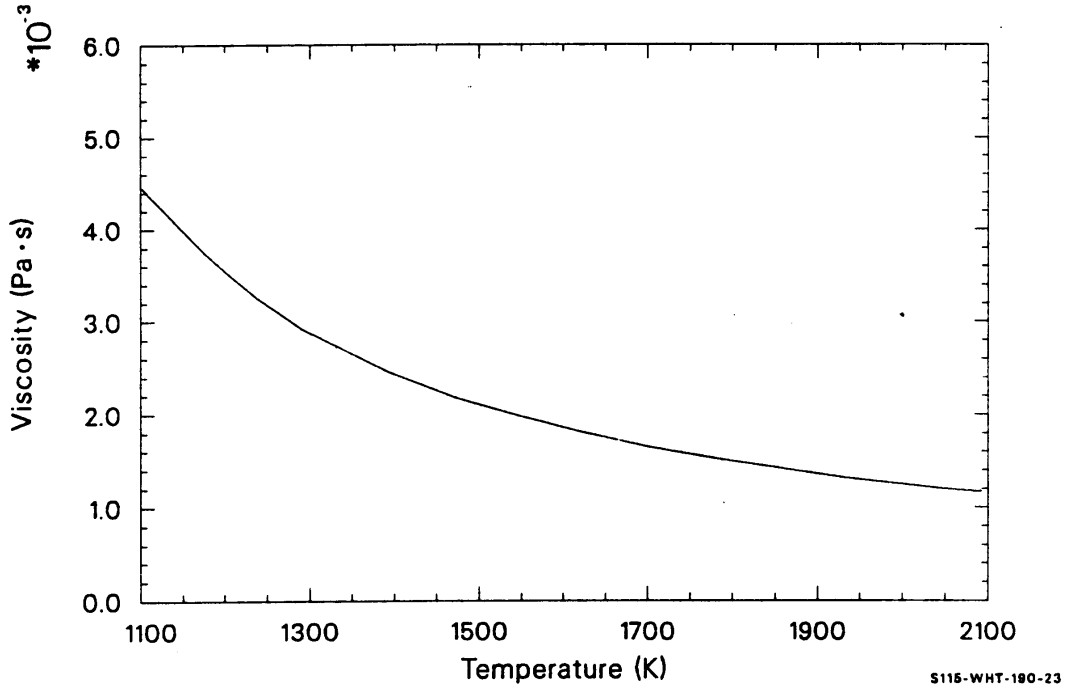

Figure 8-12. Viscosity of silver-indium-cadmium absorber.

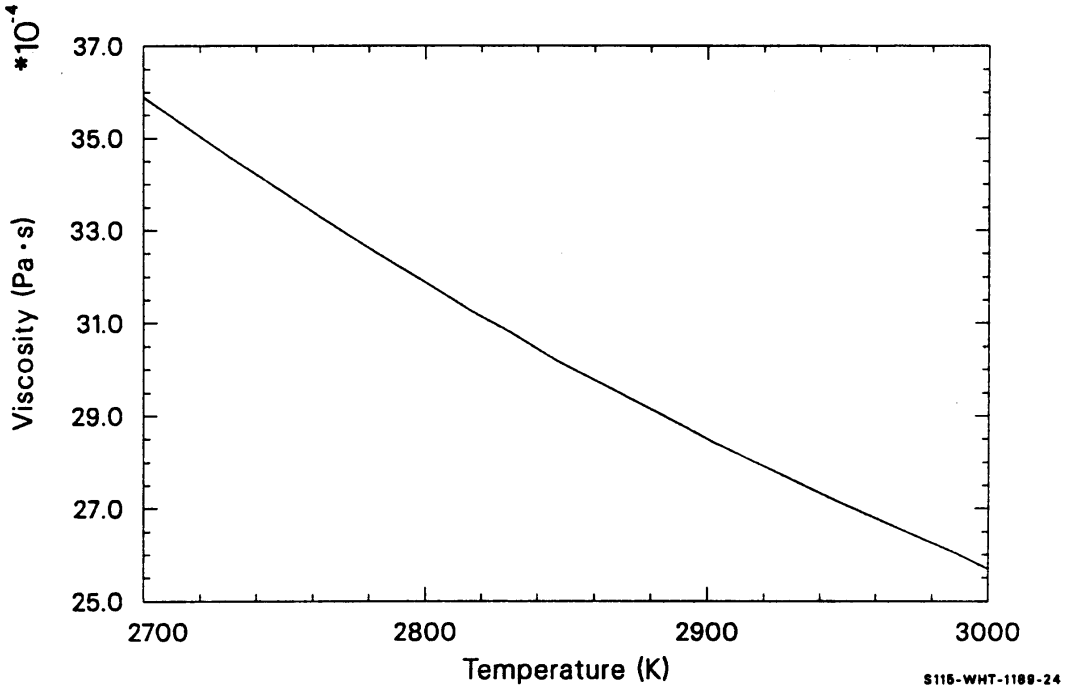

Figure 8-13. Viscosity of boron carbide absorber.

9. CADMIUM

9.1 Specific Heat (CDCP)

The specific heat is calculated by subroutine **CDCP** as a function of temperature. The temperature dependent specific heat[9-1] values are shown in Table 9-1. Linear interpolation is provided for temperature calls which fall between tabular values. Regardless of the input temperature, a specific heat value is always returned. Calls to **CDCP** that are outside the table range will be returned with either the first or last table value. **CDCP** also returns the flag **IERR** that is normally 0, but will be set to 1 if the input temperature lies outside the range 300 K to 4000 K.

Table 9-1. Cadmium specific heat as a function of temperature.

Temperature (K)	Specific Heat [J/(Kg•K)]
298.15	231.3
400.0	241.8
500.0	252.6
594.0	263.7
594.001[a]	264.4

a. liquid phase.

9.2 Thermal Conductivity (CDTCON)

Thermal conductivity is calculated by subroutine **CDTCON** as a function of temperature. The temperature dependent thermal conductivity[9-1] values are shown in Table 9-2. Linear interpolation is provided for temperature calls that fall between tabular values. Regardless of the input temperature, a thermal conductivity value is always returned. Calls to **CDTCON** that are outside the table range will be returned with either the first or last table value. **CDTCON** also returns the flag **IERR** that is normally 0, but will be set to 1 if the input temperature lies outside the range 300 K to 4,000 K.

Table 9-2. Cadmium thermal conductivity as a function of temperature.

Temperature (K)	Thermal Conductivity [W/(m•K)]
273.15	97.5
293.15	97.0
303.15	96.8
333.15	96.2
373.15	95.3
403.15	94.7
433.15	94.2
473.15	92.9
503.15	91.9
533.15	90.8
573.15	88.9
594.0	87.9
594.001[a]	41.6
600.0	42.0
700.0	49.0
800.0	55.9
1,040.0	72.5

a. liquid phase.

9.3 Density (CDDEN)

Density is calculated by subroutine **CDDEN** as a function of temperature. The temperature dependent density[9-1] values are shown in Table 9-3. Linear interpolation is provided for temperature calls which fall between tabular values. Regardless of the input temperature, a density value is always returned. Calls to **CDDEN** that are outside the table range will be returned with either the first or last table value. **CDDEN** also returns the flag **IERR** that is normally 0, but will be set to 1 if the input temperature lies outside the range 300 K to 4,000 K.

Table 9-3. Cadmium density as a function of temperature.

Temperature (K)	Density (kg/m^3)
273.15	8,670
303.15	8,640
333.15	8,610
363.15	8,580
403.15	8,541
433.15	8,511
473.15	8,470
503.15	8,439
533.15	8,406
573.15	8,360
594.	8,336
594.01[a]	8,020
602.0	8,010
623.0	7,990
773.0	7,820
873.0	7,720

a. liquid phase.

9.4 Enthalpy (CDENTH)

The enthalpy of cadmium is calculated by subroutine **CDENTH** as a function of temperature. The temperature dependent enthalpy[9-1] values are shown in Table 9-4. **CDENTH** also returns the flag **IERR** that is normally 0 but will be set to 1 if the input temperature (**T**) lies outside the range 300 k to 4,000 K. Regardless of the input temperature, an enthalpy is always returned. If the temperature is outside the table range, either the first or last tabular value of enthalpy will be returned. Included in the input call to **CDENTH** is the call variable and **TREF**. **TREF** is the reference temperature at which the enthalpy is calculated. This is normally 298 K. Note that if **T** ≤ 298.0 or if **T** ≤ **TREF**, then the returned enthalpy value is zero.

Table 9-4. Cadmium enthalpy as a function of temperature.

Temperature (K)	Enthalpy (J/kg)
298.0	0.0
400.0	24,050.0
500.0	48,770.0
594.0	72,960.0
594.001[a]	128,050.0
600.0	129,650.0
800.0	182,510.0
1,000.0	235,370.0

a. liquid phase.

9.5 References

9-1 A. Cronenberg, *Handbook of Material Melt Properties for Savannah River Plant Accident Analysis Studies*, ESA-SCDAP-101, (available from Engineering Science and Analysis), April 1989.

10. GRID SPACER MATERIAL (INCONEL)

Material properties for Inconel, which include melting temperature, enthalpy, thermal conductivity and density, are available in the MATPRO library. This information is discussed below.

10.1 Melting Temperatures (HPROP)

The subroutine **HPROP** provides Inconel 718 melting temperatures. No input information is required.

For Inconel 718, page 267 of Reference 10.1-1 reports a melting range of 1,533 through 1,609 K. These numbers are used for the solidus and liquidus temperatures of Inconel grid spacers.

10.2 Enthalpy Correlations (USERP[a])

Enthalpy is calculated by subroutine **USERP** as a function of temperature. The temperature dependent enthalpy values are shown in Table 10-1.[10.1-1] Linear interpolation is provided for temperature calls which fall between tabular values. Calls to **USERP** that are outside the table range will be returned with either the first or last table value. The reference temperature for enthalpy is 0 K.

Table 10-1. Enthalpy of Inconel as a function of temperature.

Temperature (K)	Enthalpy (J/kg)
298	127,420
373	160,100
473	205,550
573	253,170
673	302,950
773	354,910
873	409,030
973	465,320
1,073	523,770
1,533	791,700
1,663	869,100
1,664	117,190
1,800	125,290

a. Presently, material properties defined by subroutine USERP are only available to COUPLE routines.

Table 10-1. Enthalpy of Inconel as a function of temperature. (Continued)

Temperature (K)	Enthalpy (J/kg)
2,000	137,200
2,200	149,100
2,400	161,010
2,600	172,920
6,000	375,360

10.3 Thermal Conductivity (USERP[a])

Thermal conductivity is calculated by subroutine **USERP** as a function of temperature. The temperature dependent thermal conductivity values are shown in Table 10-2.[10.1-1] Linear interpolation is provided for temperature calls which fall between tabular values. Calls to **USERP** that are outside the table range will be returned with either the first or last table value.

Table 10-2. Thermal conductivity of Inconel as a function of temperature.

Temperature (K)	Thermal Conductivity [W/(m•K)]
298	11.45
373	12.68
473	14.27
573	15.85
673	17.44
773	19.03
873	20.62
973	22.21
1,073	23.80
6,000	23.80

a. Presently, material properties defined by subroutine USERP are only available to COUPLE routines.

10.4 Density (USERP[a])

Density is treated by subroutine **USERP** as a constant value. The constant density value returned by **USERP** is 8000 kg/m^3.[10.1-2]

10.5 References

10.1-1 C. T. Lynch (ed.), *Handbook of Materials Science, Volume II: Metals, Composites, and Refractory Materials*, Cleveland, OH: CRC Press, Inc.

10.1-2 S. Touloukian et al., *Thermophysical Properties of Matter*, The TPRC Data Series, New York, Plenum Publishing Corp., February 1978.

a. Presently, material properties defined by subroutine USERP are only available to COUPLE routines.

11. ZIRCONIUM-URANIUM COMPOUNDS

Extension of the MATPRO materials properties package to high temperatures requires consideration of mixtures and compounds that are not formed until zircaloy cladding melts. One approach to providing the properties of molten mixtures of core material has been to define standard compounds of core materials--Corium A, Corium E, Corium AX1, Corium EX1, Corium EX2, Corium EX3, etc.[11-1] This approach has been avoided here because deciding when to switch from properties of one kind of melt to another would needlessly complicate serious efforts to model severe core damage. The six different types of corium listed above are replaced with a single class of material whose properties vary with zirconium, uranium, and oxygen concentration in the subroutines originally supplied with MATPRO and with zirconium, uranium, stainless steel, oxygen, Ag-In-Cd, and/or B_4C in newer versions of the subcodes described in this section.

In the older versions of the subcodes, concentrations of iron, chrome, nickel, silver, indium, cadmium, and other low melting components have been ignored because compounds rich in these components will probably migrate to cooler regions of the core before the melting temperature of zircaloy is attained. In the newer versions of the subcodes, only the concentrations of chrome, nickel, and a few other low melting components have been ignored. Since both versions are supplied, a discussion of each subcode version will be included in this section.

Data for all the properties modeled in this section are very scarce, so most of the subcodes use interpolations of materials properties that are available--the properties of UO_2, ZrO_2, and zircaloy in the original version and these core component elements plus FeO, Fe_2O_3, Fe_3O_4, silver, and B_4C in the newer version. These materials are used as a basis for interpolation rather than the properties of elemental uranium, zirconium, and oxygen because UO_2, ZrO_2 and zircaloy more closely approximate the compositions of interest.

For Zr-U-O compounds, a Gibbs triangle plot[11-2] of the compositions of Zr-U-O compounds (as shown in Figure 11-1) illustrates this point. It can be shown that the composition of a mixture of any two ternary Zr-U-O alloys will lie on a straight line joining the points representing the original compositions on a Gibbs plot. Severe core damage will melt zircaloy (represented here as mostly zirconium) that has been previously oxidized to some state between oxygen stabilized zircaloy, Zr(O), and ZrO_2. This melt will dissolve and mix with UO_2. The gross compositions of interest are thus most likely to lie in the shaded region of the plot. (Some uranium rich phases, which could melt and flow out of the hot region, are the only known exceptions to this general observation.)

When interpolated properties are used, the atomic fraction of each core material in the corium compound is input and is converted to a mole fraction using the following relation:

$$mfc_i = \frac{af_i}{\sum_{i=1}^{n} af_i} \tag{11-1}$$

where

mfc_i = mole fraction of the i-th core component in the compound

af_i = atomic fraction of the i-th core component in the compound

n = number of core components in the compound.

An inspection of Equation (11-1) reveals several limitations:

First,

$$1 = \sum_{i=1}^{n} af_i \tag{11-2}$$

and thus all but one of the three atomic fractions must be input. Also, the atomic fraction of oxygen must lie in the range

$$af_u \le \frac{\sum_{i=1}^{n} af_i - \sum_{j=1}^{m} afo_j}{2} \le \sum_{j=1}^{m} afo_j \tag{11-3}$$

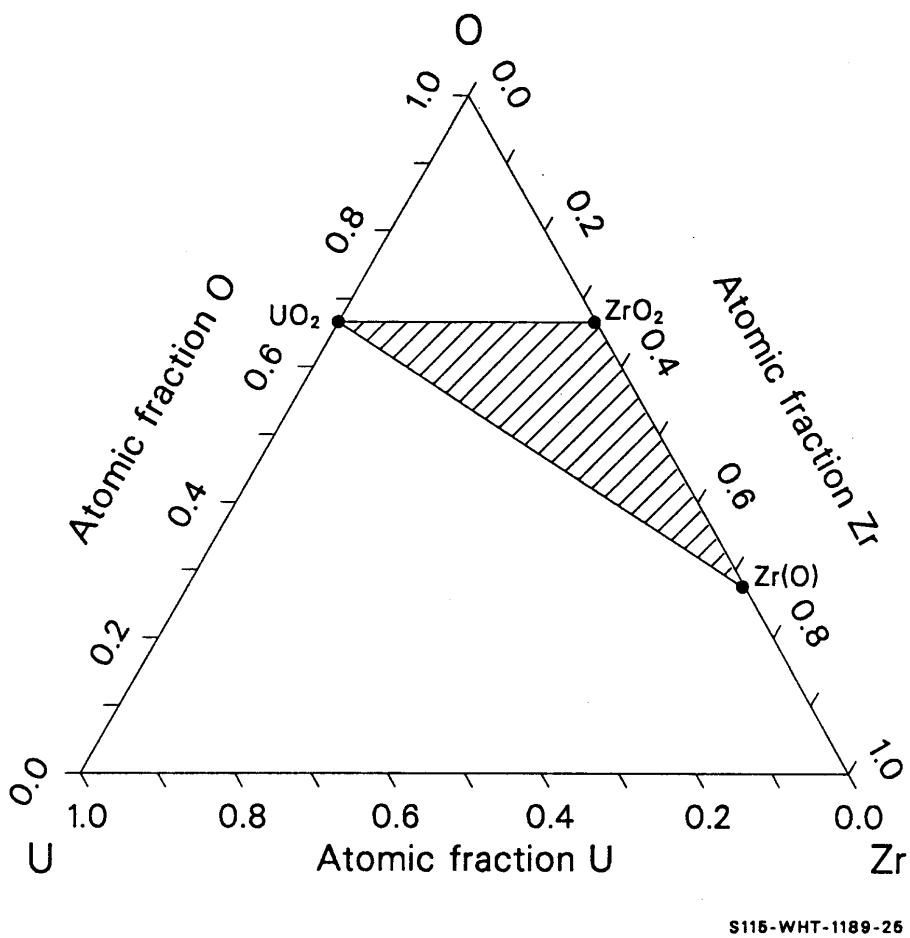

Figure 11-1. Compositions of Zr-U-O compounds on a Gibbs triangle plot.

where

af_i	=	atomic fraction of the i-th component in the compound
afo_j	=	atomic fraction of the j-th component that reacts with oxygen in the compound
af_u	=	atomic fraction of uranium in the compound
n	=	number of core components in the compound
m	=	number of core components that react with oxygen in the compound.

If Equation (11-1) is to return physically meaningful positive fractions. The right-hand inequality means that the compound must not be oxidized beyond a metal dioxide, and the left-hand inequality requires that at least enough oxygen must be present to oxidize the uranium to UO_2. With uranium and zirconium as the only components in the core compound that react with oxygen, Figure 11-1 shows that the right-hand inequality requires the compound to lie below the line drawn between the points labeled UO_2 and ZrO_2. The left-hand inequality requires that the compound lie above a line from the point labeled UO_2 to the point labeled Zr. In this case, all of the shaded triangle lies within this region; so all compounds formed out of UO_2 and zircaloy oxidized as far as ZrO_2 will be in the acceptable range.

All subcodes which use Equation (11-1) check for acceptable ranges of oxygen concentration and raise or lower the presumed oxygen content to force it to fall within the range given by Equation (11-3). An error message is printed when the range is exceeded.

In the older, more limited versions of the MATPRO core materials properties subroutines, for input values of af_u and af_{Zr} that imply that $(1 - af_u - af_{Zr})/2$ is greater than $af_u + af_{Zr}$, the input values of af_u and af_{Zr} are replaced by

$$af_{u1} = \frac{af_u}{3\,(af_u + af_{Zr})} \tag{11-4}$$

$$af_{Zr1} = \frac{af_{Zr}}{3\,(af_u + af_{Zr})} \tag{11-5}$$

where

af_u	=	atomic fraction of uranium in the compound
af_{Zr}	=	atomic fraction zirconium in the compound
af_{u1}	=	revised atomic fraction of uranium in the compound
af_{Zr1}	=	revised atomic fraction of zirconium in the compound.

Inspection of Equations (11-2), (11-4), and (11-5) shows that the transformation preserves the uranium-to-zircaloy ratio but decreases $(1 - af_{u1} - af_{Zr1})/2$ to $af_{u1} + af_{Zr1}$.

For input values of af_u and af_{Zr} that imply that $(1 - af_u - af_{Zr})/2$ is less than af_u, input values of a_{fu} and af_{Zr} are replaced by

$$af_{u1} = \frac{af_u}{3af_u + af_{Zr}} \tag{11-6}$$

$$af_{Zr1} = \frac{af_{Zr}}{3af_u + af_{Zr}} \tag{11-7}$$

Inspection of Equations (11-2), (11-6), and (11-7) shows that this transformation preserves the uranium-to-zircaloy ratio but increases $(1 - af_{u1} - af_{Zr1})/2$ to af_{u1}.

The above described transformations are not used in the later version of the core materials properties subroutines. However, since the older versions of these subroutines are contained in the MATPRO package along with the newer versions, where applicable, descriptions of both routines are included in this document.

References

11-1 S. Nazare, G. Ondracek, and B. Schulz, "Properties of Light Water Reactor Core Melts," *Nuclear Technology*, *32*, 1977, pp. 239-246.

11-2 F. Rhines, *Phase Diagrams in Metallurgy and Their Development and Application*, New York: McGraw-Hill Book Company, 1956, pp. 110-113.

11.1 Zirconium Uranium Oxygen Compound Melting, Solution, and Precipitation (PSOL, PLIQ, ZUSOLV, COEF)

11.1.1 Introduction

Mechanistic modeling of severe core damage processes in LWRs requires models to describe the melting of core materials and the solution of UO_2 fuel by liquid zircaloy. In particular, the temperature at which a liquid phase first appears during the heating of a Zr-U-O compound, the solidus temperature, is required to model the structural failure of reactor core material. The temperature at which the last solid phase disappears during heating, the liquidus temperature, is required to determine the amount of solid core material that can be dissolved by molten zircaloy.

Three subcodes were developed to model the melting and solution properties of Zr-U-O compounds. The solidus temperature as a function of the atomic fraction zircaloy and the atomic fraction oxygen is modeled in the PSOL subcode. The PLIQ subcode returns the liquidus temperature using the same fractions required by PSOL.

The ZUSOLV subcode models solution behavior. Given the temperature, solvent composition, and solute composition, it determines whether the solvent, usually zircaloy with some oxygen, is supersaturated. If the solvent is supersaturated, the fraction that will freeze and the equilibrium composition of the solid and liquid phases is calculated. If the solvent is not supersaturated at the given temperature, the saturation composition of the liquid phase and the atomic fraction of the solute, usually uranium dioxide, is calculated.

The subcode COEF calculates the coefficients a and b of the equation ax + b, the equation of a line, and the intersection coordinates of two lines. The coordinates of two points on a line are input into the subcode if the equation of the line is to be calculated, and the constant and dependent variable for each line is input if the intersection of two lines is to be calculated. This subcode is used exclusively with ZUSOLV to calculate positions on isopleths in determining the composition of Zr-U-O mixtures.

All three subcodes are based on analytical expressions for the liquidus and solidus phase boundary

compositions in the ternary Zr-U-O system. These expressions, which are given in the model development section, were produced by interpolating the liquidus and solidus compositions determined as a function of temperature for the several available binary systems or isopleths for which liquidus and/or solidus temperatures as a function of composition are known. The analytical expressions are used with standard metallurgical techniques, the lever rule and the mixing rule, to calculate the solution parameters given by ZUSOLV. PSOL and PLIQ employ a matrix that provides an approximate inversion of the analytical expressions for composition as a function of temperature. The matrix uses a grid of 100 positions to represent the range of possible compositions and assigns a fixed temperature to each grid position.

11.1.2 Data for the Zr-U-O System

The equations for the solidus and liquidus surfaces were obtained from numerous temperature composition phase diagrams, which are available in the literature. In this section, all of these diagrams have been redrawn to a common scale and units of atomic fraction so that they might be easily compared and checked for consistency.

11.1.2.1 Binary Systems. Solidus and liquidus temperatures of zirconium-oxygen mixtures have been published by Domagala and McPherson[11.1-1] and modified by Ruh and Garrett.[11.1-2] Figure 11-2 shows a phase diagram drawn from these references. The diagram of Domagala and McPherson was

converted from weight fraction to atomic fraction using the expression

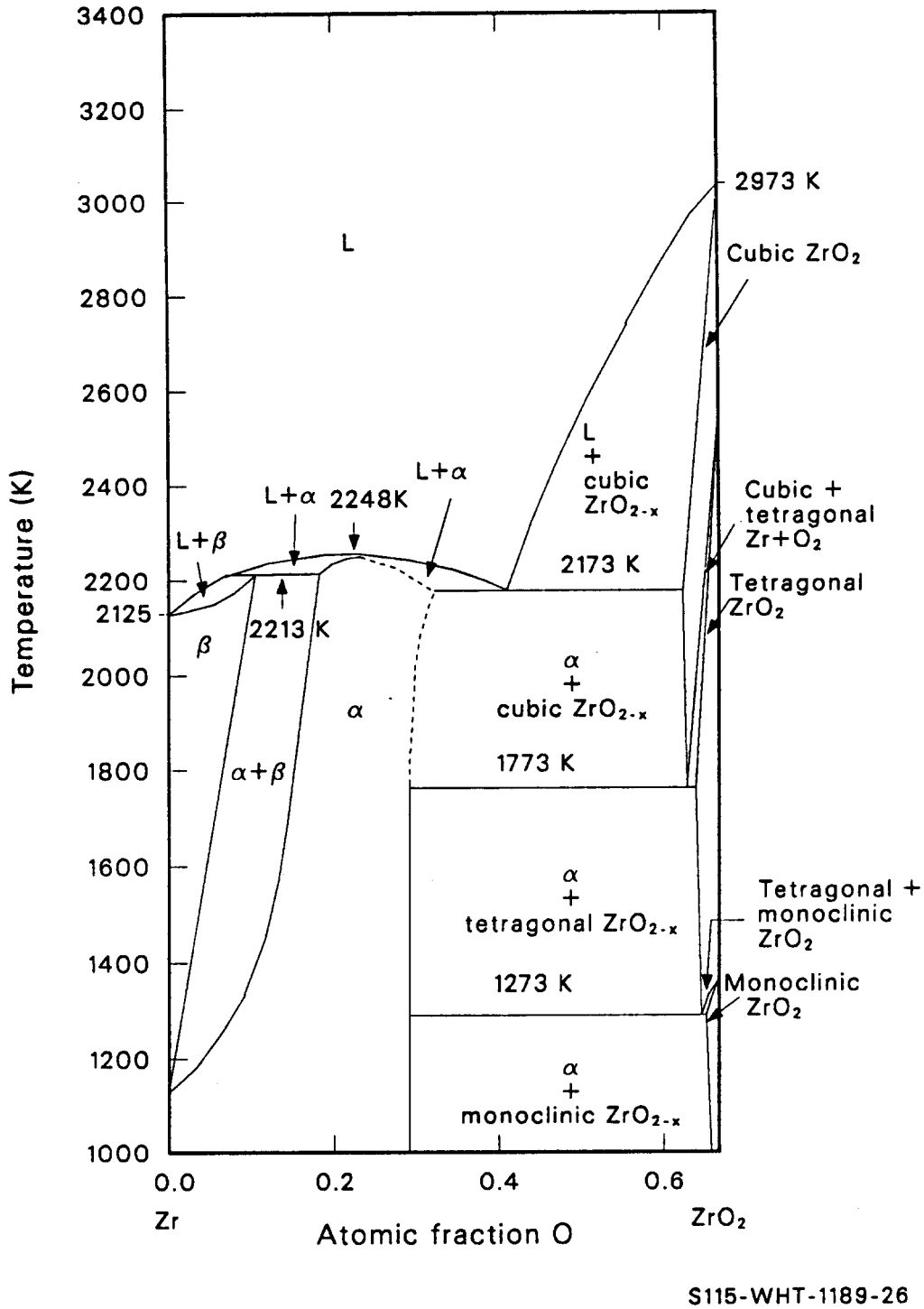

Figure 11-2. Zirconium-zirconium dioxide phase diagram.

$$f_0 = \frac{f_0^{mass}/16}{f_0^{mass}/16 + (1 - f_0^{mass})/91.22} \tag{11-8}$$

where

f_o = atomic fraction of oxygen in a Zr-O compound

f_0^{mass} = mass fraction of oxygen in a Zr-O compound.

The solidus curve is made up of several segments, one above the beta phase, one above the alpha phase, and one above the cubic ZrO_2 phase. The liquidus is composed of the two segments under the liquid region.

Figure 11-3 is a temperature composition plot for the U-O binary system, taken from Roth et al.[11.1-3] Their diagram was converted to atomic fraction oxygen using the relation

$$f_0 = \frac{R}{1 + R} \tag{11-9}$$

where R is the oxygen-to-metal ratio (atoms oxygen/atoms uranium).

The figure shows four solidus segments enclosing the UO_2 region, two liquidus segments under the L_1 phase, and another two liquidus segments under the L_2 phase. Latta and Fryxell[11.1-4] have published detailed solidus and liquidus temperature data for the curves above 2700 K in Figure 11-3. Their data are shown in Figure 11-4 and reproduced in Table 11-1.

Figure 11-5 shows an isopleth extending from $Zr_{0.7}O_{0.3}$ (approximately the composition of alpha phase zirconium saturated with oxygen) to $U_{0.33}O_{0.67}$ (the composition of uranium dioxide written in atomic fraction units). The isopleth was presented as a quasi-binary section by Skokan.[11.1-5] This presentation is in conflict with the phase diagram reproduced as Figure 11-2, which shows noncongruent melting of the alpha phase (the liquid-plus-alpha region between the alpha phase and liquid regions near 0.3 atomic fraction oxygen in Figure 11-2).

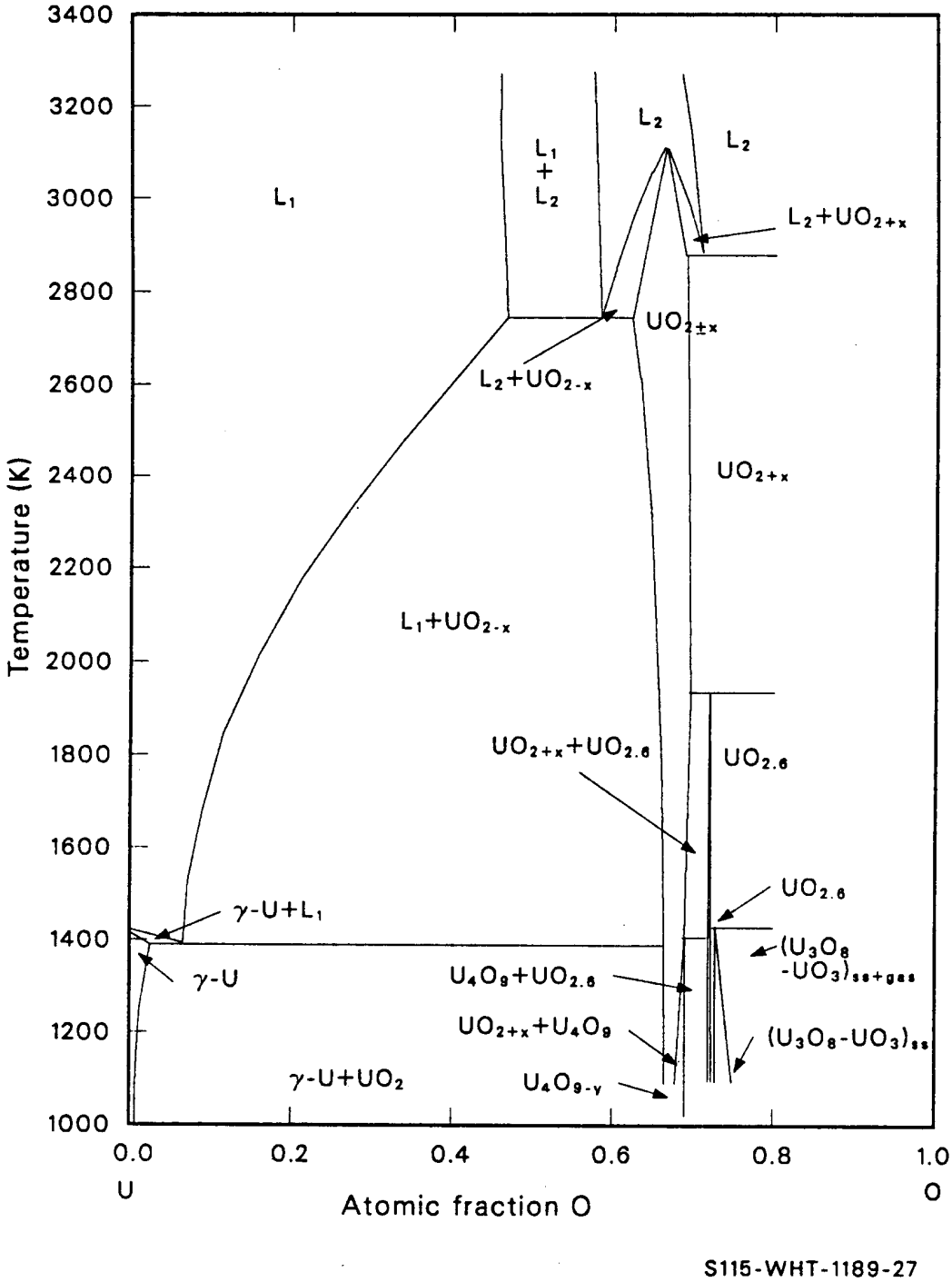

Figure 11-3. Uranium oxygen phase diagram.

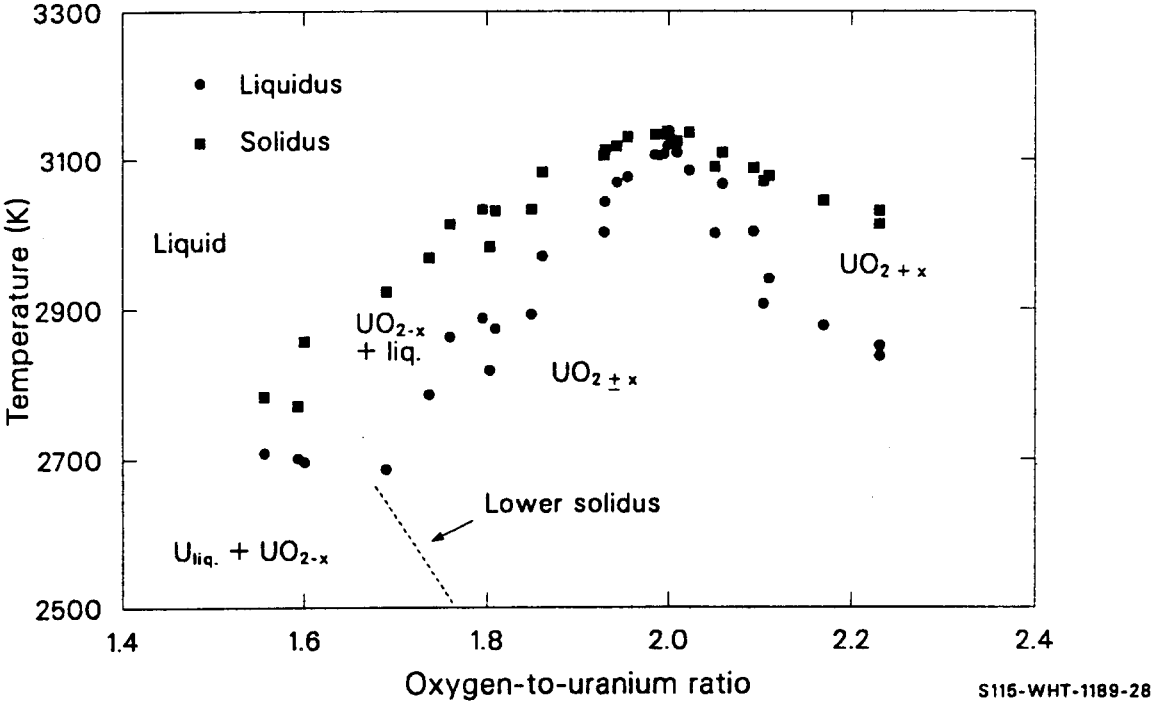

Figure 11-4. Solidus and liquidus temperatures of uranium oxides according to Latta and Fryxell.

Table 11-1. Solidus and liquidus temperatures of UO_{2+x} from Latta and Fryxell.

Sample No.	Pretest O/U	Post-Test O/U	Solidus (K)	Liquidus (K)
221	2.23	-	2,837	3,031
217	2.23	-	2,851	3,013
188	2.184	2.169	2,878	3,045
201	2.13	2.109	2,940	3,078
192	2.12	2.103	2,907	3,071
303	2.095	2.092	3,003	3,088
208	2.095	2.050	3,001	3,090
172	2.058	2.058	3,067	3,109
204	-	2.022	3,085	3,136
193	2.019	2.009	3,109	3,125
212	1.998	1.998	3,118	3,138

Table 11-1. Solidus and liquidus temperatures of UO_{2+x} from Latta and Fryxell. (Continued)

Sample No.	Pretest O/U	Post-Test O/U	Solidus (K)	Liquidus (K)
190	1.997	2.008	3,118	2,138
194	1.997	2.000	3,120	3,135
209	1.993	1.995	3,107	3,133
189	1.980	1.990	3,105	3,133
146	1.980	1.985	3,106	3,133
153	1.956	1.955	3,076	3,130
138	1.943	1.943	3,069	3,118
184	1.920	1.930	3,043	3,113
150	1.890	1.929	3,002	3,105
154	1.856	1.861	2,970	3,083
177	1.809	1.795	2,888	3,033
156	1.803	1.849	2,893	3,033
159	1.793	1.809	2,874	3,031
129	1.75	1.803	2,818	2,983
104	1.790	1.759	2,863	3,013
164	1.736	1.736	2,786	2,968
166	1.662	1.689	2,686	2,923
222	1.60	-	2,696	2,857
168	1.556	-	2,708	2,783
207	1.50	1.593	2,701	2,771

The UO_2-ZrO_2 quasi-binary system according to Romberger et al.[11.1-6] is shown in Figure 11-6. The liquidus and solidus exhibit a minimum at a 0.5-0.5 mix of the two components, and the liquidus dips sharply to touch the solidus at this minimum. Recent data presented by Hofmann[11.1-7] suggest that the $U_{0.33}O_{0.67}$ rich solidus does not rise as fast as shown in Figure 11-6. Hofmann finds a solidus temperature in the range 2,793 to 2,893 K for 0.1 mole fraction ZrO_2 (0.1 atomic fraction $Zr_{0.33}O_{0.67}$) and in the range 2,796 to 2,842 K for 0.25 mole fraction ZrO_2.

Figure 11-7 is a reproduction of the liquidus and solidus curves of the U-Zr binary system.[a] The components are mutually soluble for temperatures above 1136 K, so the solidus and liquidus form the clas-

a. P. Hoffman, private communication, EG&G Idaho, Inc., 1985.

sic lens shaped, two-phase region for such systems.

11.1.2.2 Ternary System Data. The only Zr-U-O system data in the temperature range from 1400 to 3100 K are the temperature composition plots published by Hofmann and Politis[11.1-8] and extended by Skokan.[11.1-5] Ternary temperature composition plot sections from these authors are reproduced as Figures 11-8 through 11-14. The figures are all plotted on a Gibbs coordinate system, which is an equilateral triangle with each vertex representing one of the three components. The fraction of each component is proportional to the distance from the side opposite the component's vertex. The system is used because it ensures that the sum of the fraction of each component is one for any gross composition plotted.

Figure 11-8, the phase diagram at 1,273 K,[11.1-8] shows no liquid phase and very limited single-phase regions along the U-O, Zr-O, and U-Zr sides. A large, three-phase region connecting α-Zr(O), (γ-U, β-Zr) with about 0.8 U, and UO_2 dominates the diagram.

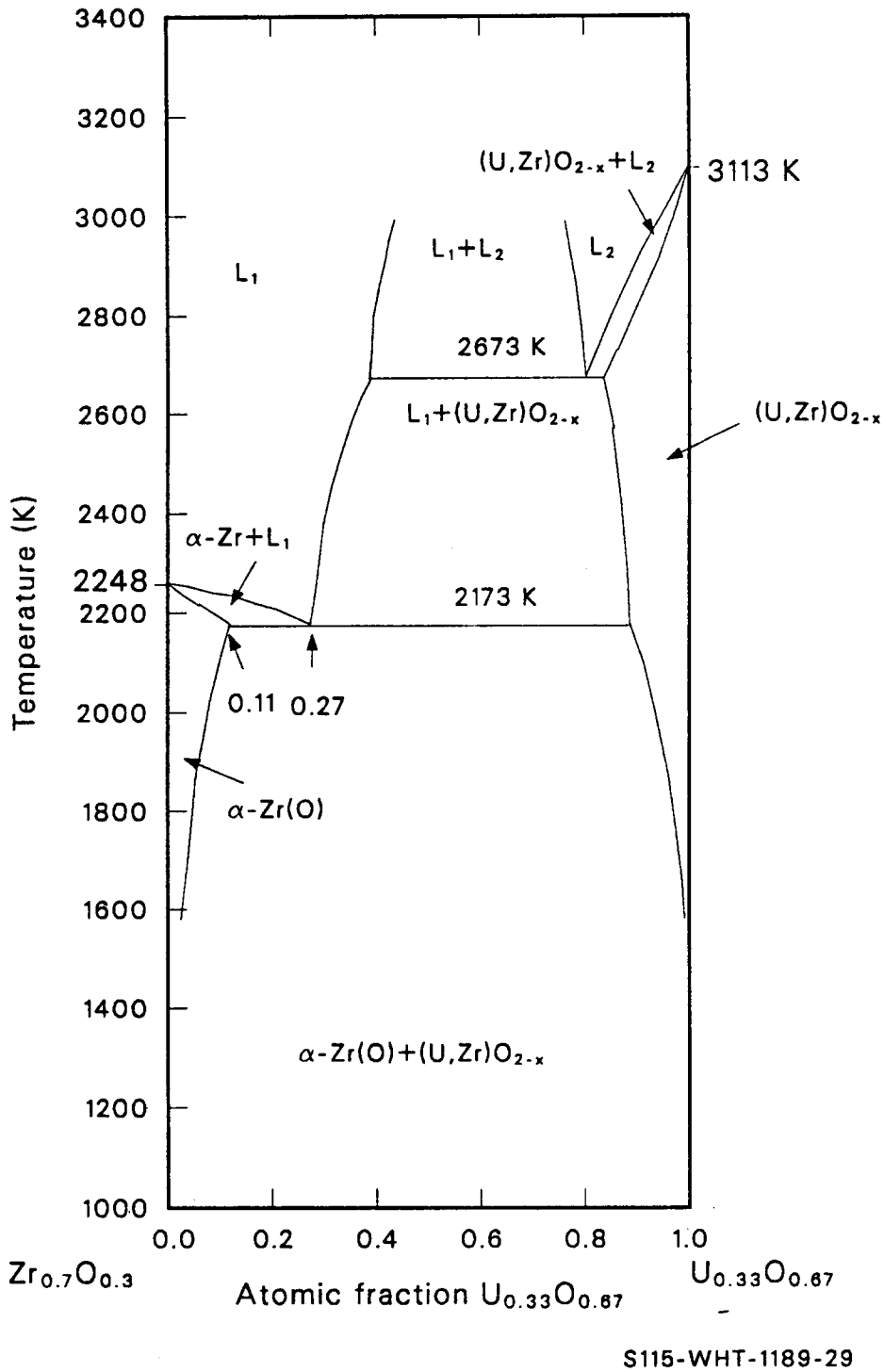

Figure 11-5. Oxygen saturated, alpha phase zirconium uranium dioxide isopleth.

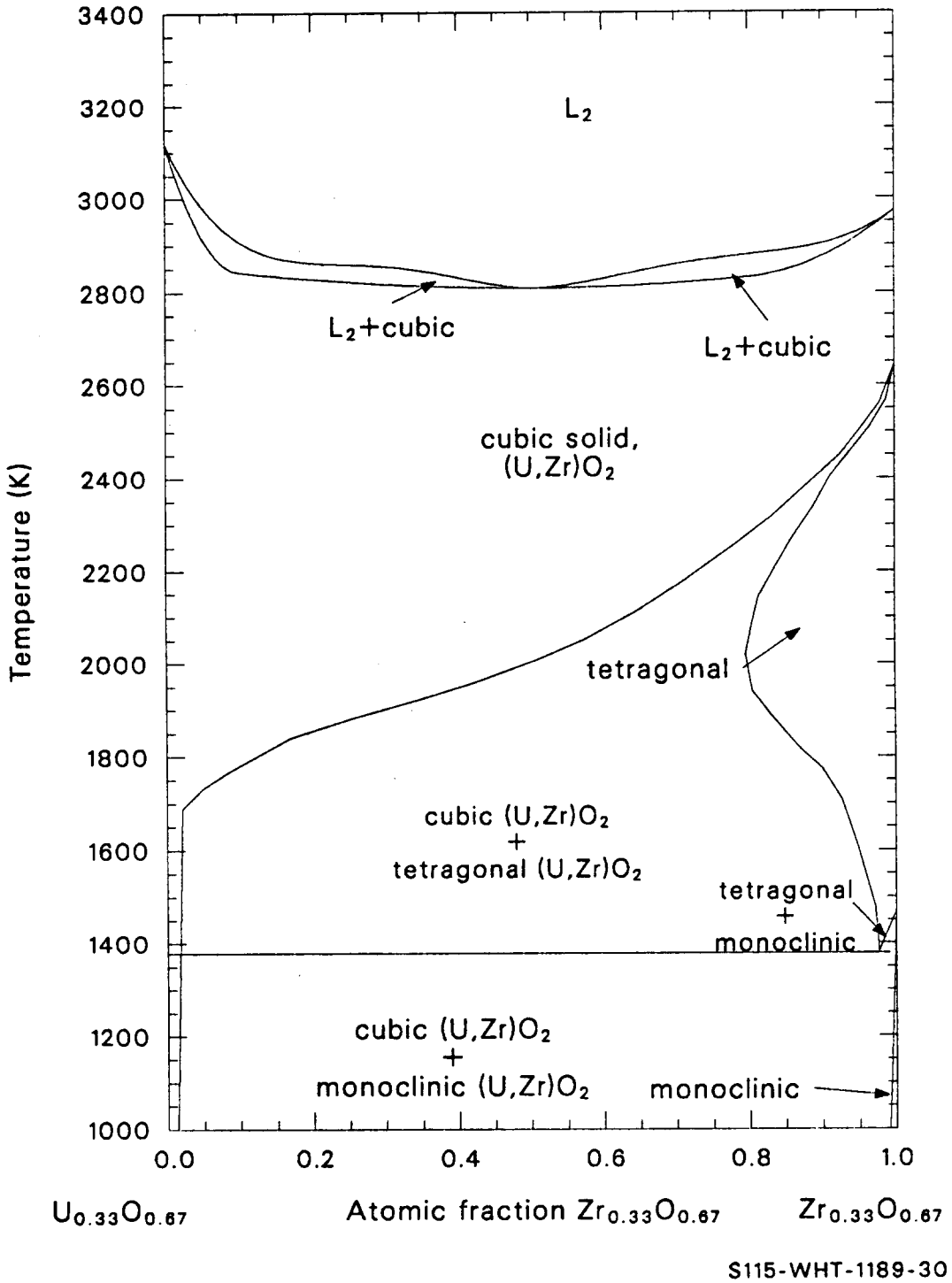

Figure 11-6. Uranium dioxide zirconium dioxide quasi-binary phase diagram.

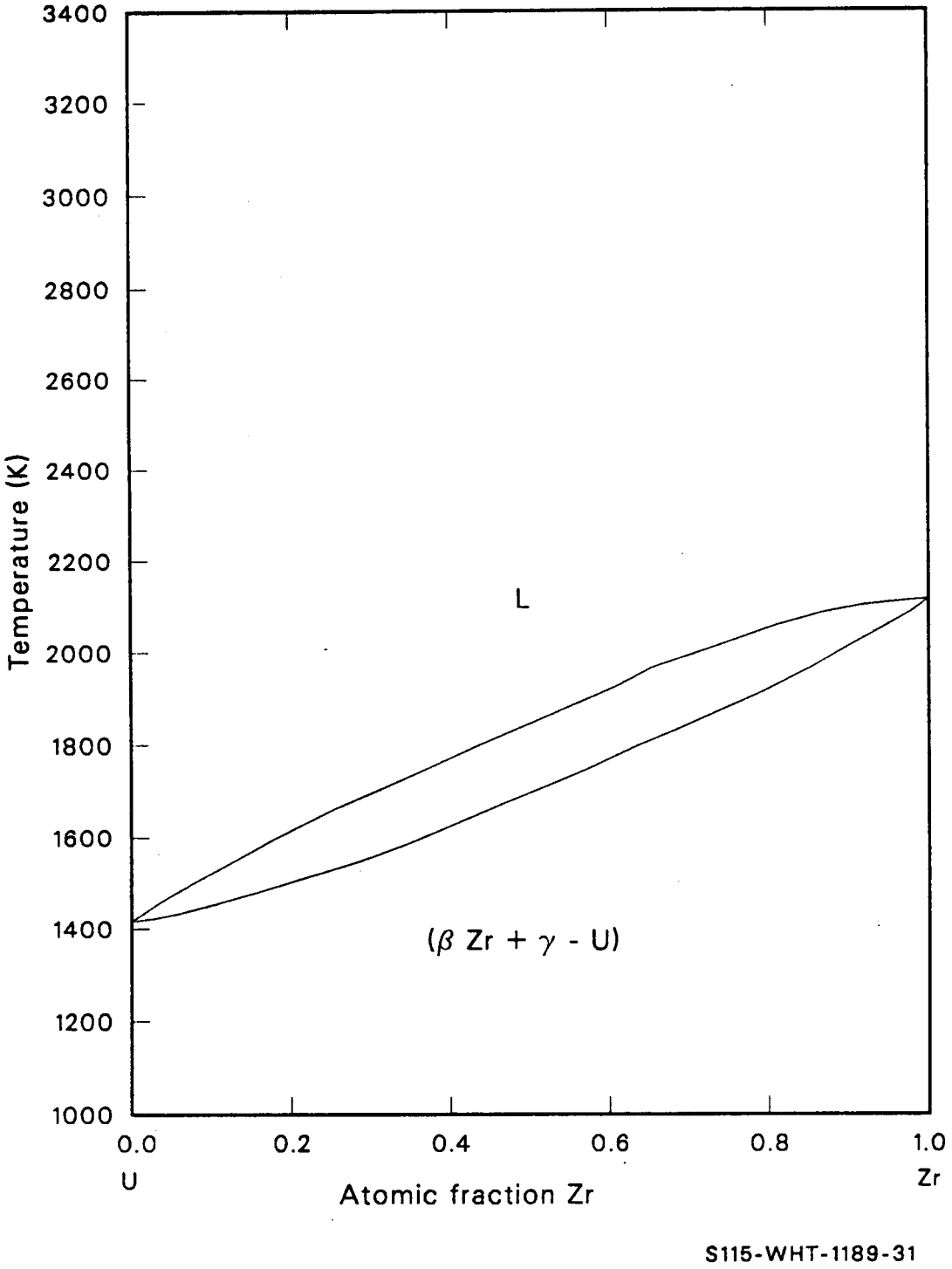

Figure 11-7. Uranium zirconium system liquidus and solidus.

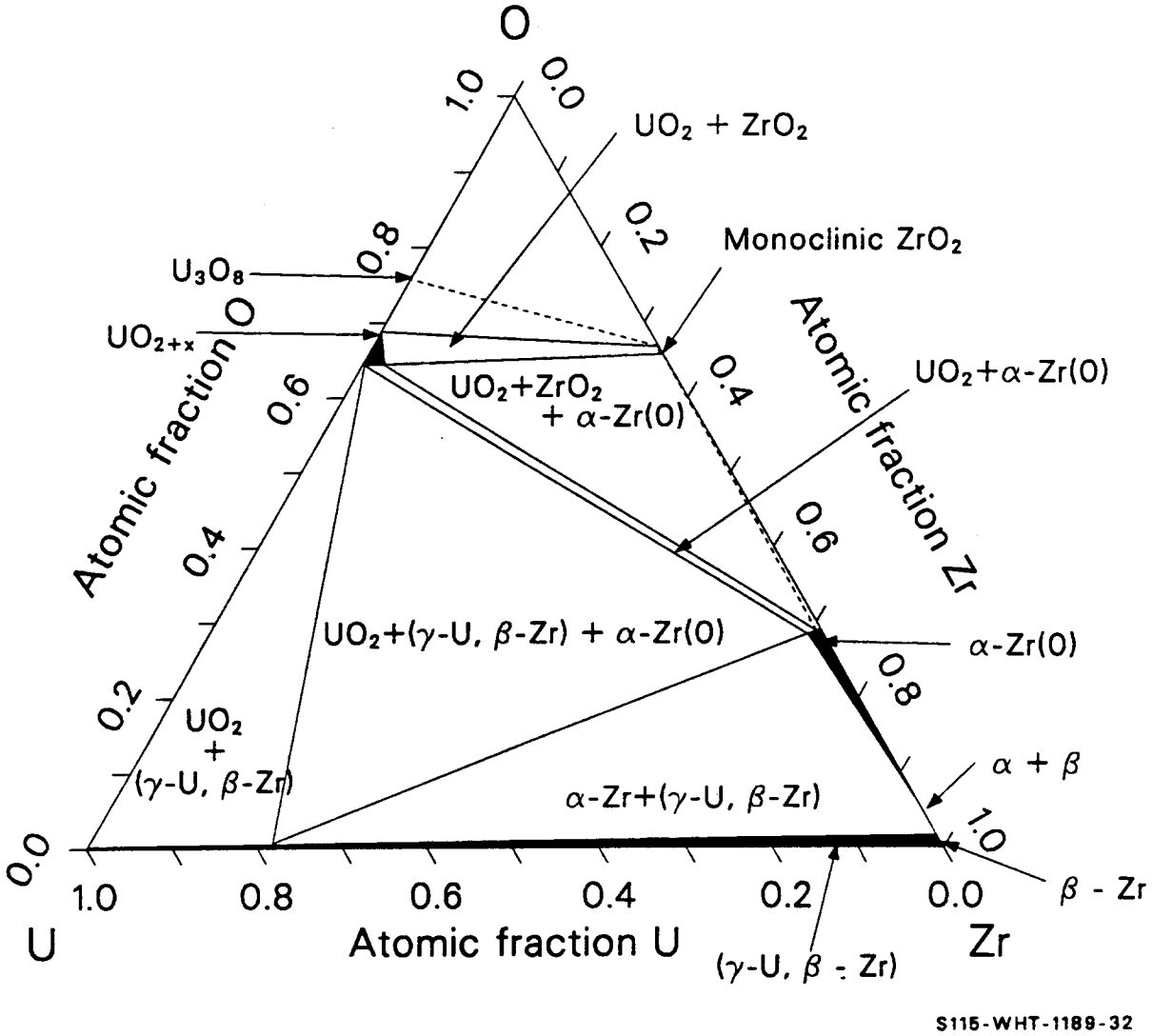

Figure 11-8. Phases of the Zr-U-O system at 1,273 K.

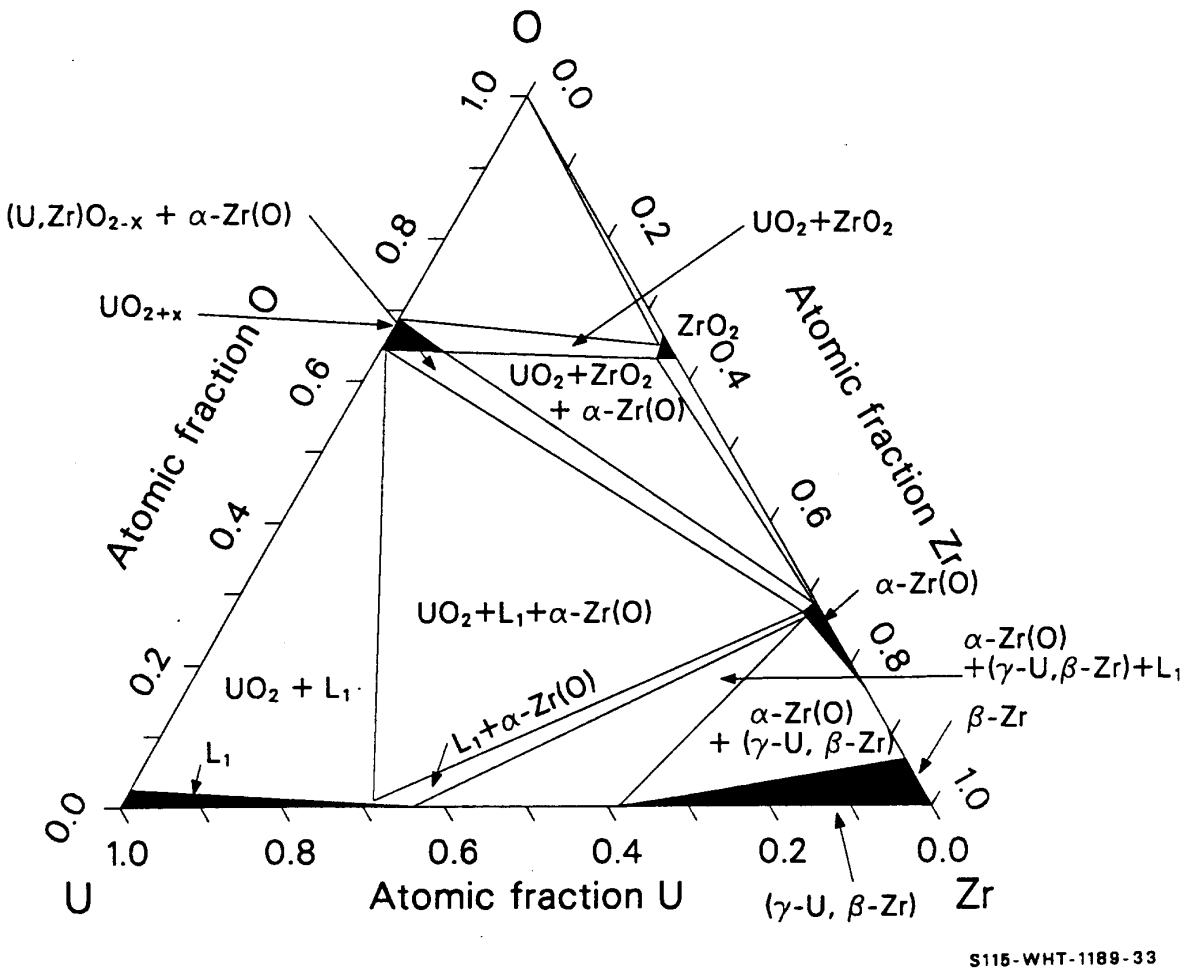

Figure 11-9. Phases of the Zr-U-O system at 1,773 K.

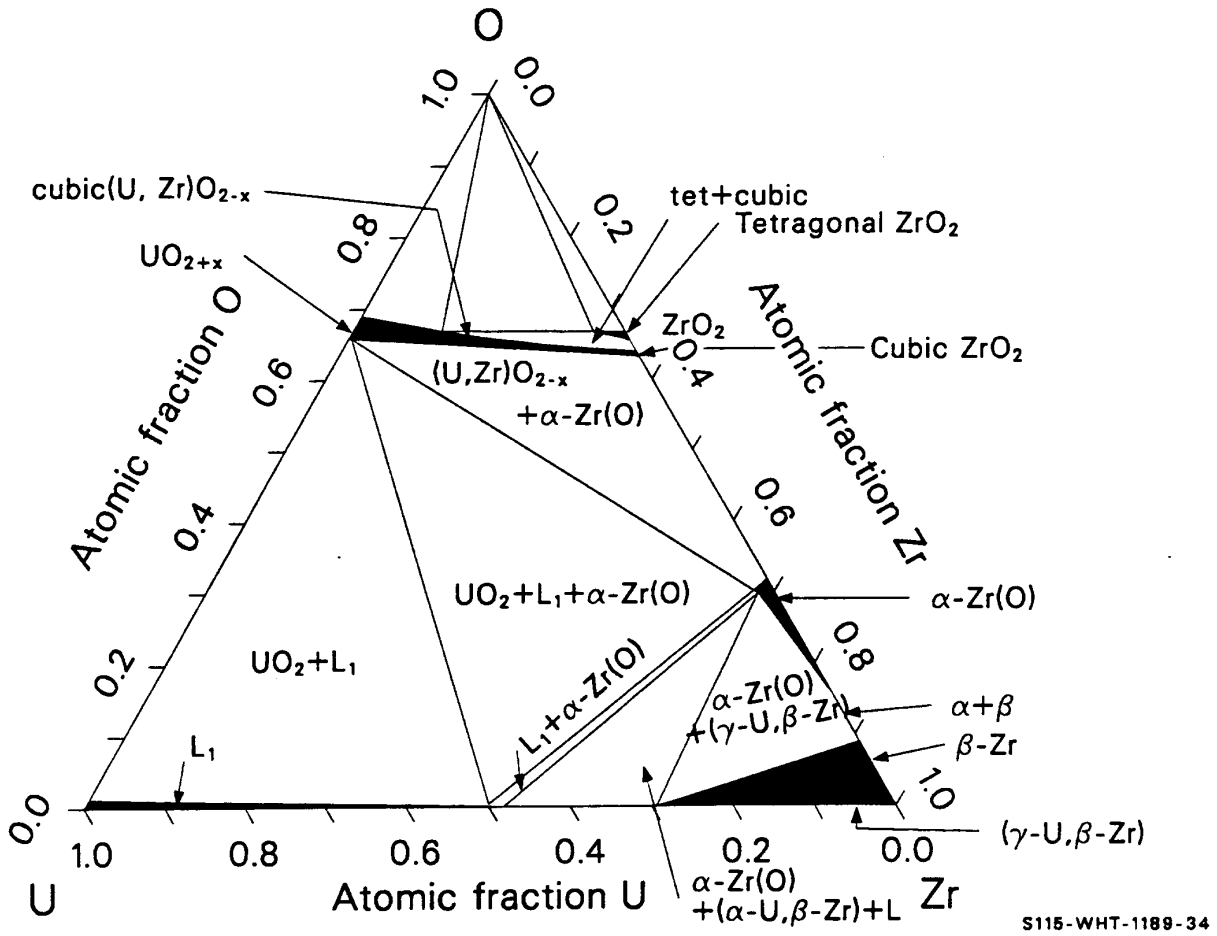

Figure 11-10. Phases of the Zr-U-O system at 1,873 K.

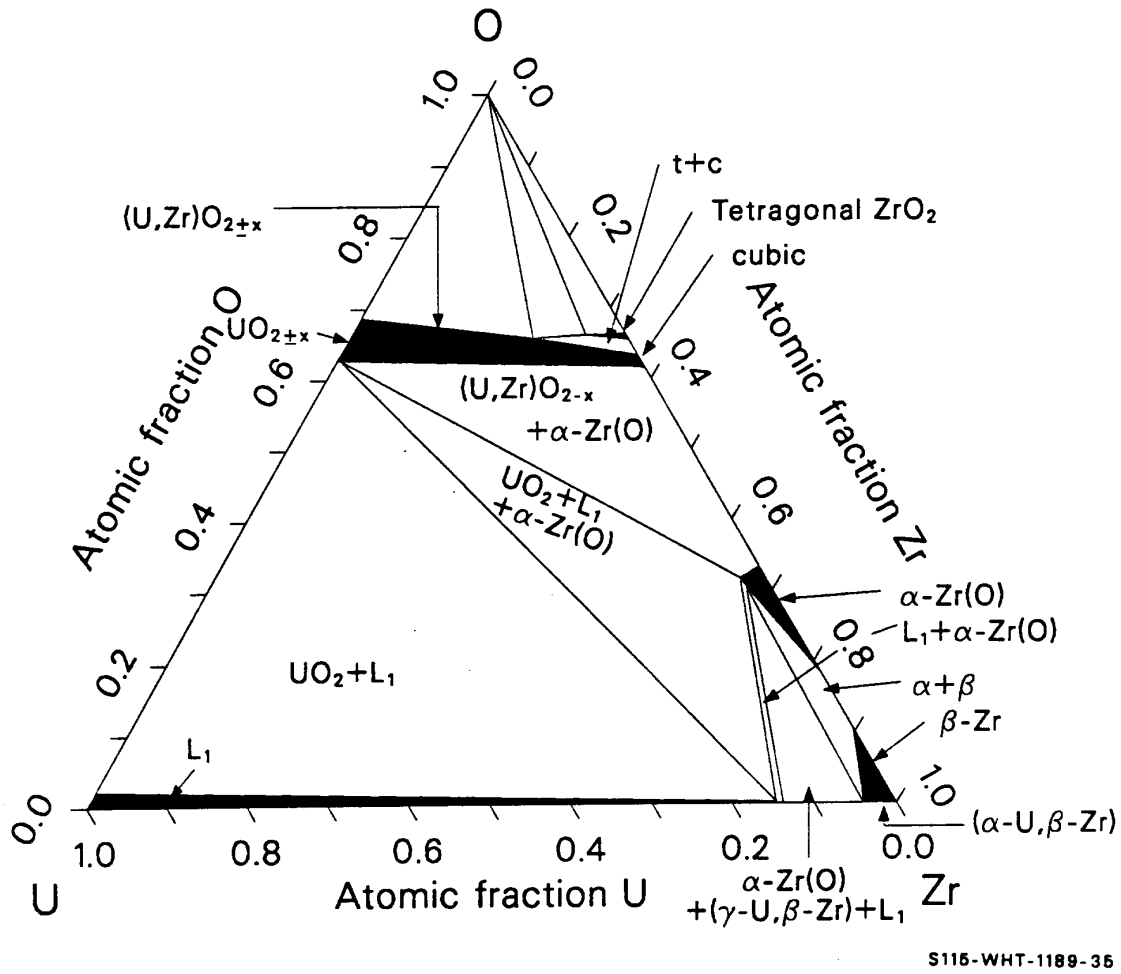

Figure 11-11. Phases of the Zr-U-O system at 2,073 K.

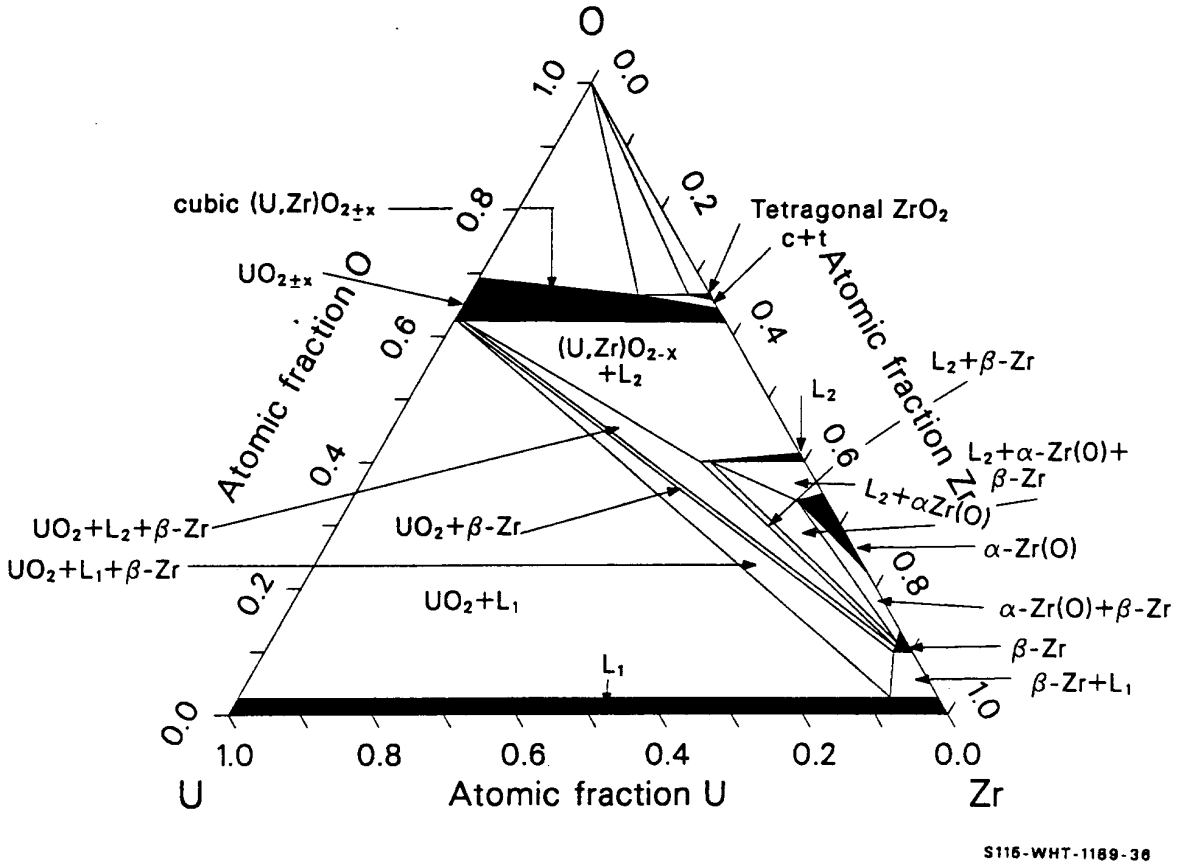

Figure 11-12. Phases of the Zr-U-O system at 2,178 K.

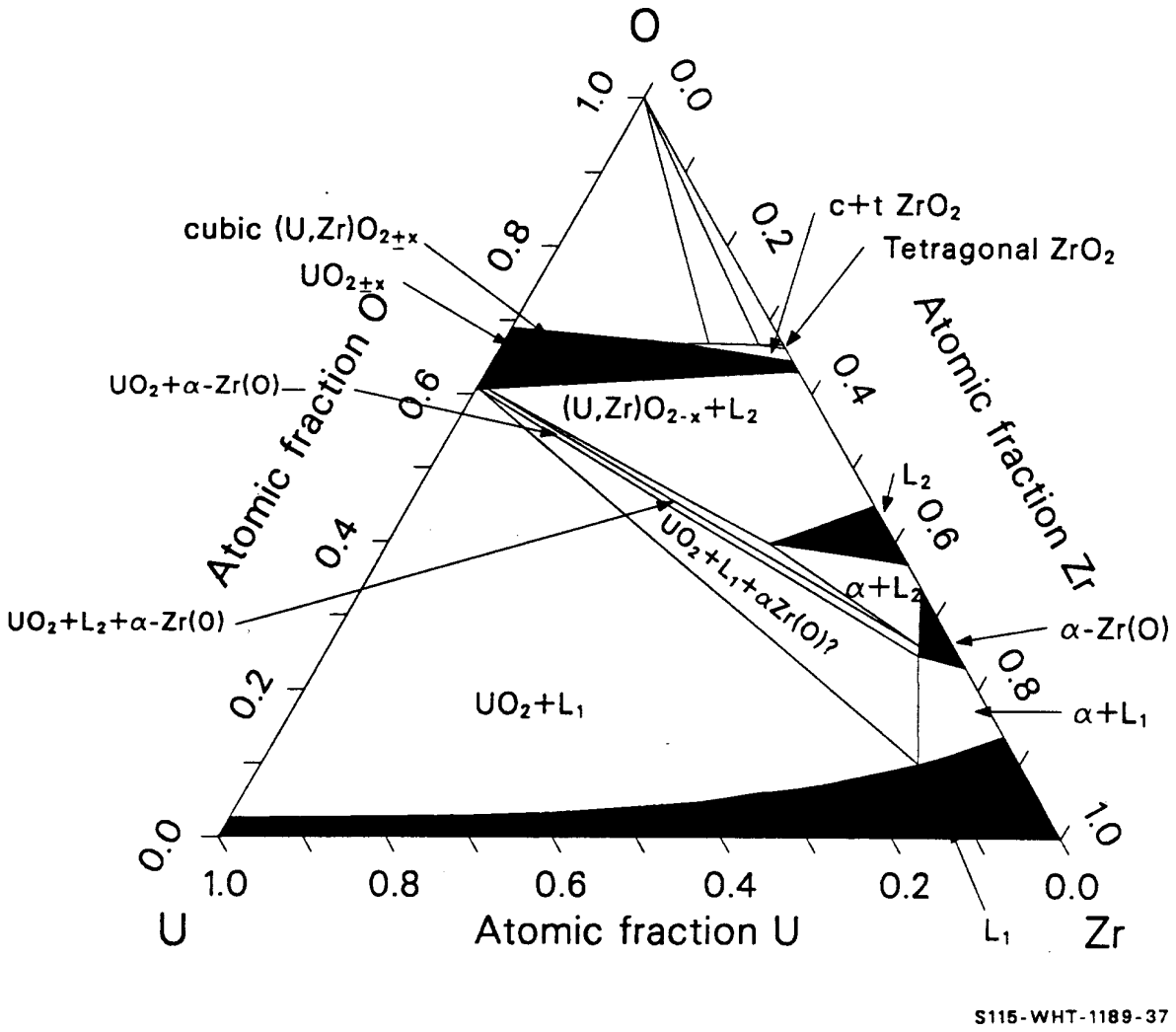

Figure 11-13. Phases of the Zr-U-O system at 2,223 K.

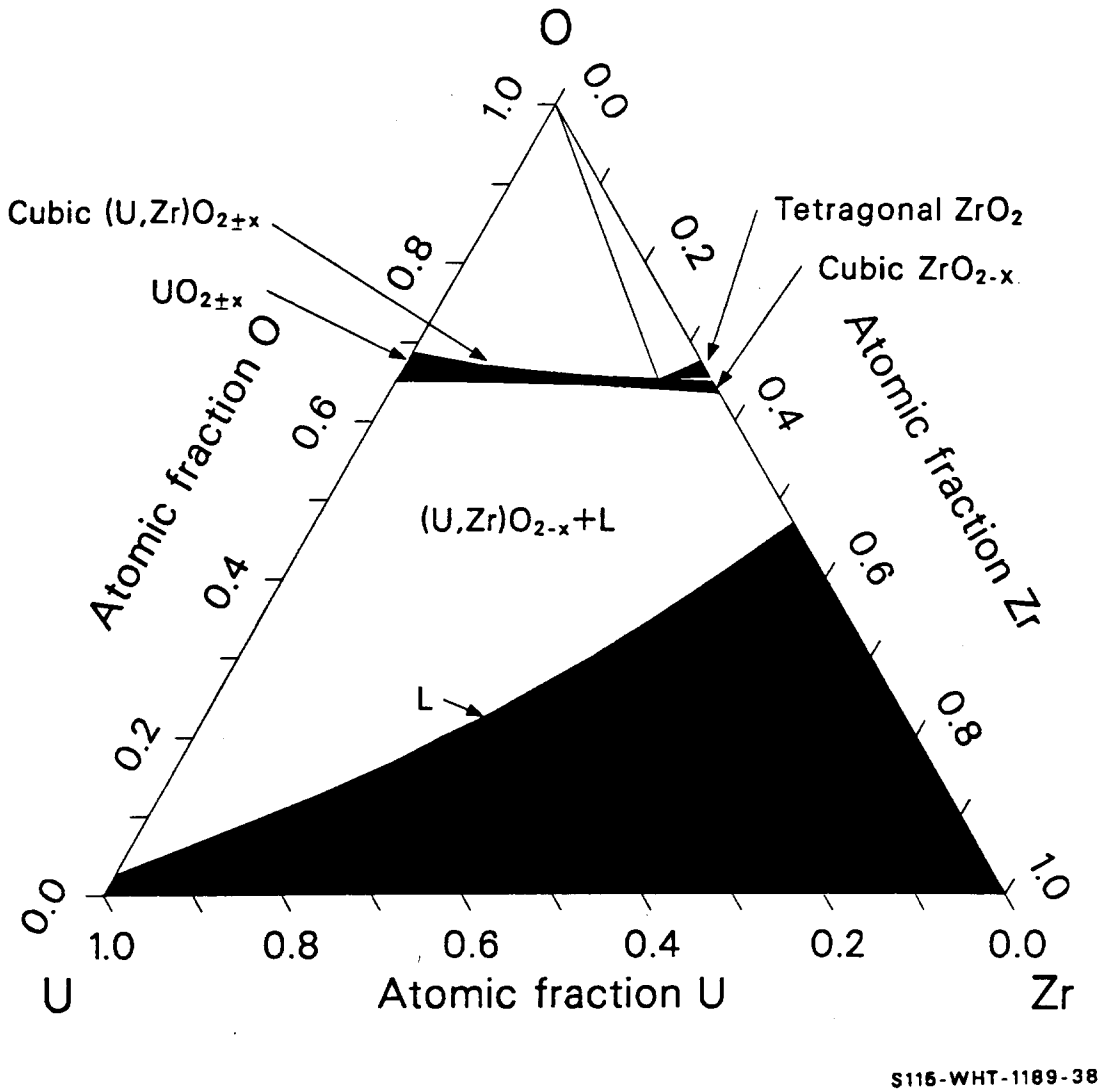

Figure 11-14. Phases of the Zr-U-O system at 2,273 K.

The 1,773 K system[11.1-8] (Figure 11-9) shows a liquid phase in the lower left-hand side of the diagram, the U-rich and O-poor region. The phase is in equilibrium with UO_2 via tie lines in the UO_2 + L region, with α-Zr(O) via tie lines in the narrow L + α - Zr(O) region, and with UO_2 and α-Zr(O) via the large, three-phase triangle that dominates the center of the phase diagram. The locations of the tie lines are not known, so the tie lines are not shown. Although most authors show the top of the UO_2 + L region as a point, it is drawn in Figure 11-9 as a short segment because the several liquid compositions at the bottom of the UO_2+ L region must connect to more than one composition at the edge of the one phase region near the UO_2 composition. The presence of the large, three phase region in the center, UO_2 + L + α - Zr(O), suggests that compositions enclosed in the triangle will experience some melting when the liquid phase passes the lowest vertex of the three-phase triangle, i.e., near 1,600 K.

Figure 11-10 shows the phase diagram at 1,873 K.[11.1-5] The right-hand vertex of the L region has

moved toward the Zr vertex of the Gibbs coordinates, in excellent agreement with the liquidus temperature shown in Figure 11-7. The right vertex of the (γ-U, β-Zr) phase is in excellent agreement with the U-Zr binary system solidus, too. A similar agreement is evident between the right-hand side of Figure 11-10 and the Zr-ZrO_2 binary system shown in Figure 11-2. However, the left-hand side of Figure 11-10 disagrees with the liquidus shown for the U-O binary in Figure 11-3. According to Figure 11-3, the liquidus should be above 0.1 atomic fraction O at 1,773 K. It is shown at about 0.02 fraction O in Figure 11-10. The two phase α - Zr(0) + L region was added to Skokan's figure to avoid showing a common boundary between three phase regions.[11.1-8]

Figure 11-11, the phase diagram at 2,073 K,[11.1-5] shows behavior similar to Figure 11-10. The U-Zr and Zr-ZrO_2 binaries are in excellent agreement with the figure, but the U-O binary would place the top left vertex of the Lregion considerably higher than it is shown on the ternary diagram. One should note that Figure 11-11 is an important addition to the binary systems data because it provides points like the left hand extreme of the α-Zr(O) region that are not available on any binary isopleth. The two phase α-Zr(0)+L region was added to Skokan's figure for 2,073 K for the same reason the region was added to Figure 11-10.[11.1-8]

Figures 11-12 and 11-13[11.1-5] show the complex behavior caused by the appearance of the oxygen rich liquid phase, L_1', that corresponds to the liquidus minimum at about 0.4 atomic fraction oxygen in Figure 11-2. The tentative diagrams presented by Skokan for 2,178 and 2,223 K were modified to include narrow two-phase regions between the UO_2 + L_1' + β-Zr and UO_2 + L_1 + β - Zr three-phase regions proposed by Skokan.

Figure 11-14, the relatively simple phase diagram at 2,273 K,[11.1-9] shows that the L_1' phase region no longer exists as a separate liquid when temperature increases 50 K above the temperature of Figure 11-13. The fairly simple system shown in Figure 11-14 is probably characteristic of the Zr-U-O system until temperatures near 2,673 K, when another oxygen rich phase, L_2 in Figures 11-3, 11-5 and 11-6, appears.

Unfortunately, no ternary system phase diagrams have been published for temperatures above 2,273 K. Data for these temperatures must be interpolated from binary phase diagrams.

11.1.3 Model Development

The expressions used in the PSOL, PLIQ, and ZUSOLV codes were developed by constructing polynomial expressions for the solidus and liquidus temperatures as a function of composition of the various binary systems, inverting these expressions to produce correlations for composition as a function of temperature, and connecting the resulting liquidus and solidus compositions with straight-line segments on the ternary phase diagram. Where additional correlations could be obtained from the ternary systems published, they were also employed.

Figure 11-15 shows the points that are connected to form the ternary liquidus, and Table 11-2 provides the analytical expressions for the compositions represented by the points. Figure 11-16 shows the points that are connected to form the ternary solidus, and Table 11-3 provides the analytical expressions for the compositions represented by the points. Dashed lines in Figure 11-16 represent tie lines across multiple-phase regions and are therefore not a section through a solidus surface in the three-dimensional, temperature composition phase diagram.

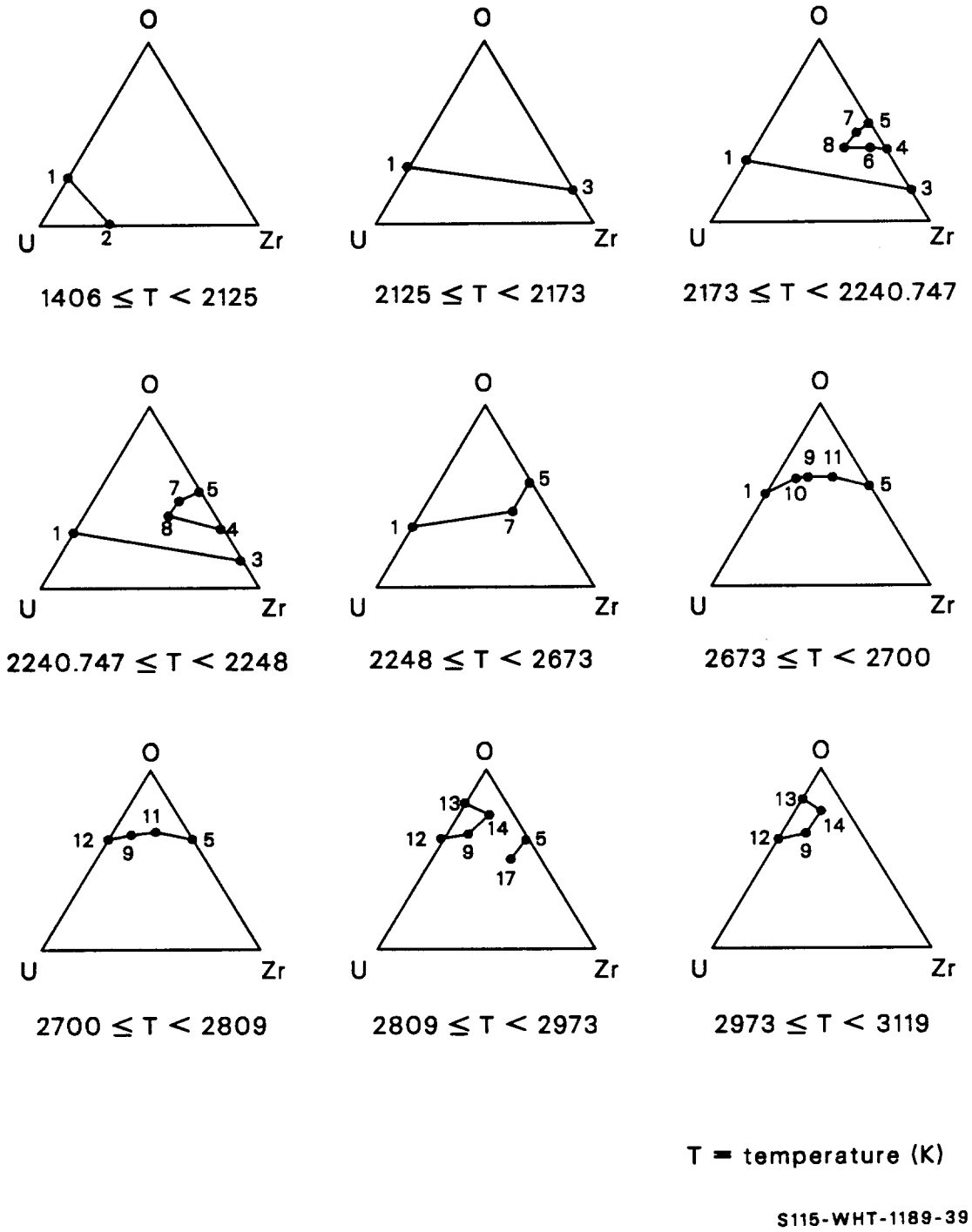

Figure 11-15. Points that are connected to form the ternary Zr-O-U system liquidus lines.

Table 11-2. Correlations for liquidus compositions.

1. L_1 boundary U-O binary system	$f_0 = \dfrac{2940.587 - \sqrt{2940.587^2 + 4833.744\,(1026.259 - T)}}{4833.744}$
2. L_1 boundary U-Zr binary system	$f_{Zr} = \dfrac{478.5 - \sqrt{478.5^2 + 238\,(1406 - T)}}{238}$
3. Zr-rich L_1 boundary, Zr-ZrO_2 binary system for $2125 \le T \le 2213$ K	$f_0 = \dfrac{1114.952 - \sqrt{1114.952^2 + 13704.72\,(2125 - T)}}{13704.72}$
For $2213 < T \le 2248$ K	$f_o = \dfrac{263.9718 - \sqrt{263.9718^2 + 1060.128\,(2182.271 - T)}}{1060.128}$
4. Zr-rich L_1' boundary, Zr-ZrO_2 binary system	$f_0 = \dfrac{694.3412 - \sqrt{694.3412^2 + 2788.519\,(2075.109 - T)}}{2788.519}$
5. O-rich L_1 and L_1' boundary, Zr-ZrO_2 binary system	$f_0 = \dfrac{1785.754 - \sqrt{1785.754^2 + 390.6488\,(764.6003 - T)}}{390.6488}$
6. Zr-rich L_1 boundary $Zr_{0.7}O_{0.3}$-$U_{0.33}O_{0.67}$ isopleth	$f_{U_{0.33}O_{067}} = \dfrac{-13.40961 + \sqrt{13.40961^2 + 829.9846\,(2240.747 - T)}}{829.9846}$
7. O-rich L_1 boundary $Zr_{0.7}O_{0.3}$-$U_{0.33}O_{0.67}$ isopleth	$f_{U_{0.33}O_{067}} = \dfrac{11234.85 - \sqrt{11234.85^2 - 27575.76\,(1883.545 + T)}}{27575.76}$
8. Forced to lie on the line from solidus point 11 to solidus point 5	interpolation
9. O-rich L_2 boundary $Zr_{0.7}O_{0.3}$-$U_{0.33}O_{0.67}$ isopleth	$f_{U_{0.33}O_{067}} = \dfrac{4930 - \sqrt{4930^2 - 6000\,(311 + T)}}{3000}$
10. Linear interpolation between point 9's location at the given temperature and point 12 at 2,700 K	location of 10 = [location of 12 at 2,700 K (T-2,673) + location of 9 at T (2,700-T)] /27

Table 11-2. Correlations for liquidus compositions. (Continued)

11. Linear interpolation between point 9's location at the given temperature and point 14 at 2,809 K	location of 11 = [location of 14 at 2,809 K (T-2,673) + location of 9 at T (2,809-T)] /136
12. O-rich substoichiometric boundary of L_2 U-O binary system	$f_O = \dfrac{2 - \dfrac{\sqrt{3119 - T}}{1610}}{3 - \dfrac{\sqrt{3119 - T}}{1610}}$
13. U-rich hyperstoichiometric boundary of L_2, U-O binary system	$f_O = \dfrac{2 + \dfrac{\sqrt{3119 - T}}{1610}}{3 + \dfrac{\sqrt{3119 - T}}{1610}}$
14. $U_{0.33}O_{0.67}$-rich L boundary, $U_{0.33}O_{0.67}$-O system for $3{,}119 \geq T \geq 2{,}989$	$f_{Zr_{0.33}O_{0.67}} = \dfrac{3119 - T}{433.3333}$
for $2{,}989 \geq T \geq 2{,}832$	$f_{Zr_{0.33}O_{0.67}} = \dfrac{443.0286 + \sqrt{443.0286^2 + 2194.367\,(2920.676 - T)}}{2194.367}$
for $2{,}832 \geq T \geq 2{,}809$	$f_{Zr_{0.33}O_{0.67}} = 0.5 - \sqrt{0.25 - \dfrac{35809.46 - T}{132001.8}}$
15. $Zr_{0.33}O_{0.67}$-rich L_2 boundary $U_{0.33}O_{0.67}$-$Zr_{0.33}O_{0.67}$ binary system for $2809 < T \leq 2821$	$f_{Zr_{0.33}O_{0.67}} = 0.5 + \sqrt{0.25 - \dfrac{5794.401 - T}{11941.6}}$
for $2{,}821 < T \leq 2{,}851.341$	$f_{Zr_{0.33}O_{0.67}} = \dfrac{4162.934 - \sqrt{4162.934^2 + 6838.223\,(327.3354 - T)}}{6838.223}$
for $2{,}851.341 < T \leq 2{,}862$	$f_{Zr_{0.33}O_{0.67}} = \dfrac{T - 2817.588}{59.2158}$

Table 11-2. Correlations for liquidus compositions. (Continued)

for 2,862 < T ≤ 2,973	$f_{Zr_{0.33}O_{0.67}} = \dfrac{793 + \sqrt{793^2 - 1160\,(3399 - T)}}{1160}$
16.	Point 15 with y coordinate increased 0.01
17. Intersection of lines from 0.7 Zr, 0.3 O to point 15 and point 5 to the $L_1/L_1 + L_2$ boundary location is given by	$f_{U_{0.33}O_{0.67}} = \dfrac{41641.97 - \sqrt{41641.97^2 - 94995.94\,(15257.48 - T)}}{94995.94}$

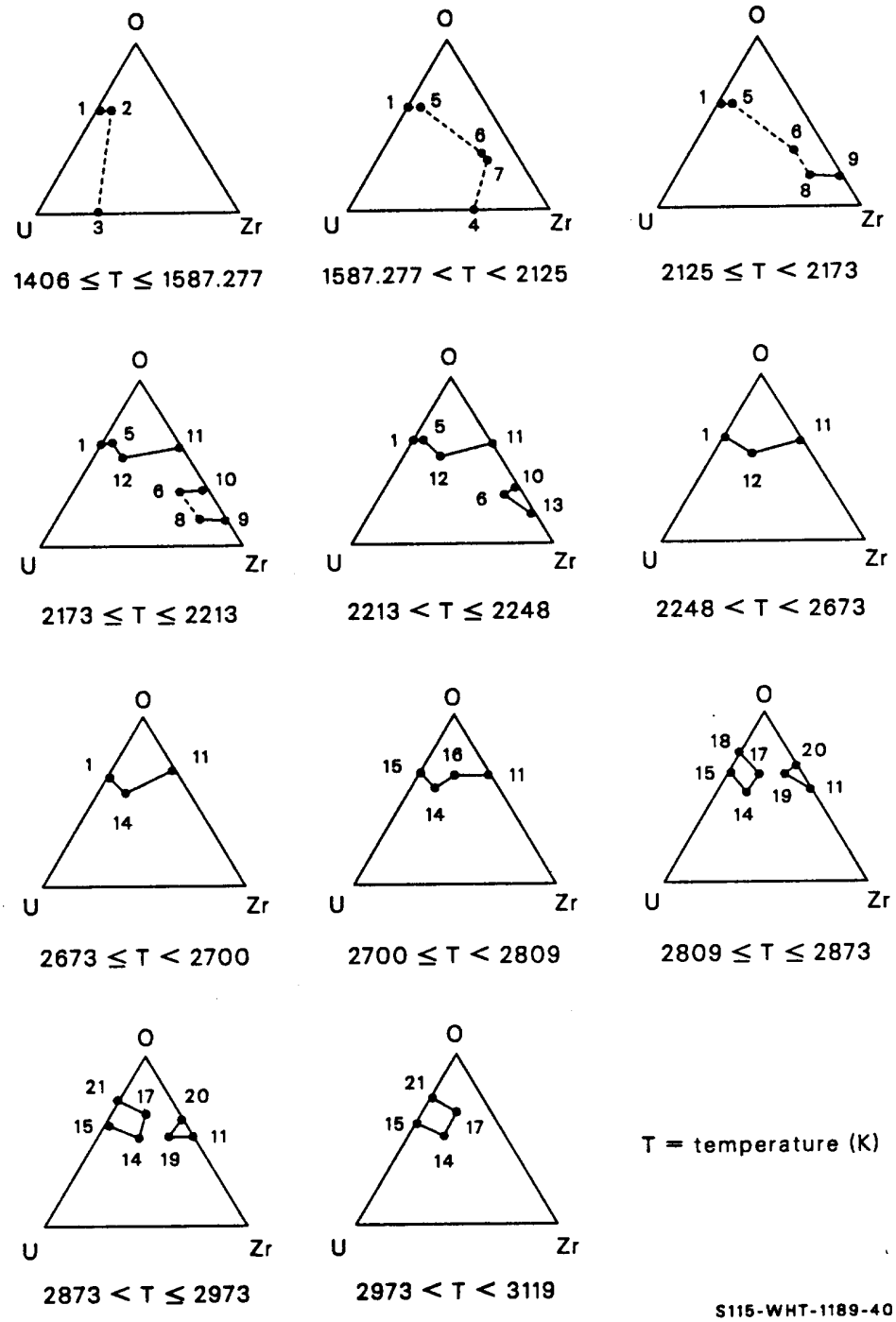

Figure 11-16. Points that are connected to form the ternary Zr-O-U system solidus lines.

Table 11-3. Correlations for solidus compositions.

1.U-rich solid UO_{2-x} boundary for T < 2,700 K, U-O binary system	$f_o = \dfrac{473984.9 + \sqrt{473984.9^2 - 763564.9\,(291499.1 + T)}}{763564.9}$
2.	Point 1 with x-coordinate increased 0.01times the ratio of the Zr content of the U-Zr binary system liquidus/0.1993
3.The U-Zr binary system liquidus	point 2 of Table 11-1
4.β-Zr, γ-U phase boundary, U-Zr binary system	$\dfrac{-208.5 + \sqrt{208.5^2 - 302\,(1406 - T)}}{302}$
5.	Point 1 with x coordinate increased 0.01
6.U-rich, O-rich extriem of the alpha zircaloy phase region.	
For $1{,}587.277 \le T < 2{,}223$	$x = 0.6248868 + T\,(2.938827\times10^{-4} + T\,(-9.967758\times10^{-8}))$
For $2{,}223 \le T \le 2{,}248$	$x = -7.207558 + T3.595666\times10^{-3}$
For $1{,}587.277 \le T\ 2{,}178$	$y = 0.5935931 + T\,(-4.90869\times10^{-4} + T1.629741\times10^{-7})$
For $2{,}178 \le T \le 2{,}248$	$y = 2.848266 - T1.71115\times10^{-3}$
7.	Point 6 displaced 0.01 parallel to the O-Zr side of the Gibbs triangle
8.U-rich, O-poor extriem of the beta phase zircaloy region	$x = 32.99604 + T\,(-2.99394\times10^{-2} + T6.984916\times10^{-6})$
	$y = -27.11131 + T\,(2.472659\times10^{-2} + T\,(-5.619063\times10^{-6}))$
9.Zr-rich boundary of the beta phase, Zr-ZrO_2 binary system	$f_o = \dfrac{-131.723 + \sqrt{131.723^2 - 5602.96\,(2125 - T)}}{5602.96}$
10.O-rich part of the alpha phase boundary, which is in equilibrium with liquid L_1', Zr-ZrO_2 binary system	$f_o = \dfrac{10100.05 + \sqrt{10100.05^2 - 40562.47\,(266.9135 + T)}}{40562.47}$
11.Zr-rich boundary of the cubic ZrO_2 phase, which is in equilibrium with liquid, Zr-ZrO_2 binary system	$f_o = \dfrac{52252.48 + \sqrt{52252.48^2 - 9551941\,(30182.27 - T)}}{95519.41}$

Table 11-3. Correlations for solidus compositions. (Continued)

12.$Zr_{0.7}O_{0.3}$-rich boundary of cubic $(U,Zr)O_{2-x}$ phase for $2{,}173 \le T \le 2{,}673$, $Zr_{0.7}O_{0.3}$-$U_{0.33}O_{0.67}$ isopleth	$f_{U_{0.33}O_{0.67}} = \dfrac{105794.3 + \sqrt{105794.3^2 - 128402.4\,(84438.99 + T)}}{128462.5}$
13.Zr-rich part of the alpha phase boundary, which is in equilibrium with liquid L_1, Zr-ZrO_2 binary system	$f_o = \dfrac{1941.412 - \sqrt{1941.412^2 + 7796.837\,(1764.588 - T)}}{7796.837}$
14.$Zr_{0.7}O_{0.3}$-rich boundary of cubic $(U,Zr)O_{2-x}$ phase for $2{,}673 \le T \le 3{,}119$ K, $Zr_{0.7}O_{0.3}$-$U_{0.33}O_{0.67}$ isopleth	$f_{U_{0.33}O_{0.67}} = \dfrac{2489.661 + \sqrt{2489.661^2 - 4179.972\,(3918 - T)}}{4179.972}$
15.U-rich solid UO_{2-x} boundary for $2{,}700 \le T \le 3{,}119$, U-O binary system	$f_o = \dfrac{2 - \dfrac{\sqrt{418.85^2 + 1469\,(3119 - T)} - 418.85}{1469}}{3 - \dfrac{\sqrt{418.85^2 + 1469\,(3119 - T)} - 418.85}{1469}}$
16.Linear interpolation between point 14's location at the given temperature and point 17 at 2,809 K	location of 16 = [location of 17 at 2,809 (T - 2,673) + location of 14 at T(2809-T)]/136,
17.$U_{0.33}O_{0.67}$-rich cubic phase boundary, $U_{0.33}O_{0.67}$-$Zr_{0.33}O_{0.67}$ binary system	
For $3{,}119 \ge T \ge 2{,}843$	$f_{Zr_{0.33}O_{0.67}} = \dfrac{107 - \sqrt{107^2 - 41.44\,(3119 - T)}}{1036}$
For $2{,}843 > T$	$f_{Zr_{0.33}O_{0.67}} = 0.5 - \sqrt{0.25 - \dfrac{(2862.125 - T)}{212.5}}$
18.O-rich solid UO_{2+x} boundary for $2{,}809 \le T \le 2{,}873$, U-O binary	$f_o = \dfrac{478156.7 - \sqrt{478156.7^2 - 67587\,(3383979 - T)}}{675870}$
19.$Zr0.33O_{0.67}$-rich cubic phase boundary, $U_{0.33}O_{0.67}$-$Zr_{0.33}O_{0.67}$ binary system	
For $2{,}809 \le T \le 2{,}832$	$f_{Zr_{0.33}O_{0.67}} = 0.5 + \sqrt{\dfrac{0.25 - (2872.889 - T)}{255.5556}}$

Table 11-3. Correlations for solidus compositions. (Continued)

For 2,832 < T ≤ 2,973	$f_{Zr_{0.33}O_{0.67}} = \dfrac{2212.5 + \sqrt{2212.5^2 - 2850\,(4548 - T)}}{2850}$
20.$Zr_{0.33}O_{0.67}$ coordinates	x = 2/3 and y = 0.5873503
21.O-rich solid UO_{2+x} boundary for 2,873 ≤ T ≤ 3119, U-O binary system	$f_o = \dfrac{37574.67 - \sqrt{37574.67^2 - 48052.59\,(31862.23 - T)}}{48052.59}$

Table 11-4 lists the liquidus equation number as identified in Table 11-2, the data that were used to construct the equation, and any appropriate comments about the derivation of the equation. The rather complex definition of point 17 given in Table 11-2 is caused by the fact that points 15 of the liquidus lines and point 19 of the solidus lines form a three phase region connecting L_1, L_2, and the ZrO_2 cubic phase. Point 17 is the L_1 vertex of the three phase region and was located as described to allow tie lines between-ZrO_2 and L_1 on the right side of point 17.

Table 11-5 lists the solidus equation number as identified in Table 11-3, the data that were used to construct the equation, and any appropriate comments about the derivation of the equation.

The equations of Tables 11-2 and 11-3 are expressions for the compositions at boundaries of the single liquid and solid phase regions as a function of temperature. In order to use these expressions with the lever rule and the mixing rule[11.1-9] to calculate fractions dissolved or precipitated, the distance between the boundaries of solid and liquid phases that are in equilibrium must be calculated. This is done by converting the composition to Cartesian coordinates centered on the lower left-hand side vertex of the Gibbs coordinate system with the transformation

$$X = f_0 \cos(60) + f_{Zr} \tag{11-10}$$

$$Y = f_0 \sin(60) \tag{11-11}$$

where

X,Y	=	Cartesian coordinates
f_o	=	atomic fraction oxygen
f_{Zr}	=	atomic fraction zircaloy.

Table 11-4. Data used to produce liquidus correlations.

Number	Coordinations	Comments
1.	(0.0655 atomic fraction O, 1,391 K) (0.347 atomic fraction O, 2,485 K) (0.454 atomic fraction O, 2,700 K)	L_1 boundary, U-0 binary system, Figure 11-3
2.	(0 atomic fraction Zr, 1,406 K) (0.5 atomic fraction Zr, 1,825 K) (1 atomic fraction Zr, 2,125 K)	Figure 11-7
3.	a. $2{,}213 < T \leq 2{,}248$ K (0.0673 atomic fraction O, 2,213 K) (0.249 atomic fraction O, 2,248 K)	The point at 2,248 K was required to be a minimum. Figure 11-2
	b. $2{,}125 \leq T \leq 2{,}213$K (0 atomic fraction O, 2,125 K) (0.0673 atomic fraction O, 2,213 K)	The slope at 2,213 K was required to equal the slope of the correlation of 3a. Figure 11-2
4.	(0.249 atomic fraction O, 2,248 K) (0.413 atomic fraction O, 2,173 K)	The point at 2,248 K was required to be a maximum. Figure 11-2
5.	(0.413 atomic fraction O, 2,173 K) (0.538 atomic fraction O, 2,573 K) (0.667 atomic fraction O, 2,973 K)	O-rich L_1 and L_1 boundary, Zr-ZrO_2 Figure 11-2
6.	(0 atomic fr. $U_{0.33}O_{0.67}$, 2,240.747 K) (0.135 atomic fr. U0.33O0.67, 2,222 K) (0.27 atomic fr. U0.33O0.67, 2,173 K)	Zr-rich L_1 boundary, Figure 11-5.
7.	(0.27 atomic fr. $U_{0.33}O_{0.67}$, 2,173 K) (0.32 atomic fr. U0.33O0.67, 2,222 K) (0.38 atomic fr. U0.33O0.67, 2,673 K)	O-rich L_1 boundary, Figure 11-5.
9.	(0.8 atomic fr. $U_{0.33}O_{0.67}$, 2,673 K) (0.9 atomic fr. U0.33O0.67, 2,911 K) (1 atomic fr. U0.33O0.67, 3,119 K)	O-rich L_2 boundary, Figure 11-5.
12.	See Table 11-3	Least squared deviation fit to the data of Latta and Fryxell
13.	See comments	Assumed symmetry about the UO_2 composition in Figure 11-3.
14.	a. $3{,}119 > T \geq 2{,}989$ K (0 atomic fr. $Zr_{0.33}O_{0.67}$, 3,119 K) (0.3 atomic fr. $Zr_{0.33}O_{0.67}$, 2,989 K)	$U_{0.33}O_{0.67}$-rich L2 boundary Figure 11-6.

Table 11-4. Data used to produce liquidus correlations. (Continued)

Number	Coordinations	Comments
	b. 2,989 > T ≥ 2,832 K (0.3 atomic fr. $Zr_{0.33}O_{0.67}$, 2,989 K) (0.4 atomic fr. $Zr_{0.33}O_{0.67}$, 2,924K) (0.4868 at. fr. $Zr_{0.33}O_{0.67}$, 2,832 K)	
	c. 2,832 > T ≥ 2,809 K (0.4868 at. fr. $Zr_{0.33}O_{0.67}$, 2,832 K) (0.5 atomic fr. $Zr_{0.33}O_{0.67}$, 2,809 K)	The point at 2,809 K was required to be a minimum
15.	a. 2,809 ≥ T ≥ 2,821 K (0.5 atomic fr. $Zr_{0.33}O_{0.67}$, 2,809 K) (0.5317 at. fr. $Zr_{0.33}O_{0.67}$, 2,821 K) b. 2,821 > T ≥ 2,851.341 K (0.5317 at. fr. $Zr_{0.33}O_{0.67}$, 2,821 K) (0.55 at. fr. $Zr_{0.33}O_{0.67}$, 2,838 K) (0.65 at. fr. $Zr_{0.33}O_{0.67}$, 2,850 K) c. 2,851.341 > T ≥ 2,862 K (0.57 at. fr. $Zr_{0.33}O_{0.67}$, 2,851.341156 K) (0.75 at. fr. $Zr_{0.33}O_{0.67}$, 2,862 K) d. 2,862 > T ≥ 2,973 K (0.75 at. fr. $Zr_{0.33}O_{0.67}$, 2,862 K) (0.85 at. fr. $Zr_{0.33}O_{0.67}$, 2,889 K) (1.00 at. fr. $Zr_{0.33}O_{0.67}$, 2,973 K)	$Zr_{0.33}0_{0.67}$-rich boundary. Figure 11-6. The point at 2809 K was required to be a minimum. Section b's range was reduced because it contained a local maximum that is not physically possible. The offending section was replaced with a linear fit, Section c.
17.	(0.38 at. fr. $Zr_{0.33}O_{0.67}$, 2,673 K) (0.4023 at. fr. $Zr_{0.33}O_{0.67}$, 2,873 K) (0.65 at fr. $Zr_{0.33}O_{0.67}$,2,821 K)	The coordinates given are for the $L_1/L_1 + L_2$ boundary Figure 11-8.

Table 11-5. Data used to produce solidus correlations.

Number	Coordinations	Comments
1.	(0.6626 atomic fraction O, 1,391 K) (0.6375 atomic fraction O, 2,514 K) (0.626825706 at. fr. O, 2,700 K)	U-rich solid UO_{2-x} boundary for T > 2,700 K Figure 11-3.
4.	(0 atomic fraction Zr, 1,406 K) (0.5 atomic fraction Zr, 1,690 K) (1 atomic fraction Zr, 2,125 K)	Figure 11-7.
6.	a. For 1,587.277 $\geq$ T > 2,223 K, x coordinate (1,273 K, 0.8374) (1,773 K, 0.8364) (1,873 K, 0.8113) (2,073 K, 0.8113) (2,178 K, 0.7896)	Ternary phase diagrams were used to provide a correlation for the x and y coordinates. The point does not appear on any available binary system.
	b. For 2,223K $\geq$ T > 2,223 K, x coordinate (2,223 K, 0.785608339) (2,248 K, 0.8755)	The first point of the set for b was generated by requiring continuity with a.
	c. For 1,587.227 $\geq$ T $\geq$ 2,178 K, y coordinate (1,273 K, 0.2339) (1,773 K, 0.2213) (1,873 K, 0.2616) (2,073 K, 0.2767) (2,178 K, 0.2948)	
	d. For 2,178 $\geq$ T $\geq$ 2,248 (2,178 K, 0.297578048) (2,248 K, 0.2156)	
8.	a. For the x coordinate (2,073 K, 0.948278264) (2,178 K, 0.9224) (2,213 K, 0.948)	Ternary phase diagrams were used. The point 2,073 K was calculated to fit the binary correlation.
	b. For the y coordinate (2,073 K, 0) (2,178 K, 0.0882) (2,213 K, 0.090066642)	
9.	(0 atomic fraction O, 2,125 K) (0.0545 atomic fraction O, 2,156 K) (0.104 atomic fraction O, 2,213 K)	Zr-rich boundary of the beta phase, Zr-ZrO_2 system. Figure 11-16. The data of Domagala and were converted from weight fractions.

Table 11-5. Data used to produce solidus correlations. (Continued)

Number	Coordinations	Comments
10.	(0.249 atomic fraction O, 2,248 K) (0.292 atomic fraction O, 2,173 K)	O-rich part of the alpha phase boundary which is in equilibrium with liquid L_1', Zr-ZrO_2 binary phase system. Figure 1. The point at 2,248 K was required to be a max.
11.	(0.6246 atomic fraction O, 2,173 K) (0.65 atomic fraction O, 2,611 K) (0.667 atomic fraction O, 2,973 K)	Zr-rich boundary of the cubic ZrO_2 phase which is in equilibrium with liquid, Zr-ZrO_2 binary phase system. Figure 11-2.
12.	(0.834 at. fr. $U_{0.33}O_{0.67}$, 2,673 K) (0.8681 at. fr. $U_{0.33}O_{0.67}$, 2,432 K) (0.8868 at. fr. $U_{0.33}O_{0.67}$, 2,173 K)	$Zr_{0.7}O_{0.3}$- rich boundary of cubic $(U,Zr)0_{2-x}$ phase for $2173 \geq T \geq 2673$ K, $Zr_{0.7}O_{0.3}U_{0.33}O_{0.67}$ isopleth. Figure 11-8.
13.	(0.249 atomic fraction O, 2,248 K) (0.182 atomic fraction O, 2,213 K)	Zr-rich part of the alpha phase boundary which is in equilibrium with liquid L_1, Zr-ZrO_2 binary system. Figure 11-1. The point at 2,248 K was required to be a maximum.
14.	(0.834 at. fr. $U_{0.33}O_{0.67}$, 2,673 K) (0.91915 at. fr. $U_{0.33}O_{0.67}$, 2,873 K) (1 atomic fr. $U_{0.33}O_{0.67}$, 3,119 K)	$Zr_{0.7}O_{0.3}$-rich boundary of cubic $(U,Zr)O_{2-x}$ phase for $2,673 \geq T \geq 3,119$ K $Zr_{0.7}O_{0.3}O_{0.67}$ isopleth. Figure 11-4.
15.	See Table 11-3	Least squared deviation fit to the data of Latta and Fryxell
17.	a. For $3119 \geq T \geq 2,843$ K (0 atomic fr. $Zr_{0.33}O_{0.67}$, 3,119 K) (0.1 at. fr. $Zr_{0.33}O_{0.67}$, 2,843 K) b. For $2843 > T \geq 2,809$ K) (0.1 at. fr. $Zr0.33^{O}0.67$, 2,843 K) (0.5 at. fr. $Zr0.33^{O}0.67$, 2,809 K)	$U_{0.33}O_{0.67}$-rich cubic phase boundary, $U_{0.33}O_{0.67}$-$Zr_{0.33}O_{0.67}$ binary system. Figure 11-8. The equation for a was required to match the slope of the equation for $2,843 > T \geq 2,809$ K at 2,843 K and 0.1 atomic fraction. Equation 6 was required to have a min at 2,809 K. Datum at 2,843 K is from Hofmann
18.	(0.6969 atomic fraction O, 1,926 K) (0.6947 atomic fraction O, 2,273 K) (0.6919 atomic fraction O, 2,873 K) $2,809 \geq T \geq 2,873$K	O-rich solid boundary for U-O binary. Figure 11-2.

Table 11-5. Data used to produce solidus correlations. (Continued)

Number	Coordinations	Comments
19.	a. For 2,809 ≥ T ≥ 2,832 K (0.5 at. fr. Zr0.33O0.67, 2,809 K) (0.3 at. fr. Zr0.33O0.67, 2,832 K)	$Zr_{0.33}O_{0.67}$- rich cubic phase boundary,
	b. For 2,832 > T ≥ 2,973 K) (0.8 at. fr. Zr0.33O0.67, 2,832 K) (0.9 at. fr. Zr0.33O0.67, 2,874 K) (1.0 at. fr. Zr0.33O0.67, 2,973 K)	$U_{0.33}O_{0.67}$-$Zr_{0.33}O_{0.67}$ binary system. Figure 11-5 The equation for a was required to have a minimum at 2,809 K.
21.	(0.6916 atomic fraction O, 2,873 K) (0.6786 atomic fraction O, 2,994 K) (0.667 atomic fraction O, 3,119 K)	0-rich solid UO_{2+x} boundary for 2,873 ≤ T ≤ 3,119 K, U-0 binary system. Figure 11-2.

In addition to the distances between compositions, calculations of the fractions dissolved or precipitated require knowledge of the tie lines connecting interacting solid and liquid phases. Since no data for tie lines are available, tie lines are assumed to progress between the limits of the two-phase regions they cross in fan shaped patterns. This is the simplest pattern that correctly joins to the binary systems at the edges and avoids the error of tie line crossing.

Calculation of the fractions dissolved or precipitated proceeds with a tedious but direct geometric approach to find the lengths and intersections required by metallurgical techniques once the tie lines are modeled. The location of the point representing the solvent composition is compared to the liquidus and solidus lines expressed in Cartesian coordinates to determine whether the solvent lies between the liquidus and solidus lines (supersaturated) or in the liquid-phase region (subsaturated). If the solvent is supersaturated, tie lines or tie triangles and the lever rule are used to calculate the fraction of the solvent that will freeze. If the solvent is subsaturated, the mixing rule is used to determine the amount of solute that must be dissolved to bring the solvent composition to the liquidus line where dissolution will stop (because additional mixing of the solute would move the gross composition into the multiple-phase region between the liquidus and solidus where formation of a solid phase would take place).

Figure 11-17 is an example showing how a calculation of the amount of UO_2 dissolved by two solvents at 2,500 K proceeds. Solvent A has 0.6 atomic fraction Zr and 0.4 atomic fraction O, while solvent B has 0.9 atomic fraction Zr and 0.1 atomic fraction O. The mixing rule shows that the solution formed when solvent A attacks UO_2 at 2,500 K contains only about 20% UO_2 (the distance from A to the liquidus along the A-UO_2 line divided by the distance from A to the point marked UO_2 on the plot). When solvent B attacks the UO_2, 55% of the solute will be contained in the solution at equilibrium. The tie lines shown as dashed lines in the figure would be used to calculate freezing from the solvent if the solvent composition had placed it in the two-phase region between the solid and liquid phase boundaries.

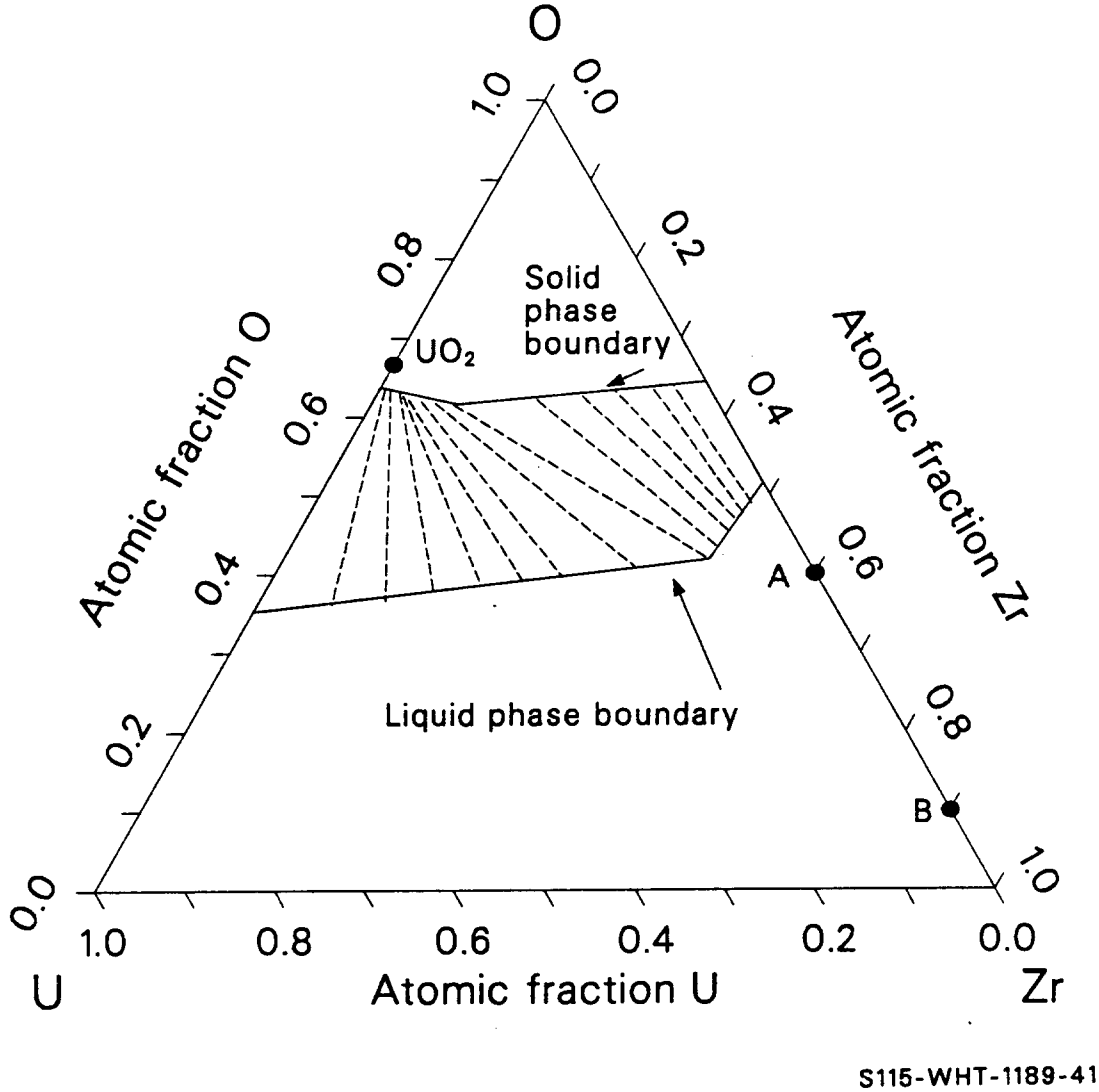

Figure 11-17. Solid and liquid phase boundaries with tie lines connecting compositions on the boundaries as they are represented for 2,500 K in the ZUSOLV code.

11.1.4 References

11.1-1 R. F. Domagala and D. J. McPherson, "System Zirconium Oxygen," *Journal of Metals, 6,* Transactions AIME 200, 1954, pp. 238-246.

11.1-2 R. Ruh and H. J. Garrett, "Nonstoichiometry of ZrO_2 and its Relation to Tetragonal-Cubic Inversion in ZrO_2," *Journal of the American Ceramic Society, 50,* 1966, pp. 257-161.

11.1-3 R. S. Roth, T. Negas, and L. P. Cook, *Phase Diagrams for Ceramists Volume IV,* The American Ceramic Society, 1981.

11.1-4 R. E. Latta and R. E. Fryxell, "Determination of Solidus-Liquidus Temperatures in the UO_{2+x} system (≤ 0.50 x < 0.2)," *Journal of Nuclear Materials, 35,* 1970, pp. 195-201.

11.1-5 A. Skokan, "High Temperature Phase Relations in the U-Zr-O System," *Fifth International Meeting on Thermal Nuclear Reactor Safety, Karlsruhe, German Federal Republic, September 9-13, 1984*, KfK 388011, December 1984, pp. 1035-1042.

11.1-6 K. A. Romberger, C. F. Bates, Jr., H. H. Stone, "Phase Equilibrium Studies in the UO_2-ZrO_2 System," *Journal of Inorganic and Nuclear Chemistry, 29*, 1966, pp. 1619-1630.

11.1-7 P. Hofmann, "SFD Singe Effects Laboratory Experiments," *Severe Fuel Damage and Source Term Research Program Review Meeting, Idaho Falls, ID, April 16-19, 1985.*

11.1-8 P. Hofmann and C. Politis, "The Kinetics of the Uranium Dioxide-Zircaloy Reactions at High Temperatures," *Journal of Nuclear Materials, 87*, 1975, pp. 375-397.

11.1-9 F. N. Rhines, *Phase Diagrams in Metallurgy, Their Development and Application*, New York: McGraw-Hill Book Company, Inc., 1956.

11.2 Specific Heat Capacity and Enthalpy (ZUCP, ZUNTHL, ZUCP1, ZUNTH1)

The function ZUCP provides the specific heat capacity of Zr-U-O compounds as a function of component concentrations and the compound temperature. ZUNTHL returns the Zr-U-O compound enthalpy as a function of component concentrations, the compound temperature, and a reference temperature for which the enthalpy will be zero. Functions ZUCP1 and ZUNTH1 provide the same information for core components.

11.2.1 Zirconium-Uranium-Oxygen Compounds

The expression used to calculate the specific heat capacity is an atomic fraction weighted average of the molar heat capacities of UO_2, ZrO_2, and zircaloy

$$C_p(c) = \frac{C_p(UO_2)\,0.207f(UO_2) + C_p(ZrO_2)\,0.123f(ZrO_2) + C_p(Zr)\,0.091f(Zr)}{0.207f(UO_2) + 0.123f(ZrO_2) + 0.091f(Zr)} \qquad (11\text{-}12)$$

where

$C_p(c)$	=	specific heat capacity of the compound (J/kg K)
$C_p(UO_2)$	=	specific heat capacity of UO_2 obtained from the FCP subcode (J/kg•K)
$C_p(ZrO_2)$	=	specific heat capacity of ZrO_2 obtained from the ZOCP subcode (J/kg•K)
$C_p(Zr)$	=	specific heat capacity of zircaloy obtained from the CCP subcode (J/kg•K)
$f(UO_2)$	=	atomic fraction of UO_2
$f(ZrO_2)$	=	atomic fraction of ZrO_2
$f(Zr)$	=	atomic fraction of zircaloy.

An analogous weighted average is used in ZUNTHL to calculate compound enthalpies. This technique has the advantage that the proper enthalpies are obtained for the limiting cases of UO_2, ZrO_2, or zir-

caloy, but the disadvantage that the heats of fusion are not constrained to appear between the solidus and liquidus temperatures of the compound.

Plots of the calculated specific heat capacity and enthalpy of a compound made up of 0.2 weight fraction UO_2 and 0.8 weight fraction ZrO_2 are shown in Figures 11-18 and 11-19.

Calculations with ZUNTHL are compared with enthalpies observed by Deem[11.2-1] for several UO_2 - ZrO_2 compounds in Tables 11-6 through 11-9. (Deem's data are presented in Tables 14 through 17 of Reference 11.2-1.) The standard error of these predictions, 2×10^4 J/kg or about 0.1 of the predicted value, is the expected standard error of the ZUNTHL function.

A similar expected standard error, 0.1 of the predicted specific heat capacity, is adopted for ZUCP.

11.2.2 Core Component Compounds

The expression used to calculate the specific heat capacity is an atomic fraction weighted average of the molar heat capacities of all components of the materials in the core.

$$C_p(c) = \frac{\sum_{i=1}^{n} C_p(i)\, af_i}{\sum_{i=1}^{n} \frac{MW_i}{100} af_i} \tag{11-13}$$

where

$C_p(c)$	=	specific heat capacity of the compound (J/kg•K)
$C_p(i)$	=	specific heat capacity of the i-th core component material obtained from the specific heat subcode for that material (J/kg•K)
af_i	=	atomic fraction of the i-th core component material
MW_i	=	molecular weight of the i-th core component material

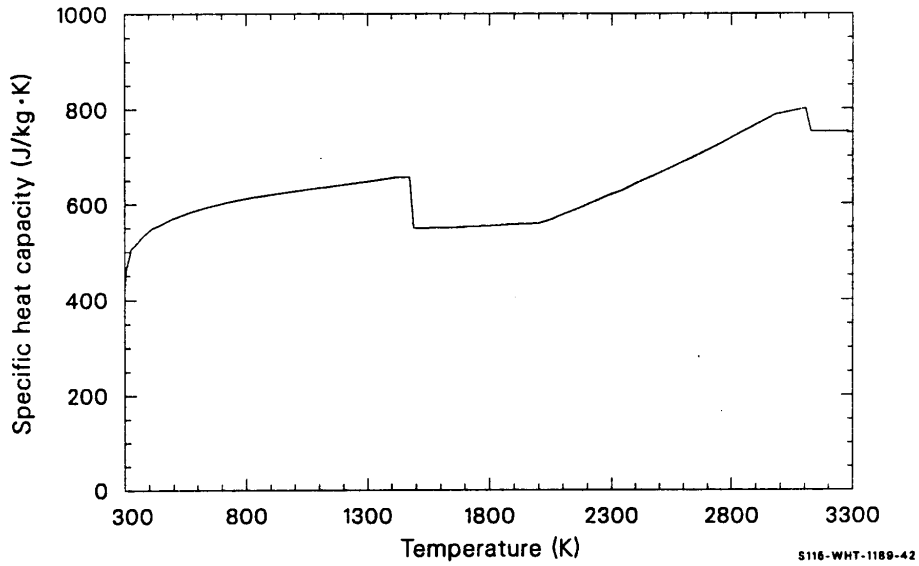

Figure 11-18. Specific heat capacity calculated for a 0.2 UO_2-0.8 ZrO_2 weight fraction compound.

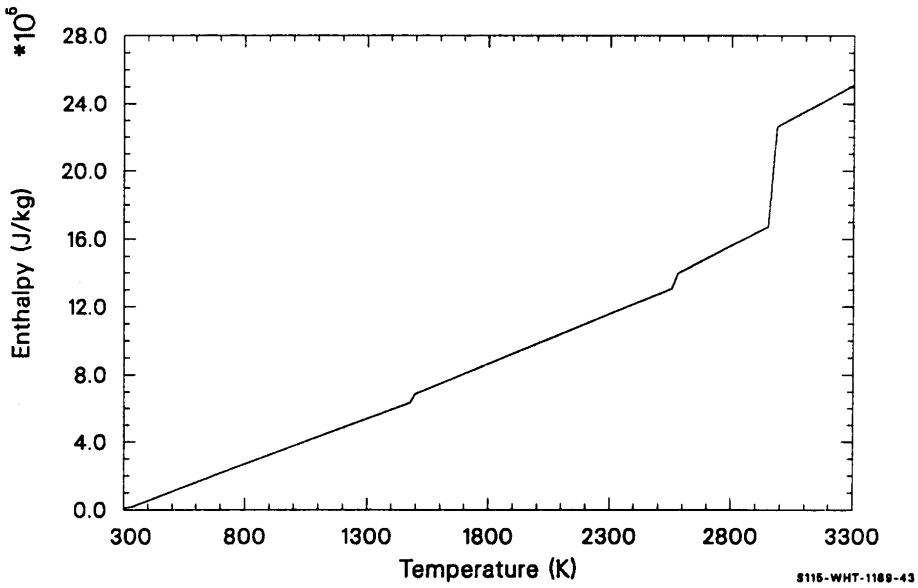

Figure 11-19. Enthalpy calculated for a 0.2 UO_2-0.8 ZrO_2 weight fraction compound.

Table 11-6. ZUNTHL calculations and Deem's data[11.2-1] for a 0.2 UO_2-0.8 ZrO_2 weight fraction compound.

Temperature (K)	Observed Enthalpy (10^4 J/kg)	Calculated Enthalpy (10^4 J/kg)
273	0.00	0.00
370	4.23	4.16
370	4.31	4.16
378	4.64	4.53
469	9.16	8.85
596	15.69	15.24
596	15.56	15.24
727	23.05	22.08
868	30.92	29.66
870	31.00	29.77
1,095	42.59	42.22
1,257	52.05	51.40
1,479	63.97	68.11
1,750	79.50	83.05
2,108	101.0	103.10
2,256	112.0	111.92

Table 11-7. ZUNTHL calculations and Deem's data[11.2-1] for 0.32 UO_2-0.68 ZrO_2 weight fraction compound.

Temperature (K)	Observed Enthalpy (10^4 J/kg)	Calculated Enthalpy (10^4 J/kg)
273	0.00	0.00
348	2.93	2.97
349	2.96	3.01

Table 11-7. ZUNTHL calculations and Deem's data[11.2-1] for 0.32 UO_2-0.68 ZrO_2 weight fraction compound. (Continued)

Temperature (K)	Observed Enthalpy (10^4 J/kg)	Calculated Enthalpy (10^4 J/kg)
371	3.95	3.93
372	3.96	3.98
390	4.74	4.75
390	4.77	4.75
408	5.57	5.54
408	5.61	5.54
541	11.97	11.63
543	11.95	11.72
690	19.20	18.82
691	19.36	18.87
829	26.21	25.76
829	26.22	25.76
947	32.30	31.78
951	32.56	31.99
1,069	37.24	38.11
1,292	49.71	49.94
1,480	60.84	63.41
1,678	70.54	73.68
1,797	75.94	79.89
1,878	81.17	84.14
1,919	82.26	86.30
1,976	86.06	89.32
2,096	93.55	95.78
2,175	100.96	100.19

Table 11-7. ZUNTHL calculations and Deem's data[11.2-1] for 0.32 UO_2-0.68 ZrO_2 weight fraction compound. (Continued)

Temperature (K)	Observed Enthalpy (10^4 J/kg)	Calculated Enthalpy (10^4 J/kg)
2,276	107.19	106.02
2,385	119.50	112.57
2,487	125.98	118.96

Table 11-8. ZUNTHL calculations and Deem's data[11.2-1] for a 0.5 UO_2-0.5 ZrO_2 weight fraction compound.

Temperature (K)	Observed Enthalpy (10^4 J/kg)	Calculated Enthalpy (10^4 J/kg)
273	0.00	0.00
339	2.33	2.32
339	2.37	2.32
367	3.41	3.37
367	3.44	3.37
383	4.02	3.99
385	3.97	4.06
401	4.76	4.69
543	10.63	10.50
547	10.83	10.67
702	17.60	17.40
702	17.62	17.40
877	25.81	25.27
878	25.66	25.31
978	30.44	29.91
979	29.96	29.96
1,102	34.98	35.70
1,243	42.05	42.38

Table 11-8. ZUNTHL calculations and Deem's data[11.2-1] for a 0.5 UO_2-0.5 ZrO_2 weight fraction compound. (Continued)

Temperature (K)	Observed Enthalpy (10^4 J/kg)	Calculated Enthalpy (10^4 J/kg)
1,273	43.43	43.82
1,484	53.39	56.46
1,521	63.64	58.19
1,796	67.66	71.20
1,889	72.17	75.66
1,995	77.74	80.82
2,086	84.60	85.34
2,188	89.66	90.60
2,297	99.33	96.47
2,430	105.94	104.01

Table 11-9. ZUNTHL calculations and Deem's data[11.2-1] for 0.94 UO_2-0.06 ZrO_2 weight fraction compound.

Temperature (K)	Observed Enthalpy (10^4 J/kg)	Calculated Enthalpy (10^4 J/kg)
273	0	0
372	2.36	2.55
372	2.55	2.55
474	5.58	5.46
596	9.25	9.15
597	9.26	9.18
728	13.41	13.29
729	13.44	13.32
870	17.96	17.87
872	18.02	17.94
1,030	23.32	23.15

Table 11-9. ZUNTHL calculations and Deem's data[11.2-1] for 0.94 UO_2-0.06 ZrO_2 weight fraction compound.

Temperature (K)	Observed Enthalpy (10^4 J/kg)	Calculated Enthalpy (10^4 J/kg)
1,108	25.15	25.76
1,314	32.72	32.77
1,492	37.11	39.24
1,816	48.45	50.81
2,071	59.66	60.56
2,265	68.58	68.68

An analogous weighted average is used in ZUNTHL to calculate compound enthalpies. This technique has the advantage that the proper enthalpies are obtained for each core component material but the disadvantage that the heats of fusion are not constrained to appear between the solidus and liquidus temperatures of the compound.

The newer versions of the subcodes, ZUCP1 and ZUNTH1, were tested by inputting identical weight fractions to those used to test ZUCP and ZUNTHL, with all other components in the core input as zero, and comparing the results. The results were identical to those shown in Figures 11-18 and 11-19. A comparison of the results obtained for several UO_2-ZrO_2 compounds using the later versions, ZUCP1 and ZUNTH1, and those obtained using ZUCP and ZUNTHL with enthalpies reported by Deem[11.2-1] showed that the results were identical. The standard error of these predictions, 2 x 10^4 J/kg, or about 0.1 of the predicted value, is the standard error of the ZUNTH1 function. A similar standard error of 0.1 of the predicted specific heat capacity is used in ZUCP1.

Calculations with ZUNTH1 were compared with enthalpies observed by Deem[11.2-1] for several UO_2-ZrO_2 compounds in Tables 11-6 through 11-9. (Deem's data are presented in Tables 14 through 17 of Reference 11.2-1.) The standard error of these predictions, 2 x 10^4 J/kg or about 0.1 of the predicted value, is the expected standard error of the ZUNTH1 function.

A similar expected standard error, 0.1 of the predicted specific heat capacity, is adopted for ZUCP1.

11.2.3 References

11.2-1 H. W. Deem, *Fabrication, Characterization, and Thermal Property Measurements of ZrO_2-Base Fuels*, BMI-1775, June 1966.

11.3 Thermal Conductivity (ZUTCON, ZUTCO1)

11.3.1 Zirconium-Uranium-Oxygen Compounds

Required inputs to ZUTCON to calculate compound thermal conductivities are the component concentrations and compound temperature. The expression used for the compound conductivity is the smaller of k_{Zr} and

$$k(c) = f(UO_2)\, k(UO_2) + f(ZrO_2)\, k(ZrO_2) + f(Zr)\, k(Zr) - 0.4\, f(UO_2)\, k(ZrO_2) + 7.8 f(UO_2)\, f(Zr) + 7.8\, f(ZrO_2)\, f(Zr) \quad (11\text{-}14)$$

where

$k(c)$	=	compound thermal conductivity (W/m• K)
$k(UO_2)$	=	UO_2 thermal conductivity obtained from the FTHCON subcode (W/m•K)
$k(ZrO_2)$	=	ZrO_2 thermal conductivity obtained from the ZOTCON subcode (W/m•K)
$k(Zr)$	=	zircaloy thermal conductivity obtained from the CTHCON subcode (W/m•K)
$f(UO_2)$	=	atomic fraction of UO_2
$f(ZrO_2)$	=	atomic fraction of ZrO_2
$f(Zr)$	=	atomic fraction of zircaloy.

Equation (11-14) is an atomic fraction weighted average of the thermal conductivities of UO_2, ZrO_2, and zircaloy modified to include cross products. The modification was added to reproduce the parabolic shape typically seen in plots of conduction versus composition in binary mixtures.[11.3-1,11.3-2]

The coefficient of the UO_2-ZrO_2 cross-product was obtained by requiring Equation (11-14) to reproduce a thermal conductivity of 1.44 W/m• K at 2,073 K for a composition of 0.315 mole fraction UO_2 and 0.685 mole fraction ZrO_2 (0.5UO_2 - 0.5ZrO_2 by weight). The thermal conductivity was obtained from a curve published as Figure 56 in Reference 11.3-3. A similar approach was used to determine the coefficient of the Zr-UO_2 cross product. A measurement from Rauch,[11.3-4] 11.09 W/m•K at 343 K for a composition of 0.80 weight fraction UO_2 and 0.20 weight fraction zircaloy, was employed. No data were found to evaluate the Zr-ZrO_2 cross product coefficient, so the Zr-UO_2 cross-product coefficient was used as an estimate.

A plot of the calculated thermal conductivity of a compound made up of 0.2 weight fraction UO_2 and 0.8 weight fraction ZrO_2 is shown in Figure 11-20.

Model predictions are compared to thermal conductivities calculated by Deem (Table 26 of Reference 11.3-3) from his data for several UO_2-ZrO_2 compounds in Tables 11-10 through 11-14. The standard error of the ZUTCON calculations is $\pm$ 1 W/m, most of which is caused by serious overprediction at low temperature and high UO_2 content.

11.3.2 Core Component Compounds

Required inputs to ZUTCO1 to calculate compound thermal conductivities are the component concentrations and compound temperature. The expression used for the compound conductivity is the smaller of k(Zr) and

$$k_c = \sum_{i=1}^{n} f(ci)\, k(ci) \tag{11-15}$$

where

k_c	=	compound thermal conductivity (W/m•K)
f(ci)	=	atomic fraction of the i-th core component
k(ci)	=	thermal conductivity of the i-th core component obtained from its thermal conductivity subcode
n	=	the number of individual core components.

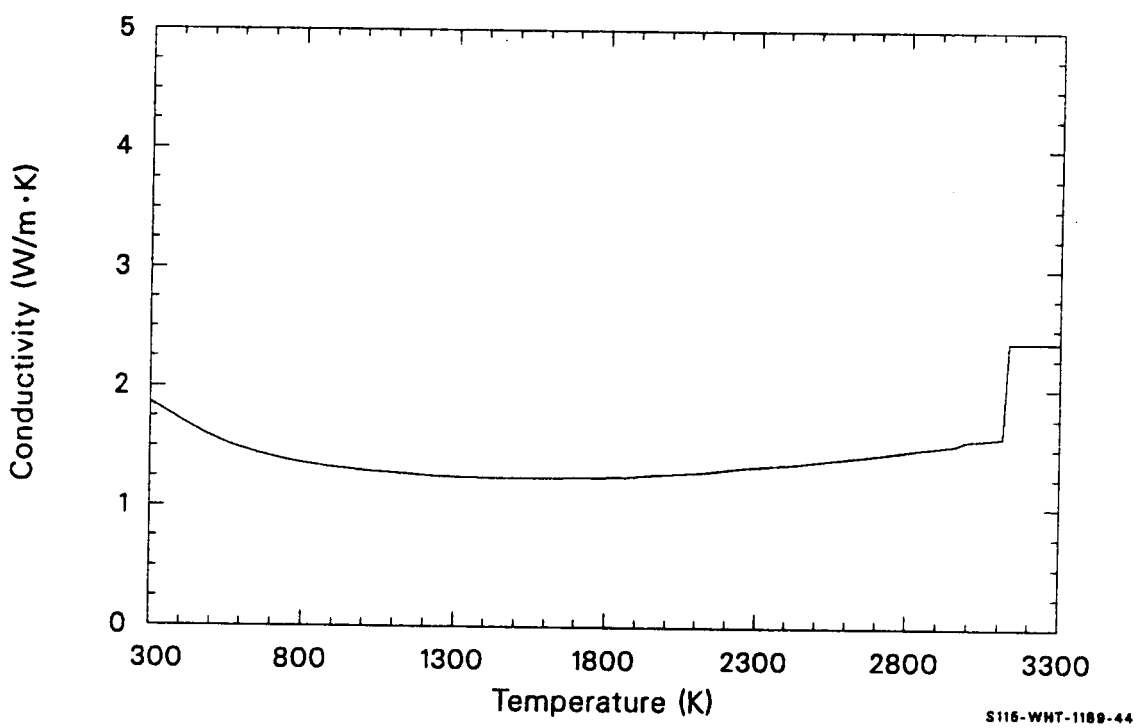

Figure 11-20. Thermal conductivity calculated for a 0.2 UO_2-0.8 ZrO_2 weight fraction compound.

Table 11-10. ZUTCON calculations and Deem's results[11.3-3] for 0.2 UO_2-0.8 ZrO_2 weight fraction compound.

Temperature (K)	Deem's Conductivity (W/m• K)	Calculated Conductivity (W/m•K)
423	2.8	1.7
473	2.6	1.6
573	2.30	1.51
673	2.42	1.43
873	2.12	1.33
1,073	1.94	1.28
1,273	1.82	1.25
1,473	1.78	1.24
1,673	1.77	1.24
1,873	1.78	1.25
2,073	1.72	1.28
2,173	1.66	1.30
2,273	1.62	1.32

Table 11-11. ZUTCON calculations and Deem's Results[11.3-3] for 0.32 UO_2-0.68 ZrO_2 weight fraction compound.

Temperature (K)	Deem's Conductivity (W/m•K)	Calculated Conductivity (W/m• K)
423	2.5	2.2
473	2.3	2.1
573	2.1	1.9
673	2.04	1.79
873	2.00	1.59
1,073	2.00	1.47

Table 11-11. ZUTCON calculations and Deem's Results[11.3-3] for 0.32 UO_2-0.68 ZrO_2 weight fraction compound. (Continued)

Temperature (K)	Deem's Conductivity (W/m•K)	Calculated Conductivity (W/m• K)
1,285	1.97	1.39
1,480	1.46	1.34
1,673	1.59	1.32
1,873	1.73	1.31
1,943	1.58	1.32
2,073	1.76	1.33
2,273	1.87	1.38

Table 11-12. ZUTCON calculations and Deem's results[11.3-3] for 0.5 UO_2-0.5 ZrO_2 weight fraction compound.

Temperature (K)	Deem's Conductivity (W/m• K)	Calculated Conductivity (W/m•K)
423	2.2	3.3
473	2.0	3.1
573	1.8	2.7
673	1.75	2.44
873	1.71	2.06
1,073	1.69	1.82
1,273	1.67	1.66
1,473	1.64	1.55
1,673	1.60	1.48
1,873	1.54	1.44
2,073	1.44	1.45
2,183	1.41	1.47
2,293	1.79	1.51
2,373	1.77	1.54

Table 11-13. ZUTCON calculations and Deem's results[11.3-3] for a low-density 0.32 UO_2-0.68 ZrO_2 weight fraction compound.

Temperature (K)	Deem's Conductivity (W/m• K)	Calculated Conductivity (W/m• K)
423	2.2	2.2
473	2.1	2.1
573	1.8	1.9
673	1.55	1.79
873	1.53	1.59
1,073	1.53	1.47
1,273	1.53	1.39
1,473	1.17	1.34
1,673	1.28	1.32
1,873	1.36	1.31
2,073	1.40	1.33
2,173	1.30	1.35

Table 11-14. ZUTCON calculations and Deem's results[11.3-3] for 0.94 UO_2-0.06 ZrO_2 weight fraction compound.

Temperature (K)	Deem's Conductivity (W/m.K)	Calculated Conductivity (W/m• K)
423	3.8	7.8
473	3.6	7.2
573	2.8	6.1
673	2.41	5.32
873	2.32	4.19
1,073	2.19	3.45
1,273	2.05	2.93
1,473	1.99	2.55

Table 11-14. ZUTCON calculations and Deem's results[11.3-3] for 0.94 UO_2-0.06 ZrO_2 weight fraction compound. (Continued)

Temperature (K)	Deem's Conductivity (W/m•K)	Calculated Conductivity (W/m• K)
1,673	1.93	2.28
1,873	1.87	2.11
2,073	1.84	2.07
2,173	1.82	2.10

Equation (11-15) is an atomic fraction weighted average of the thermal conductivities of all core components. Where all core materials were considered, cross products were not used to obtain the total thermal conductivity of the core materials.

Model predictions using ZUTCO1 were compared to thermal conductivities calculated by Deem (Table 26 of Reference 11.3-3) from his data for several UO_2-ZrO_2 compounds in Tables 11-10 through 11-14. The standard error of the ZUTCO1 calculations is $\pm$ 1 W/m, most of which is caused by serious overprediction at low temperature and high UO_2 content.

11.3.3 References

11.3-1 F. Rhines, *Phase Diagrams in Metallurgy and Their Development and Application*, New York: McGraw-Hill Book Company, 1956, pp. 110-113.

11.3-2 B. Abeles, "Lattice Thermal Conductivity of Disordered Semiconductor Alloys at High Temperatures," *Physical Review, 131*, 1963, pp. 1906-1911.

11.3-3 H. W. Deem, *Fabrication, Characterization, and Thermal Property Measurements of ZrO_2 Base Fuels*, BMI-1775, June 1966.

11.3-4 W. G. Rauch, *Uranium Zirconium Cermets*, ANL-5268, 1954.

11.4 Thermal Expansion and Density (ZUTEXP, ZUDEN, ZUTEX1, ZUDEN1)

11.4.1 Zirconium-Uranium-Oxygen Compounds

The function ZUTEXP calculates the thermal expansion strain of Zr-U-O compounds as a function of composition, temperature, and a reference temperature for which the thermal expansion strain will be zero. ZUDEN returns the compound density as a function of composition and density.

The expression used to calculate thermal expansion strains in ZUTEXP is

$$\varepsilon_c = \frac{2.46f(UO_2)\,\varepsilon(UO_2) + 2.12f(ZrO_2)\,\varepsilon(ZrO_2) + 1.39f(Zr)\,\varepsilon(Zr)}{2.46f(UO_2) + 2.12f(ZrO_2) + 1.39f(Zr)} \tag{11-16}$$

where

ε_c	=	compound thermal strain (m/m)
$\varepsilon\ (UO_2)$	=	UO_2 thermal strain obtained from the FTHEXP subcode (m/m)
$\varepsilon\ (ZrO_2)$	=	ZrO_2 thermal strain obtained from the ZOTEXP subcode (m/m)
$\varepsilon\ (Zr)$	=	isotropic Zr thermal strain obtained from the CTHEXP subcode with COSTH2 = 1/3 and COSFI2 = 1/2(m/m)
$f(UO_2)$	=	atomic fraction of UO_2
$f(ZrO_2)$	=	atomic fraction of ZrO_2
f(Zr)	=	atomic fraction of zircaloy.

This expression is a component volume fraction weighted average of the component strains. The volume fraction of each component is

$$f_V\,(i) = \frac{\dfrac{f\,(i)\,m\,(i)}{\rho\,(i)}}{\displaystyle\sum_{j=1}^{3} \dfrac{f\,(j)\,m\,(j)}{\rho\,(j)}} \tag{11-17}$$

where

$f_V(i)$	=	volume fraction of i-th component (m3/m3)
f(i)	=	mole fraction of i-th component
m(i)	=	mole weight of i-th component (kg/g mole) (0.270 for UO_2, 0.123 for ZrO_2, and 0.091 for Zr)
ρ (i)	=	density of i-th component (kg/m^3) (10,980 for UO_2, 5,800 for ZrO_2, and 6,550 for Zr).

Expression (11-16) is derived by assuming that the compound is made up of components which produce independent thermal strains. The initial volume is thus

$$V_0 = V_0\,(UO_2) + V_0\,(ZrO_2) + V_0\,(Zr) \tag{11-18}$$

$$= f\,(UO_2)\,V_0 + f\,(ZrO_2)\,V_0 + F\,(Zr)\,V_0 \tag{11-19}$$

where

$V_0\,(UO_2)$, $V_0\,(ZrO_2)$, and $V_0\,(Zr)$ = initial component volumes (m^3) and f (UO_2), f (ZrO_2), and f (Zr) = component volume fractions (m^3/m^3).

The component volume after some thermal strain is

$$V = V_0\ (UO_2)\exp(3\varepsilon\,(UO_2)) + V_0\,(ZrO_2)\exp(3\varepsilon\,(ZrO_2)) + V_0\,(Zr)\exp(3\varepsilon\,(Zr)) \tag{11-20}$$

or

$$V \approx V_0\,(UO_2)\,(1 + 3\varepsilon\,(UO_2)) + V_0\,(ZrO_2)\,(1 + 3\varepsilon\,(ZrO_2)) + V_0\,(Zr)\,(1+3\varepsilon\,(Zr)) \quad . \tag{11-21}$$

The compound volume strain, ε_{c_v} is

$$\varepsilon_{c_v} = \frac{V - V_0}{V_0} \quad . \tag{11-22}$$

$$\approx \frac{V_0\,(UO_2)\,3\varepsilon\,(UO_2) + V_0\,(ZrO_2)\,3\varepsilon\,(ZrO_2) + V_0\,(Zr)\,3\varepsilon\,(Zr)}{V_0\,(UO_2) + V_0\,(ZrO_2) + V_0\,(Zr)} \tag{11-23}$$

$$= f_V\,(UO_2)\,3\varepsilon\,(UO_2) + f_V\,(ZrO_2)\,3\varepsilon\,(ZrO_2) + f_V\,(Zr)\,3\varepsilon\,(Zr) \quad . \tag{11-24}$$

Replacement of the compound volume strain by three times the compound linear strain and substitution using Equation (11-17) completes the derivation of Equation (11-16).

The expression used in ZUDEN to calculate compound densities is

$$\rho_c = \frac{0.27f\,(UO_2) + 0.123f\,(ZrO_2) + 0.091f\,(Zr)}{\dfrac{0.270f\,(UO_2)}{\rho\,(UO_2)} + \dfrac{0.123f\,(ZrO_2)}{\rho\,(ZrO_2)} + \dfrac{0.091f\,(Zr)}{\rho\,(Zr)}} \tag{11-25}$$

where

ρ_c	=	compound density(kg/m^3)
$\rho\,(UO_2)$	=	UO density obtained from the FDEN subcode (kg/m^3
$\rho\,(ZrO_2)$	=	ZrO density obtained from the ZODEN subcode (kg/m^3)
$\rho\,(Zr)$	=	zircaloy density obtained from the CDEN subcode (kg/m^3).

Equation (11-25) is derived by assuming that each compound component contributes a volume equal to the volume the component would have as a free substance. The compound density is thus the total mass divided by the total volume

$$\rho_c = \frac{\sum_{i=1}^{3} N f_i m_i}{\sum_{i=1}^{3} \dfrac{N f_i m_i}{\rho_i}} \tag{11-26}$$

where N is the number of moles present in the compound. Cancellation of the common factor N and substitution of the component mole weights in Equation (11-26) yields Equation (11-25).

Plots of the calculated thermal expansion strain and density of a compound made up of 0.2 weight fraction UO_2 and 0.8 weight fraction ZrO_2 are shown in Figures 11-21 and 11-22.

Model predictions are compared with thermal expansion strains and densities measured at 293 K by Deem (Table 12 of Reference (11.4-1) for several UO_2-ZrO_2 compounds in Tables 11-15 through 11-19. The standard error of the ZUTEXP function calculations is $\pm$ 1.0 x 10^{-2}, and the standard error of the ZUDEN function calculations is $\pm$ 3 x 10^{2}. These standard errors are recommended as the expected standard errors of the ZUTEXP and ZUDEN function calculations.

11.4.2 Core Component Compounds

The function ZUTEX1 calculates the thermal expansion strain of core component compounds as a function of composition, temperature, and a reference temperature for which the thermal expansion strain will be zero. ZUDEN1 returns the compound density as a function of composition and density.

The expression used to calculate thermal expansion strains in ZUTEX1 is

$$\varepsilon_c = \frac{\sum_{i=1}^{n} Aaf_i \varepsilon_i}{\sum_{i=1}^{n} Aaf_i} \tag{11-27}$$

where

ε_c	=	compound thermal strain (m/m)
ε_i	=	i-th core component thermal strain obtained from its individual thermal strain subcode (m/m)
n	=	number of core components in the compound
af_i	=	atomic fraction of the i-th core component in compound
A	=	constant for each core component (Table 11-20).

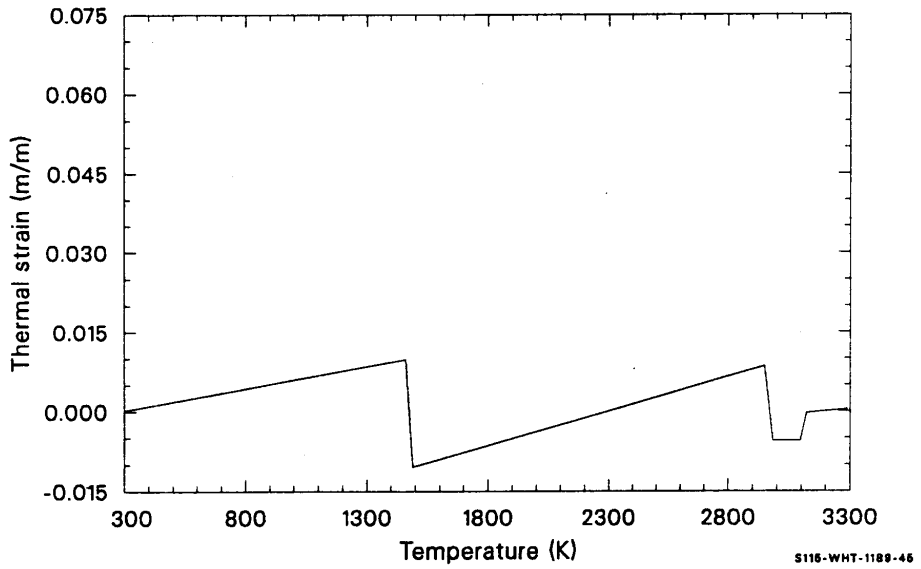

Figure 11-21. Thermal strain calculated for a 0.2 UO_2-0.8 ZrO_2 weight fraction compound.

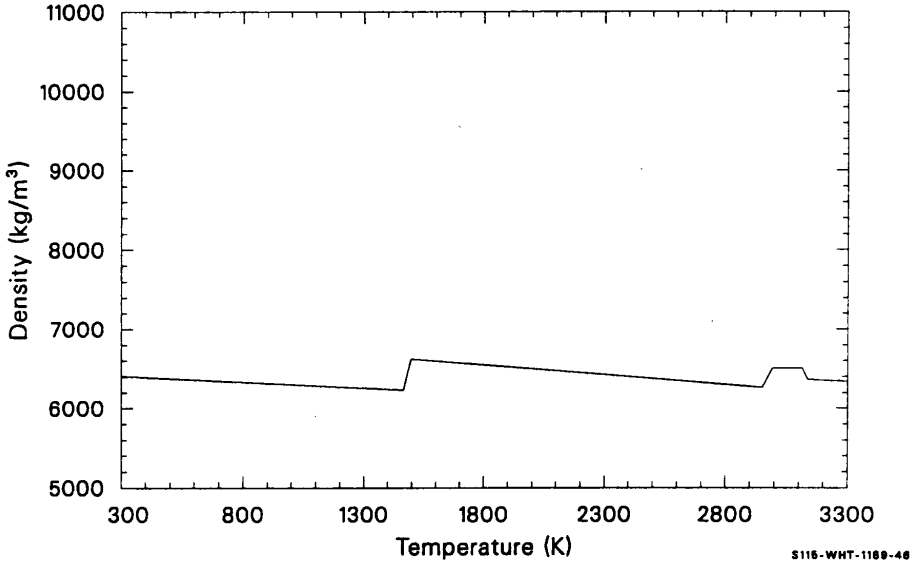

Figure 11-22. Density calculated for a 0.2 UO_2-0.8 ZrO_2 weight fraction compound.

Table 11-15. ZUTEXP calculations and Deem's data[11.4-1] for a 0.2 UO_2-0.8 ZrO_2 weight fraction compound.

Temperature (K)	Observed Strain (10^{-2} m/m)	Calculated Strain (10^{-2} m/m)
293	0	0
373	0.03	0.06
473	0.09	0.15
573	0.18	0.23
598	0.20	0.24
636	0.00	0.27
673	-0.33	0.31
873	-0.08	0.47
1,073	0.15	0.63
1,273	0.38	0.80
1,473	0.59	0.97
1,673	0.81	-0.84
1,873	1.04	-0.57
2,073	1.28	-0.31
2,273	1.58	-0.05

Table 11-16. ZUTEXP calculations and Deem's data[11.4-1] for 0.32 UO_2-0.68 ZrO_2 weight fraction compound.

Temperature (K)	Observed Strain (10^{-2} m/m)	Calculated Strain (10^{-2} m/m)
293	0	0
473	0.17	0.07
673	0.40	0.31
873	0.65	0.48
1,073	0.88	0.65
1,273	1.11	0.82

Table 11-16. ZUTEXP calculations and Deem's data[11.4-1] for 0.32 UO_2-0.68 ZrO_2 weight fraction compound. (Continued)

Temperature (K)	Observed Strain (10^{-2} m/m)	Calculated Strain (10^{-2} m/m)
1,473	1.35	1.00
1,673	1.57	-0.61
1,873	1.81	-0.35
2,073	2.05	-0.08
2,273	2.33	0.18

Table 11-17. ZUTEXP calculations and Deem's data[11.4-1] for a 0.5 UO_2-0.5 ZrO_2 weight fraction compound.

Temperature (K)	Observed Strain (10^{-2} m/m)	Calculated Strain (10^{-2} m/m)
293	0	0
473	0.16	0.15
673	0.37	0.32
873	0.61	0.50
1,073	0.84	0.68
1,273	1.08	0.87
1,473	1.32	1.06
1,673	1.56	-0.21
1,873	1.80	0.05
2,073	2.08	0.33
2,273	2.46	0.59

Table 11-18. ZUTEXP calculations and Deem's data[11.4-1] for 0.94 UO_2-0.06 ZrO_2 weight fraction compound.

Temperature (K)	Observed Strain (10^{-2} m/m)	Calculated Strain (10^{-2} m/m)
293	0	0
473	0.17	0.18
673	0.39	0.37
873	0.63	0.58
1,073	0.87	0.80
1,273	1.13	1.03
1,473	1.41	1.27
1,673	1.67	1.29
1,873	1.94	1.56
2,073	2.22	1.84
2,273	2.54	2.12

Table 11-19. ZUDEN calculations and Deem's compound density data[11.4-1]

Composition (weight fractions)	Observed Density (10 kg/m)	Calculated Density (10 kg/m)
0.2 UO_2-0.06 ZrO_2	6.26	6.40
0.32 UO_2-0.8 ZrO_2	6.81	6.83
0.5 UO_2-0.5 ZrO_2	7.62	7.59
Low density 0.32 UO_2-0.68 ZrO_2	6.46	6.83
0.94 UO_2-0.06 ZrO_2	9.92	10.04

This expression is a component volume fraction weighted average of the component strains. The volume fraction of each component is

$$f_{V_i} = \frac{\frac{f_i m_i}{\rho_i}}{\sum^{n} \frac{f_j m_j}{\rho_j}} \tag{11-28}$$

where

f_{V_i}	=	volume fraction of i-th core component (m^3/m^3)
f_i	=	mole fraction of i-th core component
m_i	=	mole weight of i-th core component (kg/g•mole)
n	=	number of core components in compound
ρ_i	=	density of i-th component (kg/m^3)

Expression (11-27) is derived by assuming that the compound is made up of components which produce independent thermal strains. The initial volume is thus

$$V_0 = \sum_{i=1}^{n} V_{0_i} \tag{11-29}$$

$$V_0 = \sum_{i=1}^{n} f_{V_i} V_o \tag{11-30}$$

where

V_{0_i}	=	initial volume of i-th core component
V_o	=	initial volume of the core components
f_{V_i}	=	volume fraction of the i-th core component
n	=	number of core components in the compound.

Table 11-20. Constants for thermal expansion strain.

Component	A
Uranium	1.28
Zirconium	1.46
Stainless steel	0.771
Uranium dioxide	2.46
Zirconium dioxide	2.12
Silver-indium-cadmium	1.07
Boron carbide	2.554
Stainless steel oxide	2.97

The component volume after some thermal strain is

$$V_0 = \sum_{i=1}^{n} V_{0_i} \exp(3\varepsilon_i) \tag{11-31}$$

or

$$V_0 \approx \sum^{n} V_{0_i} \exp\,(1 + 3\varepsilon_i) \tag{11-32}$$

where

V	=	component volume strain
ε_i	=	thermal expansion strain of the i-th core component.

The compound volume strain, ε_{c_v}, is

$$\varepsilon_{C_v} = \frac{V - V_0}{V_0} \tag{11-33}$$

or

$$V_0 \approx \sum_{i=1}^{n} \frac{3\varepsilon_i V_{0_i}}{V_{0_i}} \tag{11-34}$$

$$V_0 \approx \sum_{i=1}^{n} 3\varepsilon_i f_{V_i} \quad . \tag{11-35}$$

Replacement of the compound volume strain by three times the compound linear strain and substitution using Equation (11-28) completes the derivation of Equation (11-27).

The expression used in ZUDEN to calculate compound densities is

$$\rho_c = \frac{\sum_{i=1}^{n} MW_i af_i}{\sum_{i=1}^{n} \frac{MW_i af_i}{\rho_i}} \tag{11-36}$$

where

ρ_c	=	compound density (kg/m^3)
ρ_i	=	density of the i-th core component obtained from its individual density subcode (kg/m^3)
MW_i	=	molecular weights for the i-th core component (kg)
af_i	=	atomic fraction of the i-th core component in the compound.

Equation (11-36) is derived by assuming that each compound component contributes a volume equal to the volume the component would have as a free substance. The compound density is thus the total mass divided by the total volume

$$\rho_c = \frac{\sum_{i=1}^{n} N f_i m_i}{\sum_{i=1}^{n} \frac{N f_i m_i}{\rho_i}} \tag{11-37}$$

where N is the number of moles present in the compound. Cancellation of the common factor N and substitution of the component mole weights in Equation (11-37) yields Equation (11-36).

Plots of the calculated thermal expansion strain and density of a compound made up of 0.2 weight fraction UO_2 and 0.8 weight fraction ZrO_2 with the other core components assumed to be zero are identical to those shown in Figures 11-21 and 11-22.

Model predictions with ZUTEX1 and ZUDEN1 were compared with thermal expansion strains and densities calculated by ZUTEXP and ZUDEN and measured at 293 K by Deem (Table 12 of Reference 11.4-1) for several UO_2-ZrO_2 compounds shown in Tables 11-15 through 11-19. The standard error of the ZUTEX1 function calculations is $\pm$ 1.0 x 10^{-2}, and the standard error of the ZUDEN1 function calculations is $\pm$ 3 x 10^{2}. These standard errors are recommended as the expected standard errors of the ZUTEX1 and ZUDEN1 function calculations.

11.4.3 References

11.4-1 H. W. Deem, *Fabrication, Characterization, and Thermal Property Measurements of ZrO_2-Base Fuels*, BMI-1775, June 1966.

11.5 Zirconium-Uranium-Oxygen Compounds Coefficients of Friction (ZUFRIC)

The function ZUFRIC returns the coefficient of friction of flowing Zr-U-O compounds. The correlations used for this coefficient are

$$F = (0.0791Re)^{-0.25}, \; Re > 7539.42 \tag{11-38}$$

$$F = \frac{64}{Re}, \; 7539.42 \geq Re > 10^{-6} \tag{11-39}$$

$$F = 6.4 \times 10^{7}, \; Re < 10^{-6} \tag{11-40}$$

where

F = compound coefficient of friction (Pa/Pa)

Re = Reynold's number (unitless).

The correlations are an engineering estimate and have an expected standard error of 0.90 of their calculated value. Figure 11-23 illustrates the coefficient of friction calculated with the ZUFRIC function.

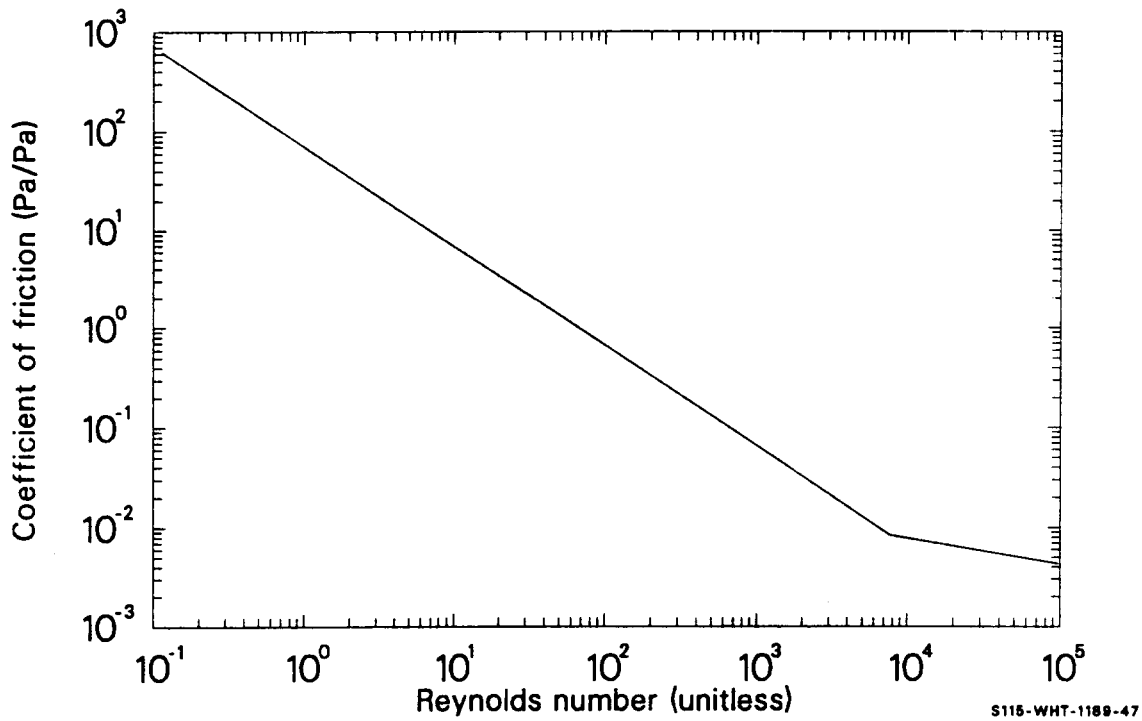

Figure 11-23. Coefficient of friction calculated with the ZUFRIC function.

11.6 Zirconium-Uranium-Oxygen Compounds Interfacial Surface Tension (ZUSTEN)

The function ZUSTEN returns the interfacial surface tension of molten Zr-U-O compounds on zircaloy cladding. The value used is

$$T = 0.45 \tag{11-41}$$

where T is the interfacial surface tension (N/m).

The value is an engineering estimate[a] and has an expected standard error of +1.0, -0.4.

a. L. J. Siefken, private communication, EG&G Idaho, Inc., October 14, 1982.

11.7 Zirconium-Uranium-Oxygen Compounds Viscosity (ZUVISC)

11.7.1 Model Development

The function ZUVISC returns an estimate of the viscosity of both solid and liquid Zr-U-O compounds as a function of the composition and temperature of the compound. The expression used to calculate viscosity for temperatures below the solidus temperature (which is provided by the PSOL function) is

$$\eta_s = 1.38 \exp\left(\frac{4.942\times10^4}{T}\right) \tag{11-42}$$

where η_s is the viscosity of solid Zr-U-O compounds (Pa• s).

This correlation is the expression used for solid UO_2 viscosity in the FVISCO subcode of MATPRO. For temperatures above the liquidus temperature, a mole fraction average of the component viscosities is used.

$$\eta_1 = f(UO_2)\,\eta(UO_2) + f(ZrO_2)\,\eta(ZrO_2) + f(Zr)\,\eta(Zr) \tag{11-43}$$

where

η_1	=	viscosity of liquid Zr-U-O compounds (Pa• s)
$\eta(UO_2)$	=	viscosity of liquid UO (Pa• s)
$\eta(ZrO_2)$	=	viscosity of liquid ZrO (Pa• s)
$\eta(Zr)$	=	viscosity of liquid Zr (Pa• s).

$\eta(UO_2)$ is calculated with the appropriate expression from the FVISCO subcode:

$$\eta(UO_2) = 1.23 \times 10^{-2} - 2.09 \times 10^{-6}\,T\ . \tag{11-44}$$

$\eta(ZrO_2)$ and $\eta(Zr)$ are calculated with correlations recommended by Nazare, Ondracek, and Schultz[11.7-1]

$$\eta(ZrO_2) = 1.22\times10^{-4}\exp\left(\frac{10500}{T}\right) \tag{11-45}$$

$$\eta(Zr) = 1.90\times10^{-4}\exp\left(\frac{6500}{T}\right) \tag{11-46}$$

For temperatures between the solidus and liquidus temperatures of the compound, an interpolation scheme is used

$$\eta = \frac{\eta_l(T - T_{sol}) + \eta_s(T_{liq} - T)}{T_{liq} - T_{sol}} \tag{11-47}$$

where

T_{sol}	=	solidus temperature (K)
T_{liq}	=	liquidus temperature (K)
η	=	viscosity of Zr-U-O compounds (Pa• s).

Figure 11-24 illustrates the effect of temperature on the viscosity of a compound composed of two-thirds mole fraction zircaloy and one-third mole fraction UO_2. The expected standard error of viscosities is $\pm$ 0.8 of the predicted value because there are no data in support of the model.

11.7.2 References

11.7-1. S. Nazare, G. Ondracek, and B. Schultz, "Properties of Light Water Reactor Core Melts," *Nuclear Technology, 32*, 1977, pp. 239-246.

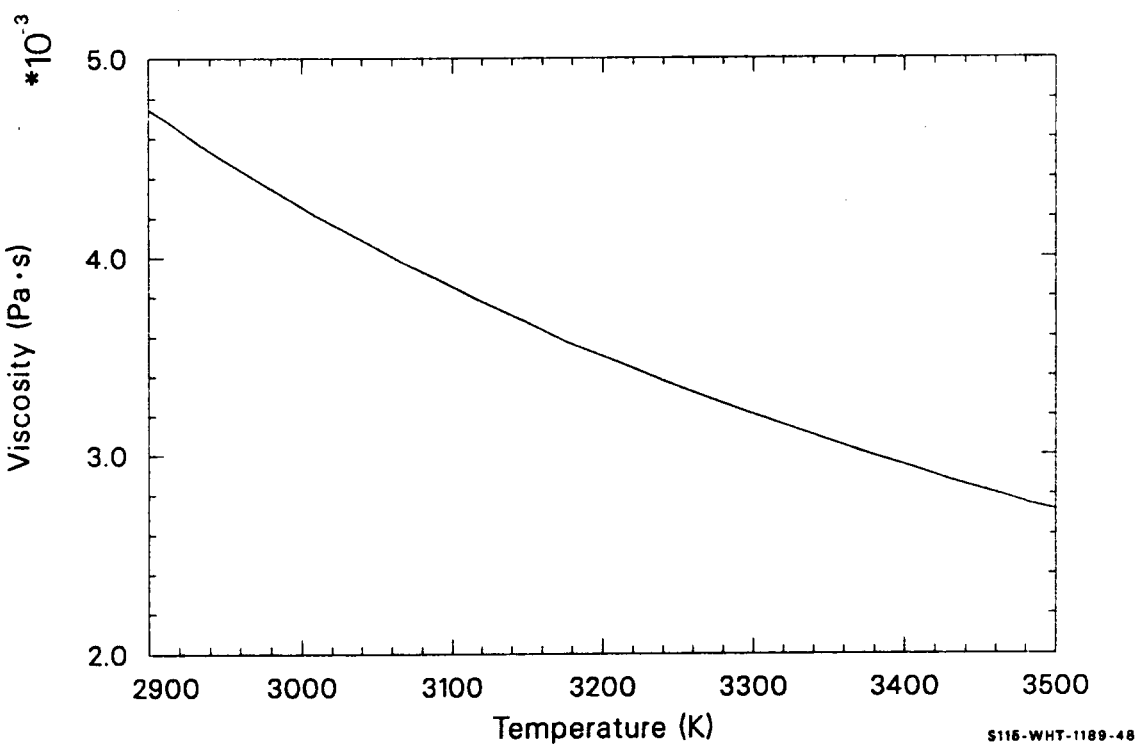

Figure 11-24. Viscosity of a compound composed of 0.33 mol% zirconium and 0.67 mol% uranium dioxide.

11.8 Heat of Solution of Uranium Dioxide by Zirconium-Uranium-Oxygen Compounds (ZUSOLN)

11.8.1 Model Development

ZUSOLN returns an estimate of the heat required to liquefy UO_2 in a zircaloy-uranium-oxygen compound as a function of the compound composition. The expression used to calculate this heat is

$$Q = \frac{1.5Z + 1.5U - 0.5}{1.5Z + 2.5U - 0.5} 2.69\times10^5 + \left(\frac{U}{1.5Z + 2.5U - 0.5}\right) 2.74\times10^5 \qquad (11\text{-}48)$$

where

Q	=	heat required to dissolve a unit mass of UO_2 in a zircaloy-uranium-oxygen compound (J/kg)
U	=	atomic fraction uranium in solvent (atoms uranium/atoms solvent)
Z	=	atomic fraction zirconium in solvent (atoms zirconium/atoms solvent).

Equation (11-48) is an interpolation between the heat of fusion for UO_2, 2.74 x 10^5 J/kg,[a] and the heat of fusion for UO_2 minus the difference in the heats of formation of ZrO_2 and UO_2 given on page 208 of Reference 11.8-1. The coefficient of the UO_2 heat of fusion is the ratio of the molecular fraction of UO_2 to the sum of fractions of UO_2 and zircaloy in the solvent. (These fractions were derived at the beginning of Section 11). Thus, when this fraction is one, UO_2 is being melted in a mixture of UO_2 and ZrO_2, so the appropriate heat is the energy necessary to melt the UO_2.

The coefficient of the first term in Equation (11-48) is the ratio of the molecular fraction of zircaloy to the sum of the fractions of UO_2 and zircaloy in the solvent. When this fraction is one, UO_2 is being dissolved in zirconium. There are no data for the heat required to do this so it was estimated by approximating the dissolution as a fusion of UO_2, followed by removal of the O_2 from the uranium and addition of the O_2 to a zirconium atom. The resultant number is very similar to the heat of fusion of UO_2.

With the current numbers, 2.69 x 10^5 and 2.74 x 10^5, use of Equation (11-48) to interpolate is not necessary. However, the large uncertainty, $\pm$ 3 x 10^5, suggests that it is prudent to maintain the equation until measurements confirm that the actual number for the heat of solution of UO_2 by zirconium is near the heat of fusion of UO_2.

Figure 11-25 illustrates the small effect of solvent composition on the heat required to dissolve UO_2.

a. This number is taken from the PHYPRP subroutine.

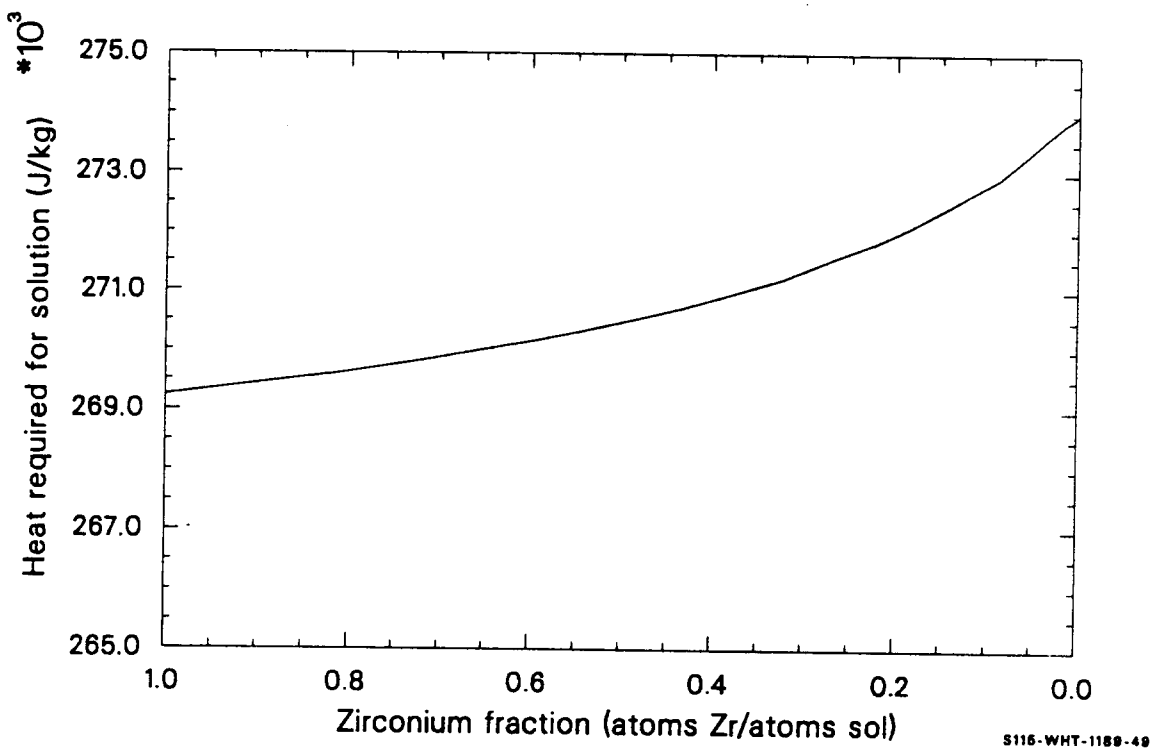

Figure 11-25. Effect of solvent composition of heat required to dissolve a kilogram of uranium dioxide.

11.8.2 References

11.8-1 C. J. Smithells and E. A. Brandes (eds.), *Metals Reference Book*, London and Boston: Butterworths (TN671 S55 1956).

11.9 Heat of Fusion of Zirconium-Uranium-Oxygen Compounds (ZUFUSN)

The subcode ZUFUSN calculates the heat of fusion of a zirconium-uranium-oxygen compound as a function of component concentration. Atomic fractions of uranium and zirconium are input into the subcode. The expression used to calculate the heat of fusion of a Zr-U-O compound is a mole fraction weighted average of the molar heats of fusion of UO_2, ZrO_2, and zircaloy

$$L = \frac{2.74\times10^5\,(0.270)\,f\,(UO_2) + 7.06\times10^5\,(0.123)\,f\,(ZrO_2) + 2.25\times10^5\,(0.091)\,f\,(Zr)}{0.270f\,(UO_2) + 0.123f\,(ZrO_2) + 0.091f\,(Zr)} \qquad (11\text{-}49)$$

where L is the heat of fusion of the Zr-U-O compound.

11.10 Coefficient of Thermal Expansion of Liquefied Mix (ZUBET1)

Subroutine ZUBET1 calculates coefficient of thermal expansion of liquefied mixture. Table 11-21. shows the required input calls.

Table 11-21. Call variable to the subroutine ZUBET1.

Call Variable	Description
afz	atomic fraction of zircaloy in mixture
afu	atomic fraction of metallic uranium
afs	atomic fraction of stainless steel
afa1	atomic fraction of silver-indium-cadmium
afa2	atomic fraction of boron carbide
afux2	atomic fraction of uranium dioxide
afzx2	atomic fraction of zirconium dioxide
afalup	atomic fraction of aluminum
aflith	atomic fraction of lithium
afcadm	atomic fraction of cadmium
afsoil	atomic fraction of soil
temp	temperature of mixture (K)

The returned coefficient of thermal expansion of a liquefied mixture is calculated by:

$$\beta = \frac{\left(\frac{\rho(T)}{\rho(T+\Delta T)} - 1\right)}{\Delta T} \tag{11-50}$$

where

ρ	=	density as a function of temperature for the mixture
T	=	temperature of mixture (K)
ΔT	=	assumed differential change in temperature (10 K).

11.11 Position of Advancing Zr-UO_2 Interface (PSUZ)

11.11.1 Summary

Subroutine PSUZ calculates the position of the advancing liquid Zr-UO_2 interface.[11.11-1] The temperature dependent propagation constant is

$$\kappa = 8.67 \times 10^{-27} e^{[1.66 \times 10^{-2} T]} \ (m^2/s). \tag{11-51}$$

where

T = input temperature of liquid Zr-UO_2 region.

Once the propagation constant has been evaluated, the position of the liquid Zr-UO_2 interface may be found by

$$x_f = \sqrt{2\kappa\Delta t - x_o^2} \ . \tag{11-52}$$

11.11.2 References

11.11-1 W. Turk, *Design & Verification of Modular Computer Models for Interpreting Rod Melting Experiments*, INEL-TR-52, February 1980.

11.12 UO_2 Solubility in Oxygen Stabilized Zircaloy (PSLV)

11.12.1 Summary

Subroutine PSLV calculates the solubility of UO_2 in oxygen stabilized zircaloy. The temperature dependent solubility, S, is found by:

$$S = \begin{cases} 0 & \text{if } T \le 2103 \text{ K} \\ 1.9143754 + T\,(1.2127195 \times 10^{-3} + 3.1857023 \times 10^{-7} T) & \text{if } T < 2673 \text{ K} \\ 2.0859332 + T\,(-1.1311691 \times 10^{-3} + 2.5104264 \times 10^{-7} T) & \text{if } T > 2673 \text{ K and } T < 3119 \text{ K} \\ 1.0 & \text{if } T > 3119 \text{ K} \end{cases} \ . \tag{11-53}$$

These expressions are interim correlations for the intersection of the line connecting UO_2 and Zr(O) and the solidus on the Gibbs plots discussed in Section 11.1. They should be used with caution because they assume a particular oxygen concentration in the initial oxygen stabilized zircaloy solvent.

11.13 Rate of Dissolution of UO_2 in Zr-U-O (DISUO2, UO2DIS, UO2SOL)

11.13.1 Introduction

Mechanistic modeling of severe core damage processes in LWRs requires models to describe the melting of core materials and the dissolution of UO_2 fuel by liquid zircaloy. The temperature of the zircaloy melt, initial oxygen content, and initial quantity of UO_2 is required to determine the amount of solid core material dissolved in molten zircaloy.

Three computer subcodes were developed to model the solution properties of Zr-U-O. The kinetics of UO_2 dissolution in melted zircaloy is modeled in DISUO2. The maximum atomic fraction of UO_2 that can be dissolved in a Zr-U-O solvent for a given temperature and solvent composition is modeled in

UO2DIS, and the remaining solid phase composition is modeled in UO2SOL.

DISUO2 is based on experimental results by Hofmann et al.[11.13-1] on the dissolution kinetics of UO_2 in melted zircaloy. Expressions for the rate of dissolution of UO_2 in melted zircaloy as a function of temperature and prior dissolution were determined from the experiments. The rate equations are used to determine additional dissolution in a time step for each intact node with melted zircaloy.

UO2DIS and UO2SOL are based on analytical expressions for the solidus phase boundary compositions in the ternary Zr-U-O system. These expressions were produced by interpolating the solidus compositions determined as a function of temperature for the several available binary systems or isopleths for which solidus temperatures as a function of composition are known. The analytical expressions that return the compositions are used with standard phase diagram techniques, the lever rule and the mixing rule, to calculate the maximum amount of UO_2 that can be dissolved by a given solvent.

11.13.2 Data for the Zr-U-O System

The equations for the solidus surfaces were obtained from numerous temperature composition phase diagrams available in the literature. In this section, all of these diagrams have been redrawn to a common scale and units of atomic fraction so that they might be easily compared and checked for consistency.

Solidus temperature curves for the zirconium oxygen mixture have been published by Domagala and McPherson[11.13-2] and modified by Ruh and Garrett.[11.13-3] The curves are made of several segments: one above the beta phase, one above the alpha phase, and one above the cubic ZrO_2 phase. Figure 11-26 shows a phase diagram drawn from these references with weight fraction converted to atomic fraction using the expression

$$f_0 = \frac{\dfrac{f_0^{mass}}{16}}{\dfrac{f_o^{mass}}{16} + \dfrac{(1 - f_o^{mass})}{91.22}} \tag{11-54}$$

where

f_o = atomic fraction of oxygen in a Zr-O compound

f_o^{mass} = mass fraction of oxygen in a Zr-O compound.

Figure 11-27 is a temperature composition plot for the U-O binary system taken from Roth et al.[11.13-4] The diagram was converted to atomic fraction oxygen using the relation

$$f_0 = \frac{OM}{1 + OM} \tag{11-55}$$

where OM is the oxygen-to-metal ratio (atoms oxygen/atoms uranium).

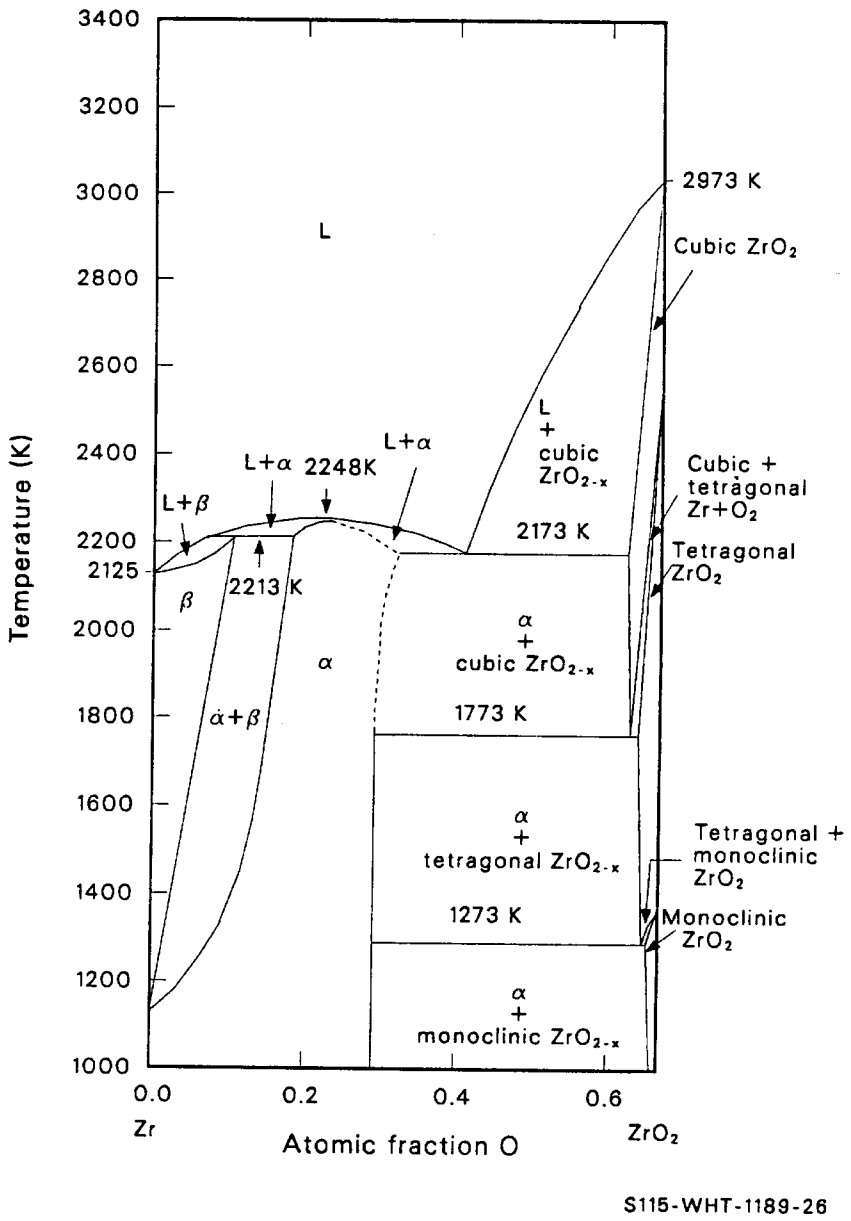

Figure 11-26. Zirconium-zirconium dioxide phase diagram.

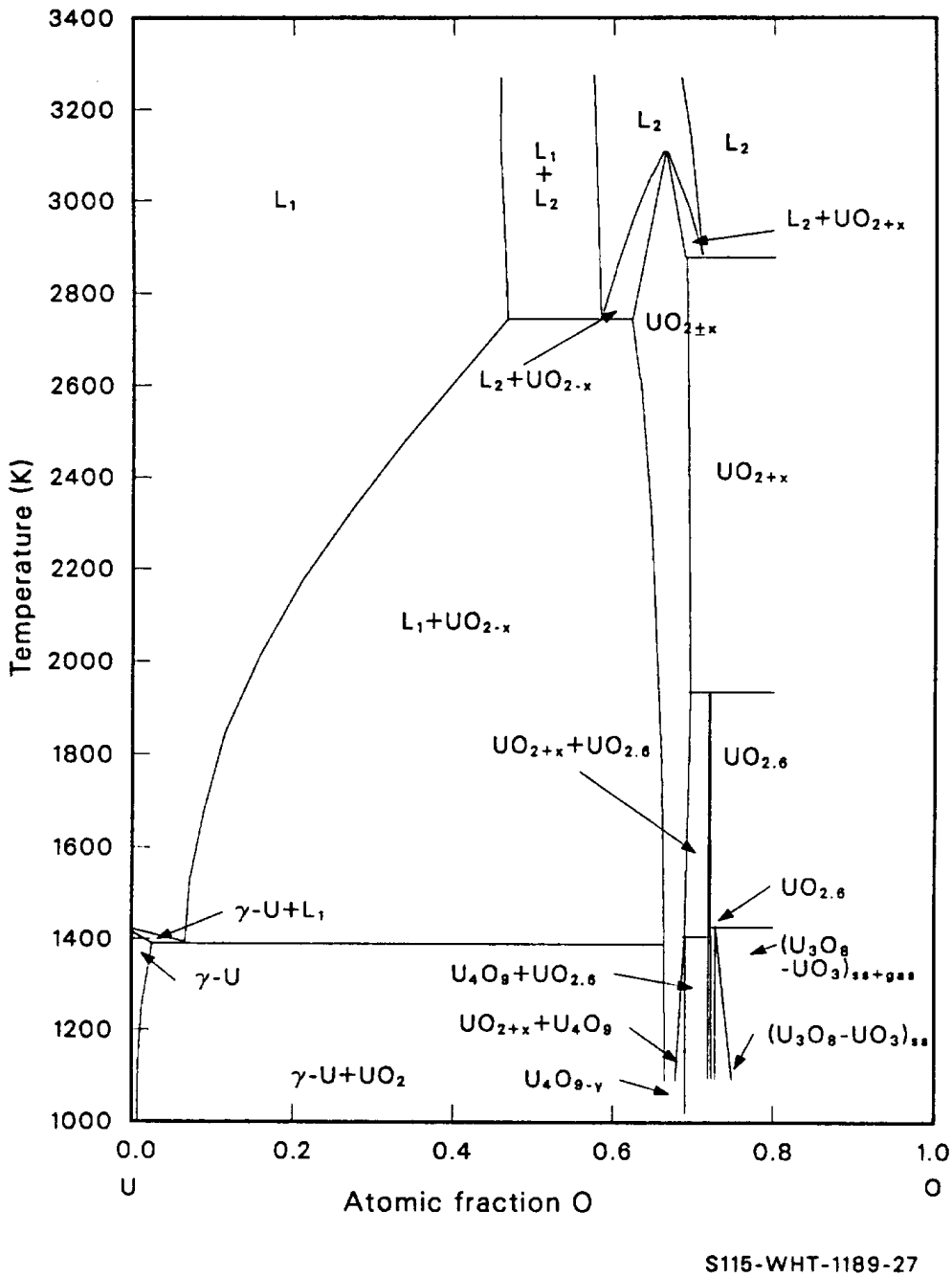

Figure 11-27. Uranium-oxygen phase diagram.

The figure shows four solidus segments enclosing the UO_2 region, two liquidus segments under the L_1 phase and another two liquidus segments under the L_2 phase. The development of the phase diagram is discussed by Hagrman in Section 11.1.

Figure 11-28 shows an isopleth (constant pressure section of the pressure temperature composition figure) extending from $Zr_{0.7}O_{0.3}$ (the approximate atomic fraction composition of alpha phase zirconium

saturated with oxygen) to $U_{0.33}O_{0.67}$ (the uranium dioxide composition written in atomic fraction units). The isopleth was presented as a quasi-binary section by Skoken.[11.13-5]

Figure 11-29 shows the UO_2-ZrO_2 pseudo-binary system based on Romberger et al.,[11.13-6] and measurements by Hofmann,[11.13-7] which indicated a sharp drop in the solidus temperature as the composition moved away from pure UO_2 or ZrO_2. The minimum melting point occurs at a composition consisting of a 0.5-0.5 mix of the two components and at a temperature of 2,810 K.

Zr-U-O ternary diagrams have been constructed from the binary diagrams and other data.[11.13-5,a] The ternary phase diagram in Figure 11-30[11.13-8] is the Zr-U-O system at 2,273 K,[a] which is just above the complexities caused by the Zr-O phase transition that occurs from 2,125 to 2,248 K. This diagram is characteristic of the Zr-U-O system until 2,673 K, when a second liquid phase (L_2 in Figures 11-27 through 11-30) appears and covers the temperature range of primary interest in fuel dissolution.

11.13.3 Model Development

The expressions used in the UO2DIS and UO2SOL subcodes were developed by constructing polynomial expressions for the solidus temperature as a function of composition for the various binary systems. Where additional correlations could be obtained from the ternary systems published, they were also employed. These expressions were then inverted to produce correlations for composition points as a function of temperature. These composition points on the ternary phase diagram are connected with straight lines to form the solidus boundary. Details of this development are presented in Section 11.1.

a. Private communication, P. Hofmann, 1985.

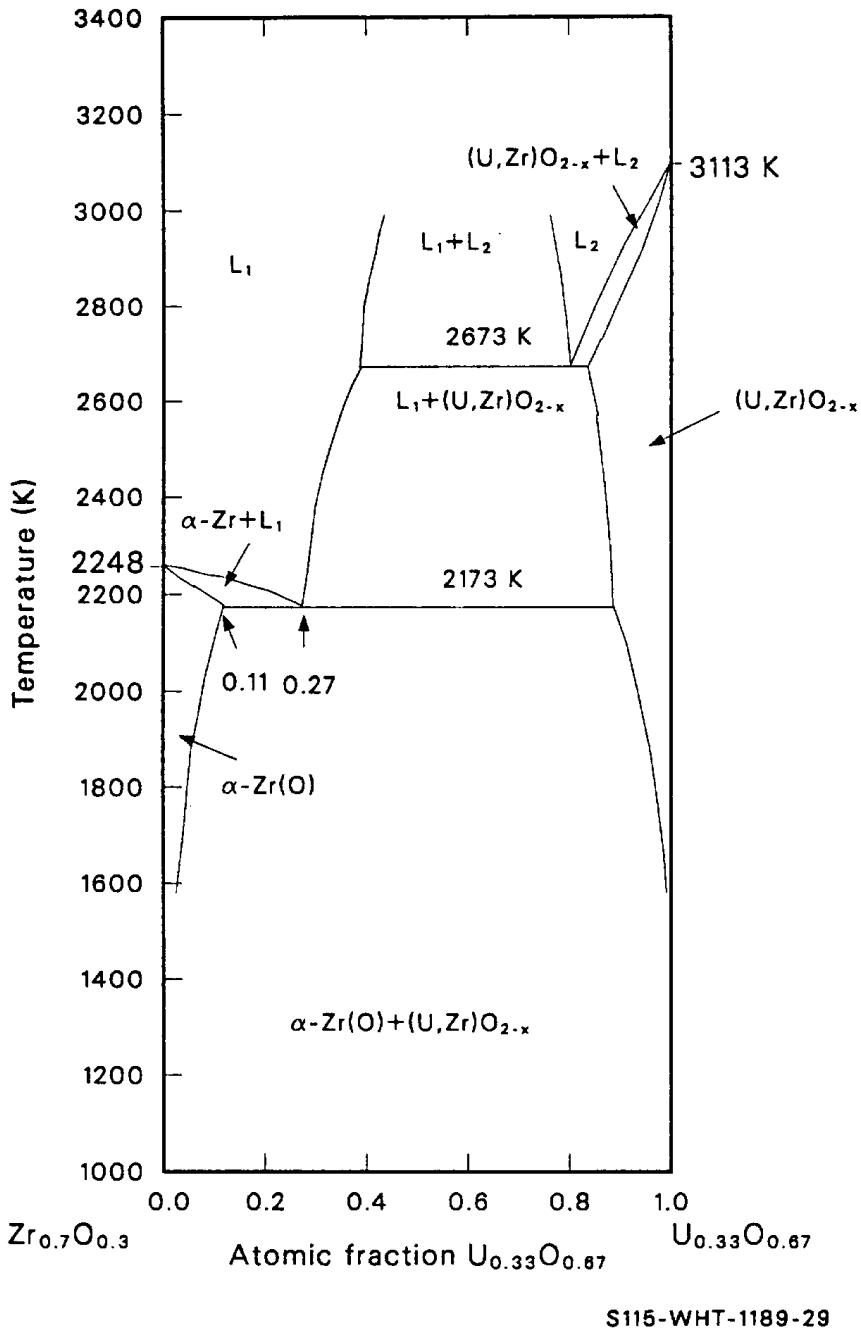

Figure 11-28. Oxygen saturated alpha phase zirconium - uranium dioxide isopleth.

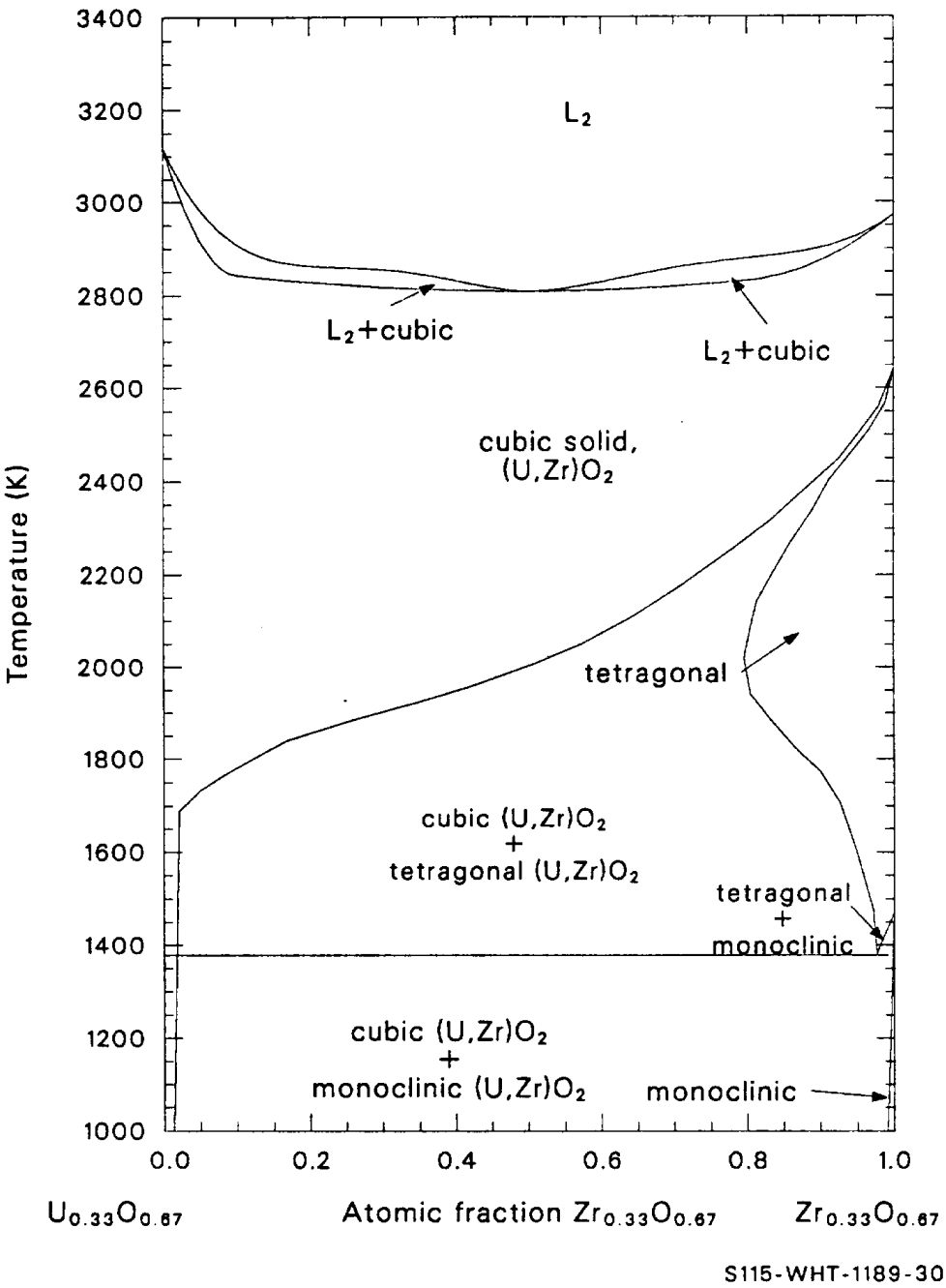

Figure 11-29. Quasi binary phase diagram for the ZrO_2-UO_2 system from Reference 11.13-6.

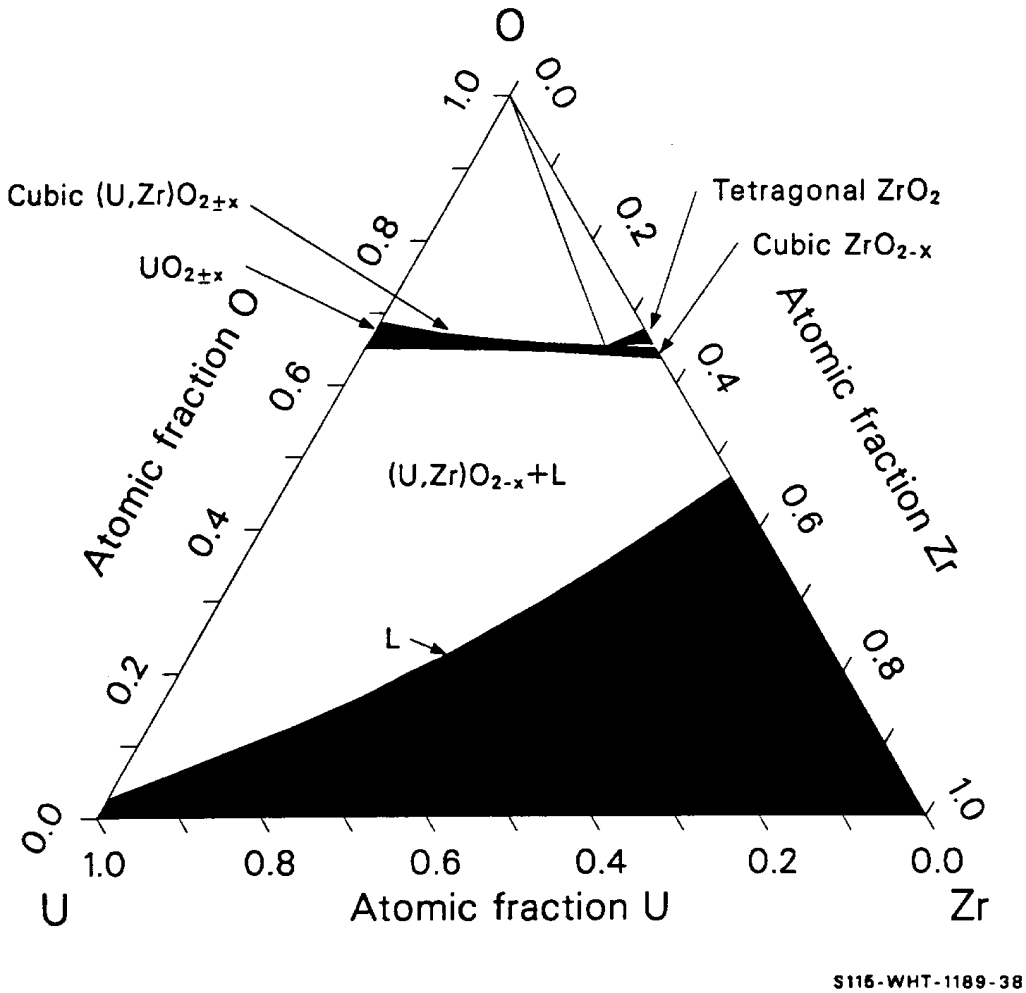

Figure 11-30. Zr-U-O isothermal section at 2,273 K according to Hofmann and Politis.

11.13.3.1 Ternary Zr-U-O Phase Diagram Models. Figure 11-31 shows the points connected to form the ternary Zr-U-O system solidus lines (detailed equations are presented in Section 11.1). Dashed lines in Figure 11-31 represent assumed tie lines across multiple phase regions and are therefore not a section through a solidus surface in the three-dimensional temperature composition phase diagram.

11.13.3.2 Calculation of Dissolution Limits. Figure 11-32 illustrates the method used to estimate the maximum fraction of UO_2 that can be dissolved in a Zr-U-O solvent and the solvent composition. Compositions that can be produced by mixing UO_2 (represented by point 4 in Figure 11-32) and a partly oxidized zirconium melt (represented by point 1) lie along the line connecting the two points. The equilibrium composition of the liquid (solvent) is represented by point 2, the liquidus where the first solid precipitates appear. The equilibrium composition of the solid (solute or precipitate) is represented by point

3, the solidus where the first liquid phase appears.

The modification recommended by Hofmann et al.[11.13-1] is to assume that the nonequilibrium slurry produced when zircaloy attacks UO_2 will continue to attack the UO_2 by dissolution along grain boundaries and removal of grains until the composition of the slurry is approximately equal to the liquidus point 3.

The lever and mixing rules state that the UO_2 fraction at 3 is the length from 1 to 3 divided by the length from 1 to 4. Thus, the line segment lengths have to be calculated. This is done using the Pythagorean theorem after converting the compositions of each point to Cartesian coordinates centered on the lower left side vertex of the Gibbs coordinate system with the transformation

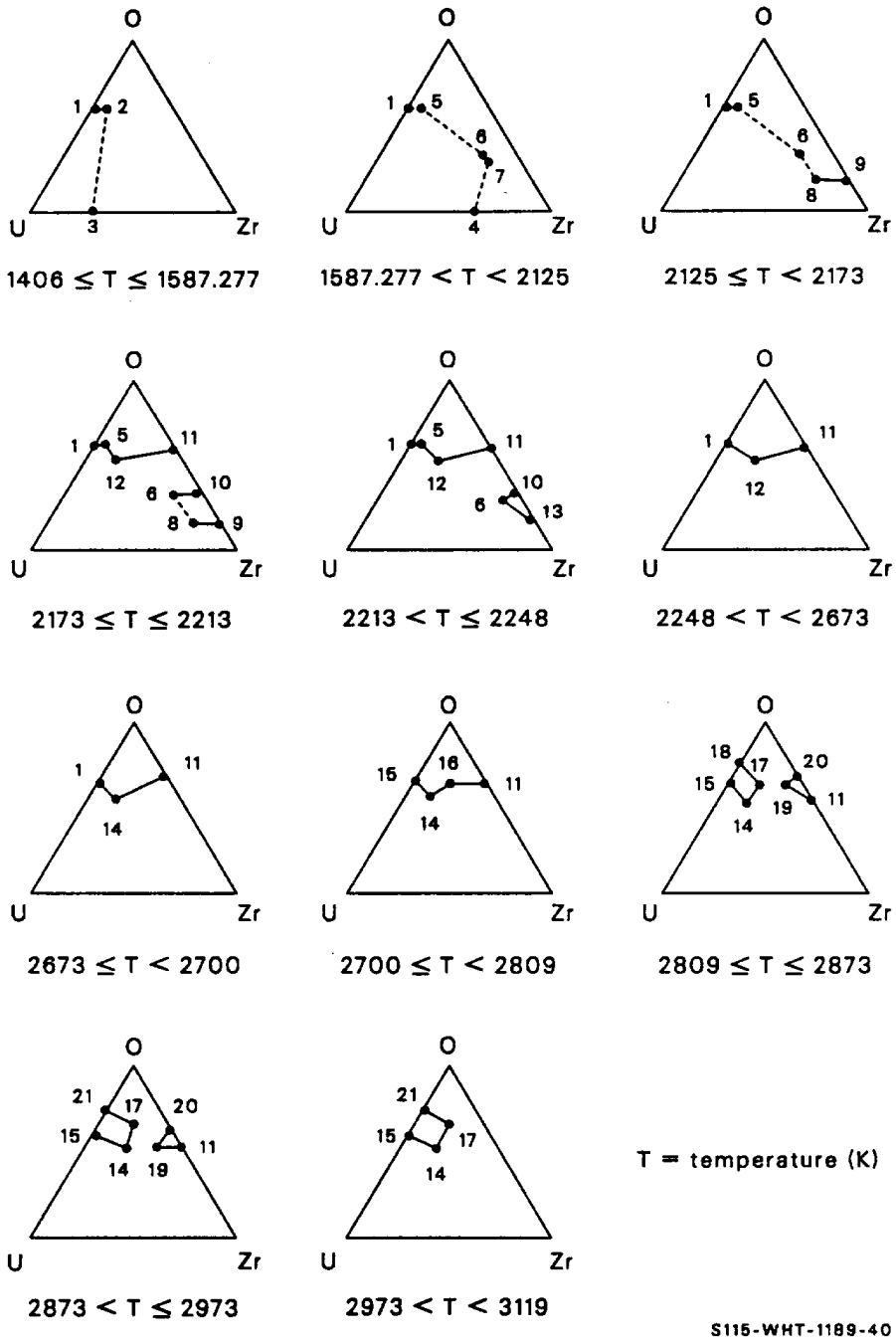

Figure 11-31. Points connected to form the ternary Zr-U-O system.

a.R. E. Latta and R. E. Fryxell, "Determination of Solidus Liquidus Temperatures in the UO_{2+x} system (≤ 0.5 x < 0.2)," *Journal of Nuclear Materials*, 35, 1970, pp. 195-201.

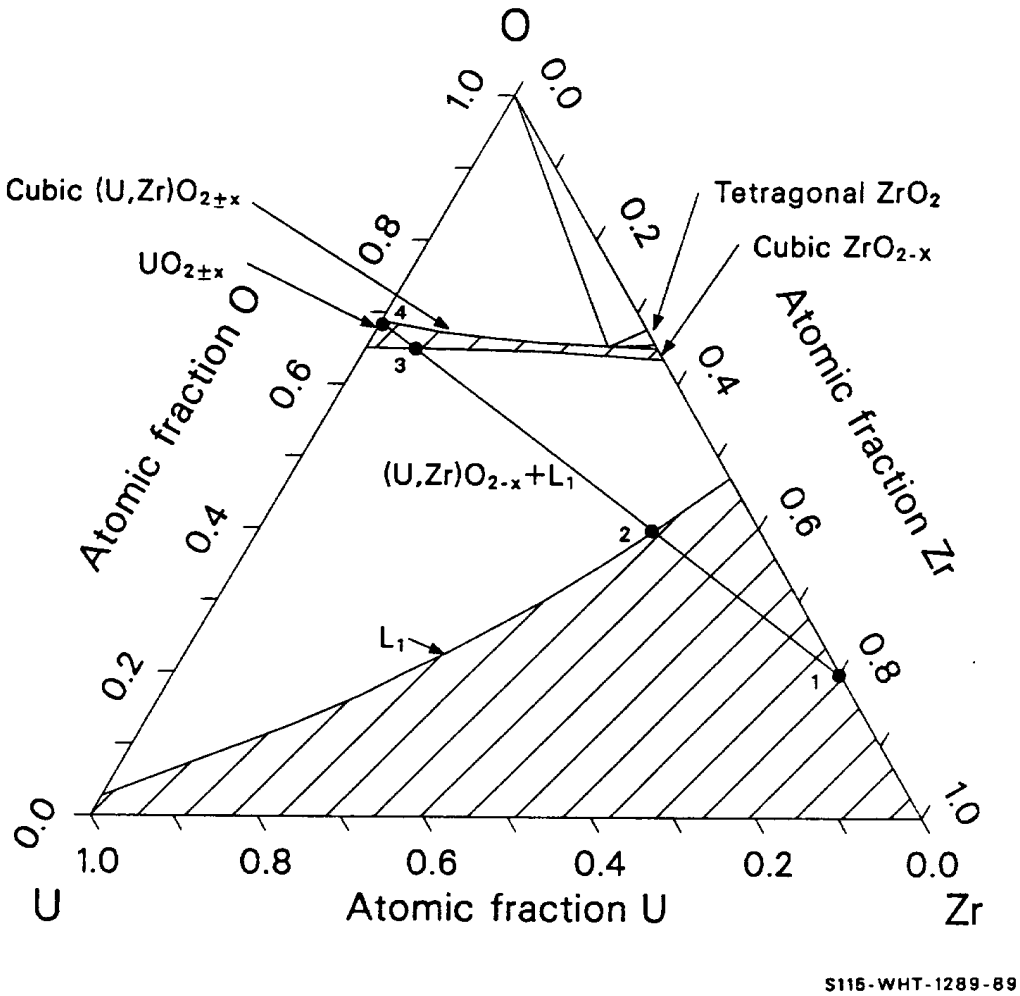

Figure 11-32. Zr-U-O isothermal section at 2,273 K according to Hofmann and Politis (revised).

$$x = f_o \cos 60 + f_{zr} \tag{11-56}$$

$$y = f_o \sin 60 \tag{11-57}$$

where

x,y	=	Cartesian coordinates
f_o	=	atomic fraction of oxygen
f_{zr}	=	atomic fraction of zirconium.

The subcode UO2SOL returns the solidus points in Cartesian coordinates as a function of temperature. The subcode UO2DIS connects the points with straight lines to form the solidus curve (the bottom of the upper shaded area of Figure 11-32) and finds the intersection (point 3 of Figure 11-32) between the solidus curve and the UO_2 solvent composition line (the line from 4 to1 in Figure 11-32). The atomic fraction of UO_2 in the solidus composition is then determined using the lever rule.

11.13.4 Uranium Dioxide Dissolution Kinetics

The reaction kinetics of molten zircaloy with solid UO_2 were investigated and reported by Hofmann et al.[11.13-1] A matrix of dissolution experiments was performed at various reaction temperatures and times with UO_2 crucibles and as received zircaloy in a nonoxidizing environment. The crucibles were then metallographically examined, and the area fraction of the $(U, Zr)O_{2-x}$ ceramic phase in the once molten solvent was measured. A set of standards was established by dissolving known amounts of UO_2 in zircaloy and then measuring the ceramic area fraction so that the ceramic area fractions measured in the experiments could be correlated with the UO_2 content of the melt.

It was found that the fuel dissolution showed parabolic behavior after a short incubation period. (The first ceramic particles do not appear in the solidified melt until about 35.8 wt% UO_2 has been dissolved.) The parabolic equation for the wt% of UO_2 in the melt was given as

$$\text{wt\% } UO_2(T,t) = 35.8 + [K(T)\, t]^{0.5} \qquad (11\text{-}58)$$

where

K	=	parabolic rate constant $[(\text{wt\% } UO_2)^2/s]$
T	=	temperature (K)
t	=	time (s).

The parabolic rate constant K was determined by fitting an Arrhenius function to the data, obtaining

$$K(T) = 1.0196 \times 10^{15} \exp(-677200/RT) \qquad (11\text{-}59)$$

where R is the universal gas constant (8.314 J/mole•K).

The surface area present in the experiments is implicit in these equations, so the data were transformed by Hofmann into equivalent uniform receding interface positions and fit to a new Arrhenius function, yielding

$$\Delta \xi\, (T, t) = [K'(T) \cdot t]^{1/2} \qquad (11\text{-}60)$$

where

$\Delta \xi$	=	displacement of the dissolution interface (cm)

$K'(T)$ = $3.85 \times 10^{19} \exp(-1067000/RT)$ = parabolic rate constant for displacement (cm^2/s).

The subcode DISUO2 calculates the increment of fuel dissolved for a time step based on the dissolution interface model. The model is implemented for incremental calculations by:

$$X_{i+1} = (X_i^2 + K'(T) \cdot t)^{1/2} \tag{11-61}$$

where

X_i = dissolution from position at time step i (cm)

Δt = time step (s).

Dissolution of UO_2 is assumed to proceed according to Equation (11-61) until maximum dissolution occurs when the solvent reaches the solidus composition. The rate equations do not consider the effect of oxidation of the solvent, but the determination of dissolution limits does.

11.13.5 References

15.5-1 P. Hofmann, H. Uetsuka, A. N. Wilhelm, and E. A. Garcia, "Dissolution of Solid UO_2 by Molten Zircaloy and its Modeling," *International Symposium on Severe Accidents in Nuclear Power Plants, Sorrento, Italy, March 1988.*

15.5-2 R. F. Domagala and D. J. McPherson, "System Zirconium Oxygen," *Journal of Metals, 6*, Transactions AIME 200, 1954, pp. 238-246.

15.5-3 R. Ruh and H. J. Garrett, "Nonstoichiometry of ZrO_2 and its Relation to Tetragonal Cubic Inversion in ZrO_2," *Journal of the American Ceramic Society, 50*, 1966, pp. 257-261.

15.5-4 R. S. Roth, T. Negas, and L. P. Cook, *Phase Diagrams for Ceramist, Volume IV*, The American Ceramic Society, 1981.

15.5-5 A. Skokan, "High Temperature Phase Relations in the U-Zr-O System," *Fifth International Meeting on Thermal Nuclear Reactor Safety, Karlsruhe, German Federal Republic, September 9-13, 1984*, KfK 388011, December, 1984, pp. 1035-1042.

15.5-6 K. A. Romberger, C. F. Bates, Jr., and H. H. Stone, "Phase Equilibrium Studies in the UO_2-ZrO_2 System," *Journal of Inorganic and Nuclear Chemistry, 29*, 1966, pp. 1619-1630.

15.5-7 P. Hofmann, "SFD Singe Effects Laboratory Experiments," *Severe Fuel Damage and Source Term Research Program Review Meeting, Idaho Falls, ID, April 16-19, 1985.*

15.5-8 P. Hofmann and C. Politis, "The Kinetics of the Uranium Dioxide Zircaloy Reactions at High Temperatures," *Journal of Nuclear Materials, 87*, 1975, pp. 375-397.

12. SILVER-ZIRCONIUM COMPOUNDS

The solubility of zircaloy in Ag-In-Cd neutron absorber material is required to calculate the amount of cladding or structural material removed by jets or flows of control rod material that result when the control rod cladding ruptures. This section describes the model and subcode (ASOLV) developed to calculate the solubility of zircaloy cladding in Ag-In-Cd neutron absorber material.

12.1 Solubility of Zircaloy Cladding in Ag-In-Cd Absorber (ASOLV)

The solubility of zircaloy in Ag-In-Cd neutron absorber material is required for calculations of the amount of cladding or structural material removed by jets or flows of control rod material that result when control rod cladding ruptures. Since the solubility is high and there is a significant mass of absorber material in reactor cores, the solution of zircaloy by absorber material can be a significant contribution to core material relocation. The possible solution of zircaloy guide tubes, which surround control rods, is also an important consideration in the analysis of the flow and freezing of the control rod material. This analysis is, in turn, important to the calculation of the amount of silver or cadmium aerosol available to carry fission products from severely damaged cores.

In the following sections, a summary is presented and the available data and observations are reviewed, followed by a discussion of the development of analytical expressions from the available data.

12.1.1 Summary

The expression used to calculate the solubility of zircaloy cladding in Ag-In-Cd absorber material is

For $1{,}234 \leq T < 1{,}410.007334$ K,

$$X = 3.785 \times 10^{-14} (T - 1{,}228)^{5.794} + 0.029 \,. \tag{12-1}$$

For $1{,}410.007334 \leq T \leq 1{,}464$ K,

$$X = -3.15545506 + T\ 2.592507834 \times 10^{-3} \,. \tag{12-2}$$

For $1{,}464 < T \leq 2{,}100$ K,

$$X = 0.4418 + T(-1.649 \times 10^{-4} + T\ 2.051 \times 10^{-7}) \tag{12-3}$$

where

T	=	temperature (K)
X	=	atomic fraction zircaloy in the solution at equilibrium saturation (atoms zircaloy/atoms solution).

For temperatures below 1,234 K, no liquids are present at equilibrium; so solution is by the negligibly slow processes of solid state diffusion. When the temperature is above 2,100 K, zircaloy melts and mixes with any silver that may be present.

Equations (12-1) through (12-3) are converted from atomic fraction to mass fraction expressions with the following relation:

$$Y = \frac{X91.22}{107.87 - X16.65} \tag{12-4}$$

where Y is the mass fraction zircaloy in the solution at saturation (mass zircaloy/mass solution).

12.1.2 Solubility Data for Ag-In-Cd on Zircaloy

At the present time, quantitative data for the solubility of zircaloy or zircaloy oxide phases in Ag-In-Cd absorber material are not available. However, quantitative data from Hagen[12.1-1] and Parker and Sutton[12.1-2-12.1-4] and binary phase diagrams for the Ag-Zr system[12.1-5-12.1-7] are sufficient for approximate modeling of the solubility of the zircaloy cladding in Ag solvents.

The quantitative data from Parker and Sutton are from instrumented fuel bundles heated by radio frequency induction. Control rods were observed to fail by reaction between stainless steel control rod cladding and a zircaloy sleeve installed to simulate reactor guide tubes. In these experiments, which did not have high pressure outside the control rods, extensive liquid metal was ejected from the control rod. It removed about one-half of the zircaloy cladding by a sort of candling process that left a heavy mass of intermetallic residue at the base of the fuel rods. The heavy mass at the base was also observed by Hagen.

The quantitative tests suggest that control rod failure and solution of zircaloy guide tubes or cladding will occur before the formation of an oxide layer of thickness sufficient to prevent absorber zircaloy interaction. For this reason, the effect of prior oxidation of zircaloy on the solubility of the zircaloy will not be considered in the development of the solubility model. The quantitative results also suggest that the minor components of the absorber and zircaloy alloys can be ignored because they are consistent with the behavior expected from Ag-Zr binary phase diagrams.

Figure 12-1 is an Ag-Zr phase diagram taken from References 12.1-5 through 12.1-7. The diagram between 0.5 and 0.65 atomic fraction zirconium is not known, but the important Zr-rich part of the diagram is well defined. Although the phase diagram is shown with temperature as the dependent variable, it can be interpreted with composition as the dependent variable. Thus, the fact that the liquidus (liquid region boundary) is at 1,466 K for a composition of 0.66 atomic fraction Zr and 0.34 atomic fraction Ag means not only that the last solid phase of the given composition disappears at this temperature, but also that compounds containing up to 0.66 atomic fraction Zr will be completely liquid at a given temperature of 1,500 K because all points to the left of the liquidus at 1,500 K are in the liquid region. Thus, silver can dissolve about twice its mass of Zr at a temperature of 1,500 K, 600 K below the melting point of Zr. The fraction increases as the temperature increases because of the positive slope of the liquidus line in the Zr-rich region. The relatively flat liquidus on the Ag-rich side of the phase diagram suggests a rapid increase in the solubility of Zr as temperature increases from 1,373 to 1,410 K.

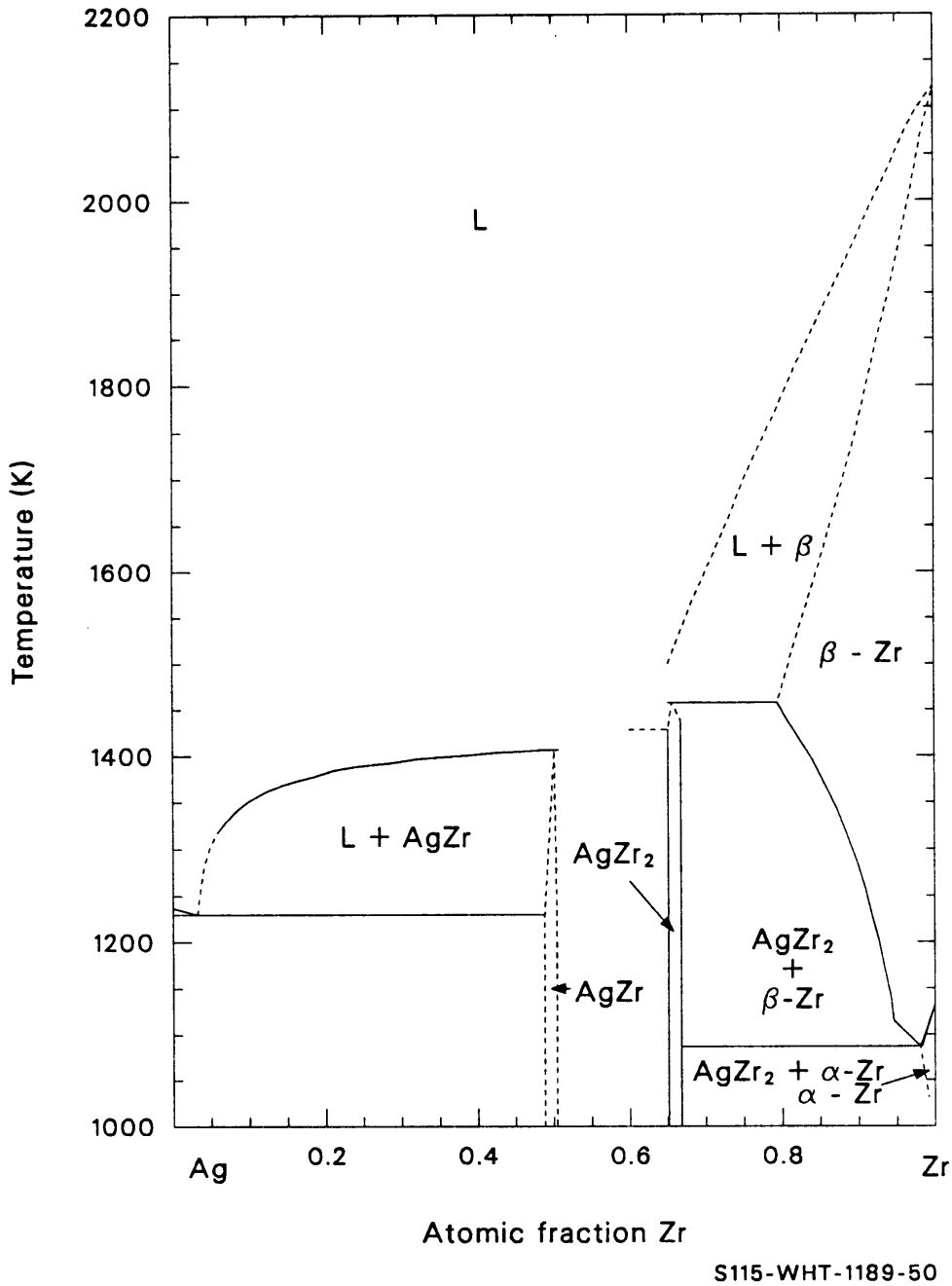

Figure 12-1. Silver-zirconium phase diagram.

12.1.3 Model Development

The expressions used in the ASOLV function were derived by finding analytical expressions for the known liquidus curves of the Ag-Zr binary phase diagram and using interpolation for the unknown region. For the Ag-rich region, the (T,X) pairs shown in Table 12-1 were taken from Hansen[12.1-5] because he

shows the individual data. The data were used to find the least squares deviation fit to a power law constrained to fit the datum at 1,228 K, given by Equation (12-1).

Hansen's data at 1,306 and 1,323 K were not used because the small numerical value of the concentrations would have dominated the fitting procedure.

To describe the Zr-rich region, the (T,X) pairs shown in Table 12-2 were taken from Elliott[12.1-6] and the MATPRO document.[12.1-8] The MATPRO temperature for zircaloy melting was used instead of Elliott's number for the melting temperature of zirconium to avoid inconsistencies in the MATPRO routines. The equation that resulted from these data as given in Equation (12-3)

The expression for the unknown region of the phase diagram is based on the assumption that there is no local maximum in the liquidus in the region. The expression is a linear interpolation between the Ag-rich and the Zr-rich liquidus curves end points, is given as Equation (12-2).

Note that the solubility is given by expressing the liquidus line as a composition versus temperature curve (instead of the more usual temperature versus composition curve) when the liquidus temperature is a monotonically increasing function of the zircaloy.

Table 12-1. Data used to find the liquidus in the Ag-rich region.

Temperature (K)	Composition (atomic fraction Zr)	Reference
1,228	0.029	Hansen
1,364	0.119	Hansen
1,380	0.20	Hansen
1,393	0.26	Hansen
1,400	0.35	Hansen
1,404	0.44	Hansen
1,408	0.51	Hansen

Table 12-2. Data used to find the liquidus in the Zr-rich region.

Temperature (K)	Composition (atomic fraction Zr)	Reference
1,464	0.064	Elliott
1,673	0.74	Elliott
2,100	1.00	MATPRO

Equation (12-4) is a conversion from atomic fraction to mass fraction. It is derived from the definition of mass fraction,

$$Y = \frac{\text{mass Zr}}{\text{mass Ag} + \text{mass Zr}} \ . \tag{12-5}$$

Division by the kilogram molecular mass of Zr and some algebra yields the expression

$$Y = \frac{X M_{Zr}}{M_{Ag} + X\,(M_{Zr} - M_{Ag})} \tag{12-6}$$

where

M_{Ag} = kg-molecular mass of Ag (kg/kg mole)

M_{Zr} = kg-molecular mass of Zr (kg/kg mole).

Equation (12-4) is obtained from Equation (12-6) by substituting the kilogram molecular mass values.

Figure 12-2 is a computer-generated graph of the calculated solubility of zircaloy in Ag-In-Cd absorber material versus temperature using the function.

12.1.4 References

12.1-1 S. Hagen, "Absorber Rod Tests in the NIELS Facility," *Severe Fuel Damage and Source Term Research Program Review Meeting, Idaho Falls, ID, April 16-19, 1985.*

12.1-2 A. P. Malinauskas and S. G. Winslow, *Monthly Highlights Report for December 1984. ORNL Projects for the NRC Office of Nuclear Regulatory Research,* p. 29.

12.1-3 A. P. Malinauskas and S. G. Winslow, *Monthly Highlights Report for February 1985. ORNL Projects for the NRC Office of Nuclear Regulatory Research,* p. 27.

12.1-4 A. P. Malinauskas and S. G. Winslow, *Monthly Highlights Report for March 1985. ORNL Projects for the NRC Office of Nuclear Regulatory Research,* p. 27.

12.1-5 M. Hansen and K. Anderka, *Constitution of Binary Alloys,* New York: McGraw-Hill Book Com-

pany, Inc., 1958.

12.1-6 R. P. Elliott, *Constitution of Binary Alloys, First Supplement,* New York: McGraw-Hill Book Company, Inc., 1965.

12.1-7 T. Lyman, ed., *Metals Handbook,* 8th Edition, 8, Metals Park, OH: American Society for Metals.

12.1-8 D. L. Hagrman, *Materials Properties Models for Severe Core Damage Analysis,* EGG-CDD-5801, May 1982.

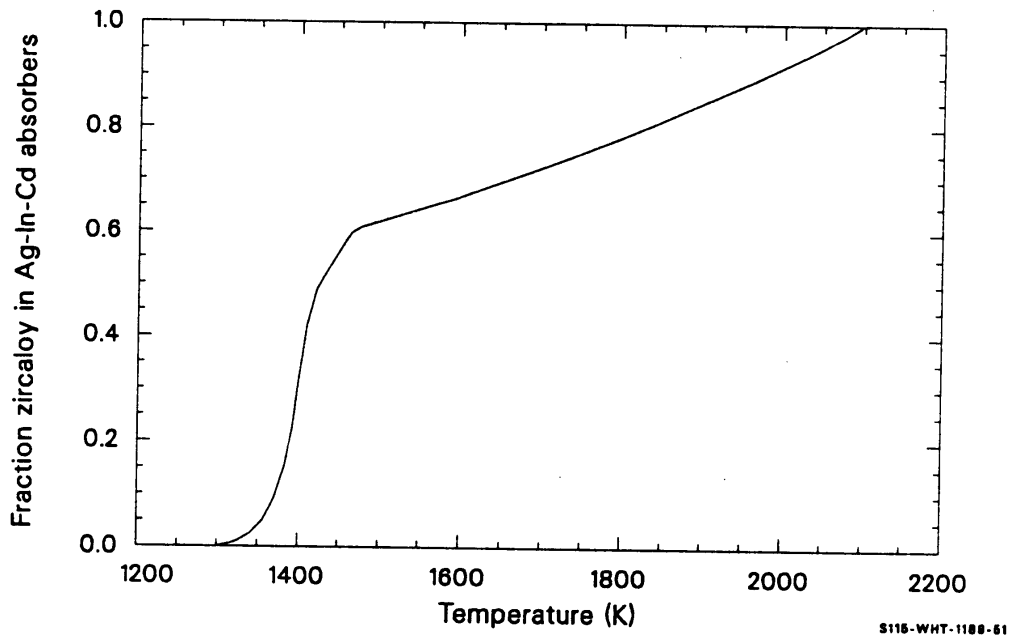

Figure 12-2. Computer generated graph of the calculated solubility of zircaloy in silver-indium-cadmium absorber material.

13. NONCONDENSABLE GASES--HELIUM, ARGON, KRYPTON, XENON, HYDROGEN, NITROGEN, OXYGEN, CARBON MONOXIDE, CARBON DIOXIDE, WATER MIXTURES

Properties of the internal gas of LWR fuel rods have been included in MATPRO. The thermal conductivity (GASCON) of 10 gases (and their mixture in any combination) is modeled, as is gas viscosity (GVISCO). Gas viscosity and thermal conductivity are modeled as functions of temperature and composition. Also included are models of specific heat capacity (GCP), effective emissivity (GMISS), and mean free path (GMFP).

13.1 Specific Heat Capacity (GCP)

The specific heat capacity of a mixture of gases at constant pressure is required to calculate the temperature of a slug of effluent proceeding from a hot core region down a pipe with walls that cool the gas. The function GCP calculates the specific heat capacity at constant pressure of a gas mixture of helium, argon, krypton, xenon, hydrogen, nitrogen, oxygen, carbon monoxide, carbon dioxide, and water vapor as a function of the mole fraction of each component and the gas temperature.

13.1.1 Model Development

The correlation used for the molar specific heat capacity at constant pressure of the monatomic gases helium, argon, krypton, and xenon is just the ideal gas expression

$$C_p = 2.5 \text{ times the gas constant} = 2.0786 \times 10^4 \text{ kg-m}^2/(\text{s} \cdot \text{kg-mole} \cdot \text{K}) \tag{13-1}$$

For hydrogen, nitrogen, oxygen, carbon monoxide, carbon dioxide, and water vapor, a second-degree polynomial correlation in temperature is employed to calculate the molar specific heat capacity. The coefficients are from Table 6.2 of Zemansky's text,[13.1-1] and they have been converted to SI units in Table 13-1.

The expressions used for the molar heat capacity of mixtures are obtained from those of the components by using a mole weighted average of the molar heat capacities

$$C_p(\text{mixture}) = \sum_{k=1}^{i} C_p(k)\, XGMIX(k) \tag{13-2}$$

where

XGMIX (k) = mole fraction of the k-th gas component (kg-moles k-th component/kg-moles of all components)

$C_p(k)$ = molar specific heat capacity at constant pressure of a pure sample of the k-th mixture component (J/kg-mole•K).

Table 13-1. Constants used to calculate C_p.

Gas	Zero Degree	First Degree	Second Degree
H_2	2.88 E+04	2.76 E-01	1.17 E-03
N_2	2.64 E+04	7.913 E+00	-1.44 E-03
O_2	2.62 E+04	1.150 E+01	-3.22 E-03
CO	2.62 E+04	8.755 E+00	-1.92 E-03
CO_2	2.87 E+04	3.573 E+01	-1.036 E-02
H_2O	2.88 E+04	1.375 E+01	-1.436 E-03

After the molar heat capacities are calculated, they are converted to the specific heat capacity per unit mass by dividing by the kg-mole weight of the mixture, which is given by

$$\text{mwt(mixture)} = \text{mwt (k) XGMIX (k)} \tag{13-3}$$

where mwt (k) is the kg-mole weight (mass) of k-th mixture component (kg/kg-mole).

13.1.2 Reference

13.1-1 M. W. Zemansky, *Heat and Thermodynamics*, 4th edition, New York: McGraw-Hill Book Company, Inc., 1957.

13.2 Thermal Conductivity, Gas Conductance, and Jump Distance (GASCON, GTHCON, GJUMP)

The heat conductance of gas-filled gaps or pores is dependent on the thermal conductivity of the gas mixture when the dimensions of the gas-filled regions are large compared to the mean distance between gas molecule collisions (mean free path of the gas molecules). When the mean free path is not smaller than the gap dimension, the conduction component of gas gap heat conductance becomes a function of the number of gas molecules present and the nature of the gas gap interfaces. This section presents data and correlations for the thermal conductivities of 10 gases of interest in fuel rod analysis. The effect of long mean free paths on gap conductance is also discussed.

13.2.1 Summary

Three functions are provided to meet various analytical needs for gas thermal conductivity. The GASCON function calculates gas thermal conductivity as a function of temperature and gas component fractions. To accomplish this, GASCON first calculates individual gas thermal conductivities through the use of Equations (13-4) through (13-7). Equation (13-8) is then used to calculate the mixture thermal conductivity. GASCON uses these equations in essentially the same form presented below. Though this is

not the most simple format possible, it serves to reduce error caused by repeated manipulation of the data. GASCON also generates, but does not return, an uncertainty term for each thermal conductivity.

The GTHCON function calculates the conduction part of gas gap heat transfer as a function of the gas conductivity, the gas pressure, and gas gap width. The conductance includes a series of resistance terms that account for the cases in which the mean free path is not smaller than the gap dimensions. These terms have been previously introduced and are explained in Section 13.2.3. The final expression, Equation (13-11), combines Equation (13-8) with the resistance terms. The equation is again used in essentially unaltered form in the code.

The GJUMP function determines an effective jump distance derived from the models used in GTHCON and GASCON. The jump distance is the mixture thermal conductivity divided by the conductance part of the gap heat conductance, or GASCON divided by GTHCON. The GASCON function is called by GJUMP.

The correlations used for pure noble or diatomic gases are all of the form

$$K = AT^{B} \tag{13-4}$$

where

k	=	thermal conductivity (W/m•K)]
T	=	gas temperature (K).

The constants A and B for each noble or diatomic gas are given in Table 13-2.

The following conductivity equations are used for carbon dioxide and steam:

$$k_{\text{carbon dioxide}} = 9.460 \times 10^{-6}\, T^{1.312}\,. \tag{13-5}$$

For $T \leq 973.15$,

$$k_{\text{steam}} = (-2.8516\times10^{-8} + 9.424\times10^{-10}T - 6.005\times10^{-14}T^{2})\,\frac{p}{T} + \frac{1.009P^{2}}{T^{2}\,(T-273)^{4.2}} + \tag{13-6}$$

$$17.6 + 5.87\times10^{-5}\,(T-273) + 1.08\times10^{-7}\,(T-273)^{2} - 4.51\times10^{-11}\,(T-273)^{3}$$

Table 13-2. Constants used in gas thermal conductivity correlations.

Gas	A	B
He	2.639×10^{-3}	0.7085
Ar	2.986×10^{-4}	0.7224
Kr	8.247×10^{-5}	0.8363
Xe	4.351×10^{-5}	0.8616
H_2	1.097×10^{-3}	0.8785
N_2	5.314×10^{-4}	0.6898
O_2	1.853×10^{-4}	0.8729
CO	1.403×10^{-4}	0.9090

$$k_{steam} = 4.44\times10^{-6}T^{1.45} + 9.5\times10^{-5}\left(\frac{2.1668\times10^{-9}}{T}P\right)^{1.3} \tag{13-7}$$

where

P = gas pressure (N/m^2).

The uncertainties of the values predicted by Equations (13-4) through (13-7) are summarized in Table 13-3.

The thermal conductivity of gas mixtures is calculated with the expression

$$k_{mix} = \sum_{i}^{n}\left(\frac{k_i x_i}{x_i + \sum_{j=1}^{n}(1-\delta_{ij})\,\psi_{ij}x_j}\right) \tag{13-8}$$

where

$$\psi_{ij} = \phi_{ij}\left(1 + 2.41\frac{(M_i - M_j)\,(M_i - 0.142M_j)}{(M_i + M_j)^2}\right) \tag{13-9}$$

and

$$\phi_{ij} = \frac{\left[1 + \left(\frac{k_i}{k_j}\right)^{1/2}\left(\frac{M_i}{M_j}\right)^{1/4}\right]^2}{2^{3/2}\left(1 + \frac{M_i}{M_j}\right)^{1/2}} \tag{13-10}$$

and

δ_{ij}	=	Kronecker Delta = 1 for i = j, 0 otherwise (unitless)
n	=	number of components in mixture (unitless)
M_i	=	molecular weight of component i (kg)
x_i	=	mole fraction of the component i (unitless)
k_i	=	thermal conductivity of the component i (W/m•K).

Table 13-3. Uncertainty of the gas thermal conductivity correlations.

Gas	Uncertainty (W/m K)
He	$8.00 \times 10^{-7}\ T^{1.5}$
Ar	$4.96 \times 10^{-10}\ T^{2.25}$
Kr	$1.45 \times 10^{-9}\ T^{2}$
Xe	$2.77 \times 10^{-8}\ T^{1.5}$
H_2	$2.10 \times 10^{-6}\ T^{1.5}$
N_2	$2.64 \times 10^{-6}\ T$
0_2	$2.34 \times 10^{-9}\ T^{2}$
CO	for T between 300 and 400 K, 0.02 K;
	for T > 400 K, 0.002 + 4/3 (T - 400) x 10^{-4} K
CO_2	$8.78 \times 10^{-12}\ T^{3}$
H_2	O0.06 K

The conduction part of the gas gap heat conductance is calculated with the equation

$$h = \sum_{i=1}^{n} \left(\frac{k_i x_i}{x_i + \sum_{j=i\neq 1}^{n} \psi_{ij} x_j} \right) \left(\frac{1}{t + \frac{\sqrt{M_i T}}{18} \left(\frac{\gamma_i - 1}{\gamma_i + 1} \right) \left(\frac{1}{a_i p} \right) \left(\frac{k_i}{x + \sum_{j=i}^{n} \delta_{ij} \psi_{ij} x_j} \right)} \right) \tag{13-11}$$

where

h	=	conduction part of the gas gap heat conductance ($W/m^2 \bullet K$)

γ_i	=	ratio of the specific heats at constant volume and constant pressure for component i (unitless)
a_i	=	a constant (provided in Table 13-4) that describes the nature of the gas gap interfaces (unitless)
t	=	gap width (m).

Details of the development of the models used in the GTHCON subcode are presented in the following sections. Section 13.2.2 is a review of the data, and Section 13.2.3 is a discussion of the model development.

13.2.2 Gas Thermal Conductivity and Accommodation Coefficient Data

Most gas thermal conductivity data are for temperatures < 500 K. At higher temperatures of interest in reactor fuel behavior analysis, interpretation of experiment measurements (power transferred across a gas-filled gap at known temperatures) is difficult. Significant energy can be transferred by convection or radiation as well as by conduction. Also, the mean free path of the gas molecules can become nonnegligible compared to gap width for some combinations of pressure, temperature, and gap width. When this happens, experiment data measure not only the bulk gas thermal conductivity but also gap surface effects and numbers of molecules available to transfer energy across the gap.

Table 13-4. Surface accommodation coefficients.

Gas	Factor a_i of Equation (13-11)	$a_{gas\text{-}zircalloy}$	$a_{gas\text{-}fuel}$
He	0.06	0.07	10.34
Ar	0.15	0.16	0.8
Kr	0.74	0.85	0.85
Xe	0.74	0.85	0.85
H_2	0.06	0.071	0.34
N_2	0.19	0.2	0.85
O_2	0.19	0.2	0.85
CO	0.19	0.2	0.85
CO_2	0.74	0.85	0.85
H_2O	0.19	0.2	0.85

Researchers usually correct their data for the effects of long mean free paths and convection by measuring power at several differing gas pressures. Since the mean free path is inversely proportional to pressure and the effect of convection is proportional to the square of the gas density (pressure),[13.2-1] it is

usually possible to find combinations of experiment dimensions and pressures where the reciprocal conductance is independent of pressure or increasing linearly with reciprocal pressure. When the data show no pressure dependence, both mean free path and convection effects can be neglected. When the linear dependence is present, gas conductivity is found by extrapolation to infinite pressure. Groups of data with equal temperature and varying pressure are fit to an equation of the form

$$\frac{1}{h} = \frac{t}{k} + \frac{\text{constant}}{P} \ . \tag{13-12}$$

Corrections for radiation heat transfer are applied when necessary by using the Stefan-Boltzmann law. In most experiments, the radiation correction is smaller than measurement uncertainty and the correction is neglected.

Data used in the development of the correlations for pure gas thermal conductivities were taken from the references listed in Table 13-5.[13.2-1 to 13.2-12] The method of correcting for long mean free paths and temperature range investigated are listed in the comment column. With the exception of the two publications by Timrot and Umanskii,[13.2-6,13.2-11] the references reported conductivities and temperatures that could be used without further analysis. The analysis of the high temperature data of Timrot and Umanskii is discussed below.

Data reported by Timrot and Umanskii are reduced power per unit length and temperatures for a coaxial cylindrical cell. The reduced power was defined to be the power per unit length that would be obtained with a small mean free path, and it was obtained from measurements of power at several pressures. The technique was similar to the approach of extrapolation to infinite pressure.

Table 13-5. Pure gas conductivity references.

Gas	Reference	Comments
He	Kannuluik and Carman[13.2-1]	Extrapolated to infinite pressure temperatures to 580 K
	Gambhir, Gandhi, and Saxena[13.2-2]	Pressure independent conductivity temperatures to 370 K
	von Ubisch[13.2-3]	Extrapolated to infinite pressure at 300 and 790 K
	Saxena and Saxena[13.2-4]	Pressure independent conductivity temperatures to 1,300 K
	Timrot and Totskii[13.2-5]	Radiation effects correction, but long mean free path correction not discussed
	Timrot and Umanskii[13.2-6]	Analysis discussed in the text of this report (Section 13.2.2) Temperatures from 800 to 2,600 K
	Zaitseva[13.2-7]	Extrapolated to infinite pressure temperatures from 350 to 800 K
	Cheung, Bromley, and Wilke[13.2-8]	Extrapolated to infinite pressure at 370 and 590 K

Table 13-5. Pure gas conductivity references. (Continued)

Gas	Reference	Comments
	Johnston and Grilley[13.2-9]	Extrapolated to infinite pressure temperatures to 383 K
Ar	Kannuluik and Carman[13.2-1]	Extrapolated to infinite pressure temperatures from 370 to 380 K
	Gambhir, Gandi, and Saxena[13.2-2]	Pressure independent conductivity temperatures from 310 to 370 K
	von Ubisch[13.2-3]	Extrapolated to infinite pressure at 300 and 790 K
	Zaitseva[13.2-7]	Extrapolated to infinite pressure temperatures from 320 to 790 K
	Cheung, Bromley, and Wilke[13.2-8]	Extrapolated to infinite pressure at 370 and 590 K
	Schafer, as quoted by Brokaw[13.2-10]	At 1,370 K
Kr	Kannuluik and Carman[13.2-1]	Extrapolated to infinite pressure temperatures from 370 to 580 K
	Gambhir, Gandhi and Saxena[13.2-2]	Pressure independent conductivity temperatures from 310 to 370 K
	von Ubisch[13.2-3]	Extrapolated to infinite pressure at 300 and 790 K
	Zaitseva[13.2-7]	Extrapolated to infinite pressure temperatures from 310 to 800 K
Xe	Kannuluik and Carman[13.2-1]	Extrapolated to infinite pressure temperatures from 370 to 80 K
	Gambhir, Gandi, and Saxena[13.2-2]	Pressure independent conductivity temperatures from 310 to 370 K
	von Ubisch[13.2-3]	Extrapolated to infinite pressure at 300 and 790 K
	Zaitseva[13.2-7]	Extrapolated to infinite pressure temperatures from 310 to 790 K
H_2	Johnston and Grilley[13.2-9]	Extrapolated to infinite pressure temperatures to 370 K
	Geier and Schafer as quoted At 1373 K by Brokaw[13.2-10]	
	Timrot and Umanskii[13.2-11]	Analysis discussed in the text of this report (Section 13.2.2)
N_2	Cheung, Bromley, and Wilke[13.2-8]	Extrapolated to infinite pressure at 380 and 590 K

Table 13-5. Pure gas conductivity references. (Continued)

Gas	Reference	Comments
	Figure 4, Keyes[13.2-12]	Temperatures from 320 to 620 K
O_2	Cheung, Bromley, and Wilke[13.2-8]	Extrapolated to infinite pressure at 370 and 590 K
O_2	Johnson and Grilley[13.2-9]	Extrapolated to infinite pressure temperatures to 380 K
CO	Johnston and Grilley[13.2-9]	Extrapolated to infinite pressure temperatures to 380 K
CO_2	Cheung, Bromley, and Wilke[13.2-8]	Extrapolated to infinite pressure at 380 and 590 K
	Johnston and Grilley[13.2-9]	Extrapolated to infinite pressure temperatures to 380 K
	Figure 4, Keyes[13.2-12]	Temperatures from 320 to 620 K

In contrast to most authors, Timrot and Umanskii correlated values of reduced power with temperature and determined their expression for gas thermal conductivity by taking the derivation of the correlation. The appropriate expression is

$$k = \frac{\ln\left(\frac{R}{r}\right) dW(T)}{2\pi dT} \tag{13-13}$$

where

W(T)	=	equation for power per unit measured in the experiment (W/m)
R	=	outer wall radius of the cell (m)
r	=	inside wall radius of the cell (m).

The analysis by Timrot and Umanskii[13.2-6] is an excellent approach to modeling thermal conductivity with data from a single experiment, but it is inconvenient for use in conjunction with the other literature data. To use Timrot and Umanskii's data with data from other references, the reported values of reduced power and temperature have been used to find approximate point-by-point conductivities. The derivative of W with respect to temperature at temperature T_i was approximated with the expression

$$\frac{dW(T_i)}{dT} \approx \frac{1}{2}\left(\frac{W_{i+1} - W_i}{T_{i+1} - T_i} + \frac{W_i - W_{i+1}}{T_i - T_{i-1}}\right) \tag{13-14}$$

where the subscript i refers to the i-th measured value in a series of measurements listed in order of increasing temperature. Equations (13-14) and (13-15) convert the data reported by Timrot and Umanskii to thermal conductivities.

When the mean free path of the gas molecules in a gap is long compared to the gap dimensions, the transfer of energy from the hot gap surface to the gas and then to the cold gap surface during individual molecular collisions becomes more important to the heat conductance than the bulk gas thermal conductivity. The experiment data of interest in this case are surface accommodation coefficients, defined by the relation

$$a_{sg} = \frac{T_2 - T_1}{T_s - T_1} \tag{13-15}$$

where

a_{sg}	=	surface accommodation coefficient for a particular gas-surface interface (unitless)
T_s	=	surface temperature of the hot gap surface (K)
T_1	=	average temperature of the gas molecules impinging on the surface (K)
T_2	=	average temperature of the gas molecules after striking and again leaving the surface (K).

Surface accommodation coefficients tend to be large for massive gas molecules, and they are increased when an intermediate gas layer is absorbed on the surface. For example, White[13.2-13] reports accommodation coefficients of 0.09, 0.041, 0.16, and 0.20 for H_2, helium, argon, and 0_2 on clean tungsten surfaces at 90 K. For heavy polyatomic molecules, accommodation coefficients are reported to be generally in the range 0.8 to 0.9. For helium on nickel with and without absorbed gas, White reported accommodation coefficients of 0.360 and 0.071 at 273 K. For helium on glass (a ceramic), the accommodation coefficient is 0.34, a value larger than the helium metal accommodation coefficients mentioned above.

Numerous sources of low temperature data were reviewed but not used in the development of the thermal conductivity model to avoid giving undue emphasis to data that have been replaced by more relevant information. These sources of data and some theoretical discussions are included in a bibliography at the end of this report.

13.2.3 Model Development and Uncertainty Estimates

Development of analytical models for gas gap conductance will be described in several steps. Initially, the data discussed in Section 13.2.2 are used to develop models for the thermal conductivity of pure gases. Uncertainties are discussed, and analytical expressions for these uncertainties are presented. The conductivity of mixed gases is discussed next, and the conduction contribution to the conductance of narrow gaps (or gas-filled fuel regions) is modeled.

An elementary treatment of gas conductivity that considers the gas to be a collection of hard spheres leads to the conclusion that the conductivity of a single-component gas is proportional to the square root of temperature, the square root of the molecular mass, and inversely proportional to the square of the molecule's diameter. The expression that results from the elementary treatment (given in most college statistical mechanics texts and therefore not repeated here) is

$$k_{ideal} = \frac{3}{2}\frac{m^{1/2}}{\sigma}K_B^{3/2}T^{1/2} \tag{13-16}$$

where

k_{ideal}	=	thermal conductivity of an idealized gas (W/m•K)
m	=	mass of the molecules (kg)
K_B	=	Boltzmann's constant (J/K)
σ	=	area of the sphere's cross section (m^2).

For real gases where the molecules have structure and distant dependent interactions, Equation (13-16) must be replaced by an equation of the form

$$K = AT^B \tag{13-17}$$

where A and B are constants for a given gas. Data referenced in Section 13.2.2 and the least-squares method were used to find the values of A and B given in the summary.

Figures 13-1 through 13-4 illustrate the correlation predictions and the data base for the monatomic gases helium, argon, krypton, and xenon. The values of B for these four gases (0.7085, 0.7224, 0.8363, and 0.8616) increase with increasing boiling temperatures (4, 87, 120, and 166 K), an indication that the increasing departure from the idealized gas temperature dependence is due to increasing intermolecular forces. This regular trend and the fact that a single exponent serves to model the extensive helium data lends confidence to the extrapolations beyond the low temperature data available for krypton and xenon.

Dashed lines in Figures 13-1 through 13-4 are the expected standard error of the correlations. Since the data show increasing scatter with increasing temperature, the expected standard error of the thermal conductivity was determined from the standard error of a new variable defined to be the thermal conductivity divided by a power of temperature. Trial values of the power were varied until the residuals of the new variable were temperature independent. Once the appropriate power was determined, the standard error of the new variable was calculated and the expected standard error of the conductivity was obtained by multiplying the standard error of the new variable by the power of the temperature.

For the diatomic molecules, H_2, N_2, O_2, and CO, the relation between the exponent B in Equation (13-5) and boiling temperatures is no longer apparent. The conductivities of these gases cannot be expected to be related in any simple fashion because they transfer energy in complex molecular rotational and vibrational modes, in addition to translational modes. The data base, correlation predictions, and expected standard errors for these gases are shown in Figures 13-5 through 13.-8.

The analysis of the diatomic gas data followed the procedure of the monatomic gases, with the exception of the determination of the expected standard error of the CO conductivity correlation. For carbon monoxide, only four data were available; and an arbitrary uncertainty of 0.02 times the thermal conductivity (typical of low temperature measurement scatter) was assigned over the temperature range of the data. The 0.02 was replaced with a linear function of temperature for temperatures > 400 K, and the coefficients in this function were determined to predict an expected standard error of 0.10 times the predicted thermal conductivity at 1,000 K.

Figure 13-9 is a comparison of the data base and correlation predictions for the thermal conductivity of CO_2. It is possible that the large exponent of temperature in the carbon dioxide correlation is due to an extreme departure from the idealized gas approximation at the low temperatures for which data are avail-

able. The vapor pressure of solid carbon dioxide is one atmosphere at 195 K,[a] and the data extend only over a range of two to three times this temperature. If the large exponent of temperature obtained from data in the range from 300 to 600 K is due to the fact that all the data are at temperatures where significant intermolecular forces are present, the exponent can be expected to decrease at temperatures > 600 K. The temperature dependence of the uncertainty has been forced higher than the dependence indicated by the limited CO_2 data to reflect this concern. A temperature cubed dependence for the expected standard error was selected because the cube is the largest exponent of temperature that gives physically reasonable conductivities over the range of solid fuel temperatures.

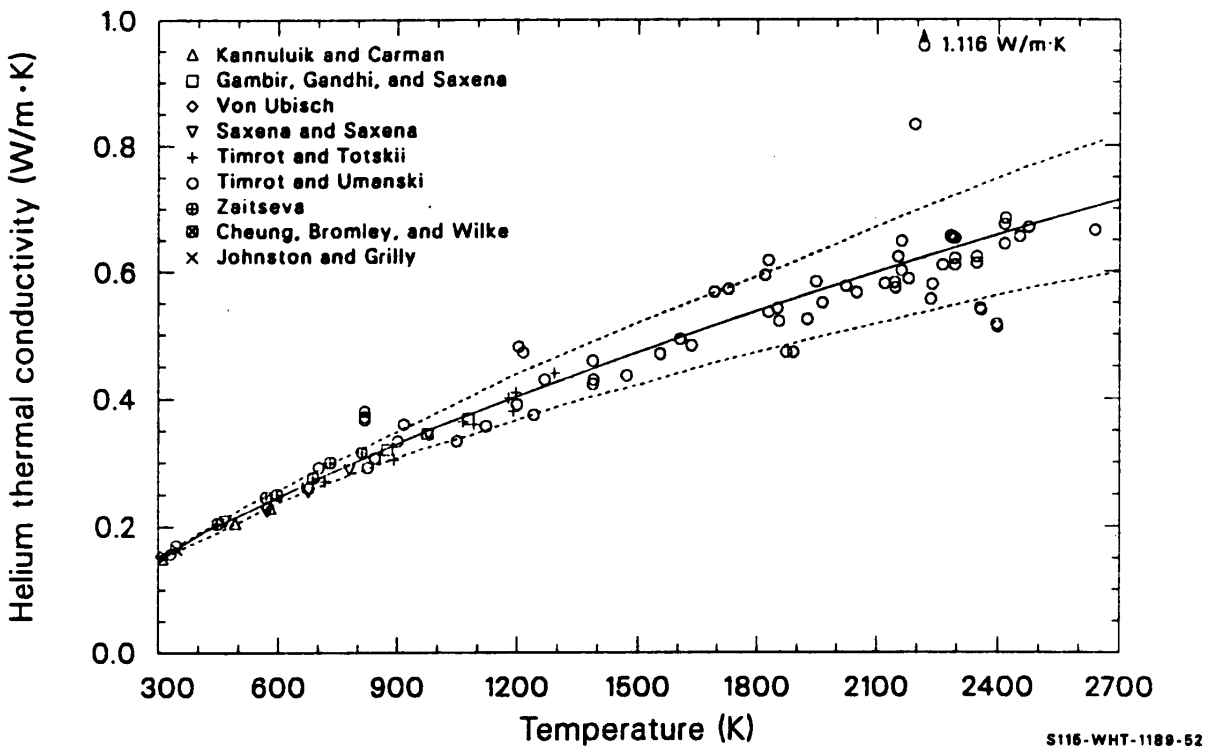

Figure 13-1. Thermal conductivity of helium as a function of temperature.

a. There is no liquid phase of CO_2 at atmospheric pressure, so the closest measure of boiling point is the one given here.

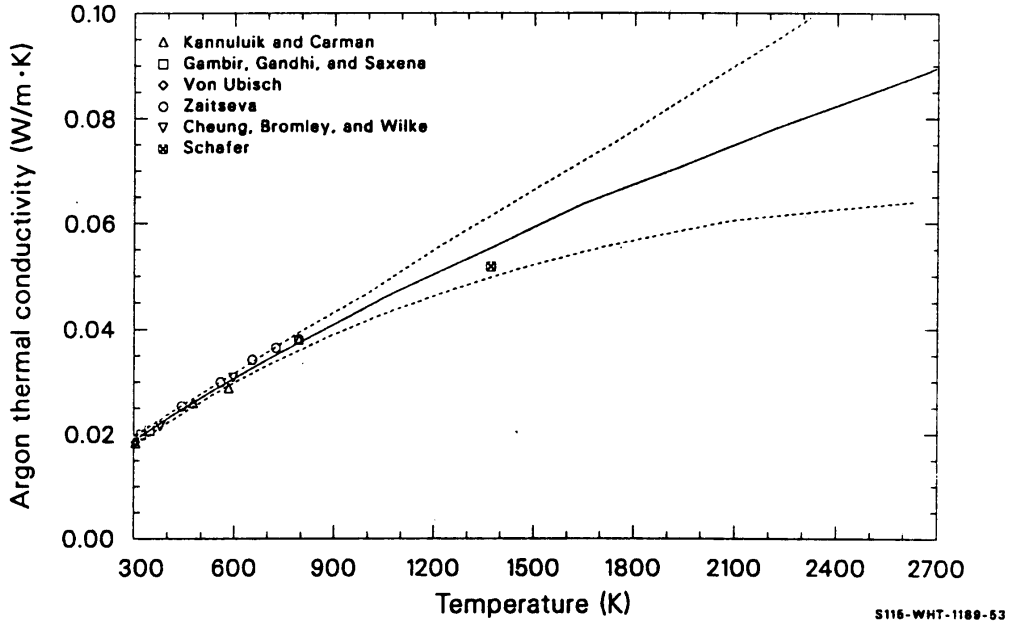

Figure 13-2. Thermal conductivity of argon as a function of temperature.

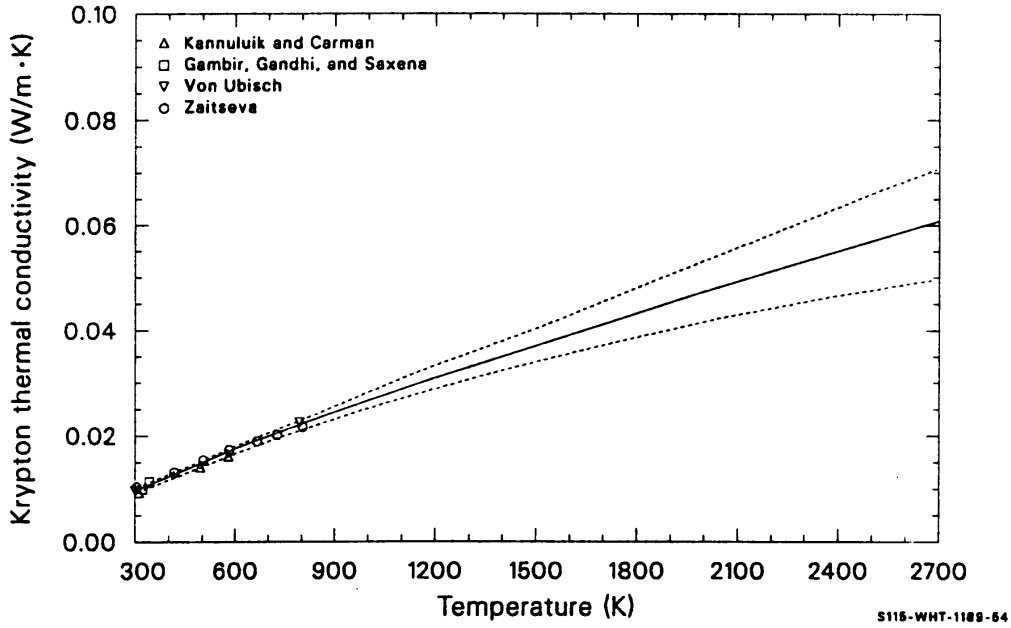

Figure 13-3. Thermal conductivity of krypton as a function of temperature

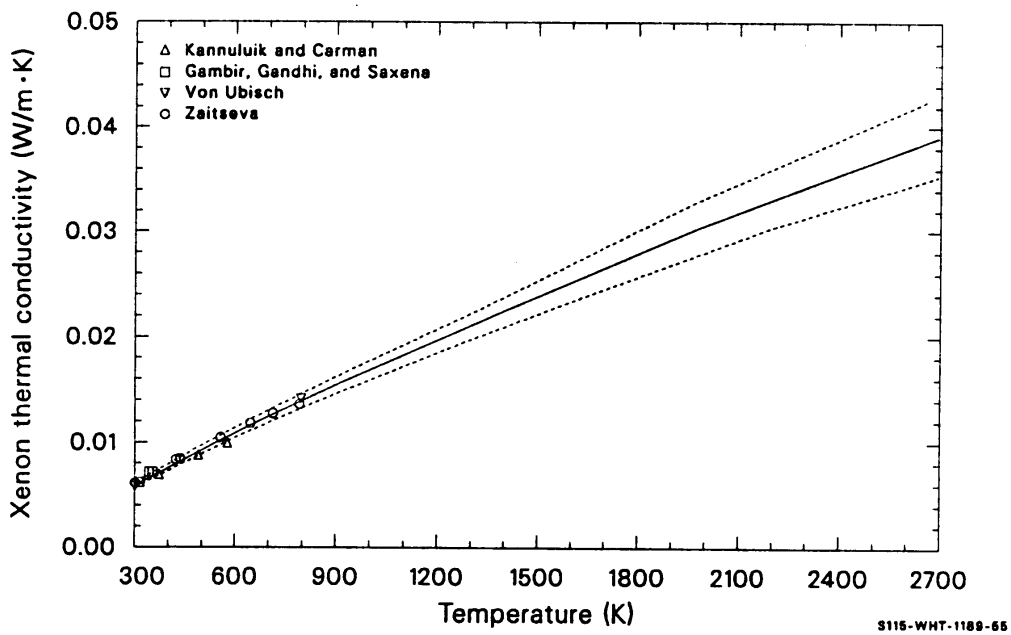

Figure 13-4. Thermal conductivity of xenon as a function of temperature.

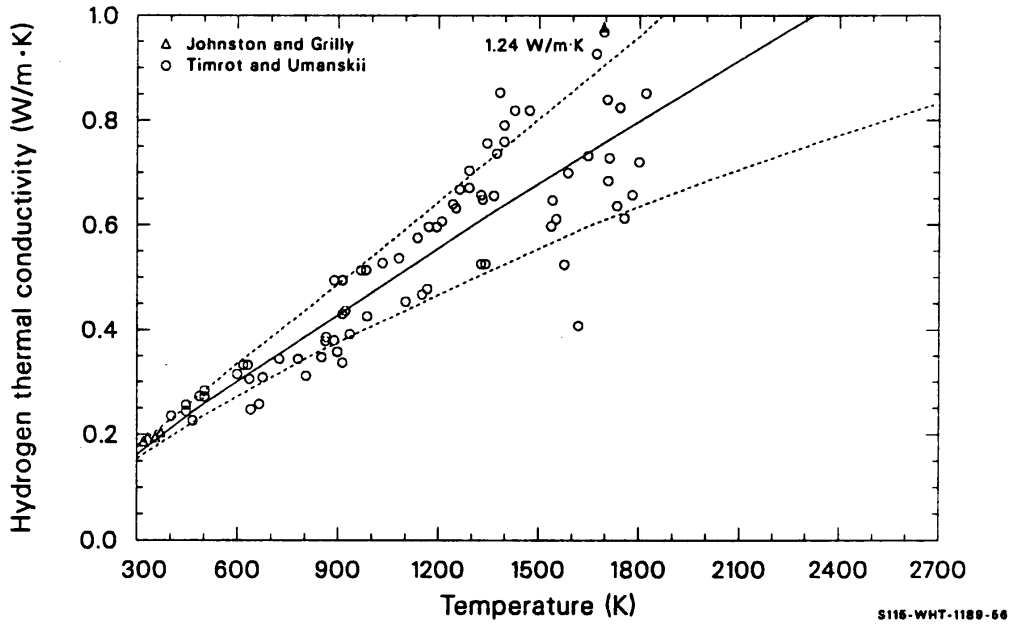

Figure 13-5. Thermal conductivity of hydrogen as a function of temperature.

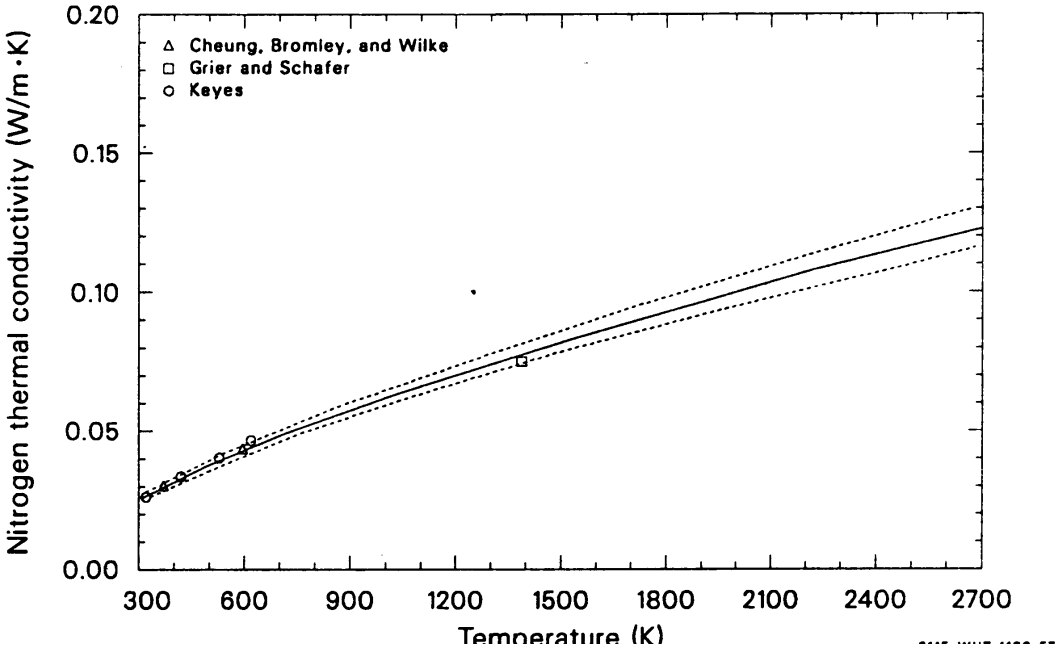

Figure 13-6. Thermal conductivity of nitrogen as a function of temperature.

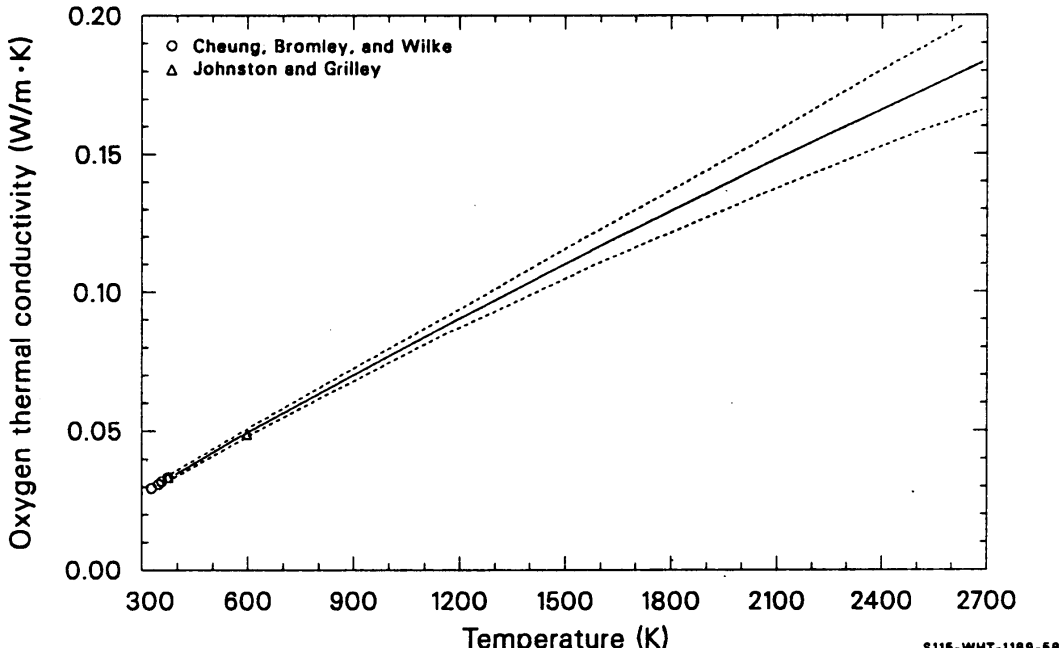

Figure 13-7. Thermal conductivity of oxygen as a function of temperature.

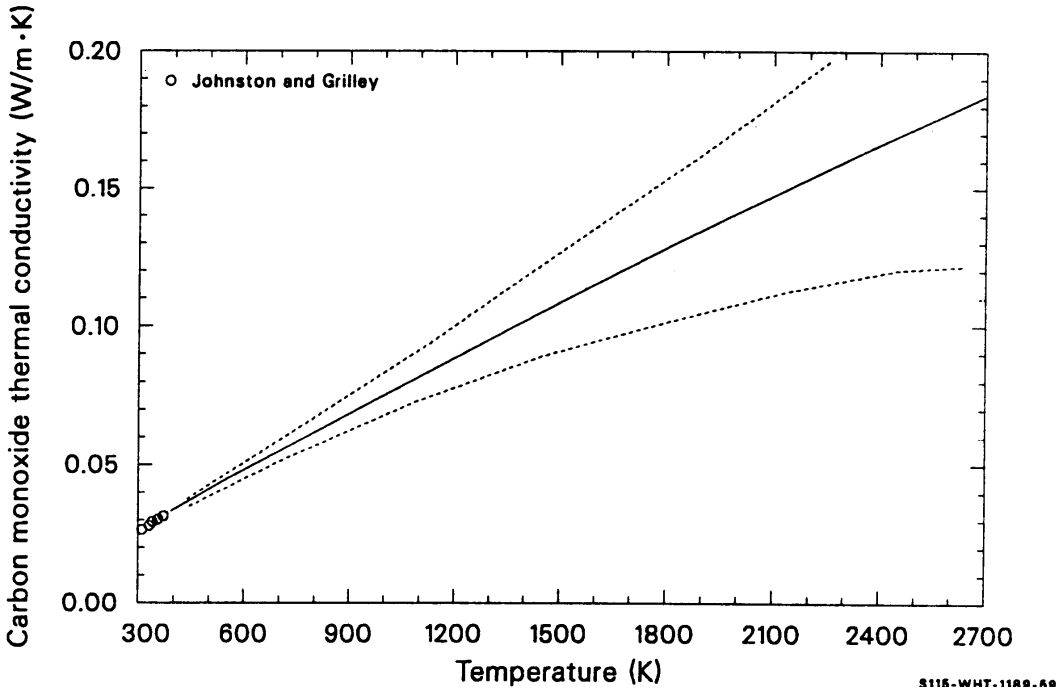

Figure 13-8. Thermal conductivity of carbon monoxide as a function of temperature.

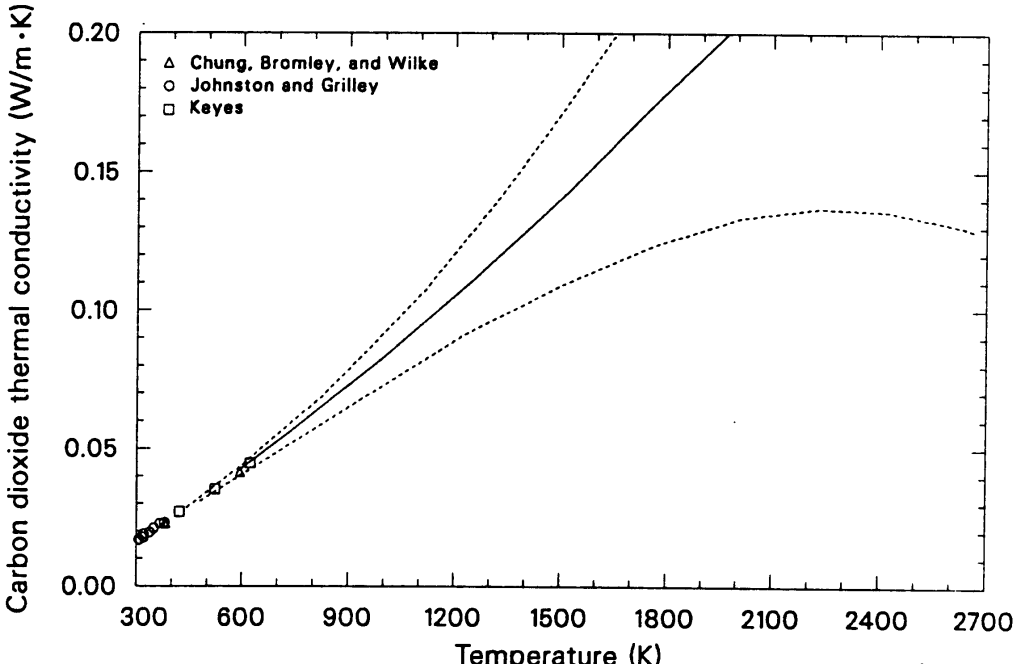

Figure 13-9. Thermal conductivity of carbon dioxide as a function of temperature.

The low temperature part of the correlation for the thermal conductivity of steam was taken from the ASME steam tables;[13.2-14] and the tolerance given in this reference, 0.06, times the conductivity, has been adopted as the expected standard deviation.

The high temperature part of the MATPRO correlation was taken from Tsederberg.[13.2-15] Tsederberg's expression was used for high temperatures because the power law he used does not become negative at high temperatures. No data were found above the 973 K limit of the ASME steam tables.

When gases are mixed, the thermal conductivity of the mixture is not simply related to the conductivities of the mixture components because the ability of each component to diffuse through the mixture is affected by the presence of all the other components. The relation between pure gas conductivities and gas mixture conductivities, Equation (13-8), is taken from the work of Brokaw.[13.2-10] Figure 13-10 is a comparison of the conductivities predicted by Equation (13-8) to data reported by Von Ubisch[13.2-3] for helium-xenon mixtures at 793 K. The measurements show excellent agreement with the conductivities predicted by Equation (13-8).

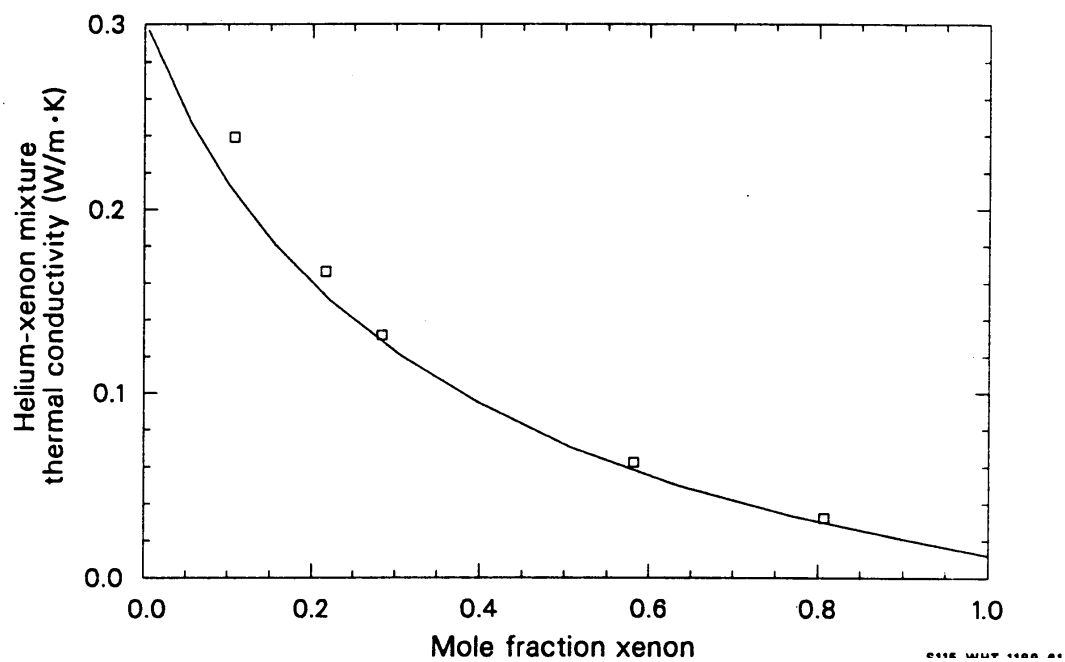

Figure 13-10. Thermal conductivity of helium xenon mixtures at 793 K.

Although less satisfactory agreement can be expected for mixtures containing diatomic molecules that transport energy in rotational and vibrational modes, Equation (13-8) is adequate for fuel rod analysis because the principal gas mixture components are monatomic.

Equation (13-11), the expression for the conduction contribution to the conductance of a gas-filled gap, is based on kinetic theory developed by Knudsen,[13.2-16] as well as the thermal conductivity correlations which have been developed. Knudsen studied low pressure gases and pointed out that molecules striking a surface do not attain thermal equilibrium with the surface in a single collision. The average speed and temperature of molecules that have just collided with a wall are somewhat less than the values

implied by the wall temperature. Knudsen derived an expression for the power per unit area transferred from a hot surface to a cold gas

$$W_S = \left(\frac{2R}{\pi M T_g}\right)^{1/2} \frac{1}{4} \left(\frac{\gamma+1}{\gamma-1}\right) P\,(T_s - T_g)\, a_{sg} \tag{13-18}$$

where

W_s	=	power per unit area transferred across the surface (W/m^2)
R	=	the gas constant (J/(K-mole)
M	=	molecular weight of the gas (kg/mole)
γ	=	ratio of the constant volume to the constant pressure specific heats of the gas (unitless)
T_g	=	temperature of the gas (K)
a_{sg}	=	surface accommodation coefficient for a particular gas surface interface.

The corresponding expression for the energy transferred from a hot gas to a cold surface is

$$W_S = \left(\frac{2R}{\pi M T_g}\right)^{1/2} \frac{1}{4} \left(\frac{\gamma+1}{\gamma-1}\right) P\,(T_s - T_g)\, \left(\frac{a_{sg}}{1-a_{sg}}\right) \tag{13-19}$$

If the mean free path of the gas molecules is long compared to the gap width, the power per unit area transferred across the gap in steady state can be found by equating the expressions for the power per unit area across the two surfaces. The resultant expression[13.2-13] is

$$W_{SS} = \left(\frac{2R}{\pi M T_g}\right)^{1/2} \frac{1}{4} \left(\frac{\gamma+1}{\gamma-1}\right) P\,(T_h - T_c)\, \left(\frac{a_{hg} a_{cg}}{a_{hg} + a_{cg} - a_{hg} a_{cg}}\right) \tag{13-20}$$

where

W_{ss}	=	power per unit area transmitted across the gap in the steady state (W/m^2)
T_h	=	temperature of the hot gap surface (K)
T_c	=	temperature of the cold gap surface (K)
a_{hg}	=	surface accommodation coefficient for the hot surface gas interface (unitless)
a_{cg}	=	surface accommodation coefficient for the cold surface gas interface (unitless).

Equation (13-20) could have been obtained less rigorously by defining a thermal impedance for each surface

$$r_S = \frac{\Delta T}{W_{SS}} \tag{13-21}$$

where

r_s = thermal impedance for surfaces S (K m^2/W)

ΔT = temperature difference between the surface and gas (K)

and adding the two series impedances that represent the surfaces to find an effective impedance for the entire gap in the limit of mean free paths that are much longer than gap width. This thermal impedance approach has been adopted to model the conductivity of a fuel rod gap when the gas mean free path is not long compared to gap width.

Single component gases are considered first. The expression for the power per unit area transferred across the gas is

$$W_B = \frac{k \Delta T_B}{t} \tag{13-22}$$

where

W_B = power per unit area transferred across a region of gas (W/m^2)

ΔT_B = temperature change across the gas (K).

The thermal impedance of the gas is

$$r_B = 1/k \tag{13-23}$$

where r_B is the thermal impedance of gas. Summation of the series thermal impedances that represent the two surfaces and the gas bulk produces the following expression for gap impedance

$$r_{eff} = \frac{t}{k} + \left(\frac{\pi M T_g}{2R}\right)^{1/2} 4 \left(\frac{\gamma - 1}{\gamma + 1}\right) + \frac{1}{aP} \tag{13-24}$$

where r_{eff} is the effective impedance of a gap containing a single component gas (m^2K/W) and $a = a_{hg} a_{cg} / (a_{hg} + a_{cg} - a_{hg} a_{cg})$. The gap conductance is the reciprocal of the effective impedance

$$h = \frac{k}{t + 4 \frac{k}{aP} \left(\frac{\gamma - 1}{\gamma + 1}\right) \left(\frac{\pi M T_g}{2R}\right)^{1/2}} \tag{13-25}$$

where h is the gap conductance for a gap containing a single component gas (W/m^2 K).

Equation (13-25) illustrates several features of gap conductance. The surface impedance term in the denominator is not important for large gaps. For gaps of a given width, the surface impedance is large at low pressures and high temperatures. Finally, the impedance term is most important for gases with large thermal conductivities.

Equation (13-11) is derived with a slight generalization of the arguments just given for a single component gas. Inspection of Equation (13-8), the expression for the thermal conductivity of gas mixtures, shows that the i-sum in the equation represents the combination of parallel impedances due to each component of the mixture. (The j-sum represents the modification of the scattering cross section seen by each

component due to the presence of all the other components.) The arguments just given for a single component gas can be repeated for impedance due to each component of the gas mixture. The resultant expression for the gap conductance due to the i-th component of the gas mixture is

$$h_i = \frac{x_i}{t + 4\frac{x_i}{a_i P_i}\left(\frac{\gamma_i - 1}{\gamma_i + 1}\right)\left(\frac{\pi M_i T_g}{2R}\right)^{1/2}} \tag{13-26}$$

where

h_i	=	gap conductance due to the i-th component of the gas mixture (W/m^2 K)
x_i	=	i-th term in Equation (13-8)
P_i	=	partial pressure of i-th component of mixture
a_i	=	value of factor a of Equation (13-23) for each gas component and the two gap surfaces (unitless)
γ_i	=	ratio of constant volume to constant pressure specific heats for component i.

The partial pressure of the i-th gas component is given in terms of the mole fraction of the component and the total pressure by the idealized gas law. The relation is

$$P_i = PX_i \ . \tag{13-27}$$

Equation (13-11) is obtained by substituting Equation (13-26) into Equation (13-25) and combining the parallel gap conductances due to each component of the mixture.

Values of V_i and M_i are contained in the GTHCON subroutine. The specific heat ratios were taken from Zemansky,[13.2-17] and the molecular weights were taken from the *Handbook of Chemistry and Physics.*[13.2-18]

The surface accommodation coefficients required to use Equation (13-11) were estimated from data and trends mentioned in Section 13.2.2. The coefficients and values of a_i that result are listed in Table 13-4. The accommodation coefficients for helium on zircaloy and fuel were approximated with helium nickel and helium glass data. Hydrogen accommodation coefficients were assumed to be approximately the same as those of helium because of the similar masses of these molecules. The accommodation coefficient for argon on zircaloy was assumed equal to the argon-tungsten coefficient. An estimate for the argon fuel coefficient was obtained by using the ratio of argon and helium coefficients on zircaloy to multiply the helium fuel coefficient. For heavy molecules (krypton, zenon, and carbon dioxide), White's estimate of 0.85 is used for the accommodation coefficients of both fuel and zircaloy. The nitrogen-zircaloy coefficient was adopted for nitrogen, oxygen, carbon monoxide, and steam because of the similar masses of these molecules. A heavy molecule estimate of 0.85 was used for the fuel surface accommodation coefficient of the nitrogen-like group because the estimate obtained from scaling up with the zircaloy surface coefficients was greater than one.

The effective jump distance calculated by GJUMP is determined with Equations (13-8) and (13-11). The mixed gas conductivity is divided by the heat conductance for a gap with zero width and with the two surface accommodation coefficient replaced by the single surface accommodation coefficient.

13.2.4 References

13.2-1 W. G. Kannuluik and E. H. Carman, "The Thermal Conductivity of Rate Gases," *The Proceedings of the Physical Society, 65*, 1952, pp. 701-709.

13.2-2 R. S. Gambhir, J. M. Gandhi, and S. C. Saxena, "Thermal Conductivity of Rare Gases, Deuterium and Air," *Indian Journal of Pure and Applied Physics, 5*, 1967, pp. 457-463.

13.2-3 H. von Ubisch, "The Thermal Conductivities of Mixtures of Rare Gases at 29°C and at 520°C," *Arikiv foer Fysik*, 16, 7, 1959, pp. 93-100.

13.2-4 V. K. Saxena and S. C. Saxena, "Measurement of the Thermal Conductivity of Helium Using a Hot Wire Type of Thermal Diffusion Column," *British Journal of Applied Physics, 1*, 1968, pp. 1341-1351.

13.2-5 D. L. Timrot and E. E. Totskii, "Dilatometric Method for the Experimental Determination of the Thermal Conductivity of Corrosive Gases and Vapors at High Temperatures," *High Temperature, 3*, 1965, pp. 685-690.

13.2-6 D. L. Timrot and A. S. Umanskii, "Investigation of the Thermal Conductivity of Helium in the Range 400 to 2400 K," *High Temperature, 3*, 1965, pp. 345-351.

13.2-7 L. S. Zaitseva, "An Experimental Investigation of the Heat Conductivity of Monatomic Gases Over Wide Temperature Intervals," *Soviet Physics Technical Physics, 4*, 1959, pp. 444-450.

13.2-8 H. Cheung, L. A. Bromley, and C. R. Wilke, "Thermal Conductivity of Gas Mixtures," *AIChE Journal, 8*, 1962, pp. 221-228.

13.2-9 H. L. Johnston and E. R. Grilley, "Thermal Conductivities of Eight Common Gases between 97 and 380 K," *Journal of Chemical Physics, 14*, 1946, pp. 223-238.

13.2-10 R. S. Brokaw, "Predicting Transport Properties of Dilute Gases," *IREC Process Design and Development, 8*, 1969, pp. 240-253.

13.2-11 D. L. Timrot and A. S. Umanskii, "Thermal Conductivity of Hydrogen and Argon," *High Temperature, 4*, 1966, pp. 289-292.

13.2-12 F. G. Keyes, *The Heat Conductivity, Viscosity, Specific Heat and Prandtl Numbers for Thirteen Gases*, NP-4621, 1952.

13.2-13 G. K. White, *Experimental Techniques in Low Temperature Physics*, London: Oxford Press, 1959, pp. 181-183.

13.2-14 *Thermodynamic and Transport Properties of Steam*, NewYork: American Society of Mechanical Engineers, 1968.

13.2-15 N. V. Tsederberg, *Thermal Conductivity of Gases and Liquids*, Cambridge: The M.I.T. Press, 1965.

13.2-16 M. Knudsen, *Kinetic Theory of Gases*, New York: John Wiley and Sons, Inc., 1950.

13.2-17 M. W. Zemansky, *Heat and Thermodynamics*, NewYork: McGraw-Hill Book Company, Inc., 1957.

13.2-18 C. D. Hodgman, ed., *Handbook of Chemistry and Physics*, Thirty Eighth Edition, Chemical Rubber Publishing Co., 1956.

13.2.5 Bibliography

1. A. D. Andrew and C. S. Calvert, *Thermal Conductivity and Viscosity of Neon, Helium, Argon, Zenon and Their Binary Mixtures*, TID-24636, April 1966.

2. A. K. Barua, "Thermal Conductivity of Eucken Type Factor for the Binary Mixtures H-He, H-Ne, H-Kr, and H-Ze," *Indian Journal of Physics, 34*, 4, 1960, pp. 169-183.

3. R. S. Brokaw, "Estimating Thermal Conductivities for Nonpolar Gas Mixtures Simple Empirical Method," *Indian Journal of Engineering Chemistry, 47*, 1955, pp. 2398-2400.

4. R. S. Brokaw, *Alignment Charts for Transport Properties, Viscosity, Thermal Conductivity, and Diffusion Coefficients for Nonpolar Gases and Gas Mixtures at Low Density*, Lewis Research Center, NASA-TR-R-81, 1960.

5. R. S. Brokaw, *Approximate Formulas for Viscosity and Thermal Conductivity of Gas Mixtures*, Lewis Research Center, NASA-TN-D-2502, November 1964.

6. F. R. Campbell and R. Des Haies, "The Effect of Gas Pressure on Fuel/Sheath Heat Transfer," *Transactions of the American Nuclear Society, 21*, June 1975, p. 380.

7. J. M. Davidson and J. F. Music, *Experimental Thermal Conductivities of Gases and Gaseous Mixtures at Zero Degrees Centigrade*, HW-29021, July 1953.

8. R. A. Dean, *Thermal Contact Conductance Between UO_2 and Zircaloy-2*, CVNA-127, May 1962.

9. B. G. Dickens, "Effect of Accommodation on Heat Conduction through Gases," *Proceedings of the Royal Society London, 143*, February 1934, pp. 517-540.

10. J. M. Gandhi and S. C. Saxena, "Correlated Thermal Conductivity Data of Rare Gases and Their Binary Mixtures at Ordinary Pressures," *Journal of Chemical and Engineering Data, 13*, 3, 1968.

11. W. C. Gardiner and K. L. Schafer, "Transport Phenomena in Gases and Intermolecular Forces," *Zeitschrift fur Elektrochemie, 60*, 1956, pp. 588-594.

12. R. S. Hansen, R. R. Frost, and J. A. Murphy, "The Thermal Conductivity of Hydrogen-Helium Mixtures," *Journal of Physical Chemistry, 68*, 7, 1964, pp. 2028-2029.

13. F. G. Keyes, "Thermal Conductivity of Gases," *Transactions of the American Society of Mechanical Engineers, 76*, 1954, pp. 809-816.

14. F. G. Keyes, "Thermal Conductivity of Gases," *Transactions of the American Society of Mechanical Engineers, 77*, 1955, pp. 899-906.

15. W. G. Kannuluik and L. H. Martin, "Thermal Conductivity of Gases at 0°C," *Proceedings of the Royal Society London, 144*, May 1934, pp. 496-513.

16. J. M. Lenoir and E. W. Comings, "Thermal Conductivity of Gases, Measurement at High Pressure," *Chemical Engineering Progress, 47*, 1951, pp. 223-231.

17. E. A. Mason, and S. C. Saxena, "Approximate Formular for the Thermal Conductivity of Gas Mixtures," *Physics of Fluids, 1*, 5, September-October 1958, pp . 361-369.

18. E. A. Mason and H. von Ubisch, "Thermal Conductivities of Rare Gas Mixtures," *Physics of Fluids, 3*, 3, May-June 1960, pp. 355-361.

19. F. J. Neugebauer, *Collection of Heat Transfer Properties of Gases at Moderate Pressures and Rules for Rapid Estimation of Missing Data*, General Electric Company, 62-GL-54, April 1962.

20. S. C. Saxena and J. P. Agrawal, "Thermal Conductivity of Polyatomic Gases and Relaxation Phenomena," *Journal of Chemical Physics, 35*, 1961, pp. 2107-2113.

21. K. L. Schafer and K. H. Grundler, "The Heat Transport in Quartz Power Gas Mixtures, A Method for the Determination of the Thermal Conductivity of Gases at High Temperatures," *Zeitschrift fur Elektrochemie, 63*, 4, 1959, pp. 449-453.

22. B. N. Srivastava and A. K. Barua, "Thermal Conductivity of Binary Mixtures of Diatomic and Monatomic Gases," *Journal of Chemical Physics, 32*, 1960, pp. 427-435.

23. K. L. Schafer and F. W. Reiter, "Method for the Measurement of Heat Conductivity at 1100°C," *Zeitschrift fur Elektrochemie, 61*, 1957, pp. 1230-1235.

24. B. N. Srivastava and S. C. Saxena, "Thermal Conductivity of Binary and Ternary Rare Gas Mixtures," P*roceedings of the Physics Society of London, B, 70*, 4, April 1957, pp. 369-378.

25. L. B. Thomas and R. C. Golike, "A Comparative Study of Accommodation Coefficients by the Temperature-Jump and Low Pressure Methods and Thermal Conductivities of Helium, Neon, and Carbon Dioxide," *Journal of Chemical Physics, 22*, 1954, pp. 300-305.

26. E. Thorton, "Viscosity and Thermal Conductivity of Binary Gas Mixtures: Xenon-Krypton, Xenon-Argon, Xenon-Neon, and Xenon-Helium," *Proceedings of the Physics Society London, 76*, 1960, pp. 104-112: "Viscosity and Thermal Conductivity of Binary Gas Mixtures: Krypton-Argon, Krypton-Neon, and Krypton-Helium," Ibid., 77, 1961, pp. 1166-1169.

27. E. Thorton and W. A. D. Baker, "Viscosity and Thermal Conductivity of Binary Gas Mixtures: Argon-Neon, Argon-Helium, and Neon-Helium," *Proceedings of the Physics Society London, 80*, 1962, pp. 1171-1175.

28. Y. S. Touloukian (ed.), "Thermal Conductivity," *Thermophysical Properties Research Center, Data Book, 2*, Chapter 1, Purdue University, 1966.

29. R. E. Walker, N. de Haas, A. A. Westenberg, "New Method of Measuring Gas Thermal Conductivity," *Physics of Fluids, 3*, May-June 1960, pp. 482-483.

30. S. Weber, "Experimental Researches on the Thermal Conductivity of Gases," *Annalen de Physik, 54*, 4, March 1917, pp. 325-356.

31. S. Weber, "Heat Conductivity of Gases," *Annalen de Physik, 82*, February 1927, pp. 479-503.

32. F. G. Waelbroech and P. Zucherbrodt, "Thermal Conductivities of Gases at Low Pressures, I. Monatomic Gases, Helium, and Argon," *Journal of Chemical Physics, 28*, 1958, pp. 523-524.

13.3 Effective Emissivity (GMISS)

The effective emissivity of a cylinder of gas is useful for calculating the approximate radiation heat transfer between a slug of effluent proceeding from a hot core region down a pipe with walls that cool the gas. Use of the effective emissivity allows the slug to be treated as an opaque source, thus avoiding the need to solve the detailed differential equations for energy transport in a nontransparent media.[13.3-1]

13.3.1 Model Development

The function GMISS calculates the effective emissivity of a cylindrical slug of gas, that is, an emissivity that can be applied as though the slug were opaque. This emissivity is a function of the gas temperature, pressure, and composition, as well as the diameter of the slug. The function accepts input mole fractions of helium, argon, krypton, xenon, hydrogen, nitrogen, oxygen, carbon monoxide, carbon dioxide, and water vapor; but the correlations used to calculate the emissivity assume that water vapor is the only nontransparent species present. Since nonsymmetrical molecules like CO_2 and (probably) CO also absorb infrared irradiation, the current (1989) version of the function may give incorrect results when more than trace amounts of these components are present.

The correlations used to calculate the effective emissivity are based on Figures 11-28 and 11-29 of Pitts and Sissom.[13.3-2] Several steps are employed in the calculations. First, an equivalent beam path length,

$$L = GPRESS \cdot XGMIX(10) \cdot DIA \tag{13-28}$$

where

L	=	equivalent path length (m)
GPRES	=	gas pressure (Pa)
XGMIX(10)	=	mole fraction water vapor in the gas (kg-moles H_2O/kg-moles gas)
DIA	=	diameter of effluent slug (m)

is calculated. Next, this length is used to determine coefficients for a correlation used to calculate the effective emissivity at 1.01 E+05 Pa (one atmosphere) pressure as a function of temperature. The expressions used for the coefficients are

$$a = -7.715 + \ln(L)\,[1.016 - 3.339E\text{-}02 \ln(L)] \tag{13-29}$$

$$b = -3.798E\text{-}03 + \ln(L)\,[4.652E\text{-}04 - 1.611E\text{-}05 \ln(L)]. \tag{13-30}$$

The expression used to calculate the effective emissivity at 1.01 E+05 Pa as a function of temperature and path length is

$$EMISS = \exp(a + bT) \tag{13-31}$$

where

EMISS	=	effective emissivity of a gas slug at 1.01 E+05 Pa
T	=	temperature (K).

The final step in calculating the effective emissivity is to multiply EMISS by a factor that depends on the gas pressure, the partial pressure of water, and the equivalent path length,

$$GMISS = EMISS \cdot CW \tag{13-32}$$

where

GMISS	=	effective emissivity of a gas slug
CW	=	factor which converts emissivity at 1.01 E+05 Pa to emissivity at the given pressure, GPRES.

Values of the factor CW are calculated with one of a series of second degree polynomials that are functions of the total pressure expressed in units of two atmospheres,

$$x = 9.872 \times 10^{-6} \cdot GPRESS \cdot 0.5 \tag{13-33}$$

Table 13-6 lists the coefficients c, d, and e of the polynomial

$$CW = c + dx + ex^2 \tag{13-34}$$

as a function of the equivalent path length.

13.3.2 References

13.3-1 R. B. Bird, W. E. Stewart, and E. N. Lightfoot, *Transport Phenomena*, NewYork: John Wiley and Sons, 1960.

13.3-2 D. R. Pitts and L. E. Sissom, *Schaum's Outline of Theory and Problems of Heat Transfer*, New York: McGraw-Hill Book Company, 1977.

Table 13-6. Coefficients used to calculate CW.

Equivalent Beam Length	c	d	e
≤ 1.5438 E+03	1.2 E-01	2.0766 E+00	6.333 E-01
1.5438 E+03 < L < 1.15785 E+04	2.0 E-01	1.8857 E+00	5.7143 E-01
1.15785 E+04< L < 2.3157 E+04	2.7 E-01	1.741 E+00	5.619 E-01
2.3157 E+04 < L < 5.4033 E+04	3.6 E-01	1.55738 E+00	5.5476 E-01
5.4033 E+04 < L < 2.3157 E+05	5.3 E-01	1.171 E+00	4.619 E-01
> 2.3157 E+05	6.0 E-01	1.0024 E+00	4.048 E-01

13.4 Viscosity (GVISCO)

Viscosity is important in describing the dynamic behavior of fluids. According to kinetic theory, for a gas having a net mass motion, molecules tend to lose forward momentum due to the proximity of stationary surfaces. This loss is described in terms of a viscosity, and it is pertinent to the flow of gas in a fuel cladding gap as well as through a cladding rupture. In particular, the rate at which gas flows into the ballooning section of a fuel rod is inversely proportional to the fill gas viscosity for narrow gaps, becoming less dependent on the gas viscosity as the gap widens and flow becomes turbulent.

13.4.1 Model Development

Bretsznajder,[13.4-1] Bird et al.,[13.4-2] and Hirschfelder et al.[13.4-3] have discussed in detail the functional relationships for viscosity, which in summary showed dependence on temperature, pressure, and gas composition. The formulation used in the routine GVISCO was taken from Bird et al. and is

$$\mu_{mix} = \sum_{i=1}^{n} \frac{X_i \mu_i}{\sum_{j=1}^{n} X_j \Phi_{ij}} \tag{13-35}$$

where

μ_{mix}	=	viscosity of gas mixture (kg/m s)
n	=	number of chemical species in the mixture
X_i, X_j	=	the mole fractions of species i and j
μ_i, μ_j	=	the viscosities of species i and j (kg/m s).

Φ_{ij} is a dimensionless parameter defined as

$$\Phi_{ij} = \frac{1}{\sqrt{8}}\left(1+\frac{M_i}{M_j}\right)^{-1/2}\left[1+\left(\frac{\mu_i}{\mu_j}\right)^{1/2}\left(\frac{M_j}{M_i}\right)^{1/4}\right]^2 \tag{13-36}$$

where M_i, M_j are the molecular weights of species i and j (kg/mole).

The viscosity of a pure monatomic species may be expressed as

$$\mu_i = 8.4411\times10^{-24}\left(\frac{\sqrt{MT}}{\sigma^2 k\frac{T}{\varepsilon}}\right) \tag{13-37}$$

where

μ_i	=	viscosity of specifies i (kg/m s)
M	=	molecular weight of species (kg/mole)
σ	=	the collision diameter (m)
T	=	absolute temperature (K)
ε	=	the maximum energy of attraction between a pair of molecules (J/molecule)
k	=	Boltzmann's constant = $1.38\text{x}10^{-23}$ (J/K).

Bird et al. state that Equations (13-35) through (13-37) are useful for computing viscosities of nonpolar gases and gas mixtures at low density from their tabulated values of the intermolecular force parameters σ and ε. Figure 13-11 shows the viscosities for three different cases calculated from Equation (13-35): (a) helium only, (b) an equal molar mixture of helium and zenon, and (c) an equal molar mixture of helium, argon, krypton, and zenon. The routine GVISCO currently allows 10 gases to be considered: helium, argon, krypton, zenon, hydrogen, nitrogen, oxygen, carbon monoxide, carbon dioxide, and steam. Additional nonpolar gases may be readily added to GVISCO if desired.

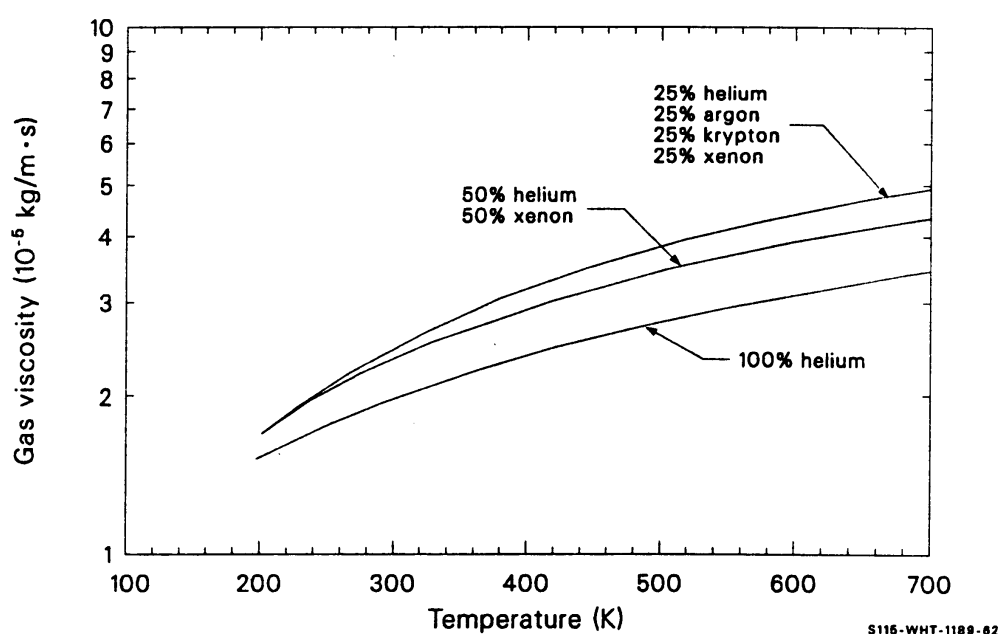

Figure 13-11. Gas viscosity as a function of temperature for pure helium, a binary mixture of helium and xenon, and for an equal molar mixture of helium, argon, krypton, and xenon.

The viscosity of steam, μ_s, is taken from Meyer et al.[13.4-4]

$$\mu_s = (0.407T - 30.8) \times 10^{-7} \tag{13-38}$$

where

μ_s	=	viscosity of steam (kg/m• s)
T	=	temperature (K).

A density correction could be applied, but examination of tabular data indicates the correction is small at typical fuel rod temperatures.

13.4.2 References

13.4-1 S. Bretsznajder, *Prediction of Transport and Other Physical Properties of Fluids*, New York: Pergamon Press, 1971.

13.4-2 R. B. Bird, W. E. Stewart, and E. N. Lightfoot, *Transport Phenomena*, New York: John Wiley and Sons, Inc., 1954.

13.4-3 J. O. Hirschfelder, C. F. Curtiss, and R. B. Bird, *Molecular Theory of Gases and Liquids*, New York: John Wiley and Sons, Inc., 1954.

13.4-4 C. A. Meyer et al., *Thermodynamic and Transport Properties of Steam*, New York: The American Society of Mechanical Engineers, 1967.

13.5 Mean Free Path (GMFP)

13.5.1 Model Development

The mean free path of gas molecules is required to calculate the rate of deposit of aerosol particles due to thermophoresis. The function GMFP calculates an approximate mean free path based on the one component ideal gas result for viscosity and the viscosity returned by the GVISCO function.[13.5-1]

$$\mu = \frac{1}{3}\rho\frac{8R\sqrt{T}}{\pi mwt}\lambda \tag{13-39}$$

where

μ	=	gas viscosity [kg/(m•s)]
ρ	=	the gas density (kg/m^3)
R	=	the gas constant, 8.31410^3 kg-m^2/(s kg-mol•K)
T	=	the gas temperature (K)
mwt	=	kg-mole weight (mass) of the gas
λ	=	mean free path of gas molecules (m).

The result is generalized to an approximate expression for mixtures by using a mole fraction weighted average of the kg-mole weight factor in the expression for the mean free path,

$$\lambda = \frac{\mu 3}{\rho} \left(\frac{\pi}{8RT}\right)^{1/2} \sum_{k=1}^{10} XGMIX(k)\ [mwt(k)]^{1/2} \tag{13-40}$$

where

XGMIX(k)= mole fraction of the k-th gas component (kg-moles k-th component/kg-moles of all components)

mwt(k) = kg-mole weight (mass) of k-th mixture component (kg/kg-mole).

13.5.2 Reference

13.5-1 R. B. Bird, W. E. Stewart, and E. N. Lightfoot, *Transport Phenomena*, New York: John Wiley and Sons, 1960, pp. 20-21.

14. VESSEL STEEL

Components of the primary coolant system, when subjected to high temperature and pressure during an accident, may fail by creep rupture prior to the failure of the reactor pressure vessel lower head. Since leakage through a ruptured primary coolant system component or a steam generator tube will reduce the system pressure, and thus affect the high pressure melt scenario, a model was developed to calculate the rupture time and creep damage term for A-508 Class 2 carbon steel, 316 stainless steel, and Inconel 600. This model uses the master creep rupture curves developed by Harris et al.[14.1-1] The subcode RUPTUR calculates the rupture time and creep damage terms for A-506 Class 2 carbon steel, 316 stainless steel, and Inconel 600. The subcode TRUPT supplies the parameters and arguments used in RUPTUR, and the subcode CALTAV calculates the average temperature during the time step.

14.1 Rupture Time and the Creep Damage Term Calculations (RUPTUR, TRUPT, CALTAV)

The subroutine RUPTUR calculates the rupture time and the creep damage term for A-508 Class 2 carbon steel, 316 stainless steel, and Inconel 600, using the master rupture curves for these materials developed by Harris et al.[14.1-1] These master rupture curves were developed using creep rupture data for the A-508 Class 2 carbon steel from creep rupture testing performed at the INEL and creep rupture data for 316 stainless steel and Inconel 600 from available literature.[14.1-2, 14.1-3] The necessary parameters and arguments used to calculate the rupture time and creep damage term are passed into RUPTUR by the TRUPT subcode. The input values needed to calculate creep rupture information are the inner and outer wall stresses (Pa), the inner and outer radii of the component(m), the average temperature during the time step (K) (calculated in the subcode CALTAV), the component material to be considered, the shape of the component, the time since the last rupture calculation, and the previous creep rupture damage term (0.0 for the first creep rupture calculation).

14.1.1 Model Description

The subcode RUPTUR calculates the rupture time and creep damage term using ksi units for stress and Rankine units for temperature. The stress value, in Pascals, input into RUPTUR is converted to ksi using the following relationship:

$$s_{ksi} = \frac{s_{si}}{6894757.2} \tag{14-1}$$

where

s_{ksi} = stress in ksi

s_{si} = stress in Pascals.

The average temperature, in Kelvin, input into RUPTUR is converted to Rankine using the following relationship:

$$T_R = 1.8T_K \tag{14-2}$$

where

T_R	=	temperature (R)
T_K	=	temperature (K).

If the temperature of the material being considered is below 900 K (1,620 R), no creep rupture calculations are performed.

For each location where a creep rupture calculation is to be performed, a creep rupture damage term is initialized to 0.0 for the first calculation (this is done in the subcode TRUPT) and the calculated damage term from RUPTUR is stored in TRUPT for use in the creep rupture calculation at the next time step. For each time step, the calculated incremental creep damage term is added to the previous term using the following equation:

$$DCREEP = DCREEP + dt/3600 \ t_r \tag{14-3}$$

where

DCREEP	=	the incremental creep damage term
dt	=	the time step
t_r	=	time in hours to rupture at the current average wall temperature and pressure.

Stress, in ksi, is calculated for cylindrical and spherical geometries in the subcode RUPTUR; whereas, if the geometry of the system is rectangular, no stress calculations are performed and the stress is set equal to 0.0. The stress calculation for a cylindrical geometry uses

$$s_{ksi} = \frac{p_i r_i - p_o r_o}{r_o - r_i} \tag{14-4}$$

and the stress calculation for a spherical geometry uses

$$s_{ksi} = \frac{p_i r_i^2 - p_o r_o^2}{r_o^2 - r_i^2} + \frac{p_i - p_o}{2} \tag{14-5}$$

where

s_{ksi}	=	stress (ksi)
p_i	=	inner pressure (ksi)
p_o	=	outer pressure (psi)
r_i	=	inside wall radius
r_o	=	outside wall radius.

The rupture time is then calculated using the average temperature, in Rankine, for each time step and the Larson-Miller parameter,[14.1-4] which is calculated using the following relationship:

$$P_{lm} = a \log(s_{ksi}) + b \tag{14-6}$$

where

P_{lm}	=	the Larson-Miller parameter
s_{ksi}	=	stress (ksi)
a,b	=	constants for each material, as shown in Table 14-1.

Using the above calculated Larson-Miller parameter, the rupture time for the required material is calculated using the Larson-Miller or Manson-Haferd equation.[14.1-5] The Larson-Miller equation is used for all materials considered in this subroutine except A-508 Class 2 carbon steel at a stress less than 14 ksi, for which a relationship developed by Manson and Haferd is used. The rupture time for those materials using the Larson-Miller equation is calculated using the following relationship:

$$t_r = 10\,(P_{lm}/T) - C \tag{14-7}$$

where

t_r	=	the rupture time
C	=	material constant value, as shown in Table 14-1
T	=	the average temperature (R).

The equation developed by Manson and Haferd used to calculate the rupture time for A-508 Class 2 carbon steel is as follows:

$$t_r = 10\,[(T - 1503.69)/P_{lm}] + C \;. \tag{14-8}$$

14.1.2 Model Development

The creep rupture data by Harris et al.[14.1-1] were used to develop the master creep rupture curves. The model used to calculate the creep rupture failure time and damage in SCDAP/RELAP5 was based upon data that came from several different sources. Since no creep rupture data for A-508 Class 2 carbon steel were available in the literature, creep rupture tests were performed at the INEL, using A-508 Class 2 carbon steel obtained from Oak Ridge National Laboratory. Data obtained from these tests are shown in Tables 14-2 and 14-3. The creep rupture data used to develop the master curves for 316 stainless steel and Inconel 600 were obtained from the literature and are shown in Tables 14-4 and 14-5, respectively.

For all materials except A-508 carbon steel with less than 14 ksi stress, the theory developed by Larson and Miller was used to determine the creep rupture failure time. For low-stress A-508 carbon steel, a relationship developed by Manson and Haferd was used to calculate the rupture time. To develop the master creep rupture curves that are the basis of this model, a least-squares fit was performed on the data. For the A-508 carbon steel, the master rupture curve, Figure 14-1, was developed using a least-squares fit of creep rupture data obtained from the INEL tests. For carbon steel, the applicability of the master rupture curve depends on the tensile strength of the material (Table 14-4). Typically, the room temperature tensile

strength of carbon steel is 551 MPa (80 ksi) to 723 MPa (105 ksi). For the INEL tests, the room temperature tensile strength was 633 MPa (92 ksi). For 316 stainless steel, the master creep rupture curve, Figure 14-2, was developed using a least-squares fit of the creep rupture data shown in Table 14-4 and a material constant value of 20; for Inconel 600, the master creep rupture curve, Figure 14-3, was developed using a least-squares fit of the data shown in Table 14-5 and a material constant value of 15.

Table 14-1. Constants used to solve creep rupture equation.

Material	Stress (ksi)	a	b	c
A-508 carbon steel	< 14	157.233	255.346	3.499
A-508 carbon steel	≥ 14	-9603.0	46454.0	20.0
316 stainless steel	< 52	-13320.0	54870.0	20.0
316 stainless steel	≥ 52	-64000.0	142000.0	20.0
Inconel 600	all	-11333.0	43333.0	15.0

Table 14-2. Creep rupture data of A-508 pressure vessel carbon steel.

Number	Temperature (K)	Stress (ksi)	Rupture Time (h)	Minimum Creep Rate Percent (h)	Time to Tertiary Creep (h)
18	900	20.41	13.7	.62	5.70
14	900	16.23	43.7	.15	12.32
5	925	16.26	9.4	1.02	3.94
15	925	14.24	23.7	.44	9.06
13	925	12.24	42.5	.25	15.03
7	950	16.21	2.449	4.56	0.92
12	950	14.26	4.6	2.66	2.09
10	950	12.17	10.1	1.10	3.77
6	975	16.23	0.440	24.15	0.19
16	975	14.23	1.117	8.99	0.51
11	975	12.22	2.664	4.87	1.23

Table 14-2. Creep rupture data of A-508 pressure vessel carbon steel. (Continued)

Number	Temperature (K)	Stress (ksi)	Rupture Time (h)	Minimum Creep Rate Percent (h)	Time to Tertiary Creep (h)
8	1,000	16.23	0.124	103.44	0.04
9	1,000	12.15	1.006	14.98	0.34
17	1,000	8.16	6.9	2.93	2.58
19	1,025	12.17	0.409	52.38	0.12
20	1,025	8.11	2.603	8.88	0.78

Table 14-3. Tensile test data of A-508 pressure vessel carbon steel.

		Proportional Limit		Yield		Ultimate		Elongation	
Specimen Number	Temp (K)	ksi	MPa	ksi	MPa	ksi	MPa	Uniform	Total
1	297	71	488	71	491	92	633	11	27
2	800	36	248	50	347	59	407	2	26
3	900	26	182	39	267	42	287	1	42
4	1,000	12	86	17	117	19	134	3	54

Table 14-4. Stainless steel creep rupture data.

	Stress (ksi) to produce rupture in			
Temperature (F)	1 h	10 h	30 h	100 h
800	64.5	64.5	64.5	64.5
850	63.3	63.3	63.5	63.3
900	62.2	62.2	62.2	62.2
950	60.0	60.0	60.0	60.0
1,000	58.5	58.5	55.0	51.7
1,050	56.0	52.9	47.5	43.4

Table 14-4. Stainless steel creep rupture data. (Continued)

	Stress (ksi) to produce rupture in			
Temperature (F)	**1 h**	**10 h**	**30 h**	**100 h**
1,100	53.5	45.1	40.0	36.4
1,150	46.5	38.4	34.0	30.5
1,200	40.0	32.7	29.0	25.6
1,250	35.0	27.8	24.3	24.1
1,300	30.0	23.7	20.8	18.0
1,350	26.0	20.0	17.5	15.0
1,400	22.5	17.1	14.8	12.4
1,450	19.5	14.6	12.6	10.5
1500	17.0	12.5	10.6	8.8

Table 14-5. Inconel 600 creep rupture data.

	Stress, psi to produce rupture in				
Temperature (F)	**10 h**	**100 h**	**1000 h**	**10,000 h**	**100,000 h**
1,000	74,000	50,000	34,000	23,000	16,000
1,200	34,000	23,000	14,500	9,400	6,000
1,400	13,000	8,400	5,600	3,600	2,400
1,600	7,500	4,800	3,000	1,900	1,200
1,800	4,400	2,800	1,800	1.150	730
2,000	2,100	1.400	920	620	420

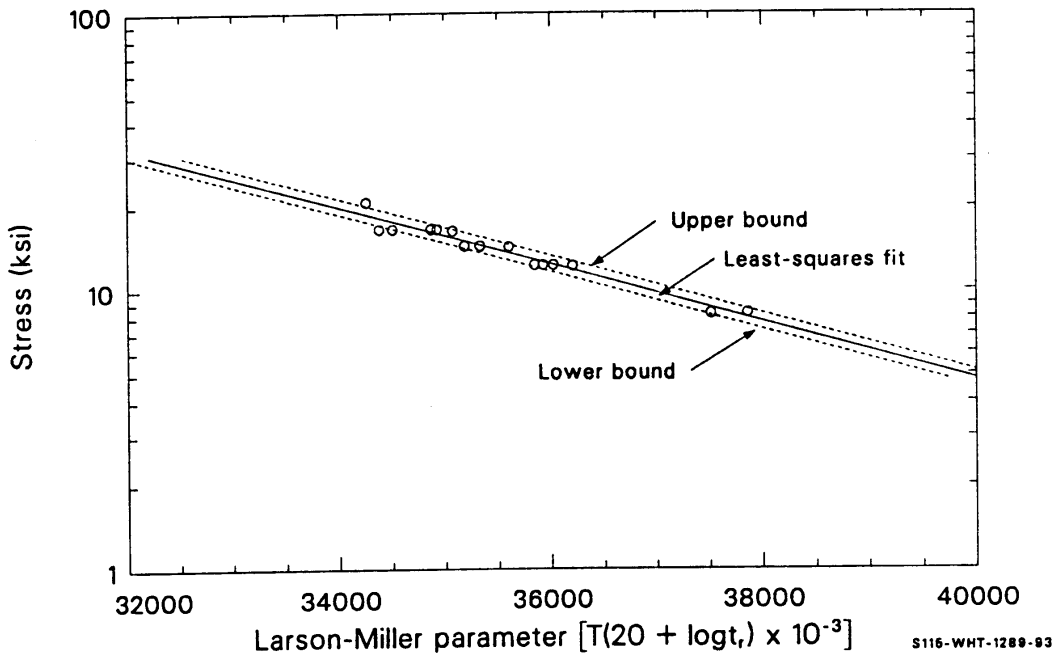

Figure 14-1. Master creep rupture curve for A-508, Class 2 carbon steel.

Creep rupture calculations are not performed if the following conditions exist in the system: the inner stress minus the outer stress is less than or equal to zero; the stress value is less than 0.01 ksi; or the value for the creep damage term is 1.0. If the incremental damage term is 1.0, then the wall has already ruptured and additional creep rupture information is not needed.

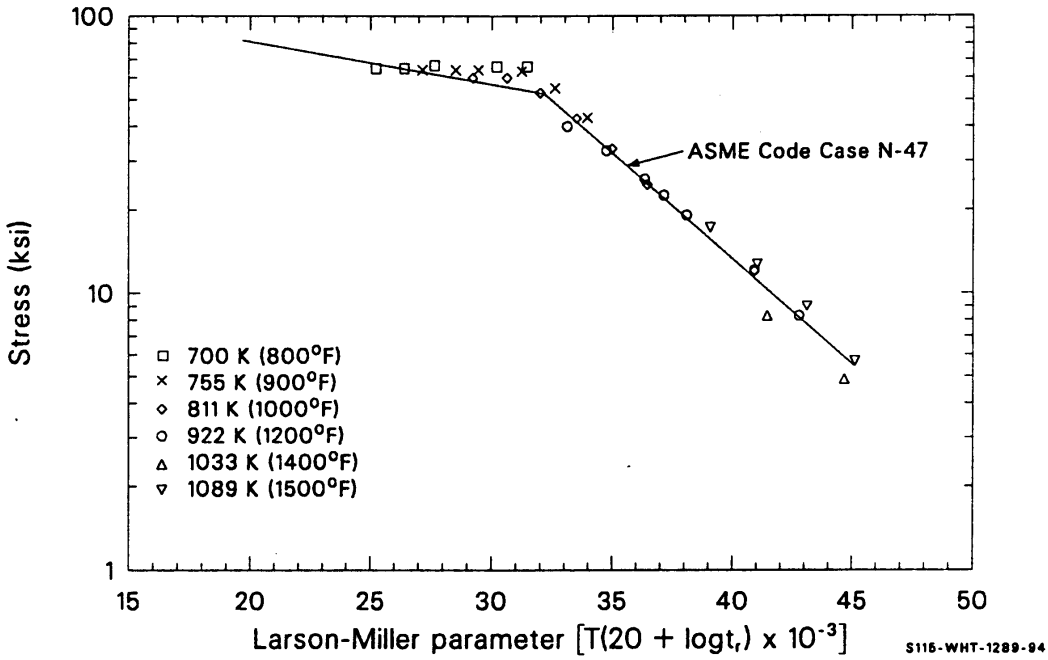

Figure 14-2. Master creep rupture curve for 316 stainless steel.

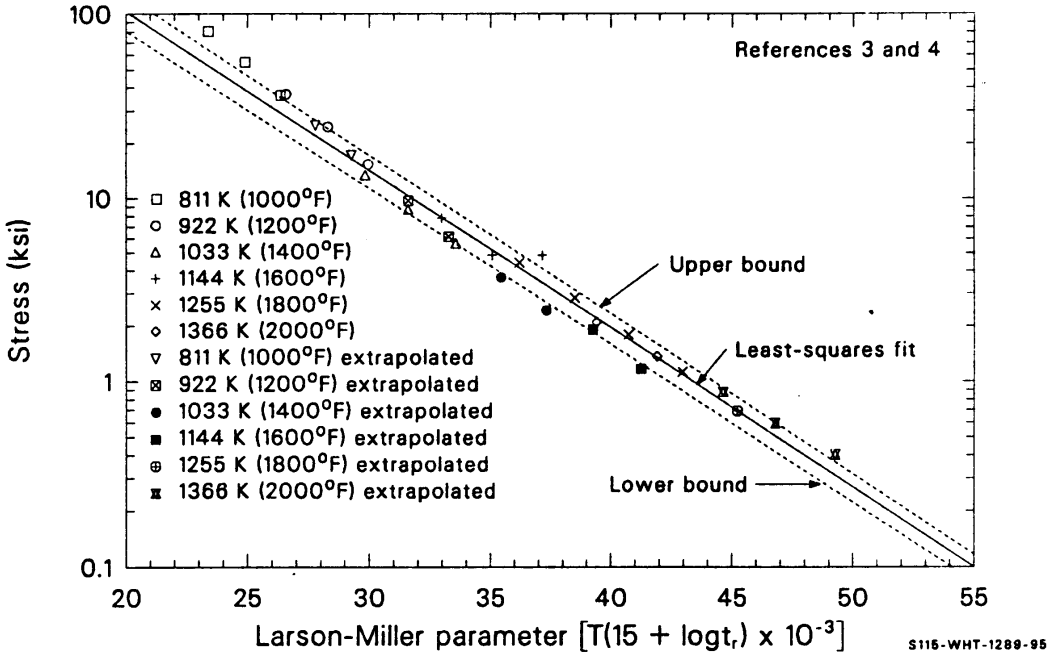

Figure 14-3. Master creep rupture curve for Inconel 600.

14.1.3 References

14.1-1 B. L. Harris, V. N. Shah, and G. E. Korth, *Creep Rupture Failure of Three Components of the Reactor Primary Coolant System During the "TMBL" Accident,* EGG-EA-7431, November 1986.

14.1-2 American Society of Mechanical Engineers, *ASME Boiler and Pressure Vessel Code Case*, N-47-22, April 5, 1984.

14.1-3 *Inconel 600 Technical Bulletin*, International Nickel Co., Inc., 5th Edition, 1978.

14.1-4 F. R. Larson and J. Miller, "A Time Temperature Relationship for Rupture and Creep Stress" *Transactions of the ASME*, July 1952, pp. 765-775.

14.1-5 S. S. Manson and A. M. Haferd, *A Linear Time Temperature Relation for Extrapolation of Creep and Stress Rupture Data*, NACA TN 2890, March 1953.

14.2 Carbon Steel

14.2.1 Enthalpy Correlations

Enthalpy is calculated by subroutine **USERP** as a function of temperature. The temperature dependent enthalpy values are shown in Table 14-6.[14.2-1] Linear interpolation is provided for temperature calls which fall between tabular values. Calls to **USERP** that are outside the table range will be returned with either the first or last table value. The reference temperature for enthalpy is 0 K.

Table 14-6. Enthalpy of carbon steel as a function of temperature.

Temperature (K)	Enthalpy (J/kg)
300	1,3500
400	18,500
600	240,000
800	300,000
1,000	365,000
1,200	435,000
1,400	515,000
1,600	615,000
1,699	657,500
1,700	687,500
1,800	723,500

Table 14-6. Enthalpy of carbon steel as a function of temperature. (Continued)

Temperature (K)	Enthalpy (J/kg)
2,000	793,500
2,200	863,500
2,400	1,003,500
2,600	1,353,500
2,800	1,703,500
3,000	2,053,500
6,000	4,153,500

14.2.2 Thermal Conductivity

Thermal conductivity is calculated by subroutine **USERP** as a function of temperature. The temperature dependent thermal conductivity values are shown in Table 14-7.[14.2-1] Linear interpolation is provided for temperature calls which fall between tabular values. Calls to **USERP** that are outside the table range will be returned with either the first or last table value.

Table 14-7. Thermal conductivity of carbon steel as a function of temperature.

Temperature (K)	Thermal Conductivity (W/m•K)
300	51.6
400	50.0
600	47.5
800	44.5
1,000	41.0
1,200	37.0
1,400	33.5
1,600	30.0
1,699	29.0
1,700	28.0
1,800	27.5
2,000	25.0

14.2.3 Density Correlations

Density is calculated by subroutine **USERP** as a function of temperature. The temperature dependent density values are shown in Table 14-8.[14.2-1] Linear interpolation is provided for temperature calls which fall between tabular values. Calls to **USERP** that are outside the table range will be returned with either the first or last table value.

Table 14-8. Density of carbon steel as a function of temperature.

Temperature (K)	Density (kg/m^3)
300	7,850
400	7,825
600	7,780
800	7,750
1,000	7,720

14.2.4 References

14.2-1 J. C. Spanner et al., *Nuclear Systems Material Handbook*, TID-26666, April 1979.

15. TUNGSTEN

15.1 Specific Heat (TUNGCP)

Specific heat is calculated by subroutine **TUNGCP** as a function of temperature. The temperature dependent specific heat[15-1] values are shown in Table 15-1. Linear interpolation is provided for temperature calls which fall between tabular values. Calls to **TUNGCP** that are outside of the table range will be returned with either the first or last table value.

Table 15-1. Specific heat of tungsten as a function of temperature.

Temperature (K)	Specific Heat (J/kg.K)
295	138.2
373	141.2
573	148.6
773	155.6
1,023	163.9
1,273	171.6
1,523	178.8
1,773	185.3
2,023	191.3
2,273	196.7
2,523	201.6
2,723	205.1
3,073	210.2

15.2 Thermal Conductivity (TUNGK)

Thermal conductivity is calculated by subroutine **TUNGK** as a function of temperature. The temperature dependent thermal conductivity[15-1] values are shown in Table 15-2. Linear interpolation is provided for temperature calls which fall between tabular values. Calls to **TUNGK** that are outside the table range will be returned with either the first or last table value.

Table 15-2. Thermal conductivity of tungsten as a function of temperature.

Temperature (K)	Thermal Conductivity (W/m•K)
573	124.7
673	122.9
773	121.2
873	119.4
1,073	161.1
1,773	114.5
1,373	111.5
1,573	108.6
2,573	96.73
2,973	93.16
3,173	91.63

15.3 Density Correlations (TUNGRO)

A constant value density[15-1] is returned by subroutine **TUNGRO**. The density value returned is 19600 (kg/m^3).

15.4 References

15-1. M. Firnhaber, K. Trambauer, S. Hagen, P. Hofmann, *Specification of the International Standard Problem ISP-31: CORA 13 Experiment on Severe Fuel Damage*, Gesellschaft für Reaktorsicherheit (GRS) mbH, August 1991.

16. UTILITIES

This section describes subcodes that are not logically part of the MATPRO library but are called often by the subcodes in the package. Subcodes described in this section are POLATE, linear interpolation; CTXTUR, texture factor calculations; QFUSON, heats of fusion; PMOLE and PMASS, mass fraction mole fraction conversions; ZUINT, the reciprocal of thermal conductivity; and ATOMFR, which calculates mass fractions of compound materials.

16.1 Linear Interpolation (POLATE, POL8)

A number of the MATPRO subcodes contain tables for a property rather than analytical expressions. POLATE and POL8 are similar subcodes used to interpolate values from tables. POLATE returns an interpolated number x(yy), using an input table consisting of up to 20 x,y pairs, whereas POL8 can handle no more than 13 x,y pairs. These interpolation subcodes are used when analytical expressions based on theory are not available or are too complex, as in the case of cladding specific heat capacity.

The POLATE or POL8 function returns the interpolated value of y(xx), using an input value of xx (the independent variable for which an interpolated dependent variable is desired), the values for the independent variable (up to 20 values for POLATE, only 13 for POL8), and the values for the dependent variable (up to 20 for POLATE, only 13 for POL8). To increase the efficiency of the POLATE or POL8 function, an estimate of the expected location of the value of the input xx in the table of numbers is also accepted. The number of the pair used in a previous interpolation is often used for this estimate.

Beginning with its initial estimated value, the index K is raised or lowered until a pair of xx_k and xx_{k+1} are found which bound xx. $Y(xx_k)$ and $Y(xx_{k+1})$ are then used to interpolate for Y(xx).

If xx is outside the range of the set of xx_k given as input, the y_k of the member of the set of xx_k closest to xx is returned by the POLATE or POL8 functions.

16.2 Cladding Texture Factors (CTXTUR)

Texture factors are required to model all structure sensitive material properties. The subroutine CTXTUR calculates the numbers needed to describe material texture for those material properties subcodes that specifically consider texture variations.[a]

16.2.1 Model Description

The input information for the subcode CTXTUR is obtained from a basal pole figure. The pole figure is a stereographic plot of the relative number of basal poles found at specified orientations. Figure 16-1 is a schematic illustration showing the relation between the basal pole intensity (concentration found from X-ray diffraction) at one orientation and the intensity on a typical pole figure. The intensity, I, at an angle h to the radial direction and u to the circumferential direction of a cladding sample, is projected from its orientation on a sphere of arbitrary diameter to the radius r and angle u in the circumferential axial plane and recorded on the plot as a number, I.

The radius r on the pole figure is related to the angle h by

a. In the MATPRO 11 package, only CELAST (Section 4.6) and CAGROW (Section 4.7) require this information.

$$\frac{r}{r_0} = \tan\left(\frac{\dot{\theta}}{2}\right) \tag{16-1}$$

where r_o is the radius of the sphere shown in Figure 16-1 and of the pole figure plot.

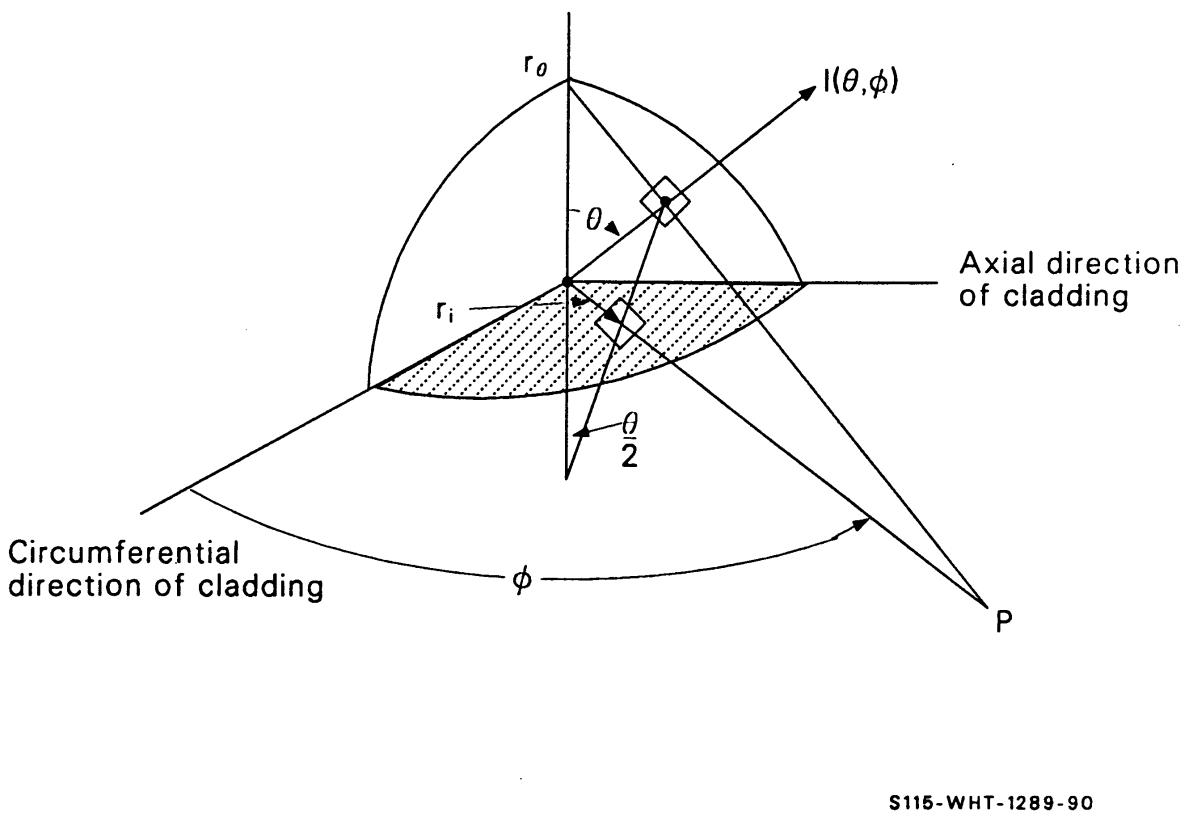

Figure 16-1. Schematic illustration showing the relation between basal pole intensity at one orientation (h,u) and the plotted value of the intensity at (r,U) on a pole figure.

The input information required by CTXTUR is a 9 X 9 array of basal pole intensities from a pole figure. If h and u are the angles defined in Figure 16-1, element (1,1) of the input array is the average intensity for h from 0 to 10 degrees and u from 0 to 10 degrees. Element (1,2) is the average intensity for h from 0 to 10 degrees and u from 10 to 20 degrees, and so on.

A typical input grid is presented in Figure 16--2. Input element (1,1) would be the average basal pole intensity in the area labeled (1,1) and so on. For the present version of this routine, the pole figure is assumed to represent material with mirror plane symmetry about the planes containing two of the three

axes so only one quadrant of the pole figure is used.

Eight volume fraction weighted averages of various cosines are returned by the CTXTUR subcode. In each case, the volume weighted average is defined by the integral

$$\langle g \rangle = \int_0^{2\pi}\int_0^{\pi} g(\theta, \phi)\, \rho(\theta, \phi) \sin(\theta)\, d\theta d\phi \tag{16-2}$$

where

g	=	any function of the angles θ and ϕ that have been previously defined
<g>	=	volume fraction weighted average of g
ρ (θ, ϕ)	=	volume fraction of grains with their c-axis oriented in the region sinθdθdϕ about θ and ϕ.

The function ρ is determined by normalizing the input average intensity values to1/4p for randomly distributed basal poles. The exact normalization equation is

$$\rho(\theta, \phi) = \frac{I(\theta, \phi)}{\int_0^{2\pi}\int_0^{\pi} I(\theta, \phi) \sin(\theta)\, d\theta d\phi} \tag{16-3}$$

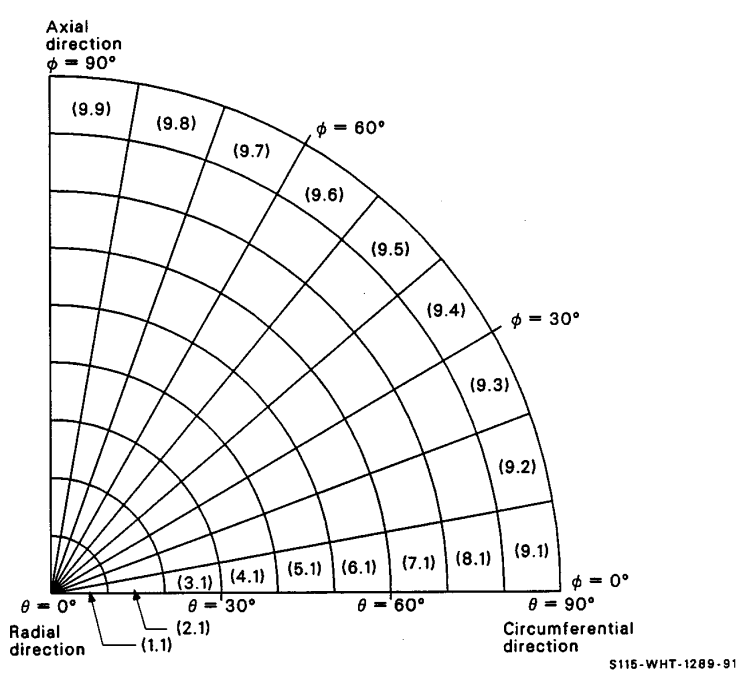

Figure 16-2. Input grid for CTXTUR subcode.

where I (θ, ϕ) is the diffracted X-ray intensity of the basal planes at (h,u), as plotted in basal pole figures.

Equation (16-3) is approximated with a sum of the average X-ray intensities, which is required input information.

$$\rho_{r,s} = \frac{\text{Input element } (r, s)}{\sum_{i=1}^{9}\sum_{j=1}^{9} \text{Input element } (i, j) \sin\theta_i \left(\frac{\pi}{18}\text{radians}\right)^2} \tag{16-4}$$

where

$\rho_{r,s}$	=	average fraction of grains with their c axis oriented in the (i,j)-th grid element
$\sin\theta_i$	=	sine of the angle θ at the center of the (i,j)-th grid element.

Once the weighting factors, $\rho_{r,s}$ have been obtained from the pole figure, the averages defined in Equation (16-2) are approximated with the sum

$$\langle g \rangle = \sum_{r=1}^{9}\sum_{s=1}^{9} \rho_{r,s} g_{r,s} \sin\theta_{r,s} \left(\frac{\pi}{18}\text{radians}\right)^2 \tag{16-5}$$

where $g_{r,s}$ is the value of g at the center of the (r,s) element.

The eight volume fraction weighted averages returned by the CTXTUR subcode are $<\cos^2\theta>$, $<\cos^4\theta>$, $<\cos^2\alpha>$, $<\cos^4\alpha>$, $<\cos^2\theta\cos^2\alpha>$, $<\cos^2\theta\cos^4\alpha>$, $<\cos^4\theta\cos^2\alpha>$, and $<\cos^4\theta\cos^4\alpha>$[a], where α is the complement of ϕ.

Several other frequently used texture factors can be obtained from the eight averages returned. For example, the cosine of the angle between the direction defined by θ and ϕ in Figure 16-3 and the circumferential direction of the cladding is

$$\cos\Psi = \sin\theta\sin\alpha \ . \tag{16-6}$$

The circumferential texture factor defined by Kearns[16.2-1] is thus

$$f_\theta = \langle\cos^2\Psi\rangle = \langle 1\rangle - \langle\cos^2\theta\rangle - \langle\cos^2\alpha\rangle + \langle\cos^2\theta\cos^2\alpha\rangle \tag{16-7}$$

where f_θ is the circumferential texture factor. Similarly, the axial texture factor of Kearns is

$$f_z = \langle\cos^2\alpha\rangle - \langle\cos^2\theta\cos^2\alpha\rangle \tag{16-8}$$

---

a. For the mirror plane symmetry assumed in this routine, some of these outputs are redundant. For instance, $<\cos^2\theta\cos^2\alpha> = <\cos^2\alpha> <\cos^2\theta>$. The extra outputs are included in case the routine needs to be generalized to consider material without mirror plane symmetry.

where f_z is the axial texture factor.

16.2.2 References

16.2-1 J. J. Kearns, *Thermal Expansion and Preferred Orientation in Zircaloy*, WAPD-TM-472, November 1965.

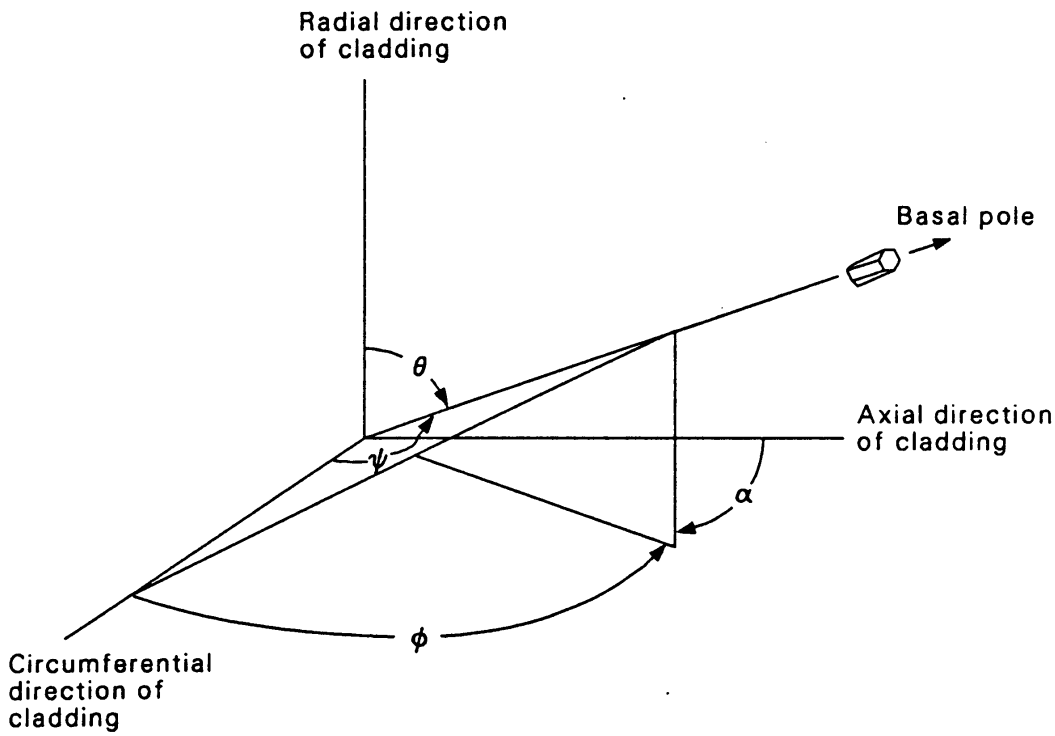

Figure 16-3. Relation between angles used in the definition of Kearn's texture factor (f_u) and angles averaged by CTXTUR subcode.

16.3 Collected Heats of Fusion (QFUSON)

QFUSON calculates the heat of fusion of uranium dioxide, zircaloy, silver-indium-cadmium or boron carbide absorber material, 304 stainless steel, Inconel 718, and zirconium-uranium-oxygen compounds. The required input data are an indicator specifying which kind of neutron absorber is to be considered and the composition of the zirconium-uranium-oxygen compound.

16.3.1 Model Development

The values of the heat of fusion used in QFUSON are given in Table 16-1. All but the last two entries of the table have been discussed in conjunction with enthalpy subcodes. For Inconel 718, the heat of fusion was estimated by multiplying the molar heats of fusion of nickel and chromium, the main compo-

nents of Inconel 718, by the atomic fraction of these elements in the alloy[a] and dividing the sum by 0.111, the weight of a gram mole of the alloy in kilograms. The elemental heats of fusion were obtained from pages 186-188 of Reference 16.3-1. For Zr-U-0 compounds, a similar mole fraction weighted average of the molar heats of fusion of $U0_2$, $Zr0_2$, and zircaloy is employed.

16.3.2 References

16.3-1 C. J. Smithells and E. A. Brandes (eds.), Metals Reference Book, London and Boston: Butterworths, 1956.

Table 16-1. Heats of fusion calculated in QFUSON.

Material	Heat of Fusion (J/kg)
Uranium dioxide	2.74×10^5
Zircaloy	2.25×10^5
Zircaloy oxide	7.06×10^5
Silver-indium-cadmium	9.56×10^4
Boron carbide	2.74×10^5
304 stainless steel	2.5×10^5
Inconel 718	3.2×10^5
Zr-U-O compound	$\dfrac{(2.74\times10^5)\,0.27f_{UO_2} + (7.06\times10^5)\,0.123f_{ZrO_2} + (2.25\times10^5)\,0.091f_{Zr}}{0.27f_{UO_2} + 0.123f_{ZrO_2} + 0.091f_{Zr}}$

16.4 Mass Fraction Mole Fraction Conversions (PMOLE, PMASS)

PMOLE is a subroutine that calculates the atomic fraction of uranium, zirconium, and oxygen in a uranium-zirconium-oxygen compound given the mass fractions of uranium and zirconium. The inverse conversion is performed by PMASS.

The expressions used to find atomic fractions from mass fractions are:

$$U = \frac{\dfrac{WU}{0.238}}{\dfrac{WU}{0.238} + \dfrac{WZ}{0.091} + \dfrac{WX}{0.016}} \tag{16-9}$$

a. A composition of 0.769 atomic fraction nickel and 0.231 atomic fraction chromium was assumed.

$$Z = \frac{\frac{WZ}{0.091}}{\frac{WU}{0.238} + \frac{WZ}{0.091} + \frac{WX}{0.016}} \tag{16-10}$$

$$X = 1 - U - Z \tag{16-11}$$

where

U	=	atomic fraction of uranium in compound (atoms uranium/atoms compound)
Z	=	atomic fraction of zirconium in compound (atoms zirconium/atoms compound)
X	=	atomic fraction of oxygen in compound (atoms oxygen/atoms compound)
WU	=	mass fraction of uranium in compound (kg uranium/kg compound)
WZ	=	mass fraction of zirconium in compound (kg zirconium/kg compound)
WX	=	mass fraction of oxygen in compound (kg oxygen/kg compound).

To find mass fractions from atomic fractions, the following expressions are used:

$$WU = \frac{0.238U}{0.238U + 0.091Z + 0.016X} \tag{16-12}$$

$$WZ = \frac{0.091Z}{0.238U + 0.091Z + 0.016X} \tag{16-13}$$

$$WX = 1 - WU - WZ\ . \tag{16-14}$$

All of these equations can be deduced by regarding the atomic weights of uranium, zirconium and oxygen (0.238 kg/g-mole, 0.091 kg/g-mole, and 0.016 kg/g-mole, respectively) as factors which convert fractions of a kilogram of compound to moles or fractions of a mole of compound to kilograms. Equations (16-11) and (16-14) are simplified forms that use the constraint that all fractions of a compound must sum to one.

16.5 Integral of the Reciprocal of Thermal Conductivity (ZUINT)

The subroutine ZUINT calculates the integral of the reciprocal of thermal conductivity (+1/K dt). Required inputs to ZUINT are the percent composition, compound temperature, and a reference temperature. ZUINT returns the integral of the reciprocal of thermal conductivity for each thermal conductivity computed in the subcode ZUTCON over a temperature range from a reference temperature $\geq$ 200 K to a compound temperature $\leq$ 3,300 K.

Calculation of

$$\int_{RFTEMP}^{ZUTEMP} \frac{1}{K} dt \tag{16-15}$$

is complicated by the fact that the thermal conductivity for each compound shows a discontinuity at phase changes. At the present time, ZUTCON simplistically assumes these phase changes occur at the phase changes of the components. To incorporate variable temperatures and the phase change discontinuities into the subroutine, the integral is divided at temperatures corresponding to these phase changes.

$$\int_{RFTEMP}^{ZUTEMP} \frac{1}{K} dt = \int_{RFTEMP}^{T} \frac{1}{K} dt + \int_{T_1}^{T_2} \frac{1}{K} dt + \ldots + \int_{T_n}^{ZUTEMP} \frac{1}{K} dt \ . \tag{16-16}$$

Integrals from T_i to T_{i+1} on the right-hand side are contained in one data statement, DTEMP, and the temperatures $T_1 \cdots T_n$ are contained in another, TEMP. The two data statements are used to evaluate all except the right and left terms on the right-hand side of Equation (16-16). The end terms, which contain no discontinuities, are evaluated with standard numerical integration techniques. This format allows any reference temperature > 200 K and any component temperature larger than the reference temperature and ≤ 3,300 K to be used. The final value for + 1/K dt is obtained by summing the contribution from each section of the curve.

16.6 Atomic Fraction (ATOMFR)

A number of MATPRO subcodes used the atomic fractions of uranium, zirconium, and oxygen to calculate the materials properties of a Zr-U-O mixture. The masses of uranium dioxide, zirconium, and oxygen due to oxidation in the mixture are input into the subcode ATOMFR; and the mass fractions of uranium and zirconium in the mixture are calculated. These mass fractions are then input into the MATPRO subcode PMOLE to calculate the atomic fractions of uranium, zirconium, and oxygen in the Zr-U-O mixture. The mass fractions of uranium and zirconium are calculated using the following relationships:

$$WTOT = WUO2 + WZR + WOX \tag{16-17}$$

where

WTOT	=	the total mass of the input materials
WUO2	=	mass of uranium dioxide
WZR	=	mass of zirconium
WOX	=	mass of oxygen due to oxidation

and

$$FU = (a \quad WUO2)/WTOT \tag{16-18}$$

where

FU	=	mass fraction of uranium
a	=	weight fraction of uranium in UO_2 = .8814814

and

FZR = WZR/WTOT

where FZR is the mass fraction of zirconium.